

10-12 may 2006
Aveiro, Portugal

SiF'06

proceedings of the
4th international
workshop
structures in fire

Paulo Vila Real
Jean-Marc Franssen
Nuno Lopes

SiF'06

proceedings of the
4th international workshop
structures in fire
volume 1

edited by
Paulo Vila Real
Jean-Marc Franssen
Nuno Lopes

ISBN 972-789-190-X



**Fourth International
Workshop
Structures in Fire**

SiF'06

Fourth International Workshop Structures in Fire

SiF'06

PROCEEDINGS OF THE FOURTH INTERNATIONAL WORKSHOP
STRUCTURES IN FIRE

University of Aveiro
Aveiro, Portugal
10-12 May, 2006

Volume 1

Paulo Vila Real
Department of Civil Engineering
University of Aveiro
Aveiro, Portugal

Jean-Marc Franssen
Department M&S
University of Liege
Liege, Belgium

Nuno Lopes
Department of Civil Engineering
University of Aveiro
Aveiro, Portugal



Department of Civil Engineering
University of Aveiro

**Proceedings of the Fourth International Workshop
Structures in Fire**

Copyright © 2006 Paulo Vila Real, Jean-Marc Franssen and Nuno Lopes

Edited by:
Paulo Vila Real
Jean-Marc Franssen
Nuno Lopes

1st Edition
May, 2006

No part of this publication may be reproduced, stored in a retrieval system, or transmitted in any form or by means, electronic, mechanical photocopying or otherwise, without permission in writing from the Publisher.

ISBN: 972-789-190-X

Published by:
UNIVERSIDADE DE AVEIRO
CAMPUS UNIVERSITÁRIO DE SANTIAGO
3810-193 AVEIRO
PORTUGAL

Editor note

Although all care was taken to ensure the integrity and quality of this publication and the information on herein, no responsibility is assumed by the publisher nor the authors for any damage to property or persons as a result of operation or use of this publication and/or use of the information contained herein.

FOREWORD

The SiF Workshops were created to form an International Forum where experts in the field of structural fire engineering could present their research activities and receive feedback from their colleagues.

The 1st SiF workshop was held in Copenhagen, Denmark in 2000, the 2nd SiF took place in Christchurch, New Zealand in 2002 and the 3rd in Ottawa, Canada in 2004, providing fire resistance researchers with the opportunity to meet, present papers, establish collaborations and discuss their work with their peers.

Following the great success of these three workshops, the University of Aveiro was selected to host the fourth International Workshop in the series SiF-Structures in Fire, which was held in Aveiro, Portugal from 10 to 12 May 2006.

The focus of the workshop was on the behaviour of structures under fire conditions. Papers were accepted on the basis of their quality and originality. Answering to the call-for-papers, 133 abstracts were received, from which 111 were selected by the Scientific Committee for possible presentation at the Workshop. These abstracts led to 91 technical papers published in these proceedings and were grouped in the following topics:

- Steel, Stainless Steel and Aluminium Structural Members
- Steel Connections
- Structural Behaviour
- Concrete Structures
- Composite Structures
- Timber Structures
- Fire Safety Engineering
- Other Topics

These proceedings include papers from 197 authors from 25 countries: Australia, Austria, Belgium, Brazil, Canada, China, Czech Republic, Egypt, Finland, France, Germany, Italy, Japan, Lithuania, Luxemburg, The Netherlands, New Zealand, Poland, Portugal, Singapore, Spain, Sweden, Switzerland, United Kingdom and United States of America.

We hope that the high quality of these contributions will develop a better understanding of the new approaches for robust design of structures under fire conditions.

Sincere thanks to the scientific committee, the workshop secretariat, the authors and the sponsoring organizations for their contribution to the success of the Workshop.

Paulo Vila Real
Chairman of the organizing committee

Jean-Marc Franssen
Chairman of the scientific committee

COMMITTEES

Organizing committee

Paulo Vila Real (Chairman)	<i>University of Aveiro, Portugal</i>
Nuno Lopes (Co-chairman)	<i>University of Aveiro, Portugal</i>
Paulo Cachim	<i>University of Aveiro, Portugal</i>
Paulo Piloto	<i>Polytechnic Institute of Bragança, Portugal</i>
João Paulo Rodrigues	<i>University of Coimbra, Portugal</i>
Joaquim Valente	<i>Technical University of Lisbon, Portugal</i>
Aldina Santiago	<i>University of Coimbra, Portugal</i>

Scientific committee

Jean-Marc Franssen (Chairman)	<i>University of Liege, Belgium</i>
Andrew Buchanan	<i>University of Canterbury, New Zealand</i>
Asif Usmani	<i>University of Edinburgh, U. K.</i>
Barbara Lane	<i>Arup Fire, U. K.</i>
Bin Zhao	<i>C. T. I. C. M., France</i>
Farid Alfawakhiri	<i>American Institute of Steel Construction, U. S. A.</i>
Guo-Qiang Li	<i>Tongji University, Shanghai, China</i>
Ildefonso Cabrita Neves	<i>Technical University of Lisbon, Portugal</i>
James Milke	<i>University of Maryland, U. S. A.</i>
Joris Fellingier	<i>Centre Information Acier, Belgium</i>
Jürgen König	<i>SP Trätek/Wood Technology, Sweden</i>
Jyri Outinen	<i>Finnish Constructional Steelwork Association, Finland</i>
Kang Hai Tan	<i>Nanyang Technological University, Singapore</i>
Kazunori Harada	<i>University of Kyoto, Japan</i>
Kuldeep Prasad	<i>N. I. S. T., U. S. A.</i>
Luís Simões da Silva	<i>University of Coimbra, Portugal</i>
Michel Njankouo	<i>University of Yaounde, Cameroun</i>
Mario Fontana	<i>E. T. H. Hönggerberg, Zürich, Switzerland</i>
Paulo Vila Real	<i>University of Aveiro, Portugal</i>
Peter Moss	<i>University of Canterbury, New Zealand</i>
Rajesh Dhakal	<i>University of Canterbury, New Zealand</i>
Richard Liew	<i>National University of Singapore, Singapore</i>
Valdir Pignatta e Silva	<i>University of São Paulo, Brazil</i>
Venkatesh Kodur	<i>National Research Council, Canada</i>

SPONSORS

FUNDAÇÃO
LUSO-AMERICANA



SUPPORTERS



TABLE OF CONTENTS

VOLUME I

FOREWORD	V
COMMITTEES	VII
SPONSORS	IX
TABLE OF CONTENTS	XI

STEEL, STAINLESS STEEL AND ALUMINIUM STRUCTURAL MEMBERS

• Time delay coefficient of temperature formulations in EC3 Part 1-2 and classification of fire protection materials Zhi-Hua WANG and Kang-Hai TAN	3
• Behavior of stainless steel sections subjected to non-homogenous temperatures Ossama M. EL-HUSSEINY, Mohamed E. EL-DIB, Ehab B. MATAR and Osama F. SALEM	13
• Experimental investigation of cold-formed steel columns subject to distortional buckling under simulated fire conditions Thanuja RANAWAKA and Mahen MAHENDRAN	29
• Analysis of restrained heated steel beams during cooling phase Guo-Qiang LI and Shi Xiong GUO	41
• Mechanical properties of thin steels at elevated temperatures Thanuja RANAWAKA and Mahen MAHENDRAN	53
• The effect of partial fire protection loss on the fire resistance reduction of steel beams Yu KANG, George V. HADJISOPHOCLEOUS and Heng AIK KHOO	63
• Heating of aluminium members exposed to natural fire conditions Johan MALJAARS, Frans SOETENS and Leen TWILT	75
• Simple thermal calculation methods for steel columns protected with steel casings and layered steel balcony slab structures Olli KAITILA and Timo KORHONEN	89
• Experimental and numerical study of a two-span steel I-Beam heated along the lower flange Kuldeep S. VIRDI and Gordon COOKE	101

<ul style="list-style-type: none"> • Studies on local buckling of heated steel columns with box sections by using finite element analyses Fuminobu OZAKI, Philipp NIEDEREGGER, Markus KNOBLOCH and Mario FONTANA 	113
<ul style="list-style-type: none"> • Proposal to the Eurocode 3 for the lateral-torsional buckling of Stainless steel I-beams in case of fire Nuno LOPES, Paulo VILA REAL, Luís SIMÕES DA SILVA, Jean-Marc FRANSSEN and Enrique MIRAMBELL 	127
<ul style="list-style-type: none"> • Light weight structures exposed to fire: a stainless steel sandwich panel Tiina ALA-OUTINEN, Peter SCHAUMANN, Olli KAITILA and Florian KETTNER 	139
<ul style="list-style-type: none"> • Numerical validation of an improved proposal to the Eurocode 3 for the lateral-torsional buckling of steel beams subjected to fire. Paulo VILA REAL, Nuno LOPES, Luís SIMÕES DA SILVA and Jean-Marc FRANSSEN 	151
<ul style="list-style-type: none"> • Testing and analysis of catenary action in unprotected steel beams subjected to fire David PROE, Ian BENNETTS and Ian THOMAS 	161
<ul style="list-style-type: none"> • A performance-based design approach for steel perimeter columns subject to fire Spencer E. QUIEL and Maria E.M. GARLOCK 	175
<ul style="list-style-type: none"> • Combined Axial Load and Moment Capacity of Fire-Exposed Beam-Columns with Thermal Gradients Maria E.M. GARLOCK and Spencer E. QUIEL 	187
<ul style="list-style-type: none"> • Investigation of simple calculation method in EN 1993-1-2 for buckling of hot rolled class 4 steel members exposed to fire C. RENAUD and B. ZHAO 	199
<ul style="list-style-type: none"> • Use of simplified methods for designing external members protection Daniel JOYEUX, Sylvain DESANGHERE, Olli KAITILA and Jose Antonio CHICA 	213
<ul style="list-style-type: none"> • Mechanical responses of a steel column exposed to a localized fire Daisuke KAMIKAWA, Yuji HASEMI, Kaori YAMADA and Masatoshi NAKAMURA 	225
<ul style="list-style-type: none"> • Fire load behavior of steel building columns with damaged spray-applied fire resistive material Stephen PESSIKI, Kihyon KWON and Byoung-Jun LEE 	235
<ul style="list-style-type: none"> • Stainless steel structures in fire Leroy GARDNER 	247
<ul style="list-style-type: none"> • Critical Behaviour of Long Span Cellular Beams in Fire Darlene RINI, Allan JOWSEY, Jose L. TORERO, Barbara LANE and Susan LAMONT 	259
<ul style="list-style-type: none"> • Behaviour in fire of thermally restrained compressed steel members. Experimental and numerical approach Manfred KORZEN, I. Cabrita NEVES, João Paulo C. RODRIGUES and Joaquim C. VALENTE 	273

- **A Novel Engineering Tool For Thermal Analysis of Structural Members in Natural Fires**
Hong LIANG and Stephen WELCH
..... 287
- **Development of a method to calculate the temperature of a column exposed to localised fire, according to the EC1 and EC3 fire parts**
Mike HALLER, Alexandra KAY and Louis-Guy CAJOT
..... 299

STEEL CONNECTIONS

- **Finite element modelling of fin plate steep connections in fire**
M. SARRAJ, I. W. BURGESS, J. B. DAVISON and R. J. PLANK
..... 315
- **Nonlinear Finite Element Modelling of Behavior of Extended End-plate Bolted Moment Connections in Fire**
Guo-Biao LOU and Guo-Qiang LI
..... 327
- **The development of a component-based connection element for endplate connections in fire**
Florian BLOCK, Ian BURGESS, Buick DAVISON and Roger PLANK
..... 345
- **Connections of unprotected steel members to fire walls**
Alexander HEISE and Peter SCHAUMANN
..... 357
- **On bolted connection with intumescent coatings**
František WALD, Michal STREJČEK and Alena TICHÁ
..... 371
- **Behaviour and design of beam-to-column connections under fire conditions**
N.H. Ramli SULONG, A.Y. ELGHAZOU LI and B.A. IZZUDDIN
..... 379

STRUCTURAL BEHAVIOUR

- **3D Modelling of bi-steel structures subject to fire**
Chaoming YU, Z. HUANG, I. W. BURGESS and R. J. PLANK
..... 393
- **Structural analysis of a heated steel portal frame by two different methods**
Gordon COOKE and Dhionis DHIMA
..... 405
- **Fire induced collapse of tall buildings**
Graeme FLINT, Asif USMANI, Susan LAMONT, Barbara LANE and José TORERO
..... 415
- **Refined plastic hinge model for the analysis of steel-framed structures under fire conditions**
Alexandre LANDESMANN and Eduardo de Miranda BATISTA
..... 427
- **Scale modelling of insulated steel framed structure testing in fire**
Ming WANG, Peter C. CHANG and James G. QUINTIERE

.....	439
• Structural fire performance of steel portal frame buildings Peter MOSS, Rajesh DHAKAL, Ming Wei BONG and Andy BUCHANAN	451
• Numerical modeling of the behaviour of a stainless steel portal frame subjected to fire Nuno LOPES, Paulo VILA REAL, Paulo PILOTO, Luís MESQUITA and Luís S. da SILVA	463
• Comparison of analytical models for fire resistance performance of steel structures Yu Guang LI, Hideki UESUGI and Takao WAKAMATSU	473
• The role of large strains and consequent mitigation measures for buildings in fire Claudio POZZI, Barbara LANE, Susan LAMONT and Alexander HEISE	487
• Fire Structure Interface and the Thermal Response of the World Trade Center Towers Kuldeep PRASAD and Anthony HAMINS	499
• Influence of concrete floor slab on stress-deformation behaviour of high-rise steel frame exposed to compartment fire Takeo HIRASHIMA, Yu Guang LI, Masaru FUJITA, Hirofumi SEGAWA, Kentaro FUJIMOTO and Hideki UESUGI	511
• Practical application of engineering methods for fire safety design of structures Jochen ZEHFUSS	519
• Tall building collapse mechanisms initiated by fire Asif USMANI, Charlotte ROBEN, Louise JOHNSTON, Graeme FLINT and Allan JOWSEY	527
• Author Index	539

VOLUME II

CONCRETE STRUCTURES

• Thermo-Mechanical behavior of concrete mixes suitable for the rehabilitation of fire-damaged tunnel liner Patrick BAMONTE, Stefano CANGIANO and Pietro G. GAMBAROVA	545
• Behaviour of reinforced concrete structures in fire Zhaohui HUANG, Ian W. BURGESS and Roger J. PLANK	561
• Factors governing the fire performance of high strength concrete systems V.K.R. KODUR and L. PHAN	573
• Fire performance of HPLWC hollow core slabs Marco BRECCOLOTTI, Annibale Luigi MATERAZZI and Ilaria VENANZI	587
• Assessment of damage in concrete structures exposed to fire. Micro and macrostructural analysis C. ALONSO	599
• Performance of carbon FRP reinforced concrete beams Muhammad Masood RAFI, Ali NADJAI, Faris ALI and Didier TALAMONA	613
• Analysis of hollowcore concrete floor slabs under fire Jeremy CHANG, Andrew H. BUCHANAN, Rajesh DHAKAL and Peter J. MOSS	623
• Modelling membrane action of model-scale slabs at ambient and elevated temperatures S. J. FOSTER, I. W. BURGESS and R. PLANK	635
• Behaviour of precast R.C. elements under fire conditions Alberto MEDA and Paolo RIVA	647
• Experimental Evaluation of Compression Resistance of HC-FST Columns After Fire Audronis Kazimieras KVEDARAS and Žygimantas BLAŽEVIČIUS	659
• Effects of thermal gradients on membrane stresses in thin slabs Anthony K. ABU, Ian W. BURGESS and Roger J. PLANK	671
• Behaviour of the UHPFRC BSI® at high temperatures J.C. MINDEGUIA, M. DHIER SAT, A. SIMON and P. PIMIENTA	683
• Experimental study of transient thermal strain and creep of an ordinary concrete at high temperatures J.C. MINDEGUIA, P. PIMIENTA, I. HAGER, C. LABORDERIE and H. CARRÉ	697

• Experimental behaviour of concrete floor slabs at ambient and elevated temperatures Colin G. BAILEY and Wee Siang TOH	709
• New NDT techniques for the assessment of fire damaged concrete structures Matteo COLOMBO and Roberto FELICETTI	721
• Transient thermal strain of Self-Compacting Concrete – with and without polypropylene fibres Bertil PERSSON	735
• Liquid/steam pressure measurement inside concrete exposed to fire Robert JANSSON	747
• Spalling of self compacting concrete Lars BOSTRÖM and Robert JANSSON	757
• Residual strength of R.C. Beams after fire Simona COCCIA and Zila RINALDI	767
• Performance of concrete in fire: a review of the state of the art, with a case study of the Windsor Tower fire Ian FLETCHER, Audun BORG, Neil HITCHEN and Stephen WELCH	779
• Performance in fire of insulated FRP-Wrapped reinforced concrete columns Ershad U. CHOWDHURY, Luke A. BISBY, Mark F. GREEN and Venkatesh K.R. KODUR	791

COMPOSITE STRUCTURES

• Generic model for a composite T-Beam at elevated temperature Mark A. BRADFORD	805
• Performance of cellular composite floor beams at elevated temperatures Ali NADJAI, Olivier VASSART, Faris ALI, Didier TALAMONA, Ahmed ALLAM and Mike HAWES	813
• Thermal and structural behaviour of orthotropic slabs in fire Xinmeng YU, Zhaohui HUANG, Ian W. BURGESS and Roger J. PLANK	825
• Fire resistance of high-strength concrete-filled steel columns Peter SCHAUMANN, Venkatesh KODUR and Oliver BAHR	837
• Numerical modelling of lateral torsional buckling for partially encased steel beams at elevated temperatures P.A.G PILOTO, L.M.R MESQUITA and Ana Ramos GAVILÁN	849
• The effect of edgebeam protection on composite structures in fire S. LAMONT, M. GILLIE and A.S. USMANI	861

- **A performance based design methodology for composite floor slabs in fire**
David LANGE, Asif USMANI, Neil CAMERON, Wolfgang WINKLER and Jose TORERO
..... 873
- **Numerical analysis of the effect of localised fires on composite steel concrete buildings**
Jean-Marc FRANSSSEN, Dan PINTEA and Jean-Claude DOTREPPE
..... 885

TIMBER STRUCTURES

- **Thermo-mechanical modelling of the timber connection behaviour under fire**
Patrick RACHER, Karine LAPLANCHE and Dhionis DHIMA
..... 899
- **Predicting the structural fire performance of solid wood-framed floor assemblies**
Noureddine BÉNICHOU
..... 909
- **In-depth temperature measurements of timber in fires**
Pedro RESZKA and Jose L.TORERO
..... 921
- **Using Commercial FEA Software Packages to Model The Fire Performance of Exposed Glulam Beams**
B.L. BADDERS, J.R. MEHAFFEY, and L.R. RICHARDSON
..... 931
- **Predicting the fire resistance of light-frame wood floor assemblies**
Steven CRAFT, George HADJISOPHOCLEOUS, Burkan ISGOR and Jim MEHAFFEY
..... 939
- **Modelling resistance of wooden I-Joists exposed to fire**
Jürgen KÖNIG and Bo KÄLLSNER
..... 951
- **Fire behaviour of timber block walls**
Andrea FRANGI and Mario FONTANA
..... 963
- **Effect on the charring rate of wood in fire due to oxygen content, moisture content and wood density**
Magdalena CEDERING
..... 975
- **Simulation of cross laminated timber boards under Fire Exposure**
J. SCHMIDT, J. KÖNIG, J. FORNATHER and K. BERGMEISTER
..... 983

FIRE SAFETY ENGINEERING

- **Segmentation of analysis/design levels for structural fire engineering**
Nestor IWANKIW
..... 993
- **Application of FSE to an industrial building**
Nicolas TAILLEFER, Dhionis DHIMA and Philippe FROMY
..... 1005

• Fire safety engineering analysis of a single storey framed building based on structural global behaviour J. DE LA QUINTANA, J. GRIJALVO, F. REY and J. UNANUA	1017
• A real fire in small apartment – a case study Valdir Pignatta e SILVA, Ricardo Hallal FAKURY, Francisco Carlos RODRIGUES and Fabio Domingos PANNONI	1023
• Accuracy in predicting the temperature evolution in compartment fires Antonín UHLÍŘ, Tomáš BAIERLE and František WALD	1035

OTHER TOPICS

• An Experimental Investigation of Gypsum Board Partition Assembly Performance Under Real Fire Exposures Samuel L. MANZELLO and Richard G. GANN	1047
• Experience with thermo imaging cameras on fire tests Jan PAŠEK, František WALD and Antonín UHLÍŘ	1059
• Thermal stresses in glazing systems in buildings Piotr TOFILO, Michael DELICHATSIOS, Ali NADJAI and Jean-Marc FRANSEN	1065
• Investigation of Fire Performance of Structural Members Incorporating Fiber Reinforced Plastic Composites used Scaled Experimental Enclosure Fires Vahid MOTEVALLI and Tahar EL-KORCHI	1077
• Author Index	1089

Steel, Stainless Steel and Aluminium Structural Members



TIME DELAY COEFFICIENT OF TEMPERATURE FORMULATIONS IN EC3 PART 1-2 AND CLASSIFICATION OF FIRE PROTECTION MATERIALS

Zhi-Hua WANG¹ and Kang-Hai TAN²

ABSTRACT

Heat transfer analysis for uniformly protected steel members exposed to fire conditions, in general, involves solving a 2D transient conduction equation with well-posed initial/boundary conditions. Current design code, i.e. EC3 Part 1-2, adopts a closed form solution from the SP approach which employs a simplified 1D characteristic heat transfer model. A virtual “time delay” has been incorporated in the analytical solution, where a portion (one-third) of capacitance of fire insulation material is added to the thermal resistance system. Results of a sensitivity study are presented in this paper to assess the validity of the time delay coefficient for different protection materials. The results indicate that for insulation with large heat capacitance, the time delay estimation in the SP approach yields significant discrepancy compared with exact solution. An alternative formula of emulation of the time delay coefficient is recommended, which expands the applicability of the EC 3 formulations to a much wider range of fire protection materials.

Moreover, the SP approach and hence the EC3 provisions, implicitly assumed that the boundary condition at the structure-fire interface is of the first kind (or Dirichlet, with prescribed temperature identical to the fire-gas temperature). The adoption of Dirichlet boundary conditions in the SP and EC3 methods implicitly assumes that heat loss through the surface heat transfer, namely, convection and radiation, is negligible for uniformly-insulated steel members. In general, this is not true. Dirichlet boundary conditions yield good approximations for fire protection materials with *high* thermal resistance and *low* heat storage in a transient process, e.g. intumescent paint. But for some other types of protection materials with comparable heat capacitance, such as web-infilled aerated blockwork, significant discrepancies are anticipated by using the EC3 equations.

¹ Project Officer, Nanyang Technological University, School of Civil and Environmental Engineering, Singapore, email: zhwang@ntu.edu.sg.

² Associate Professor, Nanyang Technological University, School of Civil and Environmental Engineering, Singapore, email: ckhtan@ntu.edu.sg.

Therefore, the assumptions in SP approach and EC3 of both the constant virtual time delay and the Dirichlet boundary conditions are closely associated with the heat capacitance of the insulation materials. A classification of different types of insulation materials according to their thermal behaviour is presented in this paper. As revealed by the classification, the applicability of the EC3 provisions is valid for a limited range of insulation materials. This paper will be instructive to fire engineers and designers as it clarifies the limitations of EC3 method inherited from the analytical solutions employed in the SP approach.

1. INTRODUCTION

Heat transfer analysis for insulated steel members exposed to fire, plays an important role in the fundamental understanding of structural fire behaviour. The SP approach [1] makes use of the lumped capacitance assumption for steel section and reduces the heat transfer model to one-dimensional (1D). Eigenfunction approach is adopted in the SP approach to solve the governing transient 1D diffusion equation with Dirichlet boundary condition. Besides, a simplified constant virtual time delay coefficient has been incorporated in the evaluation of the step function of the SP approach, rendering a closed form solution possible for design purpose. The coefficient for the time delay was derived based on the assumption that the heat capacitance of the insulation materials is negligibly small as compared against that of steel. The SP approach is shown to be efficient and is capable of predicting the temperature response with reasonable accuracy for steel members protected by insulation materials with small heat capacitance, such as intumescent paint [2]. The closed form formulation was therefore adopted by the current EC 3 provisions [3].

However, it is common engineering practice to use insulation materials with high capacitance, such as concrete and brick, which in turn, results in solution difficulties in the SP approach and EC 3 provisions, inherited from the two simplifications, i.e. constant time delay coefficient as well as Dirichlet boundary. Alternatively, Melinek and Thomas [4] suggested a solution scheme which makes use of Laplace transform and the more realistic Robin boundary condition with prescribed heat flux. An exact time delay coefficient was derived in [4] and confirmed by the sensitivity study conducted by Wang and Tan [5]. More detailed discussion on heat conduction in solids and relevant mathematical solution techniques with a general problem setting can be found in [6, 7].

This paper further investigates the effect of two simplifications inherited in the SP approach and therefore in the current Eurocode 3. Basically, both can be traced back to one root, namely, the assumption of negligible heat capacitance of the insulation materials. The findings will be of great importance for engineers to gain a fundamental understanding in the classification of insulation materials in fire protection design.

2. DEFINITION OF HEAT TRANSFER MODEL

Based on the lumped capacitance assumption, that is, temperature distribution within a steel section is uniform, a physical 2D heat transfer domain for an insulated steel member subjected to fire, can be reduced to a 1D characteristic model, as shown in Fig. 1.

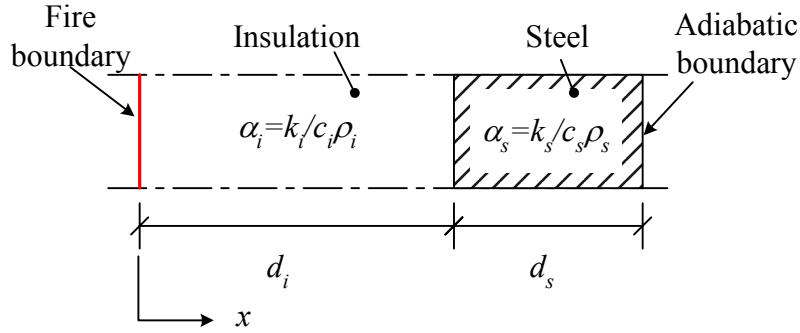


Fig. 1 – Schematics of condensed 1D heat transfer model

For simplicity in calculations, it is assumed that the thermal properties of both steel and insulation materials are isotropic and homogenous, i.e. independent of spatial coordinates and temperature. The governing 1D transient heat equation is given by:

$$k_i \frac{\partial^2 T(x,t)}{\partial x^2} - c_i \rho_i \frac{\partial T(x,t)}{\partial t} = 0 \quad (1)$$

where k_i , c_i and ρ_i are the thermal conductivity, specific heat and density of insulation, respectively, with subscript 'i' denoting the properties of insulation.

A lumped heat capacitance (per unit cross-sectional area) for steel, Q_s , is assumed at $x = d_i$:

$$Q_s = c_s \rho_s d_s = \frac{c_s \rho_s}{(A_p/V)} \quad (2)$$

where c_s , ρ_s and d_s are respectively the specific heat, density and characteristic thickness of steel section, and A_p/V is the section factor of insulated steel members, and is given in [3].

Without loss of generality, the boundary temperature at $x=0$ is normalized to zero, by simply introducing a new state variable $\theta(x,t)$, which is defined as the normalized temperature:

$$\theta(x,t) = T(x,t) - T_0 \quad (3)$$

where T_0 is the temperature prescribed at the surface $x=0$. This transformation of variable is valid because the terms presented in Eq. (1) are all in partial derivative forms. The normalized boundary conditions for derivation of the transient temperature response due to initial condition, or alternatively termed as *step functions*, are given by:

$$\theta(0,t) = 0 \quad (4)$$

$$-k_i \frac{\partial \theta(d_i,t)}{\partial x} = Q_s \frac{\partial \theta(d_i,t)}{\partial t} \quad (5)$$

Note in Eq. (4), a fixed temperature is specified at the fire-insulation interface, which implies that the surface heat transfer resistance by convection and radiation is ignored (infinite heat transfer coefficient) and a Dirichlet (type 1) boundary condition is adopted instead. The boundary condition at $x = d_i$, i.e. Eq. (5) has apparent physical meaning that when the steel layer is considered as a lumped mass, the heat flux entering this system through the insulation-steel layer balances the rate of heat storage change in the system. The initial condition for the entire domain is given by:

$$\theta(x,0) = \theta_0 \quad (6)$$

Let $\theta(x,t)/\theta_0$ denote the solution, i.e. the step function, of temperature response corresponding to the governing Eq. (1) together with the well-posed conditions in Eqs. (4) to (6). A dimensionless heat capacitance μ is defined as

$$\mu = \frac{Q_i}{Q_s} = \frac{c_i \rho_i d_i (A_p/V)}{c_s \rho_s} \quad (7)$$

In the case that the heat capacity of insulation, Q_i is negligibly small compared to Q_s , a closed form approximation was proposed in the SP approach [1], as:

$$\theta_s(t)/\theta_0 = \begin{cases} 1 & \text{for } t \leq t_d \\ \exp\left(-\frac{t-t_d}{\tau}\right) & \text{for } t > t_d \end{cases} \quad (8)$$

where $\theta_s(t) \equiv \theta(d_i, t)$ is the steel temperature response; t_d the time delay of steel temperature response due to the retardant effect by insulation. The term τ is the thermal time constant, given by:

$$\tau = R_i (Q_s + Q_i/3) = \frac{c_s \rho_s d_i}{(A_p/V) k_i} \left(1 + \frac{\mu}{3}\right) \quad (9)$$

where $R_i = d_i/k_i$ is the thermal resistance of insulation.

Bearing in mind that the fire boundary condition hitherto has not yet come into the heat transfer model, it is clear from Eq. (8) that the time delay t_d is an intrinsic parameter of the step function $\theta(x,t)/\theta_0$, i.e. the thermal response system comprising the insulation and the lumped steel section is independent of the fire condition. It should be noted in Eq. (9), one third of the insulation capacitance is added to the steel according to Wickstrom [1], which has been verified by Melinek and Thomas [4] as an expression for the long-term time constant. The steel temperature response with respect to various τ values is presented in Fig. 3. The time delay t_d is estimated by comparing the results of Eq. (8) with the exact solutions, and is computed in [1] as:

$$t_d = \frac{\mu\tau}{8} \quad (10)$$

Defining the dimensionless time delay coefficient as $t_d^* = t_d / \mu\tau$, it can be seen from Eq. (10) that the SP approach adopted a constant numerical value, 1/8 to be precise, for t_d^* .

3. TEMPERATURE FORMULATIONS

With the assumption of constant thermal properties, temperature response can be calculated for insulated steel members subjected to a time-varying boundary condition, (e.g. fire condition) using the principle of superposition (Duhamel's theorem, [6, 7]), as:

$$T_s(t) = T_0 + \int_0^t \theta_g(t-\xi) d(1 - \theta_s(\xi)/\theta_0) \quad (11)$$

where $\theta_g(t)$ is the prescribed time-varying heating curve, i.e. fire conditions. In this paper, the standard ISO 834 fire curve is assumed as the heating condition for simplicity. Discussions and results that follow can be extended to natural fire conditions by substitution with no theoretical difficulties. The standard heating curve (above initial temperature) is given by Eurocode 1 [8],

$$\theta_g(t) = 345 \log_{10}(8t + 1) \quad (12)$$

where t is time (in minute).

SBN [9] adopts an approximate expression for the standard fire curve in terms of a sum of exponential terms, as:

$$\theta_g(t) = \sum_{j=0}^3 B_j \exp(-\beta_j t) \quad (13)$$

where B_j and β_j are constants given in Table 1.

Table 1: Constants in the SBN approximation of the ISO 834 fire curve

j	0	1	2	3
$B_j (^{\circ}\text{C})$	1325	-430	-270	-625
$\beta_j (\text{h}^{-1})$	0	0.2	1.7	19

Substituting Eq. (8) and Eq. (13) into Eq. (11), the steel temperature is obtained for $t > t_d$ as:

$$T_s(t) = T_0 + \sum_{j=0}^3 \frac{B_j}{1 - \beta_j \tau} \left\{ \exp[-\beta_j(t - t_d)] - \exp[-(t - t_d)/\tau] \right\} \quad (13)$$

and for $t \leq t_d$, $T_s(t) \equiv T_0$. Eq. (13) is known as the SP approach for temperature response of insulated steel structures exposed to standard ISO 834 fire.

When temperature-dependent material properties are to be incorporated in the analysis, instead of the closed form solution given by Eq. (13), a time-stepping scheme is required to calculate the temperature increments for a given time interval. An approximate time derivative is given by Wickstrom [1] as:

$$\frac{dT_s}{dt} = \frac{T_g - T_s}{\tau} - (e^{\mu/10} - 1) \frac{dT_g}{dt} \quad (14)$$

The term involving the derivative of T_g at the right hand side of Eq. (14), is due to the retardant (sink) effect of insulation where the time delay is incorporated. Eq. (14) is adopted by EC3 in terms of finite difference form, and the increment of steel temperature ΔT_s within a time interval Δt is given by:

$$\Delta T_s = \frac{k_i A_p / V}{c_s \rho_s d_i (1 + \mu/3)} (T_g - T_s) \Delta t - (e^{\mu/10} - 1) \Delta T_g, \quad (\Delta T_s \geq 0, \text{ if } \Delta T_g > 0) \quad (15)$$

where $\Delta t \leq 30$ s for insulated steel members.

An alternative form of solution for computation of the time derivative of steel temperature response is given by the ECCS recommendations [10] as:

$$\frac{dT_s}{dt} = A'(T_g - T_s) - B' \frac{dT_g}{dt} \quad (16)$$

where .

$$A' = \frac{1}{(R_i + 1/h) Q_s (1 + \mu/N)} \quad (17)$$

$$B' = \frac{b}{1 + N/\mu} \quad (18)$$

$$h[T_g(t) - T(0, t)] = -k_i \frac{\partial T(0, t)}{\partial x} \quad (19)$$

with N and b as weighting factors, and h the combined heat transfer (first order) coefficient of surface heat transfer at the fire-insulation interface. In the SP approach, the Dirichlet boundary (with prescribed temperature) is assumed at the fire-insulation interface. As implied by Eqs. (4) and (11), the final Dirichlet boundary condition applied at $x = 0$ after incorporation of Duhamel's integral, can be written as

$$T(0, t) = T_g(t) \quad (20)$$

As compared to the Robin (type 3, with prescribed heat flux induced from ambient temperature) boundary condition in Eq. (19), the heat transfer model using the Dirichlet Eq. (20) is reduced to the limiting case with $h \rightarrow \infty$. Thus, there is no heat loss through surface heat transfer and the outer surface temperature of insulation is identical to the fire gas temperature, i.e. $T_{sur}(t) \equiv T_g(t)$. The weighting factors N and b are associated with the ratio of heat capacitance of insulation to steel, i.e. $\mu = Q_i / Q_s$. It is shown in Eq. (17) that a portion $1/N$ of the insulation capacitance is incorporated in the evaluation of time constant $1/A$ and the factor b is incorporated in the evaluation of retardant effect, B of the insulation. The weighting factors N and b have been determined by Melinek and Thomas [4] using Laplace transform. For the limiting case $h \rightarrow \infty$:

$$b = \frac{1 + \mu/4}{2(1 + 5\mu/8)} \quad (21)$$

$$N = 2(b + 1) \quad (22)$$

Values of N and b for $h \rightarrow \infty$ are listed in Table 2.

Table 2: Values of the weighting factors b and N for $h \rightarrow \infty$

μ	∞	1	0.5	0.2	0.1	0
N	2.4	2.77	2.86	2.93	2.96	3
b	0.2	0.38	0.43	0.47	0.48	0.5

Based on Eqs. (16) to (19), an analytical formulation of the time delay has been proposed by Melinek and Thomas [4], as:

$$\frac{t_d}{\tau} = \ln \frac{\alpha}{\alpha - \beta} \approx \frac{\mu}{6 + 2\mu} \quad (23)$$

where

$$\alpha, \beta = \frac{A'}{2B'} \left(1 \pm \sqrt{\frac{1 - 3B'}{1 + B'}} \right) \quad (\alpha > \beta) \quad (24)$$

The terms $1/\alpha$ and $1/\beta$ possess respectively the physical meanings as the short-term and long-term time constants in the evaluation of steel temperature response using Eq. (16), as detailed in [4]. It is noteworthy that the expression for the long-term time constant $1/\beta = R_i(Q_s + Q_i/3)$ for the limiting case $h \rightarrow \infty$, is identical to the time constant τ in Eq. (9) of the SP approach.

4. EFFECT OF LARGE INSULATION CAPACITANCE

4.1. Time delay coefficient

Wang and Tan [5] conducted a sensitivity study and investigated the effect of large heat capacitance of the insulation materials. The result of the sensitivity study is shown in Fig.

2. The scattered points in Fig. 2 represent the “optimal” time delay coefficients obtained by statistical means by comparing Eq. (8) with the exact series solutions obtained from eigenfunction approach. When μ is small, ECCS [10] recommended that the heat sink effect due to heat capacitance (the capacity for heat storage) of insulation materials can be neglected from temperature prediction. It can be shown in Fig. 2, when $\mu < 0.5$, the numerical values of t_d/τ is immaterial as the total time delay is negligible. It is also clear that the time delay coefficient in the SP approach, i.e. Eq. (10), can only predict the time delay accurately up to the range $\mu < 1.5$. On the other hand, the formulation derived by Melinek and Thomas as shown in Eq. (23) is able to estimate the time delay for a much wider range, i.e. the heat capacitance of insulation can be as high as 10 times that of the steel section ($\mu = 10$), which practically covers all the application of insulated steel members in engineering design. It is also interesting to note that in Eq. (23), the exact expression has a limit when $\mu \rightarrow \infty$, given by

$$\lim_{\mu \rightarrow \infty} \frac{t_d}{\tau} = \lim_{\mu \rightarrow \infty} \ln \frac{\alpha}{\alpha - \beta} \approx 0.31 \quad (25)$$

while the approximate expression $t_d/\tau \approx \mu/(6+2\mu)$ has a limit of 0.5 for $\mu \rightarrow \infty$. However, for practical consideration, this approximation as a handy algebraic function rather than the usage of logarithm function yields reasonably accurate results when μ does not exceed 10.

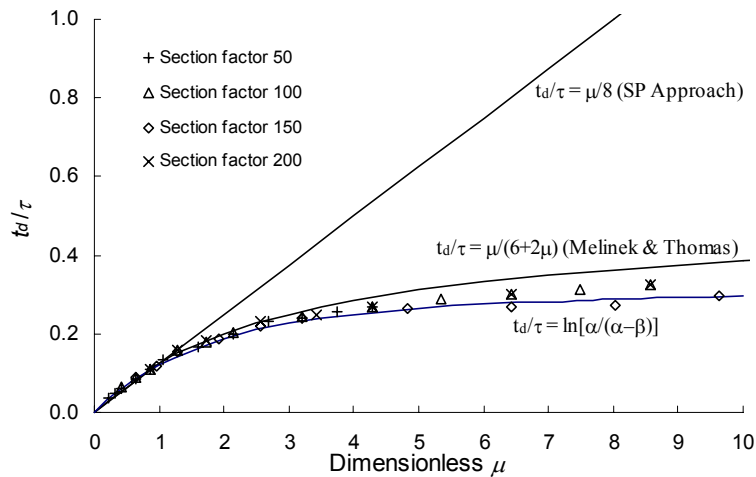


Fig. 2 – Comparison of time delay estimation by different formulas

Comparisons of steel temperature predictions using different time delay formulations are plotted in Fig. 3 against the exact solutions. It is demonstrated that the use of Eq. (23) in the case of high heat capacitance of insulation ($\mu = 3.26$) improves the accuracy of prediction significantly.

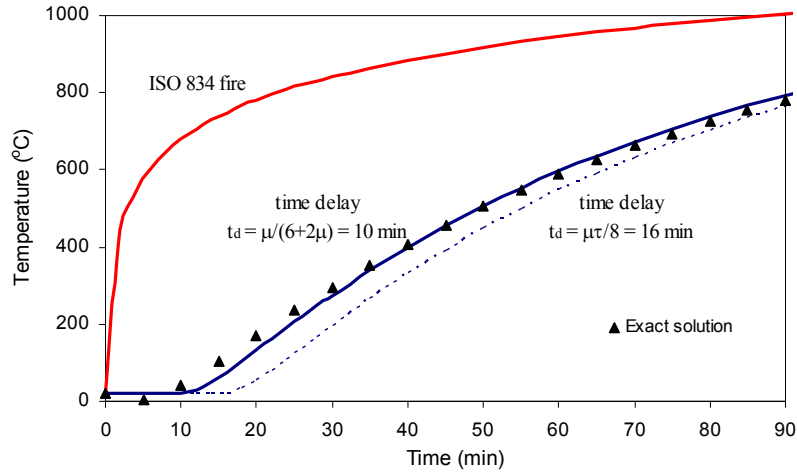


Fig. 3 – Comparison of steel temperature response predicted using different time delay against exact solutions ($\mu = 3.26$)

4.2. Boundary conditions

Investigation on the sensitivity of different types of boundary conditions, i.e. Dirichlet boundary in Eq. (15) (SP approach) or Robin boundary in Eq. (16) (ECCS approach), was conducted by Wong and Ghajel [11]. Their finding suggested that for insulation with relatively high heat capacitance or high conductivity, such as concrete, the use of Dirichlet boundary, assuming the outer surface temperature of insulation is identical to the fire gas temperature, as shown in Eq. (20), in EC 3 formulations may give rise to significant discrepancy in steel temperature predictions.

This can be argued intuitively as that: for an insulation with high conductivity or high heat capacitance, the temperature rise due to heating of the ambient fire gas can be effectively conducted through (with high k_i) or stored within (with high $\rho_i c_i$) the insulation layer. This relative ease of heat transfer through fire-insulation interface will in turn induce a non-negligible temperature difference between the temperatures of fire gas and the outer surface of insulation $T_g(t) > T(0,t)$, and eventually violate the basic assumption of Dirichlet boundary.

5. CONCLUSIONS

In this paper, investigations on two major assumptions in EC 3 formulations for temperature prediction of insulated steel members are presented, i.e. the constant time delay coefficient and Dirichlet boundary condition for approximation of fire conditions. It is shown that for insulation with low heat capacitance, the simplified EC 3 provision is capable of predicting the steel temperature response with reasonable accuracy. However, for insulation with relatively high heat capacitance (or high conductivity), both simple numerical treatments in the EC 3 formulations must be released or refined to broaden its applicability range. That is, the exact formulation of time delay coefficient using Eq. (23) instead of Eq. (10) must be adopted. Besides, a more realistic Robin boundary (Eq. (19)) instead of Eq. (20) should be incorporated in the temperature formulation to cater for non-negligible heat loss due to surface heat transfer at the fire-insulation interface.

6. REFERENCES

- [1] Wickstrom, U, "Temperature analysis of heavily-insulated steel structures exposed to fire", *Fire Safety J.*, Vol. 9, pp. 281-285, 1985.
- [2] Tan, KH, Wang, ZH and Au, SK, "Heat transfer analysis for steelwork insulated by intumescent paint exposed to standard fire conditions", *Proceedings of the Third International Workshop, Structure in Fire, SiF'04*, pp 49-58, Ottawa, Canada, 2004.
- [3] prEN 1993-1-2, "Eurocode 3: Design of Steel Structures – Part 1-2: General Rules – Structural Fire Design, Stage 49 draft", CEN, Brussels, 2003.
- [4] Melinek, SJ and Thomas, PH, "Heat flow to insulated steel", *Fire Safety J.*, Vol. 12, pp. 1-8, 1987.
- [5] Wan, ZH and Tan, KH, "Sensitivity study of time delay coefficient of heat transfer formulations for insulated steel members exposed to fire", *Fire Safety J.*, Vol. 41 (1), pp. 31-38, 2006
- [6] Carslaw, HS and Jaeger, JC, "Conduction of heat in solids, 2nd ed.", Oxford University press, New York, 1959.
- [7] Ozisik, MN, "Heat conduction, 2nd ed.", John Willey & Sons Inc, NJ, 1993.
- [8] prEN 1991-1-2, "Eurocode 1: Actions on Structures – Part 1-2: General Actions – Actions on structures exposed to fire, 3rd draft", CEN, Brussels, 2001.
- [9] SBN, "Swedish building code 1975", National Board of Physical Planning and Buildings, 1975.
- [10] ECCS Technical Committee 3, "European Recommendations for the Fire Safety of Steel Structures", Elsevier Scientific Publishing Company, Amsterdam, 1983.
- [11] Wong, MB and Ghajel, JI, "Sensitivity analysis of heat transfer formulations for insulated structural steel component", *Fire Safety J.*, Vol. 38, pp. 187-201, 2003.



BEHAVIOR OF STAINLESS STEEL SECTIONS SUBJECTED TO NON-HOMOGENEOUS TEMPERATURES

Ossama M. EL-HUSSEINY¹, Mohamed E. EL-DIB²,
Ehab B. MATAR³ and Osama F. SALEM⁴

ABSTRACT

Full utilization of the special features of stainless steel has not been possible due to lack of technical data on certain design aspects such as the fire resistance of stainless steel structures. During fire, stainless steel structures are influenced by the elevated temperatures where, the modulus of elasticity and the yield stress decrease with temperature increase. The behavior of stainless steel cold-formed sections at high temperatures was studied through the development of a computer program studying six different cold-formed stainless steel profiles. The bending moment capacities about x and y axes of stainless steel beams at elevated temperatures were determined under different linear and non-linear temperature distributions models. However, the effects of width / thickness ratio of the cross section and providing stiffener lips on the cross section capacity as well as on local buckling were discussed. A stainless steel structure was taken as a real applied example in which the critical temperature and the time of total collapse were calculated.

KEYWORDS

Stainless steel, Fire resistance, Cold-formed, Linear temperature distribution models, Non-linear temperature distribution models, Local buckling, Critical temperature.

¹ Professor, Zagazig University, Department of Structural Engineering, Zagazig, Egypt.
email: bect@tedat.net.eg

² Associated Professor, Zagazig University, Department of Structural Engineering, Zagazig, Egypt.
email:

³ Lecturer, Zagazig University, Department of Structural Engineering, Zagazig, Egypt.
email: ehab_bmatar@yahoo.com

⁴ Lecturer Assistant, Zagazig University, Department of Structural Engineering, Zagazig, Egypt.
email: osfik2003@yahoo.com

1. INTRODUCTION

The use of stainless steel in structural and architectural applications is an increasing trend due to material attractive appearance, corrosion resistance, ease of maintenance and low life cycle cost. The metallurgical microstructure of stainless steels may be ferritic, martensite, austenitic or austenitic-ferritic. Each group has different properties with respect to strength, corrosion resistance and ease of fabrication. This research is limited to austenitic stainless steel (Polarit 725). Although significant progress has been made over the last ten years in the development of design guidance for structural stainless steel, the fire resistance of stainless steel has received less attention. Stainless steel has wide use applications especially in elevated temperature environments such as boilers and pressure vessels and are not necessarily suitable for design in building structures. The elevated temperatures data in material standards in Euro code 3 Part 1.2 [1] are usually given up to 550 °C, whereas in fire engineering, behavior at higher temperatures is of interest.

Two different techniques have been used in fire problems. The first one is used for the newly designed steel structures where, the required capacity of the cross section can be evaluated in fire condition or at the expected fire temperature. The second technique is used for evaluating existing steel structures where, the critical temperature at which the structure starts to collapse can be determined under the applied loads. The time interval at which the structure collapses is calculated according to the critical temperature, which causes the structure collapse by using the standard fire curve ISO 834 [2].

The most important difference between stainless and carbon steel is the plateau of the stress-strain curve, that, the stress-strain relationship of austenitic stainless steel is non-linear and there is no well defined yield stress. The stress-strain relationship of stainless steel at elevated temperatures is necessary for determining the load-bearing capacity of structures under fire conditions. Therefore, the change of yield stresses (σ_y) of austenitic stainless steel (Polarit 725) was presented depending on the change in temperature using non-linear developed equations based on the experimental tests carried out by Ala-Outinen [3].

During fire, a typical temperature distribution across stainless steel sections is not available. The presence of architectural thermal separators causes non-homogeneity of the distribution of temperatures across the cross section. In order to represent the actual fire, many trials were made in order to simulate the actual distribution of fire on the cross section. Linear models were suggested depending on researches carried out by J. KRUPPA [4] assuming linear temperature distributions across the cross section depending on many experimental observations while non-linear models were suggested depending on researches carried out by McLaughlin [5].

2. OBJECTIVES AND RESEARCH PLAN

The main objective of this research is to evaluate the bending moment capacity about centroidal axes of different cold-formed stainless steel sections at elevated temperatures. The cross sections are subjected to general case of loading; cross-sections also were analyzed under different temperature distributions depending on the fire conditions and their locations relative to walls and slabs. Six different cold-formed cross sections including unstiffened and stiffened C, Z, rectangular hollow sections and I-shaped cold formed sections as shown in Fig. 1. The integration technique was used numerically in incremental steps to calculate the bending capacity of the cross sections. The equilibrium at plastic condition was considered. The study also discussed the effect of width / thickness ratio of the cross section elements and the effect of adding stiffener lips to the cross section bending moment capacity. A comparison

between the strengths of the cross sections due to linear and non-linear temperature distribution models was also presented in order to identify the best temperature distribution model, which has good agreement with experimental results. In order to achieve the objectives of this research, computer program (SCFSA) [6] was developed in order to analyze different cold-formed stainless steel cross sections.

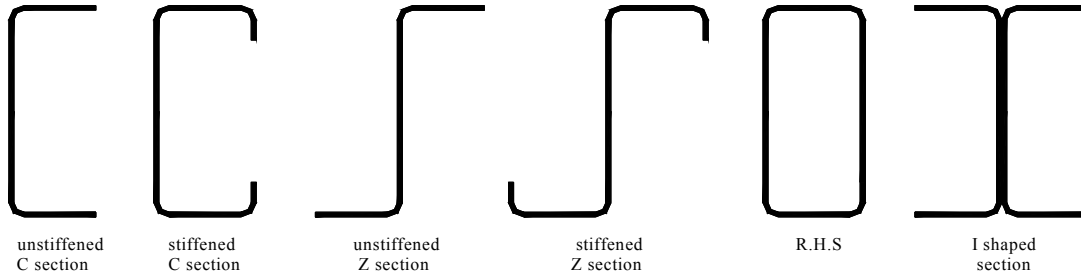


Fig. 1 -The studied stainless steel cold-formed sections.

3. MODELING OF STAINLESS STEEL MECHANICAL PROPERTIES AT HIGH TEMPERATURES

Each cross section was divided into small elements. Each element has its temperature according to the defined temperature distribution model. The change of yield stresses (σ_y) was presented depending on the change in temperature using non-linear developed equations based on the experimental tests carried out by Ala-Outinen [3] as follows:

$$\sigma_y(T) = 0.0022(T)^2 - 1.0888(T) + 308.95 \quad (\text{For } 20^\circ\text{C} \leq T \leq 300^\circ\text{C}) \quad (1)$$

$$\sigma_y(T) = -0.0001(T)^2 - 0.0601(T) + 205.15 \quad (\text{For } 300^\circ\text{C} < T \leq 700^\circ\text{C}) \quad (2)$$

$$\sigma_y(T) = -0.4250(T) + 410.333 \quad (\text{For } 700^\circ\text{C} < T \leq 900^\circ\text{C}) \quad (3)$$

Fig. 2 presents the relation between the 0.2% proof stress of austenitic stainless steel (Polarit 725) and temperature from the experimental data and the developed equations which emphasize a good correlation.

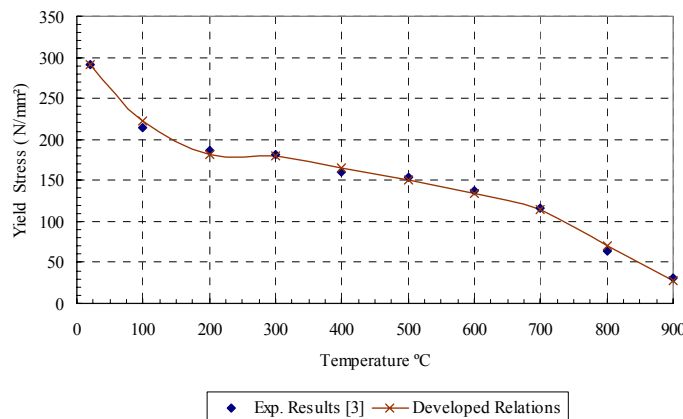


Fig. 2 - Change of yield stress of (Polarit 725 stainless steel) at high temperatures.

In case of cold-formed stainless steel sections, the effect of local buckling must be taken into consideration. Therefore, the stress is governed by the critical buckling stress which is calculated according to the following equation [7]:

$$\sigma_{cri} = \frac{\eta k \pi^2 E_o}{12 (1 - \nu^2) (w/t)^2} \quad (4)$$

Where:

σ_{cri} = critical local buckling stress in (N / mm²).

η = plasticity reduction factor.

k = buckling coefficient.

E_o = initial elastic modulus in (N / mm²).

ν = Poisson's ratio.

w = width of element in (mm).

t = thickness of element in (mm).

However, the modulus of elasticity (E_o) changes with temperature. Therefore, the following equations were developed based on the available test data of the relation between the modulus of elasticity of stainless steel (Polarit 725) and temperature, which were presented by Ala-Outinen [3].

$$E_o(T) = -1.55(T)^2 + 186(T) + 174900 \quad (\text{For } 20^\circ\text{C} \leq T < 200^\circ\text{C}) \quad (5)$$

$$E_o(T) = -23(T) + 153200 \quad (\text{For } 200^\circ\text{C} \leq T \leq 600^\circ\text{C}) \quad (6)$$

$$E_o(T) = 1.10(T)^2 - 2050(T) + 976000 \quad (\text{For } 600^\circ\text{C} < T \leq 900^\circ\text{C}) \quad (7)$$

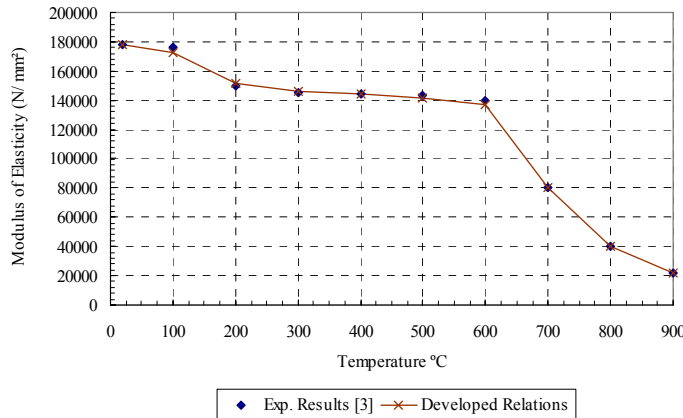


Fig. 3 - Change of modulus of elasticity of (Polarit 725 stainless steel) at high temperatures.

Fig. 3 presents the relation between the modulus of elasticity of austenitic stainless steel (Polarit 725) and temperature from the experimental data and the developed equations.

Substituting the three previous equations (5) through (7) into equation (4) in order to evaluate the critical stress (σ_{cri}), which governs the local buckling of compressed element at higher temperatures, therefore, other three equations were developed as follows:

$$\sigma_{cri} (i) = K * \pi^2 * ((-1.55 * (T)^2 + 186 * (T) + 174900) / (12 * 0.91 * (w/t)^2)) \quad (\text{For } 20^\circ\text{C} \leq T < 200^\circ\text{C}) \quad (8)$$

$$\sigma_{cri}(i) = K * \pi^2 * ((-23*(T)+153200) / (12* 0.91 *(w/t)^2)) \quad (9)$$

(For 200 °C ≤ T ≤ 600 °C)

$$\sigma_{cri}(i) = K * \pi^2 * ((1.1*(T)^2 -2050*(T)+976000) / (12* 0.91 *(w/t)^2)) \quad (10)$$

(For 600 °C < T ≤ 900 °C)

Where, the buckling coefficient (K) is to be taken 4.0 for stiffened compressed elements and 0.425 for unstiffened compressed elements. However, when the critical local buckling stress (σ_{cri}) of a compressed element exceeds its yield stress (σ_y) at any temperature, the governing stress is considered to be the yield stress while, for tensioned elements the governing stress is the yield stress (σ_y).

4. MODELS OF LINEAR AND NON-LINEAR TEMPERATURE DISTRIBUTION

In this research, different linear and non-linear temperature distribution models were studied for different cross sections. Fig. 4 shows for example the different three linear temperature distribution models and their separators positions for the unstiffened C cold formed section.

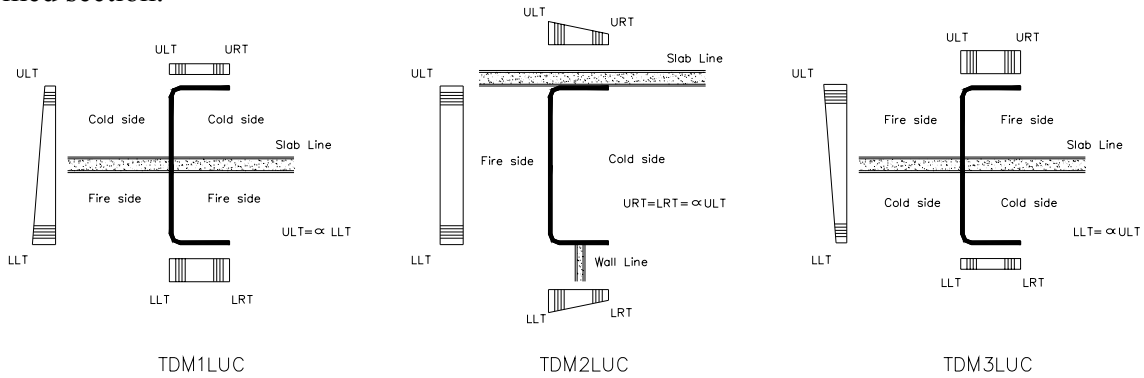


Fig. 4 - Linear temperature distribution models for unstiffened C cold formed section.

In the first temperature distribution model (TDM1LUC), as shown in Fig. 4, the fire is applied to the lower tensioned flange side, while the upper compressed flange side is assumed to be in room air temperature (20 °C). In the third temperature distribution model (TDM3LUC), the fire is applied to the upper compressed flange side, while the lower tensioned flange side is assumed to be in room air temperature (20 °C). The slope of the web or flange gradient line (α) is varied according to the degree of fire proof of the slab or partition where (α) takes values 0, 0.2 or 0.4. In the second temperature distribution model (TDM2LUC) the fire is applied to the left side, while the right side is assumed to be in room air temperature (20 °C).

For non-linear models there are several positions of cross sections with respect to the internal separators. In this research three common non-linear cases were taken for each cross section. Fig. 5 shows the temperature distribution of the three non-linear cases (A, B and C) for unstiffened C cold-formed section.

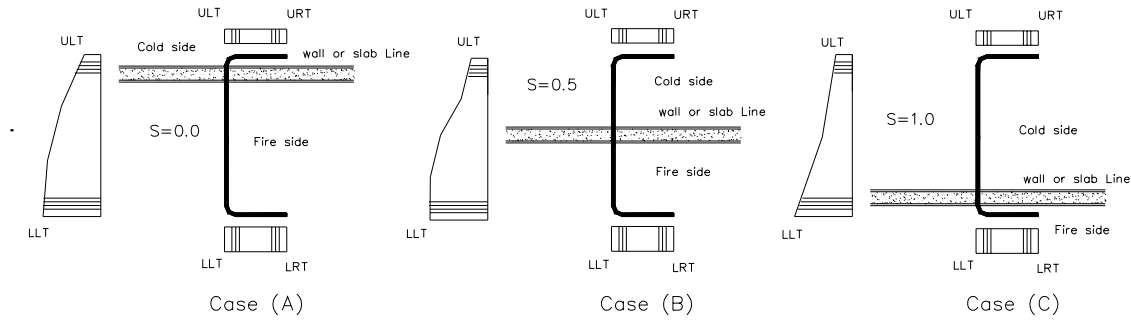


Fig. 5 - Non-linear temperature distribution models for unstiffened C cold-formed section.

The temperature values are calculated as a function of the inside high temperature (T_i) (fire temperature), and the outside temperature (T_o) (room temperature).

The temperature difference between flanges (ΔT) is calculated from the following equation [5];

$$\Delta T = [0.55 - 0.30 * (S - 0.25)^2] * (T_i - T_o) \quad (11)$$

Where the factor (S) is called the "exposure factor" that recognizes the portion of the web exposed to cold air. This exposure factor (S) is equal to 0.0 for the face-exposed condition, 0.5 for the semi-exposed condition, and 1.0 for the fully exposed condition.

The mean temperature for the section is represented by the following equation [5];

$$T_m = T_o + (0.47 - 0.22 S) * (T_i - T_o) \quad (12)$$

The values of the element temperature in the hot and cold sides are given by the following equations [5], respectively:

$$T(y) = T_L \left[1 - \frac{(T_L - T_u)}{T_L} (y/h)^2 \right] \quad (13)$$

$$T(y) = T_L \left[1 - \frac{(T_L - T_u)}{T_L} (y/h)^{0.5} \right] \quad (14)$$

Where (y) is the vertical distance of the centroid of the element from the x-axis lying at the lower boundary of the cross section and (h) is the height of the section. In the previous equations (13) and (14), (T_L) is the temperature of the lower flange and (T_u) is the temperature of the upper flange which can be calculated from the following equations [5], which can be applied along the width of the flanges.

$$T_L = T_o + [1.0 - 0.07 S - 0.3 S^2] * (T_i - T_o) \quad (15)$$

$$T_u = T_o + [0.2575 - 0.5 S - 0.15 S^2] * (T_i - T_o) \quad (16)$$

5. AGREEMENT BETWEEN DEVELOPED NUMERICAL MODELS AND EXPERIMENTAL RESULTS

Results obtained from this research were compared with available experimental test results carried out by Baddoo and Burgan [8]. This test program consisted of fire tests on four columns (length 3.4 m) and two beams supporting concrete slab (span 4.25 m) with structural

material of grade 1.4301 (304) austenitic stainless steel, (Polarit 725). One of the beam specimens was a rectangular hollow section, formed by two cold-formed channels welded together flange tip to flange tip. The other specimen was an I-shaped section, formed by two cold-formed channel sections welded together back to back. Regarding experimental test results of the two cross sections, it was noticed that, the developed SCFSA numerical model results were always in the safe side. They are lower than the experimental results by about 14% for the rectangular hollow cold-formed section and by about 7% for the I-shaped cold formed section at 500 °C and by about 40% and 60% at high temperatures respectively as shown in Fig. 6.

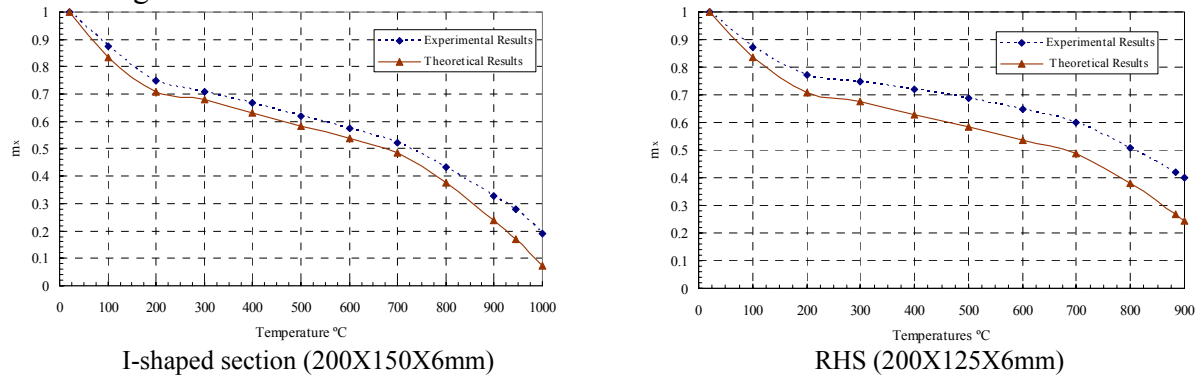


Fig. 6- Comparison of experimental and theoretical results for cold-formed I-shaped and RHS.

6. PROPOSED PROGRAM (SCFSA) RESULTS

The capacity of any of the six studied cross sections in this research depends on many parameters, but mainly it depends on the choice of the temperature distribution model, which affects significantly the strength of the cross section. The capacity of the cross section under different temperature distribution models was expressed by a utilization factor which is the ratio between the resisted bending moments at higher temperatures to that at room temperature. In this research the results of one of the six studied cross sections, which is the unstiffened C cold-formed section is presented. Figs. 7 and 8 show the relation between the temperature and the utilization factor of bending moment about x and y axis respectively, for the three different linear temperature distribution models. The unstiffened C cold-formed section (200X100X4 mm) has h/t for the web equal to 46, and b/t for the flanges equal to 23, which satisfy the recommendations of the specification for the design of cold-formed stainless steel structural members [9]. Generally, all these figures show that as the temperature increases the utilization factors m_x and m_y decrease for all temperature distribution models.

In the first model (TDM1LUC) the utilization factors of bending moment about x-axis (m_x) at 500°C with different values of temperature gradient slope ($\alpha = 0.0, 0.2$ and 0.4) are 0.69, 0.66 and 0.62 respectively, while at 900°C the utilization factors are 37%, 33% and 30% respectively. In the second model (TDM2LUC) the utilization factors at 500°C are 64%, 62% and 61% respectively and at 900°C the utilization factors are 35%, 32% and 30% respectively. In the third model (TDM3LUC) the utilization factors at 500°C are 75%, 69% and 64% respectively and at 900°C the utilization factors are 40%, 34% and 30% respectively.

Consider the three different linear models at constant value of ($\alpha = 0.0$). The second temperature distribution model (TDM2LUC) was found to give lower utilization factors (m_x)

than the first and the third temperature distribution models. At 500°C, the cross section resists in the first, second and third models by about 69%, 64% and 75% from its bending moment capacity about x-axis respectively. At 900°C the cross section resists by about 37%, 35% and 40% from its bending capacity respectively. This is because in the second temperature distribution model (TDM2LUC) the web of the section is directly exposed to fire and that increases its temperature up to (T_{max}), and since the web forms a large portion of the section, therefore, the cross section with this model has lower utilization factors than with the other two models. The third model (TDM3LUC) was found to give higher utilization factors than the first one although the flange which has high temperature is the compression one. This is because, the rate of decrease of the yielding stress with the increase in temperature is much pronounced than that of the local buckling stress, therefore, the governing stress at high temperatures is almost the yield stress rather than the local buckling stress.

It was also observed that the rate of moment capacity reduction is steep as the temperature increased up to 200°C, where, the cross section loses about 22%, 25% and 18% of its bending moment capacity in the first, second and third models respectively. Then the rate was a little flattened as the temperature increased up to 600°C, where, the cross section loses about 35%, 40% and 29% of its capacity respectively. Then the rate increased again as the temperature increased over 600°C, where, the cross section loses about 63%, 65% and 60% of its capacity respectively at 900°C.

For the three different linear models at constant value of ($\alpha=0.0$). The three models do not differ a lot up to 300°C. Over 300°C the second temperature distribution model (TDM2LUC) was found to give lower utilization factors (m_y) than the first and the third models. At 500°C the cross section is still resisting in the first, second and third models about 80%, 77% and 80% from its bending moment capacity respectively.

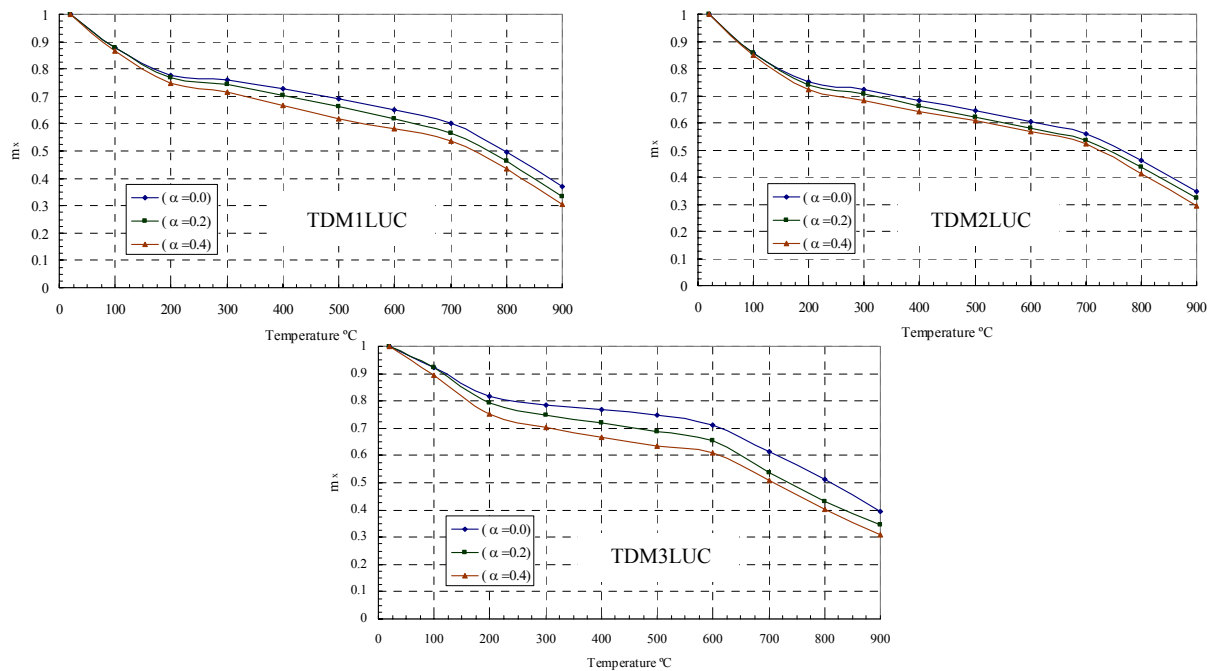


Fig. 7 - Utilization factors of beam for bending moment about x-axis for unsiffened C Cold-formed section for the three linear models.

It was observed that, the first and the third models were found to give equal utilization factors of bending moment about y-axis. This is because, the tension and compression portions are equal in both the upper and lower flanges and the allocation of fire do not differ the utilization factors of the first model than those of the third model. It was also noticed that the rate of moment capacity reduction is steep as the temperature increased up to 200°C for the first and the third models and up to 300°C for the second model, where, the cross section loses about 16% of its capacity for the first and the third models up to 200°C and 17% for the second model up to 300°C. Then the rate was little flattened as the temperature increased up to 600°C for the first and the third models and up to 700°C for the second model, where, the cross section loses about 23% of its capacity for the first and the third models and 27% for the second model up to 700°C. Then the rate increased again as the temperature increased over 600°C for the first and the third models and over 700°C for the second model, where, the cross section loses about 45% of its capacity for the first and the third models and 66% for the second model at 900°C.

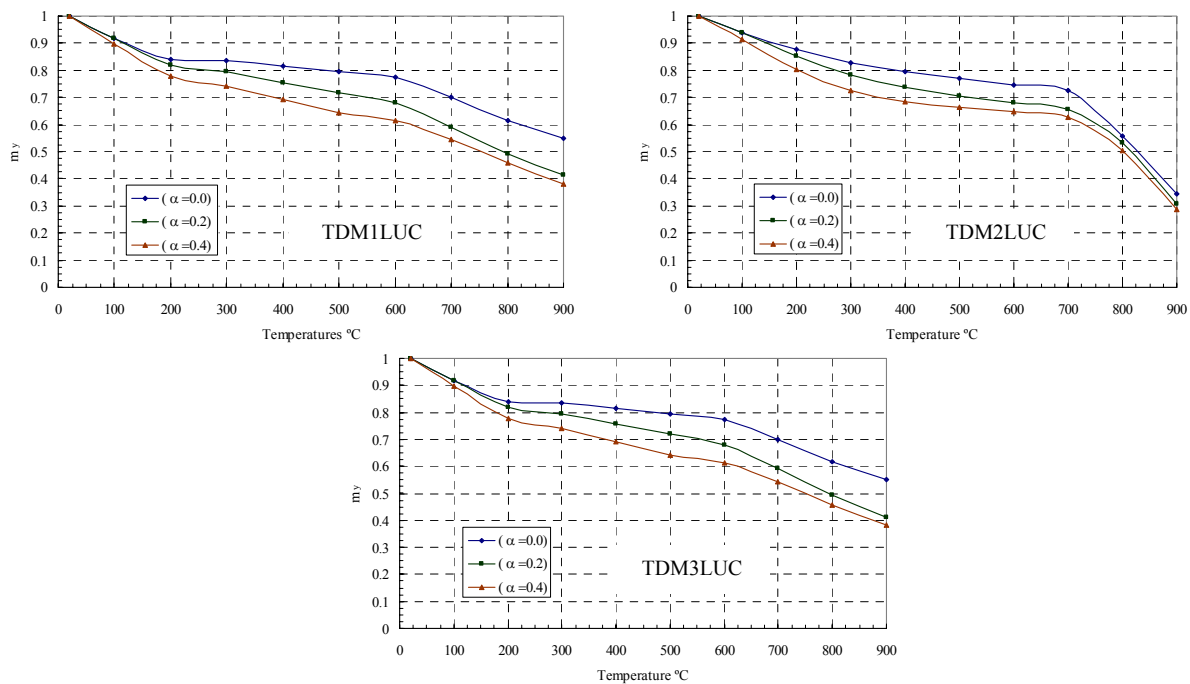


Fig. 8 - Utilization factors of beam for bending moment about y-axis for un-stiffened C Cold-formed section for the three linear models.

Fig. 9 shows the relation between the temperature and the utilization factors of the bending moment about x and y axes for the studied three non-linear model cases, where these cases differ according to the value of the "exposure factor" (S) as discussed earlier. The rate of moment capacity reduction about x-axis is steep as the temperature increased up to 200°C for cases (A) and (B) and up to 300°C for case (C), where, the cross section loses about 26% and 21% of its bending moment capacity for cases (A) and (B) respectively, and 20% of its capacity for case (C). Then the rate was little flattened as the temperature increased up to 700°C for cases (A) and (B) and up to 900°C for case (C), where, the cross section loses about 47%, 36% of its capacity for cases (A) and (B) respectively, and 31% of its capacity for case

(C). Then the rate increased again as the temperature increased over 700°C for cases (A) and (B), where, the cross section loses about 75% and 54% of its capacity respectively at 900°C.

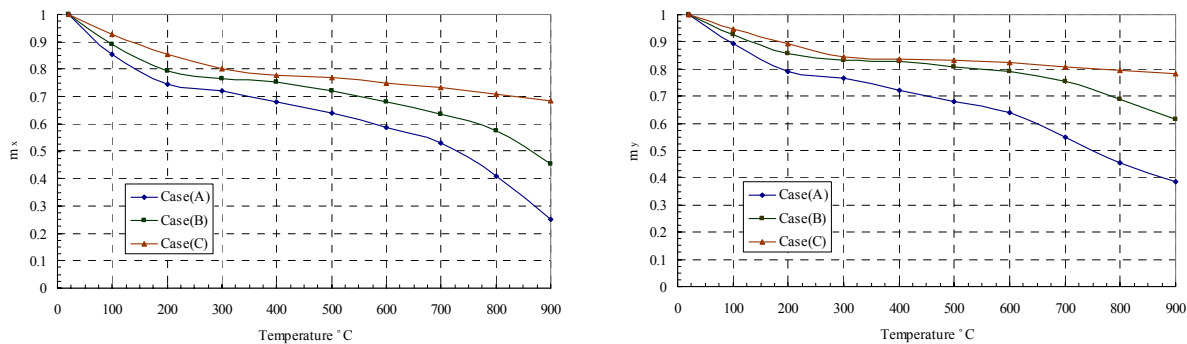


Fig. 9 - Utilization factors of beam for bending moment about x and y axes for un-stiffened C Cold-formed section for the three non-linear model cases.

For the utilization factors of the bending moment about y-axis for the studied three non-linear cases, the rate of moment capacity reduction is steep as the temperature increased up to 200°C for cases (A) and (B) and up to 300°C for case (C), where, the cross section loses about 21% and 14% of its bending moment capacity for cases (A) and (B) respectively, and 15% of its capacity for case (C). Then the rate was a little flattened as the temperature increased up to 600°C for cases (A) and (B) and up to 900°C for case (C), where, the cross section loses about 36%, 21% of its capacity for cases (A) and (B) respectively, and 22% of its capacity for case (C). Then the rate increased again as the temperature increased over 600°C for cases (A) and (B), where, the cross section loses about 61% and 39% of its capacity respectively at 900°C. Generally, it was noticed that the cross section is stronger when most parts of the cross section are exposed to cold air as in case (C) while in case (A), most parts of the cross section are in fire side therefore, the cross section is weaker.

6.1 Comparison between Linear and Non-linear Temperature Distribution Models

A comparison between the utilization factors of bending moments about x and y axes of the non-linear temperature distribution model (TDMNLUC) case (B) with those of the first linear temperature distribution model (TDML1UC) with all values of temperature gradient slopes ($\alpha = 0.0, 0.2$ and 0.4), shows that the non-linear model give higher utilization factors than those of linear model for both bending moments about x and y axes as shown in Fig. 10. Linear distribution model with temperature gradient slope of ($\alpha = 0.0$) yields better correlation with non-linear models than other temperature gradient slopes.

For utilization factors of bending moment about x-axis, the linear model with all values of temperature gradient slopes ($\alpha = 0.0, 0.2$ and 0.4) were found to give lower utilization factors than the non-linear model, where, at 500°C the utilization factors of the linear model are 0.69, 0.66 and 0.62 for (α) equal to 0.0, 0.2 and 0.4 respectively, while at the same temperature the utilization factor of the non-linear model is 0.72. At 900°C the utilization factors of the linear model are 0.37, 0.33 and 0.30 for (α) equal to 0.0, 0.2 and 0.4 respectively, while at the same temperature the utilization factor of the non-linear model is 0.46. However, it was observed that linear models with different values of (α) give lower utilization factors of bending moment about x-axis than those of the non-linear model of case (B) by about (4%, 9% and 16%) for (α) equal to 0.0, 0.2 and 0.4 respectively at 500 °C and by about (24%, 39% and 53%) respectively at 900°C.

It was observed that linear models with different values of (α) give lower utilization factors of bending moment about y-axis than those of non-linear models of case (B) by about (3%, 12% and 26%) for (α) equal to 0.0, 0.2 and 0.4 respectively at 500°C and by about (11%, 48% and 60%) respectively at 900°C.

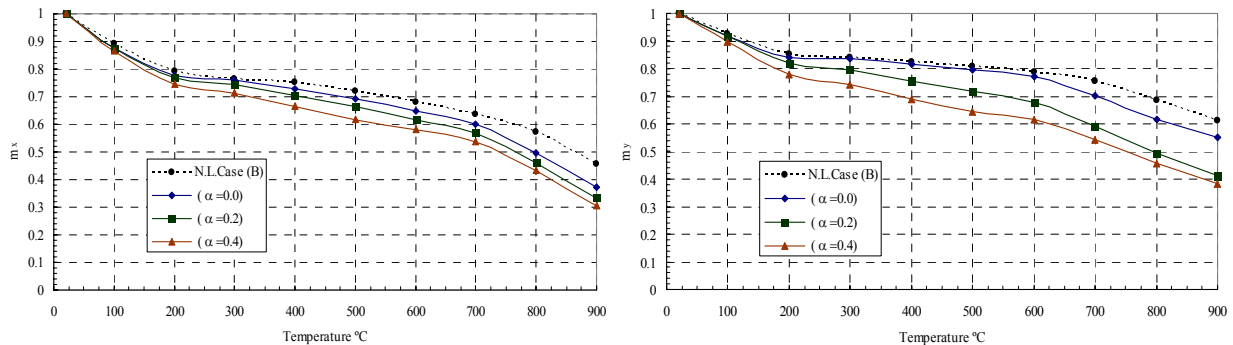


Fig. 10 - Comparative curves of utilization factors of beam for bending moment about x and y Axes for linear and non-linear temperature distribution models.

6.2 Local Buckling Effect on the Moment Capacity of Stainless Steel Profiles

The local buckling of the compressed flat parts of any cross section affects the governing critical stresses of these parts. This research takes into account the effect of local buckling of the compressed parts of any cross section subjected to fire. Fig. 11 represents the difference between considering the effect of local buckling on the cross section bending moments capacities and not considering that effect for unstiffened C cold formed section with first linear temperature distribution model (TDM1LUC) using different values of temperature gradient slope, (α) equal to (0.0, 0.2 and 0.4). However, in Fig. 11, the relationship between temperature and the ratio between bending moment capacity about x-axis of the cross section when considering the local buckling effect and without considering the local buckling effect is plotted. As shown in that figure, it was observed that as the temperature increased the effect of considering local buckling decreased, where at room temperature the ratio is equal to 80%. At 500 °C the bending capacity ratio is equal to 83%, 87% and 89% for (α) equal to 0.0, 0.2 and 0.4 respectively. At 900 °C the bending capacity ratio is equal to 86%, 90% and 92% for (α) equal to 0.0, 0.2 and 0.4 respectively. For bending moment capacity about y-axis of the cross section when considering the local buckling effect and without considering it as shown in Fig. 11, it was observed that as the temperature increased the effect of considering local buckling decreased, where at room temperature the ratio is equal to 73%. At 500 °C the bending moment capacity ratio is equal to 84%, 88% and 90% for (α) equal to 0.0, 0.2 and 0.4 respectively. At 900 °C the bending moment capacity ratio is equal to 86%, 91% and 93% for (α) equal to 0.0, 0.2 and 0.4 respectively.

This means that as the temperature slope gradient increases the moment capacity ratio increases also. This was referred to the rate of decrease of yielding stress with the increase in temperature is much pronounced than that of the critical stress which is a function in Young's modulus.

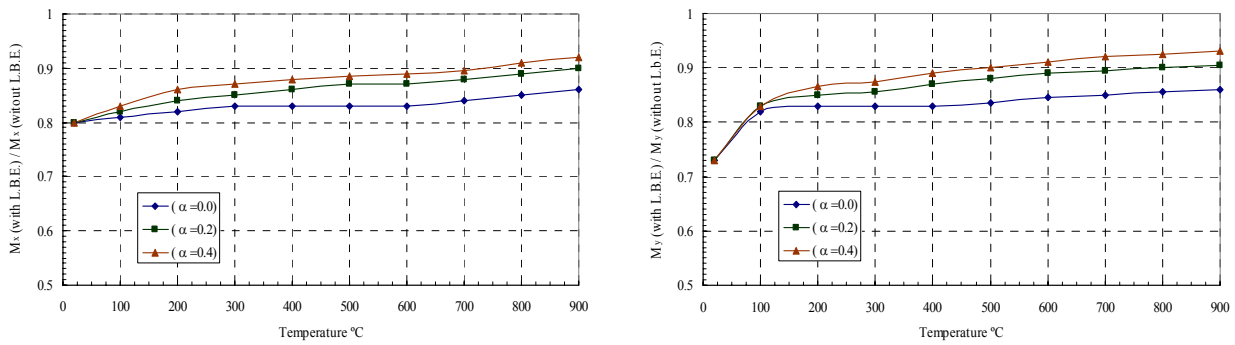


Fig. 11 - Comparison between bending moment capacities about x and y axes with or without Considering local buckling effect for (TDM1LUC)

6.3 Effect of Width / Thickness Ratio on the Cross Section Bending Moment Capacity

The width / thickness ratio of the compressed flat parts affects significantly the critical local buckling stress. As the width / thickness ratio increases the critical local buckling stress decreases, especially for large width / thickness ratios which are limited as indicated in the specification for the design of cold-formed stainless steel structural members [9].

The effect of width / thickness ratio on the bending moment capacity, was studied on un-stiffened C cold-formed section using the first linear temperature distribution model (TDM1LUC) with constant value of (α) which equal to zero. The chosen cross sections have different thicknesses which were changed between 2.0, 3.0 and 4.0mm. Therefore, in the first case with ($t = 2.0\text{mm}$), the flange width thickness ratio equal to (47) and the web width / thickness ratio equal to (94). In the second case with ($t = 3.0\text{mm}$), the flange width / thickness ratio equal to (31) and the web width / thickness ratio equal to (62). And in the third case with ($t = 4.0\text{mm}$), the flange width / thickness ratio equal to (23) and the web width / thickness ratio equal to (46). All the previous width / thickness ratios are within limits [9].

Fig. 13 represents the relationship between the temperature and the bending moment capacity about x and y axes of the cross section with different thicknesses. As shown in that figure it was observed that, as the temperature increases the utilization factors of bending moment about both x and y axes decrease for all thicknesses. At 500 °C the utilization factors of bending moment about x-axis are 92%, 79% and 69% for un-stiffened C cold formed section with thicknesses equal to 2mm, 3mm and 4mm respectively. Moreover, at 900 °C the utilization factors of bending moment about x-axis are 60%, 44% and 37% respectively. It was observed that, as the temperature increases the utilization factors of bending moment decrease for large thicknesses more than for small thicknesses. This is referred to the fact that, for small width / thickness ratios as in case of ($t = 4.0\text{mm}$), the governed stress of the compression parts of the cross section is controlled by the yielding stress, for large ratios as in case of ($t = 2.0\text{mm}$) the maximum stress is rather controlled by the local buckling critical stress. However, the rate of decrease of yielding stress with the increase in temperature is much pronounced than that of the local buckling critical stress which is a function of Young's modulus and width / thickness ratio.

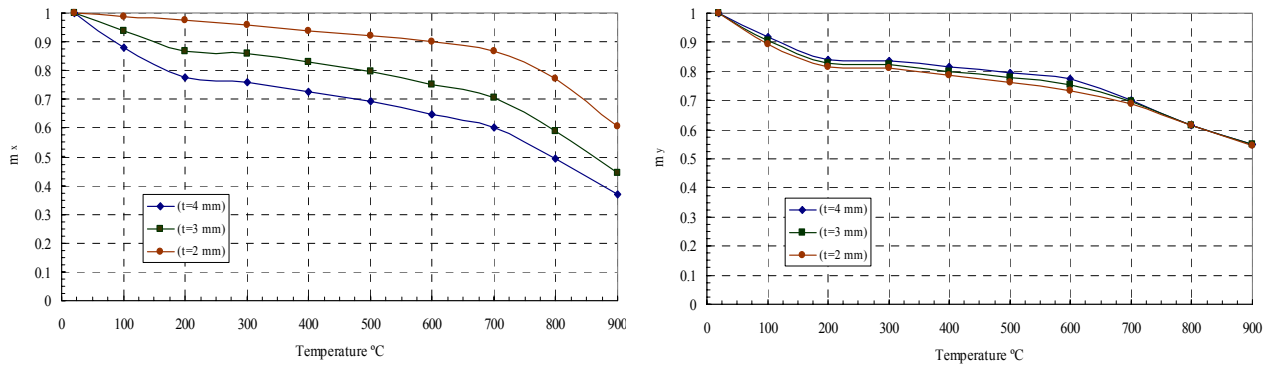


Fig. 13 - Comparison between bending moment capacity about x and y axes of unstiffened C Cold-formed section with different thicknesses using (TDM1LUC).

For the bending moment capacity about y-axis of the cross section with different thicknesses, as shown in that figure it was observed that, as the temperature increases, the utilization factors of bending moment about y-axis decrease for all different thicknesses nearly with the same value. This is because; the thickness of the C cold-formed cross section does not affect the moment of inertia about y-axis as it affects the moment of inertia about x-axis.

7. APPLIED NUMERICAL EXAMPLE

A roof system consists of light weight concrete slab placed on the top of stainless steel simply supported beams of 6m span and 2 m spacing as shown in Fig. 14. The cross section of the stainless steel beams is assumed to be a rectangular hollow cold-formed section 200x100x6mm. Each beam is divided into six elements as shown in Fig. 15. The used material is stainless steel Polarit (725) and the beam is loaded by an equivalent uniform load $w = 0.5 \text{ t/m'}$.

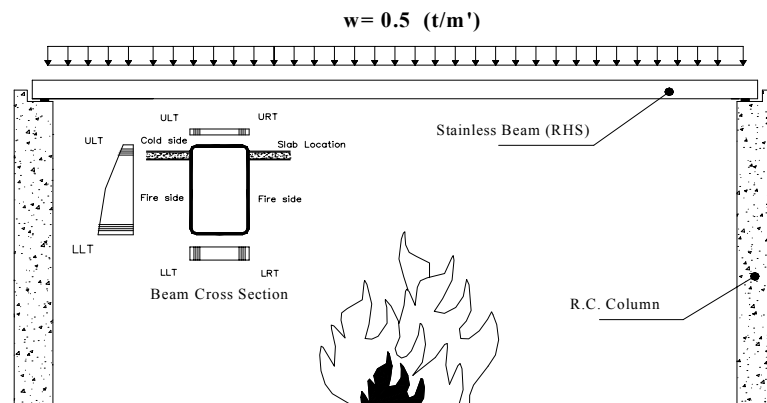


Fig. 14 - Dimensions and loads of the studied beam.

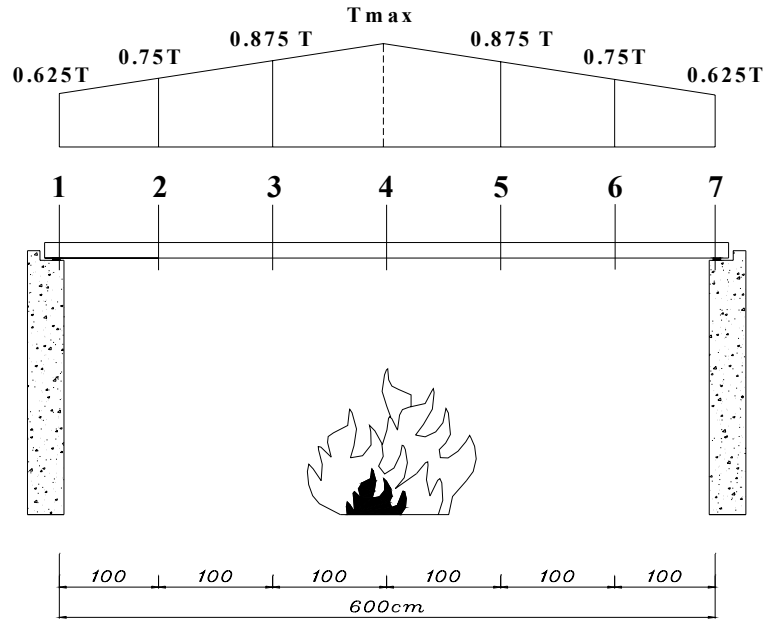


Fig. 15 - Sections and temperature distribution of the studied beam.

7.1 The Temperature Distribution in Fire Action

The linear temperature distribution along the beam is considered having a value (T_{max}) occurring at section (4) at mid span according to the experimental studies carried out by J. KRUPPA [4]. The temperature values decrease linearly, it is equal to ($0.625 T_{max}$) at sections (1) and (7) as shown in Fig. 15. The temperature distribution across the cross section is considered as non-linear distribution for the beam cross sections as described in temperature distribution model (TDMNLRHS) case (A) using an exposure factor ($S=0.0$).

The applied loads are assumed to be constant, while the temperature values are applied in increments till a plastic hinge is developed, and thus a plastic failure mechanism occurs. The mechanism of failure depends on the geometry, the dimensions of the structure, the type of loads and the type of supports. The temperature, at which the plastic hinge in the mechanism of failure forms, is considered as the critical temperature.

7.2 Results of the Applied Example

The results of the studied beam described in Fig. 14 are tabulated in table 1. The bending moment capacity (M_x) of the cross sections at the room temperature and the bending moments about x-axis resulted from the applied loads were calculated. The ratios of the calculated bending moments to the plastic bending moment capacity were presented in table 1 as $m_x = M_x / M_{px}$ (utilization factor).

The capacity of each section of the studied beam is calculated from the results curve of the non-linear temperature distribution case (A) of the rectangular hollow cold-formed section. The values of the utilization factors calculated at a maximum fire temperature equal to 100 °C

are compared to the actual utilization factors caused by the working loads at room temperature for all of the seven sections. It was found for all sections that, the utilization factors calculated at a maximum fire temperature equal to 100 °C are still higher than the actual utilization factors caused by the working loads at room temperature and no plastic hinges are formed at fire temperature equal to 100 °C. Then the temperature increased to 300 °C and still no plastic hinges are formed yet. Then the temperature increased to 500 °C and still no plastic hinges are formed yet. At fire temperature equal to 620 °C, it was noticed that for section (4) the utilization factor of bending moment about x- axis (m_x) which, is equal to 52.7% is lower than the actual utilization factor (m_x) caused by the working loads which is equal to 52.8%, therefore, a plastic hinge formed at section (4) and the mechanism of failure is then completed as beam collapse.

The critical temperature of the studied beam under the applied loads and the assumed temperatures is equal to 620 °C. This means, when the fire temperature reaches this critical temperature, the structure will collapse. Also, the time of collapse is determined to be illuminant using the ISO 834 Time Temperature Curve [2].

		1	2	3	4
Bending Moment Ratio	M_x / M_{px}	0.0	0.293	0.469	0.528
T=100°C	T	62.5	75	87.5	100
	m_x	0.897	0.876	0.855	0.835
T=300°C	T	187.5	225	262.5	300
	m_x	0.723	0.699	0.687	0.675
T=500°C	T	312.5	375	437.5	500
	m_x	0.669	0.639	0.611	0.584
T=600°C	T	375	450	525	600
	m_x	0.639	0.606	0.573	0.538
T=620°C	T	387.5	465	542.5	620
	m_x	0.633	0.603	0.561	0.527 *

Table 1 - Results of the Applied Example

8. CONCLUSIONS

From the analysis carried out using the computer program (SCFSA) and within the range of assumptions and variables, the following conclusions are deduced:

- 1- The critical temperature, at which a stainless steel structure may collapse in fire conditions, depends not only on the applied working loads, the dimensions of the cross section, the geometrical shape of the structure and the considered cross section but also on the temperature distribution along the structure elements and across their cross sections.
- 2- The allocation of slab and walls with respect to the stainless steel beam cross section affects the utilization factor. Wherever, the slab or walls protect most of the cross section from temperature increase, the capacity of the section is increased markedly.

- 3- It is observed that up to 200°C the rate of reduction of cross section capacities for linear or non-linear models is steep and nearly the section loses only between 10 to 30 % of its capacity. During the temperature increase up to nearly 600°C, the rate of capacity loss is lesser and over nearly 600°C the rate begins to increase rapidly up to failure. It is to be noticed that the rate of reduction of cross section capacities with high temperature is coherence with the yield stress and the local buckling critical stress reduction with high temperatures.
- 4- It is observed that with the temperature increase, the effect of considering local buckling decreases. This is referred to the fact that the rate of decrease of yielding stress with the increase in temperature is much pronounced than that of the local buckling critical stress which is a function of Young's modulus.
- 5- Increasing of width / thickness ratios of the compression flat parts of the cross section decreases significantly the bending moment capacity of the cross section, especially at low temperatures rather than at high temperatures. For small width / thickness ratios, the governed stress of the compression parts of the cross section is controlled by the yielding stress while for large ratios the governed stress is rather controlled by the local buckling critical stress.

9. REFERENCES

- [1] ENV 1993-1-2. 1995. EUROCODE 3, Design of Steel Structures - Part 1.2, Structural Fire Design. Brussels: European Committee for Standardization (CEN), (1995).
- [2] RECOMMENDATIONS ISO R 834, Organization International De Normalization, No ISO / R 834, (1968).
- [3] ALA-OUTINEN, TIINA, "Fire Resistance of Austenitic Stainless Steels Polarit 725 (EN 1.4301) and Polarit 761 (EN 1.4571). ", Espoo 1996, Technical Research Center of Finland, VTT Tiedotteita- Meddelanden- Research Notes, Finland, (1996).
- [4] KRUPPA, J. AND ARNAULT, P., "Resistance Au Feu Des Poutres Isostatiques En Acier", Revue Construction Metalique, Vol. 1, No.1, (1975).
- [5] E.R. MACLAUGHLIN, "Temperature Effect on Tall Steel Framed Buildings", Part 1- Response of Steel Columns Subjected to Temperature Exposure, AISC National Engineering Conference. Pittsburgh. (1970).
- [6] SCFSA PROGRAM, A developed computer program, based on Matlab program version 5.3 (R11), to be linked .www. Mathworks.com
- [7] GJ. VAN DEN BERG, "The Behavior of Cold-Formed Stainless Steel Structural Members", Journal of Constructional Steel Research, Vol. 46, No.1-3, and ISSN: 0143-974X, (1998).
- [8] N.R. BADDOO AND B.A. BURGAN, "Fire Resistant Design of Austenitic Structural Stainless Steel", the steel Construction Institute, Journal of Construction Steel Research, Vol. 46, paper No. 243, Silwood Park, Ascot SL5 7QN.
- [9] AMERICAN SOCIETY OF CIVIL ENGINEERING, "Specification for the Design of Cold-Formed Stainless Steel Structural Members.", (1991).



EXPERIMENTAL INVESTIGATION OF COLD-FORMED STEEL COLUMNS SUBJECT TO DISTORTIONAL BUCKLING UNDER SIMULATED FIRE CONDITIONS

Thanuja RANAWAKA¹ and Mahen MAHENDRAN²

ABSTRACT

In recent times, light gauge cold-formed steel sections have been used extensively in residential, industrial and commercial buildings as primary load bearing structural components. However, these members are susceptible to various buckling modes including local and distortional buckling, and their ultimate strength behaviour is governed by these buckling modes. Fire safety design of building structures has become increasingly more important in recent times and hence there is a need to assess the performance of light gauge cold-formed steel structures under fire conditions. However, the buckling behaviour of light gauge cold-formed steel members under fire conditions is not well understood. Therefore a research project was undertaken to investigate the distortional buckling behaviour of light gauge cold-formed steel structures under axial compression. Experimental studies were first used to investigate the distortional buckling behaviour of a series of compression members with two cross-sections and various thicknesses (0.6 to 0.95 mm) at elevated temperatures. The sections were made of both lower and higher grade steels (G250 and G550). Steady state tests were undertaken at temperatures in the range of 20 to 800°C. Degradation of mechanical properties was included in the design procedure to predict the compression capacities at varying temperatures. Predicted member capacities were then compared with experimental member capacities and appropriate recommendations were made about the current design procedures. This paper presents the details of this experimental investigation and the results.

1. INTRODUCTION

Light gauge cold-formed steel sections are more economical than traditional heavy hot-rolled steel sections. They have a high strength to weight ratio compared to the thicker hot-rolled members. The use of very thin (0.42 to 1.2 mm) cold-formed steels has increased

¹ PhD Student, Queensland University of Technology, School of Urban Development, GPO Box 2434, Brisbane, QLD 4001, email: t.ranawaka@qut.edu.au

² Professor of Structural Engineering, Queensland University of Technology, School of Urban Development, GPO Box 2434, Brisbane, QLD 4001, email: m.mahendran@qut.edu.au

rapidly around the world due to the development of advanced manufacturing technologies. However, the knowledge and understanding of the behaviour of cold-formed steel members is limited, particularly at elevated temperatures. Local and distortional buckling are the most common failure modes of short light gauge cold-formed steel compression members. Therefore in order to determine the capacity of steel compression members, both local and distortional buckling modes should be considered. However, local buckling mode has been thoroughly investigated at both ambient and elevated temperatures and there is a wealth of knowledge on this topic (Lee et al., 2003)¹. On the other hand, there is limited research on the relatively new distortional buckling behaviour of cold-formed steel members at ambient and elevated temperatures. For these reasons a series of laboratory experiments was carried out to determine the distortional buckling failure behaviour of light gauge cold-formed steel compression members at elevated temperatures in the range of 20 to 800°C. This paper presents the details of this experimental investigation and the results.

2. EXPERIMENTAL INVESTIGATION

2.1 Test Specimen

An experimental study was carried out first to investigate the structural behaviour of light gauge cold-formed steel compression members, which were subjected to distortional buckling failure mode at ambient temperature. Suitable light gauge cold-formed steel cross sections were determined based on the available literature review, elastic buckling analyses and the constructability of the sections. This led to the choice of two sections, lipped C-sections with and without additional lips (see Figure 1). The required column length and the cross-sectional dimensions were obtained based on the buckling stress plots of the compression members from Thin-wall program (Papangelis and Hancock, 1998)² based on finite strip analyses, and the finite element program ABAQUS (HKS, 2004)³. Both low and high strength steels were considered since they are commonly used in Australia. High strength steel G550 with a nominal yield strength of 550 MPa and low strength steel G250 with a nominal yield strength of 250 MPa were used. The thickness of cold-formed steels was varied from 0.6 mm to 0.95 mm. i.e. 0.6, 0.8, and 0.95 mm. The test specimen length (L) was varied from 190 mm to 290 mm with respect to the thickness and the section type. Additional lengths of 5 mm were provided for each top and bottom end to allow for the fixing of specimens to the end plates. Table 1 shows the selected dimensions.

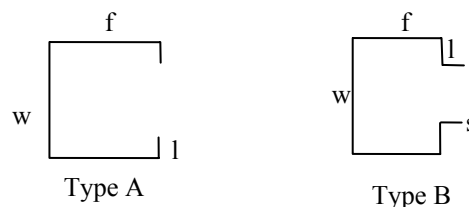


Figure 1 Designed Sections for Experiments

Table1 Selected Dimensions of Type A and Type B Sections in mm

Section Type	Nominal Thickness (mm)	w	f	l	s	Length (mm)
A	0.60	30	30	5	-	200
	0.80	30	30	5	-	180
	0.95	30	35	5	-	180
B	0.60	40	30	5	10	280
	0.80	40	30	5	10	240
	0.95	40	30	5	10	220

2.2 Test Set-up

The fixed-end condition was used in the experiments since the test set-up is simpler than that of pin-end conditions. Further, in the case of pin-end specimens, an additional moment is created due to the shift in the line of axial compression force after the elastic buckling failure. This may complicate the problem. Specially designed end plates with a groove were used to provide the required fixed-end conditions. The groove depth was 5 mm as it was adequate to fix the specimen to the end plates accurately. Pyrocrete 165 coil grout was selected as the filling material since it has a higher strength at elevated temperatures.

2.3 Test Procedure at Ambient Temperature

Eighteen steel columns from each grade (G250 and G550) were tested. The test specimens with the fixed-end plates were then placed between the large cross heads of a universal testing machine (Tinius Olsen) and loaded in axial compression until the specimens failed. Figure 2 shows the overall test set-up. The out-of-plane deflections of both flanges were measured using 20 mm LVDTs at mid-height and 5 mm away from the flange-lip junction for Type A specimen. The out-of-plane deflections of one flange and one lip were measured for Type B specimens. The shortening of the specimen was also recorded during the tests by the Tinius Olsen testing machine.

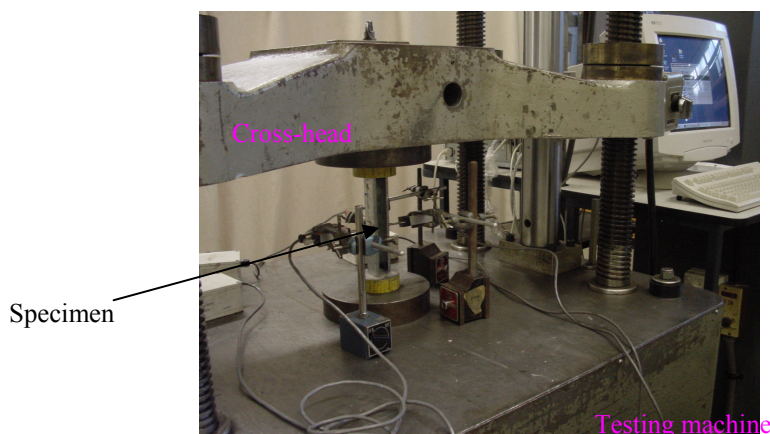


Figure 2 Overall Test Set-up at Ambient Temperature

2.4 Test Procedure at Elevated Temperatures

A series of experiments was undertaken to investigate the distortional buckling behaviour at elevated temperatures. More than 120 tests were carried out including the tests at five different temperatures. A specially designed electrical furnace which is now available in the QUT structural laboratory was used to simulate fire conditions in the experiments (see Figure 3). Temperature in the furnace was controlled by a microcomputer based temperature indicating system, and the rate of temperature increase was adjustable. Four glow bars were used to heat the furnace electrically. The glow bars were placed in the furnace to ensure evenly distributed heat throughout the furnace. The air temperature inside the furnace was measured by two thermo couples located inside the furnace. An additional portable thermometer was used externally and attached to the specimen to measure the specimen temperature so that the accuracy can be increased. Two shafts were used to fix the specimen and to apply the compression load to the specimens. The bottom end of the shaft was fixed while the load was applied via its top end.

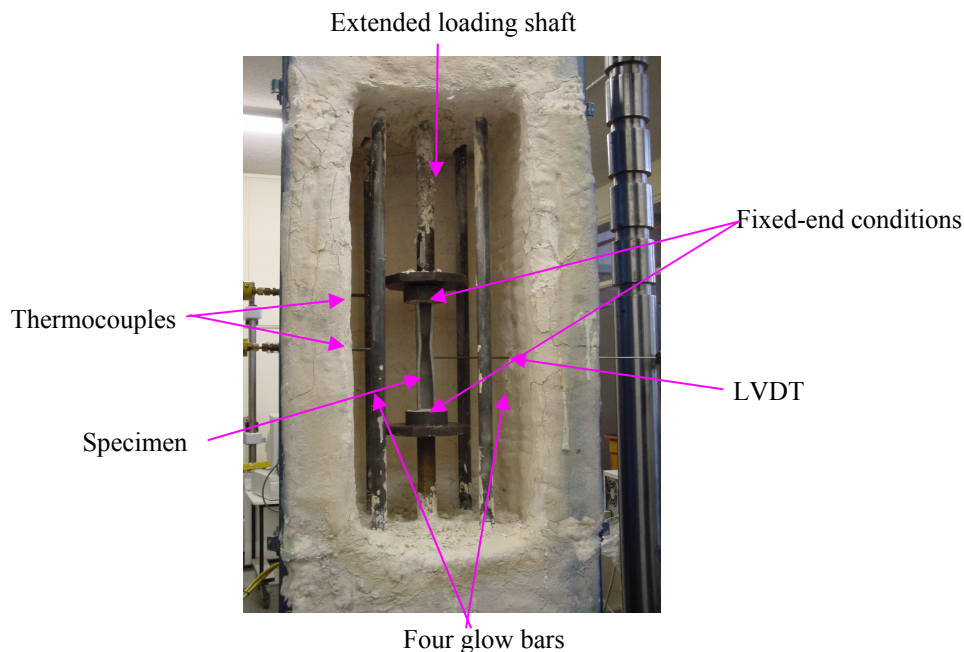


Figure 3 Overall Test Set-up at Elevated Temperatures

All the experiments were undertaken in the steady state condition since difference between the transient state and steady state test methods is negligible (Lee et al., 2003). The furnace was first heated up to the required temperature. It was then maintained for about 20 minutes so that the specimen also reached the required temperature. The applied load on the specimens due to thermal expansion was carefully observed during the heating process and the specimen was allowed to freely expand when the temperature was increased. An automatic temperature controller was used to ensure the upper limit of the temperature.

The temperature range chosen in this study was from ambient temperature to 800°C at intervals of 150°C, i.e., 200, 350, 500, 650 and 800°C. The specimen temperature measured by thermometer and the air temperature measured by thermocouples were observed during the test period. It was noticed that the air temperature measured by the thermocouples and the specimen temperature measured by the thermometer were the same. The specimens were loaded until they failed while maintaining the pre-selected temperatures after the furnace reached a steady state condition. Horizontal displacement was measured at the mid height of

the specimens to observe the flange deformation during the test. Axial shortening of the specimen was also measured.

2.5 Test Results

Figure 4 shows the typical axial compression load versus out-of-plane deflection and axial shortening graphs for 0.95 mm G250 Type A specimen while Figure 5 shows the ultimate load reduction with increasing temperature for both low and high strength steels of 0.95 mm Type A specimens.

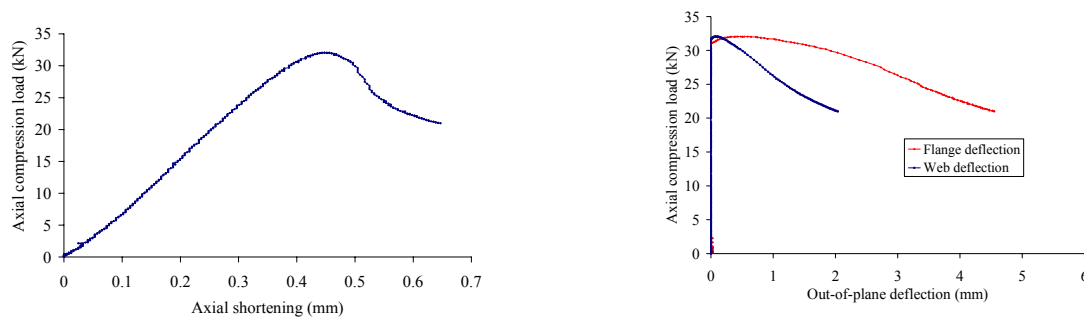


Figure 4 Load-Deformation Curves for 0.95 mm G250 Type A Specimen

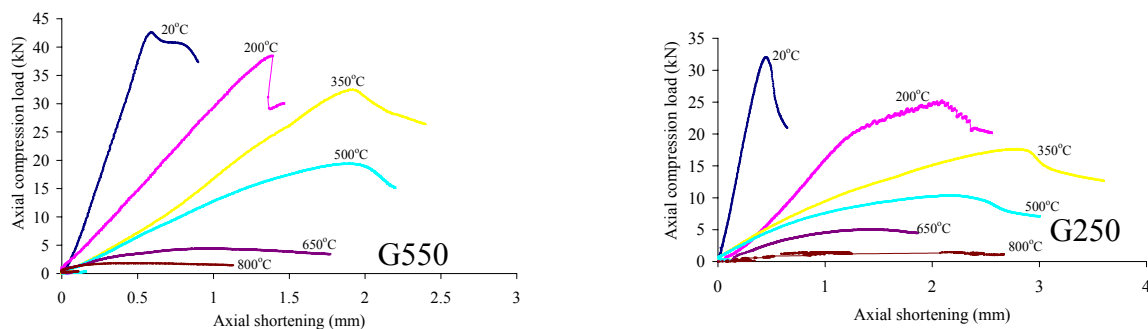


Figure 5 Comparison of Buckling Behaviour with Respect to the Temperature and the Steel Grade for 0.95 mm Steels

2.6 Buckling Modes

Two main types of distortional buckling failure modes were observed at ambient temperature while three different types were observed at elevated temperatures. Ambient temperature test results showed that column fails by both flanges moving inwards or outwards. In addition to these two modes, many test columns failed due to one flange moving outward while the other flange moving inward at elevated temperatures (see Figure 6). However, the cross sectional dimensions and length of test specimens used at elevated temperatures were the same as those at ambient temperature. The end conditions were fixed for all the specimens. The only difference was the temperature. Therefore it is clear that temperature can affect the failure modes. On the other hand the imperfections can also influence the failure modes of the specimens.

However, the different types of buckling occur mainly because of the thickness, steel grade, section types, temperature and imperfection. The experimental results suggest that imperfections and temperatures have governed the failure mode rather than other parameters. They showed that the failure modes of the three nominally identical columns were different even though the failure loads were about the same.

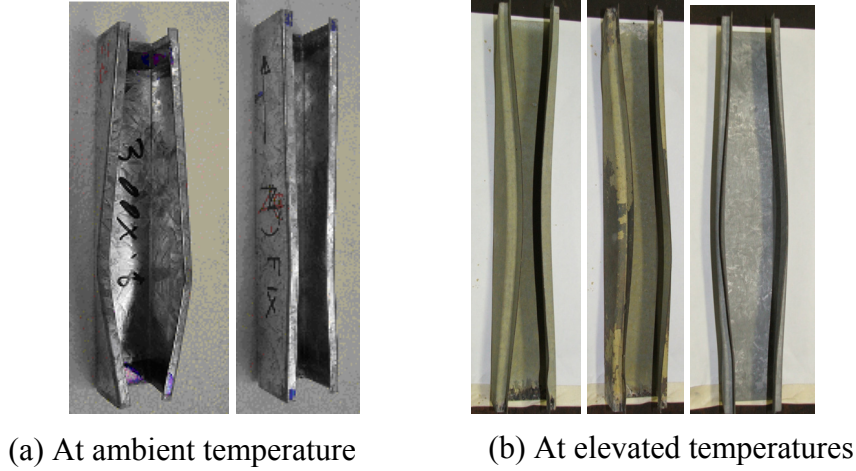


Figure 6 Main Buckling Modes

3. COMPARISON OF TEST RESULTS WITH PREDICTIONS FROM CURRENT DESIGN EQUATIONS

3.1 Ambient Temperature

3.1.1 AS/NZS 4600

The ultimate loads obtained from the tests were compared with the available design equations in the Australian/New Zealand Standard, AS/NZS 4600 (SA, 1996)⁴ for cold-formed steel structures. Only AS/NZS 4600 presents the distortional buckling equations among the various design standards (see Equation 1)

$$\blacklozenge \text{ For } f_{od} > f_y/2: \quad P_n = Af_n = Af_y \left(1 - \frac{f_y}{4f_{od}} \right) \quad (1(a))$$

$$\blacklozenge \text{ For } f_y/13 \leq f_{od} \leq f_y/2: \quad P_n = Af_n = Af_y \left[0.055 \left(\sqrt{\frac{f_y}{f_{od}}} - 3.6 \right)^2 + 0.237 \right] \quad (1(b))$$

where A = Area of the full cross-section, f_y = Yield strength of steel, f_n = Ultimate strength of the specimen, f_{od} = Elastic distortional buckling strength.

According to AS/NZS 4600 (Clause 1.5.1.5), the yield strengths of 0.6 and 0.8 mm G550 steels should be taken as 90% of the corresponding values or 495 MPa whichever is the lesser. Therefore reduced yield strengths were used in Equation 1 to calculate the distortional buckling capacity of the 0.6 and 0.8 mm specimens. Table 2 provides the predicted ultimate loads and the average ultimate load from experiments.

Table 2 presents the experimental and predicted ultimate loads from Equations 1 (a) and (b) of AS/NZS 4600. The mean values are 1.07 and 1.0 for low and high strength steels, respectively while the COV is about 0.04 for Type A specimens. The mean values of Type B specimens are 1.18 and 1.14 for low and high strength steels, respectively while the COV of low strength steel is 0.127. Therefore it can be concluded that although AS/NZS 4600 predictions are for both types of sections, the Type A specimens show a very good agreement while Type B specimen values are more conservative. Therefore the accuracy of AS/NZS 4600 design rules should be further investigated by considering other types of light gauge steel sections.

Table 2 Comparison of Predicted Ultimate Loads from Equation 1 with Test Results at Ambient Temperature

Specimen	Ultimate Load (kN)		Exp./Predicted	
	Predicted	Exp.	Actual	Mean/COV
A0.6-550-20	19.02	19.70	1.04	1.000
A0.8-550-20	30.70	31.10	1.01	0.040
A0.95-550-20	44.55	42.90	0.96	
B0.6-550-20	18.89	24.10	1.28	1.140
B0.8-550-20	34.15	39.60	1.16	0.127
B0.95-550-20	54.09	53.60	0.99	
A0.6-250-20	12.37	12.80	1.03	1.070
A0.8-250-20	19.08	20.40	1.07	0.042
A0.95-250-20	28.11	31.40	1.12	
B0.6-250-20	12.76	15.70	1.23	1.180
B0.8-250-20	22.57	26.00	1.15	0.039
B0.95-250-20	32.60	37.50	1.15	

In addition the comparison of predicted ultimate loads from Equation 1 with test results is shown in Figure 7. Lau and Hancock (1987)⁵ developed Equation 1(a) whereas Kwon and Hancock (1992)⁶ developed Equation 1(b) to extend Lau and Hancock's curve for slender sections which may buckle in the distortional mode in the post-buckling range.

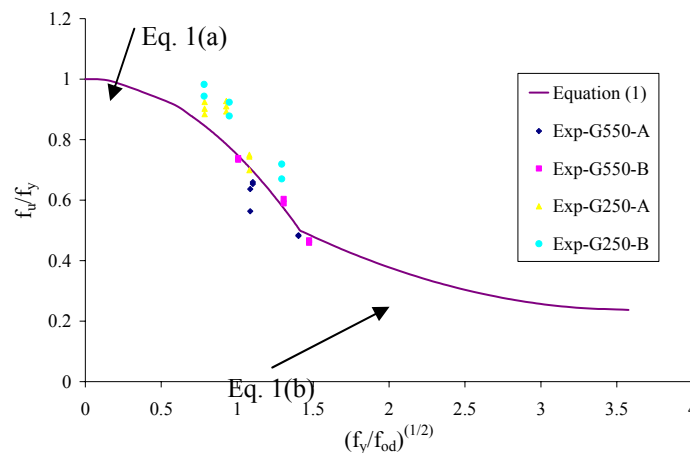


Figure 7 Comparison of Equation 1 Predictions with Test Results at Ambient Temperature

The measured yield strength from the tensile coupon test results were used to non-dimensionalise the test results as given in Hancock (1998)⁷. f_{od} was determined from finite element analyses for the tested specimens. Figure 7 shows a good agreement between test results and Equation 1. Therefore based on Table 2 and Figure 7 it can be concluded that the design equations in AS/NZS 4600 are reasonably accurate for light gauge cold-formed steel compression members (C-section and C-section with additional lips) at ambient temperature.

3.1.2 Direct strength method

The direct strength method proposed by Schafer and Pekoz (1998)⁸ is one of the alternative methods to determine the strength of cold-formed steel members. The direct strength method includes the distortional buckling of cold-formed steel compression members. Therefore the predictions of the direct strength method were compared with the test results in this research. However, it must be noted that the direct strength method was calibrated by using the available test data for concentrically loaded compression members with pin ends (AISI, 2004)⁹. Equation 2 presents the ultimate load of the compression members which fail by distortional buckling mode.

$$\begin{aligned}
 &\lambda \leq 0.561 \\
 &\text{And} \\
 &\lambda > 0.561
 \end{aligned}
 \quad
 \begin{aligned}
 P_n &= Af_n = Af_y \\
 P_n &= Af_n = Af_y \left[1 - 0.25 \left(\frac{f_{od}}{f_y} \right)^{0.6} \right] \left[\frac{f_{od}}{f_y} \right]^{0.6}
 \end{aligned}
 \quad (2)$$

where,

$$\lambda = \sqrt{\frac{f_y}{f_{od}}}$$

Note: All the symbols are the same as in Equations 1(a) and (b).

Table 3 and Figure 8 show the comparison of test results with Equation 2 predictions. As shown in Table 3 and Figure 8 the direct strength method predicts the ultimate strength of compression members reasonably well which failed from distortional buckling at ambient temperature. As stated earlier although the direct strength method was developed based on the results of pin-ended compression members, the results show that it can also be used for fixed-end conditions. However, the experimental to predicted ultimate load ratio varies from 0.873 (unsafe) to 1.188 (conservative).

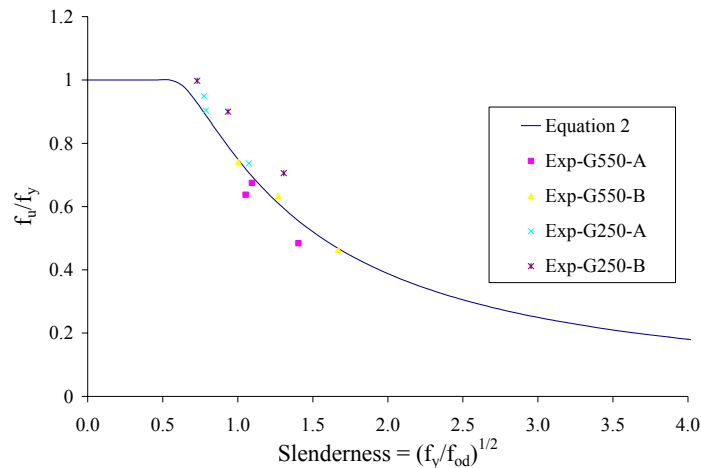


Figure 8 Comparison of Equation 2 Predictions with Test Results at Ambient Temperature

Table 3 Comparison of Predictions from Equation 2 with Test Results at Ambient Temperature

Specimen	Ultimate Load (kN)		Exp./Predicted	
	Predicted	Exp	Actual	Mean/COV
A0.6-550-20	22.58	19.7	0.873	0.909/ 0.057
A0.8-550-20	35.10	31.1	0.886	
A0.95-550-20	44.27	42.9	0.969	
B0.6-550-20	24.35	24.1	0.99	1.006/ 0.027
B0.8-550-20	38.14	39.6	1.038	
B0.95-550-20	54.07	53.6	0.991	
A0.6-250-20	12.30	12.8	1.041	1.039/ 0.021
A0.8-250-20	20.07	20.4	1.016	
A0.95-250-20	29.66	31.4	1.059	
B0.6-250-20	13.21	15.7	1.188	1.134/ 0.050
B0.8-250-20	22.82	26.0	1.139	
B0.95-250-20	34.86	37.5	1.076	

3.2 Elevated Temperatures

3.2.1 AS/NZS 4600

Although AS/NZS 4600 design rules are available for the prediction of distortional buckling failure loads of compression members, they are limited to ambient temperature conditions. Therefore they were modified to predict the ultimate loads at elevated temperatures by substituting the appropriate reduced yield strengths at relevant temperatures in the original equations (Equation 1). The reduction factors for yield strength and elasticity modulus of the steels used in this study are given in another paper at this conference (Ranawaka and Mahendran, 2006)⁹.

AS/NZS 4600 specifies a reduction factor of 0.9 for the yield strength of 0.6 and 0.8 mm G550 steels. However, it is given only for ambient temperature conditions. Therefore two different cases were considered for elevated temperatures for these steels. In Case 1, no reduction factor was used (Pred.1), but in Case 2 the reduction factor of 0.9 was used with the

appropriately reduced yield strengths at elevated temperatures (Pred.2). All the parameters were based on experimentally measured values.

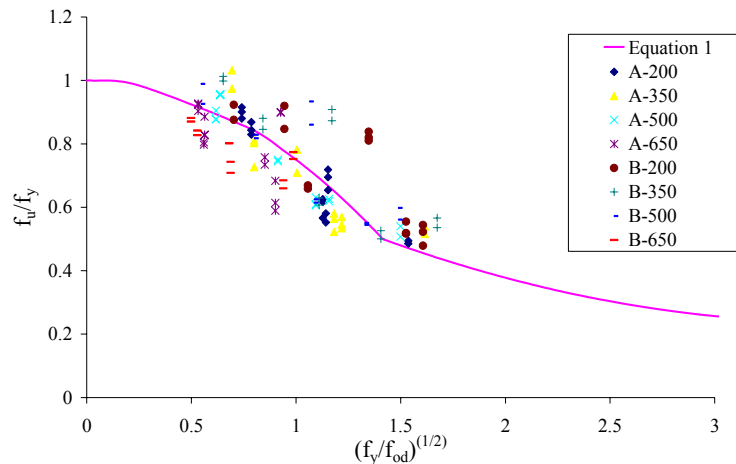


Figure 9 Comparisons of Equation 1 Predictions (Case 1) with Test Results at Elevated Temperatures

Table 4 Comparison of Predictions from Equation 1 (Cases 1 and 2) with Test Results at Elevated Temperatures

Specimen	Ultimate Load (kN)		Exp. (kN)	Exp/Pred. ₁		Exp/Pred. ₂	
	Pred. ₁	Pred. ₂		Actual	Mean/COV	Actual	Mean/COV
A0.6-550-200	18.274	17.084	15.198	0.832	0.814/ 0.087	0.890	0.873/ 0.081
A0.6-550-350	15.370	14.397	13.568	0.883		0.942	
A0.6-550-500	8.407	7.839	6.946	0.826		0.886	
A0.6-550-650	3.310	3.054	2.367	0.715		0.775	
A0.6-250-200	10.635		9.302	0.875	0.860/ 0.015		
A0.6-250-350	6.798		5.886	0.866			
A0.6-250-500	4.485		3.829	0.854			
A0.6-250-650	2.254		1.906	0.845			
B0.6-550-200	20.418	17.430	20.874	1.022	1.001/ 0.112	1.198	1.098/ 0.126
B0.6-550-350	17.245	16.000	18.713	1.085		1.170	
B0.6-550-500	9.477	8.894	10.046	1.060		1.130	
B0.6-550-650	3.809	3.562	3.189	0.837		0.895	
B0.6-250-200	10.858		14.630	1.347	1.162/ 0.145		
B0.6-250-350	7.521		9.119	1.212			
B0.6-250-500	5.129		5.871	1.145			
B0.6-250-650	2.627		2.477	0.943			
A0.8-550-200	32.369	30.539	27.191	0.840	0.900/ 0.080	0.890	0.964/ 0.101
A0.8-550-350	27.041	25.748	23.743	0.878		0.922	
A0.8-550-500	14.670	13.769	12.903	0.880		0.937	
A0.8-550-650	4.224	3.832	4.242	1.004		1.107	
A0.8-250-200	17.937		17.280	0.963	0.928/ 0.055		
A0.8-250-350	11.094		10.234	0.923			
A0.8-250-500	7.348		7.118	0.969			
A0.8-250-650	3.708		3.184	0.859			
B0.8-550-200	31.949	31.408	32.922	1.030	0.981/ 0.097	1.048	1.032/ 0.084
B0.8-550-350	26.713	24.925	28.397	1.063		1.139	
B0.8-550-500	14.957	14.530	14.685	0.982		1.011	
B0.8-550-650	5.171	4.714	4.383	0.848		0.930	
B0.8-250-200	20.521		23.071	1.124	1.026/ 0.111		
B0.8-250-350	12.976		14.500	1.117			
B0.8-250-500	8.715		8.455	0.970			
B0.8-250-650	4.563		4.078	0.894			

Figure 9 shows the comparison of predictions from Equation 1 (Case 1) and the test results while Table 4 presents the results for 0.6 and 0.8 mm steels. A reasonable agreement between the predictions and test results can be seen with mean and COV values of 0.965 and 0.128, and 0.992 and 0.126 for the two cases considered here. However, when compared with the results from ambient temperature, Equation 1 predictions have become unconservative (compare results of Tables 2 and 4). Therefore these equations should be further modified by considering additional test and numerical results for elevated temperature conditions.

3.2.2 Direct strength method

As for the AS/NZS 4600 design rules, the direct strength method was also developed for ambient temperature conditions. Therefore the direct strength method equations were modified by including the reduced yield strength obtained in this research to determine the distortional buckling failure loads. The additional reduction factor of 0.9 for 0.6 and 0.8 mm G550 steels was not used (Case 1). Figure 10 compares the ultimate loads predicted by the direct strength method with test results.

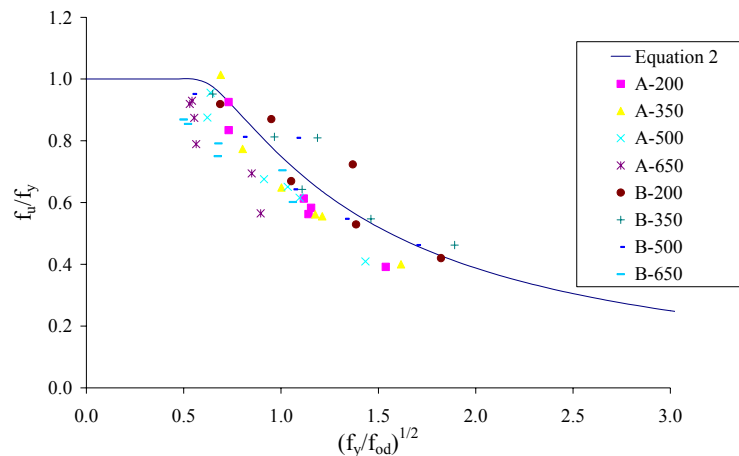


Figure 10 Comparisons of Equation 2 Predictions (Case 1) with Test Results at Elevated Temperatures

As shown in Figure 10 the direct strength method does not accurately predict the ultimate strength of compression members at elevated temperatures which failed from distortional buckling. The direct strength method over-predicts the ultimate load of many specimens and is conservative for some specimens. The ratio of the experimental to predicted ultimate load varied from 0.761 to 1.145 with an overall mean of 0.921 and a COV of 0.123 (Case 1). Therefore it can be stated that the direct strength method is reasonably accurate but not safe for all the specimens at elevated temperatures. As stated earlier the direct strength method was developed using the results of pin-ended compression members and for ambient temperature conditions. Therefore more results are required to assess the accuracy of direct strength method for elevated temperature conditions.

4. CONCLUSIONS

A series of experiments was undertaken at ambient and elevated temperatures to investigate the distortional buckling behaviour of light gauge cold-formed steel compression members. Both low and high strength steels were considered with the nominal thicknesses of

0.6, 0.8 and 0.95 mm. The experimental results were then compared with predictions from the available design rules based on AS/NZS 4600 and the direct strength method. The results showed that both methods are reasonably accurate at ambient temperature. The modified equations taking into account the reduced yield strength and elasticity modulus of steel at elevated temperatures appear to be adequate, but their accuracy has decreased when compared with results for ambient temperature conditions. It can be concluded that, since current design rules are developed for ambient temperature conditions, their applicability to elevated temperature conditions is questionable. Further studies into the distortional buckling behaviour of compression members at elevated temperatures are continuing at the Queensland University of Technology in order to develop improved design equations.

5. REFERENCES

- [1] Lee, J., (2004), Local Buckling Behaviour and Design of Cold-Formed Steel Compression Members at Elevated Temperatures, PhD thesis, Queensland University of Technology, Brisbane, Australia.
- [2] Papangelis, J.P. and Hancock, G.J. (2000), THIN-WALL 2.0, The University of Sydney, Sydney, Australia.
- [3] Hibbitt, Karlsson & Sorensen, Inc. (2002), ABAQUS/Standard User's Manual, Version 6.3, New York, USA
- [4] Standards Australia (1996), AS/NZS 4600, Cold-formed Steel structures, Sydney, Australia.
- [5] Lau, S. C. W. and Hancock, G. J. (1987) Distortional Buckling Formulas for Channel Column, Journal of Structural Engineering, Vol. 113, pp. 1063-1078.
- [6] Kwon, Y.B. and Hancock, G.J. (1992). Design of Channels Against Distortional Buckling, Research Report no. R660, University of Sydney, Sydney, Australia
- [7] Hancock, J. (1998), Design of Cold-Formed Steel Structures, Australian Institute of Steel Construction, 3rd Edition, Sydney, NSW, Australia
- [8] Schafer, B.W. and Pekoz, T. (1998) Direct Strength Prediction of Cold-formed Steel Members using Numerical Elastic Buckling Solutions, Proceedings of the Fourteenth International Specialty Conference on Cold-formed Steel Structures, Missouri, USA, pp.137-144.
- [9] AISI (2004), Specification for the Design of Cold-Formed Steel Structural Members, American Iron and Steel Institute, Washington, D.C.
- [10] Ranawaka, T. and Mahendran, M. (2006) Mechanical Properties of Thin Steels at Elevated Temperatures, To be presented at the 4th International Workshop on Structures in Fire, Aveiro, Portugal.



ANALYSIS OF RESTRAINED HEATED STEEL BEAMS DURING COOLING PHASE

Guo-Qiang LI¹ and Shi Xiong GUO²

ABSTRACT

Observations from experiments and real fire indicate that restrained steel beams have better fire-resistant capability than isolated beams. Due to the effects of restraints, a steel beam in fire condition can undergo very large deflections and the run away damage may be avoided. However disgusting damages may occur in the beam-to-column connections, which is thought to be mainly caused by the enormous axial tensile forces in steel beams when temperature decreases. Over the past ten years, the behaviour of restrained steel beams subjected to fire during heating has been investigated in detail through experimental and theoretical methods, and some practical and simplified approaches for analysis of this behaviour have been proposed. While the performance of restrained steel beams during cooling has not been so deeply studied. For the safety evaluation and repair of structures against fire, more detailed investigation on the behaviour of restrained beams subjected to fire during cooling is necessary. When the steel temperature decreases, the elastic modulus and yield strength of steel recover, and the contraction force in restrained steel beams will be produced. In this study, an incremental method is proposed for analyzing the behaviour of restrained steel beams subjected to cooling. In each temperature decrement, the development of deformation and internal forces of a restrained beam is divided into two steps. One step is to consider the effect caused by recovery of elastic modulus of steel, and the other step is to consider the contraction force generated by temperature decrease in the beam. In this way, the behaviour of restrained steel beams during cooling phase in fire can be easily analyzed. At last, the proposed approach is validated by FE method.

Keywords: steel structure, restrained beam, fire resistance, cooling

¹ Professor, Tongji University, college of civil engineering, 1239 Siping Road, Shanghai 200092 P. R. China
email: gqli@mail.tongji.edu.cn

² PHD student, Tongji University, college of civil engineering, 1239 Siping Road, Shanghai 200092 P. R. China
email: guosxnr@163.com

1. INTRODUCTION

Observations from experiments and real fire indicate that restrained steel beams have better fire-resistant capacity than isolated beams^[1,2]. However the damages of the connections of restrained beams to columns are still noticeable in fire, which is thought to be mainly caused by the enormous axial tensile forces in steel beams when temperature decreases. Fig. 1 shows the damages in the beam-to-column connection found in the fire attack to a tall steel building in TaiPei Science and Technology Park. Over the past ten years, the behaviour of restrained steel beams during fire heating has been investigated in detail through experimental and theoretical studies^[3-6], and some practical and simplified approaches for modeling this behaviour have been proposed^[7,8]. While few research on the performance of restrained steel beams during fire cooling has been conducted, except some studies on the strain reversal of steel during cooling carried out by El-Rimawi et al^[9] and Bailey et al^[10] and others. Considering the important effects on the beam-to-column connections due to the contraction force, theoretical investigation on the behaviour of restrained steel beams during fire cooling is necessary.



Fig. 1 Damages to beam-column connections in Taipei Science and Technology Park

2. THE BEHAVIOUR OF RESTRAINED STEEL BEAMS DURING FIRE HEATING AND COOLING

The behaviour of a restrained beam during heating can be divided into 4 stages according to the development of axial force in the beam, as shown in Fig.2. The development of the deflection of the beam in each stage is shown in Fig.3.

In stage I, the beam is in elastic state. Compressive axial force is induced in the beam by thermal expansion and increases with temperature elevation. In stage II, the beam goes into elasto-plastic state. The compressive force in the beam begins to decrease, until it becomes to zero. In stage III, the beam is in elasto-plastic, while the axial force in the beam goes into tension. In stage IV, the axial tensile force in the beam reaches the maximum and then begins to decrease with the reduction of the steel strength. In stage II ~IV, plastic strain is produced and accumulated in the beam with temperature increasing. When temperature begins to decrease, because the plastic strain is maintained and the beam is restrained at the ends, contraction will be aroused and the tensile axial force in the beam will be increased, as indicted by the dashed line in Fig 2. On the other hand, deflection of the beam is reversed a bit due to the recovery of the elastic modulus of steel and the increase of the axial tensile force in the beam during cooling, as shown by the dashed lines

in Fig.3.

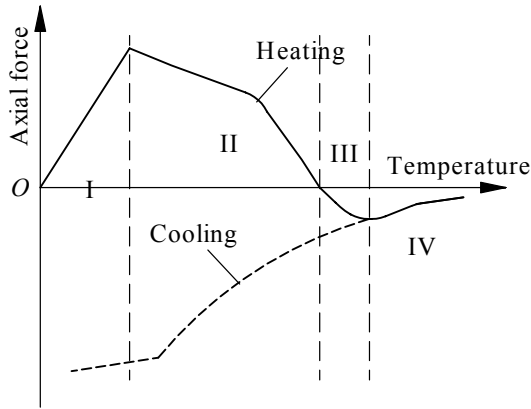


Fig. 2 Development of axial force in a restrained beam subjected to heating and cooling

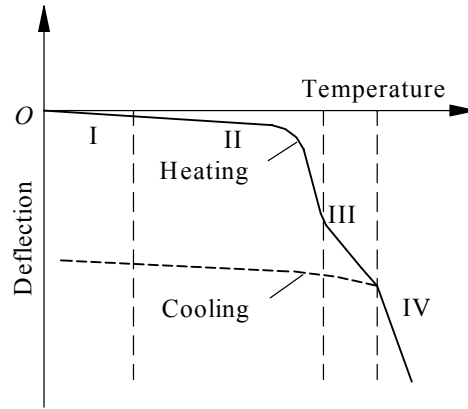


Fig. 3 Development of deflection of a restrained beam subjected to heating and cooling

3. EQUILIBRIUM OF RESTRAINED STEEL BEAM IN LARGE DEFLECTION STATE

Restrained steel beams in fire condition can undergo very large deflection, so the effect of geometric non-linearity, which is normally ignored in isolated beams, must be considered. A typical model of a restrained beam is shown in Fig.4, in which L is the span of the beam; k_a is the stiffness of the axial restraint at ends; k_r is the stiffness of the rotational restraint; F is the axial force in the beam; M_{end} and M_{mid} are the resistant bending moments at the end and middle.

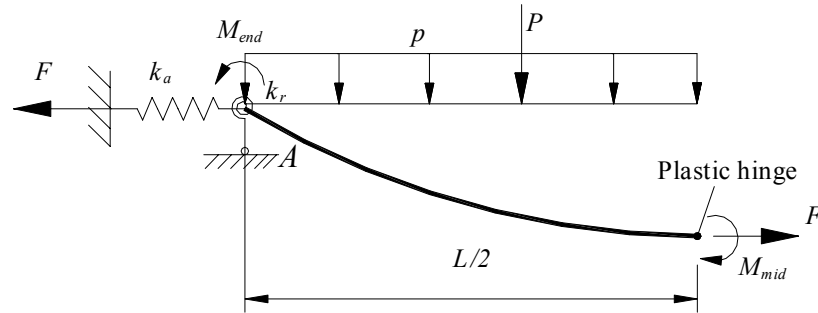


Fig. 4 The model of a restrained steel beam

The equilibrium equation of moments in the beam involving the effect of geometric non-linearity can be expressed as:

$$M_{end} + M_{mid} - M_{eff} + F\delta = 0 \quad (1)$$

where δ is the vertical mid-span displacement and M_{eff} is the moment about end A induced by the applied load on the beam.

The axial force in the beam can be determined by:

$$F = (\alpha L \Delta T - \lambda \frac{\delta^2}{L}) k_{e,a} \quad (2)$$

where α is the coefficient of thermal expansion of steel; ΔT is the temperature increase; λ is a factor relevant to the deflection curve of the beam; $k_{e,a}$ is the effective axial stiffness of the beam, which can be derived by

$$\frac{1}{k_{e,a}} = \frac{2}{k_a} + \frac{1}{k_{bT}} \quad (3)$$

where k_{bT} is the axial stiffness of the beam at temperature T .

4. THE STIFFNESS OF RESTRAINED STEEL BEAMS

In this study, the axial stiffness of the restraint to the beam, k_a , is assumed to be constant, but the axial stiffness of the beam, k_{bT} , varies widely in different stages. Since the effective axial stiffness of the beam is dependent on k_{bT} , the study of k_{bT} is needed. In order to simplify the study, the temperature distribution at the beam cross section is assumed to be uniform.

Given the beam is elastic and its deflection is very small, the axial stiffness of the beam can be simply determined by

$$k_{bT} = \frac{E_T A}{L} \quad (4)$$

where E_T is the elastic modulus of steel at temperature T ; and A is the cross-sectional area of the beam.

If the beam is elastic but its deflection is large, the axial stiffness of the beam must account for the effect of geometric non-linearity due to deflection. Based on the energy conservation principle, k_{bT} can be obtained by the following equation^[11]:

$$\begin{aligned} \frac{1}{k_{bT,e}} = & \int_0^l \frac{\sqrt{1 + f'(x)^2} f^2(x)}{E_T I} dx + \int_0^l \frac{1}{E_T A \sqrt{1 + f'(x)^2}} dx \\ & - \frac{k_{e,r}}{EL / L} \frac{\int_0^l \sqrt{1 + f'(x)^2} f(x) dx}{\int_0^l \sqrt{1 + f'(x)^2} dx} \int_0^l \frac{\sqrt{1 + f'(x)^2} f(x)}{E_T I} dx \end{aligned} \quad (5)$$

where E is the elastic modulus of steel at ambient temperature; $f(x)$ is the function of deflection curve of the beam; and $k_{e,r}$ is the effective stiffness of the restrained beam, which can be determined with

$$\frac{1}{k_{e,r}} = \frac{L}{EI} + \frac{2}{k_r} \quad (6)$$

where k_r is the rotational stiffness of the restraints to the ends of the beam.

If plastic hinge occurs in the beam, the axial stiffness of the beam will be sharply reduced. According to plastic theory, the relationship between the moment, M , and axial force, F , at the plastic hinge in the beam can be expressed as:

$$\begin{cases} \frac{M}{M_p} + \omega \left(\frac{F}{F_p} \right)^2 = 1 & \text{Neutral axis in the web} \\ \zeta \frac{M}{M_p} + \left| \frac{F}{F_p} \right| = 1 & \text{Neutral axis in the flange} \end{cases} \quad (7)$$

where M_p is the plastic moment capacity of the beam; F_p is the plastic axial force capacity of the beam; ω and ζ are factors relevant to the type of the cross-section of the beam, and given by

$$\omega = \frac{(2 + \mu_t)^2}{\mu_t(4 + \mu_t)}, \quad \zeta = \frac{4 + \mu_t}{2(2 + \mu_t)} \quad (8)$$

where μ_i is the ratio of the cross-sectional area of the web to one flange of the beam.

For a beam without rotational restraints at the ends, $M_{\text{end}}=0$, so Eq.(1) is changed to:

$$F\delta = M_{\text{mid}} + M_{\text{eff}} \quad (9)$$

Work out the expression of M_{mid} from Eq.(7) and substitute into Eq.(9), then the derivative of F with respected to δ can be obtained by:

$$\frac{dF}{d\delta} = \begin{cases} -\frac{F}{2\omega \frac{M_p F}{F_p^2} + \delta} & \text{Neutral axis in the web} \\ -\frac{F}{\frac{M_p}{\zeta F_p} + \delta} & \text{Neutral axis in the flange} \end{cases} \quad (10)$$

Given temperature is kept constant, the relationship of the relative displacement of the two ends of the beam, u , and the deflection at the mid span of the beam, δ , can be expressed as:

$$u = \lambda \frac{\delta^2}{L} \quad (11)$$

Then

$$\frac{du}{d\delta} = 2\lambda \frac{\delta}{L} \quad (12)$$

Therefore, according to the differential equations (10) and (12), the axial stiffness of the beam with plastic hinge and large deflection can be determined by:

$$k_{bT,p} = \frac{dF}{du} = \begin{cases} -\frac{F}{2\omega \frac{M_p F}{F_p^2} + \delta} \cdot \frac{L}{2\lambda\delta} & \text{Neutral axis in the web} \\ -\frac{F}{\frac{M_p}{\zeta F_p} + \delta} \cdot \frac{L}{2\lambda\delta} & \text{Neutral axis in the flange} \end{cases} \quad (13)$$

Similarly, for a beam with end rotation fully restrained, the axial stiffness of the beam with plastic hinge and large deflection can be derived as:

$$k_{bT,p} = \frac{dF}{du} = \begin{cases} -\frac{F}{4\omega \frac{M_p F}{F_p^2} + \delta} \cdot \frac{L}{2\lambda\delta} & \text{Neutral axis in the web} \\ -\frac{F}{2\frac{M_p}{\zeta F_p} + \delta} \cdot \frac{L}{2\lambda\delta} & \text{Neutral axis in the flange} \end{cases} \quad (14)$$

5. ANALYSES OF RESTRAINED BEAMS DURING COOLING

In order to simplify this analysis, the temperature distribution over the cross-section of the beam is assumed to be uniform. When the steel temperature decreases from T_1 to T_2 , the elastic modulus and yield strength of steel recover, with increase of the stiffness and the load bearing capacity of the beam. At the same time, the contraction force, ΔF , will be produced by the temperature decrease, as shown in Fig.5(a). Therefore, the behavior of

restrained beams during cooling is mainly dominated by the recovery of the elastic modulus and the contraction force.

For analyzing the behaviour of the restrained beam during cooling, the temperature incremental approach is employed. In each temperature decrement, $\Delta T = T_2 - T_1$, the change of the beam can be divided into two steps. In the first step, the steel temperature decreases from T_1 to T_2 with all the forces and moments applied on the beam kept constant. In this step, the beam contracts, and the steel elastic modulus and yield strength recover, as shown in Fig.5 (b). In the second step, the incremental tensile axial force, ΔF , resulted from contraction, is applied at the ends of the beam, as shown in Fig.5 (c).

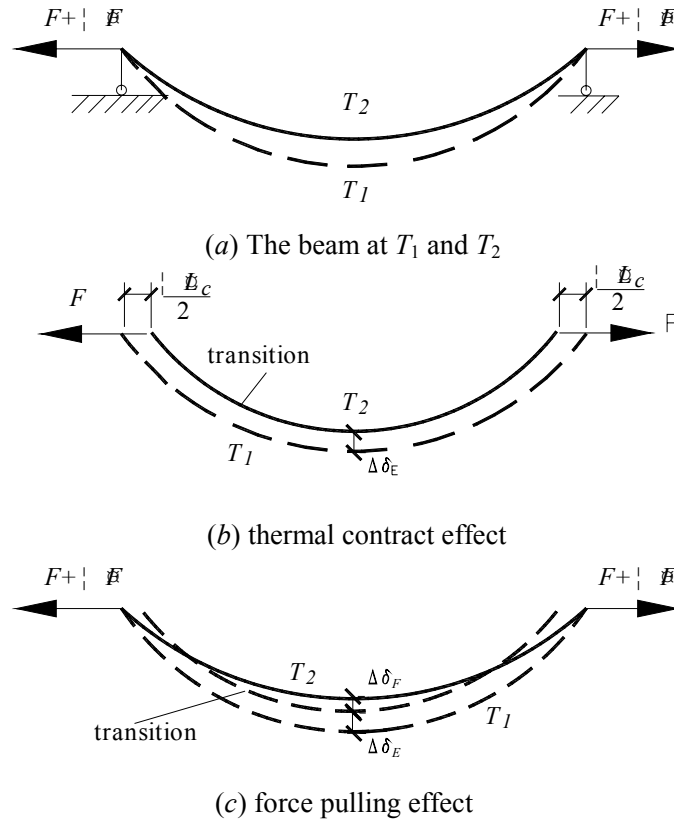


Fig. 5 Division of the change of the restrained beam during cooling

5.1 Deflection induced by recovery of the elastic modulus of steel

The stress-strain relation of steel when unloading is assumed to be as Fig.6. According to the theory of El-Rimawi et al^[9] about strain reversal when temperature decreases, the stress and strain can be assumed to change as shown in Fig.7. The plastic strain at both temperatures T_1 and T_2 is the same as ε_y . At temperature T_2 , when the stress is σ_{y1} , the strain is $(\varepsilon_{T1} - \sigma_{y1} / E_{T1} + \sigma_{y1} / E_{T2})$.

According to the above assumption about strain reversal during cooling, the change in deflection of restrained beams due to recovery of the elastic modulus can be analyzed approximately by the following method, as shown in Fig.8. At T_1 , the change in mid-span deflection with the load increasing follows the track OA . Using a factor δ_T to relate the mid-span elastic deflection to the load as below:

$$s_{T_1} = \frac{\delta}{p} = \frac{c_L}{E_{T_1}} \quad (15)$$

where c_L is a factor dependent on the span of the beam and the type of loads on the beam.

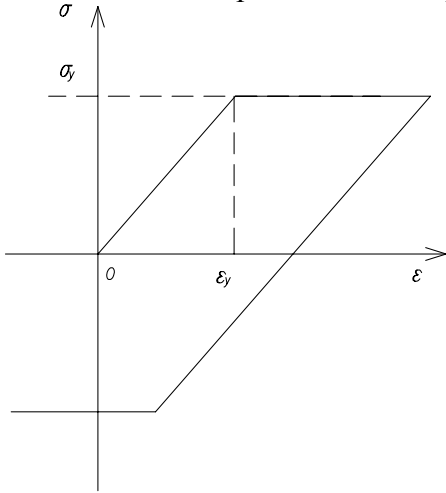


Fig. 6 Stress-strain curve of steel when unloading

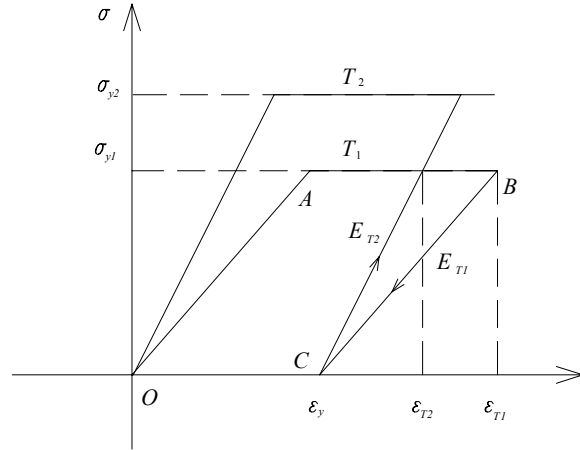


Fig. 7 Reversal of stress in cooling

Suppose the deflection of the beam at temperature T_1 is δ_{T_1} . When temperature decreases, if the plastic deflection is maintained, the deflection will follow the track $A-C-B$, as shown in Fig. 8. Then the deflection at temperature T_2 can be determined by:

$$\delta_{T_2} = \delta_{T_1} - ps_{T_1} + ps_{T_2} \quad (16)$$

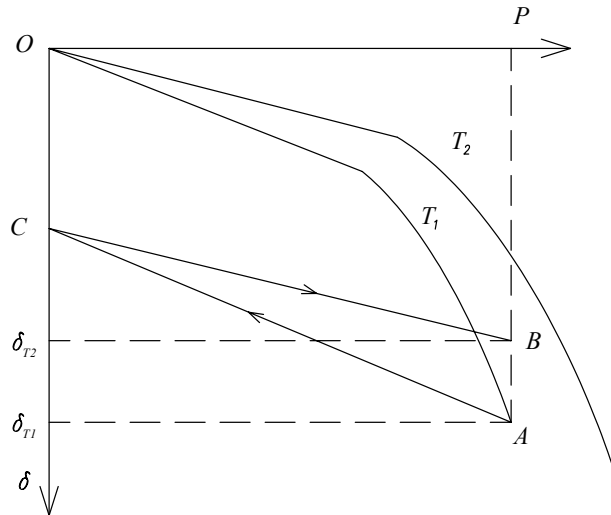


Fig. 8 Deflection reversal of restrained beam

At ambient temperature, under the action of p , the displacement is given by

$$\delta_0 = s_0 p = \frac{c_L}{E_0} p \quad (17)$$

According to Eq.(15) and(17),

$$ps_{T_1} = \delta_0 E_0 / E_{T_1}, \quad ps_{T_2} = \delta_0 E_0 / E_{T_2}$$

Thus the mid-span deflection of the beam at temperature T_2 can be expressed as:

$$\delta_{T_2} = \delta_{T_1} - \delta_{rev,E} \quad (18)$$

where $\delta_{rev,E}$ is the deflection reversal induced by the recovery of the elastic modulus, given by

$$\delta_{rev,E} = \delta_0 E_0 \left(\frac{1}{E_{T_1}} - \frac{1}{E_{T_2}} \right) \quad (19)$$

5.2 Contraction force generated by temperature decrease

In the second steps as shown in Fig. 5(c), the relative displacement of the ends of the beam is induced by the incremental tensile axial force, ΔF . Because the steel strength recovers with temperature decreasing, as shown in Fig. 9, then at the beginning the displacement change of the beam ends can be treated as elastic. After the plastic hinge occurs, the plastic displacement change of the beam is generated. Then the complete relative displacement change of the ends due to ΔF can be divided into two parts, i.e. the elastic part, Δu_e , and the plastic part, Δu_p . Accounting for the geometric compatibility, the following equation must be satisfied:

$$\Delta u_e + \Delta u_p = \alpha \Delta T L \quad (20)$$

where $\Delta T = T_2 - T_1$.

ΔF can be determined by:

$$\Delta F = \Delta u_e k_{e,ae} + \Delta u_p k_{e,ap} \quad (21)$$

where $k_{e,ae}$ is the effective axial restraint stiffness when the beam is in elastic state; and $k_{e,ap}$ is the effective axial restraint stiffness when the beam is in plastic state.

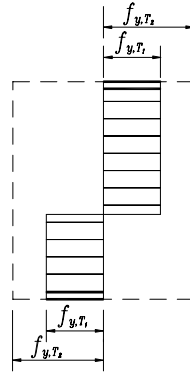


Fig. 9 Recovery of steel strength with temperature decreasing

5.3 The deflection reversal due to contraction force

When the steel temperature decreases from T_1 to T_2 , if ΔF is not so large to lead the beam into plastic, the deflection reversal of the beam induced by ΔF can be obtained with the energy conservation principle^[11]:

$$\delta_{rev,F} = \frac{2}{E_{T_2} I} \int_0^{\frac{L}{2}} \left(\frac{1}{2} x \right) [f(x) \Delta F] \sqrt{1 + (f'(x))^2} dx$$

for simply-supported beams (22a)

$$\delta_{rev,F} = \frac{2}{E_{T_2} I} \int_0^{\frac{L}{2}} \left(\frac{L}{8} - \frac{1}{2}x \right) [M_c - f(x)\Delta F] \sqrt{1 + (f'(x))^2} dx$$

for rotationally restrained beams (22b)

$$\text{where } M_c = \frac{\Delta F \int_0^L \sqrt{1 + f'(x)^2} f(x) dx}{\int_0^L \sqrt{1 + f'(x)^2} dx}.$$

5.4 The total deflection during cooling

When temperature decreases from T_1 to T_2 , given ΔF is small and the plastic hinge does not occur, the total deflection of the beam at temperature T_2 can be determined by

$$\delta_{T_2} = \delta_{T_1} - \delta_{rev,E} - \delta_{rev,F} \quad (23)$$

If ΔF is very large and the plastic hinge occur, the deflection of the beam has to be worked out through the equilibrium equation of the beam. For a beam with end rotation fully restrained, assume M_{mid} and M_{end} to be M_p , then the deflection of the beam at temperature T_2 can be derived from Eq.(1):

$$\delta_{T_2} = \frac{M_{eff} + 2M_p}{F} \quad (24)$$

where M_p is the plastic moment capacity of the beam at temperature T_2 .

Similarly, for a simply-supported beam,

$$\delta_{T_2} = \frac{M_{eff} + M_p}{F} \quad (25)$$

The complete behaviour of the restrained beam during fire cooling can be analyzed step by step, until the steel temperature decreases to ambient.

6. VALIDATION

In order to validate the method proposed in this paper, the performance of a restrained steel beam in fire cooling predicted by this method is compared with the results obtained by FE method. The section of the beam is H400X200X8X12, and the span is 8m. The lateral displacement of the beam is supposed to be fully restrained, so no lateral buckling will occur. The steel of the beam is Q235, of which the yield strength is 235MPa, and the steel property at elevated temperature is determined according to the EUROCODE 3^[12]. The rotations of the ends are fully restrained, and the axial stiffness of the restraints is $0.1k_b$. The uniform distributed load applied on the beam is 33.33kN/m, which gives a load ratio of 0.7.

The FE analysis is carried out by ANSYS 6.0^[13], a commercial FE package. The comparisons of the developments of the deflection and axial force obtained by the proposed method and FE method are shown respectively in Fig.10 and Fig.11. The beam is firstly heated and then cooled down from 600°C.

It can be seen that the predictions by the method proposed in this paper and the FE method are in accordance.

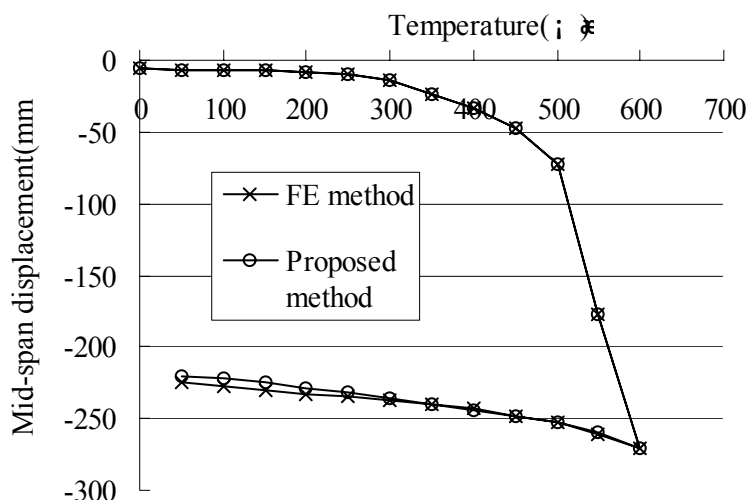


Fig. 10 Comparison of deflections predicted by FE method and the proposed method

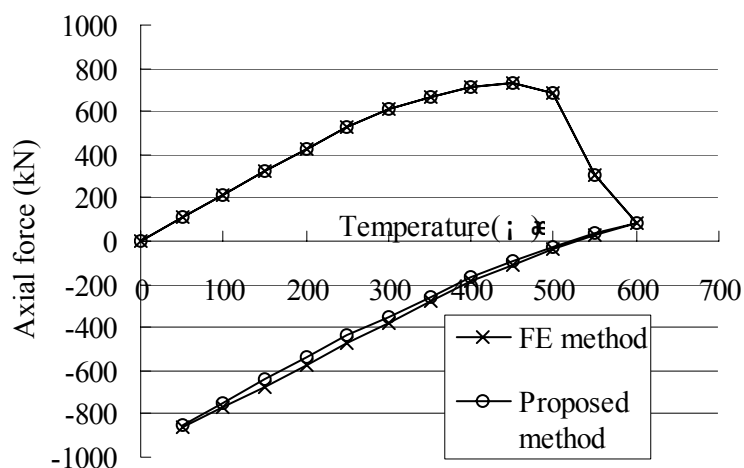


Fig. 11 Comparison of axial forces predicted by FE method and the proposed method

7. CONCLUSION

In this paper, the performance of restrained steel beams during fire cooling is investigated. A practical incremental method for analyzing this performance is proposed. Using this approach, the developments of deflection and axial force in a restrained steel beam during fire cooling can be simply obtained. The effectiveness of the method proposed is validated by FE method.

8. REFERENCES

- [1] Steel Construction Institute. (1991) *Structural fire engineering investigation of Broadgate phase 8 fire*. June, Ascot.
- [2] Wang Y.C. (2002), *Steel and Composite Structures: Behaviour and design for fire safety*. Spon Press, London.
- [3] Li G.Q., He J.L. and Jiang S.C. (2000), "Fire-resistant experiment and theoretical calculation of a steel beam". *China Civil Engineering Journal*, 32(4), 23-26.

- [4] Liu T.C.H., Fahad M.K. and Davies J.M. (2002), "Experimental investigation of behaviour of axially restrained steel beams in fire". *Journal of Constructional Steel Research*, 58(9), 1211-1230.
- [5] Huang Z.F. and T K.H. (2002), "Structural response of a steel beam with a frame during a fire", *Proceedings of the Third International Conference on Advances in Steel Structures*, Vol. II, 1111-1118.
- [6] Yin Y.Z., Wang Y.C. (2004), "A numerical study of large deflection behaviour of restrained steel beams at elevated temperatures", *Journal of Constructional Steel Research*, 60(7), 1029-1047.
- [7] Yin Y.Z., Wang Y.C. (2005a), "Analysis of catenary action in steel beams using a simplified hand calculation method, Part 1 : theory and validation for uniform temperature distribution", *Journal of Constructional Steel Research*, 61(2), 188-211.
- [8] Yin Y.Z., Wang Y.C. (2005b), "Analysis of catenary action in steel beams using a simplified hand calculation method, Part 2 : validation for non-uniform temperature distribution", *Journal of Constructional Steel Research*, 61(2), 213-234.
- [9] El-Rimawi J.A., Burgess I.W. and Plank R.J. (1996), "The treatment of strain reversal in structural members during the cooling phase of a fire", *Journal of Constructional Steel Research*, 37(2), 115-134.
- [10] Baily C.G., I. Burgess W. and Plank R.J. (1996), "Analyses of the effect of cooling and fire spread on steel-framed buildings", *Fire Safety Journal*, 26(4), 273-293.
- [11] Li G.Q. and Guo S.X. "Analysis of restrained steel beams subjected to temperature increasing and descending". The third International symposium on steel structures. Korea, 2005.3.
- [12] European Committee for Standardization (CEN). DAFT ENV 1993-1-2, Eurocode 3: *Design of steel structures, part 1.2 : General rules/structural fire design*, 2001.
- [13] ANSYS. Structural analysis guide. ANSYS Inc. 2002.



MECHANICAL PROPERTIES OF THIN STEELS AT ELEVATED TEMPERATURES

Thanuja RANAWAKA¹ and Mahen MAHENDRAN²

ABSTRACT

In recent times, light gauge cold-formed steel sections have been used extensively in residential, industrial and commercial buildings as primary load bearing structural components. This is because cold-formed steel sections have a very high strength to weight ratio compared with thicker hot-rolled steel sections, and their manufacturing process is simple and cost-effective. Despite the importance of fire safety design of building structures, the buckling behaviour of light gauge cold-formed steel members under fire conditions is not well understood. Therefore a research project was undertaken to investigate the buckling behaviour of light gauge cold-formed steel structures under axial compression. As the first step in this research project, mechanical properties of thin, cold-formed steels were determined at elevated temperatures. Tensile coupon tests were undertaken to determine the mechanical properties (yield stress and modulus of elasticity) and the stress-strain curves for a range of thicknesses, 0.6, 0.8 and 0.95 mm, made of both lower and higher grade steels (G250 and G550 steels). Steady state tests were undertaken at temperatures in the range of 20 to 800°C. Test results showed that significant deterioration of these important mechanical properties occurred at elevated temperatures depending on the steel grade. Currently available reduction factors cannot be used safely for thin cold-formed steels. This paper presents the details of the experimental investigation and the results.

1. INTRODUCTION

A greater understanding of the mechanical properties of steel enables the development of accurate and cost effective fire design methods for steel structures. The mechanical properties of light gauge cold-formed steels reduce significantly with increasing temperatures. The deterioration of the mechanical properties, yield strength and elasticity modulus, affects

¹ PhD Student, Queensland University of Technology, School of Urban Development, GPO Box 2434, Brisbane, QLD 4001, email: t.ranawaka@qut.edu.au

² Professor of Structural Engineering, Queensland University of Technology, School of Urban Development, GPO Box 2434, Brisbane, QLD 4001, email: m.mahendran@qut.edu.au

the strength of cold-formed steel structures significantly. However, the deterioration of the mechanical properties of light gauge cold-formed steels at elevated temperatures has not been investigated adequately. This is despite the fact that light gauge cold-formed steels are commonly used in Australia. Therefore an improved knowledge and understanding of mechanical properties at elevated temperatures is required to improve the available design methods or to develop new design methods. Hence an extensive experimental study into the deterioration of mechanical properties of light gauge cold-formed steels at elevated temperatures was conducted to derive accurate reduction factors of mechanical properties.

2. EXPERIMENTAL INVESTIGATION

Lee et al. (2003)¹ undertook a series of tensile coupon tests at elevated temperatures to determine the mechanical properties of light gauge cold-formed steels at elevated temperatures. However, it was found that the strain and temperature measuring methods they adopted in the experiments were not adequate and hence their measured values and the developed equations were not accurate. Therefore improved test methods and devices were used in this research to determine the mechanical properties and stress-strain curves at elevated temperatures accurately.

Strain gauges and/or conventional extensometers can be attached to the tensile coupon specimens in their testing at ambient temperature. However, these two methods have some drawbacks at elevated temperatures. In order to eliminate these shortcomings, a contact free Laser Speckle Extensometer which was developed by the Austrian Company Messphysik GmbH was used in this research project. This new expensive device gives accurate results even at very high temperatures when the overall test set-up is provided adequately.

2.1 Test Method

Three types of test methods are currently used to investigate the behaviour of steel structures under fire conditions, namely, steady-state test, transient-state test and ISO test (ISO, 1999)². Both the transient state and ISO test methods are based on temperature variations under a constant load while the steady state method is based on a constant temperature with increasing load. In this research, the steady state test method was used to determine the mechanical properties of light gauge cold-formed steels due to its simplicity and accurate data acquisition. Many other researchers have also used the steady state test method for the same reasons (Feng et al., 2003³, Outinen, 1999⁴). On the other hand Outinen (1999) and Lee et al. (2003) carried out both steady state and transient state tests and showed that the difference between steady state and transient state test results is negligible.

2.2 Test Specimen

The dimensions of tensile test specimens were decided based on AS 1391 (SA, 1991)⁵ as shown in Figure 1. Base metal thickness was determined for each specimen and was used in the mechanical property calculations. Both low and high strength steels were considered with nominal yield strengths of 250 MPa and 550 MPa, respectively. Temperatures were selected from 20°C to 800°C at different intervals for elevated temperatures. A total of 115 tests was undertaken in this study.

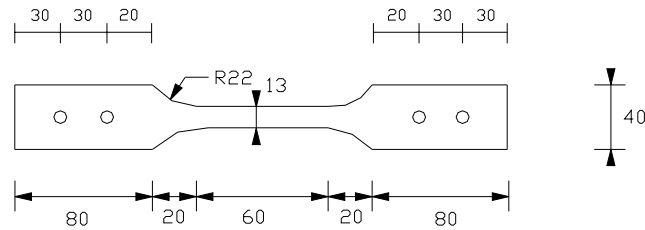


Figure 1 Dimensions of Tensile Test Specimens

2.3 Test Rig and Procedure

All the tensile coupon tests were carried out in the Structures Laboratory at the Queensland University of Technology. The available electrically heated furnace was used for the simulated fire tests in this research project. Figure 2 shows the test specimen inside the electrical furnace. Four glow bars were set inside the furnace so that the specimen was heated uniformly. Two thermocouples were used to measure the inside temperature. An additional thermometer was attached to the specimen to measure the specimen temperature during testing. The elevated temperatures selected in this study were 100°C, 200°C, 350°C, 500°C, 650°C and 800°C. The heating rates were set between 10°C/min and 25°C/min. The specimen temperature measured by thermometer and the air temperature measured by thermocouples were found to be the same.

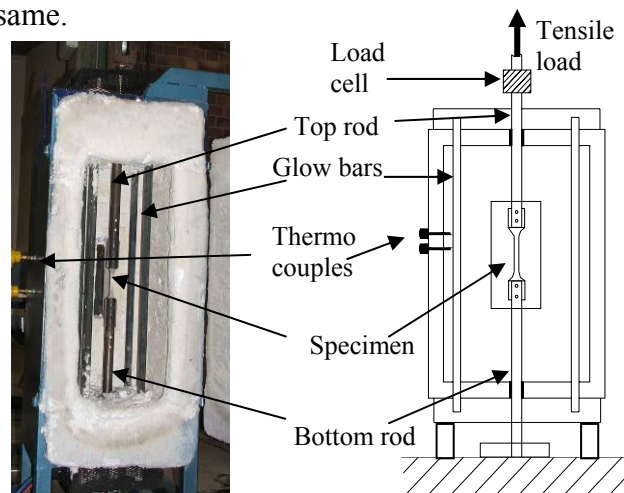


Figure 2 Test Rig

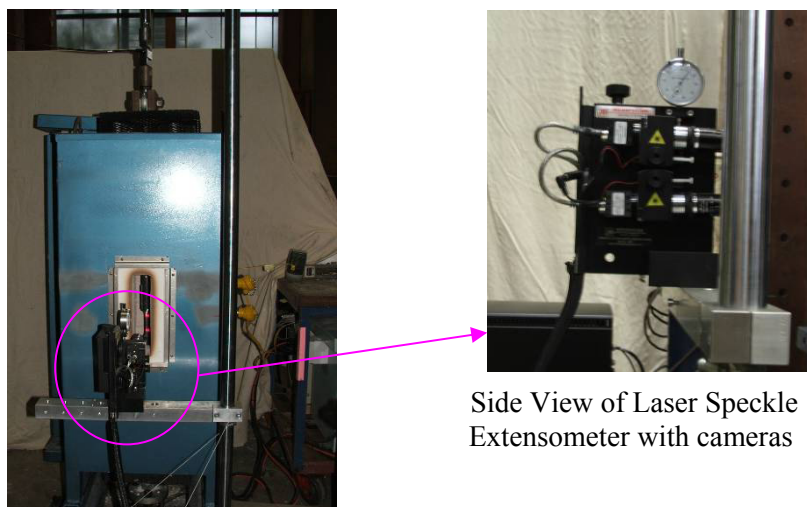


Figure 3 Test Set-up Showing Load Application and Strain Measurements

As shown in Figure 3 a laser speckle extensometer was located behind the furnace and was used to measure the strains in the middle of the specimen while the tensile load was being applied. The laser speckle extensometer contains a computer based video processor to measure the strains. The yield strength, the elasticity modulus and the stress-strain curves were obtained from the tensile test results.

3. DETERIORATION OF MECHANICAL PROPERTIES

3.1 Yield Strength

Normally the 0.2% proof stress method was used to determine the yield strength of steel at ambient temperatures. Most researchers used the 0.2% proof stress method while some of them used 0.5%, 1.5% and 2.0% of total strain to determine the yield strength at elevated temperatures. Therefore all of these methods were used in this study to determine the yield strength of light gauge cold-formed steels at elevated temperatures. Figure 4 shows the typical stress-strain curves obtained at ambient temperature. The yield strength based on the 0.2% proof stress method was measured from the intersection of the stress-strain curve and the proportional line off-set by 0.2% strain level. The strengths at 0.5%, 1.5% and 2.0% strain levels were measured from the intersection of stress-strain curve and the non-proportional vertical line specified at given strain values (see Figure 4).

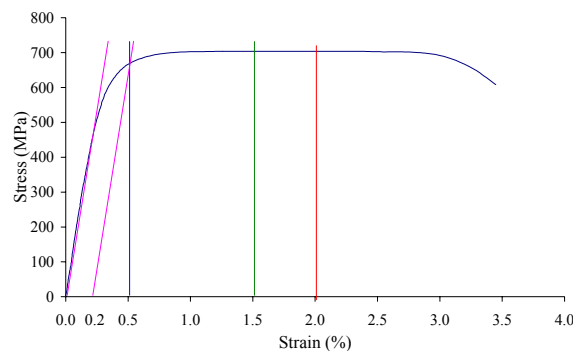


Figure 4 Typical Stress-Strain curve of 0.6 mm G550 steel at 20°C

The reduction factors at elevated temperatures were calculated as the ratio of yield strength at elevated temperatures ($f_{y,T}$) to yield strength at ambient temperature ($f_{y,20}$). They were determined based on various strain levels (Figure 4). Table 1 gives the yield strength reduction factors for 0.6 mm G550 steel for a range of strain levels while Figure 5 presents the yield strength based on 0.2% proof stress method for all the steels tested here. According to Figure 5, high strength steel shows higher reduction factors at low temperatures than low strength steels. Low strength steels lose their strength more rapidly at lower temperatures than high strength steels. There is a considerable difference in the degradation of yield strength between low and high strength steels in the range of 200°C to 500°C. However, when the temperature increases beyond 400°C, high strength steel loses its strength more rapidly than low strength steel. However, the steel thickness does not appear to have a significant influence on the reduction factors.

Table 1 Yield Strength Reduction Factors ($f_{y,T}/f_{y,20}$) based on Various Strain Levels

Temperature (°C)	0.6 mm G550 steel			
	0.2%	0.5%	1.5%	2.0%
20	1.000	1.000	1.000	1.000
100	0.970	0.968	1.000	1.000
200	0.956	0.947	0.996	0.994
350	0.838	0.814	0.897	0.896
500	0.403	0.402	0.461	0.471
600	0.118	-	-	-
650	0.097	0.099	0.105	0.107
800	0.030	0.030	0.031	0.031

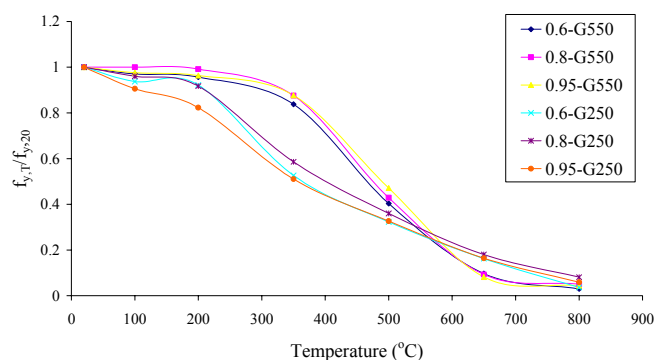


Figure 5 Yield Strength Reduction Factor versus Temperature for Different Steel Grades and Thicknesses

3.2 Elasticity Modulus

Elasticity modulus is also one of the most important mechanical properties needed in cold-formed steel design for fire safety. Therefore the elasticity modulus reduction factors were also measured with respect to the temperatures. The elasticity modulus was determined from the initial slope of the stress-strain curves. The reduction factors were then calculated as the ratio of the elasticity modulus at elevated temperature (E_T) to that at ambient temperature (E_{20}). Figure 6 shows the reduction factors of elasticity modulus versus temperature for both low and high strength steels. According to Figure 6 the influence of the steel grade or thickness is negligible.

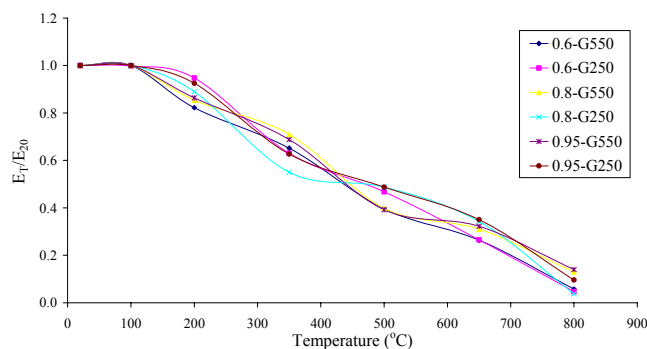


Figure 6 Elasticity Modulus Reduction Factors versus Temperature for Different Steel Grades and Thicknesses

4. DISCUSSION OF RESULTS

4.1 Comparison of Reduction Factors with Current Cold-formed Steel Design Standards

The yield strength and elasticity modulus reduction factors at elevated temperatures were compared with those in relevant cold-formed steel design standards. BS 5950-8 (BSI, 1990)⁶ and Eurocode 3 Part 1.2 (ECS, 1993)⁷ were considered for this purpose. Figure 7(a) shows the strength reduction factors for both low and high strength steels from this research, Eurocode (ECS, 1993) and BS 5950-8 (BSI, 1990). As shown in the figure there is a significant difference between the reduction factors obtained from this research and the current steel design standards. Figure 7(b) shows the comparison of elasticity modulus reduction factors from this research and Eurocode. The elasticity modulus reduction factors obtained from Eurocode overestimate the many values for both low and high strength steels.

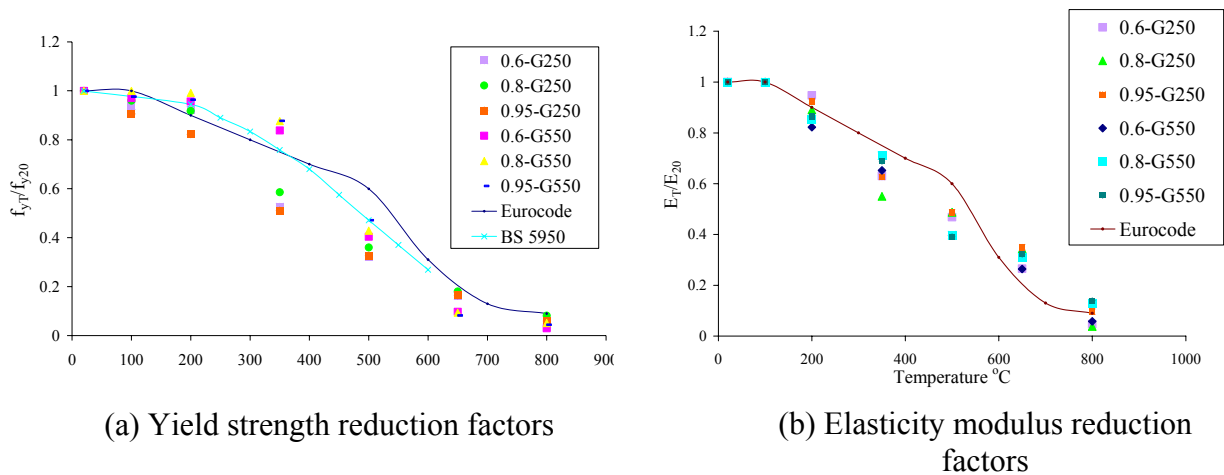


Figure 7 Comparison of Reduction Factors with Current Steel Design Standards

4.2 Comparison of Reduction Factors with Available Research Results

Outinen (1999) provided reduction factors for both yield strength and elasticity modulus by undertaking tests on 2 mm S350GD+Z (minimum yield strength of 350 MPa) steel specimens. Chen and Young (2004)⁸ also carried out high temperature tests to obtain the mechanical properties of 1 mm G550 steel and provided reduction factors for both yield strength and elasticity modulus. Both Outinen's (1999) and Chen and Young's (2004) values were compared with the reduction factors obtained from this research. Figure 8(a) compares the yield strength reduction factors obtained from this research and others' research results. The reduction factors presented by Chen and Young (2004) and Outinen (1999) for yield strength agree well for lower temperatures, but disagree for other temperatures. As shown in Figure 8(b) the elasticity modulus reduction factors presented by Chen and Young (2004) overestimate the reduction factors. Outinen's reduction factors agree reasonably well at some temperatures, but disagree at other temperatures.

In summary currently available reduction factors for both yield strength and elasticity modulus cannot be used in the design of light gauge cold-formed steel structures at elevated temperatures.

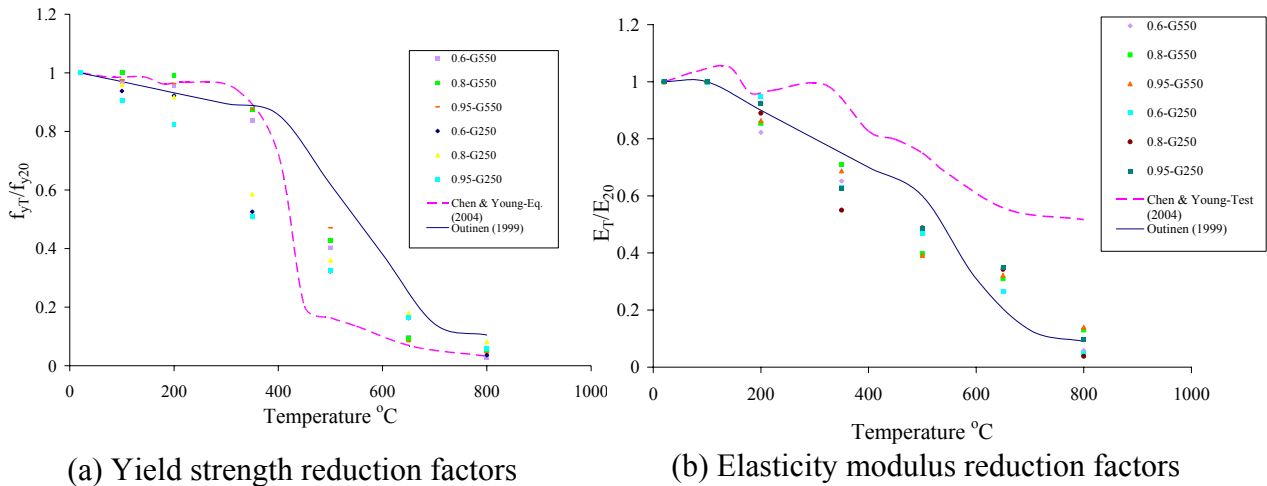


Figure 8 Comparison of Reduction Factors at Elevated Temperatures with Other Researchers' Results

4.3 Comparison of Reduction factors for Cold-formed and Hot-rolled Steels

As stated in the SCI Publication (1993)⁹, the reduction of strength of cold-formed steels at elevated temperatures is more than that of hot-rolled steels and is about 10 to 20%. The reduction factors stated in BS 5950-8 (BSI, 1990) also confirm this. In order to obtain the difference between the reduction factors of hot-rolled and cold-formed steels the available design standards, AS 4100 (SA, 1998)¹⁰ and BS 5950-8 (BSI, 1990) were considered. As shown in Figure 9 the yield strength and elasticity modulus reduction factors presented in AS 4100 and BS 5950-8 for hot-rolled steel overestimate the reduction factors of cold-formed steels obtained from this research in most cases. Therefore it is clear that the reduction factors obtained for hot-rolled steels cannot be used to design the cold-formed steel structures under fire conditions.

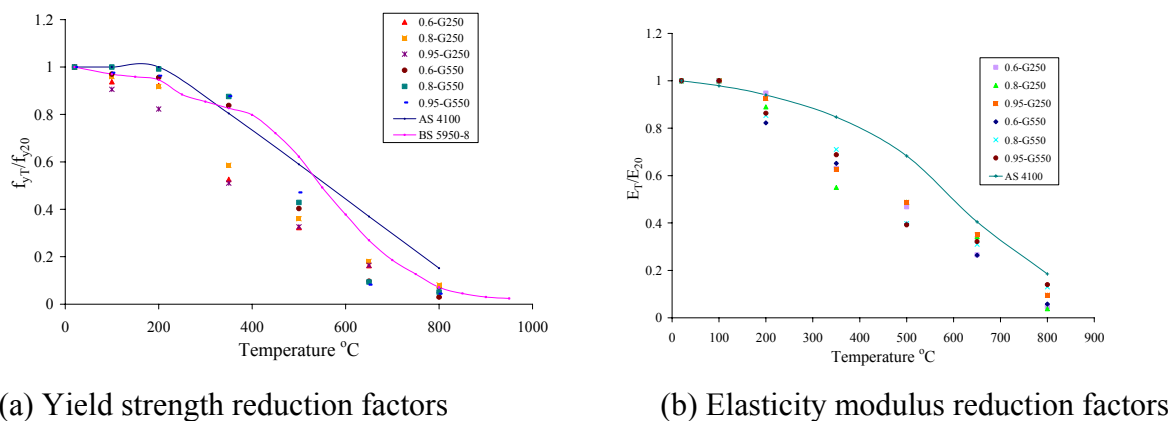


Figure 9 Comparison of Reduction Factors for Cold-formed and Hot-rolled Steels

5. PREDICTIVE EQUATIONS FOR MECHANICAL PROPERTIES

5.1 Yield Strength

Based on the yield strength results obtained from the tensile coupon tests at various temperatures, empirical equations were developed to determine the reduction factors for light gauge cold-formed steels. Since the temperature is the main factor causing the degradation of yield strength of steel, they were developed as a function of temperature. Other researchers (Olawale and Plank, 1998¹¹; Outinen et al., 1999 and SA, 1998) also determined the yield strength reduction factors as a function of temperature. The reduction factors obtained from the 0.2% proof stress method were used in deriving the empirical equations.

As shown in Figure 5, considerable differences were observed in the reduction factors of low and high strength steels. Therefore separate equations were developed for low and high strength steels. The reduction factors of high strength steels show three main regions while low strength steels show two main regions. The high strength steel shows a linear reduction in strength up to 200°C due to increasing temperatures. It then has a non-linear reduction due to the meteorological behaviour and the loss of strength gained due to cold-working. However, the latter effect is minimal up to about 500°C. Therefore the reduction factors of high strength steel are higher than that of low strength steel. However, the strength gain due to cold-working is lost when the temperature is above 500°C as seen by the sudden loss of strength (see Figure 5). Hence there is hardly any difference between low and high strength steels beyond 500°C. Three different equations were developed for high strength steels considering the three main regions. Since low strength steels do not have any strength gain due to cold-working it has only two regions. Therefore two equations were developed for them.

Equations 1(a) to (c) and, 2(a) and (b) present the reduction factors ($f_{y,T}/f_{y,20}$) for high and low strength steels, respectively. Figures 10(a) and (b) show the comparison of experimental results and the predictions of Equations 1 and 2, respectively. As shown in Figure 10 there is very good agreement between the test results and predicted values from Equations 1 and 2.

For G550 steels

$$\frac{f_{y,T}}{f_{y,20}} = -0.00016T + 1.0003 \quad 20^\circ C \leq T \leq 200^\circ C \quad (1a)$$

$$\frac{f_{y,T}}{f_{y,20}} = 0.97 - \frac{(T - 200)^{1.81}}{58500} \quad 200^\circ C < T < 600^\circ C \quad (1b)$$

$$\frac{f_{y,T}}{f_{y,20}} = -0.00037T + 0.3363 \quad 600^\circ C \leq T \leq 800^\circ C \quad (1c)$$

For G250 steels

$$\frac{f_{y,T}}{f_{y,20}} = -0.0007T + 1.014 \quad 20^\circ C \leq T \leq 200^\circ C \quad (2a)$$

$$\frac{f_{y,T}}{f_{y,20}} = 3.7 - \frac{(T - 74)^{0.15}}{0.736} \quad 200^\circ C < T \leq 800^\circ C \quad (2b)$$

where $f_{y,T}$ and $f_{y,20}$ are the 0.2% proof stress at elevated and ambient temperatures, respectively and T is the temperature.

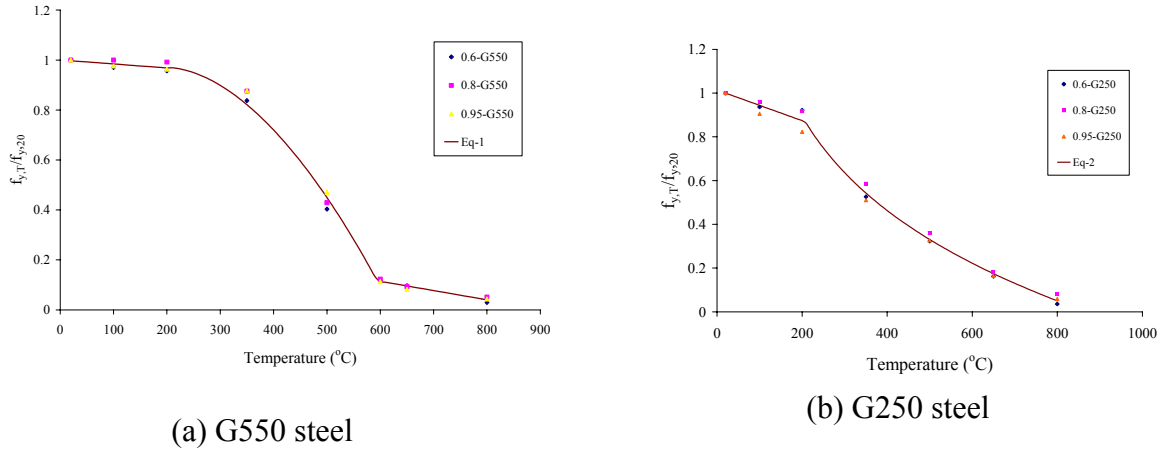


Figure 10 Comparison of Predicted Yield Strength Reduction Factors with Test Results

5.2 Elasticity Modulus

Elasticity modulus also deteriorates with the temperature as yield strength and is one of the important factors determining the buckling behaviour of light gauge steel members. Therefore empirical equations were developed for elasticity modulus with respect to temperature. Unlike in yield strength, the influence of steel grade is negligible on the reduction of elasticity modulus. The influence of steel thickness is also negligible. Therefore the steel grade and thickness were not considered in developing the predictive equations.

Experimental results show that the elasticity modulus remains the same up to about 100°C. Beyond this there is a linear reduction. Therefore a linear equation was generated to predict the elasticity modulus reduction factors at elevated temperatures (see Equation 3b). The calculated values from the equations are compared with the test values in Figure 11. It is clear that the predicted values agree well with the test results.

$$\frac{E_T}{E_{20}} = 1 \quad 20^\circ C \leq T \leq 100^\circ C \quad (3a)$$

$$\frac{E_T}{E_{20}} = -0.0013T + 1.1297 \quad 100^\circ C < T \leq 800^\circ C \quad (3b)$$

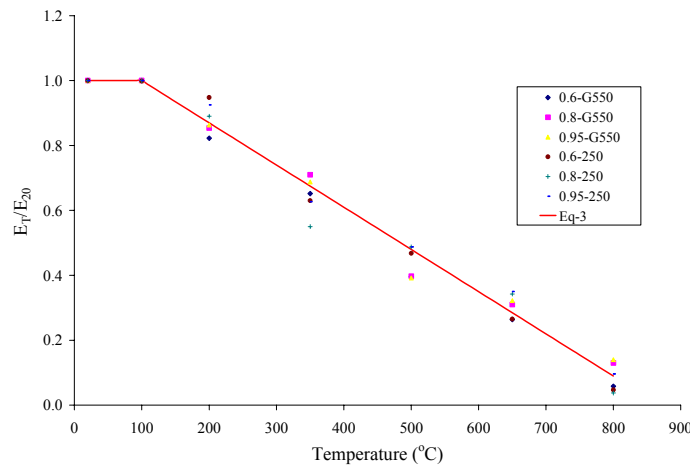


Figure 11 Comparison of Predicted Elasticity Modulus Reduction Factors with Test Results

6. CONCLUSION

This research was based on a detailed experimental study into the mechanical properties of thin cold-formed steels at elevated temperatures. Tensile coupon tests were undertaken for three different thicknesses and two different steel grades at seven different temperature levels to determine the important mechanical properties. The results showed that the steel grade has an influence on the yield strength while there is no clear relationship between the elasticity modulus and the steel grade or thickness. Current literatures including various steel design standards do not present accurate reduction factors for both yield strength and elasticity modulus of light gauge cold-formed steels at elevated temperatures. By considering all the results from this research, a new set of predictive equations was generated for both yield strength and elasticity modulus at elevated temperatures. The use of such accurate mechanical properties developed from this research will lead to safe design of light gauge cold-formed steel structures under fire conditions.

7. REFERENCES

- [1] Lee, J., Mahendran, M. and Makelainen, P. (2003) Prediction of Mechanical Properties of Light Gauge Steels at Elevated Temperatures, *Journal of Construction Steel Research*, pp. 1517-1532
- [2] ISO 834-1 (1999), *Fire-Resistance Tests-Elements of Building construction, Part 1-General Requirements*, International Organisation for Standardisation, Switzerland.
- [3] Feng, M., Wang, Y. C. and Davies J. M. (2003) *Structural Behaviour of Cold-formed Thin-walled Short Steel Channel Columns at Elevated Temperatures, Part 1: Experiments*, *Thin-Walled Structures*, Vol. 41, No. 6, pp.543-570.
- [4] Outinen, J. (1999) *Mechanical Properties of Structural Steels at Elevated Temperatures*, Licentiate Thesis, Helsinki University of Technology, Finland
- [5] Standards Australia (SA) (1991), AS 1391-1991, *Methods for Tensile Testing of Metal*, Sydney, Australia.
- [6] British Standards Institution (BSI) (1990), BS 5950, *Code of Practice for Fire Resistance Design, Structural Use of Steelwork in Building, Part 8*, London, UK.
- [7] Eurocode 3 (1996) CEN ENV 1993-1-2, *Design of steel structures, General rules, Structural Fire Design*, Brussels
- [8] Chen, J. and Young, B. (2004) *Mechanical Properties of Cold-formed Steel at Elevated Temperatures*, *Proceeding of Seventeenth International Speciality Conference on Cold-formed Steel Structures*, University of Missouri-Rolla, Orlando, Florida, USA, pp.437-465
- [9] Steel Construction Institute (SCI) (1993), *Building Design Using Cold Formed Steel Sections: Fire Protection*, Silwood Park, Ascot
- [10] Standards Australia (SA) (1998), AS 4100, *Steel Structures*, Sydney, Australia
- [11] Olawale, A.O. and Plank R.J. (1988), *The Collapse Analysis of Steel Columns in Fire Using a Finite strip Method*, *International Journal for Numerical Methods in Engineering*, 26, pp.2755-2764.



THE EFFECT OF PARTIAL FIRE PROTECTION LOSS ON THE FIRE RESISTANCE REDUCTION OF STEEL BEAMS

Yu KANG¹, George V. HADJISOPHOCLEOUS² and Heng AIK KHOO³

ABSTRACT

The spray-on protective coating is a frequently used fire protection of steel beams. Since the spray-on protective coating may be damaged during the service life of the protected beams, it is necessary to estimate the effect of this damage on the fire resistance of a steel beam. A numerical study was carried out to investigate the fire resistance reduction of protected steel beams caused by partial loss of spray-on fire protection. Hot-rolled I-shape steel beams according to CAN/CSA-G40.20/G40.21-98 specifications were used in this study. Heat transfer and structural analyses were conducted on the studied beams to predict the cross-section moment capacity of steel beams during the standard fire exposure. The study shows that partial loss of spray-on fire protection can cause a significant cross-section moment capacity reduction for protected steel beams exposed to the standard fire. The effect of fire protection loss on the cross-section moment capacity reduction is strongly dependent on the area of protection loss. Besides, the cross-section moment capacity reduction is also affected by several other factors, such as damage shape, damage location, damage penetration and the weight of steel section.

1. INTRODUCTION

It is known that unprotected steel structures do not have the desirable resistance against fire because the temperature of unprotected steel members increases rapidly due to the high thermal conductivity of steel. Spray-on insulation coatings are widely used to protect steel structures against fire because spray-on protective materials can efficiently slow down

¹ Research Associate, Carleton University, Department of Civil and Environmental Engineering, Ottawa, Canada,
email: ykang@connect.carleton.ca.

² Professor, Carleton University, Department of Civil and Environmental Engineering, Ottawa, Canada,
email: george_hadjisophocleous@carleton.ca.

³ Assistant Professor, Carleton University, Department of Civil and Environmental Engineering, Ottawa, Canada,
email: heng_khoo@carleton.ca.

heat transfer from the fire to the steel, and hence lower the rate of steel temperature increase. However, spray-on materials are often rather soft, and the protective coatings can be easily damaged during service, resulting in a possible fire resistance reduction for the steel member that is being protected. Thus, it is essential that the effect of partial protection damage on the fire resistance of steel members be understood.

A few numerical studies have been carried out to investigate the effect of partial spray-on protection damage. Tomecek and Milke [1] carried out a two-dimensional finite element study to investigate the effect of spray-on protection loss on the fire resistance of steel columns. Ryder et al. [2] conducted another investigation on the same subject by three-dimensional finite element analyses. These researches only focused on local steel temperature rise at the damaged region and used a temperature limit as the fire resistance criterion. Nevertheless, the effect of partial protection damage on the fire resistance of steel beams has not yet been investigated. Moreover, the investigation should look into the actual load-carrying capacity and deflection of steel members in order to obtain a more rational assessment of fire resistance. This study only looks at the reduction in the load-carrying capacity of steel beams during the ISO 834 standard fire exposure.

2. METHODOLOGY

This study focused on protected simply supported steel beams with partial loss of spray-on fire protection. Steel beams used in the study were CAN/CSA-G40.20/G40.21-98 [3] Grade 350W standard hot-rolled steel I-beams listed in CISC [4]. Five I-shape sections, W410×74, W410×60, W310×60, W310×39 and W250×24, were considered.

Spray-on mineral fiber was used as the fire protection of the steel beams. The fire protection was applied uniformly along the perimeter of the beam cross-section. Two protection thicknesses, representing 1- and 2-hour fire resistance ratings for a fully protected steel member, were considered in this study. The protection thickness was estimated using a simple equation provided by Lie [5], given as

$$d_i = \frac{25.4R}{(1.03W / D + 42)}, \quad (1)$$

where d_i (mm) is the thickness of protection, R (minute) is fire resistance, W (kg/m) is the weight of the steel section per unit length, D (mm) is the heated perimeter. Equation (1) was originally developed to estimate the protection thickness required for a designed fire resistance rating of a steel column subjected to the ASTM E119 standard fire exposure. It was adopted because the beams in this study were assumed to be exposed to fires on four sides, and the time-temperature curve of the ASTM E119 fire is very similar to that of the ISO 834 fire, especially in the first two hours.

The study was based on numerical analysis. A two-stage analysis, a heat transfer analysis followed by a structural analysis, was carried out on each studied beam to predict the cross-section moment capacity during the standard fire exposure. The numerical heat transfer analysis simulated the temperature rise of a steel beam exposed to the ISO 834 standard fire exposure, and the structural analysis calculated the cross-section moment capacity of a beam from the resulting temperature distributions.

In this study, standard fire resistance tests were simulated using two- and three-dimensional finite element analyses. There are two heat transfer processes involved in the standard fire resistance test modelling. One is heat transfer within the specimen, and the other one is the heat exchange at the specimen boundary. In this study, heat transfer within

the specimen is transient heat conduction in a solid body. Thermal properties of both steel and the fire protection material, including density, specific heat, thermal conductivity, and moisture content (for the fire protection material only), are needed in modelling the heat transfer process within a protected steel beam. Thermal properties of the spray on protective material were adopted from ECCS [6], and they are shown in Table 1. For the steel section, EC3 [7] recommended specific heat and thermal conductivity of steel at elevated temperatures were used, and the density of steel, which is 7850 kg/m^3 , was considered to be constant with temperature.

Table 1. – Thermal properties of spray-on mineral fibre material, from ECCS

Density (kg/m^3)	Thermal conductivity (W/mK)	Specific heat (J/kgK)	Equilibrium Moisture content (%)
300	0.12	1200	1

Heat exchange at the specimen boundary is by convection and radiation. The heat flux on the exposed surface, q'' (W/m^2), is given by

$$q'' = h_c (T_f - T_s) + \Phi \epsilon_{\text{res}} \sigma (T_f^4 - T_s^4) \quad \text{with} \quad (2)$$

$$\epsilon_{\text{res}} = \frac{\epsilon_f \epsilon_s}{\epsilon_f + \epsilon_s - \epsilon_f \epsilon_s}, \quad (3)$$

where h_c ($\text{W/m}^2\text{K}$) is the convection heat transfer coefficient, taken as $25 \text{ W/m}^2\text{K}$ for the standard fire (EC1 [8]), T_f (K) is the fire temperature, T_s (K) is the surface temperature, Φ is the view factor, conservatively taken as 1.0, σ is the Stefan-Boltzmann constant, ϵ_{res} is the resultant emissivity, ϵ_f is the flame emissivity, taken as 0.8 (Purkiss [9]), and ϵ_s is the surface emissivity, taken as 0.625 for the steel surface (Purkiss) and 0.9 for the fire protection surface (Ryder et al. [2]).

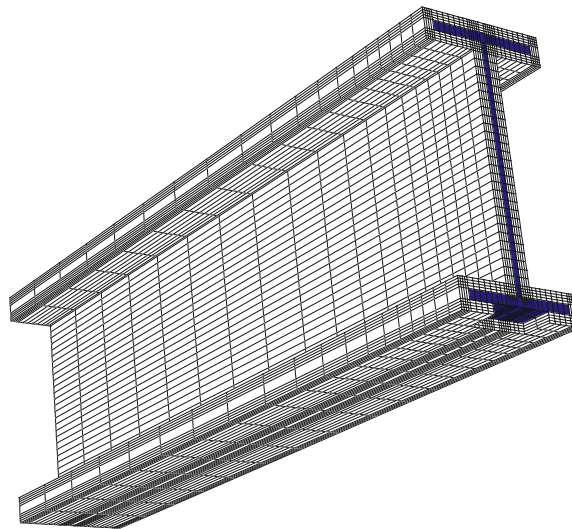


Fig. 1– Finite element heat transfer model of a beam with the bottom flange protection loss

The heat transfer analysis was implemented using finite element software ABAQUS [10]. Two-and three-dimensional finite element models were developed to model the ISO

834 standard fire tests. Two-dimensional models were used to model the cross-section of fully protected and unprotected steel beams, and three-dimensional finite element models were used to model protected beams with partial protection loss. Solid heat transfer elements DC2D4 and DC3D8 were employed respectively for two- and three-dimensional models. The three-dimensional models were symmetric models with the plane of symmetry passing through the mid-span of the beam. Figure 1 shows a three-dimensional model of a protected steel beam with partial protection loss on the flange. It can be seen that the fire protection loss was modeled by removing elements at the designed damage area. A standard fire test was simulated by conducting a transient heat transfer analysis on a finite element model. Heat flux at the model boundaries was calculated based on the ISO 834 standard time-temperature curve and the boundary conditions described by Equations (2) and (3). A user subroutine written in FORTRAN code was employed to apply heat flux on the boundary. The temperature profile of the steel beam during heating was obtained through the heat transfer analysis.

Since no experimental work was included in this study, test data for model validation were obtained from existing published literature. The test data from Ryder et al. [2] were used for model validation. The data were from a fire resistance test that measured the average steel temperature of a W250×73 (W10×49 in imperial designation) steel column covered with 19 mm of spray-on fire protection under an ASTM E119 standard fire exposure. Two two-dimensional heat transfer analyses were carried out to simulate this test; one was based on the ASTM E119 standard fire curve and the other one was on the ISO 834 standard fire curve. The measured average steel temperature and the results of the heat transfer analyses are compared in Figure 2. It can be seen that the modeled steel temperatures based on these two standard fire curves are similar, and they are in good agreement with the test data.

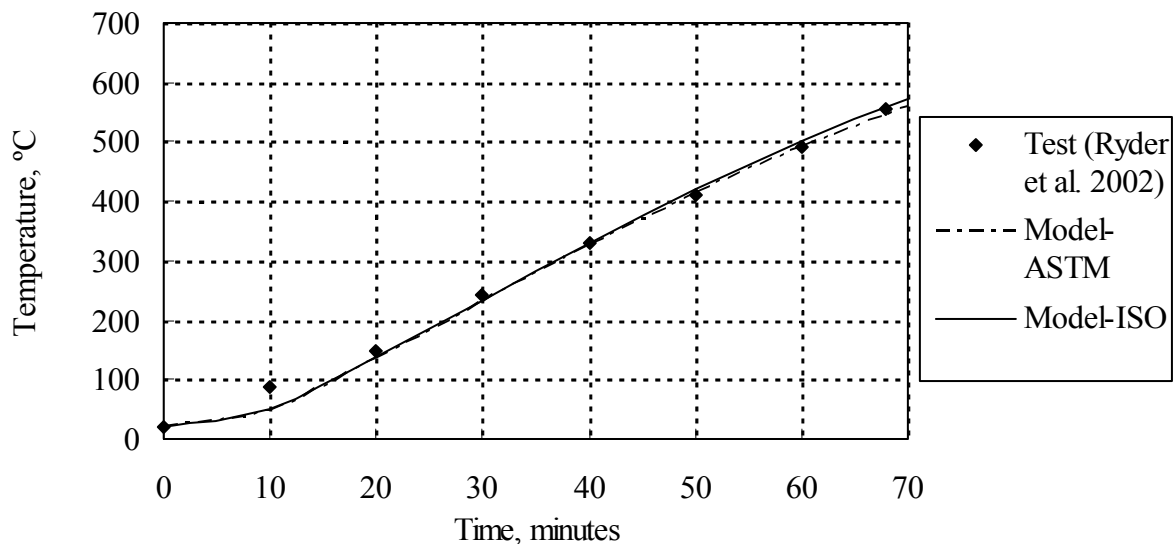


Fig. 2 – Average temperature of a W10×49 steel column with 19 mm of protection

The structural analysis was carried out based on the classical pure bending theory. When a beam is subjected to pure bending, the plane section initially perpendicular to the neutral axis of the beam remains plane and perpendicular to the neutral axis. For a cross-section with a non-uniform temperature distribution, the moment capacity M_f is given by

$$M_f = \sum_{i=1}^n \sigma_i A_i y_i, \quad (4)$$

where n is the number of elements in the cross-section, A_i is the area of element i , y_i is the distance from the neutral axis to the centroid of the element i and σ_i is the average stress of element i . For a steel beam cross-section with no residual stress and with an increasing curvature, the fibre furthest from the neutral axis yields first, and the yield moment $M_{y,f}$ can be given by

$$M_{y,f} = \sum_{i=1}^n \varepsilon_{y,T,0} k_{E,T,i} \frac{E A_i y_i^2}{Y_0}, \quad (5)$$

where $\varepsilon_{y,T,0}$ is the yield strain of the furthest fibre, Y_0 is the distance between the yielded fibre and the neutral axis and $k_{E,T,i}$ is the reduction factor of elastic modulus at steel temperature T_i . If the cross-section is able to undergo large rotation without any local buckling or distortional buckling, the plastic moment capacity may be reached. Thus, the plastic moment $M_{p,f}$ can be calculated by

$$M_{p,f} = \sum_{i=1}^n k_{y,T,i} f_y A_i y_i, \quad (6)$$

where f_y is the yield stress of steel at normal temperature and $k_{y,T,i}$ is the reduction factor of yield stress at steel temperature T_i . Since the study was confined to standard hot-rolled steel beams, it is unlikely that local buckling on the compression elements occurs before yielding is reached. Besides, steel sections are usually categorized into several classes in design codes, depending on the width-to-thickness ratio of their elements under compression. The width-to-thickness ratio limit is associated with the ratio of elastic modulus to the yield strength. This section classification concept was employed in the structural analysis, with the width-to-thickness ratio limit of a plate based on the reduced elastic modulus and yield strength at elevated temperatures.

The structural analysis was implemented using Visual Basic programs. The EC3 [7] mechanical model was adopted in the programs to describe the mechanical properties of steel at elevated temperatures. The temperature profile of a steel beam cross-section was the input data of a structural analysis. By carrying out a structural analysis, the moment capacity of a cross-section during a designed standard fire exposure was obtained.

3. RESULTS AND DISCUSSIONS

This study focused on the moment capacity reduction at the mid-span cross-section of a steel beam. Since the protection loss area is symmetric about the mid-span of a beam, when the beam is exposed to fire, the mid-span is expected to experience the largest reduction of moment capacity. In addition, the effect of protection loss on the cross-section moment capacity reduction along the length of a beam was also investigated.

3.1 W410x74 Beams

The relative cross-section moment capacities for fully protected W410×74 beams and W410×74 beams with symmetric bottom flange protection loss are plotted against

fire-exposure time in Figures 3 and 4, respectively for 1- and 2-hour fire resistance ratings. The relative cross-section moment capacity is the ratio of the cross-section moment capacity at elevated temperatures to that at normal temperature. The size of each protection loss in length \times length (cm \times cm) is provided in the figures, and the symbol L for beams 1BF11 and 2BF11 represents the full length of a beam. It can be clearly seen that the cross-section moment capacity of a beam with partial protection loss reduces faster than that of its fully protected counterpart. This result is due to the high local temperature profile at the mid-span cross-section due to the partial protection loss.

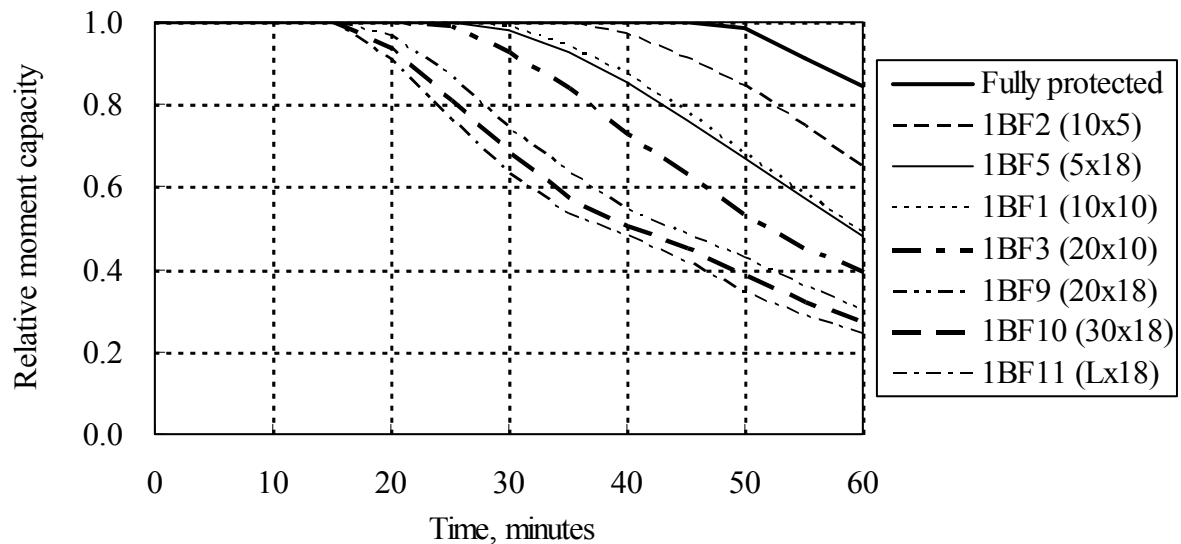


Fig. 3 – Relative cross-section moment capacities for 1-hour rating W410 \times 74 beams with full protection or with symmetric bottom flange protection loss

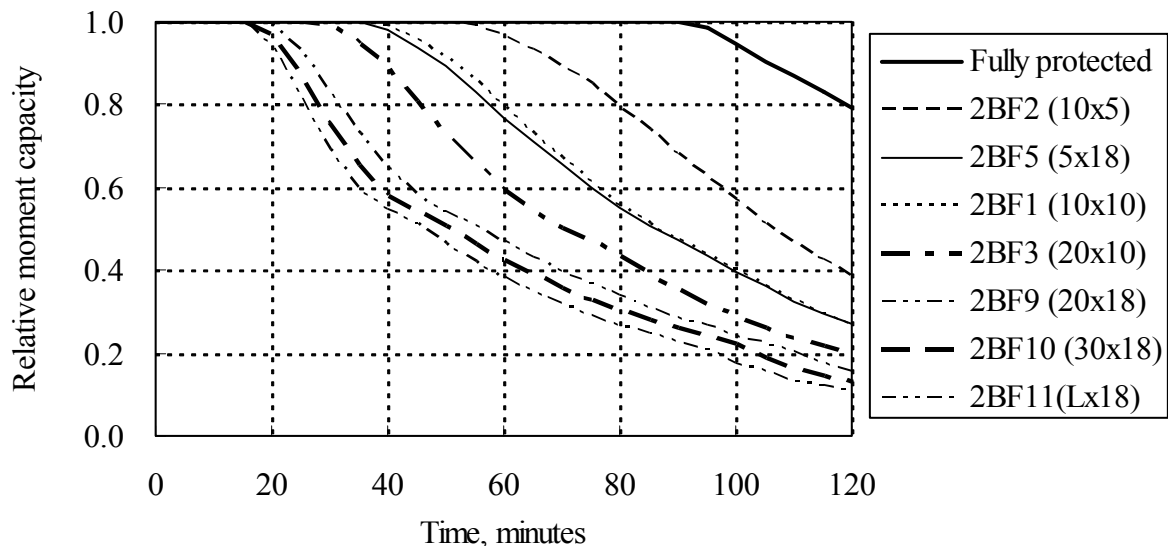


Fig. 4 – Relative cross-section moment capacities for 2-hour rating W410 \times 74 beams with full protection or with symmetric bottom flange protection loss

The reduction of cross-section moment capacity strongly depends on the area of protection damage; the larger the damage area, the greater the reduction of the moment capacity. For example, as shown in Figure 4, the cross-section moment capacity of beam

1BF3 (200 cm² protection loss) drops to 39% of its initial value after 1 hour of standard fire exposure, while that of beam 1BF2 (50 cm² protection loss) remains 65% after the same period of exposure.

The reduction of the cross-section moment capacity is also affected by the shape of the damage. The influence of damage shape can be found by comparing the results between beams 2BF4 and 2BF8 in Figure 5. Both beams 2BF4 and 2BF8 have a protection loss area of 180 cm², but the width to length ratio of the damage is 1.8 for beam 2BF4 and 0.56 for beam 2BF8. It is noted that the length of the damage is in the longitudinal direction of a beam. It can be seen that the cross-section moment capacity of beam 2BF4 decreases faster than that of beam 2BF8 during the first 100 minutes, but they decrease at nearly the same rate thereafter. The reason is related to the heat entering from the damage area. At the early stage of fire exposure, the fire temperature rises very fast, and the temperature of the bottom flange increases rapidly before the heat entering from the damage area is conducted away. Therefore, a wider damage shape leads to a faster rate of the local temperature increase in the mid-span cross-section due to a wider opening, resulting in a faster reduction rate of moment capacity. According to the time-temperature curve of the standard fire, the fire temperature rises very slowly after a certain time. As a result, the temperature profile of the mid-span cross-section becomes more uniform as time progresses. Thus, the influence of damage shape on the moment capacity reduction diminishes. These phenomena indicate that a larger width to length ratio of protection damage results in a greater reduction in the moment capacity during early stages of standard fire exposure, but this effect becomes smaller for longer fire-exposure time. Overall, the shape of the damage has much less influence than the area of the damage.

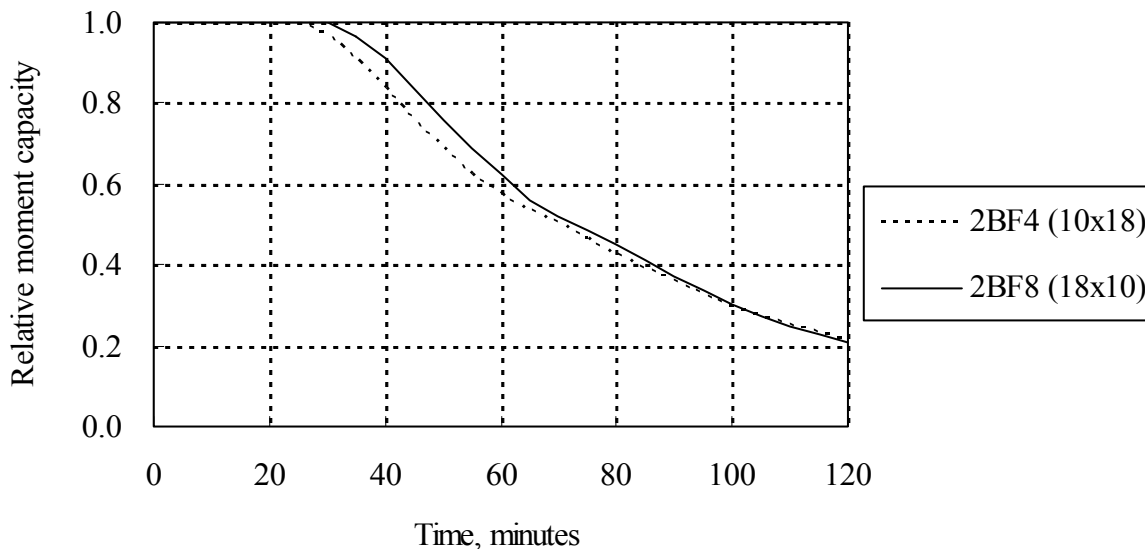


Fig. 5 – Relative cross-section moment capacities for W410×74 beams 2BF4 and 2BF8

Since the fire resistance reduction strongly depends on the area of protection loss, it is possible to characterize the fire resistance reduction using simple equations with respect to the area of protection loss. Hence, the reduction of fire resistance F_r is defined in terms of the ratio of the fire resistance of a beam to its original fire resistance rating, given as

$$F_r = 1 - \frac{R_f}{R_{f,0}}, \quad (7)$$

where R_f is the time taken for the moment capacity of a beam with a protection loss to drop to the level equal to a fully protected beam at its rated time, and $R_{f,0}$ is the fire resistance rating of the fully protected beam. Two equations are proposed in the following to describe the fire resistance reduction of W410×74 beams with the bottom flange protection loss respectively for 1- and 2-hour fire resistance ratings. For 1-hour fire resistance rating, the fire resistance reduction is given by

$$F_r = 0.635 - \frac{508}{(800 - A_L^{1.4734})}, \quad (8)$$

where A_L is the area of the protection loss. For 2-hour fire resistance rating, the fire resistance reduction is given by

$$F_r = 0.79 - \frac{316}{(400 - A_L^{1.4379})} \quad (9)$$

Figure 6 shows the fire resistance reductions from Equation (8) along with the analytical results.

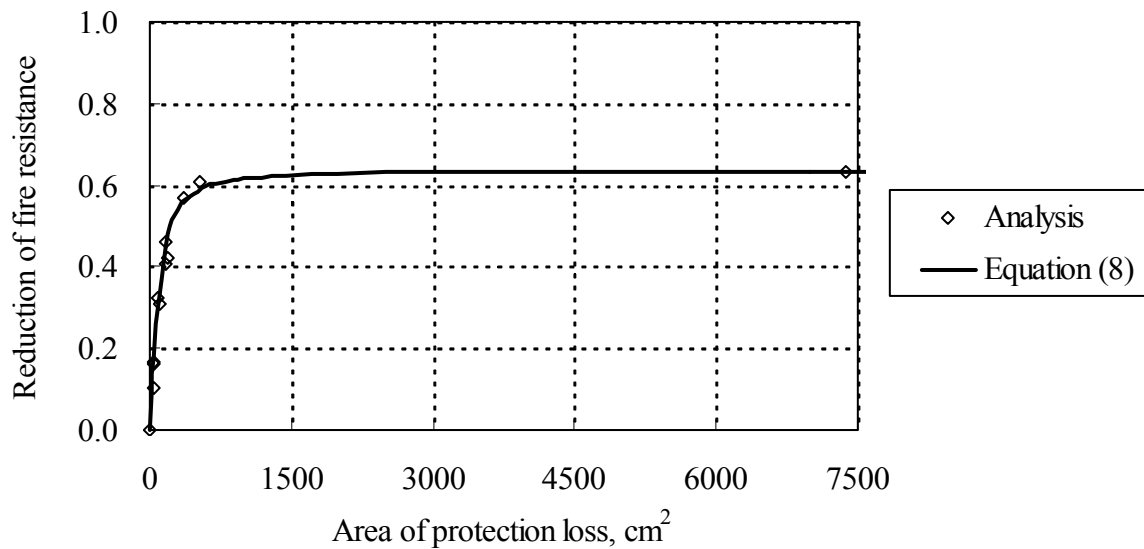


Fig. 6 – Fire resistance reductions of 1-hour rating W410×74 beams with the bottom flange protection loss

Figure 7 compares the reduction of the cross-section moment capacity for 1-hour rating W410×74 beams with protection loss on the bottom flange and on the web. It can be seen that the flange protection damage has a greater effect on the cross-section moment capacity reduction than the web protection damage. Even among the web protection loss, a protection loss close to the flange (1W2) has a greater effect on the moment capacity reduction than a protection loss at the mid-height of the web (1W1). This is to be expected since the difference in the moment capacity is related to the contribution of different regions of a cross-section to the cross-section moment capacity. Because the flange has a greater contribution to the cross-section moment capacity than the web, the weakening of the flange results in a greater reduction in moment capacity than the weakening of the web. Similarly, beams with the web protection loss closer to the flange have a greater effect on the moment capacity reduction than those with the protection loss at the mid-height of the web. On the other hand, protection loss on the top flange is found to have identical effect on the reduction of the cross-section moment capacity as that on the bottom flange. The reason is that the W410×74 section is stocky enough to reach the plastic moment capacity at elevated

temperatures regardless of whether the protection loss is on the bottom or top flange.

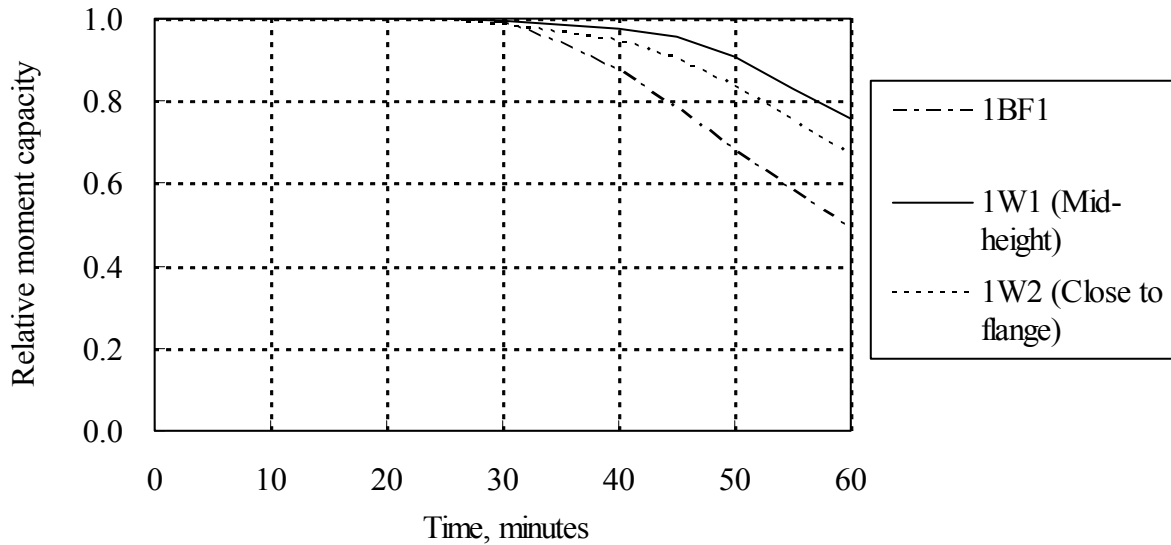


Fig. 7 – Relative cross-section moment capacities for 1-hour rating W410×74 beams with protection loss on the bottom flange or on the web

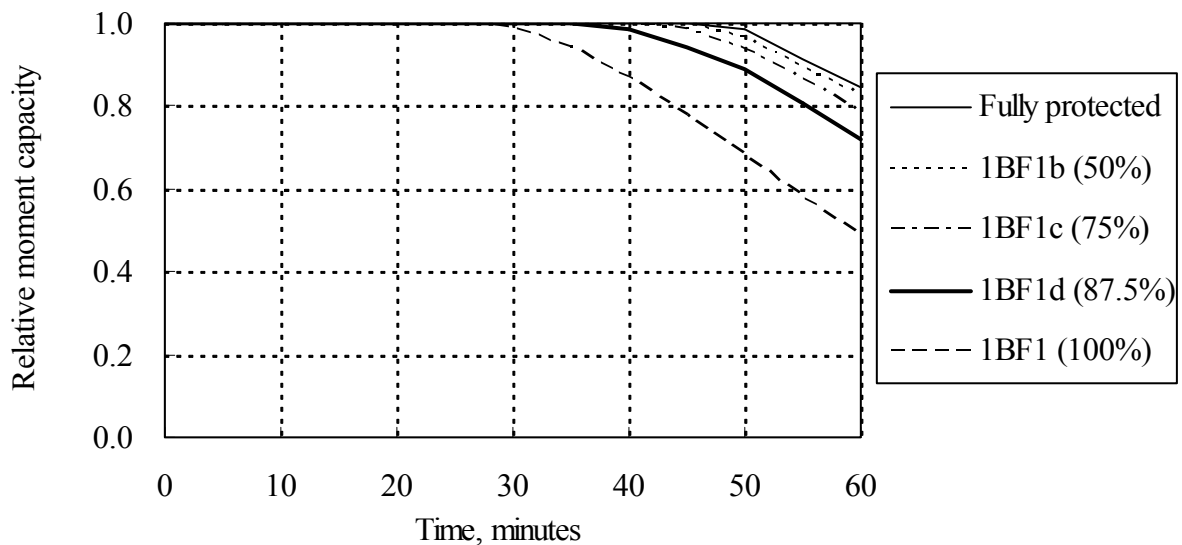


Fig. 8 – Relative cross-section moment capacities for 1-hour rating W410×74 beams with various depths of bottom flange protection loss

The effect of the penetration of the protection damage was also investigated. The investigation was carried out on W410×74 beams with a 10 cm × 10 cm size protection loss on the bottom flange. The damage penetration is respectively equal to 100%, 87.5%, 75%, or 50% of the designed protection thickness of a beam. Reductions of the cross-section moment capacity are compared in Figure 8 for 1-hour fire resistance rating beams. It can be seen that a deeper damage penetration results in a larger reduction of the cross-section moment capacity due to a standard fire exposure. Besides, it can also be observed that the effect of protection loss on the reduction of the cross-section moment capacity is relatively small if the damage does not fully penetrate the protective coating, even when the remaining protection at the damage area is very thin. For example, after 1 hour of standard fire

exposure, the relative cross-section moment capacity of beam 1BF1d (with a damage of 87.5% of the protective coating) is only about 15% lower than that of the fully protected beam. The reason may partly be attributed to the great difference between the conductivity of steel and the protective material, with the conductivity of steel being about 400 times higher. Hence, heat can be conducted in the steel section at a high rate, resulting in a relatively low temperature profile in the steel cross-section even with only a thin layer of protection at the damage area.

3.2 Beams of Different Sections

An investigation was conducted to compare the effect of protection loss between beams of different steel sections. Cross-section moment capacity reductions of protected steel beams associated with several other steel sections were predicted. Since the cross-section moment capacity reduction is different between fully protected beams of different sections but with identical fire resistance rating, a modified relative moment capacity is used in the comparison to make the effect of the protection loss comparable. The modified relative moment capacity is defined as the ratio of the cross-section moment capacity of a beam with protection loss to that of its fully protected counterpart.

Figure 9 compares cross-section moment capacity reductions between 1-hour rating W410×74 and W410×60 beams with symmetric protection loss of 10 cm × 10 cm size on the bottom flange. W410×74 and W410×60 beams have similar depths, but the weight per unit length of a W410×74 beam is 26% greater than that of a W410×60 beam. It can be seen that the moment capacity reduction of a W410×60 beam is greater than that of a W410×74 beam. Although not shown, similar result is found when comparing the moment capacity reduction between a W310×39 and a W310×60 beam. These results indicate that a beam of a lighter section has a greater reduction of the moment capacity in a fire than that of a heavier section if they both have an identical protection loss. The reason may be due to the heat capacity difference between a lighter section and a heavier section. This investigation suggests that Equations (8) and (9) have to be modified for different beam sections.

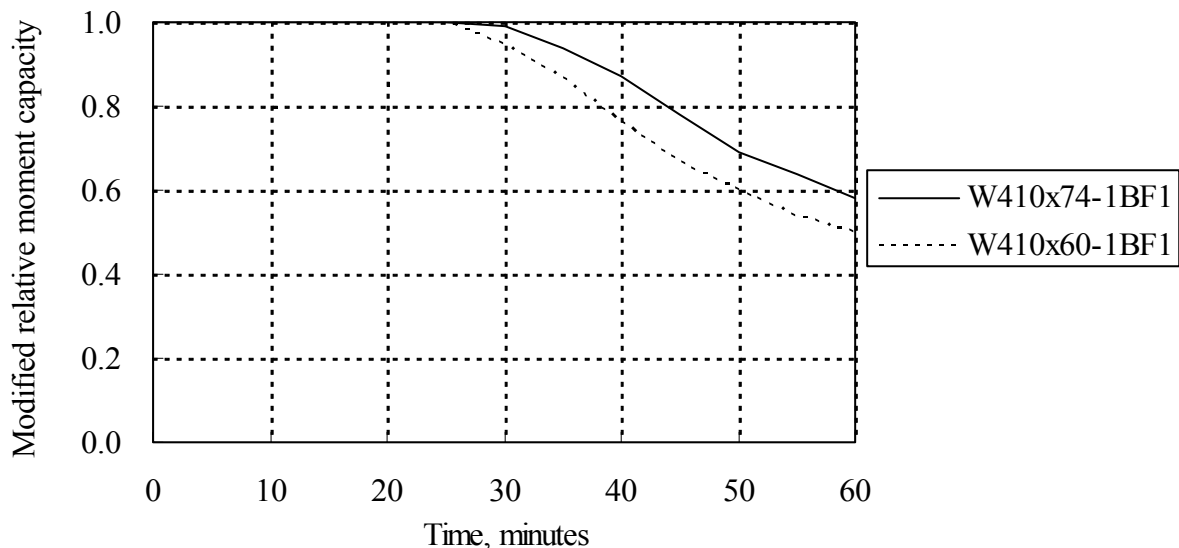


Fig. 9 – Modified relative cross-section moment capacities for 1-hour rating W410×74 and W410×60 beams with protection loss on the bottom flange

3.3 Cross-Section Moment Capacity along the Length

The influence of protection loss along the length of beams was also investigated. Figure 10 presents modified cross-section moment capacities along the length for 1-hour fire resistance rating W410×74 beams with symmetric bottom flange protection loss after 1 hour of standard fire exposure. It is noted that the origin of the abscissa in Figure 10 represents the centerline of the damage, and its value represents the longitudinal distance from the damage center along the length. The results confirm that the largest reduction of the moment capacity occurs on the mid-span of a beam. It can be seen that the effect of partial protection loss on the reduction of the moment capacity is very significant at cross-sections within the damage area. However, the effect of protection loss decreases rapidly with distance from the damage area. Taking beam 1BF4 for example, the modified relative cross-section moment capacity is only 0.46 at the edge of the damage area (50 mm from the damage center), and it increases to 0.89 at 200 mm from the damage center. For 1-hour fire resistance rating W410×74 beams, the affected distance is about 40 cm from the edge of the damage area after 1 hour of standard fire exposure.

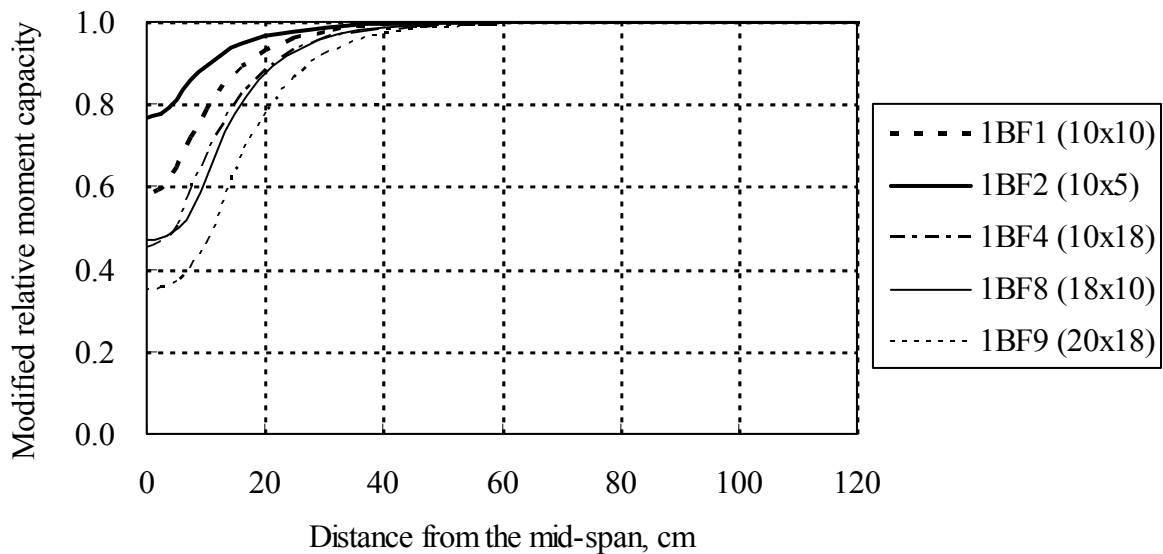


Fig. 10 – Modified relative cross-section moment capacities after 1 hour of standard fire exposure for 1-hour rating W410×74 beams with symmetric bottom flange protection loss

4. CONCLUSIONS

Overall, the study shows that partial loss of spray-on fire protection will cause a reduction of the cross-section moment capacity for protected steel beams exposed to the standard fire. The effect of fire protection loss on the cross-section moment capacity reduction strongly depends on the area of protection loss, and it is also affected by other factors, such as damage shape, damage location, damage penetration and section weight.

The reduction of the cross-section moment capacity strongly depends on the area of protection loss; the larger the area of protection loss, the greater the reduction in moment capacity. For W410×74 beams with the bottom flange protection loss at the mid-span, the fire resistance reduces rapidly with the damage area when the damage area is less than about 500 cm². The rate of reduction reduces as the damage area increases. The fire resistance reduction approaches a limit when the protective coating at the bottom is completely removed. This limit is about 0.635 for 1-hour original fire resistance rating W410×74 beams and about

0.79 for 2-hour original fire resistance rating W410×74 beams. The reduction of the cross-section moment capacity is also affected by the shape of protection damage. A larger width to length ratio of the damage results in a larger reduction of moment capacity during early stages of standard fire exposure, but this effect diminishes for a longer fire-exposure time. Overall, the effect of damage shape is much less than that of the area of the damage.

The reduction of the cross-section moment capacity also depends on the location of protection loss. The flange protection loss has a greater effect on the moment capacity reduction than the web protection loss. For beams with the web protection loss, the damage closer to the flange has a greater impact on the moment capacity reduction than that located away. For beams with a small area of protection loss, the depth of damage penetration has relatively minor effect on the cross-section moment capacity unless the damage has fully penetrated the protective coating. In addition, the influence of protection loss appears to be greater for a lighter steel section than for a heavier steel section.

On the other hand, the effect of partial protection loss on the moment capacity reduction is very significant at cross-sections within the damage area, but this effect decreases rapidly with distance from the damage area. The affected distance is about 40 cm from the edge of the damage area after 1 hour of standard fire exposure for 1-hour rating W410×74 beams.

5. REFERENCES

- [1] Tomecek, D.V. and Milke, J.A., "A Study of the Effect of Partial Loss of Protection on the Fire Resistance of Steel Columns," *Fire Technology*, Vol. 29, pp. 4-21, 1993.
- [2] Ryder, N.L., Wolin, S.D. and Milke, J.A., "An Investigation of the Reduction in Fire Resistance of Steel Columns Caused by Loss of Spray-Applied Fire protection," *Journal of Fire Protection Engineering*, 12: 31-44, 2002.
- [3] CAN/CSA-G40.20/G40.21-98, General Requirement for Rolled or Welded Structural Quality Steel/Structural Quality Steel, Canadian Standards Association, Rexdale, Ontario, Canada, 1998.
- [4] CISC, Handbook of Steel Construction, 8th Edition, Canadian Institute of Steel Construction, Willowdale, Canada, 2004.
- [5] Lie, T.T., Structural Fire Protection, American Society of Civil Engineers, New York, USA, 1992.
- [6] ECCS, Fire Resistance of Steel Structures, ECCS Technical Note No. 89, Technical Committee 3, European Convention for Constructional Steelwork, Brussels, Belgium, 1995.
- [7] EC3, Eurocode 3: Design of Steel Structures - Part 1-2: General Rules - Structural Fire Design, European Committee for Standardization, Brussels, Belgium, 1995.
- [8] EC1, Eurocode 1: Actions on structures - Part 1-2: General actions - Actions on structures exposed to fire, European Committee for Standardization, Brussels, Belgium, 2002.
- [9] Purkiss, J.A., Fire Safety Engineering Design of Structures, Butterworth-Heinemann, Oxford, UK, 1996.
- [10] ABAQUS Version 6.4.1, ABAQUS/ Standard User's manual, Hibbitt, Karlsson & Sorensen Inc, 2004.



HEATING OF ALUMINIUM MEMBERS EXPOSED TO NATURAL FIRE CONDITIONS

Johan MALJAARS¹, Frans SOETENS² and Leen TWILT³

ABSTRACT

Although the use of aluminium in structural applications has increased in recent years, the behaviour in fire is not yet well known. Compared to steel, the mechanical properties at elevated temperatures reduce more significantly. Therefore, fire design of aluminium structures requires considerable attention.

This paper considers heating of aluminium members on the basis of a Natural Fire Safety Concept. A parameter study was carried out to determine in which cases aluminium has to be insulated, to determine the relation between the critical temperature of the member and the required insulation thickness and to determine the influence of the application of active measures on the required insulation thickness for aluminium members.

1. INTRODUCTION

Aluminium alloys are applied more and more as material for load bearing members in structures such as fast ferries, living quarters on drilling platforms, helicopter decks, etc. Most aluminium alloys applied in such structures have a melting temperature between 550 and 600 °C. According to the data in the Eurocode for fire design of aluminium structures, EN 1999-1-2 [1], the strength of these alloys reduces from 80 to 20 % of the strength at room temperature between approximately 180 and 350 °C (figure 1). Based on a ratio between the extreme value of the design load at room temperature and the load in fire design of about 0,5,

¹ Ph.D. Researcher, TNO and Eindhoven University of Technology, The Netherlands, email johan.Maljaars@tno.nl

² Professor, TNO and Eindhoven University of Technology, The Netherlands, email frans.soetens@tno.nl

³ Senior researcher, TNO, The Netherlands, email leentwilt@hotmail.com

the critical temperatures of aluminium alloy members are approximately 150 up to 350 °C⁴. Because of these low temperatures aluminium structures are sensitive to fire.

To evaluate the fire resistance of a structure, either the standard temperature-time curve, or the Natural Fire Safety Concept (NFSC) as specified in the Eurocode for fire design, EN 1991-1-2, can be used [2]. The latter option may be advantageous for structures that are sensitive to fire, as the NFSC gives a more realistic approximation of the gas temperature. This is due to the fact that it considers the actual layout of the compartment. Moreover it provides the possibility to take active measures into account in the fire safety design.

This paper gives the results of a study on heating of aluminium members exposed to natural fire conditions for various compartments layouts. First, the layouts considered are presented together with the resulting gas temperature-time curves. Subsequently, the maximum temperature of unprotected aluminium members exposed to these temperature conditions are given. Finally, for each of the layouts, the insulation thickness required to maintain the temperature below the critical temperature is determined.

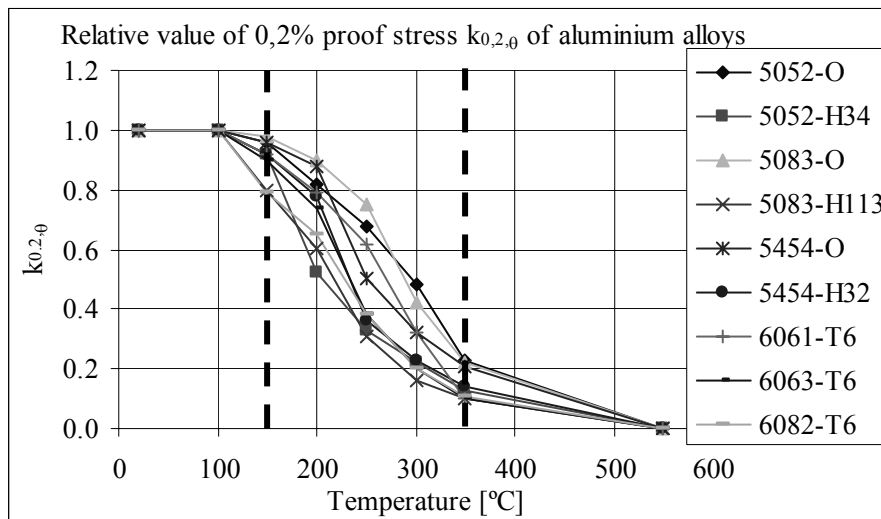


Fig. 1 – Relative strength of some aluminium alloys according to EN 1999-1-2

2. GAS TEMPERATURE FOR COMPARTMENTS CONSIDERED

2.1 Selection of fire parameters

The NFSC is developed in recent projects and co-sponsored by the EU. Some backgrounds on the NFSC are given in Schleich et al [3].

The NFSC takes into account the most important parameters influencing the temperature in a specific fire compartment. These parameters are:

- The compartment size;
- The ventilation condition, determined by the amount, size and height of the openings (windows and doors) in the compartment. The opening factor O , representing the ventilation condition, is defined according to equation (1);

⁴ According to EN 1999-1-2, it may be assumed that, using simple calculation models, no structural failure will occur if the temperature of the aluminium member does not exceed 170 °C

- The energy exchange between the compartment and the walls, ceiling and floor of the compartment (the boundary enclosure);
- The fire load density, defined as the potential energy of all combustible materials per unit floor area;
- The type of combustible material, determining:
 - o The maximum rate of heat release (RHR_f), defined as the maximum amount of energy released by the fire per unit time and per unit floor area;
 - o The fire growth rate (t_α) of the combustible material, i.e. the time [s] to reach a rate of heat release of 1 MW.

$$O = \frac{A_v \sqrt{h_{eq}}}{A_t} \quad \text{with} \quad h_{eq} = \frac{\sum_i A_{v,i} h_i}{A_v} \quad (1)$$

With: O = Opening factor [$\text{m}^{1/2}$];

A_v = Total area of vertical openings in all walls [m^2];

$A_{v,i}$ = Area of vertical opening 'i' [m^2];

A_t = Total area of boundary enclosure [m^2];

h_i = Height of vertical opening 'i' [m];

h_{eq} = Weighted average of window heights on all walls [m].

In most cases, the amount and types of combustible materials in a fire compartment during lifetime of the structure are not exactly known in the design stage and should be determined on the basis of a statistical analysis. Therefore, recommended values for the 80 % fractile of the characteristic fire load density ($q_{f, char, 0.8}$) are provided in EN 1991-1-2. These depend on the occupancy of the compartment. To determine the design fire load density ($q_{f, d}$), the characteristic fire load density should be multiplied by the following partial factors:

- Factor to take into account the risk of fire activation, based on the compartment floor area (δ_{q1});
- Factor to take into account the risk of fire activation, based on the type of activity (δ_{q2}) (e.g. manufactory of paints, museum etc);
- Factors to take into account the presence of active measures (δ_{ni}). Some active measures and their reduction factors are given in table 1, taken from EN 1991-1-2. When combining active measures, the respective factors shall be multiplied ($\Pi \delta_{ni}$).

Hence, the design value of the fire load density follows from:

$$q_{f, d} = q_{f, car} \cdot \delta_{q1} \cdot \delta_{q2} \cdot \Pi \delta_{ni} \quad (2)$$

(Symbols given above.)

Table 1 – Factors δ_{ni} on the fire load density for active fire fighting measures

Active measure	δ_{ni}
Water extinguishing system	0.61
+ 1 independent water supp	0.87
+ 2 independent water supp	or 0.7
Fire detection by heat	0.87
Fire detection by smoke	or 0.73
Automatic alarm transmission	0.87
Work fire brigade	0.61
Off site fire brigade	or 0.78
Staircase overpressure	0,9

In the current study, the gas temperature-time relations were evaluated for in total 72 compartments layouts. The fire parameters are selected in such a way, that a wide range of – realistic – temperature-time curves is obtained.

Two compartment sizes are considered:

- Length x width = 20 m x 10 m, height = 3 m with a flat roof. For this compartment, $\delta_{q1} = 1,47$;
- Length x width = 40 m x 20 m, height = 3 m with a flat roof. $\delta_{q1} = 1,7$. It should be noted that the NFSC was not validated for such a large compartment. Nonetheless, this case is considered because such large compartment sizes are applied often in practice.

Three occupancies are considered:

- Dwelling, with relatively high value for $q_{f, char, 0.8}$, equal to 948 MJ/m². Other fire parameters are: $RHR_f = 250 \text{ kW/m}^2$, $t_\alpha = 300 \text{ sec}$, $\delta_{q2} = 1,0$;
- Office, with an intermediate value for $q_{f, char, 0.8}$, equal to 511 MJ/m². $RHR_f = 250 \text{ kW/m}^2$, $t_\alpha = 300 \text{ sec}$, $\delta_{q2} = 1,0$;
- Transport (e.g. train station), with a low value for $q_{f, char, 0.8}$, equal to 104 MJ/m². $RHR_f = 250 \text{ kW/m}^2$, $t_\alpha = 600 \text{ sec}$, $\delta_{q2} = 0,85$.

Four opening configurations are considered. In the graphs in this paper, different opening sizes are indicated with different greyscales of the curves:

- The two walls in length direction of the compartment are open from floor to ceiling over their full length; no openings in the other walls. In case of the small compartment with a floor area of 20 m x 10 m: $O = 0,358 \text{ m}^{1/2}$. In case of the large compartment with a floor area of 40 m x 20 m: $O = 0,212 \text{ m}^{1/2}$;
- The two walls in width direction are open from floor to ceiling over their full length; no openings in the other walls. For the small compartment: $O = 0,179 \text{ m}^{1/2}$. For the large compartment: $O = 0,106 \text{ m}^{1/2}$;
- One wall in width direction is open from floor to ceiling over its full length; no openings in the other walls. For the small compartment: $O = 0,090 \text{ m}^{1/2}$. For the large compartment: $O = 0,053 \text{ m}^{1/2}$;
- One wall in width direction is open from floor to ceiling over half its length. For the small compartment: $O = 0,045 \text{ m}^{1/2}$. For the large compartment: $O = 0,027 \text{ m}^{1/2}$.

A lightweight boundary enclosure was applied for all layouts in combination with an insulation layer for the entire compartment. Similar boundary enclosures are applied regularly in living quarters on drilling platforms and ships.

Three sets of active measures are considered, indicated in table 2:

- Off site fire brigade, $\delta_n = 0,78$. In the figures, this set of active measures is indicated with solid diamonds;
- Off site fire brigade, automatic fire detection by smoke and automatic alarm transmission to the fire brigade, $\Pi\delta_n = 0,50$. In the figures, this is indicated with crosses;
- Off site fire brigade, detection by smoke, automatic alarm transmission and an automatic extinguishing system with one independent water supply, $\Pi\delta_n = 0,26$. In the figures, this is indicated with open triangles.

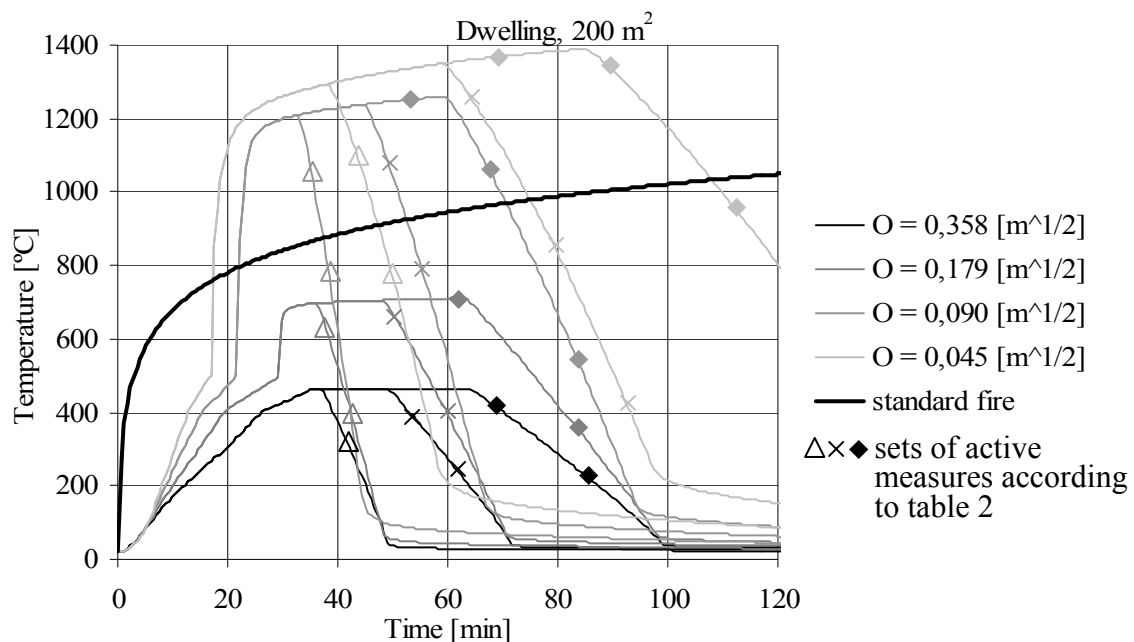
Table 2 – Reduction factors on the fire load density for active fire fighting measures

Active measure	$\Pi\delta_h$	0,78	0,50	0,26
	δ_h			
Water extinguishing system + 1 independent water supp	0.61			△
	0.87			△
Fire detection by smoke	or 0.73		×	△
Automatic alarm transmission	0.87		×	△
Off site fire brigade	or 0.78	◆	×	△

2.2 Resulting temperature-time curves

For each of the compartment layouts given above, the gas temperature was determined with the software OZONE vs. 2.2. With OZONE, the fire compartment is divided into two zones with uniform temperature per zone and a possible switch to one zone. The temperature in each zone is determined numerically. For some backgrounds, see Cadorin et al [4].

A selection of the resulting gas temperature – time curves is given in figures 2 and 3 for dwellings and transport buildings respectively. The different grey-scales indicate different opening factors. The curves marked by different symbols are the results of the sets of active measures applied⁵. In every case considered, the longer fires are the result of calculations with few active measures (only off-site fire brigade) and the shorter fires are the result of calculations with all active measures considered in this study. The black curve gives results of the standard temperature-time curve.

Fig. 2 – Gas temperature-time curves for dwelling occupancy with fire compartment 200 m²

⁵ Remember that, in the calculations, the effect of the active measures is accounted for via the fire load density.

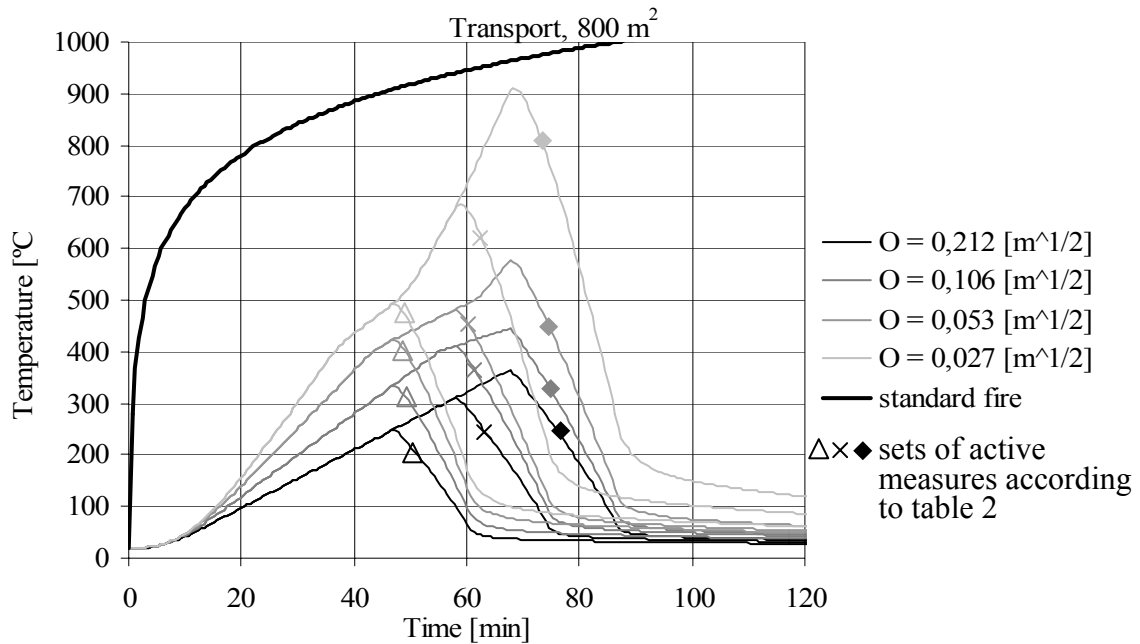


Fig. 3 – Gas temperature-time curves for transport occupancy with fire compartment 800 m²

Based on the results, it was concluded that for most layouts the opening factor influences the maximum temperature and the design fire load density mainly influences the fire duration. Only in case of very low fire load densities and a low fire growth rate, such as for the transport buildings, the maximum rate of heat release (RHR_f) is not yet reached at the end of the fire, so that the fire load density also influences the maximum temperature.

Depending on the layout of the compartment, the maximum temperature in the NFSC may be lower or higher than the temperature after two hours of exposure to the standard fire.

3. TEMPERATURE OF UNPROTECTED ALUMINIUM MEMBERS

3.1 Thermal properties of aluminium alloys

To determine the temperature of bare members exposed to the temperature curves of the previous paragraph, the thermal properties of aluminium have to be known. These properties are determined in tests for many alloys at room temperature. At elevated temperature, however, the test results given are in most cases limited to pure aluminium. The data given below origin from Kammer [5], Davis [6], Brandes [7], DinNenno [8] and Holman [9] and correspond with the values given in EN 1999-1-2:

- The coefficient of thermal conductivity λ is dependent on the alloy. At room temperature, λ varies from 110 to 230 W/mK. At 500 °C, the λ of pure aluminium is 250 W/mK. Thus, the λ of aluminium is several times higher than that of steel (55 W/mK at room temperature and 40 W/mK at 500 °C). In view of those values, the temperature can be assumed as uniform throughout the thickness for both steel and aluminium members.
- The specific heat c of aluminium alloys at room temperature is approximately 870 to 900 J/kgK. The value for pure aluminium at 500 °C is determined at 1100 J/kgK. This is about twice the value for steel. However, the density ρ of aluminium is 1/3 of that of steel, so that the thermal capacitance ($c\rho$) is approximately 2/3 of that of steel.

- The emissivity of plain aluminium ε varies from 0.05 to 0.20. EN 1999-1-2 specifies a value of 0,3, which is lower than the value for steel (EN 1993-1-2 gives a value of 0,7). However, in most realistic fires the member will be covered with soot. For such a case, EN 1999-1-2 prescribes a value of 0,7. This value is used in the current study.

3.2 Maximum member temperatures

The member temperature can be determined using the simple calculation model for heating of unprotected members in EN1999-1-2, which is equal to the simple calculation model for steel. Because of the uniform temperature through thickness, the temperature of a member depends solely on the section factor, defined as the exposed surface area of the member (A_m) divided by its volume (V).

In this study, two aluminium members were considered, both exposed at four sides:

- A square hollow section with a width of 50 mm and a wall thickness of 10 mm (section factor $A_m/V = 125 \text{ m}^{-1}$);
- A square hollow section with a width of 50 mm and a wall thickness of 1 mm (section factor $A_m/V = 1020 \text{ m}^{-1}$).

Figure 5 gives an example of the temperature-time curve of the aluminium sections exposed to certain natural fire conditions. For reference, also the temperature of a steel section with section factor equal to 125 m^{-1} is given. Note that the melting temperature of aluminium alloys is 570 to 600 °C, so that the temperature-time curve is only realistic up to this temperature.

The maximum temperature of the members is shown to be almost equal to the gas temperature. This was found for all cases considered.

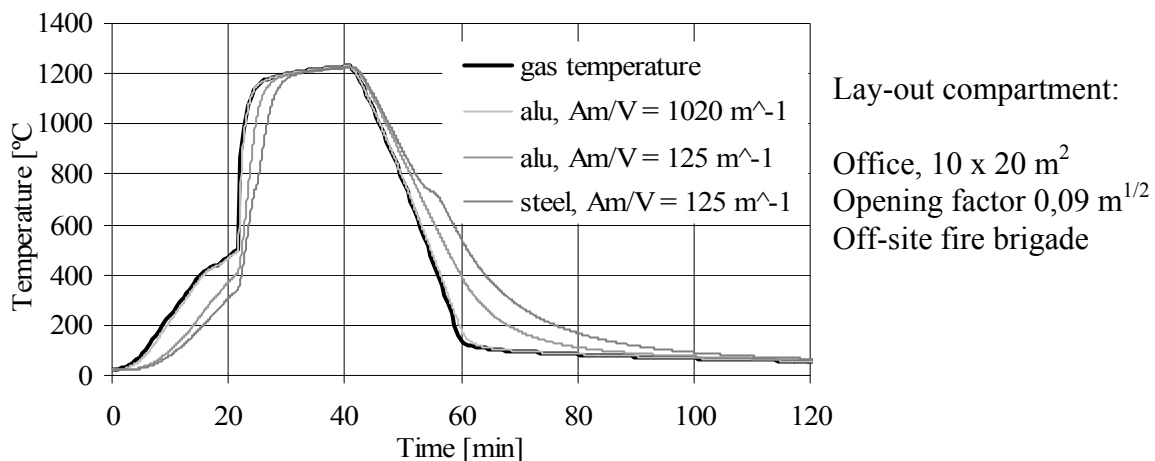


Fig. 5 – Example of unprotected member temperature when exposed to a certain NFSC

The maximum temperature of aluminium members exposed to natural fire conditions is therefore – in practice – approximately equal to the maximum gas temperature. Hence, for unprotected members, the maximum gas temperature is a proper indication whether non-insulated aluminium members may be applied.

To evaluate the fire resistance of a member, two criteria are considered:

- Criterion 1. The structure should remain its load bearing function during the entire fire;
- Criterion 2. The structure should remain its load bearing function for 30 minutes after fire breakout.

These criteria do not necessarily correspond with the criteria set in practice to structures evaluated on the basis of the NFSC. The authors do not intend to introduce new criteria to be used in practice with this. The reason to apply these criteria in the current study is for the purpose of a comprehensive evaluation only.

Figures 6, 7 and 8 give a selection of the maximum temperature of unprotected aluminium members exposed to natural fire conditions. The selected critical temperatures of 150 up to 350 °C are indicated with dashed lines.

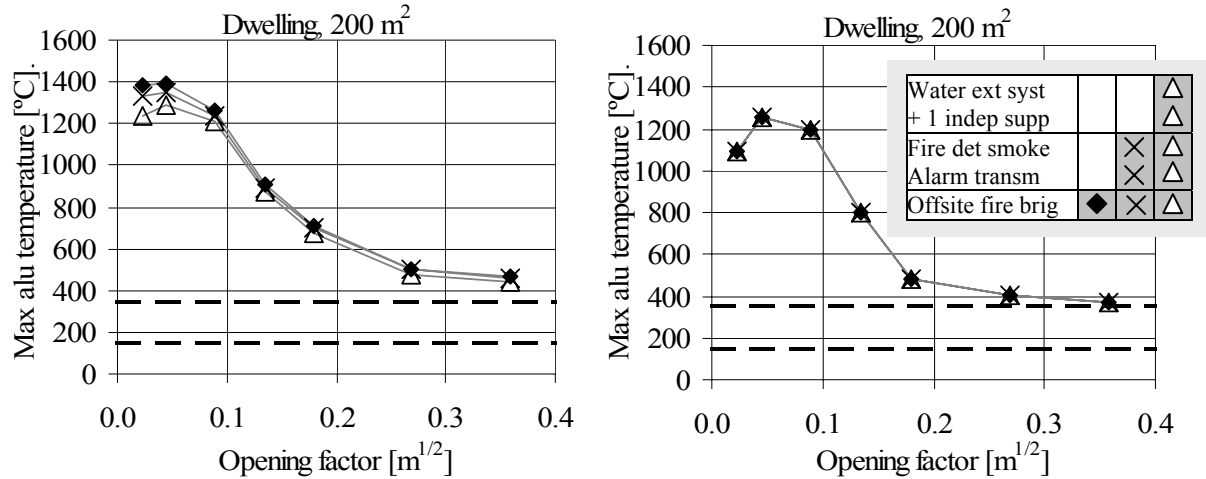


Fig. 6 – Max temperature of unprotected alu members for different sets of active measures for dwellings, area 200 m² (left-hand graph: crit. 1, right-hand graph: crit. 2)

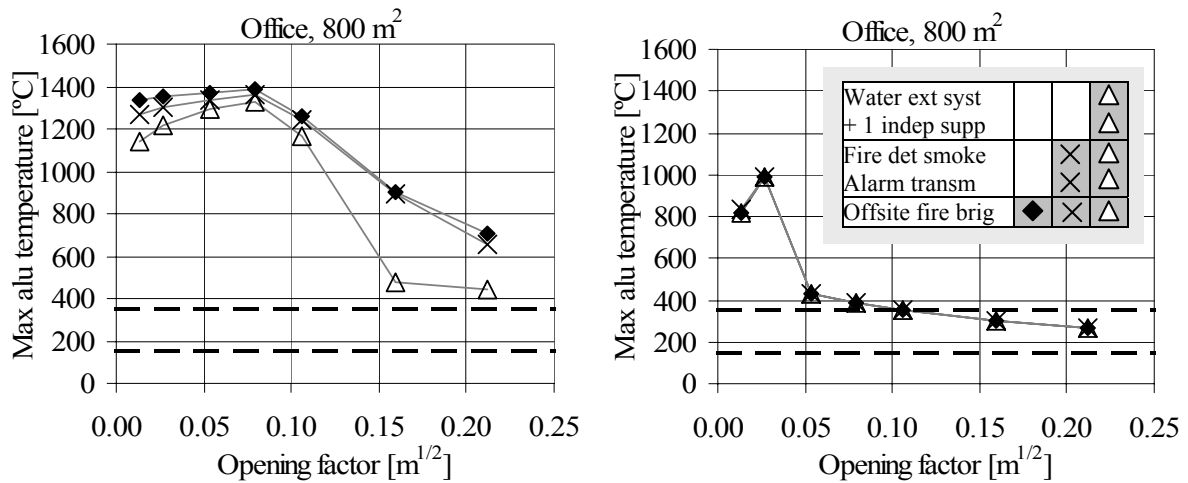


Fig. 7 – Max temperature of unprotected alu members for different sets of active measures for offices, area 800 m² (left-hand graph: crit. 1, right-hand graph: crit. 2)

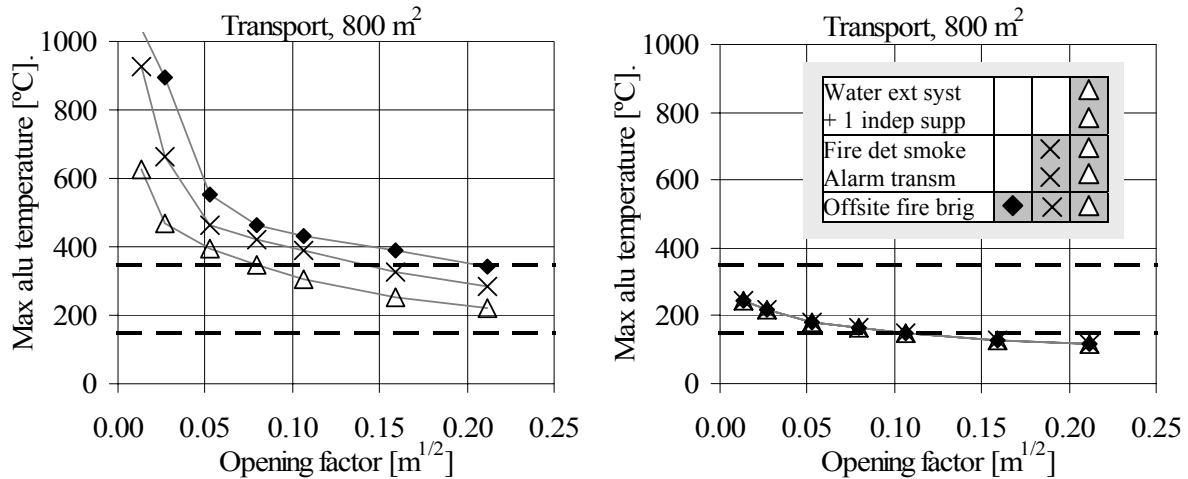


Fig. 8 – Max temperature of unprotected alu members for different sets of active measures for transport function, area 800 m² (left-hand: crit. 1, right-hand: crit. 2)

Conclusion is that, in case of (the mild) criterion (2) and a compartment with high opening factors and low fire load density, the temperature is in the range of selected critical temperatures. Hence, in such cases insulation is not always required. In case of (the severe) criterion (1), the member has to be insulated in almost all situations, however not for transport buildings with high opening factors. From tentative calculations results – not shown here – one can conclude that insulation is also required in case of a fire design based on the standard fire, for required fire resistances of 30 or more.

The figures show that active measures only reduce the maximum member temperature in the NFSC in case of a very low fire load density. This is due to the fact that the member temperature is almost equal to the gas temperature, and that the gas temperature remains at its maximum during a certain period.

4. HEATING OF INSULATED MEMBERS

4.1 Thermal properties of the insulation material

For all temperature-time curves resulting from the compartment layouts considered, the insulated member temperature was determined with 2D finite element models in the finite element program DIANA.

Physical properties of insulation materials are determined in standardised tests on heated steel sections. However, a standard test procedure to determine the thermal properties of the insulation material in case of aluminium sections does not exist. In this study, a fictitious – but not unrealistic – relation between thermal conductivity and temperature was applied (see figure 9). The density and the specific heat were assumed to remain unchanged during heating: $\rho_p = 60 \text{ kg/m}^3$ and $c_p = 1030 \text{ J/kgK}$. Insulation materials with such a low density are commonly used to protect aluminium load-bearing components.

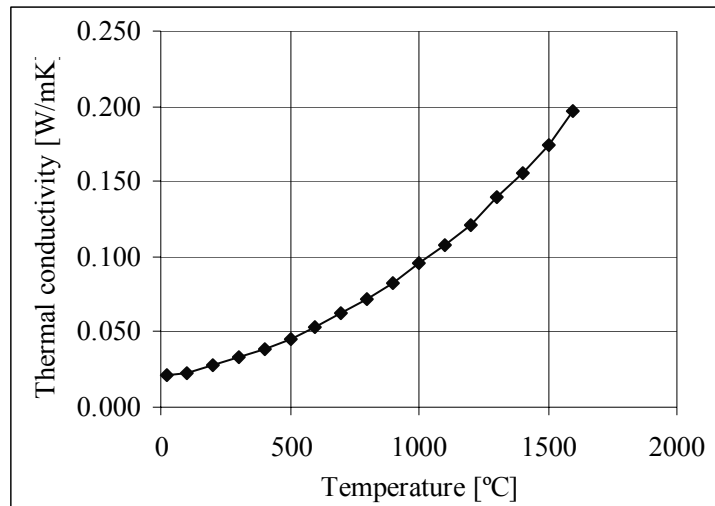


Fig. 9 – Relation between thermal conductivity and temperature of the insulation applied in the finite element models

4.2 Examples of heating curves

As an example, figure 10 gives the temperature development as a function of the time of the insulated slender section ($A_m / V = 1020 \text{ m}^{-1}$) - with various thicknesses of the insulation layer - exposed to natural fire conditions. The values in the legend represent the thickness of the insulation layer. The thicknesses are chosen in such a way that the maximum member temperature is in the range of the critical temperatures, i.e. 150 to 350 °C.

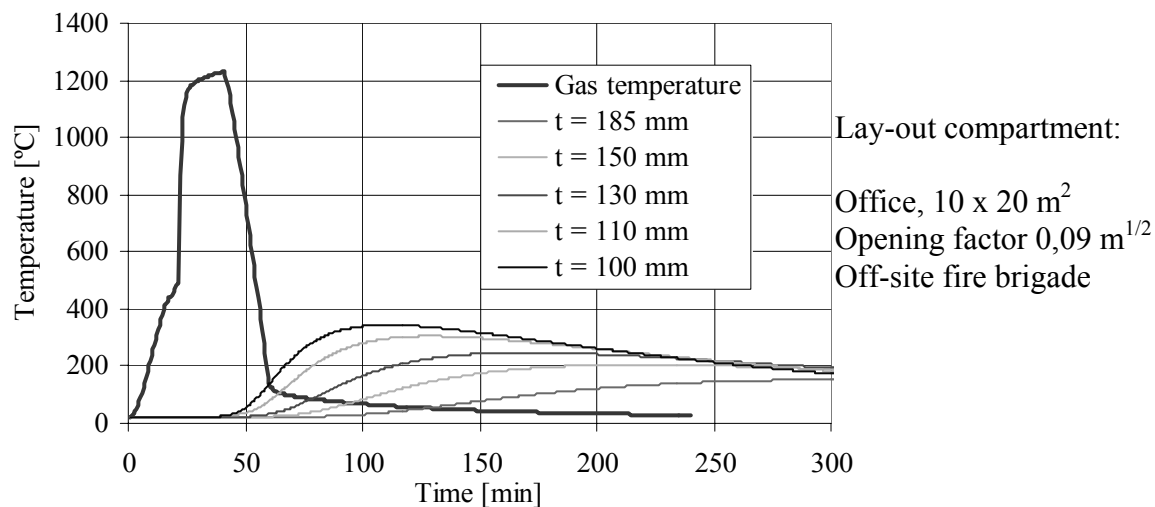


Fig. 10 – Temperature development in the insulated slender section ($A_m / V = 1020 \text{ m}^{-1}$) exposed to natural fire conditions

The required insulation thickness appears to be very thick. In practice, this may result in uneconomic and/or difficult to apply solutions. The figure also shows that the aluminium member needs to be so heavily insulated, that the aluminium temperature may still increase several hours after the decay phase has started. In this respect, an insulation material with a low thermal capacitance and a low thermal conductivity may be beneficial.

The mechanical properties of some aluminium alloys depend on the thermal exposure period. Note that the values for the relative proof stress in EN 1999-1-2 are valid for thermal

exposure periods of up to 2 hours. These values cannot be used in NFSC without checking the validity for such long thermal exposure periods.

In this study, no attention was paid to the problems indicated above.

4.3 Parameter study on the required insulation thickness

For the temperature-time curves of members with a certain insulation thickness in figure 10, the maximum member temperature can be determined and be presented as a function of the insulation thickness. This has been done for all compartments considered for the slender section ($A_m/V = 1020 \text{ m}^{-1}$) and the stocky section ($A_m/V = 125 \text{ m}^{-1}$) with various thickness of the insulation layer. Figures 11, 12 and 13 give some examples of the maximum member temperature as a function of the insulation thickness. The left-hand graphs in the figures refer to criterion 1: 'the structure should survive the fire' and the right-hand graphs to criterion 2: 'the critical temperature may not be reached within 30 minutes after fire ignition'. The different greyscales of the curves indicate different opening factors and different symbols indicate different sets of active measures (i.e. different design fire load densities) according to table 2. The curves correspond to the compartment layouts for which the gas temperature is given in figures 2 and 3. Note that the scales of the horizontal axes of the left and right hand graphs of figs. 11 to 13 are not equal.

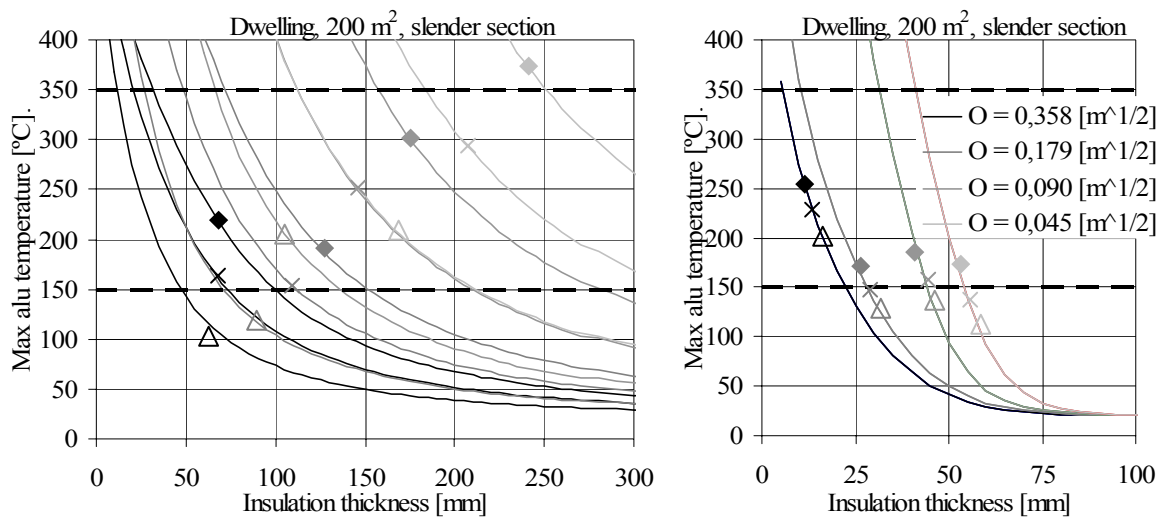


Fig. 11 – Relation between insulation thickness and maximum member temperature for dwellings, area 200 m², $A_m/V = 1020 \text{ m}^{-1}$ (left-hand: crit. 1, right-hand: crit. 2)

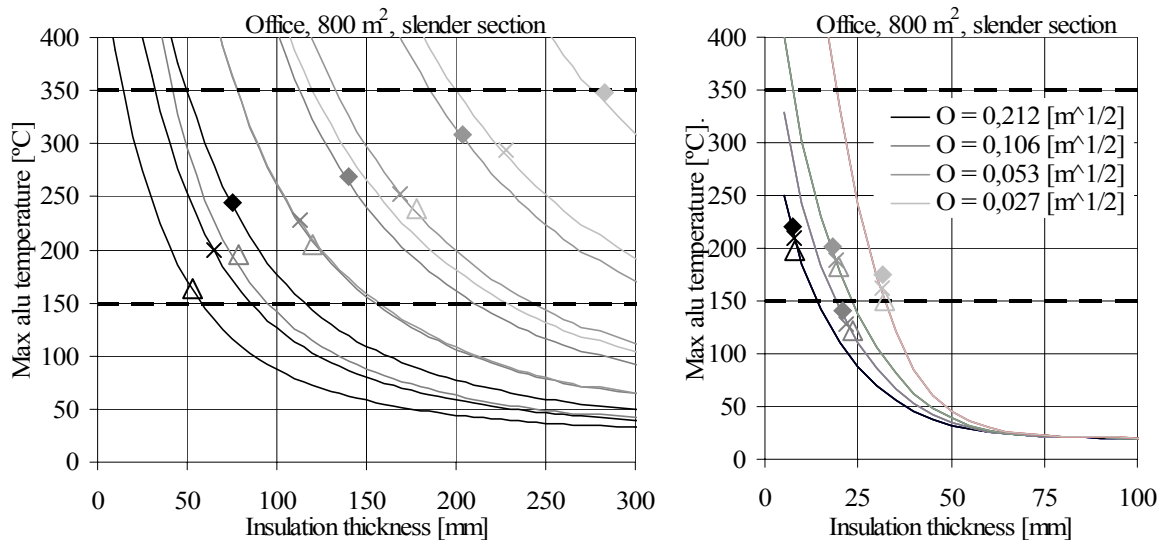


Fig. 12 – Relation between insulation thickness and maximum member temperature for offices, area 800 m², $A_m/V = 1020 \text{ m}^{-1}$ (left-hand: crit. 1, right-hand: crit. 2)

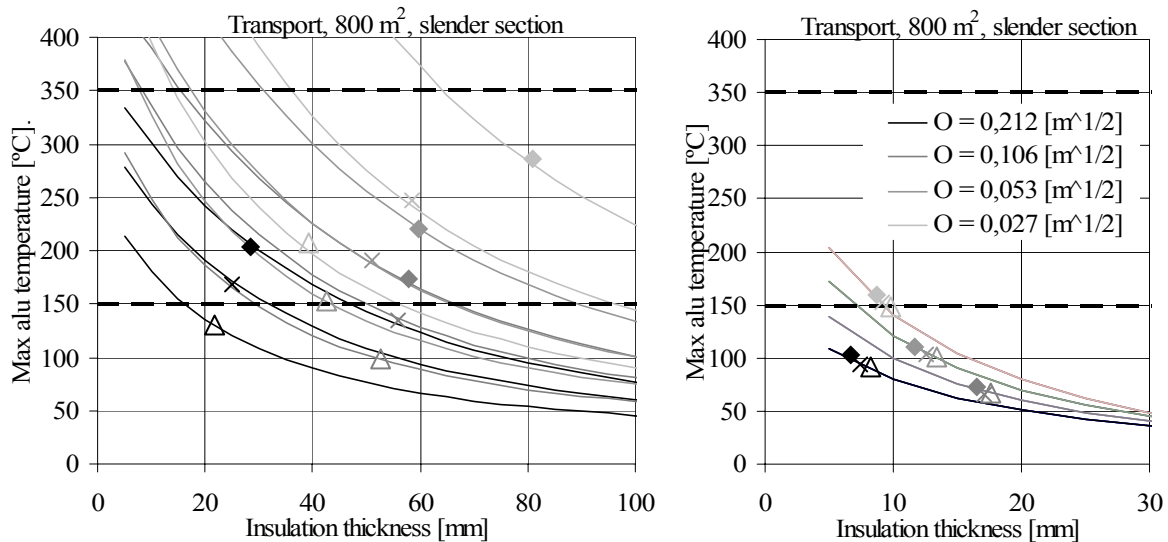


Fig. 13 – Relation between insulation thickness and max member temperature for transport buildings, area 800 m², $A_m/V = 1020 \text{ m}^{-1}$ (left-hand: crit. 1, right-hand: crit. 2)

The parameter study showed that, in case of criterion (1), the required insulation thickness in order to remain below the critical temperature depends both on the maximum temperature and on the fire duration. Contrary to non-insulated members, active measures reduce the required insulation thickness (via the reduction of the design fire load density and thereby the fire duration). This is not the case for criterion (2) which is caused by the fact that the decay phase has not yet started 30 minutes after fire ignition.

The curves also show that a considerable increase in insulation thickness is required in order to reduce the maximum member temperature, especially in case of the transport occupancy. For most cases, the insulation layer has to be 15 % up to 60 % thicker in order to reduce the member temperature with 50 °C. To maintain the temperature at 170 °C, the insulation layer has to be 1,5 to 3,5 times the thickness required for 350 °C. From calculations based on the standard temperature-time curve – not shown here – it was concluded that the extra insulation required to reduce the member temperature with 50 °C is 5 % up to 30 %. To

maintain the temperature at 170 °C, the insulation layer has to be 1,4 to 2,5 times the thickness required for 350 °C.

This significant amount of extra insulation indicates that it is important to accurately determine the critical temperature of aluminium members, especially when the design is based on natural fire conditions.

The results show that the variation in insulation thickness required is up to a factor 10 for the natural fire conditions considered. Also, the two criteria selected result in a large difference in required insulation thickness. Therefore, selection of an appropriate fire scenario and an appropriate fire resistance time in the design is crucial.

5. CONCLUSIONS

- The temperature development in non-insulated, typical aluminium members (i.e. section factor 125 m^{-1} or beyond), exposed to natural fire conditions is practically the same as the gas temperature development in the fire compartment; hence, in order to evaluate the structural behaviour of such members, no separate thermal response analysis is necessary;
- If structural fire safety requirements are set, the use of non-insulated aluminium members is only feasible in exceptional cases, i.e. in situations with very small fire load densities (e.g. transport buildings), possibly in combination with active fire protection measures and significant ventilation conditions;
- To meet structural fire safety requirements for building categories such as dwellings and offices, it is – not only under standard fire conditions, but also under natural fire conditions – generally necessary to insulate the aluminium members, even if active fire safety measures are taken.
- The required thickness of fire insulation on aluminium members is significantly larger than that on steel members under similar conditions; as a consequence, under natural fire conditions, a significant temperature increase in the aluminium temperature during the cooling down period of the fire may occur, possibly leading to (unexpected) failure in the last phase of the fire; hence, there is a need to develop fire insulation materials for aluminium with both a low thermal conductivity and a low thermal capacitance.
- When analysed under natural fire conditions, a reduction of the critical temperature of aluminium members from 350 °C (= maximum value attainable in practice) to 170 °C (= default value according to the Eurocode EN 1999-1-2) results in an increase in the required insulation thickness of 50 to 250%; the corresponding reduction factors, based on a standard fire approach amounts 40 to 150%. In addition, the insulation layer required in order to keep the aluminium temperature below 170 °C is for many compartment layouts so thick that it may be uneconomical, difficult or even impossible to apply this insulation layer. Hence there is a need to accurately determine the critical temperature of aluminium members, while the use of natural fire safety design is strongly recommended.

6. ACKNOWLEDGEMENT

This research was carried out under project number MC1.02147 in the framework of the Strategic Research programme of the Netherlands Institute for Metals Research in the Netherlands (www.nimr.nl).

The Aluminium Centrum, Bayards Aluminium Constructions, Corus, Nedal Aluminium and Alcoa Building and Construction systems are kindly acknowledged for their contribution to this research.

7. REFERENCES

- [1] EN 1999-1-2, Eurocode 9: Design of aluminium structures – Part 1-2: General Rules – Structural fire design, September 2003
- [2] EN 1991-1-2, Eurocode 1: Actions on structures – Part 1-2: General actions – Actions on structures exposed to fire
- [3] Schleich J.B., Cajot L.G., et al. *Valorisation project - Natural Fire Safety Concept* ECSC Research 7215-PA/PB/PC –042-057, D-E-F-I-NL-UK & ECCS, 1999-2001
- [4] Cadorin, J.F., Pintea, D. and Franssen, J.M. *The design fire tool ozone V2.0 – Theoretical description and validation on experimental fire tests*, 1st draft, Université de Liège, département M&S, Rapport interne SPEC/2001-01, 2004
- [5] Kammer, C. *Aluminium Taschenbuch teil 1, Grundlagen und Werkstoffe*, Aluminium Verlag Düsseldorf 2002. ISBN 3-87017-274-6
- [6] Davis, J.R. *ASM specialty handbook, Aluminum and aluminum alloys*, ASM International, 1993, ISBN 0-87170-496-X
- [7] Brandes, *Smithells Reference Book*, Butterworth, 1983, ISBN 0-40871053-5
- [8] DinNenno, *The SFPE Handbook of Fire Protection Engineering*, Society of Fire Protection Engineers, 2002, ISBN 0-8776-5451-4
- [9] Holman, J.P. *Heat Transfer*, McGraw-Hill Publishing Company, 1990, ISBN 0-07-909388-4



SIMPLE THERMAL CALCULATION METHODS FOR STEEL COLUMNS PROTECTED WITH STEEL CASINGS AND LAYERED STEEL BALCONY SLAB STRUCTURES

Olli KAITILA¹ and Timo KORHONEN²

ABSTRACT

The use of external steel columns will highlight the structural system of the building, allow for different architectural effects and decrease the thermal effects of a building fire on the load-carrying structures. However, some fire protection for external steel columns will usually still be necessary. One way to provide this protection is to use thin steel sheet casings.

Mainly CHS-, RHS-, H- and I-columns are considered in this study. The load-bearing structural steel or stainless steel column is protected by a thin steel sheet casing also made of structural or stainless steel.

Simple calculation methods in 1D and 2D have been developed in order to determine the temperature development of the steel casings and columns when external gas temperatures are known. The 1D-method is applicable when both the structure and the fire exposure are cylindrically symmetric, e.g. for CHS-sections under standard EN 1363-1: 1999 (ISO 834) fire. It can also be used for RHS-sections without an important error. The 2D-method can be used also in the case of asymmetric fire exposure and/or cylindrically asymmetric steel profiles, e.g. H- and I-profiles.

The methods have been validated on the basis of a standard fire test and natural fire tests carried out using the VTT façade test rig. Very good agreement between calculations and test results was found using the 1D-method and also the 2D-method under symmetric fire exposure. The agreement is not quite as good for the 2D-method under asymmetric fire exposure. Higher asymmetry leads to less accurate results due to the high nonlinearities in temperature distributions. However, the results are mostly conservative for these cases as well.

A 1D-temperature calculation method for layered steel balcony structures has also been developed by VTT. However, due to lack of space, only a short presentation of this method can be included in this paper.

¹ Senior Research Scientist, D.Sc. (Tech.), VTT Technical Research Centre of Finland, P.O.Box 1000, FI-02044 VTT, Finland, email: olli.kaitila@vtt.fi, Tel: +358 20 722 4862, Fax: +358 20 4815

² Research Scientist, D.Sc. (Tech.), VTT Technical Research Centre of Finland, P.O.Box 1000, FI-02044 VTT, Finland

1. INTRODUCTION

The ECSC project N° 7210 PR380 “Development of Design Rules for the Fire Behaviour of External Steel Structures” ran from 1.7.2002 until 31.12.2005. The partners in the project were CTICM (coordinator), TNO, ProfilARBED, LABEIN and VTT. The main objectives of the research were the following:

- To improve the existing model for determining the thermal actions on external bare, insulated or shielded structural elements, taking into account radiative and convective heating by external flames and by the openings of the fire compartment itself.
- To extend the existing physical model for temperature development within structural elements (steel or composite) by including transient state conditions and, when necessary, the effects of fire protection systems such as fire insulation and thermal shielding, taking into account heat transfer across air gaps.
- To verify the developed models on the basis of experimental results and to adapt the models, where appropriate.
- To develop simple rules on the heating of bare or protected external steel sections, steel sections away from a localised fire and balconies, in case of fire.

VTT was the responsible partner for Work Package 4, where the main objective was to develop simple thermal calculation methods for steel columns protected with steel casings, and for balcony slab structures, with the aim of incorporating the methods in the structural Eurocodes.

Simple calculation methods in 1D and 2D have been developed in order to determine the temperature development of the steel casings and columns when external gas temperatures are known. The 1D method is applicable when both the structure and the fire exposure are rotationally symmetric, e.g. for CHS-sections under EN 1363-1: 1999¹ (ISO834) standard fire. It can also be used for RHS-sections without an important error being made. The 2D method can be used also in the case of asymmetric fire exposure and/or rotationally asymmetric steel profiles, e.g. H- and I-profiles. Only the more generally applicable 2D-method will be discussed here due to space limitations. The calculation methods have been validated on the basis of fire tests carried out at VTT during the course of the present project.

Fig. 1 shows the types of structures that are considered in this study. The load-bearing structural steel or stainless steel column is protected against external fires by a thin steel sheet casing also made of structural or stainless steel.

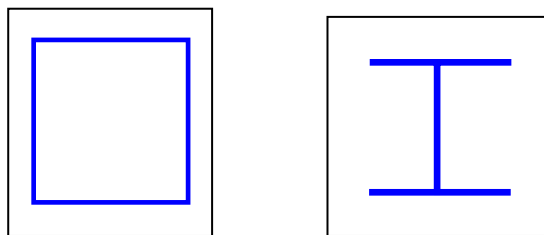


Fig. 1 — RHS- and H-section protected with a steel sheet casing.

A 1D-temperature calculation method for layered steel balcony structures was also developed by VTT during the ECSC Project PR 380. However, due to lack of space, only a short presentation of this method can be included in this paper.

2 2D-THERMAL CALCULATION METHOD FOR STEEL COLUMNS

2.1 Mathematical formulation

The basic case considered is shown in Fig. 2 for an H-profile. There are a total of seven unknown temperatures: $T_1 \dots T_4$ are lumped temperatures of the four sides of the protective casing, T_5 , T_6 and T_7 are the lumped temperatures of the top flange, the web and the bottom flange, respectively. The external gas (flame) temperatures $T_{g1} \dots T_{g4}$ are assumed to be known as functions of time on all four sides of the column.

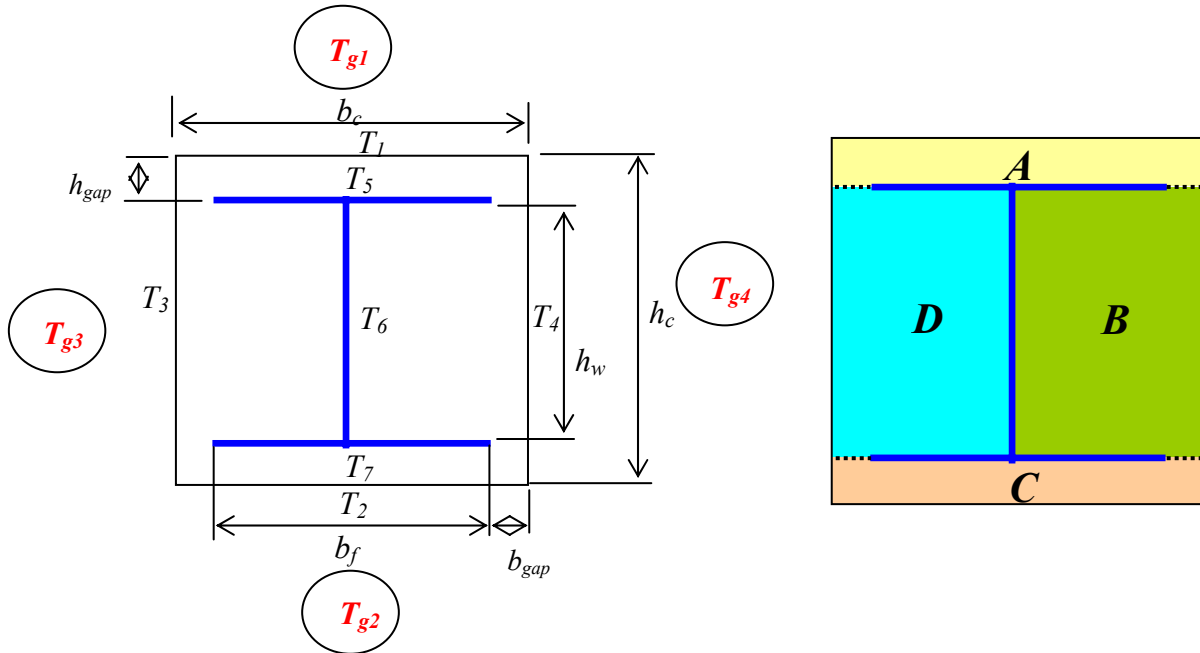


Fig. 2 — H-profile protected with a thin steel sheet casing.

When the gaps between the flange surfaces and the casing (h_{gap}) and the flange edges and the casing (b_{gap}) are small, it can be assumed that the casing and the column form four individual enclosures (A, B, C and D) separated from each other by the web and flanges, as shown on the right in Fig. 2. Heat transfer is calculated separately in each of these four enclosures. The resulting lumped casing and column temperatures ($T_1 \dots T_7$) are then added up from calculations in each of the four cavities to obtain the resulting temperature of each structural member. In the following, the different elements of the casing and the column are referred to by the index i ($i = 1 \dots 7$). The ordinary differential equations (ODE) to be solved can then be written in matrix form as shown in Eq. (1), where the matrix **C** is diagonal (lumped) as given in Eq. (2). ρ_i is the density [kg/m^3], c_i is the specific heat [J/kgK], A_i is the surface area per unit length [m^2/m] and d_i is the thickness [m] of element i .

$$\mathbf{C} \dot{\mathbf{T}} = \mathbf{q}_f + \mathbf{q}_A + \mathbf{q}_B + \mathbf{q}_C + \mathbf{q}_D \quad (1)$$

$$\mathbf{C}_{7 \times 7} = \begin{bmatrix} \rho_1 c_1 A_1 d_1 & 0 & 0 & 0 & 0 & 0 & 0 \\ 0 & \rho_2 c_2 A_2 d_2 & 0 & 0 & 0 & 0 & 0 \\ 0 & 0 & \rho_3 c_3 A_3 d_3 & 0 & 0 & 0 & 0 \\ 0 & 0 & 0 & \rho_4 c_4 A_4 d_4 & 0 & 0 & 0 \\ 0 & 0 & 0 & 0 & \rho_5 c_5 A_5 d_5 & 0 & 0 \\ 0 & 0 & 0 & 0 & 0 & \rho_6 c_6 A_6 d_6 & 0 \\ 0 & 0 & 0 & 0 & 0 & 0 & \rho_7 c_7 A_7 d_7 \end{bmatrix} \quad (2)$$

Vector $\dot{\mathbf{T}}$, as given in Eq. (3), gives the time derivatives of the temperatures to be calculated. \mathbf{q}_f is the flux vector to the casing due to external flames and hot gases, as given in Eq. (4). ε_i is the emissivity [-] of element i .

$$\dot{\mathbf{T}} = \begin{bmatrix} \dot{\mathbf{T}}_1 & \dot{\mathbf{T}}_2 & \dot{\mathbf{T}}_3 & \dot{\mathbf{T}}_4 & \dot{\mathbf{T}}_5 & \dot{\mathbf{T}}_6 & \dot{\mathbf{T}}_7 \end{bmatrix}^T \quad (3)$$

$$\mathbf{q}_f = \begin{bmatrix} A_1 \varepsilon_f \varepsilon_1 \sigma (T_{g1}^4 - T_1^4) + A_1 h_f (T_{g1} - T_1) \\ A_2 \varepsilon_f \varepsilon_2 \sigma (T_{g2}^4 - T_2^4) + A_2 h_f (T_{g2} - T_2) \\ A_3 \varepsilon_f \varepsilon_3 \sigma (T_{g3}^4 - T_3^4) + A_3 h_f (T_{g3} - T_3) \\ A_4 \varepsilon_f \varepsilon_4 \sigma (T_{g4}^4 - T_4^4) + A_4 h_f (T_{g4} - T_4) \\ 0 \\ 0 \\ 0 \end{bmatrix} \quad (4)$$

Vectors \mathbf{q}_A , \mathbf{q}_B , \mathbf{q}_C and \mathbf{q}_D give the contributions of the enclosures A, B, C and D, respectively, to Eq. (1). Each vector includes four nonzero terms corresponding to the element numbers that make up the cavity. For instance, for cavity A, terms corresponding to elements $i = 1$, $i = 3$, $i = 4$ and $i = 5$ are nonzero, while terms corresponding to elements $i = 2$, $i = 6$ and $i = 7$ are zero. The individual nonzero terms q_i for vectors \mathbf{q}_A , \mathbf{q}_B , \mathbf{q}_C and \mathbf{q}_D are calculated using Equation (5)², where J_i is the radiosity [W/m²] of element i , F_{ij} is the radiation view factor from element i to element j and n is the number of surfaces in the enclosure other than surface i (here $n = 3$).

$$\mathbf{q}_i = -A_i (J_i - \sum_{j=1}^n F_{ij} J_j) \quad (5)$$

The radiosities J_i can be calculated from Equation (6)³, where δ_{ij} is the Kronecker delta defined as $\delta_{ij} = 1$, when $i = j$, and $\delta_{ij} = 0$, when $i \neq j$, and σ is the Stefan-Boltzmann constant, $\sigma = 5.67 \times 10^{-8}$ W/m²K⁴.

$$J_j = \frac{\varepsilon_j \sigma T_j^4}{\sum_{i=1}^n [\delta_{ij} - (1 - \varepsilon_i) F_{ij}]} \quad (6)$$

The radiation view factors, F_{ij} , for parallel and perpendicular planes in a rectangular enclosure can be calculated using Eqs (7)², respectively, where w_i and w_k are parallel surfaces ($w_k = w_i$) and w_j is perpendicular to w_i and w_k . Note that in the enclosure $\sum_{j=1}^4 F_{ij} = 1$ and $0 \leq F_{ij} \leq 1$.

$$F_{ik} = \sqrt{1 + \left(\frac{w_k}{w_i}\right)^2} - \frac{w_k}{w_i}; \quad F_{ij} = \frac{1 + \frac{w_j}{w_i} - \sqrt{1 + \left(\frac{w_j}{w_i}\right)^2}}{2} \quad (7)$$

Finally, the group of ODEs (Eq. (1)) can be solved for the time derivatives of temperatures $T_1 \dots T_7$ at each time step. The equations can be easily expanded for use with RHS-columns by adding one unknown temperature for the fourth column side.

2.2 Validation of calculation method

In 2003 and 2004, a total of five large scale structural fire tests were carried out at the Fire Research testing facilities of VTT Building and Transport in Espoo, Finland, within the ECSC project PR 380. The six column types used in all five tests are presented in Table 1. Of these, column type 1 with intumescent paint protection (M-RHS-Paint) was not considered for these calculations.

The first of the five tests was carried out in a horizontal furnace and involved a total of six unloaded structural steel or stainless steel short columns with different types of fire protection tested according to the EN 1363-1:1999 (ISO 834) standard fire curve. These test results provide data for the validation of the simple calculation method for the temperature development of a steel column protected with a steel casing and subjected to a symmetric fire load.

Table 1 — Column types used in tests.

Col. #	Short name	F / V [1/m]	Column description
1	M-RHS-Paint	206	S355 RHS 150x150x5 column protected with intumescent paint protection
2	S-RHS-Sbox	206	Stainless steel (AISI 304) RHS 150x150x5 column with 1.0 mm thick stainless steel (AISI 304) casing
3	M-RHS-Sbox	206	S355 RHS 150x150x5 column with 1.0 mm thick stainless steel (AISI 304) casing
4	S-RHS-Unp	206	Stainless steel (AISI 304) RHS 150x150x5 column, unprotected
5	M-RHS-Mbox	206	S355 RHS 150x150x5 column with 1.0 mm thick pvdf-coated structural steel casing
6	M-HEA-Mbox	212	S355 HE 200 A - column with 1.0 mm thick pvdf-coated structural steel casing

M = Mild steel column

Mbox = Mild steel casing

S = Stainless steel column

Sbox = Stainless steel casing

The other four tests were carried out using the VTT façade testing rig under natural fire conditions and included the same six types of columns as the horizontal furnace test. The columns were placed in front of a fire room window at different locations as shown in Table 2 and Fig. 3. The column temperatures were measured at the mid-height and the head of the window and 800 mm above the window (1960 mm, 2760 mm and 3560 mm from the floor, respectively).

Table 2 — Column specimen types and locations in natural fire tests.

Test number	Test date	Column 3: Side Column (SC)	Column 2: Centre Left Column (CLC)	Column 1: Centre Right Column (CRC)
1	28.5.2004	T1-C3: M-RHS-Mbox	T1-C2: S-RHS-Sbox	T1-C1: M-RHS-Sbox
2	4.6.2004	T2-C3: S-RHS-Sbox	T2-C2: M-RHS-Sbox	T2-C1: S-RHS-Unp
3	11.6.2004	T3-C3: M-RHS-Sbox	T3-C2: M-HEA-Mbox	T3-C1: S-RHS-Sbox
4	18.6.2004	T4-C3: M-HEA-Mbox	T4-C2: M-RHS-Paint	T4-C1: M-RHS-Mbox

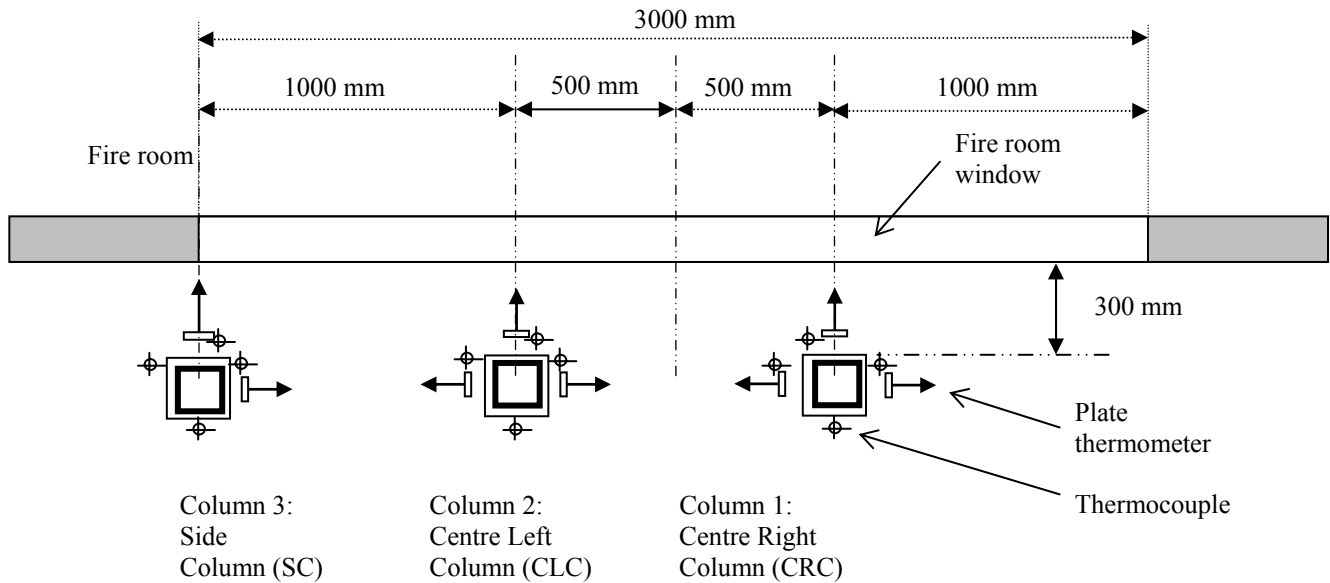


Fig. 3 — Placing of the columns in front of the fire room window in natural fire tests.

The material properties used in the validation procedure were based on prEN 1993-1-2: 2003⁴ and are specified in Table 3. The emissivity of flames was taken as $\varepsilon_f = 1.0$ and the heat transfer coefficient from flames to the steel surface was $h_f = 25 \text{ W/m}^2\text{K}$. The convection in the cavity was assumed to happen linearly and was modelled as conduction through the air inside the cavity. The conductivity of air as function of temperature was taken from Incropera & DeWitt².

Table 3 — Material properties used in the validation models.

	Structural steel	Stainless steel
Specific heat [J/kgK]	Eq. (3.2) in prEN 1993-1-2: 2003	Eq. (C.2) in prEN 1993-1-2: 2003
Density [kg/m ³]	7850	7850
Emissivity [-]	0.7	0.4 ... 0.6

Figures 4-5 show examples of calculation and test results for an HEA-column and an RHS-column, respectively, in the standard fire test and a natural fire test. A very good agreement was generally achieved for the case of symmetric fire loading. However, the relative complexity of the asymmetric fire scenario did not always allow a very accurate reproduction of the test results. It has to be noted that the real situation is very complex and includes problems such as very strong asymmetry of the fire exposure around and along the axes of the column and casing, and the asymmetry of the cross-section itself. Also, especially heat conduction within the cross-section and along the vertical axes of the casing and column, and radiation and convection

in the enclosure between the casing and column and inside the rectangular hollow section are complicated phenomena. All these effects cause dissemination of heat in the structure. In Figures 4-5, ϵ_{ps_c} and ϵ_{ps_s} are the emissivity values used for the casing and the column, respectively.

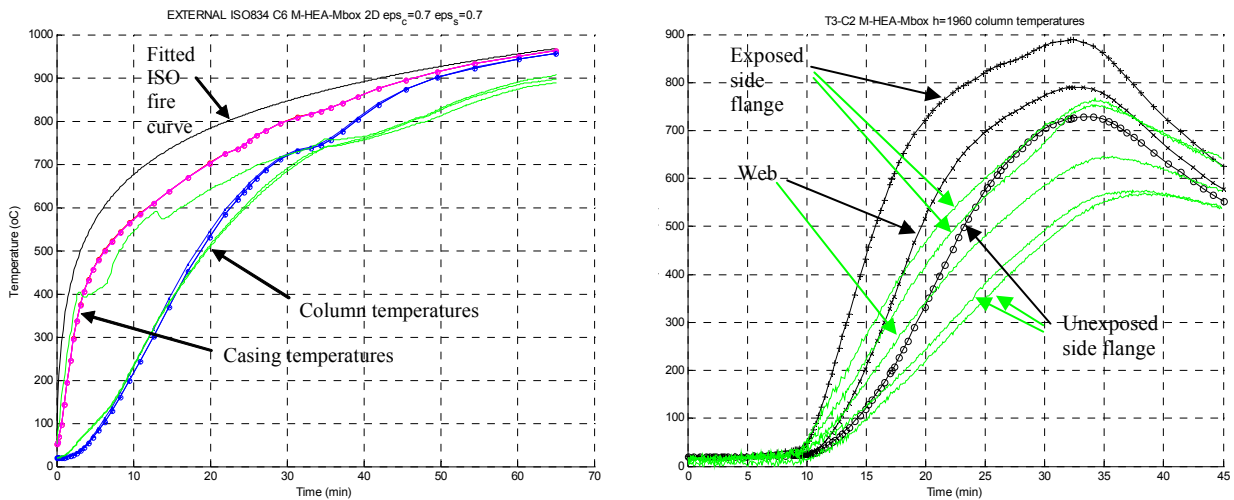


Fig. 4 — Calculated (lines with markers) and measured (full green lines) temperatures of column M-HEA-Mbox in standard fire test (left) and natural fire test (right).

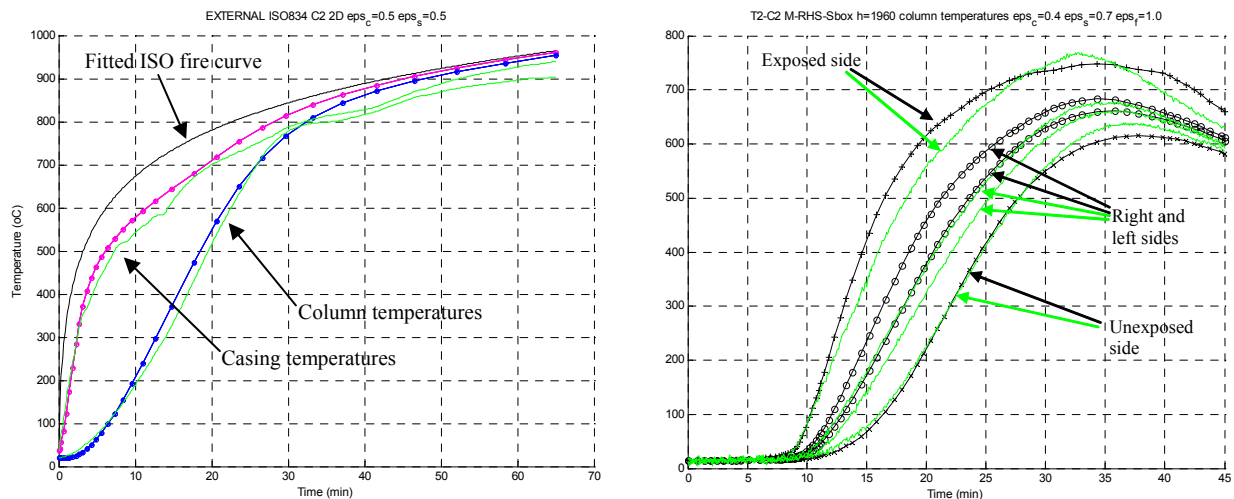


Fig. 5 — Calculated (lines with markers) and measured (full green lines) temperatures of column S-RHS-Sbox in standard fire test (left) and M-RHS-Sbox in natural fire test (right).

Clearly, none of the effects taking place along the vertical axis of the structure are taken into account in the two-dimensional calculation method. Thus, when fire temperatures measured around the hottest cross-section of a column during a fire test are used as the basis for the 2D-calculation, the heat fluxes to other (cooler) parts of the column are not taken into account. This will lead to higher steel temperatures in calculations. The analysis is thus on the safe side when the hottest cross-section is considered, but it is obviously difficult to gain a very accurate understanding of the temperature distribution along the height of the column.

On the other hand, the measured temperatures on the unexposed side of the column were in many cases found to be higher than the calculated temperatures. This is explained by the fact that heat conduction within the cross-section of the steel member is not taken into account in the calculations.

Further problems in the validation of any calculation method against test results from a real fire test (as opposed to a furnace test) are obviously caused by the highly local nature of the temperature fields and the strong heat fluxes present around the columns. When considering a gas temperature measurement at a location between the mid-height and the lower edge of a fire room window, the measurements can be strongly affected by the cold air flowing into the fire room from the outside. It is hard to tell, then, what the actual temperature is that should be used in the calculation. Also, when considering a cross-section that is at least partly engulfed in flames and the gas temperatures are measured at a certain distance from the column or casing, it is possible that the gas temperature measurement shows a lower value than the steel temperature measurement.

Another factor is that the temperatures reach very high values quite quickly after flashover. Are the thermocouples always accurate at such fast temperature variations and at such high temperatures? Also, what are the factors, besides different radiation view factors and possible flow of cold air from behind, that cause the large differences between plate thermometer and wire thermocouple measurements at the same location, as was experienced during the fire tests? What temperature should then be used in the modelling?

When performing checks on the calculations, it was very quickly noticed that the value of emissivity used for the different elements has an important influence on the results.

2.3 Calculation software

2.3.1 Input data, usage and output data

The calculation methods are relatively straightforward to use, once they have been programmed as computer code. For this research, the programming was carried out using Matlab[®] 7.0.1⁵, but any other available and suitable programming language can be used as well. The program files will be available free of charge from the authors by email request after the project ECSC PR 380 has been officially closed (later this year).

An attempt has been made to make the usage of the Matlab[®]-programs relatively easy. The user should open the `_input.m` -file of the program, which can be done using a normal text editor or the Matlab[®] M-file editor. The file lists a number of variables that should be given a value. The user should change the given values when necessary, according to the structure to be analysed. The input requests can be divided in three categories:

1. geometric dimensions
2. material properties
3. initial temperatures and temperature development of fire

After this, the program can be run from the Matlab[®] command window. The default output includes a listing of all input data given by the user in the input file, a table with calculated temperature data on different sides of the casing and column as functions of time and a figure including this results data.

2.3.2 Limitations to the use of the programs

Because the programs have been developed for the purposes of the present study and the available test data to check the sensibility of the programs to changes of the different parameters has been limited, there are some restrictions to the use of the programs.

The casings tested and considered in this study have been made of steel sheet with a thickness of 0.8 - 1.0 mm. The casing temperature has been lumped into one node in the methods, so no heat conduction is considered through the casing. Because of this limitation, it is suggested that the calculation methods should be used with caution when the steel sheet

thickness is less than 0.8 mm or more than 1.0 mm. On the other hand, though, increasing the steel sheet thickness leads to more thermal resistance and lower temperatures, so no upper limit to the steel sheet thickness of the casing need be set.

The columns tested within this project were of types RHS 150×150×5 and HEA 200. Other available tests included columns of types RHS 200×200×10 and UBP 254×254×71. The range of F/V-value of these column types was 104 1/m to 212 1/m. The calculation methods can be used at least for this range of F/V-values of columns. Using the methods for lower or higher F/V-values should be done with caution.

The fire gas temperatures used in this study were based either on the EN 1363-1:1999¹ (ISO 834) standard fire curve or fire loads from natural fire tests. No problems were noticed in the use of these temperature data. There is no inherent limitation to the type of fire gas temperature development used in the calculations. However, especially when considering natural fires where the heat exposure varies strongly as a function of place and time, special care should be given to the choice of cross-sections to be analysed. As a basic rule, the hottest cross-section should be chosen for analysis, but it can also be that the critical cross-section is not the one with the highest local temperature but for instance the one with the highest average temperature.

The increase of the air gap dimensions between the casing and the column seem to lead to increased conservatism in the calculation results. Therefore no maximum value really needs to be given for the air gap. Besides, it should be limited by practical architectural, structural and economical design considerations. Making the air gap larger does not provide much additional fire safety, since the radiation inside the cavity is still considered to happen inside a closed system. On the other hand, a *small gap* is assumed, so, the casing should not be in physical contact with the sides of the column.

3. THERMAL CALCULATION METHOD FOR LAYERED BALCONY SLABS

3.1 Bases of method

BalconySlab.m is a code developed by VTT to calculate the heat transfer through layered balcony slab structures. The program has been written using Matlab[®]. The use of the method is in fact not limited to balcony slabs; it can be used for any type of layered structure that can be simplified to 1D, if the material thermal properties are known with sufficient accuracy.

The program solves 1-dimensional basic heat transfer equations for a slab, which may consist of several layers, some of which may be air gaps. One side of the slab is assumed to be heated by a fire and the other side is assumed to be open to constant ambient conditions. The fire temperature may be given as a user-defined time series or one of two different analytical fire curves (Wickström's parametric fire curve or the EN1363-1:1999¹ (ISO 834) standard fire curve) may be used.

A number of commonly used structural materials are included in the material library of the program, but the user may include further materials by programming them in the open source code. In addition to structural materials, air gaps can be included in the succession of layers. The radiation terms at the fire exposed (bottom) surface and at the unexposed (top) surface of the balcony slab have been linearized, which is necessary in order to render the program stable.

3.2 Modelling of air gaps within balcony slab structure

As noted, there may be air gaps (layers) in the balcony slab. The thermal properties of air are calculated using ambient pressure. Convective heat transfer is not modelled in the air gap. Instead, heat is transferred through the air gap by thermal conductivity (which is quite low) and by thermal radiation. The calculation of radiation heat transfer in the air gap is carried out by using an effective thermal conductivity, which contains the radiative part. Thus, only the temperature-dependent thermal conductivity of air is modified by the radiative part, otherwise the air gap is modelled similarly to any other material layer, i.e. by using conductive heat flux equations. This approximation is better for thin air gaps than for thick air gaps, because convection is not important in very thin gaps and the radiation part is closer to the 1-dimensional (semi-infinite) result.

Thermal radiation is treated as it would be for a vacuum between the materials. Let the left side material have an emissivity ε_1 and the right side material ε_2 . The surface temperatures of the materials are T_1 and T_2 , respectively, and the width of the vacuum between the semi-infinite solid material layers is d . The positive x -direction is chosen as the positive direction for heat transfer as given by Eq. (8). The denominator in Eq. (8) includes the effects of reflections between the surfaces of the air gap. ΔT is the temperature difference between the surfaces ($T_2 - T_1$).

$$\dot{q}'' = \dot{q}_r'' = \frac{\sigma(T_2^4 - T_1^4)}{\frac{1}{\varepsilon_1} + \frac{1}{\varepsilon_2} - 1} = \frac{\sigma(T_2^2 + T_1^2)(T_2 + T_1)}{\frac{1}{\varepsilon_1} + \frac{1}{\varepsilon_2} - 1} \Delta T = -\frac{k_{eff,vac}}{d} \Delta T \quad (8)$$

Thus, the radiative heat transfer through a vacuum may be formulated as heat conduction through an effective material, whose thermal conductivity $k_{eff,vac}$ is given by Eq. (9), and the thermal inertia is equal to zero, i.e. $\rho c = 0$. This is a good approximation for air, because of its low density. Note, that the temperature will vary linearly in the vacuum gap between layers, when the effective thermal conductivity is used.

$$k_{eff,vac} = \frac{\sigma \cdot d \cdot (T_2^2 + T_1^2)(T_2 + T_1)}{\frac{1}{\varepsilon_1} + \frac{1}{\varepsilon_2} - 1} \quad (9)$$

If the cavity is filled with air, then ρc is not equal to zero, and there will be some thermal inertia and a small thermal flux due to the conductivity of air (N.B. the convective part is assumed to be zero here). Thus the air gap is modelled by adding the effective vacuum conductivity (radiation term) to the conductivity of air and then treating the air gap like any other material layer. The temperature will vary almost linearly inside the air gap (due to the low density of air), but this is not usually correct due to the neglected convection terms. For thin air gaps, the approximation is usually very good, because not much energy is needed to heat the air layer and the edge effects are not important for the radiation part.

3.3 Calculation results

As an example of calculation results, Figures 6-8 show comparisons with available test results for calculation model *Balc1_b* that is a balcony slab consisting of the following layers:

- Exposed side
 - Rock wool insulation (140 kg/m^3), 30 mm
 - Air gap (varying thickness depending on c-s)
 - Str. steel sheeting Rannila RAN 45 ER, 0.9 mm
 - Air gap (varying thickness depending on c-s)
 - RHS $3 \times 50 \times 50$ beams
 - Wood grills made of $28 \text{ mm} \times 95 \text{ mm}$ boards
- Unexposed side

A fairly good agreement of results was obtained in this case, although the calculated steel sheet temperatures are actually a little lower than the highest measured temperatures. The calculated wood grill temperatures show quite a good agreement with the measured curves. It should be noted that the measured temperatures are from different locations in the balcony slab, while the calculated temperatures correspond to the most severe case.

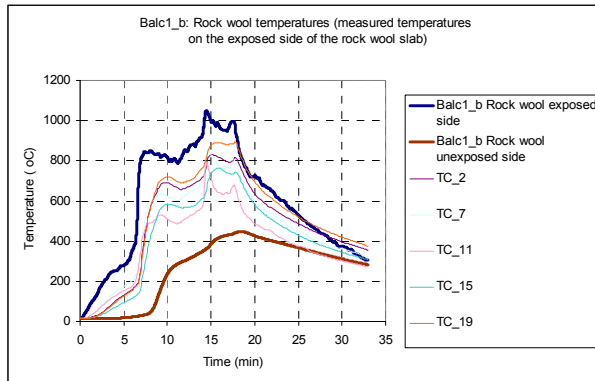


Fig. 6 — Comparison of temperatures on insulation surfaces (Rock wool 140 kg/m^3) from calculation model *Balc1_b* and test.

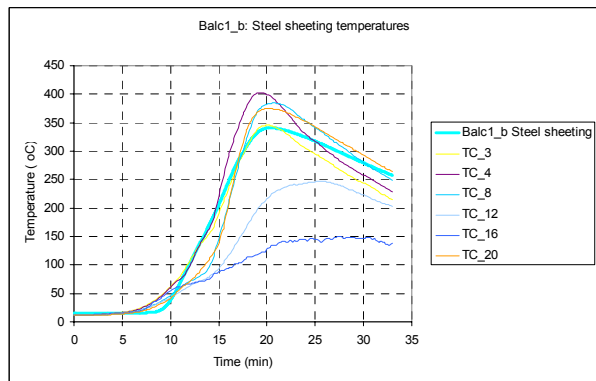


Fig. 7 — Comparison of interior steel sheeting (RAN 45 R) temperatures from calculation model *Balc1_b* and test.

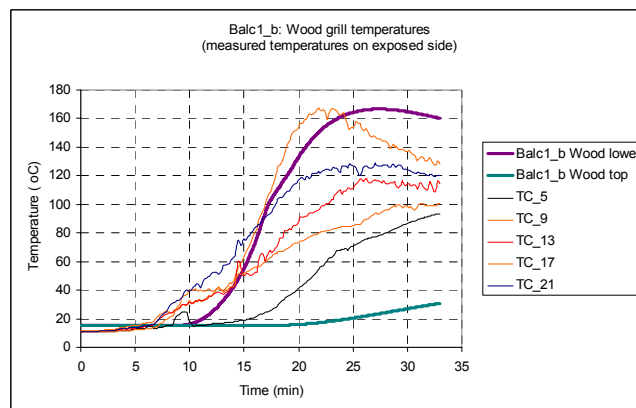


Fig. 8 — Comparison of wood grill temperatures from calculation model *Balc1_b* and test.

4. SUMMARY AND CONCLUSIONS

In the frame of ECSC Project PR 380, simple calculation methods for the temperature development of structural or stainless steel columns protected with structural or stainless steel casings have been developed and validated on the basis of a furnace test with temperature development according to the EN1363-1:1999 standard fire curve and natural fire tests carried out on the VTT façade test rig. Very good agreement between calculations and test results was found using the 1D-method and also the 2D-method under symmetric fire exposure. The agreement is not quite as good for the 2D-method under asymmetric fire exposure. In fact, the more asymmetric the fire exposure is, the less accurate are the results. This is explained by the high nonlinearities in temperature distributions during these tests. However, the results are mostly conservative for these cases as well. Further comparisons to other available test results were also carried out and good agreement was found.

The proper choice of emissivity values is essential for the calculations. It is recommended on the basis of the available test results that for stainless steel, an emissivity value equal to at least $\varepsilon = 0.5$ should be used. If more safety is required, the value can be raised to $\varepsilon = 0.6$. For structural steel, the value of emissivity $\varepsilon = 0.7$, as recommended by prEN 1993-1-2: 2003⁴, seems appropriate.

The test results available for the validation of the calculation methods represented only a small fraction of all possible structural entities of this type. The test results covered the following range of variables:

- F/V-values of steel columns: 104 1/m - 212 1/m
- casing steel sheet thickness: 0.8 mm - 1.0 mm
- air gap distance between column and casing: 12 mm - 40 mm

The method can be used also outside these limits, but it is suggested that strong caution be used when doing so. In any case, the results obtained using these calculation methods are meant to be indicative and full guarantee cannot be given about their conservatism in all possible design cases. The limited availability of suitable test results for the testing and full validation of these calculation methods does not allow the methods to be considered fully valid.

Also a 1D-temperature calculation method for layered steel balcony structures was developed by VTT during the ECSC Project PR 380. A fairly good agreement of results was obtained in this case, although the calculated steel sheet temperatures are actually a little lower than the highest measured temperatures. The calculated wood grill temperatures show quite a good agreement with the measured curves.

Computer codes using Matlab[®] 7.0.1 have been written for the practical usage of these calculation methods. The computer codes will be available from the author free of charge after the official closing of the ECSC Project PR380.

5. REFERENCES

- [1] EN1363-1: 1999: Fire resistance tests – Part 1 : General requirements, CEN 1999.
- [2] Incropera, F.P., DeWitt (2002), D.P., *Fundamentals of Heat and Mass Transfer*, Fifth Edition, John Wiley and Sons, U.S.A.
- [3] Siegel & Howell (1972), *Thermal Radiation Heat Transfer*, McGraw-Hill Book Company, U.S.A.
- [4] prEN 1993-1-2: 2003 *Eurocode 3: Design of Steel Structures Part 1.2: General rules, Structural fire design*, CEN, European Committee for Standardisation, 2003.
- [5] Matlab[®], Version 7.0.1, The MathWorks, Inc.



EXPERIMENTAL AND NUMERICAL STUDY OF A TWO-SPAN STEEL I-BEAM HEATED ALONG THE LOWER FLANGE

Kuldeep S. VIRDI¹ and Gordon COOKE²

ABSTRACT

Experiments have been made on a 2-span continuous steel I-section beam heated along one flange to elevated temperatures. The reaction force needed to suppress mid-span deflection due to thermal bowing was measured as heating progressed. As expected, the reaction force predicted by a simple elastic analysis agreed poorly with the test results, but the FAUST computer program, based on nonlinear inelastic analysis, gave excellent correlation with the test results.

1. INTRODUCTION

Fire Engineering calculations are generally carried out on the basis of isolated members such as beams and columns assumed to be heated uniformly along the length. In practice there may be beams which span continuously between several supports. Of course, structural frames are assemblages of beams and columns, whose response under fire is complex. Realistically, in a continuous structure, fire will develop in one compartment while the adjacent compartments remain at ambient temperatures. Tests have been carried out at Cardington on a composite frame, where selected members were exposed to fire, cited in Ref [1]. The Cardington tests show conclusively the importance of interaction between members exposed to fire and other connected members in the frame. This paper describes tests carried out on a two-span beam where the bottom flange was heated in one span only. Advantage was taken to study the response of the two-span beam with the bottom flange heated in both spans. The tests have been used to validate a finite-difference based method of material and geometric nonlinear analysis for calculating the response under fire of frames made of steel and composite beams and columns.

¹ Professor, School of Engineering and Mathematical Sciences, City University, London, UK
email: k.s.virdi@city.ac.uk

² PhD, Fire Safety Consultant and Visiting Professor, City University, London, UK
email: gordon@cookeonfire.com

A simplified analysis of the two-span beam may be based on the principle of allowing the beam to first deflect due to thermal bowing and then to apply a force to return the deflection at the middle support to a zero value. Indeed this procedure is the only realistic approach for calculating the restraint forces in the structure, unless a more rigorous method of analysis is used. The principles on which the nonlinear inelastic analysis used in the paper is described briefly.

2. EXPERIMENTS

The beam (initially straight with shape ACE) heated along the lower flange would, if unrestrained, bow down to the shape AFE as shown in Fig. 1. When restrained at mid-span the deflected shape is ABCDE. In the experiments² the mid-span restraint force was provided using a strong beam (not shown in the figure below) so that the ends of the specimen were held down while the centre of the specimen was pushed up to counteract the thermal bowing. The restraint force was provided with the aid of a compression load cell and a screw-jack at mid-span while measurement was made to ensure there was zero deflection at mid-span.

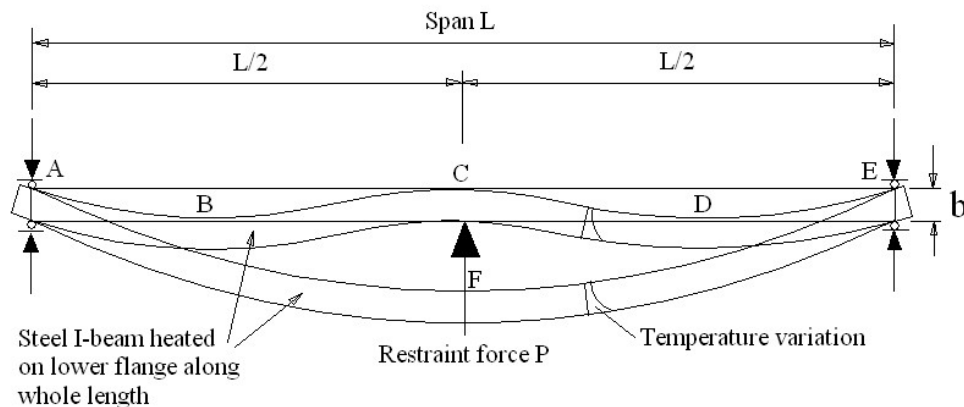


Fig 1 - Practical beam restraint conditions simulated in the experiments.

2.1 Specimens

Two experiments were performed on the smallest hot rolled steel I-section 'joist' (beam) commercially available in the UK. This was a RS joist, 104mm deep by 44mm wide by 7.35kg/m. A nominal span of 1500mm was used. The section has slightly tapered flanges and a stated nominal second moment of area about the major axis of 152.3cm^4 . A check on the steel composition showed that the steel corresponded most closely to an ordinary mild steel (Grade 43 of BS 4360). The steel had an unusually high 0.2% proof stress of 421 N/mm^2 and an upper limit ultimate tensile strength of 517 N/mm^2 when compared with a BS 4360 Grade 43 values of 255 N/mm^2 for yield strength and $430\text{--}510\text{ N/mm}^2$ for ultimate tensile strength. It could be assumed to have an E value of 210 kN/mm^2 for theoretical analysis purposes.

2.2 Apparatus

The apparatus comprised the specimen test beam supported at the ends by steel restraint frames which were fixed to a steel I-section strong beam $305 \times 165 \times 54\text{kg/m}$ as shown in Fig. 2 and Fig. 3. Central restraint against downward thermal bowing of the specimen was provided by a compression load transducer resting on the strong beam,

surmounted with a purpose-made hand-adjusted screw jack with ball race incorporated and a 25mm thick high density insulation packing piece. The packing piece was in contact with the lower flange of the specimen and this meant that the beam was not heated over the 100mm length. Kaowool blanket was placed around the packer at mid-span to reduce heat loss. A check on vertical deflection of the centre of the specimen relative to its ends was achieved with a steel straight edge bearing on the specimen at its ends and with an electrical connection at the centre – as soon as the beam moved down an electric lamp would go out and the screw jack would be adjusted to bring the top of the beam at mid-span to the same level as the ends. Between measurements the straightedge was stored in a water-filled trough so that as heating continued it would not be affected by thermal bowing caused by the plume of hot air rising past the heated assembly.

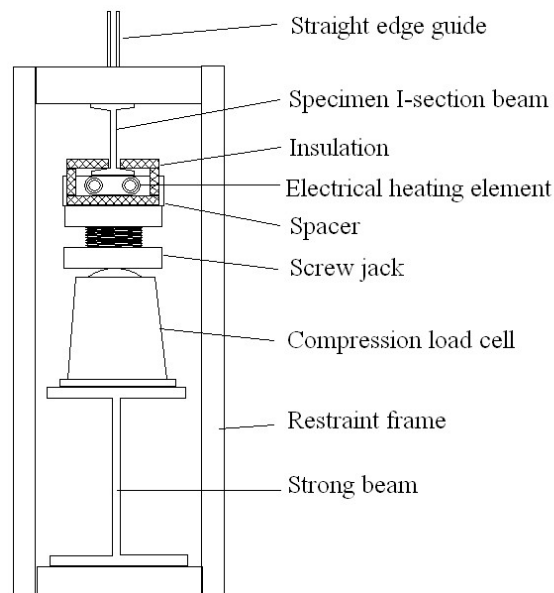


Fig. 2 - Vertical section through test rig.

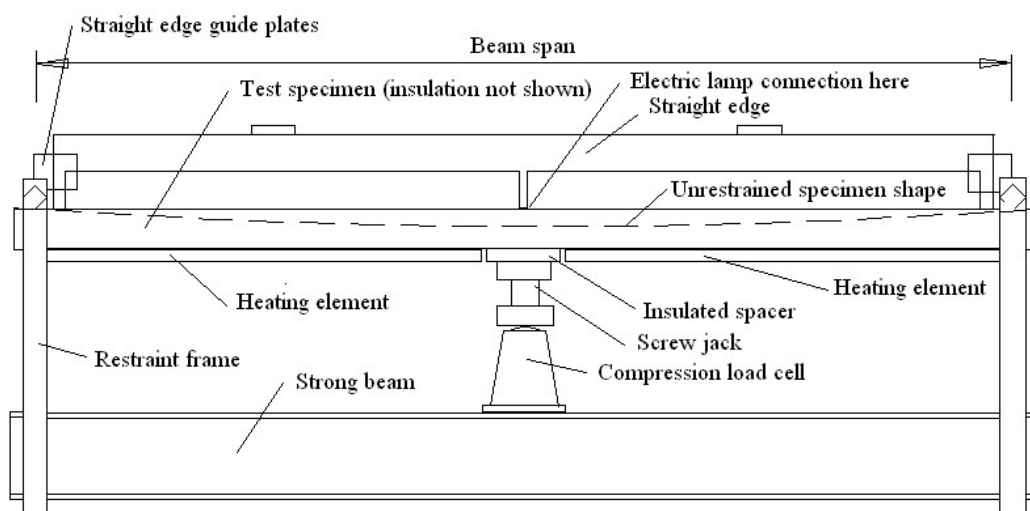


Fig. 3 - Schematic of test rig.

2.3 Heating

Heating along the lower flange was achieved using 680mm long by 30mm wide by 30mm thick high-temperature flexible ceramic insulated electrical heating elements rated at 3.5kW operated at 60V (requiring the use of transformers) which were capable of operating at 1050°C. These were held against the lower flange by steel tie wires. The ceramic insulation on the heating elements was in short lengths so that the heating element could flex without restraining the bending of the test specimen. The lower flange and heaters were insulated with 25mm strips of Kaowool ceramic fibre insulation board held on with steel wire ties (Fig. 2).

2.4 Temperatures

To obtain comprehensive data of temperature along the length and across the depth, 12 stations of chromel-alumel thermocouples were used, spaced at 128mm centres along the length. At each station 5 thermocouples were fixed, spaced at nominally 25mm apart over the depth. Thus 60 thermocouples were used, as shown in Fig. 4.

2.5 Restraint force

The load cell used was a calibrated pillar type compressive load transducer of 100mm height and 8 tonne rating. The hand-operated screw jack incorporated a ball-bearing race so that it was easily possible to adjust the jack to maintain zero vertical deflection at mid span.

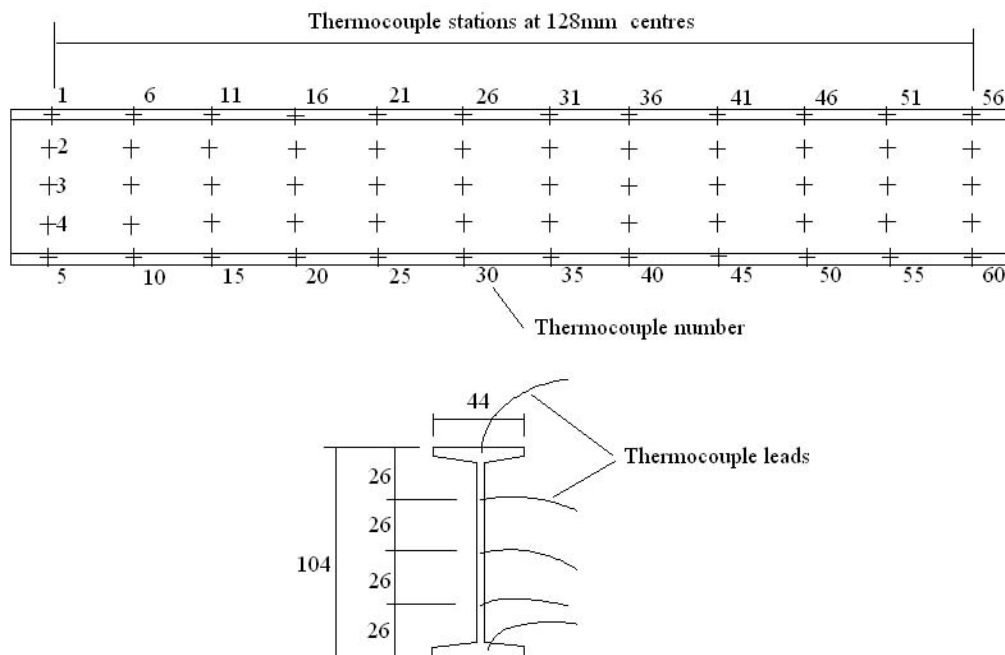


Fig. 4 - Positions of thermocouples in the steel beam.

2.6 Experimental procedure

For one test two heating elements and associated Kaowool insulation were present. In the half flange heated test the unwanted heating element and Kaowool were not present. These two tests were made using the same specimen and this was justified by the knowledge that the residual strength properties of mild steel heated were not greatly affected by heating

and cooling: the permanent reduction in strength was approximately 25 N/mm^2 and 50 N/mm^2 after heating to temperatures of 600°C and 700°C respectively.

One or both of the heating elements were switched on and the data loggers started. Every 2 minutes, just before the data logger began recording the 60 channels, the cool straightedge was placed in position and the screw jack adjusted until the lamp lit and the jack was continually adjusted to maintain zero deflection. It was frequently removed from the rig to cool it in the water trough. This procedure was repeated until the end of each experiment.

2.7 Results of experiments

A typical set of temperature profiles across the depth of the section at quarter span at times of 12, 24 and 32 minutes are given in Fig.5 for the beam heated along whole of the flange. The hot flange recorded a maximum temperature of 700°C .

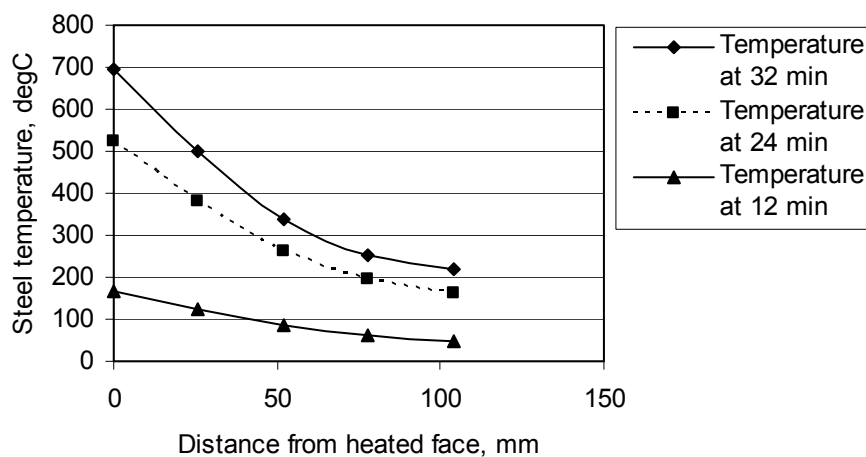


Fig. 5 - Typical temperature profiles for beam heated along whole flange.

Fig. 6 shows the variation of the maximum hot flange temperature along the length of the beams for both the whole flange heated and the half-length heated experiments. It should be noted that the profile for the whole flange heated case is at 32 minutes, while the half-length heated profile is for 38 minutes.

The experimental restraint force data are plotted in Fig. 7 below. It should be noted that when whole flange was heated, there appears to have been some redistribution of stresses, showing the restraint force nearly constant while the heating continued. After this stage, the restraint force required had to be reduced to keep the central support at zero deflection. The half-length heated case shows a similar brief plateau, however, at a much later stage. It is difficult to assess whether this is related to the phase change phenomenon in steel.

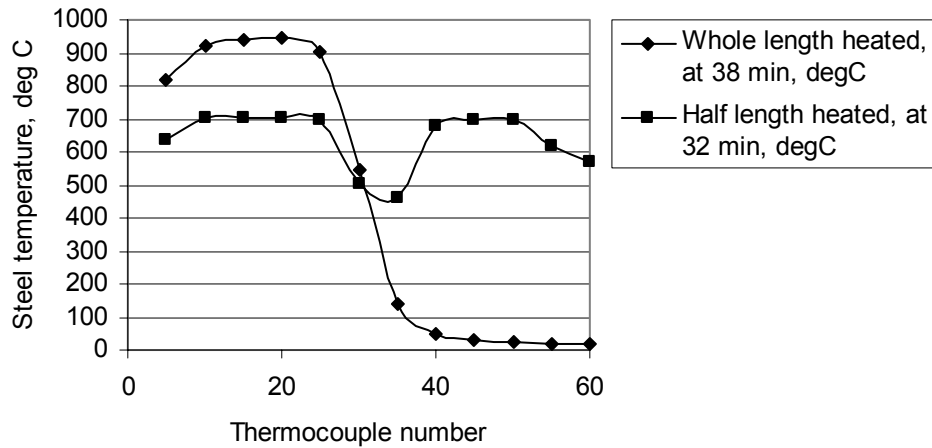


Fig. 6 - Variation of hot flange temperature with length.

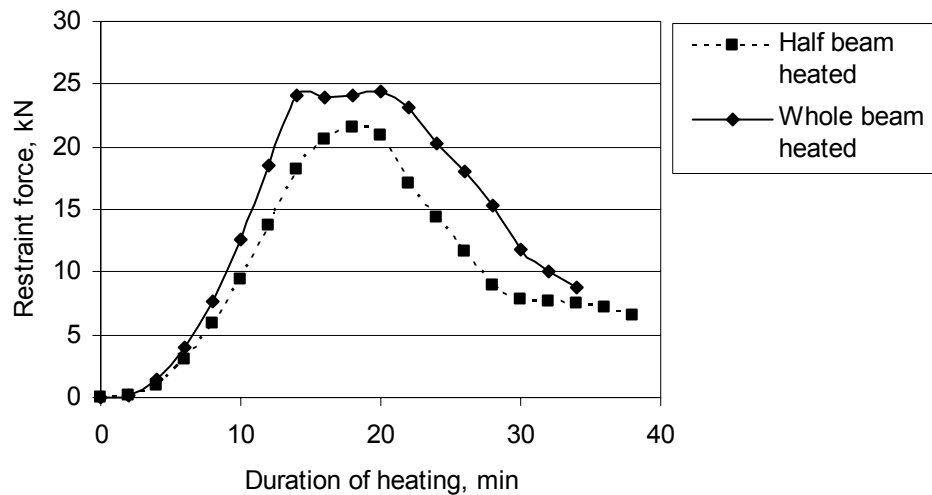


Fig. 7 - Experimental mid-span restraint force for the two tests.

3. ELASTIC THEORY

It can be shown² that a steel beam of span L and depth d subjected to a linear temperature difference T across the depth will, if it is not restrained, bow into a circular arc such that the mid-span deflection is:

$$\Delta = \frac{\alpha T L^2}{8d}$$

(1)

where α = coefficient of linear thermal expansion of steel ($14 \times 10^{-6}/^{\circ}\text{C}$). It is sufficiently accurate to assume that T is the difference between the hot flange temperature and the cold flange temperature for a steel I-section when calculating thermal bowing deflection of steel I-sections. If, in the deflected form, a restraint force P is applied upwards at mid-span to the beam to produce zero deflection at mid-span, then using the principle of superposition (which only applies in the elastic domain), the force so applied is equal to the force needed to sustain

zero displacement at mid-span, as in the experiment. Thus the force needed to ‘straighten out’ the deflected beam can be obtained from the well-known relation

$$\Delta = \frac{PL^3}{48EI}$$

(2)

where E = Elastic modulus (210kN/mm² for steel). Transposing and substituting for Δ gives

$$P = \frac{6EI\alpha T}{Ld}$$

(3)

As heating continues T increases and E decreases (to approximately 145 kN/mm² at 800°C). E is assumed to vary with temperature as in the steel Eurocode 3 Part 1.2³.

The calculated restraint force for the experiment in which the whole of one flange is heated is shown in Fig. 8 below. Hence, the stress:

$$f = \frac{My}{I} = \frac{PLy}{4I}$$

(4)

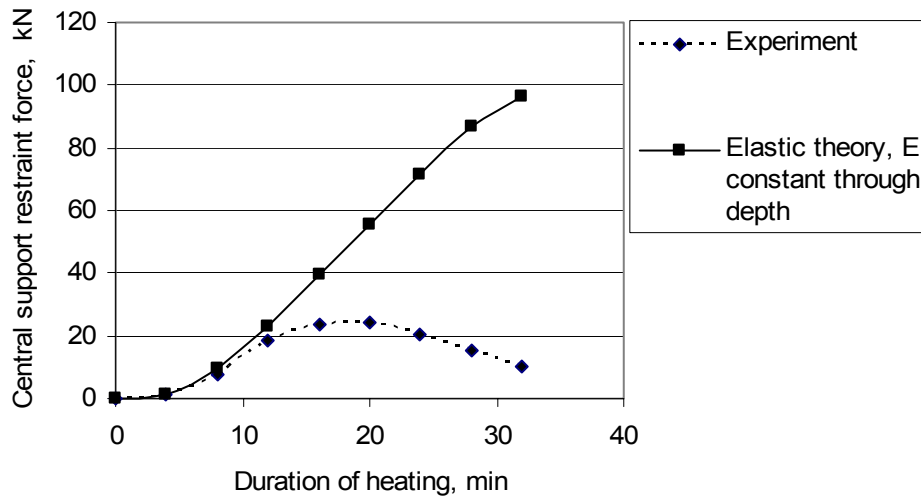


Fig. 8 - Experimental and theoretical mid-span restraint force based on elastic analysis.

If the stress f exceeds nominally 250N/mm² the material has yielded and the restraint force will be less than that assumed in an elastic analysis. Fig. 8 gives the comparison of experimental and theoretical restraint force for the condition when whole of the lower flange is heated. It is clear that an elastic analysis over-predicts the restraint force. By substitution in Equation 4, the stress was found to be 295N/mm² at 12 minutes, indicating that the steel had yielded.

4. INELASTIC ANALYSIS

The stability response of isolated restrained beam-columns has previously been studied by Viridi and Dowling^{4,5} and Viridi⁶. The numerical method is based on the application of finite differences for the calculation of deflected shape of the beam-column for increasing values of the applied member loading. A generalised Newton-Raphson approach was adopted for speedy convergence. The method has been extended to the fire analysis of

framed structures⁷. The method is capable of dealing with arbitrarily defined cross-sections, stress-strain characteristics, joint characteristics, and initial imperfections.

4.1 Modelling of frames

A frame may be viewed as an assemblage of members forming a structural skeleton. A general member in the structure can be represented by a beam-column of finite length. A typical member A-B in a space frame is shown in Fig. 9.

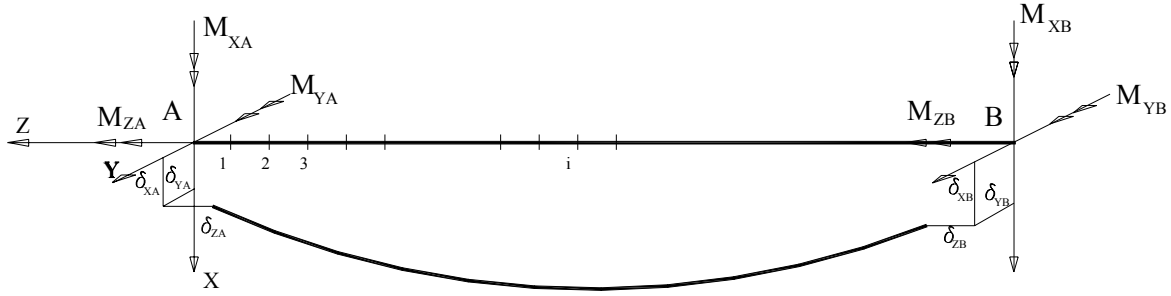


Fig. 9 – A typical member in a space frame,

4.2 Equilibrium deflected shape of members

The equilibrium deflected shape of a typical beam-column is obtained by subdividing it into a number of segments and establishing conditions of equilibrium at the segmental stations. For given end forces, the external moments at a station need to be in equilibrium with the internal moments induced by the curvatures due to deformations, and where applicable, torsional warping. Internal moments are computed using the moment-thrust-curvature relations as described by Viridi and Dowling⁴.

The Newton-Raphson method suggests that if $M(w)=0$ is a function of w , a better approximation w_{k+1} for an assumed value w_k can be given by:

$$w_{k+1} = w_k - [M'(w_k)]^{-1} M(w_k) \quad (5)$$

where, $M'(w_k)$ is the matrix of derivatives of $M(w_k)$ with respect to w_i at iteration k . By replacing the function M by $\{M_{in}(w) - M_e(w)\}$ and rearranging

$$[M'_{in} - M'_e] \{w_{k+1} - w_k\} = -\{M_{in} - M_e\} \quad (6)$$

where $\{M_{in} - M_e\}$ is the vector of differences of internal moments to external moments and has $(2n+2)$ elements, where n is the number of subdivisions in the member, and $\{w_{k+1} - w_k\}$ is the vector of corrections to the deflections. It follows that the term $[M'_{in} - M'_e]$ is a matrix of $(2n+2) \times (2n+2)$ elements. The method of forming these matrices efficiently is explained in detail in Ref [5] and Ref [7].

In the original formulation, the above solution was based on solving for deflections. In the present formulation, the solution is for moments along the length, but the two approaches are interchangeable.

4.3 Equilibrium nodal deformations of the frame

The global deformation vector $\{\Delta\}$ at nodes i and j is transformed to member axes as follows

$$\{\delta\} = [T] \{\Delta\} \quad (7)$$

where $\{\delta\}$ is the vector of member deformations at ends A and B with respect to member local axes and $[T]$ is the transformation matrix between local and global axes. The end forces obtained from member equilibrium deflected shape calculations are now checked for equilibrium at nodal points. If these forces are not in equilibrium, then corrections to nodal deformations must be made.

For the beam-column shown in Fig. 9, the member end forces $\{p\}$ are functions of member deformation $\{\delta\}$.

$$\{p\} = \{p(\delta)\} \quad (8)$$

These end forces are transformed to global forces $\{P\}$ using the member transformation matrix $[T]$. If the external nodal forces were represented by $\{F\}$, the unbalanced nodal forces $\{R\}$ may be written as:

$$\{P\} - \{F\} = \{R(\Delta_r)\} \quad (9)$$

where $\{\Delta_r\}$ are the global deformations at the r th iteration. The aim of the iteration is to reduce all the unbalanced forces to an acceptably small value. The generalised Newton-Raphson method suggests that an improved set of deformations $\{\Delta_{r+1}\}$ is given by

$$\{\Delta_{r+1} - \Delta_r\} = - [K(\Delta_r)]^{-1} \{R(\Delta_r)\} \quad (10)$$

where, $[K]$ is a matrix representing variations in nodal forces corresponding to changes in nodal deformations. By substituting $\{R\}$ in terms of $\{P\}$ and $\{F\}$

$$\{\Delta_{r+1} - \Delta_r\} = - [K]^{-1} (\{P_r\} - \{F\}) \quad (11)$$

The matrix of influence coefficients, or the numerical stiffness matrix $[K]$, is formed by calculating the changes in member end forces required for small increments in end deformations. For example, to calculate the terms corresponding to axial forces and deformations, end B is restrained for all six degrees of freedom. The end A is also restrained in all directions except for the displacement along z -axis. Forces and moments required for equilibrium are then calculated. It should be noted that, since this "stiffness matrix" is computed numerically, the procedure can be applied to arbitrarily defined cross-sections, stress-strain characteristics, joint characteristics, and initial imperfections.

4.4 Ultimate load

The equilibrium deflected shapes of a frame is calculated as described in previous section, for increasing values of applied loads. As the principal variable, that is, the load factor, is increased, the stiffness of the structure reduces and eventually vanishes. The maximum value of the load at which equilibrium deflected shape for a member or a converged solution for nodal deformations is found, is defined as the ultimate load of the structure.

A computer program *FAUST* based on the method outlined above has been used for an inelastic analysis of the two-span beam described above.

4.5 Results from the *FAUST* program

The two tests were modelled as accurately as possible as far as geometry is concerned. Each member is divided into 15 segments along the length. The I shape of the joist was modelled as three rectangles, with flanges of thickness 6.1mm and web thickness of 4.3mm. The fire-dependent stress-strain curves for steel were in accordance with Eurocode 3 Part 1.2³. The characteristic strength for steel, based on measurements described above, was adopted as 255N/mm². The temperature distribution adopted was as shown in Fig. 5 and Fig. 6 above. As reported above, the measured temperatures at corresponding points along the length in the heated zones were very nearly uniform. Hence, the temperature profiles were averaged for corresponding points along the length, and these average values were used as constant for the heated zones.

The calculated reaction forces for the case of both spans heated are compared with the corresponding observed values in Fig. 11. The comparison for the case of only one span heated is shown in Fig. 12. The program *FAUST* is shown to give excellent correlation with experiments. The wavy nature of the response is attributed to the variation in the recorded temperatures.

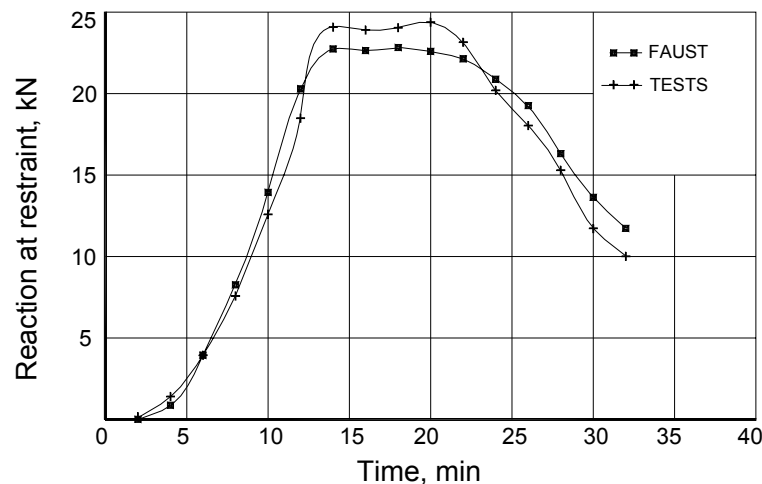


Fig. 11 - Mid-span restraint force (both spans heated).

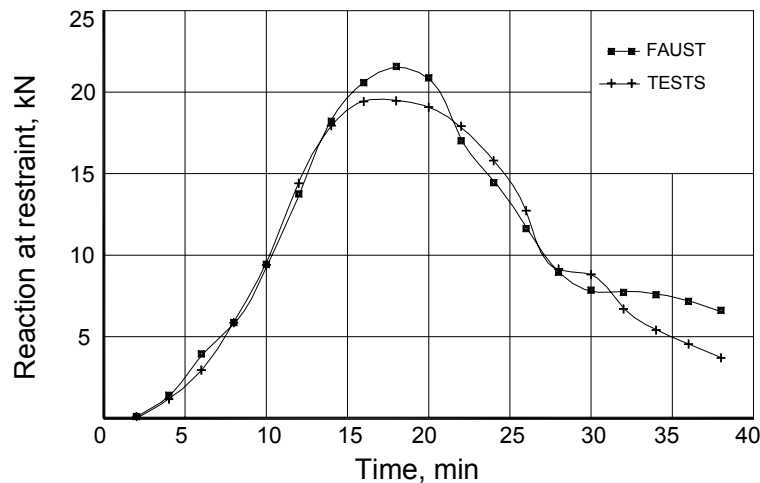


Fig. 12 - Mid-span restraint force (one span heated).

5. CONCLUSIONS

An experiment has been successfully completed on a model steel beam when heated to elevated temperatures over the whole length of one flange and similarly when heated over half the length of one flange. Data of temperature profiles and mid-span restraint force have been collected which are useful for validating theoretical models. It is shown that elastic analysis greatly over predicts the mid-span restraint force due to early local yielding and this method cannot be used. Calculations including temperature gradients, nonlinear temperature dependent stress-strain curves and based on the finite difference method, as implemented in the program *FAUST*, have been shown to give excellent correlation with the experimental results.

6. ACKNOWLEDGMENT

The computational work described in the paper was developed under a project funded by the UK Engineering and Physical Sciences Research Council. The contribution of the first author's colleague, Dr P Ragupathy is gratefully acknowledged. The second author is also grateful for the use of experimental facilities of the Fire Research Station of the Building Research Establishment.

7. REFERENCES

- [1] Wang Y C, An analysis of the global structural behaviour of the Cardington steel-framed building during the two BRE fire tests. *Engineering Structures*, May 2000, vol. 22, no. 5, pp. 401-412.
- [2] Cooke G M E, The structural response of steel I-section members subjected to elevated temperature gradients across the section, PhD thesis, City University, London, Sept 1987, pp 450.

- [3] EN 1993-1-2 Eurocode 3 Part 1.2, Structural fire design
- [4] Viridi, K S and Dowling, P J, The ultimate strength of composite columns in biaxial bending. Proceedings of the Institution of Civil Engineers, Part 2, Mar, 1973.
- [5] Viridi, K S and Dowling, P J, The ultimate strength of biaxially restrained columns. Proceeding of the Institution of Civil Engineers, Part 2, Mar, 1976.
- [6] Viridi, K S, Design of circular and rectangular hollow section columns. Journal of Constructional Steel Research, Vol 1, No 4, pp 35-45, 1981.
- [7] Ragupathy, P, Nonlinear Analysis of precast concrete frames. PhD Thesis, City University, London, 1994.



STUDIES ON LOCAL BUCKLING OF HEATED STEEL COLUMNS WITH BOX SECTIONS BY USING FINITE ELEMENT ANALYSES

Fuminobu OZAKI¹, Philipp NIEDEREGGER², Markus KNOBLOCH² and Mario
FONTANA³

ABSTRACT

In the present paper, local buckling behavior of steel columns with box sections at high temperatures is investigated by using a finite element analysis. Firstly, we describe a finite element modeling for a non-linear shell element. Secondly, we try to compare numerical results with past experimental results on steel stub columns at high temperatures. Finally, we discuss a typical case when the local buckling of the column occurs during a fire, by analyzing the heated column subject to a horizontally forced displacement due to a thermal elongation of the adjacent heated beam. From the above analysis, it was recognized that the local buckling of the heated steel column has a significant influence and decreases its fire resistance.

¹ Post Doctoral Researcher of the 21st Century COE Program, Tokyo Univ. of Science,
(Former Guest Researcher, Swiss Federal Inst. of Tech. (ETH), Inst. of Structural Eng. (IBK))
Center of Fire Sci. and Tech., 2641 Yamazaki, Noda-shi, Chiba, 278-8510, Japan.

e-mail: fuminobu_ozaki@yahoo.co.jp

² Research Assistant, Swiss Federal Inst. of Tech. Zurich (ETH), Inst. of Structural Eng. (IBK)
ETH-Hoenggerberg, CH-8093, Zurich, Switzerland.

e-mail: philipp.niederegger@ibk.baug.ethz.ch and markus.knobloch@ibk.baug.ethz.ch

³ Professor, Swiss Federal Inst. of Tech. Zurich (ETH), Inst. of Structural Eng. (IBK)
e-mail: fontana@ibk.baug.ethz.ch

1. INTRODUCTION

Designing steel structures against a fire, we must especially verify fire resistance of steel columns which are main structural members. When the column, in particular, has a large plate width – thickness ratio, a local buckling phenomenon in the heated column may occur during the fire. In this case, there is a possibility that the column will collapse by local buckling at an early fire stage ahead of the other collapse modes, for instance overall buckling. The main purpose of this study is to investigate the local buckling behavior of the steel column at high temperatures by using a finite element analysis. In the finite element analysis, non-linear improved shell elements which have been proposed by Nakagawa and Suzuki [1] are used. The shell element model is described in the first part of this paper. In the next part, we compare numerical results with experimental results obtained from past steel stub column tests at the high temperature (Hirashima et al. [2]). Finally, we discuss a typical case when local buckling of the column occurs during the fire, by analyzing a heated column subject to a horizontally forced displacement due to a thermal elongation of an adjacent heated beam numerically.

2. FINITE ELEMENT MODELING FOR THE SHELL ELEMENT

2.1 Descriptions of Displacement Fields in the Shell Element

Fig-1 shows a schematic diagram of the shell element used in this study. Its shape is a rectangular which has side lengths $2a$ and $2b$. The shell element has eight independent nodes; there are four corner nodes (Node 1, 2, 3 and 4) and four middle nodes (Node 4, 5, 6 and 7). Fig-2 shows the nodal degrees of freedom at the Node 1, 5 and 7. In the element, non-dimensional coordinate axes ξ , η and ζ are respectively set. Each corner node has three translational degrees of freedom in directions of coordinate axes ξ , η and ζ , and also has four rotational degrees of freedom in the directions of rotational angles ϕ , θ , ϕ_w and θ_w . Each middle node has one translational degree of freedom. To improve compatibility of the rotational displacements on boundaries of the adjacent elements, each corner node has two independently rotational degrees of freedom ϕ_w and θ_w in the in-plate direction. The shell element has, therefore, 32 nodal degrees of freedom in total.

To determine displacement fields in the element, we use shape functions defined by the following equations (1) - (3). Displacements u , v and w at arbitrary points in the element are described as the follows [1],

$$u = [[A'], [B], [C]] \{u\} \quad (1),$$

$$v = [[A''], [B'], [D]] \{v\} \quad (2),$$

$$w = [[A], [C], [D]] \{w\} \quad (3).$$

Where,

$$\{u\}^T = \{u_1, u_2, u_3, u_4, u_5, u_6, \phi_1, \phi_2, \phi_3, \phi_4\}, \quad \{v\}^T = \{v_1, v_2, v_3, v_4, v_7, v_8, \theta_1, \theta_2, \theta_3, \theta_4\},$$

$$\{w\}^T = \{w_1, w_2, w_3, w_4, \phi_{w1}, \phi_{w2}, \phi_{w3}, \phi_{w4}, \theta_{w1}, \theta_{w2}, \theta_{w3}, \theta_{w4}\},$$

$$[A] = \begin{bmatrix} \frac{1-\xi}{2} \frac{1-\eta}{2}, & \frac{1+\xi}{2} \frac{1-\eta}{2}, & \frac{1+\xi}{2} \frac{1+\eta}{2}, & \frac{1-\xi}{2} \frac{1+\eta}{2} \end{bmatrix},$$

$$[A'] = \begin{bmatrix} -\frac{1-\eta}{2} \frac{1-\xi}{2} \cdot \xi, & \frac{1-\eta}{2} \frac{1+\xi}{2} \cdot \xi, & \frac{1+\eta}{2} \frac{1+\xi}{2} \cdot \xi, & -\frac{1+\eta}{2} \frac{1-\xi}{2} \cdot \xi \end{bmatrix},$$

$$[A''] = \begin{bmatrix} -\frac{1-\xi}{2} \frac{1-\eta}{2} \cdot \eta, & -\frac{1+\xi}{2} \frac{1-\eta}{2} \cdot \eta, & \frac{1+\xi}{2} \frac{1+\eta}{2} \cdot \eta, & \frac{1-\xi}{2} \frac{1+\eta}{2} \cdot \eta \end{bmatrix},$$

$$[B] = \begin{bmatrix} (1-\xi^2) \cdot \frac{1-\eta}{2}, & (1-\xi^2) \cdot \frac{1+\eta}{2} \end{bmatrix},$$

$$[B'] = \begin{bmatrix} (1-\eta^2) \cdot \frac{1-\xi}{2}, & (1-\eta^2) \cdot \frac{1+\xi}{2} \end{bmatrix},$$

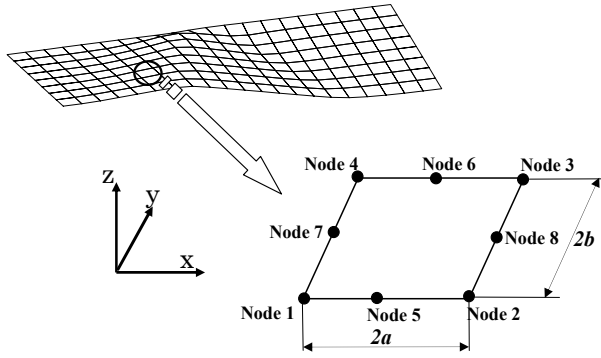


Fig-1 8 nodes shell element

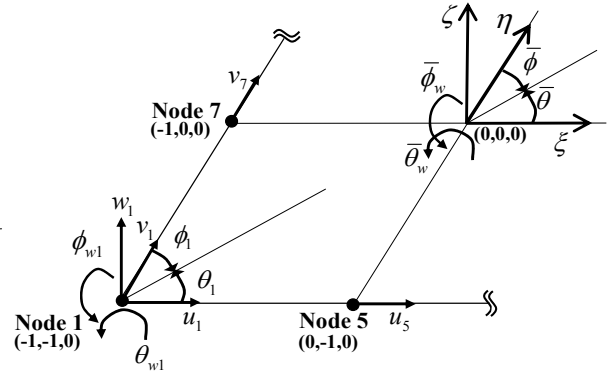


Fig-2 Nodal displacements

$$[C] = \begin{bmatrix} \frac{(1+\eta)(1-\eta)^2}{4} \cdot \frac{1-\xi}{2}, & \frac{(1+\eta)(1-\eta)^2}{4} \cdot \frac{1+\xi}{2}, & -\frac{(1-\eta)(1+\eta)^2}{4} \cdot \frac{1-\xi}{2}, & -\frac{(1-\eta)(1+\eta)^2}{4} \cdot \frac{1+\xi}{2} \end{bmatrix},$$

$$[D] = \begin{bmatrix} \frac{(1+\xi)(1-\xi)^2}{4} \cdot \frac{1-\eta}{2}, & -\frac{(1-\xi)(1+\xi)^2}{4} \cdot \frac{1-\eta}{2}, & -\frac{(1-\xi)(1+\xi)^2}{4} \cdot \frac{1+\eta}{2}, & \frac{(1+\xi)(1-\xi)^2}{4} \cdot \frac{1+\eta}{2} \end{bmatrix}.$$

Each nodal displacement on the boundary lines must be continuous. In the cases of the translational nodal displacements $\{u_{1-4,5,6}\}$, $\{v_{1-4,7,8}\}$ and $\{w_{1-4}\}$, each nodal displacement on the boundary lines is continuous so that its direction agrees with a general coordinate axis. On the other hand, this is not capable of being concluded in the cases of the rotational nodal displacements $\{\phi_{1-4}\}$, $\{\theta_{1-4}\}$, $\{\phi_{w1-4}\}$ and $\{\theta_{w1-4}\}$. This is because these nodal displacements are not rotational angles based on the general coordinate axes but they are based on each side line of the element. The latter depend on the direction of each side line. For this reason, we need to re-describe the shape functions by using the general coordinate axes.

Now, we set the general coordinate axes $\bar{\phi}$, $\bar{\theta}$, $\bar{\phi}_w$ and $\bar{\theta}_w$ as in the Fig-2. For instance, we can get the relationship between the rotational angle $\bar{\phi}_w$ and the displacement w , or,

$$\bar{\phi}_w = \frac{\partial w}{\partial y} \quad (4).$$

By using the rotational nodal displacements $\{\bar{\phi}\}$, $\{\bar{\theta}\}$, $\{\bar{\phi}_w\}$ and $\{\bar{\theta}_w\}$ based on the general coordinate axes, we can get the following equations.

$$u = [[A'], [B]] - [C] [[A'_\eta], [B_\eta]], b[C]] \{ \bar{u} \} \equiv [U] \{ \bar{u} \} \quad (5)$$

$$v = [[A''], [B']] - [D] [[A''_\xi], [B'_\xi]], a[D]] \{ \bar{v} \} \equiv [V] \{ \bar{v} \} \quad (6)$$

$$w = [[A] - [C] [[A_\eta]] - [D] [[A_\xi]], b[C], a[D]] \{ \bar{w} \} \equiv [W] \{ \bar{w} \} \quad (7)$$

Where,

$$\{ \bar{u} \} = {}^T \{ u_1, u_2, u_3, u_4, u_5, u_6, \bar{\phi}_1, \bar{\phi}_2, \bar{\phi}_3, \bar{\phi}_4 \}, \quad \{ \bar{v} \} = {}^T \{ v_1, v_2, v_3, v_4, v_7, v_8, \bar{\theta}_1, \bar{\theta}_2, \bar{\theta}_3, \bar{\theta}_4 \},$$

$$\{ \bar{w} \} = {}^T \{ w_1, w_2, w_3, w_4, \bar{\phi}_{w1}, \bar{\phi}_{w2}, \bar{\phi}_{w3}, \bar{\phi}_{w4}, \bar{\theta}_{w1}, \bar{\theta}_{w2}, \bar{\theta}_{w3}, \bar{\theta}_{w4} \}.$$

2.2 Relationship between Strains and Nodal Displacements

To analyze geometrically non-linear problems, strains ε_x , ε_y and γ_{xy} in the element are given by the equations (8), (9) and (10).

$$\varepsilon_x = u_x - zw_{xx} + 0.5(u_x^2 + v_x^2 + w_x^2) \quad (8)$$

$$\varepsilon_y = v_y - zw_{yy} + 0.5(u_y^2 + v_y^2 + w_y^2) \quad (9)$$

$$\gamma_{xy} = u_y + v_x - 2zw_{xy} + u_x u_y + v_x v_y + w_x w_y \quad (10)$$

We can also describe incremental strains by using the above equations, that is,

$$\Delta \varepsilon_x = \Delta u_x - z \Delta w_{xx} + u_x \Delta u_x + v_x \Delta v_x + w_x \Delta w_x \quad (11),$$

$$\Delta \varepsilon_y = \Delta v_y - z \Delta w_{yy} + u_y \Delta u_y + v_y \Delta v_y + w_y \Delta w_y \quad (12),$$

$$\Delta \gamma_{xy} = \Delta u_y + \Delta v_x - 2z \Delta w_{xy} + \Delta u_x u_y + u_x \Delta u_y + \Delta v_x v_y + v_x \Delta v_y + \Delta w_x w_y + w_x \Delta w_y \quad (13).$$

Upon substituting the equations (5) - (7) into the equations (11) - (13), we obtain the relationship between the incremental strains and the incremental nodal displacements, that is,

$$\begin{Bmatrix} \Delta \varepsilon_x \\ \Delta \varepsilon_y \\ \Delta \gamma_{xy} \end{Bmatrix} = \begin{bmatrix} (1+u_x)[U_x], & v_x[V_x], & -z[W_{xx}] + w_x[W_x] \\ u_y[U_y], & (1+v_y)[V_y], & -z[W_{yy}] + w_y[W_y] \\ (1+u_x)[U_y] + u_y[U_x], & (1+v_y)[V_x] + v_x[V_y], & -2z[W_{xy}] + w_x[W_y] + w_y[W_x] \end{bmatrix} \begin{Bmatrix} \Delta \bar{u} \\ \Delta \bar{v} \\ \Delta \bar{w} \end{Bmatrix} \quad (14).$$

The above equation (14) is abbreviated by the following equation.

$$\{ \Delta \varepsilon \} = [B_{el}] \{ \Delta \bar{\varphi} \} \quad (15)$$

2.3 Constitutive Material Law

A law of elasto-plastic constitutive equation in the directions of multi-axes for a non-elastic material is based on the law of Prandtl – Reuss [3], and we get the incremental stress – incremental strain relationship under a state of a plane stress. In this case, an incremental stress – incremental strain relationship can be generally described by the following equation.

$$\begin{Bmatrix} \Delta \sigma_x \\ \Delta \sigma_y \\ \Delta \tau_{xy} \end{Bmatrix} = \begin{bmatrix} D_{ep11}, D_{ep12}, D_{ep13} \\ D_{ep22}, D_{ep23} \\ sym & D_{ep33} \end{bmatrix} \begin{Bmatrix} \Delta \varepsilon_x \\ \Delta \varepsilon_y \\ \Delta \gamma_{xy} \end{Bmatrix} \quad (16)$$

The above equation (16) is abbreviated by the following equation.

$$\{\Delta\sigma\} = [D_{ep}]\{\Delta\varepsilon\} \quad (17)$$

2.4 Equilibrium Equation of Force on the Element

An equilibrium equation of force for the above shell element is given by using the principle of virtual work. Now, we consider the state in which both internal forces and external forces are in equilibrium at time t . And, we consider the next state in which the time gains from t to $t + \Delta t$. Where, the Δt means a small incremental time. The equilibrium equation of forces at time $t + \Delta t$ is given by the following equation.

$$\iiint_V (\sigma_x^{t+\Delta t} \delta\varepsilon_x^{t+\Delta t} + \sigma_y^{t+\Delta t} \delta\varepsilon_y^{t+\Delta t} + \tau_{xy}^{t+\Delta t} \delta\gamma_{xy}^{t+\Delta t}) dx dy dz = \{\delta\bar{\varphi}\}^T \{F\}^{t+\Delta t} \quad (18)$$

Where,

$\{F\}$: Each pair of nodal force vectors with respect to the nodal displacement $\{\bar{\varphi}\}$.

$^{t+\Delta t}$: Various quantities at time $t + \Delta t$

The virtual strains $\delta\varepsilon_x^{t+\Delta t}$, $\delta\varepsilon_y^{t+\Delta t}$ and $\delta\gamma_{xy}^{t+\Delta t}$ at the time $t + \Delta t$ are given by

$$\delta\varepsilon_x^{t+\Delta t} = \delta\varepsilon_x^t + \Delta u_x \delta u_x + \Delta v_x \delta v_x + \Delta w_x \delta w_x \quad (19),$$

$$\delta\varepsilon_y^{t+\Delta t} = \delta\varepsilon_y^t + \Delta u_y \delta u_y + \Delta v_y \delta v_y + \Delta w_y \delta w_y \quad (20),$$

$$\delta\gamma_{xy}^{t+\Delta t} = \delta\gamma_{xy}^t + \Delta u_x \delta u_y + \delta u_x \Delta u_y + \Delta v_x \delta v_y + \delta v_x \Delta v_y + \Delta w_x \delta w_y + \delta w_x \Delta w_y \quad (21).$$

On the other hand, the stress at the time $t + \Delta t$ can be given by the following equation.

$$\{\sigma^{t+\Delta t}\} = \{\sigma^t\} + [D_{ep}]\{\Delta\varepsilon\} \quad (22).$$

Substituting the equations (19) – (21) and (22) into the equation (18), we get

$$\begin{aligned} \int_V [\{\delta\varepsilon^t\}^T [D_{ep}]\{\Delta\varepsilon\} + \sigma_x^t (\Delta u_x \delta u_x + \Delta v_x \delta v_x + \Delta w_x \delta w_x) + \sigma_y^t (\Delta u_y \delta u_y + \Delta v_y \delta v_y + \Delta w_y \delta w_y) \\ + \tau_{xy}^t (\Delta u_x \delta u_y + \delta u_x \Delta u_y + \Delta v_x \delta v_y + \delta v_x \Delta v_y + \Delta w_x \delta w_y + \delta w_x \Delta w_y)] dV \\ = \{\delta\bar{\varphi}\}^T \{F^{t+\Delta t}\} - \int_V \{\delta\varepsilon^t\}^T \{\sigma^t\} dV \end{aligned} \quad (23).$$

From the second term to the forth term in a left side of the above equation (23), we can rewrite them by using the shape functions, or,

$$\begin{aligned} \sigma_x^t (\Delta u_x \delta u_x + \Delta v_x \delta v_x + \Delta w_x \delta w_x) + \sigma_y^t (\Delta u_y \delta u_y + \Delta v_y \delta v_y + \Delta w_y \delta w_y) \\ + \tau_{xy}^t (\Delta u_x \delta u_y + \delta u_x \Delta u_y + \Delta v_x \delta v_y + \delta v_x \Delta v_y + \Delta w_x \delta w_y + \delta w_x \Delta w_y) \\ = \{\delta\bar{u}\}^T [\sigma_x^t [U_x]^T [U_x] + \sigma_y^t [U_y]^T [U_y] + \tau_{xy}^t ([U_x]^T [U_y] + [U_y]^T [U_x])] \{\Delta\bar{u}\} \\ + \{\delta\bar{v}\}^T [\sigma_x^t [V_x]^T [V_x] + \sigma_y^t [V_y]^T [V_y] + \tau_{xy}^t ([V_x]^T [V_y] + [V_y]^T [V_x])] \{\Delta\bar{v}\} \\ + \{\delta\bar{w}\}^T [\sigma_x^t [W_x]^T [W_x] + \sigma_y^t [W_y]^T [W_y] + \tau_{xy}^t ([W_x]^T [W_y] + [W_y]^T [W_x])] \{\Delta\bar{w}\} \\ \equiv \{\delta\bar{\varphi}\}^T [C_\sigma] \{\Delta\bar{\varphi}\} \end{aligned} \quad (24).$$

Finally, we can get the following equation by using the equation (24).

$$\int_V [B_{el}]^T [D_{ep}] [B_{el}] + [C_{\sigma}] dV \cdot \{\Delta \bar{\varphi}\} = \{F^{t+\Delta t}\} - \int_V [B_{el}]^T \{\sigma^t\} dV \quad (25).$$

The above equation (25) is an incremental control equation to give the relationship between the incremental nodal displacements and the incremental nodal forces. This recurrence equation, for instance, can be solved by using the Newton-Raphson method.

3. COMPARISONS OF NUMERICAL RESULTS WITH EXPERIMENTAL RESULTS

3.1 Numerical Model of Stub Column Tests

In this paragraph, validity and applicability for the above finite element modeling are verified by the past experimental results on the stub columns at high temperatures. Hirashima et al. have conducted experiments to investigate behavior and strength of heated stub columns

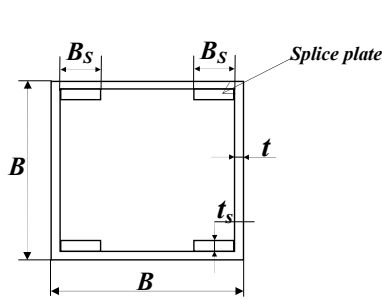


Fig-3 A Section of Specimen

Table-1 Various quantities of specimens

	B/t = 25	B/t = 30
Plate width B_s (mm)	150	135
Plate thickness t (mm)	6	4.5
Specimen height H (mm)	450	405
Splice plate width B_s (mm)	25	25
Splice plate thickness t_s (mm)	9	9

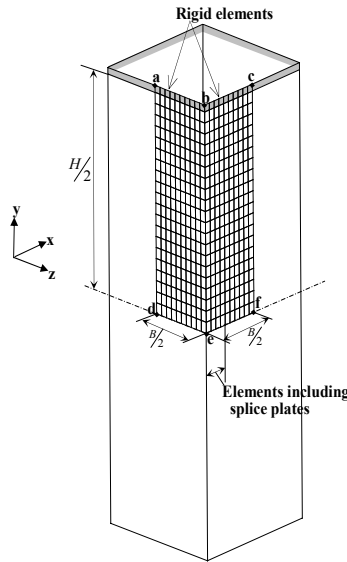


Fig-4 (a) A numerical model [Model 1]

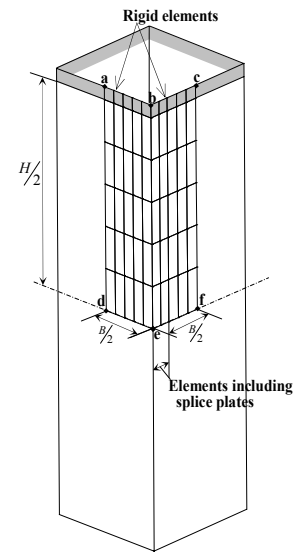


Fig-4 (b) A numerical model [Model 2]

under a condition when a compressive force was gradually increased while keeping a specimen temperature, constant [2]. The temperature range is RT, 400°C, 500°C, 600°C. Two types of specimens with square sections were used. These specimens were made by four steel plates, and each edge of the plate was welded. Plate width - thickness ratios B/t (B : plate width, t : plate thickness) of the specimens are respectively 25 and 30. The aspect ratio H/B (H : height of specimen) is 3, constant.

Fig-3 shows a sectional area of the specimen, and Table -1 shows its dimensions. In the specimen, four splice plates were used so as to avoid collapsing the welded edge lines during the experiment. The splice plates were welded on the edge lines of the specimen. The splice plate have the bigger thickness than the plate thickness, it is, therefore, considered that the former have an influence upon the behavior and the strength of the specimen.

Figs-4 (a) and (b) show two types of analytical models used for the finite element analysis. As in the Figs-4, the number of shell elements in between the models 1 and 2 is different. The

models 1 and 2 respectively have 400 and 50 equally rectangular shell elements. A reason why two different types of the models are used in this study is as follows; by using the above finite element modeling, we can obtain an advantage if we are capable of analyzing the 3-D behavior with the small number of the elements. This is because the shell element has the detailed displacement fields by using a lot of degrees of nodal freedoms even to 32. It is considered that this point contributes to shorten a computational time and a computational complexity, in particular, in the case when we analyze the 3-D behavior of the member. To verify validity of this point, the model 2 was also used.

In the consideration of symmetry of the specimen, a partial column model consisted of two quarter plates was used. Plate - sections welded the splice plates have the plate thickness added both splice plate and specimen plate thickness. To apply the compressive force on the top of the specimen uniformly, we used rigid elements at tops of the model. Boundary conditions of both line a-b and b-c in the Figs-4 (a) and (b) are respectively fix ends in the consideration of actual experimental conditions. For analyzing the buckling phenomena of the symmetrically analytical model, we applied initial imperfections in the model. They were given by minute uniformly distributed loads on the lines d-e and e-f. Values of the loads were, for the all analytical cases, determined so that out-plate deflections of both points d and f respectively correspond with $B/1000$ and $-B/1000$. The compressive force from the top line in the model was applied, by controlling the displacement at the point b.

3.2 Stress and Strain Relationships

Stress σ – strain ε relationships used in the finite element analysis are shown in Figs-5(a), (b) and (c). In the Figs-5, solid lines show the stress – strain relationships obtained by coupon tests [2], and dash lines show them used in the finite element analysis. The latter were determined by using the following equation [4].

$$\sigma(\varepsilon) = \max \{ \sigma_1(\varepsilon), \sigma_2(\varepsilon) \} \quad (26)$$

$$\sigma_1(\varepsilon) = \min \{ E\varepsilon, \sigma_{yt} \}, \quad \sigma_2(\varepsilon) = f_1(\varepsilon) + f_2(\varepsilon),$$

$$f_1(\varepsilon) = \frac{E_o \varepsilon}{\left\{ 1 + \left(\varepsilon / \varepsilon_o \right)^n \right\}^{\frac{1}{n}}}, \quad f_2(\varepsilon) = \frac{E_t \varepsilon}{\sqrt{1 + \left(\varepsilon / \varepsilon_2 \right)^2}},$$

$$E_o = E - E_t, \quad \varepsilon_o = \sigma_o / E_o, \quad \varepsilon_2 = 0.05$$

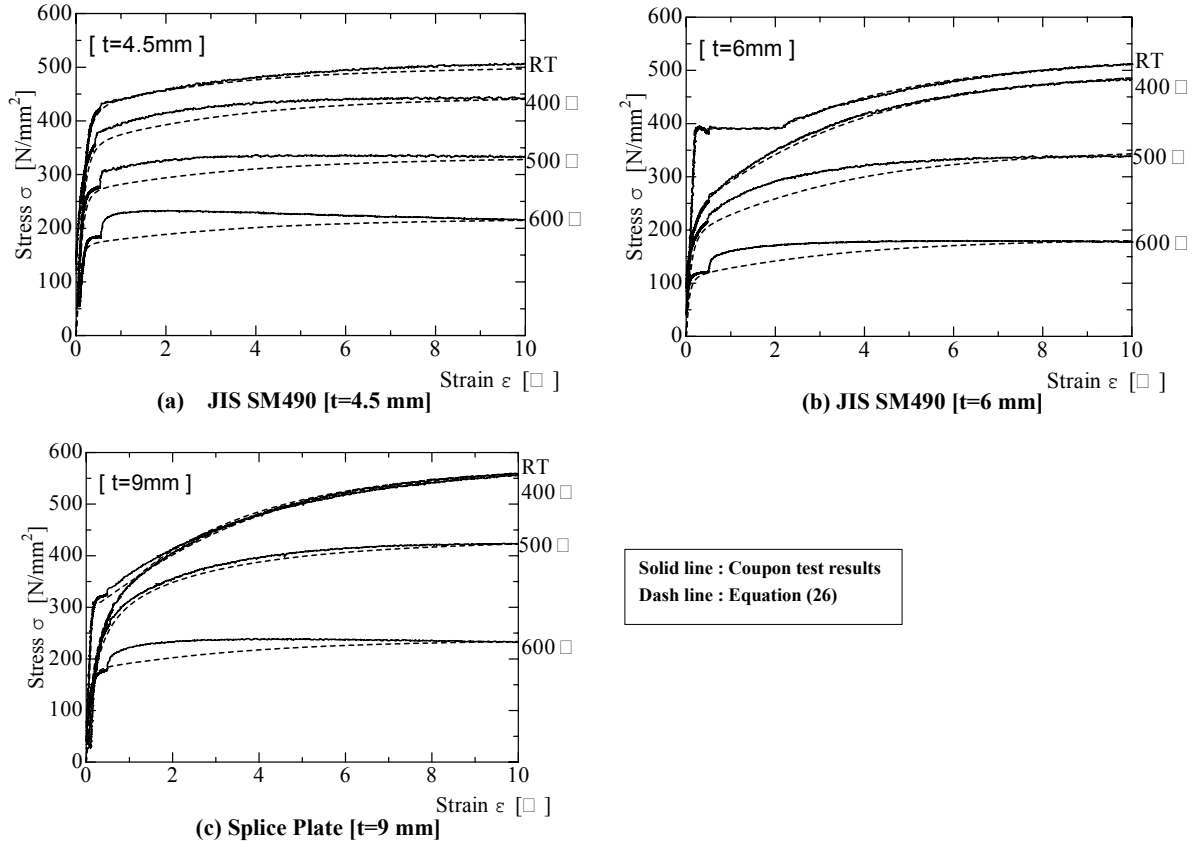


Fig-5 Stress – strain relationship

In the above equation,

E : Young's modulus

σ_{yt} : Yield stress in the case when a material has a plastic flow

E_o : Coefficient on strain hardness

σ_o : Stress to determine a tensile strength

n : Coefficient on the shape of equation.

Hirashima et al. have reported that a strain velocity of the coupon test was changed from 0.3 % /min to 10 % /min at a strain point $\varepsilon = 0.5$ % [2]. As the result, we recognize that the stress, in particular, at the high temperature suddenly rises at this strain point as in the Figs-5. In the finite element analysis, this sharp rise of the stress is not taken into account, and the stress – strain relationship over the strain $\varepsilon = 0.5$ % was determined so that its stress and the coupon test result are approximately agreed at the strain point $\varepsilon = 10$ %.

3.3 Analytical Results

Fig-6 (a) and (b) show the analytical results compared with the experimental results. In Figs-6, dots show the experimental results, and both solid and dash lines show the numerical results. A vertical axis and a transverse axis in the Figs-6 respectively show an average stress $\sigma_o (= P / A)$ and an average strain $\varepsilon_o (= \delta_v / H)$. Where, P means the compressive

force, A means a total sectional area including the splice plates and δ_v means a shortening of the specimen.

As in the Fig-6, we can recognize that the numerical results and the experimental results in the all cases agree approximately. We can also recognize that there are not qualitative differences in between the models 1 and 2. In Fig-7, a deflection figure of the numerical model 1 after the local buckling occurred are shown.

From the above analytical results, it is considered that we can accurately analyze the 3-D behavior even if we use the numerical model which has the small number of the shell elements, such the model 2.

4. ANALYTICAL EXAMPLES OF THE HEATED COLUMN SUBJECTED TO A HORIZONTALLY FORCED DISPLACEMENT AT THE TOP

4.1 Numerical Model

In this paragraph, we discuss the analytical case of the heated column during the fire stage. Generally, when the fire occurs in a fire compartment, the heated column may be subject to a pushing deformation due to the thermal elongation of the adjacent heated beam in the compartment (Fig-8). The column is subject to an anti-symmetric bending moment with raising a member temperature. In this case, there is the possibility that local buckling occurs at the top or bottom of the column where compressive force due to both axial force and bending moment is superposed. The column is, in particular, subject to large thermal elongation in the case when the heated beam has a long span length. It is considered that the fire resistance of the column may decrease by local buckling occurred at an early fire stage. We discuss this problem by using the finite element analysis.

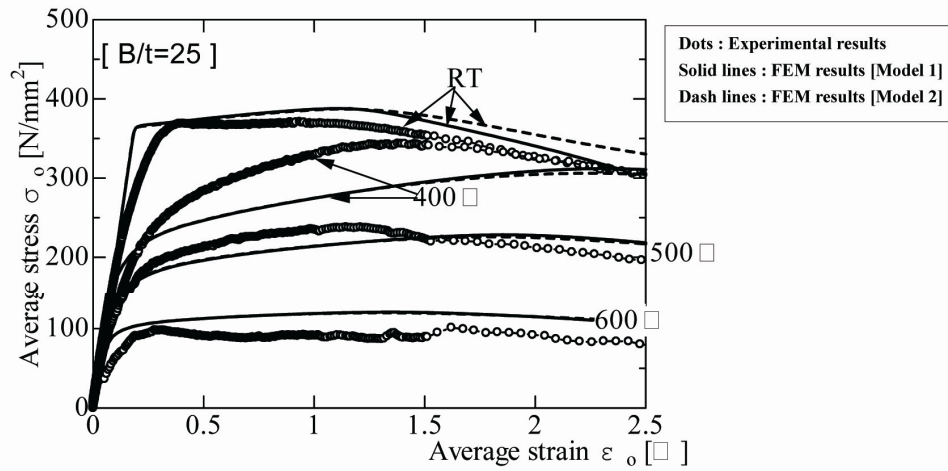


Fig-6 (a) Analytical Results [B/t = 25]

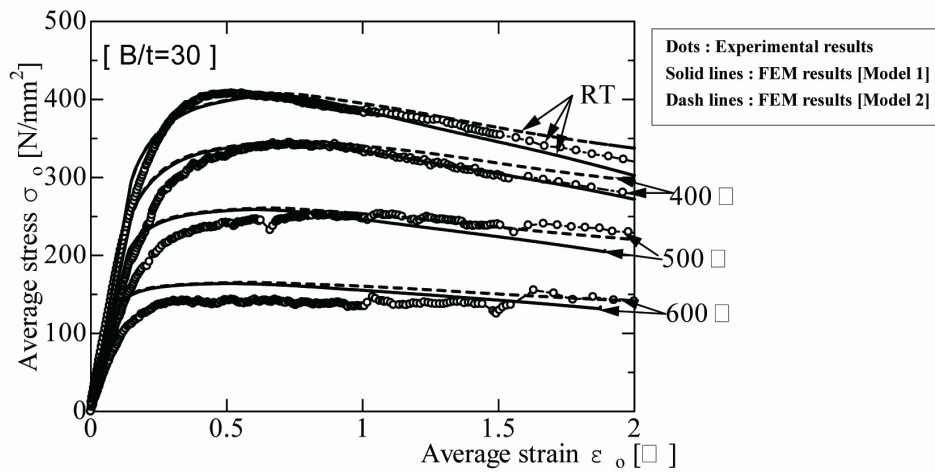


Fig-6 (b) Analytical Results [B/t = 30]

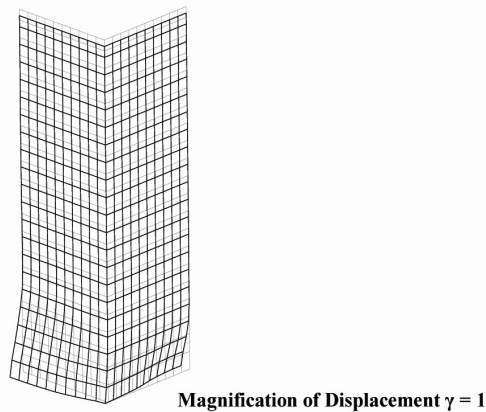


Fig-7 Displacement figure after the local buckling occurred (B/t = 30, 600°C, [Model 1])

In Fig-9, the numerical model of the heated column is shown. As in Fig-9, its top is pushed sideways by the horizontally forced displacement δ_H which is equivalent to the

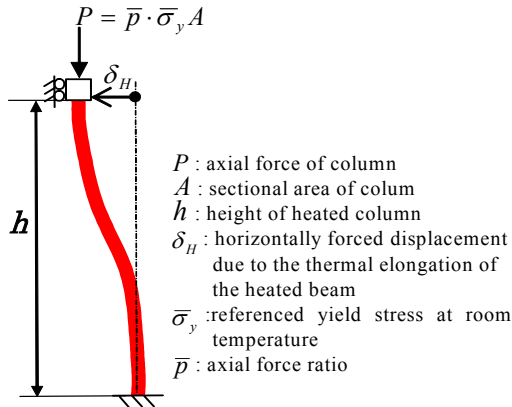


Fig-9 A numerical model of the heated column with the horizontally forced displacement

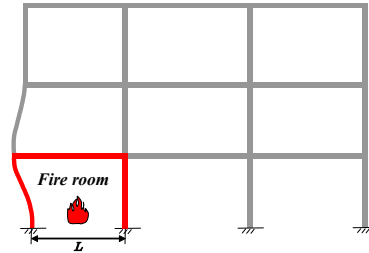


Fig-8 A multi-storied steel frame with a fire compartment room

Table -2 Analytical parameters

Column section	BOX-350-350-10
Column height h (mm)	3500
Axial force ratio \bar{p}	0.3
Width – Thickness ratio B/t	35
Beam span – Column height ratio L/h	3

thermal elongation of the adjacent beam. The value of δ_H is given by the following equation.

$$\Delta\delta_H = \alpha \cdot L \cdot \Delta T \quad (27)$$

Where,

α : Linear coefficient of elongation on the steel ($=12 \times 10^{-6} \text{ } 1/^{\circ}\text{C}$)

L : Span length of the heated beam

T : Member temperature.

From the equation (27), the horizontally forced displacement δ_H is increasing with raising the member temperature T . Analytical parameters of this model are shown in the Table-2. The span length of the heated beam L is three time longer than the column height h .

Fig-10 shows the formulated stress – strain relationships used in this analytical case. The steel grade is JIS SM490, and its referenced yield stress $\bar{\sigma}_y$ at room temperature is standardized by $\bar{\sigma}_y = 325 \text{ N/mm}^2$ [4]. The stress – strain relationships at the high temperatures are given by the equation (26), whose coefficients $E, \sigma_{yt}, E_o, \sigma_o, n$ are the functions of the temperature [4].

In the numerical analysis, the member temperature T of the column is uniform and gradually increasing while keeping the axial force P , constant.

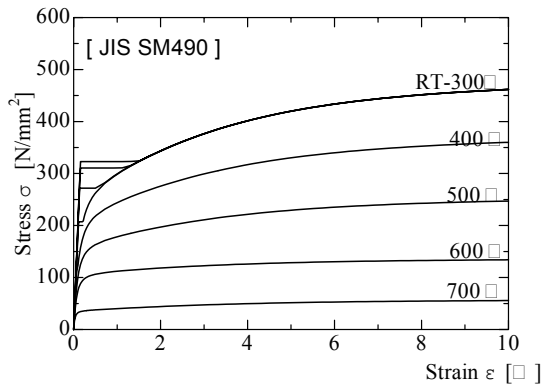
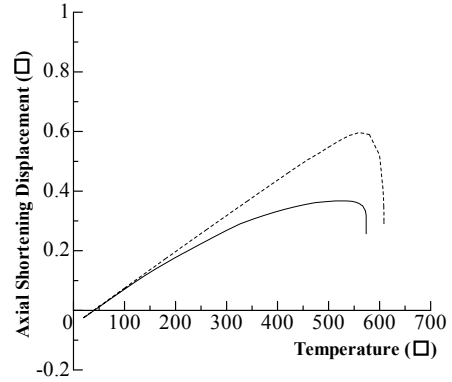


Fig-10 Stress – strain relationship at high temperature



Solid line : Numerical result of the heated column with the horizontally forced displacement
Dash line : Numerical result of the centrally loaded compressive heated column

Fig-11 Numerical results [B/t=35]

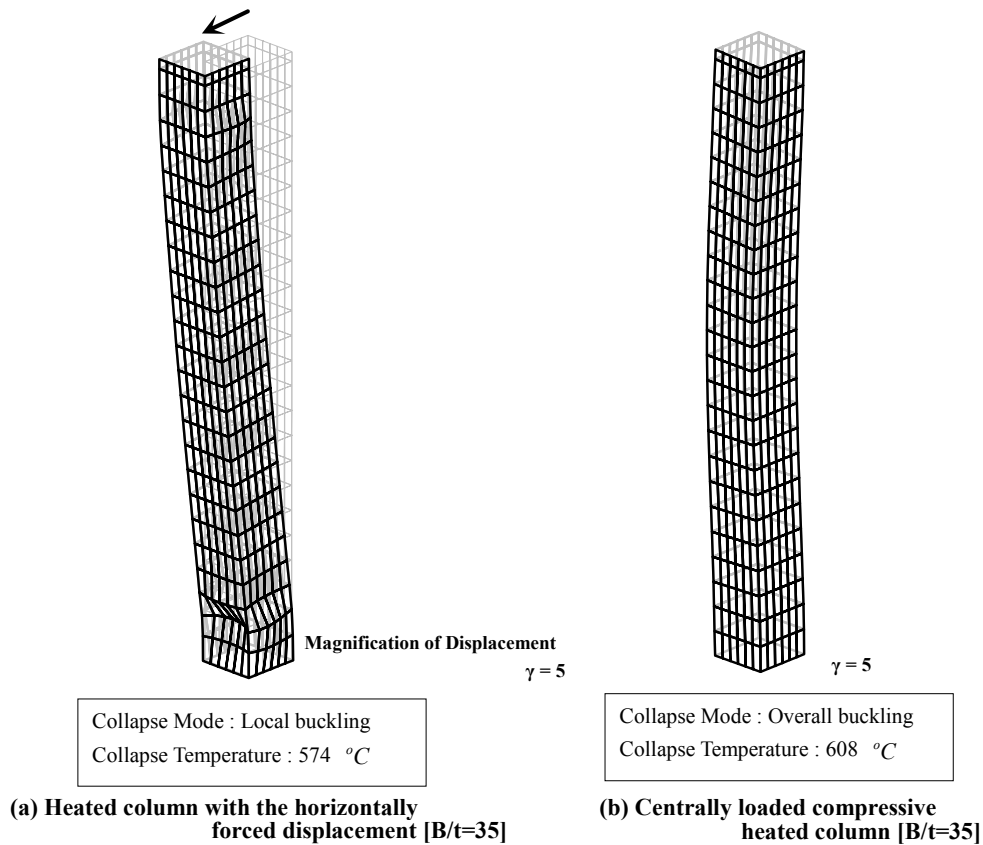


Fig – 12 Displacement figures at the collapse temperature

4.2 Numerical Results

Fig-11 shows the numerical results of the above case. These are the relationships between the temperatures and the axial displacements of the heated column. For reference, the analytical result in the case when the horizontally forced displacement δ_H does not occur, that is, in the case of the centrally loaded compressive column is shown in the same graph. In accordance with the numerical analysis, local buckling occurred at both top and bottom of the

column by increasing the horizontally forced displacement. The heated column, however, does not collapse immediately at that time. The heated column can sustain the axial force and the member temperature is further rising. This is because the heated column has a stable residual strength in the post local buckling region, as is seen in the Figs-6 (a) and (b). Finally, this column could sustain the axial force up to 574°C . As in the Fig-11, we can recognize that the axial displacement of the heated column is rapidly decreasing around this temperature. On the other hand, the centrally loaded compressive column could sustain the axial force up to 608°C (the dash line in the Fig-11). Hence, the collapse temperature of the former case is 34°C lower than it of the latter one. This is because the centrally loaded compressive column did not show the local buckling during the analysis and it finally collapsed by overall buckling. Figs - 12 (a) and (b) respectively show the displacement figures at the collapse temperature. We can see the local buckling deformations at both top and bottom of the column as in the Fig-12 (a), and also the arrow-like deflection of the column due to the overall buckling as in the Fig-12 (b).

From the above numerical examples, it is considered that local buckling may occur in the column by the thermal elongation of the adjacent heated beam and this has an influence to decrease the fire resistance of the column.

5. CONCLUSION

Main conclusions of this study are:

1. We were able to analyze 3-D non-linear behavior of the heated members by the finite element modeling developed for the study. This has the advantage to be capable of analyzing the behavior accurately even if the analytical model has small number of the elements.
2. We verified the reliability of the finite element analysis by past experimental results of the steel stub column at high temperature. We recognized that the past experimental results and our numerical ones agree well.
3. Heated columns in a fire compartment may be pushed sideways by the thermal elongations of the adjacent heated beam with raising the temperature. In this case, there is the possibility that local buckling occurs at the top or bottom of the heated column. We discussed the analytical case of the heated column subjected to the horizontally forced displacement at its top by using the finite element analysis. From the analytical case, we recognized that local buckling of the heated steel column has a significant influence and decreases its fire resistance.

6. ACKNOWLEDGMENT

The authors sincerely acknowledge offers of highly valuable experimental results on steel stub columns at high temperature from Dr. Takeo Hirashima and Prof. Dr. Hideki Uesugi, Chiba University, Japan.

7. REFERENCES

- [1] Hirofumi Nakagawa and Hiroyuki Suzuki : “Ultimate Temperatures of Steel Beams Subjected to Fire”, J. of Steel Construction Eng., Japan, Vol. 6, No.22, June 1999, (In Japanese).
- [2] Takeo Hirashima et al. : “A Study on Strength-Deformation Capacity of Steel Members at Elevated Temperature”, J. of Structural Eng., Vol. 46B, March 2000, (In Japanese).
- [3] R. Hill : “The Mathematical Theory of Plasticity”, Clarendon Press, Oxford, 1950.
- [4] Architectural Inst. of Japan : “Recommendation for Fire Resistant Design of Steel Structures”, January 1999, (In Japanese).



PROPOSAL TO THE EUROCODE 3 FOR THE LATERAL-TORSIONAL BUCKLING OF STAINLESS STEEL I-BEAMS IN CASE OF FIRE

Nuno LOPES¹; Paulo VILA REAL²; Luís SIMÕES da SILVA³;

Jean-Marc FRANSSSEN⁴ and Enrique MIRAMBELL⁵

ABSTRACT

Eurocode 3 states that stainless steel structural elements, subjected to high temperatures, must be designed with the same expressions of the carbon steel elements. However, knowing that the stress-strain relationship of stainless steel is different from the carbon steel, it is expected that the design procedure, for structural elements resistance of this two materials, should be different.

Recent studies showed that, the formulae, for lateral-torsional buckling resistance of stainless steel beams at high temperatures, in Eurocode 3, do not give good results, being on the unsafe side for some cases. This justifies the presentation of new formulae that approximates better the real behaviour of structural elements in stainless steel, at high temperatures. This new formulae were based on numerical study using the program SAFIR, which was modified to take into account the material properties of the stainless steel.

1. INTRODUCTION

For more than three decades, there was an enormous research effort, by the steel industry and the academics, to investigate the behaviour of steel structures subjected to fire,

¹ Research Assistant, University of Aveiro, Department of Civil Engineering, 3810-193 Aveiro, Portugal, email: nuno_lopes@civil.ua.pt.

² Professor, University of Aveiro, Department of Civil Engineering, 3810-193 Aveiro, Portugal, email: pvreal@civil.ua.pt.

³ Professor, University of Coimbra, Department of Civil Engineering, 3030 Coimbra, Portugal, email: luisss@dec.uc.pt.

⁴ Professor, University of Liege, Department M&S, Liège, Belgium, email: jm.franssen@ulg.ac.be.

⁵ Professor, Universitat Politècnica de Catalunya, Dep. Enginyeria de la Construcció, Barcelona, Spain, email: enrique.mirambell@upc.edu

resulting in the development of a number of design rules¹, which were incorporated within the structural Eurocodes. More recently, research works have been oriented towards stainless steel structures. Although some progress has been made in the knowledge of the behaviour of stainless steel structures at room temperature, fire resistance design has received less attention.

At elevated temperature stainless steel has a better retention of strength than carbon steel. A comparison of the reduction factor for the yield strength of grade 1.4301 stainless steel with that of structural carbon steel (as defined in EN 1993-1-2²) is shown in Fig. 1, where $f_{y,\theta}$ refers to the nominal yield strength at temperature θ , and f_y refers to the nominal yield strength at room temperature. This figure demonstrates the better material properties of stainless steel at elevated temperature.

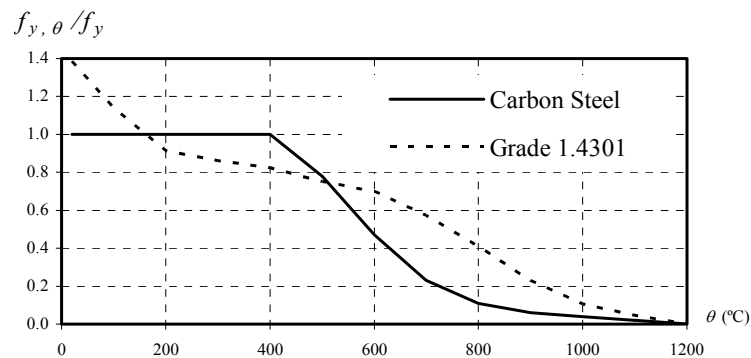


Fig. 1 – Reduction factor for the yield strength at high temperature.

Stainless steel has countless desirable characteristics for a structural material^{3, 4}. Although its use in construction is increasing, it is still necessary to develop the knowledge of its structural behaviour. Stainless steels are known by its non-linear stress-strain relationships with a low proportional stress and an extensive hardening phase. There is not a well defined yield strength, the conventional limit of elasticity at 0.2% being usually considered.

The EN 1993-1-4¹ “Supplementary rules for stainless steels” gives design rules for stainless steel structural elements at room temperature, only making mention to its fire resistance by doing reference to the fire part of the Eurocode 3, EN 1993-1-2². Recently, in 2002, the Euro Inox and the Steel Construction Institute published the second edition of the “Designers Manual for Structural Stainless Steel”⁵, where it is referred that the formulae, for the lateral-torsional buckling of beams and for the flexural buckling of columns, are based in the formulae for carbon steel elements at high temperatures. Despite both carbon and stainless steel exhibiting different constitutive laws, whereby stainless steel presents a pronounced non-linear behaviour even for low stress values, the stainless steel design rules are based on the ones developed for carbon steel.

Part 1-1 of Eurocode 3⁶ recently introduced significant changes in the evaluation of the lateral-torsional buckling resistance of steel beams at room temperature that improves the conservative approach of the ENV 1993-1-1⁷ in case of non uniform bending. For the same reasons, an alternative expression^{8, 9} for beams was proposed in case of fire with lateral-torsional buckling, ensuring the compatibility and coherence between part 1-1 (general rules and rules for buildings)⁶ and part 1-2 (structural fire design)², as well as supplying a simple, competitive, and safe procedure. This new proposal^{8, 9} follows the same rationale as in part 1-1 of Eurocode 3, also taking into consideration the influence of the loading type.

In this paper a brief description of the prescribed formulations in Eurocode 3, for the lateral-torsional buckling of stainless steel beams in case of fire, is first presented, followed by the presentation of the expressions of the Eurocode 3 for the safety evaluation of lateral-

torsional buckling of carbon steel elements at high temperatures. A proposal for the lateral-torsional buckling in case of fire made by the authors¹¹, that improves the behaviour of the lateral-torsional buckling curves from part 1-2 of Eurocode 3, is also presented. Finally, a new design procedure for the lateral-torsional buckling of stainless steel beams subjected to high temperatures, based in the carbon steel elements design formulae is proposed. This procedure was calibrated using the program SAFIR¹⁰, a geometrical and material non linear finite element code, that has been adapted according to the material properties defined in EN 1993-1-4¹ and EN 1993-1-2², to model the behaviour of stainless steel structures.

2. CASE STUDY

A simply supported beam with fork supports, as shown in figure 2, was chosen to explore the validity of the beam safety verifications. Regarding the bending moment variation along the member length, five values, (-1, -0.5, 0, 0.5 and 1), of the ψ ratio (see fig. 2) have been investigated as well as a mid span concentrated load and a uniformly distributed load.

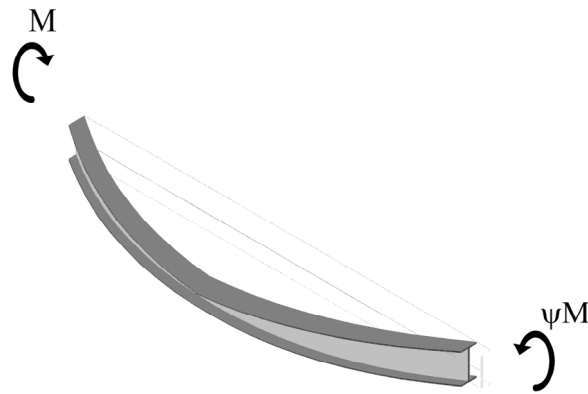


Fig. 2 – Simply supported beam with non-uniform bending.

The following welded cross-sections were used: IPE 220 steel section (representative of $h/b = 2$), HEA 500 steel section (representative of $h/b < 2$) and IPE 500 steel section (representative of $h/b > 2$). Stainless steel grade 1.4301 (also known as 304) was studied for each cross-section. A uniform temperature distribution in the cross-section was used so that comparison between the numerical results and the Eurocode could be made. In this paper, the temperatures chosen were 400, 500, 600 and 700 °C, deemed to cover the majority of practical situations.

In the numerical simulations, a lateral geometric imperfection given by the following expression was considered:

$$y(x) = \frac{l}{1000} \sin\left(\frac{\pi x}{l}\right) \quad (1)$$

where l is the length of the beam. An initial rotation around the beam axis with a maximum value of $l/1000$ radians at mid span was also considered.

The adopted residual stresses follow, the typical patterns for carbon steel welded sections, considered constant across the thickness of the web and flanges. The distribution is shown in figure 3, and has the maximum value of f_y (yield strength)¹².

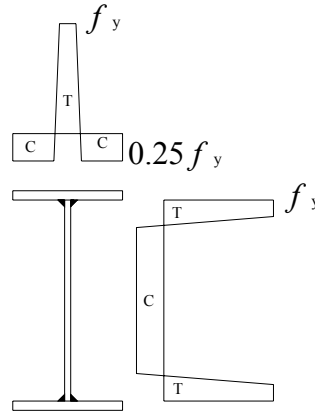


Fig. 3 – Residual stresses: C – compression; T – tension.

3. EUROCODE 3 FORMULAE FOR THE LATERAL-TORSIONAL BUCKLING OF STAINLESS STEEL ELEMENTS AT HIGH TEMPERATURES

For stainless steel beams subjected to high temperatures, part 1-4 of Eurocode 3 refers that the same formulation prescribed for carbon steel elements should be used, according to the EN 1993-1-2², where the lateral-torsional buckling resistant moment for class 1 and class 2 cross-sections, is

$$M_{b,fi,t,Rd} = \chi_{LT,fi} W_{pl,y} k_{y,\theta} f_y \frac{1}{\gamma_{M,fi}} \quad (2)$$

where $\chi_{LT,fi}$ is given by

$$\chi_{LT,fi} = \frac{1}{\phi_{LT,\theta} + \sqrt{(\phi_{LT,\theta})^2 - (\bar{\lambda}_{LT,\theta})^2}} \quad (3)$$

with

$$\phi_{LT,\theta} = \frac{1}{2} \left[1 + \alpha \bar{\lambda}_{LT,\theta} + (\bar{\lambda}_{LT,\theta})^2 \right] \quad (4)$$

In this expression the imperfection factor α depends on the steel grade and is determined with

$$\alpha = 0.65 \sqrt{235 / f_y} \quad (5)$$

The non-dimensional slenderness for lateral-torsional buckling at high temperatures is given by

$$\bar{\lambda}_{LT,\theta} = \bar{\lambda}_{LT} \left[\frac{k_{y,\theta}}{k_{E,\theta}} \right]^{0.5} \quad (6)$$

where:

$\bar{\lambda}_{LT}$ is the lateral-torsional buckling slenderness at room temperature;

$k_{E,\theta}$ is the reduction factor for the young's modulus;

$k_{y,\theta}$ is the reduction factor for the yield strength determined by

$$k_{y,\theta} = \left[f_{0.2p,\theta} + k_{2\%,\theta} (f_{u,\theta} - f_{0.2p,\theta}) \right] \frac{1}{f_y} \quad (7)$$

where:

$f_{0.2p,\theta}$ is the proof strength at 0.2% plastic strain;

$k_{2\%,\theta}$ is the correction factor for determination of the yield strength $f_{y,\theta}$;

$f_{u,\theta}$ is the tensile strength.

The stainless steel mechanical and thermal properties at high temperatures, used in this paper, can be found in part 1-2 of Eurocode 3².

4. FORMULAE FOR THE LATERAL-TORSIONAL BUCKLING OF CARBON STEEL ELEMENTS AT HIGH TEMPERATURES

The new proposal for the lateral-torsional buckling of carbon steel beam elements^{8, 9} adopts, following EN 1993-1-1⁶, a modified reduction factor for the lateral-torsional buckling $\chi_{LT,fi,mod}$, given by


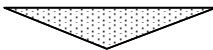
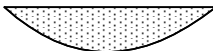
$$\chi_{LT,fi,mod} = \frac{\chi_{LT,fi}}{f} \quad \text{but} \quad \chi_{LT,fi,mod} \leq 1 \quad (8)$$

where f depends on the loading type and is determined with

$$f = 1 - 0.5(1 - k_c) \quad (9)$$

k_c is a correction factor determined according to table 1.

Table 1 – Correction factors k_c for the new proposal.

Moment distribution	Class 1, 2, 3 sections
	k_c
 $-1 \leq \psi \leq 1$	$0.6 + 0.3\psi + 0.15\psi^2$ but $k_c \leq 1$
	0.79
	0.91
Note: for others bending diagrams $k_c = 1$.	

To take into account the cross-section type and the steel grade S460, the imperfection factor α given by equation (5), is written as a function of a severity factor β ⁸

$$\alpha = \beta \sqrt{235 / f_y} \quad (10)$$

with the severity factor, for welded sections, given in table 2.

Table 2 – Values of the severity factor, β .

Cross-section	limits	β	
		S235, S275, S355, S420	S460
Welded I section	$h/b \leq 2$	0.70	0.75
	$h/b > 2$	0.80	0.85

5. LATERAL-TORSIONAL BUCKLING PROPOSALS FOR STAINLESS STEEL ELEMENTS AT HIGH TEMPERATURES

The proposal made by the authors^{8, 9} for lateral-torsional buckling of carbon steel beams, described in section 4, was tested with stainless steel beams subjected to high temperatures.

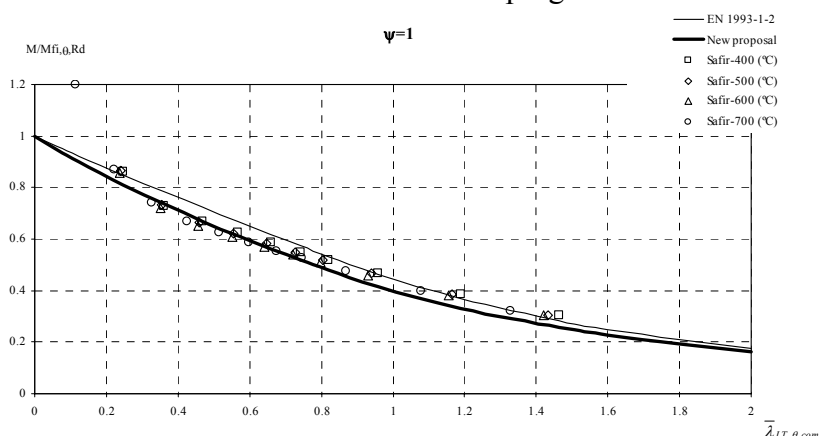
As it can be observed for $\psi = 1$ in figures 4, 5 and 6, the curves resulting from the Eurocode 3 are not on the safe side. To improve this result a new severity factor β , given in table 3, different from the one defined in table 2 for carbon steel, is proposed for the lateral-torsional buckling of stainless steel beams.

Table 3 – Values of the severity factor, β for stainless steel 1.4301.

Cross-section	limits	β
Welded I section	$h/b \leq 2$	0.85
	$h/b > 2$	1.00

6. PARAMETRIC STUDY

Results for stainless steel beams subjected to lateral-torsional buckling at high temperatures are shown in figures 4, 5 and 6, for three values, (-1, 0 and 1) of the ψ ratio, a mid span concentrated load and a uniformly distributed load. The figures compare the curves obtained using part 1-2 of Eurocode 3, described in section 3 of this paper (denoted “EN 1993-1-2”), the curve obtained with the new proposal presented in section 5 (denoted “New proposal”), and the numerical results obtained with the program SAFIR.



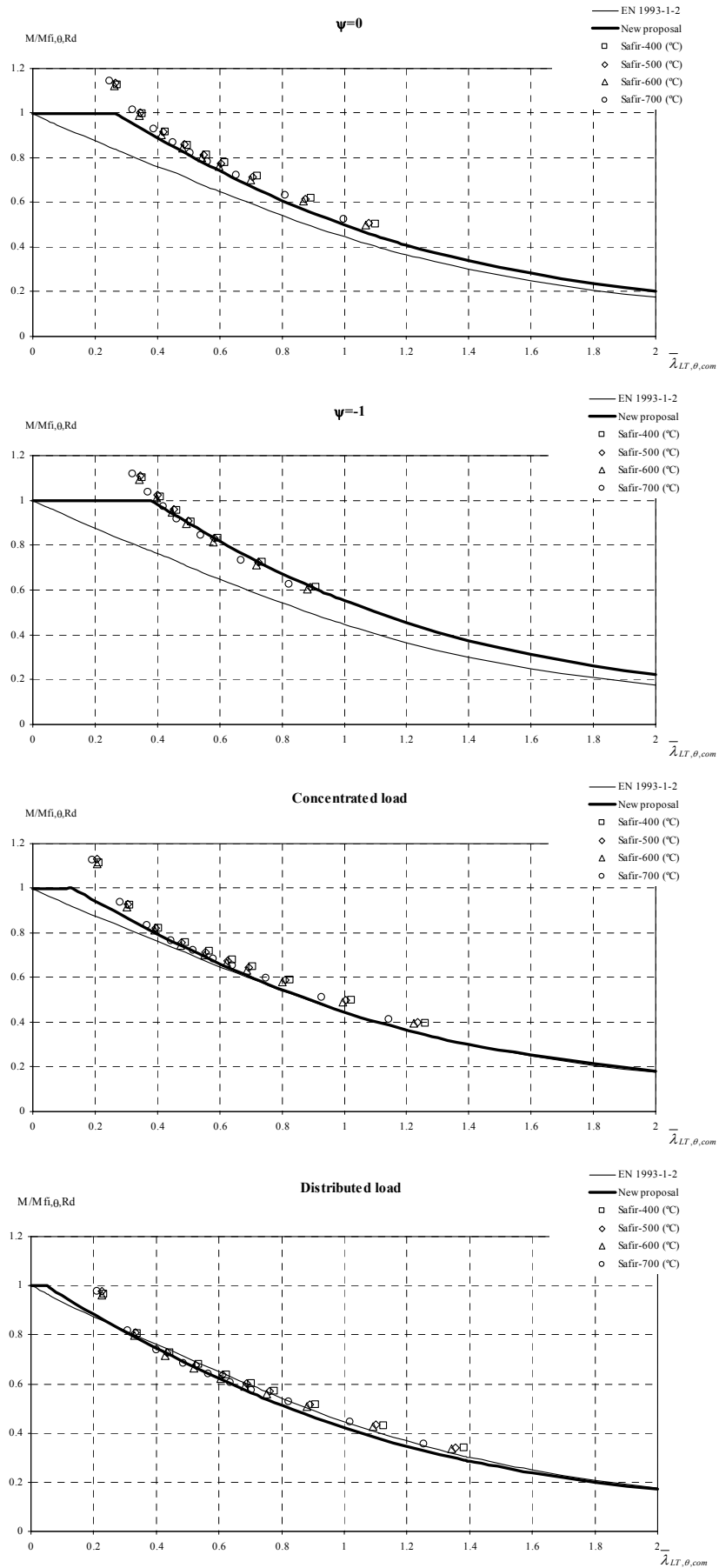
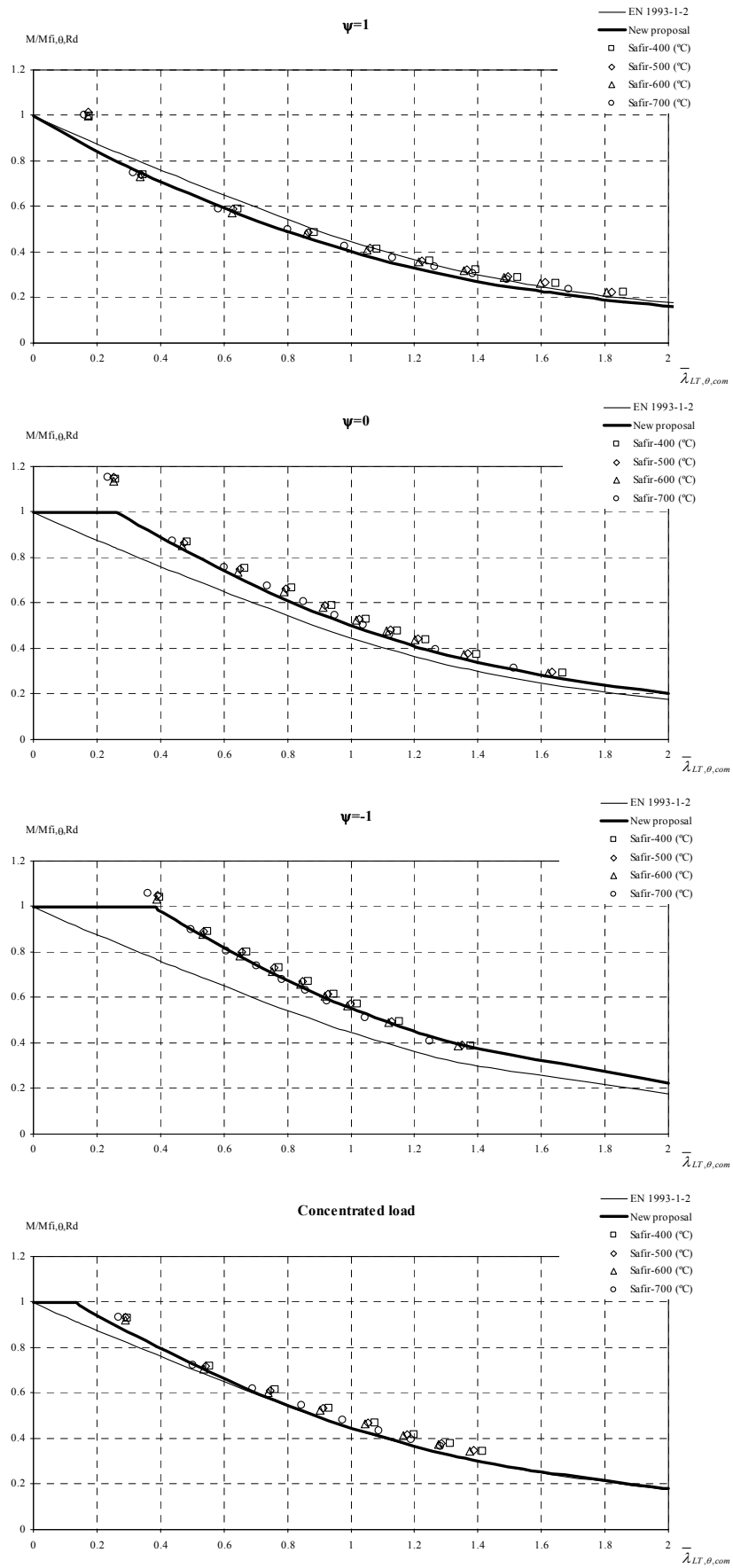


Fig. 4 – Lateral-torsional buckling in stainless steel HEA500 beams.



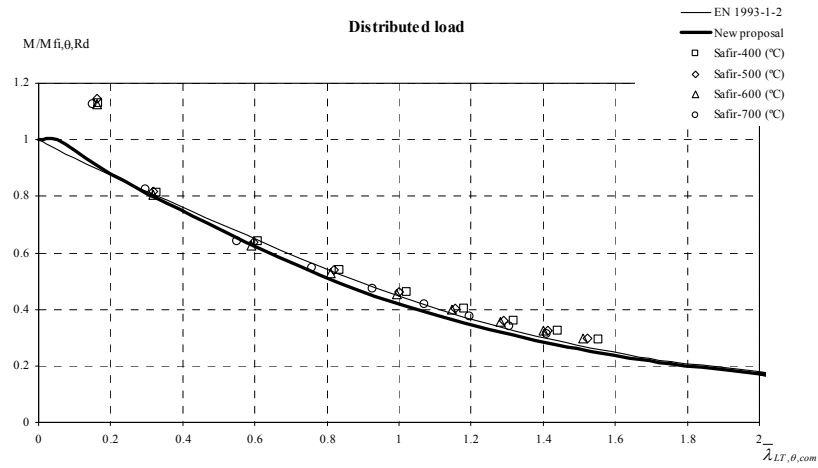
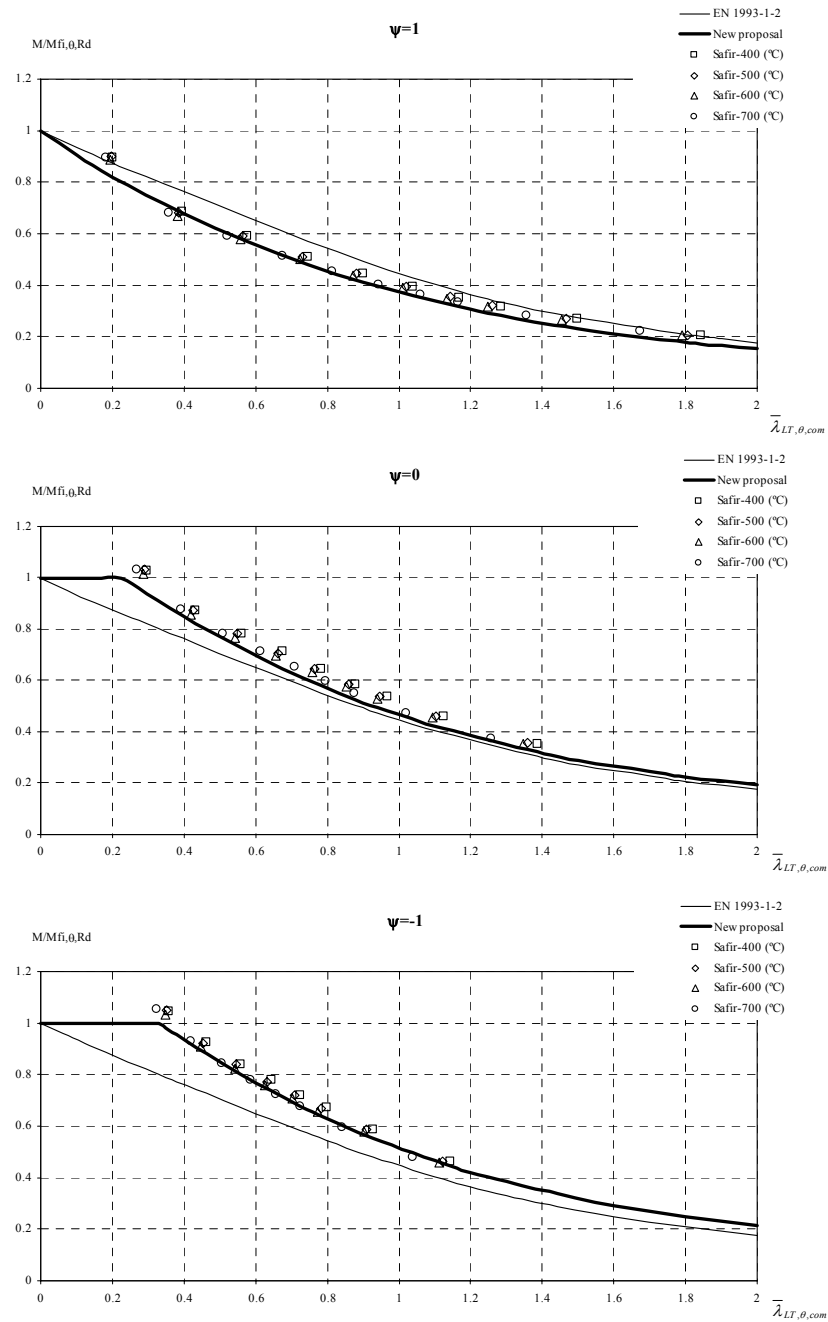


Fig. 5 – Lateral-torsional buckling in stainless steel IPE220 beams.



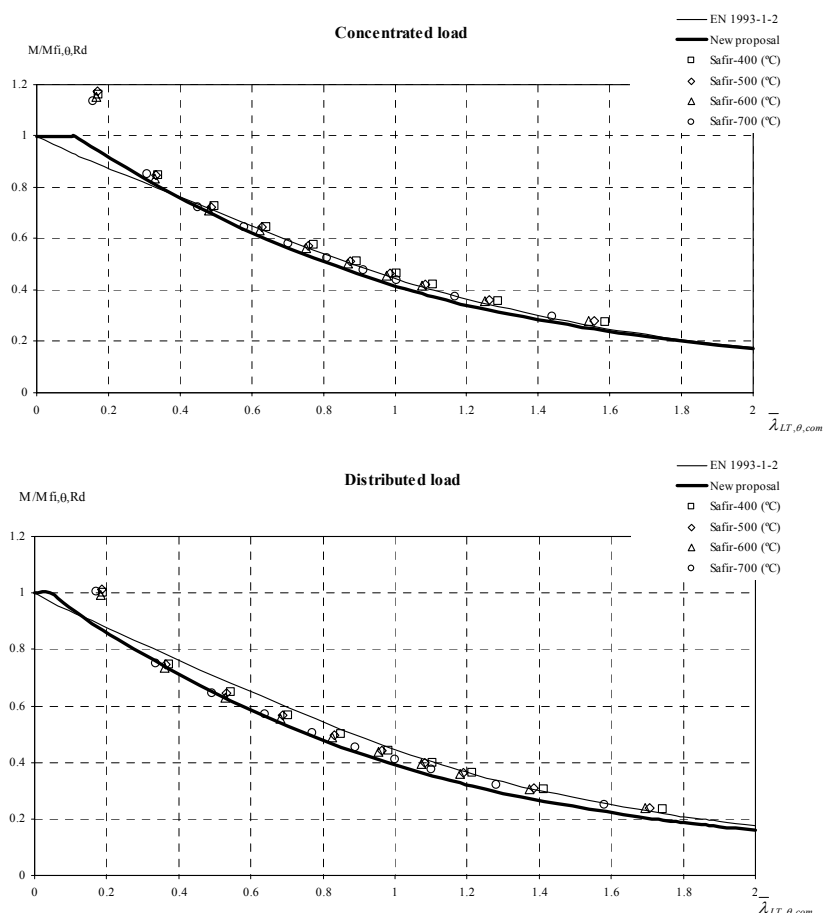


Fig. 6 – Lateral-torsional buckling in stainless steel IPE500 beams.

7. CONCLUSIONS

Figures 4, 5 and 6 show that the proposal made by the authors^{8, 9} for the lateral-torsional buckling of carbon steel beams at high temperatures (considering the influence of the loading type), gives results that are in good agreement with the numerical results obtained with the program SAFIR for stainless steel beams, provided that the new imperfection factor is determined using the severity factor defined in table 3.

It should be pointed out that these results were obtained only for the stainless steel grade 1.4301. Knowing that the other stainless steel grades mentioned in part 1-2 of Eurocode 3 exhibit different stress-strain relationships from the stainless steel 1.4301, it is to be expected that future work will suggest some changes in the proposal presented here, taking into account the influence of the steel grade.

8. REFERENCES

- [1] European Committee for Standardisation, EN 1993-1-4 “Eurocode 3, Design of Steel Structures – part 1-4. General rules – Supplementary Rules for Stainless Steels”, Brussels, Belgium, 2004.
- [2] European Committee for Standardisation, EN 1993-1-2 “Eurocode 3: Design of Steel Structures - Part 1-2: General rules - Structural fire design”, Brussels, Belgium, April 2005.

- [3] Gardner, L., “The use of stainless steel in structures” Prog. Struct. Engng Mater., 2005.
- [4] Imma Estrada Palacios, “Shear Design of Stainless Plate Girders”, PhD Thesis, Universitat Politècnica de catalunya, Barcelona, 2005, 2005.
- [5] Euro Inox e Steel Construction Institute “Designers Manual for Structural Stainless Steel”, 2002.
- [6] European Committee for Standardisation, EN 1993-1-1 “Eurocode 3, Design of Steel Structures – part 1-1. General rules and rules for buildings”, Brussels, Belgium, 2003.
- [7] European Committee for Standardisation, ENV 1993-1-1 “Eurocode 3, Design of Steel Structures – part 1-1. General rules and rules for buildings”, Brussels, Belgium, 1992.
- [8] Vila Real, P.M.M., Lopes, N., Simões da Silva, L. and Franssen, J.-M., “Numerical validation of an improved proposal to the Eurocode 3 for the lateral-torsional buckling of steel beams subjected to fire”, fourth international workshop Structures in Fire SiF’06, University of Aveiro, Aveiro, 10-12 of May of 2006.
- [9] Vila Real, P.M.M., Lopes, N., Simões da Silva, L. and Franssen, J.-M., “Lateral-Torsional Buckling of Unrestrained Steel Beams Under Fire Conditions: Improvement of EC3 Proposal”, Computer & Structures, ELSEVIER, 82/20-21 pp. 1737-1744, 2004.
- [10] Franssen, J.-M., “SAFIR. A Thermal/Structural Program Modeling Structures under Fire”, Proc. NASCC conference, American Inst. for Steel Constr., Baltimore, USA, April 2003.
- [11] Lopes, N., Vila Real, P.M.M., Piloto, P., Mesquita, L. e Simões da Silva, L., “Modelação numérica da encurvadura lateral de vigas I em aço inoxidável sujeitas a temperaturas elevadas”, Congreso de Métodos Numéricos en Ingeniería, Granada, Spain, 2005.
- [12] Chen W. F. and Lui E. M. Stability design of steel frames. CRC Press, 1991.



LIGHT WEIGHT STRUCTURES EXPOSED TO FIRE: A STAINLESS STEEL SANDWICH PANEL

Tiina ALA-OUTINEN¹, Peter SCHAUMANN²,
Olli KAITILA³ and Florian KETTNER⁴

ABSTRACT

A new type of laser-welded stainless steel sandwich panel with rock wool insulation has been developed by Kenno Tech Ltd. It is the aim of the present study, conducted in the frame of the RFCS project “Stainless Steel in Fire”, to prove that a fire resistance of 30 to 60 minutes can be achieved without additional active or passive fire protection. The sandwich panel system has been tested in small and large scale fire tests to investigate the thermal and load bearing behaviour of the element exposed to fire. Furthermore, numerical models have been established. This contribution focuses on the presentation of the thermal and mechanical numerical analysis, which were performed with the general purpose FE-software packages *ABAQUS/Standard* and *COMSOL Multiphysics*. As the mechanical response of the structural element has no influence on the heating of the member, the thermal and mechanical problems could be solved separately. Thermal analysis have been performed in 2D with *ABAQUS/Standard* and *COMSOL Multiphysics* considering material nonlinearities. The results of the two programs are compared to each other and to the test results. The mechanical analysis was performed with *ABAQUS/Standard* using a three-dimensional shell model and considering material nonlinearities, buckling analysis and the effect of high temperatures on the structural behaviour. The results are compared to fire tests.

1 M.Sc. (Tech.), VTT Technical Research Centre of Finland, P.O. Box 1000, FI-02044 VTT, Finland
email: tiina.ala-outinen@vtt.fi

2 Professor, University of Hannover, Institute for Steel Construction, Appelstr. 9a, 30167 Hannover, Germany
email: schumann@stahl.uni-hannover.de

3 D.Sc. (Tech.), VTT Technical Research Centre of Finland, P.O. Box 1000, FI-02044 VTT, Finland
email: olli.kaitila@vtt.fi

4 Research Assistant, University of Hannover, Institute for Steel Construction, Appelstr. 9a, 30167 Hannover, Germany, email: kettner@stahl.uni-hannover.de

1. INTRODUCTION

The RFSC-project (Contract No RFS-CR-04048) “Stainless Steel in Fire” seeks to develop more comprehensive and economic design guidance on structural stainless steel members and connections in fire. This includes specific unprotected products meeting the requirements for 30 and 60 minutes fire resistance. The project covers tests on materials, members and connections, numerical analysis and development of design guidance. The comprehensive final report will provide design guidance in a suitable format for inclusion in European standards, accompanied by web-based design software.

This paper deals with a new type of laser-welded stainless steel sandwich panel developed by Kenno Tech Ltd. and analysed in the frame of the project. The sandwich panel consists of two stainless steel sheets as cover plates and V-profiles comprising the web of the section, as shown in Fig. 1. The voids are filled with insulation material, e.g. rock wool, to improve the thermal behaviour. It is the aim of the study to prove that a fire resistance of 30 to 60 minutes can be achieved without additional active or passive fire protection.



Fig. 1 – Stainless steel sandwich panel.

The main structural benefit of this type of welded metal sandwich panels is a high strength to weight ratio, which means advantages for transport and installation at the building site. Previously, these types of structures have been made of carbon steel, but new welding techniques have made it possible to produce them also from stainless steel. The main applications for the sandwich panels are in transportation, ship building, construction industry and process industry, especially where the advantages of stainless steel (resistance to corrosion, increased strength in fire situation, sanitary applications, low maintenance costs) can be beneficial.

2. STRUCTURAL FIRE TESTS

An unloaded small scale and a loaded large scale test have been carried out at the VTT Fire Research testing laboratory on the corrugated core sandwich panels with rock wool insulation fabricated by the Finnish company Kenno Tech Ltd. The dimensions of the specimens were decided on the basis of computed results and are shown in Fig. 4. The total thickness of the sandwich panels was 124.5 mm and the stainless steel grade was EN 1.4301. The spaces between the core elements were filled with blowing rock wool with a density of 115 kg/m^3 , calculated on the basis of the small scale test specimen. The thermal action followed the EN 1363-1: 1999¹ (ISO 834-1) standard fire curve. The temperatures measured by furnace thermocouples were averaged automatically, and the average was used for controlling the furnace temperature. Temperature readings were taken at each thermocouple at intervals of 10 s.

The small scale test was carried out in the cubic furnace on a specimen with horizontal dimensions equal to approximately $1250 \times 1250 \text{ mm}$. The element was installed onto the top opening of the furnace so that its bottom surface was exposed to heating and the top surface was open to the testing hall.

The cross-section of the insulated floor construction in the large scale test was similar to that in the small scale test. The floor consisted of two equal panels with a seam in the middle. The width of one full panel was 1504 mm, the length 5405 mm and the thickness 125 mm. The total width of the furnace ceiling was 3015 mm. The test specimen was loaded during the test. The calculated variable action at normal temperature was 250 kg/m² and in the fire situation 50 % of that. The elements were installed onto the top opening of the furnace so that their bottom surfaces were exposed to heating. The top surface was covered with an 11 mm thick and 2708 mm wide chipboard. The seam between the panels was protected with a stainless steel casing and rock wool insulation attached from underneath, as shown in Fig. 2.

Unfortunately, the installation of the blowing rock wool was not successful for the large scale test specimen and there were several areas of very low insulation density. This caused scatter in the temperature measurements and the failure of the specimen in terms of fire separating function at a relatively early stage.

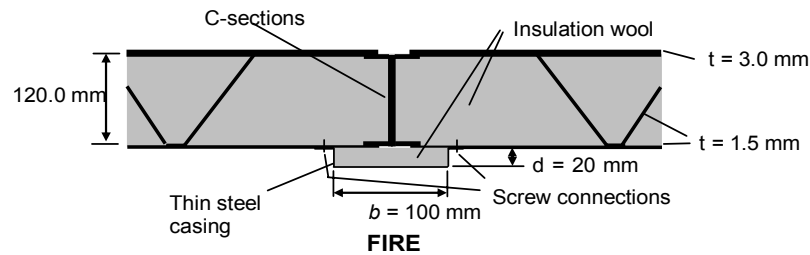


Fig. 2 – Cross-section of test specimens showing seam between floor panels in large scale test.



Fig. 3 – Large scale test setup: furnace (left) and applied variable loads (right).

3. MATERIAL MODELS

3.1 Thermal material properties

The thermal properties of stainless steel were determined according to EN 1993-1-2². The thermal properties of the blowing rock wool used in the tests were not directly available. Models for rock wool slabs of densities 30 kg/m³ (wool30) and 140 kg/m³ (wool140) had been determined by VTT on the basis of earlier tests, so these were expected to provide upper and lower bounds for the temperature calculations. The specific heat capacities c for wool30 and wool140 were taken as 900 J/kgK and 800 J/kgK, respectively. The thermal conductivities λ (W/mK) were modelled according to Eq. (1) for wool30 and Eq. (2) for wool140, where T is the insulation temperature (°C).

$$\lambda = 0.034 - 0.00016T + 1.09 \cdot 10^{-6} T^2 \quad (1)$$

$$\lambda = 0.0341 - 0.0095(T/100) + 0.0034(T/100)^2 \quad (2)$$

3.2 Mechanical material properties for stainless steel

A model for the mechanical material properties for stainless steel at elevated temperatures can be obtained from EN 1993-1-2², where the stress is given as a function of strain, temperature and alloy. The general formulation for the stress-strain relationship is shown on the left in Fig. 4 and it is evaluated at different material temperatures on the right.

Stainless steel has no distinctive yield stress in comparison to conventional structural steel and consequently no horizontal plateau but is given as continuously increasing function as shown in Fig. 4. For steel with no yield plateau the nominal strength value is defined by the proof stress at 0.2 % plastic strain $f_{0.2p}$.

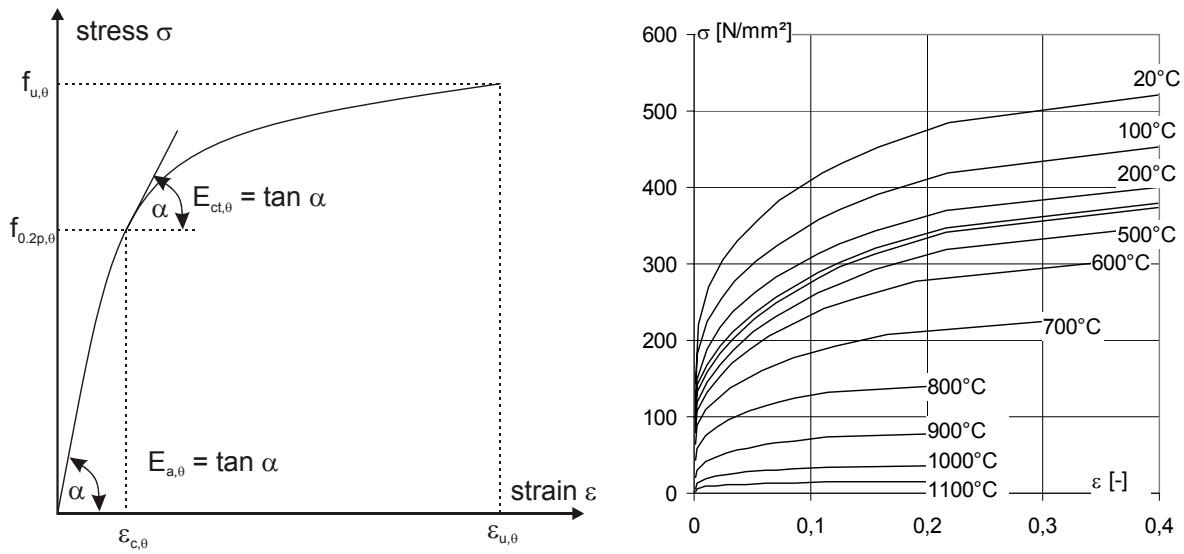


Fig. 4 – General stress-strain formulation (left) and evaluation at different temperatures (right) for stainless steel EN 1.4301 according to EN 1993-1-2.

For the numerical studies in *ABAQUS*, true stresses and logarithmic strains were used as given in Eq. (3) and Eq. (4), respectively.

$$\sigma_{true} = \sigma_{nom} (1 + \varepsilon_{nom}) \quad (3)$$

$$\varepsilon_{ln}^{pl} = \ln(1 + \varepsilon_{nom}) - \frac{\sigma_{true}}{E} \quad (4)$$

Furthermore, EN 1993-1-2² gives an approach for the thermal elongation according to Eq. (5), but for the use in *ABAQUS*, a constant thermal expansion coefficient was derived from Eq. (5), as given in Eq. (6).

$$\Delta L/L = (16 + 4.79 \cdot 10^{-3} \theta_a - 1.243 \cdot 10^{-6} \theta_a^2) \cdot (\theta_a - 20) \cdot 10^{-6} \quad (5)$$

$$\alpha_\theta = \frac{d(\Delta L/L)}{d\theta} \approx 1.8 \cdot 10^{-5} \quad (6)$$

4. THERMAL FE-MODELLING

4.1 General model information

The thermal analysis for the floor slab was done using *COMSOL Multiphysics*³ and *ABAQUS/Standard*⁴ with two-dimensional incremental temperature calculation of the cross section using the Finite Element Method. The two models are illustrated in Fig. 5. In *ABAQUS*, only a small part of the cross section was modelled in order to improve efficiency by taking advantage of symmetry conditions. In *COMSOL*, a larger cross-section could be modelled without problems due to high calculation times.

Three- and four-node elements with linear shape functions were used in *ABAQUS* for the implementation of the stainless steel parts and the rock wool including direct heat flux between the two materials. In *COMSOL*, the meshing is done automatically by the program using triangular linear elements. The thermal boundary conditions were taken as adiabatic at symmetry boundaries for both models. The thermal action on the bottom surface of the slab was modelled according to the standard temperature-time curve as defined in EN 1363-1: 1999¹ (ISO 834-1) with convective and radiative heat transfer ($\alpha_c = 25 \text{ W/(m}^2\text{K)}$; $\varepsilon_{res} = 0.2$ in *ABAQUS* and $\varepsilon_{res} = 0.4$ in *COMSOL*). On the unexposed (top) surface of the slab, the heat loss was implemented with a constant ambient temperature of 20°C and convective heat transfer with $\alpha_c = 9 \text{ W/(m}^2\text{K)}$ in *ABAQUS* and $\alpha_c = 4 \text{ W/(m}^2\text{K)}$ in *COMSOL*. Additionally, radiation heat transfer from the unexposed surface to the ambient was considered in *COMSOL* with an emissivity of $\varepsilon_{res} = 0.4$ (EN 1991-1-2: 2002⁵). Fig. 5 also shows temperature plots at analysis times of 30 and 60 minutes.

Because a material model for the blowing rock wool used in the tests was not available, the calculation was performed with rock wools of density $\rho = 30 \text{ kg/m}^3$ (wool30) and $\rho = 140 \text{ kg/m}^3$ (wool140). The application of the low density rock wool 30 led to slower heat flux in the area of the web than in the area of pure rock wool. This phenomenon can be explained by the thermal diffusivity a , which is defined in Eq. (7)

$$a = \frac{\lambda}{c \cdot \rho} \quad \left[\frac{\text{mm}^2}{\text{s}} \right] \quad (7)$$

The thermal diffusivity defines the diffusion of heat in a medium and depends on thermal conductivity λ , which is higher for steel than for the insulation material, as well as on density ρ and thermal capacity c . The thermal diffusivity is plotted in Fig. 6 as a function of the material temperature for stainless steel and two different rock wools. The comparison demonstrates that for temperatures higher than 400°C, the values for wool30 are higher than the values for stainless steel and high density rock wool, which leads to the effect shown on the right in Fig. 6.

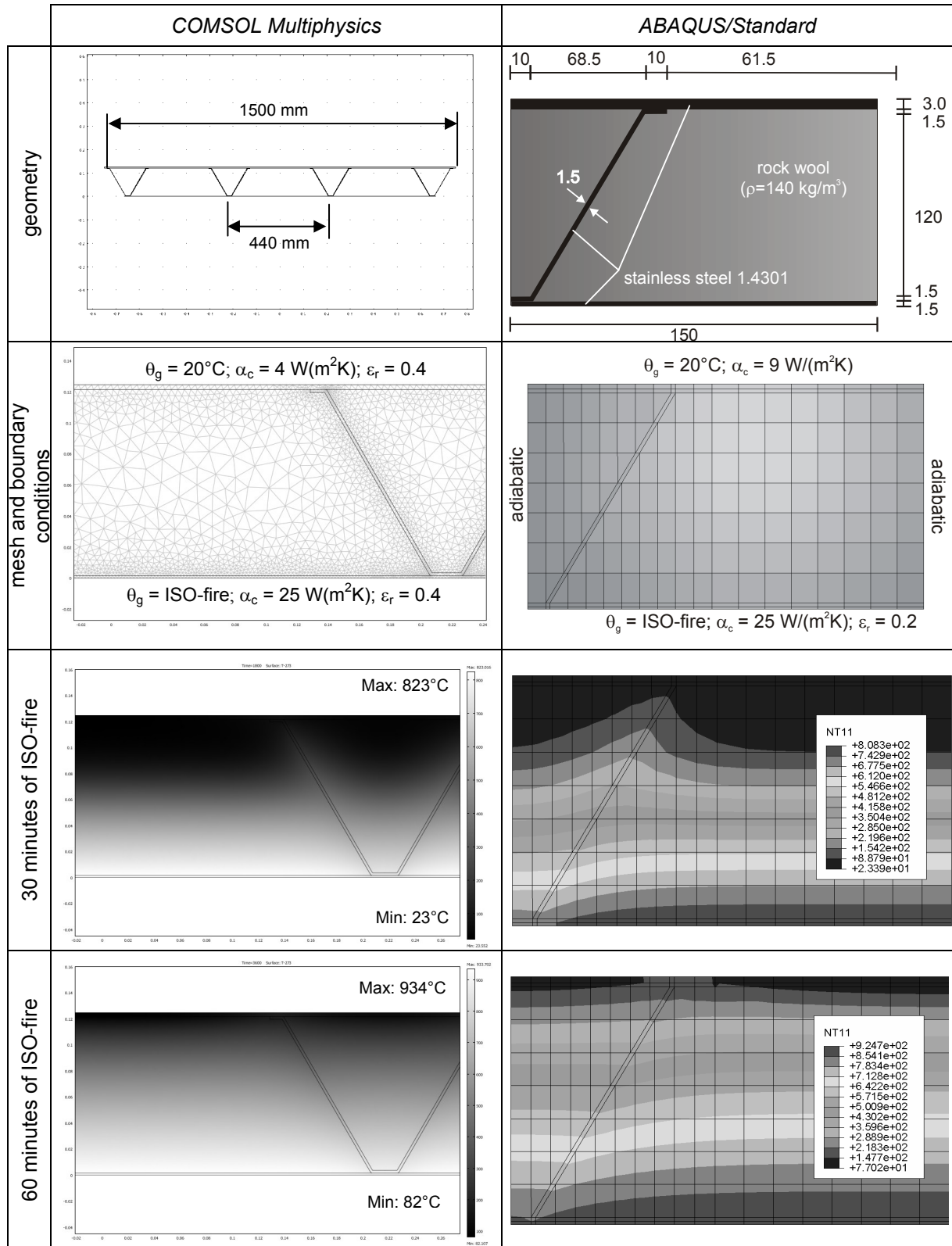


Fig. 5 – Thermal modelling in *COMSOL* and *ABAQUS*.

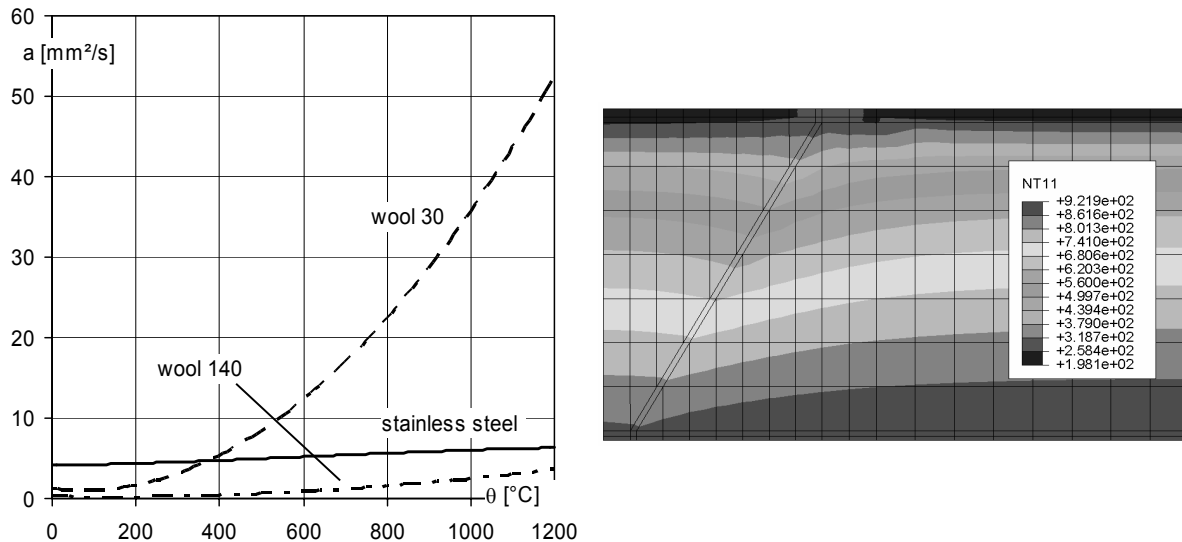


Fig. 6 – Thermal diffusivity of stainless steel, rock wool 30 and 140 (left) and temperature distribution after 30 minutes ISO-fire with rock wool 30 (right).

4.2 Comparisons between numerical calculations and measured temperatures

The results of the numerical analysis using *COMSOL* and *ABAQUS* were compared with the measured temperatures of the small and large scale fire tests and are illustrated in Fig. 7. The temperatures are divided in three diagrams: for the upper flange of the steel profile (unexposed side), the middle of the web and the lower sheet (exposed side). All measured values that refer to the same part of the cross section (e.g. lower sheet), but are disposed over the area of the test specimen, are plotted in small dotted lines. An average value was calculated from these measured values and is shown as a thick line. The results of the numerical calculations are plotted for rock wool 30 and 140.

For the small scale test, the comparisons show that the numerical calculations are conservative in relation to the average values of the measured temperatures. Furthermore, the results with high density rock wool lie closer to the measured values of the small scale test. Unfortunately, due to the problems in blowing rock wool installation, there is a lot of scatter in the results of the large scale test. This makes comparisons with calculations difficult and these results should be considered with caution. However, fairly good agreement between *ABAQUS* and *COMSOL* analysis results can be seen here as well.

When comparing the average temperatures of small and large scale tests, it is obvious that the temperatures at the unexposed side are about 100 % higher in the large scale test, while the temperatures at the exposed side are nearly the same. These circumstances lead to different temperature gradients over the height of the member and this will be significant regarding the deflection (cf. section 5.3).

The Eurocodes define insulation criteria for separating members: the temperature at the unexposed side of the member must not exceed 140 $^\circ\text{C}$ as average and 180 $^\circ\text{C}$ as peak value. The measured temperature results reveal that the insulation criterion I 60 is met in the small but not in the large scale test.

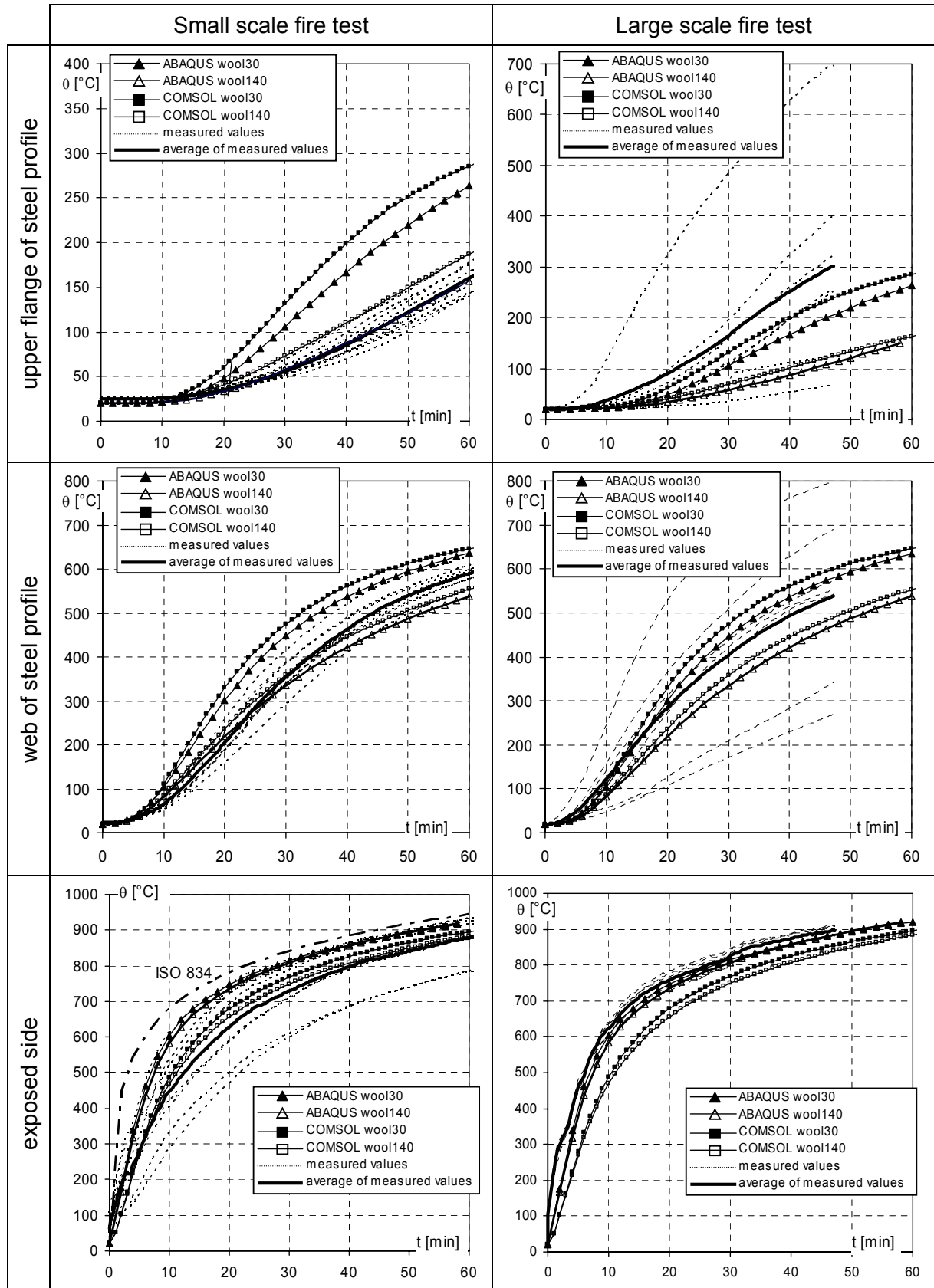


Fig. 7 – Comparisons between numerical calculations and measured temperatures from fire tests.

5. MECHANICAL FE-MODELLING

5.1 ABAQUS-model

A three-dimensional *ABAQUS*-model was set up for a load bearing calculation using S4R shell elements with reduced integration. Only a small part of the test specimen was implemented to reduce the size of the model and hence the required calculation time. The model represents one half of a rib, because the V-profiles of the floor element cause a one-way spanning load bearing behaviour so that the load-carrying in transverse direction is negligible. The boundary conditions were applied as shown in Fig. 8.

The numerical studies were performed in five steps:

1. Identification of buckling modes by linear buckling analysis to determine imperfections
2. Application of the imperfect geometry obtained in step 1
3. Application of mechanical loads
4. The loaded sandwich panel is subjected to the heating according to the small scale fire test
5. Load increasing with constant temperature distribution of 60 minutes of ISO-fire

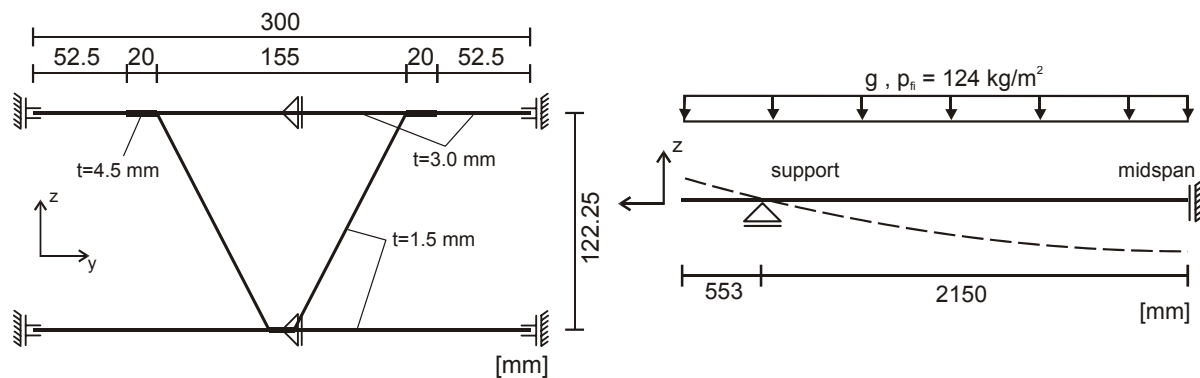


Fig. 8 – Geometry and boundary conditions of the ABAQUS-model: continuous boundary conditions along the edges (left) and at the ends of the rib (right).

5.2 Determination of imperfections – Linear buckling analysis

For a realistic estimation of the load bearing capacity, geometric imperfections must be considered in the analysis. The imperfections are simulated by superposing the FE-model with scaled buckling mode shapes determined in a linear buckling analysis with a basic state considering vertical loading, material nonlinearities and different temperature fields. The comparison of the different basic states revealed that the magnitude of the eigenvalues differed, but not the buckling shape. Finally, the imperfection has been developed from a superposition of two buckling modes, which are presented in Fig. 9: one for the compression zone in the upper flange at midspan and the other for the compression zone at the support. A common maximum magnitude for the imperfections was applied according to Eq. (8). The buckling mode shape according to Fig. 9 is scaled with ω and superposed with the perfect geometry.

$$\omega = b / 200 = 155.0 / 200.0 = 0.775 \text{ mm} \quad (8)$$

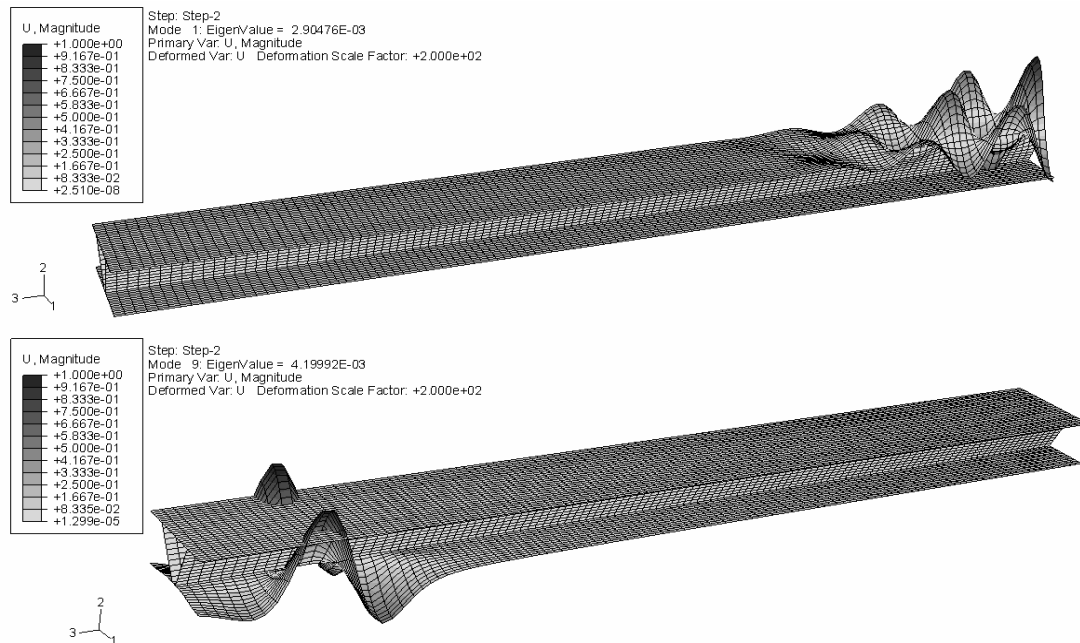


Fig. 9 – Buckling modes for the two compression zones at midspan and at support.

5.3 Load bearing behaviour of the sandwich panel subjected to ISO-fire

Finally, the sandwich panel with the imperfect geometry was subjected to the temperatures determined in the small scale fire test (rf. section 2). The analysis procedure is described in 5.1. The deformed shape is presented in Fig. 10 with a contour-plot showing Mises-stresses after 60 minutes of ISO-fire. Further investigation of the strains showed that no significant plastification occurred.

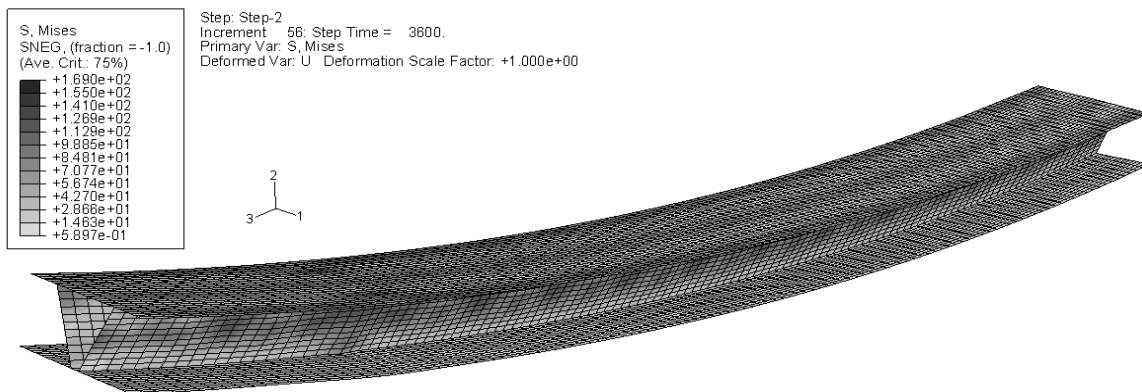


Fig. 10 – Deformed *ABAQUS*-model and Mises-stresses after 60 minutes of ISO-fire (no amplification).

The nodes at midspan and at the end of the cantilever arm at the lower sheet in the middle of the two webs were chosen as reference nodes for the time-displacement curve in Fig. 11. In addition to vertical deflections resulting from the external loading, thermal bowing determined according to simplified equations for the deflection midspan Eq. (9) and at the end of the cantilever arm Eq. (10) is depicted in Fig. 11.

$$w_{\theta,m} = \frac{L^2}{8} \alpha_T \frac{\Delta\theta}{d} \quad (9)$$

$$w_{\theta,c} = \frac{L_c}{2} \alpha_T \frac{\Delta\theta}{d} \cdot (L + L_c) \quad (10)$$

where d distance of the upper and lower flange
 $\Delta\theta$ temperature gradient
 α_T expansion coefficient
 L span between supports
 L_c span of the cantilever arm

The comparisons in Fig. 11 (left) between measured values and the results of the *ABAQUS* analysis show significant differences for the deflection at midspan w_m . The deflection governed by thermal bowing, as derived from Eq. (9) and (10) is also plotted in Fig. 11. Obviously, the total deflection during 60 minutes of ISO-fire in *ABAQUS* is governed by thermal bowing, and not by the effects of the mechanical loads and the loss in bending stiffness due to high steel temperatures. The reason for the differences between the test and the numerical analysis is the application of small scale fire test temperatures on the numerical model, because those values differ from the temperatures measured in the large scale test (see Fig. 7). Therefore the thermal bowing determined from the large scale temperatures are plotted in Fig. 11 as well. The maximum deflection thus obtained fits well with measured values of the large scale test.

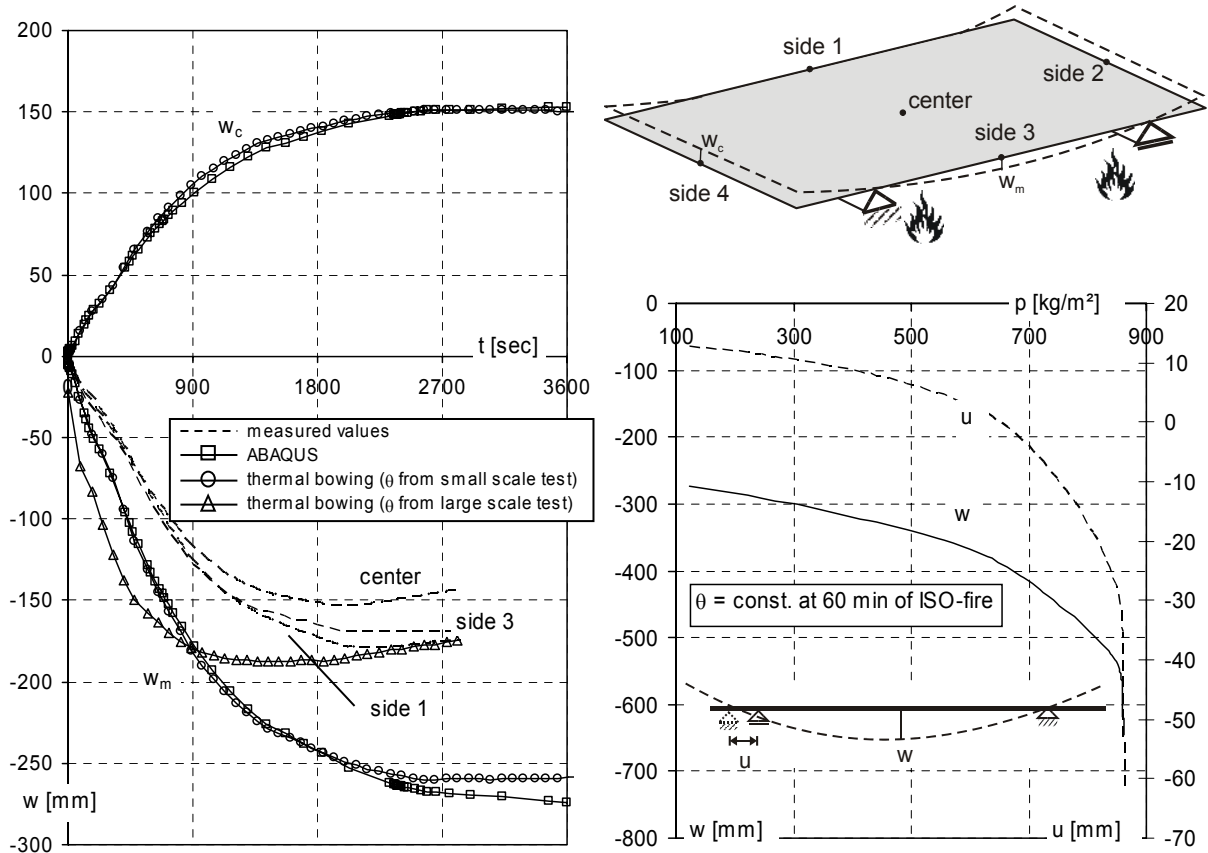


Fig. 11 – Deflections at various points (left) against time and vertical and horizontal displacements at midspan and at support against loads at constant temperatures of 60 min ISO-fire (right).

Overall, the deflections show that the requested fire resistance of 60 min for load bearing capacity was reached and failure did not occur. For this reason, a load bearing calculation was performed following the heating of 60 minutes of ISO-fire with constant temperatures and increasing live loads. The results for the deflection at midspan and the horizontal displacement at support are plotted on the right side of Fig. 11. An ultimate load $p \approx 800 \text{ kg/m}^2$ for the structural member can be estimated from the graphs for R 60 due to rapidly increasing deflections. However, the large deflections due to thermal bowing may define a lower limit state for serviceability.

6. SUMMARY AND CONCLUSIONS

This contribution presented a new type of laser-welded stainless steel sandwich panel with rock wool insulation developed by Kenno Tech Ltd. and analysed in the frame of the RFCS-project “Stainless Steel in Fire”. Two fire tests have been performed with the element subjected to ISO-fire: an unloaded small scale test to analyse the temperature development and a large scale test with additional live load. Numerical and test results on the thermal and load bearing behaviour were demonstrated and explained.

Two-dimensional thermal analyses were performed using commercial FEM-software packages *COMSOL Multiphysics* and *ABAQUS/Standard*. The thermal analysis results from the two FEM-codes showed good agreement with each other and with the average values of the measured temperatures from the small scale test. However, the temperatures of the large scale test scatter because the installation of the blowing rock wool was not successful for the test specimen and there were several areas of very low insulation density.

A three-dimensional shell model has been set up in *ABAQUS* for the investigation of the load bearing behaviour of the panel. The model considered imperfections determined from linear buckling analysis, non-linear material behaviour of stainless steel and large deformations. The results demonstrated that the requested fire resistance of 60 min for load bearing capacity was reached and failure did not occur. However, the deflections up to 60 minutes of ISO-fire action were mainly governed by thermal bowing, not by the effects of the mechanical loads and the loss in bending stiffness due to high steel temperatures. Furthermore, the deflections determined using *ABAQUS* were obviously higher than in the large scale test. The reason was that in *ABAQUS*, the temperatures of the small scale test were applied on the structural model and the upper sheet in the large scale test shows higher temperatures than in the small scale test due to the insulation cavities. Thus the large scale test specimen had a smaller temperature gradient and hence smaller deflections due to thermal bowing.

Furthermore, the live load on the ABAQUS-model was continuously increased until failure could be observed due to rapidly increasing deflections.

7. REFERENCES

- [1] EN 1363-1: 1999 *Fire resistance tests – Part 1: General requirements*, CEN European Committee for Standardization, Brussels, Belgium, 1999.
- [2] EN 1993-1-2 *Eurocode 3: Design of steel structures - Part 1.2: General rules, Structural fire design*, CEN European Committee for Standardization, Brussels, Belgium, 2005.
- [3] COMSOL Multiphysics© Version 3.2, *User's Guide*, COMSOL AB, 2005
- [4] ABAQUS/Standard© Version 6.5-1, *User's Manual*, ABACOM Software, 2004
- [5] EN 1991-1-2: 2002 *Eurocode 1 Actions on structures - Part 1-2: General actions - Actions on structures exposed to fire*, CEN European Committee for Standardization, Brussels, Belgium, 2002.



NUMERICAL VALIDATION OF AN IMPROVED PROPOSAL TO THE EUROCODE 3 FOR THE LATERAL-TORSIONAL BUCKLING OF STEEL BEAMS SUBJECTED TO FIRE

Vila Real, P.M.M.¹; Lopes, N.²; Simões da Silva, L.³ and Franssen, J.-M.⁴

ABSTRACT

Significant changes have been introduced in the recently approved EN version of part 1-1 of Eurocode 3, in the evaluation of the lateral-torsional buckling resistance of unrestrained beams at room temperature when compared to the approach of ENV 1993-1-1, that is over-conservative in the case of non-uniform bending.

Numerical modelling of the lateral-torsional buckling of steel beams at elevated temperature has shown that the beam design curve from EN 1993-1-2 is also over-conservative for loadings other than uniform bending.

Based on the newly proposed methodology for cold design from the EN 1993-1-1, an improved proposal for the lateral-torsional buckling of unrestrained steel beams subjected to fire is presented in this paper that addresses the issue of the influence of the loading type, the steel grade, the pattern of the residual stresses and the cross-section type on the resistance of the beam, achieving better agreement with the numerical behaviour while maintaining safety. This proposal is based on extensive numerical simulations on rolled and equivalent welded cross-sections considering the influence of the ratio h/b , between the depth h and the width b of the cross-section, the influence of the load type, the influence of different steel grades and the influence of the residual stresses (hot-rolled or welded sections).

A statistical study of the results is performed, showing the accuracy of the improved proposal presented in this paper.

¹ University of Aveiro, Dep. Civil Engineering, 3810 Aveiro, Portugal,
Email: pvreal@civil.ua.pt.

² University of Aveiro, Dep. Civil Engineering, 3810 Aveiro, Portugal,
Email: nuno_lopes@civil.ua.pt.

³ University of Coimbra, Dep. Civil Engineering, 3030 Coimbra, Portugal,
Email: luisss@dec.uc.pt.

⁴ University of Liege, Department M&S, Liège,
Email: jm.franssen@ulg.ac.be.

1. INTRODUCTION

Recently, Vila Real et al. [1, 2, 3] proposed an alternative expression for the lateral-torsional buckling resistance of unrestrained beams under fire loading. This change, already incorporated in part 1-2 of EC3 [4], was triggered by the identification of the unconservative nature of the previous expression [5] for the case of a simply-supported beam with fork supports under uniform bending.

Also recently, during the conversion of Eurocode 3 from ENV to EN status, the project team introduced in EN 1993-1-1 [6] significant changes in the evaluation of the lateral-torsional buckling resistance of unrestrained beams at room temperature compared to the over-conservative approach of ENV 1993-1-1 [7] in the case of non-uniform bending. It is desirable that the former compatibility and coherence between part 1-1 (General rules and rules for buildings) [6] and part 1-2 (Fire design) [4] is restored.

In a previous paper by the authors [8], a new proposal for the evaluation of the lateral-torsional buckling of beams in case of fire was presented that followed the same format as the cold-design expressions. In particular, a correction factor f was introduced, that accounted for the beneficial effect resulting from reduced plastic zones connected with variable bending along the beam [9]. In a subsequent paper, Vila Real et al. [10] have studied the influence of the steel grade (S235 to S460), the cross-sectional shape and the pattern of residual stresses (rolled and welded sections), on the lateral-torsional buckling of steel I-beams under fire conditions. It was indeed concluded that the influence of all these parameters must be taken into account, which was not the case on the previous proposal from the authors [8], which only considered the influence of the loading type.

The study was carried out using more than 5000 numerical finite element simulations with the specialized finite element code SAFIR [11], which is a finite element code for geometrical and material non-linear analysis, specially developed at the University of Liege for studying structures subjected to fire.

It is the objective of the present paper to present the statistical study that has supported the improved proposal presented in reference [10].

2. THE LATERAL-TORSIONAL BUCKLING CODE PROVISIONS OF PART 1.2 OF EUROCODE 3

According to EN 1993-1-2, the design buckling resistance moment of a laterally unrestrained beam with a class 1 or 2 cross-section type, is obtained as follows:

$$M_{b,fi,t,Rd} = \chi_{LT,fi} W_{pl,y} k_{y,\theta,com} f_y \frac{1}{\gamma_{M,fi}} \quad (1)$$

where $\chi_{LT,fi}$, is given by

$$\chi_{LT,fi} = \frac{1}{\phi_{LT,\theta,com} + \sqrt{[\phi_{LT,\theta,com}]^2 - [\bar{\lambda}_{LT,\theta,com}]^2}} \quad (2)$$

with

$$\phi_{LT,\theta,com} = \frac{1}{2} \left[1 + \alpha \bar{\lambda}_{LT,\theta,com} + (\bar{\lambda}_{LT,\theta,com})^2 \right] \quad (3)$$

The non-dimensional slenderness $\bar{\lambda}_{LT,\theta,com}$ (or $\bar{\lambda}_{LT,fi}$, if the temperature field in the cross-section is uniform) is given by

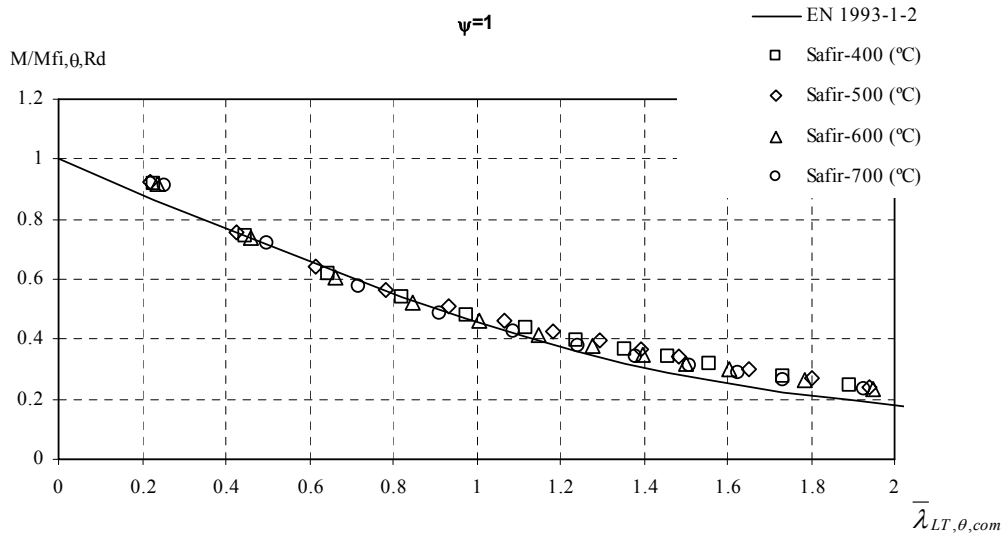
$$\bar{\lambda}_{LT,\theta,com} = \bar{\lambda}_{LT,fi} = \bar{\lambda}_{LT} \sqrt{\frac{k_{y,\theta}}{k_{E,\theta}}} \quad (4)$$

where $k_{y,\theta}$ denotes the reduction factor for the yield strength of steel at the steel temperature θ_a reached at time t and $k_{E,\theta}$ is the reduction factor for the slope of the linear elastic range at the steel temperature θ_a reached at time t .

The imperfection factor α , is a function of the steel grade and is given by:

$$\alpha = 0.65 \sqrt{235 / f_y} \quad (5)$$

This proposal, presented for the first time by Vila Real et al. in 1999 [1] and published in 2001 [2], was based on the study of the behaviour of the European hot rolled profile IPE 220, in steel grades S235 and S355 submitted to uniform bending. Figure 1 shows the accuracy of this proposal.



a)

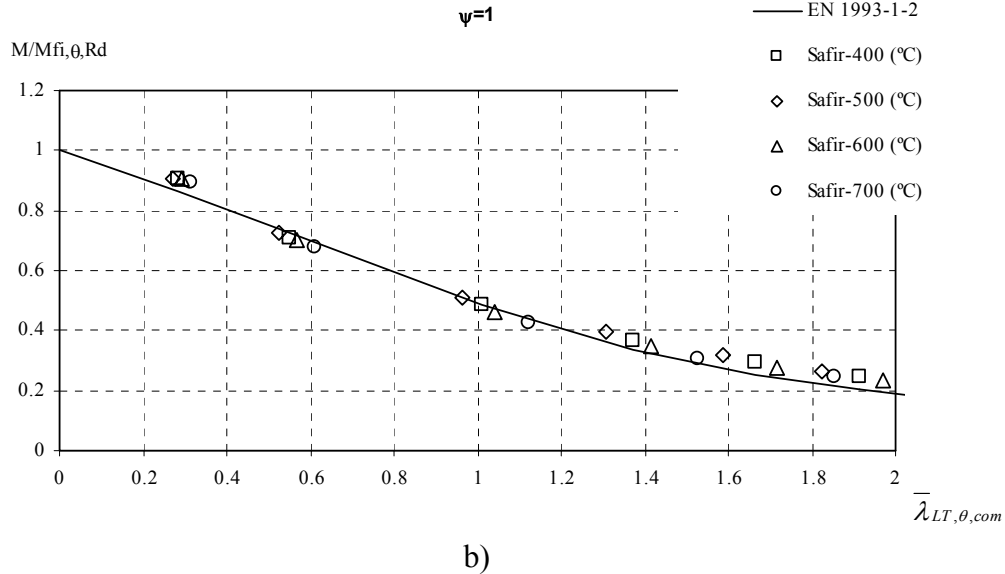


Fig. 1 – Numerical results for an IPE 220: a) S235; b) S355. Comparison with EN 1993-1-2.

During the conversion of Eurocode 3 from ENV to EN status, the project team has accepted this proposal which, it is now known, presents unsafe values for some type of profiles, as can be seen in figure 2 for the case of a welded IPE 500 in steel grade S460.

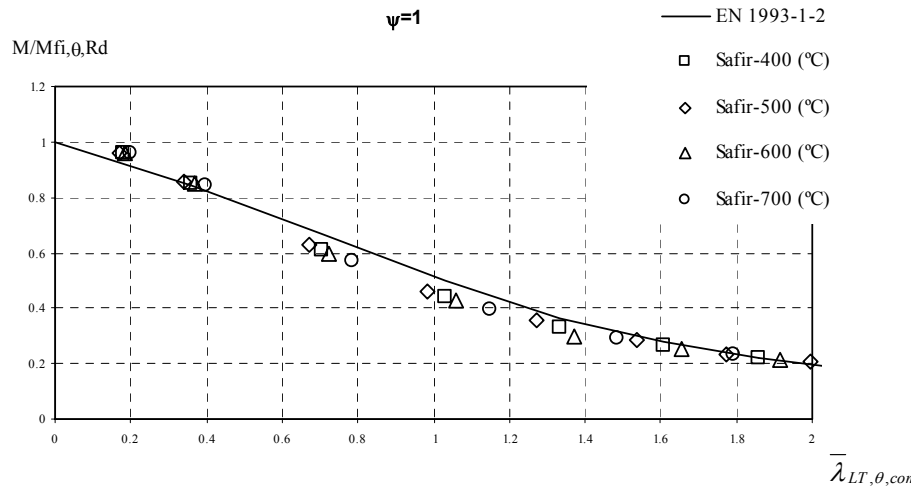


Fig. 2– Numerical results for an welded IPE 500 in steel grade S460. Comparison with EN 1993-1-2.

3. A NEW PROPOSAL

To take into account the steel grade, the type of the cross-section and the effect of the residual stresses, equation (5), which defines the imperfection factor α , is rewritten as a function of a severity factor β [10]

$$\alpha = \beta \sqrt{235 / f_y}, \quad (6)$$

the severity factor being given in Table 1.

Table 1 - Values of the severity factor, β

Cross-section	limits	β	
		S235, S275, S355, S420	S460
Rolled I section	$h/b \leq 2$	0.65	0.70
	$h/b > 2$	0.75	0.80
Welded I section	$h/b \leq 2$	0.70	0.75
	$h/b > 2$	0.80	0.85
Other cross-sections	-	0.80	0.85

To take into account the moment distribution between the lateral restraints of members, the authors have proposed a modified reduction factor given by [8,10]:

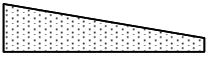
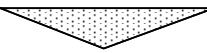
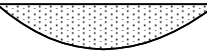
$$\chi_{LT,fi,mod} = \frac{\chi_{LT,fi}}{f} \quad \text{but} \quad \chi_{LT,fi,mod} \leq 1 \quad (7)$$

where

$$f = 1 - 0.5(1 - k_c) \quad (8)$$

and k_c is a correction factor according to Table 2, established by numerical adjustment to match as closely as possible a representative sample of finite element numerical results.

Table 2 - Correction factors k_c for the new proposal.

Moment distribution	Class 1, 2, 3 sections
	k_c
 $-1 \leq \psi \leq 1$	$0.6 + 0.3\psi + 0.15\psi^2$ but $k_c \leq 1$
	0.79
	0.91

Note: for others bending diagrams $k_c = 1$.

With this new proposal the results for the welded IPE 500 in steel grade S460 shown in the figure 2 are improved, as illustrated in figure 3.

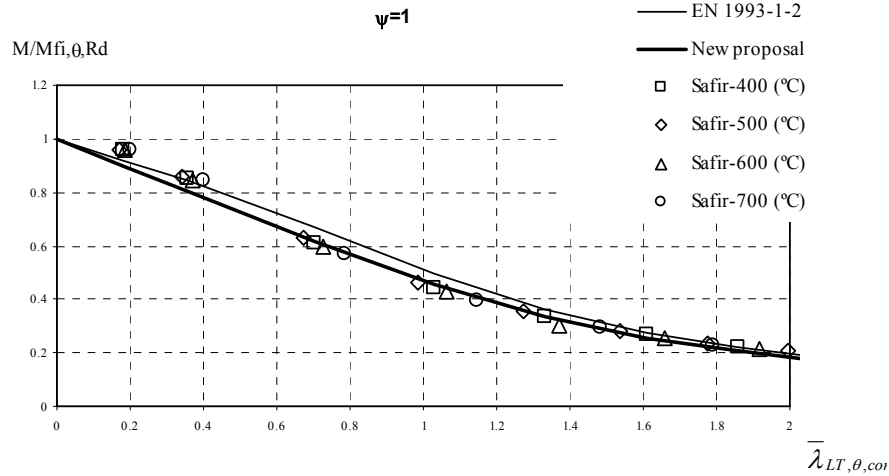


Fig. 3– Numerical results for an welded IPE 500 in steel grade S460.
Comparison with EN 1993-1-2 and the new proposal.

4. STATISTICAL EVALUATION

The values of the severity factor β defined in the Table 1 were chosen so that the new proposal has the same degree of accuracy as the formulae of the EN 1993-1-2 for a hot rolled IPE 220 submitted to uniform bending [1,2].

For each chosen severity factor, it is possible to evaluate the ratio between the analytical value of the ultimate design lateral torsional buckling resistance moment, $M_{ult,i}^{Analytical}$ and the corresponding SAFIR moment. This ratio is also the ratio between the analytical and the SAFIR lateral torsional buckling coefficient as follows:

$$x_i = \frac{M_{ult,i}^{Analytical}}{M_{ult,i}^{SAFIR}} = \frac{\chi_{LT,i}^{Analytical}}{\chi_{LT,i}^{SAFIR}} \quad (9)$$

The proposal is safe if it leads to values of x_i lower than 1, and unsafe for values higher than 1, (see figs. 7 to 9).

The average value, μ , and the standard deviation, σ , were calculated as:

$$\mu = \frac{\sum_{i=1}^n x_i}{n} \quad (10)$$

$$\sigma = \sqrt{\frac{\sum_{i=1}^n (x_i - \mu)^2}{n-1}} \quad (11)$$

The results obtained with EN 1993-1-2 for the hot rolled IPE 220 in steel grades S235 and S355 are shown in figure 4. The average value and the standard deviation for this case are, respectively, $\mu = 0.929$ and $\sigma = 0.078$. When EN 1993-1-2 is used with hot rolled and

welded IPE 220 steel section (representative of $h/b = 2$), HEA 500 steel section (representative of $h/b < 2$) and IPE 500 steel section (representative of $h/b > 2$), in steel grades, S235, S355 and S460 (see fig. 5) the average value and the standard deviation are, respectively, $\mu = 0.969$ and $\sigma = 0.075$. If the new proposal is used with hot rolled and welded IPE 220, HEA 500 and IPE 500, in steel grades, S235, S355 and S460 (see fig. 6) the average value and the standard deviation take the values $\mu = 0.943$ and $\sigma = 0.066$, respectively.

Figure 7 shows the ratio x_i given by eq. (9) when EN 1993-1-2 is used with the hot rolled IPE 220 in steel grade S235 and S355 submitted to uniform bending moment. The maximum unsafe error is 5.3% and the average error is 2.5%. If EN 1993-1-2 is used with hot rolled and welded IPE 220, HEA 500 and IPE 500, in the steel grades, S235, S355 and S460 (see fig. 8) these values increase to 12.8% and 4.6%, respectively.

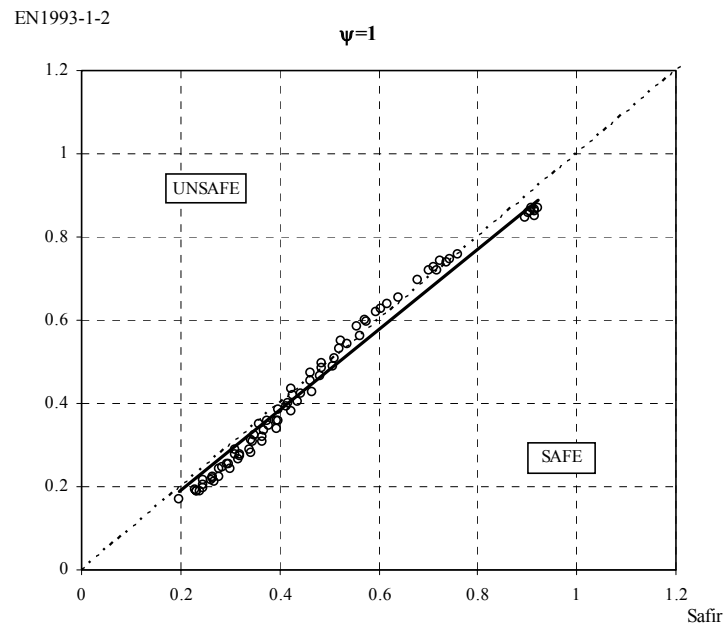


Fig. 4 –Comparison between EN 1993-1-2 and numerical results for the hot rolled IPE 220 in steel grade S235 and S355 ($\mu = 0.929$, $\sigma = 0.078$).

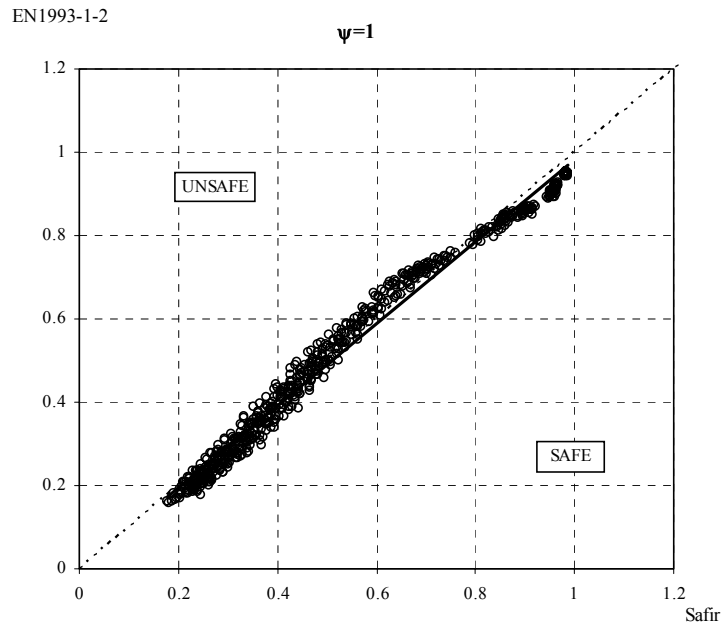


Fig. 5 –Comparison between EN 1993-1-2 and numerical results for the hot rolled and welded HEA 500, IPE 220 and IPE 500 in steel grade S235, S355 and S460 ($\mu = 0.969$, $\sigma = 0.075$).

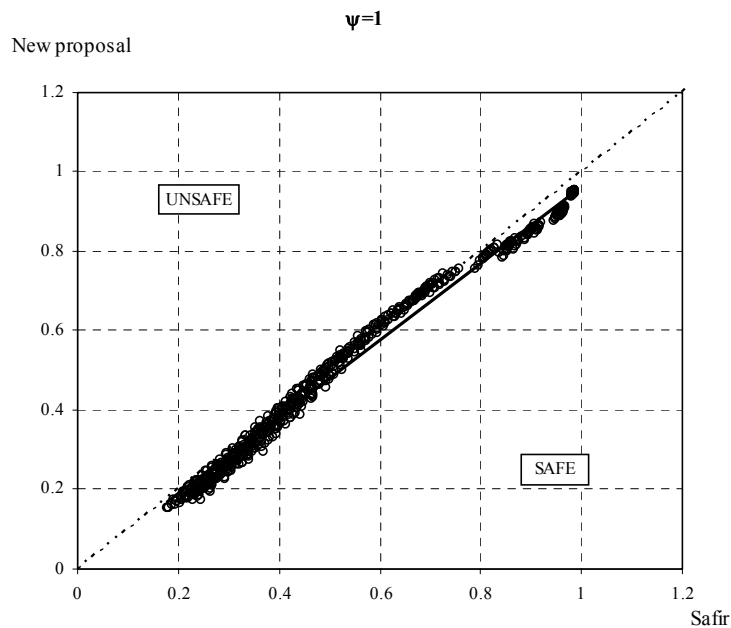


Fig. 6 –Comparison between the new proposal and numerical results for the hot rolled and welded HEA 500, IPE 220 and IPE 500 in steel grade S235, S355 and S460 ($\mu = 0.943$ and $\sigma = 0.066$).

The severity factor of Table 1 was derived so that the accuracy of the new proposal was similar to the accuracy of the proposal of the EN 1993-1-2 for the case it was based, i.e., for the case of the hot rolled IPE 220 in steel grade S235 and S355. The new proposal gives the results shown in figure 9, with the same unsafe error of 5.3% as for the EN 1993-1-2 and an average error of 1.8%.

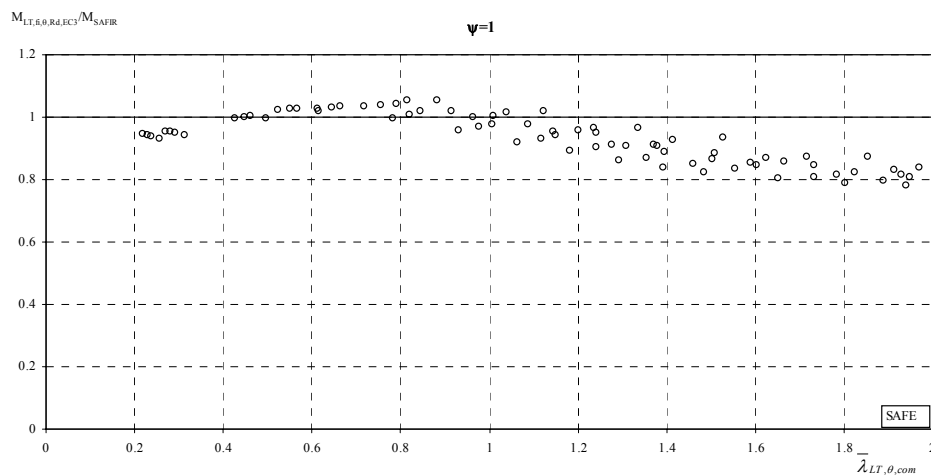


Fig. 7 –Ratio x_i for EN 1993-1-2 with hot rolled IPE 220 in steel grade S235 and S355. (maximum unsafe error 5.3% and average error 2.5%)

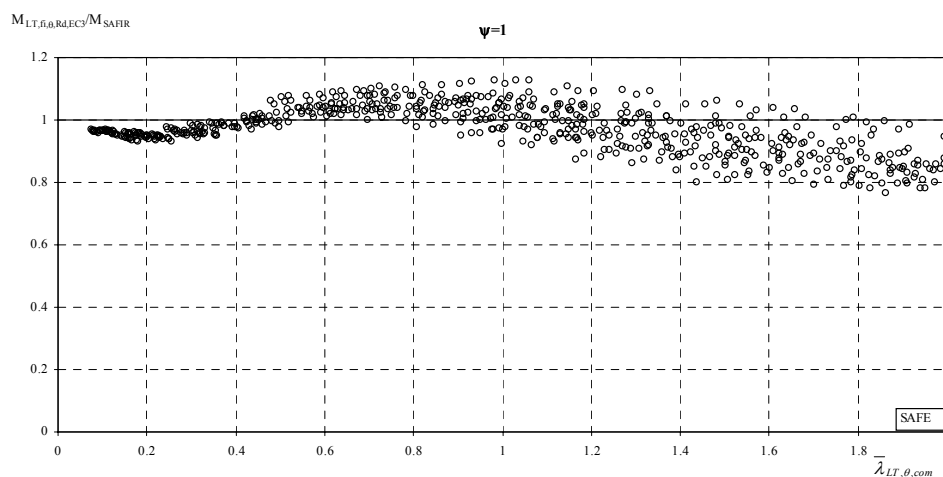


Fig. 8 –Ratio x_i for EN 1993-1-2 with the hot rolled and welded HEA 500, IPE 220 and IPE 500 in steel grade S235, S355 and S460, (maximum unsafe error 12.8% and average error 4.6%)

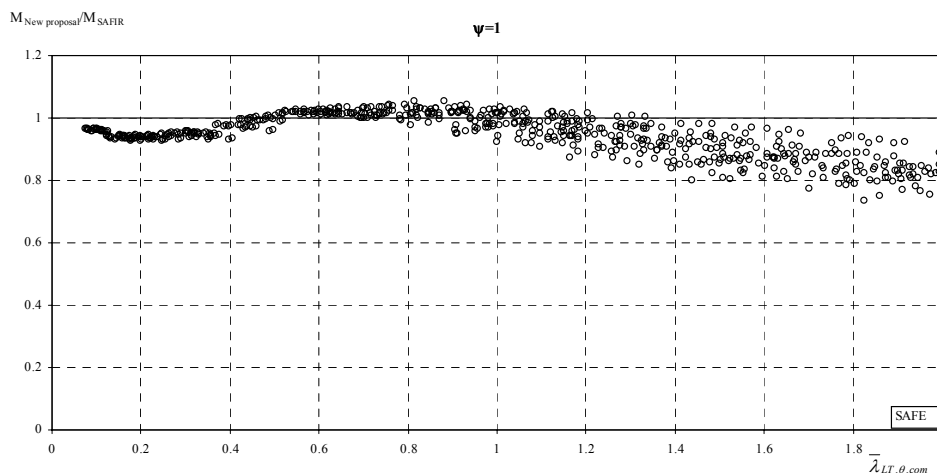


Fig. 9 –Ratio x_i for the new proposal with the hot rolled and welded HEA 500, IPE 220 and IPE 500 in steel grade S235, S355 and S460, (maximum unsafe error 5.3% and average error 1.8%)

5. CONCLUSIONS

An improvement of a previous proposal from the authors [8] for the lateral-torsional buckling resistance of unrestrained beams under fire loading which takes into account the influence of the steel grade, the type of the cross-section and the residual stresses (hot-rolled or welded sections) [10], was validated, in this paper, by a statistical study. It was shown that the proposal from the EN 1993-1-2 is not safe for some cross sections, which is not the case for the new proposal due to the introduction of a severity factor obtained to ensure the same level of accuracy that the EN 1993-1-2 formulae present for the hot rolled IPE 220 in steel grade S235 and S355.

6. REFERENCES

- [1] Vila Real, P.M.M. and Franssen, J.-M. Lateral buckling of steel I beams under fire conditions - Comparison between the EUROCODE 3 and the SAFIR code. internal report No. 99/02 , Institute of Civil Engineering – Service Ponts et Charpents – of the University of Liege, 1999.
- [2] Vila Real, P.M.M. and Franssen, J.-M. Numerical Modelling of Lateral Buckling of Steel I Beams Under Fire Conditions – Comparison with Eurocode 3. Journal of Fire Protection Engineering, Vol. 11, No. 2, , pp. 112-128, USA, 2001.
- [3] Vila Real, P.M.M., Piloto, P.A.G. and Franssen, J.-M. A New Proposal of a Simple Model for the Lateral-Torsional Buckling of Unrestrained Steel I-Beams in Case of Fire: Experimental and Numerical Validation. Journal of Constructional Steel Research, Elsevier, Vol. 59/2, pp. 179-199, 2003.
- [4] European Committee for Standardisation. EN 1993-1-2, Eurocode 3, Design of Steel Structures – part 1-2. General rules – Structural fire design. Brussels, Belgium, 2005.
- [5] European Committee for Standardisation. ENV 1993-1-2, Eurocode 3, Design of Steel Structures – part 1-2. General Rules – Structural fire design. Brussels, Belgium, 1995.
- [6] European Committee for Standardisation. EN 1993-1-1, Eurocode 3, Design of Steel Structures – part 1-1. General rules and rules for buildings. Brussels, Belgium, 2005.
- [7] European Committee for Standardisation. ENV 1993-1-1, Eurocode 3, Design of Steel Structures – part 1-1. General rules and rules for buildings. Brussels, Belgium, 1992.
- [8] Vila Real, P.M.M., Lopes, N., Simões da Silva, L., Franssen, J.-M. Lateral-Torsional Buckling of Unrestrained Steel Beams Under Fire Conditions: Improvement of EC3 Proposal. Computers & Structures, Elsevier, Vol. 82, pp. 1737-1744, 2003.
- [9] Boissonnade, N., Greiner, R. and Jaspart, J.P. Rules for member stability in EN 1993-1-1. Background documentation and design guidelines. ECCS Technical Committee 8 – Stability, 4th draft, 2005.
- [10] Vila Real, P.M.M., Lopes, N., Simões da Silva, L., Franssen, J.-M., An Improved Proposal to the Eurocode 3 for the Lateral-Torsional Buckling of Steel Beams in Case of Fire, submitted to the Journal of Constructional Steel Research, Elsevier, December 2005.
- [11] Franssen, J.-M., SAFIR. A Thermal/Structural Program Modelling Structures under Fire. Engineering Journal, A.I.S.C., Vol. 42, No. 3, pp. 143-158, 2005.



TESTING AND ANALYSIS OF CATENARY ACTION IN UNPROTECTED STEEL BEAMS SUBJECTED TO FIRE

David PROE¹, Ian BENNETTS² and Ian THOMAS³

ABSTRACT

The use of unprotected steel beams in sprinkler-protected office buildings has been increasing in Australia over the past ten years. This has been justified using performance-based assessments, taking into account firstly the high reliability of the sprinkler system and secondly the robust performance of the floor system in fire resulting from the interconnection between the elements of structure. In this context, quantification of the catenary action developed in the steel beams is of interest, and a study of this mode of support has been commenced.

Two fire tests have been conducted on steel beams supported in catenary action. A numerical analysis program has been written, based on moment-curvature methods. The material model for steel used in this analysis was that proposed by Poh. This model includes an explicit calculation of creep strain. Experimental and analytical results were compared. Reasonable agreement was obtained for Test 1, but in Test 2 the observed strength was greater than that calculated. Further investigation of this difference will be undertaken.

Keywords: fire tests, fire performance, numerical analysis, structural analysis, unprotected steel, catenary action, creep, steel structures

1. INTRODUCTION

There are now numerous examples in Australia of multistorey steel-frame buildings in which the majority of the steel beams are unprotected. Examples in the Melbourne CBD include the office building at 140 William Street, the RACV headquarters (office, hotel, public assembly) building in Bourke Street, the BHP Billiton office building in Lonsdale Street, the office building at 50 Lonsdale Street and the building on the Southern Cross site at the corner of Bourke and Russell Streets. These buildings range in above-ground height from 18 to 42 storeys, and they have more than 90% of the total beam length unprotected. In

¹Assoc. Professor, Centre for Environmental Safety and Risk Engineering (CESARE), Victoria University, Melbourne, Australia; email: david.proe@vu.edu.au (formerly at Ove Arup Pty Ltd, Melbourne)

²Principal Risk Consultant, Noel Arnold Pty Ltd; email: ian.bennetts@noel-arnold.com.au (formerly CESARE)

³Professor, CESARE, Victoria University, Melbourne, Australia; email: ian.thomas@vu.edu.au

addition, two buildings in Singapore have recently been approved with unprotected steel, being the 16-storey twin-tower National Library building and the 4-storey Ang Mo Kio retail/bus interchange complex. These buildings all incorporate sprinkler protection throughout, generally incorporating enhancements above the minimum regulatory requirements, and typically have steel beams which act in composite action with the floor slab.

Regulatory approval on these buildings has been obtained using performance-based assessments, taking into account firstly the high reliability of the sprinkler system and secondly the robust performance of the floor system in fire resulting from the interconnection between the elements of structure. Evidence of the robust performance of such floor systems has been obtained from the large-scale fire testing which has been conducted, in particular an early series of fire tests on a full-scale steel frame structure in the USA by Iding and Bresler^[1], the testing to model the 140 William Street building in Australia^[2] and the testing of an 8-storey full-scale model building at Cardington in the UK^[3].

In this context, an understanding of the performance of the floor system at high temperatures and large deflections is important. A useful step in this direction is quantification of the behaviour of the steel beams. When an unprotected steel beam reaches a temperature in fire at which it is unable to fully support the applied vertical load in bending action, its interconnection to the surrounding structure may enable it to be supported by the development of horizontal forces at its ends. The load is then partly supported in catenary action, as for a flexible cable which is pulled at its ends. As the temperature continues to increase, the transition from bending action to catenary action progresses. The current study explores this transition.

Any study of steel beams in catenary action must account for the high temperatures and stresses which are associated with this mode of behaviour. Under such conditions, the influence of elevated-temperature creep can be important. Fortunately, a comprehensive constitutive model for steel at elevated temperatures has recently been developed by Poh^[4], based on an extensive series of elevated-temperature laboratory tensile tests conducted at BHP Research. This model includes explicit evaluation of creep strain as a function of temperature, stress and time. This model will be used in the analysis of the tests conducted.

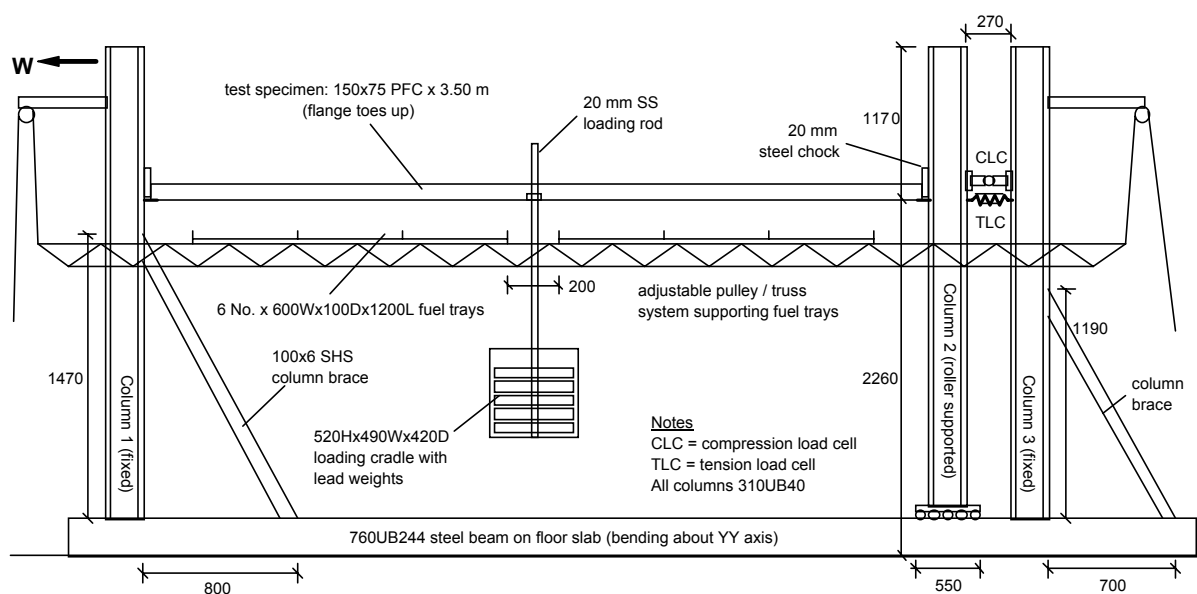


Figure 1 : Elevation of Experimental Setup

2. EXPERIMENTAL SETUP

The test setup consisted of a steel beam with pinned ends and stiff restraint against horizontal movement. A constant vertical load was applied, and the beam was heated from below via trays of burning methylated spirits.

As shown in Figures 1 and 2, the steel beam was supported between three steel columns, labelled Columns 1, 2 and 3. Column 1 at the west (left) end was fixed in position. At the east (right) end the beam was connected to Column 2, which was supported at its base on rollers and was thus free to move horizontally. This column was in turn tied via two load cells to Column 3, which was fixed in position. Column 2 thus provided vertical support for the beam, while Column 3 provided horizontal support.

The horizontal force between Columns 2 and 3 was measured via two load cells, a larger one for compression forces (calibrated to 200 kN) and a smaller one for tension forces (calibrated to 50 kN), as shown in Figure 1. The tension cell was located at the same height (± 5 mm) as the steel connecting plate on the other side of the column, while the compression cell was located approximately 80 mm above this point. The compression cell was arranged so that its parts would freely separate when moved apart and thus would not carry any tensile force. Similarly, the tension cell was connected with sufficient clearance in the connecting bolt holes such that it would only carry tensile forces and not compressive forces. The operation of these cells was verified by loading prior to the fire tests. The stiffness of each of the cells was very high, resulting in almost no measurable horizontal movement of the end of the beam (relative movement was measured between Columns 2 and 3).

The ends of the beam were supported via a steel plate welded to the column and bolted to the bottom surface of the PFC, as shown in the photograph in Figure 3. A steel chock was placed loosely between each end of the test specimen and the adjacent column, in order to directly transfer compressive forces between the beam and the column and avoid compressive buckling of the steel connecting plate. Large compressive forces were expected as the beam expanded thermally during the early part of the test.



Figure 2 : Photograph of Experimental Setup



Figure 3 : Photograph of End Connection

A central point load was applied via lead weights and kept constant throughout the test. The lead weights were supported in a steel cradle hanging from a stainless steel rod of 20 mm diameter which passed through the beam. The applied loads were as shown in Table 1.

The test specimen was a Grade 300 Plus hot-rolled parallel-flange channel section (PFC) of nominal size 150 mm x 75 mm x 17 kg/m, supplied by OneSteel Pty Ltd. It was bent about its weak (YY) axis, oriented with the web at the bottom and the two flange tips up. A single length of PFC was cut to form the two test specimens. Measured dimensions of the section are shown in Figure 4. Table 1 shows the measured yield stresses of the section.

Two tests were conducted. Test 1 was performed in two parts, which will be referred to as Test 1a and Test 1b. In Test 1a, the fuel was used up before significant horizontal force had developed. As it was necessary for the trays to cool before adding more fuel, this test was continued on a later date as Test 1b, using the same specimen as Test 1a. A new test specimen was used for Test 2. The tests were conducted at Victoria University, Melbourne. In Test 1, vertical shielding panels were used on each side of the specimen to partially contain the heat. In Test 2, an additional shielding panel was used above the specimen, in order to further increase the steel beam temperatures. The methylated spirits was ignited and allowed to burn freely until it was completely consumed.

Continuous measurements were recorded of steel temperatures at numerous locations, vertical deflection at midspan and axial force at one end.

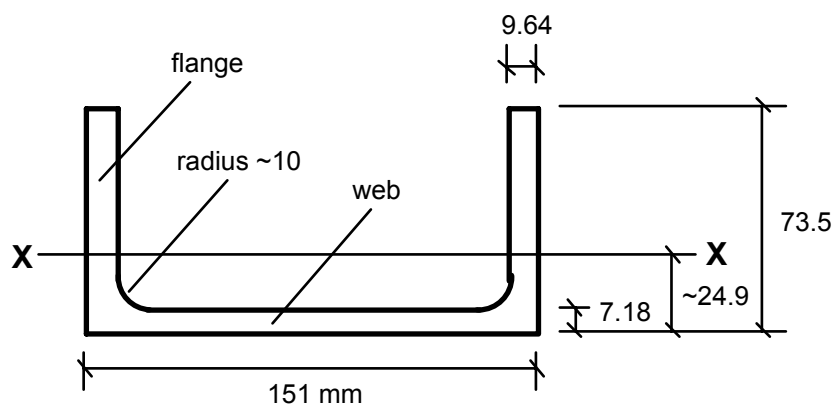


Figure 4 : PFC Cross-Section

Table 1 : Measured Yield Stresses of PFC Section

	flange	web
0.2% proof stress	357	377
upper yield	346	372
lower yield	342	360

Table 2 : Applied Loading

	Test 1 (1a & 1b)	Test 2
beam span	3.54 m	3.54 m
mass of loading rod and cradle (kg)	40 kg	40 kg
mass of lead weights (kg)	560 kg	860 kg
steel beam self-weight, based on measured dimensions (kg/m)	18.8 kg/m	18.8 kg/m
midspan bending moment (kNm)	5.50	8.10

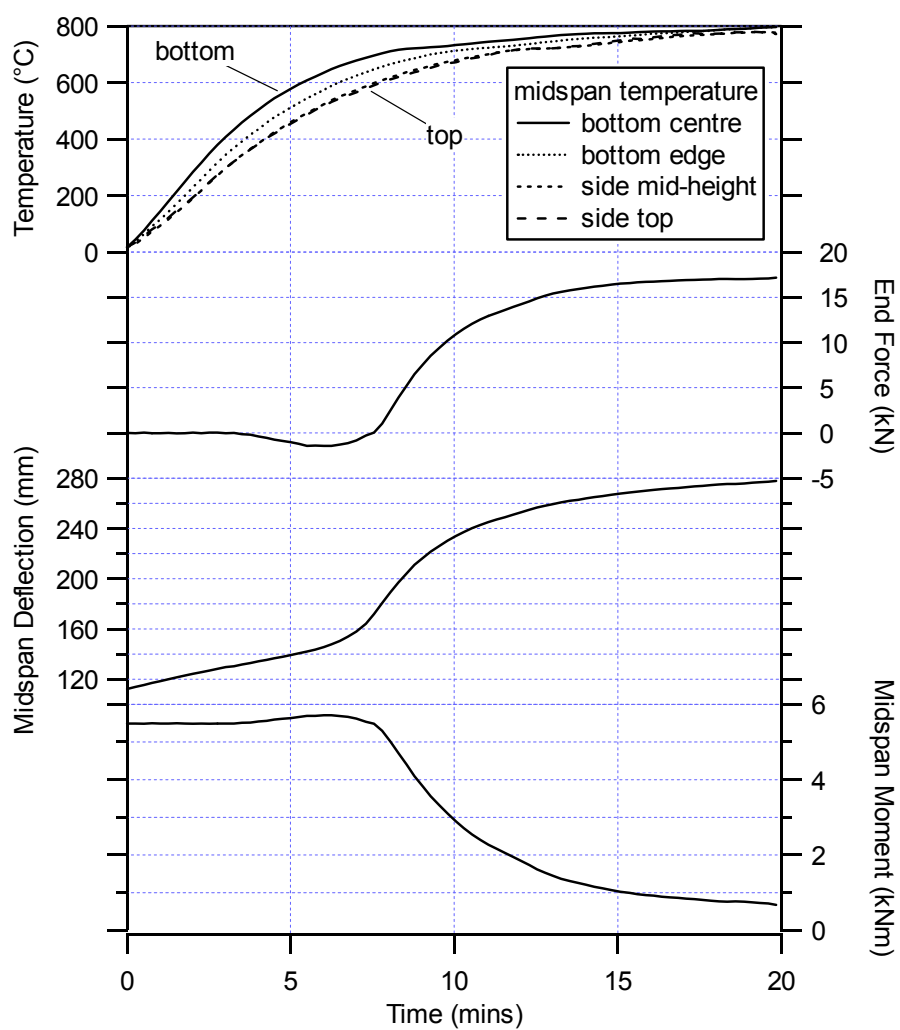


Figure 5 : Results of Test 1b

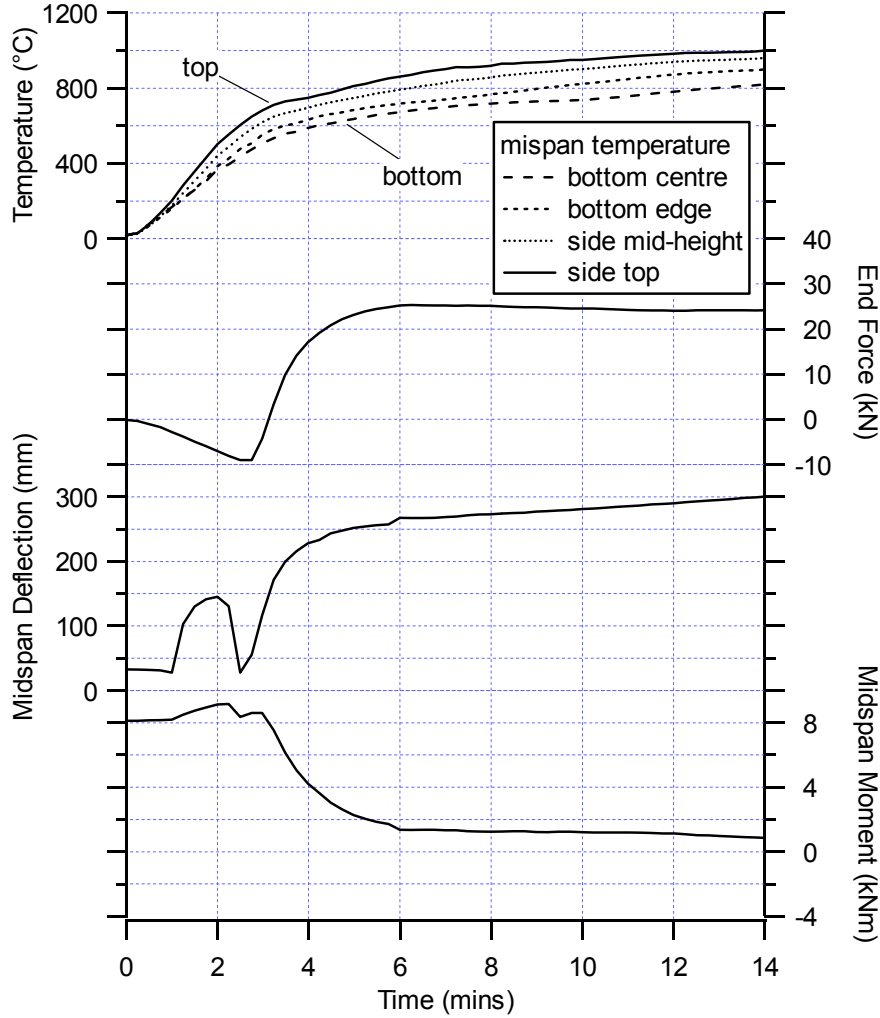


Figure 6 : Results of Test 2

3. EXPERIMENTAL RESULTS

The test results for each of Tests 1b and 2 are summarised in Figures 5 and 6 respectively. These graphs show the temperature profile over the cross-section at midspan, the end force and the midspan deflection. They also show the internal bending moment at midspan (with hogging moment shown as positive), which was calculated as follows:

$$M_i = M_e - F\delta \quad (1)$$

where –

M_i = internal moment about bottom of section (where axial load was applied at ends)

M_e = external moment due to applied loads = $(PL/4) + (w_{self}L^2/8)$

F = end force (with tensile force positive)

δ = midspan deflection (with downward deflection positive)

P = midspan point load; L = length; w_{self} = self-weight uniform loading

In both Tests 1b and 2, the measured rate of deflection of the steel beam increased as the support mechanism was undergoing the transition from bending action to catenary action (when the end force changed from compression to tension) but then reduced to a much lower rate for the remainder of the heating period. It was thus observed that the development of catenary support was a gradual and stable process.

4. MATERIAL MODEL

A comprehensive constitutive model for steel at elevated temperatures has been published by Poh. This material model is based on extensive elevated-temperature coupon testing at BHP Melbourne Research Laboratories, using the same type of steel as used in the catenary test specimens. It includes the following strain components:

$$\begin{aligned}\varepsilon_{tot} &= \varepsilon_{th} + \varepsilon_{\sigma} + \varepsilon_c \\ \varepsilon_f &= \varepsilon_{tot} - \varepsilon_{th} = \varepsilon_{\sigma} + \varepsilon_c\end{aligned}$$

where –

ε_{tot} = total strain

ε_{th} = thermal strain (or thermal expansion), dependent on temperature

ε_{σ} = stress-inducing strain, dependent on temperature and stress (σ)

ε_c = creep strain, dependent on temperature, stress and time

ε_f = free strain

It may be seen that the material model includes an explicit creep term, whereas other models such as those in Eurocode 3 and BS5950.8 include creep strains only implicitly. Thus, under these codes there are only two components of the total strain, being the thermal strain and the stress-inducing strain. The stress-inducing strain implicitly includes a certain amount of creep strain, and the amount corresponds to the strain rate which was used in the original tensile testing which formed the basis of the material models (with a lower strain rate incorporating more creep).

The creep equations of Poh's model are presented in a form which is based on constant temperature and stress being applied at a point in the material for a period of time, as this was the basis of the experimental measurements on which the equations were based. In the current application, both temperature and stress will be continuously changing with time. Poh's report presents various alternative methods of applying the model to this case, and recommends that the "strain-hardening rule" be adopted. This approach is used in the current application.

A conceptual problem arises in this application of the creep equations and the strain-hardening rule. For creep occurring over an interval from time t_1 to time t_2 , the equations depend on the actual values of t_1 and t_2 rather than on the time increment ($t_2 - t_1$). Since the creep equations are highly non-linear, the result will thus be different, for example, if t_1 is 10 mins and t_2 is 11 mins than if t_1 is 60 mins and t_2 is 61 mins. Thus, the definition of time zero will affect the result.

The analysis of a steel member as it undergoes a transition from bending strength to catenary strength necessarily involves stress reversal, or unloading, of some or all fibres of the cross-section. At ambient temperature, it is well known that steel which has been loaded beyond the elastic range does not retrace its original stress-strain path upon unloading. This phenomenon is known as the "Bauschinger effect", as described by Horne^[5].

At elevated temperature, the Bauschinger effect is logically associated only with the stress-inducing strain component. The stress-inducing strain at which the material behaviour becomes non-linear is similar to that at ambient temperature, but the transition from linear to non-linear is less distinct. The Bauschinger effect has been incorporated into the analysis method, with an option to perform the analysis either with or without this effect, in order to investigate its importance. The analysis results reported in the current paper include this effect in all cases.

In order to compare Poh's material model with other more simplified models available, a calculation procedure has been set up for a one-dimensional analysis, representing a test

coupon subjected to any desired strain history. This model has been run for a uniformly increasing total strain and the resulting stress in the steel has been calculated. By plotting this stress versus total strain, values of 0.2% and 2% proof stress have been obtained.

Figure 7 shows the effective yield stress values obtained using this method, along with curves published in Eurocode 3 and AS4100. It may be seen that there is little difference between the 0.2% and 2% proof stress values above a steel temperature of 650°C. The Eurocode curve corresponds closely with the 2% proof stress at 50 millistrain/min up to 750°C, and above 850°C corresponds closely with a strain rate of 2 millistrain/min. The simple linear relationship from AS4100 gives close agreement with the curve for 0.2% proof stress with no creep up to a temperature of 750°C, above which it corresponds to a progressively increasing creep contribution, being below the 2 millistrain/min curve for temperatures above 850°C.

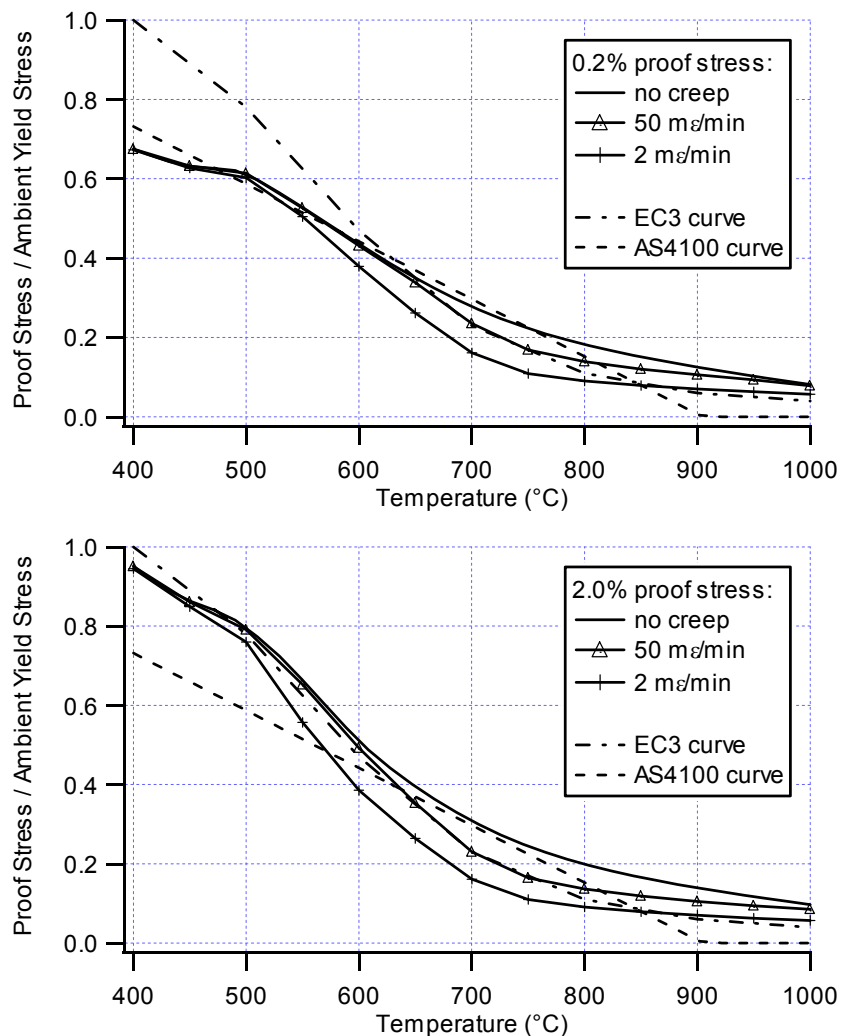


Figure 7 : Effective Yield Stress Versus Temperature

5. ANALYSIS METHOD

The numerical analysis procedure is formulated on the assumption that plane sections remain plane at elevated temperature. Iterative solution techniques are used to calculate a linear distribution of total strain such that equilibrium is achieved at any time and at any cross-section. Both moment equilibrium and axial force equilibrium are required to be

achieved, ie (a) internal moment about bottom of section equal to applied moment about bottom of section; and (b) internal axial force equal to applied end force. The total strain includes explicit determination of thermal strain, stress-inducing strain and creep strain.

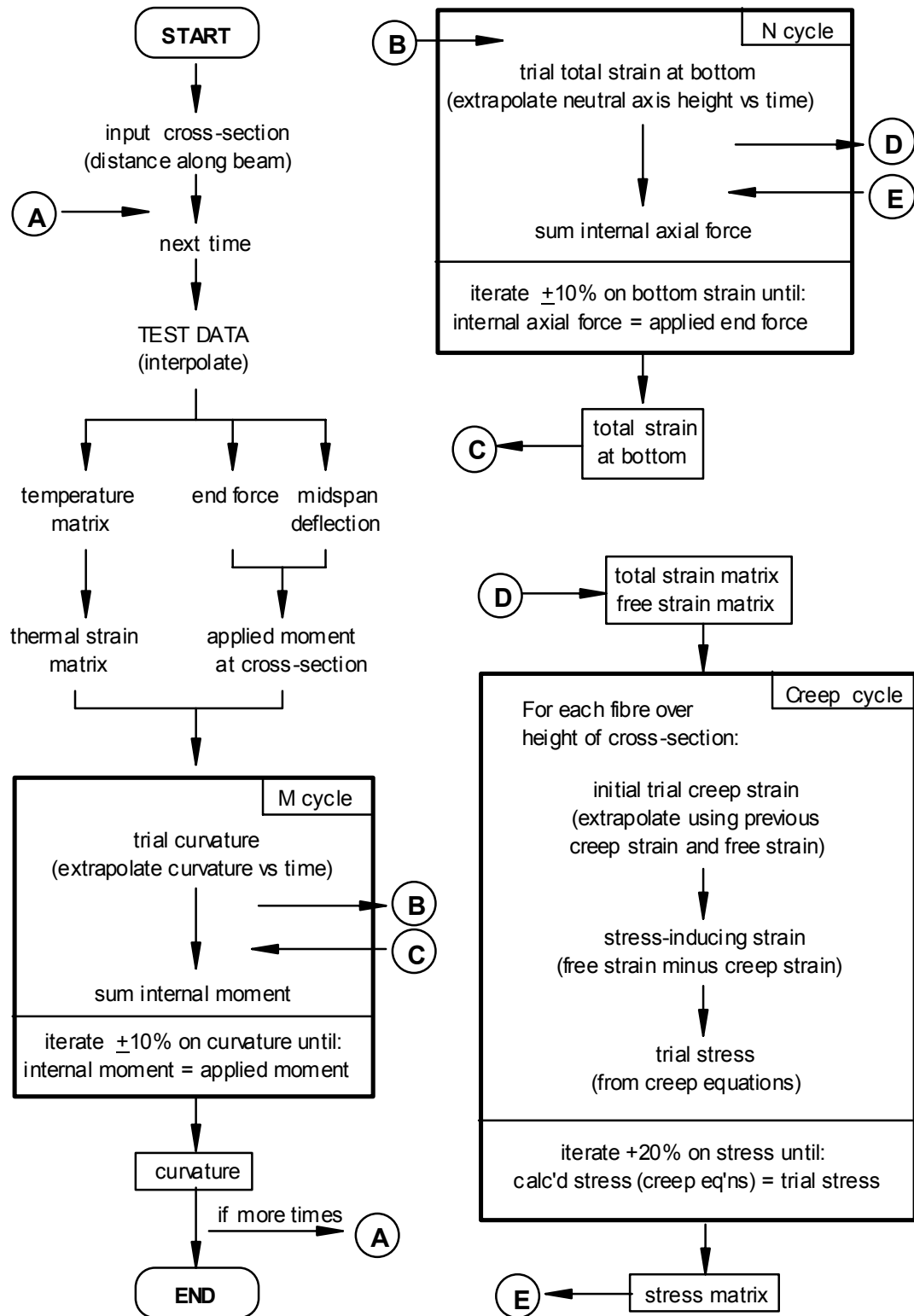


Figure 8 : Flowchart Showing Numerical Analysis Procedure

The calculation procedure is illustrated in detail in Figure 8. It utilises the measured midspan deflection and end force to calculate the internal moment at any cross-section along the length of the beam. Thus, it does not attempt to predict the deflection or the end force. This internal moment is used in an iterative trial-and-error procedure to calculate the curvature at every point along the beam. These curvature values are integrated along the beam to calculate the midspan deflection, which then can be compared back against the measured value of midspan deflection.

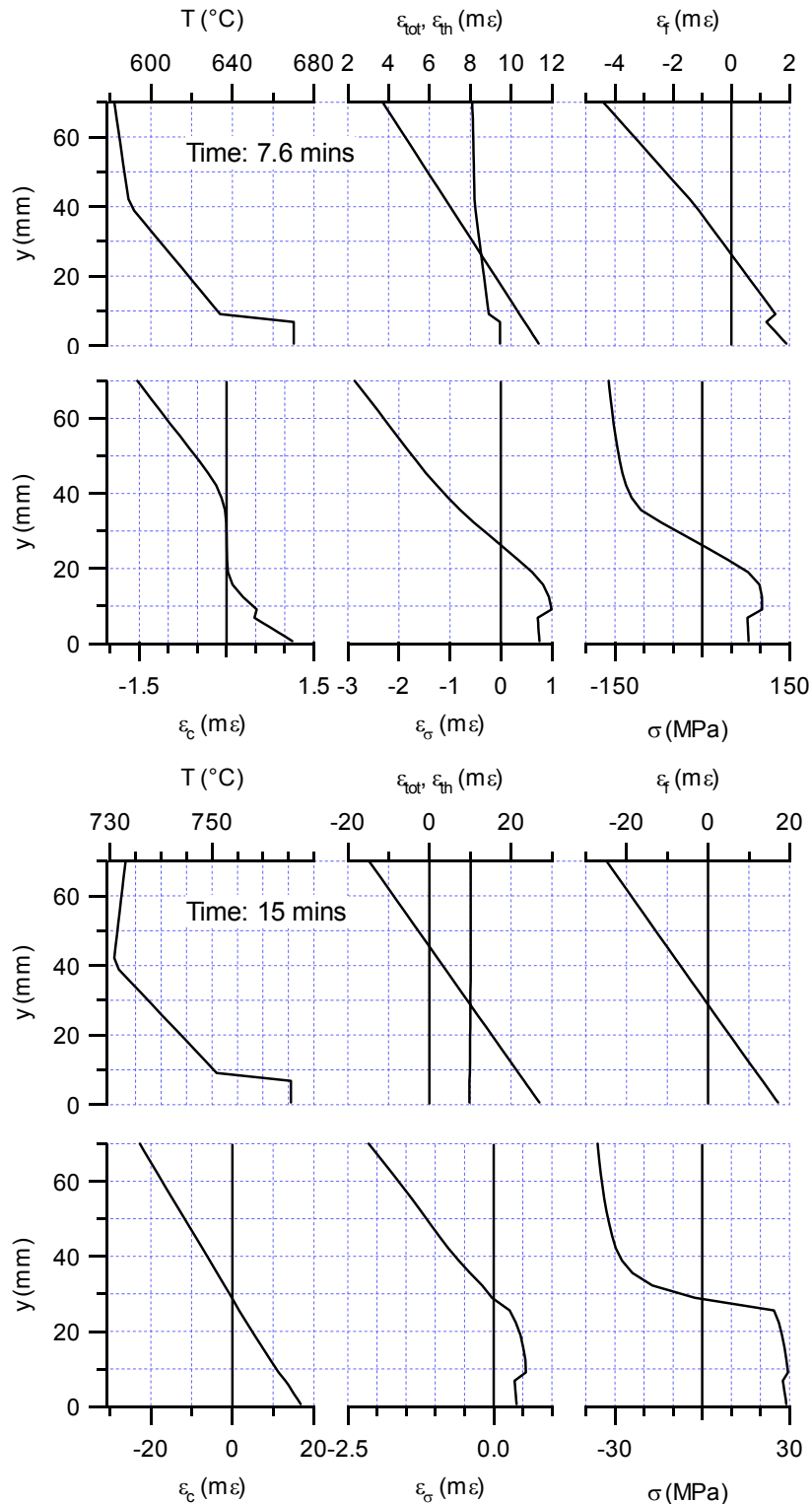


Figure 9 : Results of Numerical Analysis, Cross-Section Parameters, Base Case

The iterative procedure is performed in small time steps from the start of the test and utilises extrapolation of the results from the previous steps to estimate the new starting values. Close control of the bounds of iteration is necessary due to the explicit inclusion of creep strain in the material model, which can easily cause successive estimates to diverge wildly if not carefully controlled.

6. ANALYSIS RESULTS FOR TEST 1b

The current version of the analysis routine is based on a single value of yield stress for the section. Given that the bending moment capacity and to a lesser extent the axial capacity are likely to depend more strongly upon the yield stress of the flanges than that of the web, the measured values for the web were used. As the upper and lower yield were both below the 0.2% proof stress, a yield stress value of 355 MPa, being slightly below the measured 0.2% yield stress of the flange, was used as the base case for the calculations.

The base case incorporated the following inputs: moment and deflection at midspan, 355 MPa yield stress, creep "on", Bauschinger "on"

Figure 9 shows an example of the cross-section temperatures, strains and stresses calculated at both 7.5 mins and 15 mins for the base case. The height (y) shown in these diagrams is measured from the bottom (web) of the PFC.

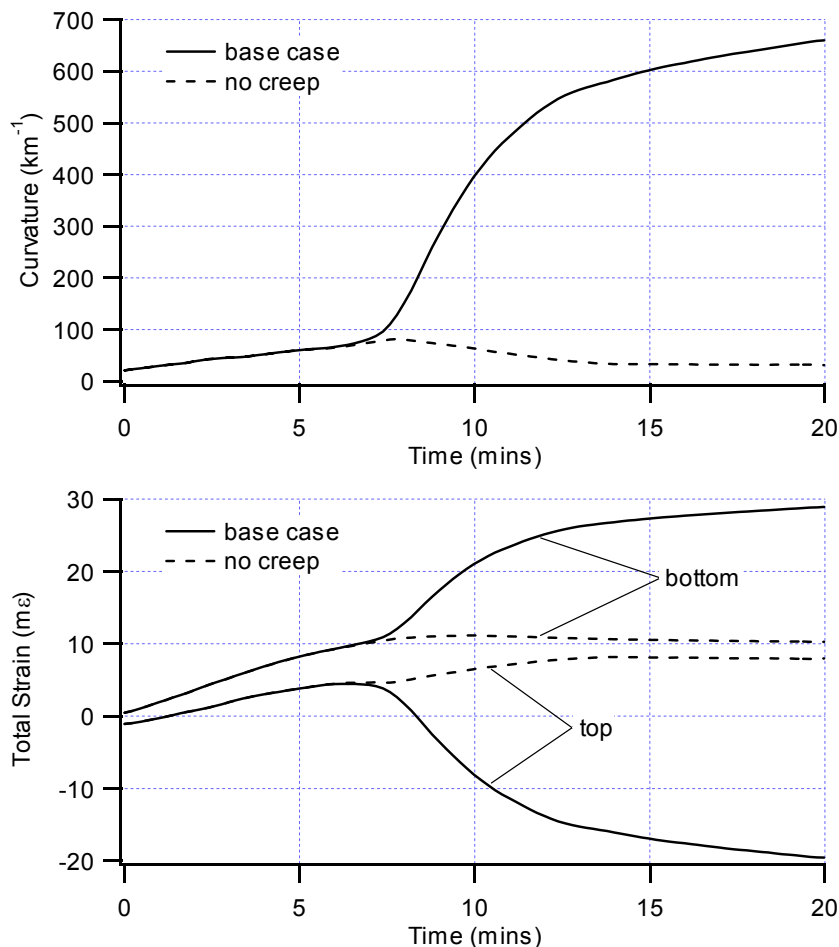


Figure 10 : Numerical Analysis Results for Midspan Cross-Section, Test 1b, Base Case and No Creep Case

Figure 10 shows the curvature, the bottom total strain and the top total strain as a function of time for the base case and for the same case with the creep strain set to zero. It may be seen that the creep component had little effect before 7 mins but had a major effect after this time. The steel temperatures at this time ranged from 560°C (top) to 670°C (bottom) within the cross-section.

An example of the integration along the length of the beam is shown in Figure 11. The curvatures are integrated to calculate slope and deflection along the length for the base case at 7.5 mins. The resultant midspan deflection of 68 mm represents the effect of the external loading and the heating. The initial deflection (out-of-straightness) of the beam without external loading at ambient temperature was 91 mm (with an additional 22 mm due to the midspan point load). For comparison with the measured deflection, this initial deflection of 91 mm must be added to the deflection calculated by integration. The calculated midspan deflections versus time are shown in Figure 12, along with the measured midspan deflections. It may be seen that reasonable agreement was obtained.

The calculations which have been performed check only that the relationship between the bending moments and the calculated curvatures at each cross-section along the length of the beam are reasonable. They do not indicate why the particular combinations of deflection and end force occurred, ie whether they were due to compatibility effects, strength effects or a combination of these. To explore this question, a calculation of midspan strength has been performed. As this calculation does not include an evaluation of strain values, an effective yield stress at any temperature is required. For this purpose, the following curves shown in Figure 7 have been used:

- Eurocode 3 curve
- Poh's material model, 2% proof stress, 2 millistrain/min

In addition, a curve has been calculated using Poh's model with 2% proof stress and 0.3 millistrain/min.

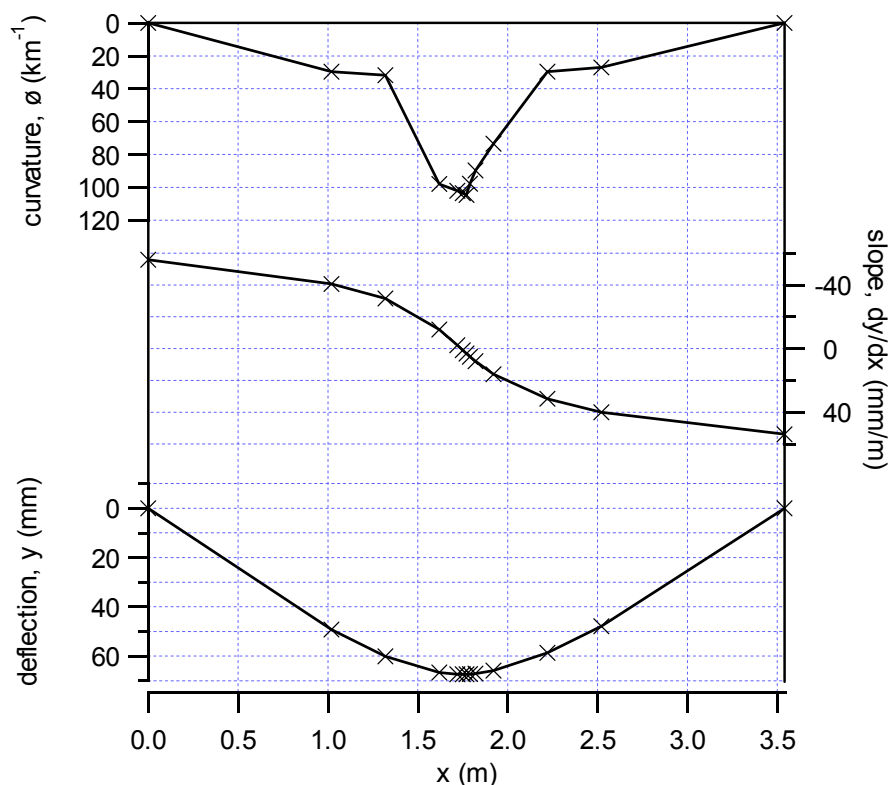


Figure 11 : Results of Integration Along Length, Base Case, 7.5 Mins

The results of this strength calculation are shown in Figure 13. It may be seen that the deflection and end force appear to have been controlled by strength from the start of catenary action (when the end force became tensile) at about 7 mins until the end of the heating period at about 20 mins. During the earlier part of the test and during the cooling period at the end of the test, the midspan strength was greater than the applied moment, and thus the deflection and end force appear to have been controlled by factors other than strength. At these times, it is expected that compatibility effects governed the behaviour, resulting from the thermal expansion or contraction of the steel and the current value of the effective axial stiffness of the deflected beam.

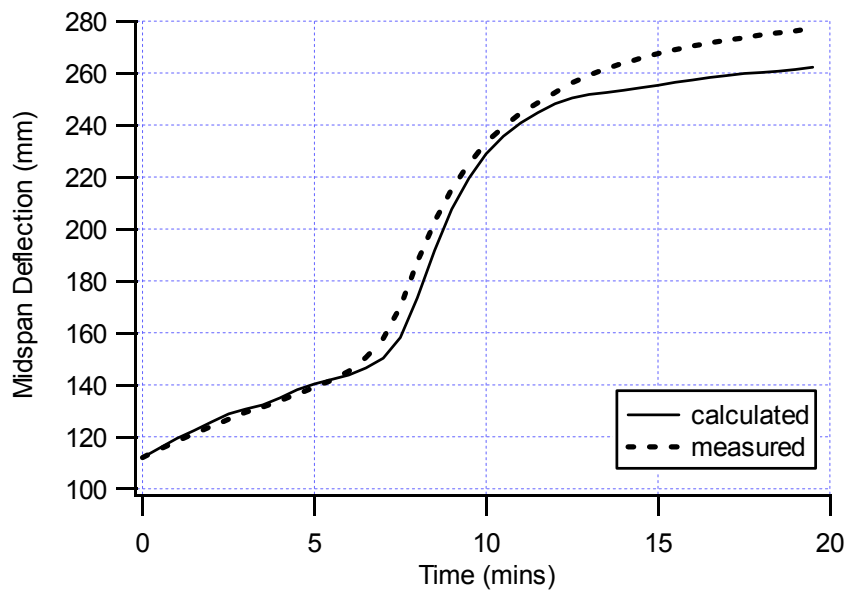


Figure 12 :Comparison of Midspan Deflections

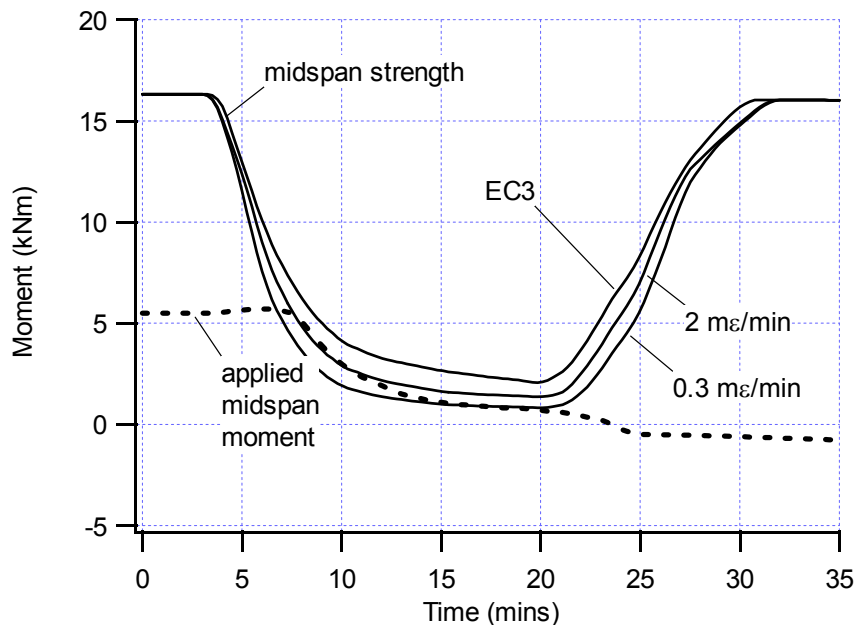


Figure 13 : Results of Strength Calculation

7. ANALYSIS OF TEST 2

The successful result obtained for Test 1 was unfortunately not repeated for Test 2. In this test the measured temperatures were higher at the top of the section than the bottom, which was the opposite of Test 1. In addition, the temperatures attained were much higher than for Test 1.

Given the shape of the cross-section, with little steel at the top of the section, higher temperatures in the top part of the section have a large impact upon the section moment capacity, greatly reducing its effective depth. Thus, as the beam went into catenary action, the iterative calculation procedure began to produce progressively larger curvatures in trying to achieve the applied moment and these eventually became unrealistically large. Hence, the calculation procedure was calculating cross-section moment capacities at midspan which were less than those measured in the test.

Numerous sensitivity studies on the input data were conducted, and none appeared to account for the observed discrepancy. Possible explanations may include:

- The strain hardening rule for creep calculations is not applicable in this case
- The local strain rate in the midspan region may have been extremely high, resulting in greater effective material strength than that captured in the tensile testing which formed the basis of Poh's material model.
- The temperatures attained were above those at which the material model gives a good fit to the tensile test data.
- There was significant inaccuracy in measured values such as the deflection or the end force, possibly due to temperature effects upon the instrumentation.
- Distortion of the steel columns supporting the test specimen, resulting in unexpected forces and moments being applied.

It is possible that Test 2 may be repeated to further investigate this discrepancy.

8. CONCLUSION

The analytical results agreed well with the experimental results for Test 1. For Test 2, the analysis showed that the beam would not be expected to support the applied loads at the measured values of end force and deflection.

The authors acknowledge OneSteel Pty Ltd for supplying funding and materials for these tests, Ove Arup Pty Ltd for providing study leave and flexible working arrangements for Mr Proe, and Victoria University for funding and the use of their facilities. They also thank Mr M Culton for his care and attention to detail in constructing the test rig and performing the tests.

9. REFERENCES

1. Bresler, B and Iding, R, "Response of Steel Buildings to Fire", Univ of California, 1980.
2. Thomas, I R, Bennetts, I D, Dayawansa, P H, Proe, D J and Lewins, R R, "Fire Tests of the 140 William Street Office Building, BHP Research, 1992.
3. Kirby, B et al, "The Behaviour of Steel Framed Multistorey Buildings in Fire, British Steel Corporation, 1999.
4. Poh, K W, "Modelling Elevated Temperature Properties of Structural Steel", BHP Research, 1996.
5. Horne, M R, "Plastic Theory of Structures", Pub. Nelson & Sons, 1971.



A PERFORMANCE-BASED DESIGN APPROACH FOR STEEL PERIMETER COLUMNS SUBJECT TO FIRE

Spencer E. QUIEL¹ and Maria E.M. GARLOCK²

ABSTRACT

This paper outlines a procedure for the performance-based design of fire-exposed perimeter columns in a steel frame. The subassembly considered for this study includes a two-storey length of the perimeter column and the beam framing into the column in the direction perpendicular to the building's exterior. When heated, this beam will expand and induce bending moment and lateral deflection in the column as well as increased axial force in the beam itself. Our proposed approach (1) predicts the steel member temperature time-history, (2) uses a simplified material model that considers non-linearity and temperature effects, and (3) analyzes a simplified structural model (i.e. an analytical model) that represents the perimeter column and beam interaction. This analytical model is used to develop closed-form solutions for beam axial force and column deflection and bending moment. The analytical model solutions are compared to the results of a more complex and detailed multi-story finite element analysis model. A comparison of these results shows that the analytical model results give reasonable and conservative estimations of structural behavior. This procedure is conducive to code-based design and has potential as a tool for predicting the behavior of steel perimeter frame sections in a severe fire.

1. INTRODUCTION

The current state of practice in the US commonly uses a *prescriptive* approach for designing structures to resist fire. Prescriptive codes state how a building is to be constructed to resist exposure to unwanted fire. Although this standard has been used by the building industry for nearly a century, the furnace-test methodology on which it is based is principally a thermal test, not a structural test, and it considers individual member behavior without consideration of

¹ Graduate Student, Princeton University, Dept. of Civil and Env. Engineering, squiel@Princeton.EDU.

² Assistant Professor, Princeton University, Dept. of Civil and Env. Engineering, mgarlock@Princeton.EDU.

how it interacts with the surrounding structure. Recent reports by the National Institute of Standards and Technology (NIST) [1] in the US and the British-based Institution of Structural Engineers [2] have called for the development of *performance-based* standards and code provisions as an alternative to current prescriptive methods. Performance-based provisions state how the structure is to perform when subjected to a wide range of fire conditions and scenarios. Specifically, both of these reports have recommended the development of a structural design methodology based on the performance of the structural frame as a whole rather than the individual components. This research addresses the recommendations of these reports specifically for the behavior of steel perimeter columns exposed to fire.

The perimeter column in a building is typically laterally braced by one beam per floor in the plane perpendicular to the exterior wall. The fire-induced structural response of this beam that frames into the perimeter column directly affects the perimeter column's behavior and the structural integrity of the frame as a whole. Previous research by the authors examined the fire response of a tall steel moment-resisting frame composed of wide-flange sections [3]. The analysis results indicated that the thermal expansion of the beams that frame into the perimeter column induce column lateral deformations and moments that can reach the plastic moment capacity of the perimeter columns. Since these beams are partially restrained from expanding by the column they develop large axial forces, potentially leading to beam failure. Once these beams, which brace the perimeter column in one plane, fail, the stability of the column, and the structure as a whole, may be compromised.

Research in recent years by professionals and academics worldwide has contributed to the development of performance-based structural-fire design standards with a variety of methods and approaches. Research such as that by Lane [4] and Gewain et. al [5] has emphasized the implementation of realistic fire temperature-time histories that use compartment fire models and consider fuel loads. These temperature curves can then be applied to the appropriate structural sections to determine thermal and mechanical response. Usmani et. al [6] have developed analytical expressions, confirmed with the results of computational finite-element modeling, which can be used to solve for the moment and midspan deflection in heated horizontal beams. Wang et. al [7] described the use of structural subframe models to effectively capture the behavior of a full fire-exposed building frame.

In the US, the use of performance-based design tools over prescriptive methods has been the exception rather than the rule even though engineering communities in other countries, most notably in Europe, have shown a greater willingness to adapt and implement performance-based standards [5]. Recently, guidelines for the performance-based structural-fire design of steel frames have been included in the 2005 edition of AISC's Steel Construction Manual [8]. These provisions include the following critical design steps: development of a design-basis fire that considers compartment size, fuel load, ventilation, and the existence of active fire protection systems such as sprinklers; prediction of the steel member temperatures via the lumped heat capacity method or, where needed, computational heat transfer analyses; and calculation of structural performance via "advanced" analysis methods or, where appropriate, via "simple" analysis methods [8]. Similar to the Eurocodes, the AISC manual references the changing material properties (most notably the modulus of elasticity and yield strength) of steel and concrete at elevated temperatures.

The AISC manual stipulates that an analysis of a structure's mechanical response must account for the deterioration of steel's strength and stiffness properties as its members' temperatures increase as well as the effects of thermal expansions and large deflection. Advanced methods must be used to capture the response of the structural frame to fire,

particularly the interaction between connected structural members [8]. Simple methods are permitted only when the assumption of uniform temperature is reasonable while support and restraint conditions remain unchanged [8]. The analytical solution presented in this paper can be classified as a “simple” method that accounts for the frame interaction of the perimeter column and the beam framing into the column perpendicular to the exterior wall. It can also serve as a verification of more complex models and their solutions.

This paper presents an analytical solution that predicts the behavior of steel perimeter columns in a fire considering its interaction with the beam that frames into it. Such a methodology has not been presented in the past and it is important for reasons described above. Three quantities are obtained from the analytical solution: (a) the column lateral deflection, (b) the bending moment induced in the perimeter column by the expanding beam, and (c) the axial force in the beam itself as it expands against the restraint provided by the column. The solution for these three variables is based on equilibrium and compatibility between the lateral deflection of the column (due to the beam’s thermal expansion) and the net axial deformation of the beam, which considers thermal expansion and axial shortening due to compression. This approach considers the interaction between the beam and column, which is essential for developing an accurate solution. The calculations can be performed using a spreadsheet because no iteration is necessary and the solution is closed-form. The analytical solution is sufficiently simple and accurate for use in performance-based design procedures.

2. PERFORMANCE-BASED METHODOLOGY

The performance-based design methodology outlined in this paper focuses on the following steps that are to be implemented after a temperature time-history of the fire has been defined: (1) prediction of the steel member temperature time-history, (2) simplification of a material model that considers non-linearity and temperature effects, and (3) analysis of a simplified structural model that represents the perimeter column and beam interaction.

2.1 Steel Member Temperature-Time History

The temperature of structural steel members may be calculated with a thermal finite element (FE) analysis or with the lumped mass method (also called the lumped heat capacity analysis). The latter method assumes that the temperature is uniform through the section’s depth. Buchanan [9] illustrates a step-by-step lumped mass solution that is implemented in a spreadsheet to calculate the change in steel temperature for members unprotected or protected by fireproofing material as the fire evolves.

In this paper we compare the lumped mass solution to a finite element solution for a beam that is heated on three sides and therefore develops a thermal gradient. The beam used for this comparison was taken from a building that experienced a severe conflagration in the last decade [3]. The beam section dimensions are shown in Fig. 1, and it has an unprotected and protected section factor of 57.6 m^{-1} and 61.4 m^{-1} ,

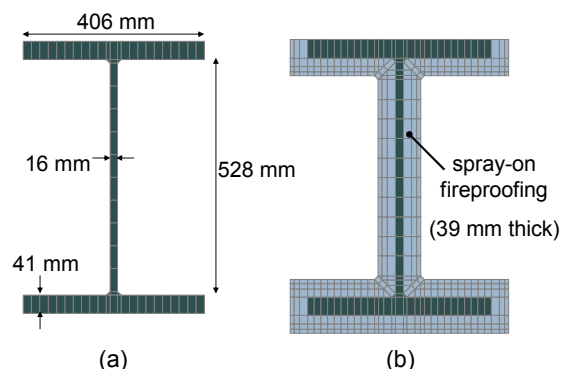


Fig. 1 - Cross-section of the beam used in this study, shown (a) unprotected and (b) protected by fireproofing (shown with finite-element discretization).

respectively, for three sides exposed the fire curve shown in Fig. 2. The post-flashover temperature time-history used for this study is taken from a previous tall building study by the authors [3]. The top face of the top flange carries the slab and is thus assumed to act as an adiabatic surface. The spray-on fireproofing is assumed to have a constant thickness of 39 mm and constant density of 240 kg/m^3 . In the lumped mass analysis, the thermal conductivity and specific heat for the fireproofing, which in reality are temperature dependent, are assumed constant (with median values of 0.12 W/m-K and 1200 J/kg-K , respectively). This was assumed to simplify the analysis and avoid iteration. In the finite element analysis, these properties are temperature dependent. The thermal FE analyses were performed using SAFIR, a software developed at the University of Liege and specifically designed for structures exposed to fire [10]. The finite-element discretization used for the unprotected and protected beam sections is shown in Fig. 1.

A comparison between the lumped mass thermal analysis results and the FE results is shown in Fig. 2. The shaded regions are “temperature envelopes,” showing the range between the maximum and minimum temperature in the beam’s cross section based on the FE results. The average beam temperature obtained from the FE analysis is also shown in Fig. 2. Examining the protected beam case, good correlation is seen between the lumped mass and thermal FE analyses.

Because the temperature envelope between the maximum and minimum temperature is narrow for the protected beam, the lumped mass solution (which assumes a uniform temperature through the section) is an accurate approximation of the section’s average temperature. Examining the unprotected beam case, the lumped mass temperature is slightly more conservative (i.e. about 40°C to 90°C greater) than the FE average temperature between 0.25 and 1 hour. During this time, the section’s maximum and minimum temperature differ by as much as 300°C , due to the fact that only three sides of the beam are exposed to a

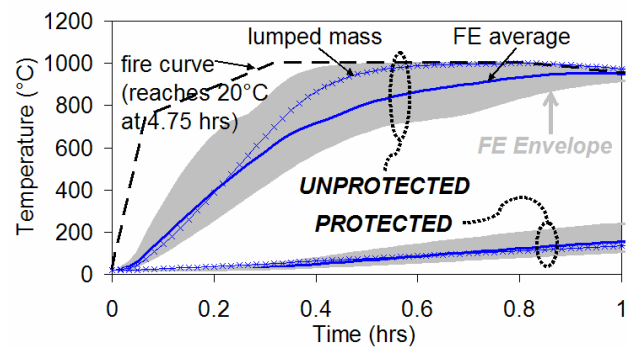


Fig. 2 - Comparison of lumped mass and thermal-FE solutions for the unprotected and protected beam (shown in Fig. 1).

rapidly increasing fire temperature. The bottom flange and web heat much quicker than the top flange, and thus non-uniform temperatures develop through the section. As noted by Buchanan [9], the presence of non-uniform temperatures can decrease the accuracy of a lumped mass solution and may bias the analytical solution toward the maximum temperatures present in the cross-section. This phenomenon is seen in Fig. 2 in the period from 0.5 to 1 hour. Therefore, the lumped mass method may be considered a conservative approach in this case.

2.2 Simplified Material Model

The structural steel material model chosen for this study is based on Eurocode [11]. Eurocode provides reduction factors for steel strength and stiffness that are a function of temperature. The yield stress (σ_y), equal to the yield stress at ambient temperature ($\sigma_{y,20}$), is multiplied by $k_{y,\theta}$, a yield stress reduction factor that becomes less than 1.0 when temperatures exceed 400°C . Similarly, the Eurocode provides a reduction factor, $k_{E,\theta}$, for the modulus of elasticity (E) which becomes less than 1.0 when temperatures exceed 100°C . The stress-strain

relationship, which is elastic perfectly plastic at room temperature, is transformed into a non-linear relationship at elevated temperatures (i.e. the proportional limit stress, σ_p , no longer equals the yield stress). This nonlinearity begins when temperatures exceed 100°C as represented by $k_{p,\theta}$, which equals the proportional limit stress divided by the yield stress at ambient temperature.

Fig. 3 represents a schematic comparison of the non-linear Eurocode stress-strain model to that of a simplified model developed for this analytical procedure. The Eurocode model requires an iterative procedure to calculate the position on the stress-strain curve if $\sigma_p < \sigma < \sigma_y$. In order to derive a closed-form analytical solution that does not require iteration, the stress-strain relationship is approximated as a tri-linear function with a constant tangent modulus (E_t) in the stress region between σ_p and σ_y (shown as the “simplified model” in Fig. 3). The strain at yield is chosen to be 0.02 as recommended by Eurocode [11]. The tangent modulus at any given time step i ($E_{t,i}$) for the simplified model may be explicitly calculated at a given temperature:

$$E_{t,i} = \frac{\sigma_{y,i} - \sigma_{p,i}}{0.02 - \sigma_{p,i}/E_i} \quad (1)$$

where subscript i in Eqn. (1) denotes σ_y , σ_p , or E at time step i . Once the member is loaded beyond its proportional limit into the tangent region at a given temperature during time step i , T_i , plastic strain develops in the steel material. The plastic strain during this step, $\varepsilon_{pl,i}$, is equal to

$$\varepsilon_{pl,i} = \left(\frac{1}{E_{t,i}} - \frac{1}{E_i} \right) (\sigma_i - \sigma_{p,i}) \quad (2)$$

where stress σ_i represents the stress at time step i .

Fig. 4 traces the evolution of stress and strain from time step $i-1$ to time step i . Assume that at time $i-1$ the member is loaded to point **A**. Based on Franssen [12], the material model assumes that the material unloads from point **A** to zero stress via modulus of elasticity E_{i-1} and reloads with stiffness E_i to the new stress-strain curve for increased temperature T_i at point **B**. The plastic strain, rather than the maximum stress level, describes the complete stress-strain history as the steel temperature changes. The stress at point **B**, on the loading path to σ_i , considers the new proportional stress limit for the material model at temperature T_i due to the development of plastic strain and is referred to as the effective proportional stress at time i ($\sigma_{peff,i}$):

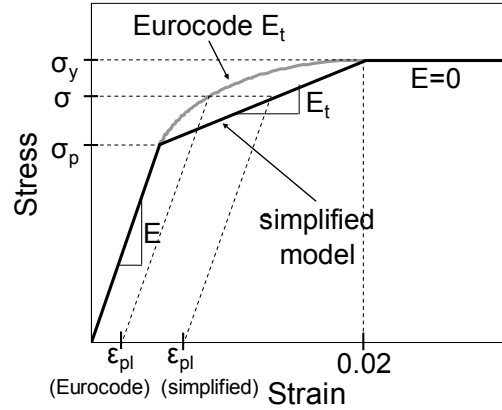


Fig. 3 - Material models for structural steel: Eurocode compared to a simplified tri-linear model.

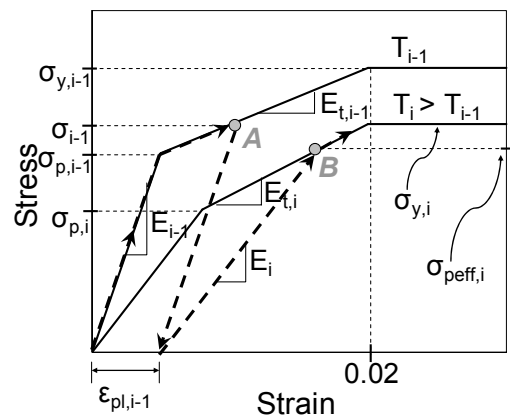


Fig. 4 - Material models for increasing temperature, showing plastic strain.

$$\sigma_{peff,i} = \sigma_{p,i} + \frac{\varepsilon_{pl,i-1} E_i E_{t,i}}{E_i - E_{t,i}} \quad (3)$$

2.3 Analytical Model

The structural models that are used to predict perimeter column response are shown in Fig. 5. The MRF of the fire-affected floors of the prototype high-rise [3] is shown in Fig. 5(a). The two stories of the perimeter column under investigation plus the beam that frames into it perpendicular to the building's exterior wall are identified in Fig. 5(a). All boundary conditions in this two-story frame sub-section, identified as the sub-assembly model in Fig. 5(b), are assumed to be fixed, providing a high level of restraint to the beam's thermal expansion and thus conservatively estimating the reactions in the beam and column. This sub-assembly can be simplified as the analytical model, shown in Fig. 5(c), in which the spring represents the flexural stiffness and strength of the perimeter column. Our objective is to use this analytical model to predict (a) the column lateral deflection (Δ), (b) the bending moment (M) induced in the perimeter column by the expanding beam, and (c) the axial force (P) in the beam itself as it expands against the restraint provided by the column.

The solutions for Δ , P and M are based on several assumptions that are explained and justified as follows:

1. The concrete floor slab is not included in the analytical model. Thermal analysis of the steel beam, however, did consider the presence of a concrete slab by assuming that the top flange acts as an adiabatic surface (i.e. it is assumed that the concrete slab prevents heat transfer to the beam that supports it). A previous study by Garlock and Quiel [3] validates this assumption through an analysis of a steel high-rise building frame.
2. The steel temperature in the beam is assumed to be uniform. Computational analysis of two subassembly frame models, one with uniform temperature in all members and the other with a vertical thermal gradient in the beam, produces nearly identical results for P and M . Beam

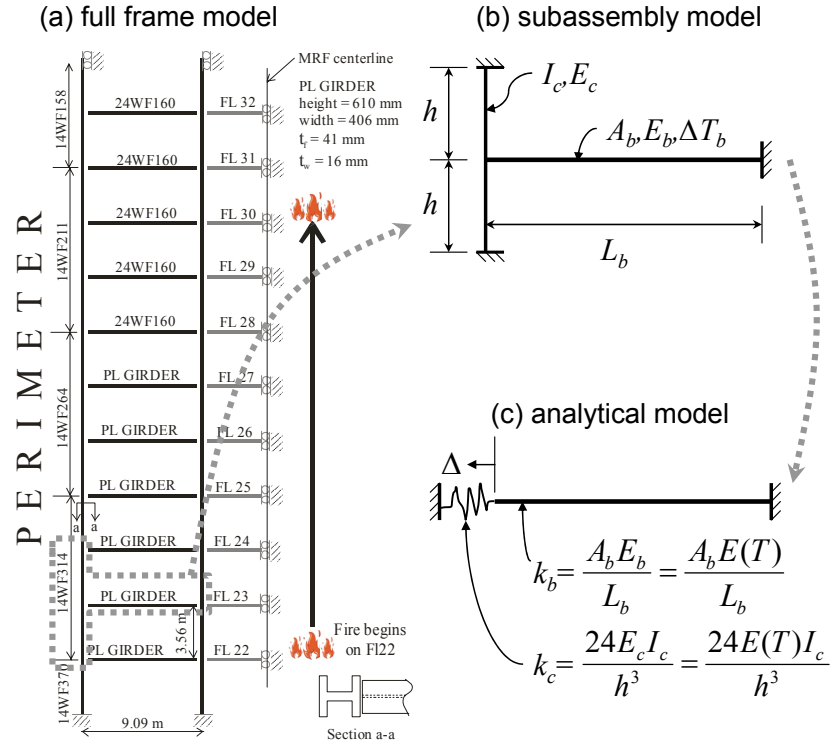


Fig. 5 - Structural models used for analysis.

curvature resulting from the thermal gradient in the beam decreases the beam's total horizontal elongation, and thus the assumption of uniform temperature in the beam is conservative for predicting maximum Δ .

3. Gravity loads are not included in the analytical model. Computational analysis of two subassembly frame models, one with and the other without applied gravity loads (including axial load on the column and distributed load on the beam), has produced results for P , M , and Δ that show close agreement.
4. The perimeter column segments above and below the beam are assumed to have the same temperature and the same length.
5. The temperatures in the perimeter column are assumed to be uniform through the section depth and along its length. For temperatures that are less than that causing a reduction in E and σ_y , this assumption has no meaning since the stiffness and strength are not affected. This will be the case in most situations where the perimeter columns are adequately protected. If a temperature gradient develops through the section depth such that the temperatures reduce σ_y , additional perimeter column moments develop [13], which are not considered in the solution.
6. The second order effects are not considered when determining M . For most cases in design, the column temperatures will not get very high and thermal bowing (and therefore the second-order M) should be negligible.

Full rotational restraint is assumed between the beam and the column in the computational subassembly models, although released rotational restraint will lead to the same solution due to assumptions 2, 3, 4, and 5. The solutions for Δ , P , and M do not consider buckling, which should be considered separately for determining the perimeter column strength. Lateral-torsional buckling is assumed not to be a concern for the beam because it is braced by the concrete floor slab and filler beams that frame into it.

Fig. 6 represents the axial force-deformation (P - Δ) relationship of the beam, which assumes uniform temperature through the section depth and the simplified material model shown in Fig. 3. It is seen that the axial force in the beam, P , is limited by yield force, P_y , equal to

$$P_y = \sigma_y A_b = k_{y,\theta} \sigma_{y,20} A_b \quad (4)$$

where A_b equals the cross-sectional area of the beam. Similarly, the proportional limit force, P_p , is equal to

$$P_p = \sigma_p A_b = k_{p,\theta} \sigma_{p,20} A_b \quad (5)$$

The initial stiffness of the beam, k_b , equals $A_b E(T)/L_b$, and the tangent beam stiffness, $k_{b,t}$, equals $A_b E_t(T)/L_b$. $E(T)$ and $E_t(T)$ are functions of temperature, as described previously.

The analytical solution for Δ , P , and M is based on compatibility between the lateral deflection of the column (due to the beam's thermal expansion) and the net axial deformation of the beam. More specifically, the deflection of the perimeter column (as represented by the spring deformation) must be equal to the combined effects of thermal expansion, axial shortening due to compression, and the development of plastic strain (ϵ_{pl}) in the floor beam. Equations (6a) and (6b) describe this relationship for time step i :

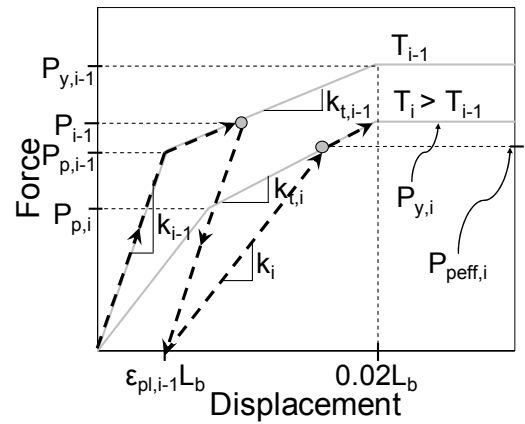


Fig. 6 - Axial force-deformation behavior of the beam.

$$\text{For } P_i < P_{p,i}: \quad \frac{P_i}{k_{c,i}} = \alpha \Delta T_{b,i} L_b - \frac{P_i}{k_{b,i}} - \varepsilon_{pl,i-1} L_b \quad (6a)$$

$$\text{For } P_{p,i} < P_i < P_{y,i}: \quad \frac{P_i}{k_{c,i}} = \alpha \Delta T_{b,i} L_b - \left(\frac{P_{p,i}}{k_{b,i}} + \frac{(P_i - P_{p,i})}{k_{b,t,i}} \right) - \varepsilon_{pl,i-1} L_b \quad (6b)$$

The subscript i in these expressions represents such values at time step i (e.g. $P_{y,i} = P_y$ at time step i). In these expressions, the coefficient of thermal expansion (α) and the original length of the beam (L_b) are assumed not to change with temperature. The spring stiffness, k_c , equals the flexural stiffness of the column (see Fig. 5(c)). Solving for P using Equations (6a) and (6b), the following expressions are obtained:

$$\text{For } P_i < P_{p,i}: \quad P_i = \frac{(\alpha \Delta T_{b,i} - \varepsilon_{pl,i-1}) L_b}{\left(\frac{1}{k_{b,i}} + \frac{1}{k_{c,i}} \right)} \leq P_{\max,i} \quad (7a)$$

$$\text{For } P_{p,i} < P_i < P_{y,i}: \quad P_i = \frac{\left[\alpha \Delta T_{b,i} - \varepsilon_{pl,i-1} - \left(\frac{P_{p,i}}{A_b} \right) \left(\frac{1}{E_{b,i}} - \frac{1}{E_{t,i}} \right) \right] L_b}{\left(\frac{1}{k_{b,t,i}} + \frac{1}{k_{c,i}} \right)} \leq P_{\max,i} \quad (7b)$$

The axial force in the beam cannot exceed $P_{\max,i}$, which equals the lesser of two possible values. The first is the yield force of the beam (P_y), described by Eqn. (4) and the second is the force that develops a local mechanism (P_m). Based on assumptions 4 and 5 described previously, the sub-assembly model will develop plastic hinges simultaneously in the beam-column interface and at the fixed column ends. Through equilibrium, one can calculate $P_{m,i}$ as

$$P_{m,i} = \frac{4M_{p,i}}{h} = \frac{4(k_{y,\theta} \sigma_{y,i} Z_c)}{h} \quad (8)$$

where Z_c is the column's plastic modulus and assuming that the temperature in the section is uniform.

By solving for P at each time step i , column moment (M_i) may be obtained by considering P_i as a point load applied at the midspan of a fixed end beam:

$$M_i = \frac{P_i h}{4} \quad (9)$$

The column deformation, Δ , is equal to the left side of Eqn. (6) with the results of Eqn. (7) substituted for P_i . Fig. 3 shows that for a given stress, σ , in the range $\sigma_p < \sigma < \sigma_y$, the plastic strain, ε_{pl} , estimated by the simplified model is significantly greater than the plastic strain estimated using the Eurocode model. Examining Eqn. (6) it is seen that Δ (represented by the left side of the equation) will be smaller if ε_{pl} is larger, especially when the ε_{pl} term becomes large relative to the other terms in the equation. To develop a more accurate solution, our studies have shown that the Eurocode material model should be used to calculate Δ during the first few time steps after σ enters the range $\sigma_p < \sigma < \sigma_y$. This adjustment will yield a smaller, more accurate estimate for ε_{pl} at a point where the strain variation between the simplified material model and the Eurocode material model is greatest. As the beam stress climbs towards σ_y , the variation between the two models diminishes, allowing for more accurate use of the simplified, tri-linear regime to calculate strain with no strain adjustments. The results from the next section will show that while Δ is sensitive

to ε_{pl} , P and M are not and therefore the simplified material model is sufficiently accurate for the calculation of these values.

3. ANALYTICAL MODEL VALIDATION

The prototype building chosen for validation of the analytical model is the One Meridian Plaza (1MP) Building of Philadelphia, PA. The discretized FE frame model and the fire model (Fig. 2) represent a reasonable approximation of the 1MP structure and the fire experienced by the structure in 1991. This model is a part of a previous study done by the authors [3]. 1MP's construction was composed of wide-flange structural steel members with a slab over a metal deck. All structural steel members (beams and columns) and metal decks were protected with spray-on fireproofing material (approximately 39 mm thick). The columns were also protected by 19-mm thick plaster boards. The structural system consisted of moment resisting frames (MRFs).

The analytical model was validated by comparison to the 2-D FE solution of the *full frame model* of 1MP that is shown in Fig. 5(a). The model includes the portion of the 1MP building affected by the fire: the twenty-first floor up to the thirty-third floor. The blown-up section in the lower right-hand corner of Fig. 5(a) indicates that the columns bend about the strong axis in the plane of the model. For the model validation study, it is assumed that the columns are fireproofed and the beams are not fireproofed. Such an assumption was made to magnify the perimeter column response to the beam's thermal behavior. Furthermore, since the columns are fireproofed, assumption 5 is valid (even though fire was applied on three sides of the column) since the maximum column temperature does not exceed 180°C [3] and therefore there is essentially no stiffness and strength reductions. The axial force in the full frame is measured in the Floor 23 beam at its interface with the perimeter column, and column moment is measured just below its interface with Floor 23. The beams and columns are heated on three sides since the top beam flange and the exterior-facing column flange are assumed to act as adiabatic surfaces. The beams and columns therefore will develop a temperature gradient through their depth. Full dead load and 25% live load were applied to the structure.

The analytical model solution was also compared to a FE *subassembly model* (Fig. 5(b)) that represented the beam on Floor 23 and the perimeter column above and below this beam (see Fig. 5(a)). The subassembly model results provide a direct validation of the analytical structural model solution. To this end, both columns are assumed to remain cold (a reasonable assumption since the full frame model analysis shows that the columns retain all of their strength and over 95% of their stiffness) and the beam temperature is assumed to be uniform through the depth. The beam temperatures are equal to the average temperature of the Floor 23 beam in the full frame model, which, as mentioned previously, has a temperature gradient and was obtained via thermal FE analysis.

The *analytical model* is shown in Fig. 5(c). It has the same assumptions as the subassembly model and it uses the simplified material model shown in Fig. 3. Two temperature time-histories are considered: one uses the results of lumped mass analysis (Analytical-LM), and the second uses the average temperature obtained from thermal FE analysis of the Floor 23 beam section from the full frame 1MP analysis (Analytical-FE). Both curves are shown in Fig. 2. Calculations for Δ , axial force in the beam, and column moment were performed at each beam temperature using an algorithm written in Matlab, a widely available mathematical analysis software. Because no iteration is necessary and the solution is explicit, these solutions could also have been obtained via spreadsheet.

Figs. 7(a), (b), and (c) show the P , M , and Δ results, respectively, for the four models described above. Examination of Fig. 7 not only serves to evaluate the analytical structural model and its limitations, but it also serves to develop an understanding of perimeter column behavior, which in this case is as follows: The heated beam expands quickly, pushing outward on the perimeter column until a local mechanism is created in the perimeter column with the formation of plastic hinges (at about 0.10 hours). At this point, both the axial force in the beam and the column moment, which is a function of the former, reach a plateau corresponding to the P_m value prescribed by Eqn. 8. Once the beam's material enters the tangent region and the temperature continues to increase, plastic strain begins to accumulate. Eventually, plastic strain and axial shortening in the beam together become larger than its thermal expansion, and all three quantities begin to decrease (i.e., the negative terms on the right side of Eqn. 6 become larger than the positive terms). This phenomenon is seen in Fig. 7 at about 0.28 hours. Note that Fig. 2 shows that at this time, the fire temperature is at its plateau and does not contribute to the decrease in the beam and column response.

Fig. 7 shows good correlation between the subassembly model results and the Analytical-FE results for P (Fig. 7(a)) and M (Fig. 7(b)), thereby validating the expressions for P (Eqn. (7)) and M (Eqn. (9)) and validating the use of the simplified material model for this application. As mentioned previously, when calculating Δ , the simplified material model underestimates Δ once the maximum is reached due to an overestimation of ε_{pl} . The Analytical-FE solution with *no adjustment* of Δ in response to this overestimation is shown in

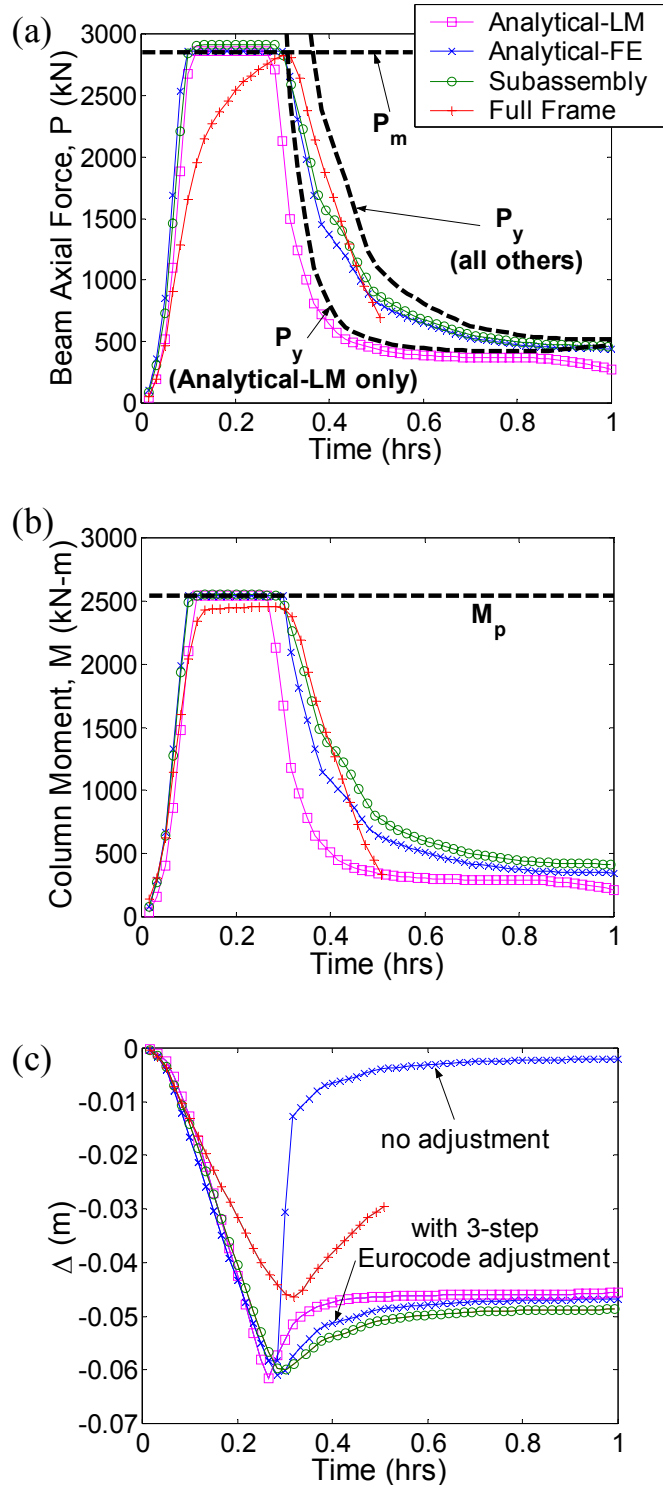


Fig. 7 - Comparison of (a) axial force in the beam and (b) bending moment and (c) lateral deflection (Δ) in the column for various structural models.

Fig. 7(c). When the *Eurocode adjustment* to Δ is applied during the first three steps after σ enters the range $\sigma_p < \sigma < \sigma_y$, the predicted values of Δ closely agree with those produced by the computational subassembly analysis, as shown by the curve in Fig. 7(c) marked Analytical-FE with a 3-step Eurocode adjustment.

The true perimeter column behavior is best represented by the full frame model since it does not have the simplifying assumptions that are inherent in the analytical model (i.e., the full frame model includes temperature gradients in the beam and column, different temperatures in the columns above and below the beam, true column boundary conditions, gravity loads, and second-order effects). By comparing the results of the full frame analysis to the Analytical-FE analysis in Fig. 7, one can see the effects of the simplifying assumptions in the analytical structural model. Examining Fig. 7(a), it is seen that the axial force in the full frame model increases at a slower rate and than in the analytical model. This is due to the formation of each of the plastic hinges developing at different times, as opposed to simultaneously as assumed in the analytical model's mechanism. Column stiffness, k_c , is overestimated in the subassembly and analytical models because the column ends are assumed to be fixed, whereas the column ends in the full frame are continuous and will have some rotational flexibility. The moment in the perimeter column is hardly affected by this difference in P as seen by the good correlation in Fig. 7(b). Fig. 7(c) shows that the analytical structural model conservatively estimates the maximum deflection in the perimeter column. Discrepancies in Δ are produced by temperature gradients in the beam as described previously.

Two approaches were previously discussed for determining the temperature in the steel section: lumped mass method and thermal FE analysis. The latter requires finite element software whereas the former can simply be done on a spreadsheet. Since one goal of the proposed methodology for determining the perimeter column behavior is to simplify the procedure and avoid complex finite element analyses, the analytical model was subject to the conservative beam temperature-time history that was obtained from a lumped mass analysis rather than the more precise FE average section temperature. This analysis is labeled Analytical-LM and the results are shown in Fig. 7. It is seen that the Analytical-LM solution correlates well to the Δ , P , and M response of the Analytical-FE solution and therefore this simplified lumped mass method can be used in lieu of finite element thermal solutions.

Overall, by comparison to the full frame analysis results, it is seen that the analytical model adequately predicts the moment time-history of the perimeter column. It also captures the maximum axial load reached in the beam, although the time-history is conservative since it assumes that the maximum axial load is reached sooner. The perimeter column deformation is overestimated (due to the uniform temperature assumption) and is therefore conservative.

4. SUMMARY AND CONCLUSIONS

This paper presented closed-form solutions for predicting the behavior of steel perimeter columns under fire and the beam framing into it (that is perpendicular to the exterior wall). The solutions were based on an analytical model, which used simplifying assumptions. The effects of these assumptions were examined by comparing the solutions of the analytical model to that of a multi-story finite element analysis of a steel frame under fire. The following observations were made by this comparison: (1) The analytical model overestimates the lateral deflection that the column experiences and is therefore a conservative approximation of this measurement; (2) the analytical model accurately predicts the bending moment that is induced in the perimeter column; and (3) the analytical model accurately predicts the maximum beam axial force and

conservatively estimates the rate of increase in axial force.

5. ACKNOWLEDGEMENTS

Mr. Quiel has been involved with this research project while on appointment as a U.S. Department of Homeland Security (DHS) Fellow under the DHS Scholarship and Fellowship Program, a program administered by the Oak Ridge Institute for Science and Education (ORISE) for DHS through an interagency agreement with the U.S Department of Energy (DOE). ORISE is managed by Oak Ridge Associated Universities under DOE contract number DE-AC05-00OR22750. All opinions expressed in this paper are the author's and do not necessarily reflect the policies and views of DHS, DOE, or ORISE.

6. REFERENCES

- [1] Gann, R.G., ed., "Final Report of the National Construction Safety Team on the Collapse of the World Trade Center Twin Towers," NIST NCSTAR 1, National Institute of Standards and Technology, Gaithersburg, MD, 2005.
- [2] IStructE, *Safety in tall buildings*, The Institution of Structural Engineers (IStructE), London, UK, 2002.
- [3] Garlock, M.E.M. and Quiel, S.E., "The Behavior of Steel Perimeter Columns in a Fire," ASCE/SEI Structures Congress, Proceedings, New York, NY, April 20-24, 2005.
- [4] Lane, B., "Performance-Based Design for Fire Resistance," *Journal of Modern Steel Construction*, AISC, December 2000, pp. 54-61.
- [5] Gewain, R.G., Iwankiw, N.R., Alfawakhiri, F., *Facts for Steel Buildings: Fire*, American Institute of Steel Construction (AISC), Chicago, IL, 2003.
- [6] Usmani, A.S., Rotter, J.M., Lamont, S., Sanad, A.M., Gillie, M., "Fundamental principles of structural behaviour under thermal effects," *Fire Safety Journal*, Vol. 36 (2001), pp. 721-744.
- [7] Wang, Y.C., Lennon, T., Moore, D.B., "The Behaviour of Steel Frames Subject to Fire," *Journal of Constructional Steel Research*, Vol. 35 (1995), pp. 291-322.
- [8] AISC, *Specification for Structural Steel Buildings – Load and Resistance Factor Design (LRFD) (ANSI/AISC 360-05) and Commentary*, American Institute of Steel Construction (AISC), Chicago, IL, 2005.
- [9] Buchanan, A.H., *Structural Design for Fire Safety*, John Wiley & Sons, Chichester, UK, 2002.
- [10] Franssen, J.-M., "SAFIR: A Thermal/Structural Program for Modeling Structures Under Fire," *Engineering Journal*, AISC, Vol. 42 (2005), No. 3, pp. 143-158.
- [11] EC3, *Eurocode 3: Design of Steel Structures. Part 1.2: General Rules – Structural Fire Design (ENV 1993-2-2:2001)*, European Committee for Standardization, Brussels, Belgium, 2001.
- [12] Franssen, J.-M., "The Unloading of Building Materials Submitted to Fire," *Fire Safety Journal*, Vol. 16 (1990), pp. 213-227.
- [13] Garlock, M.E.M. and Quiel, S.E., "Combined Axial Load and Moment Capacity of Fire-Exposed Beam-Columns with Thermal Gradients," 4th International Workshop for Structures in Fire, Proceedings, Aveiro, Portugal, May 10-12, 2006.



COMBINED AXIAL LOAD AND MOMENT CAPACITY OF FIRE-EXPOSED BEAM-COLUMNS WITH THERMAL GRADIENTS

MARIA E.M. GARLOCK¹ and SPENCER E. QUIEL²

ABSTRACT

Current practice for the design of steel beam-columns (i.e. members under combined axial load and bending) subject to fire calculates the capacity of these members assuming a uniform temperature distribution through the depth of the section. This assumption may be acceptable for some members, but there are cases where the member will be heated non-uniformly, thereby developing a thermal gradient through its depth. This paper analyses the effects of thermal gradients on the combined axial load (P) – moment (M) capacity of beam-columns and compares the capacity of members with temperature gradients to those with uniform temperature profiles. The prototype beam-columns used in this study are wide-flange (WF) steel sections that are part of a high-rise moment-resisting steel building. This study considers the effects of plate thickness, section depth, and the direction of bending (i.e. strong vs. weak axis) on the P-M capacity envelope. Results show that a thermal gradient may have a significant effect on the capacity of beam-columns, and evaluations that are made assuming a uniform temperature through the section may lead to overestimations or underestimations of the true strength of the section.

1. INTRODUCTION

Beam-columns are defined as members that are subject to axial load (P) plus bending moment (M). Current practice for the design of steel beam-columns subject to fire calculates the capacity of these members assuming a uniform temperature distribution through the depth of the section. This assumption may be acceptable for some members, but there are cases where the member will be heated non-uniformly, thereby developing a thermal gradient through its depth. For example, beams that support a slab, a column on the perimeter face of the building, and a steel column constructed in a wall will experience unsymmetrical thermal gradients in a fire, which may greatly alter the axial load – moment (P-M) capacity of the section.

Wang et al. [1] have considered the effects of non-uniform temperature distributions on the failure temperature and failure times of column sections with different load levels and

¹ Assistant Professor, Princeton University, Dept. of Civil and Env. Engineering, mgarlock@Princeton.EDU.

² Graduate Student, Princeton University, Dept. of Civil and Env. Engineering, squiel@Princeton.EDU.

slenderness ratios. Their numerical analyses showed that columns with low slenderness and non-uniform temperature distributions developed a larger flange temperature at failure than columns with uniform temperature distributions. While their analyses described the capacity *trends* of columns with different temperature distributions, their study did not evaluate the combinations of P and M that lead to this failure. Such an evaluation is especially important today with the ever increasing use of software to predict the behavior of structures in fire. Such software produces member forces and moments and the user must be able to evaluate such results in the context of the strength of the section.

This paper examines the combined P-M capacity of several representative steel sections that are unevenly heated. If the temperatures are high enough to reduce the yield stress, the resulting thermal gradient will shift the position of the resultant axial force, induce additional bending moments, and alter the section's P-M capacity. Depending on the combination of applied loading, this alteration may provide a conservative or non-conservative estimate of capacity when compared to the P-M capacity considering uniform temperature. In this paper, P-M capacity envelopes obtained from analysis of unevenly heated sections are verified with the results of finite element frame analyses that implement these sections. The effects of the section's plate thickness, depth, and its direction of loading (i.e. strong vs. weak axis) are also addressed.

2. PROTOTYPE SECTIONS

The authors have recently concluded a study of a high-rise steel moment-resisting frame (MRF) structure under fire [2]. Eleven floors and one and one-half bays of this MRF were analyzed under combined gravity and fire loads. This research has shown that the thermal expansion of the beams that frame into the perimeter columns (perpendicular to the exterior face) induce lateral deformations and large moments in these columns. The perimeter columns are therefore subjected to axial compression (through gravity loading) and bending moment (through thermal expansion of the beam that frames into them). In this study, the perimeter column was oriented such that the flange was parallel to the exterior wall and the thermal finite element analyses assumed fire applied on all surfaces except the flange on the building's exterior. The beams themselves, since they are partially restrained by the column, are subject to large axial forces as they try to expand as they are heated. Since these beams carry gravity load, they are also under bending. Both the perimeter columns and beams therefore behave as beam-columns, and both element types are used as examples in this paper.

From the previous study of the high-rise MRF [2], two specific cases will be examined: One case has the beams in the frame protected (i.e., fireproofed) and the columns unprotected (BpCu), and another case has the beams in the frame unprotected and the columns protected (BuCp). The details of the BpCu and BuCp analyses and models are given in [2]. Our study will examine the beam on Floor 23 of the previously studied MRF and the perimeter column just below Floor 23. The column section is a W14x314 and the beam is a built-up plate girder with dimensions similar to a W24x207. The fire used for this study has a growth phase as well as a decay phase and was based on the true fire-event of the prototype building [2]. The outside face (flange) of the perimeter column and the top flange of the beam are assumed to act as adiabatic surfaces and fire was applied on all other sides.

Fig. 1 shows the isotherms of the beam and column section at the time of "failure", which is 41 minutes for the column (in analysis BpCu) and 32 minutes for the beam (in analysis BuCp). In the BpCu analysis, failure is clearly the collapse of the frame as the columns can no longer

support the structure above. In the BuCp analysis, failure is the collapse of the beam, at which time the analysis terminates because convergence can no longer be achieved. Fig. 1 also shows the discretization used in the analyses, where the section is divided into numerous fibers. Fig. 2(a) shows a 3D plot of the distribution of temperature through the depth of the section over time for the column prototype. To produce this plot, the temperature in each row of fibers is averaged. Since the web has a thinner plate than the flanges, it has a higher temperature. Fig. 2(a) shows how this distribution changes over time, where towards 90 minutes the temperature through the depth becomes nearly uniform and equal to the fire temperature. Fig. 2(b) relates these temperatures to a reduced yield stress (σ_y) that is based on Eurocode [3]. It is seen that as the temperatures become constant through the depth of the section, so does σ_y .

Our objective is to examine the axial loads and moments in these beam and column sections at the time of failure and compare them to the P-M capacity envelope based on constant σ_y (which is currently used for design today) and to the P-M capacity envelope based on σ_y as a function of the temperature gradient. The derivation of the P-M capacity envelope with varying σ_y is developed in the next section.

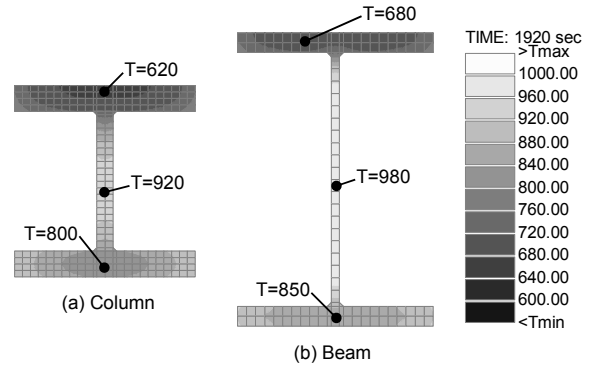


Fig. 1 – Isotherms in the prototype sections at the time of “failure,” shown with finite element discretization (a) for the column at $t = 41$ minutes and (b) for the beam at $t = 32$ minutes.

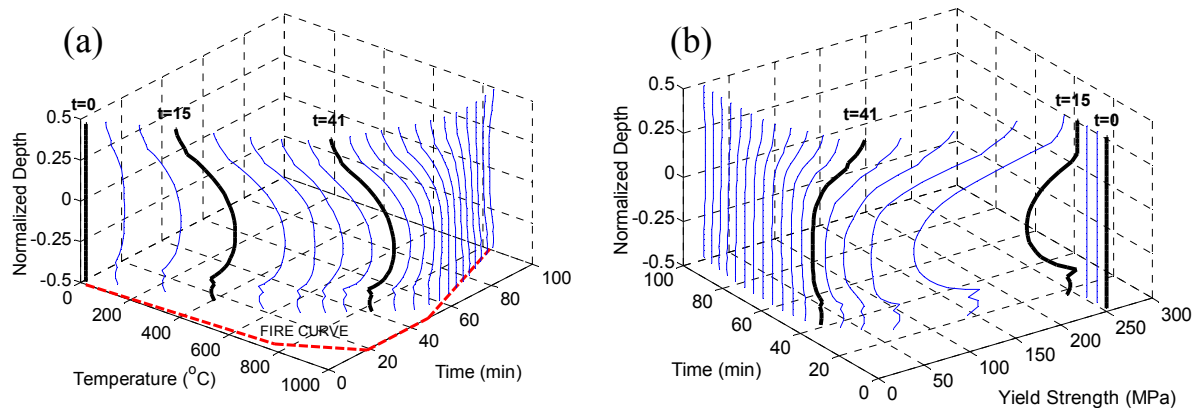


Fig. 2 – Three dimensional plots of (a) temperature (with the fire curve) and (b) yield strength through the normalized depth of the section with time.

3. DERIVATION OF THE P-M CAPACITY ENVELOPE WITH VARYING σ_y

In this section, we derive the P-M capacity envelope of a beam-column with varying σ_y through its depth. Global buckling, local buckling, and residual stresses are not considered since such an inclusion would be outside the scope of this paper. The example that will be used to explain the derivation of the P-M capacity envelope assumes that the WF section shown in Fig. 3(a) is exposed to fire on all sides (represented by the dotted lines) except the top flange. The

resulting temperature profile during the initial stages of the fire is schematically represented by Fig. 3(b). This temperature profile is similar to that shown in Fig. 2(a) for a time equal to about 25 minutes. Assuming that these temperatures through the section have exceeded the value corresponding to a reduction in yield stress, the σ_y profile is schematically represented by Fig. 3(c); the larger the temperature, the smaller the σ_y of the steel material. The yield force capacity of the section, P_y , is calculated by integrating σ_y times the area through the depth of the section, where σ_y has the same sign (i.e., all in compression or all in tension as shown in Fig. 3(c) and (e)). If the section is under bending and the axis of zero strain, i.e., the neutral axis (NA), equals the location of the plastic neutral axis (PNA), then P equals zero and the moment (M) equals the plastic moment capacity of the section (M_p). Such a case is represented in Fig. 3(e).

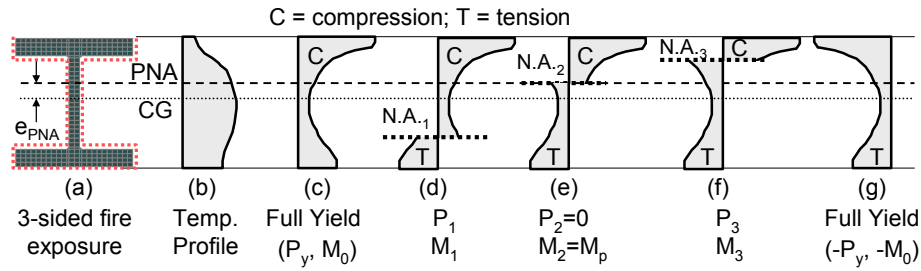


Fig. 3 – Temperature and yield stress profiles with the position of the neutral axial (NA) at various locations.

Regardless of where the NA is located, the axial load P carried by the section at its capacity is calculated by integrating σ_y over its area, where σ_y must retain its sign (positive or negative) in compression or tension:

$$P = \int_A \sigma_y dA \quad (1)$$

The moment is calculated by integrating σ_y times the distance (z) to the reference axis over the section's area, where σ_y and z retain its sign:

$$M = \int_A \sigma_y z dA \quad (2)$$

For the cases when P is not equal to zero, the value of moment will depend on the reference axis chosen. For example, Fig. 4(a) shows P acting at the PNA and the internal moment calculated using the PNA as the reference axis, M_{PNA} . If the reference axis were the center of gravity (CG) of the section (as is the case in Figs. 4(b) and (c)), the moment about this axis, M_{CG} , equals:

$$M_{CG} = M_{PNA} - P e_{PNA} \quad (3)$$

where e_{PNA} equals the distance from the CG to the PNA. Positive moment is defined as creating tension on the top (cooler) flange, and positive P equals compression. This sign convention will be used throughout this paper.

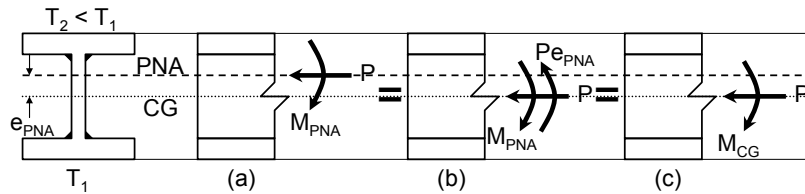


Fig. 4 – Resultant internal forces in a cross-section with a thermal gradient.

Each point on the P-M capacity envelope represents a specific location of the NA. Therefore, to develop the P-M capacity envelope of a section, the NA is progressively moved through the depth of the section and the stresses are integrated. For example, Figs. 3(c) through 3(g) represent five discrete points on the P-M capacity envelope as the NA moves from the below the section's bottom flange to above its top flange. Fig. 5 shows the *normalized* P-M capacity envelope for the case shown in Fig. 3. In this plot P and M are normalized by P_y and M_p , respectively, which are calculated as described above. The envelope shown in Fig. 5 is drawn for the case where the PNA is the reference axis and for the case where the CG is the reference axis, i.e., (P, M_{PNA}) and (P, M_{CG}) , respectively. Point A on these envelopes represents the case where the whole section has yielded in compression as shown in Fig. 3(c). Note that in this case, a moment exists in the section even when summed about the PNA. This moment disappears if the reference axis equals the position of the resultant of σ_y . The direction of this moment is reversed when the moments are considered about the CG. Eqn. (3) reveals that this is due to P times e_{PNA} being larger than M_{PNA} . Point B represents the case where the tension and compression forces in the section are equal and therefore $P = 0$ as shown in Fig. 3(e). All points that lie on the P-M capacity envelope in between points A and B represent the neutral axis moving from the bottom flange to the PNA, as shown in Fig. 3(d). Point C in Fig. 5 represents the entire section yielding in tension as shown in Fig. 3(g). All points that lie on the P-M capacity envelope in between points B and C represent the neutral axis moving from the PNA to above the top flange, as shown in Fig. 3(f). The same procedure leads one from point C to point A; for example, point B' is based on Fig. 3(e) except the area that was in tension is now in compression, and vice versa.

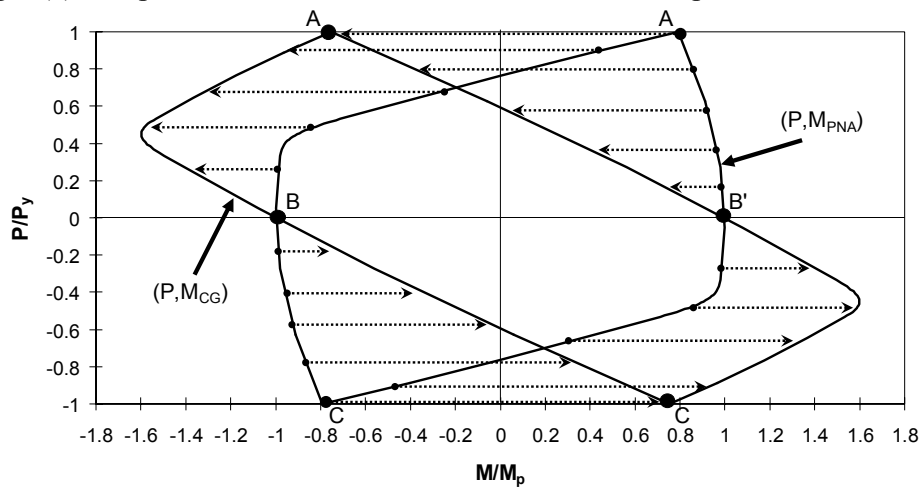


Fig. 5 – Normalized P-M capacity envelopes for an unevenly heated WF section.

The procedure described above was validated by comparison to a finite element solution. The P-M capacity envelope of the W14x314 column section at time of failure (where the temperatures are shown in Fig. 1) is shown in Fig. 5. This result was derived by using the procedure described above implemented as an algorithm written in Matlab, a widely available mathematical analysis software. These results were verified with SAFIR, a finite element software developed at the University of Liege that was specifically designed for structures exposed to fire [4]. A W14x314 column section (pinned at the bottom and with a vertical roller at the top as shown in Fig. 6) was subject to fire on three sides as discussed above. This column has a low slenderness ratio (KL/r) roughly equal to 20, and failure therefore precluded instability.

The temperature profile in the section was kept constant and equal to that shown in Fig. 1(a) and Fig. 2 (i.e. at $t = 41$ minutes) and the axial load P was kept constant as well. The moments, which were equally applied at both ends, were linearly increased until the SAFIR analysis terminated due to the development of a negative stiffness. This procedure was repeated for a range of P/P_y values from 0.1 to 0.9. The normalized P and M points at this time that the analysis terminated are shown as grey points in Fig. 6. Close agreement is seen between these points and the P-M envelope that was obtained by the procedure defined in this section, where the envelope is based on M_{CG} so that it can be directly compared to the computer output. These finite element analyses therefore validate the procedure for developing the P-M capacity envelope.

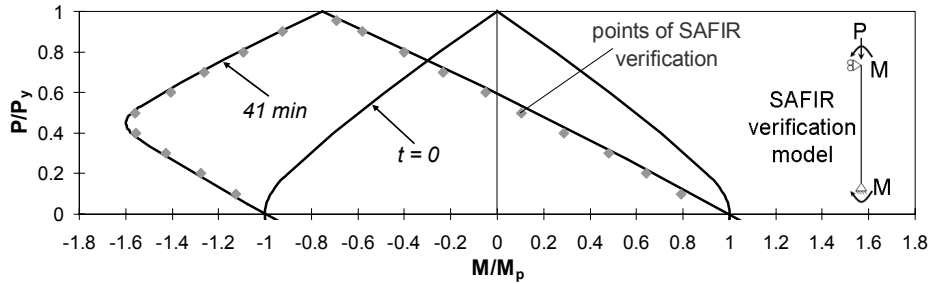


Fig. 6 – Computational verification of the shifted P-M envelope for the unevenly heated W14x314 section at $t = 41$ minutes (structural model and loading shown in the insert).

4. COMPARISON WITH CONSTANT σ_y P-M CAPACITY ENVELOPE

If the temperature through the section is uniform, or if the temperatures have not reached a state where σ_y is reduced, the normalized P-M capacity envelope is the same as that of ambient temperature since σ_y is constant through the depth. Neglecting stability and residual stress effects, the normalized P-M capacity envelope based on constant σ_y through the depth is estimated in the following three ways:

- (1) Using the method described in the previous section, the *exact* P-M capacity envelope based on the section geometry is derived.
- (2) The P-M capacity envelope is estimated using an *AISC* approach [5], where:

$$\text{For } P/P_y > 0.2: \quad \frac{P}{P_y} + \frac{8}{9} \frac{M}{M_p} = 1 \quad (4a)$$

$$\text{For } P/P_y < 0.2: \quad \frac{1}{2} \frac{P}{P_y} + \frac{M}{M_p} = 1 \quad (4b)$$

- (3) The P-M capacity envelope is estimated using a *Eurocode* approach [3], where:

$$\frac{P}{P_y} + \frac{M}{M_p} = 1 \quad (5)$$

Fig. 7 plots these three envelopes and shows that the second and third envelopes are conservative design approximations of the exact capacity envelope, whose solution is not as simple to apply in practice as the design approximations.

Current practice for the design of structures in fire assumes uniform temperature, and therefore constant σ_y , through the depth of the section [3]. Therefore the normalized P-M capacity envelope shown in Fig. 7 would apply. For comparison purposes, we will examine the

prototype column section with the temperature profile shown in Fig. 2(a) at 41 minutes and compare the P-M capacity of this section assuming constant σ_y to that based on the true temperature profile. Fig. 8 compares the *constant σ_y P-M capacity envelope* (using method (1) described above) to the *true P-M capacity envelope* that is determined with σ_y varying as shown in Fig. 2(b) for $t = 41$ minutes. In this example and in the examples to follow, the true P-M capacity envelope is calculated by using the CG as the reference axis (i.e., using M_{CG} as opposed to M_{PNA}). The reason for this is that later on we will use these envelopes to examine some finite element results, which are based on a reference axis at the CG. The following is observed by comparing the two envelopes:

- The true P-M capacity envelope shifts and distorts from the constant σ_y P-M capacity envelope. This true envelope is moving with time as the section heats unevenly. Fig. 8 shows the envelope for a specific time, but Fig. 2(b) shows that the σ_y profile changes with time and therefore the P-M envelope also changes with time.
- Fig. 8 shows that the assumption of uniform temperature through the depth of the section can be conservative in some cases (i.e., the light grey areas) and unconservative in other cases (i.e., the dark grey areas). We will now examine examples where the constant σ_y P-M capacity envelope can be conservative and other examples where this envelope can be unconservative.

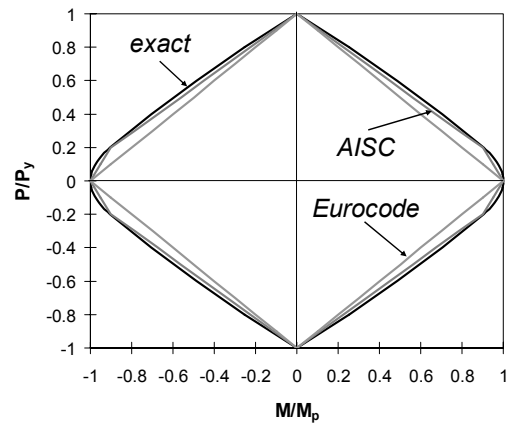


Fig. 7 – P-M capacity envelopes assuming uniform temperature through a symmetric member cross-section.

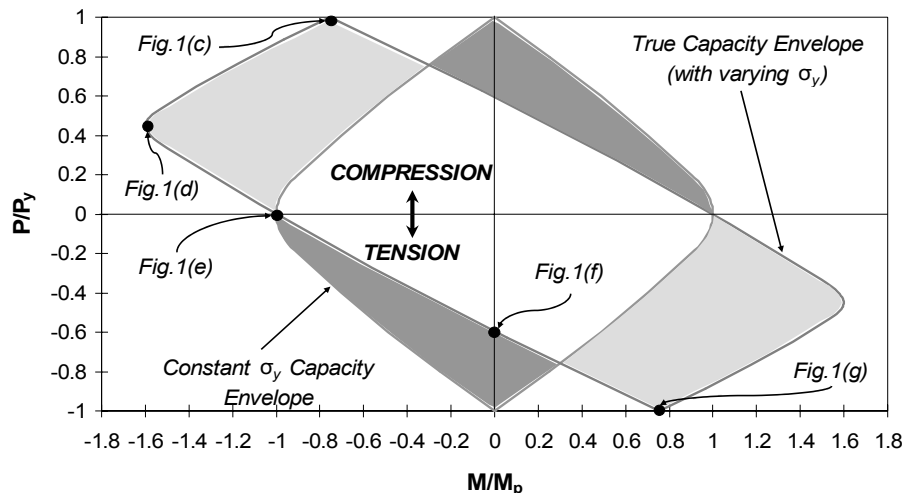


Fig. 8 – Comparison of P-M capacity envelopes for a W14x314 section with at $t = 0$ minutes (i.e. uniform temperature) and at $t = 41$ minutes (i.e. non-uniform temperature).

Before continuing our discussion, it is important to understand the behavior of a perimeter column that is unevenly heated. Fig. 9 shows that when a beam framing into a perimeter column

is heated, it expands (as shown in Fig. 9(a)) and induces moments in the perimeter column (called $M_{CG(\text{beam})}$). At “cooler” temperatures, i.e. before the material properties are affected by temperature, the *resultant* (P) of the internal axial stresses acts at the CG of the perimeter column (Fig. 9(b)). When the perimeter column is heated on all sides except at the building’s exterior, P moves toward the cooler flange and no longer coincides with the CG (Fig. 9(c)). Since P no longer acts at the CG, another moment, opposite in direction to $M_{CG(\text{beam})}$ develops when the moment is measured about the CG. This moment, labeled $M_{CG(e)}$, equals P times the eccentricity e as shown in Fig. 9(c), where e is the distance from the CG to the location of the resultant P. Therefore, at the time that $M_{CG(e)}$ becomes greater than $M_{CG(\text{beam})}$ the moments in the perimeter column reverse direction.

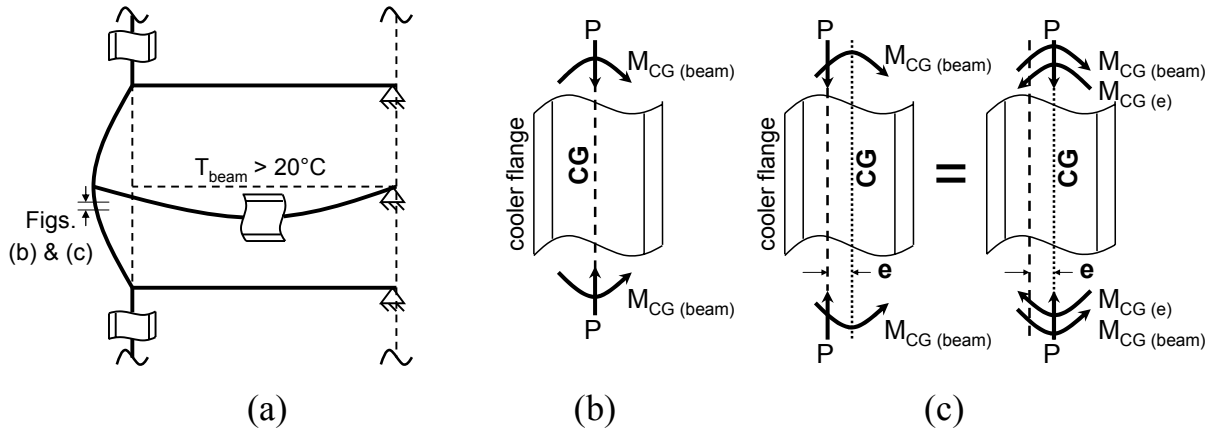


Fig. 9 – Perimeter column behavior assuming uneven heating: (a) frame behavior (b) column behavior at cool temperatures and (c) column behavior at hotter temperatures.

Fig. 10 plots the path of P and M in the perimeter column of analysis case BpCu, and the moment reversal due $M_{CG(e)}$ becoming greater than $M_{CG(\text{beam})}$ is seen to initiate at $t = 15$ minutes. Towards the end of the analysis, these points cross the constant σ_y P-M capacity envelope (i.e., $t = 0$ envelope), which would, by traditional calculations, indicate failure. The analysis however continues until the true P-M capacity envelope is reached, at which time the analysis becomes unstable and terminates since the structure has now failed. The BpCu analysis results therefore show that the constant σ_y P-M capacity envelope can be conservative for predicting the strength of perimeter columns in MRFs.

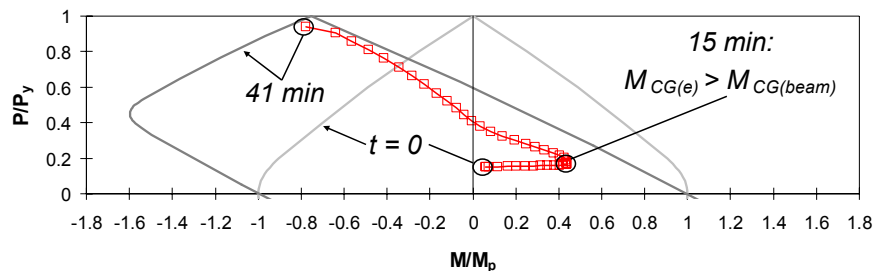


Fig. 10 – Results of the BpCu analysis for the W14x314 perimeter column.

By noting that the P/P_y ratio in Fig. 10 at time = 0 is less than 0.2, we can conclude that stiffness considerations (i.e., limiting wind drift) controlled the design of the prototype structure. If the perimeter column were designed with a larger initial P/P_y ratio, which is the case when the

column section size is not controlled by stiffness limitations (e.g., if the column were not a part of a MRF), then it is conceivable that the constant σ_y P-M capacity envelope (i.e., $t = 0$ envelope) would have been unconservative for design. Such an evaluation is being researched by the authors for future publication.

The P-M capacity envelope for constant σ_y can be unconservative in estimating the strength of heated beams. The behavior of this beam is similar to the perimeter column behavior shown in Fig. 9(b) and (c). A temperature gradient will develop in the beam due to the presence of a slab, and if the temperatures are high enough, the resultant P will move towards the top flange and the moments will eventually reverse direction. Fig. 11 plots the path of P and M of the beam framing into the perimeter column of analysis case BuCp. The moments that are plotted are equal to the beam moments at the face of the column (i.e., at the support). Fig. 11 shows that the beam's P-M behavior is bounded by the true P-M capacity envelope, which is reached before the constant σ_y P-M envelope (i.e., $t = 0$ envelope) that is used for design.

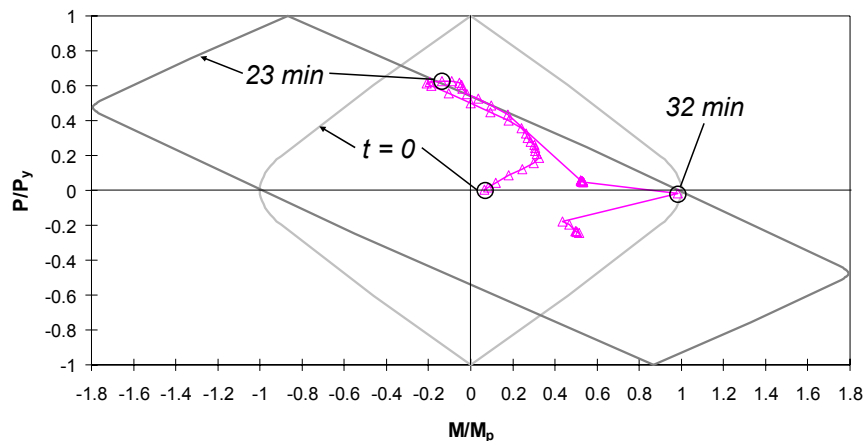


Fig. 11 – Results of the BuCp analysis for the W24x207 floor beam.

The combined P and M in the analysis shown in Fig. 11 hit the true P-M envelope at $t = 23$ minutes at which time the P/P_y ratio begins to decrease, predominantly due to a decrease in P as the beam starts to sag. This decrease in P will reverse the direction of moment once again since the P times eccentricity e component of the bending moment will also decrease (see Eqn. (3)). Towards the end of the analysis at $t = 32$ minutes, catenary action develops (i.e., the beam is hanging), as seen by the negative P/P_y values. The analysis terminates after a couple of seconds of tensile behavior due to structural instability. The authors have found that the inclusion of a concrete slab in the beam model will result in less midspan deflection and slightly less axial force in the steel beam, but the general behavior will be similar. Neglecting the slab can therefore be considered a conservative case.

5. EFFECTS OF SECTION SIZE AND DIRECTION OF AXIS LOADING

Analyses indicate that the maximum shift and distortion of the P-M capacity envelope (relative to the constant σ_y capacity envelope) is independent of section size. For example, three W14 sections were subject to a thermal analysis with fire applied on three sides: W14x53, W14x159, and W14x314. The W14x159 has roughly half the plate thickness of the W14x314, and the W14x53 has roughly half the plate thickness of the W14x159. The normalized P-M

capacity envelopes for each section is shown in Fig. 12 for time = 0 and for the time when the shift in the envelope was maximized. The average section temperature at the time of maximum shift was 861°C, 853°C, and 848°C for the W14x53, W14x159, and W14x314 sections, respectively. The temperature difference (i.e. thermal gradient) between the top and bottom flange in each of the three sections was roughly 175°C, 180°C, and 160°C for the W14x53, W14x159, and W14x314 sections, respectively. It is seen that while it took longer for the larger columns to reach the maximum envelope shift, the maximum shift in all three cases is similar.

A similar comparison can be used to demonstrate the effects of section depth. Fig. 13 shows a comparison of the maximum envelope shift for the W14x159 section and a W24x160 section, both of which have roughly the same plate thickness. The average temperature for the W24x160 section at the time of maximum shift was 873°C, and the approximate temperature difference between its flanges was 180°C. As seen in Fig. 13, the maximum envelope shifts show close agreement with regard to both their shape and the time at which they occur. Section depth therefore does not significantly affect the normalized P-M capacity envelope.

Until now this paper has only considered *strong axis* loading, as shown in Fig. 3, where the section is bending about the strong axis and the temperature gradient is parallel to the web. It is possible to have *weak axis* loading, where the section is bending about the weak axis and the temperature gradient varies parallel to the flange. Such a case may be found, for example, in a perimeter column that is oriented with the web parallel to the exterior face. A W14x314 section (250 MPa grade steel) was subject to two thermal analyses: One analysis assumed that the fire was applied on the outside faces of the flanges and on one side of the web. This represents the weak axis loading case as shown by the sketch in Fig. 14(a). Another analysis assumed that only the top flange was not exposed to fire, thus representing the strong axis loading case, also sketched in Fig. 14(a). Fig. 14(a) and (b) plot the temperature and yield strength distributions

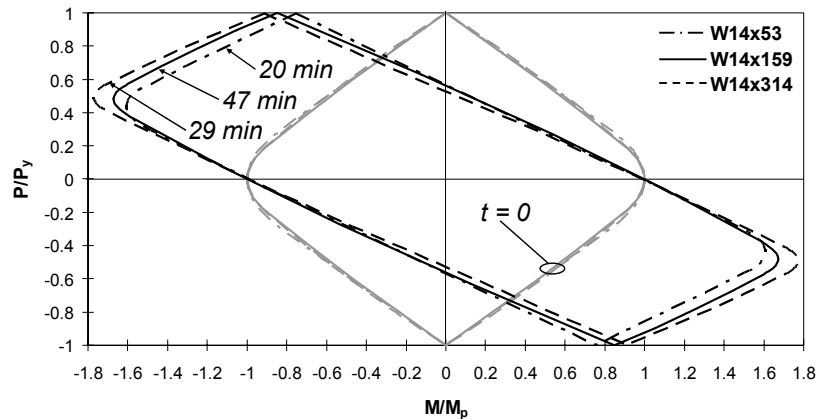


Fig. 12 – Comparison of P-M capacity envelopes for sections with similar depth and varying plate thickness.

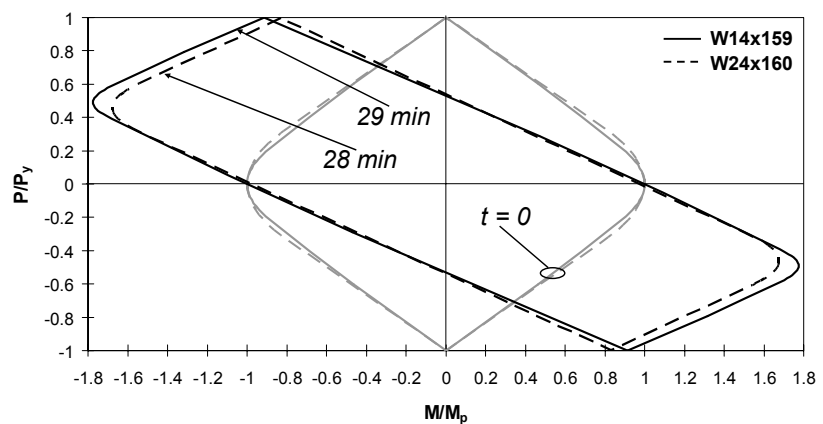


Fig. 13 – Comparison of P-M capacity envelopes for sections with varying depth and similar plate thickness.

through the section for both cases at time = 25 minutes. It is seen that for the weak axis case since the web is no longer parallel to the direction of the gradient, the bulge on the web in T and σ_y that is seen in the strong axis case is not seen in this case.

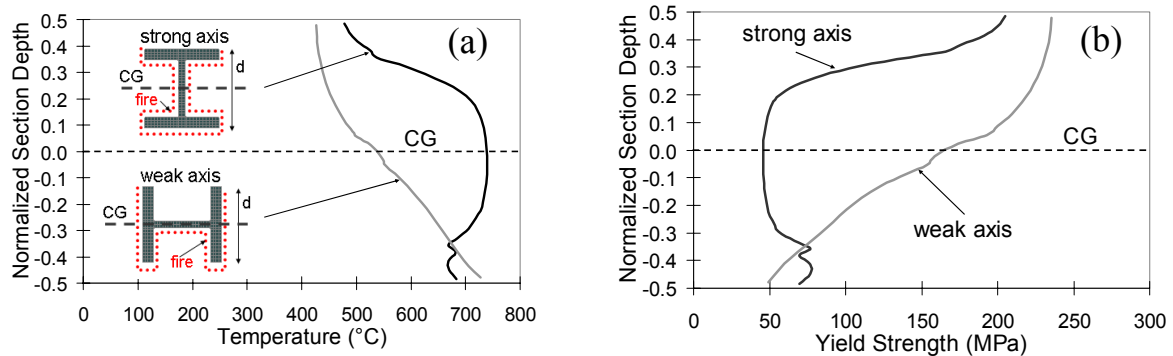


Fig 14 – Comparison of (a) temperature and (b) yield strength profiles over the normalized section depth for W14x314 sections with strong and weak axis loading at $t = 25$ minutes.

The effect that this different loading orientation has on the P-M capacity envelope is shown in Fig. 15, which plots the normalized P-M capacity envelope for the case of constant σ_y through the depth ($t = 0$) and for the case that considers the varying σ_y (at $t = 25$ min.). Fig. 15 shows that the shape of the two curves at $t = 0$ minutes is different such that the strong axis envelope is smaller than the weak axis envelope although both cross the same points on the M/M_p and P/P_y axes. Also, it is seen that both the strong axis and weak axis envelopes shift and distort as σ_y changes through the depth. The shift and distortion in the weak axis case, however, is slightly less than the strong axis case.

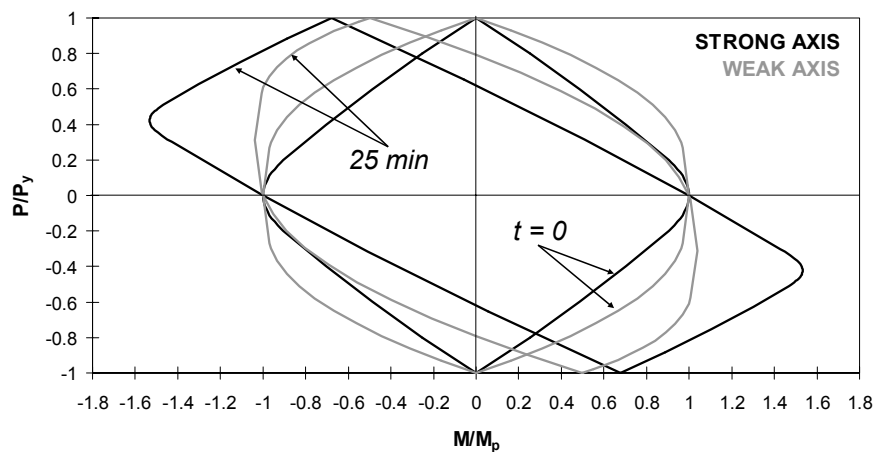


Fig 15 – Comparison of P-M capacity envelopes for W14x314 sections with strong and weak axis loading.

6. SUMMARY AND CONCLUSIONS

This paper demonstrated the effects of temperature gradient on the combined axial load – moment (P-M) capacity of steel wide-flanged sections. Members that experience uneven heating, such as perimeter columns or beams carrying a floor slab, will develop a thermal gradient

through their depth. This paper examined the P-M capacity envelope of several representative steel sections that are unevenly heated. If the temperatures are high enough to reduce the yield stress, the resulting thermal gradient will shift the position of the resultant axial force, induce additional bending moments, and alter the P-M capacity envelope. Depending on the combination of applied loading, the P-M capacity envelope that is calculated based on uniform temperature through the section (as done in practice today) may provide a conservative or unconservative estimate of the true capacity, which considers temperature gradient. This was found to be the case for sections of varying plate size, varying depth, and for bending about both the weak axis and strong axis.

7. ACKNOWLEDGEMENTS

Mr. Quiel has been involved with this research project while on appointment as a U.S. Department of Homeland Security (DHS) Fellow under the DHS Scholarship and Fellowship Program, a program administered by the Oak Ridge Institute for Science and Education (ORISE) for DHS through an interagency agreement with the U.S Department of Energy (DOE). ORISE is managed by Oak Ridge Associated Universities under DOE contract number DE-AC05-00OR22750. All opinions expressed in this paper are the author's and do not necessarily reflect the policies and views of DHS, DOE, or ORISE.

8. REFERENCES

- [1] Wang, Y.C., Lennon, T., Moore, D.B., "The Behaviour of Steel Frames Subject to Fire," *Journal of Constructional Steel Research*, Vol. 35 (1995), pp. 291-322.
- [2] Garlock, M.E.M. and Quiel, S.E., "The Behavior of Steel Perimeter Columns in a Fire," ASCE/SEI Structures Congress, Proceedings, New York, NY, April 20-24, 2005.
- [3] EC3, *Eurocode 3: Design of Steel Structures. Part 1.2: General Rules – Structural Fire Design (ENV 1993-2-2:2001)*, European Committee for Standardization, Brussels, Belgium, 2001.
- [4] Franssen, J.-M., "SAFIR: A Thermal/Structural Program for Modeling Structures Under Fire," *Engineering Journal*, AISC, Vol. 42 (2005), No. 3, pp. 143-158.
- [5] AISC, *Specification for Structural Steel Buildings – Load and Resistance Factor Design (LRFD) (ANSI/AISC 360-05) and Commentary*, American Institute of Steel Construction (AISC), Chicago, IL, 2005.
- [6] Quiel, S.E. and Garlock, M.E.M., "A Performance-based Design Approach for Steel Perimeter Columns Subject to Fire," 4th International Workshop for Structures in Fire, Proceedings, Aveiro, Portugal, May 10-12, 2006.



INVESTIGATION OF SIMPLE CALCULATION METHOD IN EN 1993-1-2 FOR BUCKLING OF HOT ROLLED CLASS 4 STEEL MEMBERS EXPOSED TO FIRE

C. RENAUD¹ and B. ZHAO²

ABSTRACT

A simple calculation method for the fire design of axially loaded steel members with class 1, 2 and 3 cross-section is available in EN version of Eurocode 3 part 1.2 (EN 1993-1-2). On the other hand, the same calculation method is also recommended, with certain specifications through an informative annex, for steel members with class 4 cross-sections. However, during the establishment of French National Annex, some numerical investigation made with the computer code ANSYS for the flexural buckling of hot rolled steel members with class 4 cross-sections at elevated temperatures shows that this simple calculation method may lead to very conservative fire resistance of this type of steel members, especially when subjected to high load ratio under fire situation.

In fact, according to the simple calculation method of EN version of Eurocode 3 (EN1993-1-2), the fire design of steel members with class 4 cross section should be performed using 0.2 % proof characteristic strength of steel in combination with a buckling curve based essentially on the characteristic effective strength of steel obtained at a strain value of 2%. This creates, from the mechanical point of view, a significant mismatch point for this simple calculation method.

In order to improve the design rules of actual Eurocode 3 for a more accurate and realistic prediction of the fire resistance of hot-rolled steel members with class 4 cross-section subjected mainly to axial loading, with the help of computer code ANSYS, a parametric study has been carried out by varying different parameters susceptible to affect the fire resistance of this type of elements, such as cross-section size, eccentricity of axial load, load ratio and buckling length, considering the standard fire exposure. On the basis of corresponding numerical results and the simple calculation approach of Eurocode 3 adopted for room temperature design, a simple calculation method has been proposed for evaluating the fire

¹ Dr., Fire Research and Engineering Section, CTICM 78470 St Rémy-lès-Cheuvreuse, France
email: chrenaud@cticm.com

² Dr. Ing., Fire Research and Engineering Section, CTICM 78470 St Rémy-lès-Cheuvreuse, France
email: binzhao@cticm.com

resistance of uniformly heated and hot-rolled I shape steel members with class 4 cross-section. It has been shown through the comparison with numerical results that the proposed calculation method is suitable to predict with a good precision the fire resistance of hot-rolled I shape steel members with class 4 cross-section under both axial load and combined loading condition. This simple calculation method has been proposed in French National Annex in the corresponding national application of EN version of Eurocode 3 part 1-2.

1. INTRODUCTION

It is well known that if the walls of steel members have high slenderness, some local instability called as local buckling will occur which could reduce largely the overall loadbearing capacity of steel members. In order to take account of such a phenomenon in room temperature design of steel members, the part 1.1 of Eurocode 3 [1] has recommended to classify steel members according to their wall slenderness and the loading condition to four different classes which means that the higher the class of steel member is, the more important the influence of local buckling over the global loadbearing capacity becomes.

The above design concept has been also introduced into the fire part of Eurocode 3 [2] for fire design of steel members. However, for a long time, the fire part of Eurocode 3 deals with the fire resistance of steel members composed of very thin walls so with high risks of local buckling, named as class 4 cross-section steel members by Eurocode, using an extremely simple rule based on a unique critical temperature of 350 °C whatever their load ratio is. Obviously, this rule could lead to a not necessary high cost of fire protection if the steel members with local buckling risks are subjected to low load ratio. As a comparison, steel members without local buckling risk have a critical temperature of at least 500 °C which could be even higher if their load ratio is lower than 0.65. With this respect, in the new version of Eurocode 3 (EN 1993-1-2), it has been incorporated in its informative annex E a simple calculation method trying to provide a design tool for fire engineers to get more detailed results for the fire resistance of such type of steel members. Apparently, for the purpose of simplicity, the calculation methods recommended in this annex for the overall load bearing capacity of class 4 cross-section steel members are referred to those given in the main part of EN 1993-1-2 for steel members with cross-section class lower than 4 considered as without local buckling risks in fire situation.

Recently, during the establishment of national application condition in France for the fire part of Eurocode 3, this informative annex has raised a lot of questions, in particular about the lack of background technical documents showing validity of the simple calculation rules of this annex. As a consequence, a parametric study has been carried out with the help of advanced calculation model ANSYS, in which the fire behaviour of different types of steel members in class 4 under different load conditions is simulated and analysed. In parallel, a comparative study has been made between the simple calculation methods and the numerical simulation on the failure temperature of the steel members analysed in parametric study. The results of the above comparison show that the simple calculation rules could lead to very conservative fire resistance of such type of steel members, especially in case of high load ratio around 0.7. For example, a failure temperature of 26 °C is even predicted by the simple calculation rules which is unfortunately fully unrealistic. This situation has firstly led to the amendment of this annex for national application in France and it is then replaced by modified simple calculation rules which are based mainly on the corresponding design rules of such type of steel members at room temperature.

Consequently, all the results of our parametric study, the analysis of existing simple calculation rules in informative annex E of EN 1993-1-2 and the modified simple calculation rules as well as their investigation with respect to advanced calculation results will be explained in detail in the following paragraphs of the present paper.

2. SHORT PRESENTATION OF SIMPLE CALCULATION RULES OF INFORMATIVE ANNEX E OF EN 1993-1-2

According to Part 1.2 of the Eurocode 3 (EN 1993-1-2), a uniformly heated class 4 steel member submitted to combined axial compression and bending moment is considered as fire resistant if following condition is satisfied:

$$\text{Strong axis: } \frac{N_{fi,Ed}}{\chi_{y,fi} A_{eff} k_{p0,2,\theta} \frac{f_y}{\gamma_{M,fi}}} + \frac{k_y M_{y,fi,Ed}}{W_{eff,y} k_{p0,2,\theta} \frac{f_y}{\gamma_{M,fi}}} \leq 1 \quad (1-a)$$

$$\text{Weak axis: } \frac{N_{fi,Ed}}{\chi_{z,fi} A_{eff} k_{p0,2,\theta} \frac{f_y}{\gamma_{M,fi}}} + \frac{k_z M_{z,fi,Ed}}{W_{eff,z} k_{p0,2,\theta} \frac{f_y}{\gamma_{M,fi}}} \leq 1 \quad (1-b)$$

Where:

- $k_y = 1 - \frac{\mu_y N_{fi,Ed}}{\chi_{y,fi} A_{eff} k_{p0,2,\theta} \frac{f_y}{\gamma_{M,fi}}} \leq 3$ with $\mu_y = (2\beta_{M,y} - 5)\bar{\lambda}_{y,\theta} + 0.44\beta_{M,y} + 0.29 \leq 0.8$
and $\bar{\lambda}_y \leq 1.1$
- $k_z = 1 - \frac{\mu_z N_{fi,Ed}}{\chi_{z,fi} A_{eff} k_{p0,2,\theta} \frac{f_y}{\gamma_{M,fi}}} \leq 3$ with $\mu_z = (1.2\beta_{M,z} - 3)\bar{\lambda}_{z,\theta} + 0.71\beta_{M,z} - 0.29 \leq 0.8$
- A_{eff} is the effective area of cross-section when subjected only to axial compression;
- W_{eff} is the effective section modulus when subjected only to bending moment about the strong axis.
- $k_{p0,2,\theta}$ is the reduction factor for the 0.2 % proof characteristic strength of steel at temperature θ ;
- f_y is the yield strength of steel at room temperature;
- $\gamma_{M,fi}$ is the partial factor for the fire situation (usually $\gamma_{M,fi} = 1$);
- $\bar{\lambda}_{y,\theta}$ is the non dimensional slenderness at temperature θ ;
- $\chi_{y,fi}$ is the reduction factor for flexural buckling in the fire design situation obtained from the relevant buckling curve;
- $\beta_{M,y}$ is a first order equivalent uniform moment factor for flexural buckling. In case of eccentric load, $\beta_{M,y} = 1.1$.

The reduction factor $\chi_{y,fi}$ for flexural buckling which depends on the relative slenderness $\bar{\lambda}_{y,\theta}$ is given by:

$$\chi_{y,fi} = \frac{1}{\varphi_\theta + \sqrt{\varphi_\theta^2 - \bar{\lambda}_{y,\theta}^2}} \quad (2)$$

where $\varphi_\theta = \frac{1}{2} \left[1 + 0.65 \sqrt{\frac{235}{f_y}} \bar{\lambda}_{y,\theta} + \bar{\lambda}_{y,\theta}^2 \right]$

The non dimensional slenderness $\bar{\lambda}_{y,\theta}$ at temperature θ is given by:

$$\bar{\lambda}_{y,\theta} = \bar{\lambda}_y \sqrt{k_{p0.2,\theta} / k_{E,\theta}}$$

where $k_{E,\theta}$ is the reduction factor of the elastic modulus at temperature θ and $\bar{\lambda}_y$ is the non dimensional slenderness at room temperature.

The effective area A_{eff} and the effective section modulus W_{eff} should be determined in accordance to part 1.5 of Eurocode 3 on the basis of material properties at 20°C.

3. PARAMETRIC STUDY OF FIRE BEHAVIOUR OF CLASS 4 CROSS-SECTION STEEL MEMBERS

In the scope of the parametric study conducted during the establishment of French National Annex, in order to have a good knowledge on the fire behaviour of hot rolled steel members, several parameters susceptible to affect the fire resistance of elements have been investigated with the computer code ANSYS [3]:

- Member length: for each section three different lengths: 3.0, 5.1, and 9.9 meters;
- Steel section: ten standard hot rolled steel profiles : HE 220 AA, HE 260 AA, HE 300 AA, HE 360 AA, HE 400 AA, HE 600 A, HE 700 B, HE 800 A, IPE 300 and IPE 500;
- Loading condition: axial load (by taking account of an eccentricity of 5 mm) and eccentric load $0.25 \times h$ and $0.5 \times h$ (h : height of the cross-section). The load is maintained constant during the simulations;
- Load level: 0.3, 0.5 and 0.7 (the load level is based on the design resistance of the members according to EN 1993-1-1 design rules).

In addition, are taken the following specific assumptions:

- Boundary conditions: steel members are hinged at both ends,
- Material mechanical properties at room temperature: yield strength equal to 355 MPa, modulus of elasticity equal to 210000 MPa and Poisson ratio equal to 0.3,
- Heating condition: uniform temperature distribution along the steel member and over its cross-section. For calculations, it's assumed that the temperature varies linearly as function of time,
- Mechanical materials properties as a function of temperature are those given by EN 1993-1-2.

As shown in figure 1, in order to take account of local buckling, steel members have been modelled with 4 node shell elements. End steel plates have been modelled using rigid elements where loading and boundary conditions have been applied. The applied distributed load on the end plates has its application direction (parallel to Z axis) kept unchanged. Initial imperfection for local buckling obtained from preliminary Eigenvalue buckling analysis has been applied with maximum amplitude of $h/200$ (web) or $b/50$ (flange). The temperature dependent value of the coefficient of thermal expansion was taken as that given in EN 1993-1-2 and was applied to the whole member.

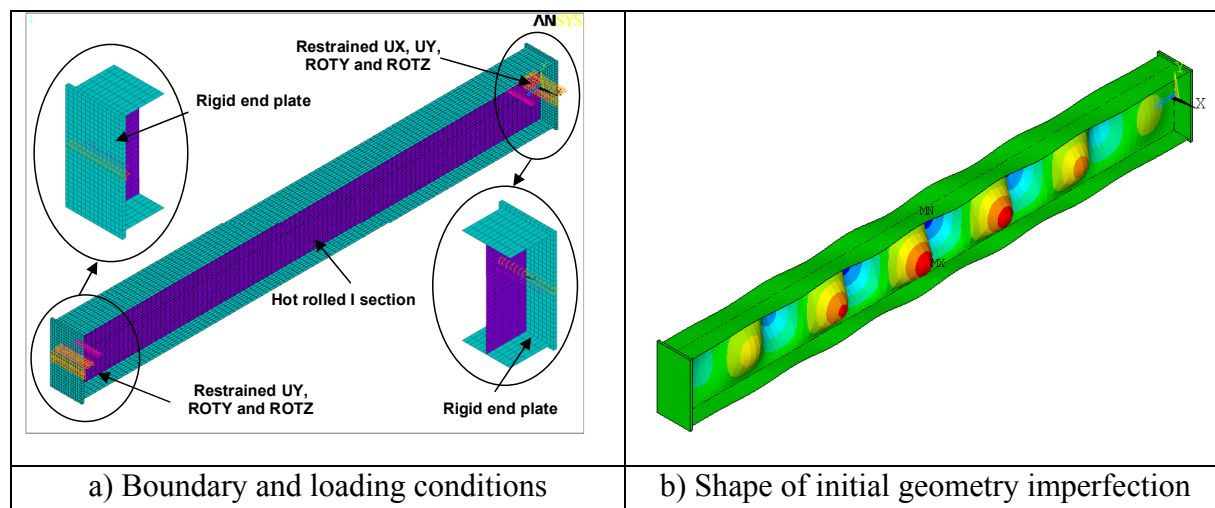


Fig. 1 – Numerical modelling of hot rolled class 4 steel members

The results of this parametric study are quite numerous. Nevertheless, only two typical results are given here in the following figure (figure 2) to show the representative failure modes of such members predicted by numerical modelling.

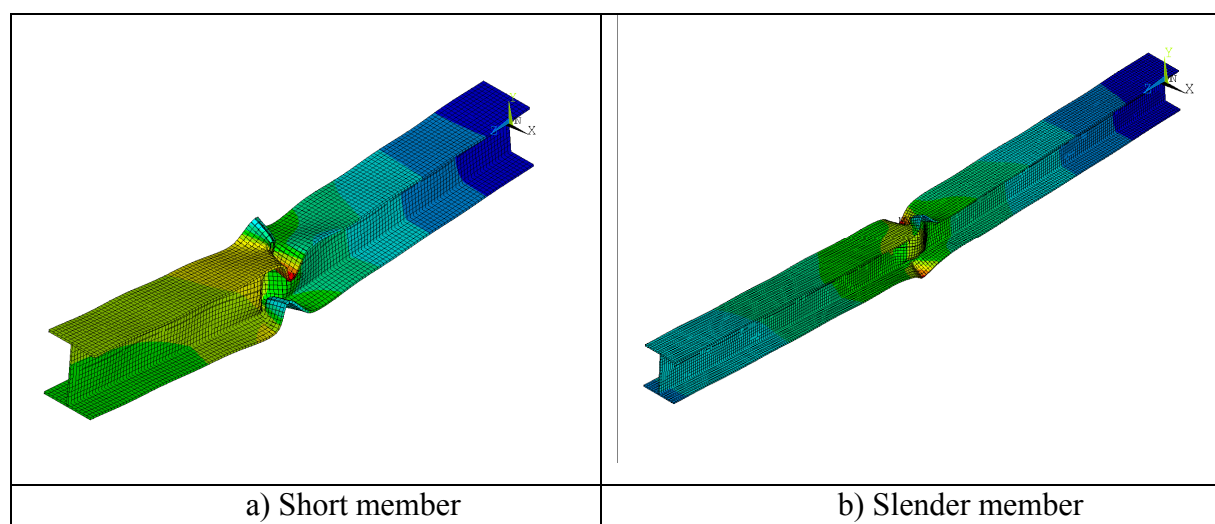


Fig. 2 – Failure modes of hot rolled class 4 steel members predicted by the numerical modelling

4. COMPARISON OF FIRE PERFORMANCE OF CLASS 4 CROSS-SECTION STEEL MEMBERS BETWEEN SIMPLE CALCULATION RULES AND NUMERICAL MODELLING

The whole results of the above parametric study have been given in comparison with the results based on the recommended simple calculation rules of EN 1993-1-2. For every cross-section, the failure temperatures (critical temperature) calculated with the simple calculation rules and those obtained numerically with ANSYS are illustrated together in figure 3 as function of load ratio and cross-section size in case of class 4 steel members submitted to an eccentric compressive load about the strong axis, with the simplified calculation results on X-axis and the numerical results on Y-axis. Figure 4 gives similar results for members under eccentric compressive load applied about the weak axis.

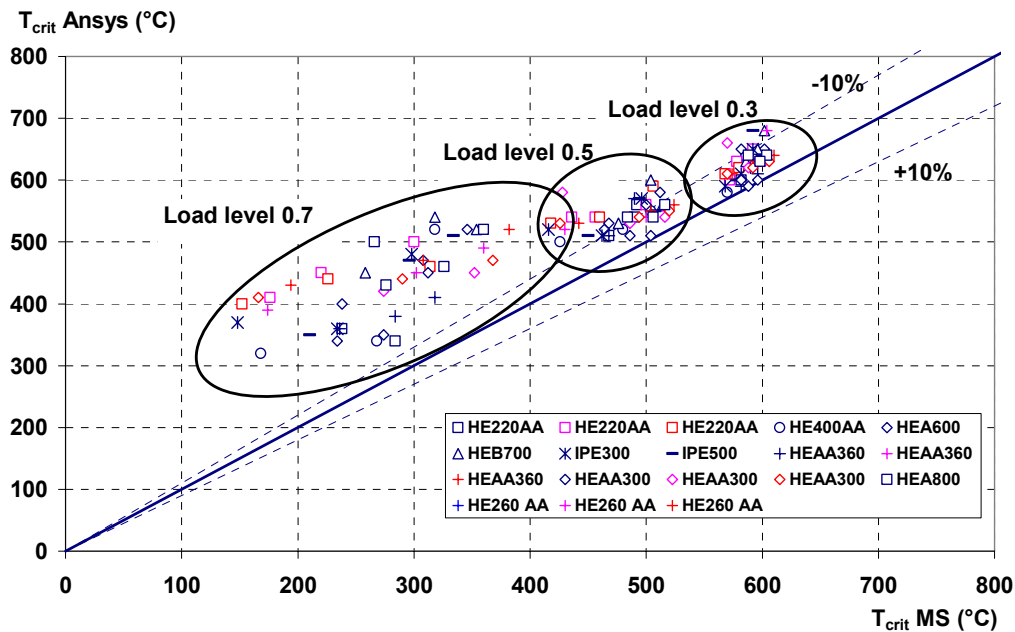


Fig. 3 – Comparison of critical temperatures calculated using simplified method (T_{crit} MS) and numerical model (T_{crit} ANSYS) – buckling about strong axis

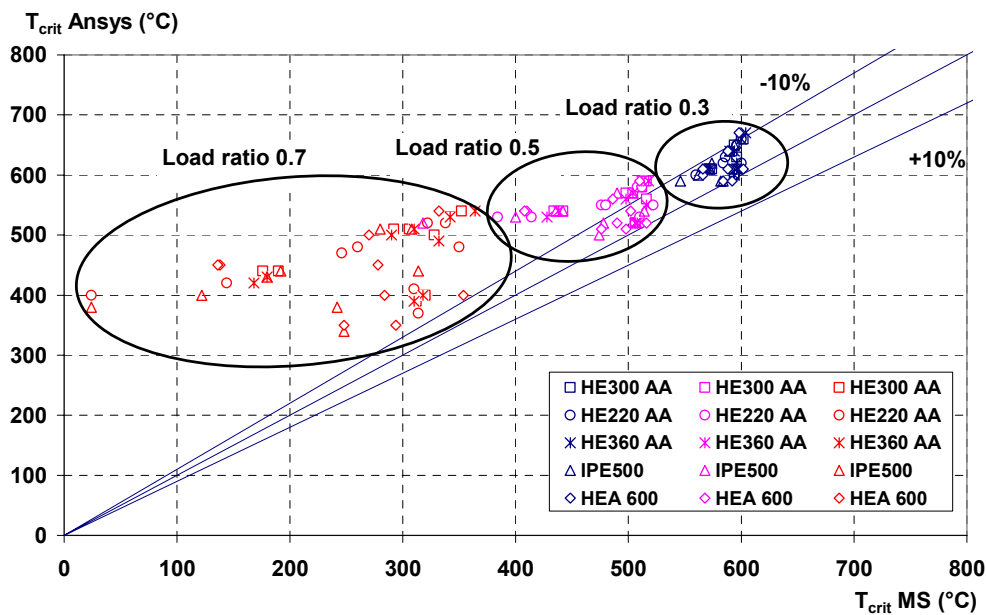


Fig. 4 – Comparison of critical temperatures calculated using simplified method (T_{crit} MS) and numerical model (T_{crit} ANSYS) buckling about weak axis

It has to be noted here that the comparison between the above two approaches is based on the load level derived from design resistance so the same absolute load values. The reason of doing so is that the applied load under fire situation will be based on simplified calculation rules only.

On the basis of the whole comparison, the following observations can be drawn:

- All points are situated on the safe side. The discrepancy between the simple calculation rules of EN 1993-1-2 and the numerical model is more significant when the buckling occurs around the weak axis.

- Globally, the existing simplified calculation rules agree quite well with the numerical model at low load levels (particularly 0.3). The difference between the simplified calculation rules and the numerical model does not exceed 15 %.
- On the contrary, the comparison shows rather big scattering for high load ratio around 0.7. The simple calculation rules could lead to very conservative fire resistance. For example, a failure temperature of approximately 24°C is even predicted by the simple calculation rules, which leads unfortunately to a fully unrealistic situation.

Such a significant difference between the simplified model and the numerical model may be explained by the fact that:

- According to EN 1993-1-2, the fire design of steel members with class 1 to 3 cross sections is based on the strength of steel at a strain value of 2 %. However, in reality the buckling of steel members will certainly occur with much smaller strain value. As a consequence, a special buckling curve has been established in order to use this strength of steel to deal with buckling. In this case, one can find that compared to buckling curves used in room temperature design, this curve is systematically lower (figure 5). As far as class 4 cross section steel members are concerned, their fire design shall be performed using 0.2 % proof characteristic strength of steel. This combination creates, from the mechanical point of view, a significant mismatch point for this simple calculation rule, leading to underestimating the fire resistance of class 4 cross section steel members in case of buckling.

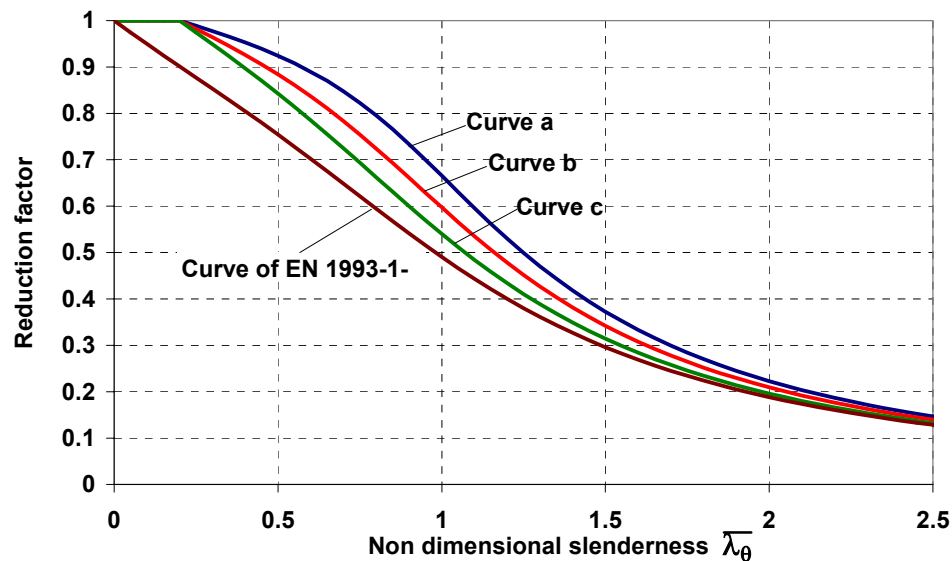


Fig. 5 – Comparison of buckling curves used in normal temperature design and fire design

Moreover, regarding the classification of steel members at elevated temperatures, according to EN 1993-1-2, they shall be classified with the method given in EN 1993-1-1 for room temperature design but with $\varepsilon = 0.85\sqrt{235/f_{y,0}}$ instead of $\varepsilon = \sqrt{235/f_{y,0}}$ in order to account for the stiffness/strength ratio of steel at elevated temperatures $k_{2\%,0}/k_{E,0}$. Nevertheless, if more attention is paid to the square root of the stiffness/strength ratio of steel at elevated temperatures based on $k_{p0.2,0}/k_{E,0}$, one can find that it remains close but always superior to one (see figure 6). This means that the slenderness of walls of steel members will

not become worse at elevated temperatures if $k_{p0.2,\theta}$ is used as strength parameter of steel in fire design. Therefore, it is not consistent to classify the steel members with $\varepsilon = 0.85\sqrt{235/f_{y,\theta}}$ in fire situation. A more right way to proceed could be to keep the same classification as that used in room temperature design.

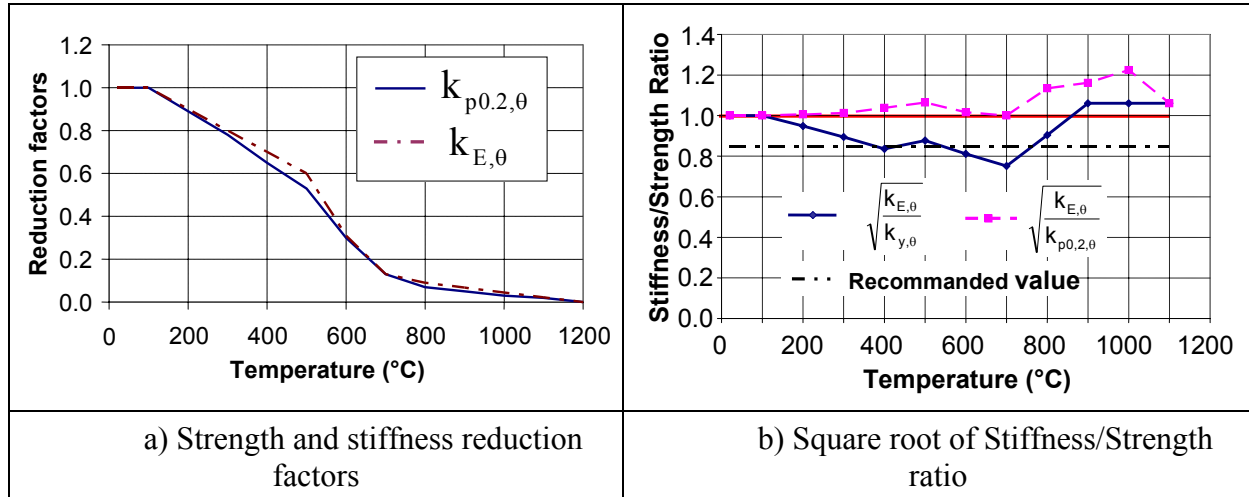


Fig. 6 – Evolution of stiffness and strength parameters as function of temperature

A third inconsistency with simple calculation rules of informative annex E of EN 1993-1-2 is related to the reduction factors of the 0.2 % proof characteristic strength of steel $f_{p0.2,\theta}$ at elevated temperatures of which the values are slightly different from those derived directly from the mathematical model for strain-stress relationship of steel at elevated temperatures (see figure 7).

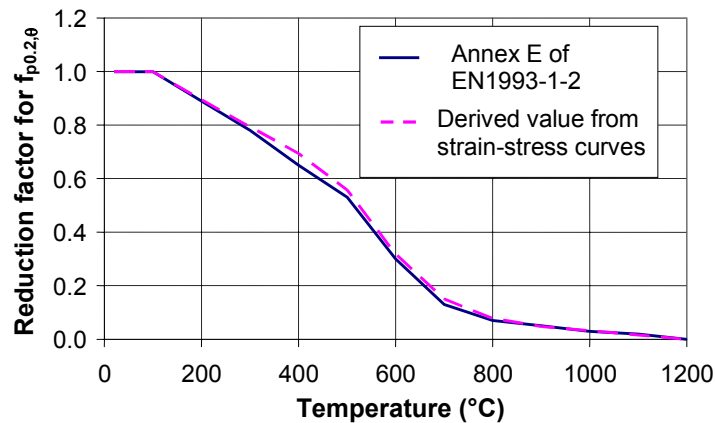


Fig. 7 – Reductions factors for $f_{p0.2,\theta}$

In conclusion, numerical investigations made with the computer code ANSYS for the flexural buckling of hot rolled steel members with class 4 cross-sections at elevated temperatures show that this simple calculation rules may lead to very conservative results and in certain cases predict fully unrealistic fire resistance of such type of steel members.

5. MODIFIED SIMPLE CALCULATION RULES FOR FIRE RESISTANCE OF CLASS 4 CROSS-SECTION STEEL MEMBERS

For the purpose of improving the situation of actual simple calculation rules of EN 1993-1-2 for hot rolled class 4 steel members, a modified calculation method is proposed which consists in using the same type of calculation approach given for steel members at room temperature in Part 1.1 of Eurocode 3, taking account of steel properties depending on temperature. The reason to propose such an approach is based on the following considerations:

- The 0.2 % proof characteristic strength of steel $f_{p0.2,\theta}$ at elevated temperatures can be considered as equivalent to the yield strength of steel f_y used in room temperature design and the square root of the stiffness/strength ratio of steel at elevated temperatures $\sqrt{k_{p0.2,\theta}/k_{E,\theta}}$ is very close to one.
- The 0.2 % proof characteristic strength of steel $f_{p0.2,\theta}$ at elevated temperatures is derived from the mathematical model for strain-stress relationship of steel at elevated temperatures.
- The engineers are normally already familiar with room temperature design rules, therefore it is very easy for them to apply the same rules in fire situation.

A full description of this simple calculation approach is given hereafter.

5.1 Main features of modified simple calculation rules for fire resistance of class 4 cross-section steel members

The buckling resistance of hot rolled class 4 steel members under axial compression in the fire situation can be obtained from:

$$N_{b,fi,Rd} = \frac{\chi_{fi}(\bar{\lambda}_\theta) \cdot A_{eff} \cdot k_{p0.2,\theta} \cdot f_y}{\gamma_{M,fi}} \quad (3)$$

where:

- A_{eff} is the effective area of cross-section under uniform axial compression;
- $k_{p0.2,\theta}$ is the reduction factor for the 0.2 % proof characteristic strength of steel at temperature θ ;
- f_y is the yield strength of steel at room temperature;
- $\gamma_{M,fi}$ is the partial factor for the fire situation;
- $\bar{\lambda}_\theta$ is the non dimensional slenderness at temperature θ ;
- χ_{fi} is the reduction factor for flexural buckling in the fire design situation obtained from an appropriate buckling curve and depending on the non-dimensional slenderness;
- $\bar{\lambda}_\theta$ is the non dimensional slenderness at temperature θ ;

The reduction factor χ_{fi} for buckling resistance in the fire design situation is determined according to:

$$\chi_{fi} = \frac{1}{\varphi_\theta + \sqrt{\varphi_\theta^2 - \bar{\lambda}_\theta^2}} \quad \text{but} \quad \chi_{fi} \leq 1.0 \quad (4)$$

With $\varphi = 0.5[1 + \alpha(\bar{\lambda}_\theta - 0.2) + \bar{\lambda}_\theta^2]$, where α is the imperfection factor corresponding to the relevant buckling curve (as function of the buckling axis and geometrical characteristics of cross-section) as defined in EN 1993-1-1.

The non dimensional slenderness $\bar{\lambda}_\theta$ at temperature θ for class 4 cross-sections is given by:

$$\bar{\lambda}_\theta = \bar{\lambda} \sqrt{k_{p0.2,\theta} / k_{E,\theta}} \approx \bar{\lambda} \quad \text{with} \quad \bar{\lambda} = \sqrt{\frac{A_{\text{eff}} f_y}{N_{\text{cr}}}} \quad (5)$$

where:

- N_{cr} is the elastic critical force for the relevant buckling mode based on the gross cross sectional properties;
- $k_{E,\theta}$ is the reduction factor of the elastic modulus at temperature θ ;

The design moment resistance of class 4 cross-section with a uniform temperature distribution may be determined from:

$$M_{\text{fi,Rd}} = \frac{W_{\text{eff}} \cdot k_{p0.2,\theta} \cdot f_y}{\gamma_{M,\text{fi}}} \quad (6)$$

Where W_{eff} is the effective section modulus when subject only to bending about relevant principal axis.

The fire resistance of class 4 cross-section steel members subjected to combined axial compression and bending requires the satisfaction of the following formula:

$$\begin{aligned} \frac{N_{\text{sd}}}{N_{\text{fi,b,Rd,y}}} + \frac{k_{yy}(M_{y,\text{sd}} + \Delta M_{y,\text{sd}})}{M_{\text{fi,b,Rd,y}}} + \frac{k_{yz}(M_{z,\text{sd}} + \Delta M_{z,\text{sd}})}{M_{\text{fi,Rd,z}}} &\leq 1 \\ \frac{N_{\text{sd}}}{N_{\text{fi,b,Rd,z}}} + \frac{k_{zy}(M_{y,\text{sd}} + \Delta M_{y,\text{sd}})}{M_{\text{fi,b,Rd,y}}} + \frac{k_{zz}(M_{z,\text{sd}} + \Delta M_{z,\text{sd}})}{M_{\text{fi,Rd,z}}} &\leq 1 \end{aligned} \quad (7)$$

Where:

- N_{sd} is the applied axial load;
- $M_{y,\text{sd}}$ and the $M_{z,\text{sd}}$ are the applied bending moments about respectively the strong (y-y) and the weak (z-z) axis;
- $\Delta M_{y,\text{sd}}$ and $\Delta M_{z,\text{sd}}$ are the additional moments about the strong (y-y) and the weak (z-z) axis due to neutral axis shifts of effective cross-section with respect to original gross cross-section;
- $N_{\text{fi,b,Rd,y}}$ is the design buckling resistance of a compressive member according to (1);
- $M_{\text{fi,b,Rd,y}}$ and $M_{\text{fi,Rd,z}}$ are the design bending moment resistances (based on the effective cross-section that is subjected to bending moment only) about respectively the strong axis (y-y) according to (3) and about the weak (z-z) axis according to (4);
- k_{yy} , k_{yz} , k_{zz} and k_{zy} are modifications factors according to EN 1993-1-1 to take account of non uniform bending moment distributions in the member about its strong (y-y) and weak (z-z) axis.

5.2 Comparison with advanced calculation model regarding the fire resistance of class 4 cross-section steel members

In order to verify the validity of proposed simple calculation rules described in the previous paragraph, the results of numerical simulation (critical temperatures) are compared to those simple calculation rules for all members investigated in our parametric study. Thus, regarding the application of simple calculation rules to evaluate the fire resistance of hot rolled class 4 steel members under eccentric compressive load, the following assumptions have been adopted:

- All non dimensional slenderness $\bar{\lambda}_\theta$ are taken equal to $\bar{\lambda}$ at 20°C due to the fact that the ratio $k_{p0.2,\theta}/k_{E,\theta}$ varies only slightly with temperature (see figure 6).
- Cross-sections are classified according to Part 1-1 of Eurocode 3 and remain unchanged at elevated temperatures.
- The effective cross-section properties of steel members (effective cross section area and effective section modulus) are determined in accordance with EN 1993-1-5 [4], i.e. based on the material properties at 20°C based on the fact that the non-dimensional plate buckling slenderness $\bar{\lambda}_p$ used to calculate the effective width of all plate elements depends on the ratio $k_{p0.2,\theta}/k_{E,\theta}$, and consequently varies very slightly with temperature.
- The possible shift e_N of the centroid of the effective area A_{eff} relative to the centre of gravity of the gross cross section and the resulting additional moment are determined using the method given in EN 1993-1-5. For double symmetric section with uniform temperature e_{Ny} and e_{Nz} are taken as zero.

The results of the above comparisons (see Figure 8) are based on the critical temperatures (as function of load ratio and cross-section size) for class 4 steel members submitted to an eccentric compressive load about the strong axis, with the simplified calculation rules on X-axis and the numerical results on Y-axis. The similar results for steel members under eccentric compressive load applied about the weak axis are given in Figure 9.

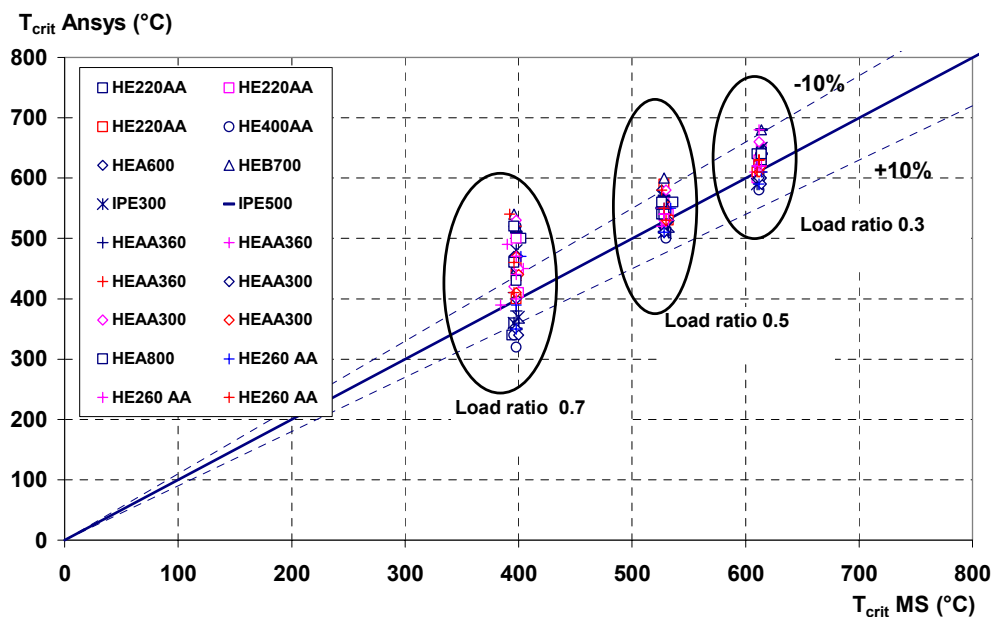


Fig. 8 – Comparison of critical temperatures calculated using simplified calculation rules (T_{crit} MS) and numerical model (T_{crit} ANSYS) – buckling about strong axis

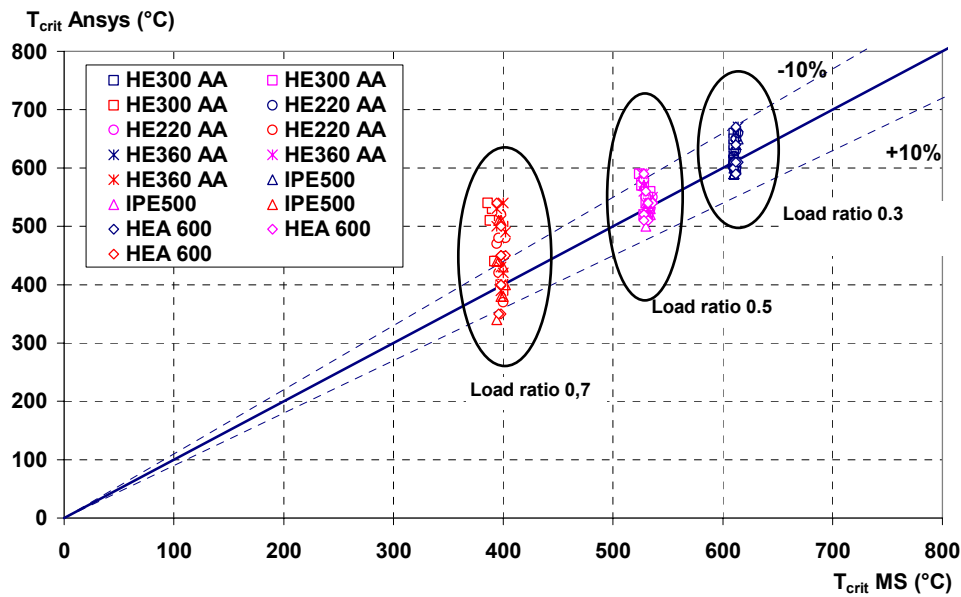


Fig. 9 – Comparison of critical temperatures calculated using simplified calculation rules (T_{crit} MS) and numerical model (T_{crit} ANSYS) – buckling about weak axis

It can be found from these results that:

- The critical temperature of steel members could have a critical temperature higher than 350°C which corresponds to the value of fixed critical temperature given in Part 1-2 of EN 1993 for all class 4 section steel elements but this critical temperature value can be considered as the appropriate value if it is used to cover all load levels of class 4 steel members.
- The critical temperatures predicted with modified simple calculation rules exhibit a quite good agreement with the critical temperatures calculated with computer code ANSYS. The difference between modified simple calculation rules and the numerical modelling is largely reduced with respect to current simple calculation rules in EN 1993-1-2, mainly at load level of 0.7.
- The critical temperatures predicted with modified simple calculation rules are globally lower than those obtained by numerical modelling, so on the safe side.
- For low load ratio (0.3 and 0.5), the maximum difference between the simplified calculation rules and the numerical model does not exceed 10%.
- For high load ratio, in some situations (low buckling length), critical temperatures given by the simplified method may be 30% lower (i.e. conservative) than the numerical temperatures (ANSYS). Even some points may be located on the unsafe side but the difference is close to 10%.

In conclusion, the modified simple calculation rules agree quite well with the numerical model and are fully suitable to predict with a good precision the fire resistance of hot-rolled I shape and class 4 cross-sections steel members under both axial load and combined loading conditions.

6. CONCLUSIONS

During the establishment of French National Annex for Part 1.2 of Eurocode 3, the mechanical behaviour of hot rolled class 4 cross-section steel members has been investigated with advanced calculation model ANSYS with a wide range of parametric simulations. The numerical results are then compared systematically with the simple calculation rules in informative annex E of EN1993-1-2 and it is derived that in some cases, these simple calculation rules could underestimate considerably the fire resistance of class 4 cross-section steel members. The mechanical analysis of these simple calculation rules has been conducted. Alternative simple calculation rules based on the corresponding numerical results and the room temperature design approach of Eurocode 3 have been proposed for French national annex. It has been shown through the comparison with numerical results that the so-called modified simple calculation rules are capable of predicting with a quite good accuracy the fire resistance of hot rolled class 4 cross-section steel columns under compression and bending.

Nevertheless, all these results are only based on advanced calculation tools without any experimental investigation. It is evident that in the future, a European research project could be initiated in this field in order to bring confident evidence about the fire behaviour of hot-rolled class 4 cross-section steel members.

7. REFERENCES

- [1] EN 1993-1-1 - Eurocode 3 " Design of steel structures " – Part 1-1: General rules and rules for buildings, CEN, May 2005.
- [2] EN 1993-1-2 - Eurocode 3 " Design of steel structures " – Part 1-2: General rules – Structural fire design, CEN, April 2005.
- [3] ANSYS, "ANSYS User's Manual for Revision 8.0 – Volume IV – Theory", Swanson Analysis SYSTEM, INC., Houston USA, 1992.
- [4] prEN 1993-1-5 - Eurocode 3 " Design of steel structures " – Part 1-5: Plated structural elements. CEN, July 2005



USE OF SIMPLIFIED METHODS FOR DESIGNING EXTERNAL MEMBERS PROTECTION

Daniel JOYEUX¹, Sylvain DESANGHERE²,
Olli KAITILA³ and Jose Antonio CHICA⁴

ABSTRACT

The annexes C in parts 1.2 of Eurocode 1 and Eurocode 3^{1, 2} are devoted to the description of a simple method aimed at estimating the heating of external bare steel structures. This method is based on a steady state assumption, restricting its validity to thermally thin sections. Indeed, sections presenting a low section factor do not systematically reach steady state temperature during the course of a real fire. So, it is not possible to accurately predict the temperature of such sections with the direct use of the simple Eurocode method.

When checking the fire stability of an external member, if the simple application of the Eurocode method leads to an unacceptable value of the temperature, an alternative approach has to be found to calculate it. This paper presents an example of the application of methods designed to estimate the temperature reached by protected and composite sections. These methods have been developed within the framework of European project partially financed by the ECSC. This work is aimed at showing how such methods can be involved to define a solution in a real context for which external members have to be protected.

1. INTRODUCTION

A European project has recently been devoted to the improvement and the extension of the existing Eurocode models about the estimation of the temperature reached by external members during a fire³. This work was intended to predict temperature development within different types of external structural elements, by including transient state effects. The verification of the current Eurocode models describing external flames has been performed on

¹ CTICM Saint Rémy lès Chevreuses, FRANCE

² CTICM Saint Rémy lès Chevreuses, FRANCE

³ VTT Espoo, FINLAND

⁴ LABEIN Bilbao, SPAIN

the basis of experimental and numerical results. Some evolutions were then suggested, in order to extend the use of these models to transient conditions, with some required modifications if needed. In parallel, an important part of this project was devoted to the development of simple models aimed at predicting the heating of various structural elements^{4,5}.

The emphasis is laid here on three types of section, namely composite section, protected section by intumescent paint, and encased section. For each type, simple methods have been developed for the prediction of the heat transfer. The aim of the present paper is not to give a thorough description of these models but rather to provide an actual illustration of the use and the benefits from such methods, compared to existing Eurocode approach. In this respect, the configuration of a real building is employed. Two fire scenarios, leading to very different fire durations, are involved in order to insist on the concept of the duration of the exposition to external thermal actions. Indeed, the introduction of time as a variable is the most important refinement of the present approach, compared to the current Eurocode one.

This paper provides first a brief description of the building. A preliminary structural study concerning the fire stability of the building has been performed and has led to the determination of critical temperatures for the structural elements. So, the goal of the presented study is to find building solutions in order to prevent structural elements to reach their critical temperature. Two values of fire load density, related to the activities existing within the edifice, are proposed. Thus, two fire scenarios are considered. For each three type of structural elements, and for each two scenario, a design of the protection is proposed to ensure the fire stability.

2. DESCRIPTION OF THE BUILDING

The considered building has 9 levels of 2.80 m height. Its facade is made of glazed frontage, so the entire facade of each room can be opened during fire. The level studied here is composed of offices and libraries. Compartment studied in level 1 is 30.0 m width and 23.0 m depth, whereas compartments of level 2 to 4 are 23.0 m on 23.0 m.

At each level, the external structure is made of columns (HEB300) linked to parallel beams (UAP270) by perpendicular members (HEA280). A picture of the external structure is given in Fig. 1, whereas the location of the members is given in Fig. 2. The present application is focused on the column.



Fig. 1 – Picture of external members

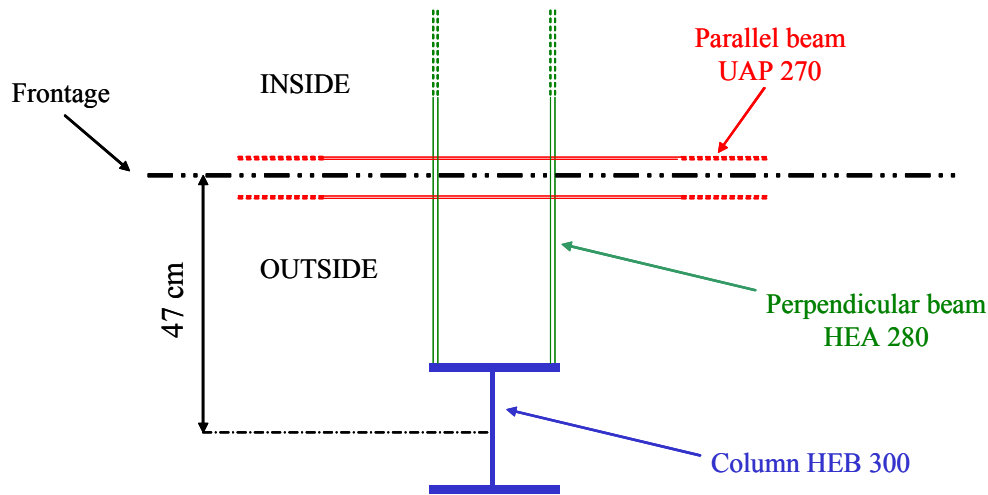


Fig. 2 – Location of external members

Detailed information is given about the mechanical characteristics of the column: the buckling length is $L_{fi} = 2,10$ m ($0,7 \times$ height $3,00$ m). The axial loads are given on the column for both representative levels:

Table 1– Mechanical loads

Level	Level 1: Library	Level 2: Office
$N_{fi,Ed}$ (kN)	1 587	1 415

According to these characteristics, the mechanical resistance of the structure is supposed to be achieved when the temperature reached by each element is below a given critical value. These critical temperatures calculated according EN1993-1-2 are summarized in Table 2 below.

Table 2 – Critical temperatures for external members

	Level 1	Level 2
Critical temperature	563°C	727°C

3. FIRE BEHAVIOUR OF UNPROTECTED STRUCTURE

The fire stability of the external column may be verified according the annexes C of the Eurocode 1 part 1.2 "actions in case of fire" for thermal action and the Eurocode 3 part 1.2 "fire behaviour of steel structures" for the thermal response. This method is a steady state method, using a balance between the incident heat flux and the heat flux lost by the steel structure, with a homogeneous temperature in section².

A parametrical study has been performed to find the worst opening configuration concerning external members. The conclusion of this study leads to the compartment geometry shown in Fig. 3. Two values of fire load density are used: 100 kg/m^2 representative of the library and 30 kg/m^2 of wood representative of the office⁶. The member is supposed to be located in the centre of the opening: no fire resistance mullion is defined in the building.

The application of Eurocodes leads to the following results given in table 2 in terms of heat flux to the different faces of the column.

The axes are shown in Fig. 3. The resulting temperature reached by the column is 764°C.

Table 3 - Heat fluxes and temperatures reached by unprotected members according to Eurocode method (Φ_z - corresponds to the face facing the opening)

Heat flux per face	Φ_{x+} (kW/m ²)	Φ_{x-} (kW/m ²)	Φ_{z+} (kW/m ²)	Φ_{z-} (kW/m ²)
	81.2	81.2	34.2	88.5

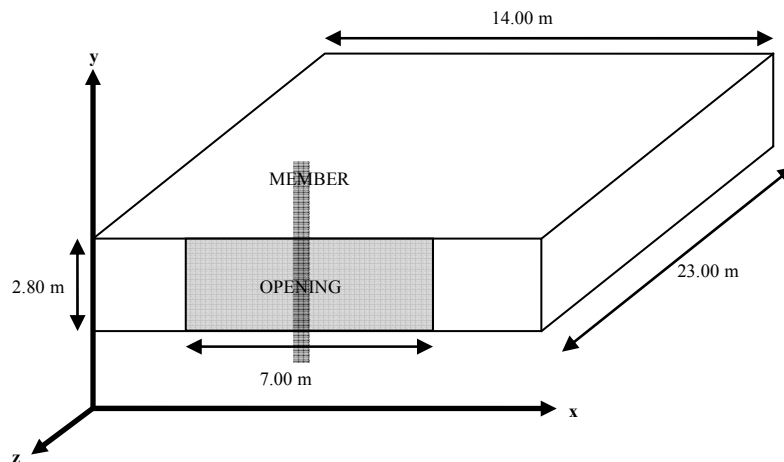


Fig. 3 – Overview of the reference compartment

Regards to the critical temperatures and the temperatures reached by the columns given here above, it can be concluded that the columns of both levels are not fire resistant and should be protected.

In such case, a transient methodology dealing with protected elements has been developed within a European project. It is then proposed to apply the method and tools developed within the present research to design the protection or chose new column section to be fire resistant, using an unsteady approach.

4. APPLICATION OF THE METHODS TO PROTECT COLUMNS

4.1 Transient approach

A pyrolysis rate is assumed in the current Eurocode model. Nevertheless, this one is defined to obtain safe results in steady state conditions. In transient conditions for external flaming, the two main parameters are the rate of heat release and duration of the thermal actions: large rate of heat release leads to large external thermal actions but a low duration, and a small rate of heat release leads to a small external thermal action with a large duration. The conclusion of the research project is to consider two different design fires from that point of view. The design fires are based on the concept of global equivalent ratio (GER), with two values: GER=1 (small external flaming conditions with large duration) and GER =1.5 (large external flaming conditions with small duration).

The rate of heat release is independent on the types of protection. The mass flux of air entering into the room is assumed to be

$$m_a = 0.5A\sqrt{H} = 16.4 \quad \text{kg/s} \quad (1)$$

In the present case, the results will be shown only for design fire of GER=1.5. Using this GER, a fuel mass flux (considering wood) is

$$m_f = m_a \frac{\Phi}{r} = 16.4 \frac{1.5}{5.7} = 4.3 \quad \text{kg/s} \quad (2)$$

So, a maximum heat release rate is 60 MW.

Using fire load densities of 100 kg/m² and 30 kg/m², this leads to the curves shown in figure 4. We assumed a t square fire (growing in 1200 s) followed by a steady period and linearly decreasing when 70% of the fire load has been consumed.

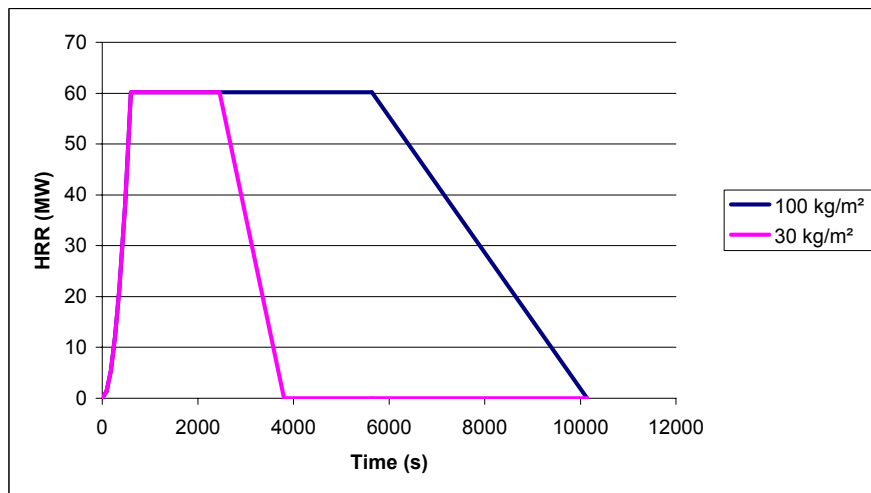


Fig. 4 – HRR curves for the two fire loads

From that curves, from the heat flux on each surface of the column is defined by the following heavy side shaped curve as a function of time. The start and the end in each case correspond to the time when HRR is defined by a GER=0.75 for which there is no external flaming (see Fig. 4).

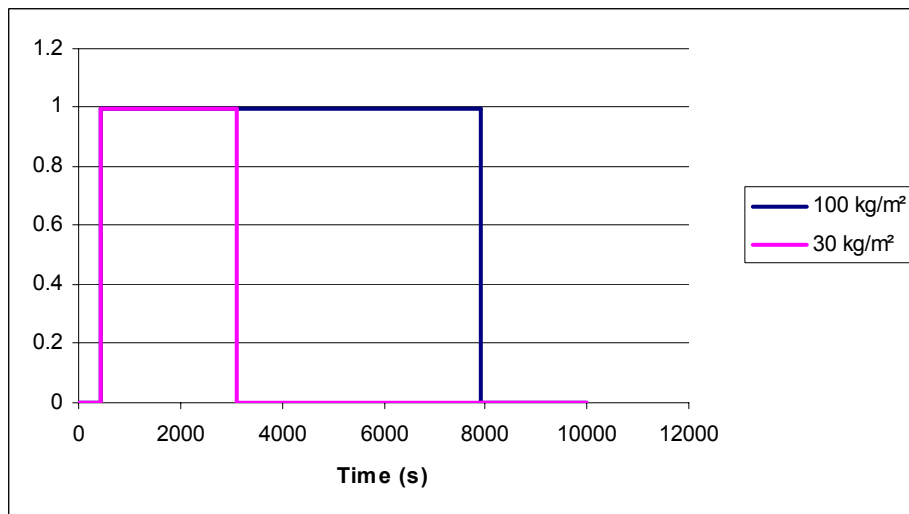


Fig. – 5 Heat fluxes curve shapes for the two fire load

The recommended values for maxima are summarized in Table 3.

Instead of the steady state temperature of the compartment coming from the Eurocode 1 part 1.2 “external flaming method”, a calculation of the temperature time curve has been performed with the zone model Ozone, using as input the mass loss rate curve defined in the exercise in order to estimate radiation from the compartment.

These heat fluxes are employed for designing three solutions of structural design or protection design:

- Protection of the column in terms of intumescent coating
- Steel box
- Composite column

4.2 Concrete filled section

Using the Eurocode equations modified in order to use possible shield effect due to flames and opening and steel geometry, the heat fluxes to the structural column is determined. From that heat fluxes, a temperature distribution of a composite section has been determined with a 2D thermal transfer model (SAFIR developed by the University of Liege). The thermal properties of steel and concrete from Eurocode 4 part 1.2 have been used.

The figure below shows the evolution of temperature within the flanges and web of the HEB 300 profile in front of the office at the height of the soffit of the opening for the level 2.

The peak temperature in the exposed flange is 576° C. If the Eurocode 3 part 2 is used to calculate resistance of the sections, it should be considered the highest temperature of the section. The critical temperature (727 °C) is higher than the peak temperature, so it results that the columns does not collapse.

The steady state calculated in the exercise (blue line in figure 6) is much higher than the transient one, above the critical temperature, leading to conservative conclusions. The exposure time is not long enough to make the profile reach the steady state temperature. To summarize, if a transient calculation is done, the profile does not need to be protected with passive protection, because collapse does not occur if the member remains unprotected.

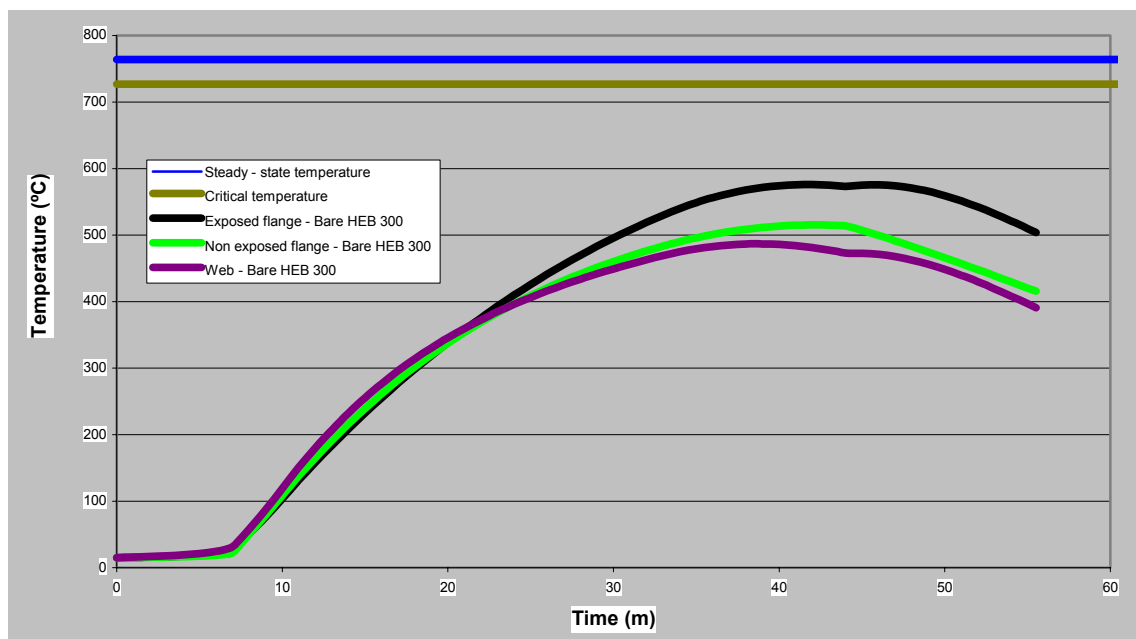


Fig. 6 – Temperatures within the HEB 300 profile in front of the office

Figure 8 shows temperature evolution in flanges and web of the HEB 300 in front of the library (level 1). As foreseen, the critical temperature is reached firstly in the exposed flange at 37 minutes and later in the non-exposed flange and the web. So, a design of composite column is proposed as shown in figure 9 to provide insulation to the steel section. A concrete partial encasement is proposed only for insulation purposes not for structural resistance. The concrete is made of siliceous aggregate with content of 100 kg/m^3 of water.

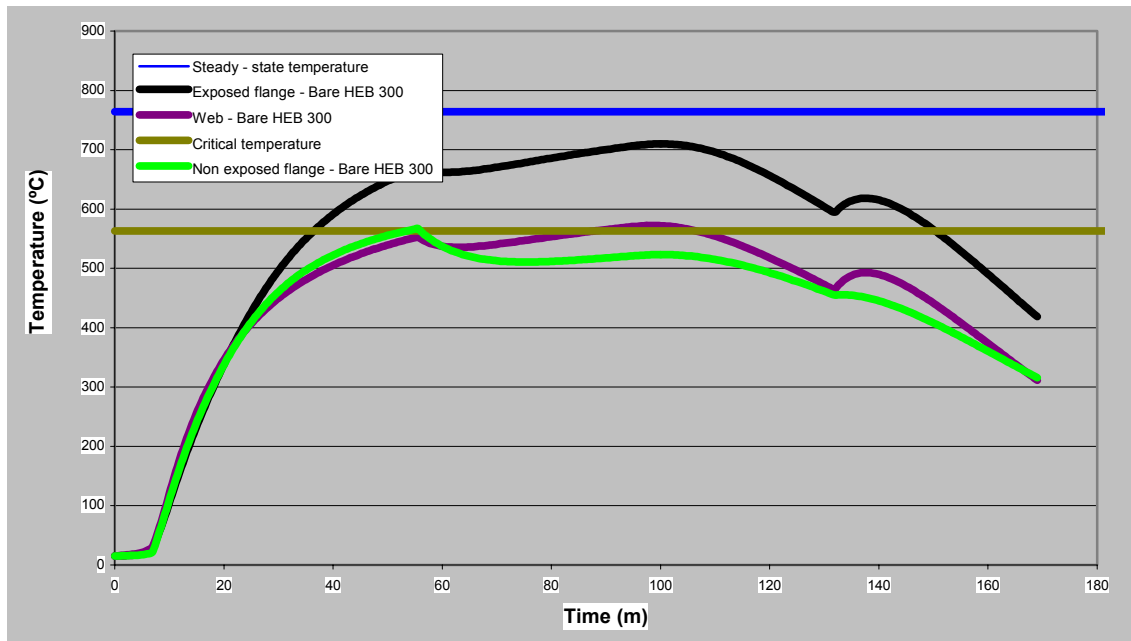


Fig. 8 – Evolution of temperature in the bare HEB 300 section for fire in the library

As a result of the concrete insulation, the exposed flange undergoes an increase of temperature by comparison with the bare section. This is due to the fact that in the composite section, the concrete core acts as a barrier that hinders the exposed flange to evacuate heat to the rest of the section. However the non-exposed flange and the web reach much lower temperatures in the composite section than in the bare section.

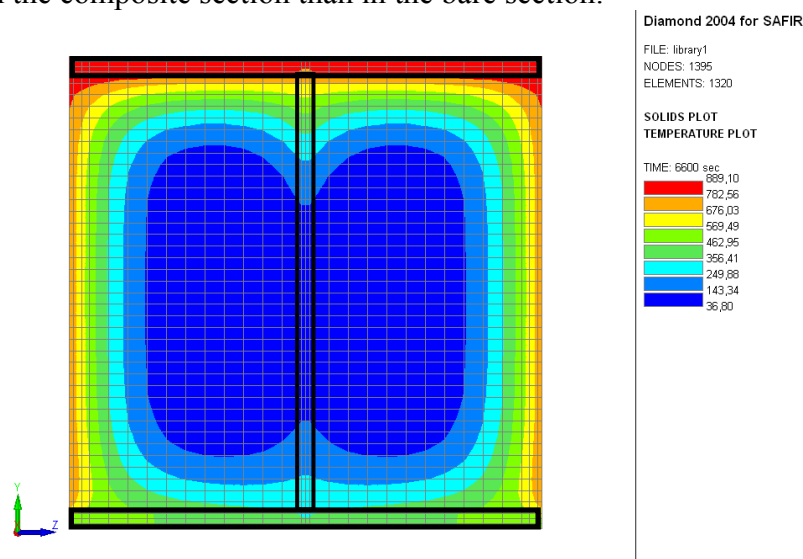


Fig. 9 – Temperature distribution within the section at 110 minutes

As a conclusion, according to the current steady state approach of the Eurocode, the encasement with concrete between flanges the column leads to a fire stability of the column.

4.3 Protected steel section

The heat fluxes curves given above in the definition of the exercise have been used as boundary conditions for heat transfer calculation, using finite element modelling. This procedure is employed here to find the thickness of the intumescent coating that has to be applied on the structure to prevent it to reach its critical temperature. Two kinds of coatings are studied here.

The apparent thermal properties of two kind of coating have been deduced from standard fire resistant tests. The intumescent coating thickness is assumed to be ten times larger than its initial value. The determination of thermal properties has been made with these assumptions. Then the application has been made by comparison with several experimental results (in case of standard test and in case of external flaming conditions).

For each simulation, the local temperatures in the middle of the web and in the flange exposed to fire have been investigated in order to have an idea of the heating of the section. Iterative calculations have led to the estimation of the minimum thickness required.

Figure 10 gives an example of the temperature field during the heating phase. This shows the effect of the coating which acts as a thermal barrier for the external heat flux. This figure corresponds to the end of the heating phase, when the heat flux begins to decrease.

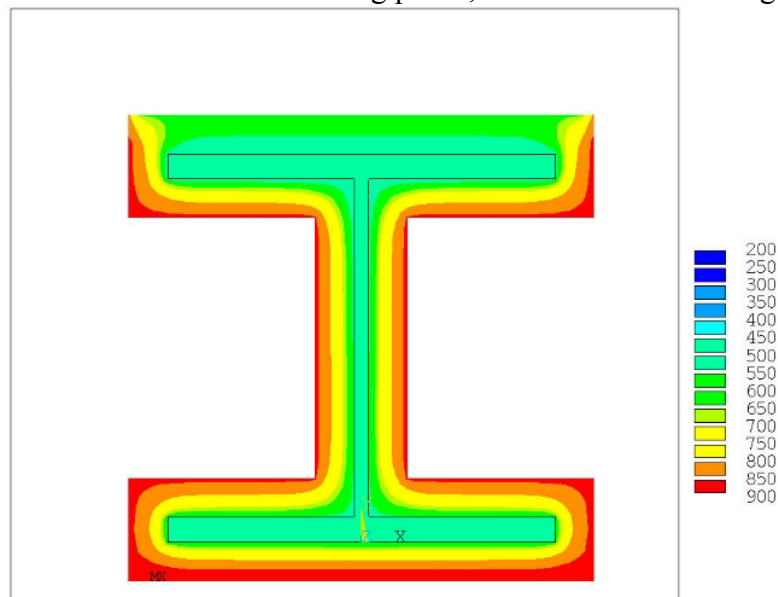


Fig. 10 – Example of temperature field in the section during the heating phase (°C)

Several calculations have been performed with different values of coating thickness for this scenario. The maximum temperatures reached by steel for the level 1 are given in the following figures:

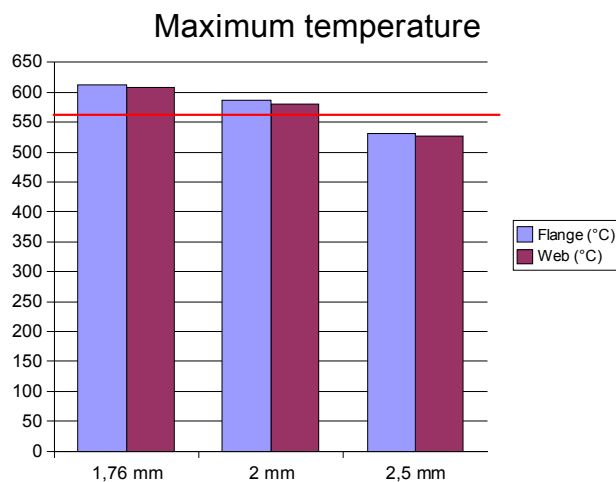


Fig. 11 – Maximum temperatures reached within the section

This study shows that a thickness of 2.5 mm is sufficient to maintain the section below its critical temperature. Figure 12 gives an example of the evolution of temperature within the section.

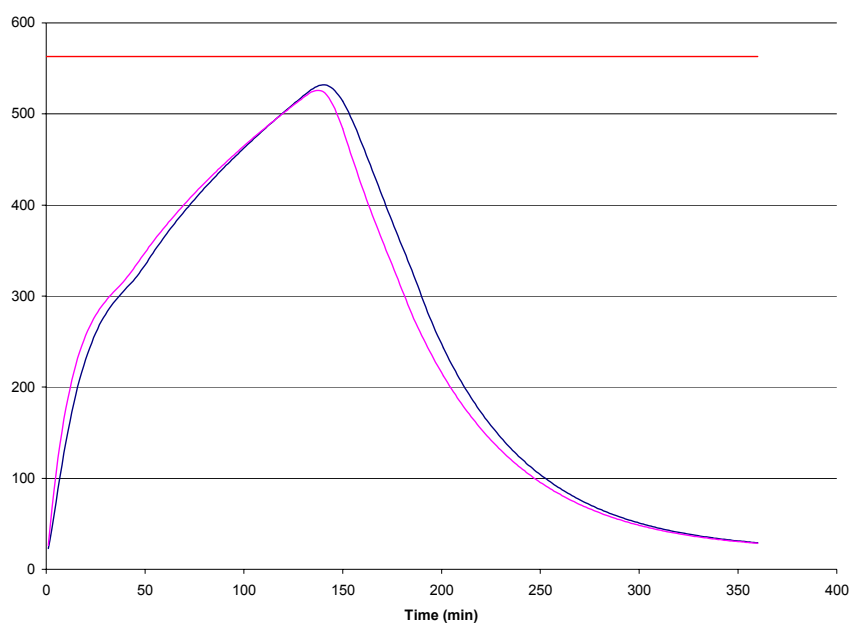


Fig. 12 – Evolution of temperature during fire in a library in the section insulated with 2.5 mm

The same procedure is done with the fire scenario at the office level. A solution proposed here is to use thickness of 0.6 mm. The corresponding curves are shown in figure 13 and figure 14.

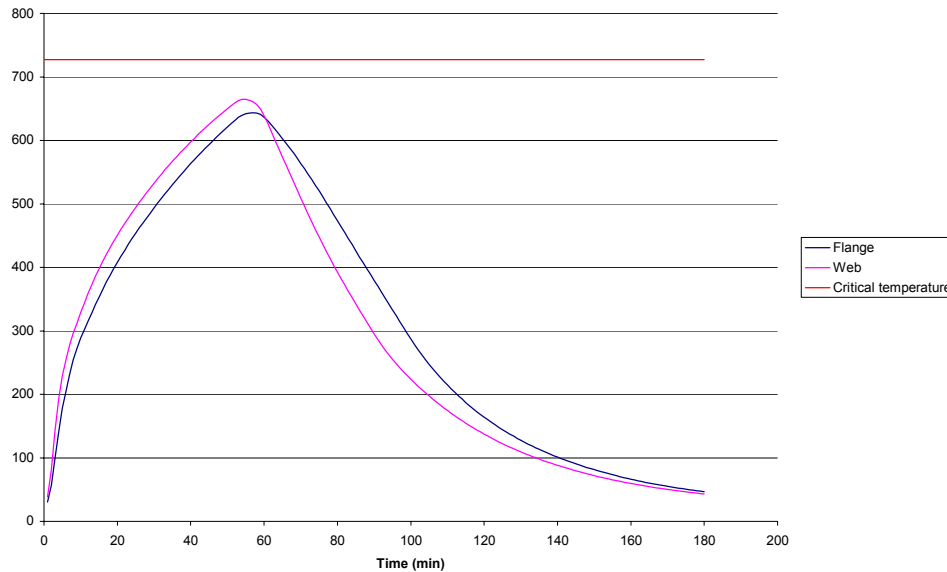


Fig. 14 – Evolution of temperature during fire in an office in the section insulated with 0.6 mm

This study has shown an illustration of the use of equivalent thermal properties for the estimation of the required thickness of intumescent paint. Two types of coating have been used and the corresponding thicknesses are close. The scenario of a fire in a library requires a thickness which is five times larger than for the scenario of a fire in an office. This is due to the difference of the duration of the fire between the two cases. A good accuracy when estimating the thickness to be applied on members is important in order to reduce the protection cost.

4.4 Encased section

A third solution is to use an encasement of the steel section by a steel box. The solution is based on different experimental tests and numerical approach developed by VTT [xx] within the European project.

Different types of encasements may be used:

- 1 mm carbon steel (Mbox) encasement, air gap 12 mm
- 2 mm carbon steel (Mbox) encasement, air gap 12 mm
- 1 mm stainless steel (Sbox) encasement, air gap 12 mm
- 2 mm stainless steel (Sbox) encasement, air gap 12 mm
- 1 mm stainless steel (Sbox) encasement, air gap 30 mm
- 1 mm stainless steel (Sbox) encasement, air gap 2 mm

In the first four cases, the air gap between the column flanges and the steel encasement was 12 mm. The calculation program is based on the assumption that the air gap is relatively small so that the heat transfer between the encasement and the column can, within reasonable accuracy, be assumed to take place in four separate compartments. On the other hand, decreasing the air gap thickness will lead to lower column temperatures. However, the differences are not too great in the practical range. Emissivity values are $\varepsilon = 0.7$ and $\varepsilon = 0.5$ for carbon and stainless steels, respectively.

Figure 15 gives the calculated temperatures for the case 3 of 1mm stainless steel encasement.

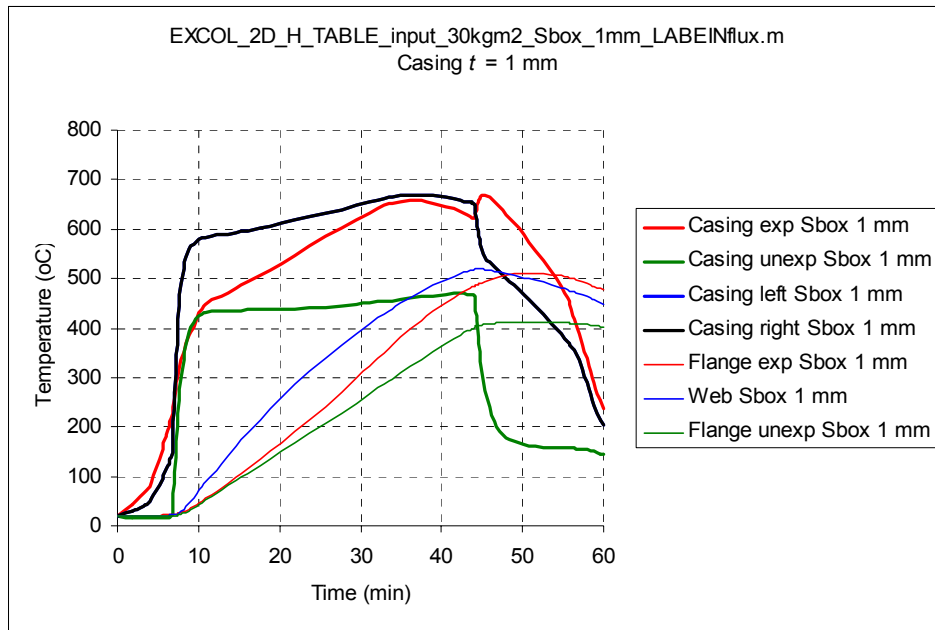


Fig. 15 – Results for 1 mm stainless steel (SBox) encasement, air gap 12 mm

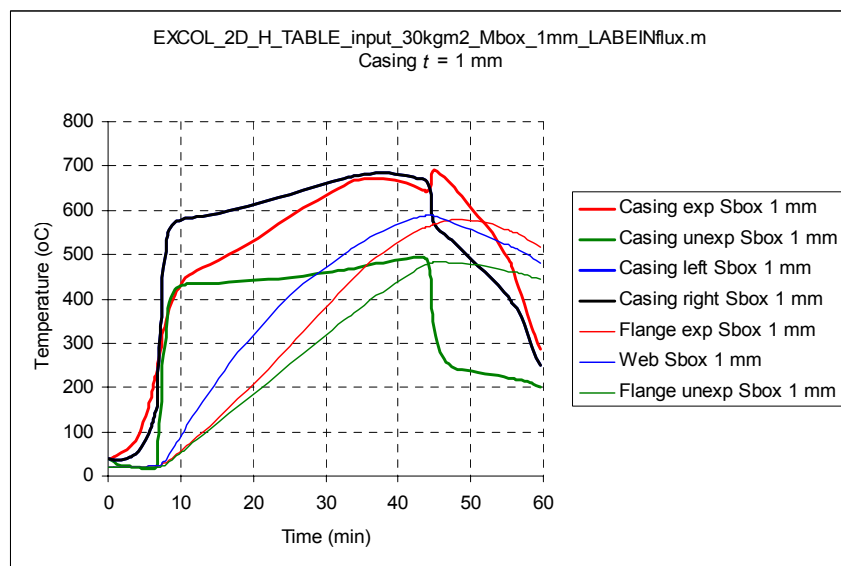


Fig. 16 – Results for 1 mm carbon steel (SBox) encasement, air gap 12 mm

It can be seen from these two figures that using a stainless steel casing (Sbox) will reduce the column temperatures by almost 100 degrees, when compared to using a carbon steel casing (Mbox). This is mainly due to the differences in emissivities between stainless steel and carbon steel. However, closer to time 60 minutes, the difference has decreased. On the other hand, increasing the casing steel thickness from 1 mm to 2 mm does not appear to have much influence on the results. Also, the influence of air gap variation is small. Nevertheless, these two solutions lead to lower temperature than the critical one.

Calculations of the level 1 corresponding to higher fire load and lower critical temperature have shown that the protection of the steel columns using a simple casing is not sufficient due to the much longer fire duration and the lower critical temperature of the columns. The temperature time curves are given in the following figure. So, for higher fire resistance times, additional or different type of fire protection has to be used.

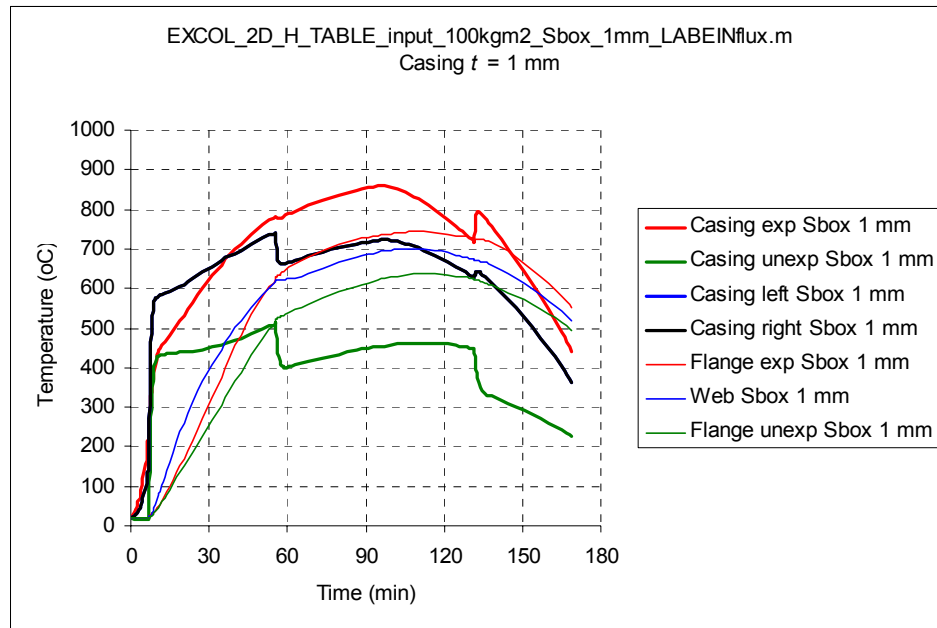


Fig. 17 – Results for 1 mm stainless steel (SBox) encasement, air gap 12 mm for the level 1.

5. CONCLUSION

The external steel columns in the present study case were considered using two methods, namely according to the Eurocode method for the steady state situation, and according to a new transient method. The current Eurocode steady state model has predicted that the fire stability of unprotected steel structure is not ensured. Then a new transient model developed within a European research has been applied. This model allows verifying protected steel structures but also composite structures. Instead of satisfying an ISO-Fire resistance rating requirements, the extension of the current model allows optimizing protection thickness or accepting solutions that are currently not be accepted. In refurbishment conditions, such approach should help designers to find solutions for the insulation of external structural elements.

6. REFERENCE

- [1] EC1 – EUROCODE 1 PART 1.2 (ENV 1991-1-2)
- [2] EC3 – EUROCODE 3 PART 1.2 (ENV 1993-1-2)
- [3] “Development of design rules for the fire behaviour of external steel structures”, ECSC contract 7210-PR380 (01/07/2002-31/12/2005)
- [4] Heat transfer model on external steel elements and external hollow sections filled with concrete, LABEIN, J. Unanua, F. Morente, Doc PR380 n° 96, 2005.
- [5] Simple Calculation Methods for the determination of the temperature increase of steel sections protected with steel casings, VTT, O. Kaitila, Doc PR380 n° 76, 2004.
- [6] Schleich J-B., Cajot L-G., *et al.* "Competitive steel buildings through natural fire safety concept." ECSC Research 7210-SA/125,126,213,214,323,423, 522,623,839,937, B-D-E-F-I-L-NL-UK & ECCS, 1994-98, Draft Final Report July 2000 - Part 1 to 5.



MECHANICAL RESPONSES OF A STEEL COLUMN EXPOSED TO A LOCALIZED FIRE

Daisuke KAMIKAWA¹, Yuji HASEMI²

Kaori YAMADA³, and Masatoshi NAKAMURA⁴

ABSTRACT

The purpose of this paper is to demonstrate mechanical responses of a square steel column adjacent to a fire source.

In this report, we conducted fire resistance experiments on a square steel column exposed to a localized fire for some restraint conditions. Square steel column (STKR400, 0.1 x 0.1 (m), 3.2mm thick and 1.6m tall) was prepared as the specimen. A 0.3m square diffusion burner was located just beside the column as the fire source. We use propane as the fuel, and its HRR is 52.5kW.

The temperature distributions and deformation of column were measured for all conditions. Additionally, the horizontal binding force at the column capital and axial force were measured for some conditions.

From these experiments, it was confirmed that large complex deformation is caused by unequal temperature distribution. We have to consider these influences on structural safety especially on buckling, although localized heating seems to be much safer than full-developed fire.

¹ Research Assistant, Waseda University, Department of Architecture, Okubo 3-4-1, Shinjuku-ku, Tokyo, 169-8555, Japan, email : d-kamikawa@suou.waseda.jp

² Professor, Waseda University, Department of Architecture, Okubo 3-4-1, Shinjuku-ku, Tokyo, 169-8555, Japan, email : hasemi@waseda.jp

³ Graduate student, School of Science and Engineering, Waseda University, Okubo 3-4-1, Shinjuku-ku, Tokyo, 169-8555, Japan, email : kahori.01@asagi.waseda.jp

⁴ Taisei Corporation, Technology center, Naze-chou 344-1, Totsuka-ku Yokohama-shi, 245-0051, Japan, email : nkmmst00@pub.taisei.co.jp

1. INTRODUCTION

If we consider such structures as atria, open car parks, railway stations, etc. in terms of fire safety design, types and location of the fire load is generally limited and specifiable. In such cases, any fire would be of a fuel-controlled type, and the fire and the effect of heating on structural members could remain localized. It may be assumed that the rise in temperature is smaller than in the event of all the members being subjected to heating by fire. It is obvious that the fire safety assessment based on assumption of full-developed-fire leads superfluous fire resistance design for such cases. To make a rational fire safety assessment, we must adopt the concept of localized fire.

From such background, the authors conducted some experiments and FEM analysis, and demonstrated the procedure to predict the temperature distributions of metal member subjects exposed to a localized fire^{1,2)}. The next problem is assessment of structural safety on the predicted thermal condition. This will be also done by some computational analysis like FEM that is common with the fire safety assessment. But we must consider the issues caused by temperature gradient that is not seen in usual fire safety assessment based upon uniform heating. There are few previous studies that deal with fire resistance experiments on members exposed to a localized fire.

Therefore, we focused on the column that has much effect on structural safety, and conducted fire resistance experiments on a square steel column exposed to a localized fire to comprehend its mechanical profile. Measurements were conducted using a model scale facility on temperature distribution, deformation of specimen, the horizontal binding force at the column capital and axial force. Four restraint configurations were chosen to investigate the fundamental profile of mechanical responses of a column exposed to a localized fire. Another purpose of this experiment is to acquire foundational data to examine the validity of numerical analysis model.

2. GENERAL DESCRIPTION OF THE EXPERIMENTS

2.1 Experimental Conditions

Although there are some patterns of geometric relationship between fire source and column, we assumed the state that a column is adjacent to a fire source. A 0.3m square diffusion burner was located just beside the column as the fire source. We use propane as the fuel, and its HRR is 52.5kW. Square steel column (STKR400, 0.1 x 0.1 (m), 3.2mm thick and 1.6m tall) was prepared as the specimen.

The mechanical response of the heated column is influenced by restraint forces of exterior frame, and these restraint conditions vary from one site to another. Therefore, we chose four fundamental restraint conditions to comprehend its property of mechanical responses. Figure 1 shows the images of experimental conditions and concepts.

For all Cases, the rotation and displacements at column bottom were restrained. In the case 1, the column capital was free from any restrains. In the case 2~4, the horizontal displacement at column capital was restrained. Additionally, the vertical displacement at column capital was also restrained in case 2, the constant vertical load (allowable stress ; 186kN) was added in the case 3. In the case 4, the vertical load was increased gradually after the temperature distribution come up to steady state.

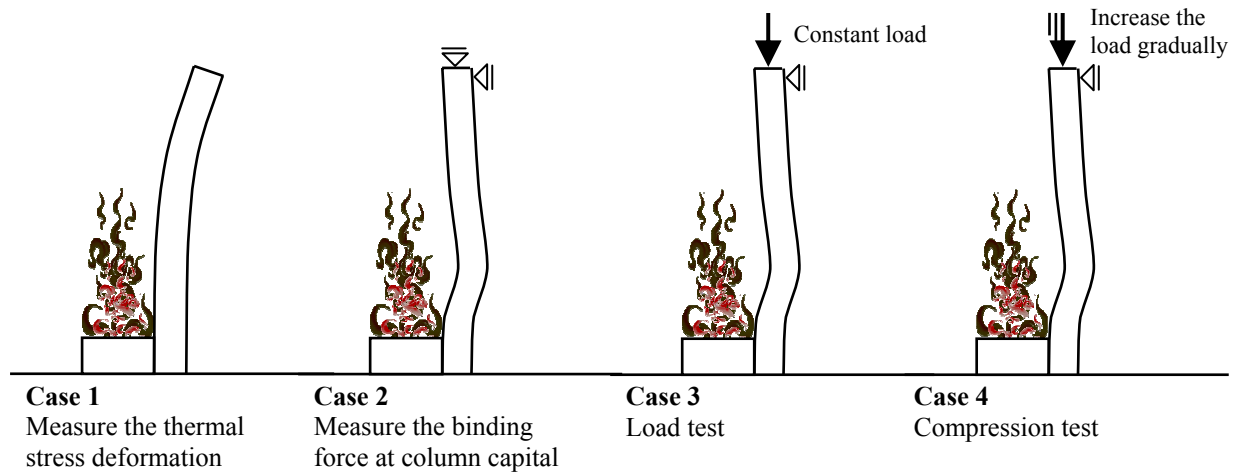


Figure 1 Images of experimental conditions and concepts

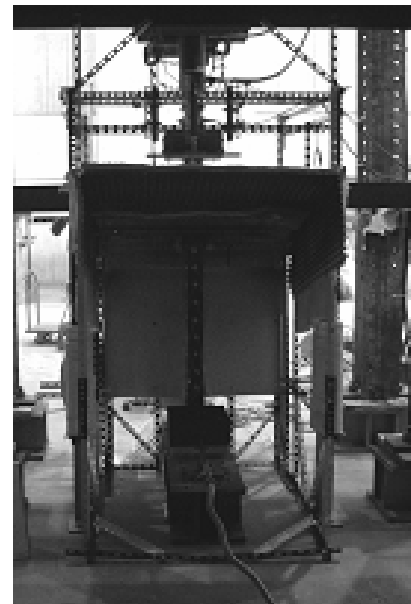
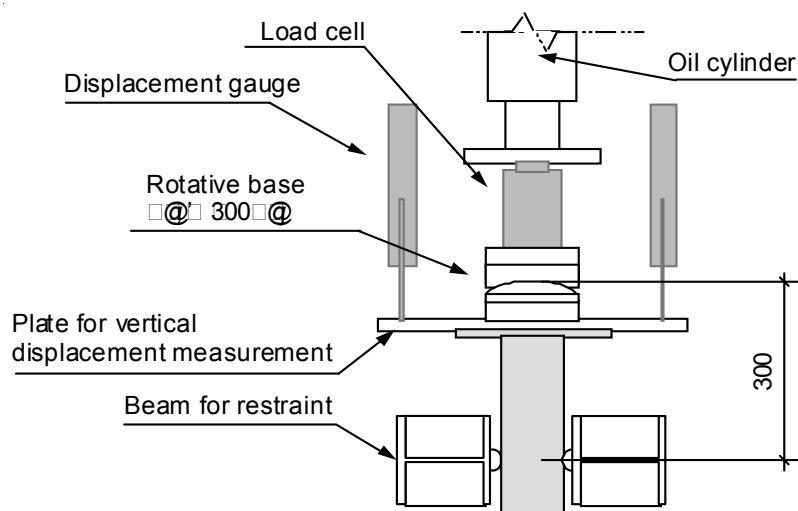
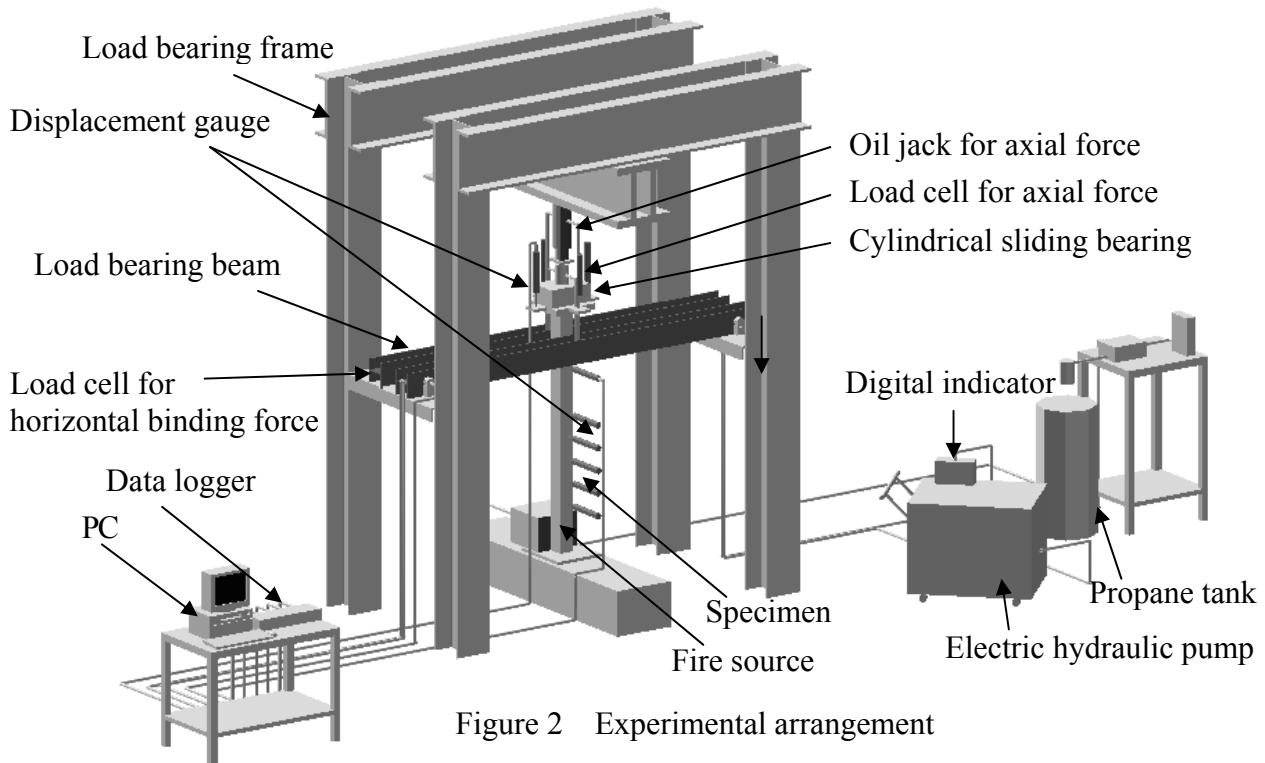
Table 1 Experimental conditions

Case No.	Restraint / axial force conditions at column capital	Measured item
Case 1	Free	Horizontal and vertical deformation
Case 2	Restrain horizontal and vertical displacement	Horizontal deformation, Horizontal and vertical binding force at column capital
Case 3	Restrain horizontal displacement, Add the constant vertical load	Horizontal and vertical deformation, Horizontal binding force at column capital, Axial force
Case 4	Restrain horizontal displacement, Increase the vertical load gradually	Horizontal and vertical deformation, Horizontal binding force at column capital, Axial force

2.2 Experimental arrangement

Figure 2,3 shows the experimental arrangement (for case 2~4). A load bearing frame was used and an oil jack (maximum output : 490kN) was set up just above the specimen. This oil jack was controlled by electric hydraulic pump, and this pump was operated according to the outputs from displacement gauges and load cell through the digital indicator. A load cell for axial force, cylindrical sliding bearing, and cruciform steel plate for vertical displacement measurement were installed between specimen and jack. The horizontal displacement at column capital was restrained by two load bearing beams. This restrained point corresponds to the focal axis of cylindrical sliding bearing. The horizontal binding force was measured by four load cells placed at each end of bearing load beams. These restraint and measurement of horizontal binding force were covered only for the direction of heated surface normal.

A 0.3m square diffusion burner was located just beside the column as the fire source, and the height of burner surface was 0.25m (from the base of column). We use propane as the fuel, and its HRR is 52.5kW. Figure 4 shows the specifications of a specimen. Square steel column (STKR400, 0.1 x 0.1 (m), 3.2mm thick and 1.6m tall) was prepared as the specimen. The partition walls for smoke exhaust were arranged around the specimen to protect experimental apparatus.



2.3 Measurement Items

In all cases, the temperature distributions of specimen surfaces, horizontal deformation and vertical displacement were measured. Temperature was measured with K-type (chromel-alumel) thermocouples ($\phi 0.65\text{mm}$) fixed on specimen surfaces with spot-welded steel foil. The location for temperature measurement is shown in Figure 4. The horizontal displacements were measured at backside surface with displacement gauges (backside means the opposite side of heated lateral). The vertical displacement of the column capital was measured with displacement gauges at the four points on cruciform steel plate above the specimen. The location for displacement measurement is shown in Figure 5.

In the case 2~4, the horizontal binding force at column capital was measured with four load cells (measuring range : 5kN) placed at each end of bearing load beams. And the axial force was measured with load cell under the oil jack (measuring range : 500kN).

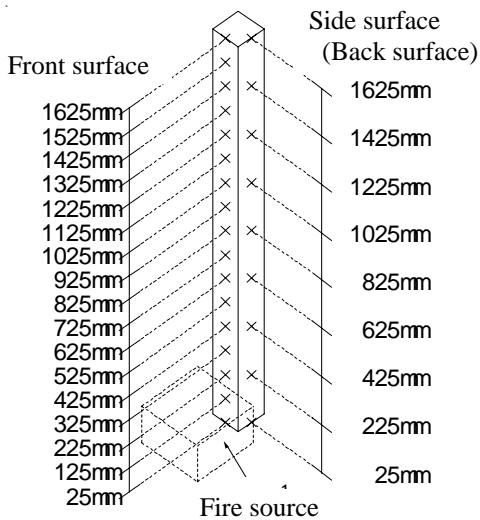


Figure 4
The location for
temperature measurement

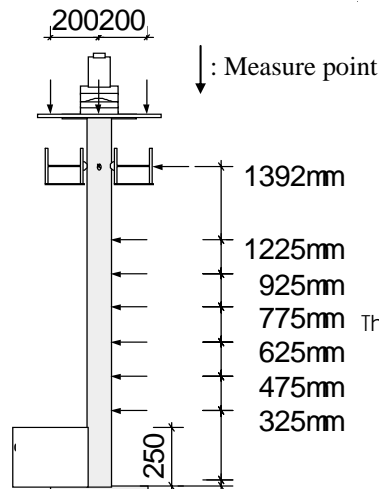


Figure 5
The location for
displacement measurement

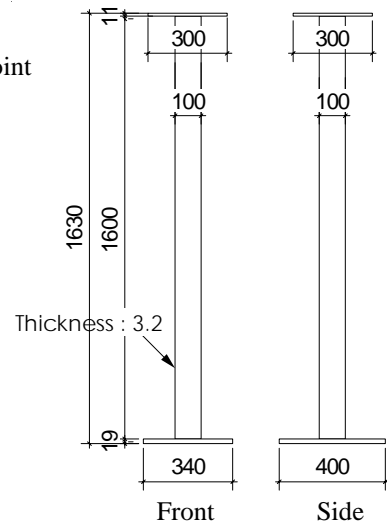


Figure 6
Specimen elevation

3. EXPERIMENTAL RESULT

3.1 Temperature Distribution

Figure 7 shows the temperature transition, and figure 8 shows temperature distribution at the steady state for the case 1. After 15 min of fire exposure, temperature of each lateral became almost steady state. In the front surface (heated surface), the peak of temperature appeared at around $z=400$ mm, and its value was 570°C at steady state. The temperature distribution and its transitions for the case 2~4 gave close agreement with that for case 1 shown in figure 7 and 8.

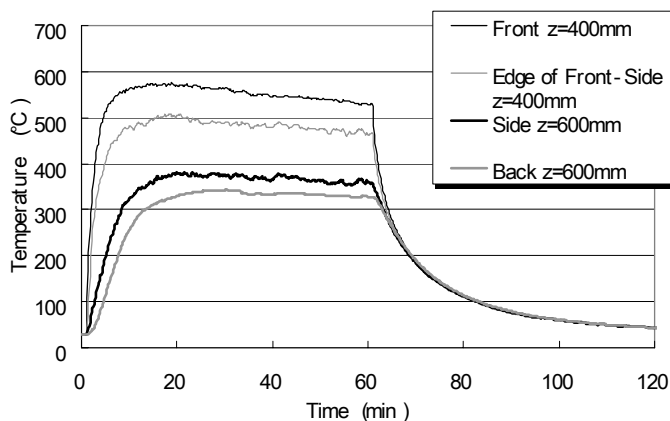


Figure 7
Temperature transition for the case 1

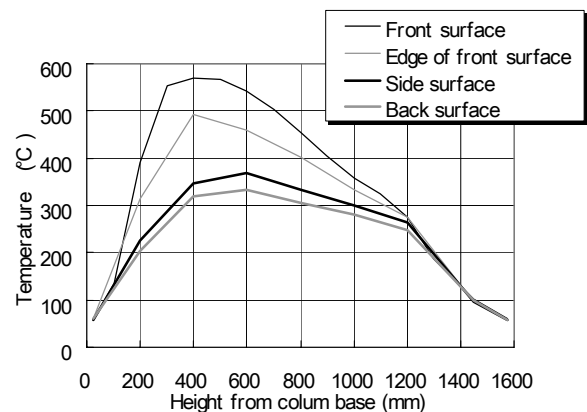


Figure 8
Temperature distribution at steady state
for the case 1

3.2 Case 1 ; Experiment for measurement on the thermal stress deformation without restraint

Figure 9 and 10 show the transition of horizontal deformation. The specimen started to bend toward backside immediately after ignition. The amount of displacement reached maximum value at around 6 min, and then the deformation decreased and became steady value. After the extinction, the deformation decreased and finally it bent toward front side slightly. This indicates the occurrence of plastic deformation at the heated surface.

The transition of vertical displacement and angle of rotation of column capital is shown in Figure 11. The expansion became almost steady state at around 15 min and its value was 5mm. The rotation angle of column capital also reached maximum value at around 6 min, and then it decreased and became steady value.

Note : The positive value of horizontal displacement means displacement toward back side.

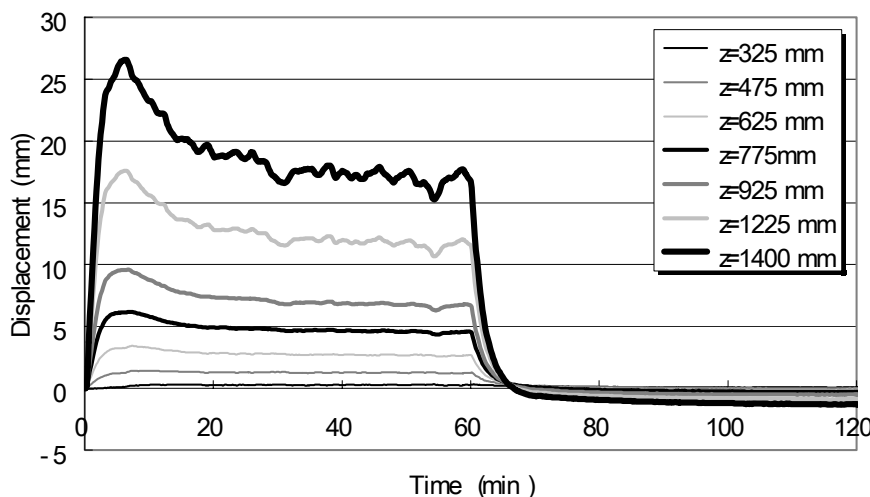


Figure 9
Transition of horizontal displacements for the case 1

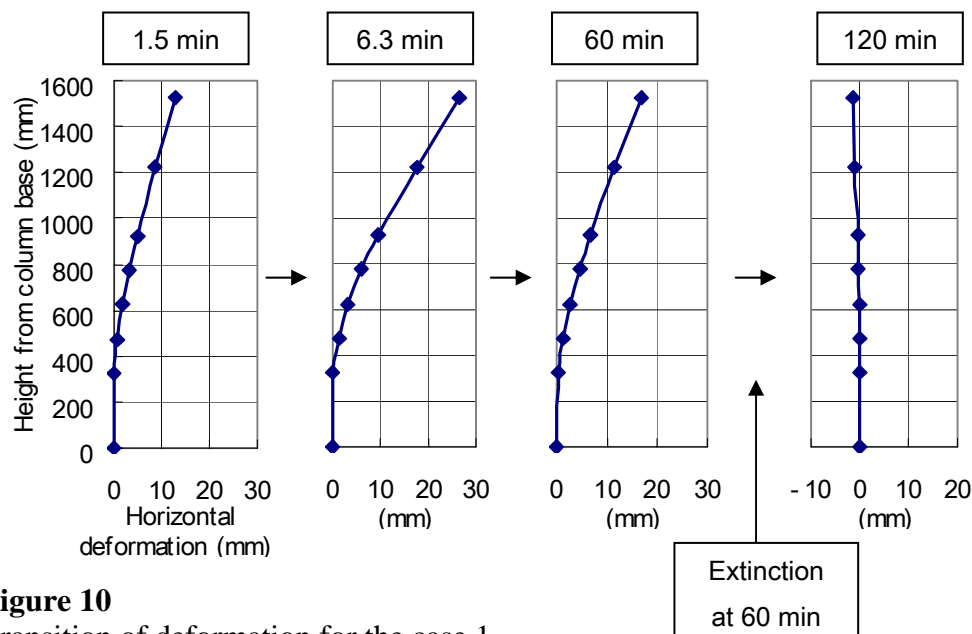


Figure 10
Transition of deformation for the case 1

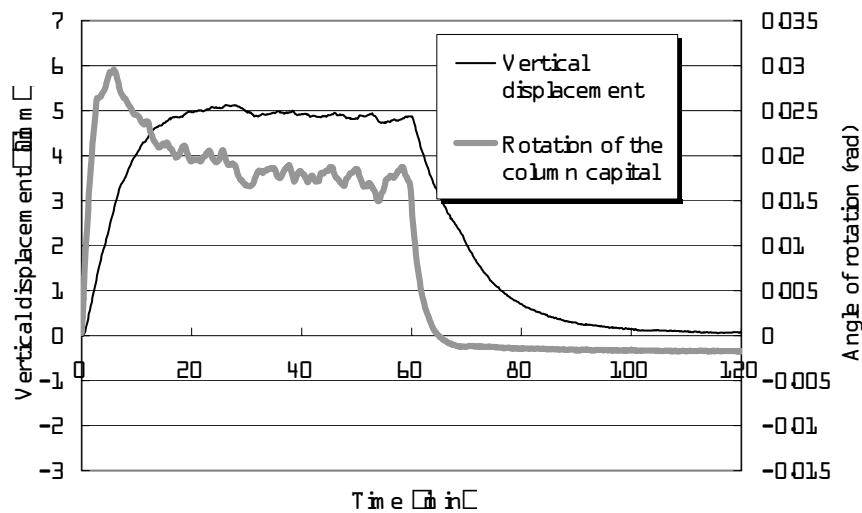


Figure 11

The transition of vertical displacement and angle of rotation of column capital for the case 1

Note : The positive value of vertical displacement means expansion.

3.3 Case 2 ; Experiment for measurement on the binding force at column capital

Figure 12 and 13 show the transitions of horizontal displacement. Figure 14 shows the transitions of vertical and horizontal binding forces at column capital.

Soon after ignition, the central region of the specimen was displaced toward burner side. The amount of displacement toward front side reached maximum value at 5 min. The height of the deformation apex was around $z=475\text{mm}$. After that, the amount of displacement decreased and the central region of the specimen became convex toward back side. After the extinction, the specimen deformed toward back side rapidly. The maximum amount of displacement toward back side was 2.5 mm at $z=475\text{mm}$. This value of displacement was measured without vertical restraint because the restraint against contraction of specimen was impossible. Therefore, the value might be smaller for the right restraint condition, because tensile force will be generated in the specimen.

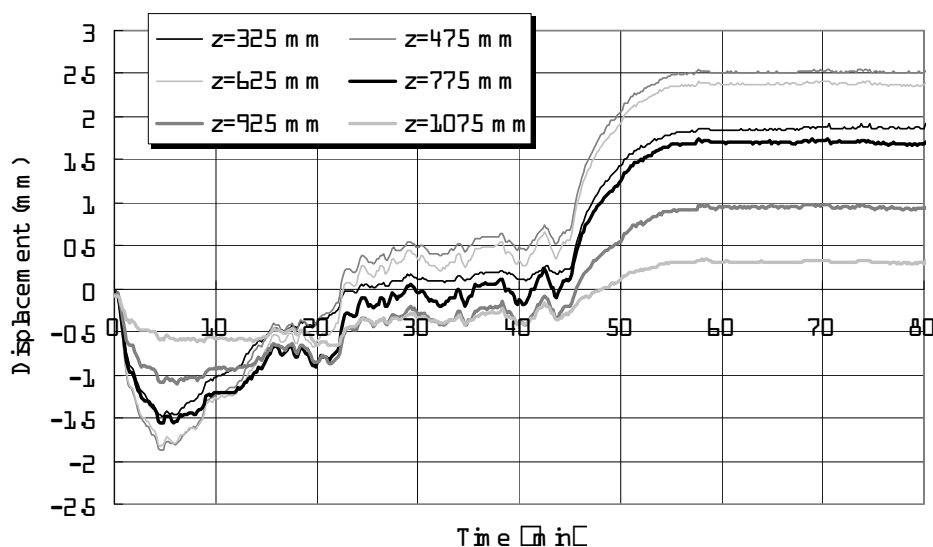


Figure 12 The transitions of horizontal displacement for the case 2

Note : The positive value of horizontal binding force means force toward back side.

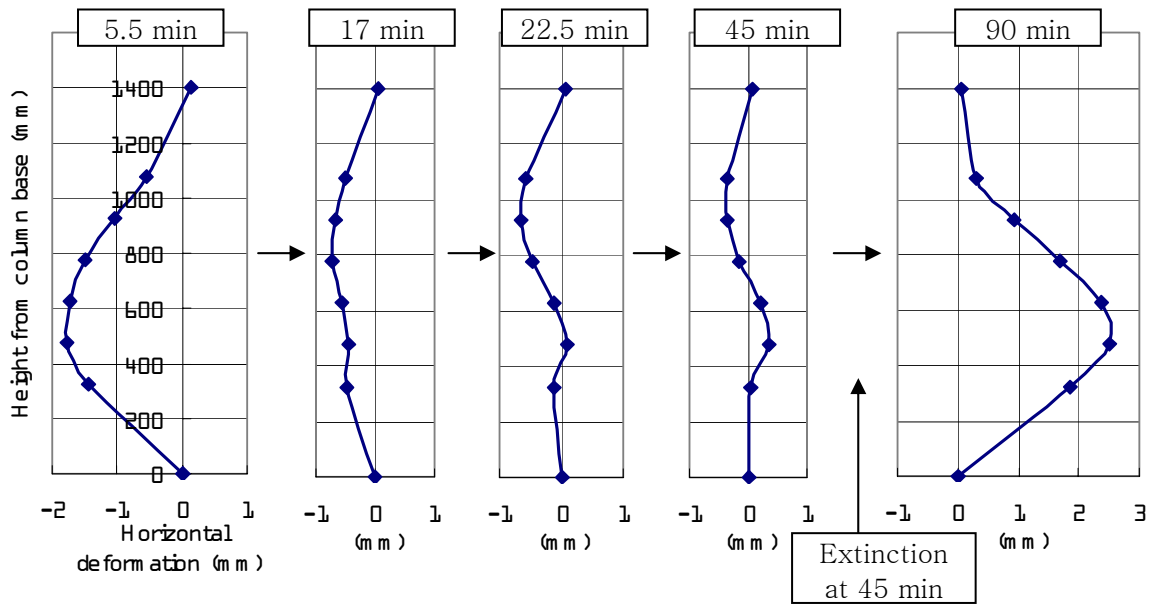


Figure 13
Transition of deformation for the case 2

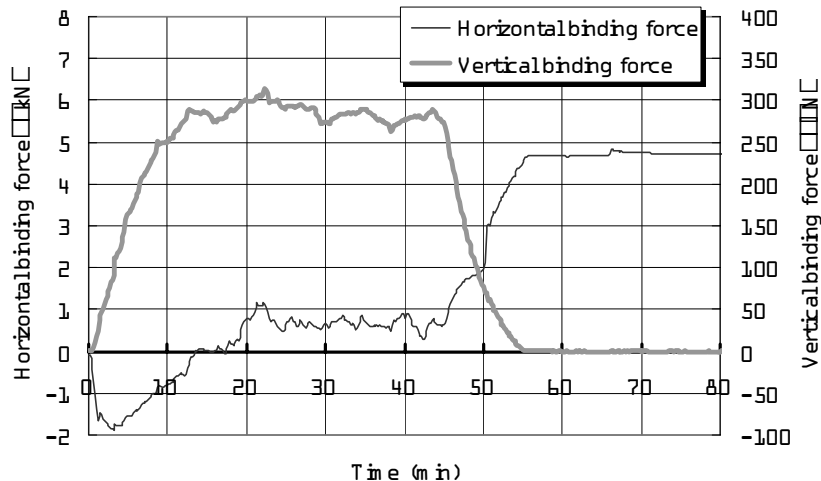


Figure 14 The transitions of binding force for the case 2

Note : The positive value of horizontal binding force means force toward back side.
The positive value of vertical binding force means force toward downward.

The horizontal binding force toward burner side appeared immediately after ignition, and it started to decrease in a few minutes at -2kN (The negative value means binding force toward front side). And then, its direction changed and became steady at around 0.8kN. The transition of horizontal displacement was similar to that of the horizontal binding force.

The vertical binding force increased linearly in first 8 min, and it reached 250kN. And then, it increased gradually and reached 310kN at 23 min. This time when the vertical binding force became the maximum is almost corresponding to the period when the displacement at hot section changed to positive value. After that, the vertical binding force decreased gradually, and became steady at 280kN. During this period, the deformed shape changed significantly, but the vertical binding force did not change so much. After the extinction, it decreased rapidly, and became 0 at 10 min from the extinction. That value seems to be negative according to the further reduction in specimen temperature if the contraction of specimen is restrained.

3.4 Case 4 ; Compression test

In this case, the compression was started after the temperature distribution became steady state (; 52min after the ignition). The axial force was added by oil jack above the specimen and increased at a rate of 10kN/min. The buckling occurred at 90 min after ignition, and the fire was extinguished at 97 min.

Figure 15 and 16 show the transitions of horizontal deformation, and figure 17 shows the transitions of axial force and vertical deformation. At 50 min after the ignition, the temperature distribution of the specimen was almost steady state and the vertical elongation of the column was 5.5 mm. Until the axial force reached around 200kN, the specimen shrank linearly against the load. And then, the rate of shrinkage increased, and buckling occurred at 374kN. The specimen was convex toward burner side at the start of compression. As the axial force increased, the hot section became convex toward back side partially. Its convex was around $z=475\text{mm}$. The horizontal transition to here is similar to that for case 2. After that, whole of specimen became convex toward back side, and finally buckling occurred at around $z=630\text{ mm}$.

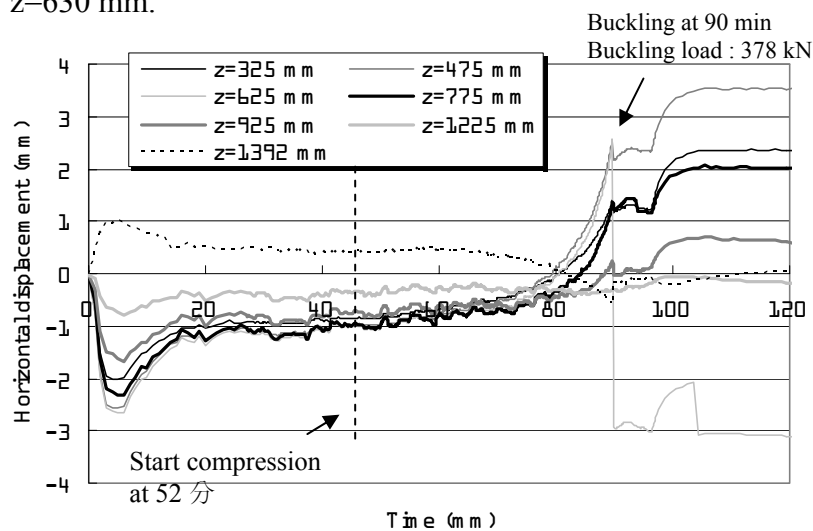


Figure 15
The transitions of
horizontal displacement
for the case 2

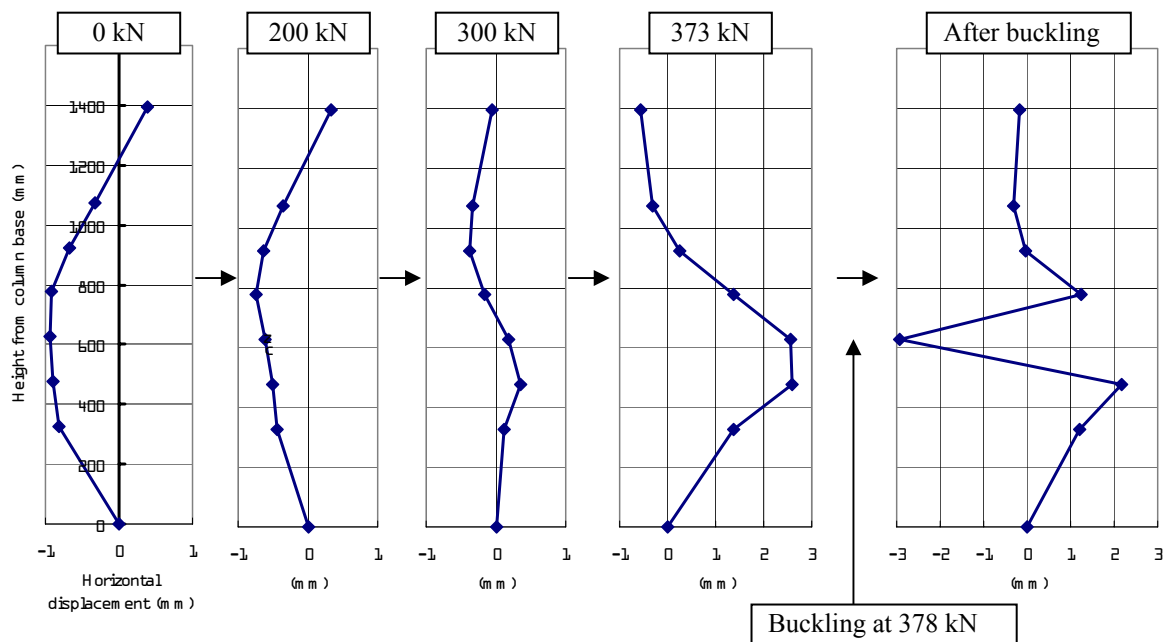


Figure 16 Transition of deformation for the case 4

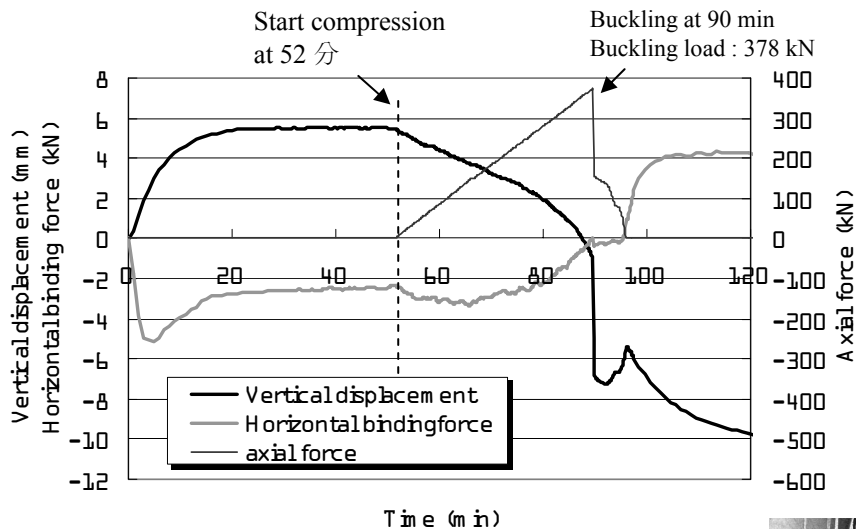


Figure 17
Transitions of axial force and vertical deformation

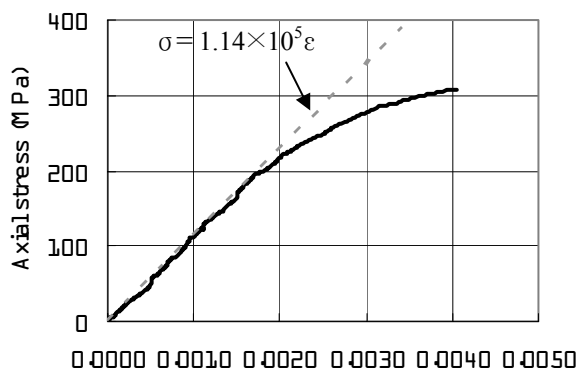


Figure 18
Relationship between axial stress and axial strain

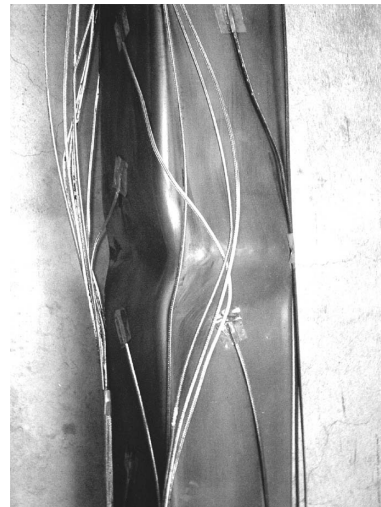


Figure 18 shows the relationship between axial stress and axial strain. The direct proportional relationship was kept until the strain reached around 0.002, and its coefficient was around 1.14×10^5 MPa, which is about half of elastic modulus at room temperature. As the axial stress increased, the strain became bigger than above relation. Buckling occurred when the axial stress was 300 MPa and strain was 0.004.

4. CONCLUSIONS

The fire resistance experiments were conducted on square steel column exposed to a localized fire and its mechanical profile was comprehended. Large horizontal deformation was caused by ununiformity of the temperature distribution. And it is confirmed that complex transitions of deformation is caused by thermal expansion and decrease in strength of steel. Although the temperature rise will be suppressed in the case of localized fire, a detailed prediction might be needed for a column because large deformation will be able to lead to buckling.

5. REFERENCE

- 1) Daisuke Kamikawa, Yuji Hasemi, Takashi Wakamatu, Koji Kagiya : Experimental Flame Heat Transfer And Surface Temperature Correlations For A Steel Column Adjacent To And Surrounded By A Pool Fire, Proceedings of IFASS 2002, 2002.6
- 2) Daisuke Kamikawa, Yuji Hasemi, Takashi Wakamatu, Koji Kagiya : Prediction of The Thermal Response of A Metal Column Exposed To A Localized Fire, Proceedings of SiF '04 THIRD INTERNATIONAL WORKSHOP STRUCTURES IN FIRE, 2004.5,



FIRE LOAD BEHAVIOR OF STEEL BUILDING COLUMNS WITH DAMAGED SPRAY-APPLIED FIRE RESISTIVE MATERIAL

Stephen PESSIKI¹, Kihyon KWON² and Byoung-Jun LEE³

ABSTRACT

Analyses were performed to examine the fire load behavior of steel H columns with damaged spray-applied fire resistive material (SFRM) subjected to concentric axial compression. The columns treated in the research are typical of multi-story steel building construction practices in the United States. Nonlinear heat transfer analyses were performed to predict the temperature distribution in the steel columns under the action of the ASTM E-119 standard fire temperature-time curve. Nonlinear structural analyses were then performed to evaluate the influence of temperature on column axial load behavior. Variables treated in the analyses include size and location (flange or web) of removed or reduced SFRM, and fire duration. The analytical approach used in the research was validated by comparing the analytical results with previous experimental fire tests reported in the literature. This paper focuses on the influence of the variables treated in the analyses on the temperature distribution in the column and the resulting axial load behavior.

1. INTRODUCTION

Analyses were performed to examine the fire load behavior of steel H columns with damaged spray-applied fire resistive material (SFRM) subjected to sustained axial compression. The objective of the research was to determine the influence of the damaged SFRM on the axial load behaviour of the columns in a fire. The columns treated in the analyses were W14x109 sections made of Grade 50 steel ($F_y = 345\text{MPa}$). The intended thickness of spray-applied fire resistive material for these columns for a 2 hour fire rating is

¹ Professor and Chairman, Lehigh University, Department of Civil and Environmental Engineering, Bethlehem PA, USA; email: pessiki@lehigh.edu.

² Research Assistant, Lehigh University, Department of Civil and Environmental Engineering.

³ Research Scientist, Lehigh University, ATLSS Center.

27 mm. This column section and this thickness of SFRM are typical of multi-story steel building construction practices in the United States.

Nonlinear heat transfer analyses were performed to predict the temperature distribution in the steel columns under the action of the ASTM E-119 standard fire temperature-time curve. Nonlinear structural analyses were then performed to evaluate the influence of temperature on column axial load behavior. Variables treated in the analyses include size and location (flange or web) of removed or reduced SFRM, and fire duration.

2. ANALYSIS PARAMETERS

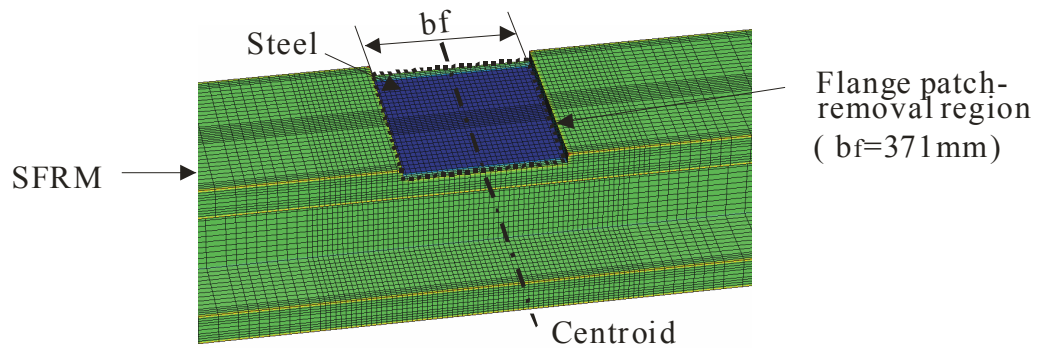
Table 1 and Fig. 1 summarize the analyses that were performed. As shown in the table, the analyses treated both the complete removal of insulation down to the bare steel (identified in the table as Patch Removal Cases), and the reduction of insulation thickness (identified in the table as Thinning Removal Cases).

The patch removal cases treated removal of SFRM on the flanges and the webs. Five different flange patch removal cases were analyzed, identified in the table as FPR1 through FPR5. Shown in the table are the dimensions of the patch removed, denoted as $(wp) \times (lp) \times (tfi,p)$ for the flange, where wp and lp are the width and length of the patch, and tfi,p is the remaining thickness of the SFRM (0 in all patch removal cases). Similarly, for the web patch removal analyses (WPR1 through WPR5), the dimensions of the patch are $(hp) \times (lp) \times (twi,p)$, where hp is the height of the web patch and twi,p is the remaining thickness of the SFRM (again, 0 in all five web patch removal cases). Examples of the finite element models for the flange and web patch removal cases are shown in Fig. 1.

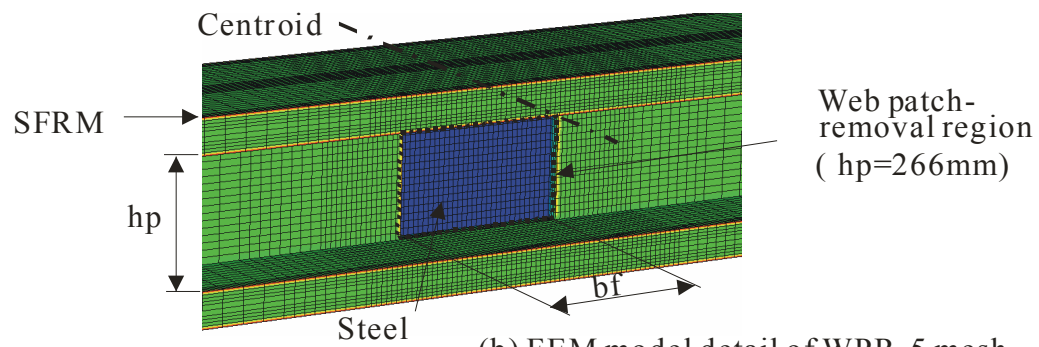
The thinning removal cases treated reduction in thickness of the SFRM on the flange (FTR1 through FTR4) and web (WTR1 through WTR4). The dimensions of the thinned regions are noted in Table 1 using the same notation described above for the patch removal cases. In all thinning removal cases, the area over which the SFRM is reduced in thickness is equal to the area of the largest patch in the patch removal cases.

Table 1. – Summary of analysis cases.

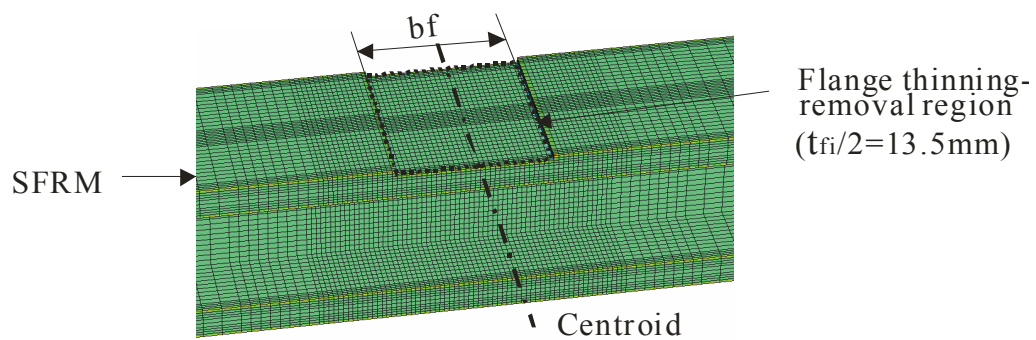
Patch Removal Cases			
(1) Flange		(2) Web	
Patch Dimension (wp)x(lp)x(tfi,p)	I.D.	Patch Dimension (hp)x(lp)x(twi,p)	I.D.
(bf)x(bf/16)x(0)	FPR1	(hi)x(bf/16)x(0)	WPR1
(bf)x(bf/8)x(0)	FPR2	(hi)x(bf/8)x(0)	WPR2
(bf)x(bf/4)x(0)	FPR3	(hi)x(bf/4)x(0)	WPR3
(bf)x(bf/2)x(0)	FPR4	(hi)x(bf/2)x(0)	WPR4
(bf)x(bf)x(0)	FPR5	(hi)x(bf)x(0)	WPR5
Thinning Removal Cases			
(3) Flange		(4) Web	
Patch Dimension (wp)x(lp)x(tfi,p)	I.D.	Patch Dimension (hp)x(lp)x(twi,p)	I.D.
(bf)x(bf)x(3tfi/4)	FTR1	(hi)x(bf)x(3twi/4)	WTR1
(bf)x(bf)x(tfi/2)	FTR2	(hi)x(bf)x(twi/2)	WTR2
(bf)x(bf)x(tfi/4)	FTR3	(hi)x(bf)x(twi/4)	WTR3
(bf)x(bf)x(0)	FTR4	(hi)x(bf)x(0)	WTR4



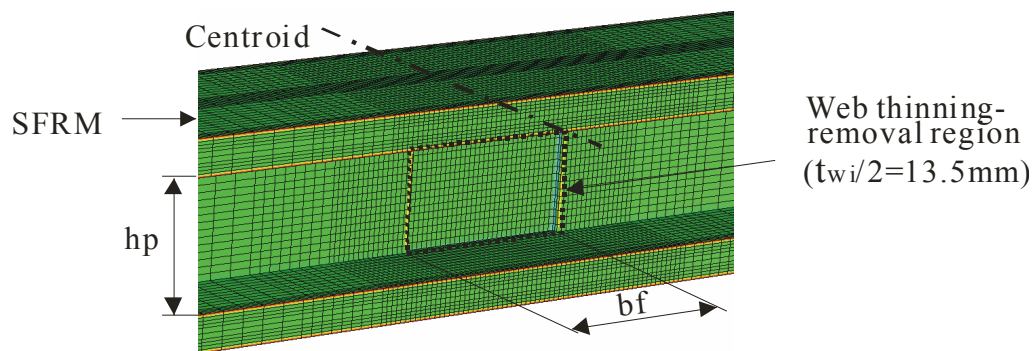
(a) FEM model detail of FPR-5 mesh



(b) FEM model detail of WPR-5 mesh



(c) FEM model detail of FTR-2 mesh



(d) FEM model detail of WTR-2 mesh

Fig. 1 – FEM model details.

3. ANALYTICAL APPROACH

The analyses performed in this research consisted of: (1) nonlinear heat transfer analyses to determine the temperature distribution as a function of time in the steel columns; and, (2) nonlinear structural analyses to determine the structural behavior as influenced by elevated temperature. All of the heat transfer analyses and structural analyses were performed using the ABAQUS which is a commercially available nonlinear finite element analysis program. Details of the program and its features are given in the User's Manual.¹

3.1 Heat Transfer Analyses

The heat transfer mechanisms included in the heat transfer analyses are conduction, convection and radiation. DC3D8 elements were used to model both the steel column and the SFRM. These elements are three-dimensional eight-node linear heat transfer elements. Thermal conductivity of the steel as a function of temperature was specified as given in the Eurocode 3.² Similarly, the specific heat of the steel as a function of temperature was specified as given in the Eurocode 3. Both the thermal conductivity and specific heat relationships are similar to the relationships given in ASCE SFP.³ Convection and radiation boundary conditions were specified where member surfaces were exposed to fire. In this research, a constant emissivity value of 0.7 was used for the steel in all analyses. Table 2 summarizes key heat transfer properties of the steel.

3.2 Structural Analyses

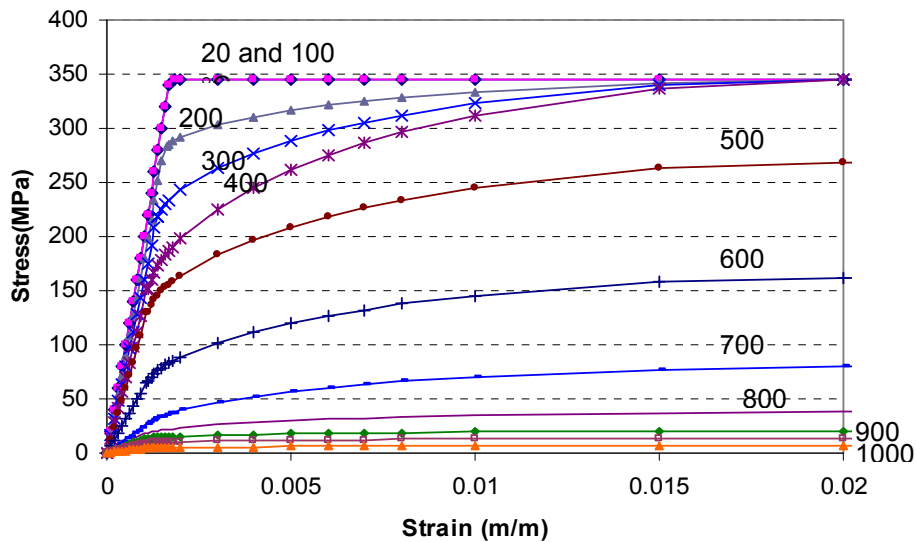
The finite element mesh used in each structural analysis was the same as the finite element mesh used in the corresponding heat transfer analysis that preceded it. This simplified the assignment of temperature history results from the heat transfer analyses as input to the structural analyses. Structural analyses were performed to determine the axial load capacity of each column at fire durations of 30, 60, 90 and 120 minutes. In each analysis, the temperature distribution at the given fire duration was applied first, followed by axial displacement to cause failure of the column in compression. The columns were modeled with pinned boundary conditions at the ends. The stress-strain properties for the steel, shown in Fig. 2, were computed using the Eurocode 3 recommendations. The SFRM was omitted from the structural analysis models since the SFRM provides negligible resistance to axial compression relative to resistance provided by the column. The thermal expansion of the steel was specified as given in the Eurocode 3. This is similar to the thermal expansion of steel given in ASCE SFP up to a temperature of about 750 °C, at which point the Eurocode provides a lower value of thermal expansion than the ASCE SFP.

3.3 Verification of Analytical Models

The analytical approach used in this research was verified in an earlier study which compared the results of finite element analyses with large-scale column tests.⁴ Finite element analyses were performed to model full-scale fire tests of steel box columns that included patch removals of insulation blanket to study the effect of the loss on insulation on column strength.⁵ Details of the experiments and the finite element analyses are given in Reference 4. It was found that good agreement could be obtained between the experiments and analyses.

Table 2. - Material properties.

	Conductivity (W/m-°C)	Specific Heat (J/kg-°C)	Density (kg/m ³)
Steel			
20 °C	53.9	440	7850
100 °C	50.7	488	
300 °C	44.0	565	
650 °C	32.4	814	
800 °C	27.3	803	
900 °C	27.3	650	
1000 °C	27.3	650	
1200 °C	27.3	650	
SFRM			
20 °C	0.042	797	240
50 °C	0.072	868	
100 °C	0.093	712	
300 °C	0.106	1086	
400 °C	0.134	1149	
600 °C	0.216	1293	
800 °C	0.275	1369	
1000 °C	0.369	1412	
1200 °C	0.407	1462	

Fig. - 2 Stress-strain relationship of $F_y = 345$ MPa steel.

4. RESULTS AND DISCUSSION

4.1 Heat Transfer Analyses

The results of the heat transfer analyses are shown in Fig. 3. Included in the figure are plots of temperature for each analysis case shown in Table 1, along with the cases where no insulation was removed and where no insulation was provided. The temperature shown for the flange patch removal and flange thinning cases is for a point on the column cross-section located at the tip of the flange at the location of the SFRM removal or thinning. The temperature shown for the web patch removal and web thinning cases is at the centerline of the web at midheight of the section at the location of the SFRM removal or thinning. The results in Fig. 3 show that removal of even a relatively small patch of SFRM leads to dramatic increases in temperature in the column cross-section at any given point in time.

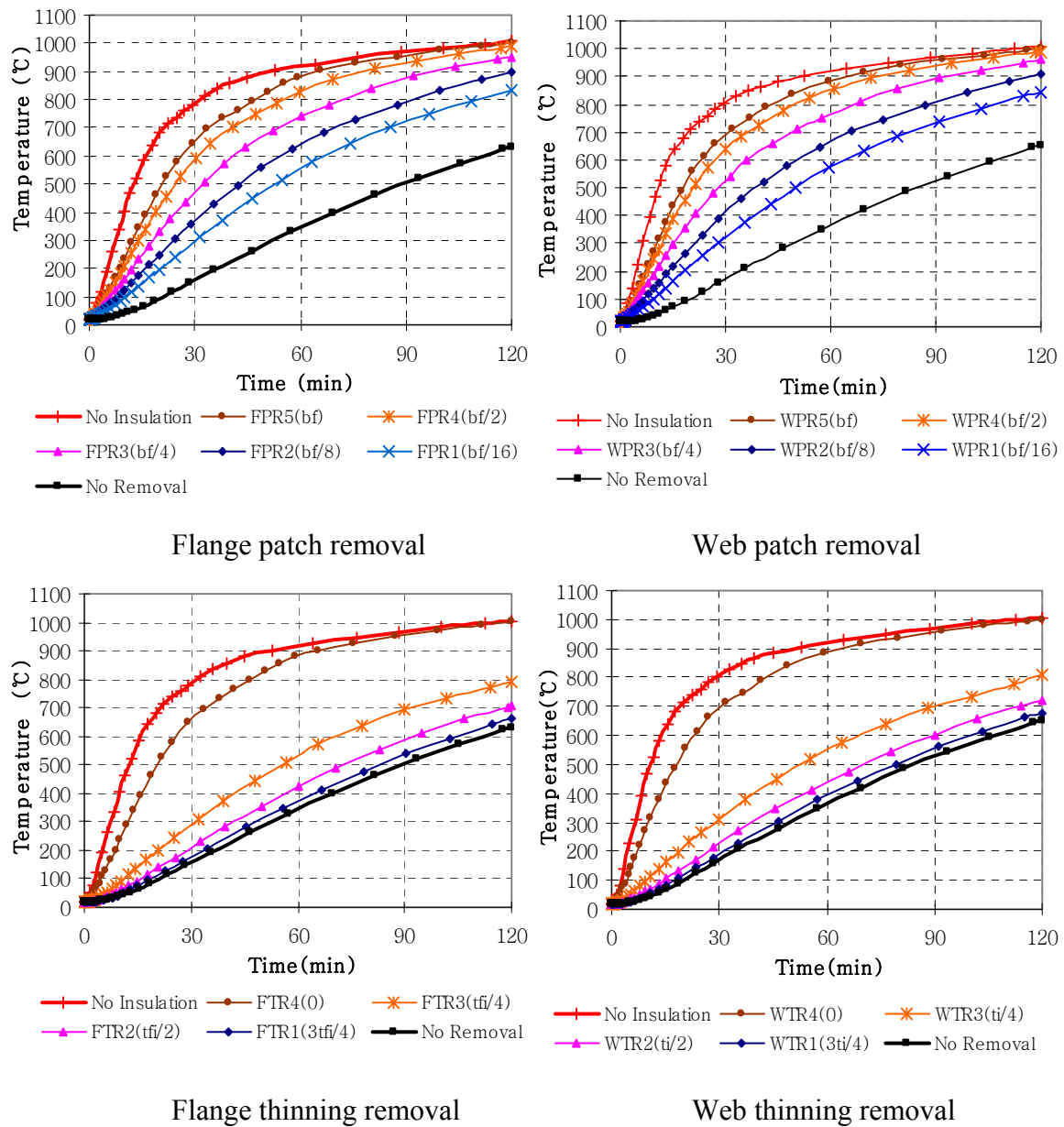


Fig. 3 – Heat transfer analyses results.

4.2 Structural Analyses

The results of the structural analyses are shown in Figs. 4 through 7. Each figure is a plot of the axial strength of the column P , normalized by the axial strength of the column P_u in the absence of a fire. The normalized axial strength P/P_u is plotted versus axial shortening. Because the analyses were performed by applying an axial displacement, the post-peak strength behavior of each column is included. Results are shown for the selected fire durations of 30, 60, 90 and 120 minutes. Figs. 4 and 5 show the results of the flange patch removal analyses and web patch removal analyses, respectively. Similarly, Figs. 6 and 7 show the results of the flange thinning analyses and web thinning analyses, respectively.

Fig. 4 shows that even relatively small removals of SFRM from the flange that are made completely to the bare steel cause dramatic decreases in column axial load capacity for fire durations in excess of 30 minutes.

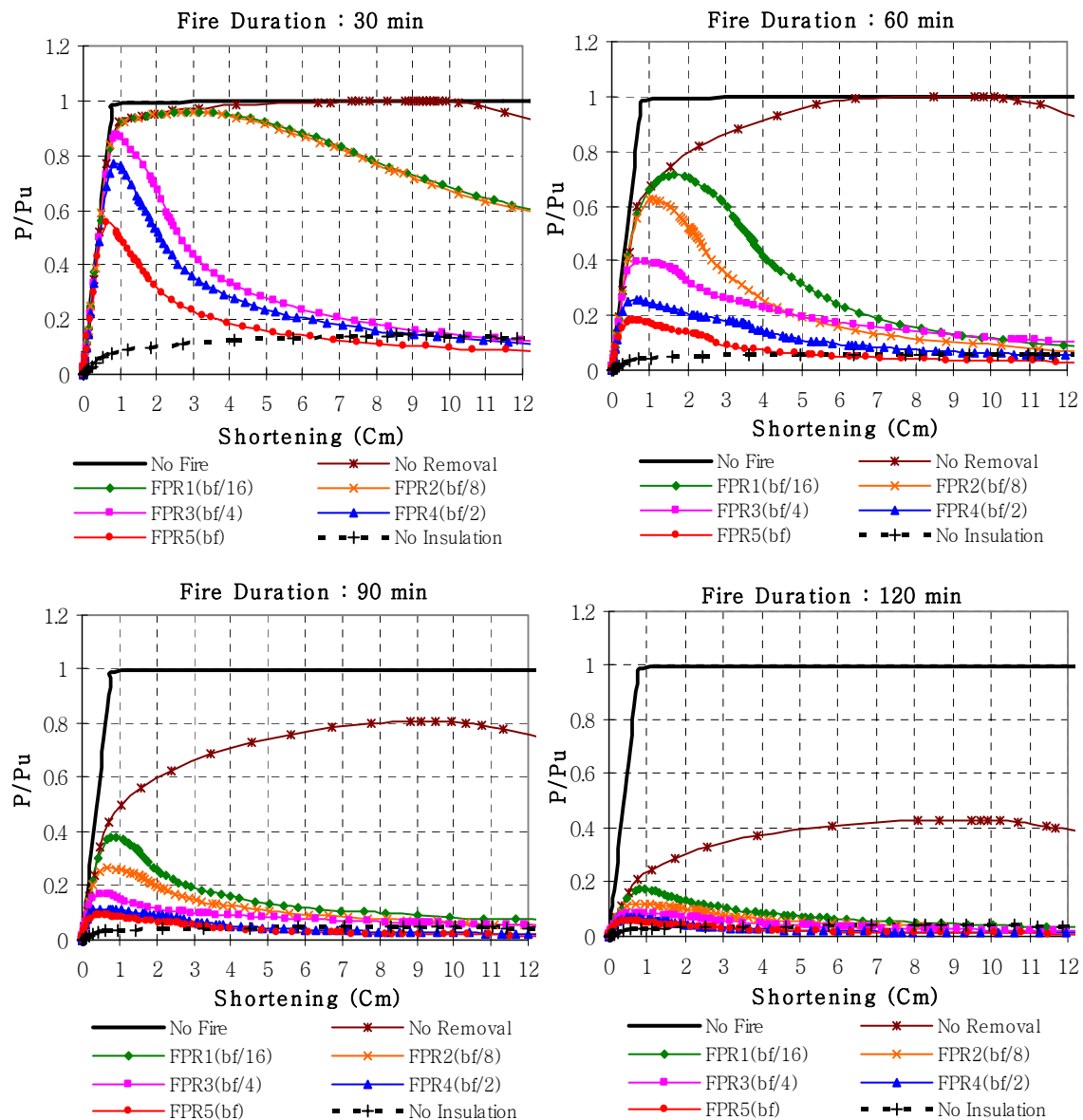


Fig. 4 – P/P_u versus column axial shortening for the flange patch removal analyses.

Fig. 4 also shows that a column with no removal of SFRM will exhibit about 80 percent of its axial load capacity at 90 minutes, and only about 42 percent of its axial load capacity at 120 minutes. This has implications for the allowable service load applied to such a column.

Fig. 5 shows the influence of removal of the SFRM to the bare steel in the column web. The reductions in axial load capacity are not as severe as they are for similar size patches in the flange at any given fire duration. Thus the column section is more sensitive to removal of the SFRM in the flange as compared to the web.

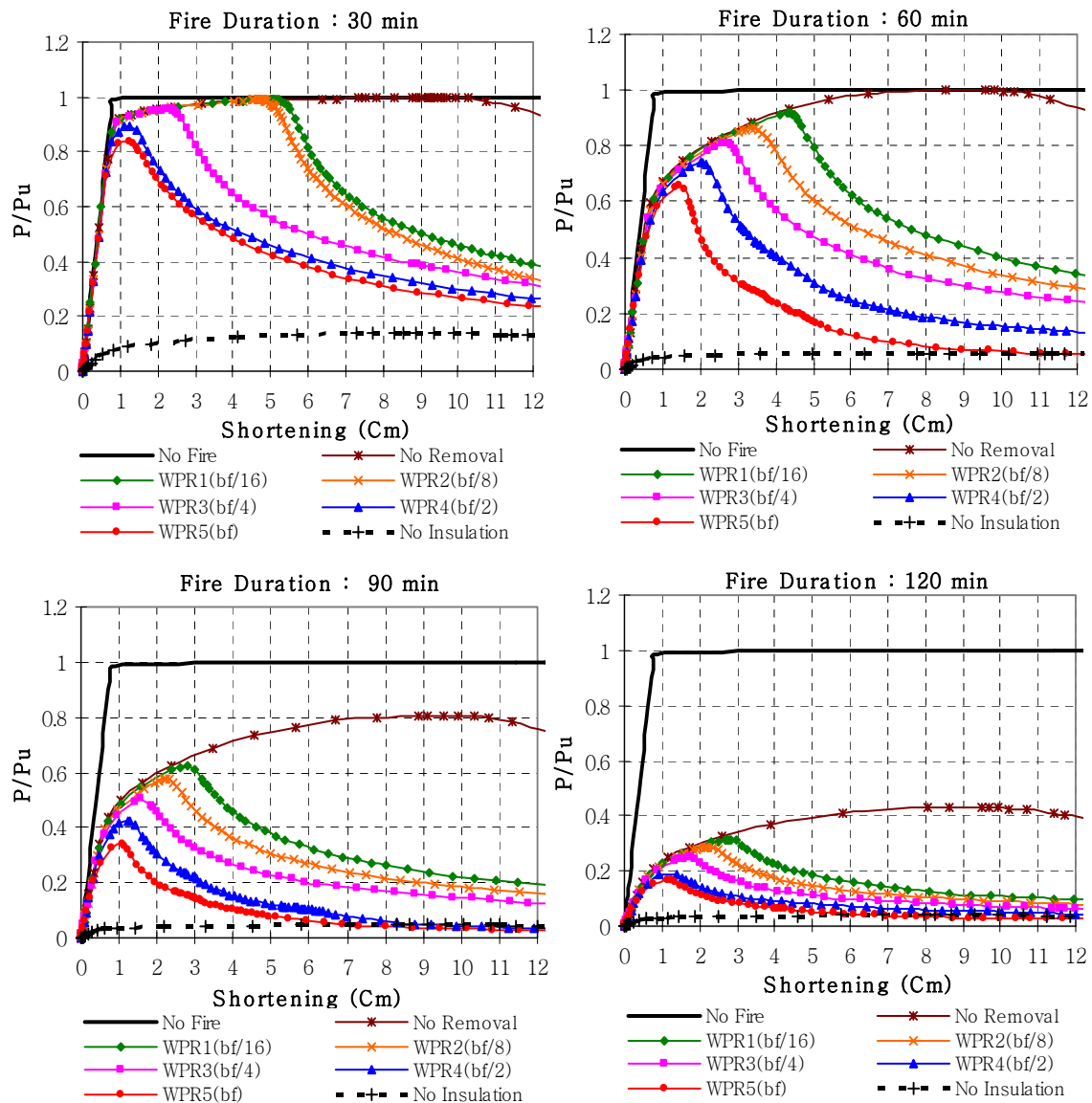


Fig. 5 – P/P_u versus column axial shortening for the web patch removal analyses.

Fig. 6 shows the influence of thinning of the SFRM on the flange. As noted earlier, the area over which the SFRM is reduced in thickness is equal to the largest patch in the flange patch removal case (bfxbf). Fig. 6 shows that the column exhibits similar axial strengths when the flange SFRM is reduced to 3/4, 1/2 and 1/4 of its intended thickness at fire

durations of 30 and 60 minutes. The axial strengths differ by greater amounts at fire durations of 90 and 120 minutes. Finally, at 30 minutes, the column exhibits significantly more axial deformation capacity for the cases where the SFRM is reduced to 3/4 and 1/2 of its intended thickness as compared to 1/4 of its intended thickness.

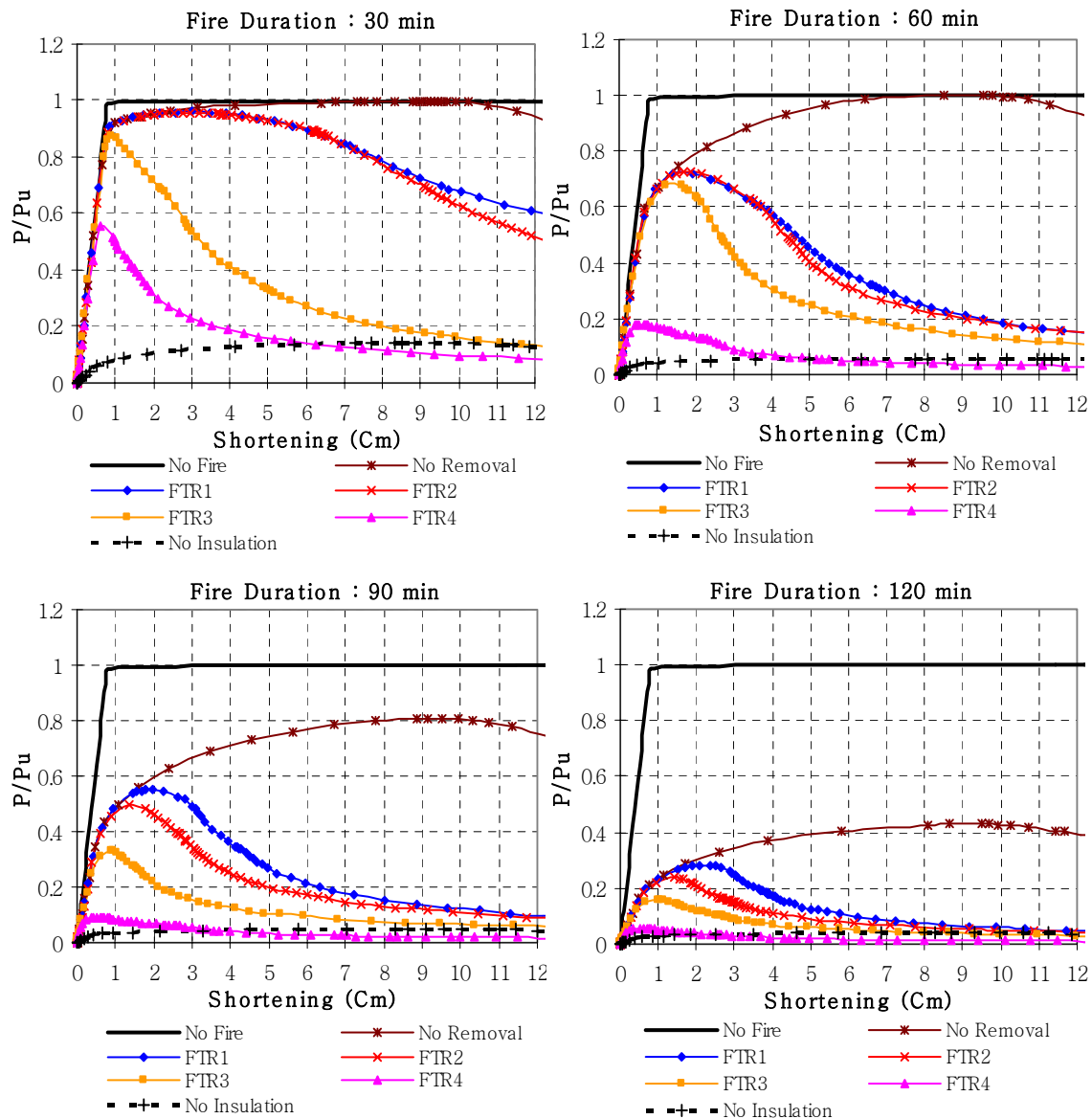


Fig. 6 – P/P_u versus column axial shortening for the flange thinning removal analyses.

Fig. 7 shows the influence of thinning of the SFRM on the web. Again, as noted earlier, the area over which the SFRM is reduced in thickness is equal to the largest patch in the web patch removal case (hixbf). In some respects, the results are similar to the flange thinning removal cases shown in Fig. 6. Fig. 7 shows that the column exhibits similar axial strengths when the web SFRM is reduced to 3/4, 1/2 and 1/4 of its intended thickness at fire durations of 30 and 60 minutes. The axial strengths differ by greater amounts at fire durations of 90 and 120 minutes.

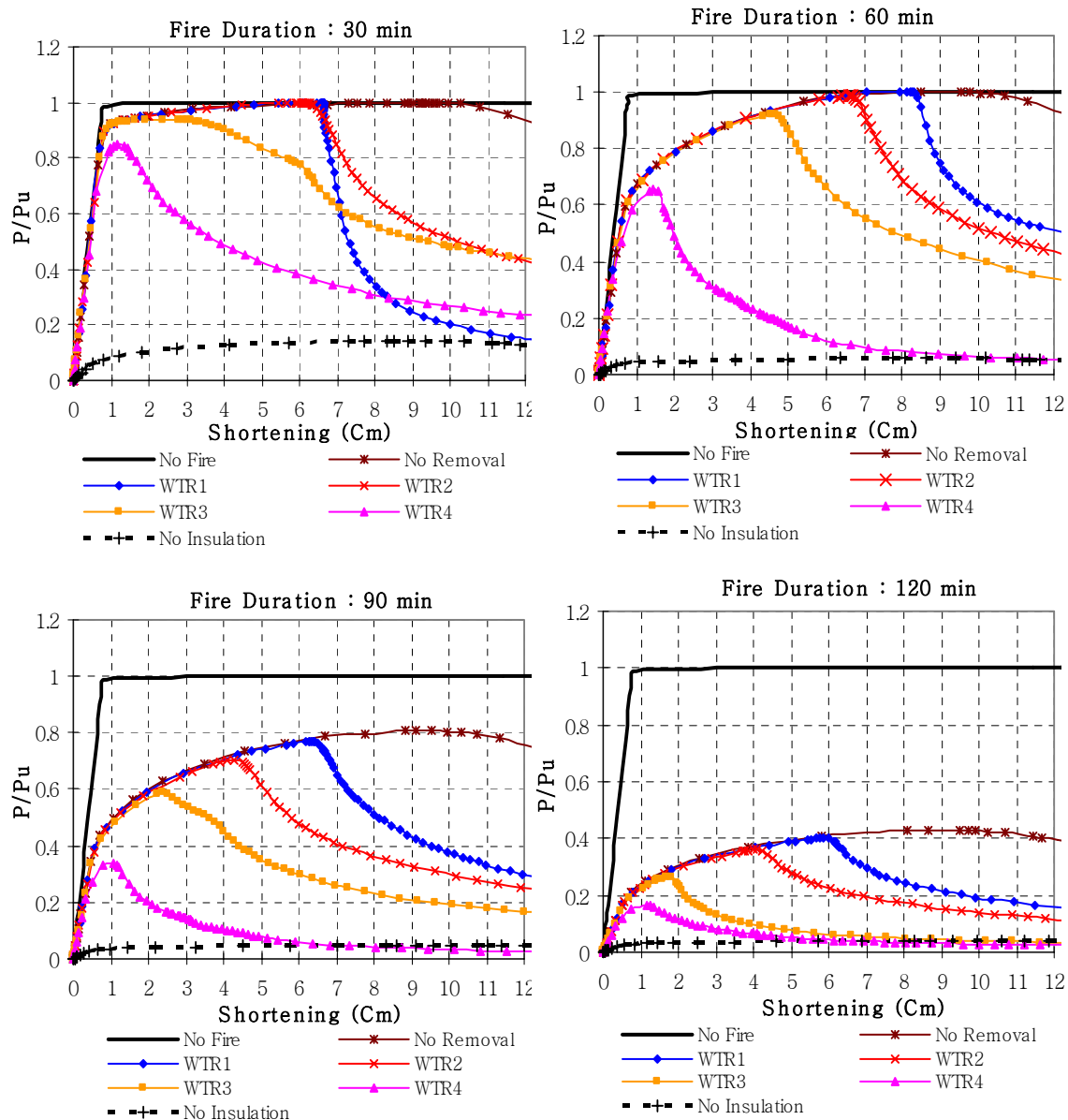


Fig. 7 – P/P_u versus column axial shortening for the web thinning removal analyses.

5. CONCLUSIONS

The following conclusions are drawn from this study: (1) The removal of even a relatively small patch of SFRM leads to dramatic increases in temperature in the column cross-section at any given point in time; (2) The removal of even relatively small amounts of SFRM from the flange that are made completely to the bare steel cause dramatic decreases in column axial load capacity for fire durations in excess of 30 minutes; (3) For a given size patch of removed SFRM, the column section axial load capacity is more sensitive to removal of the SFRM from the flange as compared to the web.

6. REFERENCES

- [1] ABAQUS Inc., ABAQUS Version 6.5 Documentation, 2004.
- [2] Eurocode 3: Design of Steel Structures - Part 1.2: General Actions – Structural Fire Design, British Standards Institution, DD ENV 1993-1-2:2001, September 2001, London, 66 pp.
- [3] American Society of Civil Engineers, Structural Fire Protection, ASCE Manual and Reports on Engineering Practice No. 78, New York, 1992, 241 pp.
- [4] Lee, B.J., Pessiki, S., “Analytical Modeling of Large-Scale Fire Tests of Steel Box Columns with Damaged Fire Resistive Insulation,” ATLSS Report in preparation, Center for Advanced Technology for Large Structural Systems, Lehigh University, Bethlehem, PA, USA.
- [5] Kohno, M., Masuda, H., “Fire-Resistance of Large Steel Columns under Axial Load,” Proceedings of the CIB-CTBUH International Conference on Tall Buildings, Malaysia, May 2003.

7. ACKNOWLEDGEMENTS

This research was funded by the P.C. Rossin College of Engineering and Applied Science at Lehigh University. Additional support was provided by Department of Civil and Environmental Engineering, and by the Center for Advanced Technology for Large Structural Systems (ATLSS) at Lehigh University. The opinions expressed are those of the authors.



STAINLESS STEEL STRUCTURES IN FIRE

Leroy GARDNER¹

ABSTRACT

The initial material cost of structural stainless steel is about four times that of structural carbon steel, due largely to the expense of the alloying elements and the relatively low volume of production. Given broadly similar structural performance, additional areas of benefit need to be identified and exploited in order to establish stainless steel as a viable alternative material for construction. In addition to the familiar benefits of corrosion resistance, low maintenance, high residual value and aesthetics, one such area is fire resistance. This paper describes experimental, numerical and analytical investigations into the elevated temperature response of stainless steel structures. Comparisons are made with the behaviour of carbon steel structures in fire and progress towards the development of structural fire resistant design guidance for stainless steel is described.

1. INTRODUCTION

Recent years have seen significant research into the response of structural stainless steel components, enabling the development and expansion of dedicated design guidance. Provisions for stainless steel are now made in design standards in Europe, North America, Australia/ New Zealand and Japan. An increase in practical applications of the material in construction has resulted [1,2,3]. However, despite considerable progress in the publication of room temperature design guidance, design rules for elevated temperatures are scarce, with only the European Standard offering guidance. Some background information is also provided as an Informative Annex in the Australia/New Zealand Standard.

The mechanical and thermal properties of stainless steel differ from those of carbon steel due to variation in chemical composition between the materials. This has implications on temperature development, strength and stiffness retention and thermal expansion, influencing the response of individual structural members and structural assemblages. Recent developments, including fire testing, numerical modelling and the development of elevated temperature design guidance for stainless steel structures are described in this paper.

¹ Lecturer in Structural Engineering, Imperial College London, Department of Civil Engineering, South Kensington Campus, London, SW7 2AZ, UK

2. MATERIAL RESPONSE AT ELEVATED TEMPERATURES

2.1 Introduction

Material properties and their response to elevated temperatures form an essential part of structural fire design. Of primary importance are the elevated temperature stress-strain characteristics, thermal expansion, thermal conductivity, specific heat and unit mass. A comparison between these properties for stainless steel and carbon steel is presented in the following sub-sections. Additionally, the two key parameters for the determination of temperature development in structural members, namely, the convective heat transfer coefficient and the emissivity (absorptivity) are introduced. More detailed discussion of the elevated temperature material properties of stainless steel are given in [4].

2.2 Strength and stiffness retention

The ability of a material to retain strength and stiffness at elevated temperature is crucial for achieving fire resistant structures. Whilst there exists a large volume of elevated temperature material data for stainless steel, these have been primarily generated for its service use in applications such as boilers and pressure vessels. Consequently, test results are generally limited to low strain levels, relatively low temperatures (around 550°C) and are primarily isothermal; the results are therefore of limited use for structural fire engineering purposes. Material behaviour at elevated temperatures was studied as part of the ECSC project 'Development of the use of stainless steel in construction', with data generated for a range of stainless steel grades, based on a programme of isothermal and anisothermal tests [5,6]. Other material studies of stainless steel at temperatures concurrent with structural fire design have also been conducted [7,8,9]. The studies have shown that, at elevated temperatures, stainless steel offers better retention of strength and stiffness than carbon steel, due to the beneficial effects of the alloying elements. A comparison of the elevated temperature performance of stainless steel and structural carbon steel is presented in Figs 1 and 2; the data are given in EN 1993-1-2 (2005) [10] and the Euro Inox/SCI Design Manual for Structural Stainless Steel [11], both of which are based on the test results reported in [5,6,7,8]. The strength reduction factors shown in Fig. 1 are for grade 1.4301 (304) austenitic stainless steel, the most widely adopted grade for structural applications, whereas the stiffness reduction factors are common to all grades (austenitic, ferritic and duplex) included in the design guidance. Strength reduction factors are defined at two strain levels: $k_{2,\theta}$ is the elevated temperature strength at 2% total strain $f_{2,\theta}$, normalised by the room temperature 0.2% proof strength f_y , whilst $k_{0.2p,\theta}$ is the elevated temperature 0.2% proof strength $f_{0.2p,\theta}$, normalised by the room temperature 0.2% proof strength f_y . EN 1993-1-2 utilises the elevated temperature strength at 2% strain for the design of Class 1, 2 and 3 cross-sections, whilst the elevated temperature 0.2% proof strength is employed for Class 4 cross-sections. At low temperatures, stainless steel has a reduction factor $k_{2,\theta}$ of greater than unity (see Fig. 1) due to use of the 2% strain limit at elevated temperatures and the substantial strain hardening that stainless steel exhibits. The stiffness reduction factor $k_{E,\theta}$ is defined as the elevated temperature initial tangent modulus E_θ , normalised by the initial tangent modulus at room temperature E_a (see Fig. 2). It should be noted that the minimum specified room temperature 0.2% proof strength for the most common structural grades of austenitic stainless steel typically ranges between 210 and 240 N/mm², whilst the Young's modulus is 200000 N/mm². Figs 1 and 2 demonstrate the superior strength and stiffness retention of stainless steel, particularly at temperatures associated with structures in fire. For a fire resistance of 30 minutes, material will be exposed to temperatures in excess of 700°C, following the standard fire curve of ISO 834-1 (1999) [12] and EN 1991-1-2 (2002) [13].

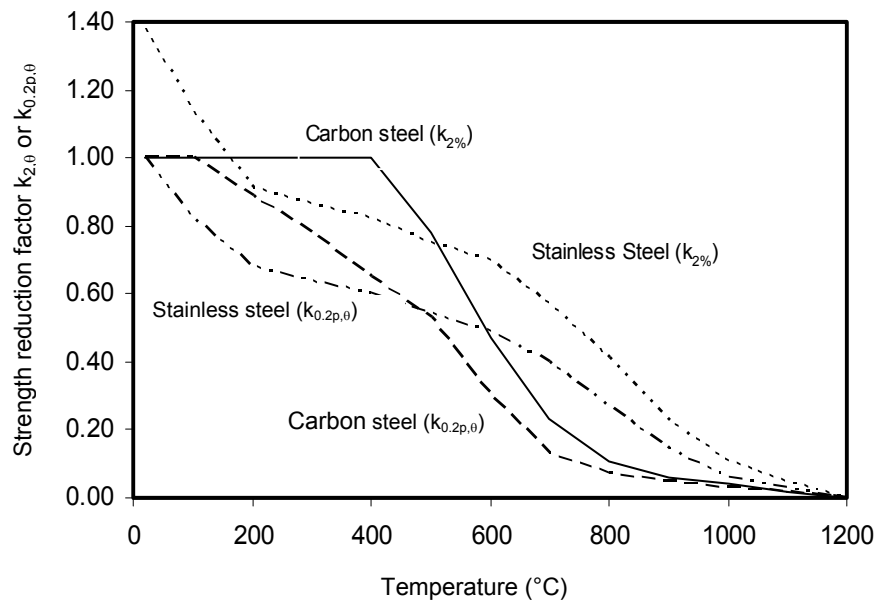


Fig. 1 – Strength reduction of stainless steel and carbon steel at elevated temperature

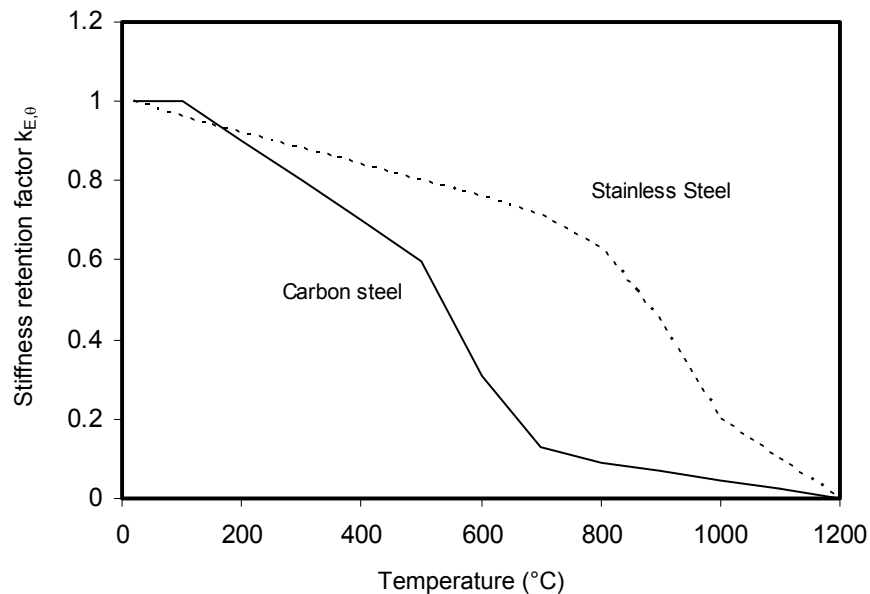


Fig. 2 – Stiffness reduction of stainless steel and carbon steel at elevated temperature

2.3 Thermal properties

This sub-section compares the key physical and thermal properties for elevated temperature behaviour (thermal conductivity, specific heat, unit mass and thermal expansion) of stainless steel and carbon steel. The variation of thermal conductivity with temperature is distinctly different for stainless steel as compared to carbon steel. The thermal conductivity of carbon steel is about 53 W/mK at room temperature and reduces steadily with temperature to a value of 27 W/mK by approximately 800°C. In this temperature region (723°C) a phase transformation occurs beyond which the thermal conductivity remains constant. The thermal conductivity of stainless steel is generally lower than that of carbon steel, rising steadily with temperature from a value of about 15W/mK at room temperature to a value of about 30 W/mK at 1200°C. The relationship is also continuous with temperature since no phase

transformation occurs in austenitic stainless steel upon heating. The effect of lower thermal conductivity will be to cause more localised temperature development in a steel frame, though it is not believed that the differences in thermal conductivity between stainless steel and carbon steel has any significant influence on the general fire performance of a structure.

Specific heat (or specific heat capacity) is the amount of heat per unit mass of a material required to raise the temperature by one degree, and is clearly an important property in controlling the temperature development in a structural member. The specific heat of stainless steel increases steadily with temperature and shows no marked discontinuities (due to the absence of any phase change). The specific heat of carbon steel is, on average, slightly higher than stainless steel, and shows the latent heat of a phase change in the region of 723°C. On average, the specific heat of carbon steel is approximately 600 J/kgK, as compared to approximately 550 J/kgK for stainless steel.

The Euro Inox/SCI Design Manual for Structural Stainless Steel [11] and EN 1993-1-2 [10] state that the unit mass (density) of both carbon steel and stainless steel may be assumed to be independent of temperature and taken as 7850 kg/m³.

Fig. 3 shows a comparison of the thermal expansion of carbon steel and stainless steel as given in EN 1993-1-2. The figure shows that stainless steel expands to a greater extent, up to 50% more than carbon steel. The effect of the higher thermal expansion has not been observed directly since no tests have been conducted on restrained stainless steel members or frames in fire. The practical implications of the higher degree of thermal expansion of stainless steel are discussed in Section 5 of this paper.

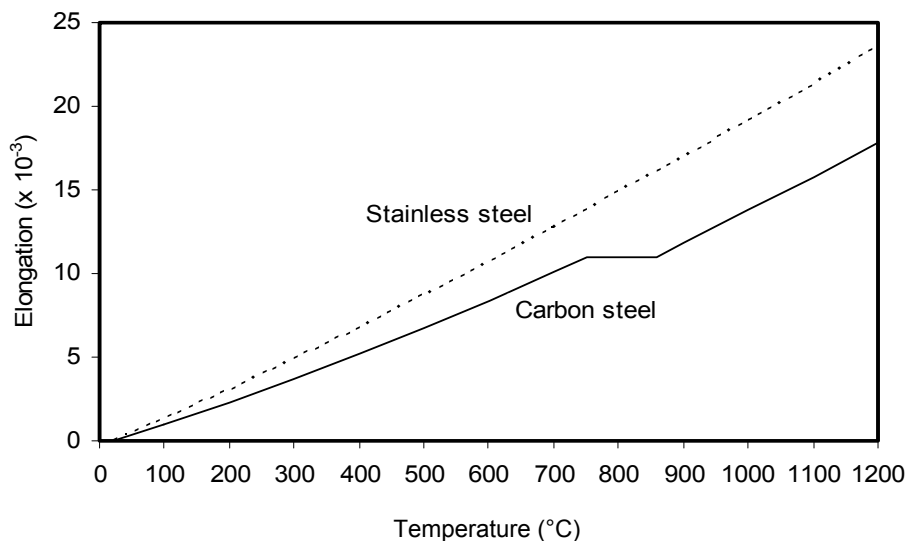


Fig. 3 – Thermal expansion of stainless steel and carbon steel at elevated temperature

2.4 Temperature development

Accurate and efficient determination of the temperature development within a structural member upon subjection to fire is paramount. Temperature development in unprotected and uniformly heated steelwork is determined in EN 1993-1-2 [10] using the simple calculation model of Eq. 1, in which $\Delta\theta_{a,t}$ is the increase in temperature (°C) in a time increment Δt (in seconds).

$$\Delta\theta_{a,t} = k_{sh} \frac{A_m / V}{c_a \rho_a} \dot{h}_{net,d} \Delta t \quad (1)$$

where k_{sh} is the correction factor for the shadow effect, A_m/V is the section factor (m^{-1}), c_a is the specific heat of the material, ρ_a is the material density (kg/m^3), and $\dot{h}_{net,d}$ is the design value of the net heat flux per unit area ($W/m^2 K$), controlled by the convective heat transfer coefficient and the emissivity.

The convective heat transfer coefficient is not a material constant, but is known to be a function of the fluid properties, the flow parameters and the geometry of the surface of the heated object [14]. The convective heat transfer coefficient is also a function of temperature, and although convection will occur at all stages of a fire, it is particularly important at low temperatures where radiation levels are low. For use with the standard temperature-time curve, EN 1991-1-2 recommends a single convective heat transfer coefficient α_c of $25 W/m^2K$. In EN 1991-1-2, this value is not dependent on the material, though alternative values are provided for different temperature-time curves (the hydrocarbon curve).

Radiative heat transfer is controlled by resultant emissivity. Emissivity is a dimensionless property that ranges between zero and unity, and depends on factors such as temperature, emission angle and wavelength. A common engineering assumption which is adopted in EN 1991-1-2 is that a surface's spectral emissivity does not depend on wavelength, and thus emissivity is taken as a constant. Tabulated emissivities for materials are widely available in literature, but show substantial variation depending, in particular, on the condition of the surface. In general, the emissivity of a polished metallic surface is very low, whilst the emissivity of dull, oxidised material approaches unity. EN 1993-1-2 adopts an emissivity ϵ_m of 0.7 for carbon steel and 0.4 for stainless steel. The suitability of the recommended values for the heat transfer coefficient and emissivity of structural stainless steel members has been assessed, based on the results of a series of temperature development tests on structural stainless steel sections, and a supporting numerical programme [4]. In total, twenty austenitic stainless steel specimens exposed to fire on all four sides and three specimens exposed on three sides (with a concrete slab on the fourth side), have been tested. All specimens were subjected to the standard fire curve defined by ISO 834-1 [12]. Fourteen specimens, tested solely to investigate the temperature development characteristics of stainless steel sections and exposed to fire on all four sides, were reported in [15]. Other temperature development data were acquired from full scale member tests conducted to determine the fire resistance of structural stainless steel components [6,15,16,17]. The deformation of the specimens during testing was assumed not to affect their temperature development. Based on a study of these results, revised values for the heat transfer coefficient and emissivity of structural stainless steel members exposed to fire were proposed. In the temperature development calculation model of EN 1993-1-2 (Eq. 1), it was proposed that emissivity be taken as 0.2 (in place of the currently adopted value of 0.4) and the heat transfer coefficient be taken as $35 W/m^2K$ (in place of the currently adopted value of $25 W/m^2K$). The revised values result in calculated temperature development characteristics that more accurately reflect observed behaviour.

3. FIRE TESTS AND NUMERICAL MODELLING

3.1 Introduction

Although knowledge of the degradation of material strength and stiffness is fundamental to understanding the performance of members in fire, full-scale elevated temperature member tests also enable the effects of instability, temperature gradients and full cross-sectional behaviour (including enhanced strength corner regions) to be studied. Owing to the impracticality and expense of generating comprehensive structural fire performance data through experimentation, a detailed, non-linear numerical modelling programme, using the finite element package ABAQUS [18], has also been performed.

3.2 Fire testing

A number of recent experimental studies of the response of unprotected stainless steel structural members exposed to fire have been performed. Fire tests on a total of 23 austenitic stainless steel columns [6,15,17,19,20] (where failure was by flexural buckling), 6 stub columns [21] and 6 laterally-restrained beams [6,15,20] have been reported. The nominal section sizes, cross-section classifications, boundary conditions, applied loads and critical temperatures for these tests have been collated and summarised in [22]. A selection of the tests has been replicated numerically, as described in section 3.3 of this paper, forming the basis for parametric studies. Deformed specimens tested as part of the ECSC project 'Development of the use of stainless steel in construction' [6,15] are shown in Figs 4 and 5.

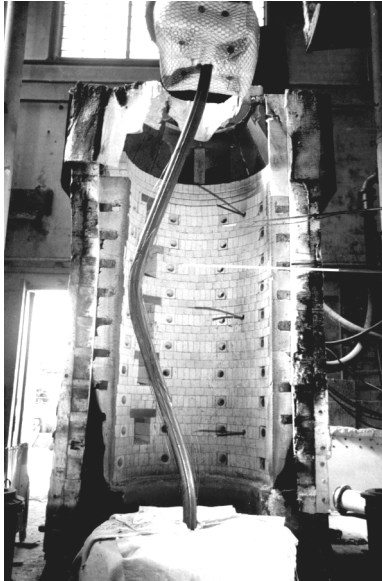


Fig. 4 – 100×75×6.0 RHS column after testing



Fig. 5 – 200×125×6.0 RHS beam after

Of the 23 column buckling tests, 4 had fixed boundary conditions whilst the remainder were pin-ended. All column buckling tests were performed on hollow sections (19 rectangular hollow sections (RHS) and 3 circular hollow sections (CHS)) with the exception of one I-section, made up of a pair of channel sections welded back-to-back. The 6 stub column tests were all Class 4 rectangular hollow sections. The 6 beam tests included one rectangular hollow section, 3 I-sections and 2 top-hat sections. All of the tested beams were supporting a concrete slab which provided full lateral restraint. There have been no tests on laterally unrestrained stainless steel beams in fire. All tests were anisothermal, whereby the load was held at a constant level and the temperature was increased (generally following the standard fire curve of ISO 834-1 (1999) [12]) until failure.

3.3 Numerical modelling

A numerical modelling study was performed to gain further insight into the buckling response of stainless steel compression members in fire, and to investigate the influence of key parameters. The finite element software package ABAQUS [18] was employed throughout the study. Analyses were conducted to simulate 12 column buckling fire tests: 4 fixed-ended and 2 pin-ended columns reported in [6,15], and 6 pin-ended columns reported in [19]. The stainless steel members were modelled using the shell elements S4R, which have 4 corner nodes, each with 6 degrees of freedom, and are suitable for thick or thin shell applications [18]. A mesh convergence study was performed to identify an appropriate mesh

density to achieve suitably accurate results whilst maintaining practical computation times. Test boundary conditions were replicated by restraining suitable displacement and rotation degrees of freedom at the column ends, and through the use of constraint equations. The replicated fire tests were performed anisothermally. This was reflected in the numerical modelling by performing the analyses in two steps: in the first step, load was applied to the column at room temperature, and in the second step, temperature was increased following the measured temperature-time relationships until failure. Imperfections were incorporated into the models by means of superposition of local and global eigenmodes.

Sensitivity studies were performed to investigate the influence of imperfections, cold-worked corner material properties and partial protection of the column ends. The studies revealed that the models were relatively insensitive to variation in imperfections, showing negligible response to changes in local imperfection amplitude and exhibiting, on average, a 6% reduction in critical temperature in response to variation of global imperfection amplitude from $L/2000$ to $L/500$ (where L is the column length). The majority of the modelled fire tests were performed on cold-formed sections, which exhibit strength enhancements in the corner regions – modelling of this strength enhancement, based on predictive expressions developed in [23], led to a 6% increase in critical temperature and improved agreement between test and finite element (FE) results. Some of the test arrangements included partial protection of the column ends from the direct effects of fire – inclusion of this protection in the FE models resulted in a 3% increase in critical temperature and improved agreement between test and FE results. Overall, it was concluded that the described FE models are capable of replicating the non-linear large deflection response of structural stainless steel members in fire.

Parametric studies were conducted to assess variation in local cross-section slenderness, global member slenderness and load level. Results were compared against those predicted by EN 1993-1-2. Variation in cross-section slenderness was achieved by considering a range of cross-section thicknesses. The results showed that Class 1 to 3 sections behave similarly, and generally follow the EN 1993-1-2 design curve. For the Class 4 sections, however, agreement was poor. The reason for this is two-fold. Firstly, the load ratio is determined by normalising the applied load by the room temperature buckling resistance – for Class 4 sections, the room temperature buckling resistance is calculated on the basis of an effective section to account for local buckling; this results in higher load ratios. Secondly, EN 1993-1-2 specifies use of the strength reduction factor corresponding to the 0.2% proof stress $k_{0.2p,0}$ for Class 4 cross-sections, whilst Class 1 to 3 sections benefit from the use of a higher 2% strain limit and adopt $k_{2,0}$. It may be concluded that the current treatment of Class 4 stainless steel sections in EN 1993-1-2 does not accurately reflect the behaviour predicted by the described FE models. Variation in member slenderness was achieved by considering a range of column lengths. As anticipated, there was a general trend showing that critical temperature reduces with increasing load ratio. The results also indicated that variation of critical temperature with load ratio is slenderness dependent. This would be expected since stocky columns are controlled primarily by material strength and its degradation, whilst slender columns are controlled primarily by material stiffness and its degradation. Since strength and stiffness do not degrade at the same rate with temperature it follows that the critical temperature of columns is slenderness dependent.

4. STRUCTURAL FIRE DESIGN

The European provisions for the design of stainless steel members in fire largely follow the carbon steel rules, with the primary differences being in the material properties. The material properties of stainless steel have been incorporated into Annex C of EN 1993-1-2 [10] to extend the scope of this document to the design of stainless steel structures in fire. Results from all available tests on stainless steel columns and beams in fire have been

compared to existing design guidance given in EN 1993-1-2 [10], the Euro Inox/ SCI Design Manual for Structural Stainless Steel [11] and proposed by CTICM/ CSM [24]. The comparisons generally revealed both conservatism and scatter of prediction in existing design methods, due, in part, to inconsistent treatment of buckling and inappropriate strain limits and member buckling curves. Revised recommendations are made herein.

At elevated temperatures, stainless steel displays superior material strength and stiffness retention in comparison to structural carbon steel (see Figs 1 and 2). Although independently important, the relationship between strength and stiffness at elevated temperature also has a significant influence on the buckling response of structural components. Currently, this concept is included in EN 1993-1-2 and the Euro Inox/ SCI Design Manual for Structural Stainless Steel for member buckling through the definition and use of an elevated temperature non-dimensional member slenderness $\bar{\lambda}_\theta$. $\bar{\lambda}_\theta$ is defined by a modification of the room temperature non-dimensional slenderness $\bar{\lambda}$, as given by Eqs. (2) and (3).

$$\bar{\lambda}_\theta = \bar{\lambda} (k_{2,\theta} / k_{E,\theta})^{0.5} \quad \text{for Class 1 to 3 cross-sections} \quad (2)$$

$$\bar{\lambda}_\theta = \bar{\lambda} (k_{0.2p,\theta} / k_{E,\theta})^{0.5} \quad \text{for Class 4 cross-sections} \quad (3)$$

The variation of $(k_{E,\theta}/k_{2,\theta})^{0.5}$ (where $k_{2,\theta}$ is based on the 2% total strain limit) and $(k_{E,\theta}/k_{0.2p,\theta})^{0.5}$ (where $k_{0.2p,\theta}$ is based on the 0.2% plastic strain limit) with temperature for stainless steel and carbon steel is shown in Fig. 6. Values of $(k_{E,\theta}/k_{2,\theta})^{0.5}$ or $(k_{E,\theta}/k_{0.2p,\theta})^{0.5}$ less than unity lead to an increase in the non-dimensional member slenderness and represents greater propensity to buckling (rather than yielding) at elevated temperature than at room temperature. For values of $(k_{E,\theta}/k_{2,\theta})^{0.5}$ or $(k_{E,\theta}/k_{0.2p,\theta})^{0.5}$ greater than unity, the reverse is true.

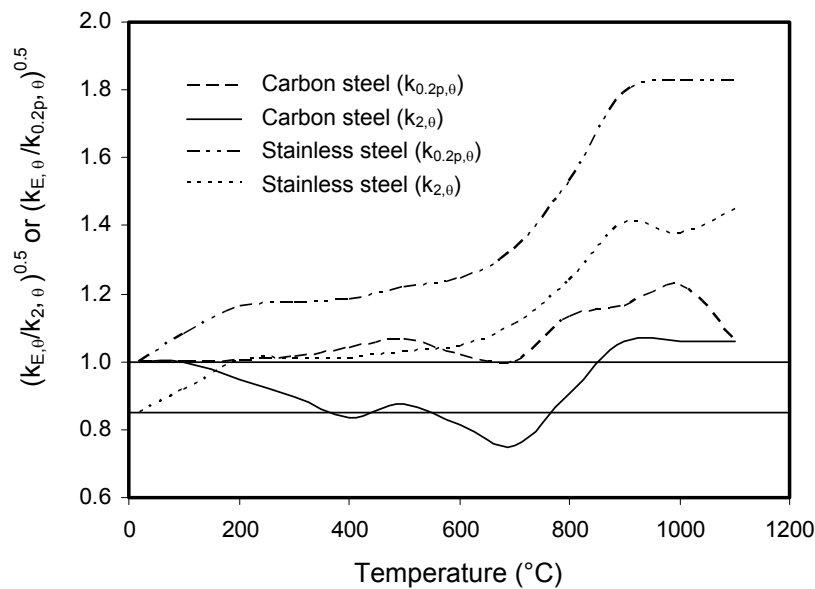


Fig. 6 – Variation of the modification factor $(k_{E,\theta}/k_{2,\theta})^{0.5}$ and $(k_{E,\theta}/k_{0.2p,\theta})^{0.5}$ with temperature

In the treatment of local buckling at room temperature, the ε factor is employed to allow for variation in material yield strength f_y . In fire, ENV 1993-1-2 (2001) [25] modified the ε factor used in section classification to reflect that loss of strength and stiffness at elevated temperatures does not occur at the same rate. Thus, at elevated temperatures ε was modified by the factor $(k_{E,\theta}/k_{2,\theta})^{0.5}$ and was defined by Eq. (4).

$$\varepsilon = \left[\left(\frac{235}{f_y} \right) \left(\frac{k_{E,\theta}}{k_{2,\theta}} \right) \right]^{0.5} \quad (4)$$

From Fig. 6, it may be seen that for the majority of the elevated temperature range, carbon steel has values of $(k_{E,\theta}/k_{2,\theta})^{0.5}$ less than unity and is therefore more susceptible to buckling (as opposed to yielding) than at room temperature; neglecting this feature leads to unsafe predictions. To simplify calculations, this factor was set as a constant of 0.85 (which was deemed an acceptably safe average value at fire limit state) in EN 1993-1-2 (2005), for both carbon steel and stainless steel. Clearly from Fig. 6, however, this factor is inappropriate for stainless steel. The Euro Inox/ SCI Design Manual for Structural Stainless Steel [11] effectively employs a modification factor of unity by adopting the room temperature classification for elevated temperature. This is more appropriate than the Eurocode 3 treatment, but still, does not correctly reflect the variation of strength and stiffness at elevated temperature exhibited by stainless steel.

It is proposed that the true variation of stiffness and strength at elevated temperature be utilised in cross-section classification and in the determination of effective section properties for stainless steel structures in fire. Thus, the ε_θ factors defined by Eqs. (5) and (6) should be determined at the critical temperature, and hence used to re-classify the cross-section. Eq. (5) may be applied to cross-sections that are Class 1 or 2 at room temperature and utilises the 2% strain limit, whilst Eq. (6) applies to cross-sections that are Class 3 or 4 at room temperature and utilises the 0.2% plastic strain limit. Eq. (6) also applies in the determination of effective section properties. The notation ε_θ is introduced to differentiate from the ε factor used for room temperature design.

$$\varepsilon_\theta = \left[\left(\frac{235}{f_y} \frac{E}{210000} \right) \left(\frac{k_{E,\theta}}{k_{2,\theta}} \right) \right]^{0.5} = \varepsilon \left(\frac{k_{E,\theta}}{k_{2,\theta}} \right)^{0.5} \quad \text{for Class 1 and 2 sections} \quad (5)$$

$$\varepsilon_\theta = \left[\left(\frac{235}{f_y} \frac{E}{210000} \right) \left(\frac{k_{E,\theta}}{k_{0.2p,\theta}} \right) \right]^{0.5} = \varepsilon \left(\frac{k_{E,\theta}}{k_{0.2p,\theta}} \right)^{0.5} \quad \text{for Class 3 and 4 sections} \quad (6)$$

From Fig. 6, it may be seen that the factors $(k_{E,\theta}/k_{2,\theta})^{0.5}$ and $(k_{E,\theta}/k_{0.2p,\theta})^{0.5}$ for stainless steel are greater than unity at elevated temperatures. The result of cross-section re-classification and the re-determination of effective section properties at the critical temperature will therefore be beneficial, and ignoring this process will be conservative. Cross-sections that are Class 4 at room temperature may become fully effective at elevated temperatures. It is further proposed that in the determination of cross-section and member resistance in fire, the strength reduction factor be based on the 2% strain limit ($k_{2,\theta}$) for Class 1 and 2 cross-sections and the 0.2% plastic strain limit ($k_{0.2p,\theta}$) for Class 3 and 4 cross-sections. Use of the strength at 2% strain for Class 3 cross-sections, as is proposed in existing design guidance seems unjustified, since local buckling would be expected before this strain level is reached.

Having established a more consistent basis for the treatment of buckling of stainless steel columns and beams in fire, comparison was made with the test results summarised in Section 3. For columns, a revised buckling curve has been proposed to provide a mean fit to the test results, which is acceptable at fire limit state. This was achieved by adopting the

general form of the room temperature buckling curves of Eurocode 3 Part 1.1, and selecting appropriate values of the imperfection parameter α and the limiting slenderness $\bar{\lambda}_0$. A comparison of the resulting fire buckling curve with $\alpha = 0.55$ and $\bar{\lambda}_0 = 0.2$ is shown in Fig. 7. Following analysis of the results it was revealed that one of the columns, Class 4 at room temperature, becomes Class 2 at elevated temperature, and its resistance is over-predicted by the proposed method. In the absence of further test results, it is recommended that cross-sections that are Class 4 at room temperature cannot be promoted beyond Class 3 at elevated temperatures.

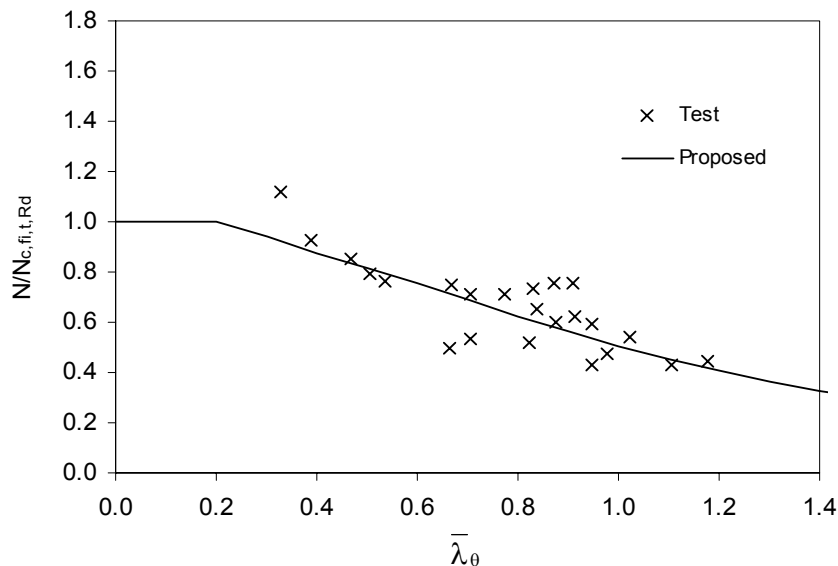


Fig. 7 – Comparison of proposed design approach with column buckling fire tests

For column buckling (23 tests), the mean proposed divided by test resistance is 1.00 with a coefficient of variation (COV) of 0.15. For stub columns (6 tests), the mean proposed divided by test resistance is 0.91 with a coefficient of variation (COV) of 0.15, whilst for beams (6 tests), the mean proposed divided by test resistance is 0.84 with a coefficient of variation (COV) of 0.19. The proposed treatment offers a more rational approach to the fire design of structural stainless steel columns and beams, yielding an improvement of 6% for column buckling resistance, 28% for stub column (cross-section) resistance and 14% for in-plane bending resistance over the current Eurocode methods. Further details are given in [22].

5. THERMAL EXPANSION

Stainless steel expands to a greater extent, up to 50% more than carbon steel (see Figure 3). Typically during component tests in fire (such as those described herein), structural members will be free to expand against the applied load, and thus no additional load is induced due to this expansion. However, in structural frames, where continuity exists between members and often fire is relatively localised, thermal expansion may be restrained by other (stiffer) parts of the structure, resulting in additional member loading. The effect of the higher thermal expansion has not been observed directly since no tests have been conducted on restrained stainless steel members or frames in fire. Given the greater thermal expansion and the ability to retain strength and stiffness to higher temperatures, additional forces will generally be experienced by restrained stainless steel structural members. The severity of the additional member forces will depend on the applied loading arrangement and on the degree of rotational and translational restraint present. Further consequences of thermal expansion may include higher axial and lateral member deformations leading to greater second order effects.

However, recent studies of the large deflection behaviour of restrained beams [26] and columns [27] have indicated that provided the integrity of the fire compartment is maintained and localised column failure (which will not occur until the resistance drops to below the applied load level) is acceptable, the effects of thermal expansion may not be very severe.

6. CONCLUSIONS

At elevated temperatures, stainless steel offers better retention of strength and stiffness than structural carbon steel, due to the beneficial effects of the alloying elements. This behaviour is reflected in EN 1993-1-2 (2005). However, in addition to knowledge of the independent degradation of material strength and stiffness at elevated temperatures, the relationship between strength and stiffness is also important, since this defines susceptibility to buckling. This concept has been recognised in EN 1993-1-2 for member buckling by the use of an elevated temperature non-dimensional member slenderness, but for local buckling of stainless steel sections, current codified treatment is inappropriate.

The results of a total of 23 column buckling fire tests, 6 stub column fire tests and 6 fire tests on laterally-restrained beams have been collated and analysed. A selection of the tests have been replicated numerically, where the importance of local and global initial geometric imperfections, residual stresses, enhanced strength corner properties and partial protection of the member ends has been investigated. From the comparisons between test and numerical results, it may be concluded that the described FE models are capable of replicating the non-linear large deflection response of structural stainless steel members in fire.

A revised buckling curve for stainless steel in fire, consistent strain limits and a new approach to cross-section classification and the treatment of local buckling are proposed. These revisions have led to a more efficient and consistent treatment of buckling of stainless steel columns and beams in fire. Improvements of 6% for column buckling resistance, 28% for stub column (cross-section) resistance and 14% for in-plane bending resistance over the current Eurocode methods are achieved.

7. ACKNOWLEDGEMENTS

The author would like to thank Kee Ng of Imperial College London and Nancy Baddoo of the Steel Construction Institute for their contribution to related research.

8. REFERENCES

- [1] Gardner, L. (2005). The use of stainless steel in structures. *Progress in Structural Engineering and Materials*. 7(2). 45-55.
- [2] Baddoo, N. R., Burgan, R. and Ogden, R. *Architects' Guide to Stainless Steel*. (1997). SCI-P-179. The Steel Construction Institute, UK.
- [3] Gardner, L. (2006). Aesthetics, economics and design of stainless steel structures. *Proceedings of the Eight International Conference on Steel, Space and Composite Structures*. 15th – 17th May, 2006. Kuala Lumpur, Malaysia.
- [4] Gardner, L. and Ng, K. T. (in press). Temperature development in structural stainless steel sections. *Fire Safety Journal*.
- [5] Zhao, B. (2000). Material behaviour at elevated temperatures: Work package 5.1. ECSC project 'Development of the use of stainless steel in construction'. Contract No. 7210 SA/842. The Steel Construction Institute, UK.
- [6] Gardner, L. and Baddoo, N. R. (2006). Fire testing and design of stainless steel structures. *Journal of Constructional Steel Research*. 62(6), 532-543.
- [7] Ala-Outinen, T. (1996). Fire resistance of austenitic stainless steels Polarit 725 (EN 1.4301) and Polarit 761 (EN 1.4571) VTT Research Notes 1760, Espoo, Finland.
- [8] Hoke, J. H. (1977). *Handbook of Stainless Steels*. McGraw-Hill.

- [9] Chen, J. and Young, B. (2006). Stress-strain curves for stainless steel at elevated temperatures. *Engineering Structures*. 28(2), 229-239.
- [10] EN 1993-1-2. (2005). Eurocode 3: Design of steel structures - Part 1.2: General rules - Structural fire design. CEN.
- [11] Design Manual for Structural Stainless Steel. (2002). Second edition. Euro Inox and the Steel Construction Institute. Building series, Volume 3.
- [12] ISO 834-1. (1999). Fire-resistance tests - Elements of building construction - Part 1: General requirements. International Organization for Standardization, Geneva.
- [13] EN 1991-1-2. (2002). Eurocode 1: Actions on structures – Part 1.2: General actions – Actions on structures exposed to fire. CEN.
- [14] Drysdale, D. (1985). An introduction to fire dynamics. 2nd Ed.. John Wiley & Sons Ltd.
- [15] Baddoo, N. R. and Gardner, L. (2000). Member behaviour at elevated temperatures: Work package 5.2. ECSC project ‘Development of the use of stainless steel in construction’. Contract No. 7210 SA/842. The Steel Construction Institute, UK.
- [16] Baddoo, N. R. and Burgan, B. A. (1998). Fire resistance design of austenitic stainless steel. Paper No. 243. 2nd World Conference on Steel Structures, San Sebastian. May 1998.
- [17] Ala-Outinen, T. (1999). Fire resistance of stainless steel structures. Proceedings of the Second European Conference on Steel Structures (Eurosteel 1999). Prague, Czech Republic, 26th-29th May, 1999. 165-168.
- [18] ABAQUS (2003). ABAQUS/ Standard User’s Manual Volumes I-III and ABAQUS CAE Manual. Version 6.4. Hibbitt, Karlsson & Sorensen, Inc. Pawtucket, USA.
- [19] Ala-Outinen, T. and Oksanen, T. (1997) Stainless steel compression members exposed to fire. VTT Research Notes 1864, Espoo, Finland.
- [20] Zhao, B. and Blanguernon, A. (2004). Member Tests in Fire and Structural Fire Design Guidance. Work package 6: Elevated Temperature Properties. ECSC project ‘Structural design of cold-worked austenitic stainless steel’. Contract No. 7210-PR-318. The Steel Construction Institute, UK.
- [21] Ala-Outinen, T. (2005). Members with Class 4 cross-sections in fire: Work package 3. ECSC project ‘Stainless steel in fire (SSIF)’. Contract No. RFS-CR-04048. VTT.
- [22] Ng, K. T. and Gardner, L. (submitted). Buckling of stainless steel columns and beams in fire. *Engineering Structures*.
- [23] Ashraf, M., Gardner, L. and Nethercot, D. A. (2005). Strength enhancement of the corner regions of stainless steel cross-sections. *Journal of Constructional Steel Research*. 61(1), 37-52.
- [24] CTICM/CSM (2005). Stainless steel column buckling behaviour at elevated temperatures – Comparison of Euro Inox and CTICM methods. Centro Sviluppo Materiali S.p.A.
- [25] ENV 1993-1-2. (2001). Eurocode 3: Design of steel structures - Part 1.2: General rules - Structural fire design. CEN.
- [26] Yin, Y. Z. and Wang, Y. C. (2004). A numerical study of large deflection behaviour of restrained steel beams at elevated temperatures. *Journal of Constructional Steel Research*. 60(7), 1029-1047.
- [27] Franssen, J.-M. (2000). Failure temperature of a system comprising a restrained column submitted to fire. *Fire Safety Journal*. 34(2), 191-207.



CRITICAL BEHAVIOUR OF LONG SPAN CELLULAR BEAMS IN FIRE

Darlene RINI¹, Allan JOWSEY², Jose L. TORERO³, Barbara LANE¹ and Susan LAMONT¹

ABSTRACT

This paper presents an investigation of the structural response of a long span cellular beam with varying section geometries while subject to various temperature-time curves. This type of beam is under investigation, in part, because of its increased use in long span building construction and its unique thermal response when protected with intumescent coatings; but more importantly, to provide an increased understanding into how these beams affect global structural response under fire conditions.

In recent years, several small-scale experimental studies have been conducted to determine the structural and thermal response of cellular beams. However, limited work has been conducted to determine how the structural fire response of long span cellular beams affect the surrounding structure in real building designs.

This study was conducted using a nonlinear, shell, finite element computational analysis of a realistic steel-frame composite structure incorporating long span cellular beams with a composite deck. A detailed parametric study was carried out varying several aspects of the section geometry including the number of web openings, end post length, size of openings, web thickness, flange thickness and span length. The aim was to investigate the affects on local buckling behavior, midspan displacements, and forces at the columns. These results were also compared with the behavior of a similar I-shaped member with no web openings with particular emphasis being given to lateral forces experienced on the columns. Different temperature vs. time curves were used, covering a wide range of fire conditions.

This preliminary study appears to indicate that long span cellular beams exposed to fire experience two buckling events prior to undergoing large displacement behavior and catenary action, as opposed to, the single buckling event witnessed in full-scale tests of traditional I sections such as at Cardington. In addition, global and local response of these

¹ Ove Arup & Partners, 13 Fitzroy St, London, W1t 4BQ, UK .

Corresponding author Email: darlene.rini@arup.com.

² PhD Student, School of Engineering and Electronics, University of Edinburgh, UK.

Email: a.i.jowsey@ed.ac.uk.

³ Professor, School of Engineering and Electronics, University of Edinburgh, UK.

Email: jltorero@staffmail.ed.ac.uk

beams is largely controlled by local web stiffness particularly in pre-buckling behavior. In all cases, overall structural instability and global collapse do not appear to be evident.

1. INTRODUCTION

Historically, the performance of structures in fire has primarily been based on the structural and thermal response of a single element under a prescribed standard temperature-time curve¹. However, little work has been conducted to determine how the structural fire response of these individual elements affect the surrounding structure. Due to the limitations and costs associated with traditional structural fire performance methods and tests, engineers and researchers have been relying more heavily on computational modeling. Advances in this technology, particularly with the use of computational fluid dynamics and finite elements packages for fire applications, has enabled more reliable insight into the global and local response of structures to realistic fire scenarios. These methods of analysis are becoming increasingly important as modern construction continues to push the envelope of design, geometry, space, size and materials. One such advance in modern construction has been the increased demand for large open spaces.

In recent years, the use of cellular steel beams has become increasingly popular in building design primarily to achieve longer spans and to reduce overall building height and steel weight costs². A cellular beam, as seen in Figure 2, is typically a wide flange beam with regular circular openings. These beams offer the flexibility of multiple internal floor configurations, as well as, a reduction in construction cost by minimizing the number of columns and structural walls. In addition, the web openings enable the reduction in overall building height by allowing building services (mechanical, electrical, plumbing etc.) to pass within the structural depth of the beam as opposed to being hung from the bottom of the elements. These added benefits make cellular beams an efficient and cost-effective material for modern building construction.

While it is evident that cellular beams offer tremendous advantages – longer spans, reduced construction costs, etc – their reduced shear capacity as a result of the web openings and Vierendeel effects can make them more susceptible to shear failure and lateral torsional buckling under ambient and fire conditions. Like any other structural beam element, cellular beams are required to achieve a certain level of fire-resistance dependent on the building's construction type, occupancy, level of active and passive protection systems, and exposure level. This fire resistance has historically been assessed using single element tests, where a single beam element is evaluated under the standard fire curve.³ However, it is difficult to extrapolate this structural test performance to real fire scenarios and building geometries where loading conditions, continuity, end conditions and local beam geometry markedly affect structural performance. In addition, typical compartments limit beam sizes to 4 meter spans, which may not predict the performance of cellular beams in long span applications.

Recent tests on cellular beams^{4,5,6,7} showed that the web of the beams between the holes (commonly referred to as the web-post) experienced higher than expected temperatures. As evident from these studies, the temperature distributions through the cross-section of cellular beams was not fully understood. Industry has spent significant time and effort addressing this shortfall and now cellular beams are designed taking this into account.^{6,7} However, the effect of long spans on overall structural performance of a frame in fire is still not well understood.

This paper, through a parametric study using the finite element code ABAQUS⁸, attempts to contribute to the understanding of the global behavior of long span cellular beams

under fire conditions and to appreciate the controlling mechanisms that lead to local failure and possibly runaway failure. The process of this study included:

- Investigation of the sensitivity of section geometry on the structural behavior of long span cellular beams exposed to a standard fire
- Investigation on whether varying the heating rate or maximum temperature plays a significant role on structural response of these beam types
- Investigation on whether increased web temperatures observed in recent fire tests significantly affect the structural fire behavior of long span cellular beams.

The focus of this paper will be on the first part of the investigation i.e. sensitivity of section geometry on the structural behavior of long span cellular beams exposed to a standard fire. The last two investigations will be addressed in future publications.

2. COMPUTATIONAL MODEL

For the first part of the investigation, a series of computational tests were derived for a long span cellular beam located in a typical interior bay illustrated in Figure 1. Imposed loads encountered in building construction were used to determine an appropriate cellular beam size and supporting structural elements for the investigation. Figure 1 and 2 indicate the geometric details, assumed loads, and support conditions of the model studied in this paper. For the first part of the investigation, several cases were developed in which a single parameter of the cellular beam section geometry was varied over a range of values (See Table 2). In some cases, the parameter in question unavoidably altered another beam characteristic. This occurred in Cases A-C in which varying the hole diameter, end post length and number of holes unavoidably changed the length of the web post.

For each proposed case, the structural model was exposed to the standard ISO 834 temperature-time curve³. The structural fire response of each respective cellular beam was then evaluated and compared with the behavior of a solid I-beam. Both the cellular beams and solid I-beam had similar geometry, structural support, loads and were subjected to the same fire. The solid beam, used for comparison, was a 670x370x183 section. The long span cellular beams and solid webbed beam were modeled assuming no protection, while the steel structure surrounding the cellular beam was protected to limit the temperature rise to 550°C for the duration of the simulation. The beam is assumed to be connected to the column along its full web height while contact between the beam flanges and the column face was not modeled.

An ABAQUS implicit solver was used to evaluate the global response of each cellular beam simulation.

In this paper, the connection forces, midspan displacements, and general buckling behavior are presented as a comparative study between the cellular beams and solid beam analyzed. The buckling of a beam is defined as the point at which deformation occurs perpendicular to the direction of loading. It is important to understand that this local buckling, however, does not necessarily result in global failure of the structure. The overall failure of the structure is defined, here, as the point at which the structure has become unstable, i.e. the loading cannot be maintained at equilibrium, or the deflection rate approaches infinity (“runaway deflection”).

The purpose of the structural model created was to include as much of a realistic long-span structure whilst small enough to run in a reasonable time, allowing for a detailed parametric study. Since the focus of the study is on the structural performance of the cellular

beam, the primary function of the supporting structural elements serves only to provide a realistic environment with continuity, load transfer, support conditions, and restraint - all of which contribute to the performance of the beam.

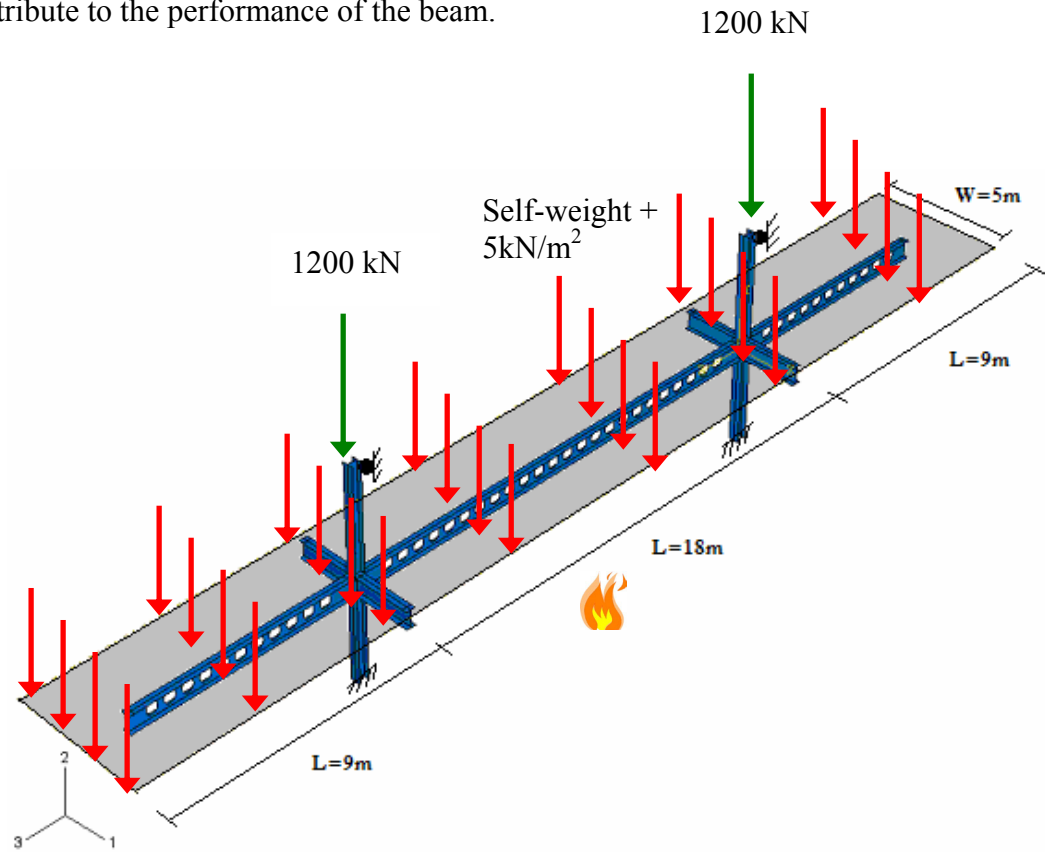


Figure 1 – Interior bay modeled in study incorporating a 18m long-span cellular beam.

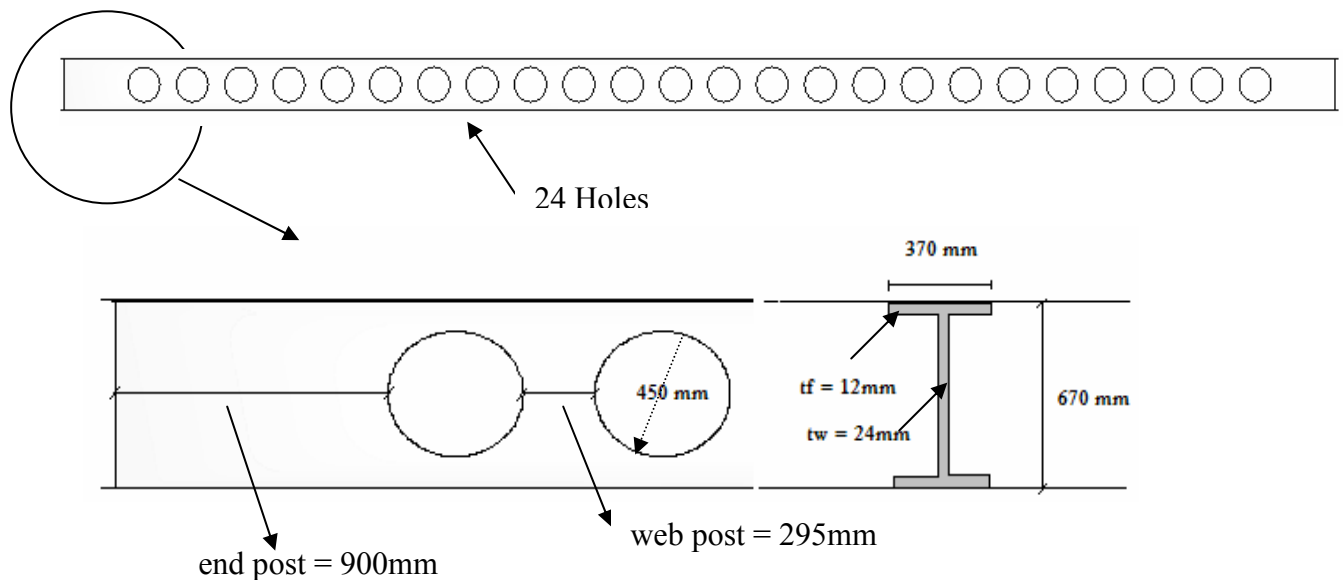


Figure 2 – Cellular beam geometric details of model in study

Table 2: Summary of proposed test cases

Scenario	Case	Hole Diameter [mm]	End Post Size [mm]	No. of Holes	Web Thickness [mm]	Flange Thickness [mm]	Bottom Flange Width [mm]	Span [mm]
Solid Beam		n/a	n/a	0	12	24	370	18000
I	a	150	900	24	12	24	370	18000
		300	900	24	12	24	370	18000
		450	900	24	12	24	370	18000
		500	900	24	12	24	370	18000
	b	450	100	24	12	24	370	18000
		450	400	24	12	24	370	18000
		450	900	24	12	24	370	18000
		450	1400	24	12	24	370	18000
	c	450	900	12	12	24	370	18000
		450	900	24	12	24	370	18000
		450	900	30	12	24	370	18000
	d	450	900	24	8	24	370	18000
		450	900	24	12	24	370	18000
		450	900	24	20	24	370	18000
	e	450	900	24	12	12	370	18000
		450	900	24	12	24	370	18000
		450	900	24	12	48	370	18000
	f	450	900	24	12	24	270	18000
		450	900	24	12	24	370	18000
		450	900	24	12	24	470	18000
	g	450	900	24	12	24	370	6150
		450	900	24	12	24	370	12000
		450	900	24	12	24	370	18000
II*	1-5	450	900	24	12	24	370	18000
III**	1-2	450	900	24	12	24	370	18000
S355 Steel, C35/45 Concrete, Rebar 420								

* In this scenario, the structural model in Figure 1-2 was exposed to time temperature curves with various max temperatures and heating rates. See Figure 3. This scenario will be the focus of a subsequent publication.

** In this scenario, the structural model in Figure 1-2 had web temperatures higher than the flanges. This scenario will be the focus of a subsequent publication.

3. THERMAL INPUT

The structural model in Figure 1 was exposed to the standard ISO-834 fire curve³ while aspects of the cellular beam geometry were varied according to Table 2.

The standard ISO 834 fire curve is represented as follows:

$$T(t) = 345 \log \left(8 \cdot \frac{t}{60} + 1 \right) + T_o \quad (1)$$

where t is in seconds and T_o is the initial or ambient temperature ($^{\circ}\text{C}$).

The heat transfer to the steel, as outlined in Eurocode 3-1-2:2001⁹, was used to determine the solid phase temperature-time curves for the mechanical analysis for the cellular beam; in addition, it was assumed to be uniformly heated through its depth and along its length. For the concrete slab, a 1-D heat transfer analysis was conducted to provide a series

of temperature-time curves at various depths in the concrete slab. These were then applied to the slab in the structural analysis by applying individual temperature-time curves to five different points through the depth of the slab (top, bottom, and $\frac{1}{4}$ points) as illustrated in Figure 3.

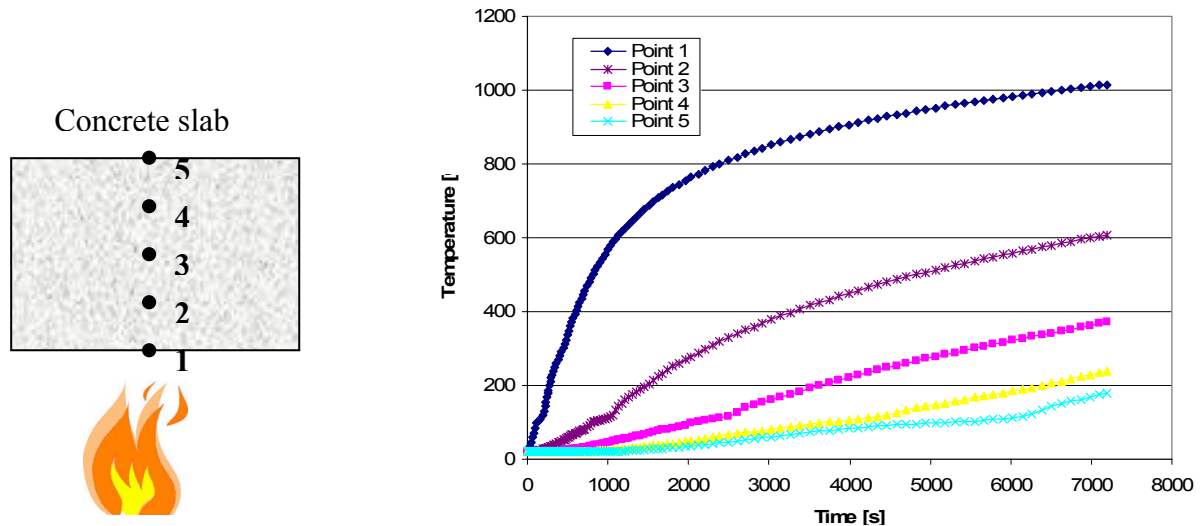


Figure 3 – Concrete slab temperature-time curves through the depth of the slab obtained from the 1-D heat transfer analysis.

4. RESULTS

The structural model as described above is evaluated from several perspectives to determine its sensitivity to different parameters. For the purpose of this paper, only general trends in buckling behavior, connections forces, and midspan displacements will be presented as they relate to variations in cellular beam section geometry and an equivalent solid beam. These trends provide an insight into the parameters that govern the local response of cellular beams in fire, as well as the implications they have for the surrounding structure.

4.1 General Buckling Behavior

Table 3 indicates the observed trends in buckling behavior with respect to buckling/yielding events, buckling mode, and buckling/yielding temperatures for each parameter analyzed in this study. In all the cellular beam cases listed in Table 2, two events were observed, where the first event was buckling or yielding of the bottom flange, and the second event was either buckling of the web post, end post or overall lateral torsional buckling (LTB) of the beam member (See Fig. 4). This response differs from the single buckling event witnessed in the solid beam tests at Cardington.¹³ In these tests, the lower flange buckled near the supports at approximately 120-150°C resulting in an increased rate of deflection and an unloading of the axial forces in the beam (towards tension).

However, in this study, the yielding of the bottom flange in the long span beams occurs at around 95-120°C but does not result in an increased rate of deflection or load reversal, as will be discussed in detail later (See Figure 5). It is not until a second buckling event – the limiting event – that an increased rate of displacement and a trend toward catenary action is observed. This behavior may be attributed to the increased depth of the beams in this study (670mm), which allow the high compressive axial forces to redistribute into the

web and temporarily stabilize the beam response. This critical buckling event, as indicated in Table 2, seems to occur at around 250-300°C, which is significantly lower than that typically sited as the limiting temperature for load bearing structural steel members (~600-800°C)^{6,7,10,11}. This lower temperature is likely the result of the realistic end conditions coupled with the increased slenderness of long span cellular beams relative to the shorter span beam configurations tested in standard fire tests.

Table 3: Trends in observed buckling behavior

Scenario	Case	Parameter Tested	Buckling Events			
			1st Event		2nd Event	
			Description	Temperature °C	Description	Temperature °C
Solid Beam				~108	Overall buckling	280-300
I	a	Diameter = 150mm	Bottom flange buckling/yielding	95-120	Overall LTB	336
		Diameter = 300mm			Overall LTB	321
		Diameter = 450mm			web post + end post	268
		Diameter = 500mm			web post	205
	b	Endpost = 100		95-105	end post	329
		Endpost = 400		130	end post	319
		Endpost = 900		95-105	web post + end post	268
		Endpost = 1400		95-105	web post	285
	c	No. of Holes = 12		95-105	end post + overall LTB	287
		No. of Holes = 24			web post + end post	268
		No. of Holes = 30			web post	202
	d	Web Thickness = 8mm		70	web post	160
		Web Thickness = 12 mm		95-105	web post + end post	268
		Web Thickness = 20 mm		122	Overall LTB	318-322
	e	Flange Thickness = 12 mm		95-105	Local bottom flange	215-365
		Flange Thickness = 24 mm			web post + end post	268
		Flange Thickness = 48 mm			web post	260
	f	Bottom Flange Width = 270 mm		95-105	web post	260-353
		Bottom Flange Width = 370 mm			web post + end post	268
		Bottom Flange Width = 470 mm			web post	296-300
	g	Span = 6150 mm		207	Overall LTB	411
		Span = 12000 mm		139	Overall LTB	292
		Span = 18000 mm		95-105	web post + end post	268

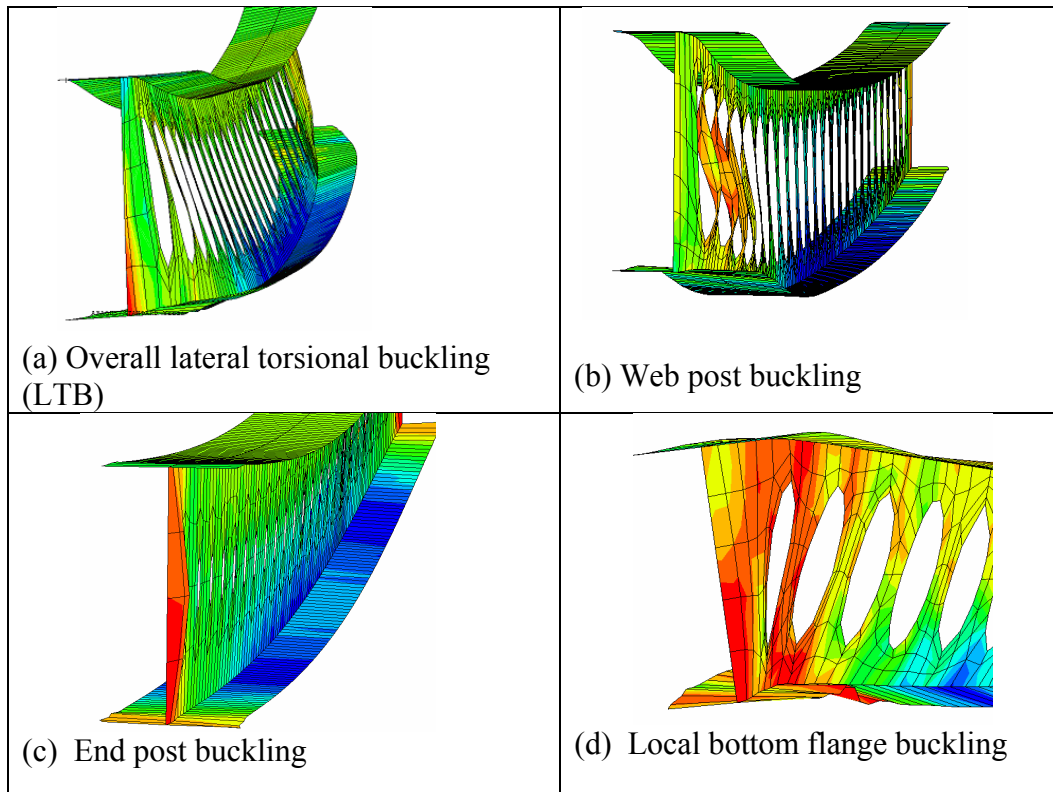


Figure 4 - Modes of behavior of cellular beams at fire limit state

As indicated in Table 3, the mode of buckling in cellular beams appears to occur in the web particularly the posts between the openings. This buckling mode is expected due to the reduced shear capacity as a result of the web openings and Vierendeel effects inherent in cellular beams. Therefore, parameters that increase web stiffness and/or strength (such as cases a-d in Table 2) have a more significant affect on the local buckling mode and overall beam response in the early stages of the analysis. In cases e-f, where the flange width and thickness were varied, little to no change was observed in the buckling mode because the limiting factor continued to be the local web stiffness and strength. So, increasing the flange width or thickness will have little benefit on local buckling modes, where the controlling parameter will still be the web stiffness. While increasing flange thickness or width may have little influence on pre-buckling response, it is expected that there will be some benefit in the post-buckling region where catenary action dominates the overall structural behavior.

The web post buckling observed for the cellular beams differs to the solid beam, which experienced overall lateral torsional buckling – a more ductile/stable buckling mode.¹² Unlike the solid beams tested in Cardington, the solid beam in this study had a more pronounced buckling event, initiating at approximately 280-300°C, as seen later. This behavior can be attributed to the longer spans in comparison to the spans tested in Cardington.

4.2 Cellular Beam Axial Forces And Midspan Displacements

Figure 5 illustrates the connections forces against temperature of the cellular beams with varying web opening diameter. Initially at 20°C, there is a local concentration of compressive forces at the bottom flange of the beam due to an initial hogging moment from the load. As the temperature in the compartment increases, the compressive forces in the beam further increase due to restrained thermal elongation and thermal bowing. This compressive force increases until local buckling or yielding of the lower flange occurs, which is observed for solid beams at Cardington at 120-150°C, as described in the literature.¹³

However, in Figure 5 and Table 3 this local buckling/yielding of the bottom flange appears to occur earlier in the fire for the cellular beams - at around 90-120°C. This could be the result of shear forces from Vierendeel bending and the longer spans causing a local increase in stress concentrations in the bottom flange near the support. For the solid beam model, this local buckling of the bottom flange is also evident at around 108°C.

After the local buckling event, the connection forces appear to stabilize as the thermal expansion induces increased deflections instead of compression. As the beam continues to heat, the deflection rate is seen to increase and a second buckling event is observed at around 250-300°C. At this point, the web posts are starting to buckle as the local web stiffness and shear capacity is overcome by the high shear forces near the supports (Fig 4b). After this point, the deflection rate grows at a higher rate and $P-\Delta$ moments increase rapidly as subsequent web-posts buckle along the length of the beam towards its center and the material properties degrade with increased temperature. These buckling events are also evident in the displacement vs. temperature plots, such as those in Figures 7 and 8. The conventional composite flexure mechanism is now replaced by tensile (catenary) mechanisms.¹³ It is interesting to note, that the system completely changes to catenary action at around 500°C. In previous tests such as those at Cardington, this event occurred much later.¹³ However, the Cardington tests incorporated a composite deck with universal beam sections at a maximum span of 9m, where tensile membrane action of the slab contributed to the performance of the structural system.

As indicated in Figure 5, the connection forces in the cellular beams do not appear to be particularly sensitive to the diameter of the web openings in the pre-buckling region of the response history. However, once buckling has occurred the larger hole diameter beam (500mm) appears to unload (change from compression to tension) at a greater rate than the smaller diameter cases. This response is likely due to the reduced web flexural stiffness of the beam with larger holes relative to the beams with the smaller holes. The buckling of the 500 mm case occurs more rapidly and the beam transitions from a flexural mechanism to a tensile mechanism, as seen in the graph. These observations were also apparent in the displacement histories, where the 500 mm case resulted in larger displacements. Similar trends occurred for the other parameters tested.

The variation in different aspects of the section geometry, except for the web thickness (Figure 6), had little affect on the pre-buckling forces in the beams. The post-buckling behavior, as discussed above for various hole diameters (Fig 5), was also observed in the other parameters studied. That is, the beams with reduced web flexural stiffness (longer end posts*, more holes*, thinner webs) experienced a more rapid transition into tensile mechanisms than the flexurally stiffer beams. (*Note: The variation of these parameters affected the dimension of the web post length, so the beams with longer end posts and the ones with more holes had shorter web posts. These web post characteristics dominated the beam behavior and were the controlling parameter for these cases.)

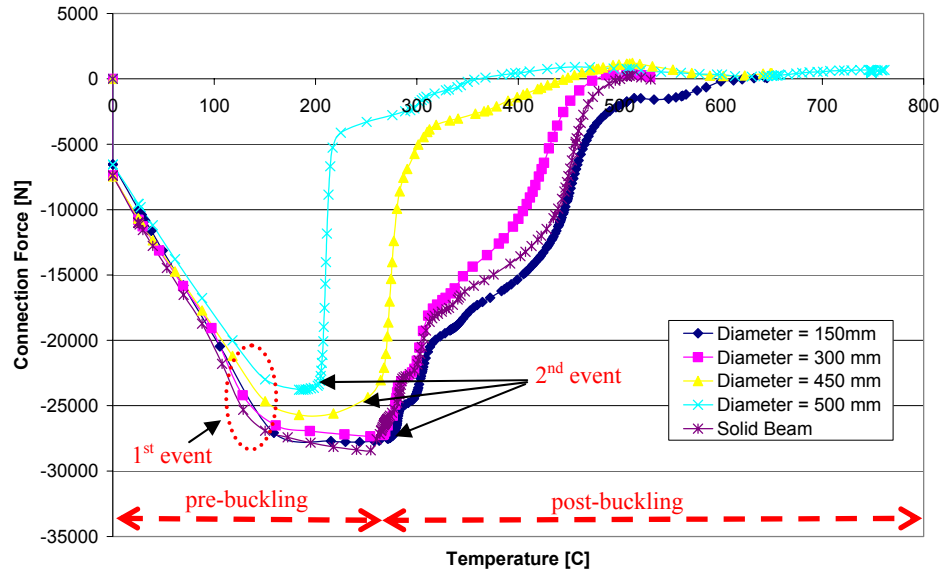


Figure 5 – Connection forces of cellular beams with various web opening diameters

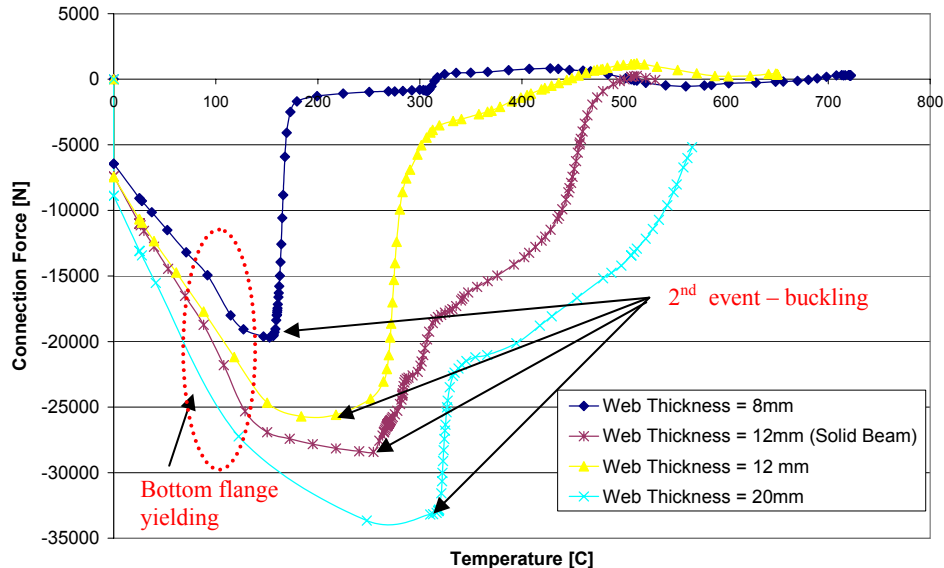


Figure 6 – Connection forces of cellular beams with various web thicknesses

Figure 6 illustrates the significant affect that increasing web thickness plays on the magnitude of the connection forces in the cellular beam. As to be expected, increasing the web thickness increases the axial force in the beam due to the increase in axial stiffness. Although increasing web thickness has resulted in increased axial forces, the buckling mode changes from web post buckling to overall lateral torsional buckling (See Fig 4.c and Table 3). This may prove to be beneficial, as lateral torsional buckling tends to be a more ductile buckling mechanism.¹² Further investigation however is needed.

It is interesting to observe that the connection forces of the cellular beam with a web thickness of 12 mm are smaller than those of an equivalent solid beam. This response is expected due to the reduced axial strength and stiffness of the cellular beam to an equivalent solid beam.

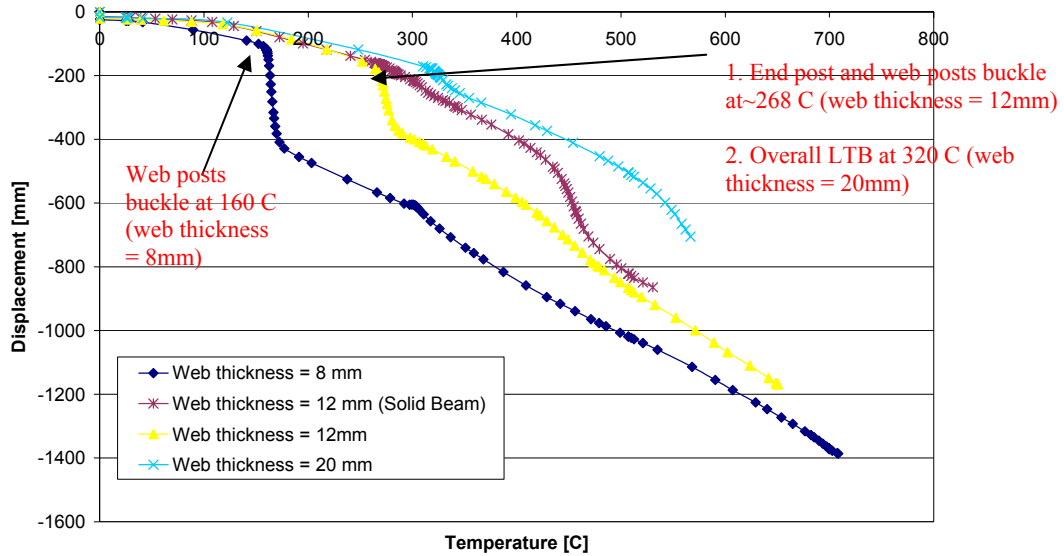


Figure 7 – Displacement versus temperature for varying web thicknesses

As described earlier, the displacement history is closely linked with the overall behavior of the structural system. Figure 7 illustrates the vertical displacement of cellular beams of varying web thicknesses with respect to temperature. Figure 8 plots the displacements versus temperature for cellular beams with varying bottom flange width. These figures reveal not only the initiation of buckling events, but also, the implications of different buckling modes on structural behavior. That is, the type of buckling mode appears to affect the displacement response of the beams.

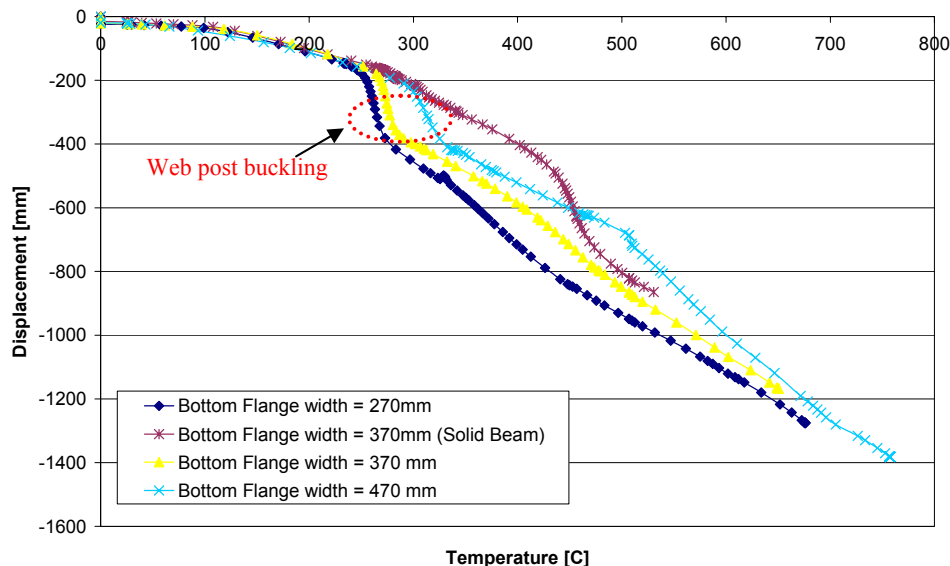


Figure 8 – Displacement versus temperature for varying bottom flange widths.

The thinner webbed cellular beams had web post buckling at around 160°C and subsequently experienced greater displacements than the thicker webbed beams that underwent end post and/or overall lateral torsional buckling modes (Fig 7). The latter buckling modes are typically more stable/ductile as evident by the lower displacement rates. The displacement vs. temperature plots from the varying diameter, number of holes, and end post simulations revealed similar results – the simulations that experienced web post buckling

tended to have increased displacement relative to those that underwent more stable buckling modes (i.e. overall lateral buckling, end post buckling, etc.) As seen in Figure 8, the displacement histories of the cellular beams with varying bottom flange widths had similar responses. In these simulations, all the scenarios experienced web post buckling. Similar trends were also observed for the cellular beams with varying bottom flange thickness.

These observations coupled with the connection force plots seem to suggest a strong correlation between buckling mode and displacement response initially after a buckling event has occurred. This correlation may alter as the simulation continues further into the post-buckling region, where catenary action becomes the dominating structural mechanism. This trend can already be seen in Figures 7 and 8, where the displacement histories are beginning to coincide. The full displacement history (up to the global failure of the structure) will be addressed in future publications.

5. CONCLUSIONS

A long span cellular beam model is evaluated from several perspectives in this study to determine its sensitivity to different parameters. The displacements, local buckling modes and connection forces of each case study were compared with a solid beam model, and general trends were observed. These details indicate the effects varying parameters have not only on global response, but local response of the cellular beam. This study suggests that the characteristics of a cellular beam's web plays a more significant role in the structural fire behavior not only in terms of the local beam response but ultimately on the surrounding structure. While other parameters do influence the structural response, it appears that the cellular beam web characteristics dominate the beam behavior, connection forces, and displacements particularly after a buckling event has occurred. While the web characteristics appear to markedly affect the pre-buckling behavior, they may not have much of a significant role in the post-buckling region where catenary action dominates the global structural response.

6. REFERENCES

-
- [1] ENV 1991-2-2:1995, Basis of design and actions on structures, Part 2-2: Actions on structures exposed to fire, British Standard Institute, 2000.
 - [2] Mac steel. www.macsteel.co.uk. 01-Oct-05
 - [3] BS 476, Fire tests on building materials and structures, Part 21 Methods for determination of the fire resistance of load bearing elements of construction, British Standard Institute
 - [4] Bailey, Colin, "Indicative fire tests to investigate the behaviour of cellular beams protected with intumescent coatings", *Fire Safety Journal*, 39 (2004), pp. 689-709
 - [5] Technical note – 'Fire engineering of cellular beams using intumescent coatings', The Structural Engineer, pp 24-25, October 2002.
 - [6] Interim guidance on the use of intumescent coatings for the protection of beams with web openings. SCI Document RT983. The Steel Construction Institute, Ascot, November 2003.
 - [7] AD269: The use of intumescent coatings for the fire protection of beams with circular web openings.

New Steel Constr 2003; 33–4.

[8] ABAQUS, Inc., Rising Sun Mills, 166 Valley Street, Providence, RI 02909-2499 USA.

[9] ENV 1993-1-2:2001, Design of steel structures, Part 1-2: Structural fire design, British Standard Institute, 2001.

[10] Liu, T.C.H and Liew, K.H. “Behaviour of cellular steel beams in fire.” Interflam Proceedings, 2004. pp157-169.

[11] Lawson, R. M., Oshatogbe, D. and Newman, G.M. “Design of Fabsec Beams in Non-Composite and Composite Applications (including Fire).” <http://www.Fabsec.co.uk>. 01/10/05.

[12] Astaneh-Asl, Abolhassan. Behavior and Design of Steel and Composite Structures. Chapter 6 - Notes. 2004.

[13] Usmani, A.S., Lamont, S. “Key events in the structural response of a composite steel frame structure in fire,” Fire and Materials, 2004: 28:281-297.



BEHAVIOUR IN FIRE OF THERMALLY RESTRAINED COMPRESSED STEEL MEMBERS EXPERIMENTAL AND NUMERICAL APPROACH

Manfred KORZEN¹; I. Cabrita NEVES²;

João Paulo C. RODRIGUES³ and Joaquim C. VALENTE⁴

ABSTRACT

Fire resistance of columns is influenced by the restraint to their axial thermal elongation. This influence has been the object of numerical and experimental research made at Instituto Superior Técnico (IST) in the past. A series of tests on small axially compressed steel elements with restrained thermal elongation was planned to be performed at IST and then compared with some real scale tests on axially compressed steel columns to be performed at the Bundesanstalt für Materialforschung und -prüfung (BAM). While at IST the restraint effect is obtained by means of a real beam located outside the furnace, the BAM test facility makes use of a hybrid sub-structuring system, where the column specimen is tested inside a furnace and the remaining structure is numerically simulated by a computer model. The paper reports on the experimental results and numerical simulations of the tests performed up to now. The correlation between the IST tests and the BAM tests on real scale columns is considered to be reasonable, although the initial load levels are not exactly similar. These first results seem to give support to the generalization of the main conclusions obtained from previous tests on small compressed steel elements and from numerical calculations, to real scale steel columns.

¹ PhD, Bundesanstalt für Materialforschung und -prüfung, Berlin, Germany
email: Manfred.Korzen@bam.de

² Associate Professor, Technical University of Lisbon, Instituto Superior Técnico, Lisboa, Portugal,
email: cneves@civil.ist.utl.pt

³ Assistant Professor, Faculdade de Ciências e Tecnologia da Universidade de Coimbra, Departamento de Engenharia Civil, Coimbra, Portugal,
email: jpaulocr@dec.uc.pt

⁴ Assistant Professor, Technical University of Lisbon, Instituto Superior Técnico, Lisboa, Portugal,
email: jvalente@civil.ist.utl.pt

1. INTRODUCTION

Experimental research has played a fundamental role on the progress of knowledge about the behavior of structures submitted to fire. Single structural members subjected to constant loading and to standard fire conditions were tested in great number during the past half century. The results of these tests, together with the investigation that was done on the mechanical properties of structural materials at high temperatures, have decisively contributed to a better understanding of the behavior of structural elements in fire. For a long period, this was also the only way to classify structural elements in fire resistance classes.

The concept of standard fire has to be abandoned and replaced by the concept of natural fire if we want realistically predict the behavior of structural members in real fires. Also, the inter-actions between structural elements during fire, due to thermal elongations, have to be taken into account. Eccentricities in the axial load acting on columns caused by the thermal elongation of beams cannot be disregarded. The restraint imposed to the thermal elongation of columns by the cold parts of the structure gives rise to a modification of the axial load acting on the column, which may negatively affect the column resistance to fire.

For steel elements, this last effect has been theoretically and experimentally studied by the authors and reported in [1, 2, 3, 4]. These tests have been done using small elements, which had the advantage of allowing a great number of tests to be performed with a limited budget within a limited period of time. In order to check out these results against real scale fire tests, a limited number of tests was planned to be performed using the fire test facilities of BAM and IST. Budget limitations played an important role on the extent of the test program.

2. EXPERIMENTAL SET-UP

2.1 IST

The experimental system for the IST tests was developed bearing in mind that the parameters to be studied should be defined and materialized as rigorously as possible, in order to guarantee a good repeatability, under the existing constraints of a limited budget and the available equipment.

The system, mounted inside a high-stiffness restraining frame, includes a reaction beam, here called stiffness-beam, used to create a restraint to the thermal elongation of the specimen, thus simulating the restraint to the elongation of a real column caused by the surrounding building structure in case of fire. The stiffness-beam is a statically determinate beam. In order to test different restraint ratios, the beam span can be changed and several INP⁵ rolled steel profiles are available (Figs. 1 and 2) [3].

⁵ Portuguese Norm NP- 339

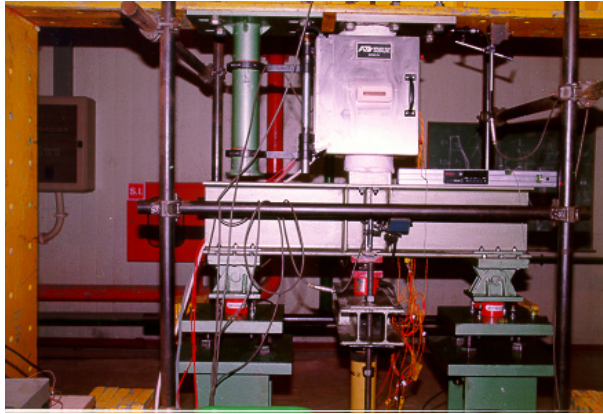


Fig. 1 Experimental set-up

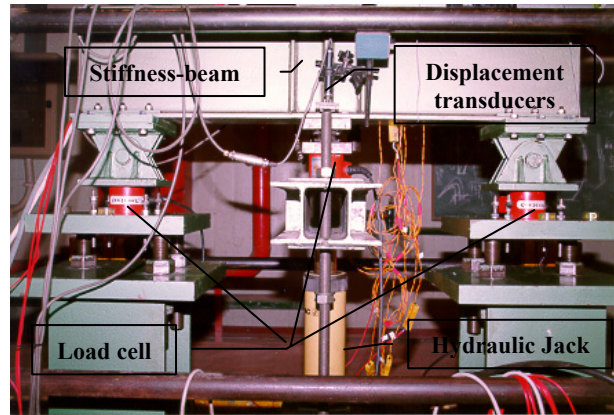


Fig. 2 Stiffness-beam, load cells and load application system

As it would be impossible to reproduce in small-scale some of the characteristics of the profiles used in steel construction, such as those resulting from the manufacturing process, steel bars with rectangular cross section were used in the tests. Their dimensions were chosen according to the slenderness values to be tested and taking into consideration the oven dimensions. The bar length between points of mooring ($h = 370$ mm) was the same in every test. Every bar had a rectangular cross-section with the bigger dimension equal to 50 mm. Therefore, the slenderness of each bar was the direct result of its thickness. Bending and buckling occurred around the weak axis.

A set of support blocks, made of stainless refractory steel, were built for these tests. They connected rigidly the test specimens to the reaction frame and to the stiffness-beam and had to withstand the forces developed during the tests without damage (Fig. 3). In the tests, the rotational stiffness of the stiffness-beam was so high that the specimens behaved as perfectly built-in.

The evolution of the restraining forces during the test was measured by two load cells placed under the stiffness-beam. This location was chosen because it was not possible to place a load cell between the support of the specimen and the stiffness-beam (Fig. 2 and 3).

At the beginning of each test, the specimen was subjected to the action of a compression load that was kept constant during the entire test. This load is intended to simulate the design value of the axial load acting on a building column in fire situation. The load was applied by a hydraulic jack to the bottom flange of the stiffness-beam while keeping its supports free to move vertically (Fig. 2).

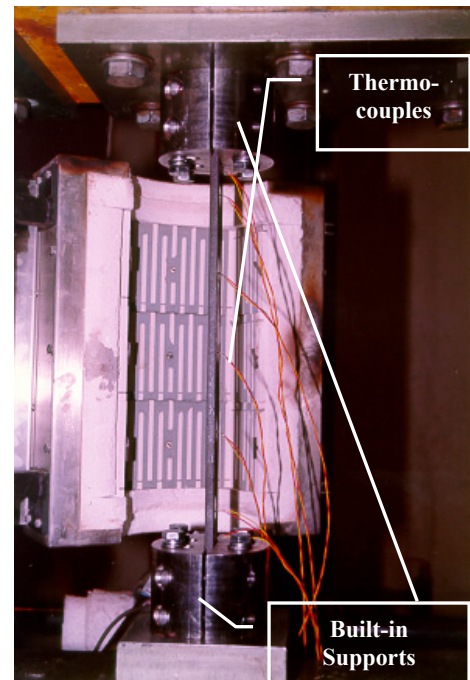


Fig. 3 Built-in bar before testing, with thermocouples

Afterwards, the supports were fixed, so that the stiffness-beam could react to the elongation of the specimen during heating. In order to achieve uniform heating conditions during the tests, an electric three-zone oven was used. This oven could reach temperatures up to 1200 °C and was controlled by computer with special software (Fig. 3).

In addition to the oven temperatures in these three zones, several other variables were measured:

- the temperature of the specimens at seven levels along the axis
- the displacements at the bottom flange of the stiffness-beam under the lower support of the heated specimen.
- and for control, the displacements of the reaction frame just above the upper support of the heated element and in several other components of the experimental system.

The experimental system used in the IST tests showed good repeatability of results and all the components performed well during the entire test programme.

2.2 BAM

A central role of the substructuring method (see e.g. [5]) plays the *BAM* column furnace (Fig. 4 (b)). Mechanical and thermal actions are applied through this device to the specimen under test. Whereas the thermal set point is a known function of time for the mean gas temperature before starting the test the mechanical set point has to be calculated online during a fire test in substructuring mode. Six electro-hydraulic control channels equipped with displacement and force sensors are available to influence the mechanical boundary conditions, i.e. two bending rotations each at top and bottom, one axial displacement at the bottom and one horizontal displacement at the top. During a substructuring test forces and moments at the boundaries of the specimen, i.e. at the upper and lower bearings of the column, are measured and utilized for the computation of the corresponding displacements and angles, which are sent to the specimen in order to keep the entire building in mechanical equilibrium with its prescribed overall boundary conditions.

This closed loop for only one channel in substructuring mode is displayed in Fig. 4 (b) – (c). According to the free body diagram in Fig. 4 (c), the experiment is *driven* by the thermal displacement, which is diminished by the mechanical displacement u^{mech} due to the stiffness c^{mod} of the surrounding environment resulting in a compressive force on the column under test. The function of the control loop is to change the (total) displacement u by moving the position of the electro hydraulic axial cylinder in such a way that the model force f^{mod} is equal to the measured force f .

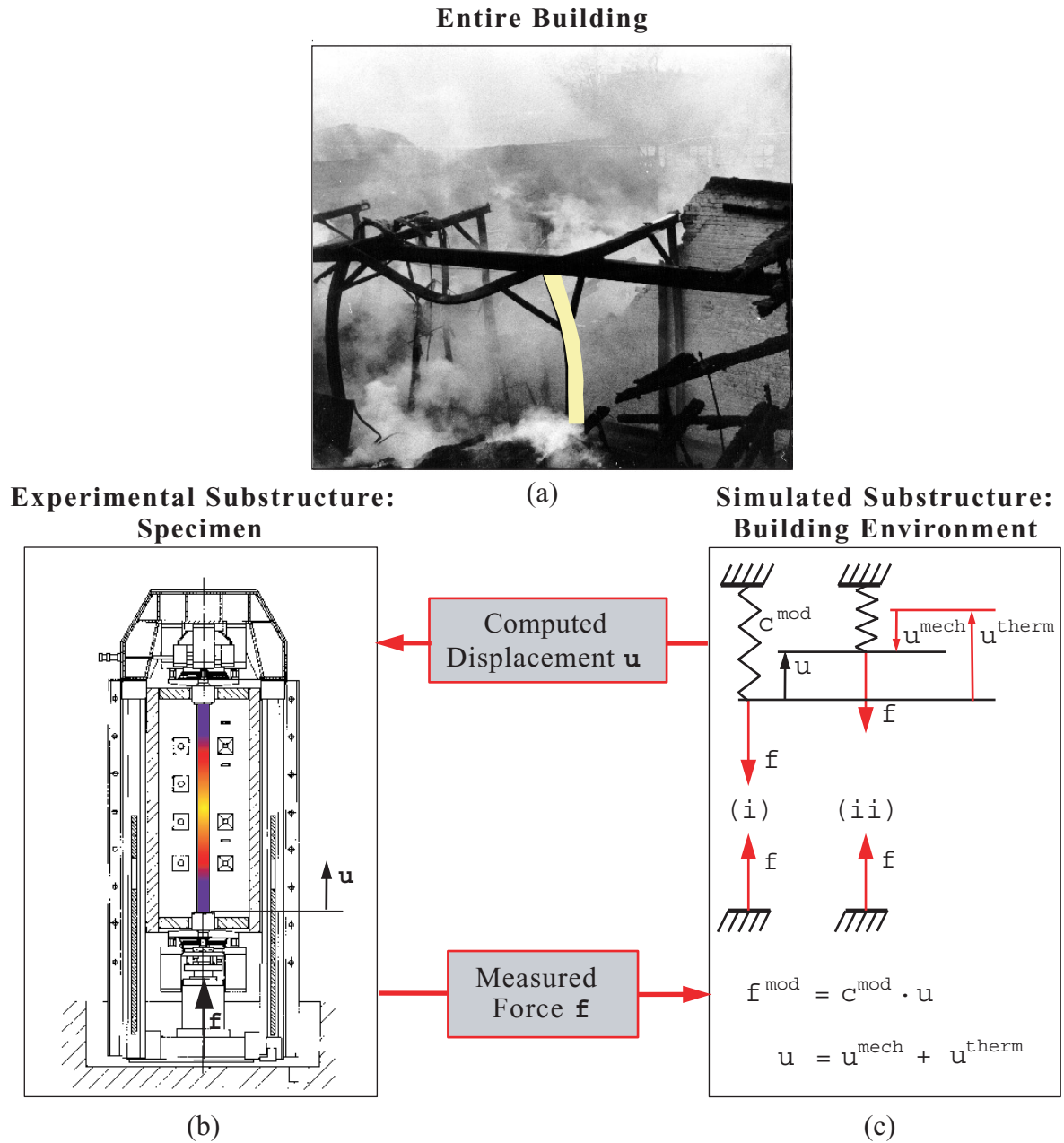


Fig. 4 – Substructuring Method – Basic Idea

3. TEST PLAN

The main objective of the test series was the identification of common features between the behavior of small axially compressed steel elements and real scale steel columns when subjected to elastic restraint to the axial elongation, in order to allow the application of the knowledge previously obtained on the basis of tests on small elements, to real columns.

One of the main correlation parameters identified was the non-dimensional stiffness ratio R , defined as the ratio between the axial stiffness K of the external system (external beam in the case of the IST tests, virtual structure in the case of the BAM tests) and the cold axial stiffness of the tested specimen (small element or column)

$$R = \frac{K}{\frac{EA}{L}} \quad (1)$$

where

E – Young's Modulus of steel at room temperature

A – Cross-sectional area of the tested specimen

L – Length of the tested specimen

Tables 1 and 2 summarize the values of the parameters used in the tests. Four values for R were chosen: 0,288; 0,173; 0,123 and 0,074 (tables 1, 2). The tests performed at IST were done using 370 mm long fixed end bars (no end rotations), with two cross-sectional dimensions: 50x20 mm and 50x12 mm. The columns tested at BAM were made of 3560 mm long steel profiles HEM 200 and HEA 140, having also fixed ends.

IST					Parameters	BAM
50x20 (mm)					Section	HEM 200
322					f_{ay} [N/mm ²]	235
32,1					λ	33,8
0,400					$\bar{\lambda}$	0,359
98					K [kN/mm]	134
0,173					R	0,173
148,15	160,43	148,14	148,17	148,32	P ₀ [kN]	1935
0,51	0,55	0,51	0,51	0,51	$P_0 / N_{fi,Rd,t=0}$	0,68
10,0	2,5	2,5	2,5	10,0	Furnace heating rate [K/min]	ISO 834
IST-1	IST-2	IST-4	IST-5	IST-6	Test n°	BAM-4
42					K [kN/mm]	57
0,074					R	0,074
			148,25	148,26	P ₀ [kN]	1935
			0,51	0,51	$P_0 / N_{fi,Rd,t=0}$	0,68
			25	5	Furnace heating rate [K/min]	ISO 834
			IST-9	IST-10	Test n°	BAM-3

Table 1 – Test Parameters ($\lambda = 32.1$ (IST), $\lambda = 33.8$ (BAM))

In the IST tests, two values for the stiffness K were chosen, 98 kN/mm and 42 kN/mm which, in combination with the two cross-section types, result in the four R values mentioned above. The stiffness values K to be used in the BAM tests were then calculated in such a way that the value of R would be the same as the one used in the IST tests.

All the tests were done on bare steel specimens. The ISO 834 standard curve was used in every BAM test, while in the IST tests four furnace heating rates were used: 2,5 K/min; 5 K/min; 10 K/min; 25 K/min.

The initial load level is defined as

$$P_0 / N_{fi,Rd,t=0} \quad (2)$$

where

P_0 – Initial applied load

$N_{fi,Rd,t=0}$ - Buckling resistance of the specimen in fire situation at time $t = 0$ (calculated with $\gamma_{M,fi} = 1$ and yield stress values experimentally obtained on probes cut from the steel profiles used for the test specimens).

In the IST tests two initial load levels were used, 0,51 and 0,54, while the corresponding initial load levels in the BAM tests were 0,68 and 0,55.

IST		Parameters	BAM
50x12 [mm]		Section	HEA 140
318		f_{ay} [N/mm ²]	269
53,4		λ	50,6
0,662		$\bar{\lambda}$	0,576
	98	K [kN/mm]	
	0,288	R	
	77,05	P_0 [kN]	
	0,54	$P_0 / N_{fi,Rd,t=0}$	
	5,0	Furnace heating rate [K/min]	
	IST-3	Test n°	
42		K [kN/mm]	22,8
0,123		R	0,123
77,14	77,08	P_0 [kN]	370
0,54	0,54	$P_0 / N_{fi,Rd,t=0}$	0,55
5	25	Furnace heating rate [K/min]	ISO 834
IST-7	IST-8	Test n°	BAM-5

Table 2 - Test Parameters ($\lambda = 53.4$ (IST), $\lambda = 50.6$ (BAM))

4. TEST RESULTS

Figs. 5 to 8 compare the test results obtained in IST using small compressed elements with the test results obtained at the BAM test facilities on real scale columns. The comparison is made on the basis of the value of the stiffness ratio R.

Figs. 5 and 6 show the experimental results obtained in the tests where the highest stiffness ratio ($R=0,173$) was used. The IST furnace heating rate makes the difference between these two graphs, 10 K/min in Fig. 5 and 2,5 K/min in Fig. 6.

One first conclusion to be drawn from these two graphs is that the loading paths of all the curves overlap quite reasonably. This is a consequence of having used the same grade of thermal restraint in every test.

The maximum restraint force and the unloading path of the BAM curve lie below the IST curves. This is a consequence of having used in the BAM test an initial load level of 0,68, which is higher than the initial load levels used in the IST tests (0,51 – 0,55). This effect can also be observed by comparing the IST-2 curve and the IST-4 and IST-5 curves in Fig. 6. The IST-2 curve lies below the IST-4 and IST-5 curves. This is a consequence of different initial load levels. The IST-2 curve corresponds to an initial load level of 0,55, while the IST-4 and IST-5 curves correspond to an initial load level of 0,51.

Comparison between the IST curves in Figs. 5 and 6 shows only a minor influence of the heating rate, in terms of maximum restraint force and corresponding temperature. The temperatures at which the unloading paths reach the initial load level are a bit lower in Fig. 6 than in Fig. 5. Nevertheless, in spite of the scattering between the IST curves, the temperatures at which the unloading paths reach the initial load level are quite similar (scatter below 50 °C). These temperatures are directly related to the fire resistance of the elements (see [1] to [4], [6]). In fact, for higher temperatures, the mechanical resistance of the element is lower than the initial acting load, which can be seen as the load share that the element must support in fire situation.

All these tests were performed on elements having a relatively low slenderness ratio (32,1 – 33,8). Therefore, the shape of the curves reflects, to a great extent, the material behaviour at high temperatures, playing the second order effects a secondary role.

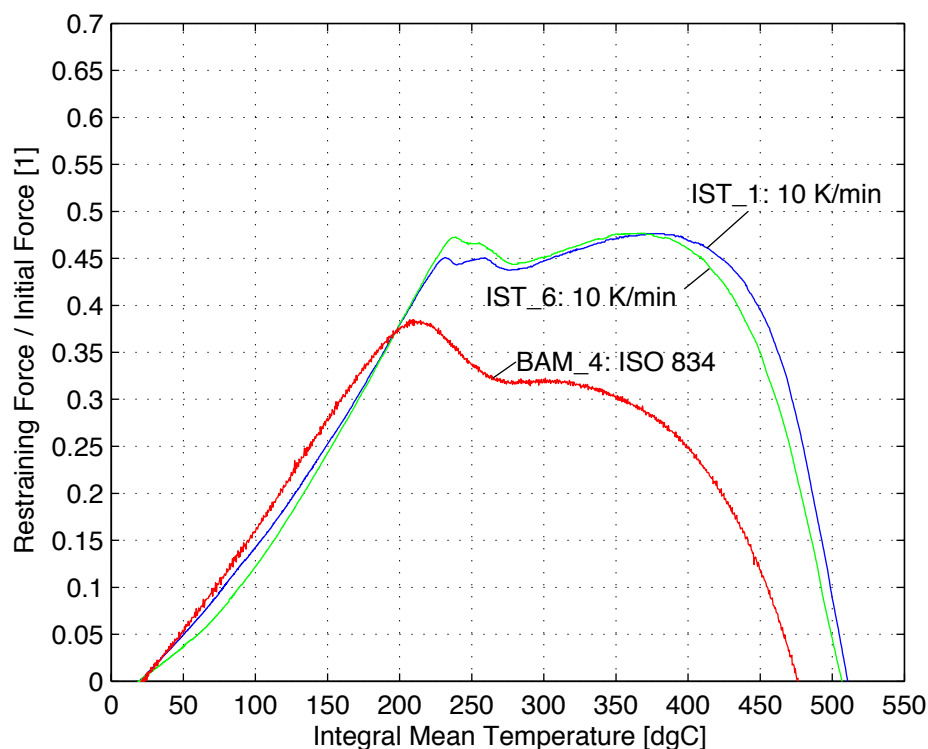


Fig. 5 – Non-dimensional evolution of restraining forces for $R = 0,173$

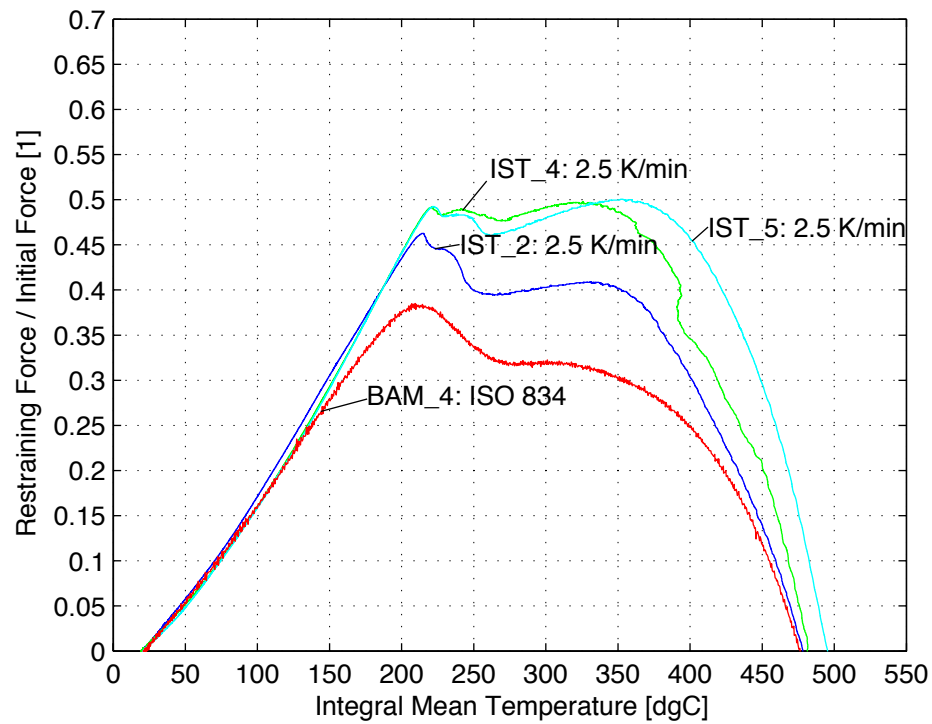


Fig. 6 - Non-dimensional evolution of restraining forces for $R = 0,173$

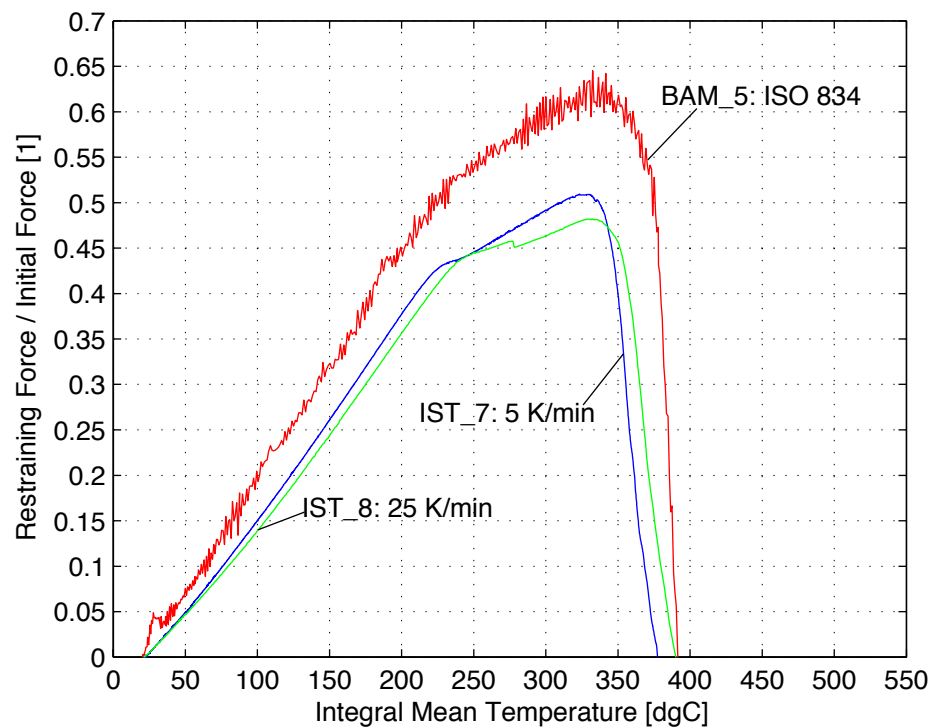


Fig. 7 - Non-dimensional evolution of restraining forces for $R = 0,123$

Fig. 7 holds for a lower stiffness ratio ($R=0,123$), approximately the same initial load level than the one used in the above IST tests, but a higher slenderness ratio (50,6 – 53,4 instead of 32,1 – 33,8).

The whole curve BAM-5 lies above the IST curves. Geometrical and material imperfections of the specimens may lead to differences between the theoretically determined and the real initial load level. This could be one explanation. The IST bars would be, in principle, more sensitive to these aspects.

The temperatures at which the unloading paths reach the initial load level show a small scatter but are now lower than in the above tests (less than 390 °C). The higher slenderness ratio is the main responsible for this reduction. The shape of the curves shows now a different pattern. The unloading path is now closer to the vertical, which is typical of low stiffness ratios [1].

Fig. 8 refers to the lowest stiffness ratio ($R = 0,074$) and the same slenderness ratio of Figs 5 and 4 (32,1 – 33,8). The loading paths show a very good correlation but the maximum restraining forces differ substantially. Here again, the difference between the initial load levels, 0,51 in the IST tests and 0,68 in the BAM test, can help explain this difference. The temperatures at which the unloading paths of the IST curves reach the initial load level are identical if Figs 8 and 5, showing the small influence of thermal restraint in columns with low slenderness ratios.

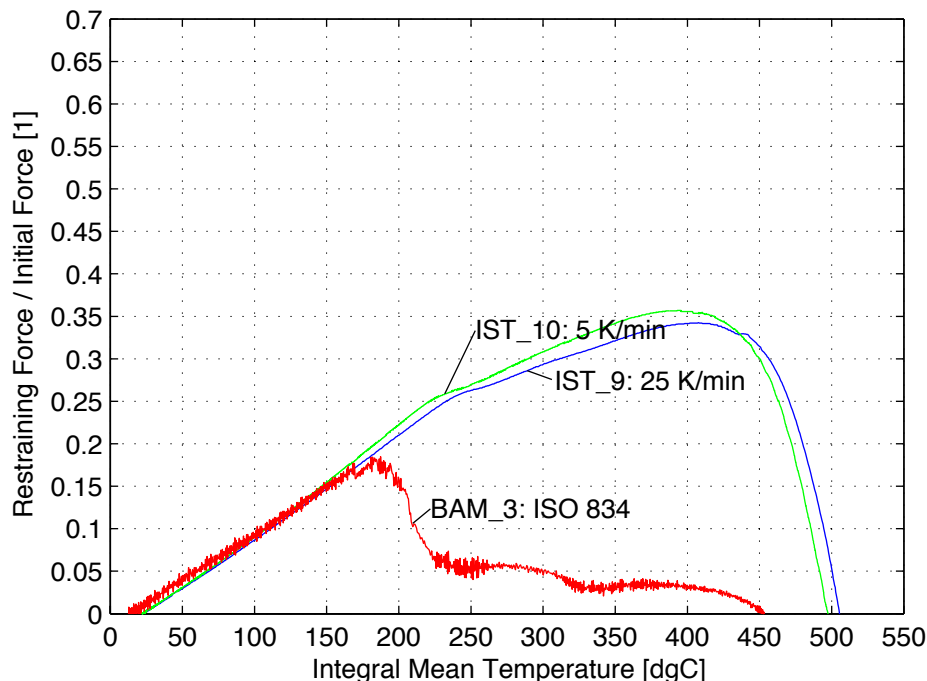


Fig. 8 - Non-dimensional evolution of restraining forces for $R = 0,074$

5. NUMERICAL SIMULATIONS

The finite element program FineFire [6] was used in the numerical simulations. The program uses an isoparametric Euler-Bernoulli beam finite element. The element was developed taking into account geometrical non-linearity and using an approximate updated Lagrangian formulation. This type of element has two nodes in the plane x, y and 3 degrees of freedom per node.

Under fire conditions, steel elements usually have a non-uniform temperature distribution along the longitudinal axis and, to some extent, in the cross sections. So, the material mechanical and thermal properties are different from point to point. These conditions are introduced into the stiffness matrix by numerical Gauss integration. The temperature dependent material properties of steel were taken from Eurocode 3 [7], namely the constitutive laws with the strain hardening option, and the thermal elongation relationships.

The non-linear equation relating the stiffness matrix of the structure to the displacement vector is solved by using the Newton-Raphson method. The stiffness matrix is updated in each iteration. The equilibrium criterion is based on out-of-balance forces. These out-of-balance forces are taken as applied forces in the next iteration.

The BAM-4 and BAM-5 tests were simulated by the program. Fifteen nodes, uniformly distributed along the column axis, were used. The node temperatures were obtained by interpolation from the measured temperature fields (Fig. 9).

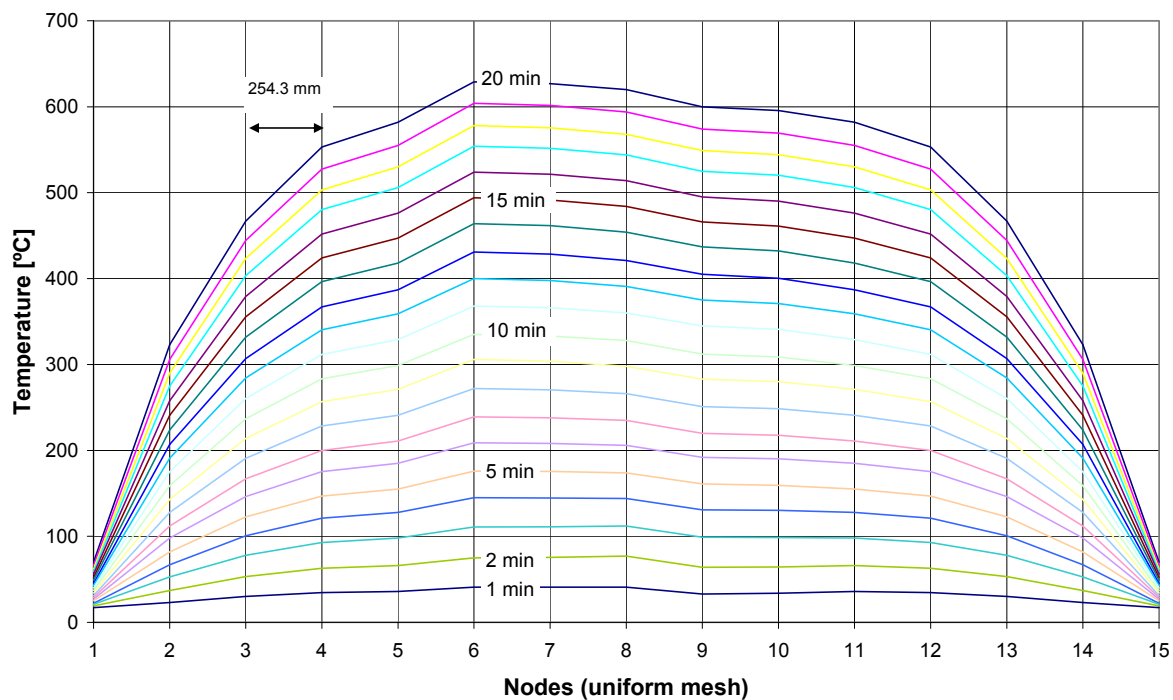


Fig. 9 – Measured temperature fields used in the simulation of the BAM-4 test

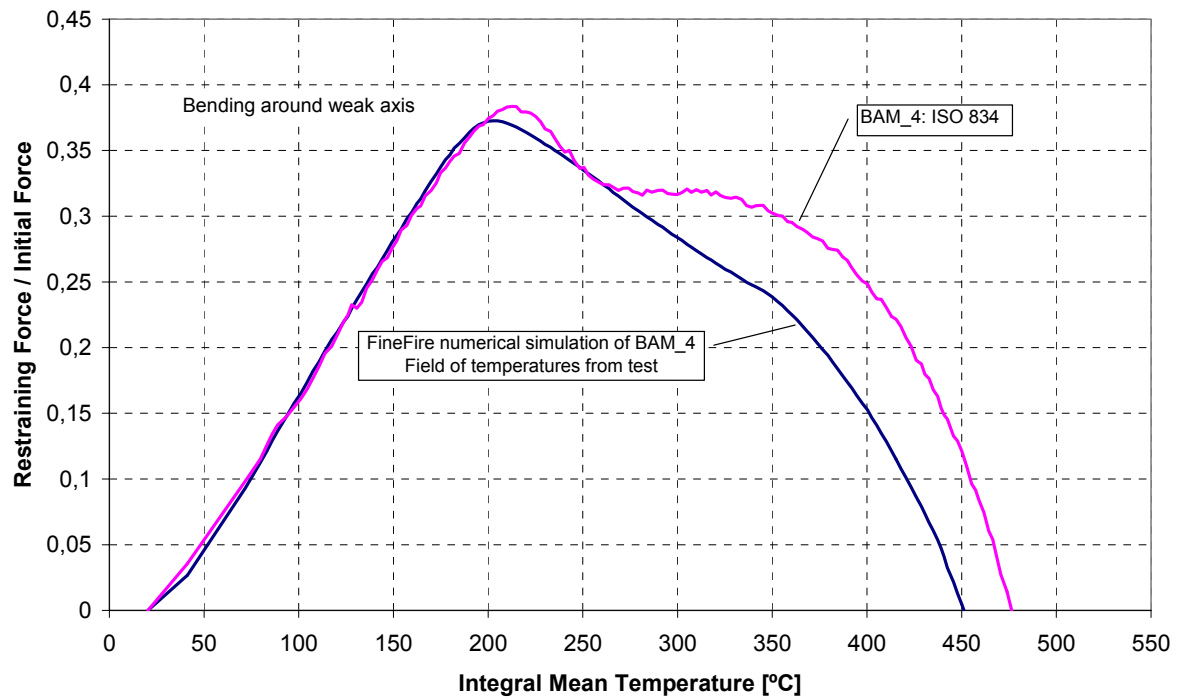


Fig. 10 – Measured and calculated evolution of restraining forces for BAM-4 test ($R = 0,173$)

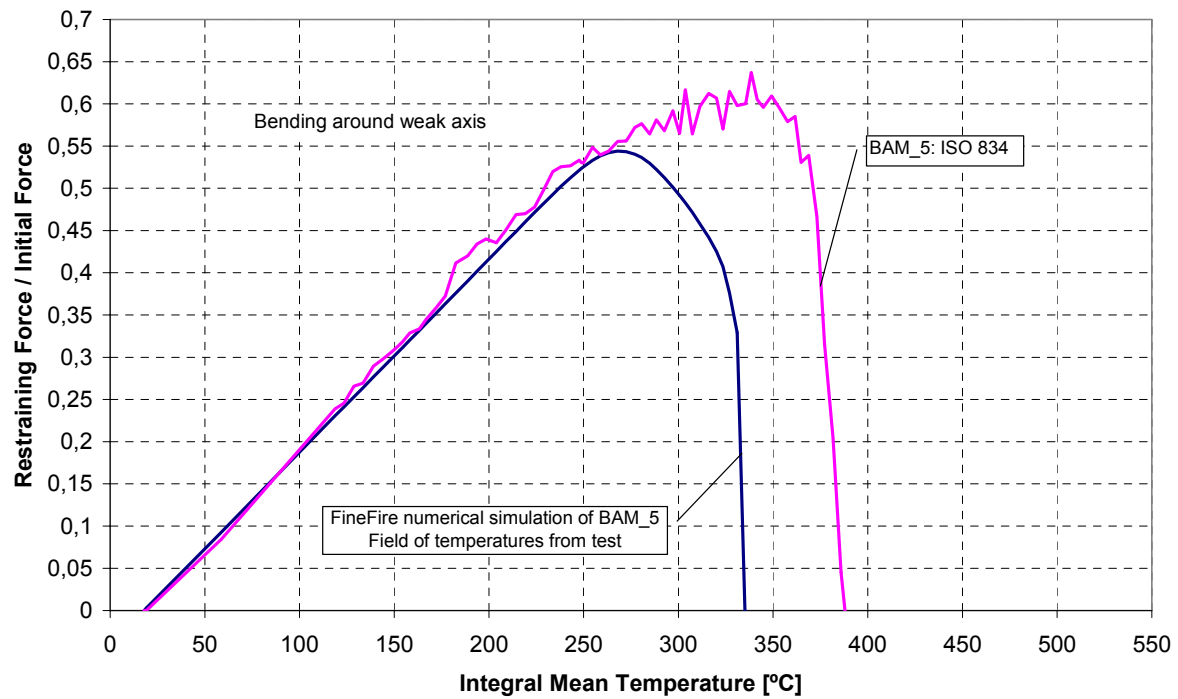


Fig. 11 – Measured and calculated evolution of restraining forces for BAM-5 test ($R = 0,123$)

Fig. 10 shows a reasonable correlation between measured and calculated values. The correlation between the loading paths is very good, showing that the planned restraint ratio was really achieved during the test. Geometrical and material imperfections of the column may lead to differences between the theoretical and the real initial load level. This would explain the worse correlation between the unloading paths.

The same comments apply to the graph of Fig. 11. The program takes into account the geometrical imperfections. If they are smaller in the real column than it was assumed in the calculations, the result could be the scatter that we see in Fig.11. A wrong measurement or low representativeness of the yield stress would have the same result.

6. CONCLUSIONS

The correlation between the series of tests performed at IST on small compressed steel elements and the tests performed at BAM on real scale columns is considered satisfactory, although the initial load levels are not exactly similar. The correlation between the BAM tests and the calculated values are also satisfactory. These first results seem to give support to the idea of generalizing the conclusions obtained in previous works ([1] to [4]), from tests on small compressed steel elements and from numerical calculations, to real scale steel columns.

Special attention was given in this work to the temperature at which the unloading path of the restraining forces reaches the initial axial load level. In a structure, this initial load may be seen as the share of the load combination in fire situation that the column is supposed to carry during fire. Indeed, when the mechanical resistance of the column has decreased below that limit, the column no longer fulfills the role it was expected to, despite the fact that global structural failure may not occur. Therefore, the steel temperature at which this occurs will define the fire resistance of the column.

Increasing the ratio of restraint to the thermal elongation of axially compressed columns will in general lead to a reduction in the fire resistance of the columns. Slender columns are the most affected. For these columns, the reduction in fire resistance may not be negligible, even in buildings where the restraint is moderate. Therefore, calculating the fire resistance on the basis of a constant axial load may lead to unsafe results.

7. ACKNOWLEDGEMENTS

The authors would like to thank GRICES – Gabinete de Relações Internacionais da Ciência e do Ensino Superior (ex. ICCTI) and DAAD – Deutscher Akademischer Austausch Dienst for supporting the travels and accommodation in the trips to each institution participating in this scientific cooperation project.

8. REFERENCES

- [1] Cabrita Neves, I. - “The Critical Temperature of Steel Columns with Restrained Thermal Elongation” - Fire Safety Journal - International Association for Fire Safety Science, Vol. 24 No. 3, 1995, Pgs. 211-227, Ed. D. D. Drysdale, University of Edinburgh, Unit of Fire Safety Engineering, Department of Civil Engineering and Building Science, School of Engineering, The King’s Buildings, Edinburgh., October, 1995.
- [2] Valente, Joaquim C.; I. Cabrita Neves – “Fire Resistance of Steel Columns with Elastically Restrained Axial Elongation and Bending”, Journal of Constructional Steel Research, Vol. 52 No. 3, pp. 319-331, December, 1999.
- [3] Rodrigues, J.P.C.; I. Cabrita Neves; J. C. Valente – “Experimental research on the critical temperature of compressed steel elements with restrained thermal elongation”, Fire Safety Journal - International Association for Fire Safety Science, Vol. 35 No. 2, 2000, Pgs. 77-98, Ed. D. D. Drysdale, University of Edinburgh, Unit of Fire Safety Engineering, Department of Civil Engineering and Building Science, School of Engineering, The King’s Buildings, Edinburgh., September, 2000.
- [4] Cabrita Neves, I.; J. C. Valente; J.P.C. Rodrigues – “Thermal Restraint and Fire Resistance of Columns” - Fire Safety Journal - International Association for Fire Safety Science, Vol. 37 No. , 2002, Pgs. 753-771, November 2002.
- [5] Korzen, M.; G. Magonette; Ph.Buchet – “Mechanical Loading of Columns in Fire Tests by Means of the Substructuring Method” - Zeitschrift für Angewandte Mathematik und Mechanik, Vol. 79, 1999, pp. S617-S618.
- [6] Valente, J. C.: Simulação do Comportamento das Estruturas Metálicas Sujeitas a Altas Temperaturas, Ph. D. thesis, Instituto Superior Técnico, 1988, (in Portuguese).
- [7] Comité Européen de Normalisation, “Eurocode 3: Design of Steel Structures - Part 1.2: General Rules - Structural Fire Design”, EN 1993-1-2, April, 2005.



A NOVEL ENGINEERING TOOL FOR THERMAL ANALYSIS OF STRUCTURAL MEMBERS IN NATURAL FIRES

Hong LIANG¹ and Stephen WELCH²

ABSTRACT

A novel CFD-based methodology for generalised thermal analysis of protected steel structures in fire has been developed, in order to overcome some of the limitations of detailed thermal analysis methods^[1]. Relying on having an appropriate balance of semi-empirical methods and detailed numerical heat transfer approaches, in order to give solutions of sufficient accuracy for structural members in a generalised fashion, the novel methodology has been developed as an essentially 1D heat transfer model^[2] with appropriate representations for 2D and 3D effects to reconstruct a quasi-3D solution. The model has been implemented both in spreadsheet format, to facilitate sensitivity studies for model verification and identification of key parameters, and as a submodel within the SOFIE RANS CFD code^[3]. Parallel calculations are performed to consider a range of parameters of interest, including member size and protection material properties, as well as uncertainties in some of the essential input parameters (such as emissivities). Model sensitivities are demonstrated, revealing the expected strong dependencies on the properties of the thermal protection materials. Initial validation is undertaken with respect to the full-scale tests on a 12m x 12m compartment at BRE Cardington^[4], comparing with the measured temperatures in a protected steel indicative, with satisfactory agreement. Predictions of steel temperatures for variations on the key input parameters will ultimately be provided as field variable predictions by the parallel calculations implemented in the CFD code, thereby providing a much more flexible means of assessing the thermal response of structure to fire than has been available hitherto. The final result is a comprehensive, but practical tool for structural fire design, with potential to improve the efficiency and safety of the relevant constructions.

Keywords: Thermal analysis; CFD; Heat transfer; Numerical modelling; Protected steel

¹ PhD student, University of Edinburgh, School of Engineering and Electronics, Edinburgh, UK,
email: H.Liang@ed.ac.uk

² Lecturer, University of Edinburgh, School of Engineering and Electronics, Edinburgh, UK,
email: S.Welch@ed.ac.uk

1. INTRODUCTION

Over the last two decades, attempts to consider more realistically the effects of fire on structures have intensified. This has been motivated in part by the introduction of performance-based codes, which make some provision for design analysis of steel-framed buildings on the basis of the predicted response of structures to "natural" fire exposures. However, in the context of "whole-frame" mechanical analyses, the member temperatures are normally still prescribed very crudely and conservatively, often taking a single worst case temperature value for an entire enclosure. More general methods are required for natural fires, which can better account for localised heating effects.

Simulations based on computational fluid dynamics (CFD) can in principle provide a much more detailed description of the thermal environment and the effects of localised heating. Nevertheless, research to date^[1] suggests that detailed thermal analysis of structural members in the context of simulations of full-scale building fires is rather problematic, considering the difference of scale between the mesh which can be afforded for the fire and that required for the thermal analysis of the structure and the high computational demands for coupled analyses. Moreover, with conventional approaches it is necessary to define in advance the specification of the structural members (i.e. section sizes, protection details, thermal properties) and this means that the results may be of very limited application. For example, if on the basis of the simulation results it is decided that any details of the specification need to be modified, or member placement changed, then the whole analysis must be repeated, including the CFD simulation. There is a clear need for much more general and flexible procedures to assess the performance of structures in fire.

In this work a novel methodology is proposed with the aim of creating a more generalised treatment by including computation of a set of "steel temperature field" parameters within the whole of the CFD calculation domain, accommodating, by means of parallel calculations, both uncertainties in the input parameters and possible variants to the specification. By predicting the member temperatures at each point in space the limitations of existing methods with regards to the position of the structural component are bypassed. And by performing parallel calculations which span the range of cases of possible interest, to provide a library of relevant solutions for any given fire scenario, the generality of the results is greatly increased. Considering the potentially great computational costs associated with the large numbers of thermal analysis calculations required (equal to the number of gas-phase cells times the number of variants studied in the parallel calculations), approximate methods are employed to reduce the full 3D thermal response problem down to treatments which are essentially 1D but which include appropriate representations of the heat transfer processes in the other dimensions to reconstruct a quasi-3D solution.

In general the novel methodology relies on having an appropriate balance of semi-empirical methods and detailed numerical heat transfer approaches, tailored to give solutions of sufficient accuracy for problems of interest. A modelling framework which exploits a simple thermal penetration model for the protection^[2], coupled to an essentially lumped parameter representation of the steel heating, has been constructed to calculate the thermal response of protected members. Newton-Raphson and Runge-Kutta procedures are used to solve for the surface temperature and to advance the solution in time, respectively, and these treatments have been further developed as submodels within the SOFIE RANS CFD code^[3]. The proposed novel methodology has been verified by performing sensitivity studies based on simple spreadsheet implementations and initial validation is reported with reference to the full-scale tests on a 12m x 12m compartment undertaken at BRE Cardington^[4].

2. MODELLING PROCESSES

2.1 Problem statement

As aforementioned, the novel methodology is developed through constructing the generalised 1D model and further considering the 2D or 3D effects within the heat transfer processes by appropriate approximations. The computations are performed in each gas-phase CFD cell in the computational domain. The generalised 1D model is constructed through analysing the heat transfer to and within an element in an idealised protected steel member exposed to heat on both faces, as shown in Fig. 1 below:

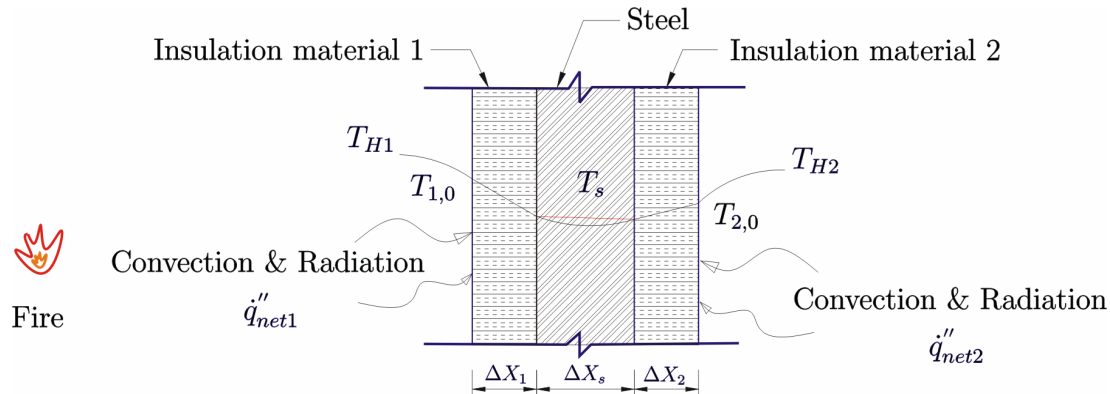


Fig. 1—Temperature distribution from a fire to a protected steel member

This element is supposed to be representative of a slice of a protected steel structure, e.g. a finite section of a flange or a web; two faces are used to allow for situations where the exposure conditions on each side might vary, encompassing also the case of hollow sections with very different exposures on the inside of the structure.

As is well-known in numerical models of heat transfer, the above situation is a strongly coupled problem, with the net heat fluxes at the gas-solid interface very much dependent on the surface temperature, but both also related to the transient thermal response of the structure itself. With simple explicit methods, large numerical errors could arise in the predictions of surface temperature. Therefore, “semi-implicit” methods are adopted here, using Runge Kutta integration to advance each timestep, and strongly link the gas- and solid-phase processes.

A relatively simple treatment has been adopted to implement the generalised 1D model itself, with a lumped parameter model being used for the steel and the coupled thermal response of the protection layer modelled with a semi-empirical treatment for transient heating, allowing for spatially and temporally varying temperature gradients within the solid. The surface temperature, protection material temperatures and the steel temperature are each updated at appropriate time intervals, which might be equal to the CFD timestep, if necessary, but can also be set to longer intervals to improve efficiency (reflecting the fact that the thermal response is normally much slower than evolution of gas-phase conditions).

The implementation of the model takes into account several possible factors which affect the transient response, in particular the temperature-dependent thermal properties, including the effects of moisture in the protection materials. This is important as these properties can have great impact on the thermal response of the structural members, and thus significant errors might occur if only constant values are used^[5].

Clearly, for a completely general or comprehensive model, 2 and 3D thermal effects must also be considered. Nevertheless, due to the multiplying computational costs, the novel

methodology described here chooses to reduce the full 3D analysis problem into quasi-3D by simply correcting the 1D model results with heat transfer process representations for the other dimensions, bearing in mind that it is sufficient to determine the “worst” case temperature in the component, and neglecting second-order errors. At present, the following effects are considered:

- Junction effects, i.e. where there is a temperature differential due to the fact that the exposure of one part of the structural component, e.g. a flange or a web, is dominant over that of a connected part;
- End effects, e.g. the cells at the extremity of the flange which are heated from different directions;
- Heat sink effects, e.g. where a beam or column is in contact with ceiling slab;
- Axial temperature gradients, e.g. where a column goes into a hot layer, or where there are significant horizontal temperature gradients.

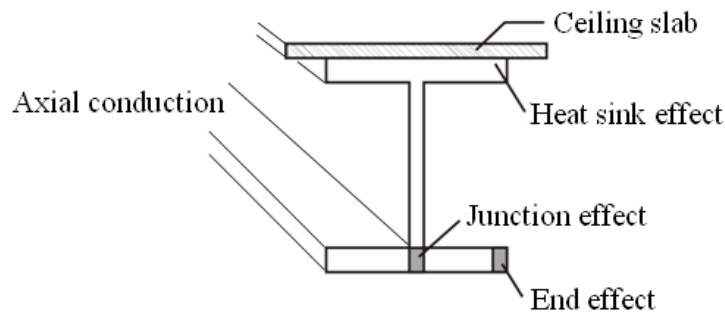


Fig. 2–Cross-section of the beam with locations of possible correction effects

One further complication which arises from the generalised nature of the method is the difficulty in determining means of representing the convective heat transfer to the component when the details of the flowfield over the surface are not specifically computed (as must be the case here). An approximate treatment is proposed, using convention correlations to the local velocities, and in most cases of practical interest radiation will be dominant anyway.

2.2 Conceptual model establishment

2.2.1 Generalised 1D model

Considering the net energy balance with surface heat transfer boundary conditions^[2], the 1D model governing equations are derived and given as below:

Energy balance equation:

$$\frac{\partial E_{system}}{\partial t} = \dot{q}_{net} \quad (1)$$

$$\text{i.e. } \rho_s \cdot c_{ps} \cdot \frac{\partial T_s}{\partial t} \cdot \Delta x_s + w_{p1} \cdot \rho_1 \cdot c_{p1} \cdot \frac{\partial T_1}{\partial t} \cdot \Delta x_1 + w_{p2} \cdot \rho_2 \cdot c_{p2} \cdot \frac{\partial T_2}{\partial t} \cdot \Delta x_2$$

$$= h_{c1} \times (T_{H1}^{(n)} - T_{1,0}^{(n)}) + \dot{q}_{r1}'' - \varepsilon_{m1} \cdot \sigma \cdot T_{1,0}^{(n)4} + h_{c2} \times ((T_{H2}^{(n)} - T_{2,0}^{(n)}) + \dot{q}_{r2}'' - \varepsilon_{m2} \cdot \sigma \cdot T_{2,0}^{(n)4})$$

The terms shown in the expanded equation here represent, respectively, the transient heating of the steel, the transient heating of each protection layer and convection, radiation and re-radiation for each surface of the protected member. The boundary conditions are supplied from the heat transfer solution for the surfaces, using the following equations:

$$\dot{q}_{net1}'' = \frac{k_1}{w_{p1}\Delta x_1} \cdot (T_{1,0}^{(n)} - T_s) \quad (2)$$

i.e.
$$h_{c1} \times (T_{H1}^{(n)} - T_{1,0}^{(n)}) + \dot{q}_{r1}'' - \varepsilon_{m1} \cdot \sigma \cdot T_{1,0}^{(n)4} = \frac{k_1}{w_{p1}\Delta x_1} \cdot (T_{1,0}^{(n)} - T_s)$$

$$\dot{q}_{net2}'' = \frac{k_2}{w_{p2}\Delta x_2} \cdot (T_{2,0}^{(n)} - T_s) \quad (3)$$

i.e.
$$h_{c2} \times (T_{H2}^{(n)} - T_{2,0}^{(n)}) + \dot{q}_{r2}'' - \varepsilon_{m2} \cdot \sigma \cdot T_{2,0}^{(n)4} = \frac{k_2}{w_{p2}\Delta x_2} \cdot (T_{2,0}^{(n)} - T_s)$$

Where:

σ is Stefan-Boltzmann constant, $5.67 \times 10^{-8} W \cdot m^{-2} \cdot K^{-4}$.

$\dot{q}_{r1}'', \dot{q}_{r2}''$ are the incident heat fluxes on each side.

$T_{1,0}^{(n)}, T_{2,0}^{(n)}$ represent the surface temperatures between the gas and the solid on each side.

T_s, T_1, T_2 are the steel and average protection layer temperatures, respectively; for the purpose of accounting for the transient energy storage in the protection layer the influence of the change of steel temperature on the protection layer temperatures is included only indirectly, referencing the rate of change on the previous timestep; a more elaborate coupling to the steel temperature change on the current step was investigated, but the effects are small and could not justify the additional computation costs incurred;

$h_{c1}, h_{c2}, \varepsilon_{m1}, \varepsilon_{m2}$ are the convection parameters and the emissivities of the protection layers.

ρ_s, ρ_1, ρ_2 are the densities of the steel and protection layers, respectively.

$\Delta x_s, \Delta x_1, \Delta x_2$ are the thicknesses of the steel and protection layers, respectively.

w_{p1}, w_{p2} are the weight factors of the protection layers, defined in terms of the thermal penetration depth of the protection, more precisely, $w_p = \min\{\frac{A_{actual}}{A_{model}} = \frac{\delta}{\Delta x_p}, 1\}$ and

$$\delta = 2 \cdot \left(\frac{k_p \cdot t}{c_p \cdot \rho} \right)^{1/2}, \text{ the instantaneous thermal penetration depth.}$$

$c_s, c_{p1}, c_{p2}, k_1, k_2$ are the specific heats of steel and protection layers, and the thermal conductivity parameters, respectively. The temperature-dependent characteristics and moisture effects are incorporated as previously^[5]. The effective values are expressed as shown in Figs. 3 and 4, as well as the equations in Tables 1 & 2, below:

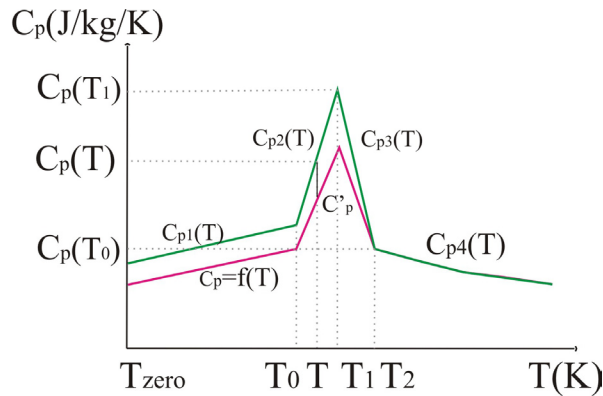


Fig. 3—Specific heat vs. temperature

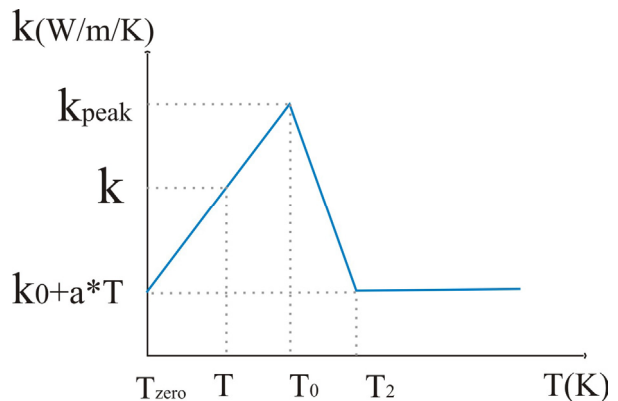


Fig. 4—Thermal conductivity vs. temperature

Table 1: Effective specific heat, c_p

$c_p = c_{p1}(T) = f(T) + c_{p,H_2O} \cdot \omega_m$	$(T_z \leq T < T_0)$	(4)
$c_p = c_{p2}(T) = f(T) + c'_{p2}(T) = f(T) + \omega_m \left[\frac{4L}{(T_2 - T_0)} \left(\frac{T - T_0}{T_2 - T_0} \right) + c_{p,H_2O} \left(\frac{T_2 - T}{T_2 - T_0} \right) \right]$	$(T_0 \leq T < T_1)$	
$c_p = c_{p3}(T) = f(T) + c'_{p3}(T) = f(T) + \omega_m \cdot \left[\frac{4L}{(T_2 - T_0)} \left(\frac{T_2 - T}{T_2 - T_0} \right) + c_{p,H_2O} \left(\frac{T_2 - T}{T_2 - T_0} \right) \right]$	$(T_1 \leq T < T_2)$	
$c_p = c_{p4}(T) = f(T)$	$(T \geq T_2)$	

Table 2: Effective thermal conductivity, k

$k = \left(\frac{T - T_z}{T_0 - T_z} \right) \cdot [k_{peak} - (k_0 + a \cdot T)] + (k_0 + a \cdot T)$	$(T_z \leq T < T_0)$	(5)
$k = \left(\frac{T_2 - T}{T_2 - T_0} \right) \cdot [k_{peak} - (k_0 + a \cdot T)] + (k_0 + a \cdot T)$	$(T_0 \leq T < T_2)$	
$k = k_0 + a \cdot T$	$(T \geq T_2)$	

The solution procedure is based upon using the heat transfer equation boundary conditions (Eqs. (2) & (3)) and iterating by the Newton-Raphson method to update the surface temperature, and thereafter, with the updated surface temperatures as boundary conditions, solving the overall energy balance Equ. (1) by the Runge-Kutta method to obtain the steel temperature. During the analysis, while using Newton-Raphson procedures to obtain the values of the surface temperatures, the convergence is checked by the absolute errors $|T_{1,0}^{(n)}(i) - T_{1,0}^{(n)}(i-1)|$ and $|T_{2,0}^{(n)}(i) - T_{2,0}^{(n)}(i-1)|$ within each time step, where n represents the time step and i represents the iteration number. By default (in the spreadsheet implementation), five iterations are carried out and reasonably good convergence typically results; in the CFD implementation, iterations are performed until a sufficient degree of convergence is achieved (e.g. 0.1% temperature error). The Runge-Kutta integration is used to accommodate rapid rates of change of gas temperature, to which thermal exposures are related in a strongly non-linear fashion via the radiation terms, and to provide an implicit element to the solution, since the evolving steel temperature is coupled back on itself via its influence on surface temperature. For simplicity, the equations for a 2nd-order Runge-Kutta procedure are provided here, as used in the spreadsheet implementation and initial CFD model, though a 4th-order method will be used in the final CFD implementation. The steel temperature at n^{th} timestep is obtained:

$$T_s^{(n)} = T_s^{(n-1)} + \frac{1}{2} (K_1^{(n)} + K_2^{(n)}) \quad (6)$$

Where, $K_1^{(n)} = \Delta t \cdot f(T_s^{(n)}, t^{(n)}) = \Delta t \cdot f(T_{1,0}^{(n)}(i_{converged}), T_{2,0}^{(n)}(i_{converged}))$,

$$\text{While, } f(T_{1,0}^{(n)}(i), T_{2,0}^{(n)}(i)) = \left\{ \begin{array}{l} h_{c1} \times (T_{H1}^{(n)} - T_{1,0}^{(n)}(i)) + \dot{q}_{r1}'' - \varepsilon_{m1} \cdot \sigma \cdot T_{1,0}^{(n)}(i)^4 \\ + h_{c2} \times (T_{H2}^{(n)} - T_{2,0}^{(n)}(i)) + \dot{q}_{r2}'' - \varepsilon_{m2} \cdot \sigma \cdot T_{2,0}^{(n)}(i)^4 \\ - \frac{(T_{1,0}^{(n)}(i) - T_{1,0}^{(n-1)}(i))}{\Delta t} \cdot \Delta x_1 \cdot w_{p1} \cdot \rho_1 \cdot c_{p1} \\ - \frac{(T_{2,0}^{(n)}(i) - T_{2,0}^{(n-1)}(i))}{\Delta t} \cdot \Delta x_2 \cdot w_{p2} \cdot \rho_2 \cdot c_{p2} \end{array} \right\} \cdot \frac{1}{\Delta x_s \cdot \rho_s \cdot c_{ps}}$$

And, $K_2^{(n)} = \Delta t \cdot f(T_s^{(n)} + K_1^{(n)}, t^{(n)}) = \Delta t \cdot f(\bar{T}_{1,0}^{(n)}(j_{converged}), \bar{T}_{2,0}^{(n)}(j_{converged}))$

$$\text{While, } f(\bar{T}_{1,0}^{(n)}(j), \bar{T}_{2,0}^{(n)}(j)) = \left\{ \begin{array}{l} h_{c1} \times (T_{H1}^{(n)} - \bar{T}_{1,0}^{(n)}(j)) + \dot{q}_{r1}'' - \varepsilon_{m1} \cdot \sigma \cdot \bar{T}_{1,0}^{(n)}(j)^4 \\ + h_{c2} \times (T_{H2}^{(n)} - \bar{T}_{2,0}^{(n)}(j)) + \dot{q}_{r2}'' - \varepsilon_{m2} \cdot \sigma \cdot \bar{T}_{2,0}^{(n)}(j)^4 \\ - \frac{(\bar{T}_{1,0}^{(n)}(j) - \bar{T}_{1,0}^{(n-1)}(j))}{\Delta t} \cdot \Delta x_1 \cdot w_{p1} \cdot \rho_1 \cdot c_{p1} \\ - \frac{(\bar{T}_{2,0}^{(n)}(j) - \bar{T}_{2,0}^{(n-1)}(j))}{\Delta t} \cdot \Delta x_2 \cdot w_{p2} \cdot \rho_2 \cdot c_{p2} \end{array} \right\} \cdot \frac{1}{\Delta x_s \cdot \rho_s \cdot c_{ps}}$$

Within these equations, the initial and intermediate surface temperatures, $T_{1,0}^n$ & $T_{2,0}^n$ and $\bar{T}_{1,0}^n$ & $\bar{T}_{2,0}^n$, respectively, are obtained through Newton-Raphson procedures to solve Eqs. (2) & (3), in conjunction with the initial steel temperature, in the first case, and the estimated steel temperature between two time steps, $T_s^n = T_s^{n-1} + K_1^{n-1}$, in the second case.

2.2.2 Quasi-3D model

Simple adoption of 1D model for thermal analysis could lead to either conservative (over-design) or non-conservative (unsafe) results. To improve the accuracy in determining the thermal responses of the structural members, a quasi-3D model has been developed which is an essentially 1D analysis, as described above, but including appropriate representations of the heat transfer processes in the omitted coordinate directions. The modelling framework which has been constructed for undertaking these calculations is based on simple physical considerations associated with different possible scenarios. For the time being, four effects are treated for which the precise nature of localised heating is important, as described below:

Junction effects

This correction accounts for the effects of the connection between two different parts of a member under differential heating, e.g. when the main exposure is from below a flange or directly onto the web. In the case where the dominant heating comes from below a flange, for cells in the region of the junction between flange and web, a possible heat sink effect to the cooler structure above the junction needs to be considered. This caters both for the case where the web is cooler, due to having no direct exposure to the dominant radiative heating, and thus some heat would possibly be lost into the web by conduction, and the case where the upper flange of the member is attached to a ceiling slab remaining cool. The effect in depressing the flange temperature can be accommodated in the quasi-3D conceptual model by including an additional term, $-k \times \left(\frac{T_s - T_{web}}{\chi} \right)$, on the right-hand side of the 1D model governing equation,

Equ. (1), where T_{web} is the independently evaluated web temperature and χ is an appropriate

lengthscale which is a function of the section geometry (section breadth & depth, and flange & web thicknesses). When the dominant heating comes directly on the web, a reverse of the above analysis can be conducted to determine the heat sink into an unexposed flange. It should be noted that in both cases, the effect of the redistribution of heat by conduction serves only to reduce the predicted peak member temperatures, meaning that the initial uncorrected 1D model predictions are expected to be on the conservative side.

End effects

Along the length of the flange, the steel temperature changes, especially for the cells in the two ends of the flange, which might be a worst case position for temperature by virtue of the fact that they are exposed to heat arriving from two different directions, i.e. their heated surface is larger. The heating might be expected to be relatively uniform when convection is dominant and a simple correction referencing the true flange surface area can be used. A more complex case results when the radiative heat flux dominates; if the radiation arrives mainly from below, then the end cell behaves no differently from any other flange cell, or may even be cooler due to the extra surface area for heat loss; if the radiation arrives *only* from the side, then conductive loss to the unexposed material elsewhere in the flange means that the end cell temperature will be depressed, and probably lower than a typical web cell temperature in the same member. At intermediate conditions, the temperature in the end cell, T_s^+ , is perturbed and needs careful consideration; a possible approximate treatment is given below:

$$T_s^+ = T_{s,avg} + \frac{\Delta T_s}{2} \quad (7)$$

Where, $T_{s,avg}$ is the average steel temperature along the flange length, which is equal to the middle point temperature, obtained from the original solution, as per Equ. (6), and ΔT_s is the temperature difference between the flange end-point and the mid-point, by considering the effects of radiation from the side: $\Delta T_s = \frac{b \cdot \dot{q}_{rad,side}}{k}$, where b is flange width.

Heat sink effects

This case considers the thermal effects when a structural member is in contact with a ceiling slab. Here, the upper flange in the model is assumed to be cooler than the rest of the member, and can be ignored. For the lower flange, heat sink effects may lead to an overly-conservative solution and a correction might be justified. The solution, together with the correction for this case, is similar to that for junction effects described above.

Axial temperature gradients

When the structure passes from a cold layer into a hot layer, i.e. a column or even in very deep section beams, the temperature changes greatly with height. The former could introduce significant modelling errors but the latter is normally likely to be less significant in terms of peak temperatures and thus is neglected here. It is however important to note that any resulting modelling errors will be on the conservative side. This can be explained by the fact that the temperatures of cells in the hot layer are reduced by axial conduction to the cooler structure below, whilst the temperatures of the cooler cells are increased - but still remain *below* those of the structure where it is exposed to the highest temperatures. The governing equation for analysis of a single cell at an intermediate height in a column running through a thermal stratified layer is:

$$h_{c1} \times (T_{H1} - T_{1,0}^{(n)}) + \dot{q}_{r1}'' - \varepsilon_{m1} \cdot \sigma \cdot T_{1,0}^{(n)4} + h_{c2} \times (T_{H2} - T_{2,0}^{(n)}) + \dot{q}_{r2}'' - \varepsilon_{m2} \cdot \sigma \cdot T_{2,0}^{(n)4} + \frac{k}{\delta_{x,upper}} \cdot (T_{s,upper} - T_s) - \frac{k}{\delta_{x,lower}} \cdot (T_s - T_{s,lower}) = 0 \quad (8)$$

Compared with 1D model governing equations, two additional correction terms $\frac{k}{\delta_{x,upper}} \cdot (T_{s,upper} - T_s)$ and $\frac{k}{\delta_{x,lower}} \cdot (T_s - T_{s,lower})$ appear, due to the heat conduction effects, where *upper* is a characteristic hot layer temperature and *lower* signifies conditions in a cold(er) layer. The significance of the correction terms depends on the location of the element in question with respect to the bounding temperatures, and they cancel for an element midway between hot and cold positions in an assumed linear temperature gradient region. Note that the model provides an approximate treatment, with $T_{s,upper}$ and $T_{s,lower}$ typically being defined at the two remote locations, thereby representing peak gradients; no attempt is made to take into account the more detailed temperature profile over the height of the column, in order to avoid the additional computational expense of performing the necessary calculations.

2.3 Verification and validation of the models

The above conceptual models are firstly implemented in a spreadsheet-based model. Representative empirical values are adopted for some terms such as the initial conditions, the dry thermal properties, moisture content, etc., and their influence has been studied by exercising the model with different sets of input parameter values. The conceptual models are also implemented into SOFIE CFD code^[3].

The performance of the model was assessed by performing sensitivity studies, looking at the effects of a range of numerical and physical parameters. Comparisons were also made with the results of a simplified version of the model, labelled “simplified method”, which advances the solution using an explicit one-step scheme, i.e. bypassing the Runge-Kutta integration used in the main method. To provide a further comparison, the simple empirical model for protected members described in Eurocode 1 is also implemented.

The test case used for verification studies is the protected steel indicative, UC254x254/73, in the full-scale tests on a 12m x 12m compartment undertaken at BRE Cardington^[4]; this member was protected with about 25mm of Fendolite MII sprayed fibre ($\rho=680\text{kg/m}^3$, $k=0.19\text{W/m/K}$). In the test a variety of thermal parameter measurements were made, encompassing conditions in the gas phase (temperatures, velocities and heat fluxes) and in the solid phase (steel temperatures in protected beams, columns and indicatives with and without protection)^[5]; this study also serves for an initial validation of the model, comparing the model predictions with the measured steel temperatures in the protected indicative.

3. PRELIMINARY RESULTS AND DISCUSSION

3.1 Simulation results

Fig. 5 shows the results of the spreadsheet-based generalised 1D model simulation. These are obtained by using the same protection materials on each side of the steel, protection thickness: $\Delta x_1 = \Delta x_2 = 25\text{mm}$ and steel flange thickness: $\Delta x_s = 14.2\text{mm}$, with moisture content 1%, fire emissivity 0.8, member emissivity 0.9 and $h_c = 8\text{W/m}^2/\text{K}^{[1]}$. The results are reasonable and in-line with expectations.

Fig. 6 shows a comparison of the predictions of steel temperature with the test. There is a reasonable agreement though some differences are apparent. The “novel” method results differ significantly from the “simplified” method, thereby justifying the effort made to introduce full coupling; the predictions of Eurocode 1 initially lie between those of the new models, but eventually exceed the measure temperatures (a conservative result); a more precise match with the test results is easily achieved by adopting a temperature dependent conductivity, with a very slight negative temperature correlation.

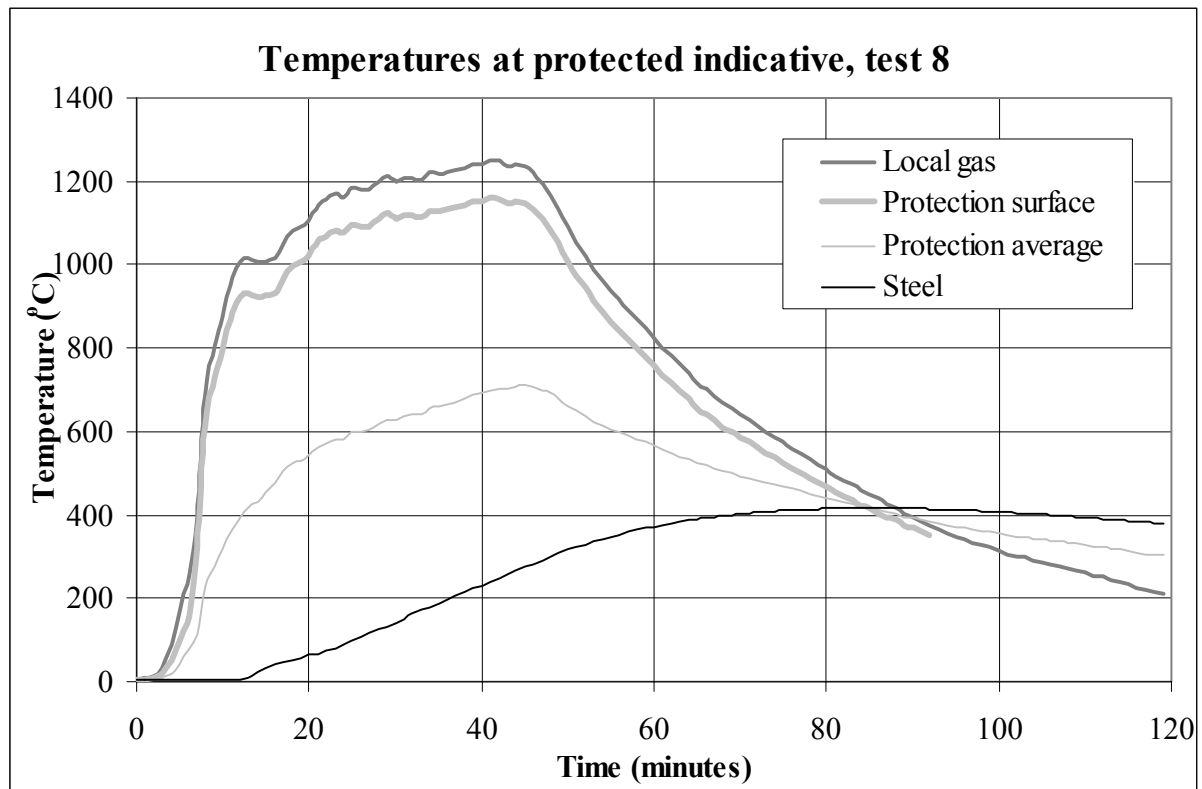


Fig. 5 –Temperature change with time using improved method

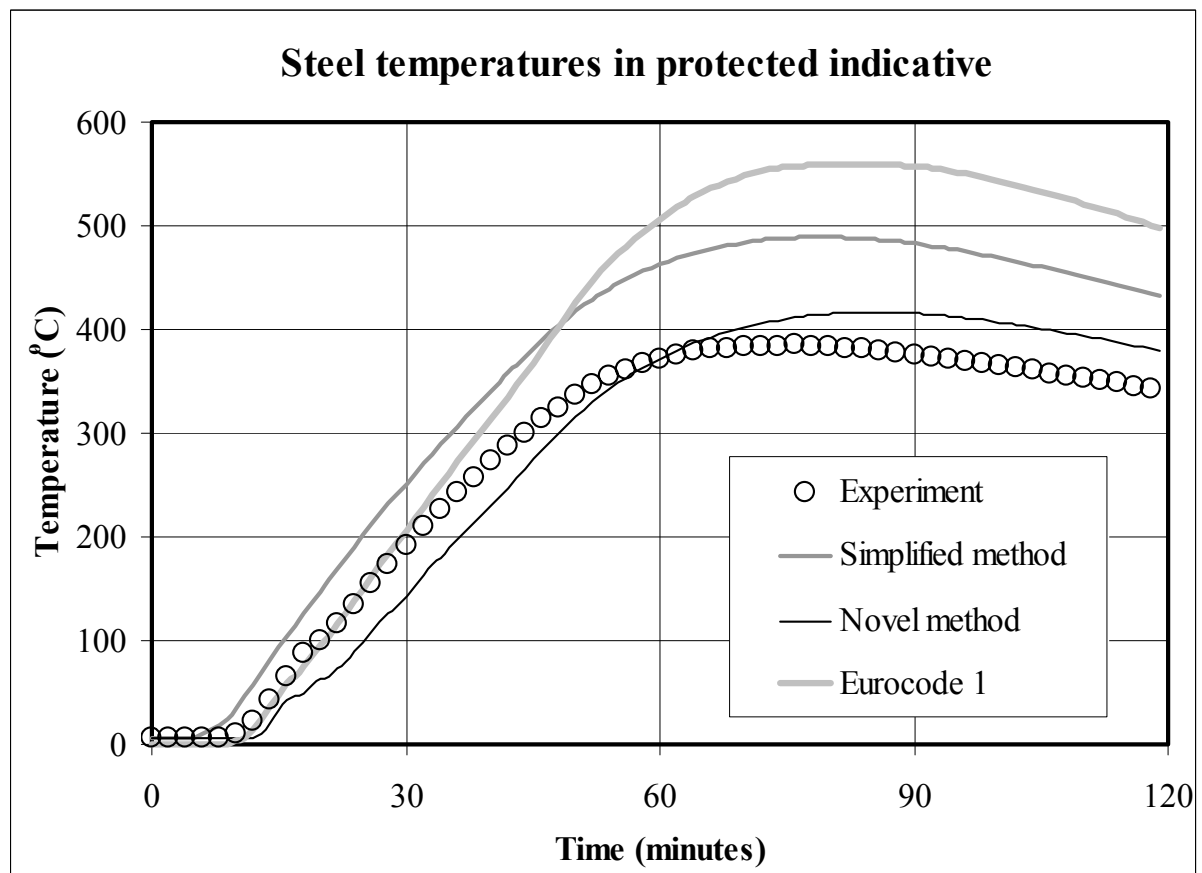


Fig. 6–Comparison of steel temperature change with time using different methods

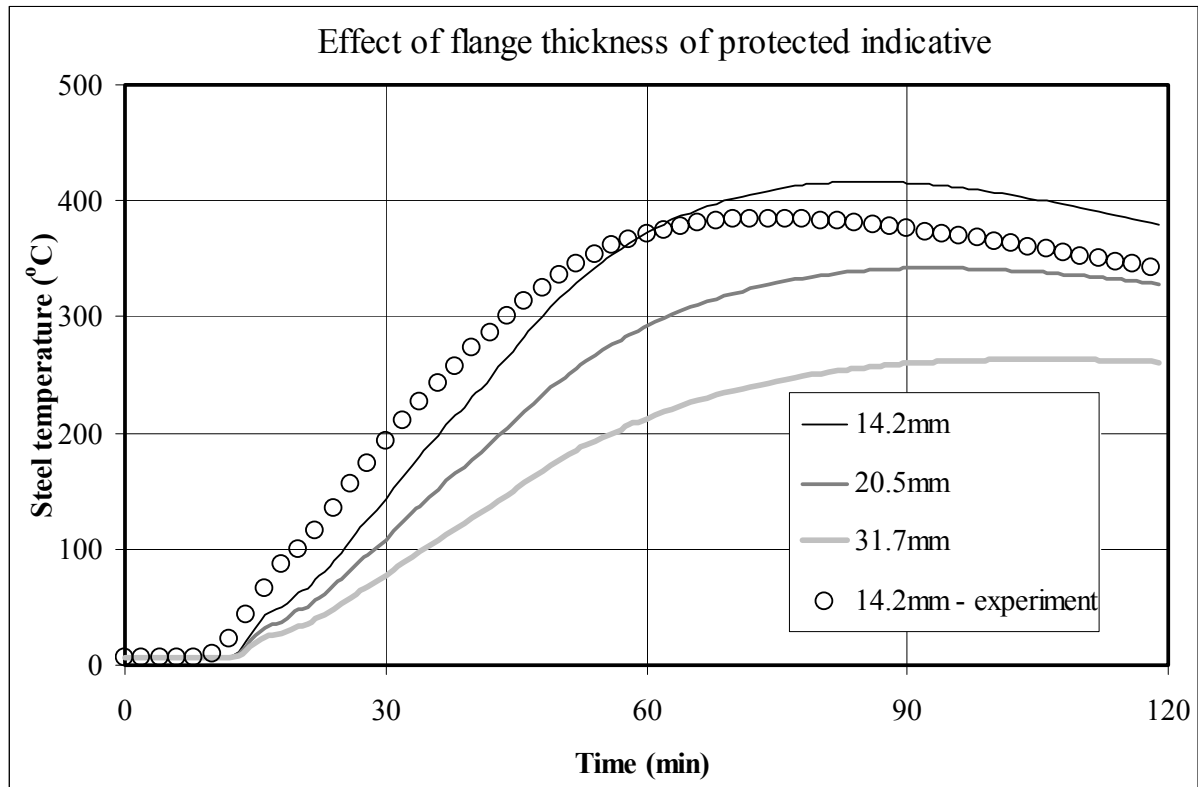


Fig. 7—Effect of flange thickness on steel temperature

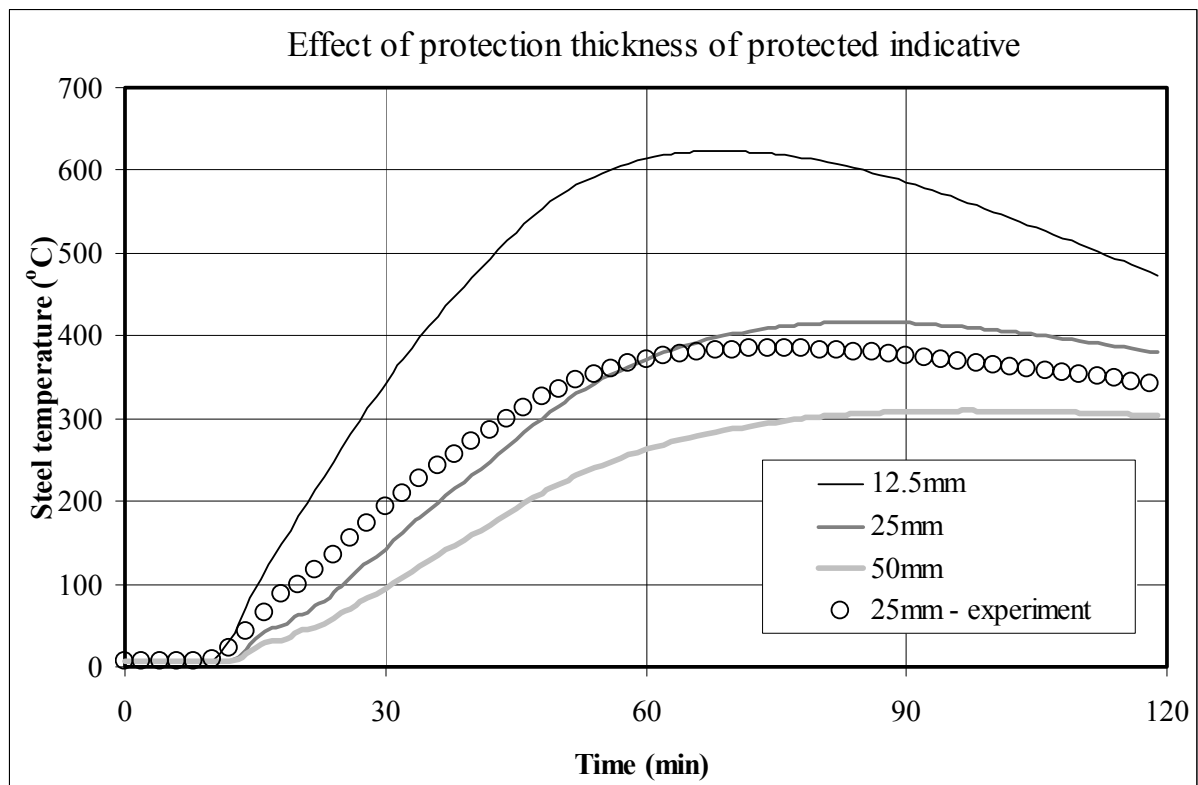


Fig. 8—Effect of protection thicknesses on steel temperature

3.2 Sensitivity study results

A couple of results from the sensitivity study are shown in Figs. 7 and 8 for the effects of changing the steel flange thickness (spanning UC 254x254/73,107,167) and the protection thickness (12.5 to 50mm). The results for changing the protection thermal conductivity mirror the latter, and show the expected strong influence of protection properties. This is the type of information which will be provided by the CFD implementation of the method.

4 CONCLUSIONS

A novel CFD-based methodology for generalised thermal analysis of protected steel structures in fire is described. The method is based on a 1D heat transfer analysis, but appropriate corrections are developed to reconstruct a quasi-3D solution. The new 1D model has been implemented both in spreadsheet format, permitting sensitivity studies for verification, and as a submodel in the CFD code. Initial results confirm the sufficiency of the algorithms adopted, and indicate some of the model sensitivities, with strong dependencies on the properties of the thermal protection materials. Comparisons with the measured temperatures in a steel indicative located in a post-flashover fire in a full-scale fire test show a sufficient agreement. Predictions of steel temperatures for variations on member and protections specifications will ultimately be provided as field variable predictions by the parallel calculations implemented in the CFD code, thereby providing a much more flexible means of assessing the thermal response of structure to fire than has been available hitherto.

5 ACKNOWLEDGEMENTS

The authors gratefully acknowledge the financial support from BRE Trust and technical supports from both BRE fire research group and the other members of the BRE Centre for Fire Safety Engineering at the University of Edinburgh.

6 REFERENCES

- [1] Kumar, S., Welch, S., Miles, S. D., Cajot, L.-G., Haller, M., Ojanguren, M., Barco, J., Hostikka, S., Max, U. & Röhrle, A., "Natural Fire Safety Concept - The development and validation of a CFD-based engineering methodology for evaluating thermal action on steel and composite structures", European Commission Report EUR 21444 EN, 150 pp., ISBN 92-894-9594-4, 2005.
- [2] Carslaw, H.S. & Jaeger, J.C. "Conduction of Heat in Solids", Oxford University, 1959.
- [3] Lewis, M.J., Moss, J.B. & Rubini, P.A., "CFD modelling of combustion and heat transfer in compartment fires", in Proc. 5th Int. Symp. on Fire Safety Science, pp. 463-474, 1997.
- [4] Lennon, T. & Moore, D., "The natural fire safety concept—full-scale tests at Cardington", Fire Safety Journal, vol 38, no. 7, pp. 623-643, 2003.
- [5] Welch, S., "Developing a model for thermal performance of masonry exposed to fire", 1st International Workshop on "Structures in Fire", Copenhagen, June 2000.
- [6] British Standard Institute. Eurocode 1: *Actions on structures – Part 1-2: General actions – Actions on structures exposed to fire*. CEN 2002.
- [7] British Standard Institute. Eurocode 3: *Design of steel structures – Part 1-2: General rules – Structure fire design*. CEN 2002.



DEVELOPMENT OF A METHOD TO CALCULATE THE TEMPERATURE OF A COLUMN EXPOSED TO LOCALISED FIRE, ACCORDING TO THE EC1 AND EC3 FIRE PARTS

Mike HALLER¹, Alexandra KAY² and Louis-Guy CAJOT³

ABSTRACT

Some simplified methods exist in the Eurocode fire parts to calculate the temperature of a steel member affected by a localised fire. Some give for instance the temperature distribution in a beam located under the ceiling or the temperature just above the fire. In all those cases we have a heat flux resulting from a radiation part and a convection part. A situation that can not yet been calculated using those methods are vertical steel members affected by localised fire in a given distance to it. This fire scenario represents nevertheless a common situation, for instance in an airport hall where a kiosk burns close to a unprotected steel column. One would in that case need to know the steel temperature in function of the column height.

This new method aims to enable the temperature of a column exposed to localised fire to be calculated at different heights up the column, based on the Eurocode methods.

¹ Mike Haller, Research engineer, Arcelor Profil Luxembourg S.A. Research Centre - Product Application

² Alexandra Kay, Student at University of Oxford

³ Louis-Guy Cajot, Department manager, Arcelor Profil Luxembourg S.A. Research Centre -Product Application

1. BACKGROUND AND AIM OF INVESTIGATIONS

For the temperature simulation in a steel profile, one can use the methods described in Annex C of EN1991-1-2. These simplified methods calculate in fact the gas temperature or the heat flux at a certain distance to the fire, which can be used to assess the temperatures in a steel member via its section factor with simplified methods according to EN1993-1-2. In cases where the flame is not impacting the ceiling, or for external fires, the first method, according to HESKESTAD can be used, which allows one to calculate the gas-temperatures at different heights in the centre of the fire. With the second method, based on the tests of HASEMI, one can calculate the heat fluxes under the ceiling in function of the distance to the fire. The problem is that none of these methods are suitable to calculate the temperatures at different heights and in a certain distance to the fire, what would be needed to calculate the temperatures in a column exposed to a localised fire. An approximation is often used with the HASEMI method, by decreasing step by step the height of the ceiling and obtaining by doing so, the temperature in different heights. This seems to be a quite conservative estimation and Research Centre of Arcelor Profil Luxembourg S.A. (APLR) tried therefore to establish in the frame of the ECSC project ^[4] a new simplified method, allowing one to calculate the temperatures in a steel column for different height.

The path that was followed at first has been to use CFD code “Sofie” as a tool, to develop such a method. Some real fire tests were used to calibrate the CFD code. Even if at the end the comparison between test and simulation results have not been too bad, the confidence in the CFD tool was not high enough to be used for the development of the method. Furthermore the simulation times have been quite high and the number of tests to be used for the calibration has not been sufficient. The results can be found in Annex to the final research report ^[4].

At last it was decided to use different existing simplified methods given in the fire parts of Eurocodes 1 and 3 and to combine them in such a way that the temperature of a column, affected by a localised fire could be calculated in function of the beam height.

2. DEVELOPMENT OF METHOD TO DEFINE TEMPERATURE DISTRIBUTION IN STEEL COLUMN HEATED BY LOCALISED FIRE

The calculations follow the methods described in the Eurocodes (ECs): Eurocode 1 Part 1-2 ^[1] and Eurocode 3 Part 1-2 ^[2]. The final objective was to model how the temperature distribution over the column height changes with time. The model would be able to cope with multiple fires, which have changing rates of heat release (RHRs), following either the Natural Fire Safety Concept (NFSC) model according to annex E of EN1991-1-2 or user defined RHR e.g. fixed car burning scenarios based on car park fire research ^[3]. The fires are to be positioned anywhere around the column. The final objective will be achieved in stages. Initially, a single fire of constant RHR, which can be placed anywhere around the column, has been considered. The fire will be considered as a single radiating rectangular surface of constant temperature, taken as the temperature at the flame mid-height. This simple model will be made more complex by considering a layered fire structure (with different temperatures at different heights), fires with changing rates of heat release, and by using multiple fires. At the very end a different shape of the fire itself has been considered.

This method has afterwards been programmed in Excel spreadsheet macros in order to validate it.

3. DEVELOPMENT OF SIMPLIFIED MODEL

This initial model takes the simplest case, previously described. The flame is of rectangular base, and stays of the same cross-section up its entire length. The method below (developed after thorough study of the ECs and other background material) is followed to determine the column temperature distribution.

Simplified Problem: Steps to Solve

1. Define flame: dimensions – width and length; rate of heat release, Q (constant)
2. Calculate flame length using EC1 Annex C eqn C.1.
3. Find temperature variation with height using EC1 Annex C eqn C.2 and C.3. Find mid-height flame temperature.
4. Position the flame around the column
5. Define column dimensions
6. Calculate flame emissivities using length and width as characteristic thickness dimensions. Use formula in EC1 Annex B eqn B.16
7. At column height “h” calculate configuration factors between all column sides which can see the flame and all the flame sides they can see. Use the envelope of receiving surfaces approximation in EC1 Annex G figure G.2. Use EC1 Annex G eqns G.2 and G.3. Define radiating surface with height equal to flame length (from (2)), and width or length defined in (1) as appropriate. (Using “G.3 External Members” method)
8. Find two overall configuration factors: one for each emissivity. Use EC3 Annex B eqn B.5.
9. Use EC3 Annex B eqn B.7 to find total radiative heat flux to the column at that height, h. Flame temperature used is the mid-height flame temperature from (3)
10. Find net radiative heat flux to the column using EC1 Annex C eqn C.9.
11. Use this value in EC3 eqn 4.25 to find the increase in temperature in a specified time increment, repeating until the temperature of the column does not change significantly (i.e. steady state conditions have been achieved).
12. Repeat for all desired heights up the column.

The user must enter inputs, which allow relevant information about the flame to be calculated. The flame length (L_f) is based on the flame equivalent diameter (D), and RHR (Q), and is calculated using the following equations:

$$L_f = -1.02D + 0.0148Q D^{2/5} \quad [\text{m}] \quad (1)$$

$$\text{with } D = (4A/\pi)^{1/2} \quad [\text{m}]$$

where A is calculated from the flame dimensions ($A = w \times l$).

The flame temperature (T) at a height, z, up the flame axis is found from:

$$T(z) = 20 + 0.25Q_c^{2/3}(z-z_0)^{-5/3} \leq 900 \quad [^\circ\text{C}] \quad (2)$$

where $Q_c = 0.8Q$

$$z_0 = -1.02D + 0.00524Q^{2/5} \quad [\text{m}] \quad (3)$$

The mid-height flame temperature is found by solving (2) at $z = L_f/2$.

The flame emissivities (ϵ) for both sides (the width and length have different emissivities) of the flame are found using:

$$\epsilon = 1 - e^{-0.3d} \quad (4)$$

where d is the appropriate flame depth. For the length emissivity, d is the width, and vice versa.

These calculations are performed in the spreadsheet and based solely on the flame dimensions and RHR of the flame.

Next, the configuration factor between the flame and column is calculated. This is a measure of how much of the radiating surface is “seen” by the column, and is based on geometry of the column and flame, and their relative positions. This calculation uses the column and flame dimensions and flame position (x^* , y^*) inputted by the user, and the calculated flame height. In this calculation, symmetry of the flame around the column is used, and all calculations are referred to the positive quadrant, in a co-ordinate system defined as shown in

Figure 0-1.

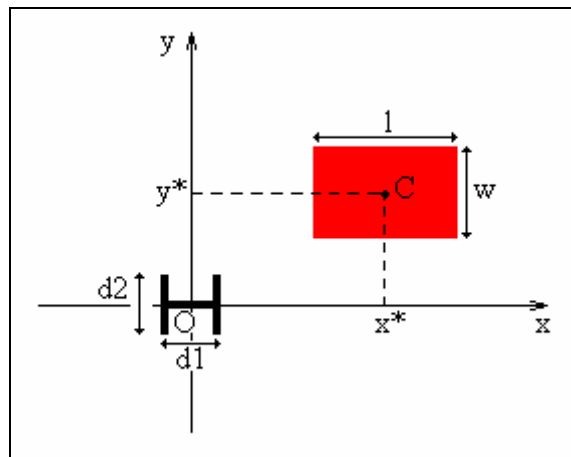


Figure 0-1 : Co-ordinate system used in model

In the models considered, only parallel or perpendicular surfaces are present. The factors are calculated using formulas in EC1-1-2 Annex G (G.2 and G.3), based on the width and height of the radiating surface under consideration, and distance between the flame surface and the column. The method used is also based on this annex.

The radiating surface seen would appear similar to below:

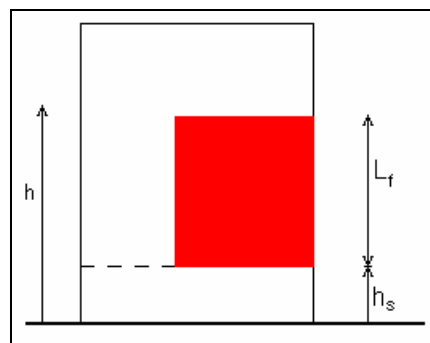


Figure 0-2 : Potential radiating surface seen from column (red area represents flame surface)

At each height where the configuration factor must be found, a horizontal line is drawn from the column to the radiating surface, and the point on the surface is marked “X”. The surface is then split so that the configuration factor from the fire part only is found, as shown below:

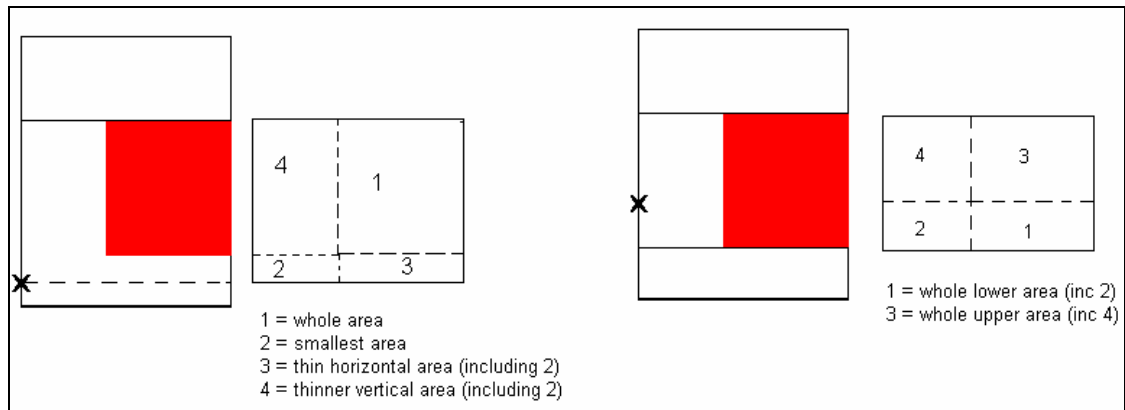


Figure 0-3 : Showing the splitting of the radiating surface for (a) height less than h_s , and (b) height greater than h_s but less than the top of the flame.

In situation (a) the total configuration factor (ϕ_T) from the fire is:

$$\phi_T = \phi_1 + \phi_2 - \phi_3 - \phi_4$$

In situation (b) the total configuration factor from the fire is:

$$\phi_T = \phi_1 - \phi_2 + \phi_3 - \phi_4$$

When the height is greater than the top of the flame, the total configuration factor is found similarly to in situation (a).

For a flame situated anywhere around a column, there are up to four total configuration factors that must be calculated at each height. Once these have been found, the overall configuration factor for each height is calculated according to EC3-1-2 Annex B Section 1.4. Care must be taken to ensure that the overall configuration factors found refer to flame sides of the same emissivity.

The data used for the configuration factors changes with flame position. There are five situations, which require slightly different inputs. These are as shown below:

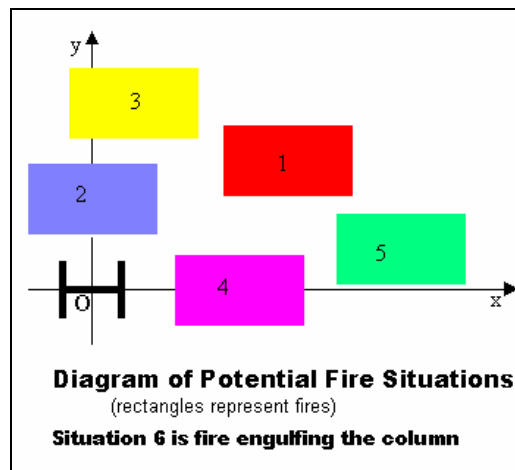


Figure 0-4 : Potential fire situations

In the spreadsheet, a “flowchart” has been implemented to assess the fire situation. The result of this is then used in the macro, to ensure the correct data is given to the configuration factor calculation tables.

Once the overall configuration factor at each height has been found, the incident heat flux (I) to the column at that height can be calculated. This calculation uses EC3-1-2 Annex B. For situations where only one flame side provides incident heat flux (i.e. there is only one emissivity) equation EC3, B.6 (5) is used:

$$I = \phi \varepsilon \sigma T^4 \quad [\text{W/m}^2] \quad (5)$$

(σ = Stephan-Boltzmann constant = $5.67 \times 10^{-8} \text{ W/m}^2\text{K}^4$)

However, if multiple sides of the flame are incident on the column, equation EC3, B.7 (6) is used:

$$I = (\phi_w \varepsilon_w + \phi_l \varepsilon_l) \sigma T^4 \quad [\text{W/m}^2] \quad (6)$$

(eq. (6) adapted from “between openings” column)

Finally, the change in temperature over time can be calculated. Firstly the increase in steel temperature over a time period is found, using:

$$\Delta T_m = (k_{sh}(A_m/V)h_{net}\Delta t)/c_a\rho_a \quad [^\circ\text{C or K}] \quad (7)$$

$$\text{where } k_{sh} = 1.0(A_m/V)_b/(A_m/V) \quad (8)$$

is the shadow coefficient. $(A_m/V)_b$ is the box value of the section factor, and (A_m/V) is the section factor. c_a is the specific heat of steel, calculated according to EC3-1-2 Section 3.4.1.2, and is temperature dependent. ρ_a is the steel density, which is taken as constant. T_m is the temperature of the column.

The net heat flux, h_{net} , is the incident heat flux minus the reflected heat flux. This is found from EC1-1-2, C.9 as:

$$h_{net} = h \varepsilon_m - h_{reflected} \quad (9)$$

$$\text{with } h_{reflected} = \alpha_c(T_m - 20) - \phi \varepsilon \varepsilon_m \sigma \{(T_m + 273)^4 - 293^4\} \quad (10)$$

where α_c is the convective heat transfer coefficient, and ε_m is the emissivity of the column (taken as 0,7). In formula (9), the incident heat flux has to be multiplied with ε_m as the steel member is not inside the hot layer.

The total temperature change in the column over time is found by adding the change in temperature, ΔT_m , to the current column temperature, to get the new column temperature, which becomes the current temperature at the next time period. The results at each height over time are tabulated, and a graph is plotted of column temperature against time for the different heights.

An Excel spread sheet has been made which, using macros, can calculate the temperature distribution over a column for a single fire with a constant rate of heat release, in any position around the column (except engulfing it). The final temperature over height graph showed a plateau over most of the flame length, due to similar configuration factors in this region and the same temperature being used for the flame. This would be solved by including different layers to the fire.

4. INCLUDING LAYERS TO THE FIRE

This problem is the same as above, in that there is a single flame positioned anywhere around a column, with a constant rate of heat release and rectangular base. However, in order to consider more accurately the temperature variation up the height of the flame, the idea of dividing the flame into several layers of different temperatures was adopted. The flame is divided as shown:

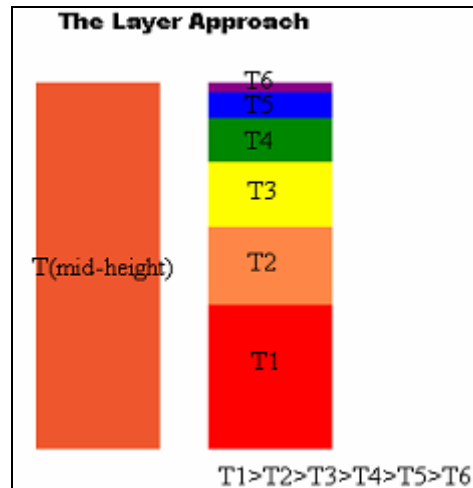


Figure 0-1: Diagram on the layer approach

The incident heat flux from the layers to a particular column height is calculated, and the total heat flux to the height is found by summing that from the individual layers. Similarly for $\phi \cdot \epsilon$ values. These values are then used in the temperature-time calculation, which is carried out as before.

In parallel with this, work by the Spanish research centre “Labein”^[4], was studied, in order to have an alternative method for comparison of our results. The simplified model followed by Labein uses an alternative heat balance equation to find the steady state temperature of a column adjacent to a localised fire. It considers a cylindrical fire.

The APLR model with layers was set up as the Labein model had been, with the same fire, and layers defined at the same points. As the model does not allow for engulfing flames, the fire was set very close to the column (about 0,02 m away). The incremented model was run, and the EC3-1-2 heat balance equation was solved.

A graph of steady state temperature against height was plotted, including results from the Labein model, the APLR simplified- and layered model. Values for the column temperature, predicted by a Labein CFD model, were also transcribed onto the graph (see Figure 0-2). The APLR simplified model showed a fairly constant temperature (about 650°C for the incremented temperature model) over the length of the flame, which dropped sharply once the height became longer than the flame height of 4,9 m. The temperature in both the APLR layers model and the Labein layers model start to drop at the same point (as the layers decrease in temperature), which was as expected as the same layer system was used in both models. This is more realistic than the sharp drop from the non-layered model, though not in keeping with the CFD predictions, which show a temperature drop from a height of about 0,5m, rather than 3,5m. The APLR layers model predicts a final temperature, which is lower than that predicted by the Labein model by approximately 100°C. With the multi layer model the flame height is no more limited to the 500°C but can be modified. By decreasing T_{\min} , the height of the global radiative surface as well as of the different layers is increased, what influences the steel temperature distribution over the height. By putting in the given example T_{\min} to 200°C, the flame height becomes 10m and the first layer increase from a thickness of 0,63m to 1,2m. While going further, with $T_{\min} = 50^\circ\text{C}$, the flame length becomes 30m with a lower layer height of 3,7m. This has as effect that the global behaviour is moreover as the one predicted by CFD even if not safe sided on the whole height.

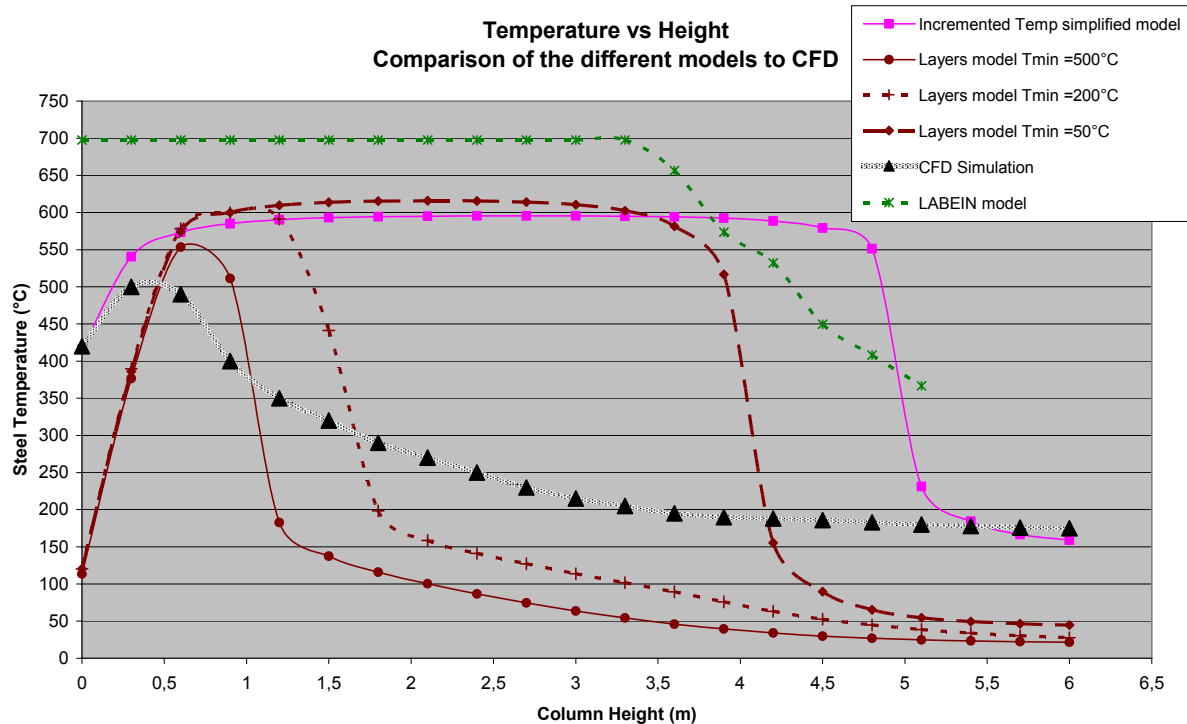


Figure 0-2: Comparison of the different models set up in the same way as the Labein model and CFD result.

5. FIRE WITH CHANGING RHR

As a next step variation of the rate of heat release was implemented. The RHR can follow one of two models: that described in Annex E of EN1991-1-2 ^[1] (NFSC model) or one defined by the user, by stating the RHR at appropriate times so that the RHR curve can be constructed. Both these methods are implemented in the spreadsheet and macro.

The NFSC curve is constructed from information in EC1-1-2 Annex E. It consists of a parabolic growing phase, followed by a phase of constant maximum RHR, and finally a linear decrease from maximum to zero. The growing phase follows the equation:

$$Q = 10^6 (t/t_\alpha)^2 \quad [\text{W}] \quad (11)$$

This phase stops once the maximum value of Q is reached, which is defined by $\text{RHR}_f \times A$, where RHR_f is the maximum rate of heat release (W/m^2) and is inputted by the user. t_α is the time needed to reach an RHR of 1MW, in seconds. The user also gives this value. Once 70% of the total fire load has been consumed, the linear decrease in RHR starts.

Once a RHR against time curve is established, all the changes this causes in flame length and temperature must be accounted for in calculations of $\phi \cdot \epsilon$ and incident heat flux. At each time, the associated flame length must be used in the configuration factor calculation, so the value of $\phi \cdot \epsilon$ also changes with time. This affects the values of incident and reflected heat flux. The change in temperature of the flame over time must also be taken into account in the incident heat flux calculation. Once values of incident and reflected heat flux over time have been found, these can be used in the column temperature calculation as before.

A spreadsheet was created to enable the calculation of column temperature for a column near a rectangular fire with changing RHR.

6. MULTIPLE FIRES

This model extends the previous “Fire with Changing RHR” model by adding more fires. As in previous models, all fires have rectangular bases and are of the same cross-section up their entire length, which is found in the same way as before. The RHR curves for each fire can follow either the NFSC curve or a curve defined by the user. The varying flame length and temperature over time of each flame mean that $\phi \cdot \epsilon$ values are variable over time, as are incident and net heat fluxes. For each flame, the $\phi \cdot \epsilon$ and incident heat flux values for each height at each time are calculated and tabulated separately. The values are summed, to give a total $\phi \cdot \epsilon$ value and a total incident heat flux value for each height over time. These total values are then used in the calculation of column temperature variation with time over the column length. As in Part III, if the flame length is calculated as negative, the $\phi \cdot \epsilon$ value is tabulated as zero.

As an example a typical car park situation was chosen with 3 cars burning close to a column. Generally using fire engineering approach, the temperature distribution in the beam is calculated using the Hasemi method from Annex C of EN 1991-1-2. With this method the temperature is obtained under the ceiling in function of the distance of the fire. As no tool exists in the past to predict the temperature in a column, the same method was sometimes used by stepwise decreasing the ceiling height. This leads nevertheless to quite conservative results. One could think of combining the Hasemi method with the one described in this report. This is done by using the Hasemi result for the part of the column that is located inside the hot layer and by this affected by radiation and convection. The new method would then be used to predict the temperature distribution in the different heights of the cold zone.

In Figure 0-1 one can see a typical fire scenario for a car park where 3 cars are burning, starting with the right hand car and spread over to the next one each 15 min. The parking bay is 2.5 m by 5 m and the beam and column is located between the 2 first cars.

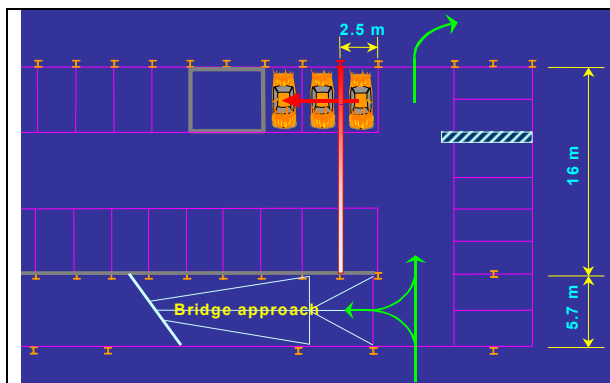


Figure 0-1: Car park fire scenario

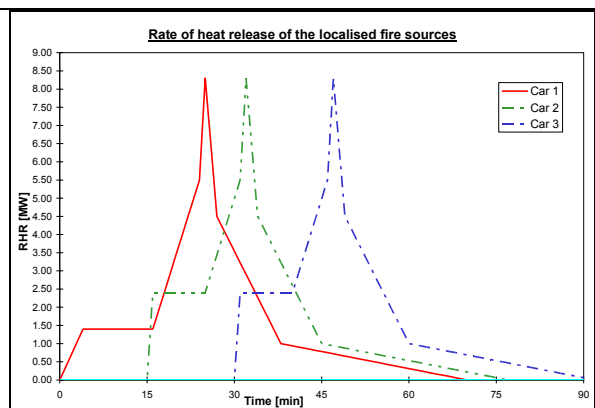


Figure 0-2: Input RHR, 3 car fire scenario ^[3]

Following the example a ceiling height of 3.6 m is assumed as well as a HEB 240 steel column. In a first step the Hasemi method is used to calculate the temperature in the steel profile in the hot layer, directly under the ceiling (see Figure 0-3). In this case a maximum temperature of 335°C are calculated for the HEB240.

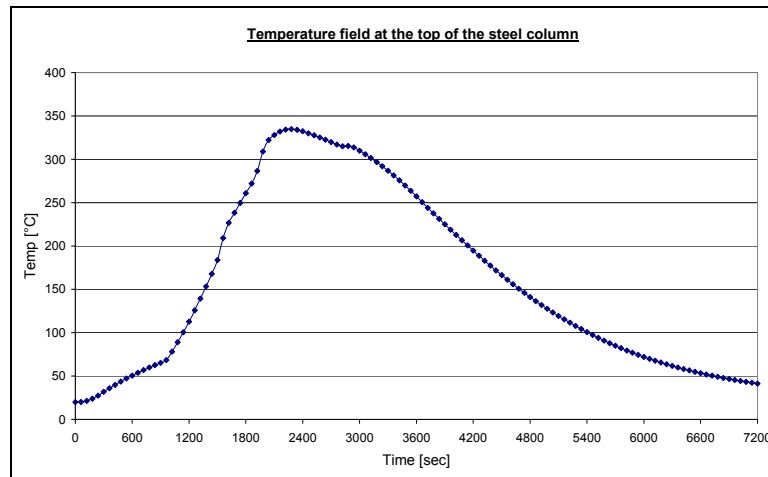


Figure 0-3: Steel temperature of the HEB 240 in the hot layer according to Hasemi

Using now the new method with rectangular multiple layer fires, the fire has been divided 8 layers, while fixing the upper layer at a temperature of 200°C, one obtain a temperature distribution in function of the columns height that reach maximal temperature of 300°C at a height of 0.6m whereas the temperatures at a height of 3.6 m gives rather low temperatures of about 80°C (see Figure 0-4). In practice the smoke layer should then be estimated (e.g. provided by smoke exhaust simulation study) and for the given height the temperature of Figure 0-3 should be used, whereas for the lower part of the column the temperature curves of Figure 0-4 according to the new developed method might be more appropriated.

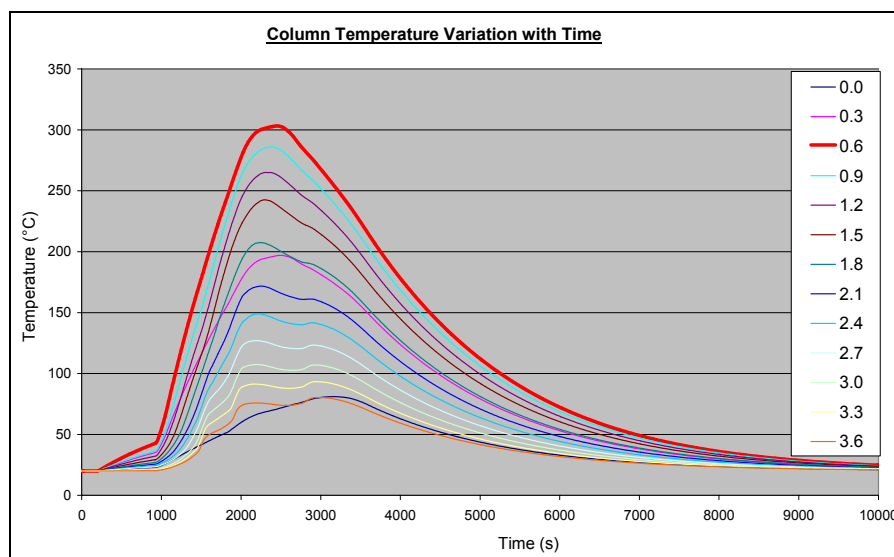


Figure 0-4: Column temperature variation resulting from the above RHR inputs.

Assuming furthermore that in this example the hot layer would have a thickness of 1.0m and combining the results of both the Hasemi and the new method (with smooth transition at interaction), one would receive a steel temperature distribution as shown in Figure 0-5.

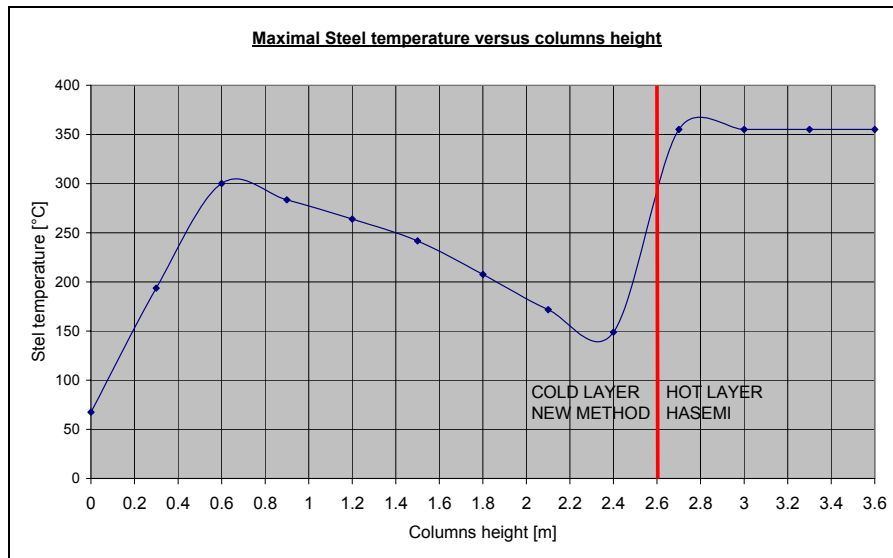


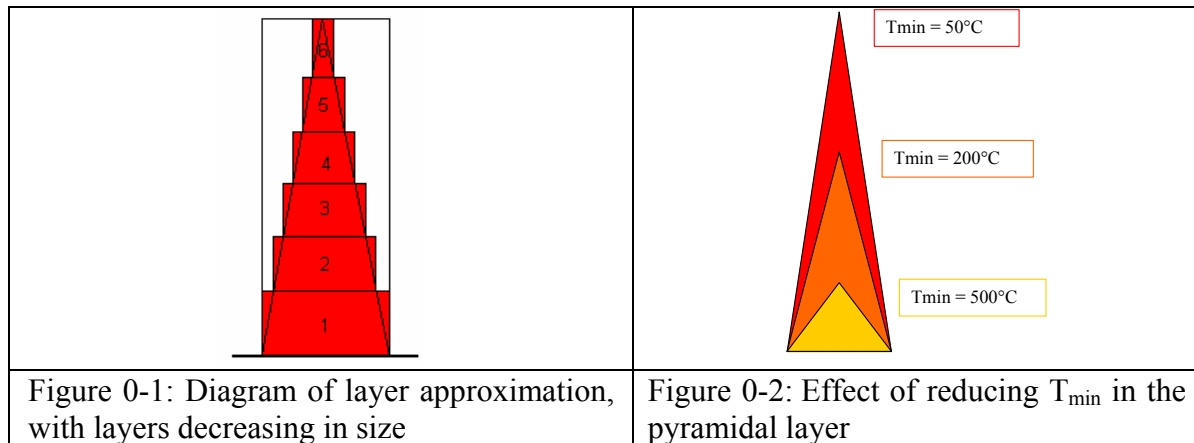
Figure 0-5: Combination of Hasemi and new method.

7. MULTIPLE FIRES WITH LAYERS

This model extends the previous “Multiple Fires” model by adding layers to the flames. The fires are the same as before. Now, the user chooses the height to which he wants the “flame” effects analysed by choosing a flame minimum temperature. This is used to calculate the “flame height”, by solving equation 2 for this temperature. Therefore, the “flame height” considered could now extend above the flame itself (as defined by the ECs). The user also chooses the number of layers to divide the flame into. Division of flame height by number of layers tells us the height of each layer. This value (which is the same for all layers) is used as the value of flame length the configuration factor calculations. The base height changes with the layer, increasing from the initial value (usually 0,3 for car fires) for the first layer, by the layer height, to give the base height for the next layer and each subsequent layer. The layer height and base height are used to find the configuration factors for the layer. The $\phi \cdot \varepsilon$ value can then be calculated in the same way as in previous models, and tabulated at each height for each layer.

Equation 2 is solved at heights from 0m to 10m every 0,2m, to find a temperature distribution over the flame height defined by the minimum temperature. Each of the heights is assigned a layer (unless it is above the flame height). The mean of the temperatures of all the heights in a layer is found, and this is taken as the temperature of the layer. This value is used in calculating its incident heat flux value.

The layers decrease in cross-section as their base height moves further up the flame axis. The first layer has cross-section equal to that inputted by the user. The flame is approximated to a pyramid, with the tip at the minimum temperature height. The dimensions of each layer are taken as the dimensions of the base of the layer defined by the pyramid at that height. The decrease in cross-section of the layers also means the emissivity of the layer decreases with increasing base height of the layer.



Once the $\phi \cdot \varepsilon$ and incident heat flux values of each layer have been found, they are summed, to give the total values for the flame at this time. The total values at each height are then tabulated in the main tables. This process is repeated at each time, to get total $\phi \cdot \varepsilon$ and incident heat flux values over time at each column height.

The temperature distribution of the column is found in the same way as before, taking the $\phi \cdot \varepsilon$ and incident heat flux time distributions at each height in turn, and finding the temperature change over time at this height.

The pyramidal model is less close to the Eurocode rules but may better reflect a real fire. It has been seen using this model that the influence of the fixed T_{min} is of higher importance as for the rectangular model. Indeed, while increasing the min temperature, the height of the pyramid is reduced and, therefore, the radiative surface at the upper part with temperature lower than T_{min} is missing. But, this is due mostly to the fact that the radiative surface at the lower part is reduced through the triangular form (see Figure 0-2). A comparison between the rectangular layer model and the pyramidal one is given in Figure 0-3, based on the car park fire scenario of §6, using different T_{min} . In order to be able to better compare the results, all four simulations were made by using an $A_m/V=999\text{m}^{-1}$ and obtaining by this gas temperatures.

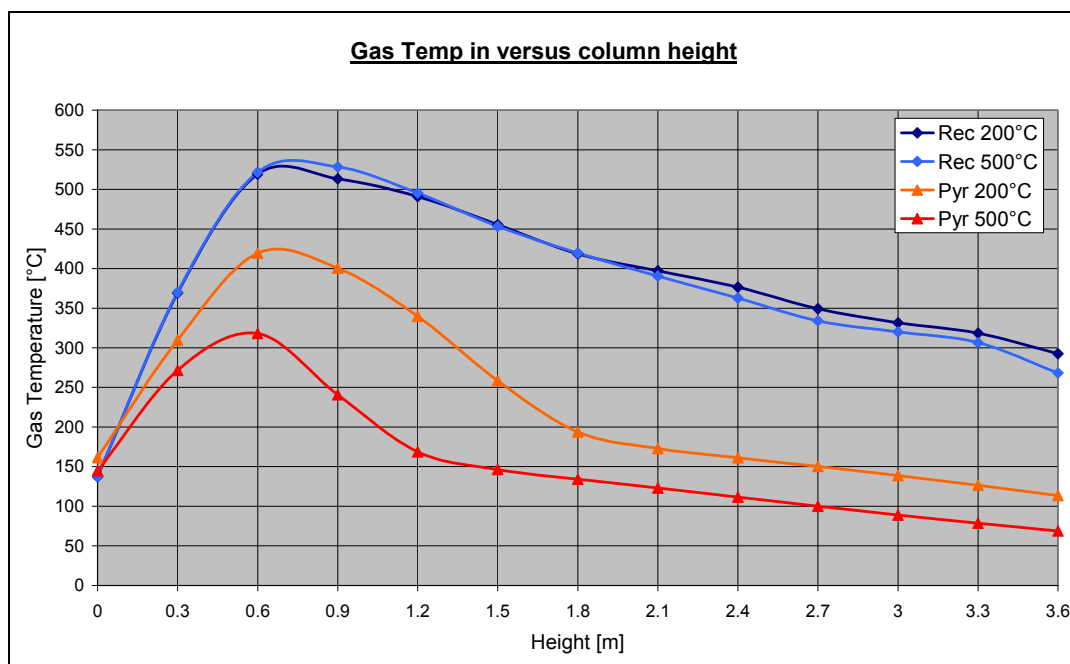


Figure 0-3: Temperature comparison for different models and layer temperatures

8. CONCLUSIONS AND POSSIBLE FUTURE IMPROVEMENTS

These models, which start based on simplified approach and one steady fire and end up with multiple fire and variable RHR with multi layer pyramidal fire shape could be used for several practical applications for which no simplified solution is yet provided. In case where CFD is not appropriated for reason of time and/or needed equipment and skills, the new methods could give a first approach of the temperature distribution in a steel column. Design situations that could be covered are e.g. columns in atriums or in airport halls as well as external structures affected by localised fire. A use for car park design may be considered as well but might be more complex as in reality the column part located in the cold zone is not only heated by the radiation coming from the fire itself but as well from radiation from the hot layer.

In short one could say that the models have furthermore to be calibrated before they could be used in practice. This is especially valid for the determination of appropriated T_{min} value. Validation of the models is furthermore needed, that could be made using either CFD or if possible real fire test data.

Several improvements could further be brought to the models:

- The model could be improved by including the option of a fire engulfing the column.
- The fact using Excel Macro is resulting in long calculation times (up to several hours). This could be improved by either programming the formulas in Visual Basic code or even better in the programming code FORTRAN.
- Shadow effects could also be accounted for in the configuration factor calculation, rather than a parameter in the temperature calculation.
- For the models using layers, the height of the top layer should be chosen automatically according to some criteria that have still to be defined, but may be linked to the real flame height instead of temperature criteria.

9. REFERENCES

- [1] EN 1991-1-2; Actions on structure exposed to Fire
- [2] EN 1993-1-2; Design of steel structures; General rules-Structural fire design
- [3] ECSC project: Development of design rules for steel structures subjected to natural fires in closed car parks; CN°: 7210/SA/211/318/518/933; 01/07/1993-30/06/1996
- [4] ECSC project: Behaviour of External Structures under Natural Fire Conditions, CN°: 7210-PR-380; 01/07/2002-31/12/2005

Steel Connections



FINITE ELEMENT MODELLING OF FIN PLATE STEEL CONNECTIONS IN FIRE

M. SARRAJ¹, I. W. BURGESS², J. B. DAVISON³ and R. J. PLANK⁴

ABSTRACT

Recent structural collapses caused by fire have focussed attention on research concerning fire safety in building design. Steel connections are an important component of any structural steel building as they provide links between the principal structural members. The evaluation of the performance of steel connections at elevated temperatures has been a topic of several research programs in the last few years. Determining the behaviour, available strength and stiffness of moment connections in fire conditions has been a dominant theme in these research works; however very little information on the behaviour of simple shear connections in fire conditions has been disseminated. Fin plate shear connections are easy to fabricate and install; as a result, they have gained popularity because of their economy. In this research, the robustness of simple fin plate beam-to-column connections is being investigated under catenary tension from highly deflected beams in fire.

A highly detailed 3D finite element model has been created using the ABAQUS software. This is a complex model accounting for material nonlinearity, large deformation and contact behaviour. Contact is critical to model the shear behaviour of the joint, and contact elements have been used at the bolt-hole interface and also at the surface between the web of the beam and the fin plate, taking into consideration friction between the surfaces. The connection model has been analysed through the elastic and plastic ranges up to failure. Bolt shear and bending, and plate and web bearing have been observed as failure modes. A comparison with available experimental data at ambient and elevated temperatures and other analytical results shows that the model has a high level of accuracy. When the connection model was extended to include an attached beam, it was found that it eventually experiences large tensile force when exposed to fire.

¹ Ph.D. , University of Sheffield, Dept of Civil & Structural Engineering, S1 3JD, UK, m.sarraj@shef.ac.uk

² Professor, University of Sheffield, Dept of Civil & Structural Engineering, S1 3JD, UK,
ian.burgess@shef.ac.uk

³ Senior lecturer, University of Sheffield, Dept of Civil & Structural Engineering,, S1 3JD, UK,
j.davison@shef.ac.uk

⁴ Professor, University of Sheffield, School of Architectural Studies, S10 2TN, UK, r.j.plank@shef.ac.uk

KEYWORDS

Structural fire engineering; fin plate joints; shear connection; large deflection; catenary.

1. INTRODUCTION

In the last three decades, over 100 fire tests have been conducted in the UK on steel structural members that include beams ¹, columns ² and connections ³⁻¹⁹. This has led to an improved understanding of the behaviour and design of steel beam-to-column connections at elevated temperatures ³⁻¹⁹ mainly associated with their moment-rotation characteristics. Using the available test data for validation, further research was conducted, simulating the connection behaviour via FE modelling ¹⁰⁻¹⁴; this provides the opportunity for wider parametric investigations and eliminates some of the limitations associated with experimental studies. More recently, simplified analytical connection component models have been developed by a few researchers ¹⁵⁻¹⁹ with the intention of simplifying connection design for fire conditions.

In fire large axial forces can often be generated in steel beams; due to the restraint to thermal expansion these forces are initially compressive. Nevertheless, at later stages the forces become tensile as catenary action starts to develop. Such action helps steel beams to survive by behaving like a suspension cable. They hang from the adjacent supporting members as a result of strength and bending stiffness losses, as shown by Liu *et al.* ²⁰. Furthermore, during the cooling stage of the fire, the deformed beams contract considerably and experience additional tension forces as described by Bailey *et al.* ²¹.

Beam-to-column connections are required to resist any resultant forces at the end of the beam and transfer them into the columns and surrounding cold structure. Consequently, for a structure to survive fire conditions, it is crucial for any connection to have sufficient strength to resist the induced actions. Recent research by Yin *et al.* ²² has shown that the level of axial force developed depends strongly on the stiffness of the joints and the surrounding structure. Evidently, overall analysis of steel structures and composite frame buildings in fire conditions needs reliable prediction methods that focus on joint stiffness as well as resistance in order to provide a realistic and safe connection design.

An assessment of previous research conducted into steel connections in fire conditions ³⁻¹⁹ gives an obvious conclusion that the investigation of simple shear connections in such conditions is almost a missing topic. The low levels of available research on fin plate shear connections in fire, together with their economical popularity, has necessitated this research.

The research presented here has focused on investigating the behaviour of fin plate shear connection in fire conditions. The creation of a reliable FE model to complement existing test results was a primary aim at the starting point of the research. Consequently, the FE model would form the main source of information and would be of great benefit when studying the influence of the connection parameters on the overall behaviour by allowing a wide ranging parametric study to be conducted which would be difficult to achieve in a laboratory environment. Additionally, the FE model results would enable a reliable simplified component model to be developed. Such a simplified model would be in demand for design/analysis software with great saving in terms of computing time. The FE model and the component model may be used to gain an insight into important issues such as the connection tying force capacity of a fin plate at ambient and elevated temperatures, bolt and plate bearing behaviour, and bolt shearing.

2. THE FINITE ELEMENT MODEL DESCRIPTION

A three-dimensional FE model of a fin plate connection was developed in order to analyse and understand the behaviour of such a connection at ambient and elevated temperatures. The starting point for this model was a simple plate with a bolt bearing against a hole (Figure 1-a). This model was then developed to form a single lap joint (Figure 1-b). Ultimately, the entire fin plate connection was then assembled and modeled using a series of lap joints in which the plate on one side was the fin plate, and the second plate was the beam web. The three main parts of the fin plate connections - beam, fin plate and the bolts (Figure 1-c) - were modelled using eight-node continuum hexahedral brick elements. This element has the capability of representing large deformation and geometric and material nonlinearity^{23, 24}. However, to capture accurately the stress behaviour in the region around the bolt holes where likely failures would initiate, an intensive mapped mesh was made within the vicinity of the bolt holes. The bolt holes were modeled 2mm larger than the bolt shank diameter and the hexagon bolt heads were modeled as cylinders. The flange of the column was modeled as a rigid surface, assuming that it was sufficiently rigid and connected to the fin plate.

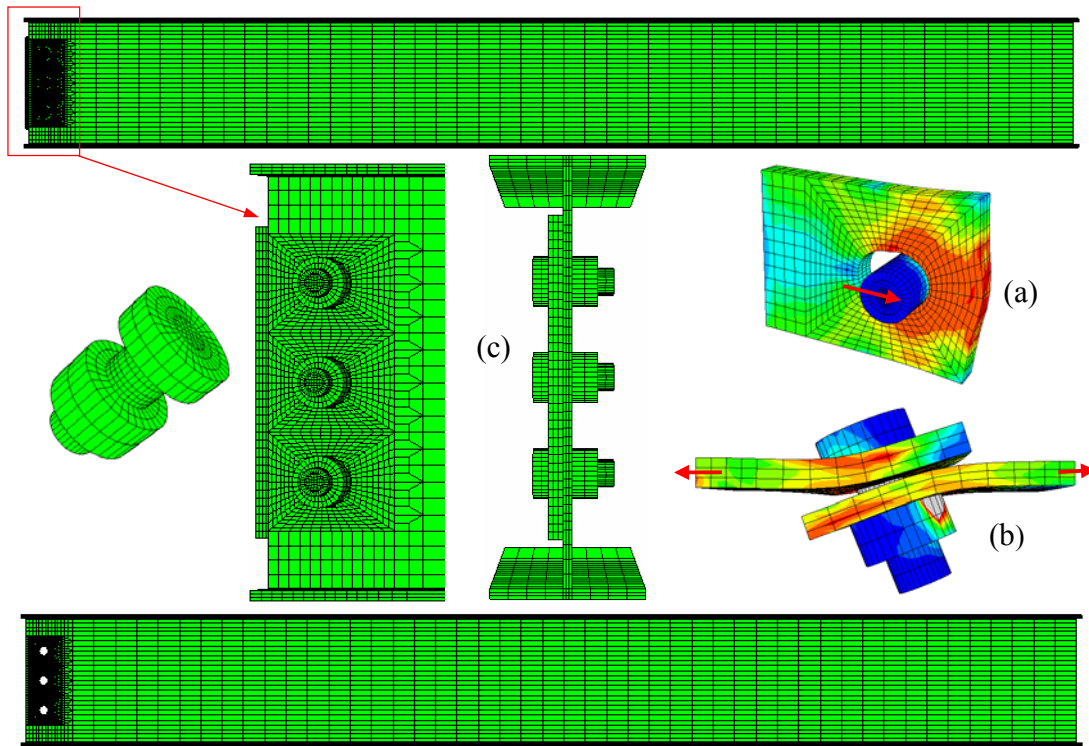


Figure 1: FE model development
(a) Single bolt in bearing (b) Lap splice (c) Fin plate and beam model

Surface-to-surface contact, with a small sliding option, was used for all the contacting surfaces to fully transfer the load from the beam web to the fin plate and, eventually, to the supporting member. The contact areas in the fin plate connection comprise the bolt shank-to-bolt holes, bolt head-to-fin plate, nut-to-beam web and fin plate-to-beam web surface (Figure 2). The contact surfaces of the bolt shank, bolt head, and bolt nut were always chosen to be master surfaces (as the bolt is of stiffer material) with all the other contact surfaces

considered as slaves. Pre-tension was not applied to the bolts during the analysis study and a friction coefficient of $\mu = 0.25$ was adopted for all the contact surfaces.

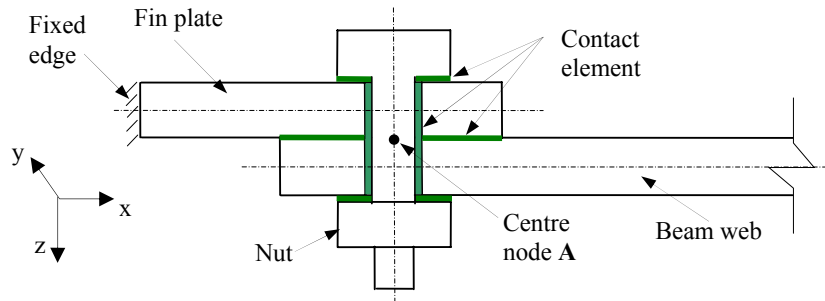


Figure 2: Contact elements distribution (Plan section on a fin plate connection)

Simulating the contact interaction between the parts of a shear joint using ABAQUS/Standard is a very (sensitive and difficult issue to achieve and at the same time it is of satisfactory accuracy when is established. The difficulties arise because of special arrangements needed to bring the connection parts into initial contact. Firstly, the mesh should be fine enough for each element's norm of the master surface to face a corresponding norm of the slave surface elements. Secondly, the load should be applied extremely slowly until contact is established. Lastly, the boundary conditions need to be assigned in a proper way to achieve a sensible behaviour at the connection and move away from any singularity problem that may arise. Therefore, each bolt was restrained at only one node (Node A) by preventing movement in the z-direction for the first analysis step, then for the later steps bolts are freed of any restraint as the contact is already established. The fin plate was fixed along the edge welded to the column flange (Figure 2). The beam was restrained at selected nodes along its flange in the z-direction to prevent lateral movement, simulating the restraint provided by the floor slab

3. VALIDATION AGAINST EXPERIMENTAL DATA AT AMBIENT TEMPERATURE

Where possible, numerical simulations should be validated against experiment results. The evaluation process for the current FE model included two stages; the first being one at ambient temperature and the second at elevated temperature. Well-documented experimental data from other researchers^{28, 29} was used for the comparison with the FE model.

3.1 Comparison of the FE model with lap joint tests at ambient temperature

Richard²⁵ reported data from several tests conducted on steel lap joints at ambient temperature. One of these tests was chosen for comparison with the finite element model analyses. The plates in the lap joint specimen were of two different thicknesses, 9.525 mm and 12.7 mm (3/8 inch, 1/2 inch). Both plates were ASTM A36 steel of yield stress 250 N/mm² and ultimate stress 400 N/mm². The bolt was ASTM A325 of 19mm (3/8 inch) diameter, installed in over-sized holes of 20.6mm (13/16 inch).

A 3-D finite element model was created for the lap joint using the material properties specified above. Comparison of the FE results with the experimental load-deflection curve (Figure 3) shows good agreement, with the same general behaviour and a maximum

difference of 6%. An observation of the FE deformation shape and mode of failure shows a similarity to what would be expected in a lap joint tensile test (Figure 4), that is bolt twisting due to the load eccentricity, and bolt shearing failure.

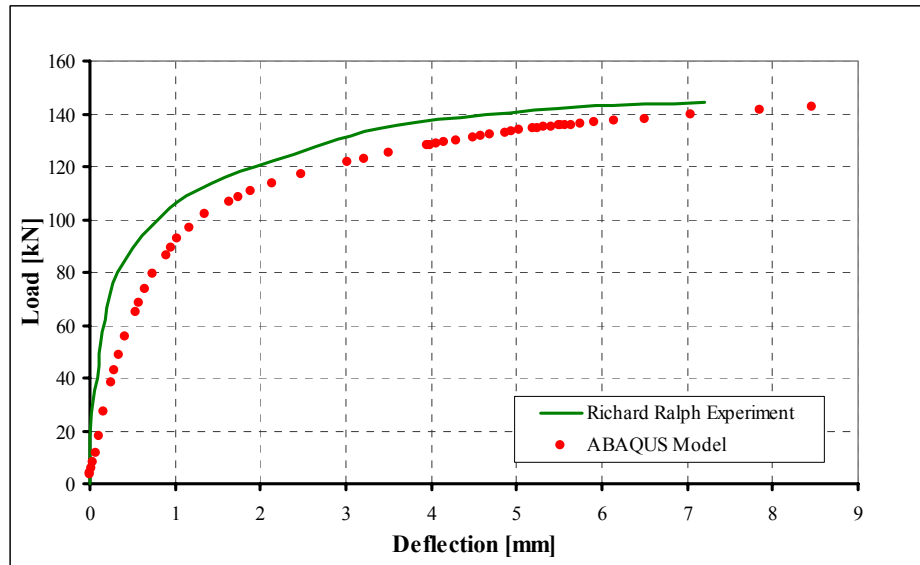


Figure 3: Load-Deflection comparisons between FE model and test data for a steel lap joint

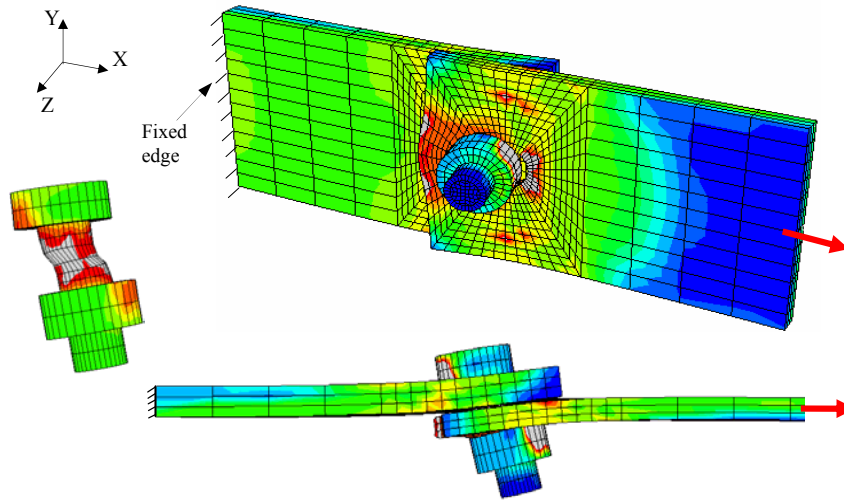


Figure 4: Steel lap joint FE model, deformation and Von Mises stress contours

3.2 Evaluation of the FEM to fin plate connection test at ambient temperature

Richard²⁵ also investigated the moment rotation characteristics of fin plate steel connections. Full scale experiments were conducted on two, three, five and seven-bolted connections. The three bolted fin plate connection test has been chosen to evaluate the capability of the finite element model to predict the moment rotation. This test was carried out on a W18×35 beam connected to a fin plate of 9.5mm (3/8 inch) thickness. Both the beam and fin plate are ASTM A36 steel. The bolts were ASTM A325 of 19mm (3/4 inch) diameter inserted into 20.6 mm (13/16 inch) over-sized hole. The final deformation and von Mises

stress contours are shown in Figure 5. It is clear from the analysis that the middle bolt acts as the centre of rotation, whereas the top hole undergoes a high deflection as the top bolt bears toward the small edge distance of the web. In contrast, the bottom bolt has to bear in the opposite direction, where the web material is not limited by the close proximity of an edge. Consequently, the bottom bolt deforms more than the top bolt and suffers high shearing stresses.

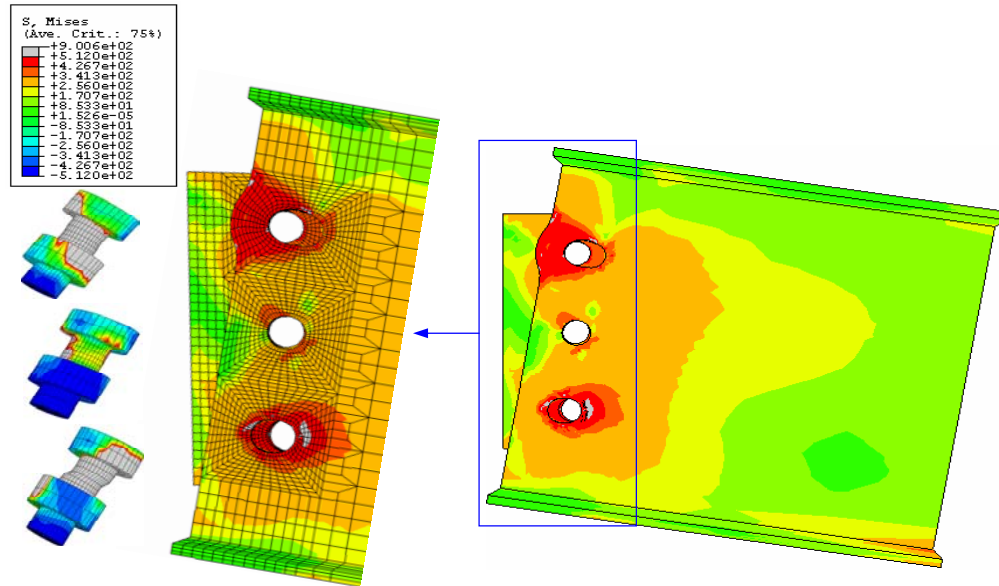


Figure 5: FE model of steel fin plate connection, deformation and Von Mises stress contours

Figure 6 shows the moment-rotation response for the FE model in comparison with the experimental results. In general, the FE model analyses agree well with the experimental data of Richard's test.

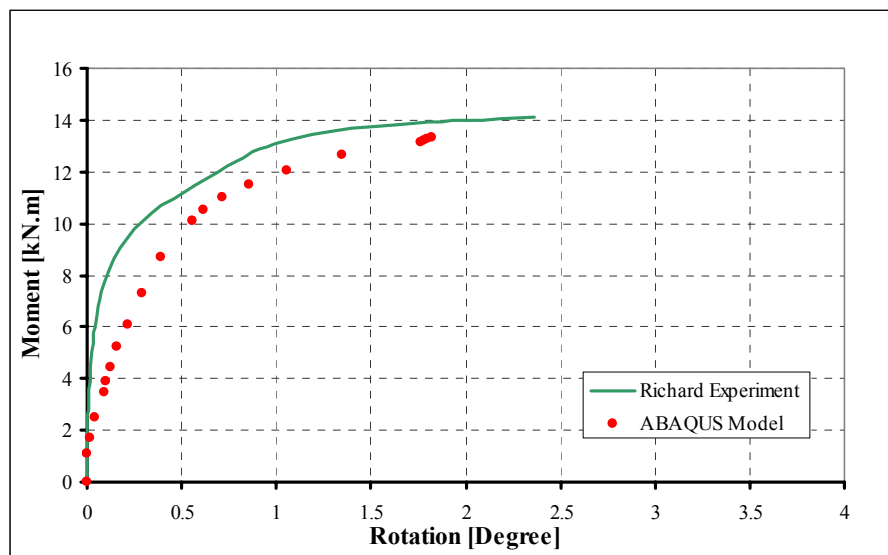


Figure 6: Moment–Rotation comparison of FE model and test data for fin plate connection

3.3 Evaluation of the FE model at elevated temperature

Although the shear behaviour of the FE model has proved satisfactory compared with test results at ambient temperature, the lack of suitable fire test data at this time for a steel fin plate connection including its supported steel beam makes it difficult to evaluate the model at elevated temperature.

Because of this lack of data, a model was created for an isolated beam and this was evaluated by comparison with existing test data. If the beam model worked well, the only remaining uncertainty about the behaviour of the complete assembly at elevated temperature would be the fin plate itself.

El-Rimawi *et al*²⁶ performed a numerical analysis using a stiffness approach to investigate different factors affecting steel beam behaviour under fire conditions. Their analyses compared well with tests conducted in the UK¹, but it has to be noted that this study did not consider the effect of axial restraint at the beam ends. For the evaluation of the current model, one of El-Rimawi's analytical results and corresponding test data for a beam under large deflections in fire conditions was used. The beam was a UB254×146×43 section spanning 4.5m, supported on roller bearings at both ends and with a uniformly distributed load of 16.34kN/m. The values of the modulus of elasticity and yield stress of steel at ambient temperature were assumed to be 205kN/mm² and 275 N/mm² respectively, and the mechanical properties of steel at elevated temperatures were assumed to follow Eurocode 3 Part 1.2²⁷. The beams supported a concrete slab on the top flange exposing it to three-side heating under fire conditions. The time-temperature relationships for the beam web and flanges are shown in Figure 7.

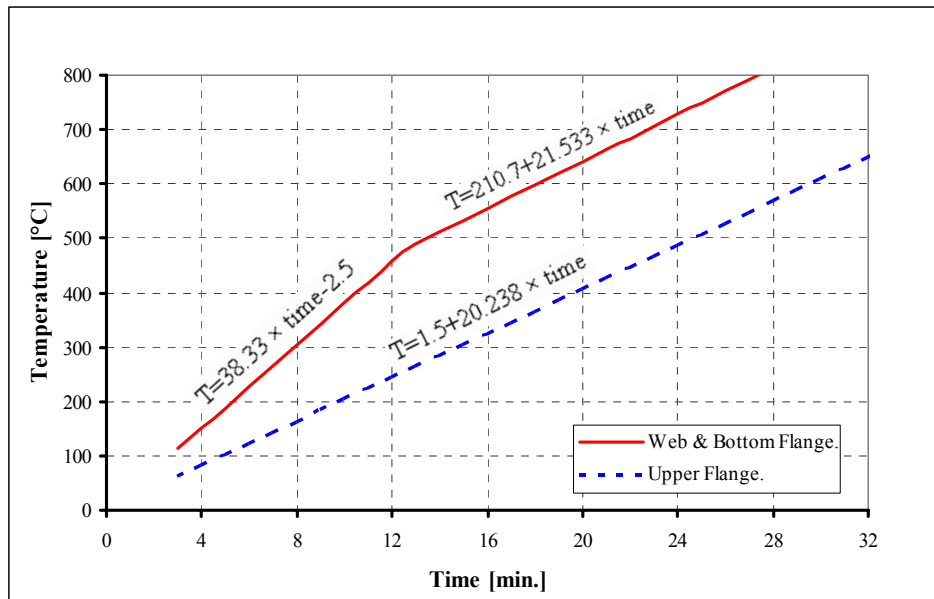


Figure 7: Time-temperature relationships used in the El-Rimawi *et al* analysis

A comparison of the beam mid span deflection against the bottom flange temperature is shown in Figure 8 for the test data, the current FE model and El-Rimawi's analysis. Additionally, the results of an independent analysis using the VULCAN software²⁸ are included. It is clear that the 3-D ABAQUS beam model is in very good agreement with the other analytical results and the experimental data.

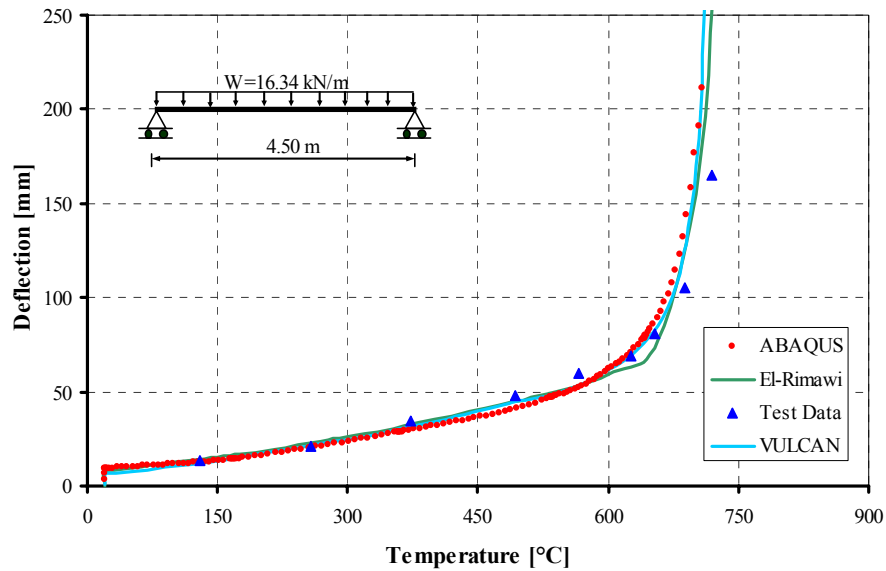


Figure 8: Comparison between Temperature-Deflection relationships of the ABAQUS simulation, El-Rimawi *et al*, test data and VULCAN software

3.4 Beam and connection behaviour in fire

In 2005 Wald and Ticha conducted a fire test on a steel fin plate connection at the Czech Technical University (Figure 9). A three-bolt fin plate connection, $6 \times 60 \times 125$ mm, was assembled using fully threaded 8.8 high strength bolts of 12 mm diameter. The beam was an IPE160 cross section 3 m long and the loads were applied by two hydraulic jacks (60 kN each) 250 mm from the beam ends. The fin plates and beam were both of Grade S235. The furnace gas temperature was controlled to follow the Cardington²⁹ fire test No. 7 for the heating and cooling stages. The deflection of the beam was recorded at the load points. A comprehensive FE model for the tested connection and supported beam was created to match the test condition. By using symmetry it was only necessary to model half of the tested beam. The deformed shape and failure mode determined by the FE analysis are shown in Figure 10 and are clearly consistent with the test observations. Bolt shearing was the predominant failure mode in the test and similarly in the FE model.



Figure 9: Wald and Ticha fin plate connection test

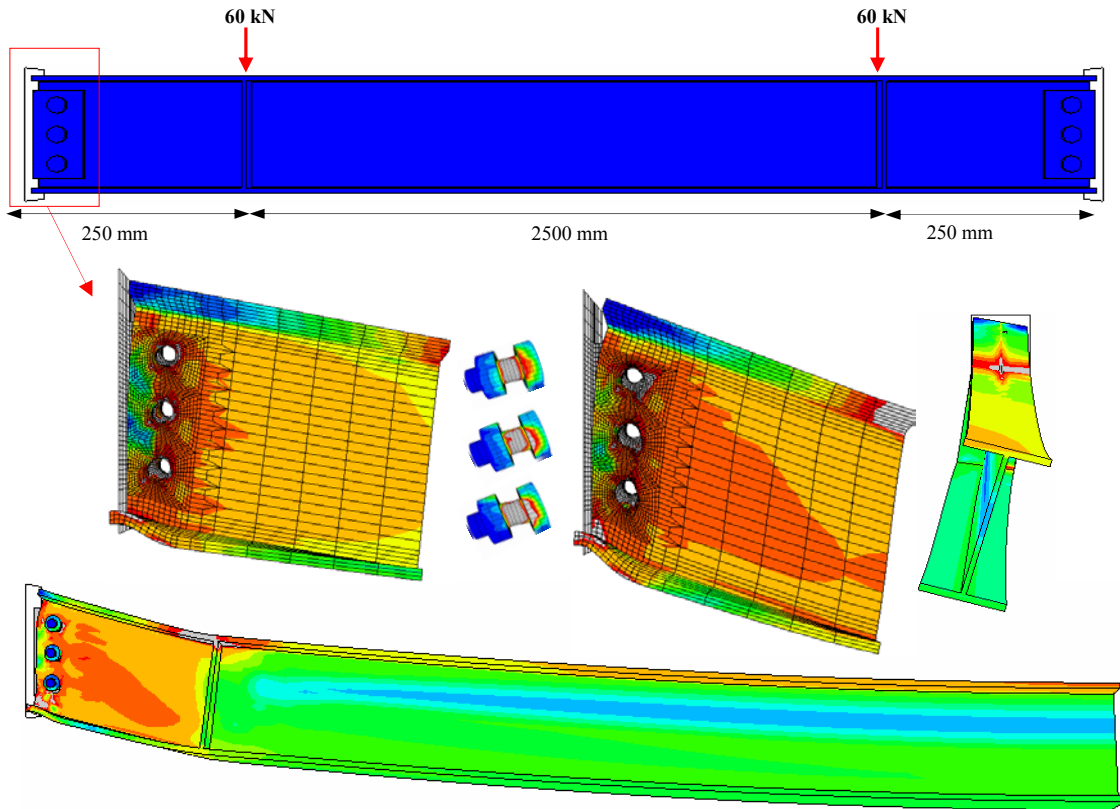


Figure 10: FE model of the tested fin plate connection and the connected beam

Comparison of the time-deflection curves for the tested beam and the FE model (Figure 11) shows a reasonable agreement. Although there are slight differences in the runaway stage it can be seen that the point at which runaway starts is approximately 32 minutes for both the test and the FE model. The complexity of the test arrangement, in particular the special lateral restraint arrangement and composite action, may account for the small differences.

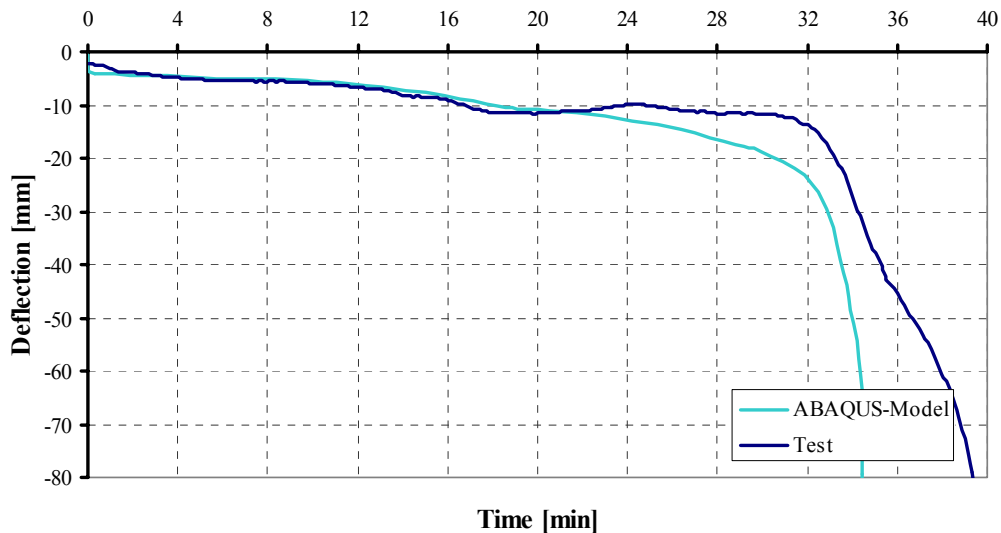


Figure 11: Time-Deflection comparisons of the FE simulation and test data

4. CONCLUSION

3D finite element models incorporating contact interaction, geometric non-linearity and non-linear material properties have been used to accurately model fin plate steel connections behaviour. The contact elements were particularly important in this context.

A connection-beam model has successfully been created and validated against the limited test data available. This can now be used in parametric studies, for example to account for different time-temperature histories.

Parametric studies of factors that influence the strength and stiffness of steel joints are difficult to control in any laboratory testing due to of the dimensional and physical variability in joints and test arrangements. Empirical parametric studies are also expensive and time consuming. The reasonable accuracy of the FE model for reproducing the experimental behaviour of steel joints makes it a useful model for both analytical and parametric studies. Although validation with experimental test data is needed, a numerical simulation carefully created and validated against test data enables cost-efficient parametric investigation that may lead to improvements in joint configuration and joint performance.

In reality this research programme has gone farther than the development of the FE model and its validation. Examination and evaluation of a component spring model assembly, at ambient an elevated temperature, for the fin plate connection is now in process. In addition, the plate bearing and bolt single shear component were introduced and described in detail.

5. ACKNOWLEDGMENT

The authors gratefully acknowledge the kind assistance of Prof. Frantisek Wald and Alena Ticha of the Czech Technical University in Prague for providing the test data for their experimental work on fin plate steel connections, and to the Engineering and Physical Sciences Research Council of the UK for their sponsorship of the principal author.

6. REFERENCES

- [1] British Steel Corporation, Compendium of UK standard fire test data on unprotected structural steel. Contract report for Department of Environment, (1987).
- [2] Shepherd, P.G., "The Performance in Fire of Restrained Columns in Steel-Framed Construction", PhD Thesis, University of Sheffield, (1999).
- [3] Kruppa, J. "Résistance en feu des assemblages par boulons", Centre Technique Industriel de la Construction Métallique, St. Remy Chevreuse, France, CTTICM Report, Document No. 1103-1, English translation available entitled "Fire Resistance of Joints with High Strength Bolts", (1976).
- [4] British Steel, "The Performance of Beam/Column/Beam Connections in the BS5950: part 8 Fire Test", British Steel (Swinden labs), Report T/RS/1380/33/82D and T/RS/1380/34/82D. Rotherham, (1982).
- [5] Leston-Jones, L.C., "The Influence of Semi-Rigid Connections on the Performance of Steel Framed Structures in Fire", PhD. Thesis, Department of Civil and Structural Engineering, University of Sheffield. (1997).
- [6] Leston-Jones, L.C., Lennon, T., Plank, R.J. and Burgess, I.W., "Elevated Temperature Moment-Rotation Tests on Steelwork Connections", *Proc. Instn. Civ. Engrs. Structs. & Bldgs*, 122, (1997) pp410-419.

- [7] Al-Jabri, K. S., Lennon, T., Burgess, I. W. and Plank, R. J. "Behaviour of Steel and Composite Beam-column Connections in Fire", *J. Construct. Steel Research*, 46 (1-3), (1998) pp308-309.
- [8] Al-Jabri, K. S., "Behaviour of Steel and Composite Beam-column Connections in Fire", PhD. Thesis, Department of Civil and Structural Engineering, University of Sheffield. (1999).
- [9] Al-Jabri, K.S., Burgess, I.W., Lennon, T. and Plank, R.J. "Moment-rotation-temperature curves for semi-rigid joints", *J. Construct. Steel Research*, 61, (2005) pp281-303.
- [10] Liu, T. C. H. "Finite Element Modelling of Behaviours of Steel Beams and Connections in Fire", *J. Construct. Steel Research*, 36, (3), (1996) pp181-199.
- [11] Liu, T. C. H. "Three-dimensional Modelling of Steel/Concrete Composite Connection Behaviour in Fire", *J. Construct. Steel Research*, 46, (1-3), (1998) pp319-320.
- [12] El-Housseiny, O. M., Abdel Salam, S., Attia, G. A. M. and Saad, A. M. "Behaviour of Extended End Plate Connections at High Temperature", *J. Construct. Steel Research*, (46), (1-3), (1998) p299.
- [13] Spyrou, S., "Development of Components Based Model of Steel Beam-to-Column Joint at Elevated Temperatures", PhD. Thesis, Department of Civil and Structural Engineering, University of Sheffield. (2002).
- [14] Al-Jabri, K. S., Seibi, A., Karrech, A., "Modelling of unstiffened flush end-plate bolted connections in fire", *J. Construct. Steel Research*, (2005), (*in press*)
- [15] Simoes da Silva, L., Aldina, S. and Paulo, V.R., "A component model for the behaviour of steel joints at elevated temperatures", *J. Construct. Steel Research*, 57, (2001) pp1169-1195.
- [16] Spyrou, S., Davison, J.B., Burgess, I.W., and Plank, R.J., "Experimental and analytical investigation of the 'tension zone' components within a steel joint at elevated temperatures", *J. Construct. Steel Research*, 60, (2004) pp867-896.
- [17] Spyrou, S., Davison, J.B., Burgess, I.W., and Plank, R.J. "Experimental and analytical investigation of the 'compression zone' components within a steel joint at elevated temperatures", *J. Construct. Steel Research*, 60, (2004) pp841-865.
- [18] Al-Jabria. K.S., "Component-based model of the behaviour of flexible end-plate connections at elevated temperatures", *Composite Structures*; 66, (2004) pp215-221.
- [19] Al-Jabri, K.S., Burgess, I.W. and Lennon, T., Plank, R.J. "Spring-stiffness model for flexible end-plate bare-steel joints in fire", *J. Construct. Steel Research*, 61, (5) pp1672-1691, (2005).
- [20] Liu, T.C.H., Fahad, M.K. and Davies, J.M. "Experimental investigation of behaviour of axially restrained steel beams in fire", *J. Construct. Steel Research*, 58, (2002) pp1211-1230.
- [21] Bailey, C.G., Burgess, I.W. and Plank, R.J. "Analyses of the effects of cooling and fire spread on steel-framed buildings", *Fire Safety Journal*, 26, (1996) pp273-293.
- [22] Yin, Y.Z. and Wang, Y.C. "A numerical study of large deflection behaviour of restrained steel beams at elevated temperatures", *J. Construct. Steel Research*, 60, (2004) pp1029-1047.
- [23] ABAQUS/Standard, User's Manual I-III, version 6.3, Hibbit, Karlsson and Sorenson, Inc. (2001).
- [24] ABAQUS, Theory Manual, version 6.3, Hibbit, Karlsson and Sorenson, Inc., Providence, RI, (2001).
- [25] Richard, R. M., Gillett P.E., Kriegh, J. D., and Lewis, B. A., "The Analysis and Design of Single Plate Framing Connections", *Engineering Journal, AISC*, 17, (2), (1980).

- [26] Burgess, I. W., El Rimawi, J. and Plank, R. J. “Studies of the Behaviour of Steel Beams in Fire”, *J. Construct. Steel Research*, 19, (2004) (1991) pp285-312.
- [27] European Committee for Standardization *EN 1993-1-2: Eurocode 3: Design of steel structures, Part 1.2: Structural fire design* (2005).
- [28] <http://www.vulcan-solutions.com/index>.
- [29] Wald, F., Simoes da Silva, L., Moore, D., Santiago, A., “Experimental behaviour of steel joints under natural fire” ECCS – AISC Workshop, June 3-4, 2004.



NONLINEAR FINITE ELEMENT MODELLING OF BEHAVIOR OF EXTENDED END-PLATE BOLTED MOMENT CONNECTIONS IN FIRE

Guo-Biao LOU¹ and Guo-Qiang LI²

ABSTRACT

A three-dimensional finite element approach for investigating the temperature field and structural behavior of extended endplate bolted moment connections in fire is presented in this paper. ANSYS 7.0 is selected for the purpose. Due to low degree of thermal-structural coupling interaction in the connection, sequential analysis, a transient thermal analysis followed by a static structural analysis where the effects of temperatures obtained from in the thermal analysis are applied as body force loads, is employed in place of direct coupling analysis. In the thermal FE model, eight-node thermal solid elements are used to represent the endplate, column, beam and bolts. Special four-node thermal surface elements overlaid onto the faces of the connection are used to simulate convection and radiation effects. The contact between column flange and endplate is idealized using four-node surface-to-surface contact elements with the hypothesis that conduction coefficient of the elements is infinite. The effects of non-uniform thermal expansion, geometric nonlinearity, temperature dependent nonlinear material behavior are taken into account in the structural FE model. Solid elements are used to discretize all of components in the endplate connection. Pretension in bolts is taken into account by defining the pretension section. Contact elements are used to model all contact problems in the connection. The validity and effectiveness of this FE approach are verified by the test results. The FE model can then be further used to predict moment-rotation-temperature relation of the connections that can be incorporated in the structural analysis of global steel frames subjected to fire.

1 INTRODUCTION

Fire resistance of connections is extremely important for maintaining the integrity of steel structures in fire. Recent fire tests on the Cardington full scale test frame and observations from real fires have demonstrated that complete structures behave very

¹ Tongji University, School of Civil Engineering, 1239 Siping Rd., Shanghai, P. R. China
email: gblou@sina.com

² Professor, Tongji University, School of Civil Engineering, 1239 Siping Rd., Shanghai, P. R. China
email: gqli@mail.tongji.edu.cn

differently from individual elements. This is partly due to the redistribution of stresses and changes in relative stiffnesses between connections and adjacent members. As a result, the survival time of the structure can be a significant improvement. However, having only very limited experimental and analytical studies carried out, current design codes give little guidelines on the fire resistance and behavior of connections at elevated temperatures. This also limits the effective use of numerical models to simulate the structural global behavior in fire, since in these models the moment-rotation-temperature characteristics of the actual semi-rigid connections is either derived from the moment-rotation characteristics at ambient temperature or idealized as fully rigid / pinned (Chiou 1992, El-Rimawi 1995).

The main objective of this paper is to establish finite element analysis procedures capable of predicting the thermal and structural behavior of bolted endplate connections in fire. ANSYS 7.0, a large-scale general-purpose finite-element package, is selected for the purpose. Due to low degree of thermal-structural coupling interaction in the connection, sequential analysis, a transient thermal analysis followed by a static structural analysis where the effects of temperatures obtained from in the thermal analysis are applied as body force loads, is employed in place of direct coupling analysis. The validity and effectiveness of this FE procedure are verified by the results of endplate connection tests.

2 TEST PROGRAM

To investigate the temperature field, structural behavior and failure mechanism, total three full scale beam-to-column extended endplate connection tests were conducted, including one at ambient temperature throughout the entire moment-rotation range and two transient state tests at different load level.

2.1 Specimens

A full-scale cruciform arrangement was chosen consisting of two H300×160×8×14 beams 2264mm long, symmetrically framing to the flanges of a single H240×240×10×16 column 1225mm long with extended endplate connections. All beams, column, and endplate were fabricated from GB specified Q235B steel. All bolts used in this test program were M20, Grade 8.8s high-strength bolts. Fig. 1 shows the details of specimen. The specimens were assembled using a torque spanner to tighten the bolts by 291 N·m torque which provided 110kN pretension in the bolts. The actual dimensions of the specimens and material properties at ambient temperature are given in table 1.

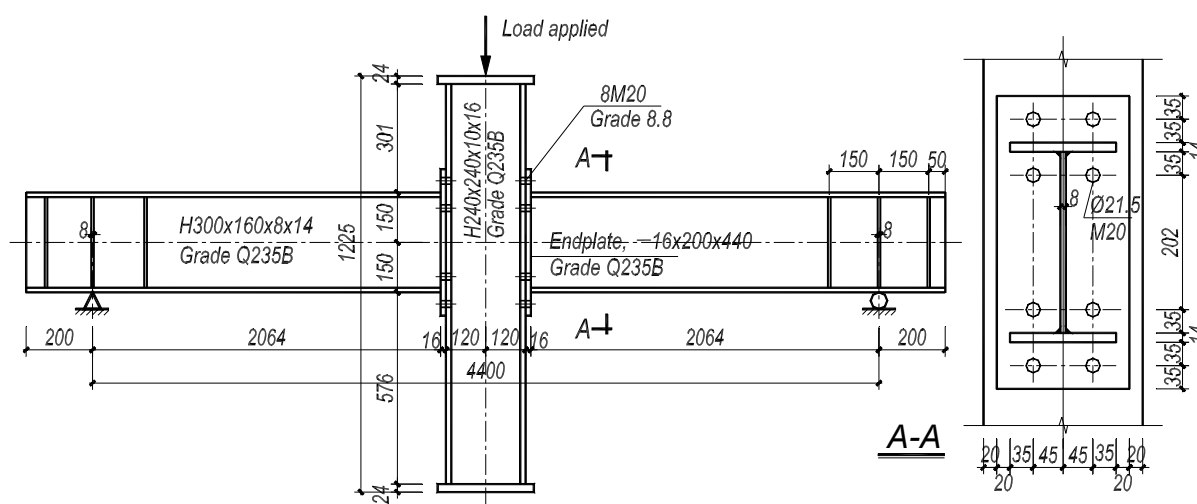


Fig. 1 Details of specimen and schematic arrangement for ambient temperature test (mm)

Table 1 Material properties at ambient temperature

Component	Grade	Thickness (mm)		Modulus (N/mm ²)	Yield strength (N/mm ²)	Tensile strength (N/mm ²)	Elongation (%)
		Nominal	Actual				
Plate	Q235B	8	7.60	2.02×10 ⁵	320.8	456.4	40.1
	Q235B	10	9.40	2.02×10 ⁵	361.7	467.7	32.4
	Q235B	14	13.90	1.99×10 ⁵	256.0	414.8	36.5
	Q235B	16	15.65	2.00×10 ⁵	249.6	421.6	36.2
bolt	8.8s	M20×60		—	—	943.3	—

Notes: The nominal effective area of bolt M20 is 244.67 mm².

2.2 Ambient temperature test

The schematic arrangement for ambient temperature test is shown in Fig. 1. An incremental load was applied to column head. A simple but reliable displacement transducers configuration, shown in Fig. 2, was employed to measure the left and right connection rotations. The connection rotation was obtained by the means of the following relationship:

$$\varphi = \varphi_{beam} - \varphi_{col} = (\Delta_{bf}^t - \Delta_{bf}^b) / h_{bf} - (\Delta_{cw}^t - \Delta_{cw}^b) / h_{bf} \quad (1)$$

where φ , φ_{beam} and φ_{col} are the connection rotation, beam rotation and column rotation respectively; Δ_{bf}^t , Δ_{bf}^b , Δ_{cw}^t and Δ_{cw}^b are the horizontal deflection of these locations illustrated in Fig. 2; h_{bf} is the distance between centerlines of upper and bottom beam flanges.

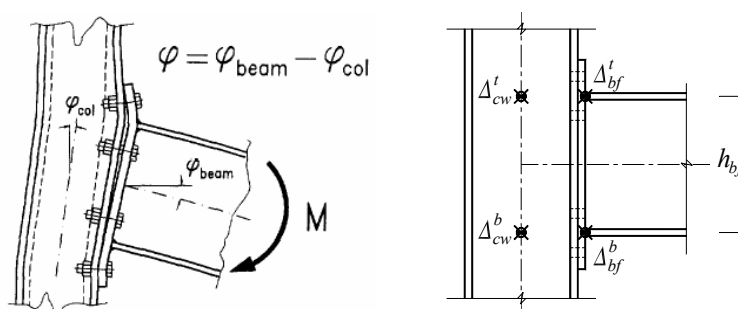


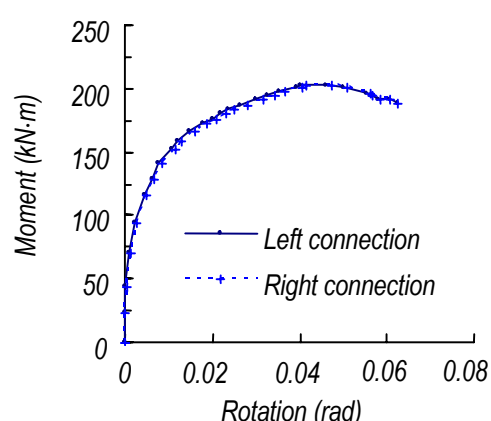
Fig. 2 Definition of connection rotation

The measured moment-rotation characteristics (M - φ curves) of the left and right endplate connections are plotted in Fig. 3(a). The failure moment was 203.17kN·m, and the limit rotations of the left and right connections were 0.0403rad (2.31°) and 0.0418rad (2.39°) respectively. Fig. 3(b) shows the failure mechanism and deformation characteristics of the specimen. These are clear from the figure: (1) failure is due to column web buckling; (2) the exterior bolts in tension zone are subjected to bending for prying action; (3) column web in tension zone little deforms; (4) the connection rotations are mainly attributed to significant deformation of column flange and endplate in tension zone.

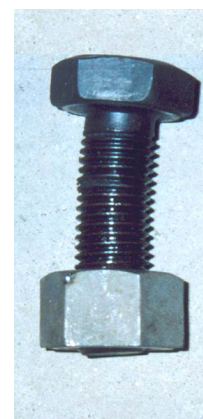
2.3 Elevated temperature tests

2.3.1 Test arrangement

The schematic arrangement for elevated temperature tests is shown in Fig. 4. Transient-state test method was employed in the tests. A constant load was applied to column head throughout the entire test. To avoid failure of exterior beams, ceramic fiber blanket was used to protect these beams. The instrumentation used for the fire tests included three displacement sensors, 16 thermocouples and load control, data record devices. The detailed test conditions are illustrated in Table 2.



(a) Moment-rotation characteristics



(b) Failure mechanism

Fig. 3 Results of ambient temperature test

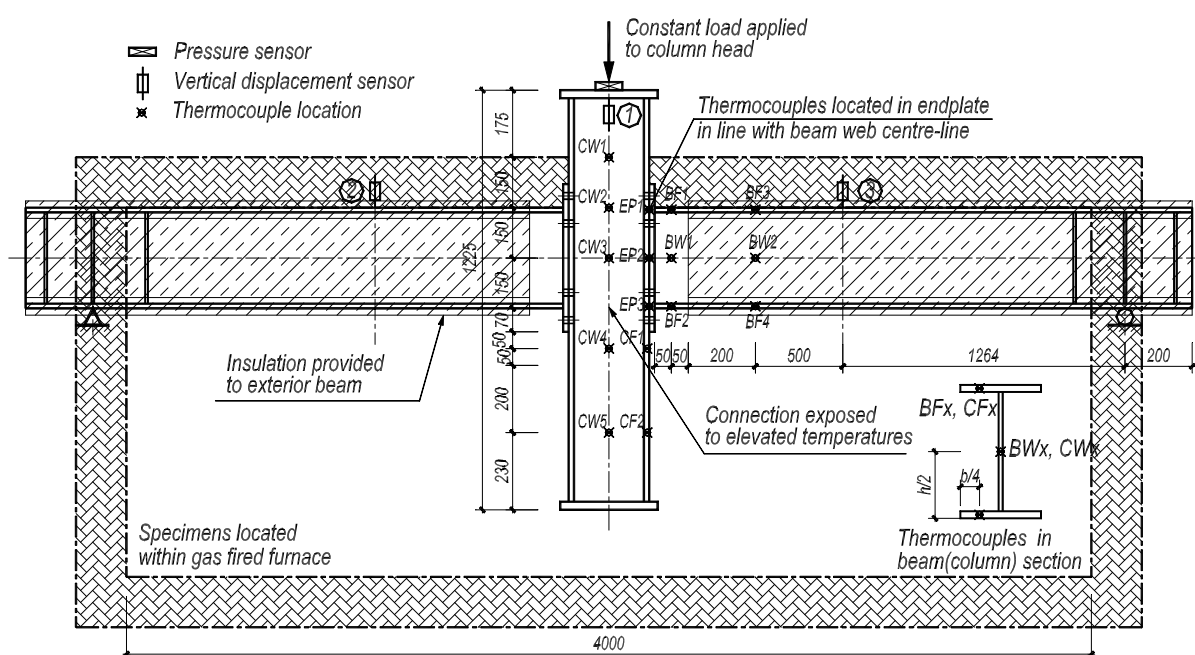


Fig. 4 Elevated temperature test schematic arrangement

Table 2 Test conditions of elevated temperature tests

Test	Test method	Fire curve	Applied load (kN)	Connection moment (kN·m)	Moment ratio
BC1F	Transient-state Test	ISO834	107.8	112.1	0.552
BC2F	Transient-state Test	ISO834	78.4	81.5	0.401

Note: Moment ratio is defined as the moment applied on the connection in fire conditions relative to the failure moment of the connection at ambient temperature test.

2.3.2 Test result

The furnace temperatures and temperatures in these specimens are shown in Fig. 5. The fire endurance and limit temperatures of the tested connections are illustrated in Table 3. It can be observed that there was a wide range variation in the temperature distribution across the beam-to-column connection. The temperature of column web was very much higher than temperatures of endplate and column flange of the connection. This may result in failure probability of column web increasing. It is clear from Fig. 6 that column web in tension zone

takes place significant plastic deformation. This is different from what happened to the same connection at ambient temperature. Therefore, it is important and necessary for connection analysis in fire to calculate temperatures of components respectively. The bending deformation of column flange and endplate in tension zone is similar to that observed at ambient temperature test, and there is a gap between column flange and endplate due to their inconsistent deformations. Fig. 7 shows deformation of high-strength bolts after testing. It is obvious that there is a bending deformation in the exterior bolts in tension zone. The interior bolts in tension zone come into necking earlier than the exterior bolts in tension zone although the temperature of the former is lower than the latter. Therefore, it can be concluded that the interior bolts undergo more tension.

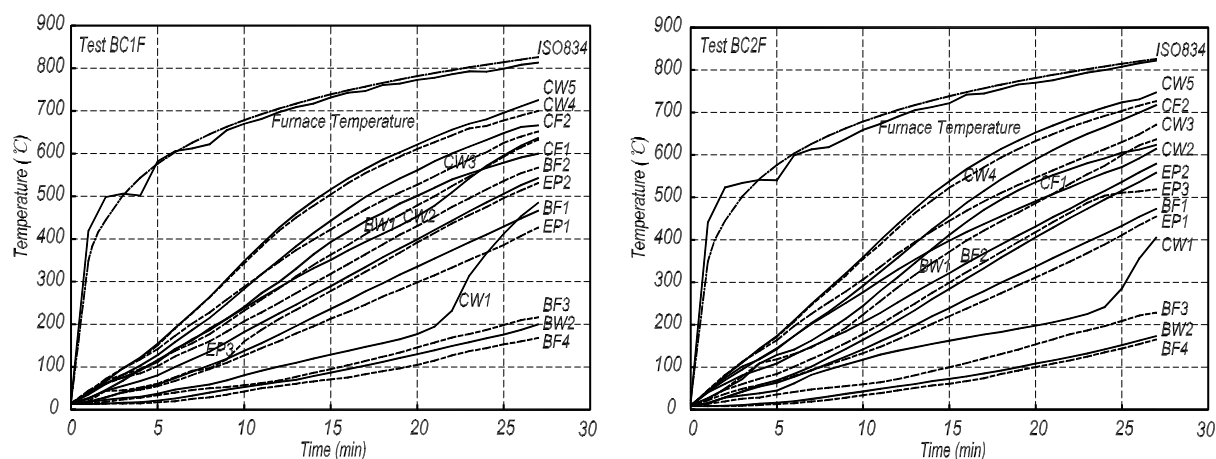


Fig. 5 Temperature-time curves recorded in fire tests on connections

Table 3 Summary of elevated temperature tests

Test	Fire endurance (min)	Limit temperature (°C)															
		CW1	CW2	CW3	CW4	CW5	EP3	EP2	EP1	CF1	CF2	BF1	BF3	BW1	BW2	BF4	BF2
BC1F	22.5	273	526	577	651	663	454	446	342	546	608	383	173	535	154	132	485
BC2F	26.0	356	592	649	716	731	514	536	434	613	700	454	222	623	163	154	559



(a) Test BC1F



(b) Test BC2F

Fig. 6 Deformation of endplate and column after testing

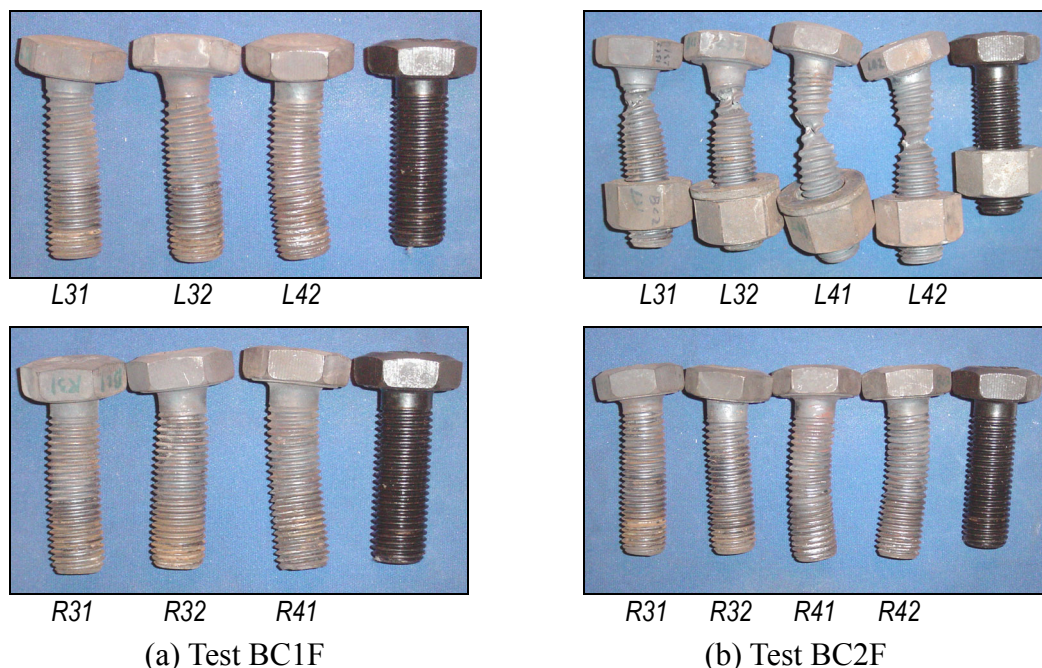


Fig. 7 Deformation of high-strength bolts after testing (L31(R31): the 3rd rank and 1st column bolt in left (right) connection)

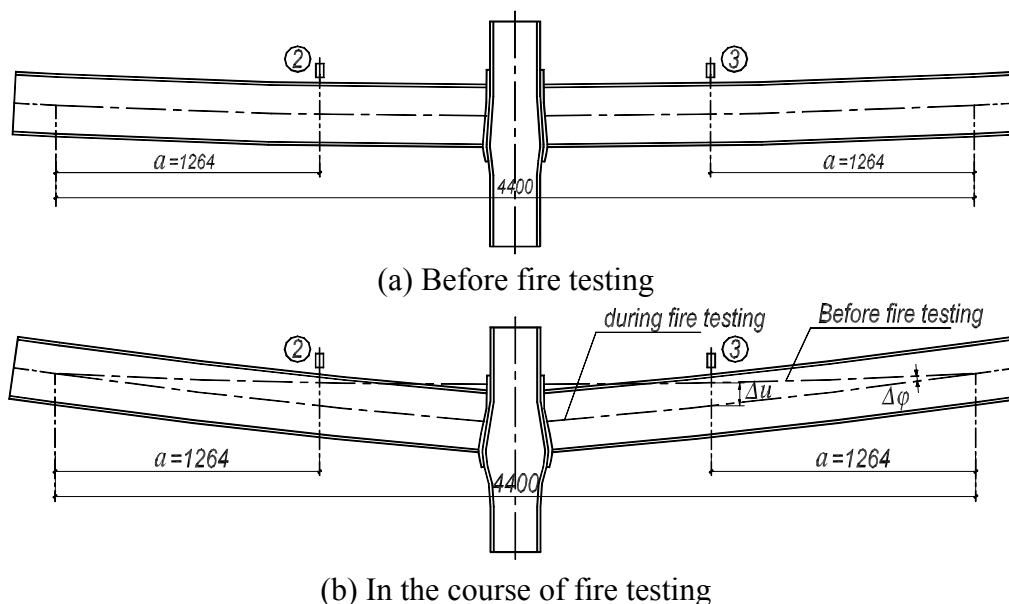


Fig. 8 Deformation of specimen during testing

Since the temperatures of insulated exterior beams are very low and closed to uniform, it can be concluded that there is no additional bending deformation produced in these beams throughout the process of fire test. That is, the rotations of these beams are totally attributed to the rotation of endplate connections. Therefore, the change of connection rotations can be obtained in terms of the measured deflections of the exterior beams (see Fig. 8). The relationship is expressed as

$$\Delta\varphi = \Delta u / a \quad (2)$$

In which $\Delta\varphi$ is the change of connection rotation in the course of fire testing, Δu is the measured deflection change of insulated exterior beam, and a is the distance as shown in Fig. 8. Rotation-time curves obtained in terms of Eq.(2) are presented in Fig. 9. The limit rotation at elevated temperature exceeds 0.1rad (5.7°) which is 2.5 times of what produced at ambient temperature. The rotation increases rapidly after 15min fire testing, correspondingly,

the mean temperature of the connections is approximately 350°C. This corresponds with the properties of steel at elevated temperatures that material strength and modulus come into degrading.

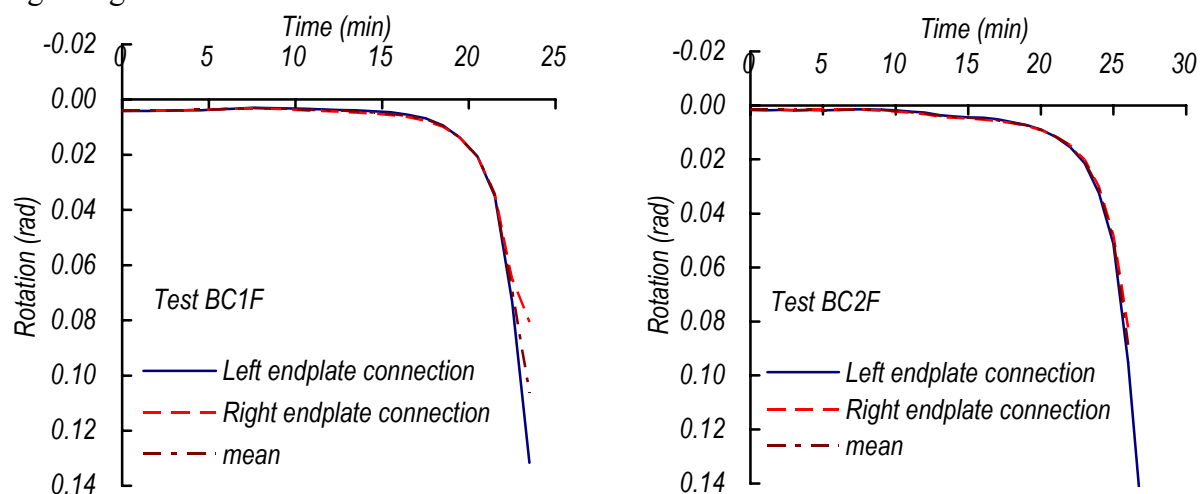


Fig. 9 Experimental rotation-time curves for test BC1F, BC2F

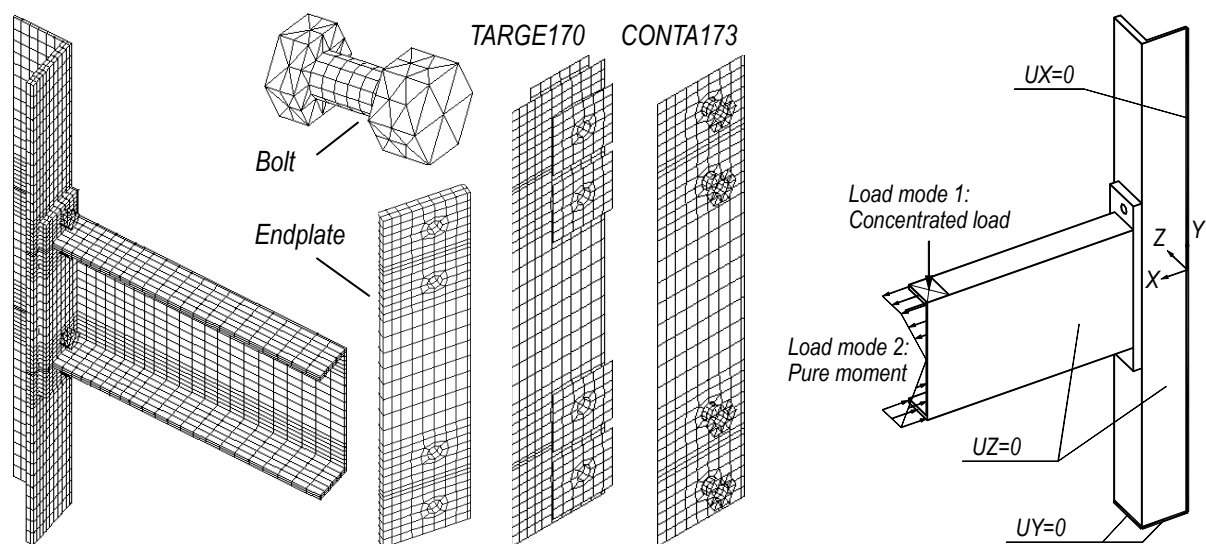
3 FINITE ELEMENT MODEL

ANSYS 7.0, a large-scale general-purpose finite-element package, was selected to simulate the behavior of high-strength bolt endplate connection in fire. Due to low degree of thermal-structural coupling interaction in the connection, sequential analysis, a transient thermal analysis followed by a static structural analysis where the effects of temperatures obtained from in the thermal analysis were applied as body force loads, was employed in place of direct coupling analysis.

3.1 Structural finite element model

The effects of non-uniform thermal expansion, geometric nonlinearity, temperature dependent nonlinear material behavior were taken into account in the structural FE model. SOLID45, eight-node solid element, was used to discretize all the components of endplate connection including endplate, column, beam and bolts. Pretensions in bolts were simulated by defining the pretension section and generating PRETS179 elements in the meshed bolt shanks. Contact elements, both TARGE170 and CONTA173, were also employed to model all contact problems in the connection including the contact between column flange and endplate, the contact between column flange and bolt shanks, the contact between endplate and bolt shanks, the contact between column flange and bolt nuts, and the contact between endplate and bolt heads. Contact problems are highly nonlinear and require significant computer resources to solve. Thus it is of efficiency for shortening solving time to determine a less contact area and to decrease the quantities of contact elements. In many cases, establishing more contact pairs can achieve the purpose presented above.

For decreasing computer resources to solve, only a quarter of endplate connection was modeled according to the principle of symmetry. To simulate the bending of steel plate accurately, it is recommended to discretize the plate in thickness direction into two layers SOLID45 elements. Fig. 10(a) shows a structural FE model with the final arrangement of mesh discretization. The structural FE model consists of approximately 7000 SOLID45 elements, 130 PRETS179 elements, 8000 nodes, 2000 TARGE170 and CONTA173 elements (totally 17 contact pairs were established).



(a) Mesh discretization of connection assembly (b) Boundary conditions and loading
Fig. 10 Structural FE model of connection assembly

3.1.1 Boundary conditions and loading

Fig. 10(b) demonstrates the boundary conditions and loads applied to the structural FE model. Nodes at the bottom of column are fully restrained in Y direction. Nodes on the plane $Z=0$ ($X=0$) are fully restrained in Z (X) direction.

It is well known that a concentrated load directly applied to a node of solid element will result in stress singularity. Thus an equivalent surface load is used to instead the concentrated load. Such transition also conduces to converge more quickly. If only moment is applied, an equivalent gradient surface load is a very efficient solution.

For FE analysis of endplate connection at ambient temperature, loads applied in sequence as follows: (1) Establish the pretension of high-strength bolt by apply a force; (2) “Lock” the pretension, that is, the effect of the initial load is preserved as a displacement. This transformation is absolutely necessary for simulating the tension reduction in the bolt in subsequent loading; (3) Add additional loads incrementally up to failure.

For FE analysis of endplate connection at elevated temperature, loads applied in sequence as follows: (1) Define reference temperature for thermal strain calculations and initial temperatures of the connection; (2) establish the pretension of high-strength bolt by apply a force; (3) “lock” the pretension; (4) add loads that the connection subjected at fire condition; (5) apply temperatures as body loads which are obtained from in the thermal analysis.

3.1.2 Material properties

For ambient analysis, the material nonlinear properties was considered by using Von Mises yield criterion with a three-linear stress-strain relationship to incorporate strain hardening as shown in Fig. 11.

Von Mises yield criterion and isotropic strain hardening rule are also used for elevated FE analysis. The stress-strain curves of steel at elevated temperatures were established by stress-strain relationship specified by EC3 Part: 1.2 (1993), but using the yield strength and elastic modulus at elevated temperatures given by the fitting equations as follows (G. Q. Li etc. 2006) (see Fig. 12 and Fig. 13):

(1) Q235 steel

Yield strength reduction factor:

$$f_{yT} / f_y = 1.0 \quad 20^\circ\text{C} \leq T_s \leq 300^\circ\text{C} \quad (3a)$$

$$f_{yT} / f_y = 1.24 \times 10^{-8} T_s^3 - 2.096 \times 10^{-5} T_s^2 + 9.228 \times 10^{-3} T_s - 0.2168 \quad 300^\circ\text{C} < T_s < 800^\circ\text{C} \quad (3b)$$

$$f_{yT} / f_y = 0.5 - T_s / 2000 \quad 800^\circ\text{C} \leq T_s \leq 1000^\circ\text{C} \quad (3c)$$

Elastic modulus reduction factor:

$$E_T / E = \frac{7T_s - 4780}{6T_s - 4760} \quad 20^\circ\text{C} \leq T_s < 600^\circ\text{C} \quad (4a)$$

$$E_T / E = \frac{1000 - T_s}{6T_s - 2800} \quad 600^\circ\text{C} \leq T_s \leq 1000^\circ\text{C} \quad (4b)$$

(2) High-strength bolt

Yield strength reduction factor:

$$f_{yT} / f_y = 1.011 - 5.5 \times 10^{-4} T_s \quad 20^\circ\text{C} \leq T_s \leq 400^\circ\text{C} \quad (5a)$$

$$f_{yT} / f_y = 1.909 \times 10^{-8} T_s^3 - 2.826 \times 10^{-5} T_s^2 + 1.125 \times 10^{-2} T_s - 0.5005 \quad 400^\circ\text{C} < T_s < 700^\circ\text{C} \quad (5b)$$

$$f_{yT} / f_y = 0.25 - 0.00025 T_s \quad 700^\circ\text{C} \leq T_s \leq 1000^\circ\text{C} \quad (5c)$$

Elastic modulus reduction factor:

$$E_T / E = \frac{32T_s - 20940}{25T_s - 20800} \quad 20^\circ\text{C} \leq T_s < 600^\circ\text{C} \quad (6a)$$

$$E_T / E = \frac{3}{32} \cdot \frac{1000 - T_s}{T_s - 475} \quad 600^\circ\text{C} \leq T_s \leq 1000^\circ\text{C} \quad (6b)$$

Where T_s is temperature of steel; f_{yT} and E_T are yield strength and elastic modulus of steel at elevated temperature respectively, f_y and E are yield strength and elastic modulus of steel at ambient temperature respectively.

Coulomb's friction model (ANSYS Inc 1994), as illustrated in Fig. 14, was employed to model the frictions between contacting surfaces. In this friction model, two contacting surfaces can carry shear stresses up to a certain magnitude across their interface before they start sliding relative to each other. The Coulomb friction model is expressed as:

$$\tau_T = \mu \sigma_N \leq \tau_{T,\max} = \tau_y \quad (7)$$

where τ_T is contact friction with units of stress; μ is coefficient of friction; σ_N is normal contact pressure; $\tau_{T,\max}$ is maximum contact friction whose value is close to yield shear stress τ_y . For steel, τ_y is given by

$$\tau_y = \sigma_y / \sqrt{3} \quad (8)$$

Where σ_y is the minimum yield stress of contacting components at corresponding temperatures.

The behavior of high strength bolted friction joist at elevated temperatures was experimentally investigated by Tanka (1979). It was considered that the main reason of the decrease of slip strength of heated friction joints depended upon the thermal relaxation of the bolt tension. The friction coefficient between contact surfaces was slightly influenced by high temperature. Therefore, in the structural FE analysis μ was taken as 0.35 for rolled clean surface without any treatment.

Possion's ratio for Q235 steel and high-strength bolt is taken as 0.3. And the coefficient of thermal expansion α_s used in the FE analysis was determined by the following formula (EC3 Part: 1.2 1993):

$$\alpha_s = 0.8 \times 10^{-8} (T_s - 20) + 1.2 \times 10^{-5} \quad (9)$$

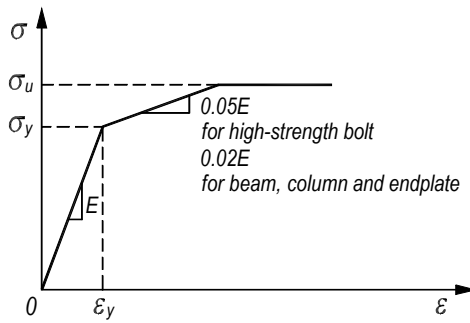


Fig. 11 Stress-strain relationship for ambient analysis

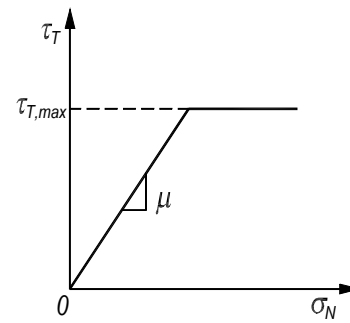


Fig. 14 Classical Coulomb friction

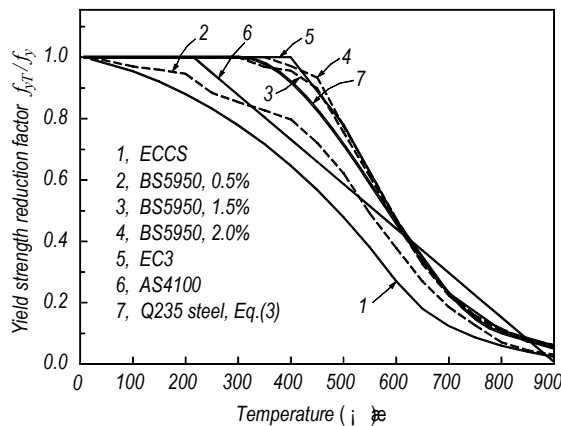


Fig. 12 Reduction factors of Q235 steel at elevated temperatures

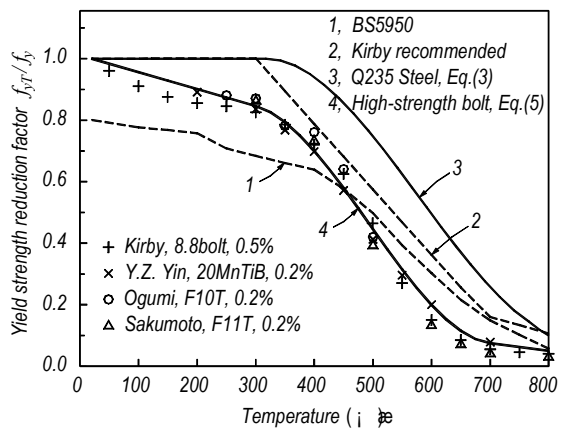
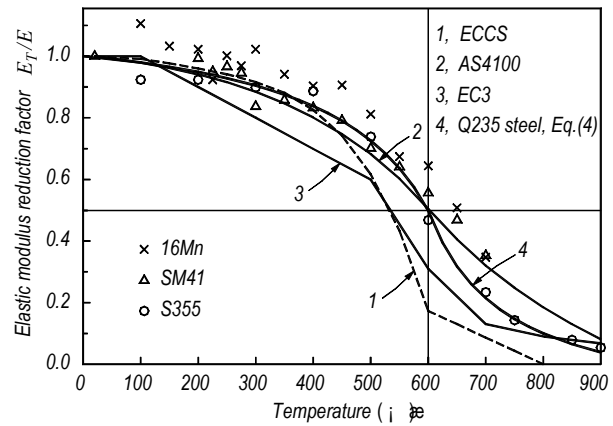
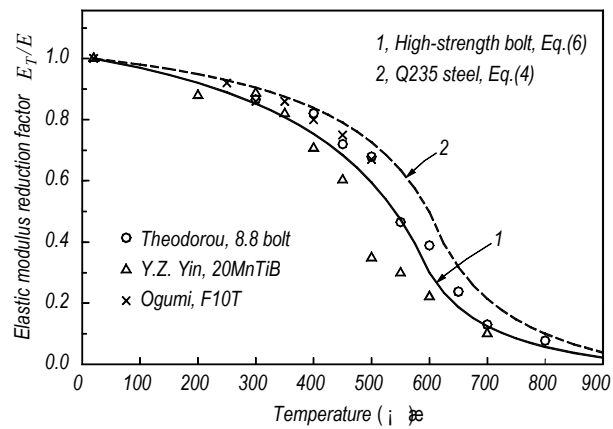


Fig. 13 Reduction factors of high-strength bolt at elevated temperatures



3.1.3 Nonlinear solution procedure

Contact problems are highly nonlinear and require significant computer resources to solve. For this type of analysis, the full Newton-Raphson method converge more quickly than the modified and initial-stiffness Newton-Raphson method. So the full Newton-Raphson method was selected to perform structural nonlinear solution. And the contact algorithm is Augmented Lagrangian Method.

3.2 Thermal finite element model

In the thermal FE model, eight-node thermal solid elements, so called SOLID 70 in ANSYS, are used to represent the endplate, column, beam and high-strength bolts. Special four-node thermal surface elements SURF152 overlaid onto the faces of the connection are

used to simulate convection and radiation effects. The contact between column flange and endplate is idealized using four-node surface-to-surface contact elements TARGE170 and CONTA173 with the hypothesis that conduction coefficient of these elements is infinite.

The comparison of results based upon different mesh patterns shows that steel plate needs to discretize four layers in its thickness direction in order to obtain solution results of acceptable error level. The mesh pattern of used thermal FE model is shown in Fig. 15. There are approximately 12000 SOLID70 elements, 2300 TARGE170 and CONTA173 elements, 4300 SURF152 elements and 13500 nodes.

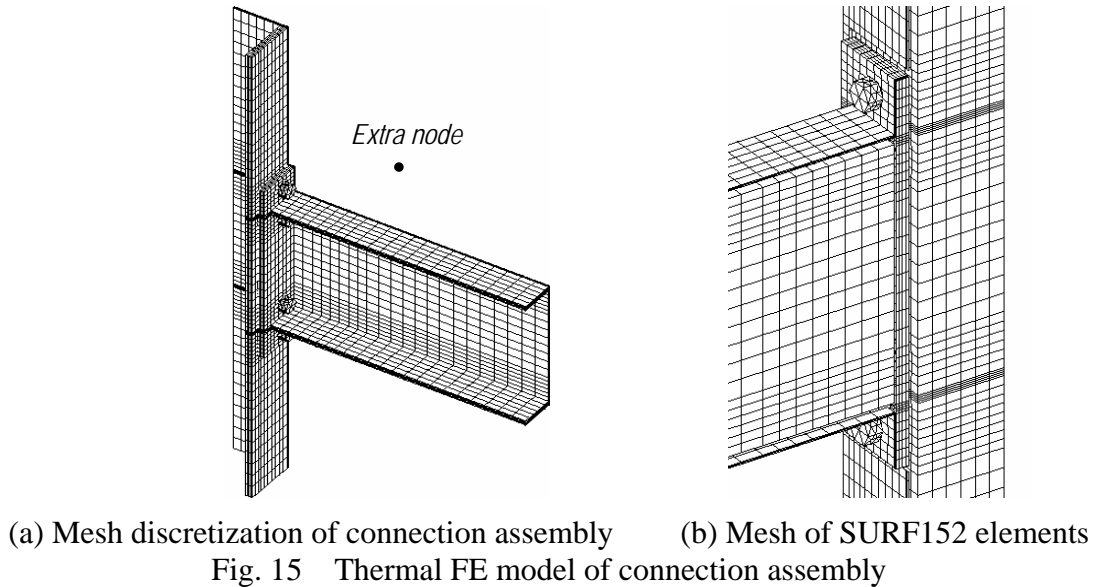
The thermal conductivity (EC3 Part: 1.2 1993) and specific heat (ECCS 1983) of steel used for thermal FE analysis are:

$$\lambda_s = 54 - 3.33 \times 10^{-2} T_s \quad 20^\circ\text{C} \leq T_s < 800^\circ\text{C} \quad (11a)$$

$$\lambda_s = 27.3 \quad 800^\circ\text{C} < T_s \leq 1200^\circ\text{C} \quad (11b)$$

$$c_s = 470 + 20 \times 10^{-2} T_s + 38 \times 10^{-5} T_s^2 \quad (12)$$

Where λ_s is thermal conductivity of steel, c_s is specific heat of steel.



4 ANALYTICAL RESULTS AND COMPARISONS

4.1 Results of thermal FE analysis

It is extremely important and difficult for thermal FE analysis to determine boundary conditions according with the practical conditions. Being scarce of true thermal properties of test furnace, the convection coefficient α_c is taken as a constant of $25\text{W}/(\text{m}^2\cdot\text{K})$, and the resultant emissivity ε_r is taken as 0.3. The comparison between analytical and experimental temperatures is illustrated in Fig. 16. The analytical temperature is higher than the experimental one. Such case is also presented in BS5950 part: 8 (see Table 4).

4.2 Results of structural FE analysis for ambient test

The analytical and experimental moment-rotation curves for ambient test are shown in Fig. 17. There is good agreement between the experimental and analytical results over the entire loading range. The analytical limit moment is $207.97\text{kN}\cdot\text{m}$, slightly higher than the experimental result by 2.35 percent.

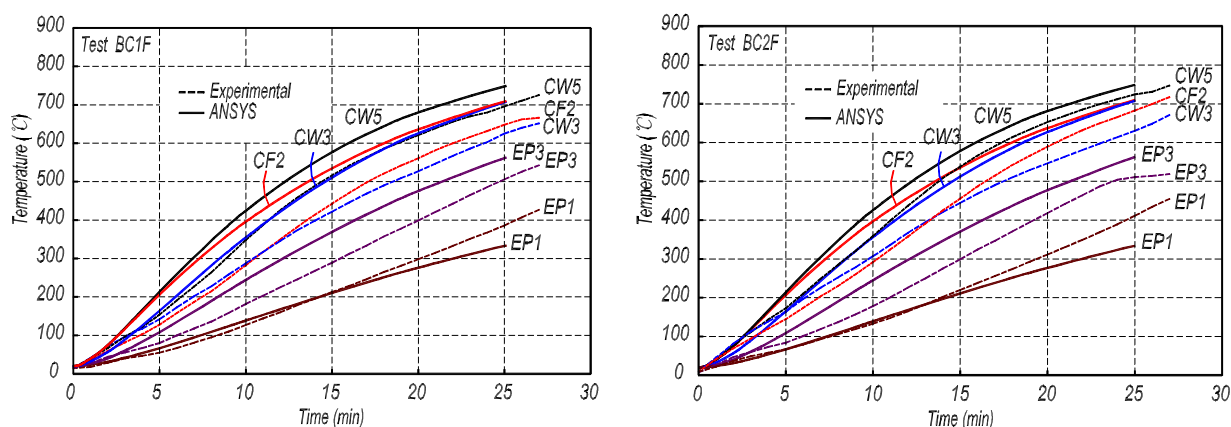


Fig. 16 Comparison between experimental and analytical temperatures

Table 4 Comparison of design temperatures given in table and Calculated temperatures by incremental formula presented in BS5950: Part 8

Temperatures (30min) for I section columns (°C)				Temperatures (30min) for I section beams (°C)			
Flange thickness (mm)	Design temperatures given in tables	Calculated temperatures by incremental formula		Flange thickness (mm)	Design temperatures given in Tables	Calculated temperatures by incremental formula	
		$\varepsilon_r=0.5$	$\varepsilon_r=0.3$			$\varepsilon_r=0.5$	$\varepsilon_r=0.3$
≤6.8	841	834	829	≤6.8	810	834	829
9.4	801	831	822	8.6	790	832	824
11.0	771	828	815	9.7	776	831	821
12.5	747	825	807	10.9	767	828	815
14.2	724	821	794	11.8	755	827	811
15.4	709	818	784	13.2	746	834	802
21.7	652	788	716	18.8	728	804	750
30.2	601	722	615	25.4	688	732	671

Bolt force in each row was obtained, as shown in Fig. 18. The two rows of bolts in compression zone of endplate connection carry almost equal forces. However, the two rows of bolts in tension zone carry unequal forces, the inner bolt carrying a larger tension than the outer one. The Von Mises stress contours at failure, contact state and pressure between column flange and endplate for ambient test are shown in Fig. 19~21. In general, the deformation characteristics established by FE analysis is in agreement with the test result. It can be observed clearly from Fig. 19 that there is significant bending deformation in the outer bolt in tension zone and a gap between column flange and endplate in compression zone. The moment/bolt force graph also reveals the phenomenon of prying action in extended endplate connection. The prying force occurs in the bolts in tension zone when 25 percent of failure moment is applied, and may exceed 40 percent of the pretension of high-strength bolt. The

maximum prying force takes place not at failure but approximately at the moment that the contact between column flange and endplate just comes into being open with assuming the column flange and endplate fully rigidity.

4.3 Results of structural FE analysis for elevated test

The analytical fire endurance of test BC1F is 21.3min, and that of test BC2F is 25.15min. Those are slightly smaller than experimental results. The analytical and experimental rotation-time curves for elevated test BC1F and BC2F are shown in Fig. 22 and Fig. 23 respectively. The analytical rotation-time curve for elevated test BC2F is very close to the experimental result. However, there is some discrepancy for test BC1F because of the error of analytical temperatures.

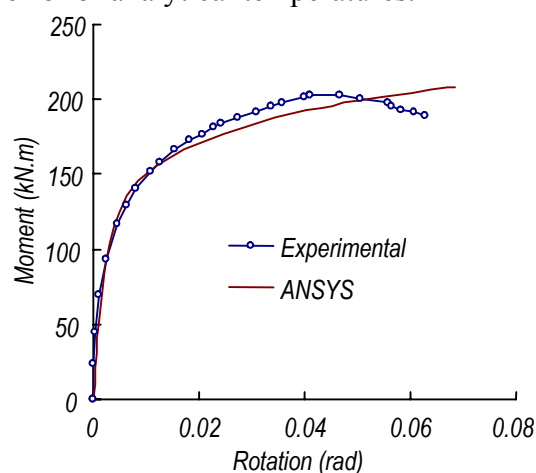


Fig. 17 Comparison between experimental and analytical moment-rotation curves for ambient test

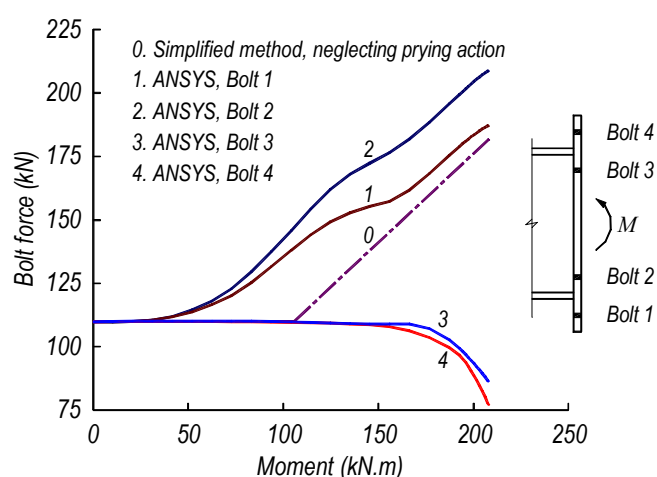


Fig. 18 Analytical bolt force for ambient test

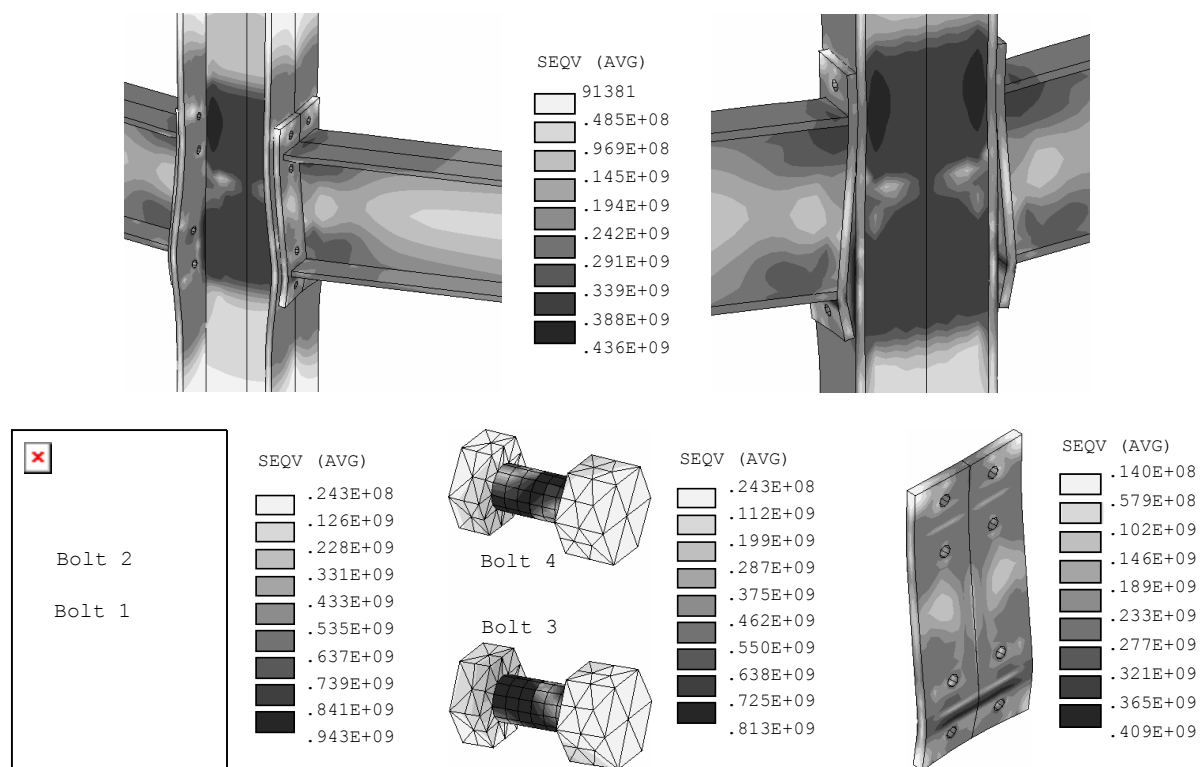
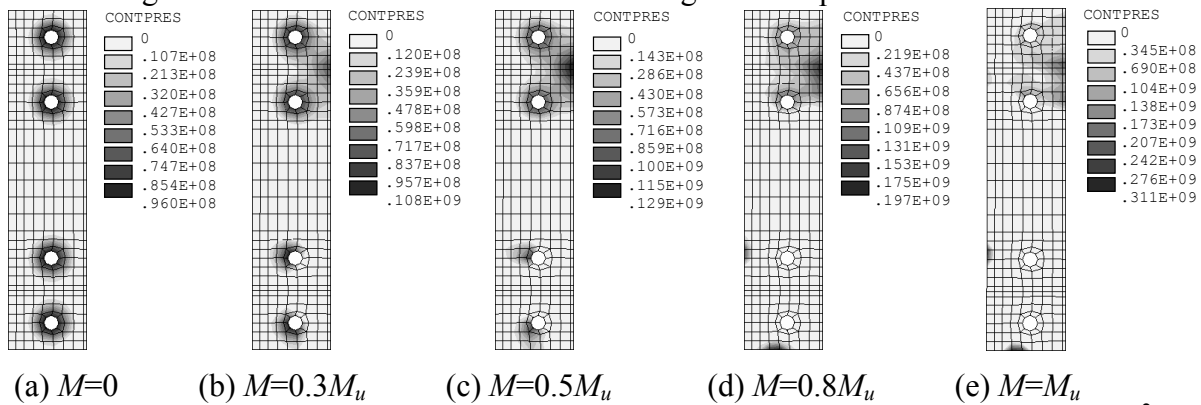
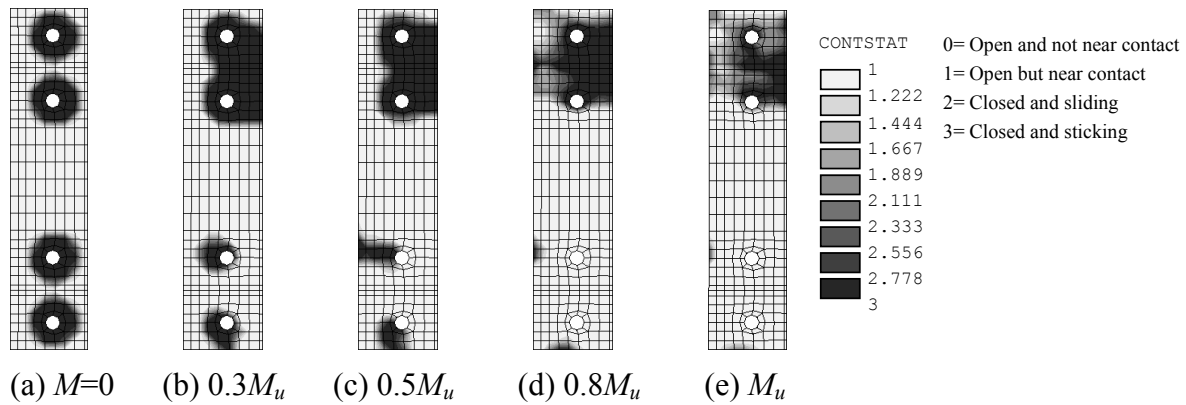
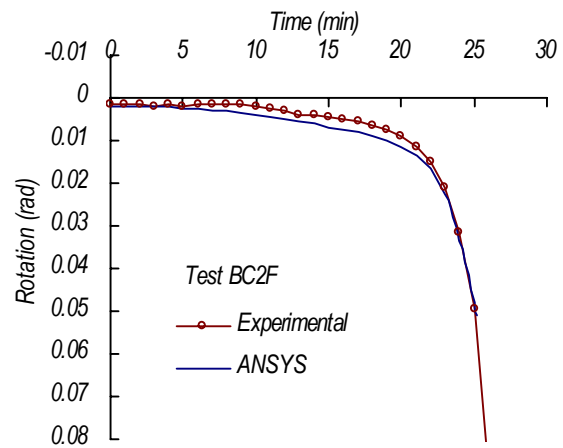
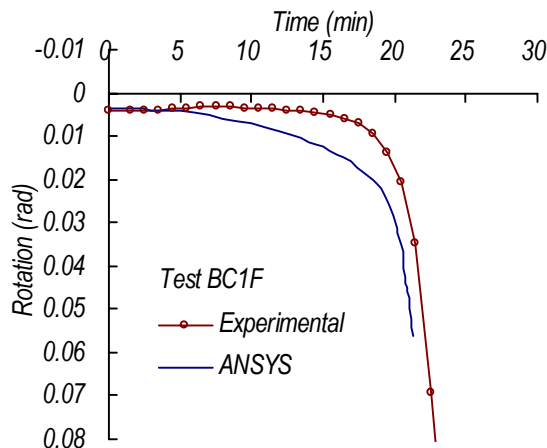


Fig. 19 Von Mises stress contour at failure for ambient test (N/m^2)



The bolt force versus mean temperature of endplate for test BC1F and test BC2F are shown in Fig. 24 and Fig. 25 respectively. The bolts in tension zone of specimen BC2F come into yielding at the failure of endplate connection, which is in great agreement with the experimental failure mechanism (see Fig. 7). All of the bolt forces at failure are lower than their initial pretension, thus it can be concluded that the difference between the bolt force produced at the end of ambient loading (corresponding to temperature 20°C in Fig. 24 and Fig. 25) and their initial pretension is due to prying action. Owing to the thermal expansion and elastic modulus decreasing with temperature increasing, the bolt pretension is released.



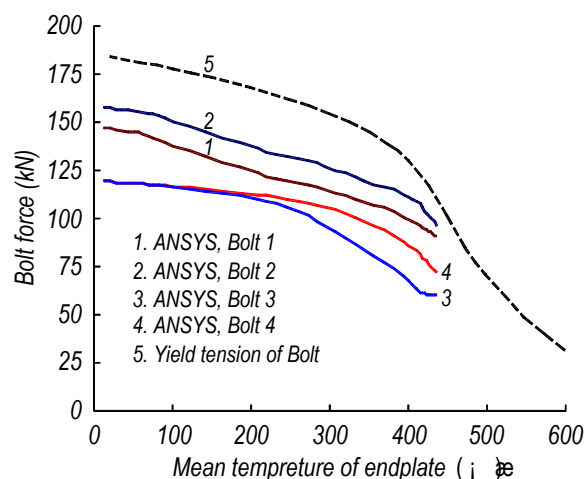


Fig. 24 Analytical bolt force for test BC1F

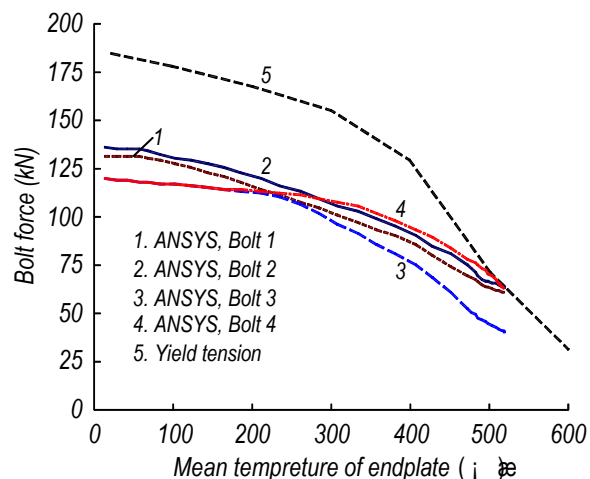


Fig. 25 Analytical bolt force for test BC2F

The Von Mises stress contours at failure, contact state and pressure between column flange and endplate for test BC2F are shown in Fig. 26~28. In general, the deformation characteristics established by FE analysis is consistent with the test result. There is significant residual tensile deformation in the column web.

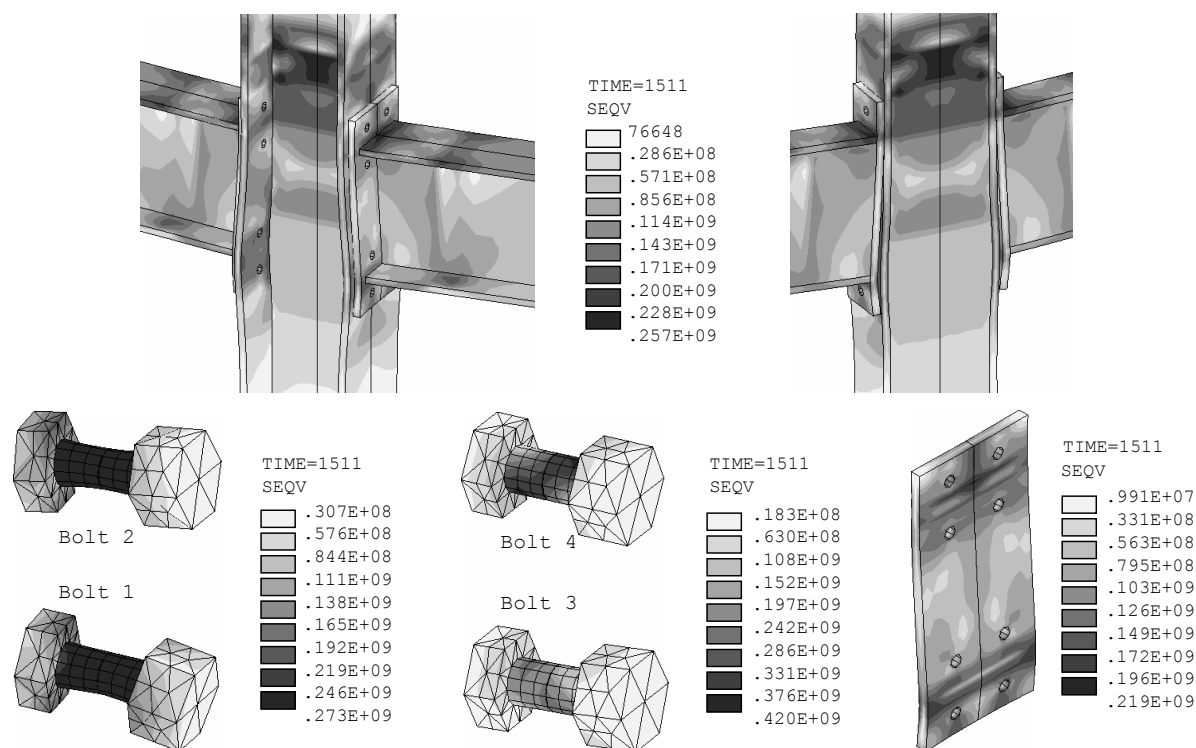


Fig. 26 Von Mises stress contour at failure for ambient test (N/m²)

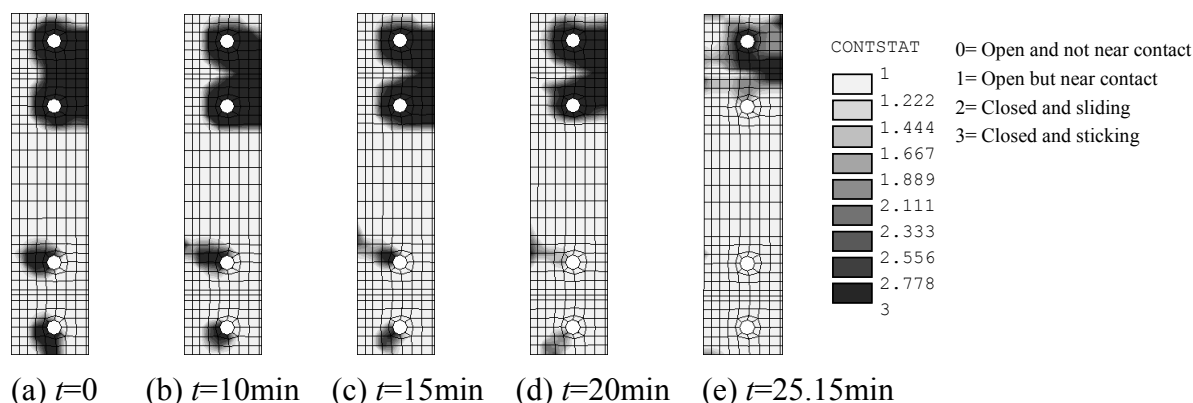


Fig. 27 Contact state between column flange and endplate for ambient test

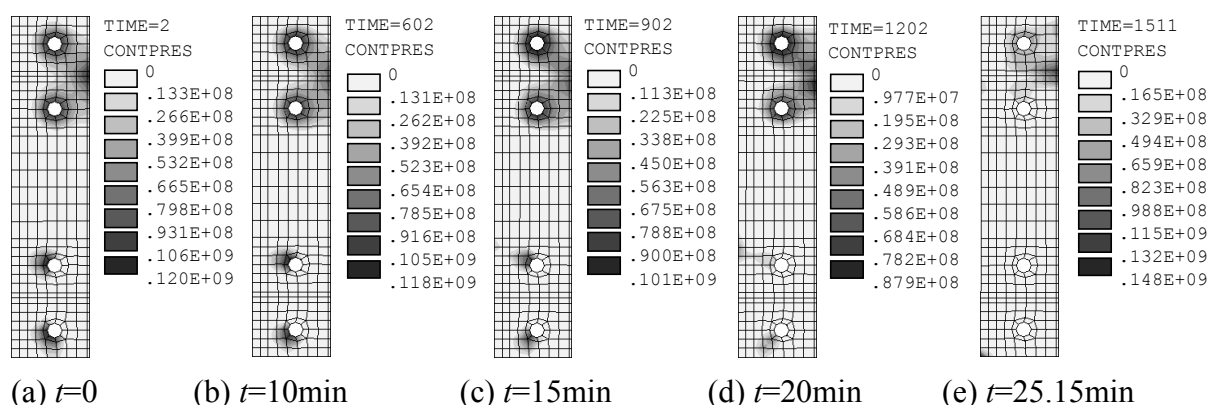


Fig. 28 Contact pressure between column flange and endplate for ambient test (N/m^2)

5 CONCLUSION

This study is focused on establishing a finite element approach for simulating the behavior of extended endplate bolted moment connections in fire. The validity and effectiveness of this FE approach are verified by the test results. The FE model can then be further used to predict moment-rotation-temperature relation of the connections that can be incorporated in the structural analysis of global steel frames subjected to fire, and to develop analytical fire-resistant design method.

6. REFERENCE

1. Al-Jabri, K.S., Burgess, I.W. and Plank, R.J.: Prediction of the degradation of connection characteristics at elevated temperature, *Journal of Constructional Steel Research*, 2004, 60(3-5), 771-781.
2. ANSYS, Inc.: Theory Manual, 001369, Twelfth Edition, SAS IP, Inc, 1994.
3. A. Tanaka, I. Kokubo and F. Furumura: Experimental study on the high strength bolted joints subjected to constant load under high temperature, *J. Struct. Constr. Eng.*, AIJ, No. 286, 13-21, 1979. (in Japanese)
4. British Standards Institution (BSI), BS 5950: The Structural Use of Steelwork in Buildings, Part 8: Code of Practice for Fire Resistant Design, 1990.
5. China Engineering Construction Society: Technical code on fire safety of steel building structures, 2006.
6. Chiou, Y. J. and Lin, Y. R.: Study on the fire response of flexibility jointed steel frames, *Computers and Structures*, 1992, 45(3), 439-451.
7. El-Rimawi, J. A., Burgess, I. W. and Plank, R. J.: The analysis of semi-rigid frames in fire—A secant approach, *Journal of Constructional Steel Research*, 1995, 33, 125-146.
8. European Committee for Standardization, ENV 1993-1-2, Eurocode 3, Design of Steel Structures, Part

- 1.2: Structural Fire Design, 1993.
9. European Convention for Constructional Steelwork (ECCS), Technical Committee 3 – Fire Safety of Steel Structures, European Recommendation for the Fire Safety of Steel Structures – Calculation of the Fire Resistance of Loadbearing Element and Structural Assemblies Exposed to the Standard Fire, Amsterdam, Elsevier, 1983.
 10. Fire-resistance tests-elements of building construction, GB/T 9978-1999. (in Chinese)
 11. G. B. Lou: Behavior and design of extended endplate moment connection with high-strength bolts in fire, PhD. Thesis, Tongji University, Jan. 2005. (in Chinese)
 12. G. Q. Li, L. H. Han, G. B. Lou and S. C. Jiang: Fire resistant design of steel structures and composite structures, China constructional industry press, Beijing, 2006. (in Chinese)
 13. International Standards Organization (ISO). ISO/CD 834-1, ISO/CD 834-2 and ISO/CD 834-3, Fire Resistance Tests — Elements of Building Construction, Part1, 2, and 3, 1990.
 14. Lawson, R. M.: Behavior of steel beam-to-column connections in fire, The Structural Engineer, 1990, 68(17), 263-271.
 15. Leston-Jones, L. C., Burgess, I. W., Lennon, T. and Plank, R. J.: Elevated-temperature moment-rotation tests on steelwork connections, Proceedings of the Institution of Civil Engineers, Structures & Buildings, 1997, 122, 410-419.
 16. Liu, T. C. H.: Moment-rotation-temperature characteristics of steel/composite connections, Journal of Structural Engineering, ASCE, 1999, 125(10), 1188-11974.
 17. Silva, L. S. da, Santiago, A., Real, P. V.: A component model for the behavior of steel joints at elevated temperatures, Journal of Constructional Steel Research, 2001, 57, 1169-1195.
 18. The Steel Construction Institute (SCI): Fire Resistant Design of Steel Structures – A handbook to BS5950: Part 8, 1990.



THE DEVELOPMENT OF A COMPONENT-BASED CONNECTION ELEMENT FOR ENDPLATE CONNECTIONS IN FIRE

Florian BLOCK¹, Ian BURGESS², Buick DAVISON³ and Roger PLANK⁴

ABSTRACT

This paper describes the development of a component-based element for endplate connections in fire. The reported research is part of an ongoing project aimed at understanding joint behaviour in fire. The paper summarises the derivation of the stiffness matrix of this new element, based on a spring model, and the incorporation of the element into the non-linear finite element program *Vulcan*. It also states the component characteristics that have been used for the individual zones of deformation in an endplate connection. Furthermore, the additional features of the element, necessary for correct response at elevated temperatures, like the consideration of the temperature distributions across the connection as well as cooling and unloading are summarised. The proposed element is then used to predict the moment-rotation curves of connection experiments at ambient and elevated temperatures. Finally, the advantages and limitations of the new high temperature connection element are listed.

1. INTRODUCTION

Traditionally, beam-to-column connections are assumed to have sufficient fire resistance due to their cooler temperatures and slower rate of heating than the members to which they are attached, caused by the large concentration of thermal mass in the connection. However, from the full-scale fire tests in Cardington and the subsequent research, it has been observed that connections are more vulnerable than assumed. This is mainly caused by the forces and deformations to which a connection is subjected during a fire, which are

¹ Research Student, Dept. of Civil & Structural Engineering, University of Sheffield, Sheffield S1 3JD, UK
Email: cip02fmb@sheffield.ac.uk

² Professor, Dept. of Civil & Structural Engineering, University of Sheffield, Sheffield S1 3JD, UK
Email: ian.burgess@sheffield.ac.uk

³ Senior Lecturer, Dept. of Civil & Structural Engineering, University of Sheffield, Sheffield S1 3JD, UK
Email: j.davison@sheffield.ac.uk

⁴ Professor, School of Architecture, University of Sheffield, Sheffield S1 3JD, UK
Email: r.j.plank@sheffield.ac.uk

significantly different from those normally assumed in design. The internal forces change from moment and shear at ambient temperature to moment, shear and compression due to restrained thermal expansion of the beams in the early and intermediate stages of a fire, and finally to shear and tension in the later stage when applied loads are supported through catenary action. It is obvious that it is very difficult to generate these loading conditions realistically through experiments, except in full-scale testing. Furthermore, a large number of experiments would be required because of the large variety of possible connection details and the structure-connection interaction.

Hence, alternative ways to investigate and design connections in-situ for the fire case are required. One such way could be the use of the Component Method to predict the detailed behaviour of a connection, in combination with a structural finite element program which is capable of simulating the non-linear behaviour of structures in fire. However, this combination is only possible if the principles of the Component Method are included into a connection element.

2. COMPONENT JOINT MODELLING

The Component Method was initially developed for the ambient temperature design of semi-rigid joints by Tschemmernegg *et al.*¹ and later introduced into the Eurocode EC3-1.8². The original feature of this method is to consider any joint as a set of individual basic spring-like components. For each component the stiffness and maximum force is computed and assembled to form a spring model which represents the behaviour of the whole joint.

In order to describe the behaviour of an isolated connection at elevated temperature, the Component Method has been used successfully by a number of researchers. Leston-Jones³ was the first to apply the method to his cruciform tests; Al-Jabri⁴ used the method to model the flexible endplate behaviour of his high temperature experiments, and Spyrou⁵ conducted a large number of high-temperature component tests and combined the investigated components using a simple two spring model. Simões da Silva *et al.*⁶ used the component models given in EC3-1.8, in combination with the temperature reduction factors given in EC3-1.2⁷, to model the above-mentioned cruciform tests. However, none of these studies combined the Component Method directly with whole-frame action. Furthermore, apart from a limited study by Spyrou, the effects of axial load on the connection in fire have not been considered. A first attempt to include high-temperature connection behaviour into the finite element program ADAPTIC using the Component Method was done by Ramli Sulong *et al.*⁸ However, from this publication it was not clear how the model was implemented into the finite element software and what was used for the individual component characteristics.

At ambient temperature however, researchers have included the detailed connection response into global frames using component-based connection elements^{9, 10, 11}. The main characteristic of these connection elements is that they are single finite elements, instead of assemblies of spring elements, which obtain their stiffness matrix from a number of translational springs. These “internal” springs represent various parts of the connection, as is assumed in the Component Method. The spring characteristics are based on analytical or empirical models. The development of such a connection element for endplate connections at elevated temperatures will be shown in the following section.

3. FORMULATION OF THE CONNECTION ELEMENT

The connection element presented in this paper has been included in the non-linear finite element program *Vulcan* as a 3D finite spring element with zero length. The proposed element is compatible with *Vulcan*'s general beam-column elements, which allow the simulation of whole steel and composite frames. Currently, the following parts of a real joint are included in the element:

1. Endplate in bending
2. Column flange in bending
3. Bolts in tension
4. Column web in compression

The first three components form the tension zone of the connection and are combined as two T-stubs in series. An additional shear spring had to be included in order to transfer the vertical load from one node to another. This shear spring is assumed to be rigid at present, but the formulation of the element allows the implementation of slip and shear failure of the bolts. It was important to position this shear spring vertically in order to uncouple the vertical and horizontal stiffnesses of the element. The shear zone in the column web is not yet included, which theoretically limits the use of the element to internal joints with equal moments in which the column web does not experience shear deformations. The assumed position of the connection element can be seen in Fig. 1(a) below.

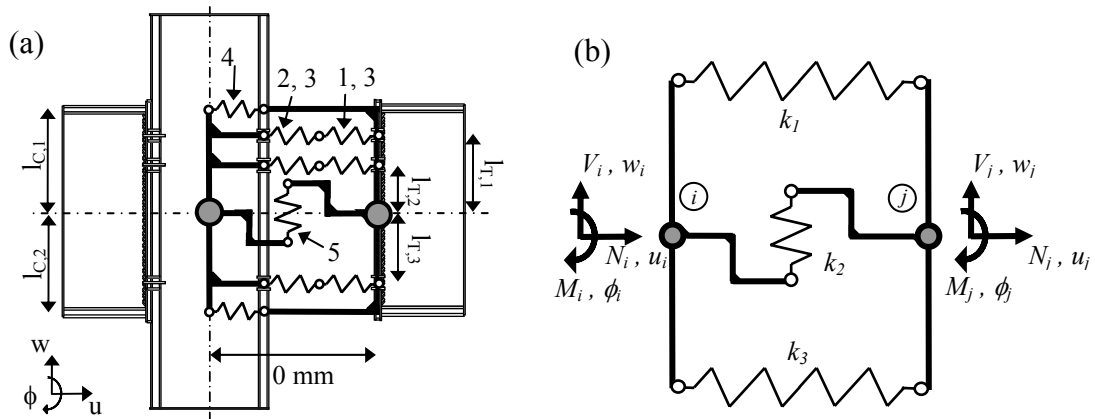


Fig. 1 - Position of the connection element within a joint (a) and a basic spring model (b)

In order to include the element into *Vulcan*, the component behaviour had to be formulated following the principles of the finite element method. Therefore, the behaviour of the connection is represented in the form:

$$\mathbf{F} = \mathbf{K}_c \mathbf{u} \quad (1)$$

However, due to the non-linear behaviour of the individual connection components in fire and also to the highly non-linear behaviour of the connected structural members, it is necessary to solve equation (1) iteratively using the tangent stiffness \mathbf{K}'_c , incremental forces $\Delta \mathbf{F}$ and displacements $\Delta \mathbf{u}$. Therefore, equation (1) is rewritten as:

$$\Delta \mathbf{F} = \mathbf{K}'_c \Delta \mathbf{u} \quad (2)$$

with

$$\Delta \mathbf{F}^T = \begin{bmatrix} \Delta N_{x,i} & \Delta V_{y,i} & \Delta V_{z,i} & \Delta M_{x,i} & \Delta M_{y,i} & \Delta M_{z,i} & \Delta N_{x,j} & \Delta V_{y,j} & \Delta V_{z,j} & \Delta M_{x,j} & \Delta M_{y,j} & \Delta M_{z,j} \end{bmatrix} \quad (3)$$

and

$$\Delta \mathbf{u}^T = \begin{bmatrix} \Delta u_i & \Delta v_i & \Delta w_i & \Delta \phi_{x,i} & \Delta \phi_{y,i} & \Delta \phi_{z,i} & \Delta u_j & \Delta v_j & \Delta w_j & \Delta \phi_{x,j} & \Delta \phi_{y,j} & \Delta \phi_{z,j} \end{bmatrix} \quad (4)$$

During the iterative process, *Vulcan* assumes $\Delta \mathbf{u}$ based on the previous step's stiffness and the connection element has to recalculate its stiffness matrix in accordance with the proposed displacements and also the updated incremental force vector $\Delta \mathbf{F}$. Both are then returned to the main routines of the program, and a convergence check, based on the out-of-balance forces, is performed. If convergence is reached, the equilibrium of the next load or temperature is calculated, otherwise the incremental displacement is varied until equilibrium is reached. The derivation of the tangent stiffness matrix of the connection element is shown in the next section.

3.1 Basic spring model and derivation of the stiffness matrix

In order to derive the stiffness matrix of the connection element, the simplest case of the element with only three springs is considered, as shown in Fig. 1(b). As in the original component method it is assumed that a joint will primarily deform in its plane, and all other out-of-plane and torsional degrees of freedom (DOF) are assumed to be rigidly connected. This reduces the problem to three DOF per node. If now each of these DOF is moved individually, as shown in Fig. 2, and the resulting spring forces are calculated, it is possible, with the help of some geometrical considerations and the spring characteristics, to derive the stiffness matrix of the basic connection element.

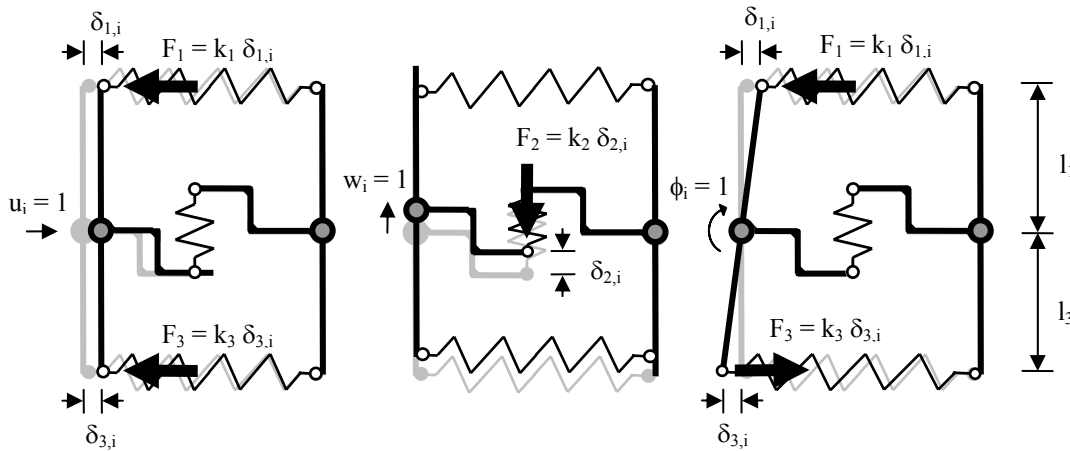


Fig. 2 - Stiffness derivation process for node i of the basic connection element

The resulting stiffness matrix for the basic two dimensional connection element, is shown in equation (5) below.

$$\mathbf{K}'_C = \left(\begin{array}{ccc|ccc} (k'_1 + k'_3) & 0 & (l_1 k'_1 - l_3 k'_3) & -(k'_1 + k'_3) & 0 & -(l_1 k'_1 - l_3 k'_3) \\ 0 & k_2 & 0 & 0 & -k_2 & 0 \\ (l_1 k'_1 - l_3 k'_3) & 0 & (l_1^2 k'_1 + l_3^2 k'_3) & -(l_1 k'_1 - l_3 k'_3) & 0 & -(l_1^2 k'_1 + l_3^2 k'_3) \\ \hline -(k'_1 + k'_3) & 0 & -(l_1 k'_1 - l_3 k'_3) & (k'_1 + k'_3) & 0 & (l_1 k'_1 - l_3 k'_3) \\ 0 & -k_2 & 0 & 0 & k_2 & 0 \\ -(l_1 k'_1 - l_3 k'_3) & 0 & -(l_1^2 k'_1 + l_3^2 k'_3) & (l_1 k'_1 - l_3 k'_3) & 0 & (l_1^2 k'_1 + l_3^2 k'_3) \end{array} \right) \quad (5)$$

However, most connections will have more than one bolt row and therefore more than one tension spring. Furthermore it is possible that, due to restrained thermal expansion, the whole connection will be under compression, which requires the implementation of a compression spring at the location of each beam flange. Hence the stiffness matrix in equation (5) is expanded to three dimensions and n bolt rows, as shown in equation (6).

$$\mathbf{K}'_C = \begin{pmatrix} K'_{11} & 0 & 0 & 0 & K'_{15} & 0 & -K'_{11} & 0 & 0 & 0 & -K'_{15} & 0 \\ 0 & \infty & 0 & 0 & 0 & 0 & 0 & -\infty & 0 & 0 & 0 & 0 \\ 0 & 0 & K'_{33} & 0 & 0 & 0 & 0 & 0 & -K'_{33} & 0 & 0 & 0 \\ 0 & 0 & 0 & \infty & 0 & 0 & 0 & 0 & 0 & -\infty & 0 & 0 \\ K'_{51} & 0 & 0 & 0 & K'_{55} & 0 & -K'_{51} & 0 & 0 & 0 & -K'_{55} & 0 \\ 0 & 0 & 0 & 0 & 0 & \infty & 0 & 0 & 0 & 0 & 0 & -\infty \\ -K'_{11} & 0 & 0 & 0 & -K'_{15} & 0 & K'_{11} & 0 & 0 & 0 & K'_{15} & 0 \\ 0 & -\infty & 0 & 0 & 0 & 0 & 0 & \infty & 0 & 0 & 0 & 0 \\ 0 & 0 & -K'_{33} & 0 & 0 & 0 & 0 & 0 & K'_{33} & 0 & 0 & 0 \\ 0 & 0 & 0 & -\infty & 0 & 0 & 0 & 0 & 0 & \infty & 0 & 0 \\ -K'_{51} & 0 & 0 & 0 & -K'_{55} & 0 & K'_{51} & 0 & 0 & 0 & K'_{55} & 0 \\ 0 & 0 & 0 & 0 & 0 & -\infty & 0 & 0 & 0 & 0 & 0 & \infty \end{pmatrix} \quad (6)$$

In which

$$K'_{11} = \sum_{i=1}^n k'_{T,i} + \sum_{i=1}^2 k'_{C,i} \quad K'_{15} = K'_{51} = \sum_{i=1}^n l_{T,i} k'_{T,i} + \sum_{i=1}^2 l_{C,i} k'_{C,i} \quad (7), (8)$$

$$K'_{33} = k'_s \quad K'_{55} = \sum_{i=1}^n l_{T,i}^2 k'_{T,i} + \sum_{i=1}^2 l_{C,i}^2 k'_{C,i} \quad (9), (10)$$

It should be noted that the lever arm l of an individual spring is measured from the reference axis, which is sited at the position of the node, positively defined in accordance with the local z-axis of the element. The governing equation (2), together with the stiffness matrix (6), forms the backbone of the connection element, but it is equally important to specify the force-displacement-temperature (F- δ - θ) behaviour of each of the individual components.

3.2 Tension spring characteristics

Traditionally, the tension components in an endplate connection are represented as a T-stub of a certain width. At ambient temperature, the force-displacement behaviour of T-stubs has been extensively studied. At elevated temperatures however, only Spyrou has investigated this component and derived simplified models, predicting multi-linear F- δ - θ relationships up to bolt failure for the three possible failure modes of a T-stub as shown in Fig. 3. The simplified models are solely based on the geometrical and material properties and the temperature of the component; these have been introduced into the connection element.

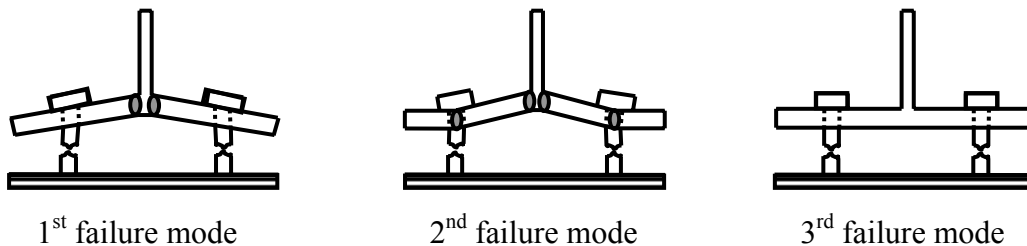


Fig. 3 - The three failure modes of a T-stub

As mentioned previously, a certain width has to be specified for the T-stub. This width ensures that the isolated T-stub behaves in similar fashion to the bolt row it represents in either the endplate or column flange. Zoetemeijer¹² specified a number of yield line patterns, which can be used to calculate this equivalent width. These have been adopted by EC3-1.8. From here, the yield line patterns for extended and flush-endplates and column flanges, as shown in Fig. 4, have been taken and implemented into the connection element.

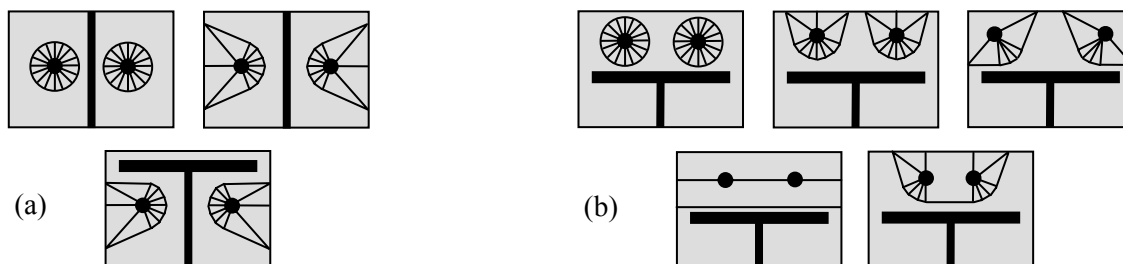


Fig. 4 - Considered yield line pattern in column flanges and flush-endplates (a) and in extended endplates (b)

If the distance between bolt rows is below a certain limit, and if the bolt rows are not separated by stiffeners, it is possible that two or more bolt rows fail together in a common yield line pattern, which reduces the strength and stiffness of the tension components. However, due to the complexity of the calculation procedure and the considerable programming effort involved, group effects have not yet been considered in the connection element.

In an unstiffened endplate connection, two T-stubs in series have to be considered per bolt row, representing the endplate and the column flange respectively. In the new element, the $F-\delta-\theta$ curves for both of these T-stubs springs are calculated initially and then, in order to satisfy equilibrium in the bolt row, the total displacement of the bolt row is distributed in accordance with the stiffness of each spring, ensuring equal forces in both springs. With the resulting tangent stiffness of both springs, an equivalent stiffness for this bolt row is calculated, and the resistance is then defined by the weaker T-stub. Further, it is assumed that each T-stub shares the equivalent bolt length equally, as is assumed as in EC3-1.8.

3.3 Compression spring characteristics

The characteristics of the compression spring (i.e. the behaviour of a column web in compression) has been studied extensively at ambient temperature. At elevated temperature, this component was also investigated by Spyrou and later by the first author of this paper¹³. In the latter study, the effects of axial load in the column section on the compression zone were investigated at elevated temperature, resulting in a simplified model for this component. This model for the $F-\delta-\theta$ relationship of the compression spring has been implemented into the connection element.

3.4 Relocation of the reference axis

If a composite structure is modelled in *Vulcan*, the position of the nodes of the slab elements as well as the beam elements is normally located at the mid-plane of the concrete slab. In order to move the beam elements into the correct position, an offset equal to the distance between the centre of the slab and the centre of the beam is used. To be fully

compatible with the other elements, the same principle has to be used with the connection element. Therefore, the same offset as for the beam elements is subtracted from the lever arm of each spring, and so the reference axis of the element is moved to the middle of the slab element. This simple modification allows the connection element to be used to model composite construction. However, shear connector elements and a fairly dense slab element mesh have to be used in order to allow the correct slippage between the beam and the slab and also the correct approximation of cracking in the concrete.

3.4 Temperature effects

The degeneration of the strength and stiffness of the connection material with increasing temperatures is included in the connection element by using the temperature-dependent strength reduction factors for mild steel given in EC3-1.2 for the column and the endplate. For the bolts, however, the temperature reduction factors derived by Kirby¹⁴ have been used. A comparison between the T-stub experiments by Spyrou and the connection element has shown that the EC3-1.2 reduction factors for bolts gave very conservative results. The Young's modulus of the bolts is reduced in accordance with the temperature reduction factors for mild steel as concluded by Spyrou.

In order to specify the temperatures of the individual components, a single time-temperature curve is used in combination with a temperature pattern. This pattern consists of temperature multipliers allowing the specification of the temperatures of the column flange, bolts and endplate for each bolt row individually, and also for the column flange and the column web in the two compression zones. This technique gives the user the capacity to consider any temperature distribution across the connection taken from experiments, analysis or design codes.

The effects of cooling on beam-to-column connections can be critical for the survival of a structure, due to the large tensile forces which are developed in the beams when the thermal strain is recovered, leaving the post-fire beams considerably shorter than they were originally due to permanent deformations¹⁵. This effect has been accounted for in the beam element in *Vulcan*, which makes it possible to expose the connection element to the correct forces during cooling of the structure. However, when high-strength bolts are heated above their annealing temperature around 600°C and allowed to cool down naturally, the strengthening effects of quenching and tempering used during manufacture of the bolts vanishes, and the bolt material returns to its base material which is considerably weaker as Kirby has observed. Unfortunately, to date there is no experimental data available on bolts which are loaded during cooling, and therefore this effect can not yet be included in the connection element. It is assumed that the bolts, as well as the material of the endplate and the column, regain their full strength when cooled down to ambient temperature.

3.5 Unloading of the connection element

As mentioned previously, when a structure starts to heat up the beams introduce compressive force, in addition to the pre-existing moment, into the connections. This causes the tension zone of the connection to unload until, if enough restraint is present, the connection is fully compressed. If in a later stage of the fire the beams cannot support the applied load in bending any more, catenary action introduces tensile forces into the connection. If this force is large enough, both compression zones in the connection unload and eventually all bolt rows are in tension. A similar effect is caused by cooling of the beam as described above. In order to respond correctly to such a changing combination of loads, a connection element for elevated temperatures needs a robust loading-unloading-reloading

approach. Therefore, the classic Massing rule with memory effects has been included into the new element. The response of the connection element simulating a symmetric connection with two bolt rows under alternating axial loads can be seen in Fig. 5 below.

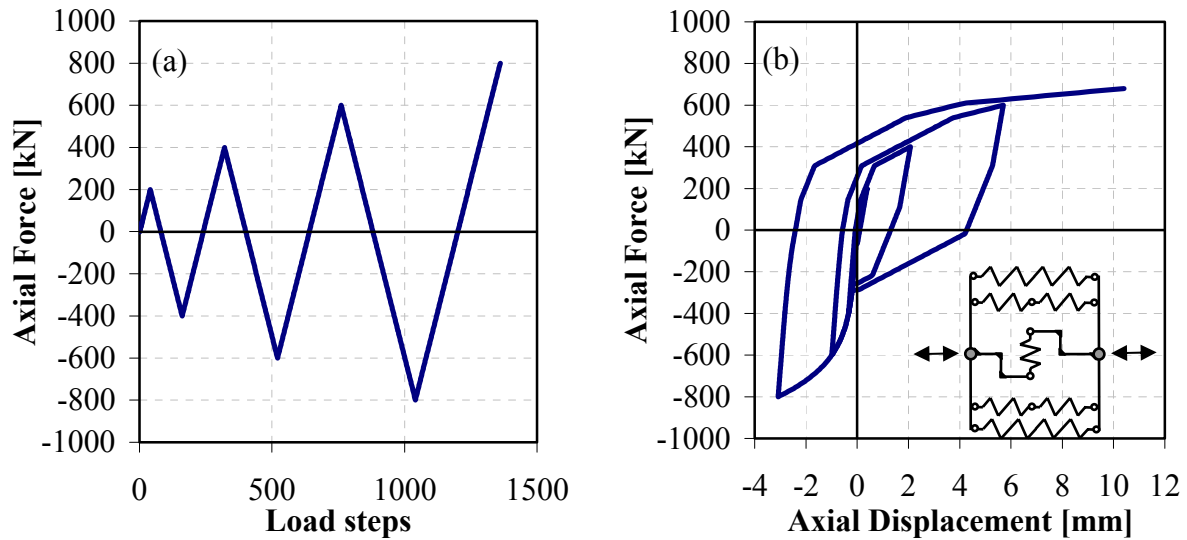


Fig. 5: Cyclic loading (a) and response (b) of the new element due to axial load

The difficulty with this approach is that the tensile and compressive forces in the connection do not act in the same place. Therefore, it is necessary, for correct prediction of the internal forces of the springs, that the compression springs are only allowed to act in compression, whereas the tension springs are allowed to act in both tension and compression, but only until the endplate at the height of the beam flange adjacent to the tension spring contacts the column. It is then assumed that all compression force is taken by the much stiffer compression spring. In reversal, when a compression spring is plastically deformed and unloads until the endplate loses contact with the column, the adjacent tension spring has to start taking load from this deformed position.

4. VALIDATION AT AMBIENT AND ELEVATED TEMPERATURES

The connection element has been validated against a number of experiments, at ambient and elevated temperatures, found in literature. Unfortunately, there are no available connection tests including axial load in the beams at elevated temperature, and therefore this novel aspect of the element could not be tested.

4.1 Ambient Temperature Experiments

In order to validate the ambient temperature behaviour of the connection element two different types of tests were used. The first test series, by Girão Coelho¹⁶, was designed to investigate the rotational capacity of the endplate side of extended endplate connections. Therefore a short beam (IPE300) was connected to a heavy column section (HE340M) by three bolt rows (M20-8.8) and endplates of varying thickness. In the first (FS1a) and second (FS2a) tests endplate thicknesses t_p of 10mm and 15mm were used, respectively.

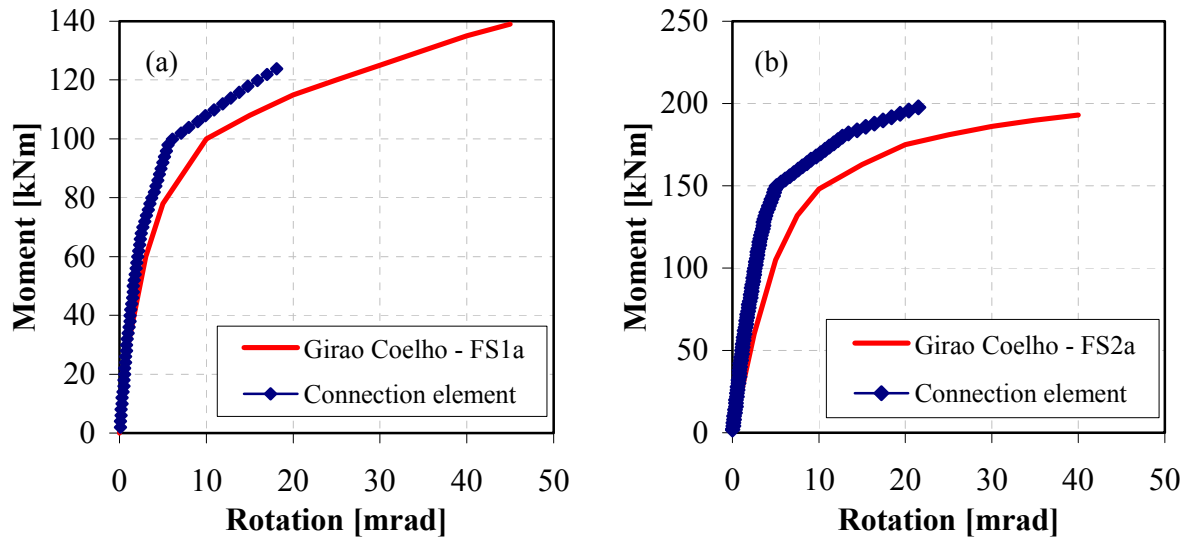


Fig. 6 - Comparison of the new element with an extended endplate tests by Girão Coelho

From Fig. 6 above, it can be seen that the new element compares reasonably well with the experimental results of both tests. However, in both tests the rotation of the connection is slightly under-predicted, which may be explained by the fact that the original yield-line patterns for the conversion between the T-stub and the real endplate have been calibrated to the ultimate resistance but are used throughout the whole test. It should be noted that for these tests the whole effective bolt length has been allocated to the endplate side of the connection, as the column flange is extremely stiff, and so the datum of the T-stub displacement in the endplate is assumed to be at the centre of the nut on the column-flange side of the connection.

The second group of experiments has been designed to fail in the compression zone of the column web. Firstly, the ambient-temperature cruciform test by Leston-Jones on flush endplate connections ($t_p = 8\text{mm}$) with three bolt rows (M16-8.8) connecting small beam (UC152x152x23) and column (UB 254x102x22) sections was modelled. The test failed by plastic buckling of the column web and large deformations of the column flange in tension. In Fig. 7(a) the good correlation between the response of the connection element and the experimental M- Φ data can be seen.

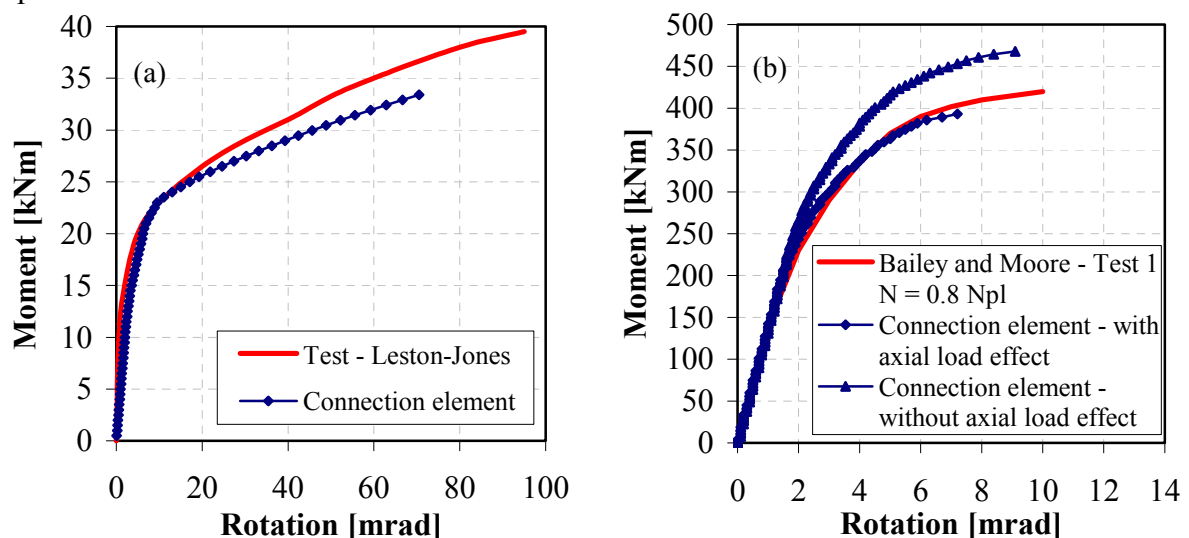


Fig. 7 - Comparison of the new element with a flush endplate test by Leston-Jones (a) and an extended endplate test Bailey and Moore (b)

The second example is again a cruciform test, conducted by Bailey and Moore¹⁷, but this time using reasonably large beam (UB457x191x74) and column (UC254x254x107) sections connected by a very stiff extended endplate ($t_p = 30\text{mm}$) and four bolt rows (M30-8.8). The test was designed to investigate the influence of axial column load ($N = 0.8 N_{pl}$) on the compression zone. As the connection element is able to account for this effect two runs were conducted, the first without consideration of the axial load and the second one with the axial load considered. From Fig. 7(b), the excellent comparison between the proposed element and the experiment can be seen, if the reducing effects of the axial column load are included.

In general, it can be said that the proposed connection element in *Vulcan* compares accurately with experimental data at ambient temperature. However, the rotational capacity is always conservatively predicted, which suggests that further refinement of the tension zone behaviour is required as the predicted rotation was limited in most cases by the fracture of the bolts, which did not always occur in the tests.

4.2 Elevated-Temperature Experiments

As part of the validation process of the new connection element, the elevated-temperature connection tests conducted by Leston-Jones have been modelled. The size of the connected sections, and the connection itself, are the same as in the ambient-temperature test discussed in the previous section. However, instead of loading the cruciform assembly until failure of the connections occurs, a constant moment was applied to the connection and then the temperature was increased by approximately $10^\circ\text{C}/\text{min}$ until failure occurred or the test had to be terminated due to spatial constraints. As a temperature distribution in the connection, the average temperature multipliers for each component over the duration of the whole test were used. In total four tests with applied connection moments ranging from 5 kNm to 20 kNm have been compared with the response of the proposed element, which can be seen in Fig. 8 below.

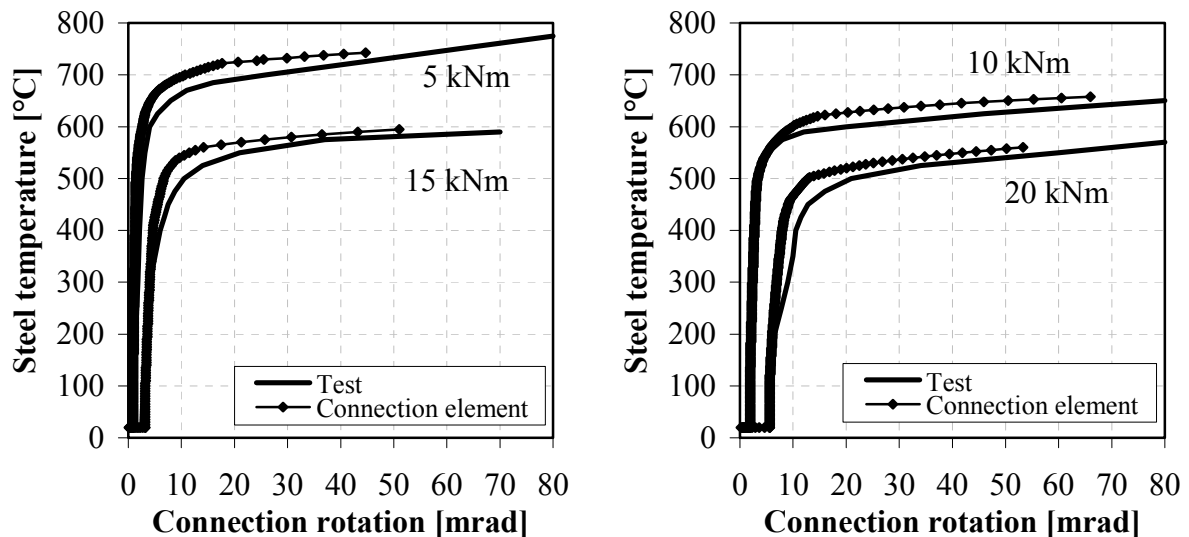


Fig. 8 - Comparison of the new element with the high-temperature tests on flush endplate connections by Leston-Jones

In general, a very good correlation is seen between the tests and the predictions of the proposed element. However, the new element under-predicts the rotations found in the test slightly, which is probably because of the non-consideration of group effects between the bolt

rows in the column flange. Also, as was observed at ambient temperature, the rotational capacities of the connections are underestimated due to bolt failure.

5. DISCUSSION

The advantages of the connection element in its present form are evident, as it opens up the possibility to combine the Component Method, and therefore detailed connection behaviour, with the overall frame action of a structure at ambient and elevated temperatures. It can deal with the changing combinations of moment and axial loading which a connection undergoes during a natural fire. Furthermore, to simulate the connection response only the geometrical and material properties of the connection are required. However, there are also a number of disadvantages associated with the connection element. The greatest is that the accuracy of response of the element depends on the accuracy of F - δ - θ models for the individual components, which do not exist for all components at present. Also, in practice the required connection details will most likely not have been designed by the time the structural fire design of a building has to be performed, which adds another iteration to the building design process. In addition, the computational time for the analysis of a structure in fire will be increased.

At present, there are still a number of limitations to the use of the connection element, which restrict its use to internal endplate joints due to a lack of calibration of the remaining components in fire. However, in theory it is possible to include all the missing components:

- Group effects in the bolt rows,
- Shear deformation in the column-web,
- Shear deformation in the beam-end zone,
- Local buckling of the bottom flange of the beam,
- Bolt behaviour during cooling.

6. CONCLUSION

In this paper, the development of a high-temperature component-based connection element has been described. The proposed element is based on the principles of the Component Method and was implemented into *Vulcan*, a non-linear finite element program specially developed for the analysis of steel and composite structures in fire. This combination of detailed connection behaviour with a realistic simulation of structures in fire can be used to increase the understanding of the complex connection-structure interaction.

However, at present this paper can only describe a practical way to develop such a connection element and only preliminary, but good, validations can be shown. Further improvements of the existing component characteristics, and investigation of the high-temperature behaviour of the remaining components, as well as more high-temperature experiments are required before the element can be used for practical design.

Nevertheless, when the remaining research is done, the safety and economy of steel and composite framed buildings could be increased significantly, as it will be possible to assess the robustness of buildings against structural collapse more accurately, which will allow an optimisation of structural design and the applied fire protection.

7. REFERENCES

- [1]. Tschemmerneegg, F., Tautschnig, A., Klein, H., Braun, Ch. and Humer, Ch., “Zur Nachgiebigkeit von Rahmenknoten – Teil 1”, Stahlbau 56, Heft 10, S. 299-306, 1987.
- [2]. CEN, “EC3: Design of Steel Structures, Part 1.8: Design of joints”, European Committee for Standardization, Document BS EN 1993-1-8:2005.
- [3]. Leston-Jones, L.C., “The influence of semi-rigid connections on the performance of steel framed structures in fire”, PhD Thesis, University of Sheffield, 1997.
- [4]. Al-Jabri, K.S., “The behaviour of steel and composite beam-to-column connections in fire”, PhD Thesis, University of Sheffield, 1999.
- [5]. Spyrou, S., “Development of a component based model of steel beam-to-column joints at elevated temperatures”, PhD Thesis, University of Sheffield, 2002.
- [6]. Simoes da Silva, L., Santiago, A. and Villa Real, P., “A component model for the behaviour of steel joints at elevated temperatures”, Journal of Constructional Steel Research 57, pp. 1169-1195, 2001.
- [7]. CEN, “EC 3: Design of Steel Structures, Part 1.2: Structural Fire Design”, European Committee for Standardization, Document BS EN 1993-1-2:2005.
- [8]. Ramli Sulong, N.H., Elghazouli, A.Y., Izzuddin, B.A., “Analytical modelling of steel connections at elevated temperature”, in the proceeding of Eurosteel 2005 – 4th European Conference on Steel and Composite Structures, Vol C, pp. 5.1-25, 2005.
- [9]. Li, T.Q., Choo, B.S. and Nethercot, D.A., “Connection element method for the analysis of semi-rigid frames” Journal of Constructional Steel Research 32, pp 143-171, 1995.
- [10]. Lowes, L.N. and Altoontash, A., “Modeling reinforced-concrete beam-column joints subjected to cyclic loading”, Journal of Structural Engineering, Vol. 129, No 12, pp. 1686-1697, 2003.
- [11]. Bayo, E., Cabrero, J.M., Gil, B., “An effective component-based method to model semi-rigid connections for global analysis of steel and composite structures”, Engineering Structures 28, pp. 97-108, 2006.
- [12]. Zoetemeijer, P., “A design method for the tension side of statically loaded, bolted beam-to-column connections”, Heron 20, pp. 1-59, 1974.
- [13]. Block, F.M., “Development of a component based finite element for steel beam-to-column connections at elevated temperatures with special emphasis on the compression zone”, PhD Thesis (in preparation), University of Sheffield, 2006.
- [14]. Kirby, B.R., “The behaviour of high-strength grade 8.8 Bolts in fire”, Journal of Constructional Steel Research 33, pp. 3-38, 1995.
- [15]. Bailey, C.G., Burgess, I.W. and Plank, R.J., “Analyses of the effects of cooling and fire spread on steel-framed buildings”, Fire Safety Journal 26, pp. 273-293, 1996.
- [16]. Giaro Coelho, A.M. “Characterisation of the ductility of bolted end plate beam-to-column steel connections”, PhD thesis, University of Coimbra, Coimbra, Portugal, 2004
- [17]. Bailey, C.G. and Moore, D.B., “The influence of local and global forces on column design”, Final Report, PII Contract No. CC1494, BRE, Garston, UK, 1999.



CONNECTIONS OF UNPROTECTED STEEL MEMBERS TO FIRE WALLS

Alexander HEISE¹ and Peter SCHAUMANN²

ABSTRACT

This paper presents two concepts to design connections for unprotected steel members to fire walls. The first option is a design concept based on maximum load bearing capacity of the bolts. In this option, the maximum reaction forces are calculated using design values for the upper limit of the load bearing capacity of the bolts. The design concept is completed including combination values for additional loads and design values to determine the resistance of the fire wall.

The second option is a connection type, which transmits only minor reaction forces to the fire wall in the case of failure of the connected beam. This type of connection is characterized by open slotted holes. The open slotted holes enable the beam to slide out of the connection without causing pull-off loads. To avoid restraining forces the slots are elongated to enable the connected beam to thermally elongate during the heating process. The design values for the load bearing capacity of the open slotted holes are determined from a statistical evaluation of tests.

The length of the slots is overestimated if it is calculated on the basis of the thermal elongation without considering the effect of the deflection due to horizontal displacement. Simple calculation methods based on numerical studies for the determination of the maximum horizontal displacement are presented.

These two options to connect unprotected beams to fire walls can be combined. Hence, it is possible to use the fire wall to transmit horizontal and vertical forces and to supersede columns and bracings. With these connections the cost effectiveness of unprotected steel constructions can be improved.

¹ Dr.-Ing., Senior Fire Safety Engineer, Arup Fire, 13 Fitzroy Street, London W1T4BQ, United Kingdom
email: alexander.heise@arup.com.

² Prof. Dr.-Ing., University of Hannover, Institute for Steel Construction, D-30167 Hannover, Germany
email: schaumann@stahl.uni-hannover.de

1. INTRODUCTION

1.1 General

It is common practice to design single storey warehouses or industrial structures for fire with very limited or no fire protection. Structural failure of these forms of single storey buildings in a fire situation is tolerated, traditionally due to the low risk of life safety that these structures present. These types of buildings typically have limited occupancy with multiple means of escape, and as such offer sufficient evacuation time.

However, the risk to the life safety for fire fighters has not traditionally been considered in the design process, and has subsequently resulted in fire-fighters primarily attacking a building using external fire-fighting measures solely. As such, the concept of property protection to minimize business interruption and property loss has become an increasingly important concept in design. This is primarily achieved by maintaining compartmentation within these large volume spaces to limit fire spread and damage to, not only the contents of the building, but also, the structure.

Minimizing property loss is achieved by sub-dividing the space with large fire walls that are structurally independent from the remainder of the building. So, when the unprotected steel structure fails, the large fire walls will remain intact. As a consequence, the unprotected steel structure is usually erected independently from the fire wall, preventing the use of the load bearing capacity of the fire wall in the structural design concept. This results in the need for additional columns and bracing.

A more cost effective solution is to connect the unprotected steel members to the fire wall. This paper presents two different design concepts for connections of unprotected steel-work to fire walls. Following these design concepts damage to the fire wall is prevented when a failure occurs to the unprotected steel members that are connected.

When connecting steel elements to fire walls two contradictory requisitions are desirable: On one hand their load bearing capacity in ambient design is aimed to be as large as possible and on the other hand the transmittable forces in case of failure should be as low as possible. The type of connection is dependent on the magnitude and the components the connection has to transmit to the fire-wall. [1]

One option is a connection, where unlimited force components can be transferred. However, the fire wall must then be designed for the maximum load bearing capacity of the connection. This connection type will be named “pull-off connection”. The other option is a connection type, which in ambient temperatures transfers vertical forces only. Due to the open slotted holes this connection is named “comb-connection”.

These two design concepts can be combined enabling the designer to find the most cost effective solution for the connection.

1.2 Pull-off connection

A pull-off connection is a connection with defined failure loads (see Fig. 2). There are a great variety of connections possible, depending on the components and the magnitude of forces, which should be transferred from the connected beam to the fire wall. However, one common element for all connections is the bolts. Given the maximum load bearing capacity of the bolts, maximum stresses can be calculated on the basis of the kinematic theorem of plastic collapse. Hereafter, an upper bound load bearing capacity of a structural element is found on the basis of an arbitrarily assumed mechanism for a kinematical chain. Therefore,

applying the resulting load bearing capacity of a connection as action to the fire wall yields also an upper bound of the reaction forces, which might stress the fire wall.

The bolts in a connection detail are typically designed to transmit both tension and shear forces. This implies that different failure scenarios must be studied to determine the governing pull-off forces. While these scenarios depend on the structural system, a two span frame can be used to simplify the analysis to get an idea of the expected forces in the actual system (see Fig. 1). These results can then be transferred to other structural systems

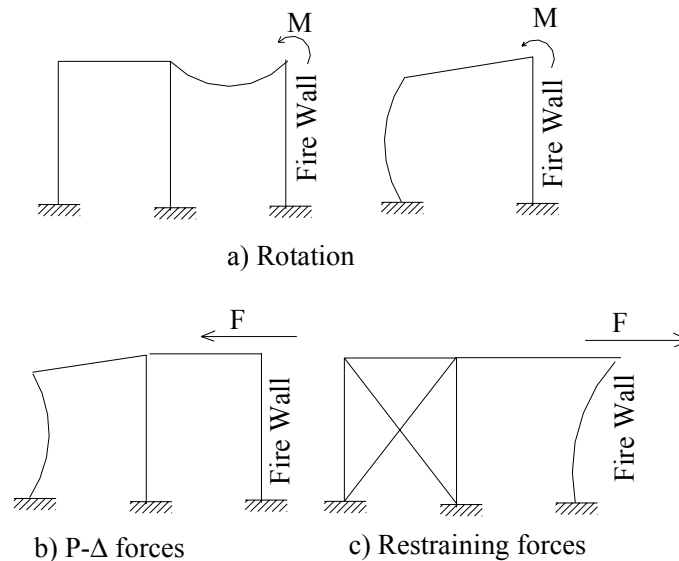


Fig. 1 – Failure scenarios for multiple span frames

Bending moments resulting from a rotation of the connection will occur if the column or the beam adjacent to the fire wall fails (see Fig. 1.a). If the column on the edge of a multiple frame fails further load cases are to be considered:

P- horizontal forces are activated if the outer column fails (see Fig. 1b).

The fire wall is also stressed by horizontal forces due to thermal expansion in indeterminate frames.

Therefore, the design of the fire wall in a multiple frame requires three different load cases. It is not necessary to study intermediate failure scenarios, since the applied reaction forces are an upper bound of the resistance capacity of the connection.

Having established a global failure mechanism, a local plastic collapse mechanism for the connection is studied (see Fig. 2).

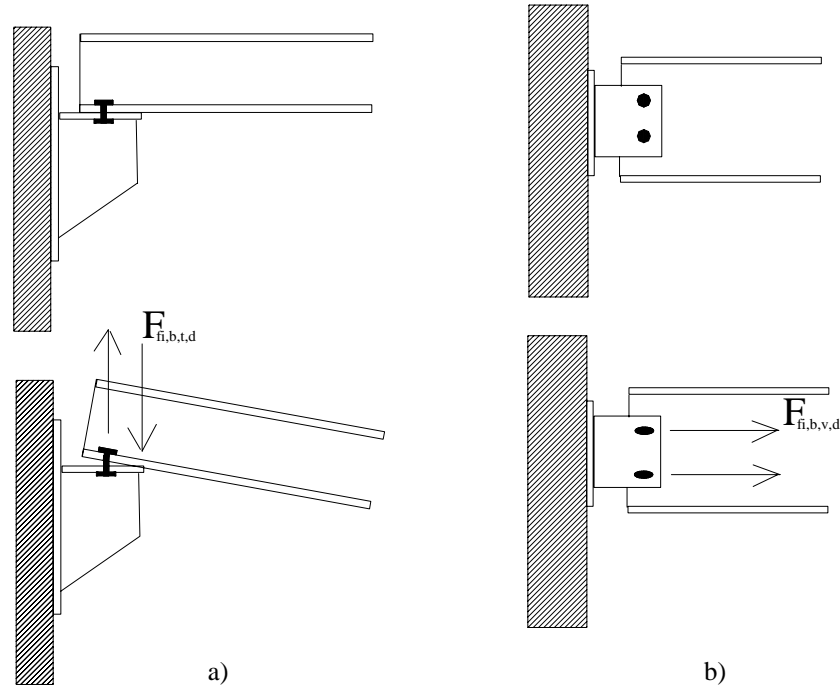


Fig. 2 – Collapse mechanism of the connections – pull off loads

A one span frame will be stressed according to Fig. 2a), with a bending moment limited by the maximum load bearing capacity of bolts in tension. In a multiple frame, additional horizontal forces may occur, which are limited by the maximum shear capacity of the bolts (see Fig. 1b,c). The maximum shear force and bending moment for the connection depicted in Fig. 2 can be calculated with the following equations:

$$F_{fi,b,t} = \gamma_{F,fi,t} f_{ub} \cdot A_s \quad (2)$$

$$F_{fi,b,v} = \gamma_{F,fi,v} 0,6 \cdot f_{ub} \cdot A_i \quad (3)$$

$F_{fi,t,d}$	maximum design tension resistance
$F_{fi,v,d}$	maximum design shear resistance
$\gamma_{F,fi,t}$	partial safety factor to determine the maximum tensile force of bolts
$\gamma_{F,fi,v}$	partial safety factor to determine the maximum shear force of bolts
A_s	tensile stress area
$A_i = A$	area of the shank
$A_i = A_s$	tensile stress area

The nominal value for the load bearing capacity is determined using the values for the tensile strength of the bolts (f_{ub}), according to EC 3-1-8 [2]. For bolts in shear, the nominal value is determined using a constant ratio of 0.6 between shear strength and ultimate strength.

The procedure to verify the fire wall is to show that the resistance capacity in a fire is greater than the loads at the fire limit state. These loads are induced by the failure of the connection. Design values for loads for the accidental situation and for the design resistance in a fire situation are needed, since the strength of the fire wall will be reduced by thermally induced degradation. The design effect of actions in the accidental situation of a fire may be calculated using eq. (4).

$$E_d = E\{(F_{fi,v,d} \text{ OR } F_{fi,t,d}) + \psi_{fi,G} \cdot G_{ki} + \psi_{fi,Q,k} \cdot Q_{ki} + \psi_{fi,S,k}\} \quad (4)$$

1.3 Comb-connections

The second option is a connection design, which transmits only minor reaction forces to the fire wall in case of failure of the connected unprotected beam. This type of connection is characterised by open slotted holes. The open slotted holes enable the failing beam to slide out of the connection without damaging the fire wall. To avoid thermally induced restraining forces, the slots are elongated, enabling thermal elongation of the connected beam during the heating process (see Fig. 3)

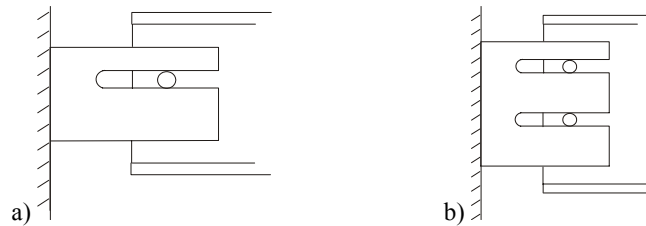


Fig. 3 – Comb connections

The torsional load bearing capacity of comb-connections is not sufficient to provide torsional support [1]. As a result, the lateral torsional buckling capacity of the beam is reduced significantly if no restraint of the rotation at the comb-connections is provided [1].

1.4 Combination of pull-off connections and comb-connections

Both design concepts can be combined (see Fig. 4).

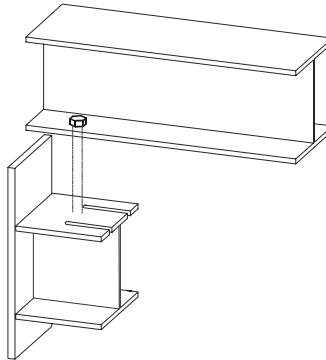


Fig. 4 – Combination of maximum tensile resistance of bolts and comb-connection

This type of connection allows the beam to slide off the bracket for load cases involving movement, which is perpendicular to the fire wall. For a load case involving rotation, a bending moment is activated, which is limited by the maximum tensional load bearing capacity of the bolts.

Practical applications of the different design concepts are presented by the authors in [3].

2. DESIGN CONCEPT BASED ON MAXIMUM LOAD BEARING CAPACITY OF BOLTS

2.1 Design values for the maximum resistance capacity of bolts

Design values for the maximum resistance capacity of bolts are determined using partial safety factors to amplify the nominal load bearing capacity of bolts (see eqs. 2 and 3). The method is based on the FORM method with determined sensitivity factors according to EN 1990 [4].

A lognormal distribution for the resistance capacity of bolts in tension and shear are assumed, for which the design value can be determined using eq. (5). The statistical uncertainty is negligible for the minimum number of tests – 92 for bolts in tension, grade 5.6 – and particularly in the context of the large number of available tests. Partial safety factors are then calculated by dividing the respective design value by the nominal value.

$$x_d = e \quad (5)$$

The statistical parameters and for lognormal distribution are determined, based on the statistical parameter presented in Table 1 and Table 2. For the statistical evaluation, a databank was created with more than 3000 test values for bolts in shear and in tension. These included test results which were provided to the authors from literature and from bolt manufacturers. The databank and the results shown in Table 1 and Table 2 are discussed in detail in [5].

Table 1 : tensile strength, number of tests, 5 % quantile, coefficient of variation and nominal values, depending on the bolt grade [5]

Grade	N [-]	$\sigma_{Z,5\%}$ [N/mm ²]	V_{σ_z} [-]	$\sigma_{Z, NEN}$ [N/mm ²]
4.6	660	392	0,12	400
5.6	92	507	0,09	500
8.8	569	839	0,05	800
10.9	1168	1049	0,04	1000

Table 1 shows that there is a good agreement between the nominal values and the 5% quantiles of the tensile strength. However, the coefficient of variation (COV) reduces with increasing tensile strength. For this reason, the design values to determine the maximum tensile force were evaluated, dependent of the bolt grade, implying that the partial safety factors for the maximum tensile force also depend on the bolt grade.

Table 2 shows the statistical parameter of the shear strength and the ratio of shear strength to ultimate strength. This ratio is equivalent to the correlation between shear strength and tensile strength.

Table 2 : shear strength, number of tests, 5 % quantile, coefficient of variation and strength ratio ($\alpha = \tau_{A,5\%} / \sigma_{Z,5\%}$) [5]

Grade	N [-]	$\tau_{A,5\%}$ [N/mm ²]	V_{τ_Z} [-]	α [-]
4.6	216	284	0,09	0,73
5.6	94	358	0,05	0,71
8.8	232	535	0,05	0,64
10.9	159	595	0,07	0,57

The COV and the strength ratio depend on the bolt grade. The strength ratio reduces with increasing grade and the COV of the shear strength differs from the COV of the tensile strength, indicating that there is no strict correlation between shear and tensile strength [5]. These variations are considered automatically calculating design values in dependency of the bolt grade.

The design value is determined as an upper quantile in dependency of the required safety level or safety index β_i and the sensitivity factor γ . The resistance of the bolts is treated as action on the structure. Therefore according to EN 1990 [4] the sensitivity factor for effects of actions γ in eq. (5) is set to -0.7.

The safety index β_i can be determined for the accidental situation in a fire considering the low probability of flash-over [6][7][8]. The probability of flash-over was assessed for industrial buildings with an average compartment area of 2500 m² [6] to 0.0606 in 50 a. The safety index for the accidental situation in a fire β_i was determined for two target failure probabilities p_t considering differing safety levels, depending on the occupancies which are separated by the fire wall [1].

Table 3 : Safety indices for the accidental situation of a fire in dependency of Safety Category I and Safety Category II [1]

Fire walls within industrial buildings Safety Category I	Fire walls which separate industrial buildings from other occupancies. Safety Category II
$\beta_i = 2,3$ ($p_t = 1.3 \text{ E-}5 \text{ p.a.}$)	$\beta_i = 3,0$ ($p_t = 1.3 \text{ E-}6 \text{ p.a.}$)

The resulting partial safety factors to determine bolts in shear and in tension are summarised in Table 4

Table 4 : Partial safety factors to determine the maximum design resistance of bolts in shear and in tension

Grade	$F_{f,t}$ bolts in tension		$F_{f,v}$ bolts in shear	
	$\beta_i = 2,3$	$\beta_i = 3,0$	$\beta_i = 2,3$	$\beta_i = 3,0$
4.6	1.44	1.52	1.64	1.72
5.6	1.35	1.41	1.40	1.43
8.8	1.23	1.26	1.31	1.34
10.9	1.19	1.22	1.24	1.29

Thus design values for the maximum resistance capacity can be determined using the partial safety factors in Table 4 and equations (2) and (3).

2.2 Combination values to determine the effects of the accidental situation in a fire.

The design effect of actions in the accidental situation of a fire may be calculated with eq. (4). The combination factors acknowledge that it is uneconomical to design for a combination of extreme values, which are improbable to occur at the same time.

In EC 1-1-2 [9] combination values for the accidental situation in a fire are recommended, which are based on the frequency of the respective load (quasi-permanent s_1 or frequent value s_2). The use of the frequent or the quasi-permanent value is a convention and is determined in the national annex of each European country.

For a consistent reliability level the failure probability of a combination of different loads should be like the reliability level achieved designing for the extreme value of one particular load only. Such combination values can be determined in two steps [10]:

The first step is the consideration of reduced sensitivity factors, taking into account the reduced effect on the failure probability of one load when additional loads also contribute to failure. A constant reduction of 40 % for additional effects of actions $\psi_{i,i}$ is proposed [4][10], discounting the variability of the sensitivity factor in dependency of the contemplated load case.

In the second step the smaller probability of extreme values occurring at the same time is considered applying the Borges-Castanheta method [10]. The idea is that from the two considered loads the extreme value of the more frequent load is determined for the larger basic period of the combining loads. It is assumed that the basic period of a fire is always smaller than the basic period of additional loads. Hence, the combination values are determined as the ratio of the extreme value during the basic period of an additional load to the respective characteristic value. The combination value is assessed for a reference period of 50 a. This model is on the safe side for more than two actions. The statistical parameter and the reference periods used to determine the combination values are presented in Table 5 and correspond to DIN 1055-100 [11].

Table 5 : Statistical Parameter [11] and resulting combination values [1]

Load	Statistical Parameter for additional loads					Combination values	
	Distribution	C.O.V. $V_{Q,50}$	Quantile	Reference Period T	Basic period	η for $\eta_{I,1} = 2,3$	η for $\eta_{I,II} = 3,0$
Dead Loads	Normal	0.10	50 %	50 a	50 a	1.17	1.19
Live Loads	Gumbel	0.40	95 %	50 a	5 a	0.42	0.46
Snow “maritime”	Gumbel	0.30	98 %	1 a	0.25 a	0.71	0.74
Snow “tempered”	Gumbel	0.15	98 %	1 a	0.125 a	0.09	0.15
Wind	Gumbel	0.20	98 %	1 a	0.008 a	0.04	0.08

Besides considering the effect of additional loads according to eq. (4) with the combination values given in Table 5, also the effect of the temperatures in the fire situation must be considered. For this the material properties and calculation methods given in the “hot” Euro-codes may be used, applying partial safety factors as presented in the following section.

2.3 Design values for the resistance of the fire wall

For a consistent safety concept also the design values to reduce the nominal resistance of the fire wall are determined using the FORM method with a determined sensitivity factor of $\alpha = +0,8$ according to EN 1990 [4].

The partial safety factors for steel and bolts are determined with eq. (5) the statistical parameter for structural steel and the resulting partial safety factors are presented in Table 6.

Table 6 Statistical parameter for structural steel and resulting partial safety factors for the resistance in a fire situation

Material	average	C.O.V.	nominal value	$M_{I,I}$ for $f_{t,I} = 2,3$	$M_{I,II}$ for $f_{t,II} = 3,0$
S 235	290 N/mm ²	0.07	235 N/mm ²	0.94	0.99
S 355	405 N/mm ²	0.06	355 N/mm ²	1.01	1.05

For bolts the same statistical parameter as for the determination of the maximum design resistance are used. The resulting partial safety factors presented in Table 7 are applied to reduce the nominal values of the resistance capacity of bolts as presented in section 0.

Table 7 Partial safety factors to determine the design resistance of bolts [1] in a fire situation

Safety index	Bolts in tension				Bolts in Shear			
	4.6	5.6	8.8	10.9	4.6	5.6	8.8	10.9
$f_{t,I} = 2,3$	1.44	1.35	1.23	1.19	1.64	1.40	1.31	1.24
$f_{t,II} = 3,0$	1.52	1.41	1.26	1.22	1.72	1.43	1.34	1.29

For concrete and reinforcement the following equation was used to determine the partial safety factor for the design resistance

$$\gamma_M = e^{\alpha \beta \xi_R - k_R \xi_F} \quad (6)$$

The COV V_R to determine the lognormal parameter ξ_R comprising model-, geometry- and material uncertainties as well as the COV V_F for the material uncertainties alone and the resulting partial safety factors are presented in Table 8.

Table 8 Partial safety factors to determine the design resistance for concrete and reinforcement [1] in the fire situation

Material	V_R	V_F	$M_{I,I}$ for $f_{t,I} = 2,3$	$M_{I,II}$ for $f_{t,II} = 3,0$
reinforcing steel	0.071	0.05	1.05	1.09
concrete	$V = 0.3$		1.06	1.25

3. COMB-CONNECTIONS

3.1 Design values for the resistance of open slotted holes

The resistance capacity of open slotted holes (see Fig. 5) is limited by the plastic resistance capacity of the plate at the restraint (A) in combination with local stresses at the interface between the bolt and the plate (B).

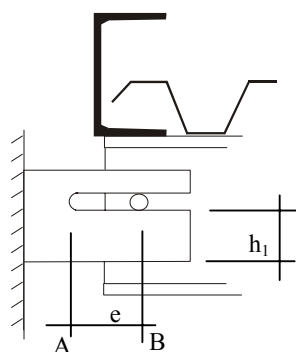


Fig. 5 – Comb-connection – Fin plate with open slotted holes

The design value is determined on basis of tests according to section D8 of EN 1990 [4] [1][12]. This is necessary because the determination of the resistance capacity on basis of FEM alone is unsatisfactory for two main reasons: One is the difficulty to model large local strains, since the stress strain relationship beyond the ultimate strain is dependent on the geometry of the specimen and the velocity in which a test is performed. The other main insecurity is in the modelling of contact at the interface between bolt and plate [1][12].

Starting point of this method is the theoretical resistance, which is the plastic resistance capacity at point A given in eq. (7) (see Fig. 5), where t is the thickness of the plate and f_y the nominal strength of the plate material.

$$P_t = \frac{h_1 \cdot t \cdot f_y}{\sqrt{16e^2/h_1^2 + 3}} \quad (7)$$

The method is suitable for a limited number of tests. The tests are used to determine a model factor and a model uncertainty, which is associated to the theoretical resistance presented in eq. (7). The method consists of a statistical evaluation of the error, comparing the theoretical resistance and the experimental resistance, where as the uncertainties of the basic variables (h_1 , t , f_y , e) are determined from literature and included as prior knowledge.

Twelve tests were performed with varying height h_1 and clearance e using M 16 bolts. The results and the setting of the test are described in detail in [12]. The experimental resistance is defined as conventional load bearing capacity and obtained from load deformation curves. It is the intersection of the tangent with the starting stiffness and a tangent where the slope is $1/10$ th respectively.

Table 9 Test parameter, deformation w and conventional resistance capacity $P_e(w)$

Test	height h_1 [mm]	clearance e [mm]	thickness t [mm]	deformation w [mm]	resistance P_e [kN]
2.1	18.7	20.0	10.2	0.47	14.40
2.2	22.3	0.3	10.2	0.92	37.01
2.3	18.8	41.1	10.2	0.66	8.22
2.4	40.7	39.9	10.1	0.97	27.52
2.5	38.9	19.7	10.1	1.28	40.42
2.6	39.4	0.3	10.1	1.93	66.03
2.7	59.2	30.4	10	1.05	50.30
2.8	58.9	20.5	10	1.35	66.45
2.9	58.9	0.9	10.2	2.18	95.56
2.10	78.8	40.5	10.1	1.70	77.54
2.11	78.8	20.5	10.1	2.25	100.03
2.12	78.5	0.3	10.1	1.52	107.76
$f_y = 293 \text{ N/mm}^2, f_u = 406 \text{ N/mm}^2$					

The statistical evaluation yields a model factor $b_e = 0.87$ and the model uncertainty $V_{be} = 0,15$ with a correlation of $\rho = 0,98$ [1][12]. These values represent the bias and uncertainty of the theoretical resistance function.

The uncertainties of the basic variables are considered as prior knowledge and taken from literature [1]. The respective values are presented in Table 10. The COV $V_{g(X)}$ of the theoretical resistance function is determined according to eq. (8), where the vector of the basic variables is $X = \{e, h, t, f_y\}$ with the statistical parameter given in Table 10 and the resistance function $g(X)$ equal to eq. (7).

$$\text{Var}(g(X_i)) = \sum \left(\frac{\partial g}{\partial X_i} \right)^2 \text{Var}(X_i) \quad (8)$$

Table 10 Statistical parameter of the basic variables [1]

X_i	$5 \text{ mm} < t < 20 \text{ mm}$	f_y	$20 \text{ mm} < h_1 < 80 \text{ mm}$	$0 < e < 60 \text{ mm}$
μ_{X_i}	t_{NOMINAL}	290 N/mm^2	h_{NOMINAL}	e_{NOMINAL}
σ_{X_i}	$0.05 \cdot t_{\text{NOMINAL}}$	20.3 N/mm^2	1 mm	3.5 mm

The resulting COV $V_{g(X)} = 0.23$ of the theoretical resistance function is the maximum value resulting from a variation of the nominal values within the limits given in Table 10.

The partial safety factor is then assessed according to EN 1990 [4] with a sensitivity factor of $\gamma_R = +0.8$ and a safety index $\beta = 3.8$ for ambient design. The statistical uncertainty associated with the small number of 12 tests is considered, too.

Thus, all the values to determine the design resistance were presented. The assessment according to EN 1990 [4] results in a partial safety factor of $\gamma_M = 2.48$ [1]. Design values are obtained dividing the theoretical resistance P_t of eq. (7) by the partial safety factor γ_M .

4. CLEARENCE

An easy way to determine the clearance e or length of the slots is to calculate the thermal elongation based on the critical temperature [13]. However, this is overly conservative, since the thermal induced horizontal displacement is reduced by large deflections before reaching this critical temperature.

Based on numerical parameter studies for simple supported and one sided fixed beams a more economical method for the determination of the maximum horizontal displacement has been worked out. The first step is the determination of the temperature at which the maximum displacement is reached. This temperature can be determined using the following diagrams (see Fig. - 6, Fig. - 7) in dependency of the ratio of the load bearing capacity M_{pl} and the stiffness EI/l as in eq. (9) as well as the utilisation factor defined in eq. (10).

$$c = \frac{M_{pl} \cdot L}{EI} \quad (9)$$

$$\mu = \frac{q l^2 / 8}{M_{pl}} \quad (10)$$

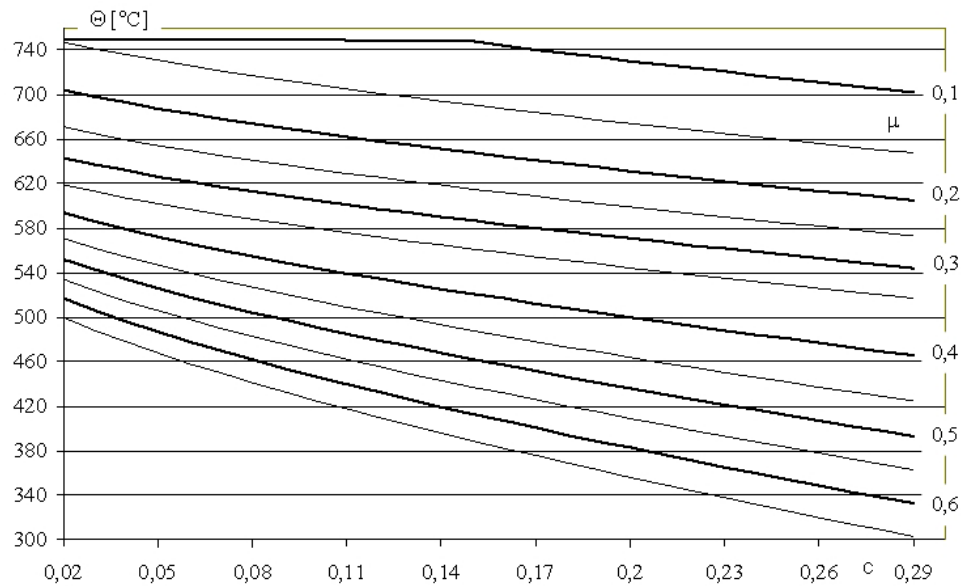


Fig. – 6: Temperature of maximum displacement of simple supported beams

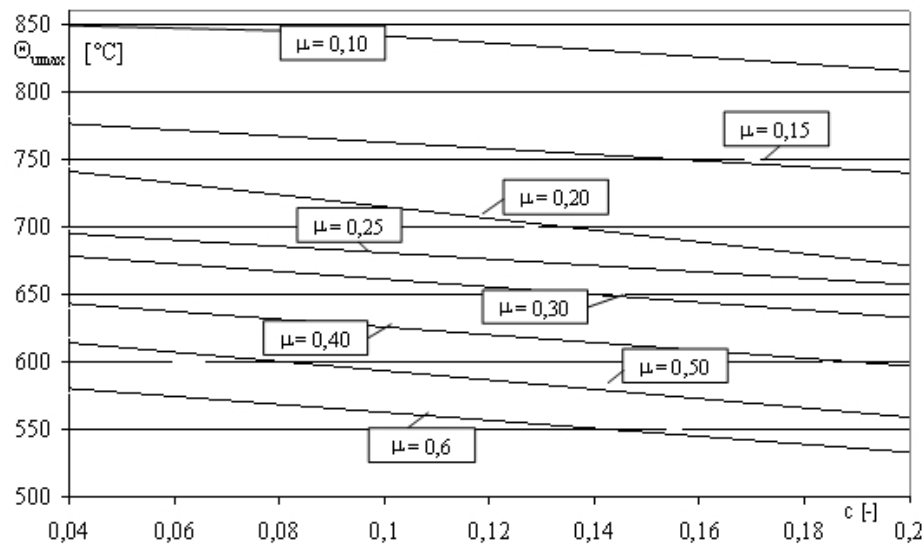


Fig. – 7: Temperature of maximum displacement of one sided fixed beams

The maximum horizontal displacement is then determined calculating the thermal elongation according to EC 3-1-2 [13]. For simple supported beams a further reduction of the

horizontal displacement can be taken into account determining the deflection at elevated temperatures and subsequently the shortening of the horizontal projection of the beam.

The deflection of the beam is determined with a powerfunction interpolating between the infinite deflection at the critical temperature and the temperature at which the proportional limit of the material is starting to show effects. The simple equations to determine the deflection at elevated temperatures are deduced and presented in [1] as well as a simple equation to determine the shortening of the horizontal projection of the simply supported beam.

If the clearance of the beam is shorter than the maximum horizontal displacement restraining forces are activated. For the case that no clearance is provided the maximum value is reached at temperatures below 140°C (S355). For this reason maximum forces based on the maximum load bearing capacity can be determined. The resulting equations are based on the slenderness and the utilisation factor at ambient design [1]. Parametric studies based on FEM showed [1] that intermediate values of the clearance can be determined interpolating linearly between the maximum force, when no clearance is provided, to the maximum horizontal displacement [1].

The resulting simple equations are tools to assess maximum movements or restraining forces and facilitate the design of connections of unprotected steel members to fire walls.

5. CONCLUSION / ACKNOWLEDGEMENT

This paper presents a consistent safety concept to design connections of unprotected steel members to fire walls. The load bearing capacity of the fire wall can be used and a more cost effective design can be achieved. The concept is based on the design of the fire wall for maximum reaction forces limited by the capacity of bolts and the design of comb connections, which allow the connected beam to expand and to slide out of the connection without stressing the fire wall.

The authors thank the German Federation of Industrial Cooperative Research Associations "Otto von Guericke" (AiF) for funding the research work and the company Goldbeckbau for providing the test specimen.

6. REFERENCES

- [1] Heise A.: Anschlüsse von Stahlbauteilen an Brandwände (Connections of steel members to fire walls- in German); Diss., Hannover 2005.
- [2] EN1993-1-8:2005: Design of steel structures - Part 1-8: Design of joints. 2005
- [3] Heise A.: Schaumann P.: Anschlüsse von Stahlbauteilen an Brandwände. Bauphysik-Kalender 2006. Verlag Ernst & Sohn, Berlin.
- [4] EN1990: 2002 Eurocode: Basis of structural design.
- [5] Schaumann P., Heise A., Scheele O.: Entwicklung von Abreißverbindungen von Stahlkonstruktionen an Brandwänden – Teil B: Auswertung von Schraubenversuchen zur Bestimmung der statistischen Parameter von Schraubenzug- und Abscherkräften, Institut für Stahlbau der Universität Hannover, 2004. Forschungsbericht 13289 N/1, AiF
- [6] DIN 18230-1: Structural fire protection in industrial buildings – Part 1: Determining the design fire resistance time, Beuth Verlag, Berlin, 1998
- [7] DIN: Grundlagen zur Festlegung von Sicherheitsanforderungen für bauliche Anlagen. Berlin. Beuth Verlag 1981
- [8] PD 7974-7:2003. Application of fire safety engineering principles to the design of buildings – Part 7: Probabilistic risk assessment.

- [9] EN 1991-1-2: 2002. Eurocode 1: Actions on structures – Part 1-2: General actions – Actions on structures exposed to fire.
- [10] ISO 2394: 1998. General Principles on reliability for structures.
- [11] Grünberg J.: Sicherheitskonzept und Einwirkungen nach DIN 1055 neu; Stahlbetonbau aktuell-Jahrbuch 2001 für die Baupraxis; Beuth, Werner; 2001
- [12] Schaumann P., Heise A.: Entwicklung von Abreißverbindungen von Stahlkonstruktionen an Brandwänden – Teil C: Drehfedersteifigkeit und Lochleibungstragfähigkeit von Kammblechverbindungen zur Übertragung vertikaler Lasten auf Brandwände, Institut für Stahlbau der Universität Hannover, 2004. Forschungsbericht 13289 N/1, AiF
- [13] EN1993-1-2:2005: Design of steel structures - Part 1-2: Structural Fire Design



ON BOLTED CONNECTION WITH INTUMESCENT COATINGS

František WALD¹, Michal STREJČEK² and Alena TICHÁ³

ABSTRACT

The paper is focussed to the temperature development in the bolted connections, which are fire protected by intumescent coating. Three tests were arranged to study the influence of coatings on bolts. On unprotected bolts in the fire protected connections was measured temperature higher till 17 % compare to protected bolts. The analytical model of prediction of the temperature of connection in EN 1993-1-2 is applied to the prediction of bolted connection in case of its installation without coating.

1. INTRODUCTION

The fire will affect the structural connections by reduction of the material properties, redistribution of internal forces and non-homogenous heating of connection components. The temperature of the steel in the region of the connection is lower than the rest of the structural member, due to the increased of thicknesses steel and the shielding effect of the connected member. By the concentration of mass in a joint, compare to connected element, is the connection heated later compare to beam and on reverse during cooling is the temperature in connection higher compare to connected beam, see [1].

The fire resistance of a bolted or a welded joint may be assumed, see [6], to be sufficient provided that the thermal resistance $(d_f/\lambda_f)_c$ of the joint's fire protection should be equal or greater than the minimum value of thermal resistance $(d_f/\lambda_f)_m$ of fire protection applied to any of the jointed members, where d_f is the thickness of the fire protection material, where for unprotected members is expected $d_f = 0$. λ_f is the effective thermal conductivity of the fire protection material. The utilization of the joint should be equal or less than the maximum value of utilization of any of the connected members and the resistance of the joint at ambient temperature should satisfy the recommendations given in EN 1993-1-8 [7]. For structural steel is now the temperature of connection predicted by two methods, the background see in [2], [3], [4] and [5]. The connection temperature may be calculated using

¹ Professor, Czech Technical University in Prague, Dept. Steel & Timber Struct., CZ166 29 Praha, Czech Rep.
email: wald@fsv.cvut.cz

² Research student, Czech Technical University in Prague, Dept. S&TS, CZ166 29 Praha, Czech Republic
email: michal.strejcek@fsv.cvut.cz

³ Research assistant, Czech Technical University in Prague, Dept. S&TS, CZ166 29 Praha, Czech Republic
email: alena.ticha@fsv.cvut.cz

the section factor A_m/V (or A_p/V) of components creating the joint, where A_m is the surface area of connection exposed to heat, A_p internal area of fire protection and V the volume of joint per unit length. For beam to column connection and beam to beam connection, which is supporting the concrete slab may be the temperature predicted from the temperature of the mid span of the beam. By this model is expected that the temperature of the connection component depends on the vertical distance from the upper part of the connected beam. The influence of mass is express indirectly in the prediction of the temperature of the lower flange at midspan.

The intumescent coatings are commonly used to provide fire protection to construction steelwork, and in some countries reached of a 40 % of multi-storey marked, see [8]. The principles by the coatings work are well understood, because the first patent on intumescent was granted as early as 1938. About one third of coatings are provided on-site. Off-site application has major features in cost savings, improved quality by better quality control, reduction of in site disruption, benefits to servicing and other follow-on trades, increased safety on-site and protection of environment. The off-side application is increasing due to the mentioned advantages, see [9]. The intumescence may be described as the reaction of active components under of influence of heat to produce significant swelling. The intumescent expands to many times their initial thickness in fire and produce carbonaceous char, which provides a thermal protective layer to any surface to which coating has been applied. Intumescent painting comprises usually a catalyst, which decomposes produce a mineral acid, a carbonific, such as starch, a binder or a resin, which softens at a predetermined temperature, and a spumific agent, which decomposed with melting of the binder. The thin film intumescent coatings are designed for internal use and typically have a dry film thickness no grater than 5 mm. They protect the steelwork for fire resistance period from 30 min till 120 min; mostly asked is 60 min. For external exposure is in the thin coatings the intumescent base coat protected by special sealer coat and decorative coat. Intumescent coating system is usually spry applied, but the application may be by brush or roller also.

The bolted structural steelwork connections with the off-site applied intumescent coatings need on-site completing of coatings of bolts after erecting of steelwork. Due to reduction in temperature in the region of connection compare to connected elements, the built up of intumescent char on the connected ply shield the fire unprotected bolts sufficiently to provide adequate fire resistance. The presented paper is directed to the influence of the shielding in time and the possibility of prediction the temperature in connection by the step by step procedure, see [8].

2. EXPERIMENTS

Three tests were performed to study the influence of fire protection of bolts in connection protected by intumescent coating. The test set up consists of stub with beam to column fin plate connection, see Fig. 1. Two stubs were installed by each test, one with painted bolts and second one with bolts without coating. The intumescent coating was prepared off-site three weeks before testing according to the operations and maintenance manual by the producer by an accredited company specialised to the fire protection finishes. The thickness of coating was tested by calibrated instrument working on the electro-magnetic induction principle. The treated part of the bolt went beyond the nut 20 mm. The tests were performed in the laboratory PAVUS a.s. in Veselí nad Lužnicí; No. 1 October 20, 2004; No. 2 May 25, 2005, see [10], and No. 3 November 11, 2005. In the second test the whole fin plate was left unprotected. First two tests were heated in the furnace following the fire curve measured during the seventh large fire test in Cardington, see [1]. During third test simulates

the gas temperature nominal fire curve. The Fig. 2 shows the test set up in test No. 2 before and after the fire test with foamed coating, see [9], and the position of the thermocouples in test No. 3. The gas temperatures as well as the average measured temperatures in connection with protected and unprotected bolts are summarised in Tab. 1 for test No. 3. The thermocouples were placed in bolts heads and in plate, 25 mm horizontally from the centre of the bolt hole, 16 thermocouples for a test. No difference in the temperature of bolts and of plate was found in case of protected bolts. For unprotected bolt the increase of the temperature of the bolts compare to the plate reached 28 °C, which is about 8 %.

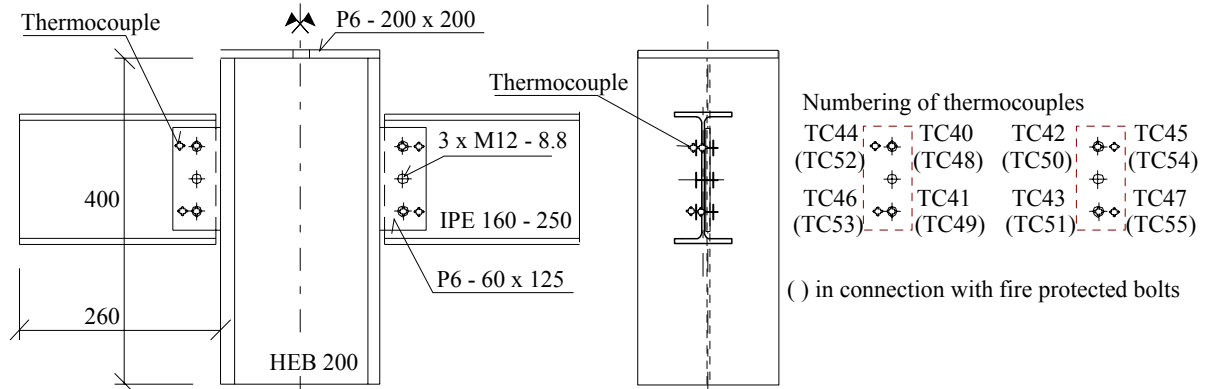


Fig. 1 – Test set up, position of thermocouples

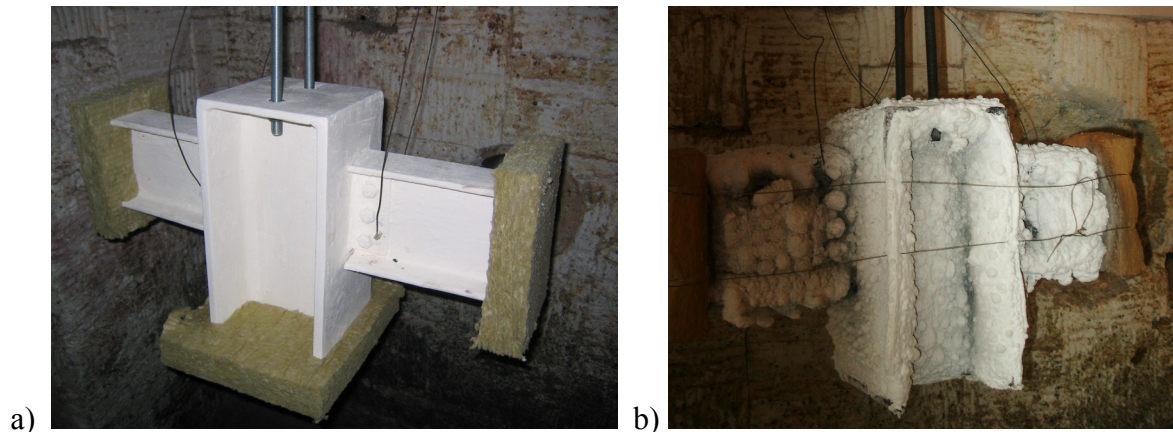


Fig. 2a – Experiment with the fire unprotected bolts in fire protected joint
a) set up before test, b) the joint with intumescent paint after foaming; test No. 2

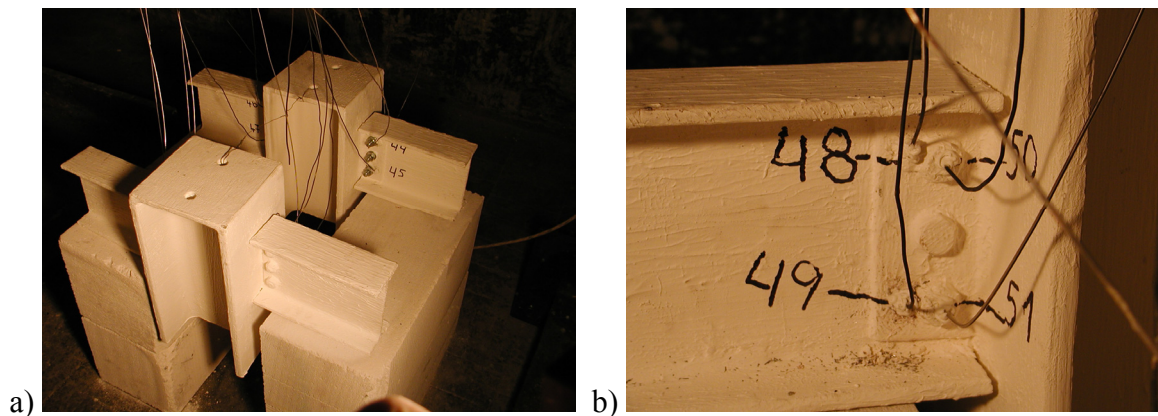


Fig. 2b – a) Test set up No. 3 before test with and without fire protected bolts;
b) position of the thermocouples in bolt head and plate

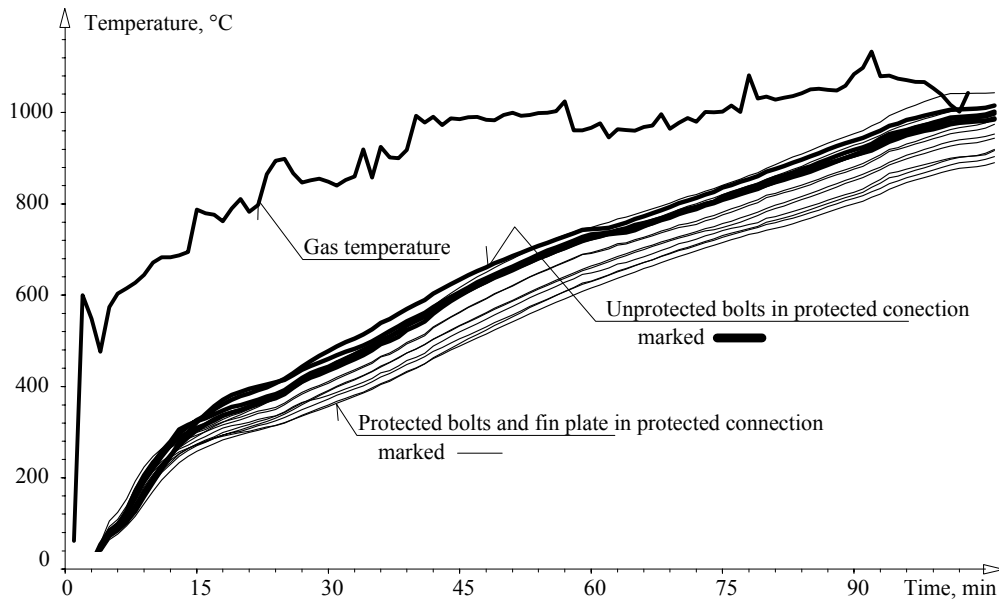


Fig. 3 – Measured temperatures in fin plate connection, test No. 3

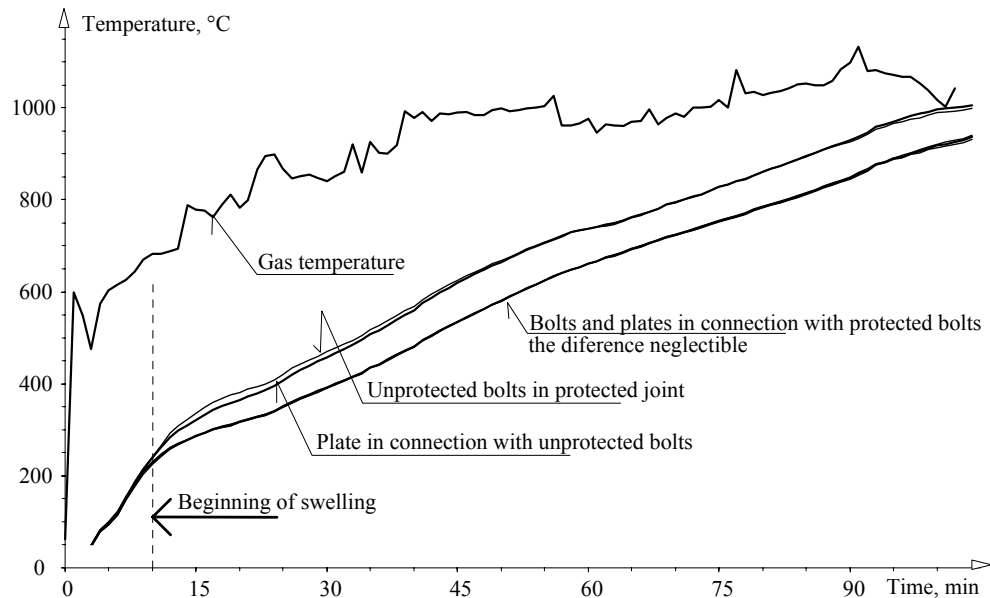


Fig. 4 – Average measured temperatures in fin plate connection, test No. 3

Tab. 1 – Average measured temperatures in fin plate connection during the test No. 3

Time, min	0	15	30	45	60	75	90	102
Average measured gas temperature, °C	12	779	840	990	977	1016	1098	1043
Protected bolts, °C	11	302	408	553	674	763	863	931
Plate by protected bolts, °C	11	300	406	552	675	767	867	940
Unprotected bolts, °C	11	359	486	643	743	840	943	999
Plate by un protected bolts, °C	11	331	467	635	749	840	949	1012
Connection temperature, protected bolts, °C	11	301	407	553	675	765	865	936
Connection temperature, unprotected bolts, °C	11	343	475	639	746	840	946	1006
Difference of temp. (bolt minus plate), protect. bolts, °C	0	2	2	1	-1	-4	-4	-9
Difference of temp. (bolt to plate), protect. bolts, %	0	-1	0	0	0	1	0	1
Difference of temp. (bolt minus plate), unprotect. bolts, °C	0	28	19	8	-6	0	-6	-13
Difference of temp. (bolt to plate), unprotect. bolts, %	0	8	4	1	-1	0	-1	-1
Increase of temperature (unprotect./protect. bolts) in %	0	14	17	16	11	10	9	7

3. ANALYTICAL PREDICTION

The temperature of a joint may be assessed using the local A/V value of the parts forming that joint, see Annex D of EN 1993-1-2 [6]. In the case of the presented test set up is the section factor for the whole set up $A_{set}/V_{set} = 188 \text{ m}^{-1}$; for fin plate only $A_{fin}/V_{fin} = 349 \text{ m}^{-1}$; and for fin plate and beam web $A_{web}/V_{web} = 212 \text{ m}^{-1}$. As a simplification a uniform distributed temperature may be assessed within the joint. In this case the temperature may be calculated using the maximum value of the ratios A/V of the connected steel members in the vicinity of the joint. For connected beam is the section factor $A_b/V_b = 303 \text{ m}^{-1}$.

The thermal properties of the fire protection material after foaming were measured as about $\rho_p = 200 \text{ kg m}^{-3}$, specific heat $c_p = 1200 \text{ J kg}^{-1} \text{ K}^{-1}$ and thermal conductivity $\lambda_p = 0,1 \text{ W m}^{-1} \text{ K}^{-1}$. The thickness of the coating after foaming was expected from the first and second tests as $d_p = 6,5 \text{ mm}$, see [8]. The temperature of connection was calculated based on the step by step prediction method for unprotected internal steelwork, eq. (4.25) in standard [6]. The results may be observed in Fig. 5, where is also demonstrated the prediction of the temperature using the step by step method for fire protected steelwork according to eq. (4.27) in document [6] with the section factor for the whole tests set up. The prediction is good and conservative for protected as well as unprotected bolts till the end of the test in 105 min. The influence of calculation of the section factor by selected sections is demonstrated in Fig. 6.

The tests show that the estimation of the section factor of the fin plate by $2000/t_p = 333 \text{ m}^{-1}$, where t_p is the fin plate thickness, is conservative. The equation $A/V = 1200/t_p$ is representing the current situation and is covering the influence of unprotected bolts in protected connection. The estimation of the temperature is valid even for the connection with unprotected fin plate, see Fig. 7.

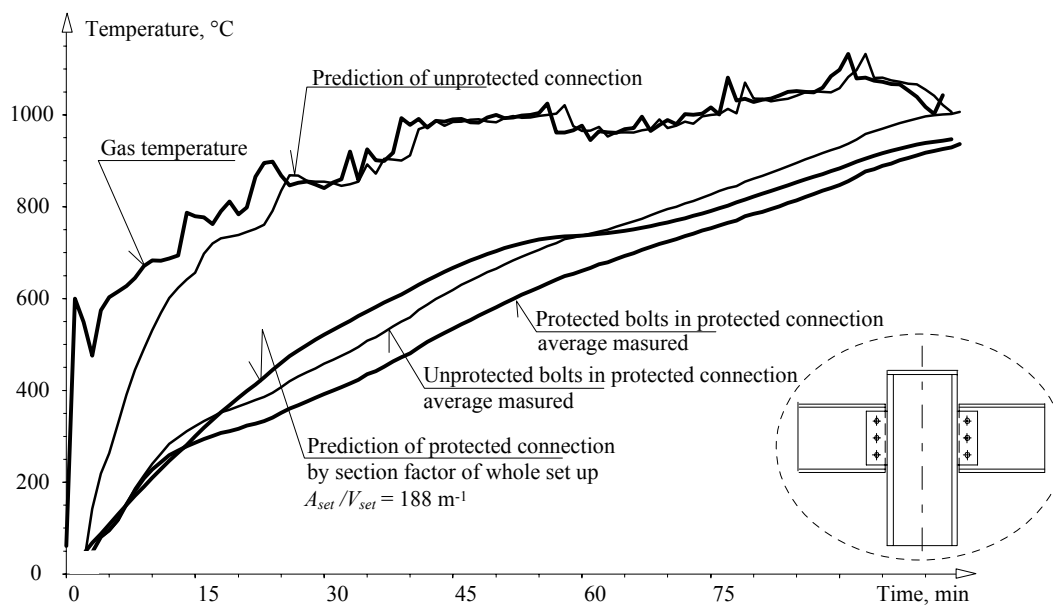


Fig. 5 – Comparison of the predicted temperature in connection to measured values in case of the protected and unprotected bolts, test No. 3

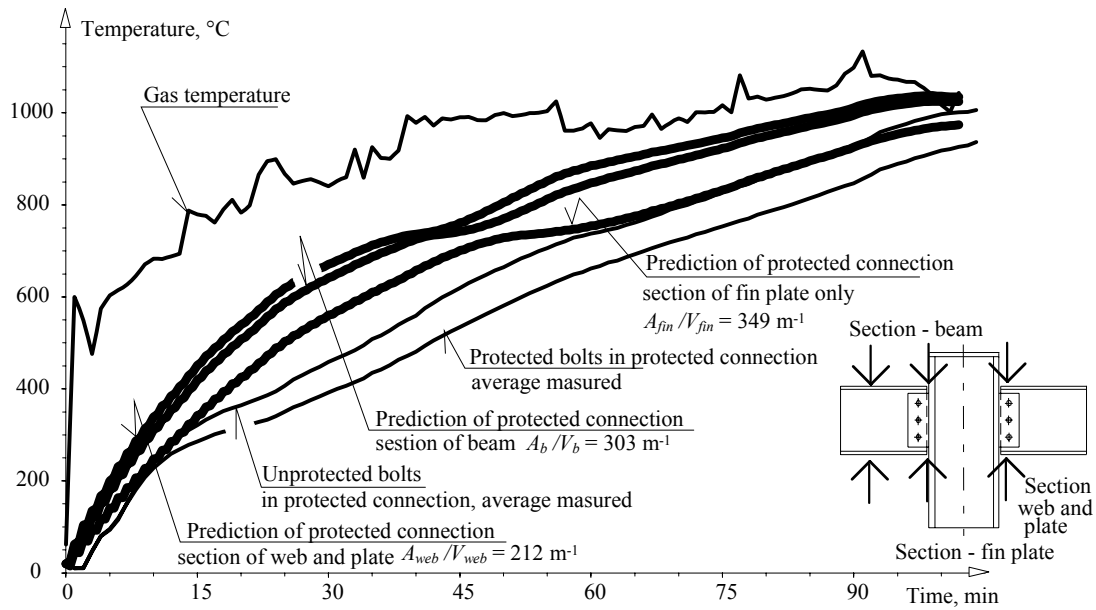


Fig. 6 – Comparison of predicted temperature in connection by section factors of the parts forming the connection to the measured values, test No. 3

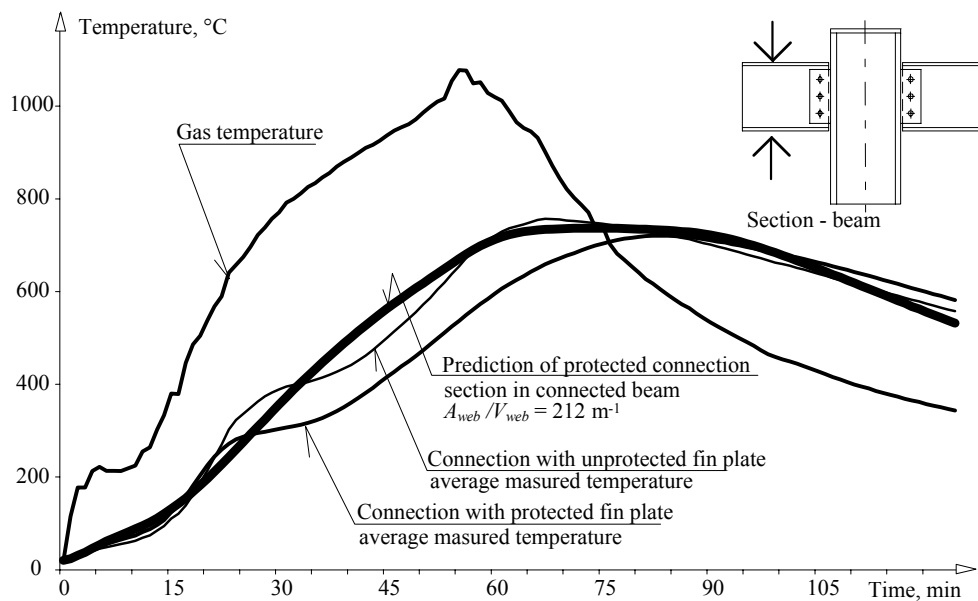


Fig. 7 – Comparison of predicted temperature in connection by section factors of the parts forming that connection to the measured values, test No. 2

4. CONCLUSIONS

The bolted fin plate connection fire protected by intumescent coating with unprotected bolts showed till 17 % higher temperature compare to the connection with protected bolts.

The test shows a conservative estimation of the connection temperature according to European standard by analytical prediction model based on the section factor of the connected member and estimated material properties of expanded coating. The conservative prediction by section factor is covering also the increase of temperature due to unprotected bolt.

To extend the result of presented tests by a FE study, which is directed to the influence of the fire scenario and to the connection geometry/type to the temperature of the connection with the fire unprotected bolts in the fire protected connection, is under preparation.

ACKNOWLEDGEMENT

The authors would like to thank the company Promat for the support with intumescent coating Promapaint[®], which was used for experiments with wet average thickness 3731 μm and dry average thickness 2500 μm which is recommended for protection of structure with $A/V = 200 \text{ m}^{-1}$ till 60 min. This outcome has been achieved with the financial support of the Czech Ministry of Education, Youth and Sports, project No. 1M680470001, within activities of the CIDEAS research centre.

REFERENCES

- [1] Wald F., Chladná M., Moore D.B., Santiago A., Lennon T.: Temperature distribution in a full-scale steel framed building subject to a natural fire, *Steel and Composite Structures*, Vol. 6, No. 2, pp.159-182, ISSN 1229-9367.
- [2] Kruppa J.: Résistance au feu des assemblages par boulons haute résistance. C.T.I.C.M., Puteaux, 1976.
- [3] Leston-Jones L.C., Burgess I.W., Lennon T., Plank R.J.: Elevated temperature moment-rotation test on steelwork connections, *Proceedings of Institution of Civil Engineers, Structures & Buildings*, 122 (4), pp. 410-419, 1997.
- [4] Al-Jabri K.S., Lennon T., Burgess I.W., Plank R.J.: Behaviour of steel and composite beam-column connections in fire, *Journal Constructional Steel Research*, Vol. 46, pp. 1-3, 1998.
- [5] The Steel Construction Institute: Enhancement of fire resistance of beams by beam-to-column connections, Technical report, SCI Publication 086, 1990.
- [6] EN 1993-1-2: 2005, Eurocode 3: Design of steel structures, General rules, Structural fire design, CEN, Brussels 2005, p. 78.
- [7] EN 1993-1-2: 2005, Eurocode 3: Design of steel structures, General rules, Design of joints, CEN, Brussels 2005, p. 133.
- [8] Newman L.C., Dowling J.J., Simms W.I.: Structural fire design: Off-side applied thin film intumescent coatings, Second edition, SCI P160, p. 39, ISBN 1-5942-162-8.
- [9] Fire protection for structural steel in buildings. 3rd Edition, Association for Specialist Fire Protection, The Steel Construction Institute and Fire Test Study Group, 2004.
- [10] Tichá A., Wald F., Uhlíř, A.: Temperature of the Fin Plate Bolted Connection Exposed to Fire, in Czech, in *Teoretické a konstrukční problémy ocelových a dřevěných konstrukcí - Lhké ocelové konstrukcie*, Bratislava, Slovak University of Technology, 2005, p. 261-266. ISBN 80-227-2298-7.



BEHAVIOUR AND DESIGN OF BEAM-TO-COLUMN CONNECTIONS UNDER FIRE CONDITIONS

N.H. Ramli SULONG¹, A.Y. ELGHAZOU LI² and B.A. IZZUDDIN³

ABSTRACT

In this paper, an analytical model for steel connections is presented and discussed. The model follows the component-based approach and is capable of simulating the behaviour of typical connection configurations in both steel and composite framed structures. Monotonic and cyclic loading conditions can be represented at ambient as well as elevated temperatures. The implementation is undertaken within the advanced finite element program ADAPTIC which accounts for material and geometric nonlinearities, and incorporates several temperature-dependant material models and structural elements. Validation of the proposed connection model is carried out by comparison against a range of available experimental results for several joint types and loading conditions. A series of sensitivity studies are then presented in order to demonstrate the scope of application of the proposed model, and to examine the influence of the connection behaviour on the overall structural performance in fire. A number of structural configurations are investigated starting from isolated members and reaching more detailed representations. Several factors are examined including connection type, boundary conditions and temperature effects. Finally, the implications of this investigation on structural fire design are assessed, and the key design parameters related to connection design are examined.

1. INTRODUCTION

Recent experimental investigations dealing with the performance of steel and composite buildings under fire conditions have provided greater insight into the actual behavioural mechanisms that occur at elevated temperature. This has led to a wide recognition of the inadequacy of current design procedures which are largely based on the response of

¹ Department of Civil Engineering, University of Malaya, 50603 Kuala Lumpur, Malaysia
e-mail: hafizah_ramli@um.edu.my

² Department of Civil and Environmental Engineering, Imperial College London, SW7 2BU, UK
e-mail: a.elghazouli@imperial.ac.uk

³ Department of Civil and Environmental Engineering, Imperial College London SW7 2BU, UK
e-mail: b.izzuddin@imperial.ac.uk

isolated members with idealised end conditions. Consequently, there has been a growing need for the development of performance-based design procedures which can provide a more rational representation of the behaviour. In order to perform further studies for the purpose of implementing new findings into design guidance, it is important to provide analytical tools, which are capable of capturing key features of the behaviour in a realistic manner. It should be noted that under fire situations, the effects of beam thermal expansion and membrane action can induce significant axial forces in the connection. In addition, due to load redistributions that occur during a fire, strain reversals frequently occur. Consequently, it is important that a connection model is able to incorporate axial load interaction effects as well as cyclic loading conditions.

This paper briefly describes the development of an analytical model for connections using the component-based approach. The model is capable of representing connection response under ambient and elevated temperature, and generalized loading conditions including possible load reversals. The model is implemented within the nonlinear finite element program ADAPTIC [1]. Several studies are carried out in order to verify the reliability and stability of the model for various connection configurations under ambient and elevated temperature conditions. Selected sensitivity studies are also presented in order to illustrate the influence of salient parameters on the local connection behaviour as well as overall structural response. Several configurations are considered covering isolated members as well as floor sub-assemblages. Finally, some design considerations related to connection response are discussed.

2. CONNECTION MODELS

2.1 Component Representation

The component-based method is employed for the connection models as it combines relatively realistic representation, based on actual geometric and material properties, with computational efficiency. The approach requires identification of active components, evaluation of force-deformation relationships and assembling of component characteristics to obtain the overall joint response.

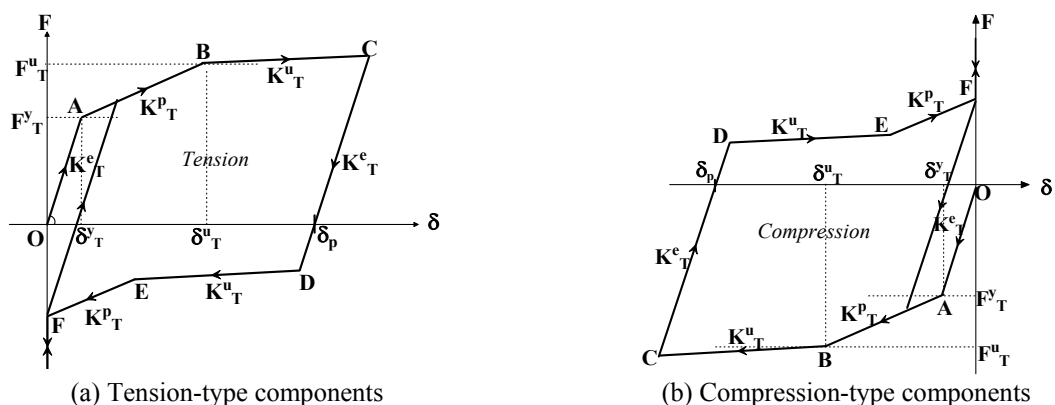


Fig.1 – Tri-linear force displacement cyclic relationships [2]

A mechanical model, which consists of two rigid bars representing the column centreline and the beam end, is typically utilised. These bars are connected by a series of nonlinear springs which model the various components. In evaluating the force-deformation relationship of each idealised component, the strength and stiffness properties are determined based on underlying mechanics principles, coupled with evidence from available experimental

studies. Tri-linear monotonic force-deformation characteristics are formulated, and then extended to account for cyclic loading, as illustrated in Fig. 1.

In this study, end-plate connections (flush and extended forms), connections with angles (top and seat and/or web angles) and fin-plate connections have been considered. Within these connection configurations, the active components identified include: bolts in tension/shear, end plate in bending, column flange in bending, beam flange in bearing, beam web in bearing/bending/tension, top/seat angle in bearing/bending/tension and plate in bearing/shear/tension. Detailed relationships and representations of force-displacement curves for the various active connection components are presented elsewhere [2]. In developing the cyclic response of the component force-deformation curve, Massing's rule is adopted for the construction of the unloading and reloading paths. In tension, active components vary depending on their geometry and position within the connection. For the compression components, it is typically assumed that only the column web in compression significantly contributes to the behaviour as suggested in previous studies [3, 4]. On the other hand, for the shear panel, the column web governs the behaviour but this component only needs to be activated when unbalanced moments exist in the connection.

To account for the influence of elevated temperature, parameters such as the elastic modulus, yield stress and ultimate strength, which represent the stiffness and strength of components, are varied with temperature. Default temperature-dependent properties are based on available information for plate and bolt materials [5, 6], but these properties are user-defined and can be modified if necessary. The model can also incorporate temperature distributions within the joint, as each component can be treated separately. Quadratic temperature variation along the depth of a segment is adopted, which enables an accurate representation of temperature in each component. It should however be noted that the effect of thermal expansion within the connection components is not included in this study.

2.2 Overall Joint Response

Non-linear procedures, based on the cyclic representation of the load-deformation temperature-dependent models of the active components, have been developed [2] and implemented within ADAPTIC [1]. For connections subjected to combined axial force and bending moment, the displacement, δ_i at any connection layer 'i' is given as:

$$\delta_i = u - \phi y_i \quad (1)$$

in which: 'u' is the horizontal displacement due to axial force, ' ϕ ' is the rotation of the connection, and ' y_i ' is the distance of the layer 'i' to the beam mid-depth.

Knowing a layer deformation ' δ_i ', the layer force ' f_i ' is obtained from the nonlinear load-deformation curve of the weakest component in the spring series. The layer force is summed up to obtain the total connection axial force 'N' and consequently the connection moment 'M', for 'n' number of layers, as follows:

$$N = \sum_{i=1}^n f(\delta_i) \quad (2)$$

$$M = -\sum_{i=1}^n f(\delta_i) y_i \quad (3)$$

The connection stiffness matrix, K is then represented as:

$$[K] = \begin{bmatrix} \left(\frac{\partial N}{\partial u} \right) & \left(\frac{\partial N}{\partial \phi} \right) \\ \left(\frac{\partial M}{\partial u} \right) & \left(\frac{\partial M}{\partial \phi} \right) \end{bmatrix} \quad (4)$$

Full details of the numerical and implementation procedures are given elsewhere [2].

2.3 Validation Studies

The connection models developed were extensively validated against available experimental results on connections subjected to ambient monotonic and cyclic loading. It should be noted however that connection tests at elevated temperature are limited, hence comparisons were made with available experimental results which do not cover all types of connection incorporated in the models. This also points out to the need for further experimental studies. In general, good agreement was obtained between the numerical simulations and experimental results. Only a couple of representative results are presented in this section to illustrate the general reliability of the models, focusing on elevated temperature situations. Details of the full-range of validation studies are reported by Ramli Sulong [2].

As a typical example for results under elevated temperature, Fig. 2 shows the comparison between analytical simulations using ADAPTIC and experimental force-displacement curves obtained for a T-stub component (Specimen AA1) tested by Spyrou [7] for different steady-state temperatures.

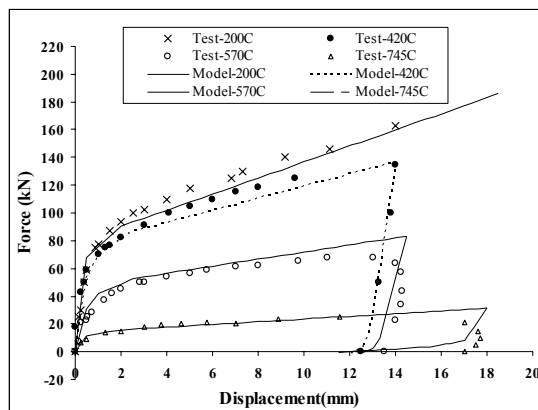


Fig. 2 - Force-displacement response of T-stub at elevated temperature for Test AA1 by Spyrou [7]

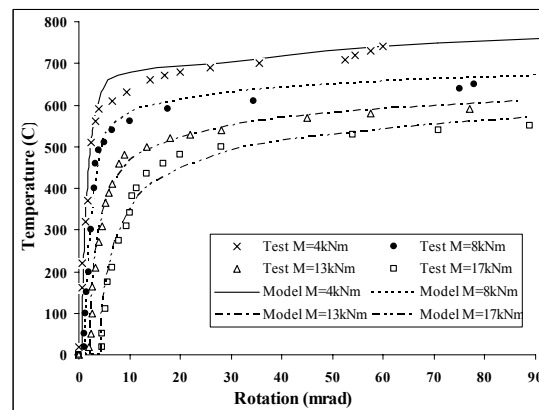


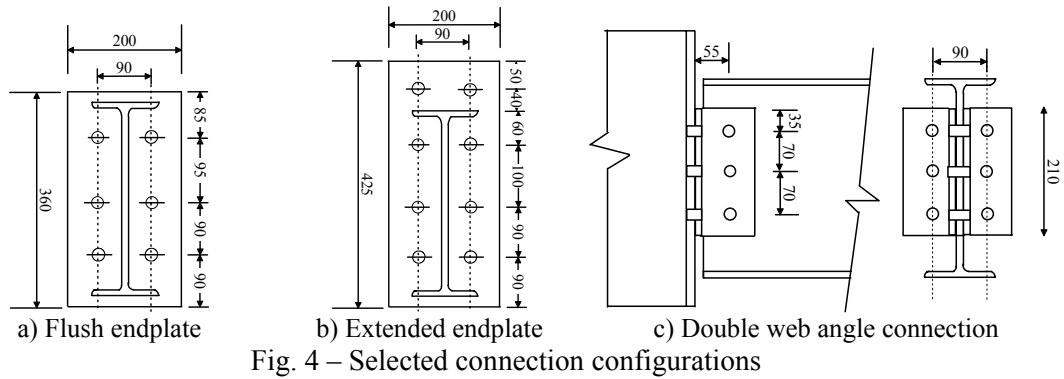
Fig. 3 - Anisothermal temperature-rotation response for flush endplate test by Al-Jabri [4]

Another example is depicted in Fig. 3 for a flush endplate connection tested at elevated temperature by Al-Jabri [4]. The figure shows the case of anisothermal loading at four levels of constant moment. The analytical-experimental comparisons are shown in terms of temperature-rotation response. As in other validation studies, good correlation between numerical simulations and experimental results is generally observed. However, some discrepancies are inevitable due to the sensitivity of the results to modelling idealisations and simplified temperature-dependent material representations.

3. PARAMETRIC INVESTIGATIONS

A series of sensitivity and parametric studies was carried out, and various factors influencing the response for steel and composite structures were investigated [2]. Emphasis was given to the influence of axial effects on the response. The main trends and observations are summarised herein.

Three connection types are examined, namely double web angles, flush endplate and extended endplate, as indicated in Fig. 4. In all cases, the connection is used in conjunction with a beam of size UB 305 x 127 x 37, column of size UC 254 x 254 x 73 and Grade 8.8 M20 bolts.



The ambient monotonic response of the three selected connections in tension, compression and moment is shown in Fig. 5a, 5b and 5c respectively. The capacity of the double web angle connection (dwa) is reached by yielding of the angle in bending followed by yielding of the column flange in bending. For the flush endplate connection (fep), plasticity is governed by yielding of the endplate in bending, followed by yielding of the column flange in bending. A similar plastic mechanism is also observed in the extended endplate configuration (extep).

In order to study the influence of connection type on the beam response, an unrestrained beam of span 5 m is subjected to a point load at mid-span. The relationships between load and displacement at mid-span are depicted in Fig. 6.

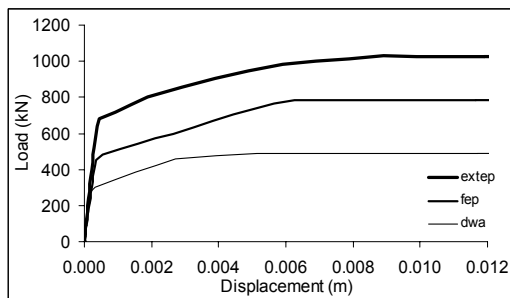


Fig. 5 a) - Load-displacement curves in tension

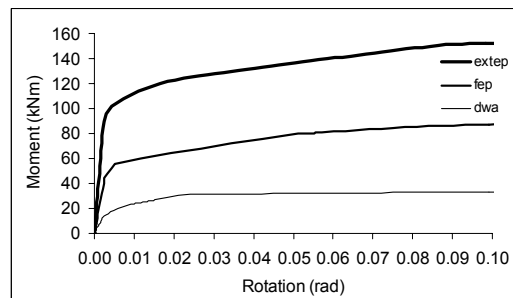


Fig. 5 c) - Moment-rotation curves

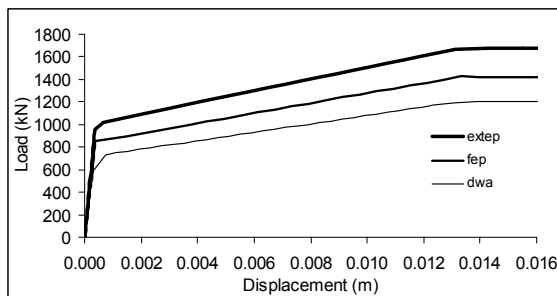


Fig. 5 b) - Load-displacement in compression

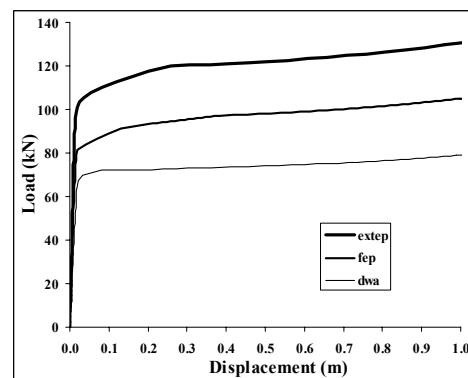
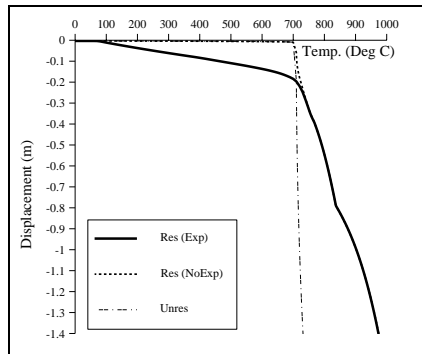


Fig. 6 - Load-displacement curves for unrestrained beam incorporating the three connections

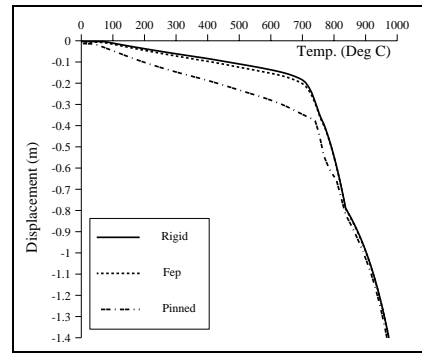
3.1 Boundary Conditions

The support conditions of a steel beam may vary from full restraint to unrestrained conditions with a range of intermediate cases offering various levels of axial and rotational restraint. Clearly, these conditions may have a significant effect on the distribution of internal

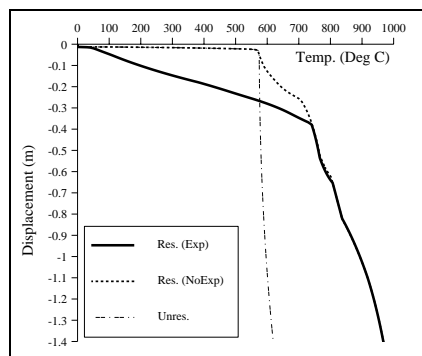
forces and deformations within a member. More accurate beam response can be represented by incorporating the actual connection details. Three support conditions are considered herein, namely rigid, pinned and the flush endplate connection (representing a semi-rigid partial strength case) with and without axial restraint. These are adopted to investigate the influence of the axial and rotational restraint of the joint on the beam response. The beam is subjected to a concentrated load at mid-span with a load ratio of 0.6 followed by a linearly increasing temperature. The temperature versus mid-span deformation curves for restrained beams with and without thermal expansion (i.e. Res. (Exp) and Res. (NoExp)), as well as the case of an axially unrestrained beam (Unres), are shown in Fig. 7a to 7c respectively.



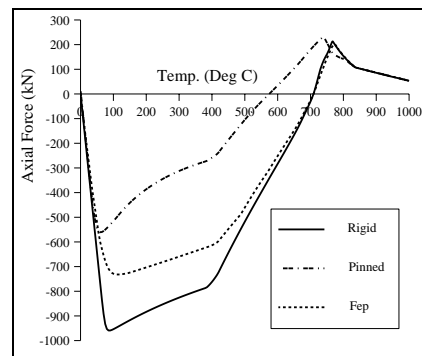
(a) rigid connection



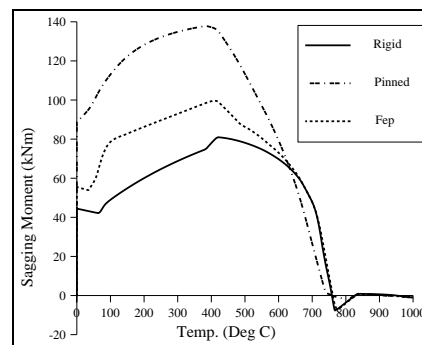
(b) flush endplate connection



(c) pinned connection



(b) axial forces at beam ends



(c) mid-span moments

Fig. 7 – Displacement-temperature response for a steel beam with various connections

Fig. 8 – Action effects in a an axially-restrained beam with various connection configurations

Generally, for all support conditions, the beam failure temperature is higher for restrained cases compared to unrestrained beams. For a restrained beam, thermal expansion causes an early buckling of the beam due to compressive loading followed by a rapid rise in displacement at mid-span. The response of the two restrained cases (with and without

expansion) is similar after around 730°C , when tensile membrane action prevails due to large displacement and loss of bending stiffness.

By comparing the restrained beam response with three support conditions, as shown in Fig. 8, the effect of rotational restraint can be observed. The restrained beam with pinned connection shows larger mid-span deformation at lower temperature due to the absence of rotational restraint at the beam end. On the other hand, beams with flush endplate and rigid connections show very similar response. By examining the axial forces at the support, the induced compressive forces vary for different support conditions depending on the rigidity of the connection. The compressive forces increase with increasing rotational restraint due to lower flexural buckling length of the beam and higher axial buckling capacity. Also, using the flush endplate connection reduces the mid-span moment compared to the pinned connection.

3.2 Temperature Effects

In this section the effect of temperature on the beam and connection response is examined. Two factors are considered here: thermal expansion and cooling. A fully restrained steel beam of 5 m span incorporating a flush endplate connection (Fig. 4a) is subjected to an initial load representing a load ratio of 0.6. Subsequently, a linear temperature history is applied uniformly along the beam up to a centroidal beam temperature T of 1000°C . For all cases, the temperature is assumed as $0.9T$ and $1.0T$ at the top and bottom of the beam section, respectively, and the connection temperature is considered as $0.7T$, uniformly distributed along its depth.

The influence of thermal expansion (i.e. with and without thermal expansion) under transient response is depicted in Fig. 9 in terms of temperature-axial load. Initially, restraint to thermal expansion induces high compressive force in the connection. Due to the applied initial load, the compressive effect is released around T of 100°C . At higher temperature (around $T = 750^{\circ}\text{C}$), the beam deflection with and without thermal expansion converge when beam tensile membrane action in the beam starts to dominate the response.

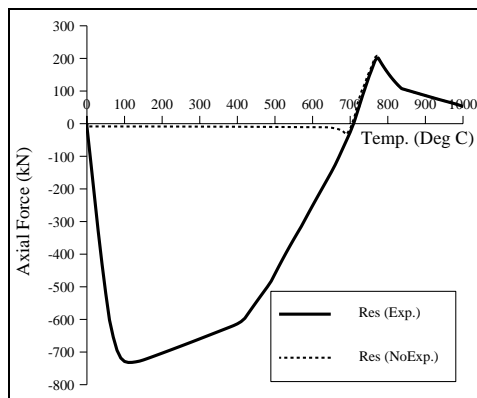


Fig. 9 - Effect of thermal expansion on the connection axial force

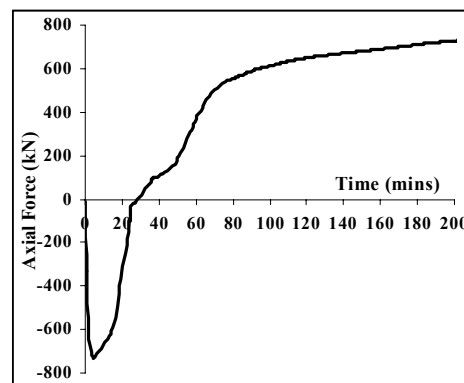


Fig. 10 - Time-axial force in the connection under the effects of heating and cooling

Recent fire tests have shown that the response in the cooling phase can also be important. This is particularly the case if significant tensile forces develop in connections. In order to illustrate this effect, the beam is assumed to follow a more realistic time-temperature representation [8]. During the cooling stage, high tensile forces are induced in the flush endplate connection as depicted in Fig. 10, approaching its tensile capacity. This highlights the importance of accounting for the full duration of fire loading in assessing structural response where in some cases the connection capacity may prove to be a limiting factor.

3.3 Composite System

In this section, the influence of connection type on the response of a restrained composite beam is examined, by considering one of the full-scale fire tests (Test 1) carried out at Cardington. Details of the composite floor models and connection configuration are given elsewhere [2, 9]. The structural model covers part of the floor as indicated in Fig. 11a. Average temperature distribution in the main elements, are considered as shown in Fig. 11b.

The overall structural behaviour of the floor system for Test 1 is presented in the time-displacement curve at mid-span of the heated beam as shown in Fig. 11c. It should be noted that, in this test, the beam deflection is largely driven by thermal expansion effects due to the high level of axial restraint from the surrounding cold structure coupled with the low effective load ratio [9].

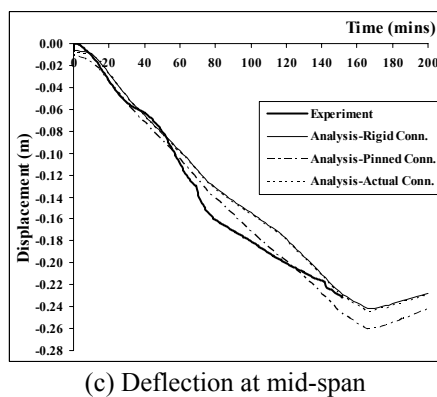
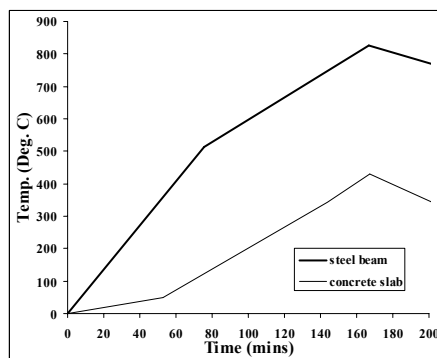
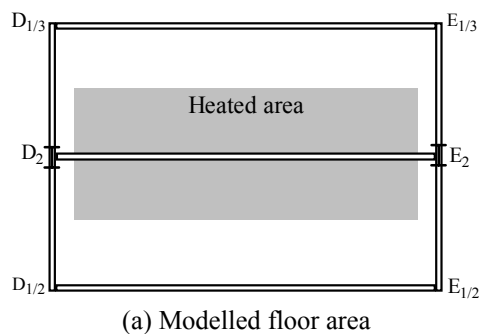


Fig. 11 - Response of composite system

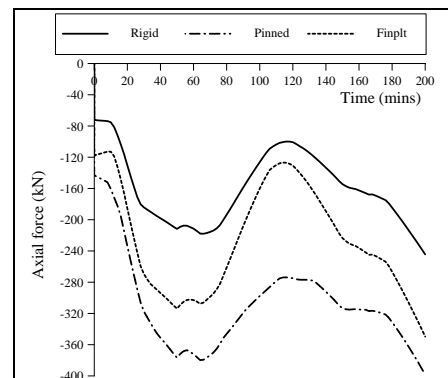
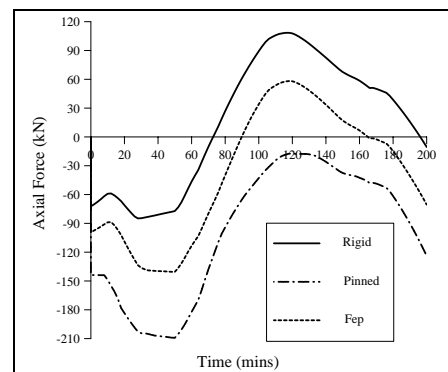
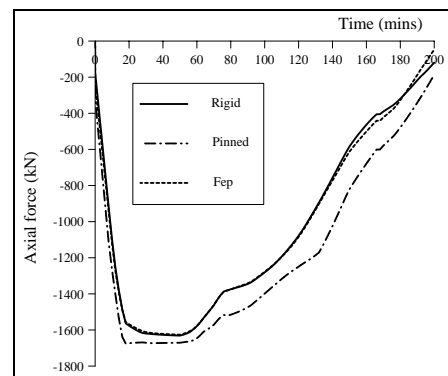


Fig. 12 – Axial force in connections

The experimental result is compared with the predicted deflection for three different beam-to-column and beam-to-beam connection conditions: i) rigid ii) pinned and iii) actual joint configurations where partial endplate is used for beam-to-column connections and finplate is used for beam-to-beam connections. Generally, the predicted models show good agreement compared to the experimental results as shown in Fig. 11c. Slight discrepancy may be attributed to the idealisation used for material properties, temperature distribution, boundary conditions and the use of a grillage model to represent the slab. More importantly, it is evident that the support condition has an insignificant influence on the overall response. This is because at higher temperature when the steel beam yields, the load is resisted by tensile forces that develop in the transverse rib slab [10]. The actual joint configuration gives virtually the same result as the rigid case because throughout the heating stage, the connection is subjected to compression; due to the location of the joint in the minor axis of the column, based on the model, high stiffness is provided by the connection. However, by comparing with the pinned joint, the floor is stiffer if the actual joint configurations are considered.

The effect of different connection conditions at the beam-to-column and beam-to-beam joints in terms of axial force is depicted in Fig. 12. Considerable levels of both strength and stiffness can be achieved by the connection compared to the pinned case and hence have a beneficial effect on the survival time of the structure.

For the heated beam, connected to the column minor axis (Grid Line 2 in Fig. 11a), the response of axial forces against time is shown in Fig. 12a. As shown in the figure, initially the force in the beam end increases with temperature in compression due to the restraint to thermal expansion. Similar trends are observed for the three different support conditions. The axial force in the flush endplate connection is similar to the rigid case because the endplate connection is very stiff in compression when the beam is connected to the minor axis of the column and the response is governed by the plastic capacity of the beam. Beyond $T = 60$ mins, changes in the compression force result from the degradation of material properties in the members.

The effect of the support condition on the unheated member at the beam-to-column joint (at the column major axis D2 in Fig. 11a) and beam-to-beam joint (at Grid Line D1/2) are shown in Fig. 12b and Fig. 12c respectively. The overall axial forces applied on the connection are small compared to the joint connected to the heated member. However, slight variations of axial forces appear for various connection conditions.

4. DESIGN CONSIDERATIONS

In this section, important aspects of connection design are discussed. In particular, emphasis is given to the influence of interaction between axial load and moment. Whilst this is not considered in detail in current design guidance [5], its importance under fire and other loading conditions has been highlighted in this work and in a number of previous studies [11-13]. Hereafter, several design aspects, which have been examined for various connection types [2], are briefly discussed for the case of a flush end plate configuration as an example.

4.1 Rotational Stiffness

Using the analytical model, the influence of the interaction between bending and axial loading on stiffness characteristics is investigated. A flush endplate configuration, shown in Fig. 13 is assumed to be connected to a beam of size UB 305 x 127 x 37. The connection is semi-rigid based on the classification of EC3.

It should be noted that in Part 1.8 of EC3 connection design does not account for significant axial loading. To assess the influence of axial loading on the rotational joint stiffness, the analytical model is utilised whereby different levels of axial load are initially applied, followed by increasing moment until the ultimate capacity is reached. The results are also compared with expressions derived by Cerfontaine and Jaspart [14] as shown in Fig 14.

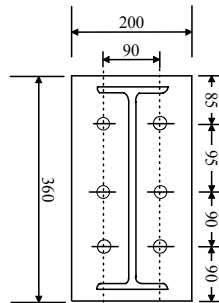


Fig. 13 – Selected connection configuration

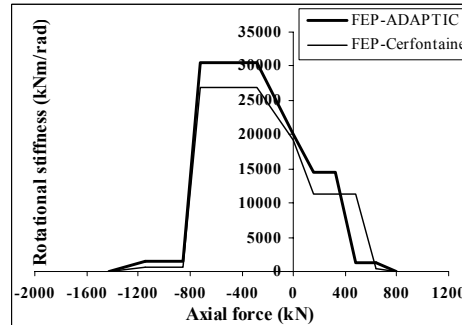


Fig. 14 – Influence of axial load on initial rotational stiffness

As indicated in the figure, the initial rotational stiffness is significantly affected by the axial loading. The slope of rotational stiffness – axial force changes at the specific level when the critical components, such as endplate, column flange in bending or column web in compression, start yielding. It should be noted that under pure moment, EC3 gives lower values compared to those obtained from the analytical model [2]. This is due to simplifications used in EC3 in relation to the location of the centre of rotation.

4.2 Strength Interaction

Using the analytical model, strength interaction curves between moment and axial load can be readily constructed. This is illustrated in Fig. 15 for the example of flush end plate. In this case, the connection is subjected to initially prescribed constant temperature and axial load followed by applied moment. Alternatively, any generalised loading procedure can be considered. The M-N interaction is represented as the ratio of N/N_t against M_{ult}/M_p , where N is the applied axial force, N_t is the axial tensile capacity of the connection in tension, M_{ult} is the ultimate moment resistance, and M_p is the moment capacity under bending action only.

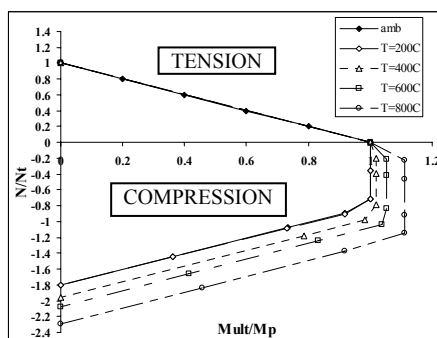


Fig. 15 – Analytical M-N interaction at various temperature levels

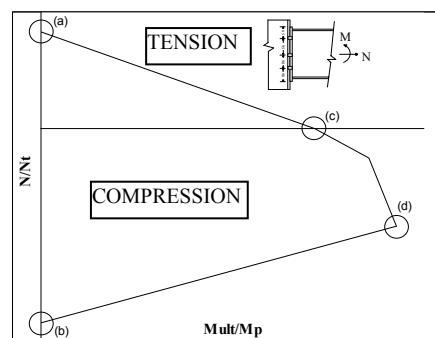


Fig. 16 - Idealised M-N interaction curves for connections

In several configurations, the normalised shape of the interaction curve is not significantly influenced by temperature effects. For the flush end plate case, depending on the N_c/N_t ratio of the connection the compressive axial force increases the moment resistance of

the joint as the pre-compression effect can benefit the components in the tension zone. However, the effect of the initial tensile forces on the joint may reduce the joint moment resistance as the tension force may activate earlier yielding of the components in tension. The M-N interaction curve in the compression region varies with temperature, where higher M_{ult}/M_p ratio is obtained as the temperature increases. This is attributed to the change of plastic mechanisms of the endplate in bending (which governs the tensile capacity of the connection), mainly due to the degradation of material properties with temperature.

Based on numerical studies of several connection types [2], relatively simple relationships can be utilised in order to derive idealised M-N interaction curves of the form shown in Fig. 16. For a given connection, points (a) to (d) in the figure can be determined without the need for detailed analysis. If component ductility is not limited, full plastic distribution can be assumed hence equilibrium considerations determine the interaction curve. The variation of slope in the curve indicates a change in the plastic mechanism in line with the location of the plastic neutral axis along the connection depth. Such idealised interaction curves can be used to determine the joint resistance subjected to any combination of moment and axial load at any temperature level. This can be of benefit not only for design considerations but also for assisting in interpreting experimental and analytical response of framed structures under fire and other loading conditions.

4.3 Deformation Capacity

The deformation capacity of a joint is obviously governed by the ductility of its constituent components. Generally, the weakest component that governs the joint moment resistance also provides the greatest contribution to the joint deformation capacity. Several studies have been conducted on the ductility of connection components [14, 15], but there is a need for further experimental investigations to quantify these effects.

As noted before, the strength interaction illustrated in Fig. 16 is based on plastic distribution. However, such curves can be readily modified to incorporate ductility limits imposed for the various components [2], hence leading to a reduced surface corresponding to lower tensile/compressive/moment resistance. For example, for a flush end plate configuration, the weakest component in tension would be the end plate in bending, whilst in compression, the column web in compression would govern. Consequently, the deformation ductility limits assigned to these components would determine the reduced interaction curve. These ductility-modified interaction curves could be readily used in assessing limiting criteria in structural frame assemblies especially for partial strength joints where the nonlinear response of the joint can affect the overall response.

5. CONCLUSION

A component-based model is utilised in this paper to assess the behaviour of isolated members and structural assemblages under fire conditions. The model can represent connection behaviour under generalised loading covering ambient and elevated temperature as well as monotonic and cyclic conditions. The influence of connection behaviour on the response of a steel beam is first discussed, followed by an examination one of the Cardington full-scale fire tests carried out on a composite arrangement. Whilst the connection can have a significant effect on the overall response of a steel beam, the contribution of the connection to the overall response in a restrained composite beam becomes significantly less pronounced as expected. Nonetheless, an appropriate representation of the joint is shown to be important for the purpose of assessing the load and deformation levels imposed on the connection itself.

Finally, design aspects related to response of connections under combined moment and axial load are examined, including stiffness and strength properties. Using the analytical model, temperature-dependent strength-interaction curves can be derived for different connection configurations. Alternatively, idealised forms of these curves can be obtained from simple equations based on equilibrium considerations. An important aspect of connection design is related to deformation capacity which can be determined based on the ductility of constituent components. In this context, strength interaction curves can be readily modified to incorporate ductility limits in various connection components although this is an aspect that appears to require further experimental examination.

6. REFERENCES

1. Izzuddin, B.A. "Nonlinear Dynamic Analysis of Framed Structures", Imperial College London, 1991.
2. Ramli Sulong, N.H., "Behaviour of Steel Connections under Fire Conditions", PhD thesis, Imperial College London, University of London, 2005.
3. Leston-Jones, L. C., "The Influence of Semi-Rigid Connections on the Performance of Steel Framed Structures in Fire", University of Sheffield, 1997.
4. Al-Jabri, K. S., "The Behaviour of Steel and Composite Beam-Column Connections in Fire", University of Sheffield, 1999.
5. European Committee for Standardisation, "Eurocode 3: Design of Steel Structures Part 1.8: Design of Joints", Brussels, 2003.
6. Kirby, B. R., "The Behaviour of High-strength Grade 8.8 Bolts in Fire", Journal of Constructional Steel Research, 33(1-2), pp. 3-38, 1995.
7. Spyrou, S., "Development of a Component-Based-Model of Steel Beam-to-Column Joints at Elevated Temperature", University of Sheffield, 2002. Bailey, C.G., Burgess, I.W., and Plank, R.J., "Analyses of the Effects of Cooling and Fire Spread on Steel-framed Buildings", Fire Safety Journal, 26(4), pp. 273-294, 1996.
8. Bailey, C.G., Burgess, I.W., and Plank, R.J., "Analyses of the Effects of Cooling and Fire Spread on Steel-framed Buildings", Fire Safety Journal, 26(4), pp. 273-294, 1996.
9. Elghazouli, A. Y., and Izzuddin, B. A., "Response of Idealised Composite Beam-Slab Systems under Fire Conditions", Journal of Constructional Steel Research, 56(3), pp. 199-224, 2000.
10. Gillie, M., Usmani, A.S. and Rotter, J.M., "A Structural Analysis of the First Cardington Test", Journal of Constructional Steel Research, 57, pp. 581-601, 2001.
11. Jaspart, J.P., Braham, M., and Cerfontaine, F., "Strength of Joints Subjected to Combined Action of Bending Moments and Axial Forces", EuroSteel '99, Prague, pp. 465-468, 1999.
12. Simoes da Silva, L., De Lima, L. R. O., Da S. Vellasco, P. C. G., and De Andrade, S. A. L., "Behaviour of Flush Endplate Beam-to-Column Joints under Bending and Axial Force", Steel and Composite Structures, 4(2), pp. 77-94, 2004.
13. Cerfontaine, F. and Jaspart, J.P., "Analytical Study of the Interaction between Bending and Axial Force in Bolted Joints", Eurosteel 2002, Coimbra, pp. 997-1006, 2002.
14. Simoes da Silva, L., and Coelho, A. G., "A Ductility Model for Steel Connections", Journal of Constructional Steel Research, 57(1), pp. 45-70, 2001.
15. Kuhlmann, U., Davison, J.B., and Kattner, M., "Structural Systems and Rotation Capacity", Proceeding of COST Conference on Control of the Semi-Rigid Behaviour of Civil Engineering Structural Connections, Liege, Belgium, pp. 167 – 176, 1998.

Structural Behaviour



3D MODELLING OF BI-STEEL STRUCTURES SUBJECT TO FIRE

Chaoming YU¹, Z. HUANG², I. W. BURGESS³ and R. J. PLANK⁴

ABSTRACT

This research is aimed at analysing the performance in fire of Bi-Steel panels used predominantly as compressive structures, such as building cores. In this paper, thermal behaviour of the Bi-Steel panel is analyzed, and a series of parametric studies are carried out. A further object of this research is to develop a non-linear procedure for modelling of the structural behaviour of Bi-Steel panels subject to fire. In this procedure, the Bi-Steel panel has been represented as an assembly of steel plates, a concrete core and steel bar connectors, using three-dimensional brick elements, and both material and geometric non-linearities are considered.

1. INTRODUCTION

Traditional steel-concrete-steel double-skin composite construction (DSC) consists of a core of concrete sandwiched between two thin steel plates. The overlapping steel studs, which act as transverse shear reinforcement, transfer the normal and shear forces between the concrete and steel plates¹. However, since each shear stud in DSC is only connected to one steel plate, there is no continuous bond maintained between the concrete core and the plates. Lack of full composite action could be one reason for the failure of this type of structure.

¹ PhD student, Department of Civil and Structural Engineering, University of Sheffield, S1 3JD, UK.
Email: c.yu@sheffield.ac.uk

² Lecturer, Department of Civil and Structural Engineering, University of Sheffield, S1 3JD, UK.

³ Professor, Department of Civil and Structural Engineering, University of Sheffield, S1 3JD, UK.

⁴ Professor, School of Architectural Studies, University of Sheffield, S10 2TN, UK.

The Bi-Steel panel, which is composed of two steel facing plates connected by an array of transverse friction-welded shear connectors and filled with concrete, was developed by Corus Group Ltd from DSC. In this structure, the steel faceplates provide resistance to both in-plane and bending forces. This is because the faceplates are equivalent to a significant area of steel reinforcement, and are in the optimal position to maximise bending resistance. The steel bar connectors are multi-functional, and provide shear reinforcement to the concrete core. They carry longitudinal shear flow between the faceplates and the concrete core, prevent buckling of the faceplates, and provide a permanent tie between the front and rear plates. Concrete provides resistance to compressive and shear forces. Normally, it is placed within the voids after panel erection has been finished on site, with the steel faceplates acting as formwork, enabling high concreting pressures to be sustained during construction. When faceplates connect to one another and to the concrete core, the entire Bi-Steel section behaves as a single composite rather than as individual elements. This structural system has several useful features, including enhanced blast and fire resistance, thickness reduction in core walls, leak resistance, and optimization of site work and site time².

At ambient temperature, the structural behaviour of Bi-Steel panels has been studied during recent years. This work has focused on analyzing the shear and tensile performance of the steel bar connectors, and the composite action between the concrete core and the steel faceplates³⁻⁶. Experimental testing and finite element methods have been used in these studies. The following structural characteristics have been found:

- 1) The Bi-Steel panel has significant shear capacity when it is subject to push-out loading. The shear strength is affected by several parameters, including plate spacing, connector spacing and shear connector diameter. A smaller connector spacing in the Bi-Steel panel produces increased slip and a lower failure load³.
- 2) The shear strength of a Bi-Steel panel with thin faceplates is governed by the strength of the plates. The shear strength of a panel with thick plates is governed primarily by the fracture strength of the friction weld⁴.
- 3) The Bi-Steel panel has high ductility and deformation capacity.

However, there have been few studies of the behaviour in fire of Bi-Steel components or structures. At elevated temperatures, the capacity of Bi-Steel panels for carrying load will be reduced. The strength and stiffness of both steel and concrete are reduced by the high temperatures, and this combines with the curvatures and stresses caused by the thermal gradient, which reduce the buckling resistance of the steel plates. Hence, the structural characteristics and stress situations within a Bi-Steel panel in fire can be very complicated.

In the building fire resistance context, it is necessary to do some detailed research in this field. For Bi-Steel panels, the calculation of fire resistance involves the determination of temperature distribution, deformation and stress under various types of loading.

2. THERMAL ANALYSIS

2.1 3D heat transfer simulation

The finite element analysis software ABAQUS was used to generate temperature

information. A Bi-Steel panel without additional fire protection, exposed to the standard ISO 834 fire, is presented for thermal analysis. Material properties are illustrated in Table 1.

Table 1 Summary of material properties used in analysis

Component	Dimension L×H×t / diameter (mm)	Density (kg/m ³)	Material grade	Strength (MPa)	Moisture content by weight (%)
Steel faceplate	200×200×15	7850	S355JR	355	
Steel bar connector	25	7850	070M20	370	
Concrete	200×200×200	2400	C45	45	5

The emissivity of the fire is taken as 0.8, and the coefficient of heat transfer by convection is $25 \text{ W/m}^2\cdot\text{K}^7$. Other values of thermal properties, such as the specific heats and the thermal conductivities of both steel and concrete, are given in EN 1994-1-2⁸.

Because of the inherent symmetry of the case, only a cuboid of Bi-Steel was considered here (see Fig. 1). Due to the basic theory of the finite element method, the model required is a mesh of nodes and elements. 3D diffusive heat-transfer solid elements (DC3D8) were chosen to represent the steel and the concrete within ABAQUS. Since the mesh density of elements has an influence on the accuracy of calculation, some sensitivity analyses had to be undertaken to determine the appropriate mesh of elements. On the basis of the results of the sensitivity analysis, the Bi-Steel model was divided into 729 DC3D8 elements and 1000 nodes. For the sake of convenience, the steel bar connector was also represented by a column of 8-node solid elements, with cross-section equal to the real area.

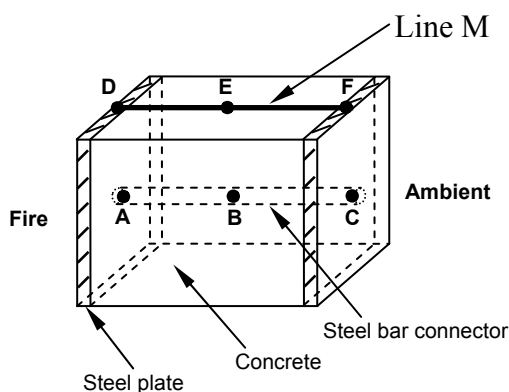


Fig. 1 – Typical 3D Bi-Steel model

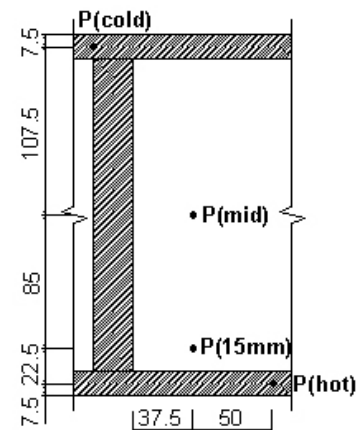
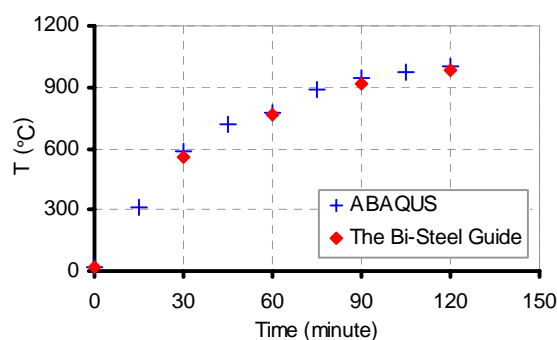
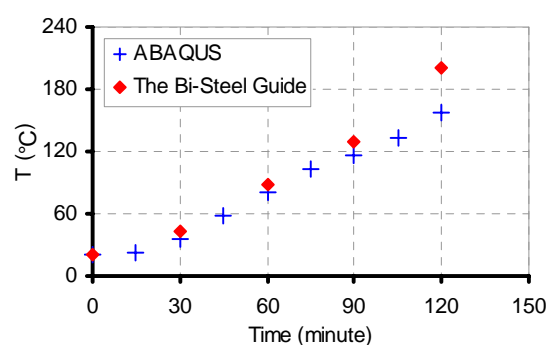
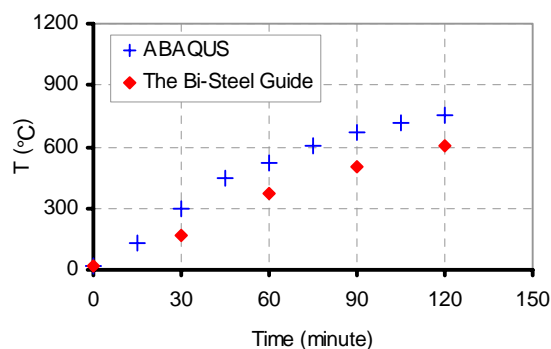
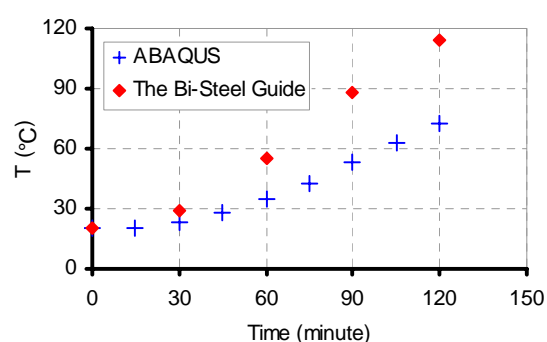


Fig. 2 – Key points used in heat transfer analysis

Uncoupled heat transfer analysis, which calculates the temperature field including the effects of conduction, forced convection and boundary radiation, but without any knowledge of the stress and deformation state being studied, was chosen as the analysis type defined within ABAQUS. Results generated were compared with the temperature values provided by the 'Bi-Steel Design and Construction Guide' (referred to as The Bi-Steel Guide in the following parts of this paper). The compared key positions are shown in Fig. 2. As the following charts (Figs. 3 to 6) show, at the point $P(hot)$, the histories of steel temperatures

However, at points $P(cold)$ and $P(15mm)$ (which is 15mm away from the heated faceplate), there are significant (up to 66%) differences in temperature between ABAQUS and The Bi-Steel Guide (Figs. 5 and 6). This inconsistency might be induced by the different values of thermal properties implied in ABAQUS analysis and The Bi-Steel Guide. In the latter case their values are not specified, even though they are based on EN 1994-1-2. Additionally, from the information provided by The Bi-Steel Guide, it seems likely that only 2D thermal analysis was conducted.

Fig. 3 – Temperatures at $P(hot)$ Fig. 4 – Temperatures at $P(mid)$ Fig. 5 – Temperatures at $P(15mm)$ Fig. 6 – Temperatures at $P(cold)$

2.2 Analysis of the influence of thermal parameters

In order to analyze the thermal behaviour of the Bi-Steel panel properly, some parametric studies have been carried out in this research. These have focused on studying the effects of heat flux, concrete moisture content, the emissivity of the fire, and the steel bar connector properties on the temperature distributions of the model.

2.2.1 Effect of heat flux

Since the nature of a real fire depends on the fire load density and ventilation conditions, it is effective to use two extreme constant heat fluxes representing a range of different fire conditions. Here, the higher heat flux employed in this paper is $40,000\text{W/m}^2$ which was calculated according to the Hydrocarbon fire curve, and the lower is $20,000\text{W/m}^2$. The temperature distributions along the steel bar connector and the line M (see Fig. 1) at 30 and 60 minutes fire time are plotted in Figs. 7 and 8. The temperature gradient between the

The temperature distributions along the steel bar connector and the line M (see Fig. 1) at 30 and 60 minutes fire time are plotted in Figs. 7 and 8. The temperature gradient between the two steel faceplates is very large. Moreover, even with extremely large heat flux, at 60 minutes the temperature of the cold surface is below 40°C.

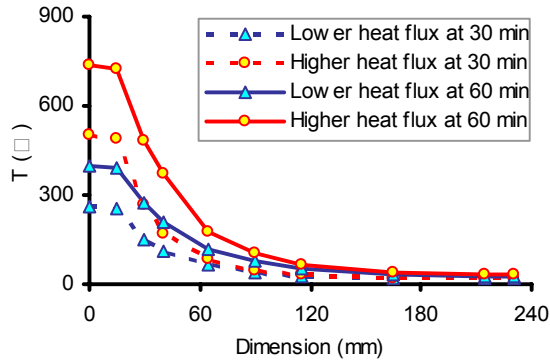


Fig. 7 – Temperature distributions along steel bar connector

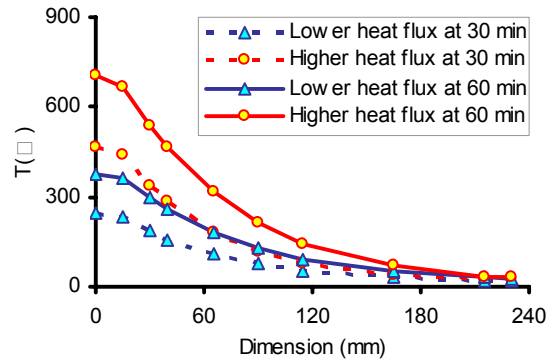


Fig. 8 – Temperature distribution along the line M

2.2.2 Effect of concrete moisture content

Since the moisture content of concrete can affect the peak value of specific heat, the temperature distribution of the model can change with it. In this paper, two values of moisture content (0% and 5% by weight) have been used in analysis. From Figs. 9 and 10 it is evident that the influence of moisture content on the temperature distribution is significant (with up to 45% difference) within the central area of the Bi-steel section, but insignificant within the area close to the hot surface. This is because, at $P(15mm)$, the fire temperature and emissivity have a greater influence on the temperature distribution than the moisture content. Overall, however, the moisture content of concrete is an important factor in the thermal analysis of the Bi-Steel panel.

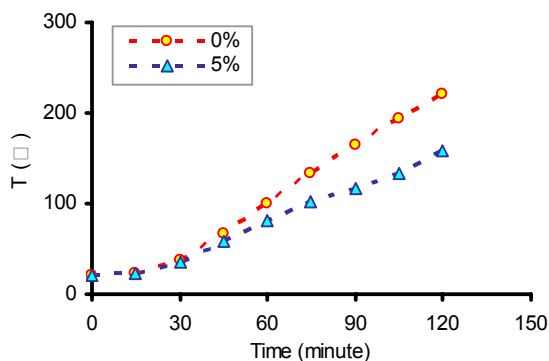


Fig. 9 – Concrete temperature variation at $P(mid)$

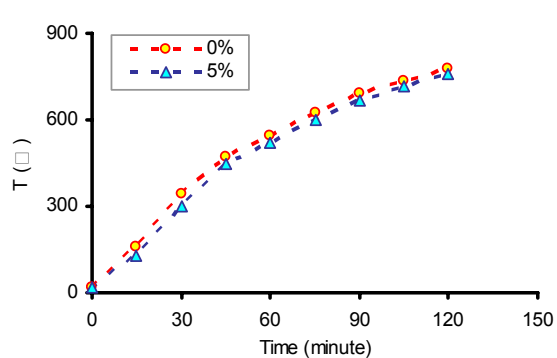
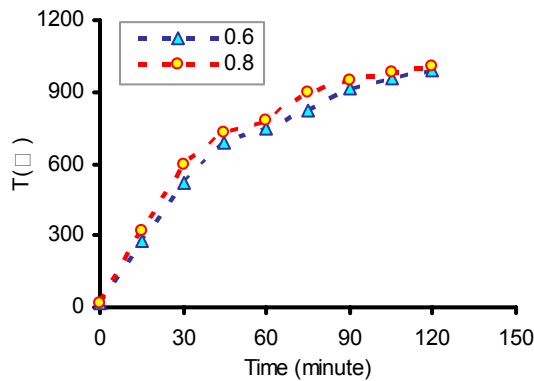
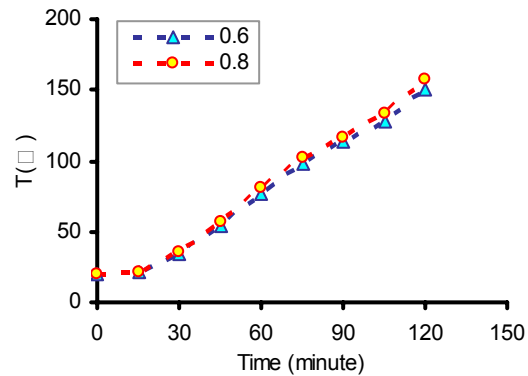


Fig. 10 – Concrete temperature variation at $P(15mm)$

2.2.3 Effect of the emissivity of fire

The emissivity of a fire is a function of the size of the flame and varies between fuel

types. Results generated by numerical modelling, in which the emissivity of fire was changed from 0.6 to 0.8, are plotted in Figs. 11 and 12. It can be seen that there is a slightly larger difference in the temperature variation of the hot steel faceplate (about 10%) than that in the temperature variation of mid-plane concrete (about 5%). Therefore, it is inferred that the fire emissivity is not a significant parameter to this temperature generation analysis.

Fig. 11 – Temperatures at $P(hot)$ Fig. 12 – Temperatures at $P(mid)$

2.2.4 Effect of steel bar connectors

According to The Bi-Steel Guide, it is not very important to model the temperature gradient accurately at points between the steel faceplates, because the behaviour of the Bi-Steel panel is dominated by faceplate behaviour. Furthermore, the reinforcement ratio in terms of the steel bar connectors is just 7.6% in the 3D model. However, it is necessary to validate whether steel bar connectors can be ignored in finite element analysis.

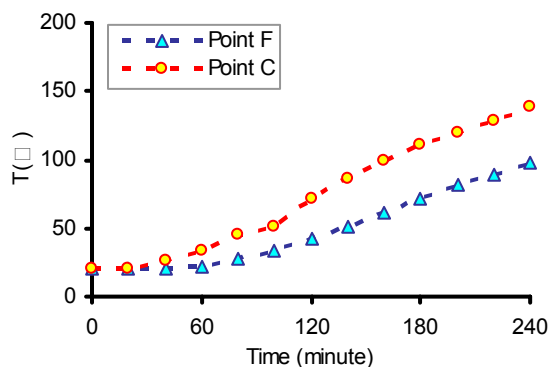


Fig. 13 – Temperatures at cold faceplate

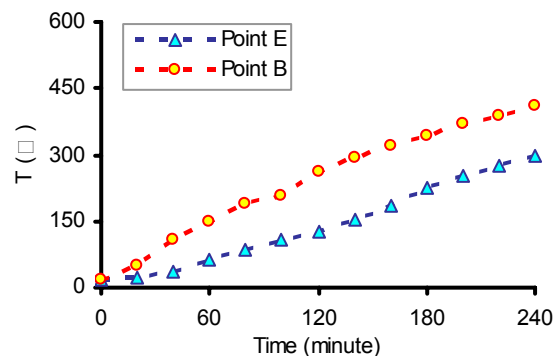


Fig. 14 – Temperatures at mid-bar

Within the analysis, three points A, B and C, whose positions along the steel bar connector are respectively at the hot faceplate, the mid-plane and the cold faceplate, were selected and compared with points D, E and F (see Fig. 1). From plotted results (see Figs. 13, 14 and 15), It can be seen that the temperature values at the compared points with the bar connector included in the model is up to 106% larger than those without the bar connector included, except for those at the heated faceplate. This is because, at the hot surface, the fire temperature and the emissivity of the fire have a greater influence on the temperature distributions within the Bi-Steel panel. Hence, in the simulation, the steel bar connectors have to be taken into account.

3. NON-LINEAR PROCEDURE FOR STRUCTURAL ANALYSIS

Before moving on to the structural analysis of a Bi-Steel panel at elevated temperature, the simulation program had to be chosen. On consulting literature reviews concerning the use of ABAQUS to model structures at high temperature, it was found that numerical problems were too severe for results to be obtained⁹. In order to confirm this, the author has tested a 3D composite structure under fire conditions in ABAQUS. It may be because the failure criteria used in the elevated-temperature concrete material model of ABAQUS are too inefficient to converge. Thus, in this research, ABAQUS was not adopted to simulate the structural behaviour of Bi-Steel panels in fire.

An in-house finite element program *Vulcan*, which provides slab, beam-column, spring and shear-connector elements, has been developed by the University of Sheffield for 3D modelling of concrete, steel and steel-framed composite structures in fire¹⁰. However, the Bi-Steel panel is a complicated three-dimensional problem. One- or two-dimensional stress-strain relationships are not adequate to represent the real behaviour of Bi-Steel panels. Hence, a three-dimensional eight-noded brick element had to be developed in order to model Bi-steel properly. Both geometric and material non-linearities were considered. A Newton-Raphson method was applied as the iteration scheme for the solution of the non-linear finite element equations. Some fundamental assumptions of the non-linear approach can be summarized as:

- 1) The displacements of brick elements may be large, but element extensions and angle changes between elements are small.
- 2) Each brick element can have a different but uniform temperature. Three-dimensional stress-strain relationships can change independently at every single Gauss point of each element, and there is no slip between elements.
- 3) In the elastic region, steel is isotropic, which means that the initial mechanical properties are the same in any direction

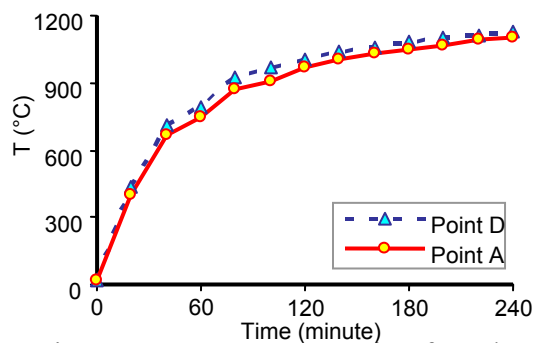


Fig. 15 – Temperatures at hot faceplate

at a material point. Concrete is isotropic, homogenous and elastic before cracking or crushing occurs.

- 4) Plastic deformations are irreversible and history-dependent. Plastic deformations of steel are hydrostatic-pressure-insensitive, but those of concrete are hydrostatic-pressure-sensitive.
- 5) The associated flow rule, which defines that the plastic potential surface has the same shape as the yield surface, has been adopted.
- 6) The plastic behaviour obeys the theory of plasticity, i.e. the stiffness of elastic unloading-reloading does not change with plastic deformations.
- 7) Concrete, on cooling down to ambient temperature of 20°C after having reached an elevated temperature, does not recover its initial compressive strength.

3.1 Geometrically non-linear brick element

In general, geometric non-linearity occurs when deformations become so large that they introduce additional internal actions. According to a study of the literature, Bathe¹¹ has set up a series of 3D isoparametric finite element formulations including material linear-elasticity. Hence, the geometrically non-linear brick element was extended to include material non-linearities for modelling of structures in fire.

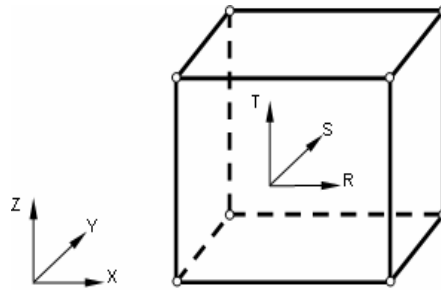


Fig. 16 – 3D eight-noded brick element

In this model, using a Total Lagrangian formulation, the basic static finite element equilibrium equation can be written as

$$({}_0^t K_L + {}_0^t K_{NL}) \cdot \Delta U = {}^{t+\Delta t} R - {}_0^t F \quad (1)$$

where ${}_0^t K_L$ is the linear-strain incremental stiffness matrix; ${}_0^t K_{NL}$ is the non-linear-strain incremental stiffness matrix; U is the vector of increments in the nodal point displacements; ${}^{t+\Delta t} R$ is the vector of externally applied nodal point loads at time $t+\Delta t$; and ${}_0^t F$ is the vector of nodal point forces equivalent to the element stresses at time t . Gaussian numerical integration is used to calculate the stiffness matrix and internal forces. Generally, the appropriate integration order depends on the matrix being evaluated and the specific finite element being considered. Here, a fully integrated 3D eight-noded element integrated at 8 Gauss points ($2 \times 2 \times 2$) is adopted. In the numerical procedure, the equilibrium relationship must be satisfied throughout the complete history of load application, so that the correct displacements can be obtained.

3.2 Material model

In the developing process of the 3D material model, a key point is to work out the

relationship between uniaxial stress-strain curves and 3D stress surfaces. For the sake of convenience, the effective stress and the effective plastic strain are defined for the multi-axial stress state such that the single $(\sigma_{\text{effective}} - \varepsilon_{\text{effective}}^p)$ curve can be calibrated against a uniaxial stress-plastic strain curve¹². Uniaxial stress-strain curves, which are documented in Eurocode 4 Part 1.2, are referenced and translated into triaxial mechanical models of steel and concrete at different temperatures.

3.2.1 Steel model

The von Mises criterion was chosen as the yield function of steel¹². It is formed as

$$f(J_2) = J_2 - k^2 = 0 \quad (2)$$

where J_2 is the second invariant of the deviatoric stress tensor. The material constant

$$k = \frac{\sigma_0}{\sqrt{3}} \quad (3)$$

where σ_0 is the uniaxial yield stress. According to the yield function, it can be seen that stress points can freely move on the yield surface which is determined by k . Thus, the determination of the material constant k , which is also called as the yield stress of material in pure shear, is very important in the numerical procedure. At elevated temperature, material degradation occurs. Both yield strength and Young's modulus decrease with increasing temperature. Hence, there is a constant value for k at every single temperature point. In other words, the yield surface is a function depending on different temperature values.

In the linear-elastic stage, the stress-strain relationship is given as Equation (4). Beyond the proportional limit, the stress point enters into elastic-plastic stage. Its relationship changes to Equation (5), and plastic strains are produced by further loading. Since an associated flow rule has been assumed, plastic strain increments can be defined using Equation (6).

$$d\sigma_{ij} = C_{ijkl} \cdot d\varepsilon_{kl} \quad (4)$$

$$d\sigma_{ij} = C_{ijkl}^{ep} \cdot d\varepsilon_{kl} \quad (5)$$

$$d\varepsilon_{ij}^p = d\lambda \cdot \frac{\partial f}{\partial \sigma_{ij}} \quad (6)$$

where C_{ijkl} is the tensor of temperature-dependent elastic stiffness; C_{ijkl}^{ep} is the temperature-dependent elastic-plastic constituent tensor, and $d\lambda$ is a non-negative scalar function that varies throughout the plastic loading history.

3.2.2 Concrete model

Since concrete has complex characteristics, it is difficult to define a general constitutive model to describe its material behaviour under various loading conditions. Over the years, some 3D constitutive concrete models have been developed for use at ambient temperature. At elevated temperatures, however, the constitutive model of concrete under

triaxial loading is still a problem. Development of an effective constitutive model, which can represent concrete stress-strain relationships either at ambient temperature or at elevated temperature, has become a major purpose of this research. The Drucker-Prager criterion¹², which is a simple modification of the von Mises criterion, but includes the influence of hydrostatic pressure on yielding, was chosen as concrete failure function. It is expressed as

$$f(I_1, J_2) = \alpha \cdot I_1 + \sqrt{J_2} - k = 0 \quad (7)$$

where I_1 is the first invariant of the stress tensor, containing the positive material constants¹³

$$\alpha = \frac{1}{\sqrt{3}} \cdot \frac{f_c - f_t}{f_c + f_t} \quad (8)$$

$$k = \frac{2}{\sqrt{3}} \cdot \frac{f_c \cdot f_t}{f_c + f_t} \quad (9)$$

in which, f_c is the uniaxial compressive strength and f_t is the uniaxial tensile strength. At elevated temperature, the failure surface shrinks with increasing temperature along the hydrostatic axis. From Equations (8) and (9) it can be seen that α and k are functions of uniaxial strengths which are temperature-dependent. Hence, the uniaxial stress-strain relationships of concrete can be introduced into the 3D failure criterion using these material constants.

3.3 Validations

After the implementation of a 3D geometric model, material model and thermal strains into *Vulcan*, some modelling was done to validate their feasibility and accuracy. In this paper, two simulations are presented.

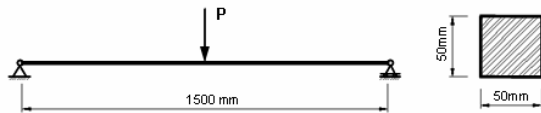


Fig. 17 – Simply supported steel beam

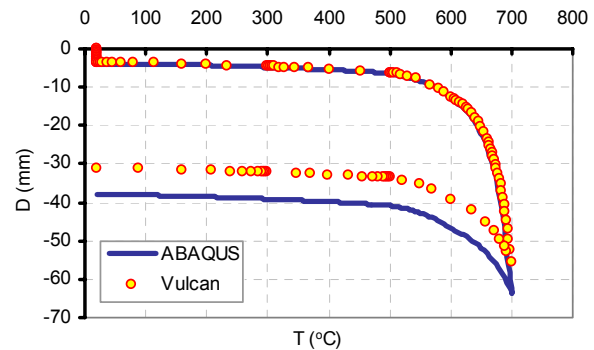


Fig. 18 – Comparisons of mid-span deflections

The first is a simply supported steel beam with 6kN concentrated load at mid-span (see Fig. 17). It is uniformly heated up to 700°C and then cooled down to 20°C. This beam was modelled by 3D brick elements within *Vulcan*, and 3D solid elements C3D8 within ABAQUS. The comparisons of deflections at mid-span are shown in Fig. 18. The trend of deformations is similar, although there is a

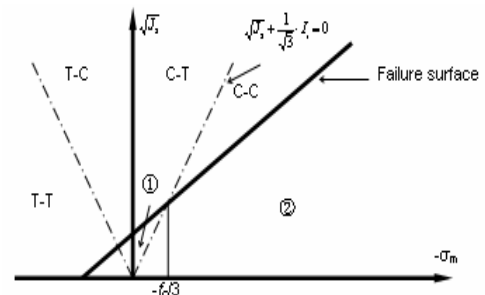


Fig. 19 – Failure zones

12% difference between the final results from *Vulcan* and ABAQUS. Moreover, before reaching 650°C, the difference is only 2% to 3% between the deflections. The reason for this could be that the plasticity models and the calculation methods for permanent strains are not identical in both programs.

In order to validate the concrete model, a concrete cube subject to different boundary conditions and thermal loads was simulated by the non-linear procedure developed. Concrete properties and loading modes are shown in Table 2. From Fig. 20, it can be seen that Case 1 failed at the uniaxial compressive strength, but Case 2 failed at an earlier stage. This is because differential thermal expansions can induce tensile forces into the concrete, so that stress points enter into Zone ① (see Fig. 19) which is much weaker and closer to the failure surface. Cases 3 and 4 are concrete confined under compression with different heating modes. Their stress state is in Zone ②. As Fig. 21 shows, their failure strengths are dramatically increased.

Table 2 Summary of modelling information

Case number	Dimension L×W (mm)	f_c (MPa)	Test load (kN)	Load mode	Thermal mode
1	100×100	49	160	Uniaxial compression	Uniform heated
2	100×100	49	160	Uniaxial compression	With temperature gradient
3	100×100	49	160	With confinement	Uniform heated
4	100×100	49	160	With confinement	With temperature gradient

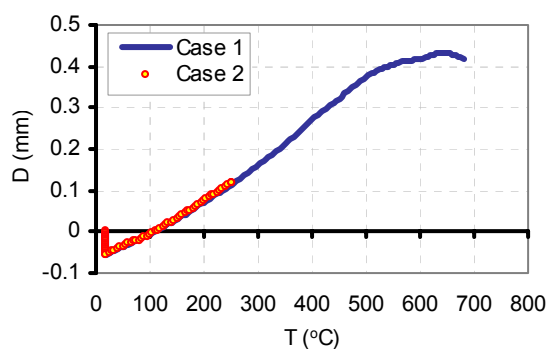


Fig. 20 – Deflection in the direction of compression

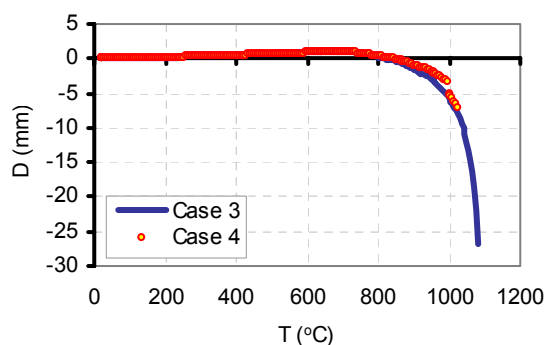


Fig. 21 – Deflection in the direction of compression

4. CONCLUSIONS

From the results of the heat transfer analyses on a Bi-Steel panel, and program validations, these points can be concluded:

- 1) In a Bi-Steel panel, there is a large temperature gradient from the heated steel faceplate to the cold steel faceplate. This thermal gradient could introduce large thermal stresses into the model.
- 2) The moisture content of concrete can affect its temperature variation significantly. The emissivity of the fire has some influence on the temperature distributions of the

Bi-Steel model, but this is not significant. The steel bar connectors have a large influence on the temperature distribution, and cannot be ignored in analysis.

- 3) The non-linear procedure developed is capable of representing the behaviour of steel and concrete structures at elevated temperatures, and analytical results are reasonable. Some structural analyses on Bi-Steel panels in fire are currently being carried out with this procedure, and the results will be reported soon.

5. REFERENCES

- [1] Roberts, T.M., and Dogan, O., "Fatigue of welded stud shear connectors in steel-concrete-steel sandwich beams", *J. Construct. Steel Research*, 45, (1998) pp301-320,
- [2] Corus Group Ltd, Bi-Steel Design & Construction Guide, Vol. 1-2, 1999.
- [3] Clubley, S.K., Moy, S.J. and Xiao, R.Y., "Shear strength of steel-concrete-steel composite panels. Part I-testing and numerical modelling", *J. Construct. Steel Research*, 59, (2003) pp781-794.
- [4] Clubley, S.K., Moy, S.J. and Xiao, R.Y., "Shear strength of steel-concrete-steel composite panels. Part II-detailed numerical modelling of performance", *J. Construct. Steel Research*, 59, (2003) pp795-808.
- [5] Xie, M., and Chapman, J. C., "Static and fatigue tensile strength of friction-welded bar-plate connections embedded in concrete", *J. Construct. Steel Research*, 61, (2005) pp651-673.
- [6] Xie, M., Foundoukos, N. and Chapman, J.C., "Experimental and numerical investigation on the shear behaviour of friction-welded bar- plate connections embedded in concrete", *J. Construct. Steel Research*, 61, (2005) pp625-649.
- [7] EN 1991-1-2, "Eurocode 1, Actions on structures, Part 1-2: General actions-Actions on structures exposed to fire", CEN, Brussels, 2002.
- [8] EN 1994-1-2, "Eurocode 4, Design of composite steel and concrete structures, Part 1-2: General rules-Structural fire design", CEN, Brussels, 2003.
- [9] Gillie, M., Usmani, A., Rotter, M. and O'Connor, M., "Modelling of heated composite floor slabs with reference to the Cardington experiments", *Fire Safety Journal*, 36, (2001) pp745-767,
- [10] Huang, Z., Burgess, I.W., and Plank, R.J., "Modelling membrane action of concrete slabs in composite buildings in fire. I: Theoretical development", *Journal of Structural Engineering, ASCE*, 129(8), pp1093-1102, 2003.
- [11] Bathe, K.J., "Finite Element Procedures", Prentice Hall, Englewood Cliffs, New Jersey 07632, 1996.
- [12] Chen, W. F., "Constitutive Equations for Engineering Material", Vol. 2: Plasticity and Modelling, Elsevier, Amsterdam-London-New York-Tokyo, 1994.
- [13] Salari, M.R., Saeb, S., Willam, K.J., Patchet, S.J., and Carrasco, R.C., "A coupled elastoplastic damage model for geomaterials", *Computer Methods in Applied Mechanics and Engineering*, 193, (2004) pp2625-2643.



STRUCTURAL ANALYSIS OF A HEATED STEEL PORTAL FRAME BY TWO DIFFERENT METHODS

Gordon COOKE¹ and Dhionis DHIMA²

ABSTRACT

A simple structural hand-analysis is presented for a steel portal frame heated in various ways. The method, called the force-displacement method, avoids the writing of program code but does involve matrix manipulation in a spreadsheet to solve the simultaneous equations formulated. The analysis gives two examples starting with an unheated single bay portal frame to introduce the analysis method; the second example considers the effects of heating one column of the frame so that it has a linear temperature gradient across the column section. The method is suitable for elastic analysis of heating effects in multi-storey frames. The results of the elastic analysis are calibrated against the SAFIR numerical finite element program and it is shown that they agree. Care is needed in the elastic analysis to ensure that no part of a member becomes plastic.

NOTATION

M = bending moment

I = moment of inertia (second moment of area of section)

L = span of beam

h = storey height

E = Elastic modulus (stress/strain)

T = increase in temperature of member

d = thickness of structural member in direction of heat flow

y = distance from neutral axis to extreme fibre

Δ = horizontal deflection at top of column

θ = rotation at end of member

α = coefficient of linear thermal expansion

σ = stress

W = external load

¹ Doctor, Fire Safety Consultant and Visiting Professor at City University, London. email: gordon@cookeonfre.com

² Doctor, Engineer in the Structures and Fire Division of CSTB, Marne la Vallee, France. email: d.dhima@cstb.fr

1. INTRODUCTION

It is sometimes desirable to know the way in which stresses and deflections develop when a frame is heated within the elastic region. In the analysis given in Example 2 below a column in a portal frame has a linear temperature gradient across the section. This effect can occur when an unprotected steel column is exposed to thermal radiation from a fire on one flange, as, for example, in an unprotected steel column placed externally opposite a window opening through which flames are jetting. The effect can also occur in internal structural members¹. The behaviour of frames subjected to heating that causes plasticity is best predicted using finite element or finite difference methods of analysis, but this level of analysis requires the use of a computer program which is not readily available or convenient to use for a one-off analysis. The force-displacement method², though confined to the elastic domain, can nonetheless provide useful data. It can be used, for example, to check under what loading and heating conditions the frame behaviour enters the plastic domain by carrying out an analysis as described and finding out if stresses have reached yield using the well known relationship $\sigma = My / I$. The two examples analysed are shown in Figure 1. In Example 2 the temperature gradient applies over the whole column height.

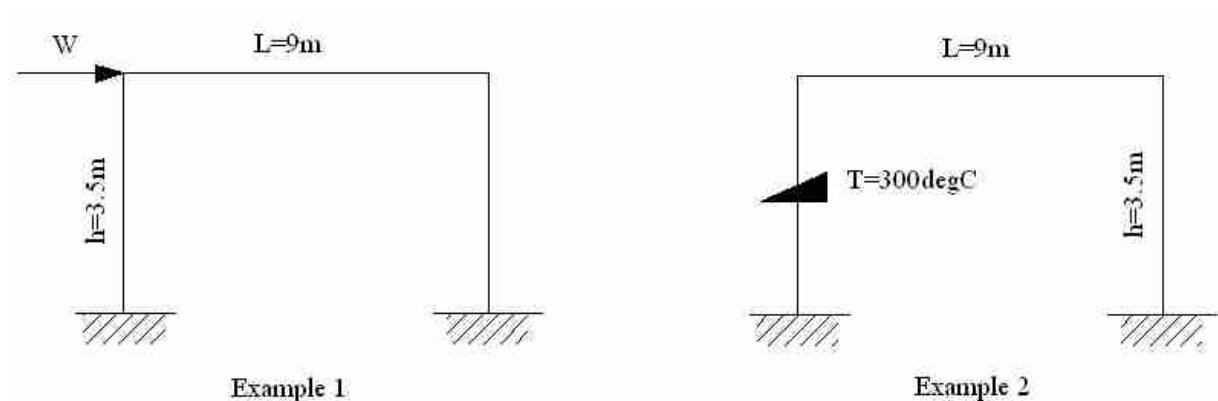


Figure 1 The two examples considered using the same frame geometry

The numerical answers in the examples relate to a portal frame having the following properties: $L = 9\text{m}$; $h = 3.5\text{m}$; $E = 210\text{kN/m}^2$. The columns are steel I-section universal columns UC 203x203x46kg/m with $I = 4035\text{cm}^4$, and the beam is a universal beam UB457x191x67kg/m with $I = 26702\text{cm}^4$. $\alpha = 0.000014/^{\circ}\text{C}$ for steel.

The force-displacement elastic analysis has been made by the first author and the SAFIR analysis by the second author.

2. ELASTIC ANALYSIS USING THE FORCE-DISPLACEMENT METHOD.

2.1 Principles of analysis

Modern structural analysis is based on energy principles and most related theories treat materials as linearly elastic. The Stiffness, Flexibility and Finite Element Methods are different to the force-displacement method² presented herein since the latter gives forces and

displacements simultaneously. Inelastic (i.e. plastic) response and time dependent stresses are not dealt with here. Actions are assumed to be static and deformations are considered small.

The method, like other analytical methods, relies on the principle of superposition – that is, if there are two or more influences acting together, their effect on stresses and deformations can be considered as additive in any sequence of their actions. If, for example, a pin-ended flexural member of stiffness EI and length L is acted upon by two bending moments, M_{12} at one end and M_{21} at the other, Figure 2, then the rotation at node 1, θ_{12} , is the rotation at 1 due to M_{12} which is $M_{12}/3EI$ plus the rotation at 1 due to M_{21} acting at node 2 which is $M_{21}/6EI$. These parameters are used in the analyses (note that $L/3EI$ and $L/6EI$ are the so-called flexibility coefficients)

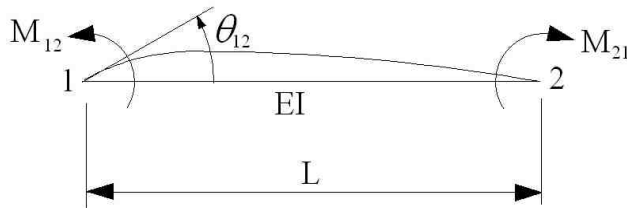


Figure 2. Principle of superposition for two bending moments acting on a member

The procedure in the analysis, using a simple fixed-base portal frame with full restraint at member joints, e.g. Figure 3, as the example, is as follows:

Step 1. The structure is assumed to deflect to its equilibrium position defined by deflection Δ .

Using intuition the direction of bending moments are marked.

Step 2. The imposed rotations at nodes in their final position are released so that all members become statically determinate and stresses are zero. The relative rotation at each node is noted.

Step 3. Statically indeterminate bending moments are applied to restore compatibility of deformation conditions at all the nodes in the structure simultaneously.

In the portal frame there are four nodes (1, 2, 3 and 4), Figure 3, and there must be four compatibility of deformation equations. An equation for equilibrium is also necessary, so that internal forces equal external forces, and in this example the external force W must equal the sum of the shear forces in the two columns (shear force = bending moment divided by member length). The set of simultaneous equations so formed can then be conveniently solved using matrix manipulation in a spreadsheet to give the unknown values of bending moment and deflection. If the assumed direction of bending moments in Step 1 is wrong, this will be indicated by a minus sign in the matrix solution – the convention is that bending moments are assumed positive if they tend to close the discontinuity (ie rotation).

The general matrix is of the form

$$[F] \begin{Bmatrix} M \\ \Delta \end{Bmatrix} = \{W\}$$

in which $[F]$ is the force-displacement matrix

$\{M\}$ is the force-displacement vector, and

$\{W\}$ is the load vector

In the following examples axial forces are ignored but they can be included in the analysis.

2.2 Example 1. Unheated portal frame with horizontal load acting

Compatibility of deformation at 1

$$M_{12} \frac{h}{3EI_c} - M_{21} \frac{h}{6EI_c} = \frac{\Delta_2}{h} = \text{rotation of column} \quad (1)$$

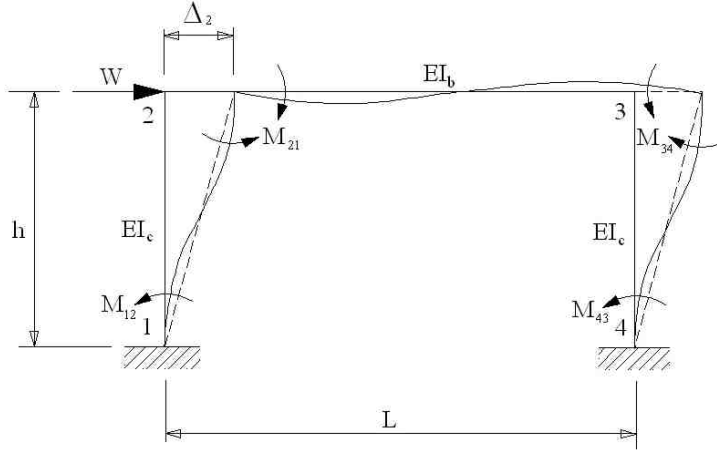


Figure 3. Parameters for the unheated portal frame with fixed bases

In the first term M_{12} is tending to decrease the angular discontinuity and is therefore positive; in the second term M_{21} is tending to increase the angular discontinuity and is therefore negative
Compatibility of deformation at 2:

$$-M_{12} \frac{h}{6EI_c} + M_{21} \frac{h}{3EI_c} + M_{21} \frac{L}{3EI_b} - M_{34} \frac{L}{6EI_b} = \frac{\Delta_2}{h} \quad (2)$$

Compatibility of deformation at 3:

$$-M_{21} \frac{L}{6EI_b} + M_{34} \frac{L}{3EI_b} + M_{34} \frac{h}{3EI_c} - M_{43} \frac{h}{6EI_c} = \frac{\Delta_2}{h} \quad (3)$$

Compatibility of deformation at 4:

$$M_{43} \frac{h}{3EI_c} - M_{34} \frac{h}{6EI_c} = \frac{\Delta_2}{h} \quad (4)$$

Equilibrium condition:

$$\frac{M_{12} + M_{21}}{h} + \frac{M_{34} + M_{43}}{h} = W \quad (5)$$

Multiplying all the above equations by $\frac{6EI_c}{h}$ and letting $A = \frac{6EI_c}{h^2}$; $B = \frac{6EI_c}{h}$; $C = 6EI_c$;

and $r = \frac{LI_c}{hl_b}$ gives the following set of equations:

$$2M_{12} - M_{21} - A\Delta_2 = 0 \quad (6)$$

$$-M_{12} + M_{21}(2 + 2r) - M_{34}r - A\Delta_2 = 0 \quad (7)$$

$$-M_{21}r + M_{34}(2r + 2) - M_{43} - A\Delta_2 = 0 \quad (8)$$

$$2M_{43} - M_{34} - A\Delta_2 = 0 \quad (9)$$

$$BM_{12} + BM_{21} + BM_{34} + BM_{43} = CW \quad (10).$$

To solve the matrix comprised of Equations 6-10 numerical values have to be substituted. Substituting these values in consistent units (m and kN) gives the following matrix for $W = 1\text{ kN}$:

2	-1	0	0	-4150	M_{12}	=	0
-1	2.796	-0.398	0	-4150	M_{21}	=	0
0	-0.398	2.796	-1	-4150	M_{34}	=	0
0	0	-1	2	-4150	M_{43}	=	0
14526	14526	14526	14526	0	Δ	=	50841

The solution is: $M_{12} = 0.92943\text{ kNm}$; $M_{23} = 0.820569\text{ kNm}$; $M_{34} = 0.820569\text{ kNm}$; $M_{43} = 0.92943\text{ kNm}$ and $\Delta_2 = 0.00025\text{ m}$. This solution has been compared with a solution given in the UK Steel Designers Manual³ and found to agree.

2.3 Example 2. Portal frame with one column non-uniformly heated across the section

In this analysis one column is heated to give a linear temperature gradient $T = 300^\circ\text{C}$ across the section. It can be shown that in its unrestrained condition the column, represented by nodes 1, 2, 3 and 4 in Figure 4, of depth d and length L bows into a circular arc, causing an end rotation of $\theta = \alpha LT / 2d$ where d is the depth of steel section measured in the direction of heat flow

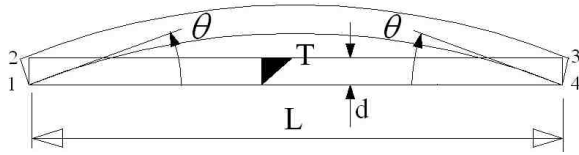


Figure 4. Thermal bowing parameters

The portal frame is shown in Figure 5 in which the rotations at node 2 are clearly illustrated. The intuitive directions of some of the bending moments are different to those in the earlier examples and so the equations for compatibility of deformation are rewritten as follows: Compatibility of deformation at 1 (noting that M_{12} and M_{21} are tending to reduce the angular discontinuity and are therefore positive):

$$M_{12} \frac{h}{3EI_c} + M_{21} \frac{h}{6EI_c} = \theta - \frac{\Delta_2}{h} = \text{rotation of column at node 1} \quad (11)$$

Compatibility of deformation at 2:

$$M_{12} \frac{h}{6EI_c} + M_{21} \frac{h}{3EI_c} + M_{21} \frac{L}{3EI_b} - M_{34} \frac{L}{6EI_b} = \frac{\Delta_2}{h} + \theta + \frac{\Delta_{v2}}{L} \quad (12)$$

Compatibility of deformation at 3:

$$-M_{21} \frac{L}{6EI_b} + M_{34} \frac{L}{3EI_b} + M_{34} \frac{h}{3EI_c} - M_{43} \frac{h}{6EI_c} = \frac{\Delta_2}{h} + \frac{\Delta_{v2}}{L} \quad (13)$$

Compatibility of deformation at 4:

$$M_{43} \frac{h}{3EI_c} - M_{34} \frac{h}{6EI_c} = \frac{\Delta_2}{h} \quad (14)$$

Equilibrium condition (assuming $M_{12} > M_{21}$):

$$\frac{M_{12} - M_{21}}{h} - \frac{M_{43} + M_{34}}{h} = 0 \quad (15)$$

As before, multiplying all the above equations by $\frac{6EI_c}{h}$ and letting $A = \frac{6EI_c}{h^2}$; $B = \frac{6EI_c}{h}$

; $C = \frac{\alpha h T_1}{2L}$; $D = \frac{\alpha h T_1}{2d}$; and $r = \frac{LI_c}{hI_b}$ and assuming $T = 300^\circ\text{C}$, gives the following set of equations:

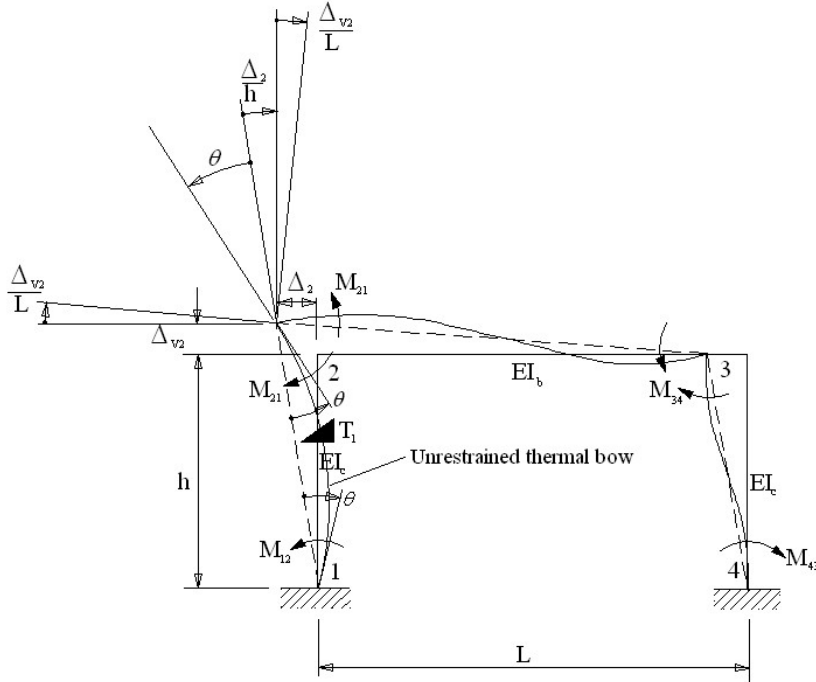


Figure 5. Portal frame with one column heated to give a linear temperature gradient across section

$$2M_{12} + M_{21} - A\Delta_2 = DB \quad (16)$$

$$M_{12} + M_{21}(2 + 2r) - M_{34}r - A\Delta_2 = DB + CB \quad (17)$$

$$-M_{21}r + M_{34}(2r + 2) - M_{43} - A\Delta_2 = CB \quad (18)$$

$$2M_{43} - M_{34} - A\Delta_2 = 0 \quad (19)$$

$$BM_{12} - BM_{21} - BM_{34} - BM_{43} = 0 \quad (20)$$

Substituting values as before gives:

2	1	0	0	4150	M_{12}	=	300.517
1	2.796	-0.398	0	-4150	M_{21}	=	303.9064
0	-0.398	2.796	-1	-4150	M_{34}	=	3.389167
0	0	-1	2	-4150	M_{43}	=	0
14526	-14526	-14526	-14526	0	Δ	=	0

The solution is: $M_{12} = 108.68\text{kNm}$; $M_{21} = 75.387\text{kNm}$; $M_{34} = 19.612\text{kNm}$; $M_{43} = 13.085\text{kNm}$ and $\Delta_2 = 0.00187\text{m}$. The temperature gradient in the column has caused a large increase in bending moment while not greatly affecting the lateral deflection.

3. NUMERICAL ANALYSIS USING SAFIR

The thermal and mechanical analysis in this study have been made with a non-linear finite element program (SAFIR) developed at the University of Liège, Belgium by Franssen⁴ et al. Thermal and mechanical analysis can be realised using a 2D or 3D model. This thermo-elastic-plastic finite elements program can take into account the large displacements and transverse thermal gradients in the mechanical calculation.

For each calculation, the loads are applied to the structure. The structure can be defined in beam, truss and shell elements. The temperature history of the structure, due to fire, is read from the files created during the temperature analysis. As the computation strategy is based on a step-by-step procedure, the following information can be obtained until failure occurs in the structure:

- Displacement at each node of the structure.
- Axial and shear forces and bending moments at integration points in each finite element.
- Strains, stresses and tangent modulus at integration points in each finite element.

In this example the portal frame is modelled with beam elements and the assumptions are:

- cross sections remain plane under bending moment
- plastic strains are only considered in the longitudinal direction of the member
- non-uniform torsion is considered
- the thermal and mechanical properties of the steel are those given in Eurocode 3 fire part 1.2⁵
- both columns of the portal frame are fully restrained at ground level.

The temperature in the heated column section is input by hand in order to have a linear thermal gradient across the section so as to copy the condition used in the above elastic analysis for Example 2: the heated and unheated flange temperatures are taken as 320 and 20°C respectively giving the required difference of 300 °C. Figure 6 gives the mesh used for the column; the mesh for the beam section is similar, having 12 elements down the web and 23 elements across the flange. The steel grade is S235 and the thermo-mechanical properties used are as in Eurocode 3. Young's Modulus (E) at 20°C is assumed to be 210kN/m² and varying with temperature.

4. COMPARISON OF RESULTS

The elastic analysis for the frame with one column subjected to a 300°C temperature gradient gave a horizontal deflection at the column head of 1.87mm whereas the SAFIR analysis gave 1.53mm. The bending moment at the top of the heated column head was 75.38kNm and 89.14kNm for the elastic and SAFIR analyses respectively. This agreement is good considering that the Elastic Modulus is assumed not to change in the elastic analysis. In both analyses the temperature gradient in the column has caused a large increase in bending moment while not greatly affecting the lateral deflection.

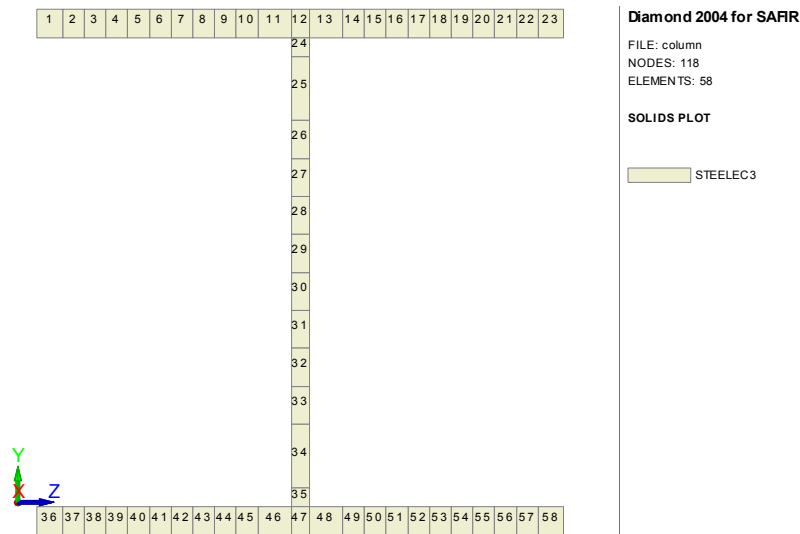


Figure 6. The mesh for the heated column

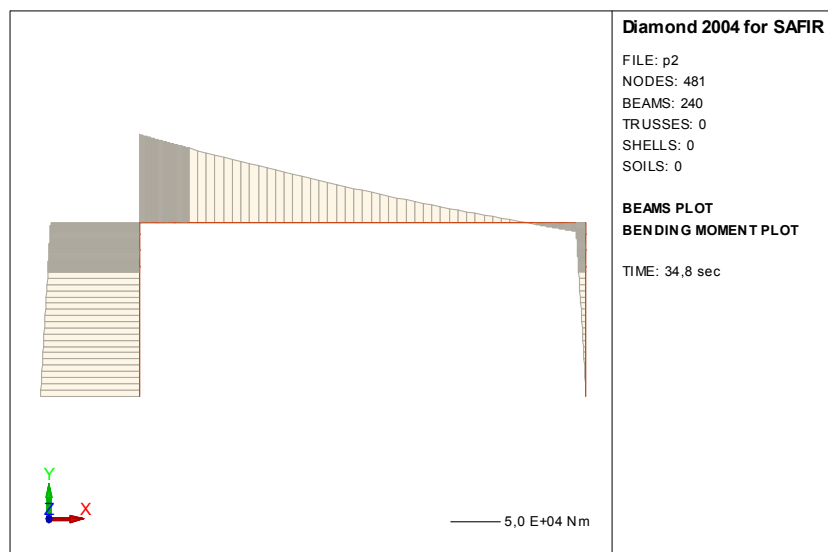


Figure 7. SAFIR bending moment diagram for the heated column condition

5. CONCLUSIONS

The use of the force-displacement method has been illustrated for the elastic analysis of a simple portal frame in which one column is heated to give a temperature gradient across the column section. The results for lateral deflection and bending moment at the top of the heated column are shown to agree well with the results obtained using the rigorous SAFIR finite element program. Care must be taken when using an elastic analysis to check that no part of a member section has entered the plastic domain.

REFERENCES

- 1 Cooke G M E, The structural response of steel I-section members subjected to elevated temperature gradients across the section, PhD thesis, City University, London, 1987
- 2 Smolira M, Analysis of tall buildings by the force-displacement method, McGraw Hill, 1975.
- 3 Steel Designers Manual, 4th edition, Crosby Lockwood, 1972, p291
- 4 Franssen, J-M., Kodur, V.K.R. and Mason, J. "User's Manuel for SAFIR : A computer Program for Analysis of structures Submitted to Fire", International Report SPEC/2000_03, 2000, University of Liege, Ponts et Charpentes, Belgium, 2000.
- 5 EUROCODE 3 Part 1.2



FIRE INDUCED COLLAPSE OF TALL BUILDINGS

Graeme FLINT¹, Asif USMANI², Susan LAMONT³, Barbara LANE¹ and José TORERO²

ABSTRACT

Research into the effects of fire on structures in recent years has been accelerating. The high profile fires in the Broadgate Phase 8, World Trade Center and Torre Windsor buildings have created an urgent need for studying the complex, fire induced, structural interactions and failure mechanisms involved in such situations. The research conducted at the Cardington test facility and subsequent modelling by a number of researchers has served well as an investigation of traditional, low rise office buildings. However further research is required to understand the response of construction forms used in high rise buildings, especially those with long span floor systems.

This paper reports on research considering the effects of fire on long span floors in tall buildings. In particular it concentrates on a collapse mechanism found to occur in structural models with fires over multiple floors. The collapse mechanism is identified in relatively simple 2D models and repeated in more realistic and complex 3D models. The mechanism affects the perimeter columns of the structure under investigation.

Keywords : Long span floor systems; multiple floor fire; progressive collapse; tall buildings.

1. INTRODUCTION

Research in the last 15 years has led to a new understanding of composite steel frame buildings in fire¹⁻⁴. This work has mainly focused upon the most common and simplest structural forms currently used; typically short-span (6-9m) rolled steel sections in frames with composite floor decks. In the aftermath of the events of 11th September 2001 and the Torre Windsor fire in Madrid, it has become apparent that other structural forms need to be investigated under fire conditions.

¹ Arup Fire, Ove Arup and Partners, 13 Fitzroy Street, London, W1T 4BQ, UK

² School of Engineering and Electronics, University of Edinburgh, Alexander Graham Bell Building, The King's Buildings, Edinburgh, Scotland, EH9 3JL, UK

³ Arup Fire, Ove Arup and Partners, 901 Market St, Suite 260, San Francisco, CA 94107

Tall office buildings around the world are supported by structural layouts that are distinctly different from regular grids of short beam spans. Such buildings generally incorporate long span floor systems comprising trusses or cellular beams, often spanning directly from a central core to the edge of the building to maximize the letable floor area and improve construction efficiency by reducing the number of columns.

Major fire events around the world have seen fire spread to multiple floors of buildings. The multi-floor fires in the World Trade Center on the 11th of September 2001 in New York were instrumental in the total collapse of several tall buildings^{5,6}. Similarly the Torre Windsor building in Madrid suffered partial collapse after a major fire event in February 2005⁷.

This paper therefore presents the results of an investigation of the effects of multi-floor fires in tall buildings incorporating long span truss floor systems. A fire has been applied over several floors and indicates a failure mechanism in the columns. The structural models used on this project represent a structure similar in form to the WTC towers design but this is not intended to be a forensic analysis of the collapses seen on the 11th of September 2001. However, comparison of results to the building responses documented in the official investigation into the WTC 1&2 collapses⁸ indicates strong similarities.

The commercial finite element modelling program ABAQUS⁹ is used to model the structure under investigation. The program can accurately predict the large displacements commonly seen in structures in fires as well as allowing for the degradation of the materials at high temperatures and the geometric effects of heating (thermal expansion and bowing).

2. MODEL DESCRIPTION

This paper presents results from an investigation of 2 and 3 dimensional models of a multi-storey office building. The models are representative of the type of construction used in the World Trade Center 1&2 towers.

All structural elements were modelled using linear beam elements (in 2D or 3D depending on analysis) and sufficiently large numbers of elements were used to allow for non-linear effects. Steel and concrete properties for elevated temperatures have been extracted from Eurocodes 2¹⁰ and 3¹¹. This data includes stress-strain curves and Young's Modulus at different temperatures. The concrete has been modelled using a "damaged plasticity" model included in ABAQUS⁹.

2.1 2D Model

Figure 1 shows the model used in the 2D analysis. A 2D slice was taken through the full 63m width of the building, including the core. This slice was primarily intended to capture the reaction of the composite floor system over the main floor truss in the outer areas, as in reference 15. 12 storeys are considered in this model to allow multiple floor fires to be considered while still allowing a reasonable distance between the fire compartments and the boundaries of the model. As the model represents a set of floors within the full structure extra loading was applied to the top of the columns to represent further floors above. This increases the load ratio in the outer columns to about 0.2. This low ratio is indicative of the small level of capacity used to support gravity loads in stressed tube structures such as the WTC towers. It does, however, allow significant P- δ moments to develop at large column displacements.

The main floors are split into outer areas supported by long span trusses and the inner, core area, supported by a beam and slab floor system. The slab has been modelled as composite with all beams and trusses but is not directly connected to the columns as would be

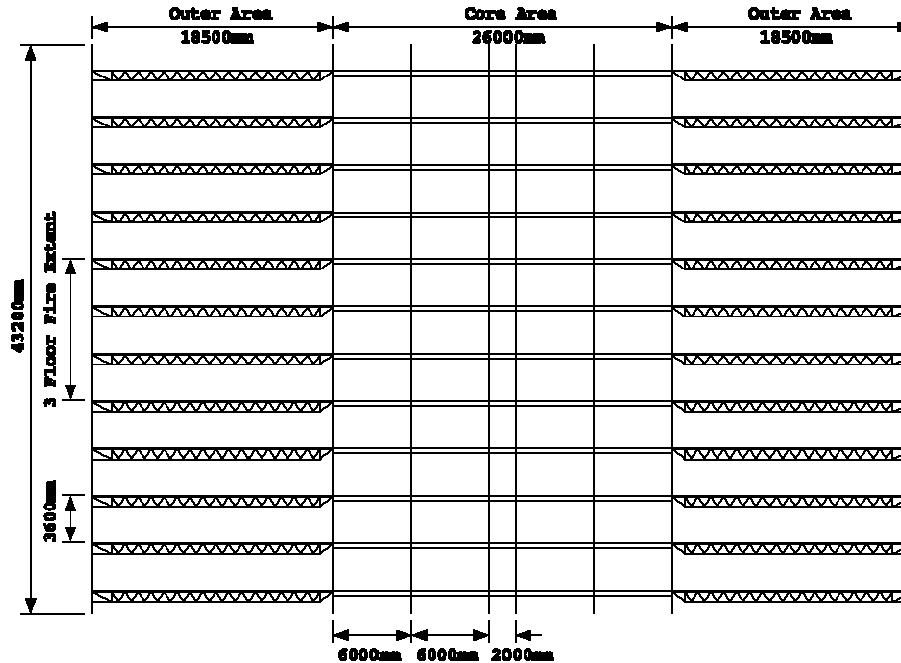


Figure 1 : 2D Model Mesh

the case in a real building.

The trusses supporting the outer areas have been modelled using the section sizes shown in Table 1. The member sizes were based on data taken from various reports^{5,12} on the structure of the World Trade Center Towers as this was a successful design of a long span truss floor system. The local effects of heating on this type of floor system were also investigated and are reported elsewhere¹³.

Member	Top Chord	Bottom Chord	Diagonal
Size (width x height)	95x38mm	130x38mm	40mm Dia.

Table 1 : Truss Member Sizes

The outer columns are 700x350mm box sections with the long sides (coming out of the page in Figure 1) made up of 6mm thick plate while the short sides (in the plane of Figure 1) are 12mm thick.

The core members have been sized using an estimate of the floor loads. Despite the fact that a 2D model was being investigated the core members were sized for the full 42x26m core of the 3D structure. The beams used in the core of this model are all 406x178x54UB sections. The columns have all been assumed as built up sections with 400x50mm flange plates and 300x30mm web plates.

In the 2D model the concrete slab has been included as a layer of 2-noded linear beam elements above the tops of the trusses and beams. The slab over the trusses is 100mm thick while the slab in the core is 125mm thick. Reinforcement has been included in the slabs as a separate group of nodes and elements running through the midpoint of the slab that are tied to the slab nodes. This reinforcement has been modelled as a smeared layer of steel with the sectional area as that given by 2 layers of welded wire mesh combined (1 layer, of 6mm diameter bars running in both directions at 100mm pitch, each in the top and bottom of the slab).

In each of these models all connections between beams/trusses and columns are assumed pinned. All connections are assumed to be perfect and connection failure has not been considered in this research. The bases of all the columns have been fully fixed in rotation and translation. The tops of the columns are fixed in rotation and horizontal translation but are allowed to translate vertically.

2.2 3D Model

Figure 2 shows a single floor of the 3D model investigated. For clarity the slab elements have been omitted. As with the 2D model 12 storeys were investigated under the effects of multiple floor fires. A symmetry model of half of the building was used to increase numerical efficiency in investigating the primary failure mechanism identified in the 2D work. The model was also created in "half resolution" to further reduce the size of the computational model. The 2D model represents a structure with columns and trusses at 1m and 2m spacing, respectively. This spacing was increased to 2m and 4m for columns and trusses respectively in the 3D model. The section sizes used in the floor trusses were increased to account for the change in resolution.

The move from full to half resolution was investigated extensively and was seen not to greatly alter the global response of the floor system¹⁴.

The loading and boundary conditions used are effectively the same as those assumed in the 2D work converted for use in a 3D model. The base of all columns was restrained in all translations and rotations while the column tops were restrained in all degrees of freedom except vertical translation. The symmetry boundary on each floor restrained the slab and transverse beams from translation in the 1 direction (as indicated in Figure 2). Rotation around the 2 axis was also restrained.

3. FIRE INPUT

In this study the compartment temperatures are based upon a generalized exponential curve given by¹⁵:

$$T(t) = T_0 + (T_{max} - T_0)(1 - e^{-at}) \quad \text{Equation 1}$$

where T_{max} and T_0 are the maximum and ambient compartment temperatures respectively. t represents the time over which the model is analysed. a is an arbitrary 'rate of heating' parameter and for the purposes of this chapter has been taken as 0.005. The applied temperature time distribution for the 100mm thick floor slab may be seen in Figure 3 which has been used for both of the models presented here.

The trusses are assumed to have no protection and are therefore assumed to equal the compartment temperature. The outer columns are assumed to be protected with a fire rated material and therefore will undergo more limited heating.

In both models the concrete slab has a realistic temperature distribution applied through its depth based on a heat transfer analysis from the fire. In the 2D model this is done by applying individual time-temperature curves to 3 different points through the depth of the slab (top surface, underside and midpoint). In the 3D model 5 discrete, equally spaced points are used to apply the temperatures through the depth of the slab from the underside to the top surface. All slabs were assumed to be heated from one side only even when it was between two floors that were on fire. This assumption is based on the amount of insulation that can normally be found on the upper side of an office building floor slab. Floor coverings, service gaps and suspended floor systems will all reduce the amount of radiation reaching the actual slab while

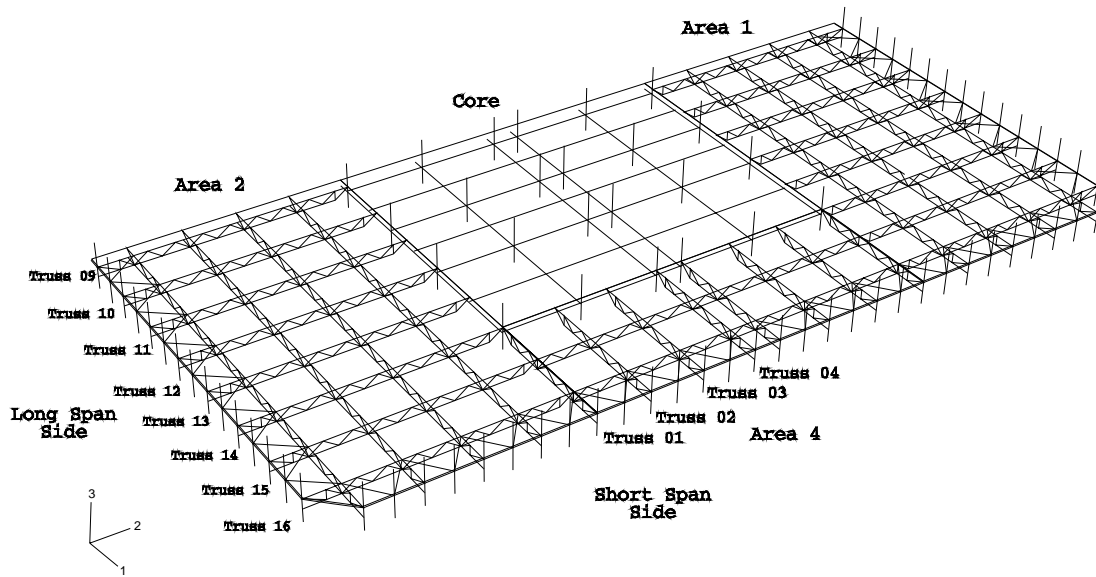


Figure 2 : 3D Model Mesh

convection will keep the hottest gasses away from the floor.

Columns in the 2D model that were situated within the fire compartment envelope were assumed to heat up at a much slower rate than the internal members of the structure. This can be attributed to higher levels of protection and having 3 sides of the member being exposed to ambient, external conditions. Thus in the 2D model the affected columns heat up linearly to 400°C over the whole analysis time. Due to numerical convergence difficulties in the 3D model the columns and spandrel beams were kept at ambient conditions.

This fire regime was applied to the outer areas of 3 stories over the mid-height of the model, as indicated by Figure 1.

The structural members affected are the outer columns, the trusses and the associated areas of concrete slab. The core members were kept entirely at ambient conditions on the assumption that integrity was maintained by the core compartmentation.

4. RESULTS

4.1 Global Response of 2D Model

Below is a description of the observed global response that ended in collapse of the 2D model after about 700s.

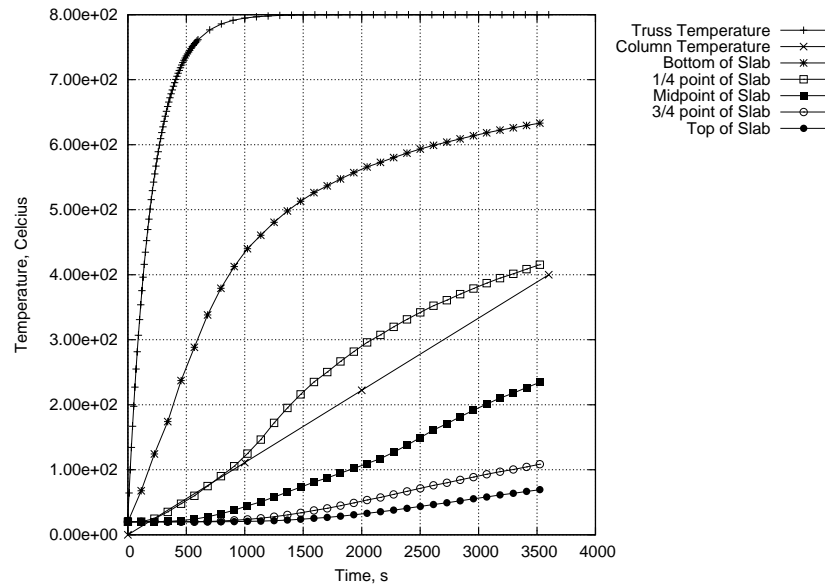


Figure 3 : Temperature Time Distributions

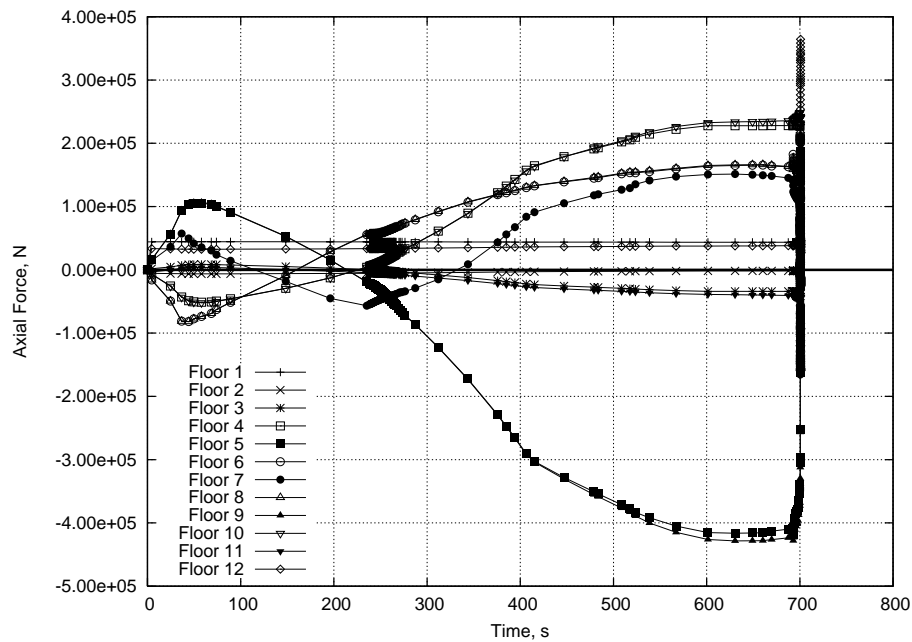


Figure 4 : Floor Membrane Forces

All the floors affected by fire (6, 7 & 8) start to expand. As the fire floors 6 and 8 are adjacent to cool floors (5 & 9), they go into high compression as they expand against the restraint provided by the column (see Figure 4). The cool interface floors (5 and 9) adjacent to the fire floors go into tension as the column is pushed out and pulls these floors outward. These floors then act as pivots on the outer columns and the next floors up/down go into compression to a lesser degree. The middle fire floor does not undergo the same forces due to the actions of the column and compatibility of displacements at that level. The expansion of the fire floors (6 and 8), at the interface of the heated and unheated floors, forces the outer columns to move into a curve. This curve means that tension is developed in the 7th floor connection as this floor is expanding at the same rate as the other fire floors while the column

at that level is moving out further due to compatibility. This phase occurs as the steel heats up rapidly over the first 200-300 seconds.

As the interface fire floors (6 & 8) begin to lose stiffness they retract and the outer columns also begin to return until the floors move into tensile membrane/catenary action and actively pull the column inward. To counter this, the cool interface floors (5 & 9) go into compression. The forces again pivot their way through the rest of the cool structure. As the interface fire floors lose stiffness they move into tension and the middle fire floor moves into compression as the column moves back in. The middle fire floor (7) is subjected to compression before large deflections in the floor take it into tension.

The movement of the column over the fire floors is directly related to the forces applied to it by the displacements of the fire floors. The outer columns at this point in the analysis can be assumed to be acting as linear springs connected to the ends of the trusses. Such movement induces moments in the columns as can be seen in Figure 5. Toward the end of the analysis (and thus the collapse of the structure) the moments in the outer columns begins to plateau. Reference to Figure 6 indicates that this is the plastic yield moment of the column section in combined bending and axial force. Thus the failure of the structure is due to plastic hinges forming at the column connections of floors 4, 7 and 9. The final displaced shape of the structure can be seen in Figure 7. In order to understand the processes involved in the movement of the outer column an analysis was conducted comparing the moments in the column taken directly from ABAQUS to those produced by theory. The outer column was simplified into a fixed ended beam as shown in Figure 8 with the fire affected floors (6, 7 & 8) being represented purely by a horizontal force. The effect of the cool interface floors, above and below the fire floors, was modelled by assuming a fixed end at that point. Simple bending theory was applied to create equations for the moment at points A, B and C as caused by forces H1, H2 and H3. These forces are the horizontal component of the forces in the truss-column connections as taken directly from ABAQUS. Additionally the $P-\delta$ moment at C was calculated using the applied load P and the horizontal deflection of point C again taken directly from the ABAQUS analysis.

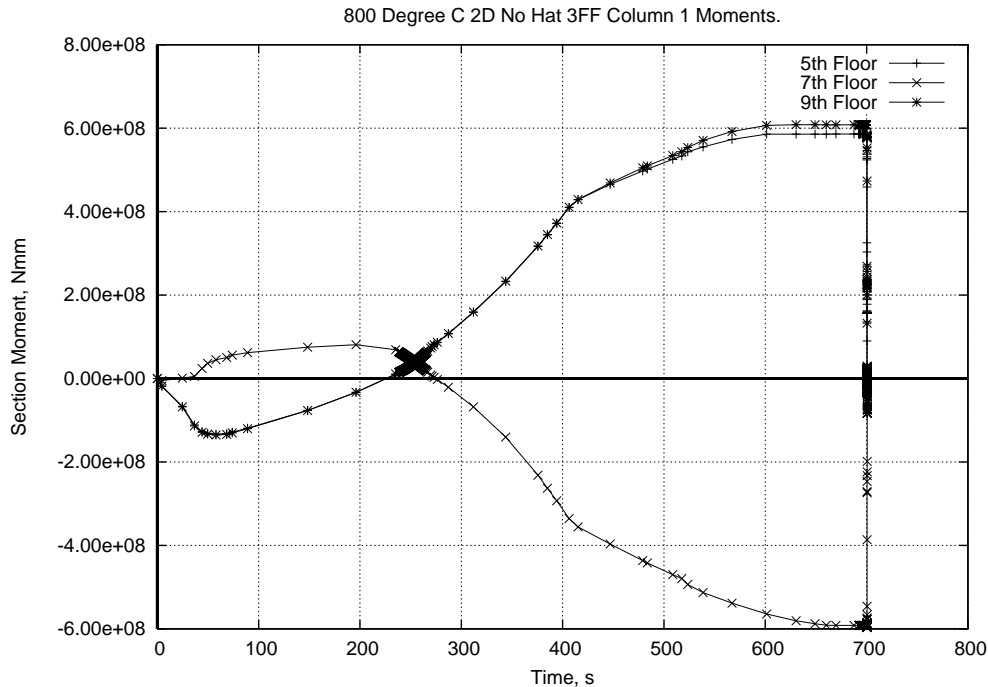


Figure 5 : 2D Model Column Moments at Hinge Positions

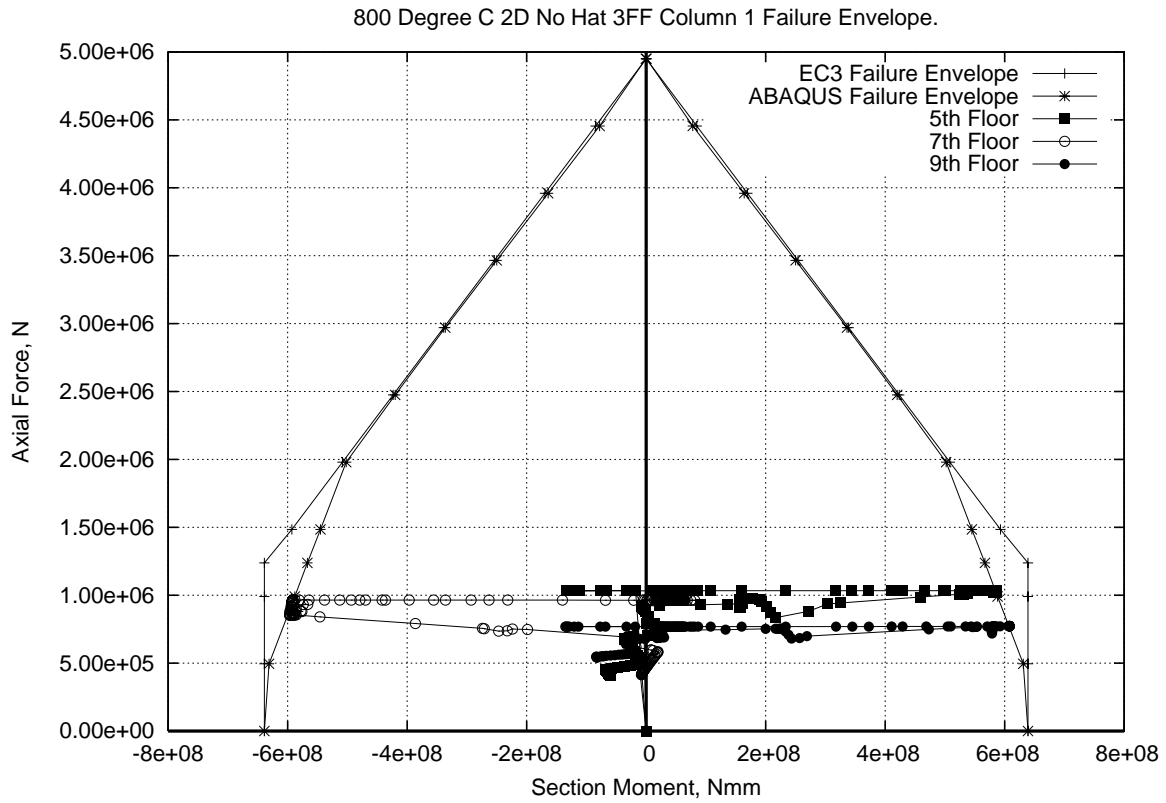


Figure 6 : Column Failure Envelope

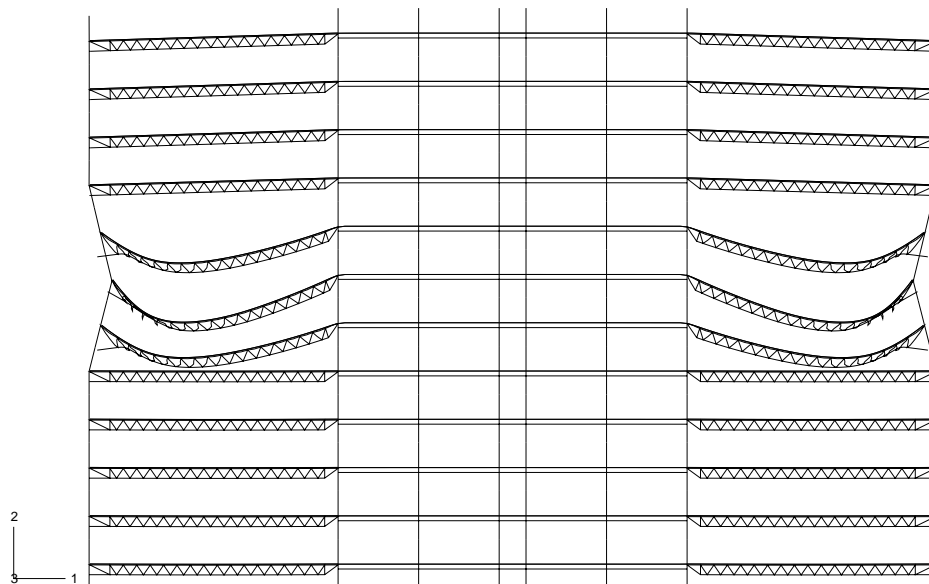


Figure 7 : Final Displaced Shape

Figure 9 shows the comparison between the figures taken from the simplified theory and those taken directly from ABAQUS. The results match very closely. For M_a and M_b the

moment can be seen to be somewhat higher for the theory but this can be explained by the choice of boundary conditions. The full ABAQUS model effectively has spring supports at floors 5 and 9 due to the continuation of the columns. The fully fixed supports assumed for the theory calculations naturally attract a higher moment. For M_c it is clear that under the conditions present in this model it is the moment caused by the floor pull in forces that is dominant. The $P-\delta$ moment grows in significance over the course of the analysis but even near collapse is smaller than the midspan moment caused by the floor forces. However as collapse progresses the $P-\delta$ moment increases at a much higher rate. When these moments are combined then the theory closely matches the model. If a larger load was applied to the column or if the column section was stiffer (therefore deflecting less) then the P -delta component of the moment would be more or less, respectively. The effects of altering column section must be carefully balanced against the forces found in the floors. A reduction in column lateral displacement will help reduce $P-\delta$ moments but will also increase connection forces leading to possible failure.

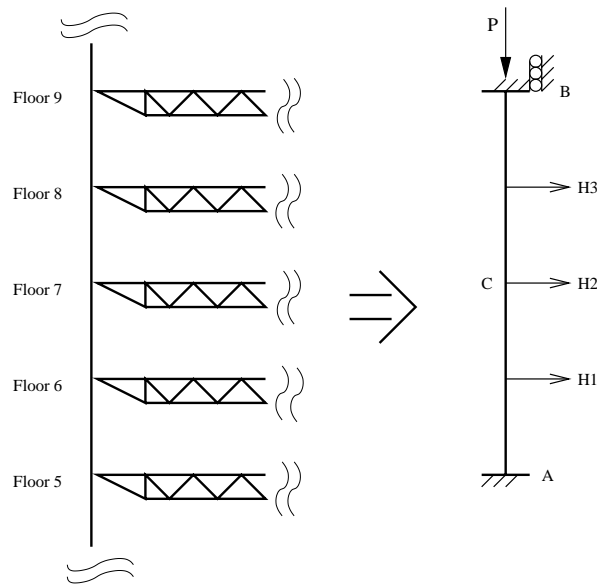


Figure 8 : Column Theory Simplification

The theory calculations did not take into account the vertical component of the fire floor connection forces but as the results match so closely it can be assumed that the effect of these vertical forces are negligible. Failure of this structure is a result of the inability of the structure to redistribute loads away from affected areas. Not only do the floors in this scenario lose the ability to provide lateral restraint to the column but they actively pull the columns out of plane. With enough displacement in the columns the ability to hold up the floors above is lost and progressive collapse is initiated.

4.2 Global Response of 3D Model

2D models have inherent limitations. The assumption in the 2D case described above that the structure was effectively an infinite extent of closely spaced truss lines may give an unrealistic response. A full 3D model allows a structure to redistribute forces through the floor membrane and can also create issues of compatibility, for instance, at corners.

In order to determine if the collapse mechanisms indicated by the 2D work were realistic a set of 3D models was investigated. As described in Section 2.2 the 3D model was based closely on the 2D model but also included a realistic distribution of structure in the 3rd dimension.

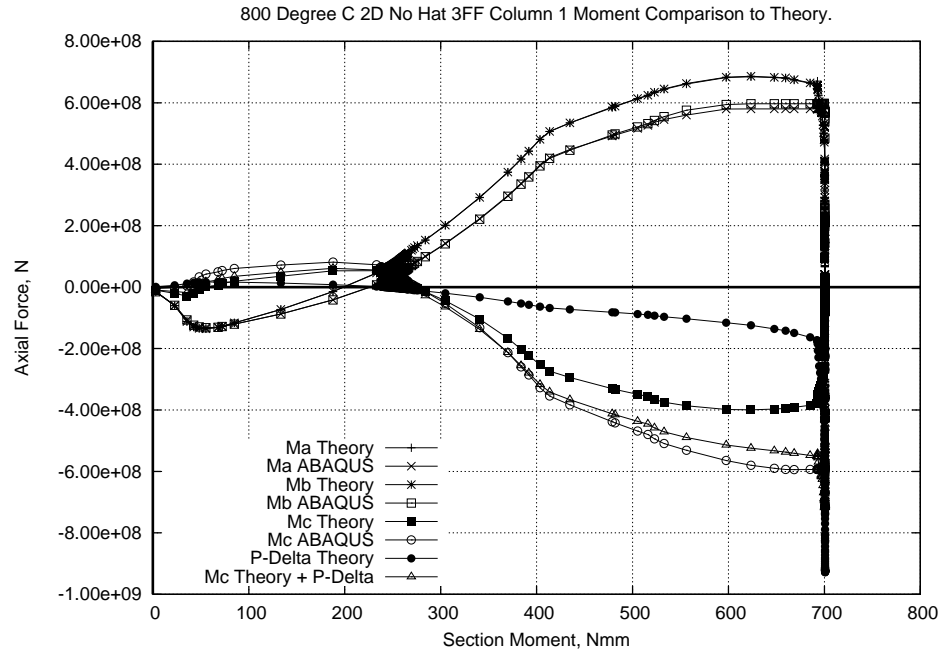


Figure 9 : Moment Theory Comparison

The response of the multi-storey 3D structure was very similar to that of the 2D analyses that preceded it. The response was again driven by the thermal expansion in the floor system. The large displacements imposed upon the floor system by the fire initially pushed the boundary columns out before increasing midspan deflections lead to catenary/tensile membrane action in the composite floors. This change in the floor geometry draws the column lines inward until they reach yield in combined bending/axial force. Figure 10 shows that the 3D model also produces the large midspan deflections typical of the 2D analyses. Inward movement of the columns is also of the same order as that indicated in the 2D analyses.

The primary difference between the 2D and the 3D analyses is that in the 3D work the response is more gradual down the long span sides of the building. As each column is affected it gradually sheds load onto the column next to it. Thus the centre of the long span sides (Truss 09 as shown in Figure 2) shows much greater deflections than the more stiff corners of the building (Truss 16).

This effect can also be seen in the moments in the columns at the lower plastic hinge location, at the 5th floor connection in Figure 11. Figure 11 also includes a direct comparison to the 2D response at the lower plastic hinge location. It can be seen that while the response in the 3D analysis occurs slightly later they are very similar. The outward push at the start of the analysis is apparent at the start of the analysis and this gradually changes into an inward pull that the columns have to resist. In the case of the 3D analysis, however, there are more columns sharing the effects of this movement and the floor is restrained, to a certain extent, by compatibility. The trusses toward the corner of the building (Trusses 15 and 16) have to maintain compatibility with the sides of the building, which limits the level of deflection that can occur. Hence Figure 11 shows an increase in moment in the columns that progresses along the column line from the centre of the building, where the trusses are relatively unrestrained, toward the corner of the building where more restraint and lower mid span deflections keep the columns from moving excessively. The 3D analysis terminated at around 1200s when a significant number of columns can be seen to have reached yield. While full collapse was not directly shown in the 3D model, analysis of the results strongly indicates that

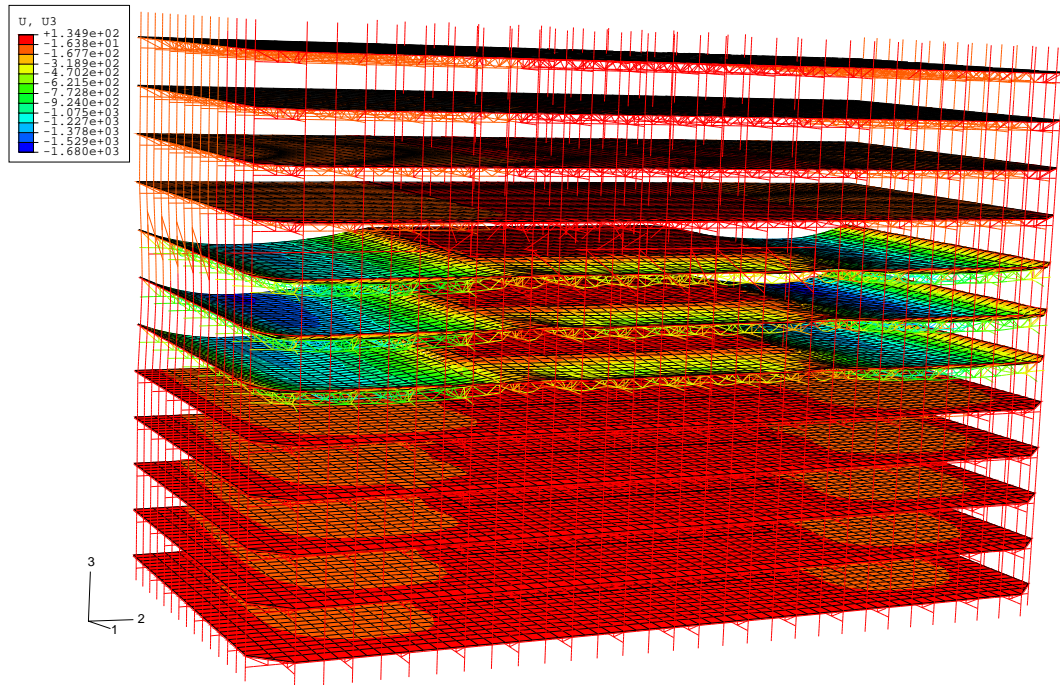


Figure 10 : 3D Model Final Floor Displacements

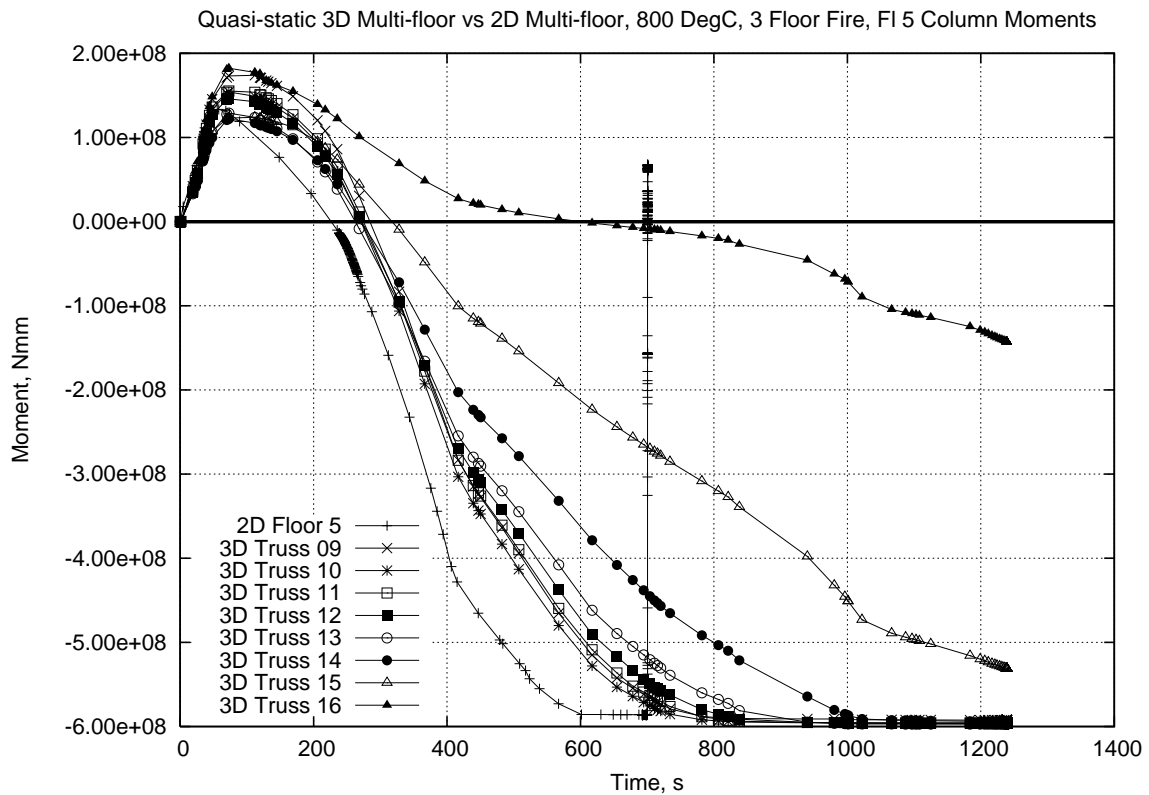


Figure 11 : 3D Column Moments at Lower Plastic Hinge

progressive collapse was being initiated in the structure. The collapse mechanism involved was again due to failure of the outer columns in combined bending/axial load.

5. CONCLUSIONS

This paper presents an analysis of a large building under fire conditions and reports on an interim stage in the investigation into the effects of fire on buildings with long span, truss based floor systems. The results match well with previous work on this project¹³.

Large displacements may be seen in the floor trusses under fire loading which can have a significant effect on the response of the columns. Global failure mechanisms are based around failure of the exterior columns after they have been drawn inward by tensile membrane action in the composite floor and form plastic hinges at floor-column interfaces.

An analysis of a similar structure in 3D showed similar structural behaviour as in the 2D work. The response of the structure was again dictated by the thermal expansion and thermal bowing of the floor system. The later response of the structure leads to apparent movement in the outer columns to the point where the columns loads can no longer be sustained. As there is no means of redistributing these column forces the outer structure collapses progressively.

6. REFERENCES

- [1] Neil Cameron (2003), "The Behaviour and Design of Composite Floor Systems in Fire", PhD Thesis, University of Edinburgh, 2003
- [2] Partners in Technology Report (2001), "Behaviour of steel framed structures under fire conditions", University of Edinburgh, 2001
- [3] S. Lamont, "The Behaviour of Multi-storey Composite Steel Framed Structures in Response to Compartment Fires", Edinburgh Uni PhD Thesis, 2001
- [4] Burgess, I.W. & Plank, R.J., "Modelling the Fire Tests on the Cardington Full-Scale Frame", Proc. 3rd Cardington Conference, November 1998.
- [5] Federal Emergency Management Agency, "World Trade Center Building Performance Study: Data Collection, Preliminary Observations and Recommendations", FEMA, May 2003
- [6] NIST, Federal Building and Fire Safety Investigation of the World Trade Center Disaster : Final report on the collapse of the World Trade Center Towers, NIST NCSTAR 1, September 2005
- [7] Ove Arup, Madrid Windsor fire: the Arup view, www.arup.com, accessed November 2005
- [8] J.L. Gross & T.P McAllister, "NIST NCSTAR 1-6 : Structural Fire Response and Probable Collapse Sequence of the World Trade Center Towers", NIST, September 2005
- [9] Hibbett, Karlsson & Sorenson Inc., "ABAQUS v6.4 & v6.5 Manuals", ABAQUS Manual Set, 2003-2005
- [10] British Standards Institution (2004), Eurocode 2: Design of concrete structures. General rules and rules for buildings, BS EN 1992-1.1:2004
- [11] British Standards Institution (2005), Eurocode 3: Design of steel structures. General rules and rules for buildings, BS EN 1993-1.1:2005
- [12] H.S. Lew, R.W. Bukowski & N.J. Carino, "Federal Building and Fire Safety Investigation of the World Trade Center Disaster : Design, Construction, and Maintenance of Structural and Life Safety Systems", NIST NCSTAR 1-1, September 2005
- [13] G. Flint, A.S. Usmani, S. Lamont, J. Torero, B. Lane, "Effect of Fire on Composite Long Span Truss Floor Systems", Journal of Constructional Steel Research, in press 2005
- [14] G. Flint, "Fire Induced Collapse of Tall Buildings", PhD Thesis, University of Edinburgh, 2005 (may be accessed at www.civ.ed.ac.uk/research/fire/thesis.html)
- [15] A.S.Usmani, Y.C.Chung and J.L.Torero. How did the WTC Towers Collapse? A New Theory. *Fire Safety Journal*, 38:501--533, 2003.
- [16] British Standards Institution (2003), Structural use of steelwork in building. Code of practice for fire resistant design, BS 5950-8:2003



REFINED PLASTIC-HINGE MODEL FOR THE ANALYSIS OF STEEL-FRAMED STRUCTURES UNDER FIRE CONDITIONS

Alexandre LANDESMANN¹ and Eduardo de Miranda BATISTA²

ABSTRACT

This paper is addressed to the application of an advanced analysis computational tool, Program SAAFE (*System for Advanced Analysis of Fire Engineering*) developed to provide an inelastic analysis of steel-framed structures under fire. A transient heat transfer analysis model is used to automatically consider the temperature gradient effects due to non-uniform exposure to fire, for both protected and non-protected cross-section. The structural inelastic behaviour is simulated up to the failure, by a second-order plastic-hinge method, extended to fire conditions, taking into account a tangent modulus model and a gradual transition from elastic to plastic regime. The following characteristics are present in the proposed approach: (i) large-displacement formulation; (ii) temperature dependent mechanical properties of the steel; (iii) combined actions of mechanic and thermal loading; (iv) geometrical and the material non-linear effects. Results from an 11-story steel-frame building are presented for different fire scenarios, the correspondent time-resistance period is evaluated, outlining the advantage of considering the steel ductility in the current design practice for steel structure under fire.

1. INTRODUCTION

The application of simplified structural analyses for fire condition, as proposed by conventional design codes [1,2], are not able to describe the actual behaviour of structures when deformations are large and the non-linear behaviour is predominant.

The steel structural stiffness (E - young modulus) and the yield limit (f_y) are considerably reduced as the temperature increases. In these situations, structural analysis shall be performed by a non-linear inelastic method, in order to accurately capture most significant effects. In this context, extensive research has been carried out in recent years based on the

¹ Adjunct Professor, Department of Structures, Faculty of Architecture and Urbanism, Federal University of Rio de Janeiro, Rio de Janeiro/RJ, ZIP 21941-590, Brazil, alandes@coc.ufrj.br.

² Adjunct Professor, Civil Engineering Program, COPPE/UFRJ, Federal University of Rio de Janeiro, POB 68.506, Rio de Janeiro/RJ, CEP 21945-970, Brazil; batista@coc.ufrj.br.

numerical simulation of steel structures subjected to fire conditions, especially with FEM developments [3,4]. As an alternative, plastic-hinge methods [5,6,7] have also been used to investigate the behaviour of structures subjected to compartment fires. Following recent applications of the Advanced Analysis concept under fire conditions [8,9], this paper presents a plastic-hinge formulation to be used in the performance-based assessment of steel-framed structures (2D) subjected to standard fires. The present numerical approach, denominated SAAFE Program (*System for Advanced Analysis for Fire Engineering*) is based on the development of the following features [9]: (i) a refined plastic lumped formulation with two interaction surfaces representing gradual stiffness degradation [6,10,11]; (ii) a tangent modulus model which includes both gradual inelastic loss of stiffness and ultimate strength of column members [6,10]; (iii) a second-order large-displacement formulation [5,13], based on the concept of Stability Functions [10,12], allowing accurate identification of instability with very little computational effort [14]; (iv) accounting for a non-homogeneous temperature distribution over the cross-section, which represents a realistic prediction of the fire effect over the structure [9]. As part of the SAAFE capabilities, a FEM program performs a 1D heat transfer analysis [15], responsible to calculate the temperature distribution over the element cross-section as presented in Section 2. The structural module performs the structural response [9], considering the mechanical properties, loading level and temperature field, the resulting non-linear equilibrium equations are solved by a Newton–Raphson incremental iterative procedure [9], as shown in Section 3. Numerical studies are carried out for an 11-storey portal frame [16] exposed to different compartmented fire conditions [17]. The computed results are presented as given in Section 4. The main conclusions are presented in Section 5.

It is important to emphasize that, results obtained with SAAFE has been previously contrasted [18] with a more sophisticated analysis program for fire design, the SAFIR program [19], being observed good agreement.

2. THERMAL ANALYSIS

A non-linear heat transfer analysis model [9,15] is proposed to simulate the effects due to the temperature gradient over the height of the cross-section, with or without insulation layers for fire protection [9]. In this approach, the section is subdivided into a predefined number (n) of segments (k) along the y -axis of the cross-section, as shown in Fig. 1, being assumed a linear temperature distribution in each element length (h_k).

The temperature dependent constitutive laws of steel [1] are adopted in the thermal procedure, which is solved by direct time integration scheme, based on a generalized trapezoidal rule [15], given as follows:

$$\left(\frac{1}{\Delta t} [M] + \omega [C + H] \right) \{ \theta \}_{n+1} = \left(\frac{1}{\Delta t} [M] - (1 - \omega) [C + H] \right) \{ \dot{\theta} \}_n + (1 - \omega) \{ R \}_n + \omega \{ R \}_{n+1} \quad (1)$$

In the previous expression (Eq. 1), vectors θ and $\dot{\theta}$ respectively represent the nodal point temperature and the corresponding temperature rate, ω is given as a temporal integration factor, adopting 0.9 [19], Δt is the fire time step (seconds), and the remaining terms are presented in Table 1.

The temperature dependent thermal properties of steel, such as the thermal conductivity (λ_k) and the steel specific heat (v_k), established by prEN 1993-1-2 [1], are incrementally considered in the present numerical procedure. The unit mass of steel (ρ_s) and the coefficient of heat transfer (μ_s) are considered to be independent of the steel temperature,

being adopted the following values: 7850 kg/m^3 and $25 \text{ W/m}^2\text{K}$. The gas temperature (θ_g) and the associated heat flux (R) are assumed to be uniformly distributed over all exposed areas of the structural member, in its longitudinal direction.

Table 1: Expressions used for the one-dimension thermal analysis approach.

Lumped mass [M]	Heat capacity [C]	Convection matrix [H]	Heat flux vector [R]
$\sum_{k=1}^n A_k h_k \rho_s \nu_k \begin{pmatrix} \frac{1}{2} & 0 \\ 0 & \frac{1}{2} \end{pmatrix}$	$\sum_{k=1}^n \frac{A_k \lambda_k}{h_k} \begin{pmatrix} 1 & -1 \\ -1 & 1 \end{pmatrix}$	$\sum_{k=1}^n \frac{1}{6} \mu_s h_k p_k \begin{pmatrix} 2 & 1 \\ 1 & 2 \end{pmatrix}$	$\sum_{k=1}^n \frac{1}{2} \mu_s \theta_g h_k p_k \begin{pmatrix} 1 \\ 1 \end{pmatrix}$

The thermal model is also responsible for establishing a link between thermal and structural analysis. In this step, equivalent cross-section properties and thermal end-forces are evaluated for each fire time step, taking into account the computed temperature in each segment (k). The expressions used in this calculation are presented in Table 2, where the elastic reduction factor $\kappa_{E,\theta}$ and the yield reduction factor $\kappa_{y,\theta}$ are taken in accordance with EC [1].

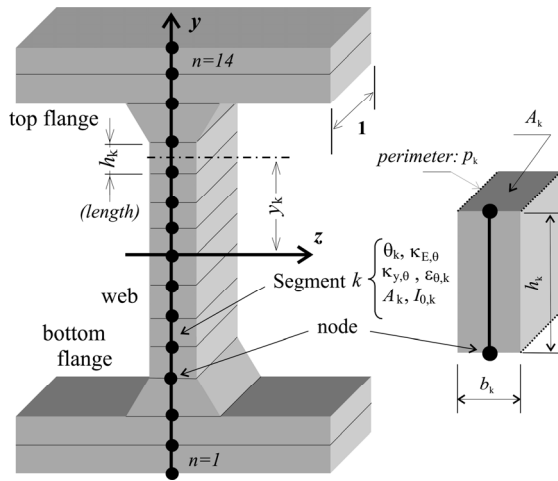


Fig. 1: One-dimension thermal model for H or I-shape cross-sections.

Table 2: Expressions used for the equivalent cross-section approach.

Cross-section area:	$A_\theta = \sum_{k=1}^n \kappa_{E,\theta,k} A_k$
Moment of inertia:	$I_\theta = \sum_{k=1}^n \kappa_{E,\theta,k} b_k h_k y_k^2$
Reference temperature:	$\theta_{ref} = \left(\sum_{k=1}^n \theta_k A_k y_k^2 \right) / I$
Inelastic axial strength:	$P_{y\theta} = \sum_{k=1}^n \kappa_{y,\theta,k} f_y A_k$
Inelastic flexional strength:	$M_{p\theta} = \sum_{k=1}^n \kappa_{y,\theta,k} f_y A_k y_k $

As a part of the proposed simplified approach, a reference temperature (θ_{ref}) is adopted to account for, in a simplified manner, a non-uniform temperature distribution over the cross-section, to be used in the plastic-hinge formulation. Thermal deformations are considered by means of Duhamel's approach [20], by the following expressions (Eq. 2) for axial (P_θ) and flexural (M_θ) forces respectively, where ε_θ is the steel thermal expansion coefficient [1]:

$$P_\theta = \sum_{k=1}^n \varepsilon_{\theta,k} (\kappa_{E,\theta,k} E) b_k h_k ; \quad M_\theta = \sum_{k=1}^n \varepsilon_{\theta,k} (\kappa_{E,\theta,k} E) b_k h_k y_k \quad (2)$$

3. STRUCTURAL ANALYSIS

3.1 Inelastic stiffness degradation

The proposed second-order refined plastic-hinge approach [9] considers the elliptical transition between elastic to plastic domains, for steel under elevated temperatures [1], by a set of inelastic reduction factors (η_θ) [9]. These factors are used to allow a gradual plastification of the cross-section for different temperature conditions, which results in a substantial loss of stiffness, leading to pronounced non-linear behaviour as the steel temperature increases. The η_θ expression, presented by Eq. (3), Fig. 2 and Table 3, is obtained by an analytical process [9], assuming a uniform temperature distribution equal to the reference temperature θ_{ref} (given in Table 2).

$$\eta_\theta = c_1 + c_2 \cdot \alpha + c_3 \cdot \alpha^2 + c_4 \cdot \alpha^3 + c_5 \cdot \alpha^4 \quad (3)$$

The α factor is based on the interaction equation proposed by the AISC-LRFD [21], being expressed in terms of the plastic strengths $P_{y\theta}$ and $M_{p\theta}$ (given in Table 2). Two interaction surfaces are adopted to represent a smooth transition from elastic to plastic domain. In this approach, the plastic strength surface for a given reference temperature is defined when the force-state parameter α , as presented in Eq. (4), is equal to unity. The initial yield surface, which delimits the elastic region, is obtained in accordance to the η_θ reduction factor, assuming the same shape of the full plastic strength surface.

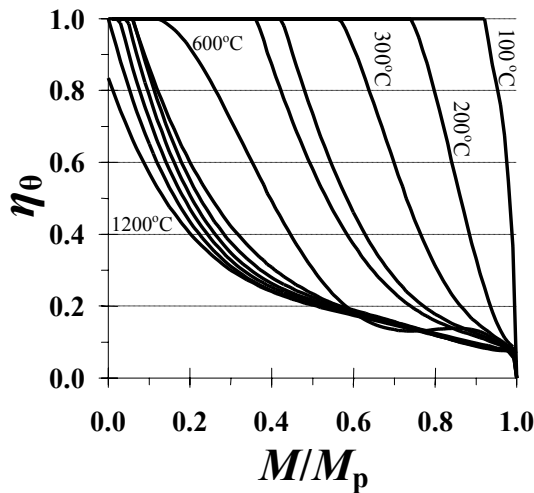


Fig. 2: Inelastic reduction factor for different steel reference temperatures.

Table 3: Coefficients of Eq. (3), used for the equivalent cross-section approach.

θ_{ref} [°C]	c_1	c_2	c_3	c_4	c_5
100	13523	-54059	80792	-53468	13213
200	-44.77	181.41	-245.94	127.25	-17.87
300	-19.66	115.98	-232.40	196.81	-60.67
400	2.70	-2.19	-10.32	17.46	-7.58
500	2.70	-5.20	-0.54	6.76	-3.64
600	0.85	3.12	-18.89	26.81	-11.85
700	1.24	-4.43	7.21	-5.57	1.62
800	1.31	-5.71	11.64	-11.08	3.92
900	1.24	-5.58	11.85	-11.63	4.2
1000	1.13	-5.09	10.94	-10.87	3.96
1100	1.00	-4.37	9.34	-9.28	3.38
1200	0.83	-3.23	6.53	-6.33	2.27

Figure 3 shows the beam-column element used in the present approach [9].

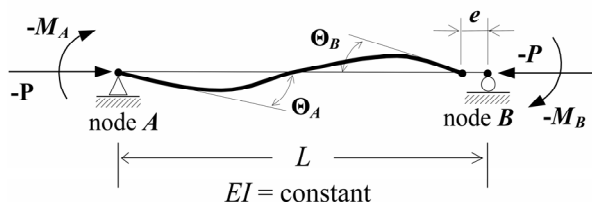


Fig. 3: Beam-column element used in the proposed approach.

$$\alpha = \begin{cases} \frac{P}{P_{y\theta}} + \frac{8}{9} \frac{M}{M_{p\theta}}, & \text{for } \frac{P}{P_{y\theta}} \geq \frac{2}{9} \frac{M}{M_{p\theta}} \\ \frac{P}{2P_{y\theta}} + \frac{M}{M_{p\theta}}, & \text{for } \frac{P}{P_{y\theta}} < \frac{2}{9} \frac{M}{M_{p\theta}} \end{cases} \quad (4)$$

The gradual plastification process is incorporated in the beam-column incremental force-displacement relationship [11] as given in Eq. (5), where the sub indices A and B are referred to the ends of the member, as shown in Fig. 3.

The tangent modulus model is used in substitution of the elastic modulus E to simulate the inelastic behaviour of compressed members under elevated temperatures. Because E_t is based on the buckling strength curves [2], such as the European fire design buckling-curve [1], it implicitly considers the axial force, member geometrical imperfections, and residual stresses on the beam-column inelastic stiffness.

$$\begin{Bmatrix} \dot{M}_A \\ \dot{M}_B \\ \dot{P} \end{Bmatrix} = \frac{E_t I}{L} \begin{bmatrix} S_{ii} & S_{ij} & 0 \\ S_{ij} & S_{jj} & 0 \\ 0 & 0 & A/I \end{bmatrix} \begin{Bmatrix} \dot{\Theta}_A \\ \dot{\Theta}_B \\ \dot{e} \end{Bmatrix} \quad \begin{aligned} S_{ii} &= \left[S_1 - \frac{S_2^2}{S_1} (1 - \eta_B) \right] \eta_A \\ S_{jj} &= \left[S_1 - \frac{S_2^2}{S_1} (1 - \eta_A) \right] \eta_B \\ S_{ij} &= \eta_A \eta_B S_2 \end{aligned} \quad (5)$$

Terms S_1 and S_2 , (Eq. 5) are referred as the stability functions [10,11,12], E_t is the tangent modulus model given by the following expression (Eq. 6) [9]:

$$\frac{E_t}{E} = 0.983 - 1.828 \left(\frac{P}{P_{y\theta}} \right) + 3.484 \left(\frac{P}{P_{y\theta}} \right)^2 - 5.534 \left(\frac{P}{P_{y\theta}} \right)^3 + 2.896 \left(\frac{P}{P_{y\theta}} \right)^4 \quad (6)$$

4. EXAMPLE OF APPLICATION: 11-STOREY FRAME

Figure 4 shows the external loading, the geometrical and the element definition for an 11-storey steel framed structure [16] to be analysed with the help of the proposed SAAFE model for different fire conditions. The cross-section dimensions and materials are given in Fig. 4d. In Fig. 4a, one can observe the lateral notional load (N_i), evaluated as defined in Appendix 7.2 of AISC/LRFD [21], applied at each frame level (i), representing the 0,2% of the gravity load combination, as given in Eq. (6), also presented in Fig. 4b. The resultant vertical load combination takes into account the nominal dead load (D), the occupancy live load (L) and the forces due to the design-basis fire (F).

$$1.2D + N_i + 0.5L + F \quad (7)$$

A localised fire region is postulated to occur at two different levels of the building, directly affecting beams and columns of the framed-structure, as shown in Fig. 4c. The exteriors columns are assumed to be partially protected to fire, particularly at its top flange, due to the exterior closing wall. On the other hand, the middle columns are assumed to be uniformly exposed to fire. The beams are also considered partially protected to the fire action due to the presence of the concrete slabs on its top flange.

It has been considered two basics fire scenario conditions, in which a compartment fire is assumed to occur at the 1st and 2nd floors, and, at the 6th and 7th floors, respectively representing the *Scenario 1* and *Scenario 2*. For each proposed scenario (1 and 2) it was also assumed two different propagation condition, denoted as A and B . For the first one (A), the flashover is considered to occur simultanely at both floor levels. In the second one (propagation condition B), flashover is assumed to start at the lower level, reaching the upper

level after elapsed 17 minutes from the beginning of the standard fire. The assumed two basic scenarios with each correspondent fire propagation conditions are given in Fig. 5.

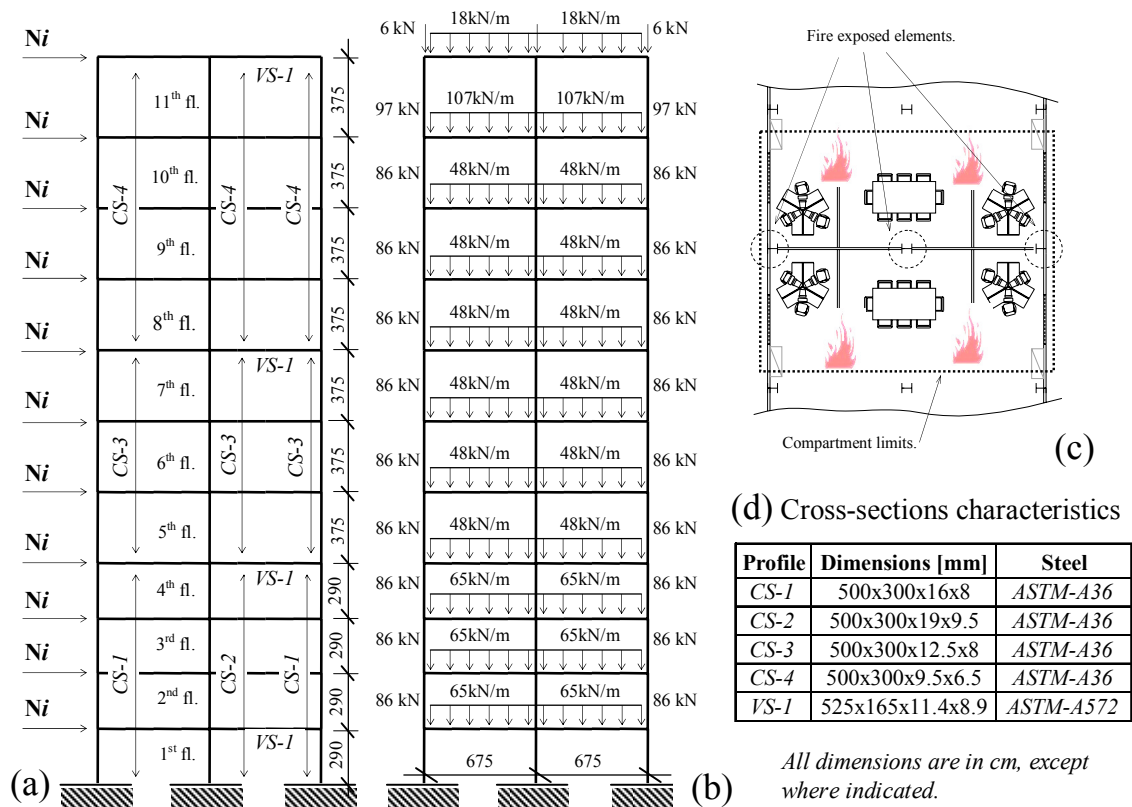


Fig. 4: Structural definition for the proposed 11-storey portal frame subjected to compartmented fire [9,16]. (a) Geometrical and cross-section definition; notional load indication (N_i), (b) Gravity load combination and horizontal dimensions, (c) compartment fire region, (d) profile dimensions and steels.

In order to assess the influence of the application of fire protection insulation materials in the global behavior and the correspondent failure time, the proposed 11-story frame was verified for four fire protection conditions. The level of protection varies from the case *NP*, non-protected to the *PA* case, in which both beams and columns are protected. Partially protection cases were also verified: *PC*, protection to the columns and *PV*, protection applied to the beams only. All the protection conditions were applied to each fire scenario, as indicated in Table 4. Being adopted a 8 mm thickness vermiculite layer, with the following characteristics: thermal conductivity $\lambda_p = 0.12 \text{ W/m}^\circ\text{C}$, specific heat $v_p = 1200 \text{ J/kg}^\circ\text{C}$, unit mass $\rho_p = 300 \text{ kg/m}^3$.

Table 4: Fire scenarios and correspondent protection cases proposed for the 11-story frame.

Scenarios		Cases	Fire Protection			
			None	Beam	Column	Both
1A	2A	NP	x			
		PA				x
1B	2B	PC			x	
		PV		x		

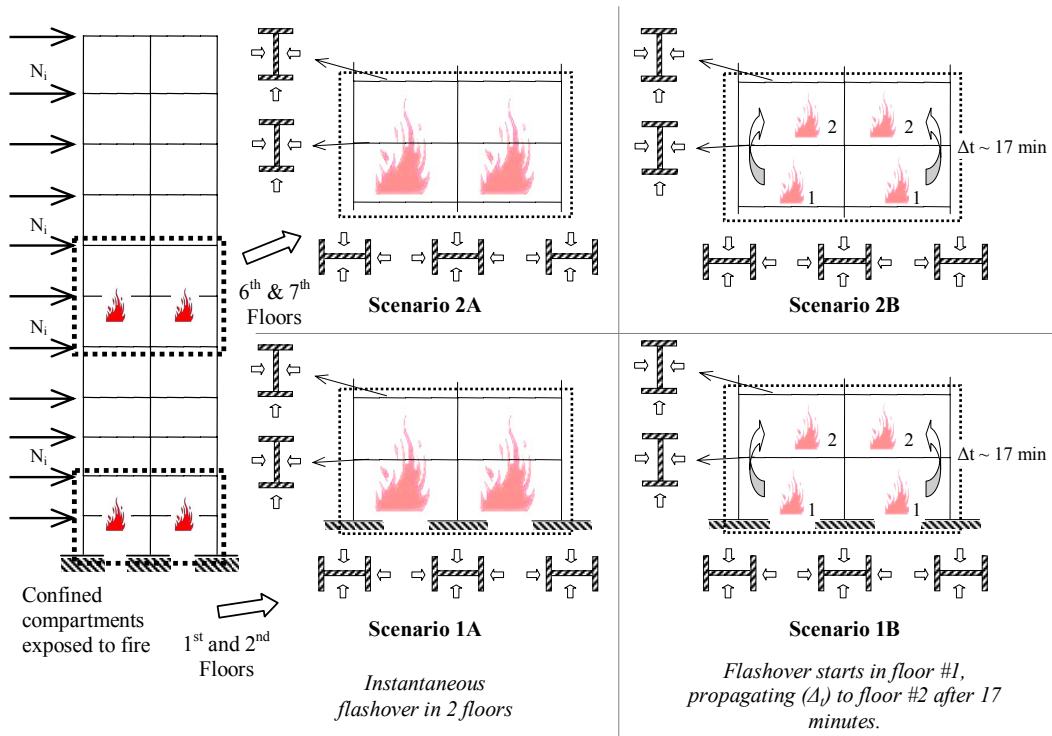


Fig. 5: Basic scenarios conditions postulated for the 11-storey portal frame building.

The obtained temperature variation (θ_{ref}) for the fire exposed elements in the confined region (Figs. 4 and 5), performed by the standard time-temperature curve [17], is shown in Fig. 6. In this, it is possible to verify the influence of the use of protection insulation and also the fire exposure condition. For the beams, the reference temperature after 1 hour is about 658°C assuming a protected condition, relatively inferior to the non-protected one which is about 940°C, very closed to the compartment ambient temperature, near to 945°C. Actually, as expected all non-protected exposed members reach temperatures very closed to the medium after elapsed 1 hour. The non-protected CS-3 cross-section exposed in 4 faces (4f) has a maximum temperature of 684°C, about 10% higher than the same section exposed in 3 faces.

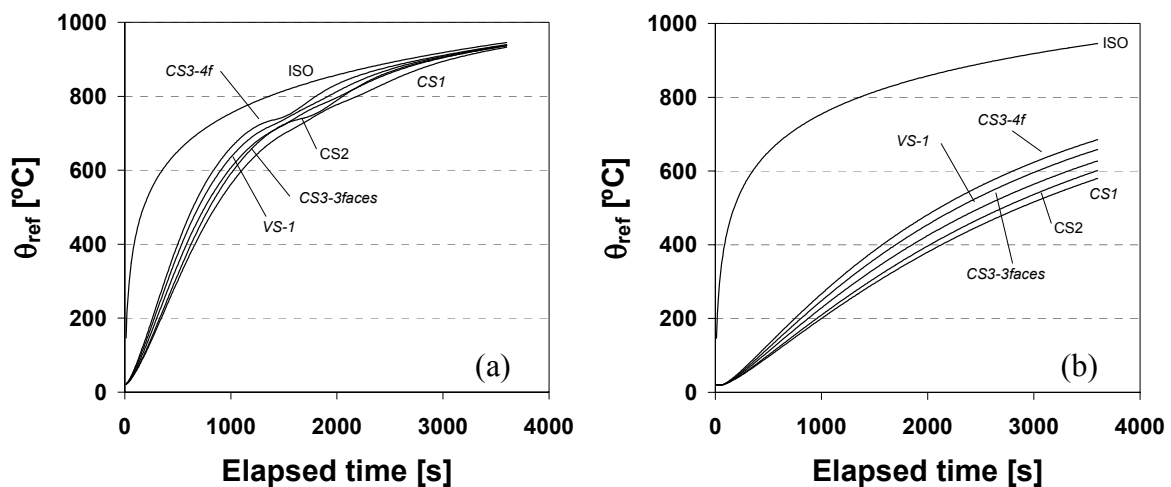


Fig. 6: Temperature variation for the fire exposed elements of the 11-story portal frame.
(a) non-protected member situation, (b) protected member situation.

A comparison between the global horizontal displacements, measured on the top of the structure (Δ_H), for all the postulated fire conditions, Fig. 5 and Table 4, obtained by the proposed approach (SAAFE) are shown in Fig. 7. For members not directly exposed to fire, it has been used the original second-order plastic-hinge approach [5,6,9,10].

Fig. 8 illustrates the non-linear structural behaviour of steel framed structures subjected to confined fire conditions, in which it is possible to verify the ability of the proposed inelastic approach [9] to capture the structural behaviour of steel framed structures subjected to confined fire conditions.

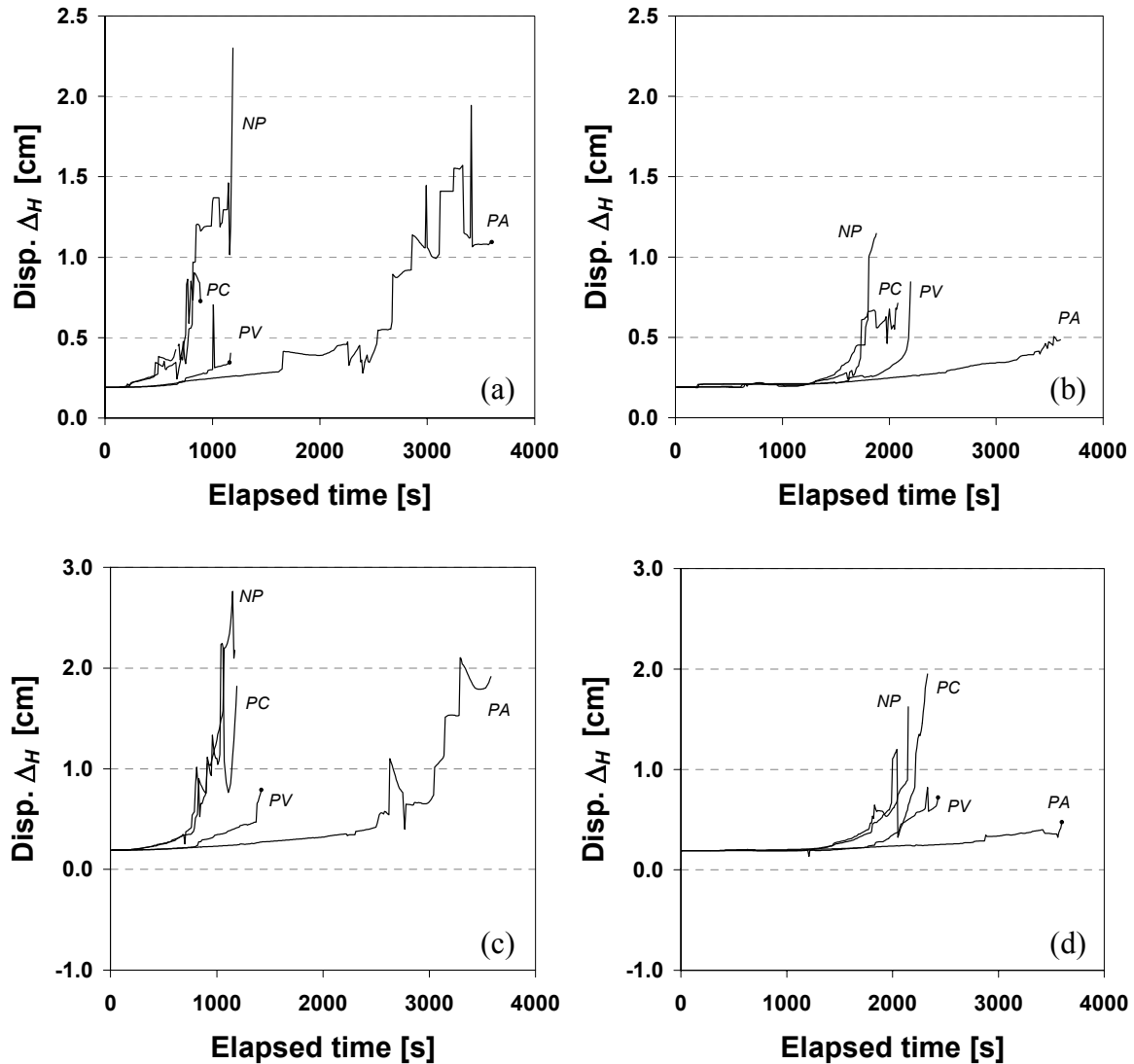


Fig. 7: Horizontal displacements for the 11-storey frame. (a) scenario 1A, (b) scenario 1B, (c) scenario 2A, (d) scenario 2B.

Based on the results obtained for the 11-story frame, it is possible to infer about the failure time, associated with the formation of an inelastic mechanism due to the postulated combined fire loading situations. Table 5 presents an estimation of the failure time for the proposed loading conditions. In general, as expected the non-protect conditions (NP) resulted to the lower ultimate time resistance, in which the case 1A was responsible for the lowest value, about 20 minutes. On the other hand, all PA cases, fully protected led to a maximum time period, over 60 minutes. The partially protection situations PV and PC

resulted a similar time period, varying from 20 to 36 minutes, very close to the *NP* results, demonstrating the necessity to performing a full protection for the proposed 11-story frame.

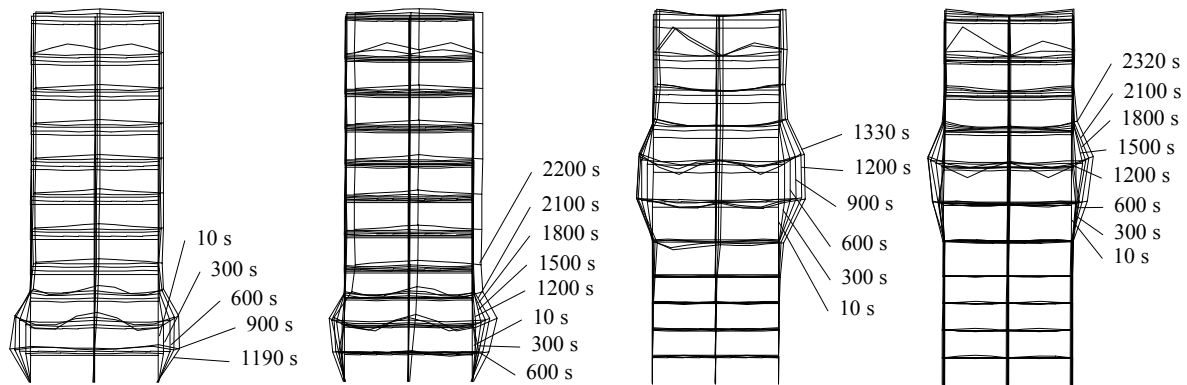


Fig. 8: Deformed configuration (30x) of the structure along the time of fire, according to ISO-834 fire curve. (a) scenario 1A, (b) scenario 1B, (c) scenario 2A, (d) scenario 2B.

Table 5: Failure elapsed time for the postulated loading scenarios obtained for 11-story frame.

Scenarios & Cases	Failure Elapsed Time [min]			
	<i>NP</i>	<i>PV</i>	<i>PC</i>	<i>PA</i>
1A	20	20	20	60
1B	32	37	35	60
2A	20	24	20	60
2B	36	41	39	60

5. CONCLUSIONS

A second-order refined plastic hinge analysis method, used to assess the performance of steel structures under fire conditions, is presented in this paper. The computational approach was developed on the basis of the Advanced Analysis concept [6], taking into account the non-linear behaviour of steel at elevated temperatures, as recommended by the prEN 1993-1-2 [1].

The model of analysis is applied to study the global behaviour of steel-framed structures exposed to different fire-heating conditions, by means of a standard time-temperature curve, allowing the identification of both local-member and global ultimate limit state of steel framed structures, including the inelastic loading redistribution. This feature represents a more economical and rational fire design than the simplified approach based on individual member capacity checks.

The computed results showed that the developed advanced analysis procedure is able to predict the critical time for different load levels. By contrast, although the proposed model is not able to accurately describe the inelastic behaviour of the beam-column elements when large flexural contributions are concerned, the global behaviour of framed structures were conveniently followed by the SAAFE computational program [9].

6. NOTATIONS

A_θ	equivalent cross-section area;
E	modulus of elasticity of steel for normal temperature design;
E_t	tangent modulus model;
I	moment of inertia for normal temperature conditions;
I_θ	equivalent moment of inertia at elevated temperature θ ;
L	beam-column length;
M_θ	bending moment at elevated temperature;
$M_{p\theta}$	equivalent flexural plastic limit strength;
P_θ	axial force at elevated temperature;
$P_{y\theta}$	equivalent squash load;
S_1, S_2	stability functions;
e	beam-column axial deformation;
f_y	yield strength;
h_k	length of the 1D thermal element;
Θ_A, Θ_B	beam-column end rotations;
ε_θ	thermal elongation of steel;
η_θ	inelastic reduction factor;
$\kappa_{E,\theta}$	elastic reduction factor of steel;
$\kappa_{y,\theta}$	yield reduction factor of steel;
θ_g	gas temperature;
θ_{ref}	cross-section reference temperature;

7. REFERENCES

- [1] EC-3 prEN 1993-1-2, European Prestandard Draft, *Eurocode 3: "Design of Steel Structures"*, Part 1.2: Structural Fire Design, CEN, Brussels (2001).
- [2] EC-3 prEN 1993-1-1, European Prestandard Draft (34), *Eurocode 3: "Design of steel structures"*, Part 1.1: General rules and rules for buildings, CEN, Brussels, 2003.
- [3] Saab, H.A., Nethercot, D.A., "Modelling of Steel Frame Behaviour under Fire Conditions", *Engineering Structures*, 1991, 13, 371-382.
- [4] Najjar, S.R., Burgess I.W., "A Nonlinear Analysis for Three-Dimensional Steel Frames in Fire Conditions", *Engineering Structures*, 1996, 18(1), pp. 77-89.
- [5] Liew, J.Y.R., 1992, "Advanced Analysis for Frames Design", *Ph.D. dissertation*, School of Civil Engineering, Purdue University, West Lafayette, IN.
- [6] Chen, W.F., Goto Y., Liew, J.Y.R., *Stability Design of Semi-Rigid Frames*. 1st New York, John Willey & Sons, Inc., 1996
- [7] Liew, J.Y.R., Tang, L.K., Holmaas, T., Choo, Y.S., "Advanced Analysis for the Assessment of Steel Frames in Fire", *Journal of Constructional Steel Research*, 1998, 47(1-2), 19-45.
- [8] Liew, J.Y.R., Tang, L.K., Choo, Y.S., "Advanced Analysis for Performance-Based Design of Steel Structures Exposed to Fire", *Journal of Structural Engineering*, 2002, 128(12), 1584-1593.
- [9] Landesmann, A., 2003, "Second-Order Inelastic Model for the Analysis of Steel-Framed Structures under Fire Conditions", *Ph.D. dissertation*, Civil Engineering Program, Federal University of Rio de Janeiro, COPPE/UFRJ (in Portuguese).

- [10] Liew, J.Y.R., White, D.W., “Second-Order Refined Plastic Hinge Analysis for Frames Design, Part 1”, *Journal of Structural Engineering*, 1993, 119(11), 3196-3216.
- [11] White, D. W., Liew, J. Y. R., Chen, W. F., “Toward Advanced Analysis in LRFD”. In: *Plastic Hinge Based Methods for Advanced Analysis and Design of Steel Frames – An Assessment of the State-of-the-Art*, Structural Stability Research Council, School of Civil Engineering, Purdue University, West Lafayette, IN, USA., 95-173, 1993.
- [12] Liew, J.Y.R., White, D.W., Chen, W.F., “Beam-Columns”, In: *Constructional Steel Design, An International Guide*, P. J. Dowling et al., ed., London, Elsevier, 105-132, 1991.
- [13] Powell, G.H., “Theory of Nonlinear Elastic Structures”, *Journal of the Structural Division - ASCE*, 1969, 95(ST12), 2687-2701.
- [14] Kim, S.E., Chen, W.F., “Sensitivity Study on Number of Elements in Refined Plastic-Hinge Analysis”, *Computers and Structures*, 1998, 66(5), 665-673.
- [15] Cook, R.D., Malkus, D.S., Plesha, M.E., *Concepts and Applications of Finite Element Analysis*, John Wiley & Sons, New York, 1989.
- [16] Silva, R.G.L., 2004, “Simplified second-order analysis of steel-framed structures”, *Ph.D. dissertation*, Federal University of Minas Gerais - UFMG, Belo Horizonte/MG (in Portuguese).
- [17] ISO 834-1, *Fire-resistance tests - Elements of building construction*, Part 1: General requirements, ISO (International Organization for Standardization), Geneva, 1999.
- [18] Landesmann, A, Batista, E.M, Alves, J.L.D., Implementation of Advanced Analysis Method for Steel Framed Structures under Fire Conditions, *Fire Safety Journal*, v.40, pp. 339-366, 2005.
- [19] SAFIR , Franssen, J.–M., Kodur, V.K.R., Mason, J., “*User’s Manual for SAFIR–2001: A Computer Program for Analysis of Structures Submitted to the Fire*”, University of Liège, Département Mécanique des Matériaux et Structures, 2000.
- [20] Gatewood, B.E., *Thermal Stress*, McGraw Hill Book Co., Inc., New York, 1957.
- [21] AISC-LRFD, Manual of Steel Construction, “*Load and Resistance Factor Design Specification for Structural Steel Buildings*”, American Institute of Steel Construction, Chicago, 1997.



SCALE MODELING OF INSULATED STEEL FRAMED STRUCTURE TESTING IN FIRE

Ming WANG¹, Peter C. CHANG² and James G. QUINTIERE³

ABSTRACT

The events of September 11th showed the combined effects of fire and structural loading on a high-rise building can be disastrous. Understanding the mechanism of structural damage caused by fire will help engineers design safer infrastructures by providing adequate resistance to failure. Contemporary research in computation fluid dynamics has produced great advances; however the physical and numerical complexities of combustion coupled with a lack of validation may lead to erroneous predictions. Physical modeling is inherently free of such complexities. One of the best known experiments was the Cardington tests which show the ability to investigate the combined effect on structures exposed to fire. The results from this full-scale experiment are reliable since it is a reproduction of a real fire in a building. However, the associated size and cost of the full-scale or large-scale models are often prohibitive. Most researchers are limited to studying the behavior of individual structural components in a furnace instead of testing a typical spatial structure. The test of structural components can show the heat transfer in specimens and the change of material properties under high temperature, but the environment in a furnace is not always similar to an actual fire. One approach to mitigate these problems is to use scale models to study the behavior of structures exposed to a real fire.

In this paper, small-scale models are used to simulate the behavior of the full-scale structures exposed to fire as the utility of such an approach is significantly easier and more cost effective to perform. Both fire and structure related parameters of the scaled models are designed based on length scale relationships derived from the governing equations of heat transfer. The wood crib fuel and the compartment wall materials are chosen properly in order to achieve a similar temperature profile as that of the prototype. The modeling of the wood

¹ Graduate Research Assistant, University of Maryland, Department of Civil Engineering, College Park, Maryland, 20742

email: wming@umd.edu

² Associate Professor, University of Maryland, Department of Civil Engineering, College Park, Maryland, 20742

email: pchang@umd.com

³ Professor, University of Maryland, Department of Fire Protection Engineering, College Park, Maryland, 20742

email: jimq@eng.umd.edu

crib fires in enclosures requires the burning time to be scaled by $s^{1/2}$ (s is the scale factor) which is suitable for the compartment fires where the heat flow is driven by gravity or buoyancy force. Based on this time scale, this paper developed the specific requirements for the scaled structural and thermal modeling. Some simplifying processes are adopted to make the scaled experiment possible. For example, the heating of the insulated steel frame is considered to be quasi-steady and the steel temperature is assumed to be uniform. Moreover, the conduction is considered to be the dominant thermal resistance for heat transfer at solid boundaries over radiation and convection. Based on these assumptions, the scaling rules for the insulation on steel are obtained, in which the insulating material and the thickness are scaled rationally. Insulated steel frames are built and placed into the scaled compartment fires. Similar steel temperature profiles are obtained from the scaled models at different scales. Scaled structural loadings are applied to the frames externally in order to achieve similar strain/stress. The structural response, such as the deflection of the beams, is also measured and observed.

This research explores how to perform small scale structural fire tests while preserving the law of similitude. It is recognized that inaccuracies may be generated because not all the phenomena can be appropriately scaled. This paper discusses and evaluates the accuracy of the use of scaled models in the study of the combined effect of fire and structural loading.

1. INTRODUCTION

Scaled models have been used to model various behaviors of full-scale structures in the lab. Wind tunnel tests [1, 2] are widely used to study the characteristics of wind-induced vibration and forces on complex structures in which the effects are often difficult to predict analytically. Structural behaviors can be simulated and predicted by conducting static and dynamic tests using scaled models [3-5]. Complex systems are difficult to understand by analytical and computational means alone, and the study of structural performance in fires can be put into this category. Many computational software packages such as ANSYS [6], ABAQUS [7], VULCAN [8, 9], SAFIR [10] and so on can perform the combined thermal and structural analysis. However, the solution obtained from these simulation packages relies on the loading applied into the computer models, and the input of loading has to be augmented by some predetermined parameters such as temperature profile, heat flow rate, heat flux, and heat generation rate, etc.. These values are usually chosen by researchers according to previous empirical data and their experience. Experimental works are required to develop the level of confidence that the computer modeling can be validated. One of the best known experiments was the Cardington tests [11, 12] which show the ability to investigate the combined effect on structures exposed to fire, and the results from the full-scale experiment are reliable since it is the reproduction of real fire disaster in a building. However, the associated high cost limits full-scale tests to be conducted sparingly. Moreover, some structures such as tall buildings, offshore oil platforms and industrial buildings are too large to be studied in a full scale. The alternative of fire testing at a reduced scale will help solve some of the problems mentioned.

Gross and Robertson [13] of the National Bureau of Standards were one of the first researchers to conduct experiments to scale wood crib fires in enclosures. Their attempt was based on matching the Froude number because they recognized that the fire plume flow was governed by the buoyancy force. In their experiment, the scaling rules applied in the design phase were basically geometric relationships, and the same compartment wall material was used for all scales. The results obtained from different scales did not compare well. A more thorough investigation of scaling of wood crib fires in enclosures was undertaken by Heskestad [14], in which some important effects were considered besides geometric scaling.

The burning rate of wood crib fires was found to be related to the flow rate of air through the internal structure of wood cribs. The relationship was formed between the ratio of free burning to that of burning inside an enclosure and a defined porosity factor, P , which was the function of the exposed surface area of crib, vertical shafts area within crib, stick spacing and stick cross section dimension. This provided a fundamental knowledge to design wood cribs for compartment fires at different scales. Recognizing the importance of the heat loss through vents via radiation and heat loss through enclosure boundaries, Heskestad [14] suggested the scaling for the material properties of the compartment walls and the scaling rules were derived from the governing equation of conduction in walls. A characteristic time defined as the fire duration was determined based on scaling of the burning rate. The validation of Heskestad's scaling laws was attempted by Croce [15]. His experimental results showed that accurate scaling was achieved by using Heskestad's hypothesis. A comprehensive review on fire scaling has been given by Quintiere [16]. Perricone [17] conducted experiments to model wood crib burning in compartments at different scales based on the scaling theory of compartment fires proposed by Quintiere and Chang [18] and Quintiere [19] which are the basis of the fire scaling adopted in this paper. It should be noted that the time scaling in [17-19] is derived by analyzing a fluid element of the fire-induced flow which is driven by the buoyancy due to the change of the density of heated gas in an enclosure.

An investigation of the feasibility of reduced scale models to extend fire testing capability to large components and assemblies was conducted by Issen [20], and the similitude requirement was proposed and evaluated by experiments. O'Connor et al. [21, 22] presented the methodology for fire resistance testing of structural components at reduced scales. The tests in these studies [20-22] showed the potential to produce similar temperature distribution and scaled structural deformation in structures at different scales. In their scaling rules, a time scale proportional to the square of the scale factor ($t \sim s^2$) was proposed for geometrically scaled specimens. This scale is based on the importance of thermal diffusion, $s \sim \sqrt{\frac{k}{\rho c}} t$. The

net incident heat flux is scaled by $\dot{q}'' = k \frac{dT}{dx} \sim s^{-1}$, which can be implemented by adjusting the

furnace temperature profiles. Their development of scaling focused on concrete structures in which the temperature gradient is significant and must be accounted for in the scaling. In contrast, we focus on steel structures protected with insulating material. Instead of adopting a furnace to generate a high temperature environment, scaled compartment fires are used to offer a more realistic fire effect on the structure. It has to be noted that the time scale used by Issen and O'Connor will not be suitable for a test in a compartment fire, where the heat flow is driven by buoyancy forces. Effects such as stress, acceleration, conduction, radiation, and convection follow different scaling laws [18]. For a scaled compartment fire, the fuel and compartment wall material have to be chosen properly in order to achieve a similar temperature profile as in the prototype. Scaled structures under such a scaled temperature profile should have similar behavior as the prototype. Using these scaled compartment fires then, scaled models can be tested. Moreover, instead of studying a single structural component, scaled steel framed structures are considered and tested in this paper.

2. SCALING OF FIRE AND STRUCTURE

The model depicted in Fig. 1 shows the fire phenomenon in a compartment. The model displays the fire burning in the compartment with a room vent. The hot gas temperature in the compartment is dependent on the difference between the heat generation rate from the fire \dot{Q} and the heat loss rate through the compartment boundaries \dot{q} .

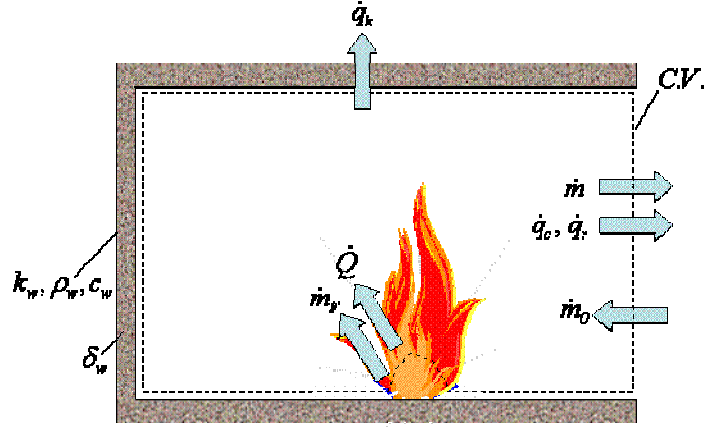


Fig. 1 – Model of compartment fire phenomena.

The total heat loss consists of the heat loss by conduction through compartment walls \dot{q}_k and radiation \dot{q}_r through the vent. This relation is expressed in the energy conservation equation:

$$\rho_{\infty} c_p V \frac{dT}{dt} + \dot{m} c_p (T - T_{\infty}) \sim \dot{Q} - \dot{q} \quad (1)$$

In a natural convection condition where there is no forced flow, the hot gas flow is driven by the buoyancy which is induced by the change of hot gas density. Therefore the burning time of the fuel needs to be scaled according to $t \sim s^{1/2}$ [18]. Based on this time scale, dimensionless groups can be produced from the energy equation. The dimensionless Π terms are given [18, 19]:

$$\Pi_f = \frac{\dot{Q}}{\rho_{\infty} c_p T_{\infty} \sqrt{gs}^{5/2}} \Rightarrow \dot{Q} \sim s^{5/2} \quad (2)$$

$$\Pi_k = \frac{\dot{q}_k}{\rho_{\infty} c_p T_{\infty} \sqrt{gs}^{5/2}} \sim \frac{\frac{k_w T_{\infty} s^2}{\sqrt{(\frac{k_w}{\rho_w c_w})t}}}{\rho_{\infty} c_p T_{\infty} \sqrt{gs}^{5/2}} \Rightarrow k_w \rho_w \sim s^{3/2} \quad (3)$$

$$\Pi_c = \frac{\dot{q}_c}{\rho_{\infty} c_p T_{\infty} \sqrt{gs}^{5/2}} \sim \frac{h_c T_{\infty} s^2}{\rho_{\infty} c_p T_{\infty} \sqrt{gs}^{5/2}} \Rightarrow h_c \sim s^{1/2} \quad (4)$$

$$\Pi_r = \frac{\dot{q}_r}{\rho_{\infty} c_p T_{\infty} \sqrt{gs}^{5/2}} \sim \frac{\sigma \epsilon T_{\infty}^4 s^2}{\rho_{\infty} c_p T_{\infty} \sqrt{gs}^{5/2}} \Rightarrow \epsilon T_{\infty}^3 \sim s^{1/2} \quad (5)$$

$$\Pi_{\delta} = \frac{\delta_w}{\sqrt{(\frac{k_w}{\rho_w c_w})t}} \Rightarrow \frac{\delta_w \rho_w^{1/2}}{k_w^{1/2}} \sim s^{1/4} \quad (6)$$

The heat loss consists of the heat loss through the room vent by convection and radiation and heat loss through the compartment walls by conduction. Π_f is used to design the fuel in a scaled model. Π_k , Π_c and Π_r can be preserved so that the total heat loss is scaled ($\dot{q} \sim s^{5/2}$). Equation (4) and (5) indicate that the proper scaling requires the change of thermal convection coefficient h_c , gas emissivity ϵ and ambient temperature T_{∞} in scaled models. However, changing these parameters may be impractical. In order to make the scaling practicable, it is

necessary to identify dominant effects and those that are negligible under typical conditions. For a compartment with low ventilation which is the case considered in this paper, the heat loss through the compartment boundaries by conduction is the most significant part of the total heat loss. Therefore, Π_k is maintained to be constant in the scaled experiment, and Π_c and Π_r are allowed not to be preserved. In this way, the properties of the wall material in the scaled models can be chosen according to Equation (3). Furthermore, the thickness of the walls can be determined by Equation (6).

Compartment fires at two scales (1/4 and 1/8, comparing to a 3.7m×3.7m×2.4m room prototype) are conducted. With two different wood crib designs at each scale, both small fire and large fire are made to represent a building fire with approximate 15-minute and one-hour durations, respectively. The details of the design of wood cribs and the experimental set-up of scaled compartment fires can be found in reference [17]. Saffil LD mat [23] was used as the wall material to built the 1/8-scale compartment and Kaowool 3000 [24] for 1/4-scale compartment. Fig. 2 shows the burning of the scaled compartment fires. Similar hot gas temperature profiles are obtained at the homologous locations as shown in Fig. 3 and they are plotted in terms of the full-scale time. The similarity of the compartment fires at two different scales is obtained successfully, and the two scaled fires are then used to scaled steel frames to obtain structural behavior in fires. It should be noted that there is a shift in the temperature profiles in the large fires as shown in Fig. 3 (b). The hot gas temperature in the 1/4-scale model reaches a relatively stable high temperature (800 to 900°C) in the early burning stage (4 to 20 minutes, full-scale time); however, in the same time range, the hot gas temperature in the 1/8-scale model remains a relatively low temperature (600 to 700°C).

Five fundamental units are involved in a quasi-static structural analysis: force (F), length (L), density (ρ), modulus (E) and time (t). Since the structural elements will be placed in compartment fires, time is scaled to $t \sim s^{1/2}$. The same structural material is usually used in scaled models, so the term of density and modulus remains independent. In structural applications, the size of structural members is to be scaled geometrically. Therefore the force (F) has to be scaled by s^2 ($F \sim s^2$) in order to keep the stress term σ independent of scale:

$$\Pi_F = \frac{\sigma s^2}{F} \Rightarrow F \sim s^2 \quad (7)$$

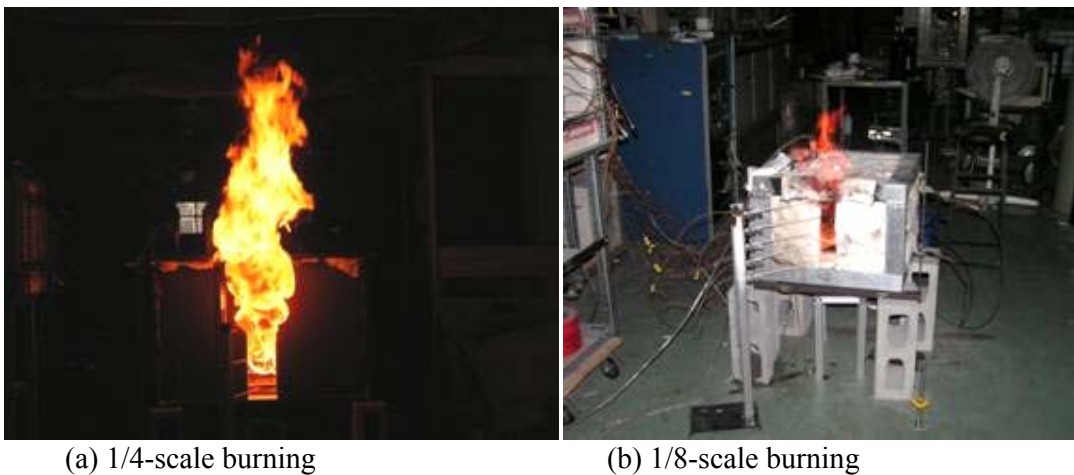


Fig 2 – Burning of scaled compartment fires

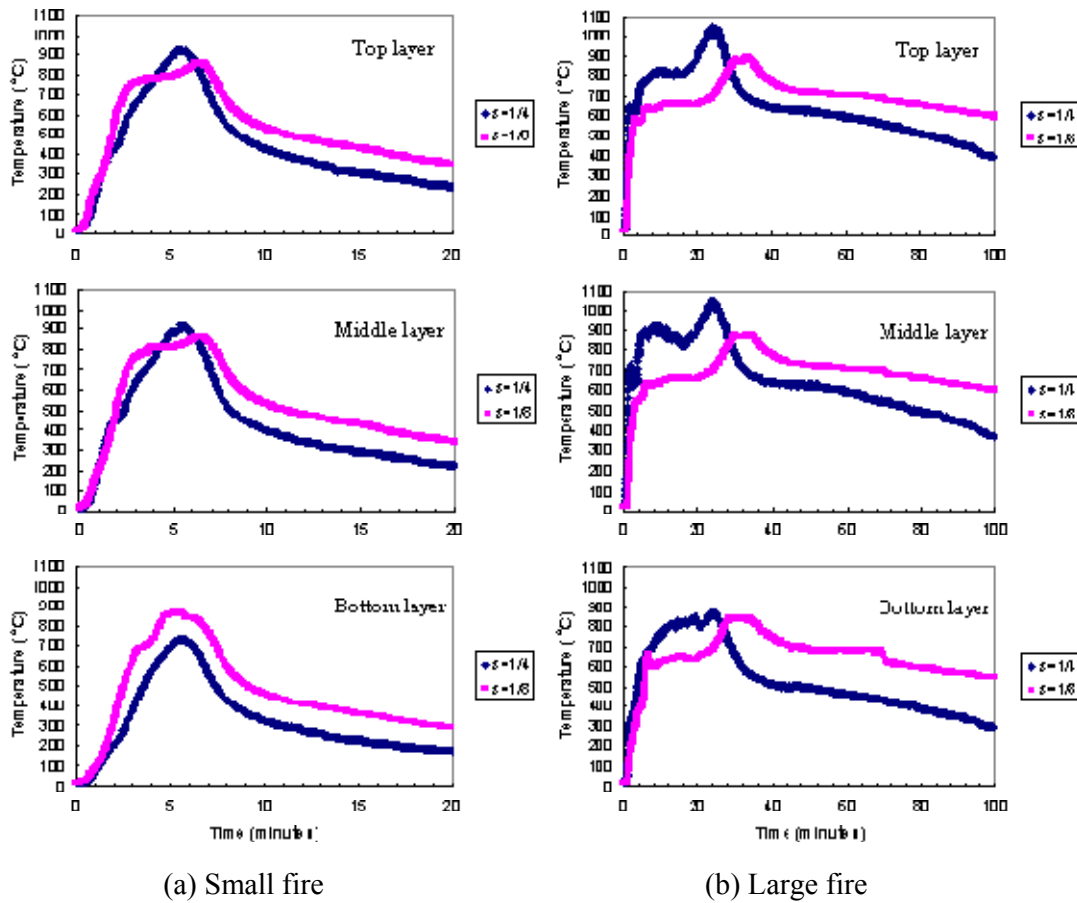


Fig. 3 – Hot gas temperature profiles in compartments, temperature vs. full-scale time

3. SCALING OF INSULATION ON STEEL

The temperature of structural elements plays an important role on the fire-induced structural performance. When we pursue the similarity of structural behaviors at different scales, the temperature in structures is one of the most important independent parameters that need to be considered. For a structure with fire proofing material, the insulation on the structure has to be scaled rationally in order to obtain similar steel temperature profile in the scaled model as that of the prototype.

Insulation scaling for scaled models can be developed from the heat transfer governing equation:

$$m_s c_s \frac{dT_s}{dt} + m_i c_i \frac{dT_i}{dt} \sim \frac{k_i}{\delta_i} A_s (T_f - T_s) \quad (8)$$

m is the mass, c is the specific heat and k is the thermal conductivity. The subscript s denotes steel, and i denotes insulation. A_s is the surface area of the insulated steel. Heat is stored in both the steel and the insulation. The effect of conduction is assumed to dominate for the heat transferring through solids compared to the effects of radiation and convection. By making equation (7) dimensionless, Equation (7) can be written:

$$\frac{k_i}{\delta_i} \sim \left(\frac{m_s c_s}{t A_s} \right) \frac{d\hat{T}_s}{dt} \left(\frac{1}{\hat{T}_f - \hat{T}_s} \right) \frac{T_\infty}{T_\infty} + \left(\frac{m_i c_i}{t A_s} \right) \frac{d\hat{T}_i}{dt} \left(\frac{1}{\hat{T}_f - \hat{T}_s} \right) \frac{T_\infty}{T_\infty} \quad (9)$$

$$\sim \frac{m_s c_s}{s^{1/2} A_s} + \frac{m_i c_i}{s^{1/2} A_s}$$

where “ \sim ” is used to denote dimensional equality, and “ $\hat{}$ ” is used to denote dimensionless variables. Furthermore, two Π terms can be obtained:

$$\Pi_i = \left(\frac{k_i}{\delta_i} \right) \left(\frac{s^{1/2} A_s}{m_i c_i} \right) \sim \left(\frac{k_i}{\delta_i} \right) \left(\frac{s^{5/2}}{\delta_i P L \rho_i c_i} \right) \sim \frac{k_i}{\delta_i^2 \rho_i} s^{1/2} \quad (10)$$

$$\Pi_s = \left(\frac{k_i}{\delta_i} \right) \left(\frac{s^{1/2} A_s}{m_s c_s} \right) \sim \left(\frac{k_i}{\delta_i} \right) \left(\frac{1}{s^{1/2}} \right) \quad (11)$$

In Equation (8) and (9), $A_s \sim s^2$, $L \sim P \sim s$, and $m_s \sim s^3$ are applied as geometry is preserved. The scaling rules used to determine the insulation in scaled models can be obtained by preserving Π_i and Π_s , and the change of insulation material or the thickness are required in order to keep Π_i and Π_s to be constant. Changing material may be sometimes impractical. Alternatively, the same insulation material as that of the prototype can be used, $k_i \sim \rho_i \sim s^0$. It should be noted that the scaling rule for insulation thickness δ_i can not be determined uniquely by substituting $k_i \sim \rho_i \sim s^0$ into Equation (9) and (10). Insulation material usually is very light weight, so the heat stored in the insulation is relatively small compared to the heat stored in the steel. Therefore, one strategy is to determine the insulation thickness in scaled models is to preserve Π_s only. Using this simplifying assumption, the scaling rules for insulation on steel are:

$$\delta_i \sim s^{-1/2} \quad \text{and} \quad k_i \sim \rho_i \sim s^0 \quad (12)$$

The scaling rules for insulation in Equation (10) are used to determine the insulation applied to small-scale models. The same insulation material will be used in scaled models as that of the prototype, and the thickness will be adjusted so that the similar steel temperature profiles will be obtained in the models at different scales.

4. SCALED STEEL FRAME TESTING

A steel framed structure built with square tube members is considered as the prototype. Fig. 4 shows the steel frame before and after it is wrapped with insulation. The small-scale frames are geometrically scaled as shown in Table 1. The insulation thickness and material are chosen according to Equation (10). SAFFIL Alumina Fibres mat [23] with thermal conductivity $k_i = 0.062 \text{ W/mK @ } 400^\circ \text{C}$ and density $\rho_i = 96 \text{ kg/m}^3$ is considered as the insulation material used in the prototype.

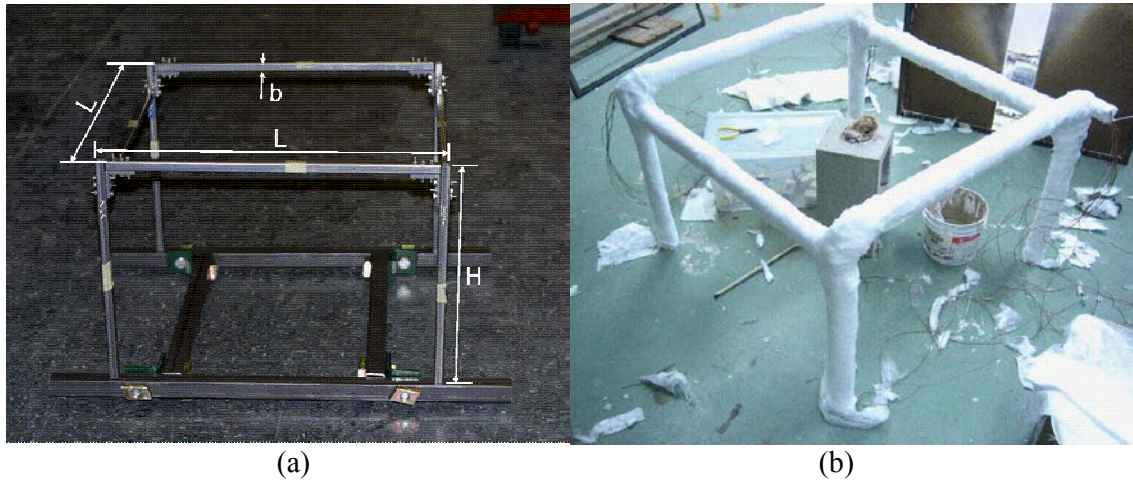


Fig. 4 – (a) Steel frame built with square tubes (b) Insulated steel frame

Table 1 – Dimension of prototype and scaled models, and insulation applied

Scale	L (mm)	H (mm)	b (mm)	δ_t (mm)	δ_i (mm)	Insulation
1	3560	2440	101.6	12.7	6.4	SAFFIL Alumina Fibres mat[23]
1/4	890	610	25.4	3.2	12.7	SAFFIL Alumina Fibres mat[23]
1/8	445	305	12.7	1.6	18.0	SAFFIL Alumina Fibres mat[23]

Two beams of the steel frame are loaded externally, and a total 127kg weight is applied to the 1/4-scale model and 31.8kg for the 1/8-scale model. Fig. 5 shows the experimental set-up of the insulated steel frames with structural loading. The steel temperature of both beams and columns is measured, and twenty K-type thermocouples are installed in each frame. Both small and large fires are conducted in each compartment, and the structural behavior such as beam deformation is also recorded.

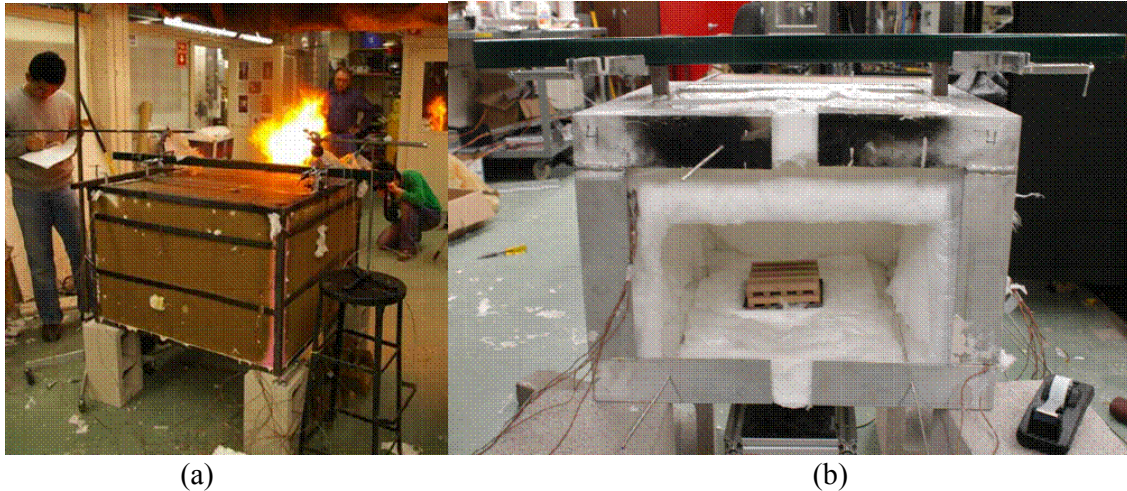


Fig. 5 – (a) 1/4-scale frame fire testing (b) 1/8-scale frame fire testing

In addition to the gravity loads on the structure, the effect of temperature is the predominant effect that results from the fire. Both maximum steel temperature and temperature-time curves play important roles on the structural response of a structure exposed to fire. The results in Fig. 3 show that the similar hot gas temperature in the compartments can be obtained by properly choosing wall materials and wood cribs design. The insulation on steel is determined by Equation (11) to obtain similar effect of heating in steel through the

insulation. Fig. 6 shows the typical temperature profiles of the beam and column in both small and large fires. The steel temperature is plotted in the full-scale time. Steel temperature profiles are obtained in 1/8 and 1/4 scales experiments. Note that the steel temperature profiles of the 1/8-scale model in the large fire is shifted to the right comparing to that of the 1/4-scale model. This shift can be traced back to the hot gas temperature profiles as shown in Fig. 3 (b) which shows a similar shift. The lower hot gas temperature in the 1/8-scale model reduces the rate of steel temperature rising, and that is why the steel temperature profiles in the 1/8-scale model are drifted and the time to reach the peak steel temperature is delayed. The hot gas temperature profiles in the small fire in Fig. 3 (a) show the good agreement and the time to reach the peak temperature is also very close. As we expect, the steel temperature profiles in the small fire agree very well as shown in Fig. 6 (a).

Fig. 7 shows the deflection of the beams under external loading. The positive value of the beam deflection in the plots indicates the downward deflection in a beam. The results show that the deflection/length profiles agree very well in small fire as shown in Fig. 7 (a), and the deflection is in elastic range and recovered to initial values because the maximum steel temperature in small fire as shown in Fig. 6 (a) is less than 200°C . The upward beam deflection is due to the thermal expansion of columns. Fig. 7 (b) shows the deflection/length profiles in large fire. The deflection in the beams is upward at the early stage and it becomes downward when the effect of steel degradation takes over the effect of the thermal expansion of columns. Unrecoverable deflection is formed in the beams.

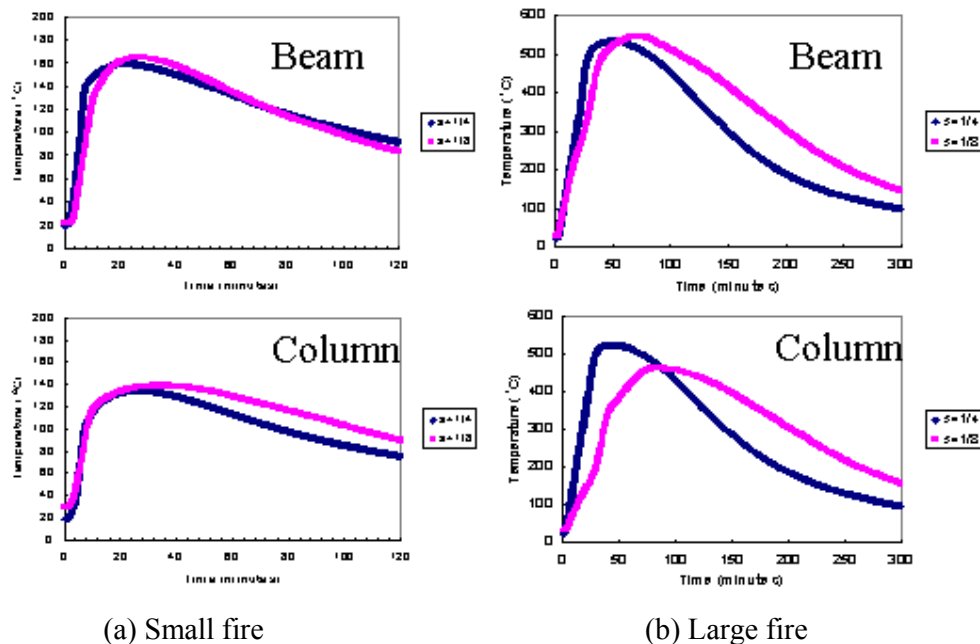
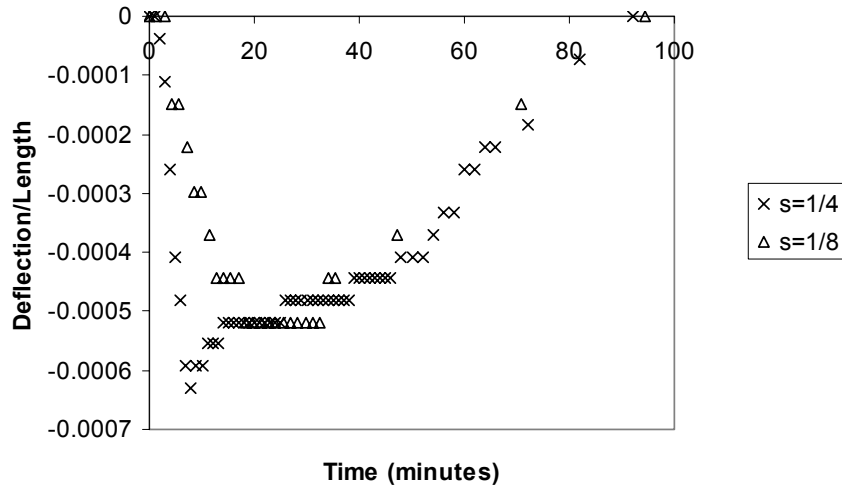
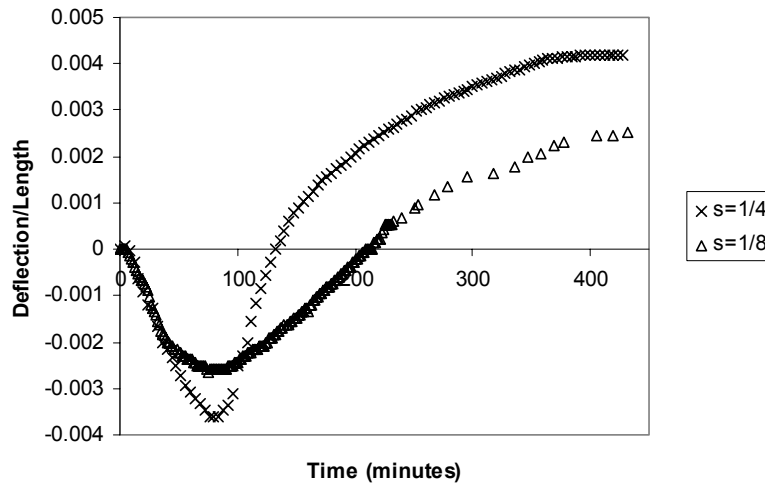


Fig. 6 – Typical steel temperature profiles in the frames, temperature vs. full-scale time



(a) Measurement in small fire



(b) Measurement in large fire

Fig. 7 – $\Delta y/L$ of steel beams vs. full-scale time

5. CONCLUSION

This paper explores the technique to simulate insulated steel structural testing in fire by using small-scale models. It provides a tool to engineers to analyze complex systems. The scaling rules for designing scaled compartment fires, structures with structural loading and insulation materials on structures are developed and presented. It offers an economical way of testing that can reveal the structures' behavior in a fire. The experimental results from the models at different scales show the similar steel temperature profiles and structural response when they are subjected to scaled fires.

REFERENCE

- [1] K.C.S. Kwok B. Samali, G.S. Wood, and J.N. Yang, "Wind Tunnel Tests for Wind-Excited Benchmark Building," *Journal of Engineering Mechanics*, 2004. **130**(4): p. 447-450.
- [2] ASCE Aerospace Division Task Committee on Wind Tunnel Studies of Buildings and Structures, "Wind-Tunnel Studies of Buildings and Structures," *Journal of Aerospace Engineering*, 1996. **9**(1): p. 19-36.
- [3] A. Jha, R. Sedaghati, and R. Bhat. *Dynamic Testing of Structures Using Scale Models*. in *Collection of Technical Papers - AIAA/ASME/ASCE/AHS/ASC Structures, Structural Dynamics and Materials Conference*. 2005.
- [4] R.J. Fay. *Scale Model Tests of Vehicle Motions*. in *International Congress and Exposition*. 1993. Detroit, MI, USA SAE Special Publications.
- [5] B.J. Wallace and H. Krawinkler, "Small-scale Model Tests of Structural Steel Assemblies," *Journal of Structural Engineering*, 1989. **115**(8): p. 1999-2015.
- [6] Inc. ANSYS, "<http://www.ansys.com>."
- [7] Inc. ABAQUS, "<http://www.hks.com>."
- [8] Z. Huang, I.W. Burgess, and R.J. Plank, "Nonlinear Analysis of Reinforced Concrete Slabs Subjected to Fire," *ACI Structural Journal*, 1999. **96**: p. 127–135.
- [9] Vulcan Solutions Limited, "<http://www.vulcan-solutions.com>."
- [10] D.I. Nwosu, V.K.R. Kodue, J.M. Franssen, and J.K. Hum, *User Manual for SAFIR: A Computer Program for Analysis of Structures at Elevated Temperature Conditions*, in *Internal Report 782*. 1999, Institute for Research in Construction, National Research Council of Canada.
- [11] D. B Moore. *Full Scale Fire Tests on Complete Buildings*. in *Proceedings of 2nd Cardington Conference*. 1996. Garston, U.K.
- [12] G.M. Newman, J.T. Robinson, and C.G. Bailey, *Fire Safe Design: A New Approach to Multi-Storey Steel-Framed Buildings*, in *SCI Publication P288*. 2000, The Steel Construction Institute.
- [13] A. F. Gross and D. Robertson, "Experimental Fires in Enclosures," *Combustion Institute Symposium on Combustion*, 1965: p. 931-942
- [14] G. Heskestad, "Modeling of Enclosure Fires," *Journal of Fire and Flammability*, 1975. **6**(3): p. 253-273.
- [15] P. A. Croce, *Modeling of Vented Enclosure Fire Part 1. Quasi-Steady Wood-Crib Source Fire*. 1978, Norwood, Massachusetts: Factory Mutual Research Corporation.
- [16] J. Q. Quintiere, "Scaling Application in Fire Research," *Fire Safety Journal*, 1989. **15**: p. 3-29.
- [17] J. A. Perricone, *Scale Modeling of the Transient Behavior of Wood Crib Fires in Enclosures*, in *Department of Fire Protection Engineering*. 2005, University of Maryland.
- [18] J.G. Quintiere and P.C. Chang. *How to Use a Scale Model to Simulate Fire and Structural Failure*. in *Designing Structures for Fire*. 2003. Baltimore.
- [19] J. G. Quintiere, *Fundamentals of Fire Phenomena*. 2006: John Wiley & Sons, Inc.
- [20] L Issen, "Scaled Models in Fire Research on Concrete Structures," *Portland Cement Association – Research and Development Laboratories – Journal*, 1966. **8**(3): p. 10-26.
- [21] D.J. O' Connor, G.W.H. Silcock, and B. Morris, "Furnace Heat Transfer Processes Applied to a Strategy for the Fire Testing of Reduced Scale Structural Models," *Fire Safety Journal*, 1996. **27**: p. 1-22.

- [22] D.J. O' Connor, B. Morris, and G.W.H. Silcock, "A Methodology for the Fire Resistance Testing of Structural Components at Reduced Scale," *Journal of Testing and Evaluation*, 1997. **25(3)**: p. 273-282.
- [23] www.unifrax.com Unifrax Corporation.
- [24] Thermal Ceramics, www.thermalceramics.com.



STRUCTURAL FIRE PERFORMANCE OF STEEL PORTAL FRAME BUILDINGS

Peter MOSS¹, Rajesh DHAKAL², Ming Wei BONG³ AND Andy BUCHANAN⁴

ABSTRACT

This paper describes a study into the fire behaviour of steel portal frame buildings at elevated temperatures using the finite element programme SAFIR. The finite element analysis carried out in this report is three dimensional and covers different support conditions at the column bases, the presence of axial restraints provided by the end walls, several different locations and severities of fires within the building, different levels of out-of-plane restraint to the columns and the effect of concrete encasement to the columns. From a large number of analyses, it is shown that the bases of the steel portal frames at the foundations must be designed and constructed with some level of base fixity to ensure that the structure will deform in an acceptable way during fire, with no outwards collapse of the walls. The analyses also show that it is not necessary for steel portal frame columns to be fire-protected unless the designer wishes to ensure that the columns and the wall panels remain standing, during and after the fire.

1. INTRODUCTION

Steel portal frame buildings with concrete tilt-up wall panels are a very common form of industrial building in New Zealand and Australia. They consist of a series of parallel steel portal frames as the major framing elements which support the roof structure. Large clear spans of up to approximately 40 metres can be achieved using steel Universal Beams (UB). Concrete tilt-up wall panels are commonly used as boundary walls as they allow fast erection and on-site fabrication. It is also common to encase all or part of the steel portal frame column

¹ Associate Professor, Department of Civil Engineering, University of Canterbury, Christchurch, New Zealand, email: peter.moss@canterbury.ac.nz

² Senior Lecturer, Department of Civil Engineering, University of Canterbury, Christchurch, New Zealand, email: rajesh.dhakal@canterbury.ac.nz

³ Engineer, Arup Fire, Brisbane, Queensland, Australia, email: kbong@arup.co.au

⁴ Professor, Department of Civil Engineering, University of Canterbury, Christchurch, New Zealand, email: andy.buchanan@canterbury.ac.nz

leg with concrete, or to use a reinforced concrete column for the lower part of the portal frame leg as shown in Fig. 1.

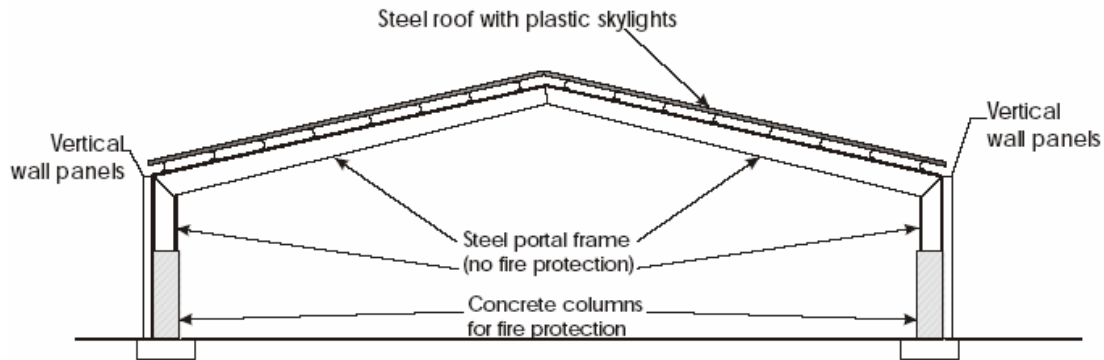


Fig. 1 - Typical industrial buildings in New Zealand¹

Several acceptable or unacceptable deformation modes of such buildings under fire are shown in Fig. 2. For the frames collapsing into the building (*inwards collapse*), it can be seen that the resulting deformation will not endanger adjacent property or persons located outside

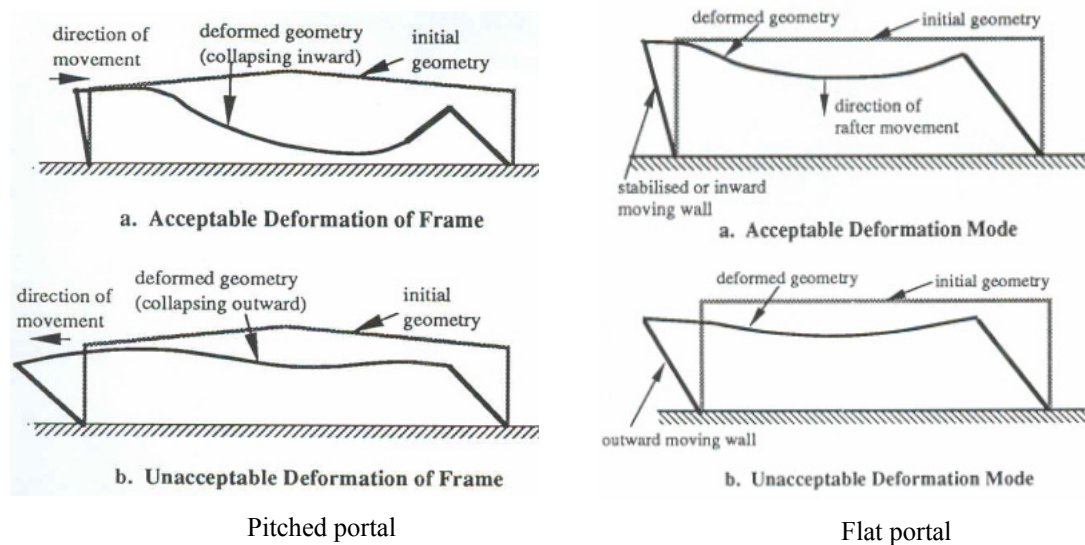


Fig. 2 - Acceptable and unacceptable deformation modes²

the building provided that the boundary walls are tied together and fall inwards as a complete unit. The inwards collapse of the walls can increase the fire separation distance to the relevant boundary and reduce the likelihood of horizontal fire spread by radiation. The inwards collapse may also extinguish the fire directly beneath the walls. In contrast, frames that *sway sideways* may collapse outwards due to P-delta effects of the walls attached and may lead to adjacent property being damaged or persons outside the building being endangered.

In the past, concrete boundary wall panels were required to remain standing after a fire, but it is now considered acceptable for the panels to collapse inwards after a period of time, provided that they remain connected to each other. However there still remains concern

that under fire conditions, the concrete panels may collapse outwards, creating a danger to fire-fighters and to adjacent property.

This study describes an analytical investigation of the fire performance of steel portal frame buildings and establishes fire design guidelines for such buildings.

2. STRUCTURAL DETAILS/DESIGN

The structure studied in this project was an industrial building formed by five parallel steel portal frames composed of 410UB54 sections. The roof structure consisted of cold-formed DHS250/15 purlins and DB89/10 brace channels. The building was designed according to the New Zealand standards^{3,4}.

The building was 40 metres long by 30 metres wide and the roof was inclined at 8°. The steel frames had a span of 30 metres and were spaced at 7.2 metres. The columns were 6 metres high and the distance from ground level to the apex of the frame was 8 metres. The purlins were spaced equally at about 1.5 metres and spanned between the steel frames. The steel sheeting was ignored in the analytical model but the self-weight was included in the analysis. The loads applied to all the analytical models are the self-weight of the steel members and the steel roofing. The calculated load ratios for the steel portal frame with ideally pinned and fixed support conditions are 0.21 and 0.18, respectively (i.e. lower load ratio signifies better fire resistance). The columns of the frames were assumed to be attached to the wall panels at the top and mid-height, and the end purlins were assumed to be supported on the end walls.

Frames with fixed and pinned bases were analysed as these provide the upper and lower bound of the base-fixity of the structure. However, fully-fixed and fully pinned bases are never achieved in reality as no real connection can provide full restraint or can allow the column base to rotate freely. Hence, a portal frame structure with partial base fixity at the supports was also analysed.

Under fire conditions, the collapse mechanisms of the walls depend on the performance of the supporting frames under elevated temperatures, providing that the connections between the walls and the frame do not fail. The concrete panels themselves were not included in the models, but were represented by appropriate restraints to the steel members. These restraints prevented the out-of-plane displacement at the top and mid-height of the columns and are required under ambient conditions to reduce the effective lengths of the columns and to prevent buckling about the weak axis.

The purlins in the end bays were connected to the concrete walls near the top of the walls (refer to Figure 3). The level of axial restraint provided by the end walls to the purlins is not well known and depends on many variables, such as the type of connection at the base, the amount of reinforcement and the thickness of the end concrete walls. In addition, it also depends on the supporting structures to which the walls are attached, the number of wall panels between the supporting structures and the types of connections used to join these structural elements together.

Two extreme cases of purlin axial restraint at these end wall connections were investigated, and they are referred to here as either *with* or *without* purlin axial restraint. The axial restraints in the steel purlins can be achieved provided the bolted end connections have sufficient axial load capacity. In a real building, the actual level of axial restraint will lie somewhere between the two extremes.

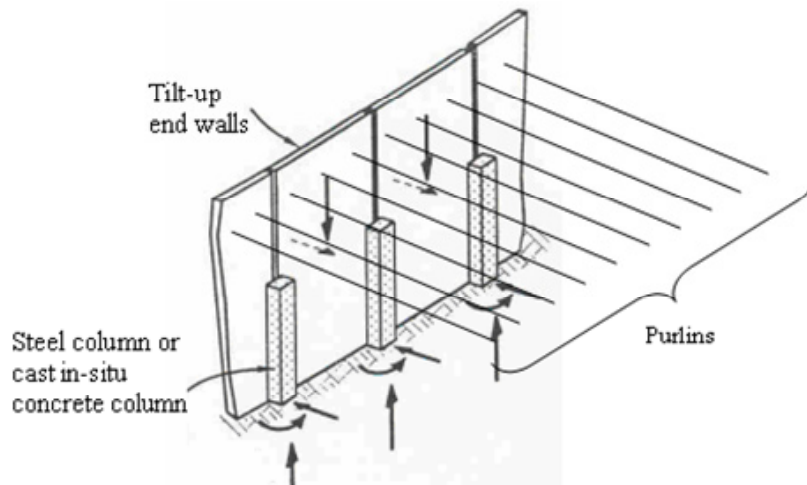


Fig. 3 Purlins in the end bays attached to tilt-up end walls

In practice, it is common to protect all or part of the steel portal frame column legs with concrete encasement. However, concrete encasement may fall off when exposed to very high temperatures or when the steel portal frame deforms excessively. In addition, when the concrete panels are trying to bow away from the supporting structures during high temperatures on one side (i.e. thermal bowing effects), the forces developed in the connections between the steel frames and the attached concrete panels will be larger due to the higher strength and stiffness of the protected steel columns. If these connections fail, the walls could collapse outwards.

Analytical models with all the steel columns protected with cast *in-situ* concrete to either full or two-thirds of the height were also analysed⁵. The analyses with columns fully encased in concrete served as the upper bound.

3. ANALYTICAL MODELLING

3.1 Fire exposure

The first step is to perform thermal analysis on the structural members using appropriate fire curves. The fire curve used in most of the analyses in this study was the ISO 834 Standard Fire⁶ (Fig. 4). However, the ISO fire is intended to represent fires in small compartments. The behaviour of a fire in a large compartment, such as warehouses or industrial buildings, is not the same as a small enclosure fire. These buildings usually have very high ceilings and large open spaces. The fire plume will have entrained a large amount of cold air when it impinges on the ceiling. The hot gases will continue to spread across the ceiling and similarly, cold air will be entrained into the ceiling jet. Therefore, the radiant heat flux from the upper hot layer may not be high enough to cause flashover. For this reason, the Eurocode External fire⁷ was used for some analyses⁵ though these are not reported herein.

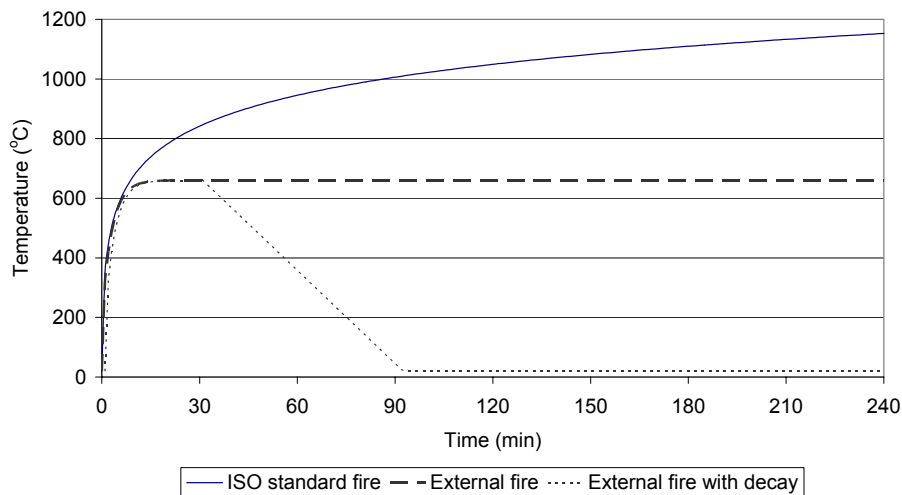


Fig. 4 Time-temperature curves used in the analysis

3.2 Structural analysis

The main purpose of the study was to investigate the different failure modes anticipated for a typical portal frame industrial structure under fire conditions. Hence, this paper focuses on the fire behaviour of the complete building and a brief description of the 3D finite element model is given below.

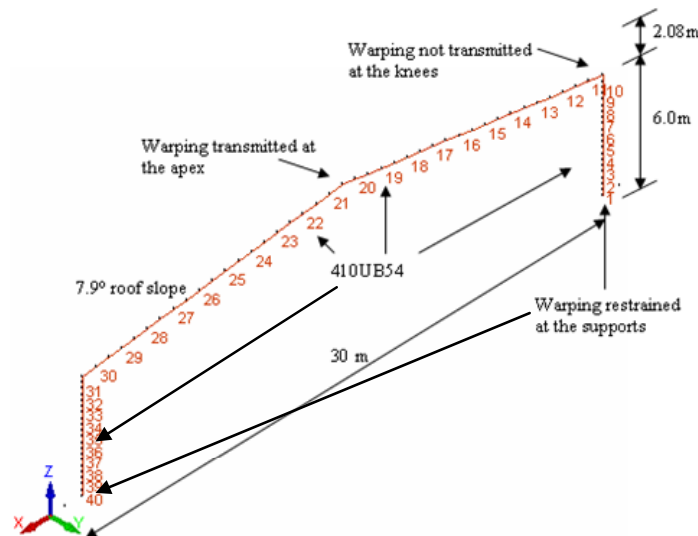


Fig. 5 Finite element modelling of one of the steel portal frames

Each of the steel portal frames was discretised into 40 beam elements as shown in Fig. 5. The nodes of the frames had seven degrees of freedom, i.e. 3 translations, 3 rotations and 1 warping. Two nodes were created at the apex of the frame, one representing the left rafter and the other the right rafter. It was assumed that full compatibility could be achieved at the apex and warping was effectively transmitted between the two nodes. Similarly, two nodes were created at the knees to represent the column and the rafter. In this case, the nodes shared the same translations and rotations but the warping between the two nodes was not transmitted. At the column bases of the frame, the warping of the cross section was restrained by the endplate.

The ends of the purlins were joined to the nodes of the rafter (i.e. via master-slave relationships between these nodes) in a way that they behave similarly to fully fixed end supports but with rotation about the vertical axis freed. In practice, the purlins will be bolted to steel cleats which are welded to the top flange of the steel rafter (Fig. 6). Some degree of fixity will be provided by the bolts to resist twisting about the longitudinal axis and in-plane deflection of the purlin. An assumption was made in the model that the bolts were able to provide full restraint against twisting about the longitudinal axis and in-plane rotation of the purlin. In terms of the warping of the purlins, it was neither transmitted to the rafter nor to the adjacent purlin since a small gap usually exists between the purlins at the support due to geometrical tolerances.

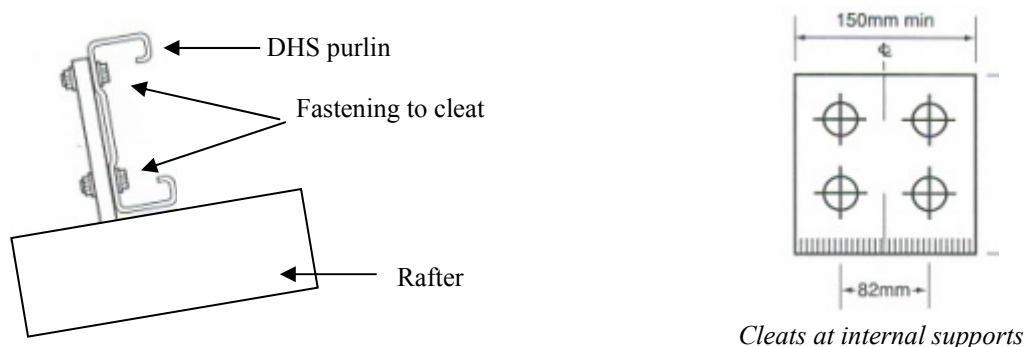


Fig. 6 Connection between purlin and steel rafter⁹

The torsional analysis calculates the elastic torsional stiffness and the warping function of the cross section at ambient temperature. In reality, the calculated value of elastic torsional stiffness will decrease during the fire due to the increased temperature and the subsequent decrease in material stiffness. It is not possible to calculate the change in the torsional stiffness as a function of time in SAFIR and only a constant value can be entered. The calculated torsional stiffness was divided by a factor of two to represent the decreased stiffness at elevated temperatures⁸.

4. RESULTS

Table 1 summarises the analytically determined failure times and collapse modes of buildings with different base support conditions, and different purlin axial restraints. The simulation end times in the table were obtained either when SAFIR was unable to converge to a solution, or when the maximum time limit of 60 minutes (arbitrarily chosen) was reached. In all cases, the whole structure is subjected to the ISO fire. For most analyses, the bottom two thirds of the columns were concrete encased to provide fire protection.

4.1 Support Conditions at the column base

4.1.1 Fixed Support Conditions

For a steel portal frame structure with bases fully fixed to the foundation, the deformation of the fire-affected roof structure (steel rafters, purlins and brace channels) is almost vertical without much sidesway. Immediately after the fire-affected roof structure starts to fail, the fire-affected frames will collapse **inwards** if the adjacent purlins are not axially restrained (Fig. 7), or the fire-affected roof structure will deform into a **catenary** if the adjacent purlins are axially restrained by the surrounding structure (Fig. 8). These failure

Table 1: Summary of analysis results

BASE FIXITY	Fire	ISO	ISO	ISO
	Fire size	100%	100%	100%
	Column protection	None	2/3 height	Full height
	Axial restraint			
PINNED	No	14.1 Sway	15.0 Sway	15.9 Sway
	Yes	19.6 Sway	16.7 Sway	17.2 Sway
PARTIAL FIXITY	No	15.6 Inwards	15.2* Inwards	
	Yes	15.9 Catenary	16.0* Catenary	
FIXED	No	14.9 Inwards	14.2 Upright	14.7 Upright
	Yes	18.5 Catenary	17.1 Catenary	19.6 Catenary

* Note: 2/3 concrete encasement applied only to the columns on one side

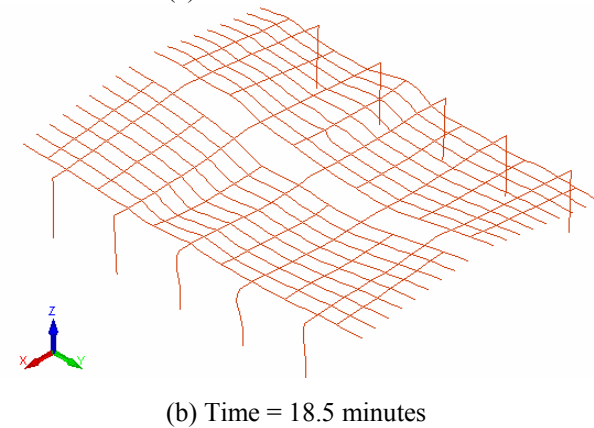
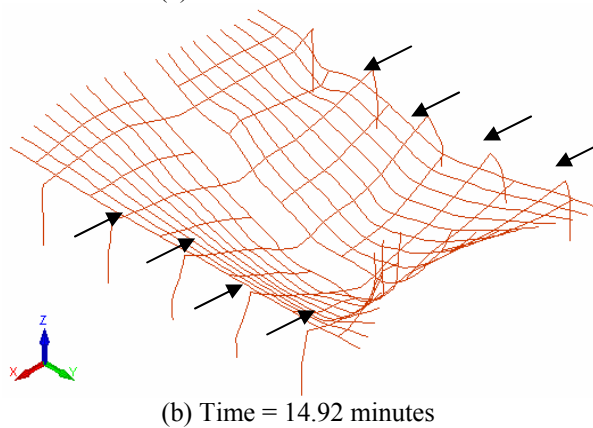
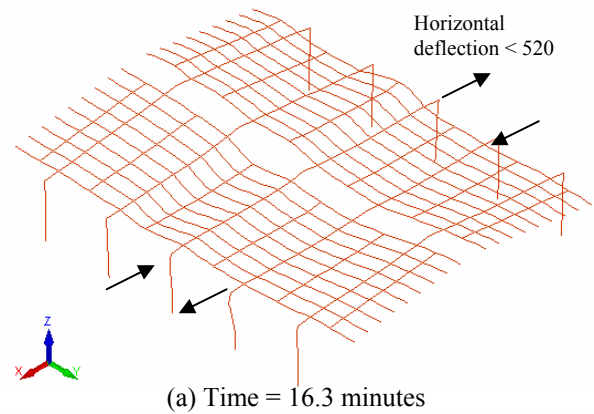
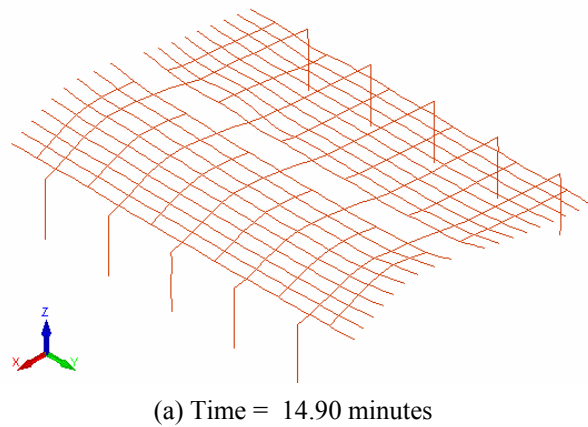


Fig. 7 Inwards collapse of the fixed support structure WITHOUT purlin axial restraint (Scale =1x)

Fig. 8 Deflected shapes immediately before and after the rapid sagging of roof of the fixed support structure and at collapse WITH purlin axial restraint (Scale =1x)

modes are acceptable provided the connections between the side walls and the supporting frames do not fail.

For the **inwards** collapse mode (i.e. no axial restraint to purlins), the initial outwards deformations of the steel columns are less than 200 mm at the top of the column and are solely due to the thermal expansion of the steel portal frame. When the fire-affected roof structure shows a snap-through failure mechanism and collapses to the ground (Fig. 7), the columns will be pulled inwards along with the collapsing rafters. Therefore, the side walls will collapse inwards provided the connections between the walls and the supporting frame do not fail.

For the **catenary** mode of failure (with axially restrained purlins), the sagging of the fire-affected roof structure into a catenary shape will push the top portions of the columns outwards to some extent (i.e. up to 520 mm at the top of the column). Providing the connections to the walls panels do not fail, the walls can still be attached to the supporting frames and held in outwards inclined positions (Fig. 8). This is acceptable according to the New Zealand concrete code¹⁰.

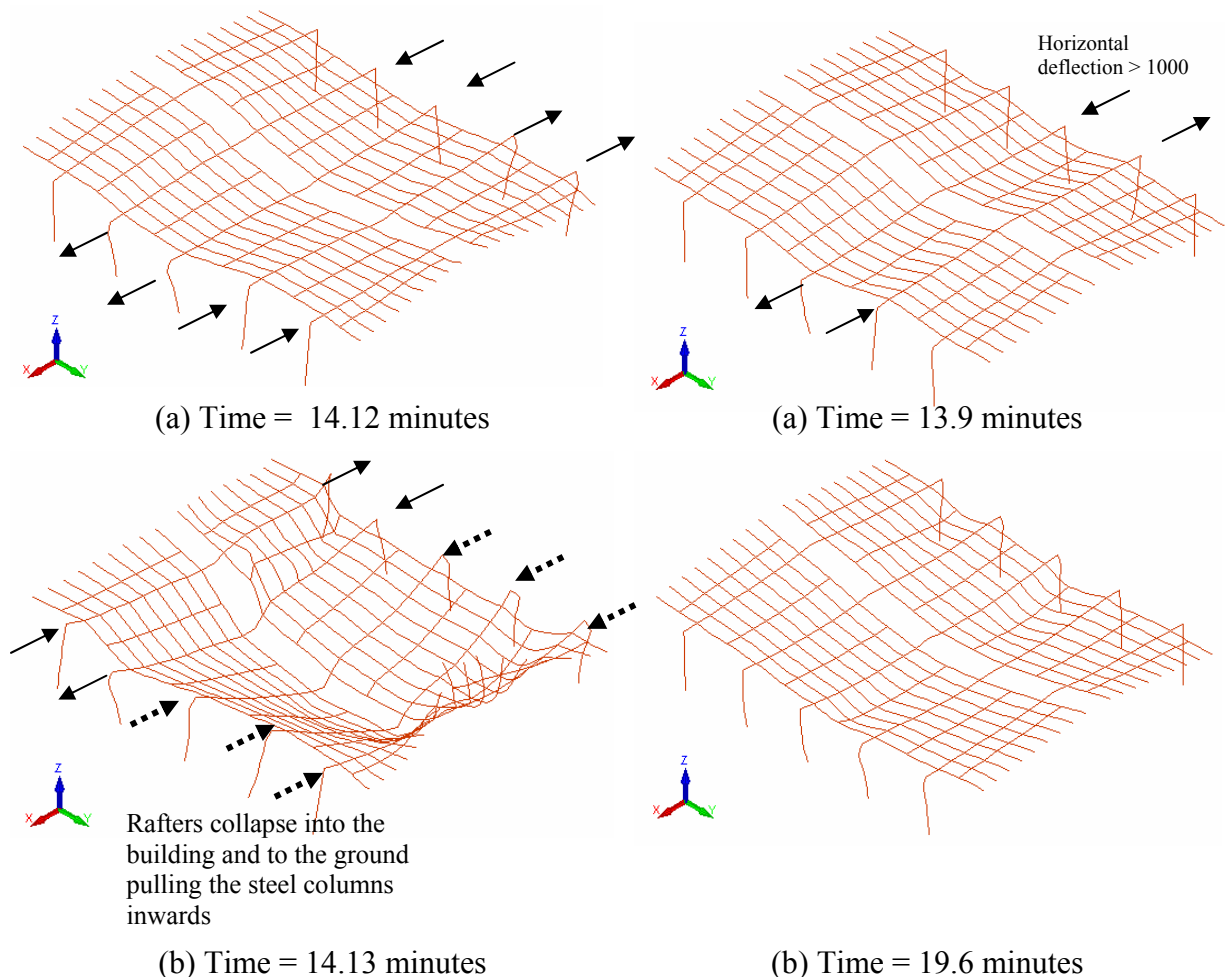


Fig. 9 Sidesways collapse of the pinned support structure WITHOUT purlin axial restraint (Scale = 1x)

Fig. 10 Deflected shapes immediately before and after the rapid sagging of roof of the pinned support structure WITH purlin axial restraint (Scale = 1x)

4.1.2 Pinned Support Conditions

For a steel portal frame structure with pinned base connections, significant **sidesway** of the fire-affected frames will occur when the fire-affected roof structure (steel rafters, purlins and brace channels) begins to fail and the sway of the fire-affected frames will result in very large horizontal deflections at the top of the columns (i.e. possibly in excess of 1 m). After that, the fire-affected roof structure will deform into a catenary if the adjacent purlins are axially restrained (Fig. 10), or in the case where the purlins are not axially restrained, the roof structure will collapse to the ground and the analyses have shown that the collapsing rafters will subsequently pull the frames inwards (Fig. 9). These failure modes are unacceptable and have been identified as the **sway** collapse mode because the large lateral deflections to one side could cause a side-sway collapse of one or more frames due to the P-delta effect related to the self weight of the walls.

4.1.3 Partially Fixed Support Conditions

Most real buildings are designed and built with partially fixed portal frame bases. The collapse mechanisms of a building with portal frames partially fixed at the base are similar to the structure with fully fixed support conditions. If the purlins fixed to the fire-affected steel frames are axially restrained by the end walls, the structure will deform into a **catenary** as shown in Fig. 12. On the other hand, without axial restraint in the purlins, the portal frame columns and the attached wall panels will collapse **inwards** (Fig. 11) when the roof structure collapses to the ground. Both of these situations are acceptable.

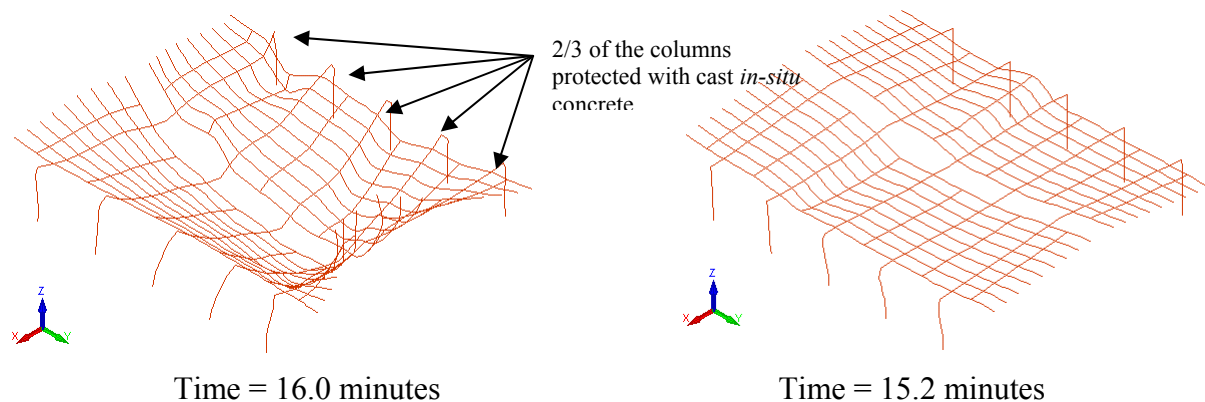


Fig. 11 Final deflected shape of the partially fixed support structure WITHOUT purlin axial restraint and 2/3 concrete encasement to right column legs (Scale = 1x)

Fig. 12 Final deflected shape of the partially fixed support structure WITH purlin axial restraint and 2/3 concrete encasement to right column legs (Scale = 1x)

4.1.4 Passive Fire Protection

For protected columns with either full or partial base fixity, the concrete encased part of the columns will not deform excessively and will remain relatively straight during the fire. If purlin axial restraints are provided by the end walls, the structure will deform into a **catenary** (Fig. 12).

In the case of pinned bases, if the rafters collapse to the ground (i.e. no purlin axial restraint), the protected columns will not collapse inwards along with them and can still be

standing **upright** after the fire (Figs 13 & 14). This is because the strength and stiffness of the concrete encased part of the steel columns are largely unaffected and the stability of the columns has not been affected. If the connections between the supporting frames and wall panels do not fail, the walls will be attached to the frames and remain standing during the fire. This is acceptable as long as the walls do not collapse outwards after the fire due to failure of the connections between the panels and the columns. However, the stability of the walls after the fire becomes an issue and the walls must resist wind loads as outwards collapse after the fire is also unacceptable.

The new New Zealand Concrete Structures Standard¹¹ will require that the connections be designed for a face load of 0.5 kPa applied to the concrete walls during the fire.

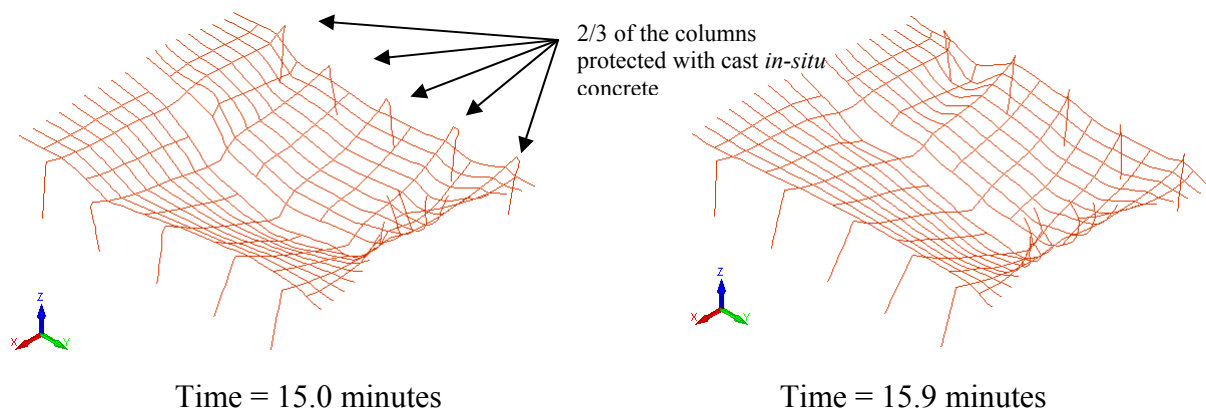


Fig. 13 Final deflected shape of the fully pinned support structure WITHOUT purlin axial restraint and with 2/3 concrete encasement to column legs (Scale = 1x)

Fig. 14 Final deflected shape of the fully pinned support structure WITHOUT purlin axial restraint and with full concrete encasement to column legs (Scale = 1x)

4.2 Steel Connections between the Side walls and the Supporting Frames

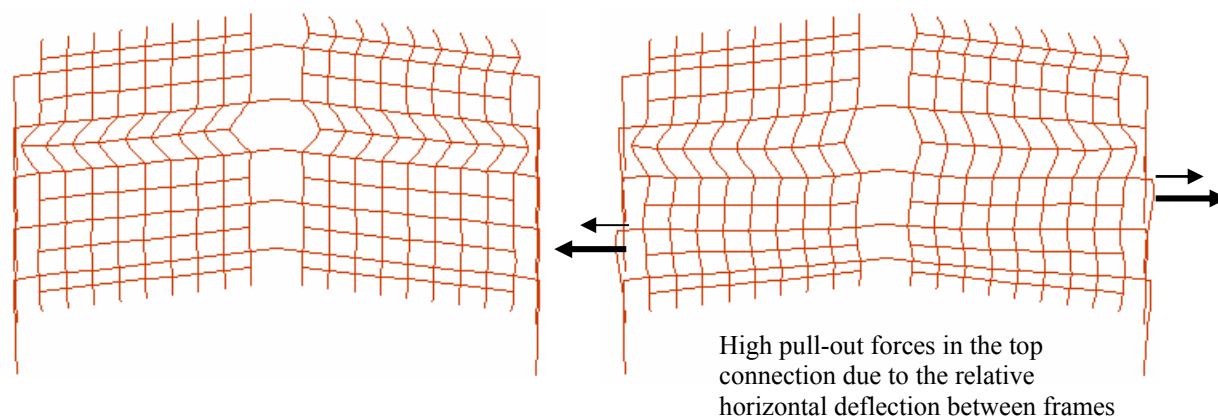
The top connections holding the walls to the supporting columns are very likely to fail due to high pull-out forces (Figure 15) as a result of the relative horizontal deflection between adjacent portal frames. This could possibly cause outwards collapse of the concrete walls if flexural capacity is not provided at the base, such as in 'pinned' base walls. This suggests that there should be more connections between the top and bottom of the wall.

5. CONCLUSIONS

The following conclusions can be drawn from the analyses carried out in this study:

- Most pin based frames fail in a sidesway mode and should not be permitted.
- All partially fixed based frames have the same failure mode as fully fixed based ones.
- For the most common case of an ISO fire occupying the whole building, without strong axial restraint of the purlins and with common column out-of-plane restraints provided by the side wall panels, structural collapse occurs at about 15 minutes.
- Full or partial base fixity, with column protection, gives good after-fire stability, with columns remaining vertical (hence much better reparability).

- The provision of concrete encasement to columns gives no benefit if the column bases are pinned.
- In order to prevent collapse in an undesirable sway mode, the level of axial restraint of the steel purlins is less important than providing some degree of flexural fixity at the bases of the portal frame columns.



(a) Deflected shape immediately before rapid sag of roof (b) Deflected shape immediately after rapid sag of roof

Fig. 15 Failure of top connection due to a pull-out mechanism - fully fixed frames with no concrete encasement (Scale = 1x))

6. DESIGN RECOMMENDATIONS

Support connections of the steel portal frames

The portal frame base connections must be detailed and designed to provide some level of rotational restraint, in order to prevent the sideways of frames and outwards collapse of wall panels.

Passive fire protection to the column legs

Assuming that the recommendation of some base fixity will always be followed, providing fire protection such as concrete encasement to the columns can ensure that the columns and walls will remain standing during and after the fire. The undesirable outwards collapse can be avoided even without concrete encasement if partial fixity is provided at the column bases.

Connections between the wall panels and the supporting frames

The wall panels must always be well connected to the supporting frames so that the outwards collapse of the panels, due to both thermal bowing of the concrete walls and outwards movement of the columns, can be prevented. This is regardless of whether or not the steel columns are fire protected. The new New Zealand Concrete Structures Standard NZS 3101:2005 will require at least two upper strong and well designed connections to the panels to ensure that the wall panels are well attached to the supporting columns.

If multiple panels are used between the supporting frames, the panels must be well connected to each other such that they act as a complete unit. An eaves tie member is recommended to keep all the walls panels connected during a fire and the connections to the

walls and supporting columns should be carefully detailed and designed to prevent outwards collapse of individual panels.

7. REFERENCES

- [1] Lim, L.C.S., Stability of Precast Concrete Tilt Panels in Fire, Fire Engineering Research Report 00/8, University of Canterbury, Christchurch, New Zealand, 2000.
- [2] Bennetts, I.D. and O’Meagher, A.J., “Single Storey Steel-framed Buildings: Support of External Walls in Fire”, BHP Structural Steel Development Group, Technical Note No.1, Australia, 1995.
- [3] Standards New Zealand, General Structural Design and Design Loadings for Buildings, NZS 4203:1992, Wellington, New Zealand, 1992..
- [4] Standards New Zealand, Steel Structures Standard, NZS 3404:1997, Wellington, New Zealand, 1997.
- [5] Bong M.W., “Structural Fire Performance of Steel Portal Frame Buildings”, Master of Engineering (Fire) Thesis, University of Canterbury, Christchurch, New Zealand, 2005.
- [6] ISO, “Fire resistance tests - elements of building construction”, ISO 834-1975, International Organization for Standardization, 1975.
- [7] EC1, “Eurocode 1: Basis of Design and Designs Actions on Structures”, ENV1992: Part 2.2: Actions on Structures Exposed to Fire, European Committee for Standardization, Brussels, Belgium, 1994.
- [8] Franssen, J.M., *personal communication*, 2004.
- [9] Dimond Industries, Hi-Span Design Manual, Manual No.9 in the Dimond Design Information Series, New Zealand, 1995.
- [10] Standards New Zealand, Concrete Structures Standard, NZS 3101:1995, Wellington, New Zealand, 1995.
- [11] Standards New Zealand, Concrete Structures Standard, NZS 3101:2006, Wellington, New Zealand, 2006.



NUMERICAL MODELLING OF THE BEHAVIOUR OF A STAINLESS STEEL PORTAL FRAME SUBJECTED TO FIRE

Nuno LOPES¹; Paulo VILA REAL²; Paulo PILOTO³;

Luís MESQUITA⁴ and Luís SIMÕES da SILVA⁵

ABSTRACT

It is known that stainless steel has a better fire performance than carbon steel, which can lead to a growing utilization of this kind of steel in structures. In fact, although more expensive than the carbon steel, structures in stainless steel can be competitive because of its smaller thermal protection need.

With the purpose of modelling by Finite Element Method the behaviour of a stainless steel framed structure, without any protection, submitted to fire, material properties of stainless steel have been introduced into SAFIR program. SAFIR is a finite element program with geometrical and material non-linear analysis, specially developed in the University of Liege for studying structures subjected to fire. The thermal and mechanical properties of the stainless steel, introduced in the SAFIR program are temperature dependent, according to the Eurocode 3. The stress strain relationship, the thermal conductivity and the specific heat are the most important material properties for structural analysis at high temperatures. Stainless steel properties are considerable different from carbon steel.

The behaviour of a frame structure will be compared in two different materials: stainless steel 1.4301 (also known as 304) and carbon steel S235. The fire resistance of the

¹ Research Assistant, University of Aveiro, Department of Civil Engineering, 3810-193 Aveiro, Portugal, email: nuno_lopes@civil.ua.pt.

² Professor, University of Aveiro, Department of Civil Engineering, 3810-193 Aveiro, Portugal, email: pvreal@civil.ua.pt.

³ Assistant Professor, Polytechnic Institute Bragança, Dep. Applied Mechanics, 5300 Bragança, Portugal, email: ppiloto@ipb.pt.

⁴ Research Assistant, Polytechnic Institute Bragança, Dep. Applied Mechanics, 5300 Bragança, Portugal, email: lmesquita@ipb.pt.

⁵ Professor, University of Coimbra, Dep. Civil Engineering, 3030 Coimbra, Portugal, email: luisss@dec.uc.pt.

stainless steel structure is 3 times higher than the one obtained with carbon steel, avoiding any fire protection material needed to fulfil the standard fire requirements.

1. INTRODUCTION

The use of stainless steel for structural purposes has been limited to projects with high architectural value, where the innovative character of the adopted solutions is a valorisation factor for the structure. The high initial cost of stainless steel, coupled with: (i) limited design rules, (ii) reduced number of available sections and (iii) lack of knowledge of the additional benefits of its use as a structural material, are some of the reasons that force the designers to avoid the use of the stainless steel in structures [1]. However, a more accurate analysis shows a good performance of the stainless steel when compared with the conventional carbon steel.

The biggest advantage of stainless steel is its higher corrosion resistance. However, its aesthetic appearance, easy maintenance, high durability and reduced life cycle costs are also important properties. It is known that the fire resistance of stainless steel is bigger than the carbon steel usually used in construction. The question of knowing if stainless steel structural elements can be used in buildings, without any fire protection, is very important, because the use of stainless steel in structures is usually due to aesthetic considerations. Eliminating the fire protection in structures will result in smaller construction costs, lower construction periods, more efficient use of interior spaces, healthier work environment and a better aesthetic appearance of the building. On the other hand, the life cycle costs of unprotected stainless steel structures are smaller than protected carbon steel structures.

Thinking in economic terms, it would be improbable that stainless steel could be chosen instead of carbon steel, due to its higher fire resistance. However, for designers that value the appearance and the durability of stainless steel, the additional benefit of having a significant fire resistance without any protection, can reverse the choice in favour of this material. In fact the stainless steel can be an excellent solution, in application where corrosion resistance and fire resistance are demanded at the same time.

Although the use of stainless steel in construction is increasing, it is still necessary to develop the knowledge of its structural behaviour.

The high corrosion resistance of the stainless steel in most of the aggressive environments has been the reason for its use in structures located near the sea, and also in oil-producing, chemical, nuclear, residual waters and food storage facilities. Its corrosion resistance results in a well adherent and transparent layer of oxide rich in chromium that forms itself spontaneous on the surface in the presence of air or of any other oxidant environment. In case it is crossed, or has some cut damage, the superficial layer regenerates itself immediately in the presence of oxygen.

The stainless steel has, at room temperature, unlike carbon steel, a non-linear behaviour, even for small stresses values. On the other hand, it does not exhibit a clearly defined yield strength. A conventional elasticity limit at 0,2% strain is usually adopted. Table 1 compares the mechanical properties of the stainless steel 1.4301 (also known as 304), used in the structure studied in this paper, with the carbon steel S235, at room temperature.

Table 1 – Steel mechanical properties at room temperature.

Mechanical properties	Carbon steel S235	Stainless steel 1.4301
Ultimate strength (MPa)	360	520
Yield strength (MPa)	235	210
Ultimate strain	> 15%	40%

In figure 1 the stress-strain relationships of carbon steel S235 and stainless steel 1.4301 at room temperature and at 600 °C [2, 3], are represented.

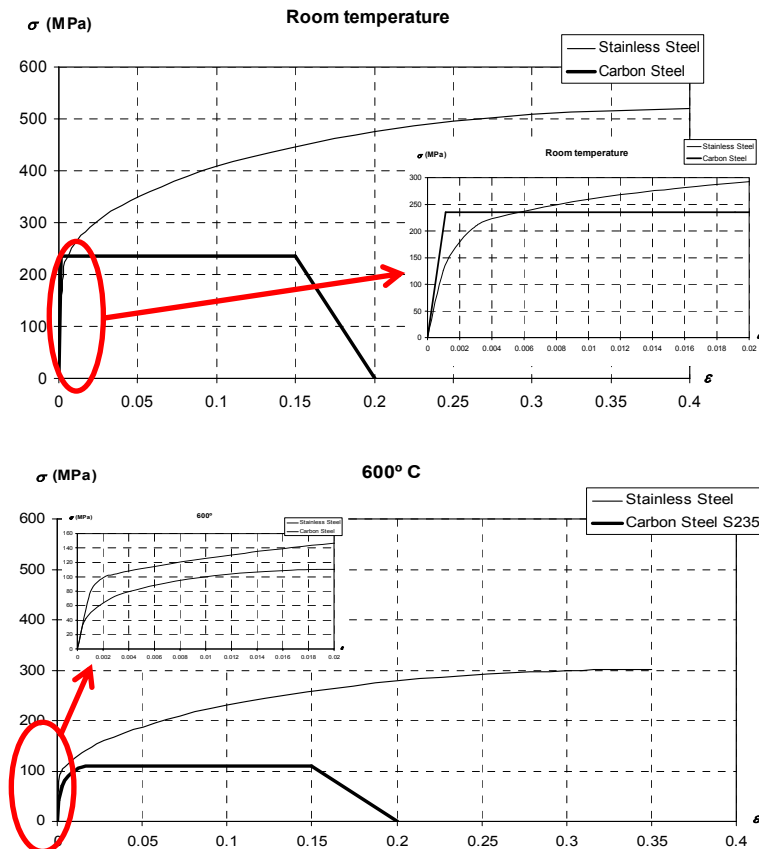


Fig. 1 – Stress-strain relationships of carbon steel S 235 and stainless steel 1.4301 at room temperature and at 600 °C.

The carbon steel S235 was chosen due to its value of the yield strength, similar to the nominal stress (0,2% proof stress) of the stainless steel 1.4301. For design purposes according to the Eurocode 3, these are the values used to check the resistance of the structural elements.

Figure 2 illustrates the differences between the thermal conductivity and the specific heat of carbon steel and stainless steel. Although the stainless steel has a thermal conductivity lower than the carbon steel, which would make one suppose slower heating speed in stainless steel, the specific heat of the carbon steel is higher, therefore there is a small difference between the temperature evolutions of both materials, as it can be observed in figure 7.

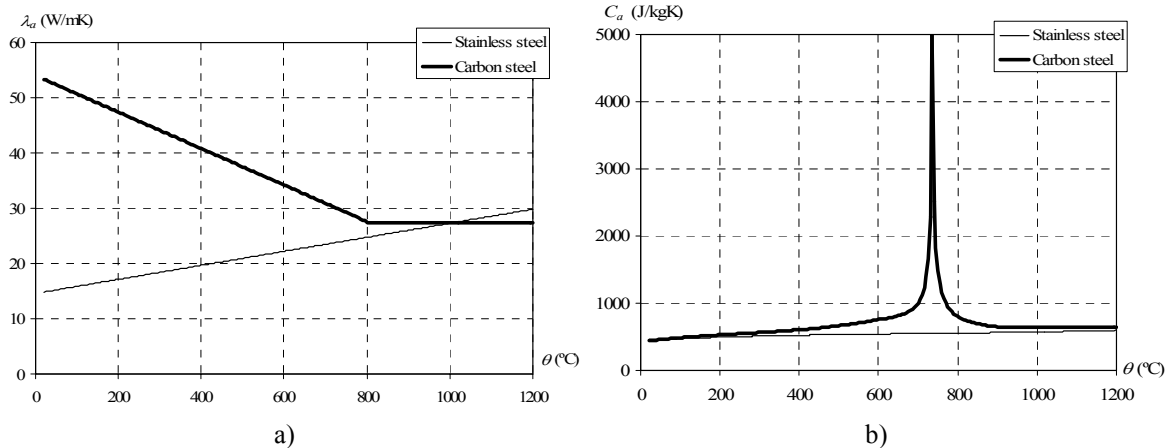


Fig. 2 – Carbon steel and stainless steel: a) thermal conductivity b) specific heat.

The fire resistance of a steel framed structure, with two spans and three stories as it is shown in figure 3, is determined in this paper. The fire resistance of this structure in S235 carbon steel is smaller than the expected standard resistance R30, while the 1.4301 stainless steel structure widely exceeds that resistance. This structure simulates an office building at an altitude of 700m. In order to account for the effects of the assembly imperfections, possible eccentricities and geometrical imperfections, an initial sway imperfection has been introduced, according to part 1.1 [4] of Eurocode 3, that corresponds to an rotation angle of 0.0033 rad.

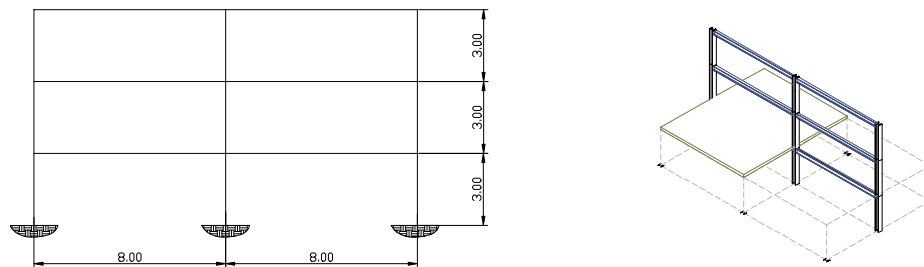


Fig. 3 – Schematic representation of the two-dimensional framed structure studied, with 5m spacing between portal frames.

2. NUMERICAL MODELLING

There are several numerical programs for structural fire resistance analysis. These programs can be based on simplified calculation methods presented in Eurocodes, or more complex programs for non-linear analysis, based in the finite element method, that are included in the advanced calculation methods of the Eurocodes. The program SAFIR [5] from the University of Liege was used in this work. This program has two distinct calculation modules, one for the thermal analysis of structure and the other for the mechanical behaviour analysis. Consequently, the non-uniform temperature evolution is calculated for each existing section type in the structure, and in a subsequent phase the mechanical module of the program reads these temperatures and determines the thermo-mechanical behaviour of the structure in a incremental static analysis. Both steps are briefly described in the following.

2.1 Thermal analysis

The thermal analysis of the program SAFIR is carried out using either three-dimensional solid elements (3D), or two-dimensional plane elements (2D). The solid elements are linear interpolated and have eight nodes, and the also linear, plane elements, can be represented by triangles with 3 nodes or quadrilateral with 4 nodes.

2.2 Mechanical analysis

The non-linear static analysis used for thermo-mechanical behaviour of the structure uses the results of the previous thermal analysis. Besides the shell finite elements, truss elements and beam elements are also available in SAFIR, being possible with the latter two, to model three-dimensional framed structures. The beam finite element is based in the Bernoulli hypothesis, where plane sections before bending deformation remains plane after deformation and the effect of the shear deformation is not considered. On the other hand this element does not take into account local buckling, therefore it should only be used as Class 1 and Class 2 sections profiles, as defined in Eurocode 3 [4].

The cross-section of the elements is simulated using a fiber model finite element, the temperature, the stress, the strain and the other material properties being considered constant in each fibre. The beam element with the fibre model, allows the consideration of residual stresses [6].

The collapse criterion of the structure is defined as the instant when the stiffness matrix becomes not positive definite, thus becoming impossible to establish the equilibrium of the structure. The program allows the use of the “arc-length” method, to solve the local failure problems that sometimes appear. In fact, in hyperstatic structures, failure in one element may not correspond to global collapse of the structure. It is possible that, beyond local failure, part of the internal forces that can not be supported by the local element, are redistributed to other structural elements, leading to a new equilibrium position.

3. ACTIONS IN STRUCTURES SUBJECTED TO FIRE

3.1 Mechanical actions

The design value of the actions effects in case of fire, should be obtained using the following accident combination as defined in the EN 1990 [7]:

$$\sum \gamma_{GA} G_k + \psi_{1,1} \cdot Q_{k,1} + \sum \psi_{2,i} \cdot Q_{k,i} + \sum A_d(t) \quad (2)$$

where

γ_{GA} – is the partial safety factor of the permanent actions in case of accident, which should take the unit value;

G_k – is the characteristic value of the permanent actions;

$Q_{k,1}$ – is the characteristic value of the main or dominant variable action;

$\psi_{1,1}$ – is the combination coefficient associated to the main or dominant variable action [7];

$\psi_{2,i}$ – is the combination coefficient associated to the remaining variable actions [7];

$A_d(t)$ - is the calculation value of the action resulting from the fire exposition and that is represented by the temperature effect in the material properties and from the indirect fire actions that results from the efforts due to the restraints to thermal elongation.

The live action considered was obtained using part 1-1 of Eurocode 1 [8]. The wind and snow actions were quantified taking into account the location and implantation of the building according to part 1-4 [9] and part 1-3 [10] of Eurocode 1.

Structural analysis corresponding to the combination of actions for accidental design situation considering the wind as the main variable action was made. Figure 4 shows the corresponding load combination.

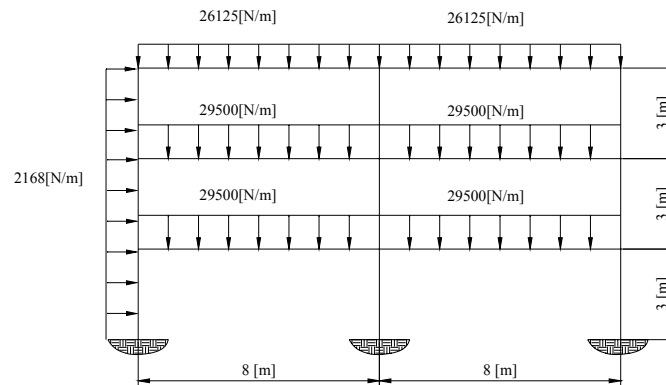


Fig. 4 – Design loads for the accidental combination where wind is the dominant variable action.

3.2 Thermal actions

In this work, the standard fire curve ISO 834 was used, which has the following analytical expression [11]:

$$\theta_g = 20 + 345 \log_{10}(8t + 1) \quad (3)$$

where:

θ_g is the gas temperature in the room subjected to fire in °C;

t is the time in min.

4. CASE STUDY

Fire resistance will be determined in the steel structure presented in figure 3, when subject to accidental conditions in compartment C4 as shown in figure 5.

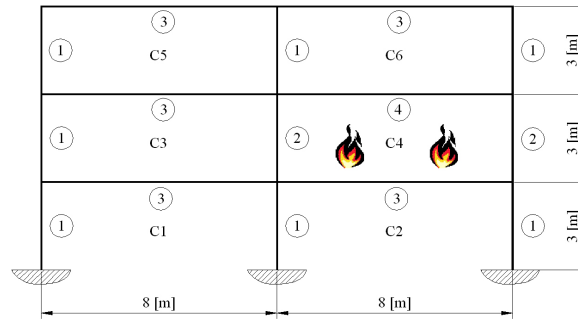


Fig. 5 – Structure with fire only in room 4.

For the structure in carbon steel the steel grade S235 was used. Structural design was made at room temperature leading to IPE 450 beam section and HEA 300 columns section. For the stainless steel structure class 1.4301 was used with a proportional elastic limit stress of 210 MPa, similar to the yield stress of the chosen carbon steel. The beams and columns sections used were the same as the structure in carbon steel.

In figure 5, different types of structural elements are numbered according to the thermal loading history. For example, the type 2 elements correspond to columns heated only in one flange. The type 4 section corresponds to a beam heated in three sides. Figure 6 illustrates these two cases.

The thermal module of the program SAFIR determines the evolution of the temperature field with time, doing a non-linear analysis, since the material thermal properties depend on the temperature and the boundary conditions are also non-linear.



Fig. 6 – a) Beam subjected to fire in three sides; b) Column subjected to fire in one side.

The temperature field obtained in the cross-section of the profiles is non uniform. Simplified methods prescribed in Eurocode 3 assume that the temperature field is uniform in the cross section of the profiles, due to the elevated steel thermal conductivity. As it can be easily understood, elevated thermal gradients may be expected in the analysed sections, which can origin significant changes in the thermo-mechanical behaviour.

Figure 7 represents the temperature evolution at a specific point of the beam cross section. It can be verified that the heating curve of the stainless steel is very similar to the heating curve of carbon steel with the exception in the range between 600 °C and 900 °C. The time delay represented for carbon steel is due to the metallurgic phase transformation and accounted by the peak in the specific heat property value of carbon steel, which that does not exists in the stainless steel, as was shown in figure 2.

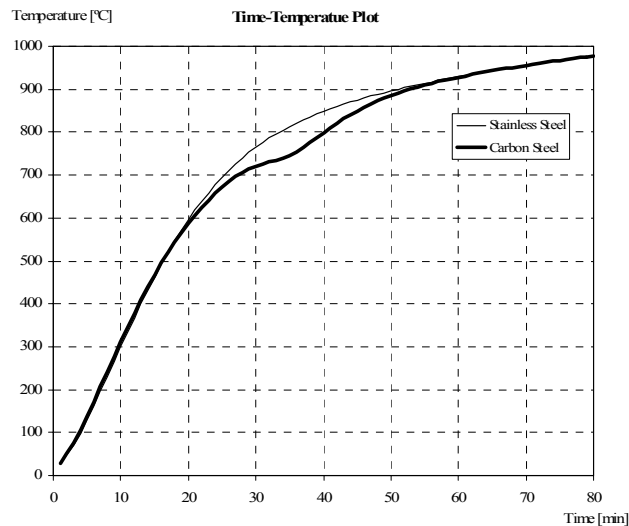


Fig. 7 – Temperature evolution in a node of the beam 4 cross section.

The beam finite elements used in the structural mesh are represented in figure 8. The deformed shape and the internal forces are determined through an incremental process, during fire, until the instant in which it is not possible to establish the equilibrium. This instant corresponds to the structure fire resistance.

The finite beam elements presents 3 nodes, with a central node that considers the non-linear axial displacement [12]. The end nodes have three degrees of freedom (two translations and one rotation) and the third node of the beam element one degree of freedom (the axial displacement), in a total of 7 degrees of freedom.

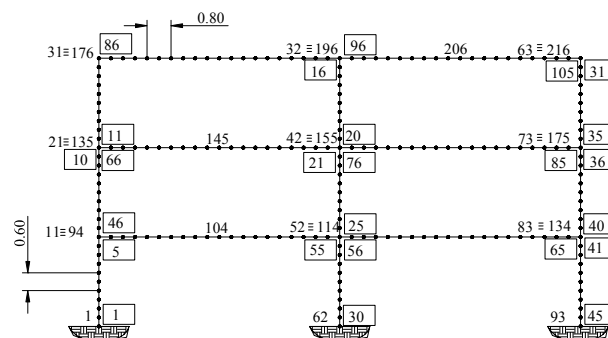


Fig. 8 – Beam elements used in the structure mesh. Nodes and elements (in box) numbering.

The deformed shape of the structure and the force diagrams can be obtained with post-processor Diamond 2004. Figure 9 presents the deformed shape, axial forces diagrams and bending diagrams at collapse of the carbon steel and the stainless steel structures. In this figures it can be observed that at collapse the deformed shape of the stainless steel structure is bigger than in the carbon steel structure, which can be justified by the fact that the stainless steel stress-strain relationship has an ultimate strain bigger than in the carbon steel, as illustrated in figure 1. It also can be observed that the bending diagrams present some differences in the two structures.

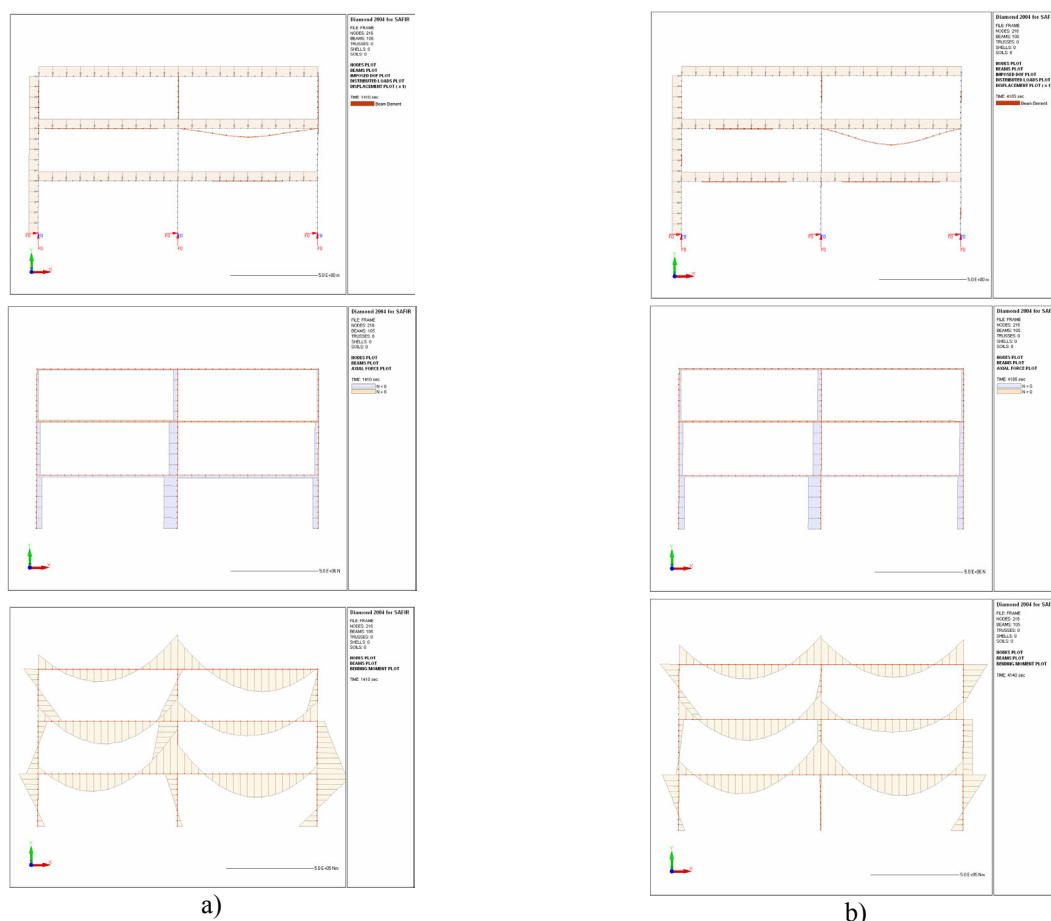


Fig. 9 – Results at failure; a) Carbon steel structure; b) Stainless steel structure (displacements scale factor of 1).

The failure in the carbon steel structure occurred after 1410 seconds (23,5 minutes) while the stainless steel structure only collapses after 4140 seconds (about 1 hour and 9 minutes), which corresponds to a fire resistance of about 3 times higher than the fire resistance of the carbon steel structure.

The fire resistance of the carbon steel structure is clearly below the standard fire resistance defined as R30, being necessary to use fire protection to fulfil the required fire resistance, which is not the case when stainless steel is used.

5. CONCLUSIONS

Fire resistance of a portal frame structure has been determined in carbon steel and in stainless steel. In both cases it has been considered that the structure was not fire protected.

The analysis was made with the program SAFIR developed, at the University of Liege, especially for the study of the behaviour of structures subjected to fire. In order to use this program in the analysis of stainless steel structures, a new stress-strain relationship material was introduced in SAFIR as well as the other mechanical and thermal properties, according the Eurocode 3.

It was concluded that the studied structure in stainless steel 1.4301 has a fire resistance 3 times higher than the fire resistance of the same structure in carbon steel S235. Concerning the standard qualification, the carbon steel structure is R15, while the structure in stainless steel is R60. This resistance allows for the utilization of the stainless steel structure without any fire protection, which increases the economic advantage of the stainless steel as a

structural material, allowing the material without protection, which is often, decisive in the choice of this kind of steel in construction. The results of the practical case presented in this paper should be seen as preliminary study. In fact, it should be determined the behaviour of the structure in carbon steel considering the stress-strain relationship allowing for strain hardening, prescribed in the Annex A of part 1-2 of the Eurocode 3.

The steel grade S235 was chosen because its yield strength is similar to the nominal stress (0,2% proof stress) of the stainless steel 1.4301.

6. REFERENCES

- [1] Gardner, L., "The use of stainless steel in structures" Prog. Struct. Engng Mater., 2005.
- [2] prEN 1993-1-4, "Eurocode 3 - Design of Steel Structures – Part 1-4: General rules – Supplementary rules for stainless steels", September 2005.
- [3] EN 1993-1-2, "Eurocode 3 – Design of steel structures – Part 1-2: General rules – Structural fire design", April 2005.
- [4] EN 1993-1-1, "Eurocode 3 – Design of Steel Structures – Part 1-1: General rules and rules for buildings", May 2005.
- [5] Franssen, J.-M., SAFIR. A Thermal/Structural Program Modelling Structures under Fire. Engineering Journal, A.I.S.C., Vol. 42, No. 3, pp. 143-158, 2005.
- [6] Vila Real, P., Cazeli, R., Silva, L., Santiago, A., Piloto, P., "The Effect of Residual Stresses in the Lateral-Torsional Buckling of Steel I-Beams at Elevated Temperature", Journal of Constructional Steel Research, ELSEVIER, 60/3-5, pp.783-793, 2004.
- [7] EN 1990, "Eurocode – Basis of structural design", April 2002.
- [8] EN 1991-1-1, "Eurocode 1 – Actions on structures – Part 1-1: Actions on Structures – Densities, self-weight, imposed loads for buildings", April 2002.
- [9] EN 1991-1-4, "Eurocode 1 – Actions on structures – Part 1-4: General actions – Wind actions", April 2005.
- [10] EN 1991-1-3, "Eurocode 1 – Actions on structures – Part 1-3: General actions – Snow loads", July 2003.
- [11] EN 1991-1-2, "Eurocode 1 – Actions on structures – Part 1-2: General actions – Actions on structures exposed to fire", Novembre 2002.
- [12] Jean-Marc Franssen, "Contributions a la Modelisation des Incendies dans les Batiments et de Leurs Effects Sur les Structures", Thèse présentée en vue de l'obtention du grade d'Agrégé de l'Enseignement Supérieur, Année académique 1997-1998, University of Liege, Belgium.



COMPARISON OF ANALYTICAL MODELS FOR FIRE RESISTANCE PERFORMANCE OF STEEL STRUCTURE

Yu Guang LI¹, Hideki UESUGI² and Takao WAKAMATSU³

ABSTRACT

In designing fire resistant building to seal off the fire within the fire compartment where it has originated, large deformation is restricted against the structural components, which configure the fire compartment. It is generally accepted to study the fire response concerning the stress deformation behavior of a structure as a planar structural frame. In order to illustrate whether the floor slab in a fire compartment exposed to fire significantly affects the behavior of the structural components, the comparisons of 3D and 2D analytical model for fire resistance performance of steel structure, have been carried out in this paper. Comparing the theoretical results with those recorded in experiments, has demonstrated that the thermal expansion of the floor slab in a fire compartment exposed to fire, will cause the structural components to produce larger deformations. And hence, the columns will be easier to reach the limit value of deflection in 3D analysis than in 2D analysis, due to the influence of the stiffness of the floor slab. Column-failure of steel structure is more likely to break out.

¹ Engineer, Tokyo University of Science, Research Institute for Science and Technology, 2641 Yamazaki, Noda-shi, Chiba, 278-8510 Japan, email: j7104710@ed.noda.tus.ac.jp

² Professor, Chiba University, Graduate School of Science and Technology, 1-33 Yayoicho, Inage-ku, Chiba-shi, Chiba, 263-8522 Japan, email: uesugi@faculty.chiba-u.jp

³ Professor, Tokyo University of Science, Research Institute for Science and Technology, 2641 Yamazaki, Noda-shi, Chiba, 278-8510 Japan, email: wakamatu@rs.noda.tus.ac.jp

1. INTRODUCTION

Buildings are designed and constructed under the assumption that a fire can break out. To assure the fire safety of a building, the main focus would obviously be to prevent the fire from spreading within the building and the collapse of the building itself. Therefore, large deformations that the structural components located on the fire zone may undergo should be restricted. In general, it is to study the fire response concerning the stress deformation behavior of a structure as a planar structural frame. But, fire is a phenomenon involving three-dimensional thermal expansion, so it is natural to treat a building structure as a 3D body when considering its behavior in a fire. Especially, the influence that the floor slab in a fire compartment exposed to fire has on the behavior of the building structure may be extremely large, it is necessary to explore how the floor slab affects the fire response of the structure when exposed to fire. The influence of floor slab on fire resistance performance of steel structure can be predicted as follows:

- The floor slab exposed directly to fire may produce larger deflections, due to the bending effect induced by the temperature differences between the heated surface and the unheated surface of the floor slab. It may cause a significant influence on the beams supporting the floor slab.
- The composite beams that consist of concrete floor slab and steel beams are relatively difficult to deflect than those simplex steel beams, therefore, the columns in 3D analysis will be leaning outwards some more, due to the elongation of the beams and the floor slab in fact.

To verify these predictions described above, in this paper the analyses of deflection behavior about the experiments in which a large full-scale frame was exposed to vehicle fire, have been carried out with the following analysis models, and the theoretical results are compared with those recorded in experiments to show the validities of the models. The models hereinafter defined will have the same meaning when used in this paper.

- Model A: 3D model which takes account of the thermal expansion of a floor slab;
- Model B: 3D model which omits the influence of a floor slab;
- Model C: 2D model which uses a planar structural frame

In addition, a steel structure with one story and one span that was under standard fire condition was analyzed to inspect the difference of analysis models as referred to above.

2. THEORETICAL BASIS OF ANALYTICAL METHOD

The degradation of the material due to the exposure to heat and the elongation due to the thermal expansion, will cause the structural members exposed directly to fire to show relatively large stresses and deformations that exceed the limits of elastic region and enter the plastic region. A non-linear analytical method of deflection behavior concerning 3D steel frame exposed to fire that takes account of the thermal expansion of floor slab, has been established [1,2]. All of the members of the building are divided into finite beam-column elements. The cross-section of each element is divided into a number of segments to allow consideration of distributions of temperature, stress and strain through the cross-section, this will enable to take the material nonlinear characteristic into account. And it is assumed that the cross-section of each element will remain within the original plane after the deformation. Using the Tangent Stiffness Method based on the Infinitesimal Displacement Theory, a convergent calculation will be made, and hence, the value for the incremental displacement will be obtained. Accumulating these incremental displacements will take the effect of geometric nonlinear characteristic into account to solve " $P-\Delta$ " interaction.

For the current study there is no basic data available on concrete placed under 2D stresses at elevated temperatures. It also provides that the temperature difference between the heated surface and the unheated surface of the floor slab exposed to fire will be extremely large, so that a large bending moment and an axial force will be produced within the floor slab restrained at the ends [3]. The main factors of the effect of the slab on the structural frame will be the bending and expanding deformations of the slab, and the effect of shear deformation of the slab will be of secondary importance. Therefore, as a simple calculation model, the floor slab is line-replaced with grid beams omitting the Wagner twist as approximately in [2]. The stiffness matrix of the grid beams at each time is calculated along the reference axis that penetrates the geometrical center of the steel beam. The uniaxial properties of concrete at elevated temperatures specified in EC4 [4] have been adopted in [2].

3. COMPARISONS OF MODELLING OF THE LARGE FULL SCALE FIRE TEST

3.1 Large Full Scale Fire Test

The steel structure of the large full-scale fire test of 3-stories type car park [5] that is thermally unprotected is shown in Figure 1. The columns of the structure are only mounted on top of two H-shaped steel members, and the bases of the inner columns are restrained using high-strength bolts. The cross-sectional dimensions of the members are shown in Table 1. The grade of steel is SS400. The deck plate (Wide-ditch gutter type 50, $t=1.2\text{mm}$) is using for the composite slab. Its reduced thickness is 100mm. The design standard strength of concrete is 21N/mm^2 . In the fire test there were 8 cars sequentially burnt at the corner of the 1st floor, as shown in Figure 2. The columns on the 1st floor and the floor slabs (shaded parts) and the beams on the 2nd floor in the area bounded by \bigcirc_{3-5} and \bigcirc_{D-E} (see Figure 3) are the members that have been exposed directly to vehicle fire. The fire-extinguishing activity began 42 minutes after ignition. The temperature and deformation of the portions that are strongly influenced by thermal expansion has been measured.



Fig. 1. Large full-scale fire test structure



Fig. 2. Vehicle on fire

Table 1. List of structural members

	1 st Floor	2 nd and 3 rd Floors
Column	\square -300 \times 300 \times 12	\square -300 \times 300 \times 9
Beam	H-400 \times 200 \times 8 \times 13	
Small beam	H-350 \times 175 \times 7 \times 11	
Floor slab	h(Reduced thickness)=100	

3.2 Modeling of the Large Full-scale Fire Test

The analyses will be performed on 3 stories portions of the car park. Model A and Model B defined in section 1 are shown in Figure 3 as a 3D model. The restraints at the base of the columns of the 1st floor are configured, based on the measurements obtained in the fire test on the displacement. Only the floor slabs that are directly exposed to vehicle fire will be included in the elasto-plastic analysis in Model A. A set of intersecting beams located approximately 1 meter apart from each other are adopted in the line-replacement of the floor slabs. Rigid joints are assumed to connect the line-replaced floor slabs to the beams supporting the floor slabs. In Model B the floor slabs are omitted. Model C is shown in Figure 4, it is the 5th line's planar frame shown in Figure 3.

In analyses the 1st floor portion of the structural frame is considered as the local substructure to the elasto-plastic analysis, and the 2nd and 3rd floors are considered as adjacent structures that will be treated elastically [6,7].

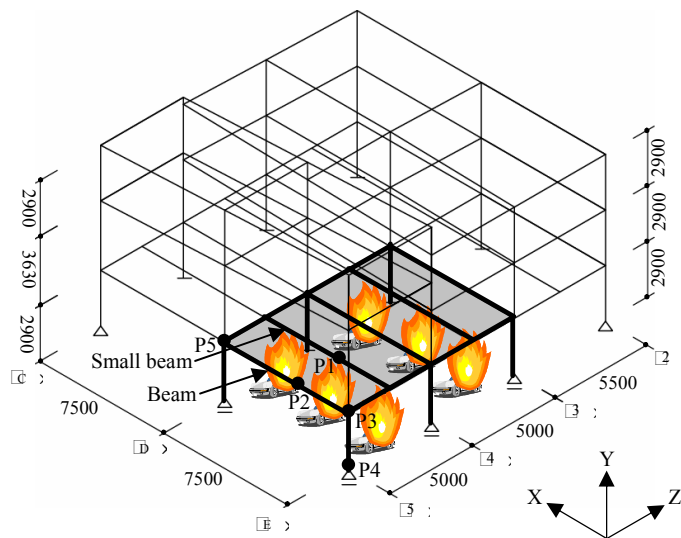


Fig. 3. Model A and Model B(omitting the slabs)

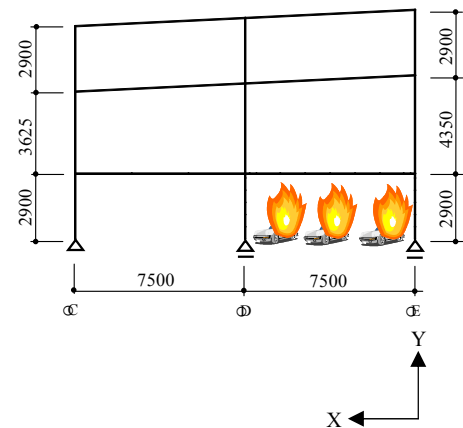


Fig. 4. Model C

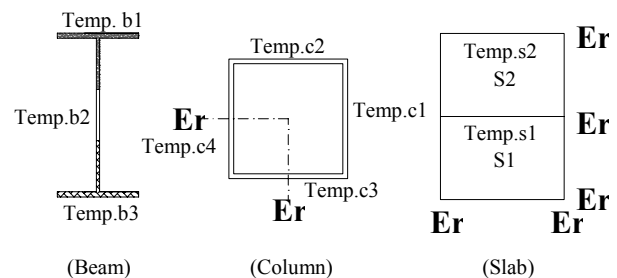
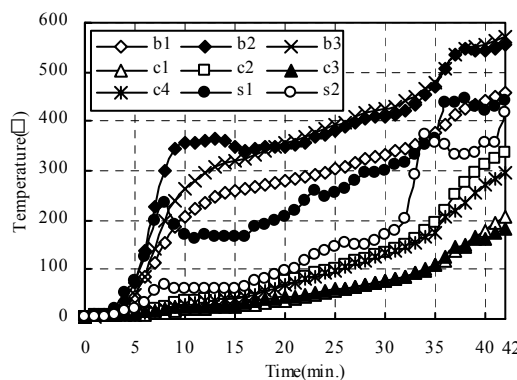


Fig. 5. Transition of temperatures in some of the structural members exposed to fire [5]

3.3 Temperatures of the Members and Stress-strain Curves for Steel Members

The temperature values obtained from the large full-scale fire test [5] are used for the members directly exposed to fire. The cross-section of each steel member is divided into several parts, a steel pipe column is divided into four parts according to the column's surface, and a H-shaped steel beam is divided into the web and the upper/lower flanges. An average temperature is calculated for each of the parts from the values obtained in the experiment along the axis of member. The average value measured in the experiment on the surface exposed to fire is used in the analysis as the temperature of the heated surface. Ignoring the influence of contained water, the temperature distribution of the floor slab is approximated using error function. Figure 5 shows the temperatures of the small beam supporting the floor "S1" bounded by $\odot_{,4}-\odot_{,5}$ and $\odot_{,D}-\odot_{,E}$, and the temperatures of the column on the 1st floor located $\odot_{,E}-\odot_{,4}$, and the temperatures for the heated surface of the slabs S1 and the slab S2. The maximum average temperature of the columns is about 260°C, About 530°C is of the beams, and about 440°C is of the heated surface of the floor slabs. The temperatures of the columns and beams not directly exposed to fire are assumed to be equal to the room temperature.

In this study, the stress-strain curves for steel members are obtained from the tensile test at elevated temperature performed on the steel members used in the large full-scale fire test. Figure 6 shows the stress-strain curves for the steel pipe columns and the H-shaped beams used in the current experiment.

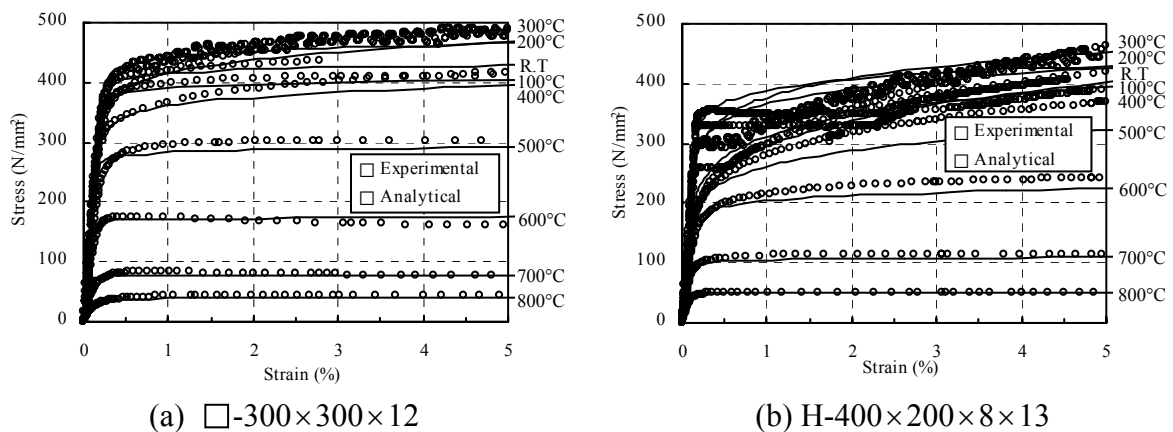


Fig. 6. Stress-strain curves for steel members (Steel grade: SS400)

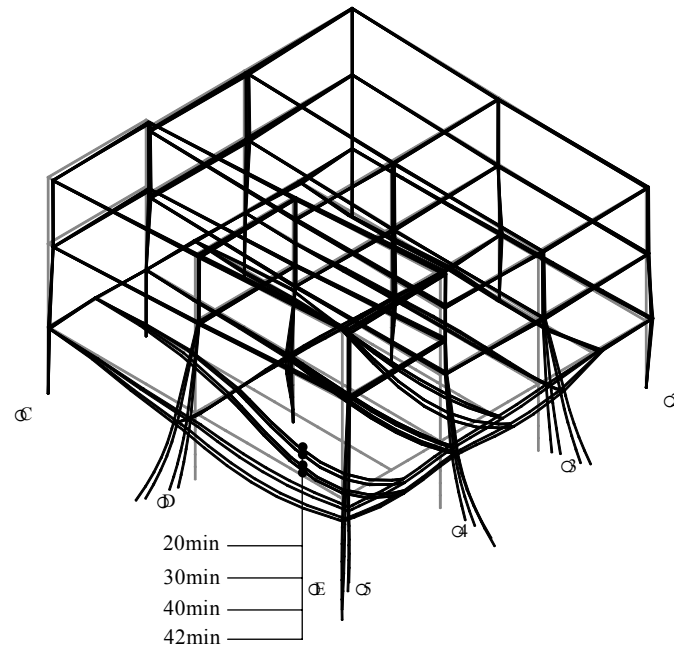
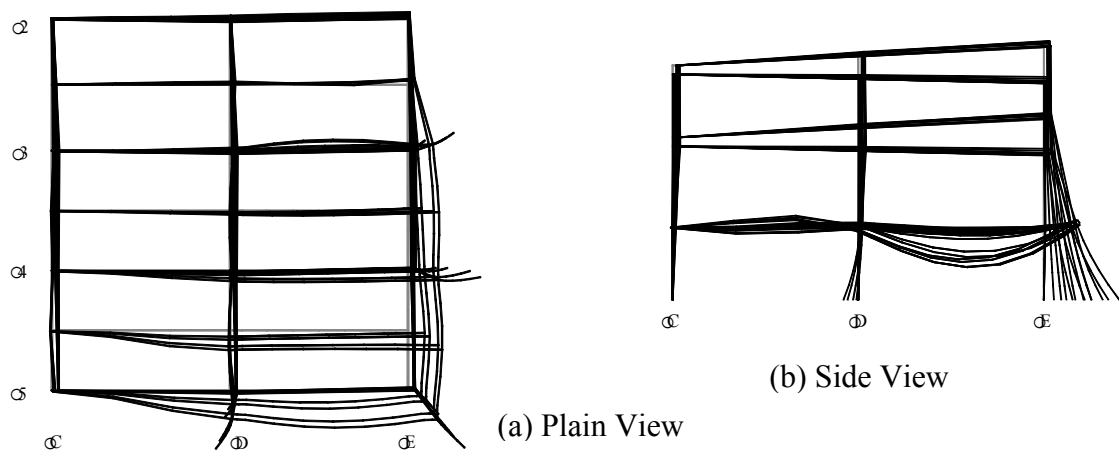


Fig. 7. Thermal deformation of the structural frame in Model A (30X magnification)

3.4 Results of Analyses and Comparisons with the Fire Test

Figure 7 shows the thermal deformation of the structural frame 20, 30, 40 and 42 minutes after ignition in Model A. As shown in Figure 7, large deformation can be seen on the columns, beams exposed to fire. Especially, at the base of the corner column located on the fire zone ($\odot, E-\odot, 5$), it is assumed to support with roller, the corner column is leaning in an oblique direction due to the 2D elongation of the beams. Therefore, an ordinary fixed column would have received an even larger bending force when exposed to fire.



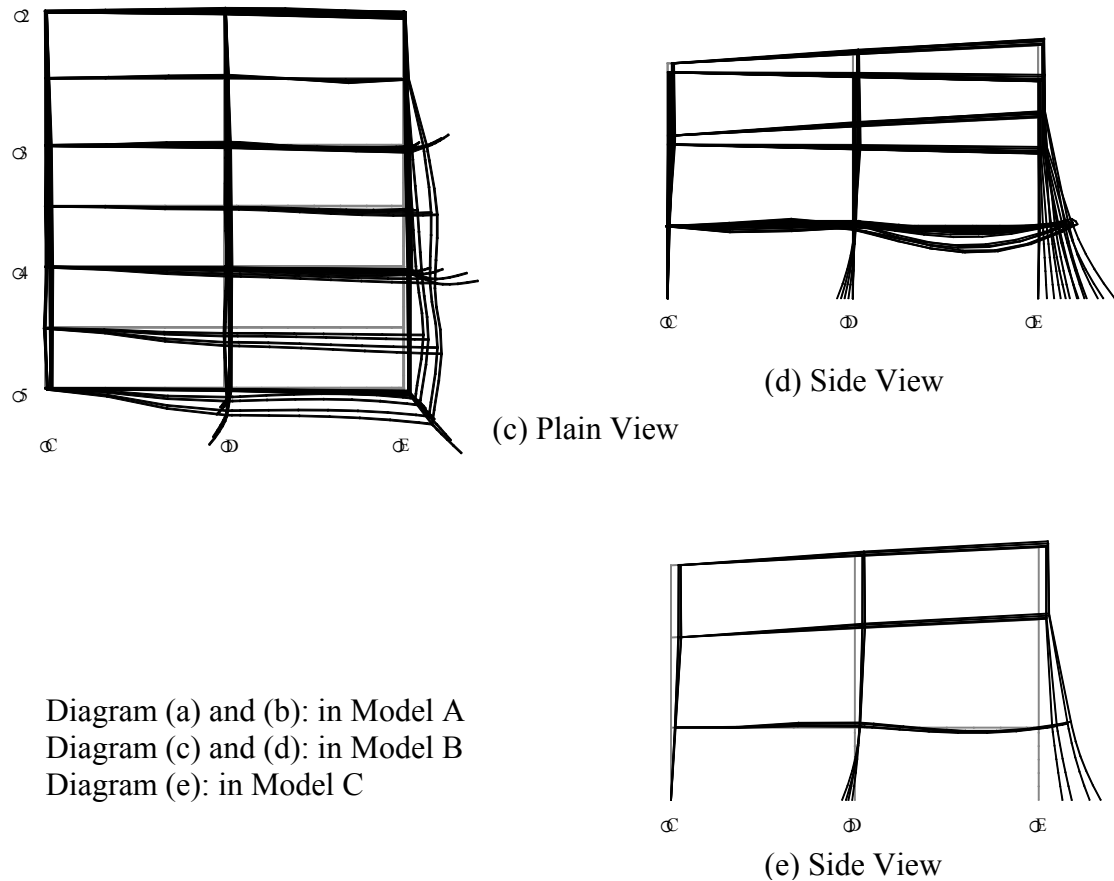
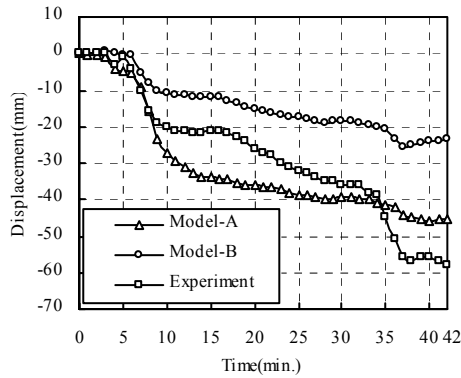
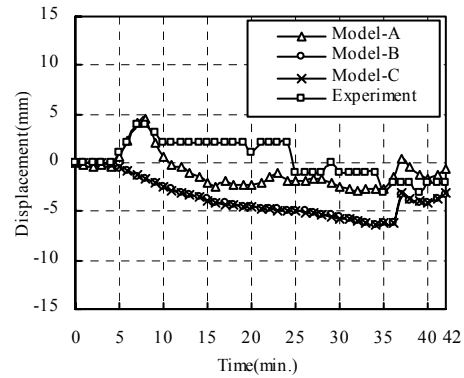


Fig. 8. Thermal deformation at Plain View and Side View

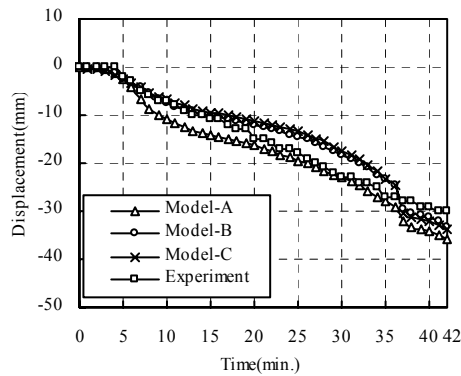
Figure 8 (a) through (e) show the thermal deformation 20, 30, 40 and 42 minutes after ignition in Model A, B and C at Plain View and Side View. First, discuss the deflection of the beam exposed directly to fire at 5th line. In the horizontal deflection, in Model A it is bowing outwards due to the thermal expansion of the floor slab, it is pushed out of the plane significantly as shown in Figure 8 (a). In Model B, as shown in Figure 8 (c), it is bowing inwards because the horizontal displacement at the top of the corner column (\odot_{E-5}) is larger than of the center column (\odot_{D-5}). It is quite likely that the beam is to laterally buckle in Model A. Then, discuss the deflection of the small beam supporting the floor slab S1. The small beam is downward deflecting considerably like a hammock with the floor slab together in Model A than in Model B as shown in Figure 8 (b) and (d), due to the influence of the floor slab. As Figure 8 (e) illustrates, in 5th line frame there is not much difference observed in the tendency of deformation in the frame plane, when comparing the results of Model C with those of Model A and B.



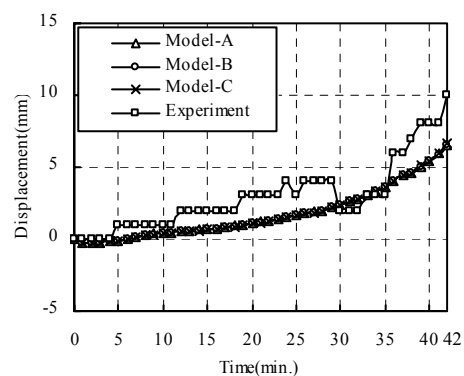
(a) Y-direction displacement at Point P1



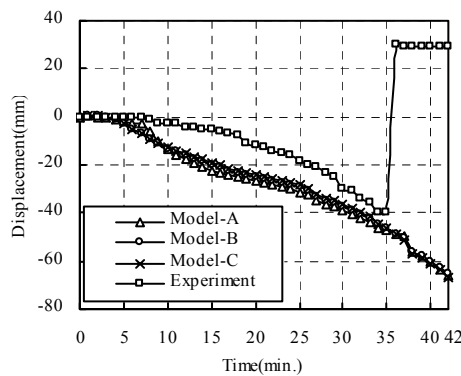
(b) Y-direction displacement at Point P2



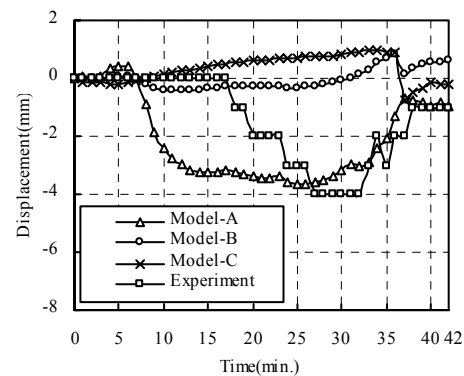
(c) X-direction displacement at Point P3



(d) Y-direction displacement at Point P3



(e) X-direction displacement at Point P4



(f) X-direction displacement at Point P5

Fig. 9. Displacement transitions at nodal points

Compare the theoretical results obtained from the analyses with those recorded in experiments. The transitions of displacement at the nodal points P1-P5 in fire zone (see Figure 3) are shown in Figure 9 (a) through (f). Figure 9 (a) indicates the vertical displacement at the center of the small beam of the 2nd floor that supports the slab S1. The analytical results in Model A and the experimental values coincide with each other largely. In the experiment, the temperatures of the heated surface of the floor slab were measured directly at these points, which are located immediately above the burning cars [5]. When considering the measured point's temperatures to the temperatures of the heated surface, the values will be higher than they should be. As a result, it will make the deflection at Point P1

for the analytical results to have larger values compared with those recorded in the experiment. In Model B, however, the analytical results show large differences compared with the experimental values. They are only about half of the experimental values. As Figure 10 shows, the floor slab exposed to fire will produce larger deformations due to the temperature differences between the heated surface and the unheated surface. The support stiffness at small beam is smaller than that at beams, therefore small beam will be affected to have more large deflection values by the bending effect of floor slab. On the other hand, beams will be raised somewhat due to the bending effect. It is the only reason for the displacement differences between Model A and Model B at Point P1. At Point P2, the center of the beam, as shown in Figure 9 (b) the analytical values in Model A agree well with those recorded in experiments. In Model B and C, the analytical values show slightly larger values compared with the experimental values. It would be considered the influence of the composite beam and the bending effect of the floor slab described above.

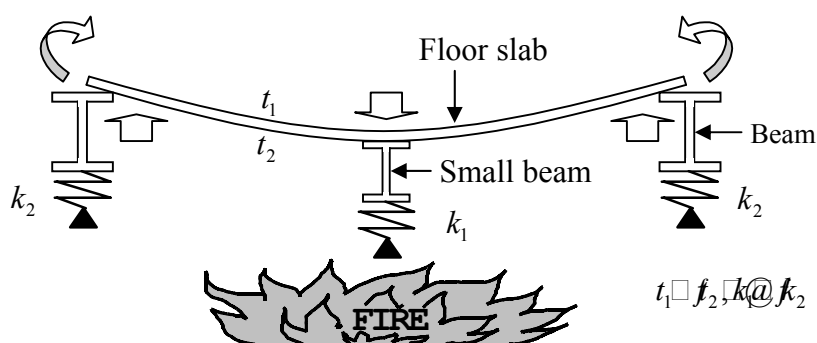


Fig. 10. Influence of the bending effect caused by the temperature difference within floor slab

At Point P3, the top of the corner column in fire zone, as shown in Figure9 (c) and (d), in the X and Y direction all of those analyses show almost similar displacement with time, and there is no significant difference observed between the results of the analyses and those recorded in the experiment. At Point P4, the bottom of the corner column, in the X direction displacement it is similar to Point P3. There is no significant difference in all of the analyses and the experiment as shown in Figure9 (e). At Point P5, the top of the center column in the 5th line frame, the analytical results in Model A coincide with the experimental values largely. Although the results in Model B and C are in opposite direction compared with the experiment, the values are quite small so that can be thought to differ only negligibly (see Figure9 (f)). This implies that the influence of the concrete floor slabs on the column's behavior in a steel structure is small when the temperatures of the structural components are less than 450°C. In Figure9 (e), the experimental value increases abruptly (approx. 70mm) in the positive direction at 35-minute mark, and remain constant after that. This is because the displacement-measuring instrument at the bottom of the corner column has gone over the limit and broken off.

4. COMPARISONS OF MODELLING FOR AN EXAMPLE UNDER STANDARD HEATING CONDITION

4.1 Analytical Structure

The abstract diagram for a steel structure with one story and one span that will be

under standard fire condition is shown in Figure 11. It is assumed that the structure is restrained with fixed bases. The cross-sectional dimensions of the members and the arrangement of bar for the floor slab are shown in Table 2. The grade of steel is SS400. The yield strength of steel is 235Mpa for SS400. Reinforcement stated in Table 2 is placed above and below the floor slab. The design standard strength of concrete is 21N/mm^2 . The load of 6.0kN is given per 1m^2 of the floor slab.

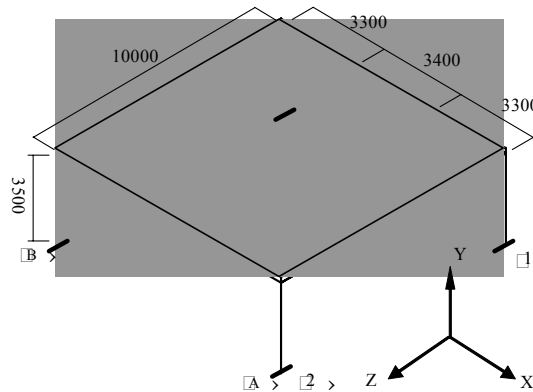


Fig. 11. Analytical structure

Table 2. List of structural members

Column	□-350×350×9×22.5	
Beam	H-400×200×8×13	
Small beam	H-400×200×8×13	
Floor slab	Thickness	150
	Long side bar	D10@200
	Short side bar	D13@100

In terms of the temperature-rise property of members, the temperature of steel member, e.g. columns, beams and small beams, shall increase uniformly at 5°C per minute because it is thermally protected from fire. The temperature within the sectional area of the steel member is assumed to be uniform. The temperature of the heated surface of the floor slab is assumed to obey to ISO834 standard heating condition.

4.2 Modeling for Analyses

The model of 3D analysis (Model A) is the same as Figure 11. All the elements for analysis are described in section 4.1. Figure 12 shows the frame that locates the 1st line of the structure as Model C, and it illustrates the load of the floor slab affecting the frame. In this example Model B is omitted to state because the small beam was broken off at the temperature of 505°C for steel members. All of the connections of different members are assumed to be rigid joint.

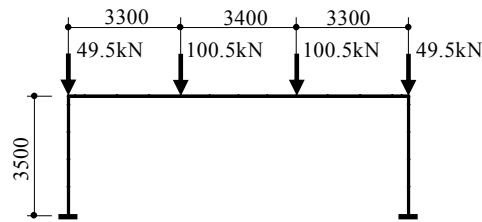


Fig. 12. Model of planar analysis (Model C)

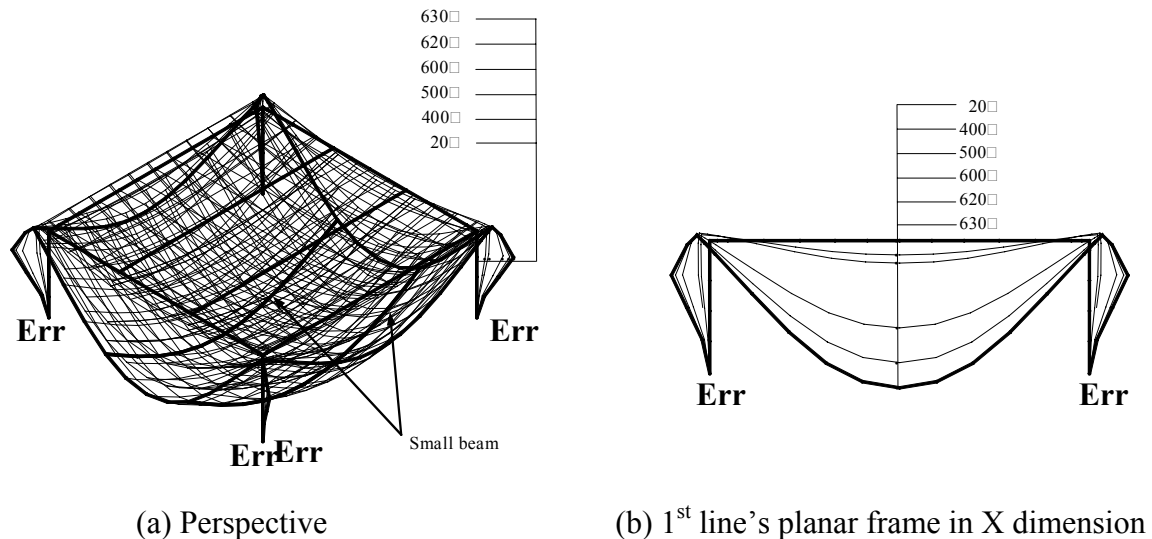


Fig. 13. Thermal deformation of the structural frame in Model A (10X magnification)

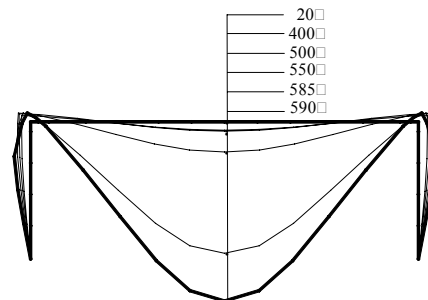


Fig. 14. Thermal deformation of the structural frame in Model C (10X magnification)

4.3 Results of Analyses and Discussions

Figure 13 shows the thermal deformation of the structure frame in Model A during the heating process. Figure 14 shows in Model C. Figure 13(a) and (b) indicate that the columns are greatly leaning outwards in an oblique direction, due to the two-dimensional elongation of the beams and the floor slab. We will examine the deformation at the center of the beam and the top of the column using Figure 13 and Figure 14. At the temperature of 630°C for steel member and 1056°C for the heated surface of the concrete, the deflection values of the beam and the column become 376.0mm and 121.5mm respectively in Model A. Based on The ECCS Design Standard [8], the existing standard of fire resistance performance evaluation

(the limit value of beam is $\delta = l^2/800H$; $\Delta = h/30$ is of column), the deflection of the beam in this example approaches the limit value of bending at the temperature of 625°C, and the column is leaning outwards successively and reaches the limit value at 625°C at the same time. The beam and the column are most likely to collapse together. But in Model C, at the temperature of 590°C for steel member, the deflection value of the beam become 433.1mm, at the same time the value of the column is 39.6mm. The deflection of the beam approaches the limit value of bending at the temperature of 585°C, and the column returns again to the original position after deflecting outwards, because the beam pull it back. Only the beam is most likely to collapse in Model C. The reason may be thought is the influence of the composite beam that consists of concrete floor slab and steel beam.

5. CONCLUSION

It is very important to model steel structure correctly when evaluating its fire resistance performance. How much to affect the fire response of steel structure for concrete slab is the key point. In this study, conceiving floor slab as a grid of intersecting beams, the analysis on the structural behavior of a large full-scale fire test has been carried out. Comparing with those analytical results which omit the influence of concrete slab and those recorded in experiments, some conclusions can be drawn as follows:

- Floor slab and small beam show larger deformation compared with the beams that support concrete slab, owing to the bending effect due to the temperature difference within concrete slab. To prevent fire from spreading within the building, the influence of concrete slab should be taken into account.
- The influence of concrete slab on the column's behavior in a steel structure is small when the temperatures of structural components are less than 450°C.

And examining an example for simple steel structure which is under ISO834 standard heating condition through the comparisons of the 3D and 2D analytical model for fire resistance performance, the following conclusions can be given:

- Steel beams supporting concrete slab approach the limit value of deflection at earlier stages of fire in planar analysis than in three-dimensional analysis that takes account of concrete slab.
- Steel columns are easier to reach the limit value of deflection in three-dimensional analysis than in planar analysis, and they are most likely to collapse when the structure is at elevated temperature.

6. REFERENCES

- [1] Becker, J., Bresler, B., “FIRES-RC --- A Computer Program for the Fire Response of Structure --- Reinforced Concrete Frames”, Report No.UCB FRG74-3, University of California Berkley, July 1974
- [2] Li Y.G., Uesugi H. and Wakamatsu T., “Three-dimensional Analysis of Deflection Behavior about Steel Frames Exposed to Fire”, Journal of Structural and Construction Engineering, The Architectural Institute of Japan, No.595, pp.151-158, September 2005(in Japanese)
- [3] Saito H., “Behavior of End Restrained Concrete Member in Fire”, B.R.I Research Paper, No.32, 1968
- [4] Commission of European Communities, “Eurocode 4-Design of Composite Steel and Concrete Structures -Part 1.2: General Rules- Structural Fire Design”, pp.52-53, 1994
- [5] Kitano T., Sugawa O., Masuda H., Ave T. and Uesugi H., “Large Scale Fire Tests of 4-Story Type Car Park (Part1: The behavior of the structural frame exposed to the fire at the deepest part of the first floor)”, Proceedings of the Fourth Asia-Oceania Symposium on Fire Science and Technology, pp.527-538, 2000
- [6] Saito H., Uesugi H., Yamaguchi M. and Kodaira A., “Thermal Stress and Deformation of Steel Structures of High Rise Buildings in Fire”, in Fire Safety Science Proceedings of the Second International Symposium, pp.719-728, 1989
- [7] Lin H.Q., Uesugi H., “Three Dimensional Analysis Method of High Rise Structure Exposed to Compartment Fire (Part 1: The formulation of restraint force and adjacent displacement for local substructure)”, Journal of Structural Engineering, The Architectural Institute of Japan, Volume 44B, pp.1-8, March 1998 (in Japanese)
- [8] ECCS(European Convention for Constructional Steelwork), “European Recommendations for the fire safety of steel structure”, Elsevier, Amsterdam-Oxford-New York (1983)



THE ROLE OF LARGE STRAINS AND CONSEQUENT MITIGATION MEASURES FOR BUILDINGS IN FIRE

Claudio POZZI¹, Barbara LANE*, Susan LAMONT* and Alexander HEISE*

ABSTRACT

As the understanding of the science of fire develops, and its resulting effect on materials and structure, more advanced validated tools are becoming available for engineers to use in the design process. As a result, as the profession continues to assess the structural fire response of composite steel framed buildings, new issues continue to be discovered and require investigation. This paper presents an insight into some specific structural fire responses observed in the non-linear analysis of a long-span floor system, including the importance of determining the location of high strains and the impact of the thermal elongation of beams on adjacent columns. From the outcomes of this case study, specific amendments to the ambient temperature design of the structure were made to ensure its robustness in fire. This knowledge will be utilised on future designs, and contribute to the ongoing understanding of real structural design for fire.

1. INTRODUCTION

The Kings Place case study has given rise to some important issues when considering stability and compartmentation of composite steel-framed buildings with long span cellular beams. Despite a good performance of the building when subjected to a parametric fire curve, failure was observed when the structure was analysed using the standard fire curve.

The columns underwent rapid vertical displacement due to the occurrence of horizontal actions and geometrical misalignment in the fire, which they were not designed for in the ambient case. Additional stresses along with material degradation have therefore undermined the structural stability in fire, and the columns could no longer withstand the load from the floors above.

¹ Corresponding Author: Dott. Ing Claudio Pozzi, Arup Fire, 13 Fitzroy Street, London, W1T 4BQ, United Kingdom

email: claudio.pozzi@arup.com

*ArupFire, 13 Fitzroy Street, London, W1T 4BQ, United Kingdom

Across the secondary protected beams and in the slab to core interface, relatively large strains were also observed. These are believed to be driven by the deflection of the slab and the boundary condition assumptions. However this is significant because it impacts compartmentation, which forms an essential part of the approvals process under the life safety requirements of the UK Building Regulations.

As the structural model was considered unsafe under the effects of this fire, methods of increasing overall robustness were therefore investigated. Specific alterations to the structure were made and these will be described in detail in this paper.

1.1 The Building

The Kings Place office building in London is a composite steel-framed structure with 8 storeys above ground and 3 basement levels. The composite floors are constructed using 130mm deep composite slabs with profiled steel decking attached by shear connectors to steel beams with circular web penetrations. The columns are universal steel column section with two changes in size (at floor 2 and 6).

2. THE STRUCTURAL FIRE ENGINEERING ANALYSIS

This paper presents the data produced from the structural fire engineering assessment of 2 of the 3 models chosen to represent the above ground structure of Kings Place. The aim of the non-linear analysis was to investigate an appropriate fire rating for the structural elements and to determine if secondary steel beams could be left completely unprotected.

2.1 Acceptance criteria

Based on the life safety requirements of the Building Regulations UK, acceptance criteria for the analysis must be based on structural stability, compartment integrity and compartment insulation.

In order to assess the structural fire response produced from the analysis, the following performance criteria were set, for the acceptance process:

Stability: the overall structure maintains its load-bearing capacity throughout the duration of the fire. No runaway deflection of the long span beams or floor system.

Horizontal compartmentation is also assessed by monitoring the rate of deflection of the composite floor. A rapid increase in deflection in any region of the floor plate implies compartmentation failure.

Vertical compartmentation via the vertical fire fighting shafts is assessed by monitoring the connections at the shaft wall to ensure that they maintain their capacity for the fire period

2.2 Fire protection strategy assessed

The fire protection layout proposed is 90 minutes fire protection to primary elements of structure (columns, edge beams and any beam directly connected to a column) with secondary elements of structure left unprotected. The core structure supporting the fire

fighting shafts will remain at 2 hours. Floor to floor compartmentation was proposed at a standard 90 minutes fire resistance.

2.3 Design Fires

If the office part of the building was designed using prescriptive guidance in the Approved Document B¹ of the Building Regulations, the structure, and all compartmentation, are recommended to achieve 120 minutes fire resistance based on building height and occupancy. An alternative rating however was proposed as part of the structural fire engineering process. In order to ascertain this, it was assumed the structure would be exposed to a credible worst-case fire scenario in one of the office floors. The credible worst-case fire scenario is determined appropriate to the level of risk (probability of occurrence based on compartment area and occupancy type), fire loading and ventilation in the building.

Some reduction of fuel load was incorporated by considering the lower probability of a fire in a sprinklered building. This still results in an overall fuel load of 35kg/m² (10kg/m² greater than the typical value for offices)². This is therefore still deemed to be conservative.

Two design fires, from a series of fire cases investigated as a function of available ventilation, were agreed with the approving authorities to represent the worst case scenarios which might occur in the building (Fig. 1):

“Short Hot” Fire – a parametric fire modelled using the equation in Eurocode 1³ assuming 100% glazing failure and flashed over whole floor. The resulting peak temperature is about 1200°C

Standard Fire - a long cool fire specified in the BS476⁴ (This was because it differed very little with a parametric fire assuming 25% glazing failure, which is currently requested in London as a reasonable worst-case scenarios check in structural fire engineering)

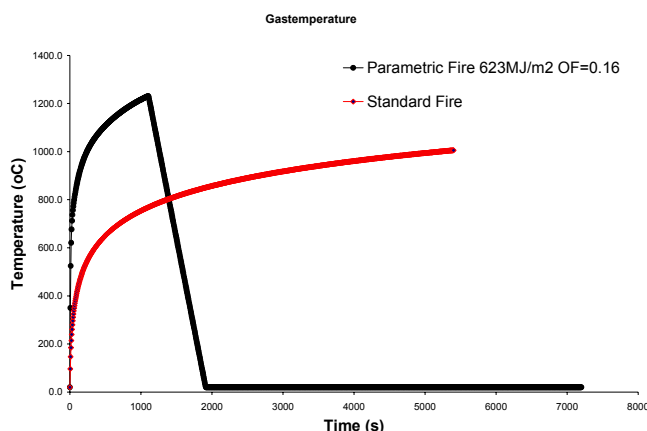


Fig. 1 –Design Fires

The “Short Hot” Fire is typically considered in design because of its high temperatures, and the short duration these high temperatures are achieved. This is because it induces higher thermal gradients within the structural elements. In addition the use of a parametric fire is very much recommended because it comprises a cooling phase, which should always form part of a structural fire assessment.

The Standard Fire has been chosen to investigate the effects of long-lasting fire with constant increase in temperature, and as a code comparison within the approvals environment.

All other fire scenarios, as a function of ventilation, were shown to fall within the boundary of the two cases adopted.

2.4 Heat Transfer

The heat transfer analysis is the second step in the structural fire analysis process. Different approaches were followed with regard to the concrete and steel materials.

The heat transfer for the concrete slab was modelled using a 1D heat transfer model in ABAQUS 6.5⁵. The slab is modelled as a flat slab of equivalent thickness, though ribs in the dovetail slab are ignored. The same assumption is used in the structural model. This reflects the approach given in Eurocode 4 Part1-2⁶. Input data to the heat transfer model complied with the recommendations for siliceous concrete material properties in Eurocode 2⁷. Moisture content in the concrete was ignored.

The Heat transfer calculations for the steelwork were conducted using the lumped mass heat transfer model in Eurocode 1² and Eurocode 3⁸ for the unprotected steel beams and protected columns. A combined use of a commercial software⁹ and the known heat transfer properties of a generic spray protection material resulted in the determination of the temperature time development of the protected beams.

2.5 Modelling Assumptions

This section describes the modelling assumptions necessary to build the structural models and to perform the non-linear finite element analyses of the structure throughout the fire duration.

When considering a single storey fire, it is necessary to select the floor that represents the worst case condition throughout the structure. Therefore the storey with the highest column load ratio (in this case the third floor) was deemed to be the worst case scenario. This is then considered to be representative of a fire on any floor plate from Level 1 – 8 (Fig. 2).

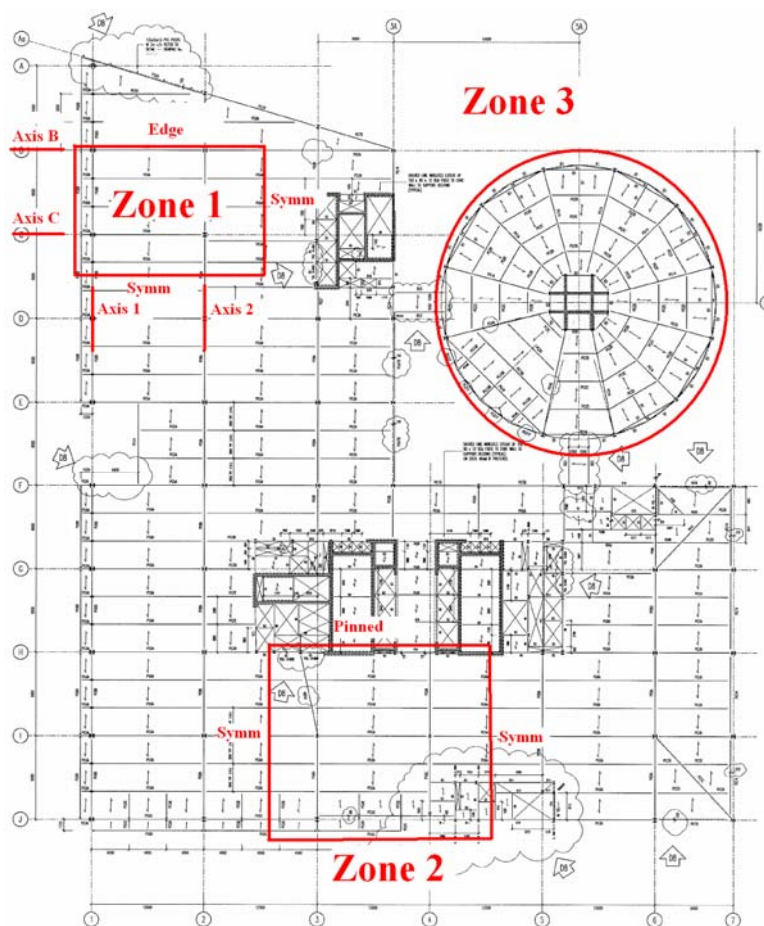


Fig. 2 – Third Floor Plan, models location and associated boundary conditions

Worst case boundary conditions were assumed for the structural models of each zone (Fig. 2). This means the resulting structural fire responses observed are on the conservative side, as less reliance on the overall floor continuity available in the model.

The boundary conditions assumed for Zone 1 makes the portion of the building weaker with respect to the real case. The edge beam condition on the north side does not take advantage of continuity of the floor plate. Furthermore, the two symmetry conditions discount the model from the beneficiary effect of the concrete core and the continuity of the floor plate on the south side.

The boundary conditions of Zone 2 might make the model slightly more redundant than the reality (the floor plate is modelled as infinitely long). However, it is believed that the fact of having ignored the steel core on the south-east side of the model might level the redundancy out.

Zone 3 does not have boundary conditions. It has been considered as a structure itself neglecting the bridges that connect it to the rest of the building.

The British Standard 5950 Part 8 2003¹⁰ was used to determine the factored design loads to the structure for the fire limit state. Subsequently, they have been applied to the model throughout the analysis.

The materials assumed in the investigation were normal weight concrete and steel. Further information about material properties under elevated temperatures were taken from Eurocode (see Table 1).

Full degradation of the stress-strain curves for both materials with temperature is allowed.

Table 1 – Material Properties

Material	Grade	Model
Steel (frame)	S355	Eurocode 3
Light weight Concrete (slab)	C35	Eurocode 2 with tensile strength equal to 5% of the compressive strength
Reinforcing mesh	Grade 460	A252, Steel mat, 8mm bars, spacing 200mm

All connections were modelled as fixed, and it was assumed failure could not occur (Note from the data obtained during the analysis, this assumption was deemed to be justified due to the low value of the connection forces shown to occur during the design fires).

The software used to perform the Finite Element Analyses (FEA) was ABAQUS⁵. The software is used throughout the world for stress, heat transfer, and other types of analysis in mechanical, structural, civil, biomedical, and related engineering applications. The code has been validated extensively for many engineering problems and in particular by University of Edinburgh^{11,12} and British Steel (now CORUS) to model composite steel and lightweight concrete structures in fire.

3. RESULTS

The most relevant results, to understand the role of induced large strains due to thermal actions, are presented in this paper only. The performance of the structure and the compartmentation under the effects of the short hot fire were found to pass the acceptance criteria. This paper concentrates on the results obtained during the standard fire only.

In summary, Zone 1 was determined to be the most vulnerable model. The Zone 2 model displayed interesting behaviour at the slab to core wall interface. The Zone 3 model showed low deflection response because of its structural robustness and short spans beams. Therefore Zone 1 and Zone 2 are presented here only.

3.1 Zone 1-Standard Fire

Although the model response was acceptable in the short hot fire, structural changes were necessary to enhance the response of the structure during the standard fire. Columns instability was observed, which meant failure of the stability acceptance criterion.

After the initial downward movement due to the load given by the above floors, the columns begin to elongate when heated. The displacement reaches values of about 25 mm before inverting its trend. At about 80 minutes all the columns showed vertical runaway with rapid increase in the downward movement whilst the temperature is still rising (Fig. 3).

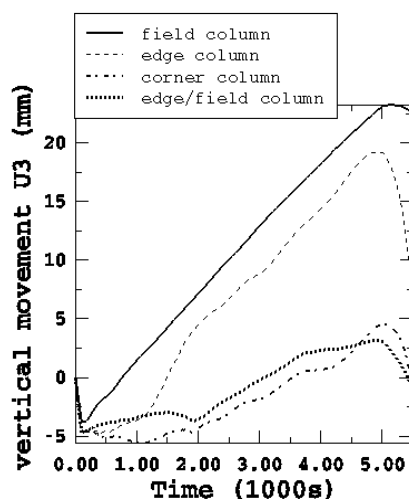


Fig. 3 - Vertical displacement over time of columns– Standard Fire

Their capacity is undermined by the lateral movement of the elements at the floor level causing bending stresses and P-Delta moments. The structural model was considered unsafe under the effects of this fire and therefore methods of increasing the robustness were investigated.

Due to large thermal elongation and consequently large displacements, the elements are required to sustain loads and actions in the fire limit state they are not traditionally designed for. Additional stresses/strains along with material degradation have therefore undermined the structural stability. This is considered to be a particular trait of long span cellular beam based construction forms.

A few options are available to increase the robustness of the structure such as increasing the columns' size, keeping the 12m span beams cooler or increasing their load bearing capacity. In this project the latter choice has been adopted in order to reach the most cost-effective solution. Therefore, the bottom flange of the 12 m span secondary protected beams connected to the columns was increased from 16 to 25 mm.

When this design change was then re-modelled, there were significant changes in the response of the structure. Column failure was shown not to occur, and this provided more robustness to the building.

Throughout the fire the columns exhibit a steady elongation along with the increasing temperatures. No vertical runaway has been recorded in this case and therefore the columns can be expected to maintain their stability. This outcome is of high importance and shows that the changes made have significantly improved the overall structural performance. When dealing with complex steel composite frames and loading conditions, it is not always easy to recognise the source of further robustness along with a cost-effective solution.

Fig. 4 shows the deflection contour of the slab at the end of the standard fire. The maximum deflection is 1600mm at the mid-span of the corner bay. The stability of the structure is maintained thanks to the tensile membrane action developing within each single bay. This phenomenon has been observed in the Cardington tests carried out in UK and it is well covered and discussed in literature.

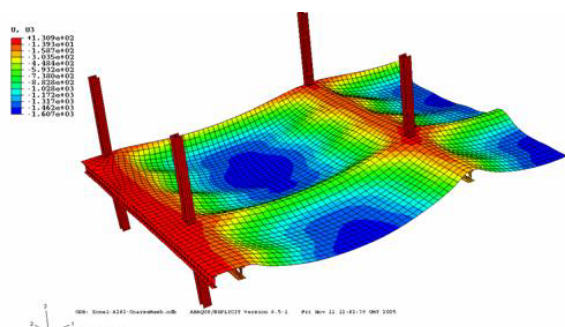


Fig. 4 – Deflection contour at the end of the fire

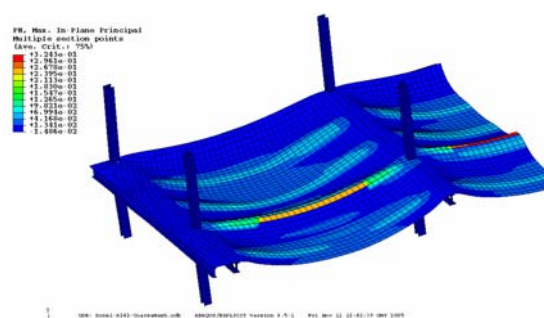


Fig. 5 – Max In-plane plastic strains in the reinforcement mesh, shorter span direction

A thorough investigation was made with regard to the total strains exhibited in this model. The software itself does not model material failure and therefore large strains can develop in the analysis although the associated stresses are negligible.

Due to the high value of deflections observed in the slab, relatively large total strains are observed across the protected secondary beams, axis C (see Fig. 2 and Fig. 5). The maximum observed strain is about 30 % in the top of the slab and 25% in the reinforcement mesh.

If full horizontal restrained is assumed acting in each panel, tensile membrane action is supported by reinforcement over the supports. However, it should also be noted that even if some local rupturing of rebar occurs, the membrane behaviour can be supported by a compressive ring in the slab which exists to form equilibrium over the supports.

3.1.1 Additional Rebars

It is assumed that the high strains are likely to cause cracks at the top face of the composite slab. The A252 mesh reinforcement provided by ambient design could rupture at strains in excess of 20% undermining compartment integrity. Therefore, additional reinforcement is proposed in the slab over the protected 12m secondary beams.

There is little benefit in adding additional reinforcement at the same height as the existing mesh because this will still have to support high strains. It is proposed instead that the reinforcement is included in the dovetail at a depth of 85mm measured from the top face of the slab. This is a typical position for rebar placed in ribs.

At this position the concrete in the model experiences about 10.7% strain assuming a linear extrapolation between 25% strain at the level of the mesh in the slab and 3% strain at the underside of the slab. This is illustrated in Fig. 6.

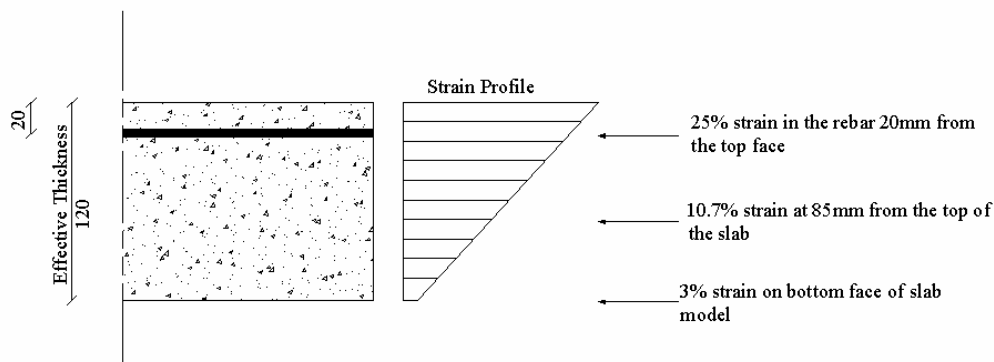


Fig. 6 – Calculation of strain at 85mm from the top side of the slab

To determine the amount of reinforcement required in the ribs over the supports an equivalent area of rebar to the A252 mesh was calculated so that the same tensile force could be carried by the new reinforcement as in the A252 mesh. The calculation takes into consideration the spacing of the ribs (152mm), relative to the spacing of the bars of the A252 mesh (200mm) and the height of the rebar in the slab (i.e. the temperature of the rebar). This calculation is presented below in Table 2.

Table 2 - Calculation of reinforcement required in the ribs of the dovetail slab over the protected beams

Variable	A252 mesh	Equivalent reinforcement in the dovetail ribs
Position of reinforcement in the slab (mm)	20mm from top face	85mm from the top face
Temperature at reinforcement after 90minutes of the standard fire (°C)	100°C	500°C
Residual strength of reinforcement (N/ mm ²)	0.96	0.5
Area of reinforcement	252 mm ² /mm	1x10mm diameter bar per dovetail rib (rib spacing is 152mm, Bar area=78.5 mm ²)

The main conservatisms in this approach are as follows:

The additional bottom and top rebar will work together in the real building limiting the potential cracks experienced by the concrete in the top surface of the slab.

A supporting compression ring will develop in the slab even if the main reinforcement ruptures as a consequence of equilibrium.

The lower rebars are expected to have a limited amount of strain up until the top rebars will eventually fail. After the assumed rupture, the strain in the lower rebars will slightly increase. It is difficult to estimate the redistribution of the forces and therefore the value of the strain at this level. However, it is believed that, due to the favourable position of the rebars into the ribs of the dovetail, the strain will hardly achieve a value close to failure.

3.2 Zone 2 – Standard Fire

The response of Zone 2 was generally better than Zone 1 mainly because of its structural layout. In this model the 12m long span cellular beams are orientated parallel to the edge side of the building causing less horizontal displacement to the edge columns. However, relatively large strains are observed at the core to slab interface and this occurs mainly because of the boundary condition assumed at the edge of the slab and the large deflection of the bay.

Large strains up to a magnitude of 20% (neglecting the strains affected by the boundary conditions at the west/east edges of the model) evolve at the concrete core on the bottom side of the slab, as shown in Fig. 7.

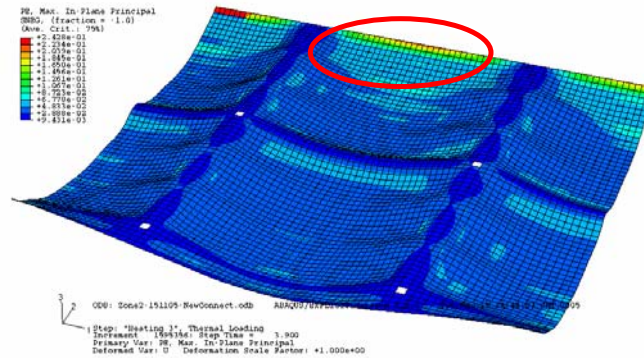


Fig. 7 - Maximum resulting plastic strain on the underside of the slab at the end of the fire

The connection between the concrete core and the dovetail slab is realised for this building using pull-out rebars which bond together the core and the slab. The concrete is not continuous because it is poured in different stages.

Given the aforementioned structural arrangement, the connection has been modelled using a pinned condition which makes the model less robust and unable to bear any bending moment. The resulting rotation at the interface is therefore greater than in the real case and the model shows a larger mid-span deflection. From a geometric perspective only, to accommodate the deflection of the bay, the edge of the slab must displace of a certain value. On the other hand, whether a gap will form at the interface must be determined considering several aspects which are not straightforward quantifiable such as: thermal elongation of the assembly, the effect of the conservative boundary condition assumption, the extent of cracking across the elements, concrete to steel bond, rebars anchorage, the overall movement of the assembly.

On this subject, the Approving Authority has determined that further provisions are required in this case to ensure compartmentation. They have requested a fire protected steel angle or similar vertical support provided at the concrete core to floor interface, firmly fixed to the core wall. It is sized to allow the slab to slide over the angle, during the effects of fire, and therefore in their view impeding compartmentation failure (Fig. 8).

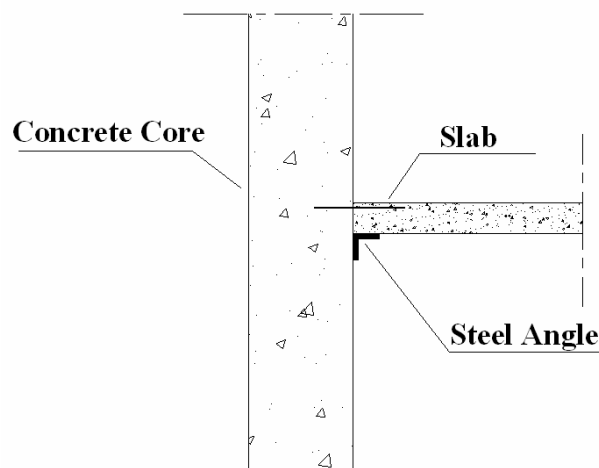


Fig. 8– Detail of the connection between slab and concrete core

The efficacy of this measure is not based on any real test or research and a thorough investigation of the matter is needed to validate the benefit of this approach.

A further provision taken in this project to limit the effect of strains was to protect to a 90min standard the secondary beams immediately adjacent to and parallel with the concrete core. This change is assumed to limit the deflection of the slab in the vicinity of the core and consequently the strains observed at the core to slab interface. However, due to time restrictions, the response of the structure with the new fire protection arrangement has not been carried out. Thus, it is difficult to assess the real benefit of such change and how it affects the secondary load-bearing mechanism of the bay adjacent to the core. The increased stiffness of this part of the assembly might create a completely different structural response in fire and give rise to new load paths.

4. CONCLUSIONS

The analysis presented in this report was used to determine if the structure could withstand an agreed, set of design basis fires when secondary steel beams are left unprotected. The non-linear finite element approach used allowed a full quantification of the structural response of the building to fire.

The Kings Place case study has given rise to some important issues when considering stability and compartmentation of composite steel-framed buildings with long span cellular beams. The choice of leaving the secondary beams unprotected relies on the secondary load bearing mechanism exhibited by the composite floor at the fire limit state. However, this paper highlights the necessity of validating this approach by checking that the structure does not contain intrinsic structural limitations which could weaken the overall response.

The first important outcome of this case study was that the structure showed enhanced stability when the bottom flange thickness of the secondary protected beams was increased.

Large strains in the slab, which might imply compartmentation failure, were mitigated by placing additional rebars across the secondary protected beams in the ribs of the dovetail in order to transfer the vertical loads to the beams and to anchor tensile membrane action.

For the concrete portions of the cores, an angle was requested by the Approving Authorities at the core wall to slab interface. Moreover, the secondary steel beams parallel with the concrete core were protected to a 90min standard. These are seen as helping to prevent compartment failure at the core edge although the benefit has not been investigated. Related concerns to this approach have been described in this paper.

It is apparent that future research is necessary in this field to understand the extent and the relevance of the issues arisen in this paper and whether consequent mitigation measures are needed and must be adopted.

5. REFERENCES

- [1] The Building Regulations 2000, Fire Safety, Approved Document B
- [2] Law M., O'Brien T., "Fire Safety of Bare External Structural Steel", Steel Construction Institute, SCI P009, 1981
- [3] BSI (British Standard Institution) BS EN 1991-1-2 Eurocode 1. Actions on structures. General actions. Actions on structures exposed to fire, 2001
- [4] BS 476: Part 20: Fire tests on building materials and structures method for measuring the rate of heat release of products, 1993
- [5] Abaqus v.6.5, Abaqus UK Ltd, The Genesis Centre, Birchwood, Warrington, WA3

7BH

- [6] BSI (British Standard Institution) BS EN 1994-1-2 Eurocode 4. Eurocode 4 - design of composite steel and concrete structures - general rules - structural fire design, 2005
- [7] BSI (British Standard Institution) BS EN 1992-1-2 Eurocode 2. Design of concrete structures. General rules. Structural fire design, 2004
- [8] BSI (British Standard Institution) BS EN 1993-1-2 Eurocode 3. Design of steel structures. General rules. Structural fire design, 2005
- [9] Fbeam 3.2, Fabsec Limited, Brooklands Court, Tunstall Road, Leeds LS11 5HL
- [10] BS5950 Part8 : Structural use of steelwork in building code of practice for fire resistant design, 2003
- [11] The University of Edinburgh, Final report of the DETR-PIT project: "Behaviour of steel framed structures under fire conditions". Technical report, 2000.
- [12] Usmani A.S. "Application of fundamental structural mechanics principles in assessing the Cardington fire tests". Structures in Fire Proceedings of the First International Workshop, Copenhagen, June 2000.



FIRE STRUCTURE INTERFACE AND THE THERMAL RESPONSE OF THE WORLD TRADE CENTER TOWERS

Kuldeep PRASAD¹ and Anthony HAMINS²

ABSTRACT

Over the past several years, there has been a resurgence of interest in studying the response of building structures to fires. Typically, the thermal loading for structural analysis of a building on fire is obtained from a standard time temperature curve or by assuming a spatially uniform enclosure temperature. This decouples the structural analysis from the fire simulations and as a result the structural response to spatially and temporally evolving fires cannot be predicted. Simulations of the effects of severe fires on the structural integrity of buildings requires a close coupling between the gas phase energy release and transport phenomena and the stress analysis in the load bearing materials. A methodology has been developed for coupling CFD simulations of fire growth with finite element models for thermal and structural analysis. A simple radiative transport model that assumes the compartment is divided locally into a hot, soot laden upper layer and a cool relatively clear lower layer is employed to predict radiative fluxes incident on sub-grid scale structural members. Thermal responses of various structural components on focus floors of World Trade Center Tower 1, coupled with realistic fire simulations are presented. One of the most striking observations that emerge from these results is the wide variation of “time-temperature” curves that hold at different points in the structure and the lack of resemblance of these curves to the “standard” time-temperature curve used in furnace tests of structural elements. Finally the thermal response is used to predict the reduction in load carrying capacity of the structure as a function of time. Sensitivity of the load carrying capacity to imperfections in fireproofing, structural damage and fire growth is discussed.

¹ Corresponding Author, Research Engineer, Building and Fire Research Laboratory, NIST, Gaithersburg, MD, email : kprasad@nist.gov.

² Group Leader, Building and Fire Research Laboratory, NIST, Gaithersburg, MD, email : ahamins@nist.gov.

1. INTRODUCTION

Following the collapse of the World Trade Center (WTC) tower, there was an active debate in the engineering community on the maximum temperature reached in the steel structure and on the role of the fires in inducing structural collapse. Some speculated that the temperatures were high enough to melt the structural steel. The fire proofing engineering community [1] considered the effect of different fireproofing thickness on steel temperature in each tower. Detailed analysis was difficult due to the complexity associated with the aircraft impact and multi-floor, spatially and temporally evolving fires. There was clearly a need to develop a methodology to predict the thermal response of the structural components coupled to the realistic fires observed on Sept. 11, fires that were ignited by the jet fuel and were subsequently fueled by the furnishings and other combustibles on each floor.

The literature on fire structural analysis is vast [2], [3], [4] and space allows a survey of some of the more recent physics-based models developed to study the collapse of the WTC towers. Usmani et al. [5] have performed a non-linear finite element analysis of a 2-D model of the WTC tower structural frame and proposed a progressive collapse mechanism due to low membrane capacity of the composite floor system. Choi et al. [6] have also carried out a 2-D finite element analysis on the behavior of light-weight floor trusses and studied the role of connections. Both these studies were limited to the use of a generalized exponential curve to represent the fire time-temperature relationship and did not include a fire decay phase.

The collapse of the WTC towers under impact and fire loading [7] has highlighted the importance of fire as a structural load and the need for an integrated analysis based on realistic thermal loading. The National Institute of Standards and Technology (NIST) recently completed a technical investigation [8] into the collapse of the WTC towers. The investigation relied heavily on four major modeling tasks; the initial aircraft impact analysis, the fire dynamic simulations, the thermal analysis of the load bearing structure and structural deterioration. The initial impact simulation is needed as input into the following three parts. It partially defines the geometry used for the fire dynamic simulations, provides guidance about insulation damage, and determines the state of the structure that survived the impact [8]. The fire dynamics [9] provides the thermal environment in the gas phase needed to determine the radiative fluxes to the exposed building surfaces. The thermal analysis determines the temperature distribution in the load bearing structure. Finally, the structural analysis integrates all the previous information to make predictions about the loads and deflections up to the point of collapse.

The methodology and results presented in this paper were a part of the NIST Investigation [8] into the collapse of the WTC towers. The objective of this paper is to describe the approach used to couple the fire simulations with the thermal and structural response of complex building assemblies. The coupling methodology is validated by comparing numerical predictions with data from large scale experiments. Uncertainty analysis on important model parameters is performed. The predicted thermal response of the structural components on focus floors of WTC 1 is presented. Thermal data is used to compute the reduction in load carrying capacity of the structure as a function of time. Finally, sensitivity of the results to imperfections in fireproofing as well as structural and fireproofing damage caused by the impact is discussed.

2. FIRE STRUCTURE INTERFACE

The coupling of fire modeling and collapse analysis of a building is dominated by radiative heat transfer from the gas phase to the structural elements. The radiation field must be determined from solutions of the radiative transport equation, which relates the incident flux to the spatial distribution of temperature and combustion products (particularly the distribution of soot particulate) as well as the enclosure geometry. Such calculations are typically performed as part of a CFD based simulation of the fire dynamics. However, the ability to couple such codes as the NIST Fire Dynamics Simulator (FDS) [9] directly to a suitable structural analysis code does not yet exist. The enormous differences in spatial and temporal length scales, differences in numerical techniques, and the complexity of the computer codes make the development of an efficient fully coupled analysis of fire-structure interactions a daunting task. In the NIST study, typical FDS simulations of fire growth and spread on one floor of the WTC tower were performed with a grid spacing of 50 cm. Typical structural components of the WTC tower such as truss rods have a 2.5 cm diameter and the perimeter columns are 35 cm on a side. It is clear that FDS cannot resolve the structural components. Since the structural components are not modeled in an FDS simulation, the radiative fluxes to the structural elements cannot be computed. A methodology was needed to predict the radiative fluxes from the hot combustion products to the sub-grid scale structural elements. The approach used for the WTC collapse analysis takes advantage of the fact that the simplest compartment can be divided into a hot, soot laden upper layer and a cool, relatively clear lower layer [10], [11] much like a “zone model”. The temperature gradients in the horizontal directions are much smaller than those in the vertical direction. The properties of the two layers are taken from suitably chosen temporal and spatial averages of the output generated by FDS. The time averages are chosen to be compatible with the time scales associated with thermal diffusion through the smallest structural members of interest. The spatial averages replace the detailed vertical temperature and absorption coefficient profiles with an effective “zone model” profile.

The layered thermal and optical properties in the gas phase allow simplification of the radiative transport equations. Let length scales in the horizontal directions \bar{x} be scaled with a length L (typically over 60 meters in the WTC towers), while the grey gas absorption coefficient κ and the length scales in the vertical direction z are scaled with H , the height of an individual floor (less than 4 meters in the WTC towers). Finally, let the integrated intensity $I(\bar{x}, z, \bar{\Omega}_x, \Omega_z)$ be normalized with respect to σT_r^4 , where σ is the Stefan-Boltzmann constant, $\bar{\Omega} = (\bar{\Omega}_x, \Omega_z)$ denotes the local direction of the radiation field, and T_r a suitable reference temperature. Then, denoting dimensionless quantities with a tilde, the radiative transport equation takes the form:

$$H/L \left(\bar{\Omega}_x \cdot \nabla_x \tilde{I} \right) + \Omega_z \frac{\partial \tilde{I}}{\partial z} = \tilde{\kappa} \left(\frac{(\tilde{T})^4}{\pi} - \tilde{I} \right) \quad (1)$$

Since the ratio $H/L \ll 1$, the terms in round brackets on the left hand side of Eq. 1 can be ignored. The remaining terms are those associated with the problem of radiative transport between plane parallel layers. For this simplified geometry, the radiative transport equation can be solved exactly and explicit formulae for the heat flux obtained as a function of the temperatures, hot layer depth, soot concentration, as well as the location and orientation of the structural element.

Figure 1 is a schematic representation of the methodology employed by the Fire Structure Interface. Fire dynamic simulations were performed for a full floor of the World Trade Center tower, and the left image shows the contour plots of gas phase temperature (maximum temperature 1100 °C). Properties of the hot layer were transferred to the finite element software for prediction of radiative fluxes to the sub-grid scale structural elements. These radiative fluxes serve as boundary conditions for a three-dimensional time dependent thermal response of the full floor structural assembly including the fireproofing (middle image). The thermal data computed using 3-D brick shaped finite elements was mapped onto the structural models consisting of beam and shell elements. The structural models (right image) are used to predict the fire induced structural response. The structural and fireproofing damage due to the aircraft impact was incorporated in the various modeling tasks.

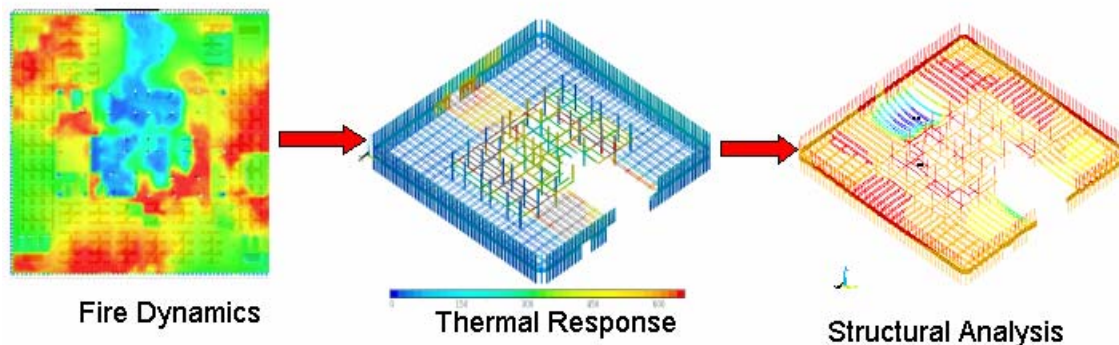


Figure 1. Schematic representation of the coupling between fire dynamics simulations (CFD) with finite element thermal and structural analysis used in NIST's World Trade Center Investigation.

3. LARGE FIRE LABORATORY EXPERIMENTS

The methodology for coupling fire simulations with the thermal response of structural elements was used extensively during NIST's Investigation into the collapse of the WTC towers. A series of large scale fire experiments were conducted at the NIST Large Fire Laboratory [12], to test that the models were accurately capturing the measured thermal response of structural elements exposed to a large fire in a compartment. Model sensitivity to changes in various experimentally derived model input parameters was also assessed.

A steel-frame compartment (3.60 m by 7.04 m by 3.82 m high) lined with 25 mm thick calcium silicate board was constructed. Several steel components (two bar-joist trusses, one thin-walled tubular column, and a simple rod) were placed in the compartment. The components were either left bare or had a fibrous sprayed-on fire protective insulation material (SFRM) applied in two nominal thicknesses (17 mm and 34 mm). The coefficient of variation ($COV = \text{Standard deviation} / \text{Mean Value}$) of the SFRM thickness ranged from 0.17 to 0.27 for the structural components. The fire was generated using liquid hydrocarbon fuels introduced by a two-nozzle spray burner onto a 1 m by 2 m pan (0.1 m deep). The fire sizes tested were between 1.9 MW and 3.4 MW to assure that the structural components were immersed in flames and hot gases. Fuels include heptane and a mixture composed of 60 percent heptane and 40 percent toluene by mass, the latter being representative of fires that yield elevated amounts of soot.

The level of agreement between the calculated and the measured values of the peak temperature for the various steel components are summarized in Table 1 and Table 2 for the un-insulated and insulated tests, respectively. Each table lists the difference, between the peak values of the measured and the simulated steel surface temperatures, normalized by the average of those temperatures, with results listed for the hottest and the coolest temperatures locations for each element. For the un-insulated components (Table 1), the results consistently under-predicted the measurements by a small percentage (absolute value of maximum difference is less than 5%). These differences are attributed to the model sensitivity to the uncertainty in the heat release rate used in the fire model. For the insulated structural components (Table 2), the numerical predictions also consistently under-predicted the measurements, and the absolute value of the differences was less than 20 %. This difference is attributed to model sensitivity to the variability in the SFRM coating thickness. Note that COV of the SFRM thickness in the experiments ranged from 0.17 to 0.27 [12], while the numerical modeling was performed with the specified mean fireproofing thickness. The comparison between experimental data and model predictions yields confidence in the analyses of the thermal environment in compartments and allows one to estimate the uncertainty in the WTC calculations.

Table 1. Percentage difference between peak values of the measured and the simulated steel surface temperatures at the hottest and coolest locations on various un-insulated components.

Element (Vertical Position)	Hottest Location	Coolest Location
Bar A	-10 %	3 %
Bar B	8 %	-2 %
Column (2.13 m above floor)	2 %	-2 %
Column (3.69 m above floor)	-3 %	-6 %
Truss A (2.89 m above floor)	-4 %	2 %
Truss A (3.29 m above floor)	-6 %	-8 %
Truss A (3.70 m above floor)	1 %	-10 %
Absolute Value of Average (Average)	4.9 % (-1.7 %)	4.7 % (-3.3 %)

Table 2. Percentage difference between peak values of the measured and the simulated steel temperatures for the hottest and coolest locations for various components with SFRM. The spray applied fireproofing has a coefficient of variance that ranges from 0.17-0.27 for structural components.

Element	Hottest Location	Coolest Location
Bar ^a	8 %	3 %
Column (0.77 m above floor)	-20 %	3 %
Column (2.13 m above floor)	-11 %	-13 %
Column (3.69 m above floor)	-30 %	25 %
Truss A (2.89 m above floor)	15 %	-15 %
Truss A (3.29 m above floor)	-15 %	-33 %
Truss A (3.70 m above floor)	-10 %	-30 %
Absolute Value of Average (Average)	16 % (-9 %)	20 % (-11 %)

a. Only one bar was used in Test 5.

4. FIRE INDUCED RESPONSE OF WORLD TRADE CENTER TOWER 1

During the course of the investigation, hundreds of preliminary calculations were performed to study the thermal response of individual structural components and full floor systems, coupled with realistic fire simulations [11]. The preliminary studies, photographic and visual evidence, and published literature, helped guide the development of global models. This section describes an application of the Fire-Structure Interface methodology described earlier to predict the global thermal response of WTC 1 for a specific set of aircraft impact damage and fire dynamic simulations.

4.1 Thermal Response of Perimeter and Core Columns

Figure 2 shows the thermal response of the perimeter columns that form the external walls of the North Tower at 6000 s after impact of the aircraft. The analysis covers eight floors of WTC 1 ranging from floors 92 through 99. There were no significant fires observed for floors below floor 92 and above floor 99. The aircraft impact on the North face of WTC 1 damaged several perimeter columns and these columns were not included in the analysis. The perimeter columns on each floor appear as lines, but each column was modeled as a three-dimensional box shaped column (see Figure 2 inset). Steel (cyan colored) is covered with 2.2 cm thick vermiculite plaster on the interior faces and 3.0 cm Blazeshield Cafco D C/F spray-on fireproofing on the exterior faces. The fireproofing on the interior faces of some columns on the South face was damaged due to the debris field (created by the aircraft impact) moving through the various floors. The columns, for which the fireproofing was damaged, heated up quickly and show significantly higher temperatures ($>600^{\circ}\text{C}$), while the columns for which the fireproofing was intact, showed moderate temperatures in the $200\text{--}300^{\circ}\text{C}$ range. The perimeter columns are all held together by a spandrel plate connection (see Figure 2 inset). The fireproofing thickness on the spandrel plate was relatively small (1.3 cm) which results in rapid heating of the spandrel plate and gradual heat conduction into the column.

Figure 2 also shows the computed time-temperature response for eight core columns (top left image). The temperature of the column varies as a function of time as the fire on each floor grows and spreads, from one location to another. It should be noted that differences in computed profiles as compared to the standard time-temperature curve could result in significant differences in the predicted structural response. In addition, simulations predict a significant temperature gradient through the cross-section, which can result in thermally induced bending and failure of the column [5], [8]. In general, the temperature of any perimeter or core column depends on the status of the fireproofing, fire intensity and duration in the vicinity of the columns as well as on the size and shape of the column.

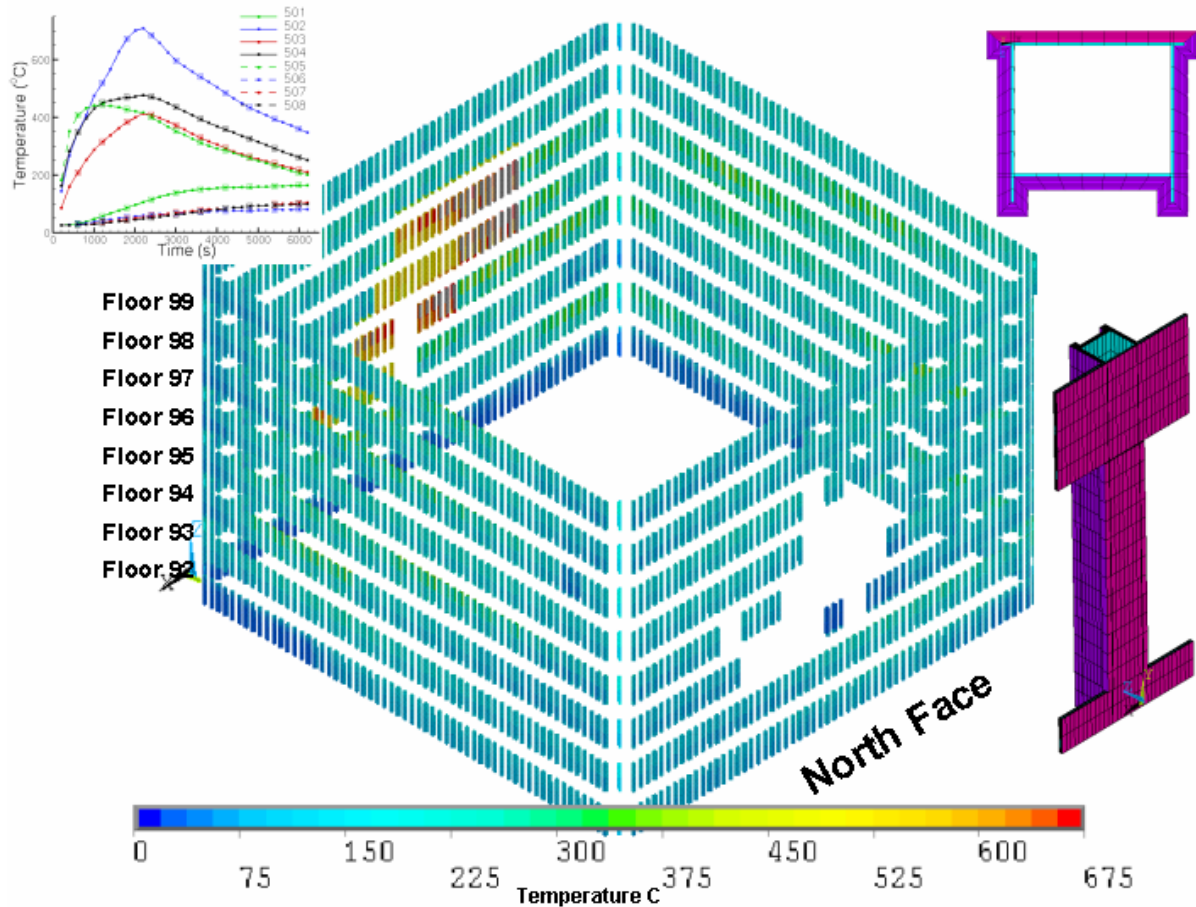


Figure 2. Computed fire induced thermal response of perimeter columns on floors 92-99, WTC 1, at 6000 s after impact of the aircraft. Figure inset (right) shows the finite element model for perimeter columns, while the sub-figure on the left shows the computed time-temperature response of eight core columns.

4.2 Thermal Response of Floor Trusses and Concrete slabs

Figure 3 shows the temperature contours in the floor trusses and core beams that supported the 96th floor concrete slab at 6000 s after impact of the aircraft. The figure also includes the perimeter and core columns for one floor above and below the concrete slab. The thermal response is coupled to the fire simulations and the structural and fireproofing damage due to aircraft impact was included in the analysis. The images on the right show a blowup of a small portion of the floor truss model illustrating the model construction and element density. Cyan colored elements have material attributes of steel while violet colored elements have attributes of fireproofing. The equivalent fireproofing thickness on the trusses in WTC 1 was estimated at 5.6 cm. Numerical simulations indicated that truss elements that have their fireproofing intact do not heat up appreciably. Truss elements for which the fireproofing has been damaged heat up very rapidly and exhibit high temperatures in the 1000-1100 °C range (depending on fire location and intensity). Figure 3 (top left sub-figure) shows the temperature response at four locations on the steel truss. The resulting time-temperature curve at any location on the steel truss is highly variable and bears no relation to the ASTM E119 curve [5].

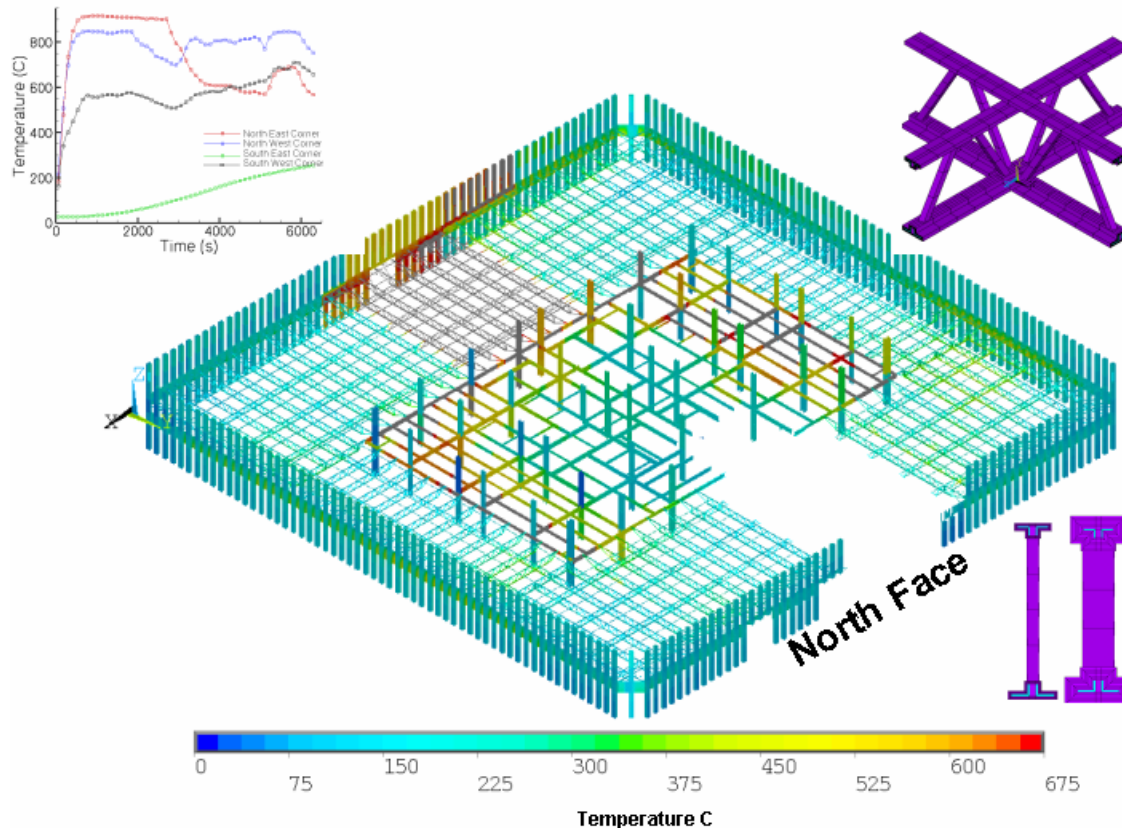


Figure 3. Computed fire induced thermal response of floor trusses and core beams supporting the concrete slab on the 96th floor of the North Tower at 6000 s after aircraft impact. Figure inset on the right shows a blow up of the model for floor trusses while the top left sub-figure shows the predicted time temperature response at four locations.

Thermal response of an 11.0 cm thick concrete slab (computed using 16 elements through its depth) shows severe temperature gradients through its thickness. The concrete slab was radiatively heated on the top and bottom faces, which results in very high surface temperature but lower temperatures in the middle layers. The severe temperature gradients can result in differential thermal expansion and out of plane bending in the concrete slab [8]. The temperatures in the concrete slab respond slowly to the spatially and temporally evolving fires as compared to the lighter floor trusses.

4.3 Reduction in Load Carrying Capacity

In order for a building to maintain its stability, the vertical load bearing members on a floor must support the weight of the building above that floor. Collapse will occur if the weight of the building above a given floor is more than the sum of the load carrying capacity of the columns. An approximate measure of the load carrying capacity of a column can be obtained from its yield strength. The yield strength is used as a measure of this capacity because the non-linear stress-strain curves approach those for an elastic-plastic model at high temperatures. Thus, after the onset of plastic behavior, no further load can be supported in any structural element exhibiting this behavior. The yield strength is temperature dependent, decreasing with increasing temperature. At temperatures of about 300 °C, steel loses about 20 percent of its yield strength. At temperatures above 600 °C, the loss of yield strength is

approximately 60 percent, and the column's ability to carry its share of the building load decreases significantly [8].

As the fire grows and spreads on any of the focus floors of each tower, the temperature of each perimeter and core column changes with time. As discussed earlier, the column temperature is a strong function of the status of the fireproofing, fire intensity in the vicinity of the column and the shape and size of the columns (See Figure 2 and Figure 3). As the temperature of a column increases with time, its load carrying capacity (product of yield strength and cross-sectional area) reduces with time. The total load carrying capacity of the structure can be approximated as the sum of the load carrying capacities of the individual columns.

Figure 4 shows the load carrying capacity of the structure for three different scenarios. The load carrying capacity is non-dimensionalized with the weight of the tower above the floor under consideration. The blue curve (top curve) in Figure 4 shows the change in the load carrying capacity of the structure as a function of time, assuming that there is no structural or fireproofing damage. Under such a scenario, the temperature of the columns does not increase significantly and this results in only a marginal decrease in load carrying capacity. The green curve (middle curve) shows the reduction in load carrying capacity over time, assuming that there is fireproofing damage on all the columns. For this case significant heating of the columns is predicted and as a result the load carrying capacity of the structure is significantly lower than that for the undamaged tower. Note, that the load carrying capacity of the individual columns could increase or decrease with time, depending on the column temperature. However, the overall load carrying capacity of the structure decreases with time for this scenario. It is conceivable that if the fire had extinguished, then the load carrying capacity of the structure would return to its undamaged value (predicted by the current analysis, although this may not happen in reality due to hysteresis effect or structural damage). The red line (bottom curve) shows the reduction in load carrying capacity over time, assuming that there is both structural and fireproofing damage. The perimeter and core columns that are damaged due to the aircraft impact are not considered in the analysis. The load carrying capacity of the structure is therefore reduced due to the impact of the aircraft even before the fires ignite (See Figure 4 red curve). This capacity is further reduced over time because of thermal heating (degradation of material properties) of the perimeter and core columns. At some point the load carrying capacity is below the dead load (shaded area in Figure 4), at which point collapse is inevitable.

The analysis presented is an upper bound estimate of the load carrying capacity of a structure and it does not account for thermal expansion and the resulting thermally induced stresses in a structure. These important features and other non-linear effects can be accounted in a detailed finite element analysis. Typical finite element analysis of the full structure under fire conditions can be computationally expensive and can exhibit convergence difficulties due to non-linear response of the structural members. The analysis presented above is an approximate but computationally efficient method for understanding the sensitivity of the various fire parameters on the load carrying capacity of the structure. To date, the goal of a fully coupled analysis has only been partially accomplished. The next step is to simulate the feedback from large deformations and local structural failures on the fire dynamics and heat transfer in complex building structures.

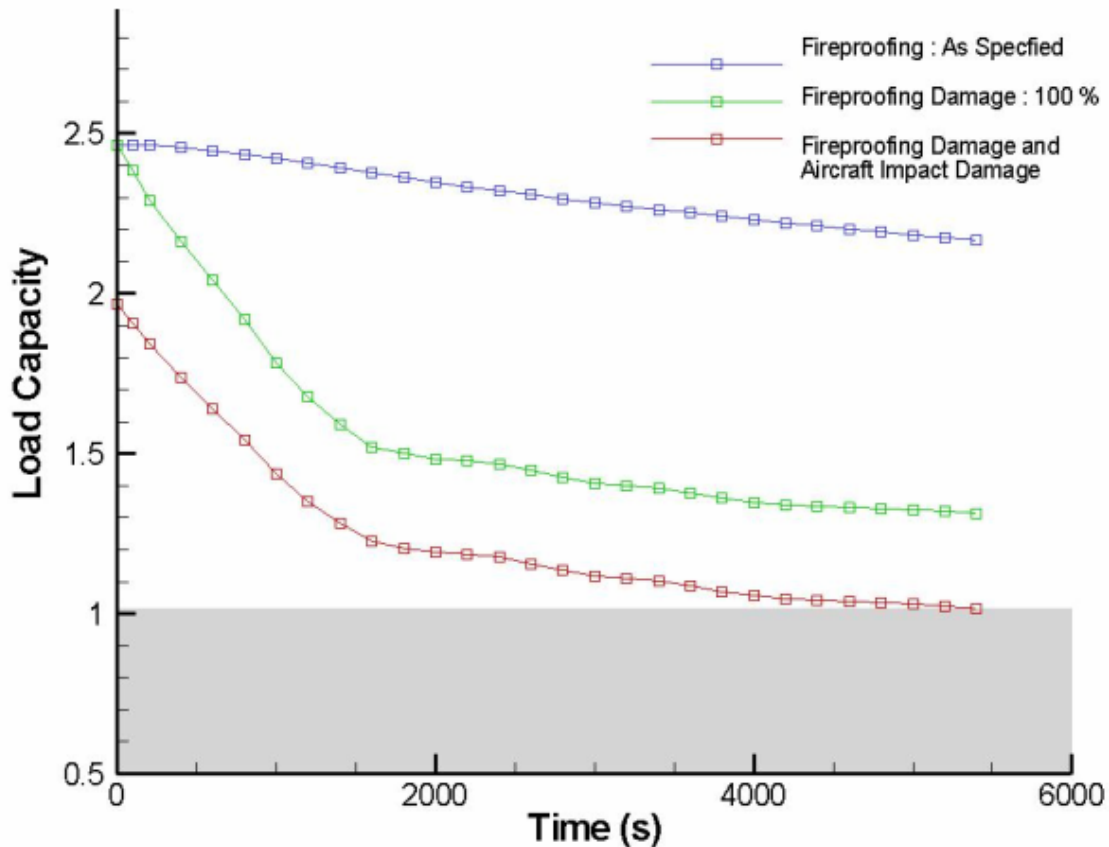


Figure 4. Load carrying capacity of the structure as a function of time for three cases: no structural or fireproofing damage (blue curve), only fireproofing damage (green curve) and both structural and fireproofing damage (red curve).

5. CONCLUSIONS

Simulation of the collapse of complex structures with fire loading requires a close coupling between computer models of fire dynamics, heat transfer and structural mechanics. A methodology has been described for coupling the Fire Dynamics Simulations with thermo-structural response of complex building assemblies. Heat transfer to sub-grid scale structural elements is calculated using a simple radiative transport model that assumes that the compartment can be locally divided into a hot sooty upper layer and a cool, relatively clear lower layer, the properties of these layers being obtained from the results of the fire dynamics simulation. The methodology has been used to predict the global thermal response of the World Trade Center Towers. Numerical simulations predict perimeter column temperature ranging from 200-300 °C for the insulated columns and 600-700 °C for the columns where the fireproofing has been damaged. Reduction in load carrying capacity as a function of time provides an approximate methodology for understanding the sensitivity of fire as well as structural and fireproofing damage on the computed structural response.

6. REFERENCES

1. Quintiere, J. G., Di Marzo, M. and Becker, R., *Fire Safety Journal*, 37, 7, (2002) 707-716.
2. Buchanan, A. H., "Structural Design for Fire Safety," John Wiley, London, 2001.
3. Bailey, C. G., and Moore, D. B., *The Structural Engineer*, London, 78, 11, (2000) 19-27.
4. Franssen, J. M., Kodur, V.K.R and Mason, J., "User's Manual for SAFIR 2002-A Computer Program for Analysis of Structures Submitted to the Fire," University of Liege, Belgium, 2000.
5. Usmani, A. S., Chung, Y. C., and Torero, J. L., *Fire Safety Journal*, 38, 6, (2003) 501-533.
6. Choi, S. K., Burgess, I. W., and Plank, R. J., "The behavior of Lightweight Composite Floor Trusses in Fire," *Designing Structure for Fire*, Society of Fire Protection Engineers and Structural Engineering Institute, Baltimore, MD, 2003.
7. World Trade Center Building Performance Study: Data Collection, preliminary observations and recommendations, *Technical report FEMA 403, Federal Emergency Management Agency*, (2002).
8. NIST (National Institute of Standards and Technology). 2005. *Federal Building and Fire Safety Investigation of the World Trade Center Disaster: Final Report of the National Construction Safety Team on the Collapses of the World Trade Center Towers*. NIST NCSTAR 1. Gaithersburg, MD, September. <http://wtc.nist.gov/NISTNCSTAR1CollapseofTowers.pdf>
9. McGrattan, K. B., Baum H. R., Rehm, R. G., Hamins, A., Forney, G. P., Floyd, J. E., Hostikka, S., and Prasad, K., "Fire Dynamics Simulator (Version 3) – Technical Reference Guide" *National Institute of Standards and Technology Report NISTIR 6783*, (2002).
10. Prasad, K. and Baum, H. R., *Proc. Combust. Inst.*, 30 (2005) 2255-2262.
11. Prasad, K. R., and H. R. Baum. 2005. *Federal Building and Fire Safety Investigation of the World Trade Center Disaster: Fire Structure Interface and Thermal Response of the World Trade Center Towers*. NIST NCSTAR 1-5G. National Institute of Standards and Technology. Gaithersburg, MD, September. <http://wtc.nist.gov/NISTNCSTAR1-5G.pdf>
12. Hamins, A., A. Maranghides, K. B. McGrattan, E. Johnsson, T. J. Ohlemiller, M. Donnelly, J. Yang, G. Mulholland, K. R. Prasad, S. Kukuck, R. Anleitner and T. McAllister. 2005. *Federal Building and Fire Safety Investigation of the World Trade Center Disaster: Experiments and Modeling of Structural Steel Elements Exposed to Fire*. NIST NCSTAR 1-5B. National Institute of Standards and Technology. Gaithersburg, MD, September. <http://wtc.nist.gov/NISTNCSTAR1-5B.pdf>



INFLUENCE OF CONCRETE FLOOR SLAB ON STRESS- DEFORMATION BEHAVIOUR OF HIGH-RISE STEEL FRAME EXPOSED TO COMPARTMENT FIRE

Takeo HIRASHIMA¹, Yu Guang LI², Masaru FUJITA³,
Hirofumi SEGAWA⁴, Kentaro FUJIMOTO⁵ and Hideki UESUGI⁶

ABSTRACT

When compartment fire occurs, a steel structural frame is three-dimensionally deformed and greatly influenced by thermal expansion of a concrete floor slab. This paper presents three-dimensional analysis of the thermal stress and deflections of a high-rise steel structure exposed to compartment fire. The results are summarized as follows:

- 1) Horizontal displacement at the top of outer columns is influenced by thermal elongation of beams and a concrete floor slab.
- 2) Deflection at the centre of beam with the floor slab is about 2 times that without the floor slab when steel temperature reaches 600°C, owing to the bimetallic effect due to the temperature gradients across the concrete floor slab.
- 3) Bending moment of beams exposed to fire with the floor slab is larger than that without the floor slab, owing to the bimetallic effect due to the temperature gradients across the concrete floor slab.

1. INTRODUCTION

The basic principle in fire engineering design of a building is to prevent the spread of fire by means of compartment elements. An important prerequisite for design is to quantitatively understand the thermal deformation of a structural frame exposed to fire heating. When compartment fire occurs, a steel structural frame is three-dimensionally deformed and greatly influenced by thermal expansion of a concrete floor slab. This paper presents three-dimensional analysis of the thermal stress and deflections of a high-rise steel structure exposed to compartment fire.

¹ Research Assoc., Chiba Univ., Faculty of Eng., 263-8522 Chiba, Japan, email: hirashima@faculty.chiba-u.jp.

² Graduate Student, Tokyo University of Science, 278-8510 Noda, Japan, email: j7104710@ed.noda.tus.ac.jp.

³ Tokyo Marine & Nichido Fire Insurance Co. Ltd., Japan, email: MASARU.FUJITA@tmnf.jp

⁴ Graduate Student, Chiba Univ., 263-8522 Chiba, Japan, email: sega-wa@graduate.chiba-u.jp

⁵ Graduate Student, Chiba Univ., 263-8522 Chiba, Japan, email: kenhappy@graduate.chiba-u.jp

⁶ Prof., Chiba Univ., Faculty of Eng., 263-8522 Chiba, Japan, email: uesugi@faculty.chiba-u.jp

2. ANALYSIS OF THERMAL STRESS AND DEFLECTIONS

2.1 Building Structure and Division into substructures

Fig.1 shows a 55-story, steel structure building used for analysis. This building has office rooms and a centre core, which contains elevators, stairs, and equipment rooms. This type of structure is called a tube structure, and resembles the structure of the World Trade Centre, but differs in that members are connected rigidly. Moreover, this building has 4 truss frame stories serving as earthquake resisting elements.

Compartment fire is assumed to occur on the 51st floor. Regarding the local characteristic of a fire incident, as shown in Fig.1, the entire structure is divided into substructures: the local substructure; the adjacent substructures; and the remaining part [1,2]. The local substructure is the part that is directly exposed to fire. Therefore, in the local substructure, the deformation behaviour is normally elasto-plastic. The adjacent substructure will be affected by thermal expansion of the local substructure. However, the influence in this region is considered to remain elastic. For the remaining part, fire-induced stress and deformations are generally negligible.

The analysis is conducted with consideration of concrete floor slab and without consideration of the same.

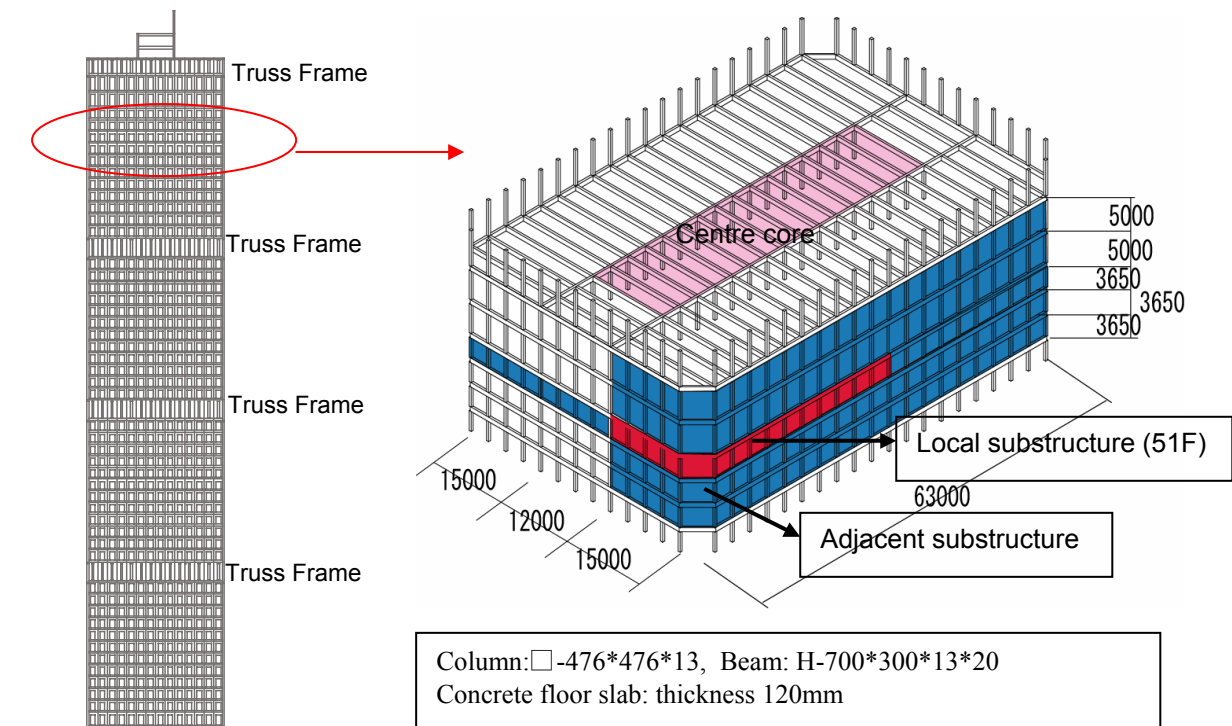


Fig.1 Analytical structure

2.2 Elasto-Plastic Analysis in the local substructure

The analysis includes the influence of material and geometrical non-linearities. The local substructure is significantly affected by the fire exposure and must be analysed in the elasto-plastic range, because of thermal elongation of steel frames and concrete floor slab exposed to fire and restraint by adjacent structural members. The equilibrium equation for the local substructure and the compatibility equation between integrated and incremental deformations are formulated in consideration of end restraint force and external joint force [1].

Elasto-plastic analysis is based on the non-linear direct stiffness formulation coupled with time step integration [3,1]. Time-dependent temperature variation is assumed to be step-wise. Temperature distribution of the member remains constant within a given time step. Strain distribution remains planar according to Bernoulli's hypothesis. Use of non-linear direct stiffness formulation based on the infinitesimal displacement theory produces a convergent calculation, which yields the value for the incremental displacement. Accumulating these incremental displacements will account for the effect of geometric non-linear characteristic.

In addition to the parallel and rotational movements, movement of a member exposed to fire in three-dimensional space will also be composed of axial rotation around the axis of the member. The principal axis of section may change following a rotational movement of the member, depending on the trajectory of rotation taken by the member. Therefore, the rotational angle of the principal axis about the section of the member is determined as a sum of the rotational angle around the axis of the member and the rotational angle of the principal axis of section depending on the trajectory of the rotating movement of the member [4].

Steel beams and steel columns, which constitute the local substructure, are longitudinally divided into segments. In the reference example, beams are divided into 16 segments and columns into 8 segments. Steel segments are further divided into subslices within the cross section; in the example, a flange is divided into 4 subslices and a web into 8 subslices.

Fig.2 shows the calculation model for the floor slab. In this study, the concrete floor slab is line-replaced with a fibre grid beam as an approximation. The main factors of the effect of the slab on the structural frame will be the bending and expanding deformations of the slab, and the effect of shear deformation of the slab will be of secondary importance. Therefore, in this study, the main focus is placed on the elongation of the floor slab due to thermal expansion and the bimetallic effect due to the temperature difference.

The service load given in nodes of the concrete floor slab is $8.9 \text{ [kN/m}^2\text{]}$.

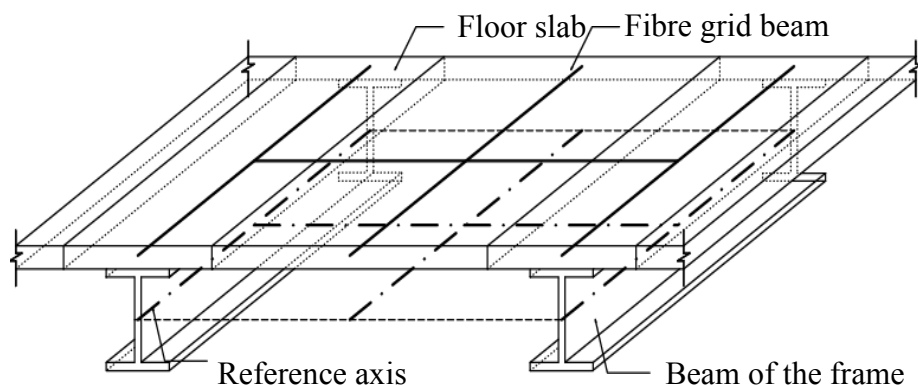


Fig.2 The calculation model for the floor slab

2.3 Temperature of steel frame and concrete floor slab

Compartment fire is assumed to occur on the 51st floor. Thermal exposure is described by the standard Temperature-time curve. Steel exposed to fire is assumed to rise in temperature at a rate of 10°C/minute in local substructure. Temperature distribution of the concrete floor slab $T_c(x, t)$ is approximated by the following error function (1), which provides the solution for a semi-infinite body:

$$T_c(x, t) = T_s + (T_0 - T_s) \operatorname{erf}\left(\frac{x}{2\sqrt{\alpha t}}\right) \quad (1)$$

T_0 : Room temperature 20 [°C]

t : Heating time [minute]

T_s : Temperature of the heated surface of the slab [°C]

x : Distance from the heated surface of the slab to the point [mm]

α : thermometric conductivity of concrete 0.5 [mm²/minute]

Temperature of the heated surface of the slab T_s is approximated by the following standard temperature-time curve:

$$T_s = 345 \cdot \log_e(8t + 1) + T_0 \quad (2)$$

2.4 Stress-Strain Curves and Thermal Strain

Total strain ε of steel at elevated temperature T [°C] is defined as the sum of the strain caused by thermal strain ε_{th} and instantaneous stress strain ε_σ .

$$\varepsilon = \varepsilon_{th} + \varepsilon_\sigma \quad (3)$$

$$\varepsilon_{th} = (10.8T + 0.00675T^2) \times 10^{-6} \quad (4)$$

$$\varepsilon_\sigma = \sigma/E_t + (\sigma/\sigma_k)^k \quad (5)$$

The parameters σ_k , k , and E_t are derived from the stress-strain curves formulated as exponential functions [5] through using the following two points. The first point is 0.2% offset point, and the second is that where strain is 20%. In this analysis, the stress-strain curves are obtained from a tensile test at elevated temperature performed on rolled steels for welding structure (SM490A) [6]. The parameters σ_k , k , and E_t determined from these curves are provided in Table 1. Fig.3 shows the stress-strain curves of steels used in analysis.

Table 1 Values of E_t , σ_k , k

Temp.	E_t [N/mm ²]	σ_k [N/mm ²]	k
R.T.	205800	594	12.4
100°C	203787	551	12.7
200°C	197749	504	13.0
300°C	187685	728	6.0
400°C	173596	595	6.8
500°C	155482	390	8.6
600°C	133342	191	17.1
700°C	107177	91	12.1
800°C	76986	84	6.5

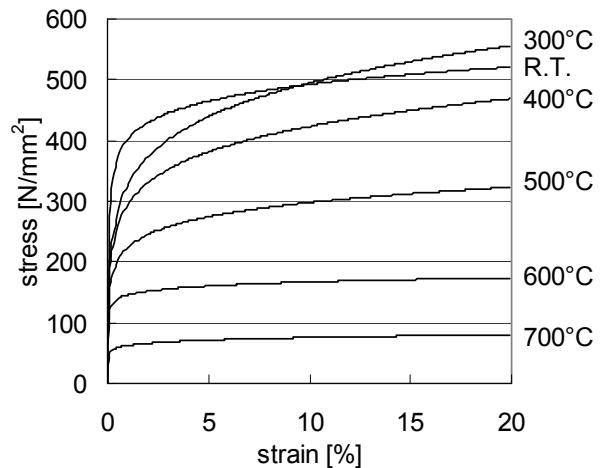


Fig.3 Stress-strain curves of steel

Total strain ε of concrete at elevated temperature T is defined as the sum of the strain caused by thermal strain ε_{th} , instantaneous stress strain ε_{σ} , and transient strain ε_{tr} [7].

$$\varepsilon = \varepsilon_{th} + \varepsilon_{\sigma} + \varepsilon_{tr} \quad (6)$$

$$\varepsilon_{th} = \begin{cases} -1.8 \times 10^{-4} + 9 \times 10^{-6} \times T + 2.3 \times 10^{-11} \times T^3 & (20 \leq T \leq 700) \\ 14.0 \times 10^{-3} & (700 \leq T \leq 1200) \end{cases} \quad (7)$$

ε_{σ} : Determined according to Eurocode No.4 [8] (See Fig.4)

$$\varepsilon_{tr} = -2.35 \times \frac{\sigma_T}{\sigma_{R,T}} \times \varepsilon_{th} \quad (8) [7]$$

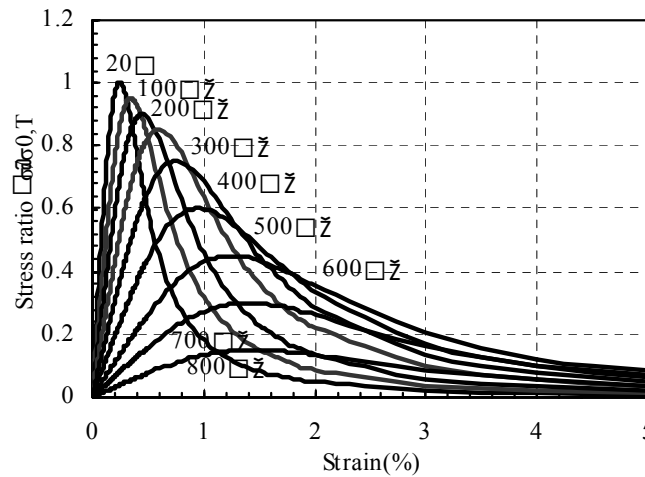


Fig.4 Stress-strain curves of concrete

3. RESULT OF THE ANALYSIS AND CONSIDERATIONS

3.1 Deflection of Frames

Fig.5 shows thermal deflection of the local substructure. In the case of without the concrete floor slab, because calculation is not converged at 560°C, Fig.6 (b) shows result at 550°C. The reason for lack of convergence is not apparent. In both of analytical results, large deflections are produced at the top of outer columns and at the centres of beams, because of thermal elongation of fire-exposed beams and restraint of adjacent members. In the case with the concrete floor slab, in addition to beams, the concrete floor slab makes the deflection of steel beams larger, owing to the bimetallic effect due to the temperature gradients across the concrete floor slab.

Fig.6 shows horizontal displacement at the top of the outer column and vertical deflection at the centre of beam in F-frame and 4-frame (see Fig.5). Horizontal displacement of the outer columns is developed according to steel temperature, because of thermal elongation of beams and the concrete floor slab. Especially, horizontal displacement of outer columns in 4-frame is influenced by thermal expansion of the concrete floor slab as shown in Fig.6 (b). Deflection at the centres of beams with the floor slab is about 2 times that without the floor slab when steel temperature reaches 600°C. This phenomenon is caused by the bimetallic effect due to the temperature gradients across the concrete floor slab. However, deflections of steel members are less than the deformation criterion recommended by ECCS [9].

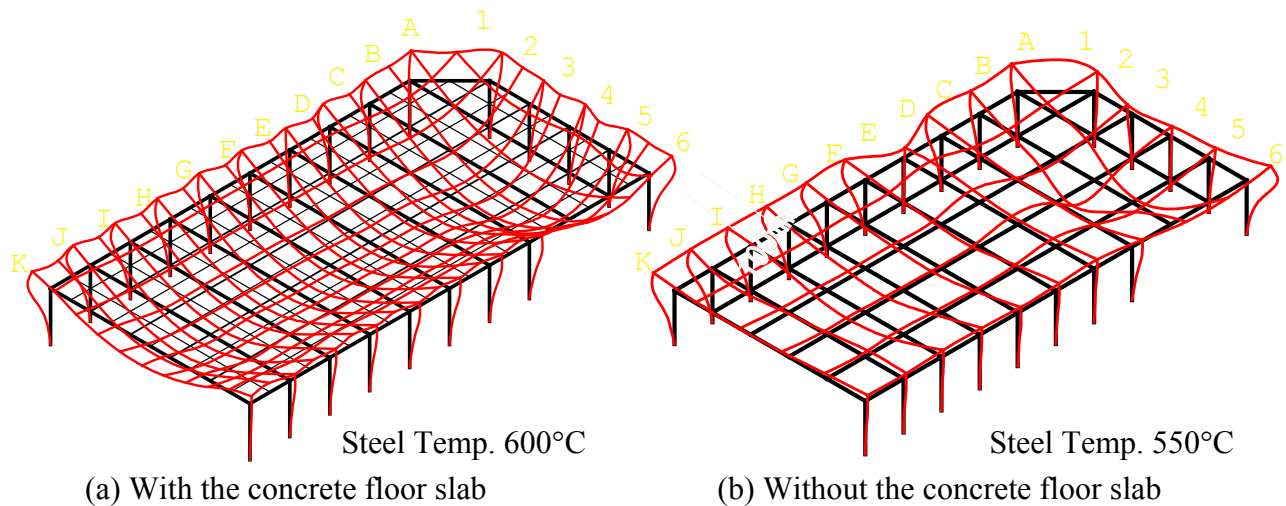


Fig.5 Thermal deflection of the local substructure

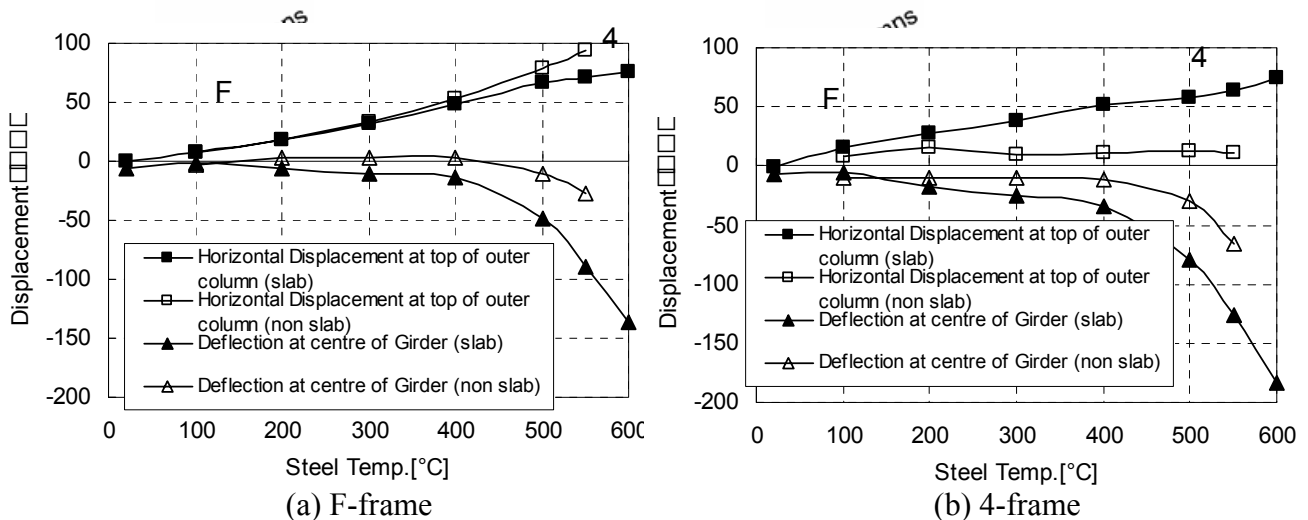
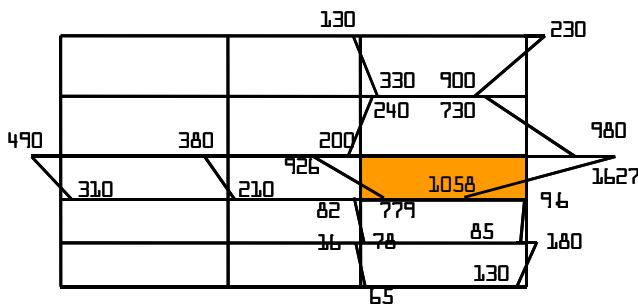
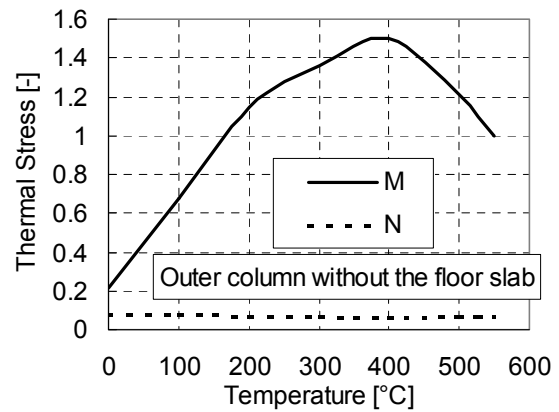
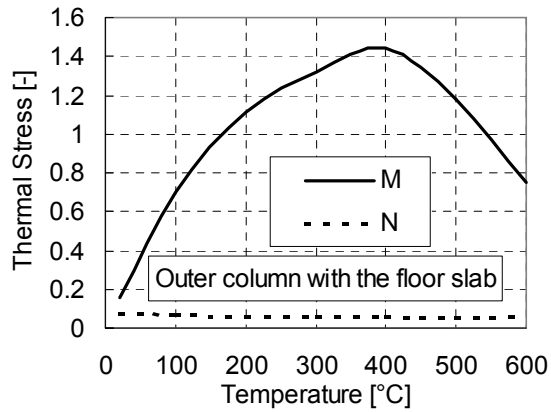


Fig.6 Thermal deflection of outer column and girder exposed to fire

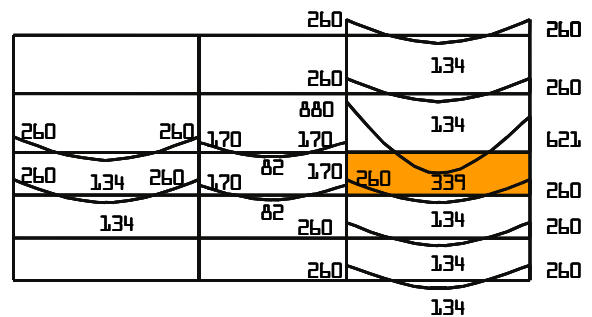
3.2 Thermal Stress of Frames

Fig.7 shows moment distribution of the F-frame at 400°C. Development of the bending moment is remarkable at the ends of the columns exposed to fire and the upstairs columns, due to thermal elongation of the fire-exposed beams and slab. These thermal stress resultants influence the adjacent steel members within two stories of the fire incident. Bending moment of the beam exposed to fire with the floor slab is about 2 times that without the floor slab, owing to the bimetallic effect due to the temperature gradients across the concrete floor slab.

Fig.8 shows Development of the thermal stresses resultant. In these figures, M is the bending moment in the form of a resultant of thermal stress divided by yielding moment of structural steel at room temperature, and N is the axial force in the form of a resultant of thermal stress divided by yielding axial force of structural steel at room temperature. As shown in Fig.8, bending moment at the top of the outer columns increases with axial force of the beams. The increases in bending moment at the centre of beam with the floor slab begin earlier than without the floor slab when steel temperature reaches 400°C.



(a) With the concrete floor slab



(b) Without the concrete floor slab

Fig.7 Moment distribution of F-frame at 400°C (Left: Column, Right: Beam, unit: kN·m)

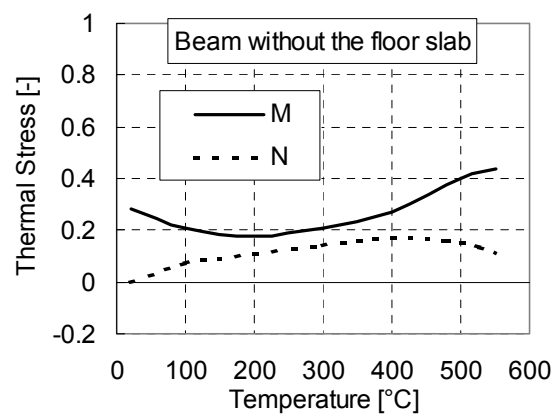
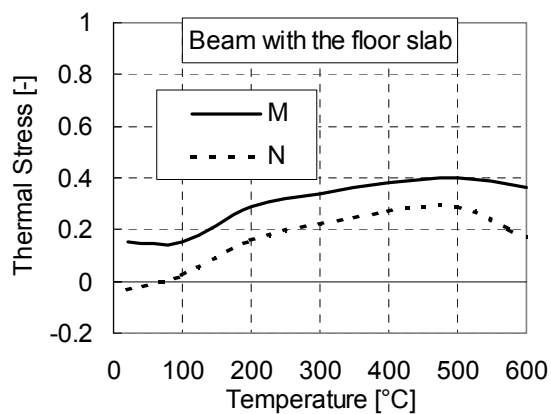


Fig.8 Development of the thermal stresses resultant

4. CONCLUSIONS

The following results are obtained by three-dimensional analysis of the thermal stress and deflections of high-rise steel structure exposed to compartment fire.

- 1) Horizontal displacement at the top of outer columns is influenced by thermal elongation of beams and a concrete floor slab.
- 2) Deflection at the centre of beam with the floor slab is about 2 times that without the floor slab when steel temperature reaches 600°C, owing to the bimetallic effect due to the temperature gradients across the concrete floor slab.
- 3) Bending moment of beams exposed to fire with the floor slab is larger than that without the floor slab, owing to the bimetallic effect due to the temperature gradients across the concrete floor slab.
- 4) Calculation without the concrete floor slab is not converged when steel temperature reaches 560°C. Clarification of the reason for lack of convergence will be the subject of future studies.

When a steel frame can sufficiently support the service load, thermal expansion of a concrete floor slab effects the deflection of the steel frame in compartment fire.

5. REFERENCES

- [1] H. SAITO, H. UESUGI, M. YAMAGICHI & A. KODAIRA, “Thermal Stress and Deformation of Steel Structures of High Rise Buildings in Fire”, Fire Safety Science – Proceedings of the Second International Symposium, 1988
- [2] H. LIN & H. UESUGI, “Three Dimensional Analysis Method of High Rise Structure Exposed to Compartment Fire (Part 1. The Formulation of Restraint Force and Adjacent Displacement for Local Sub-structure)”, Journal of Structural Engineering Vol.44B, Architectural Institute of Japan, March 1998 (in Japanese)
- [3] Becker, J., Bresler, B., “FIRES-RC--- A Computer Program for the Fire Response of Structure --- Reinforced Concrete Frames”, Report No.UCB FRG74-3, University of California Berkley, July 1974
- [4] Yuguang Li, Huiqun Lin, Takeo Hirashima, Hideki Uesigi and Takao Wakamatsu, “An Analytical Method of Deflection Behavior Concerning Three-dimensional Steel Frame Exposed to Fire which takes Account of the Thermal Expansion of a Floor Slab”, Fire Science and Technology, Vol.24, No.4, 2005
- [5] J. Hult (Author), Sumio Murakami (Translation): A Course in the Mechanics of Solids #4: Creep in Engineering Structures, Baifukan, December 1973
- [6] Takeo HIRASHIMA and Hideki UESUGI, “Load-bearing Capacity of H-shaped Steel Columns under Local Buckling at Elevated Temperature”, 8th International Symposium on Fire Safety Science, pp.211-222, 2005
- [7] Anderberg, Y. and Thelandersson, S.: Stress and Deformation Characteristics of Concrete at High Temperatures 2. Experimental Investigation and Material Behavior Model, Division of structural Mechanics and Concrete Construction, Lund Institute of Technology, Bulletin No.54, Sweden, 1976
- [8] Commission of European Communities: Eurocode 4-Design of Composite Steel and Concrete Structures -Part 1-2: General Rules- Structural Fire Design, 1994
- [9] Design Manual on the European Recommendations for the Fire Safety of Steel Structure, ECCS-Technical Committee3 Fire Safety of Steel Structure, 1985



PRACTICAL APPLICATION OF ENGINEERING METHODS FOR FIRE SAFETY DESIGN OF STRUCTURES

Jochen ZEHFUSS¹

ABSTRACT

In this contribution, it is shown by means of examples of existing buildings and new constructions, how “traditional” requirements in building regulations may be compensated by performance-based fire safety design. In existing buildings, constructed in the 1960s, the reinforced concrete elements often have a fire rating lower than R 90 due to the reinforcement being insufficiently covered. The building regulations in Germany usually require a fire resistance R 90 for load bearing and integrity elements. With a performance-based design, which is embedded in a fire safety concept, a sufficient fire resistance of the elements can be proven without being dependent on constructive measures. Therefore, both the fire exposure and the structural behavior of the elements have to be realistically considered. In consultation with the building authority and the fire department, a design fire is specified. On this basis, the fire exposure of the natural fire is simulated. The structural response of the elements exposed to the natural fire is calculated with advanced calculation methods.

For the newly erected steel construction of a shopping center of an open car park, the structure is designed with engineering methods. For the structural elements of the car park, the building authority, first of all, required a fire resistance of R 90 because the car park is erected on top of the shopping center. Applying engineering methods, the building authority and the fire department can be persuaded to refrain from the R 90 requirement. Taking into account the fire exposure of a natural fire and the overall structural behavior of the load bearing system, the requirements for the girders can be reduced to R 30. Generally, the applications show that an interlocking between realistic fire exposure and fire design of the structure is required for an optimum fire safety design.

¹ Dr. Jochen Zehfuss, diploma'd engineer, hhpberlin, Fire Safety Engineers, Berlin, Germany
email: J.Zehfuss@hhpberlin.de

1. INTRODUCTION

As a matter of principle, in Germany, the requirements in terms of fire safety on structural components and load bearing structures are laid down in the building regulations by the federal states and in the corresponding special building regulations. These requirements are generally based on the results of fire tests on single components according to the standard temperature-time curve (ISO 834). A risk-oriented analysis of the fire hazard, as well as the application of engineering methods in the analysis of load bearing structures in terms of fire resistance and fire safety (performance-based design), may therefore be implemented only in the individual case after having obtained the consent of the responsible construction supervisory authorities and fire departments. A reduction of requirements in terms of fire safety, as well as the application of engineering methods, will be approved, as in the case of the renovation of existing buildings, in the cases in which no conversion is undertaken or, as a consequence of such conversion, the structural facility will be expected to have a lower fire load, and [in the cases] in which the adherence to fire safety requirements pursuant to the Building Ordinances would result in a disproportionately high expenditure of time and money.

2. GENERAL APPROACH

At the beginning of a performance-based fire safety design, the fire scenario must first be specified. This results in close coordination with the authorities involved, the fire department, and the builder-owner. On the basis of the fire scenario, the design fire will be determined, which as a general rule will be given as an energy release rate according to [1]. For determination of the fire scenario and the design fire frequently the experiences of the involved fire department are incorporated. The temperature-time sequence of the thermal effects will be determined by means of the natural fire method in accordance with [1], which has been published in Germany, but has not been recognized up to now in construction supervisory procedures.

The determination of the fire exposure according to the natural fire method leads, in particular, to a more realistic analysis of the temperature development in larger compartments. The standard temperature-time curve (ISO 834) was developed to describe the fire sequence in residential buildings. In the natural fire method, the actually existing framework conditions in terms of fire safety are taken into consideration, such as fire loads, ventilation conditions, and room geometry. The temperatures thus determined frequently exceed the standard temperature-time curve in the initial phase. After reaching the maximum temperature, the temperatures fall again, whereas the standard temperature-time curve consistently rises. In the case of the natural fire method, the structural component or load-bearing structure must resist the stress from the beginning of the fire until the end. By means of security factors for the estimated fire loads and the size of the ventilation ducts, an adequate and quantifiable safety level will be guaranteed. Fire extinguishing measures on the part of the fire department will not be taken into consideration in the calculation. Normally, it can be assumed that fire extinguishing measures will occur after approximately 30 to 40 minutes, with the fire ceasing earlier than assumed in the calculation.

The load-bearing structure analysis in terms of fire safety or, respectively, the dimensioning of structural components occurs by means of the fire safety parts of the Eurocodes as, for example, in [items] [2] and [3]. The application of the advanced calculation methods, however, again requires the consent of the Construction Supervisory Authority.

The fire resistance of the structural components will be proven by means of the general calculation methods of the Eurocodes. With the help of a thermal and mechanical analysis,

taking into account the temperature-dependent material properties of construction materials and the temperature-related forced tensions, the load and deformation behavior of the components enduring the fire impact will be calculated, that is, a fire test will be simulated.

3. MANAGEMENT AND OFFICE BUILDINGS

3.1 General Remark

A performance-based safety design is to be implemented for a management and office building in Saarbrücken (in south-west Germany), in which a sufficient fire resistance of the load-bearing structures is to be proven. The building was built as a massive construction in the 1960's. According to the building permit issued then, the load-bearing structures (supports, ceilings, and load-bearing walls) correspond to fire resistance class R 90. It was, however, determined that due to the low cover of the reinforcement, in particular in the case of the ceiling slabs, these could not be given the fire resistance class R 90, according to the fire safety standards applicable at the time, but rather corresponded only to fire resistance classes R 60 or R 30.

It could be proven through the performance-based fire safety design that, as a general rule, the structural components had a sufficient fire resistance if a realistic natural fire was assumed as thermal impact and the evaluation in terms of fire resistance and fire safety was implemented using the full capacity of the load-bearing reserves by means of the advanced calculation method. In the following text, the fire safety design of a ceiling of an office space will be presented as an example.

3.2 Determination of the Thermal Impact on the Ceiling

The ceiling (Pos. 7.03) is located above the office space on the ground floor in the area of axes A-C/(3)-(5). It is a ribbed beam ceiling. The ribbed beam ceiling cannot be rated with any fire resistance class ($< R 30!$) because of the small width of the ribs and the thin concrete covering of the reinforcement.

The office space is separated by massive fire-resistant partitions from the adjacent usage units. The room geometry will be presented in Fig. 1. Due to the size of the office, a fire in the office space in the area of axes A-B/(3)-(5) will be authoritative.

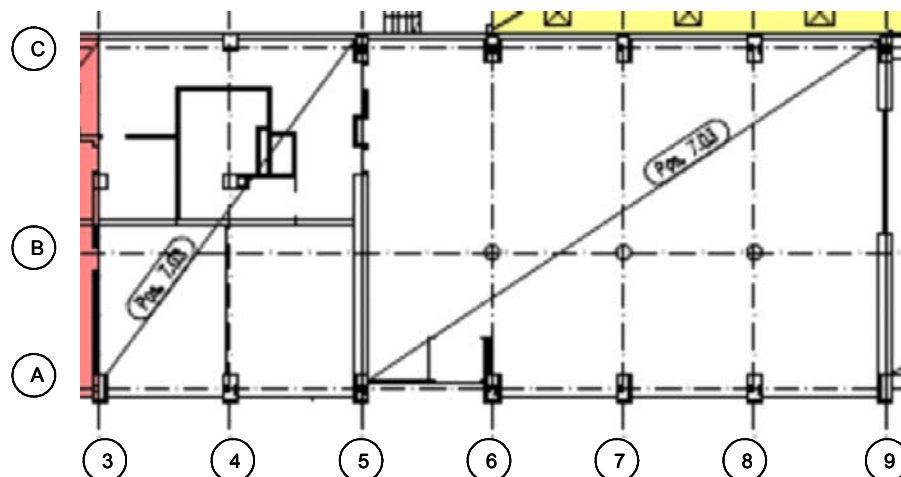


Fig. 1 – Room Geometry

Framework conditions of fire in the office room of axes A-B/(3)-(5) on the ground floor:

Floor space of office room:	= 74 m ²
Height:	= 3.50 m
Fire load density pursuant to [1]:	q = 511 MJ/m ² (for office usage)
Fire load:	Q = 511 MJ/m ² * 74 m ² = 37814 MJ
Thermal properties of the enclosing components:	b = 1500 J/(m ² s ^{0,5} K)
Openings (glazing):	h _w ≈ 3.0 m; b _w ≈ 9 m => A _w = 27.0 m ²
Maximum energy release rate:	18.5 MW

In Fig. 2 the temperature-time curve of the natural fire calculated according to the simplified natural fire model iBMB Parametric Fire Curves as set out in [4] and [5] illustrated (dotted lines “natural fire”). After 38 minutes, the maximum temperature of 789°C will be reached. In the time thereafter, the fire will die down because of the to a large extent composed fire loads. After 60 minutes the hot gas temperature is less than 400°C.

For the thermal analysis, to be on the safe side, a temperature impact covering the entire area of the ribbed beam ceiling is assumed for the entire area of the office room. In Fig. 2, the temperature-time sequence simulated according to [6] is shown at the reinforcement with an axis distance of 2.8 cm as well as at several points of the cross-section. The maximum temperature in the load-bearing reinforcement is 542°C after 40 minutes.

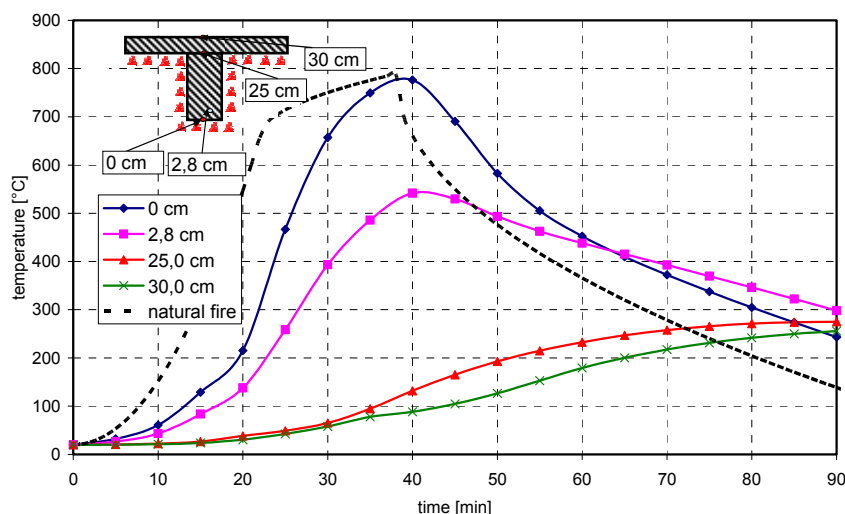


Fig. 2 – Temperature-Time Sequence of the Natural Fire and Simulated Temperature Distribution in the Cross-Section of the Structural Component

3.3 Mechanical Analysis of the Ceiling

The investigated ceiling consists of a single axis spanned two-span reinforced concrete ribbed beam ceiling with a span width of 7.80 m (axes A-B) and 5.40 m (axes B-C). Concrete with a

cylinder strength of approximately 20 N/mm² was used as construction material. The yield stress of the reinforcement is 420 N/mm².

Fig. 3 shows the sequence of the deflection of the ribbed beam ceiling determined by means of a simulation according to [6] in a fire impacted field on the axes A-B (l = 7.4 m). The maximum deflection will be reached after 40 minutes.

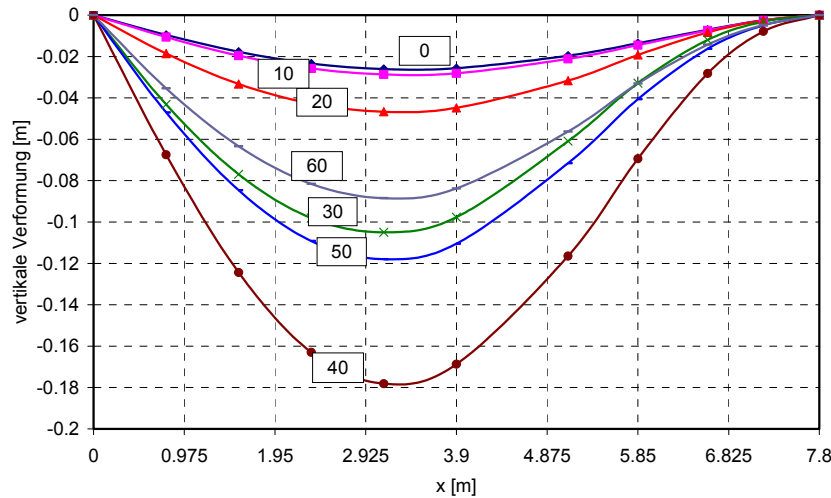


Fig. 3 – Deflection of the Ribbed Beam Ceiling in a Fire Impacted Field

Fig. 4 shows the sequence of the moment of action $M_{sd,fire}$ and the moment of resistance $M_{Rd,fire}$ in the field and support area of the ribbed beam ceiling. With an increase in heat of the concrete cross-section and the reinforcement, the stiffness and strength of the construction material decreases, so that the moment of resistance $M_{Rd,fire}$ will be reduced. As a result of the rotation obstruction, in the area of the middle support and the non-uniform heating of the cross-section, a negative moment occurs. The moment of support will be greater as the temperature of the cross-section increases, and the span moment will be reduced.

The moment of resistance remains greater than the moment of action in the span area as well as in the support area during the entire duration of the fire. After 40 minutes, the moment of resistance in the support area has been reduced to $M_{Rd,fi,hog} = 80$ kNm/m and in the span area it [has] dropped to $M_{Rd,fi,span} = 63$ kNm/m. The moments of action, however, with $M_{sd,fi,hog} = 77$ kNm/m and, in the span area, with $M_{sd,fi,span} = 39$ kNm/m, are smaller than the moment of resistance, so that the ribbed beam ceiling resists the fire and does not fail.

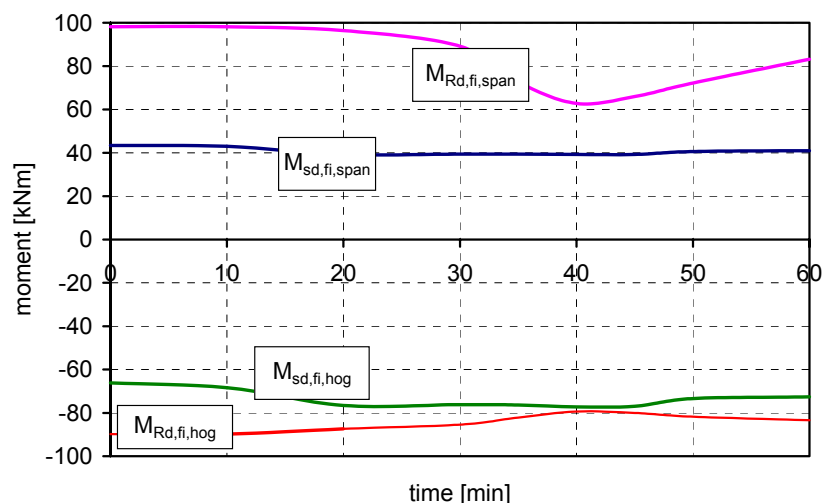


Fig. 4 – Sequence of $M_{sd,fi,span}$ and $M_{Rd,fi,hog}$ in the Fire Impacted Field of the Ribbed Beam Ceiling

4. OPEN CAR PARK

As a matter of principle, in Germany, no requirements as to fire resistance are required for the load-bearing structures of open car parks, so that such load-bearing structures can be built using an unprotected steel construction. If the garage however has a direct connection with another building, the load-bearing structures of the open car park will have the same requirements in terms of fire resistance as those of the load-bearing structures of the building. For an open car park which was built on top of a shopping center in Northern Germany, the Construction Supervisory Authority had initially required a fire resistance R 90 for the load-bearing structures. The load-bearing structures of the garage were to be constructed using a steel-frame construction. The girders were connected with the ceiling slab so that they were dimensioned as steel-composite components in the structural engineering calculations. It was agreed with the Construction Supervisory Authority that the requirements for the fire resistance of the girders could be reduced if the fire resistance of the load-bearing structures was proved by means of performance-based fire safety design on the basis of the Eurocodes /1/ and /3/.

The assignment for the fire safety design occurred after the completion of the structural engineering calculations, when the construction of the load-bearing structures of the garage had already begun, so that the optimized construction of the connections was no longer possible in terms of fire safety. Because of the large span of the girders, comparatively large, massive steel sections (HEA 600 and larger) were used.

By means of the fire safety design it was shown, in a first step, that the girders, which were designed as continuous beams, could be constructed as being unprotected. Because of the heating of over 700°C the composite girders obstructed in deforming longitudinally are stressed by axial forces of up to 10 MN. In the case of girders which are designed as single components in the structural engineering calculations, the high axial forces in the area of the connection cannot be transferred. The structural components providing horizontal reinforcement have not been sufficiently dimensioned to absorb the high axial forces.

In a second step, evidence of the stability against collapse of the overall load-bearing structure could be provided regarding the R 30 protected girders. Through reducing the temperatures of the girders to a maximum of 450°C, the axial forces developing due to the prevention of

expansion were considerably reduced, so that any and all connections and the absorption of horizontal forces could be proven.

In comparison to the steel-composite construction with small spans and smaller steel profiles, it could be determined that

In the case of a locally limited fire, the heating up of a massive profile can cause very large axial forces, which must be able to be absorbed by the reinforced construction. At the connections, the transfer of load functions only where the steel girders have been constructed as continuous beams, because the ceiling slab is not sufficient to transfer the large axial forces in the connection area.

In the case of more filigree constructions with smaller steel profiles, there are considerably smaller axial forces, that could be transferred via the ceiling slab at the connection points. The arrangement of bolts in slotted holes may significantly reduce the axial forces. (cf. /4/).

It has been shown that in case of an optimized fire safety design,
which realistically takes into account the thermal actions (natural fire),
in which, by applying advanced calculation methods, load-bearing reserves can be utilized, and
in case of an optimization of connections or, respectively supporting points,
evidence of a considerably higher fire resistance can be proved than when using the standard design (ISO 834).

5. REFERENCES

- [1] EN 1991-1-2. Eurocode 1 – Actions on Structures. Part 1-2: General Actions – Actions on structures exposed to fire.
- [2] EN 1992-1-2. Eurocode 2 – Design of concrete structures. Part 1-2. General rules – Structural fire design.
- [3] EN 1993-1-2. Eurocode 3 – Design of steel structures. Part 1.2: General rules – Structural fire design.
- [4] Hosser, D.; Zehfuss, J.: Behaviour of Structural Systems Exposed to Natural Fires Considering the Failure of Substructures and Repair. Third International Workshop Structures in Fire, Ottawa, May 2004.
- [5] Zehfuss, J.: Bemessung von Tragsystemen mehrgeschossiger Gebäude in Stahlbauweise für realistische Brandbeanspruchung. Dissertation. Department of Civil Engineering. Braunschweig University of Technology, 2004.
- [6] Hass, R.; Quast, U.; Rudolph, K.: STABA-F. A Computer Program for the Determination of Load-Bearing and Deformation Behaviour of Uni-axial Structural Elements under Fire Action. Institute of Building Materials, Concrete Structures and Fire Protection, Braunschweig University of Technology, 1985.



TALL BUILDING COLLAPSE MECHANISMS INITIATED BY FIRE

Asif USMANI¹, Charlotte ROBEN², Louise JOHNSTON²,
Graeme FLINT¹ and Allan JOWSEY³

ABSTRACT

This paper introduces the hypothesis of two possible failure mechanisms for tall buildings in multiple floor fires. This paper extends the previous work done on the WTC towers by investigating more "generic" tall building frames made of standard universal beam and column sections to determine whether the same collapse mechanisms are obtained. The outcome of this paper enables the development of a simple stability assessment method for tall buildings in multiple floor fires.

1. INTRODUCTION

Since the events of September 11, 2001 there has been considerable interest in understanding the collapse of the tall buildings in fire. Whole structure response analyses with the aim of establishing the precise collapse mechanisms for WTC tower like structures were carried out by the research group at University of Edinburgh in collaboration with Arup. The two main failure mechanisms established in this work are illustrated in Figure 1. Figure 1 (a) shows a mechanism that would occur if a stiff column was supported by a relatively weak (in membrane compression) floor system^{1,2}. If however the floors were stiff enough a conventional plastic hinge mechanism seems to establish³ as a result of the moments imposed upon the column by the floors in tension and P- δ moments, shown in Figure 1 (b). These mechanisms are based on analyses that assume that no connection failure occurs. This assumption allows the focus to be on "global" behaviour as it can be reasonably assumed that this would produce a useful upper bound reference collapse scenario. Local effects such as connection failure, local cracking of concrete, failure shear connectors and their endless

¹ Doctor, University of Edinburgh, School of Civil and Environmental Engineering,
email: asif.usmani@ed.ac.uk, G.R.Flint@ed.ac.uk

² Undergraduate student, University of Edinburgh, Department of Civil and Environmental Engineering, ,
email: C.C.Roben@sms.ed.ac.uk, L.S.Johnston@sms.ed.ac.uk

³ PhD student, University of Edinburgh, School of Civil and Environmental Engineering, ,
email: A.I.Jowsey@ed.ac.uk

permutations could potentially produce a whole range of alternative collapse scenarios, which could reasonably be assumed to produce earlier failures than the reference scenarios (although this is not by any means certain). In a design context local effects can really only be considered properly in a probabilistic rather than deterministic manner.

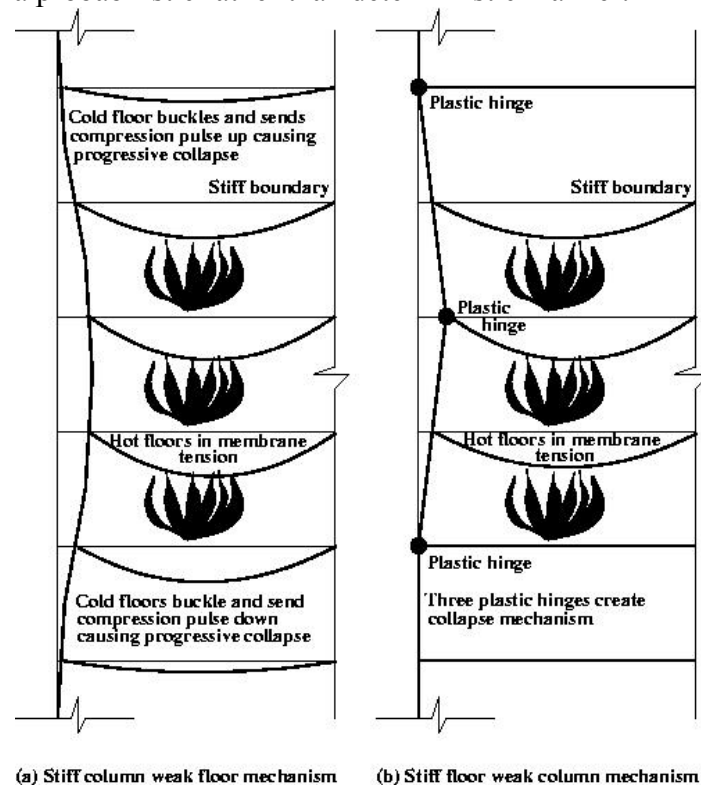


Fig.1 – Suggested collapse mechanisms for WTC towers structure in fire

All previous analyses were carried out using models similar to the WTC towers (using tubular column and truss members for the floor support). This paper extends the previous work by investigating more "generic" tall building frames made of standard universal beam and column sections to determine whether the same collapse mechanisms are obtained. Furthermore, a first attempt is made to develop some generally usable indicator of the propensity of a fire induced collapse in a tall building based on the key parameters of fire severity, number of floors affected and relative column and floor stiffness

2. MULTI-STOREY FRAME MODEL

A more conventional composite steel frame model was constructed to determine that the collapse mechanisms discovered in the context of WTC towers analyses based on the long span truss floor system could be generalised to include more conventional structures. Figure 2 shows the model details.

This is a composite floor system, where the beams and columns are universal beam and column sections respectively. The beams are laterally restrained by the stiff concrete core but are free to rotate. They are fully fixed to the column, which in turn is fixed at the bottom but restrained only in the horizontal direction at the top. The concrete slabs are designed to act compositely with the beams and are connected with multiple point constraints. All sections are modelled using 2-D beam elements. The structure is subjected to loading on the beams and the column. Each beam supports a UDL which includes the self weight of the

concrete slab as well as the imposed load. The column is subjected to a point load which represents the additional floors above the analysed structure. To compare the behaviour of the models several parameters were changed to obtain a wide variety of results. This includes changing loads, section sizes and spans. The assumed material properties are in accordance with Euro Code 3-1.

To model the fire, a generalised exponential curve is chosen to represent the time-temperature relationship and is given by

$$T(t) = T_0 + (T_{\max} - T_0) (1 - e^{-\alpha t}) \quad (1)$$

where, T_{\max} is maximum compartment temperature, T_0 is the initial or ambient temperature, and α is an arbitrary ‘rate of heating’ parameter. For the purpose of this research the maximum and ambient temperature are taken as 800°C and 20°C respectively, α is taken to be 0.005 and the time t is taken as 3600 seconds.

The fire affects floors 6, 7 and 8. The steel is assumed to be unprotected and thus has a uniform temperature equal to that of the fire, shown in Figure 3. The columns are assumed to be protected and are restricted to a maximum temperature of 400°C at the end of the heating period, which is a conservative estimate. The concrete slabs have a non-uniform temperature distribution and follow the temperatures shown in Figure 4.

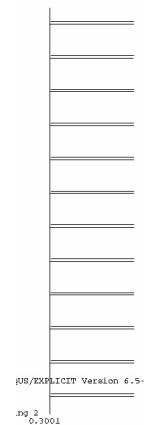
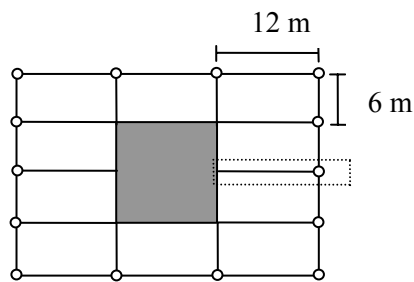


Fig. 2 – Typical plan of a multi-storey frame model and Model cross section adopted

the Finite Element

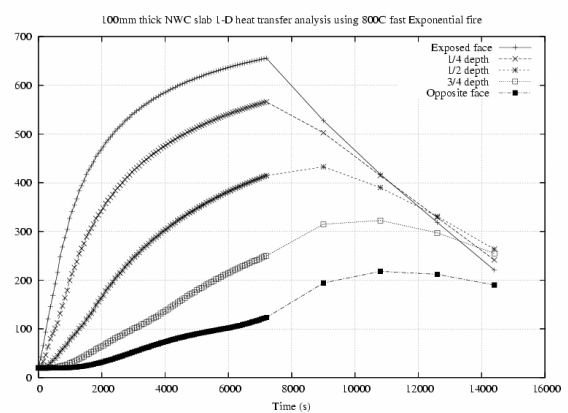
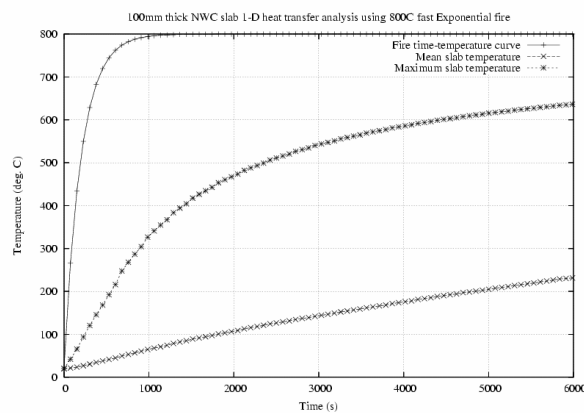


Fig.3 – Generalised fire curve and concrete temperatures through the slab

3. MODELLING RESULTS

Figure 4 shows the deformed collapsed shapes for two different models, essentially reproducing the two mechanisms shown in Figure 1. The weak floor model shows a clear plastic collapse with three hinges forming at the floors above and below the fire floors and at the centre fire floor. The stiff floor model shows that the column forces the floor below the fire floors to buckle, thus increasing the loading on the floor below and starting a progressive collapse.

The horizontal deflection of the column is plotted for both models and can be found in Figure 5. Initially both show a negative displacement, indicating the outward movement of the column due to the thermal expansion of the beams. The weak floor model shows that the fire floors quickly deflect in the positive direction as the beams are pulling it in. As the column increasingly pushes against the floors below the fire these buckle and the column moves inward at these lower floors.

The stiff floor model however, shows that only the fire floors deflect further and that no movement of the column occurs at any other point. This coincides with the three hinge failure assumption that the collapse is localised.

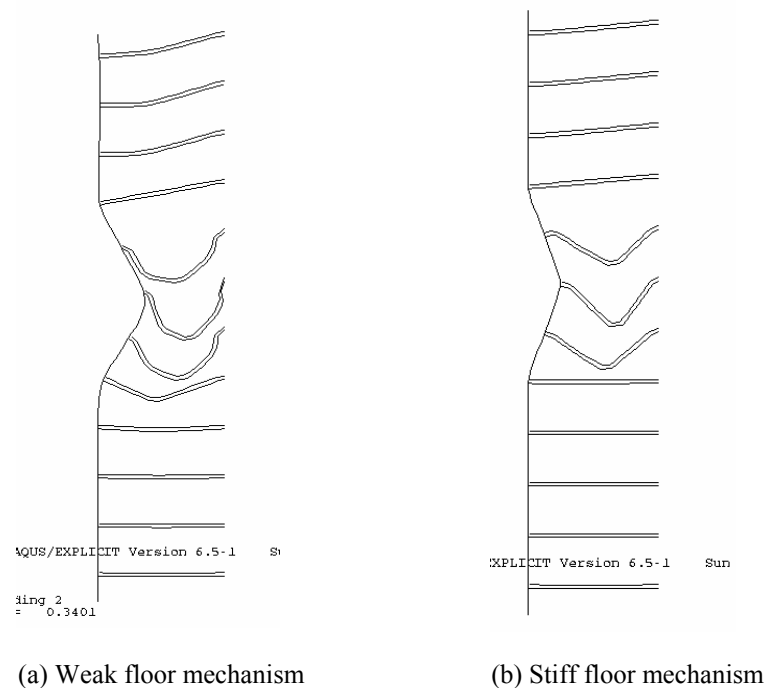
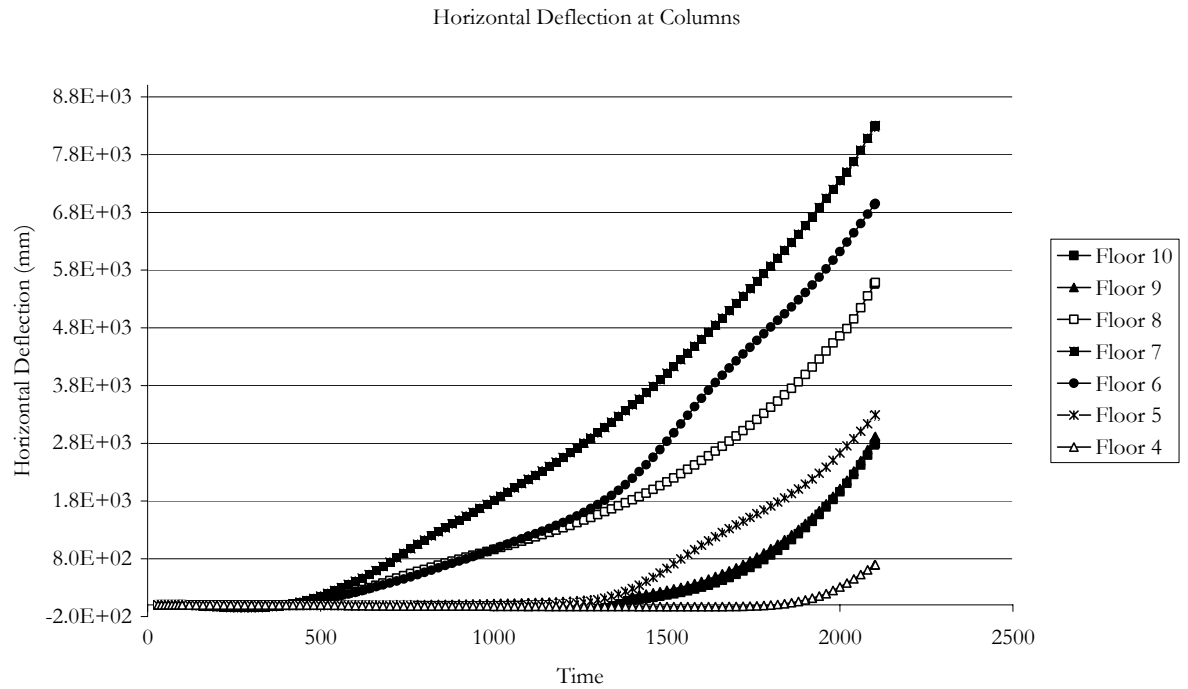
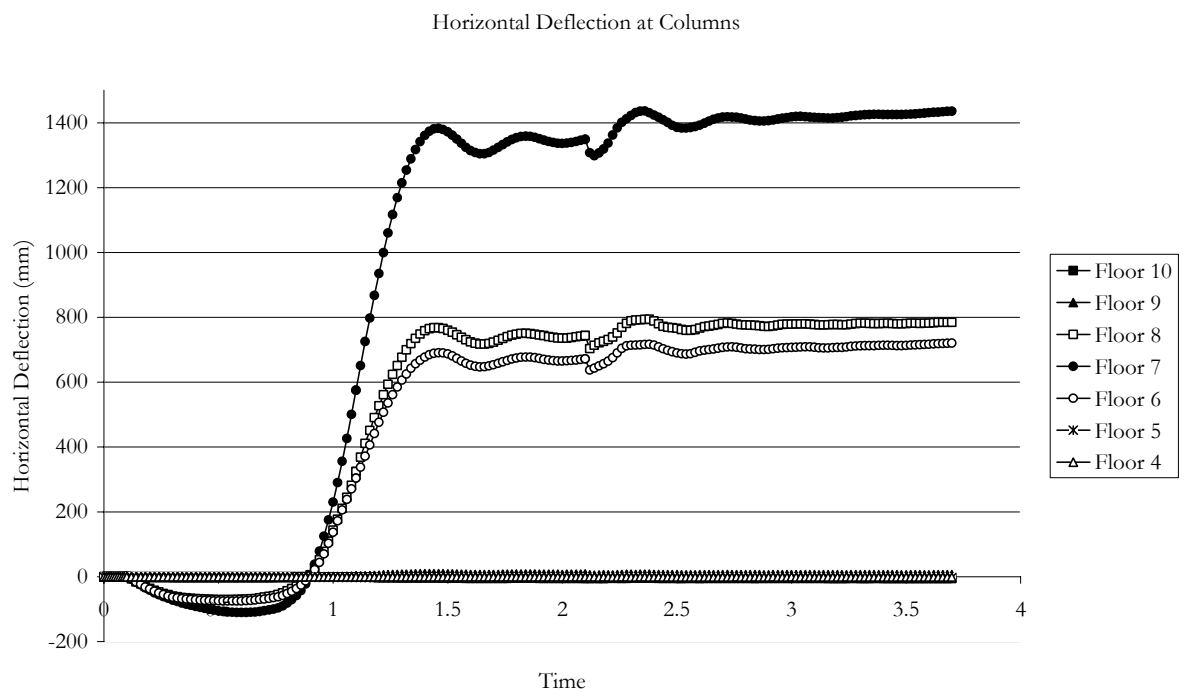


Fig. 4 – Deflected shapes with a buckling and plastic collapse respectively

The vertical deflection for the weak beam model shown in Figure 6 indicates that each section of the column deflects downwards starting with all the floors above the fire floors and gradually each consecutive floor follows. The stiff floor model initially has an upward movement due to the thermal expansion of the column. As the column is being pulled in and the collapse movement is initiated there is a sharp increase in vertical deflection for all the fire floors and those above. Floors 4 and below do not encounter any deflection.

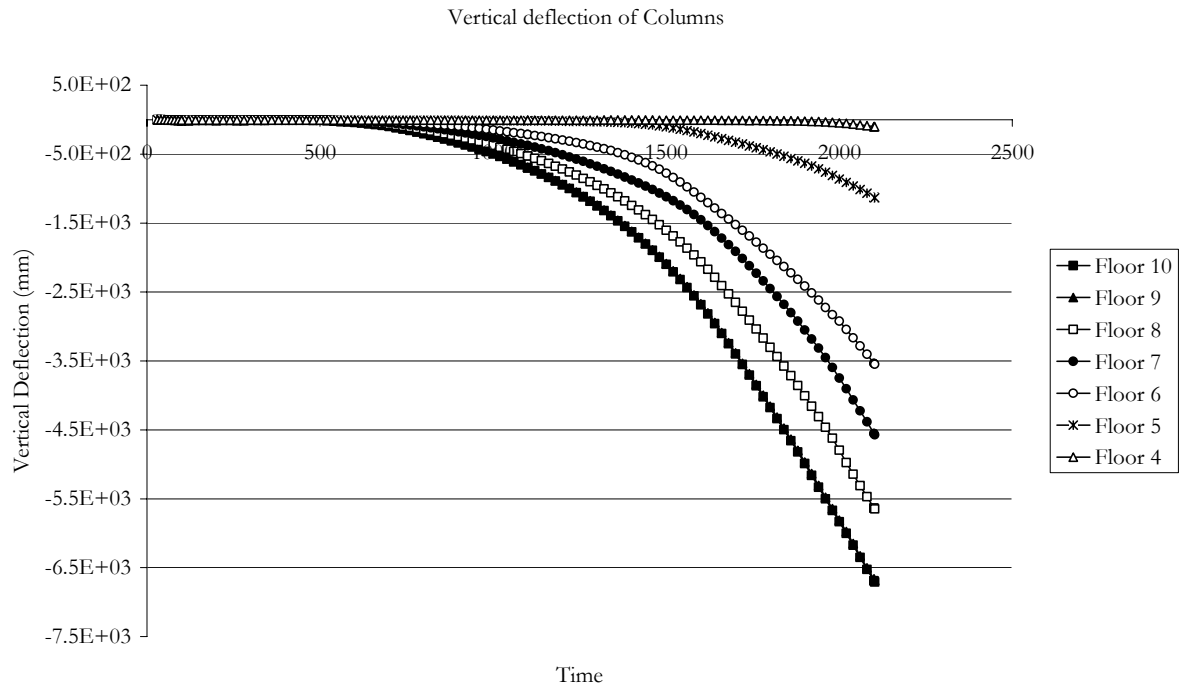


(a) Weak floor mechanism

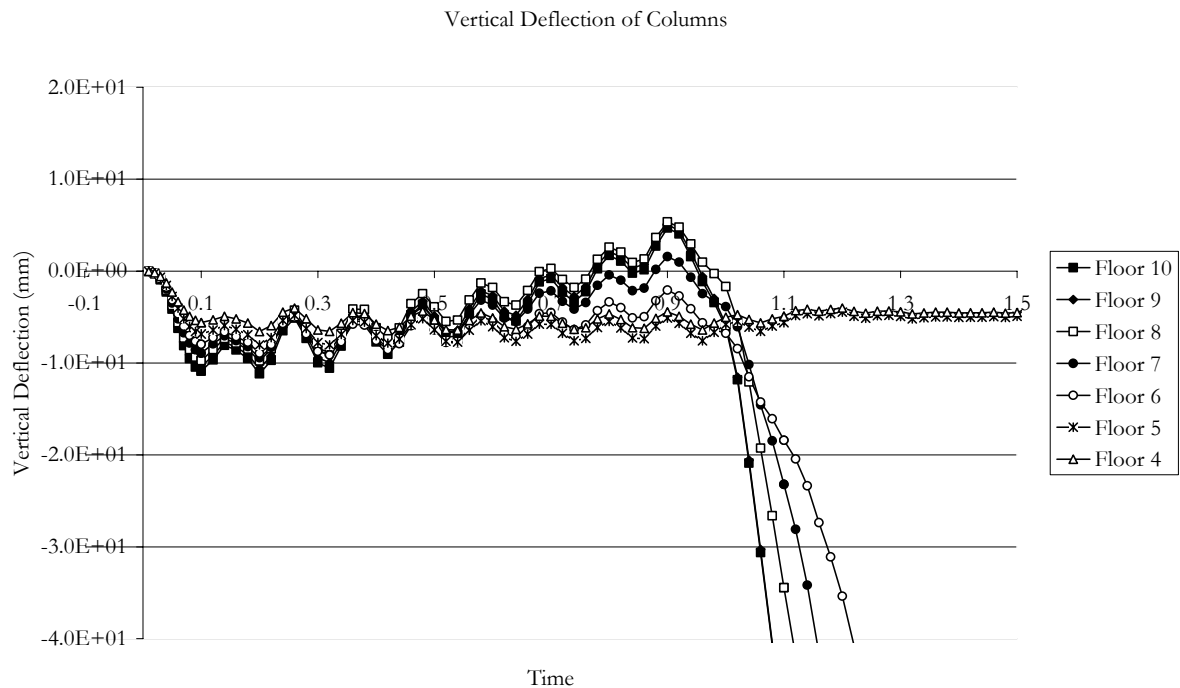


(b) Stiff floor mechanism

Fig.5. – Horizontal deflections of columns



(a) Weak floor mechanism



(b) Stiff floor mechanism

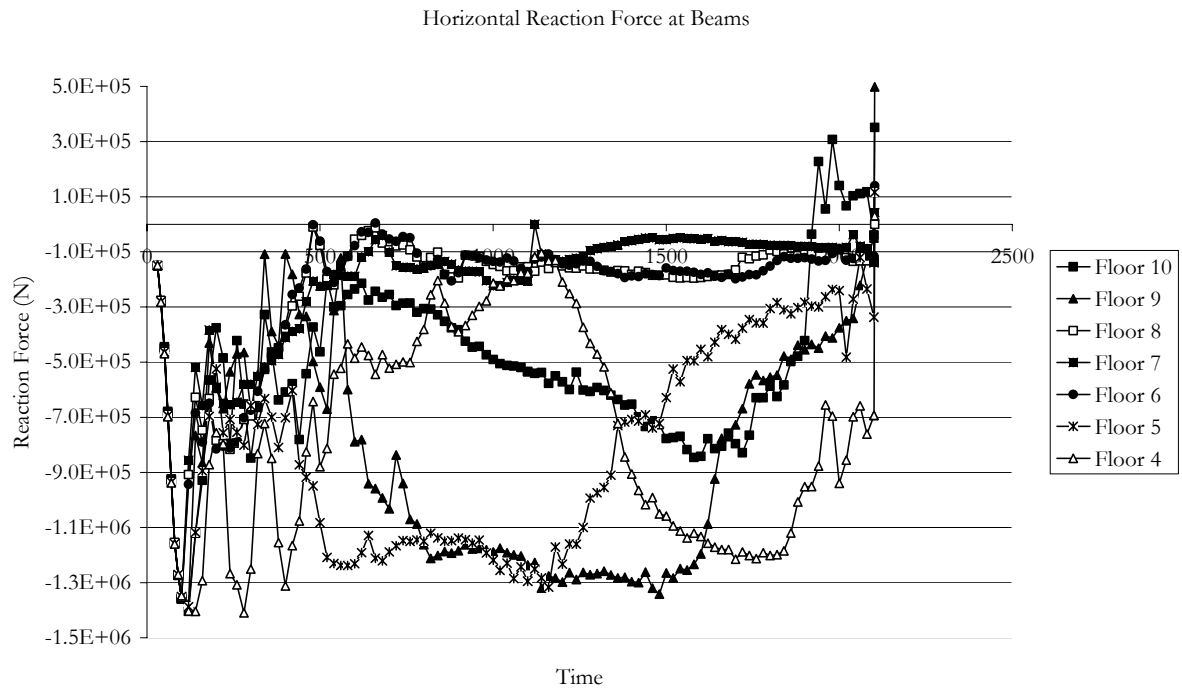
Fig.6 – Vertical deflection of columns

The horizontal reactions at the beam connection to the stiff core show the change in membrane forces over time in Figure 7. The weak floor model indicates that all floors go into an initial state of compression. The three fire floors rapidly reduce in compression until a very small reaction remains. All three floors have buckled at this stage. Floor 5, immediately

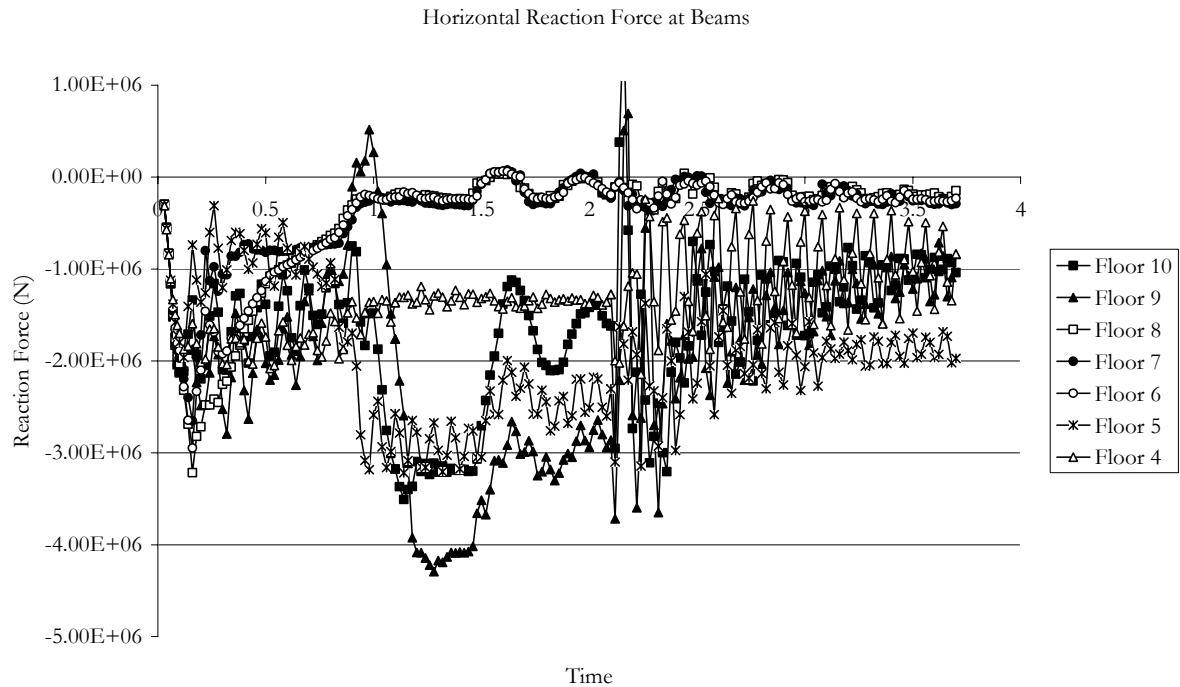
below the fire floors, experiences an increased reaction as the floors above take a reduced amount. When floor five buckles due to the increased force from the column, the reaction quickly reduces. Now floor 4 sees a rapid increase, until this floor buckles. The progressive failure of floors is thus clearly visible from this graph.

The stiff floor system in Figure 7 (b) also starts off with an immediate compression. The three fire floors buckle and during this process the reaction force reduces. At the same time the force is being redistributed to floors 5 and 9, immediately above and below the fire floors. As these floors are relatively strong no further buckling occurs and the column forms hinges to allow for inward movement of the column due to the deformation of the beams.

Research done by Flint³ shows several floors are in tension rather than compression. The exact reason for why the behaviour seen here is different is yet unknown.



(a) Weak floor mechanism



(b) Stiff floor mechanism

Fig.7 – Horizontal reaction forces at the beams

The section capacity of the column is shown in the interaction diagram of the loading and moments in Figure 8. This relates to the section moment for both models in Figure 9 as it shows when plastic hinges are formed. The weak floor model shows that hinges are formed at floor 5, 7 and 9. Although this is similar to the stiff floor model, the overall behaviour is significantly different. As the hinge forms at floor 5, the moment at floor 4 increases until that too hinges. This in turn affects the column at floor 3 which also hinges soon after. This clearly indicates the progressive collapse of the floors and column.

When comparing the section moments at the column and beam connections with the section capacity of the column, hinges can be seen.

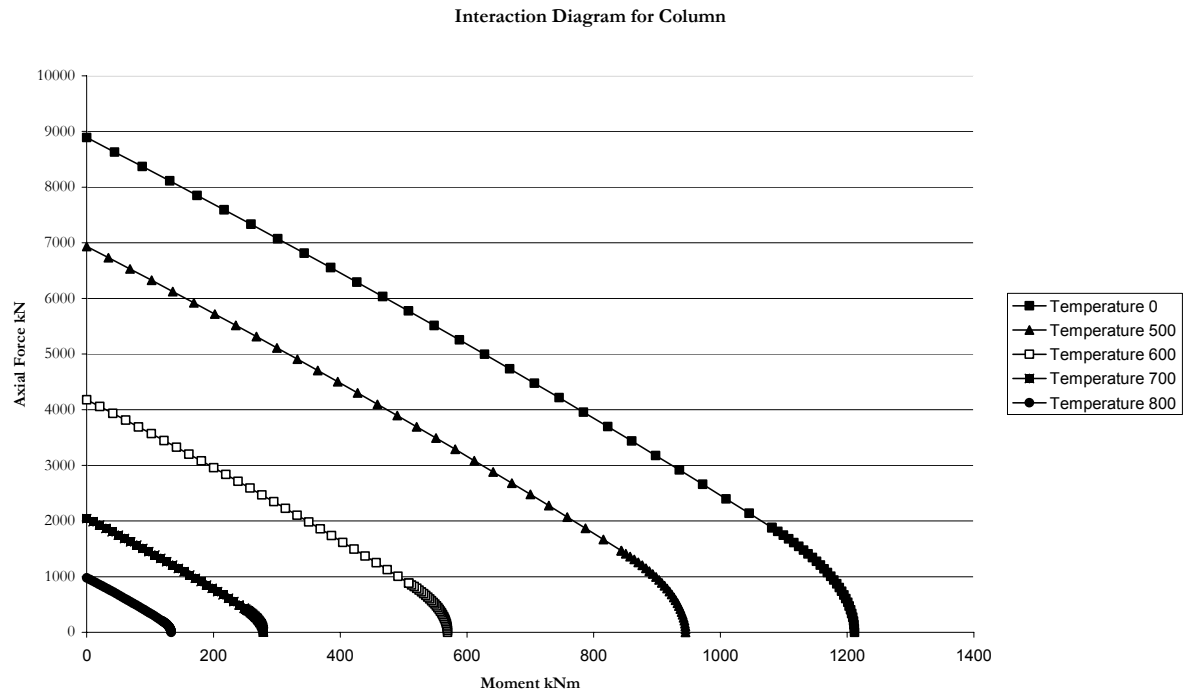
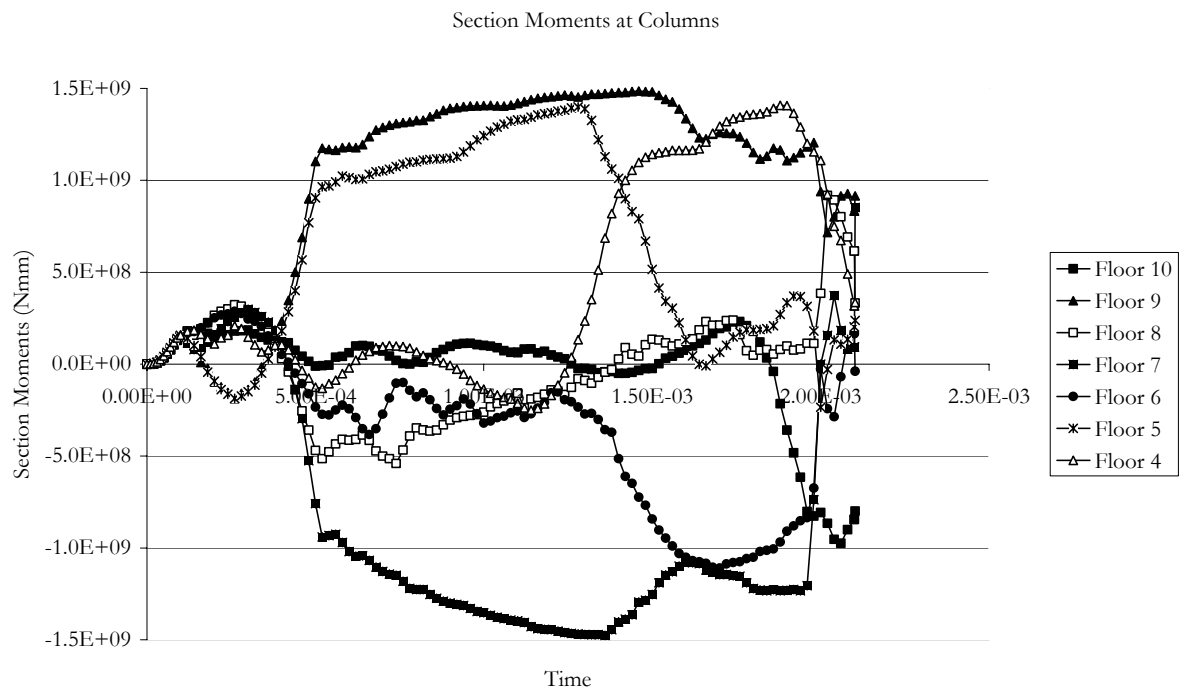
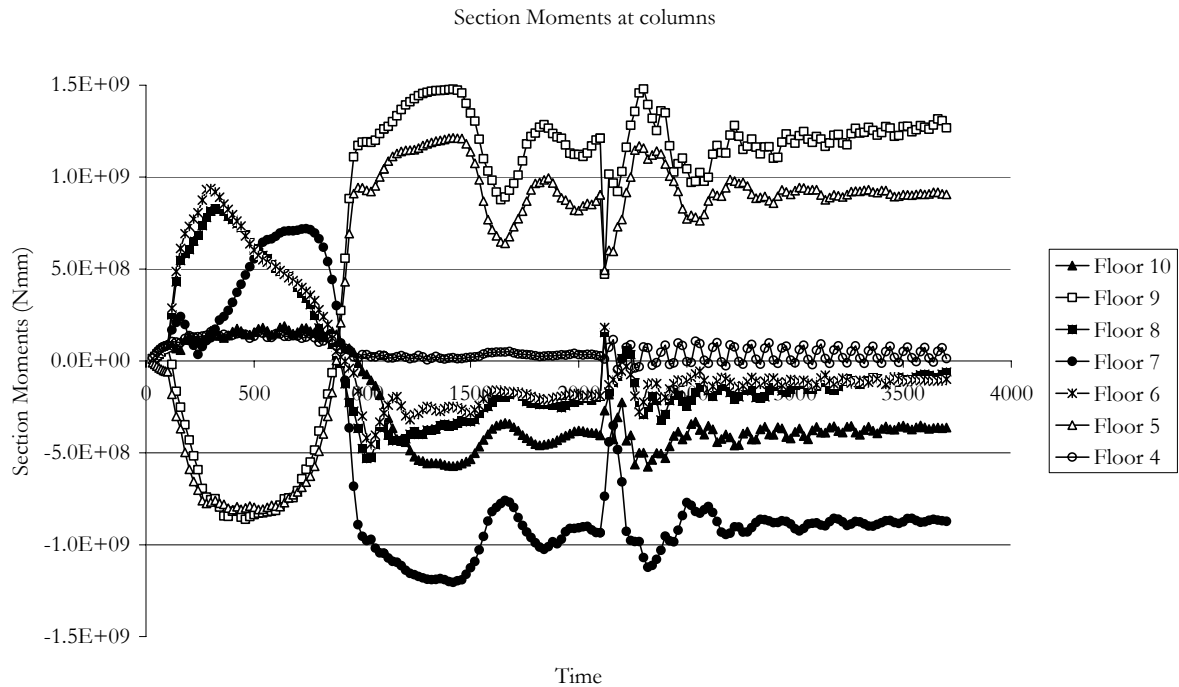


Fig.8 – Interaction Diagram for Column



(a) Weak floor mechanism



(b) Stiff floor mechanism

Fig.9 – Section moments at the column and beam connection

4. A SIMPLE STABILITY ASSESSMENT METHOD FOR TALL BUILDINGS IN MULTIPLE FLOOR FIRE

Figure 10 illustrates a simple method for assessing the stability of columns in tall buildings in multiple (or single) floor fires. The method may be described as follows:

1. Determine the limiting tensile membrane forces in the floors affected by fire. This will involve calculations to obtain the thermally induced displacements and membrane forces in the floor. A detailed description of these can be seen in reference 4.
2. From the membrane forces obtain the moments induced in the columns at the “pivot” floors (adjacent to the fire floors) and the middle fire floor. If an approximation of the column internal displacement can be made, additional P- Δ moments can be calculated.
3. At this point there are two possible mechanisms:
 - a. Calculate the reaction of the pivot floors as shown in Figure 9 (lowest pivot floor is most critical) counteracting the membrane “pull-in” forces (include an appropriate percentage of the column load to this, as the column lateral support requirement is increased due to loss of support at the fire floors). If the floor membrane is unable to provide the reaction calculated, a weak floor failure becomes possible.
 - b. If the floor is able to provide the reaction required, check the temperature dependent moment-force interaction diagram for the column to ensure that the column has not reached the yield surface (and thus formed a plastic hinge). If this is the case then stiff floor failure can occur.

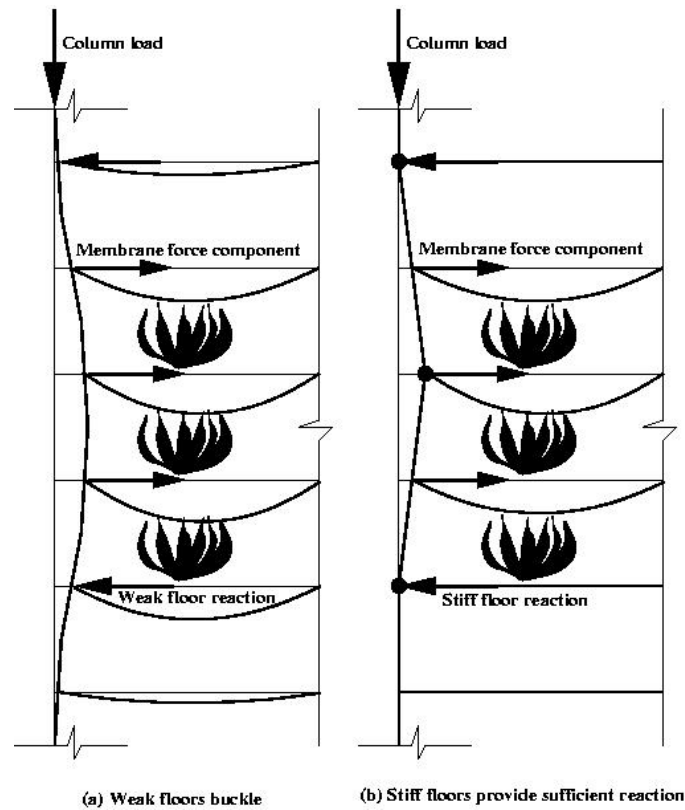


Fig.10 – Mechanics of fire induced collapse in weak and stiff floor buildings

5. CONCLUSION

This paper introduces the hypothesis of two possible failure mechanisms for tall buildings in multiple floor fires. The hypothesis is tested by creating a finite element model of a standard steel frame composite structure. The results of the modelling indicate that the two different failure mechanisms do indeed occur. This conclusion is very important and powerful as it enables the development of a simple stability assessment method for tall buildings in multiple floor fires. A very preliminary exposition of what such a method may entail is also described in the previous section.

6. REFERENCES

- [1]. A.S.Usmani, Y.C.Chung and J.L.Torero. How did the WTC Towers Collapse? A New Theory. *Fire Safety Journal*, 38:501--533, 2003.
- [2]. A.Usmani, Stability of the World Trade Center Twin Towers structural frame in multiple floor fires. *Journal of Engineering Mechanics*, ASCE, 131:654--657, 2005
- [3]. G.R.Flint, *Fire Induced Collapse of Tall Buildings*, PhD thesis, University of Edinburgh, 2005. Available at <http://www.civ.ed.ac.uk/research/fire/thesis.html>
- [4]. N.J.K.Cameron, *The Behaviour and Design of Composite Floor Systems in Fire*, University of Edinburgh, 2004. Available at <http://www.civ.ed.ac.uk/research/fire/thesis.html>

AUTHOR INDEX

ABU, Anthony K.	659
AIK KHOO, Heng	63
ALA-OUTINEN, Tiin	139
ALI, Faris	613, 813
ALLAM, Ahmed	813
ALONSO, C.	599
BADDERS, B. L.	931
BAHR, Oliver	837
BAIERLE, Tomáš	1035
BAILEY, Colin G	709
BAMONTE, Patrick	545
BATISTA, Eduardo de Miranda	427
BÉNICHOU, Nouredine	909
BENNETTS, Ian	161
BERGMEISTER, K.	983
BISBY, Luke A	791
BLAŽEVIČIUS, Žygimantas	63
BLOCK, Florian	345
BONG, Ming Wei	451
BORG, Audun	779
BOSTRÖM, Lars	757
BRADFORD, Mark A.	805
BRECCOLOTTI, Marco	587
BUCHANAN, Andrew H	451, 623,
BURGESS, Ian W	315, 345, 393, 561, 635, 659, 825
CAJOT, Louis-Guy	299
CAMERON, Neil	873
CANGIANO, Stefano	545
CARRÉ, H.	697
CEDERING, Magdalena	975
CHANG, Jeremy	623
CHANG, Peter C.	439
CHICA, Jose Antonio	213
CHOWDHURY, Ershad U.	791
COCCIA, Simona	767
COLOMBO, Matteo	721
COOKE, Gordon	101, 405
CRAFT, Steven	939
DAVISON, Buick	315, 345
DELICHATSIOS, Michael	1065
DESANGHERE, Sylvain	213
DHAKAL, Rajesh	451, 623
DHIERSAT, M.	683
DHIMA, Dhionis	405, 899, 1005
DOTREPPE, Jean-Claude	885
EL-DIB, Mohamed E.	13
ELGHAZOULI, A.Y.	379
EL-HUSSEINY, Ossama M.	13
EL-KORCHI, Tahar	1077
FAKURY, Ricardo Hallal	1023
FELICETTI, Roberto	721

FLETCHER, Ian	779
FLINT, Graeme	415, 527
FONTANA, Mario	113, 963
FORNATHER, J.	983
FOSTER, S. J.	635
FRANGI, Andrea	963
FRANSSEN, Jean-Marc	127, 151, 885, 1065
FROMY, Philippe	1005
FUJIMOTO, Kentaro	511
FUJITA, Masaru	511
GAMBAROVA, Pietro G	545
GANN, Richard G.	1047
GARDNER, Leroy	247
GARLOCK, Maria E.M.	175, 187
GAVILÁN, Ana Ramos	849
GILLIE, M.	861
GREEN, Mark F.	791
GRIJALVO, J.	1017
GUO, Shi Xiong	41
HADJISOPHOCLEOUS, George	63, 939
HAGER, I.	697
HALLER, Mike	299
HAMINS, Anthony	499
HASEMI, Yuji	225
HAWES, Mike	813
HEISE, Alexander	357, 487
HIRASHIMA, Takeo	511
HITCHEN, Neil	779
HUANG, Zhaohui	393, 561, 825
ISGOR, Burkan	939
IWANKIW, Nestor	993
IZZUDDIN, B.A.	379
JANSSON, Robert	747, 757
JOHNSTON, Louise	527
JOWSEY, Allan	259, 527
JOYEUX, Daniel	213
KAITILA, Olli	89, 139, 213
KÄLLSNER, Bo	951
KAMIKAWA, Daisuke	225
KANG, Yu	63
KAY, Alexandra	299
KETTNER, Florian	139
KNOBLOCH, Markus	113
KODUR, Venkatesh	573, 791, 837
KÖNIG, Jürgen	951, 983
KORHONEN, Timo	89
KORZEN, Manfred	273
KVEDARAS, Audronis Kazimieras	63
KWON, Kihyon	235
LA QUINTANA, J. de	1017
LABORDERIE, C.	697
LAMONT, Susan	259, 415, 487, 861
LANDESMANN, Alexandre	427
LANE, Barbara	259, 415, 487

LANGE, David	873
LAPLANCHE, Karine	899
LEE, Byoung-Jun	235
LI, Guo-Qiang	41, 327
LI, Yu Guang,	473, 511
LIANG, Hong,	287
LOPES, Nuno	127, 151, 463
LOU, Guo-Biao	327
MAHENDRAN, Mahen	29, 53
MALJAARS, Johan	75
MANZELLO, Samuel L.	1047
MATAR, Ehab B.	13
MATERAZZI, Annibale Luigi	587
MEDA, Alberto	647
MEHAFFEY, Jim	931, 939
MESQUITA, Luís	463, 849
MINDEGUIA, J.C.	683, 697
MIRAMBELL, Enrique	127
MOSS, Peter	451, 623
MOTEVALLI, Vahid	1077
NADJAI, Ali	613, 813, 1065
NAKAMURA, Masatoshi	225
NEVES, I. Cabrita	273
NIEDEREGGER, Philipp	113
OZAKI, Fuminobu	113
PANNONI, Fabio Domingos	1023
PAŠEK, Jan	1059
PERSSON, Bertil	735
PESSIKI, Stephen	235
PHAN, L.	573
PILOTO, Paulo	463, 849
PIMIENTA, P.	683, 697
PINTEA, Dan	885
PLANK, Roger	315, 345, 393, 561, 635, 671, 825
POZZI, Claudio	487
PRASAD, Kuldeep	499
PROE, David	161
QUIEL, Spencer E.	175, 187
QUINTIERE, James G.	439
RACHER, Patrick	899
RAFI, Muhammad Masood	613
RANAWAKA, Thanuja	29, 53
RENAUD, C.	199
RESZKA, Pedro	921
REY, F.	1017
RICHARDSON, L. R.	931
RINALDI, Zila	767
RINI, Darlene	259
RIVA, Paolo	647
ROBEN, Charlotte	527
RODRIGUES, Francisco Carlos	1023
RODRIGUES, João Paulo C.	273
SALEM, Osama F.	13
SARRAJ, M.	315

SCHAUMANN, Peter	139, 357, 837
SCHMIDT, J.	983
SEGAWA, Hirofumi	511
SILVA, Valdir Pignatta e	1023
SIMÕES DA SILVA, Luís	127, 151, 463
SIMON, A.	683
SOETENS, Frans	75
STREJČEK, Michal	371
SULONG, N.H. Ramli	379
TAILLEFER, Nicolas	1005
TALAMONA, Didier	613, 813
TAN, Kang-Hai	3
THOMAS, Ian	161
TICHÁ, Alena	371
TOFILO, Piotr	1065
TOH, Wee Siang,	709
TORERO, Jose	259, 415, 873, 921
TWILT, Leen	75
UESUGI, Hideki	473, 511
UHLÍŘ, Antonín	1035, 1059
UNANUA, J.	1017
USMANI, Asif	415 527, 861, 873
VALENTE, Joaquim C.	273
VASSART, Olivier	813
VENANZI, Ilaria	587
VILA REAL, Paulo	127, 151, 463
VIRDI, Kuldeep S.	101
WAKAMATSU, Takao	473
WALD, František	371, 1035, 1059
WANG, Ming	439
WANG, Zhi-Hua	3
WELCH, Stephen	287, 779
WINKLER, Wolfgang	873
YAMADA, Kaori	225
YU, Chaoming	393
YU, Ximmeng	825
ZEHFUSS, Jochen	519
ZHAO, B.	199

10-12 may 2006
Aveiro, Portugal

SiF'06

proceedings of the
4th international
workshop
structures in fire

Paulo Vila Real
Jean-Marc Franssen
Nuno Lopes

SiF'06

proceedings of the
4th international workshop
structures in fire
volume 2

edited by
Paulo Vila Real
Jean-Marc Franssen
Nuno Lopes

ISBN 972-789-190-X



**Fourth International
Workshop
Structures in Fire**

SiF'06

Fourth International Workshop Structures in Fire

SiF'06

PROCEEDINGS OF THE FOURTH INTERNATIONAL WORKSHOP
STRUCTURES IN FIRE

University of Aveiro
Aveiro, Portugal
10-12 May, 2006

Volume 2

Paulo Vila Real
Department of Civil Engineering
University of Aveiro
Aveiro, Portugal

Jean-Marc Franssen
Department M&S
University of Liege
Liege, Belgium

Nuno Lopes
Department of Civil Engineering
University of Aveiro
Aveiro, Portugal



Department of Civil Engineering
University of Aveiro

**Proceedings of the Fourth International Workshop
Structures in Fire**

Copyright © 2006 Paulo Vila Real, Jean-Marc Franssen and Nuno Lopes

Edited by:
Paulo Vila Real
Jean-Marc Franssen
Nuno Lopes

1st Edition
May, 2006

No part of this publication may be reproduced, stored in a retrieval system, or transmitted in any form or by means, electronic, mechanical photocopying or otherwise, without permission in writing from the Publisher.

ISBN: 972-789-190-X

Published by:
UNIVERSIDADE DE AVEIRO
CAMPUS UNIVERSITÁRIO DE SANTIAGO
3810-193 AVEIRO
PORTUGAL

Editor note

Although all care was taken to ensure the integrity and quality of this publication and the information on herein, no responsibility is assumed by the publisher nor the authors for any damage to property or persons as a result of operation or use of this publication and/or use of the information contained herein.

FOREWORD

The SiF Workshops were created to form an International Forum where experts in the field of structural fire engineering could present their research activities and receive feedback from their colleagues.

The 1st SiF workshop was held in Copenhagen, Denmark in 2000, the 2nd SiF took place in Christchurch, New Zealand in 2002 and the 3rd in Ottawa, Canada in 2004, providing fire resistance researchers with the opportunity to meet, present papers, establish collaborations and discuss their work with their peers.

Following the great success of these three workshops, the University of Aveiro was selected to host the fourth International Workshop in the series SiF-Structures in Fire, which was held in Aveiro, Portugal from 10 to 12 May 2006.

The focus of the workshop was on the behaviour of structures under fire conditions. Papers were accepted on the basis of their quality and originality. Answering to the call-for-papers, 133 abstracts were received, from which 111 were selected by the Scientific Committee for possible presentation at the Workshop. These abstracts led to 91 technical papers published in these proceedings and were grouped in the following topics:

- Steel, Stainless Steel and Aluminium Structural Members
- Steel Connections
- Structural Behaviour
- Concrete Structures
- Composite Structures
- Timber Structures
- Fire Safety Engineering
- Other Topics

These proceedings include papers from 197 authors from 25 countries: Australia, Austria, Belgium, Brazil, Canada, China, Czech Republic, Egypt, Finland, France, Germany, Italy, Japan, Lithuania, Luxemburg, The Netherlands, New Zealand, Poland, Portugal, Singapore, Spain, Sweden, Switzerland, United Kingdom and United States of America.

We hope that the high quality of these contributions will develop a better understanding of the new approaches for robust design of structures under fire conditions.

Sincere thanks to the scientific committee, the workshop secretariat, the authors and the sponsoring organizations for their contribution to the success of the Workshop.

Paulo Vila Real
Chairman of the organizing committee

Jean-Marc Franssen
Chairman of the scientific committee

COMMITTEES

Organizing committee

Paulo Vila Real (Chairman)	<i>University of Aveiro, Portugal</i>
Nuno Lopes (Co-chairman)	<i>University of Aveiro, Portugal</i>
Paulo Cachim	<i>University of Aveiro, Portugal</i>
Paulo Piloto	<i>Polytechnic Institute of Bragança, Portugal</i>
João Paulo Rodrigues	<i>University of Coimbra, Portugal</i>
Joaquim Valente	<i>Technical University of Lisbon, Portugal</i>
Aldina Santiago	<i>University of Coimbra, Portugal</i>

Scientific committee

Jean-Marc Franssen (Chairman)	<i>University of Liege, Belgium</i>
Andrew Buchanan	<i>University of Canterbury, New Zealand</i>
Asif Usmani	<i>University of Edinburgh, U. K.</i>
Barbara Lane	<i>Arup Fire, U. K.</i>
Bin Zhao	<i>C. T. I. C. M., France</i>
Farid Alfawakhiri	<i>American Institute of Steel Construction, U. S. A.</i>
Guo-Qiang Li	<i>Tongji University, Shanghai, China</i>
Ildefonso Cabrita Neves	<i>Technical University of Lisbon, Portugal</i>
James Milke	<i>University of Maryland, U. S. A.</i>
Joris Fellingier	<i>Centre Information Acier, Belgium</i>
Jürgen König	<i>SP Trätek/Wood Technology, Sweden</i>
Jyri Outinen	<i>Finnish Constructional Steelwork Association, Finland</i>
Kang Hai Tan	<i>Nanyang Technological University, Singapore</i>
Kazunori Harada	<i>University of Kyoto, Japan</i>
Kuldeep Prasad	<i>N. I. S. T., U. S. A.</i>
Luís Simões da Silva	<i>University of Coimbra, Portugal</i>
Michel Njankouo	<i>University of Yaounde, Cameroun</i>
Mario Fontana	<i>E. T. H. Hönggerberg, Zürich, Switzerland</i>
Paulo Vila Real	<i>University of Aveiro, Portugal</i>
Peter Moss	<i>University of Canterbury, New Zealand</i>
Rajesh Dhakal	<i>University of Canterbury, New Zealand</i>
Richard Liew	<i>National University of Singapore, Singapore</i>
Valdir Pignatta e Silva	<i>University of São Paulo, Brazil</i>
Venkatesh Kodur	<i>National Research Council, Canada</i>

SPONSORS

FUNDAÇÃO
LUSO-AMERICANA



SUPPORTERS



TABLE OF CONTENTS

VOLUME I

FOREWORD	V
COMMITTEES	VII
SPONSORS	IX
TABLE OF CONTENTS	XI

STEEL, STAINLESS STEEL AND ALUMINIUM STRUCTURAL MEMBERS

• Time delay coefficient of temperature formulations in EC3 Part 1-2 and classification of fire protection materials Zhi-Hua WANG and Kang-Hai TAN	3
• Behavior of stainless steel sections subjected to non-homogenous temperatures Ossama M. EL-HUSSEINY, Mohamed E. EL-DIB, Ehab B. MATAR and Osama F. SALEM	13
• Experimental investigation of cold-formed steel columns subject to distortional buckling under simulated fire conditions Thanuja RANAWAKA and Mahen MAHENDRAN	29
• Analysis of restrained heated steel beams during cooling phase Guo-Qiang LI and Shi Xiong GUO	41
• Mechanical properties of thin steels at elevated temperatures Thanuja RANAWAKA and Mahen MAHENDRAN	53
• The effect of partial fire protection loss on the fire resistance reduction of steel beams Yu KANG, George V. HADJISOPHOCLEOUS and Heng AIK KHOO	63
• Heating of aluminium members exposed to natural fire conditions Johan MALJAARS, Frans SOETENS and Leen TWILT	75
• Simple thermal calculation methods for steel columns protected with steel casings and layered steel balcony slab structures Olli KAITILA and Timo KORHONEN	89
• Experimental and numerical study of a two-span steel I-Beam heated along the lower flange Kuldeep S. VIRDI and Gordon COOKE	101

<ul style="list-style-type: none"> • Studies on local buckling of heated steel columns with box sections by using finite element analyses Fuminobu OZAKI, Philipp NIEDEREGGER, Markus KNOBLOCH and Mario FONTANA 	113
<ul style="list-style-type: none"> • Proposal to the Eurocode 3 for the lateral-torsional buckling of Stainless steel I-beams in case of fire Nuno LOPES, Paulo VILA REAL, Luís SIMÕES DA SILVA, Jean-Marc FRANSSSEN and Enrique MIRAMBELL 	127
<ul style="list-style-type: none"> • Light weight structures exposed to fire: a stainless steel sandwich panel Tiina ALA-OUTINEN, Peter SCHAUMANN, Olli KAITILA and Florian KETTNER 	139
<ul style="list-style-type: none"> • Numerical validation of an improved proposal to the Eurocode 3 for the lateral-torsional buckling of steel beams subjected to fire. Paulo VILA REAL, Nuno LOPES, Luís SIMÕES DA SILVA and Jean-Marc FRANSSSEN 	151
<ul style="list-style-type: none"> • Testing and analysis of catenary action in unprotected steel beams subjected to fire David PROE, Ian BENNETTS and Ian THOMAS 	161
<ul style="list-style-type: none"> • A performance-based design approach for steel perimeter columns subject to fire Spencer E. QUIEL and Maria E.M. GARLOCK 	175
<ul style="list-style-type: none"> • Combined Axial Load and Moment Capacity of Fire-Exposed Beam-Columns with Thermal Gradients Maria E.M. GARLOCK and Spencer E. QUIEL 	187
<ul style="list-style-type: none"> • Investigation of simple calculation method in EN 1993-1-2 for buckling of hot rolled class 4 steel members exposed to fire C. RENAUD and B. ZHAO 	199
<ul style="list-style-type: none"> • Use of simplified methods for designing external members protection Daniel JOYEUX, Sylvain DESANGHERE, Olli KAITILA and Jose Antonio CHICA 	213
<ul style="list-style-type: none"> • Mechanical responses of a steel column exposed to a localized fire Daisuke KAMIKAWA, Yuji HASEMI, Kaori YAMADA and Masatoshi NAKAMURA 	225
<ul style="list-style-type: none"> • Fire load behavior of steel building columns with damaged spray-applied fire resistive material Stephen PESSIKI, Kihyon KWON and Byoung-Jun LEE 	235
<ul style="list-style-type: none"> • Stainless steel structures in fire Leroy GARDNER 	247
<ul style="list-style-type: none"> • Critical Behaviour of Long Span Cellular Beams in Fire Darlene RINI, Allan JOWSEY, Jose L. TORERO, Barbara LANE and Susan LAMONT 	259
<ul style="list-style-type: none"> • Behaviour in fire of thermally restrained compressed steel members. Experimental and numerical approach Manfred KORZEN, I. Cabrita NEVES, João Paulo C. RODRIGUES and Joaquim C. VALENTE 	273

- **A Novel Engineering Tool For Thermal Analysis of Structural Members in Natural Fires**
Hong LIANG and Stephen WELCH
..... 287
- **Development of a method to calculate the temperature of a column exposed to localised fire, according to the EC1 and EC3 fire parts**
Mike HALLER, Alexandra KAY and Louis-Guy CAJOT
..... 299

STEEL CONNECTIONS

- **Finite element modelling of fin plate steep connections in fire**
M. SARRAJ, I. W. BURGESS, J. B. DAVISON and R. J. PLANK
..... 315
- **Nonlinear Finite Element Modelling of Behavior of Extended End-plate Bolted Moment Connections in Fire**
Guo-Biao LOU and Guo-Qiang LI
..... 327
- **The development of a component-based connection element for endplate connections in fire**
Florian BLOCK, Ian BURGESS, Buick DAVISON and Roger PLANK
..... 345
- **Connections of unprotected steel members to fire walls**
Alexander HEISE and Peter SCHAUMANN
..... 357
- **On bolted connection with intumescent coatings**
František WALD, Michal STREJČEK and Alena TICHÁ
..... 371
- **Behaviour and design of beam-to-column connections under fire conditions**
N.H. Ramli SULONG, A.Y. ELGHAZOU LI and B.A. IZZUDDIN
..... 379

STRUCTURAL BEHAVIOUR

- **3D Modelling of bi-steel structures subject to fire**
Chaoming YU, Z. HUANG, I. W. BURGESS and R. J. PLANK
..... 393
- **Structural analysis of a heated steel portal frame by two different methods**
Gordon COOKE and Dhionis DHIMA
..... 405
- **Fire induced collapse of tall buildings**
Graeme FLINT, Asif USMANI, Susan LAMONT, Barbara LANE and José TORERO
..... 415
- **Refined plastic hinge model for the analysis of steel-framed structures under fire conditions**
Alexandre LANDESMANN and Eduardo de Miranda BATISTA
..... 427
- **Scale modelling of insulated steel framed structure testing in fire**
Ming WANG, Peter C. CHANG and James G. QUINTIERE

.....	439
• Structural fire performance of steel portal frame buildings Peter MOSS, Rajesh DHAKAL, Ming Wei BONG and Andy BUCHANAN	451
• Numerical modeling of the behaviour of a stainless steel portal frame subjected to fire Nuno LOPES, Paulo VILA REAL, Paulo PILOTO, Luís MESQUITA and Luís S. da SILVA	463
• Comparison of analytical models for fire resistance performance of steel structures Yu Guang LI, Hideki UESUGI and Takao WAKAMATSU	473
• The role of large strains and consequent mitigation measures for buildings in fire Claudio POZZI, Barbara LANE, Susan LAMONT and Alexander HEISE	487
• Fire Structure Interface and the Thermal Response of the World Trade Center Towers Kuldeep PRASAD and Anthony HAMINS	499
• Influence of concrete floor slab on stress-deformation behaviour of high-rise steel frame exposed to compartment fire Takeo HIRASHIMA, Yu Guang LI, Masaru FUJITA, Hirofumi SEGAWA, Kentaro FUJIMOTO and Hideki UESUGI	511
• Practical application of engineering methods for fire safety design of structures Jochen ZEHFUSS	519
• Tall building collapse mechanisms initiated by fire Asif USMANI, Charlotte ROBEN, Louise JOHNSTON, Graeme FLINT and Allan JOWSEY	527
• Author Index	539

VOLUME II

CONCRETE STRUCTURES

• Thermo-Mechanical behavior of concrete mixes suitable for the rehabilitation of fire-damaged tunnel liner Patrick BAMONTE, Stefano CANGIANO and Pietro G. GAMBAROVA	545
• Behaviour of reinforced concrete structures in fire Zhaohui HUANG, Ian W. BURGESS and Roger J. PLANK	561
• Factors governing the fire performance of high strength concrete systems V.K.R. KODUR and L. PHAN	573
• Fire performance of HPLWC hollow core slabs Marco BRECCOLOTTI, Annibale Luigi MATERAZZI and Ilaria VENANZI	587
• Assessment of damage in concrete structures exposed to fire. Micro and macrostructural analysis C. ALONSO	599
• Performance of carbon FRP reinforced concrete beams Muhammad Masood RAFI, Ali NADJAI, Faris ALI and Didier TALAMONA	613
• Analysis of hollowcore concrete floor slabs under fire Jeremy CHANG, Andrew H. BUCHANAN, Rajesh DHAKAL and Peter J. MOSS	623
• Modelling membrane action of model-scale slabs at ambient and elevated temperatures S. J. FOSTER, I. W. BURGESS and R. PLANK	635
• Behaviour of precast R.C. elements under fire conditions Alberto MEDA and Paolo RIVA	647
• Experimental Evaluation of Compression Resistance of HC-FST Columns After Fire Audronis Kazimieras KVEDARAS and Žygimantas BLAŽEVIČIUS	659
• Effects of thermal gradients on membrane stresses in thin slabs Anthony K. ABU, Ian W. BURGESS and Roger J. PLANK	671
• Behaviour of the UHPFRC BSI® at high temperatures J.C. MINDEGUIA, M. DHIER SAT, A. SIMON and P. PIMIENTA	683
• Experimental study of transient thermal strain and creep of an ordinary concrete at high temperatures J.C. MINDEGUIA, P. PIMIENTA, I. HAGER, C. LABORDERIE and H. CARRÉ	697

• Experimental behaviour of concrete floor slabs at ambient and elevated temperatures Colin G. BAILEY and Wee Siang TOH	709
• New NDT techniques for the assessment of fire damaged concrete structures Matteo COLOMBO and Roberto FELICETTI	721
• Transient thermal strain of Self-Compacting Concrete – with and without polypropylene fibres Bertil PERSSON	735
• Liquid/steam pressure measurement inside concrete exposed to fire Robert JANSSON	747
• Spalling of self compacting concrete Lars BOSTRÖM and Robert JANSSON	757
• Residual strength of R.C. Beams after fire Simona COCCIA and Zila RINALDI	767
• Performance of concrete in fire: a review of the state of the art, with a case study of the Windsor Tower fire Ian FLETCHER, Audun BORG, Neil HITCHEN and Stephen WELCH	779
• Performance in fire of insulated FRP-Wrapped reinforced concrete columns Ershad U. CHOWDHURY, Luke A. BISBY, Mark F. GREEN and Venkatesh K.R. KODUR	791

COMPOSITE STRUCTURES

• Generic model for a composite T-Beam at elevated temperature Mark A. BRADFORD	805
• Performance of cellular composite floor beams at elevated temperatures Ali NADJAI, Olivier VASSART, Faris ALI, Didier TALAMONA, Ahmed ALLAM and Mike HAWES	813
• Thermal and structural behaviour of orthotropic slabs in fire Xinmeng YU, Zhaohui HUANG, Ian W. BURGESS and Roger J. PLANK	825
• Fire resistance of high-strength concrete-filled steel columns Peter SCHAUMANN, Venkatesh KODUR and Oliver BAHR	837
• Numerical modelling of lateral torsional buckling for partially encased steel beams at elevated temperatures P.A.G PILOTO, L.M.R MESQUITA and Ana Ramos GAVILÁN	849
• The effect of edgebeam protection on composite structures in fire S. LAMONT, M. GILLIE and A.S. USMANI	861

- **A performance based design methodology for composite floor slabs in fire**
David LANGE, Asif USMANI, Neil CAMERON, Wolfgang WINKLER and Jose TORERO
..... 873
- **Numerical analysis of the effect of localised fires on composite steel concrete buildings**
Jean-Marc FRANSSSEN, Dan PINTEA and Jean-Claude DOTREPPE
..... 885

TIMBER STRUCTURES

- **Thermo-mechanical modelling of the timber connection behaviour under fire**
Patrick RACHER, Karine LAPLANCHE and Dhionis DHIMA
..... 899
- **Predicting the structural fire performance of solid wood-framed floor assemblies**
Noureddine BÉNICHOU
..... 909
- **In-depth temperature measurements of timber in fires**
Pedro RESZKA and Jose L.TORERO
..... 921
- **Using Commercial FEA Software Packages to Model The Fire Performance of Exposed Glulam Beams**
B.L. BADDERS, J.R. MEHAFFEY, and L.R. RICHARDSON
..... 931
- **Predicting the fire resistance of light-frame wood floor assemblies**
Steven CRAFT, George HADJISOPHOCLEOUS, Burkan ISGOR and Jim MEHAFFEY
..... 939
- **Modelling resistance of wooden I-Joists exposed to fire**
Jürgen KÖNIG and Bo KÄLLSNER
..... 951
- **Fire behaviour of timber block walls**
Andrea FRANGI and Mario FONTANA
..... 963
- **Effect on the charring rate of wood in fire due to oxygen content, moisture content and wood density**
Magdalena CEDERING
..... 975
- **Simulation of cross laminated timber boards under Fire Exposure**
J. SCHMIDT, J. KÖNIG, J. FORNATHER and K. BERGMEISTER
..... 983

FIRE SAFETY ENGINEERING

- **Segmentation of analysis/design levels for structural fire engineering**
Nestor IWANKIW
..... 993
- **Application of FSE to an industrial building**
Nicolas TAILLEFER, Dhionis DHIMA and Philippe FROMY
..... 1005

• Fire safety engineering analysis of a single storey framed building based on structural global behaviour J. DE LA QUINTANA, J. GRIJALVO, F. REY and J. UNANUA	1017
• A real fire in small apartment – a case study Valdir Pignatta e SILVA, Ricardo Hallal FAKURY, Francisco Carlos RODRIGUES and Fabio Domingos PANNONI	1023
• Accuracy in predicting the temperature evolution in compartment fires Antonín UHLÍŘ, Tomáš BAIERLE and František WALD	1035

OTHER TOPICS

• An Experimental Investigation of Gypsum Board Partition Assembly Performance Under Real Fire Exposures Samuel L. MANZELLO and Richard G. GANN	1047
• Experience with thermo imaging cameras on fire tests Jan PAŠEK, František WALD and Antonín UHLÍŘ	1059
• Thermal stresses in glazing systems in buildings Piotr TOFILO, Michael DELICHATSIOS, Ali NADJAI and Jean-Marc FRANSSEN	1065
• Investigation of Fire Performance of Structural Members Incorporating Fiber Reinforced Plastic Composites used Scaled Experimental Enclosure Fires Vahid MOTEVALLI and Tahar EL-KORCHI	1077
• Author Index	1089

Concrete Structures



THERMO-MECHANICAL BEHAVIOR OF CONCRETE MIXES SUITABLE FOR THE REHABILITATION OF FIRE-DAMAGED TUNNEL LINERS

Patrick BAMONTE¹, Stefano CANGIANO²
and Pietro G. GAMBAROVA³

ABSTRACT

Five concrete mixes containing three types of aggregate (siliceous, calcareous and basalt) and three types of cement (blended, blast-furnace and portland), but no silica fume or fly ash, and no fibers, are investigated in this research project, in order to have information about the temperature sensitivity of 15 cementitious composites ($f_c = 40\text{-}75$ MPa) to be used in fire-damaged tunnels, for the rehabilitation of the liner, or in new tunnels. Since the structural behavior during and after a fire depends on the interaction between the mechanical properties (either “hot” or “residual”) and the thermal properties of the concrete, here the residual mechanical properties are investigated (compressive and tensile strengths, elastic modulus), as well as the mass per unit volume and the thermal diffusivity, and comparisons are made with the indications given by EC-2 “Fire Design”. On the whole, the results of previous studies on the subject are confirmed, but in several cases a rather unexpected closeness of the residual behavior to the hot behavior is observed, as well as a non marginal role for the cement type.

1. INTRODUCTION

Several dramatic fires have occurred in the last ten to fifteen years in railway and road tunnels, in most cases with heavy human losses, high socio-economical consequences and serious structural damages¹. Among the 5 major fires since 1996 in heavily-trafficked tunnels (English Channel 1996; Mont Blanc and Tauerns 1999, S.Gothard 2001 and Frejus 2005), the second should be remembered as the most serious in terms of human and economical losses (close to 40 casualties; close to 350 millions of Euros, evenly divided between the costs for tunnel rehabilitation and updating, and the costs for traffic rerouting, revenue losses included.

¹PhD Research Associate, Department of Structural Engineering, Milan University of Technology, 20133 Milan, Italy, e-mail: bamonte@stru.polimi.it.

²Senior Researcher, CTG-Italcementi, Bergamo, Italy, email: s.cangiano@itcgr.net.

³Professor, Department of Structural Engineering, Milan University of Technology, 20133 Milan, Italy, e-mail: pietro.gambarova@polimi.it.

As it is well known, the fundamental requirements for any temperature-resistant concrete are (a) to keep the mechanical properties during and after a fire as close as possible to the original ones, (b) to have a sufficiently-large thermal diffusivity in order to limit the thermal gradients in massive lightly-reinforced structures, in order to prevent the spalling of the concrete layers closest to the heated surface^{2,3}, and (3) to have a rather low thermal diffusivity to protect the reinforcement from the heat flux, especially in thin-walled R/C structures.

Within this context, (1) the water content of the mix and of the aggregates, (2) the aggregate-cement ratio, (3) the type of the aggregates, (4) the stress state during the heating, and (5) the type of porosity play a major role⁴. As a matter of fact, contrary to open porosity with interconnected pores, closed porosity with small pores increases the spalling tendency³ (this is typical of high-performance silica-fume concretes). Furthermore, for the same porosity, increasing the average pore size – as done by the heat - decreases the compressive strength^{2,9}. Other factors, as the cement type and the heating rate (provided the thermal gradients are $< 1^{\circ}\text{C}/\text{mm}$) have minor consequences on concrete mechanical behavior. However, the cement type has a remarkable influence on the thermal conductivity and diffusivity of the concrete and – consequently – on its insulation properties⁴.

With specific reference to the residual properties – that are the core of this paper – the overview of previous studies³ shows that basalt aggregate ensure the best residual compressive strength, while the results regarding calcareous and siliceous aggregates are rather contradictory (according to several tests, limestone – i.e. calcareous - aggregate is little affected by the temperature up to 400°C in terms of compressive strength; according to other results, the tensile strength decreases twice as much in calcareous than in siliceous concretes).

As for the cement type, blast-furnace slag cement and portland cement indicate no significant differences in terms of compressive-strength decay after a thermal cycle, but the strength recovery – a few days after the thermal cycle – is higher in the former case. The further strength loss after cooling and the subsequent strength recovery depend on the storage conditions after cooling (in water or in air) and on the timelength elapsed since the cooling (a few days or a few weeks). Many results show that the lowest residual strength is reached 2-4 weeks after the cooling⁵.

Because of the high amount of crystallization water, siliceous aggregate is more sensitive to fire and high temperature than either calcareous and basalt aggregates, the latter having an edge over the former because of its more homogeneous microstructure (either crystalline or vitreous⁶). However, the complexity of the comparison between siliceous and calcareous aggregates derives also from the crystalline form of the siliceous aggregate, that plays a non-marginal role, since – for instance – flint aggregate¹² makes the concrete very sensitive to high temperature, because of the dissociation of the crystallization water contained in opal and calcedonium.

As for the thermal properties, siliceous aggregate gives the concrete a higher conductivity and diffusivity than calcareous aggregate, and much higher than basalt aggregate. Furthermore, rich mixes lead to a lower diffusivity, because of the low diffusivity of the cement mortar and are more affected by the temperature than lean mixes.

Most of the previous considerations are confirmed by several studies published in the last ten to fifteen years. Concretes with pozzolanic cement are more sensitive than those with portland cement⁵. There are no major differences in the heat-induced strength loss in NSC and HPC ($f_c = 38\text{-}118\text{ MPa}$) containing granite aggregates and portland cement⁷. The same conclusions were reached later⁷ with reference to HPC ($f_c = 74\text{-}83\text{ MPa}$) containing granite or limestone aggregates, and portland cement with 8% silica fume. In the case of high contents of silica fume and/or fly ash (for instance⁹ $c = 358\text{ kg}/\text{m}^3$ with $\text{sf}/c = 15\%$ and $\text{fa}/c = 39\%$, portland cement, granite aggregate, with/without polymer or steel fibers) HPC is definitely

more temperature-sensitive than NSC. This is somewhat contradicted by a later overview¹⁰, where many previous data by other authors are compared with those obtained at NIST (4 mixes, $f_c = 41\text{-}75\text{MPa}$, portland cement type I, limestone aggregate, $w/c = 0.22\text{-}0.57$, $sf = 0$ and 11%): according to this study, the relationship between the hot and residual compressive strength is complex (decreasing the w/b ratio leads to smaller strength losses in the residual conditions; the presence of silica fume has no statistically significant effect on the mechanical properties). However, some detrimental effects due to silica fume appear in the results of the Project HITECO¹¹, concerning both the hot and the residual properties.

Finally, focussing the attention on the hot properties of silica-fume HPC¹² ($f_c = 74\text{-}84\text{MPa}$, portland cement, siliceous and carbonate aggregates) it appears that siliceous aggregate has an edge - between 100 and 600°C - in terms of compressive strength, but much less in terms of elastic modulus, while the presence of steel corrugated fibers decreases a little the compressive strength at any temperature, but reduces substantially the loss of the elastic modulus, with no major effects on the stress-strain curve.

This overview of previous literature allows us to indicate clearly the objectives of the present study, that investigates the residual behavior and the thermal diffusivity for:

- 5 mixes (lean and rich mixes);
- 3 cement types (blended, with blast-furnace slag and portland);
- 3 aggregate types (natural round siliceous, crushed calcareous and crushed basalt).

On the whole, 15 concretes were characterized (5 mixes x 3 aggregate types). All mechanical tests were residual-unstressed ($T = 20\text{-}600^\circ\text{C}$).

2. MATERIALS

As shown in Table 1, the starting point of this research project was: 5 mixes and 3 types for the coarse aggregate (the fine aggregate was natural sand):

- Mixes 1 and 2: lean mixes with low/medium-fineness blended cement containing a limited amount of calcareous filler (6-20% by clinker mass, organic-carbon $< 0.20\%$).
- Mix 3: lean mix with medium-fineness blast-furnace slag cement containing a limited amount of granulated slag in the clinker (33-65% by clinker mass).
- Mixes 4 and 5: lean and rich mixes respectively, with high-fineness portland cement.
- Siliceous aggregate: natural, round, river-bed gravel with maximum size $d_a = 20\text{ mm}$.
- Calcareous aggregate: crushed, rather flaky with maximum size $d_a = 16\text{ mm}$.
- Basalt aggregate: crushed, rather flaky with maximum size $d_a = 16\text{ mm}$.

The superplasticizer is a commercially-available mix of sulfonated polymers, in the form of a dark brown aqueous solution (solid fraction 40%).

The 15 concretes can be roughly divided into 3 categories: (1) ordinary concretes with $f_c = 41\text{-}47\text{ MPa}$, Numbers 91-95 and 105; (b) high-performance concretes with $f_c = 56\text{-}66\text{ MPa}$, Numbers 96,97,106,108,109 and 116; and (c) high-strength concretes with $f_c = 69\text{-}75\text{ MPa}$, Numbers 98,110 and 120.

3. TEST SPECIMENS AND THERMAL CYCLES

Fourteen cylinders were cast for each concrete in plastic pipes ($\varnothing \times h = 95 \times 210\text{ mm}$, total number 210), were cured at 20°C , 92% R.H. for 28 days, and then rested at 20°C , 70% R.H. until the thermal cycles and the tests. All cylinders were cut at their extremities to avoid any possible lack of homogeneity due to the initial and final phases of concreting (final size

	Mix 1	Mix 2	Mix 3	Mix 4	Mix 5
Concrete No.	94	91	92	93	106
Aggregate type ($d_a = 20$ mm)	Natural round siliceous aggregate				
Cement type	II/A-LL 32.5 R	II/A-LL 42.5 R	III/A 42.5 R	I 52.5 R	I 52.5 R
Cement content (kg/m^3)	350	380	380	360	450
Superplast. Superflux NF-Axim	0.70%	0.50%	0.33%	0.35%	1.25%
w/c	0.48	0.47	0.47	0.50	0.35
Mass per unit volume (kg/m^3)	2373	2348	2363	2388	2393
Compressive strength (MPa)	41.1	41.0	43.3	41.5	64.7

Concrete No.	95	96	97	98	110
Aggregate type ($d_a = 16$ mm)	Crushed calcareous aggregate				
Cement type	II/A-LL 32.5 R	II/A-LL 42.5 R	III/A 42.5 R	I 52.5 R	I 52.5 R
Cement content (kg/m^3)	350	400	400	360	450
Superplast. Superflux NF-Axim	1.00%	1.00%	1.10%	1.04%	2.00%
w/c	0.48	0.42	0.42	0.50	0.35
Mass per unit volume (kg/m^3)	2403	2414	2424	2388	2439
Compressive strength (MPa)	44.0	58.8	56.5	68.5	74.6

Concrete No.	105	108	116	109	120
Aggregate type ($d_a = 16$ mm)	Crushed basalt aggregate				
Cement type	II/A-LL 32.5 R	II/A-LL 42.5 R	III/A 42.5 R	I 52.5 R	I 52.5 R
Cement content (kg/m^3)	350	400	400	360	450
Superplast. Superflux NF-Axim	1.43%	1.30%	1.25%	1.30%	2.00%
w/c	0.48	0.42	0.42	0.50	0.35
Mass per unit volume (kg/m^3)	2591	2591	2591	2581	2600
Compressive strength (MPa)	47.4	56.5	64.1	66.4	73.6

Table 1 – Mix design; workability class: calcareous and siliceous aggregates S4; basalt aggregate S3; before concreting, all aggregates were in saturated, dry-surface conditions.

$\varnothing \times h = 95 \times 190$ mm). Then each cylinder was cut into a shorter cylinder and a disk, in order to have 180 specimens for testing in compression (Fig.1a) and as many specimens (disks) for testing in indirect tension (by splitting, Fig.1b, size $\varnothing \times t = 95 \times 40$ mm).

One hundred and eighty specimens were required by the numbers of the concretes (15), of the reference temperatures (4 levels: 20, 200, 400 and 600°C, Fig.2) and of the repetitions (3 specimens to be tested in each sub-case). Fifteen specimens were required for the evaluation of the thermal diffusivity (each was instrumented with 2 thermocouples, both placed in the mid-section, one close to the surface and the other along the axis, Fig.1c). Finally, fifteen specimens were kept aside for the repetition of any possible unsuccessful test and for checking the compressive strength in the virgin conditions at the end of the experimental program (the tests spanned over a 4-month period).

The thermal cycles are sketched in Fig.2, while the differential temperature ΔT to be measured under controlled heating conditions (between 100 and 900°C in this study) and instrumental in the evaluation of the thermal diffusivity is indicated in Fig.1d.

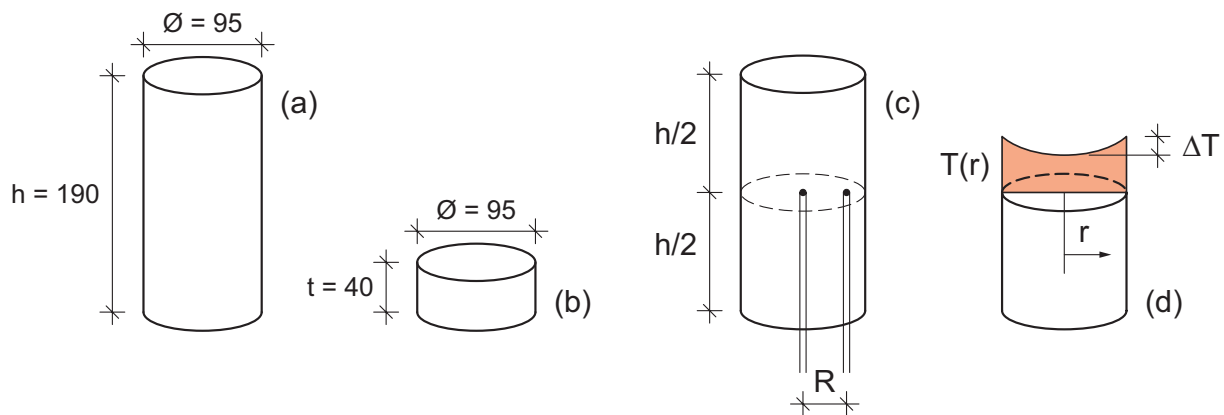


Fig.1 – Specimens: (a) cylinders; (b) disks; (c) instrumented cylinders for the evaluation of the thermal diffusivity (distance of the thermocouples $R = 35$ mm); and (d) typical temperature distribution in the mid-height section.

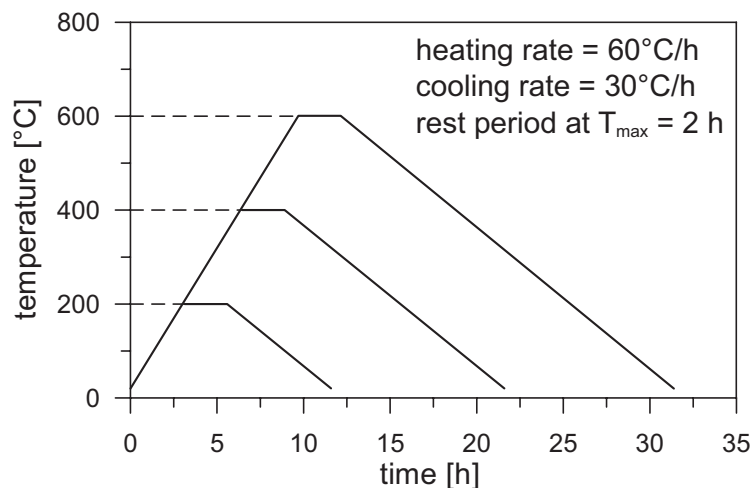


Fig. 2 – Thermal cycles.

4. TEST MODES AND INSTRUMENTATION

For each temperature level (20, 200, 400 and 600°C) and for each concrete (15 concretes), 3 cylinders were tested in compression in a force-controlled mode, by using an hydraulic press (capacity 1000 kN). The tests were performed 1-2 weeks after the thermal cycle. Before

loading the cylinders up to failure, 2 of them were instrumented with a couple of LVDTs (base-length $\Delta T = 50$ mm), to measure the shortening as a function of the load and to evaluate the elastic modulus E_c in accordance with the Italian Norm UNI 6556 (very close to the RILEM Norm for the “stabilized modulus” = secant modulus between the onset of unloading and the onset of reloading in the third cycle, with $\sigma_{\min} = 3.5\%f_c$ and $\sigma_{\max} = 40\%f_c$). Only in a few cases a third value of E_c was needed, since test repeatability was generally very good.

The failure mode in compression consisted mostly of vertical or subvertical cracks (Fig.3b), or double-cone fracture (Fig.3d), but often the vertical cracks were accompanied by either a diagonal cracked band (Fig.4c) or wedge-shaped fragments (Fig.3a), with no significant differences in terms of compressive strength.

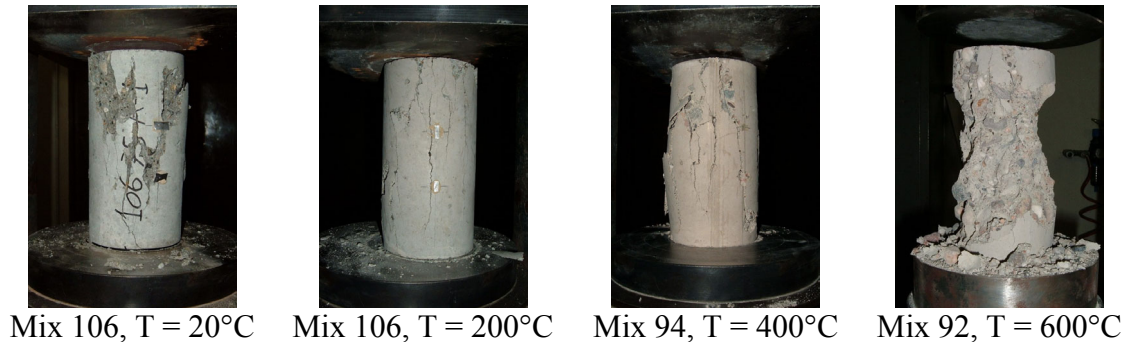


Fig. 3 – Typical failures in compression.

The indirect-tension tests were carried out according to RILEM, by placing two wooden strips at the extremities of the vertical diameter of each disk and loading it in an hydraulic press (capacity 250 kN). The scatter of the results was larger than in compression, but still limited.

The mass per unit volume ρ was evaluated after each thermal cycle, on the basis of the mass and size of each specimen.

As already mentioned, 15 cylinders were slowly heated from 20 to 900°C, in order to evaluate the thermal diffusivity, which is the key parameter in heat transmission by conduction ($D = \lambda \rho^{-1} c^{-1}$, where λ is the thermal conductivity, ρ is the mass per unit volume and c is the specific heat). Once the differential temperature ΔT (Fig.1d) is known at each temperature level T , it is possible to evaluate the diffusivity D as follows:

$$D = v_h R^2 / (4 \Delta T) \quad [L^2/t]$$

where v_h is the mean heating rate of the specimen and R is the distance between the axes of the outer and inner thermocouples (Fig.1c). The former relationship hold (a) after the initial thermal transient ($T > 150^\circ\text{C}$, as a reference), and (b) for long cylinders ($h \geq 2\phi$), a constant heating rate, and space-invariant thermal and physical properties inside the specimen¹³. Note that D is an “equivalent diffusivity” since the effects of such different phenomena as phase changes (from water to steam, $T = 100\text{-}200^\circ\text{C}$), chemical reactions (from portlandite to quicklime and water, $T = 450\text{-}500^\circ\text{C}$; from calcium carbonate to quicklime and carbon dioxide = calcination, $T > 700^\circ\text{C}$) and crystalline changes (from α to β quartz, $T = 550\text{-}600^\circ\text{C}$) are lumped together.

An electric furnace was used for running all the thermal processes ($T_{\max} = 1000^\circ\text{C}$; $\max \Delta T/\Delta t = 13^\circ\text{C}/\text{minute}$). The temperature inside the chamber and the heating rate were controlled by a PID controller (Proportional-Integral-Derivative), which was connected to the built-in thermocouple of the furnace. The signals of all the thermocouples were recorded and processed by a suitable data- acquisition system¹⁴.

5. TEST RESULTS AND COMMENTS

The residual mechanical properties of all the concretes examined in this project exhibit a more or less marked decrease because of the temperature-induced damage. Only in a few cases the compressive and tensile strengths increase (between 20 and 300°C), but this occurrence is mostly limited to basalt aggregates and to high-fineness portland cement (Fig.4). As for the elastic modulus, in no cases the residual values are larger than the original values (Fig.5).

On the whole, the compressive strength is parameter least affected by the temperature ($f_c^T/f_c^{20} = 55-90\%$ at 400°C), while the elastic modulus is the most affected ($E_c^T/E_c^{20} = 35-50\%$ at 400°C) and the indirect tensile strength is in between ($f_{ct}^T/f_{ct}^{20} = 40-70\%$ at 400°C, Fig.6). More specifically:

- For each aggregate type, both in compression (Fig.4) and in tension (Fig.6), the strength-temperature curves of the highest-grade and lowest-grade concretes envelope all the other curves, and show that basalt and calcareous concretes are less affected by the temperature at least up to 400°C. In the best concretes (either calcareous or basalt) the compressive and tensile strengths increase between 20°C and 350°C up to +5-6% with respect to virgin conditions. Furthermore, in compression and in the lowest-grade concretes, the basalt aggregate practically nullifies the effects of the temperature up to 400°C, while calcareous and siliceous aggregates bring in – on the whole – 20% and 40% losses respectively.
- In calcareous and siliceous concretes the elastic moduli are comprised within a narrow band and evolve in pretty much the same way (Fig.5), whatever the mix or the aggregate might be, while in basalt concrete the spread between the highest-grade and the lowest-grade concretes is more pronounced.
- On the whole, in compression siliceous and calcareous concretes lose roughly 2/3 of their original strength, after being exposed to 600°C, while basalt concretes definitely lose less (roughly 1/2), see Fig.4. The situation is worse for the elastic modulus (-70/75% for basalt and calcareous, and -85% for siliceous concrete), see Fig.5, and for the tensile strength, where the loss after being exposed to 600°C is close to 60-70% in basalt and calcareous concretes, and is above 80% in siliceous concretes (Fig.6).
- In the range $T = 20-600^\circ\text{C}$, NSC and HPC ($f_c^{20} = 41-66 \text{ MPa}$) lose little more than 60%, while the loss is higher for high-strength concretes (close to 70% for $f_c^{20} = 69-75 \text{ MPa}$), with reference to the compressive strength. As for the elastic modulus and tensile strength, on the whole there are no sizable differences among NSC, HPC and HSC.
- Among NSCs and HPCs ($f_c^{20} = 41-66 \text{ MPa}$, Fig.4), siliceous and basalt concretes seem to be the most and the least affected by the temperature, with the calcareous concretes in an intermediate position, closer to siliceous concretes than to basalt concretes. The same applies to the elastic modulus (Fig.5), but less clearly, since the spread of the values is definitely more limited than for the compressive and tensile strengths.
- Among HSC's ($f_c^{20} = 69-75 \text{ MPa}$, Fig.4), the single basalt concrete investigated in this study behaves better than the two calcareous concretes in terms of tensile strength (Fig.6), while the elastic moduli of the 3 concretes are very similar (Fig.5).
- For the same strength in compression at 20°C, blast-furnace cement and blended cement tend to be equally effective with calcareous aggregate; however, with siliceous and basalt aggregates, blended cement has an edge over blast-furnace cement; the same occurs in the case of the elastic modulus and of the tensile strength, for any aggregate type.
- On the whole – and with reference to calcareous and basalt aggregates – blended cement tends to be more effective than portland cement in guaranteeing a better residual behavior.

- With either calcareous or basalt aggregates and portland cement, medium water/cement ratios affects more the compressive strength than low water/cement ratios (for roughly the same strength at 20°C); this is clear in compression and tension, but not for the elastic modulus (where – as already mentioned – the spread of the values is definitely lower).
- In Mixes 1 and 2 (low/medium-fineness blended cement, medium cement content), and 3 (medium-fineness blast-furnace cement, medium cement content), basalt and siliceous aggregates always lead to the best and to the worst performance respectively, not always below 250°C but always above 300°C; the situation is the same for the elastic modulus in Mixes 1 and 2, while in Mix 3 the situation is reversed, but the moduli are so close that the differences are meaningless.
- In Mix 4 (high-fineness portland cement, medium cement content) the situation is not so clear, but on the whole basalt aggregate still ensures the best performance.
- With reference to compression (Fig.4), in Mix 5 (high-fineness portland cement, high cement content), basalt and calcareous aggregates are almost equivalent up to 400°C; above 350°C siliceous aggregates catches up and above 400°C calcareous and siliceous aggregates are almost equivalent; however, basalt aggregate is still better. In tension (Fig.6), the basalt concrete is the best and the siliceous concrete is the worst, while in terms of elastic modulus calcareous and basalt concretes behave very similarly above 500°C (Fig.5), while the single siliceous concrete has an edge below 500°C.
- On the whole, basalt aggregate (closely followed by calcareous aggregate), blended cement and medium water-cement ratios seem to diminish the dependence of the concrete on high-temperature.
- In all concretes, the higher the concrete strength, the closer the residual compressive strength to the hot compressive strength (EC-2, see Fig.8 for calcareous concretes).

With reference to the mass per unit volume (Fig.7a), siliceous and calcareous aggregates are very close in terms of mass loss after a thermal cycle, while basalt concretes undergo higher losses, with a trend that at 600°C is still sizeable.

As for the thermal properties, and specifically the thermal diffusivity, siliceous and calcareous concretes tend to have the same diffusivity, while basalt concretes have a definitely lower diffusivity (-30%). Furthermore, in siliceous and basalt concretes the diffusivity is almost constant between 200 and 600°C, while tends to be a linearly-decreasing function of the temperature in calcareous concretes (Fig.7b). More specifically:

- In all concretes, the larger the water/cement ratio, the greater the diffusivity, more with portland cement than with blended cement, with the blast furnace cement in an intermediate position; the relationship between the diffusivity and the water content seems to be roughly linear, more in calcareous than in siliceous concretes (Fig.7c).
- In calcareous and siliceous concretes portland cement brings in a greater diffusivity than blended and blast furnace cements.

6. CONCLUDING REMARKS

Fifteen structural concretes have been investigated in this study, to compare different mix designs (5), aggregate types (3) and cement types (3) in terms of insulating capabilities and mechanical properties during and after a fire respectively.

The many test results obtained show that the concretes containing basalt aggregate, blended cement (with calcareous filler) and medium-low water-cement ratios have an edge in ensuring structural concrete a good high-temperature behavior. This should be taken in due consideration since the initial phase of the design of heat-sensitive structures.

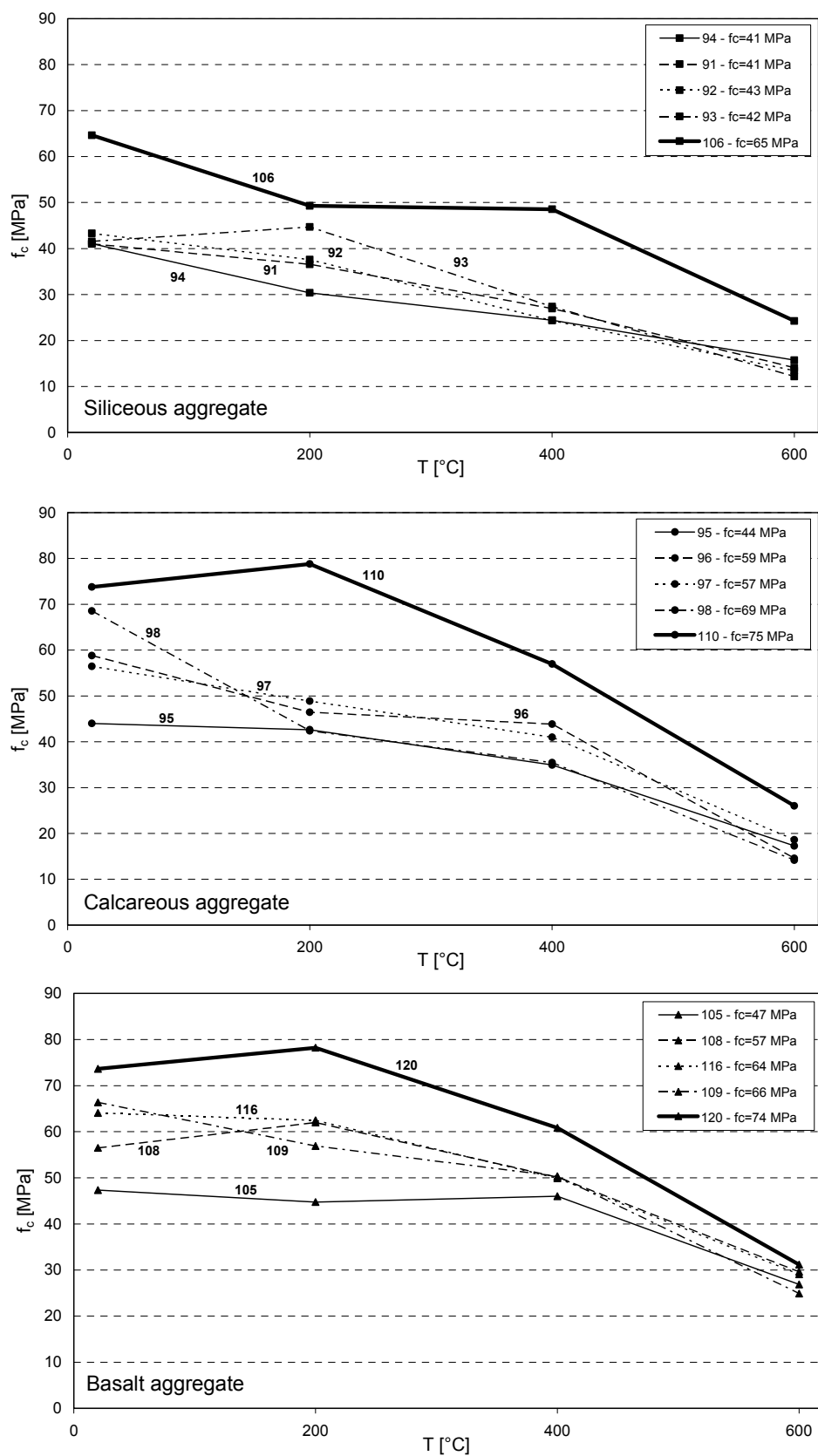


Fig. 4 – Residual compressive strength: (a) siliceous; (b) calcareous; and (c) basalt aggregates.

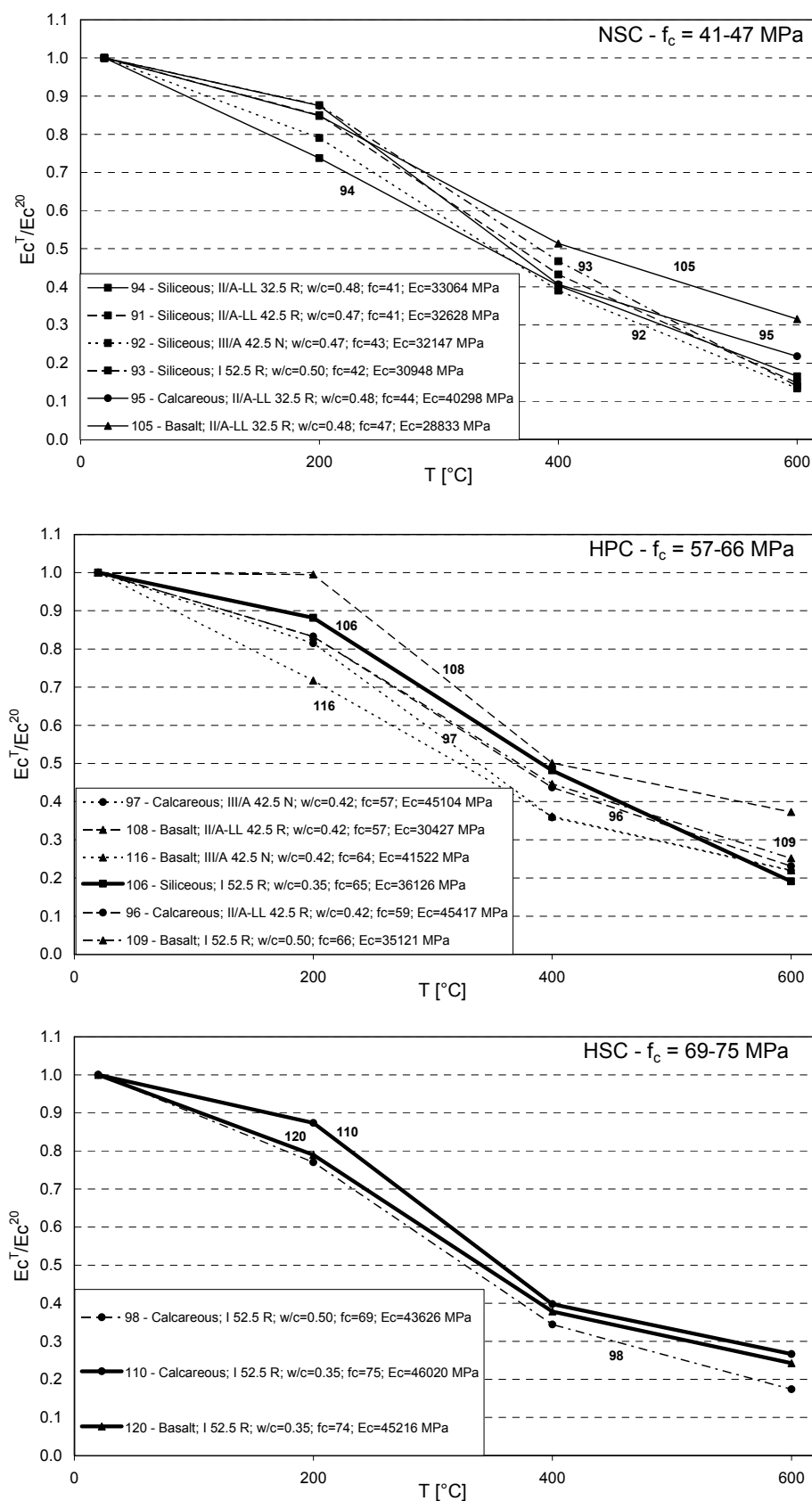


Fig. 5 – Residual elastic modulus: (a) NSC; (b) HPC; and (c) HSC.

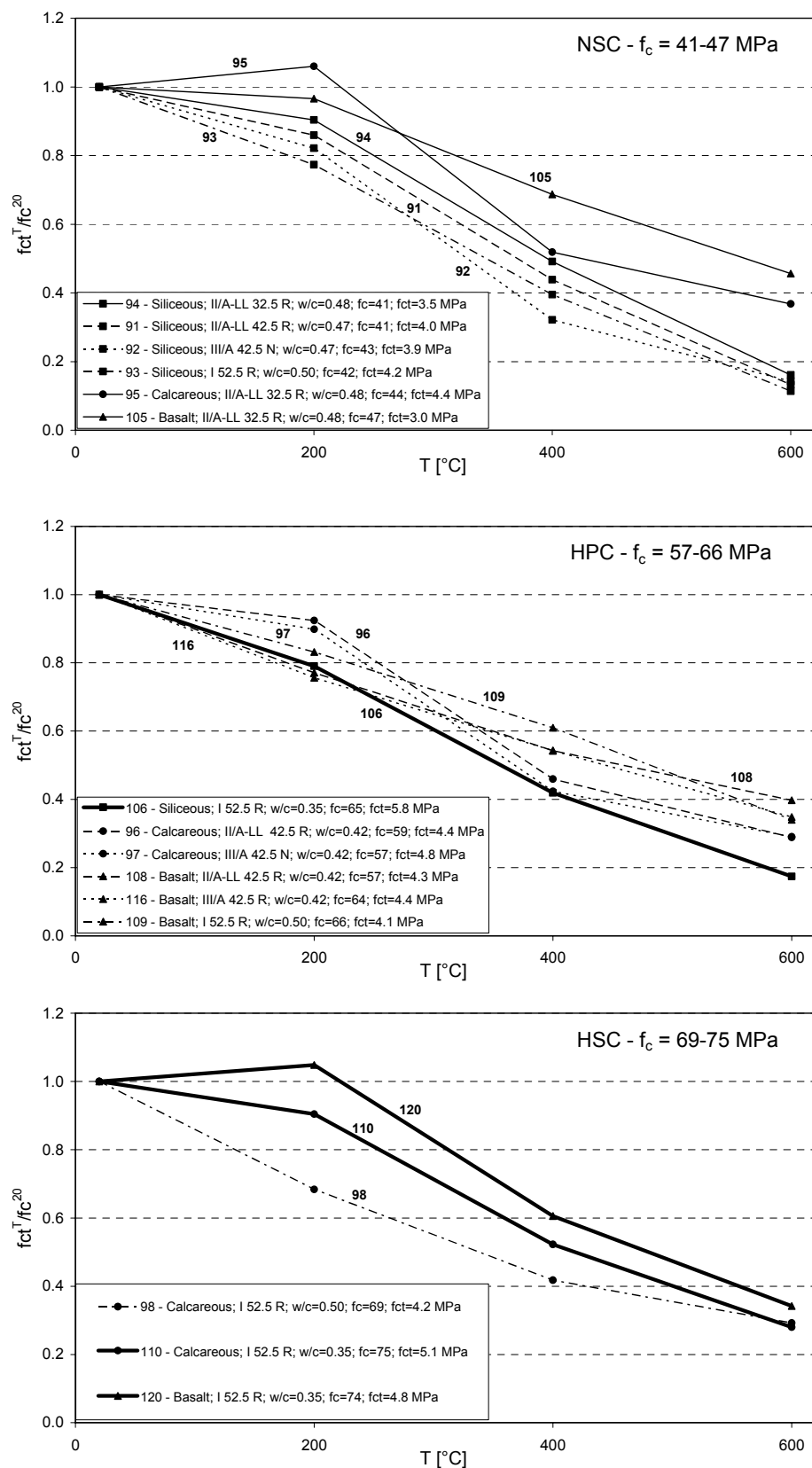


Fig. 6 – Residual indirect tensile strength: (a) NSC; (b) HPC; and (c) HSC.

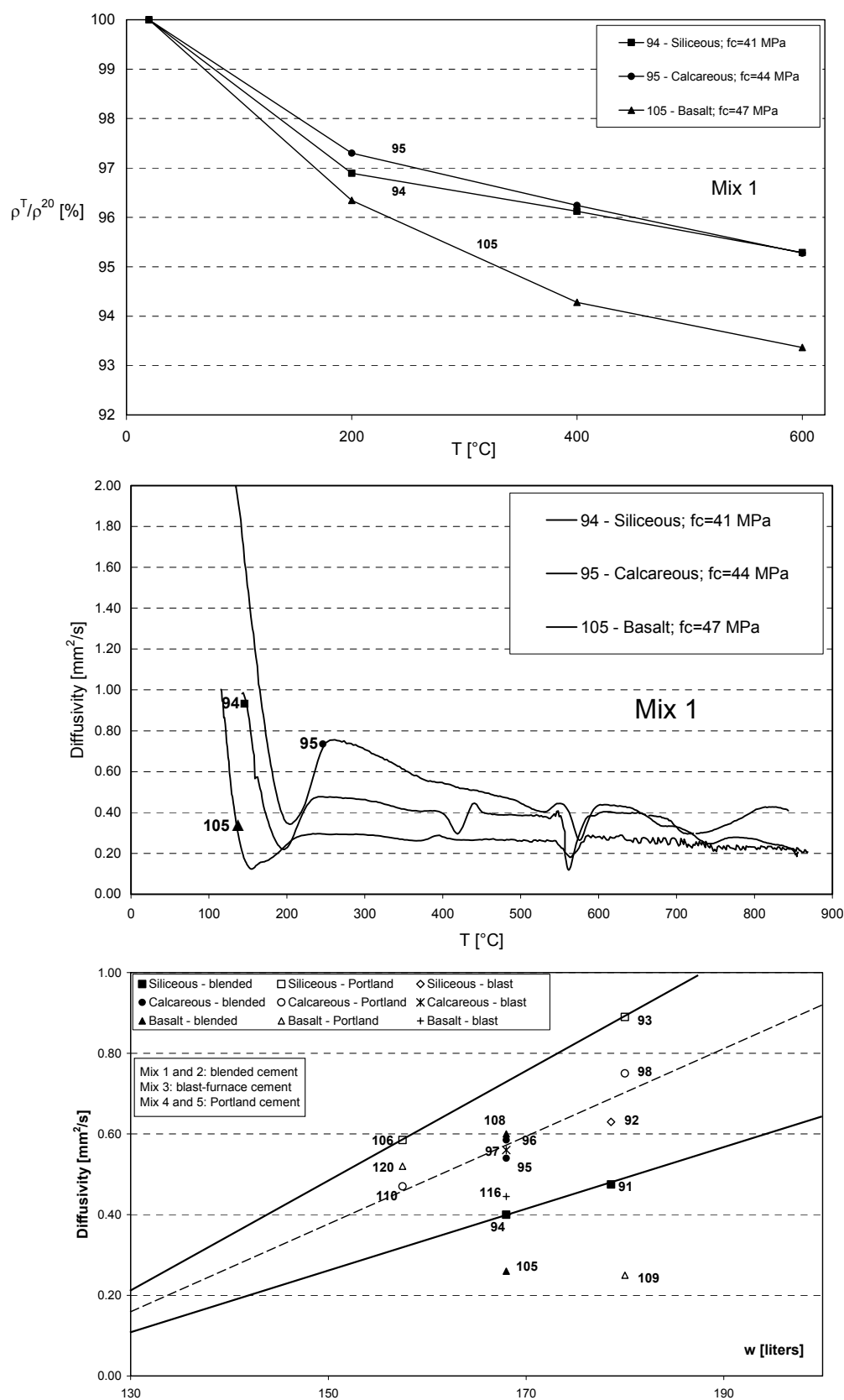


Fig. 7 – Typical examples of mass loss (a) and thermal diffusivity (b); and thermal diffusivity versus water content (c) for all the concretes investigated in this project.

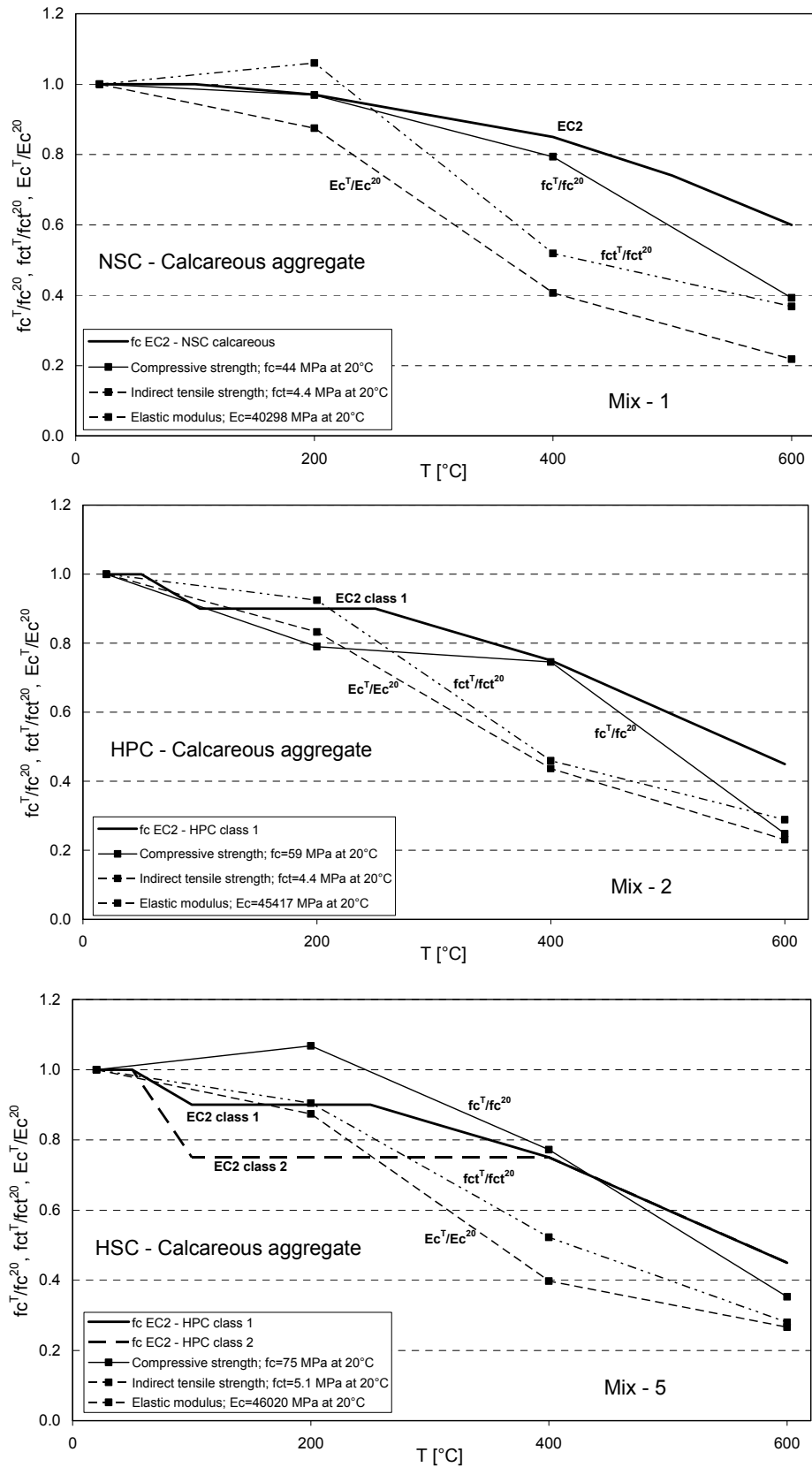


Fig. 8 – Mechanical decay of calcareous concretes and EC-2 “Fire Design” (strength at high temperature): (a) Mix 1 – blended cement; (b) Mix 3 – blast-furnace slag cement; and (c) Mix 5 – portland cement. EC2-Class 1: $f_c = 55\text{-}60$ MPa and EC2-Class 2: $f_c = 70\text{-}80$ MPa.

7. ACKNOWLEDGEMENTS

This project was financed by the firm CTG-Italcementi (Bergamo, Italy) within the European Project UPTUN “Cost-Effective, Sustainable and Innovative Upgrading Methods for Fire Safety in Existing Tunnels”. The tests were performed by Riccardo Billi, Francesca Busnelli and Marco Quaglia in partial fulfillment of their MS-Degree requirements. The suggestions by the Co-ordinator of UPTUN Work Package 4, MS Eng. Franco Corsi (ENEA, Rome, Italy) and by MS Eng. Francesco Santonicola (CTG-Italcementi) are also gratefully acknowledged.

8. REFERENCES

- [1] Caner A., Zlatanic S. and Munfah N. (2005): “Structural Fire Performance of Concrete and Shotcrete Tunnel Liners”, ASCE-J. of Structural Engrg., V.131, No.12, 1920-1925.
- [2] Khoury G. A. (2000): “Effect of Fire on Concrete and Concrete Structures”, Progress in Structural Engineering Materials, V.2, 429-447.
- [3] Kalifa P., Chéné G. and Gallé C. (2001): “High-Temperature Behaviour of HPC with Polypropylene Fibres from Spalling to Microstructure”, Cement and Concrete Research, No.31, 1487-1499.
- [4] Schneider U. (Editor, 1985): “Properties of Materials at High Temperatures : Concrete”, RILEM, Publ. by the Dept. of Civil Engrg. of the Univ. of Kassel (Kassel, Germany), 131 pp.
- [5] Papayianni and Valiasis T. (1991): “Residual Mechanical Properties of Heated Concrete Incorporating Different Pozzolan Materials”, Materials and Structures, V.24, 115-121.
- [6] Neville A.M and Brooks J.J (1999): “Concrete Technology”, Publ. by Longman Group, UK, 438 pp.
- [7] Chan Y. N., Peng G. and Chan J. K. W. (1996): “Comparison between High-Strength Concrete and Normal-Strength Concrete Subjected to High Temperature”, Materials and Structures, V.29, 616-619.
- [8] Hoff G.C., Bilodeau A. and Malhotra V.M. (2000): “Elevated Temperature Effects on HSC Residual Strength”, ACI-Concrete Int., No.4, 41-47.
- [9] Chan Y.N., Luo X. and Sun W. (2000): “Compressive Strength and Pore Structure of HPC after Exposure to High Temperature up to 800°C”, Cement and Concrete Research, V.30, 247-251.
- [10] Phan L.T. and Carino N.J. (2002): “Effects of Test Conditions and Mixture Proportions on Behavior of High-Strength Concrete Exposed to High Temperatures”, ACI-Materials J., V. 99, No.1, 54-66.
- [11] Cheyrezy M. (2001): “Compressive Strength of HPCs at High Temperature”, Proc. Int. Workshop on Fire Design of Concrete Structures – *fib* Task Group 4.3, ed. by N.P. Høj, Malta, March 2001, 2-7.

- [12] Cheng F.P., Kodur V.K.R. and Wang T.C. (2004): "Stress-Strain Curves for High-Strength Concrete at Elevated Temperatures", ASCE-J. of Mat. in Civil Engrg., V.16, No.1, 84-90.
- [13] Khoury G.A., Sullivan J.E. and Grainger B.N. (1984): "Radial Temperature Distributions within Solid Concrete Cylinders under Transient Thermal States", Magazine of Concrete Research, V.36, No.128, 146-154.
- [14] Felicetti R. and Gambarova P.G. (1998): "Effects of High Temperature on the Residual Compressive Strength of High-Strength Siliceous Concretes", ACI Materials J., V.95, No.4, 395-406.



BEHAVIOUR OF REINFORCED CONCRETE STRUCTURES IN FIRE

Zhaohui HUANG¹, Ian W. BURGESS² and Roger J. PLANK³

ABSTRACT

In the past two decades, a significant amount of research has been conducted into the performance of composite steel-framed structures in fire. However, the same level of development has not taken place for other forms of construction. In terms of reinforced concrete construction, design is still based on simplistic methods which have been developed from standard fire tests that do not necessarily represent real building behaviour. This makes it very difficult, if not impossible, to determine the level of safety achieved in real concrete structures, or whether an appropriate level of safety could be achieved more efficiently. In this study detailed analyses of a reinforced concrete structure subject to a standard fire regime are carried out. The building is designed to Eurocode 2 and represents a commercial office building. In order to study the interactions between the cool and hot zones of the structure, a series of analyses has been carried out for different extents and positions of localised fire compartments. It is clear that adjacent cool structure provides considerable restraint and continuity, increasing the fire resistance of the structure within the fire compartment. Relatively small areas of tensile membrane force are formed within the concrete slabs, and large areas are subject to compressive membrane action during the fire. As a result the downstand concrete beams experience enhanced tension during the fire, especially in the early stages, which is mainly carried by their tensile reinforcement. It is therefore very important to keep the temperature of beam reinforcement within certain limits. Eventual structural collapse in the studies is always due to column failure, and it is clear that the performance of columns is vitally important to the survival of reinforced concrete buildings in fire.

¹ Lecturer, Department of Civil & Structural Engineering, University of Sheffield, Sheffield, S1 3JD, UK;
Email: z.huang@sheffield.ac.uk

² Professor, Department of Civil & Structural Engineering, University of Sheffield, Sheffield, S1 3JD, UK;
Email: ian.burgess@sheffield.ac.uk

³ Professor, School of Architectural Studies, University of Sheffield, S10 2TN, UK;
Email: r.j.plank@sheffield.ac.uk

1. INTRODUCTION

The behaviour of structures exposed to fire is usually described in terms of the concept of fire resistance, which is the period of time under exposure to a standard fire time-temperature curve at which some prescribed form of limiting behaviour occurs. In performance-based design this limiting behaviour may be defined as real structural collapse or as a failure of integrity (which allows fire-spread to occur), but is more usually defined in terms of a deflection limit. Current design codes ^{1, 2} have taken a step towards full performance-based design by allowing designers to treat fire as one of the basic design limit states, taking account of:

- Non-uniform heating due to partial protection, which may be inherent in the framing system or specially applied,
- The level of loading in the fire limit state, using partial safety factors lower than those used for ultimate limit states, because of the relative improbability of such accidental conditions,
- Realistic stress-strain characteristics of materials at elevated temperatures.

The main limitation of these codified approaches is that they are based on the behaviour under test of isolated simply supported members, usually heated according to the standard ISO834 time-temperature curve³. In real buildings structural elements form part of a continuous assembly, and building fires often remain localised, with the fire-affected region of the structure receiving significant restraint from cooler areas surrounding it. The real behaviour of these structural elements can therefore be very different from that indicated by standard furnace tests.

In 1995-96 six large fire tests were carried out on a full-scale composite building at the BRE Fire Research Laboratory at Cardington⁴. The tests made it clear that unprotected steel members could have significantly greater fire resistance within real multi-storey buildings than when tested as isolated members. This was undoubtedly due to interaction between the heated members within the fire compartment, the concrete floor slabs (both heated and unheated) and the adjacent composite frame structure. If such interactions are to be used by designers in specifying fire protection strategies, as part of an integrated limit state design process, then this can not practically be based on testing because of the extremely high implicit costs. It is therefore becoming increasingly important that software models be developed to enable the behaviour of such structures under fire conditions to be predicted with sufficient accuracy.

A number of researchers have developed numerical modelling approaches to the behaviour of reinforced concrete structures in fire conditions. Ellingwood and Lin⁵, and Huang and Platten⁶, developed planar modelling software for reinforced concrete members in fire, and a simpler model has been developed by Lie and Celikkod⁷ for the high-temperature analysis of circular reinforced concrete columns. In the major general-purpose finite element codes this kind of numerical modelling is often attempted, but the degradation of material properties tends to be simplified, and the finite element formulations used are often inappropriate for efficient set-up and analysis of concrete and composite buildings under fire attack.

The specialised finite element program *Vulcan* has been progressively developed over the past decade⁸⁻¹¹ at the University of Sheffield for three-dimensional modelling of the structural behaviour of composite and steel-framed buildings in fire. In this program a non-linear layered finite element procedure has been developed⁹ for predicting the structural response of reinforced concrete slabs subjected to fire^{9, 10}. Also a more robust three-dimensional 3-noded beam-column element with general cross-section has been developed for

modelling of steel and reinforced concrete frames in fire conditions¹¹. These developments have provided a powerful tool to carry out 3D analysis of reinforced concrete structures in fire.

In this study a generic 37.5m x 37.5m normal-weight reinforced concrete structure comprising four floors has been considered, with realistic loading conditions and structural layout. In order to develop a better understanding of the interactions between the cool and hot zones of the structure, a series of analyses has been carried out for different extents and positions of localised fire compartments.

2. THEORETICAL BACKGROUND OF THE PROGRAM

In the 3D non-linear finite element procedure which is the theoretical basis of *Vulcan*, a reinforced concrete building is modelled as an assembly of finite beam-column and slab elements. It is assumed that the nodes of these different types of element are defined in a common reference plane, as shown in Fig. 1. The reference plane is assumed to coincide with the mid-surface of the concrete slab element. Its location is fixed throughout the analysis.

The beam-columns are represented by 3-noded line elements. The model is based on a formulation proposed by Bathe¹² for geometrically non-linear modelling of elastic beams. The cross-section of the beam-column is divided into a matrix of segments, and each segment may have different material, temperature and mechanical properties. The complications of structural behaviour in fire conditions, such as thermal expansion, degradation of stress-strain curves, failure of concrete segments by cracking and crushing, and yielding of steel member or reinforcement segments, are included. The details of the formulations of beam-column elements and the constitutive modelling of concrete and steel at elevated temperatures have been presented previously¹¹.

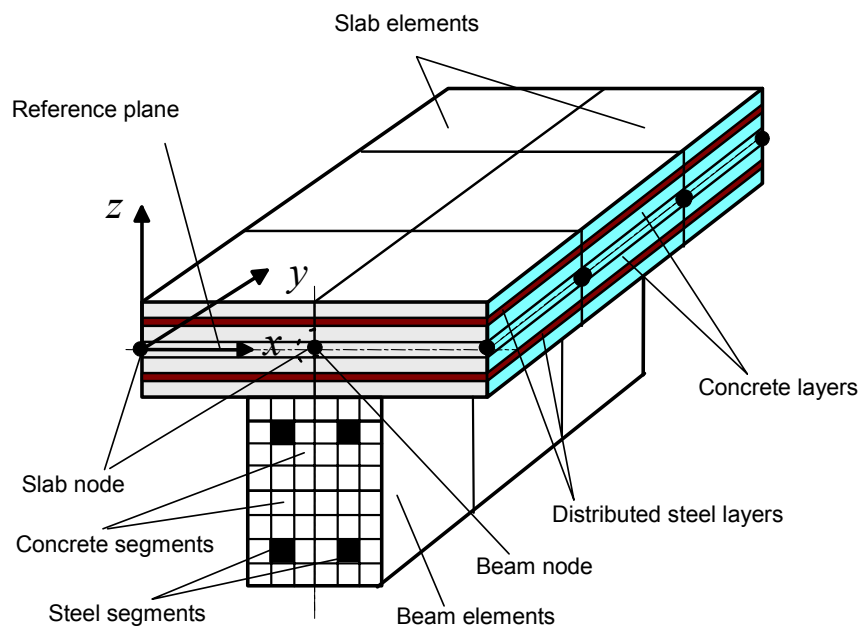


Fig. 1 – Division of reinforced concrete structure into beam and slab elements.

In this program a non-linear layered finite element procedure has been developed for predicting the structural response of reinforced concrete slabs subjected to fire^{9, 10}. The procedure is based on Mindlin/Reissner (thick plate) theory, and both geometric and material non-linearities are taken into account. The slab elements are sub-divided into concrete and reinforcing steel layers to take into account temperature distributions through the thickness of

slabs, thermal strains and material degradation for each layer, and failure layer-by-layer based on stress levels at Gauss points.

3. ANALYSIS OF REINFORCED CONCRETE STRUCTURE WITH WHOLE FLOOR HEATED

This study is based a generic 37.5m x 37.5m normal-weight reinforced concrete structure comprising four floors with 4.5m storey height and five 7.5m x 7.5m bays in each direction, which is subject to the ISO384 Standard Fire (see Fig. 2). The building is designed to Eurocode 2¹³ and BS8110¹⁴, and represents a commercial office building. The characteristic loads are assumed to be:

- Self-weight (assuming concrete density of 24kN/m³): 7.5kN/m²
- Raised floor: 0.5kN/m²
- Ceiling and services: 0.5kN/m²
- Partitions: 1.0kN/m²
- Imposed load: 2.5kN/m²

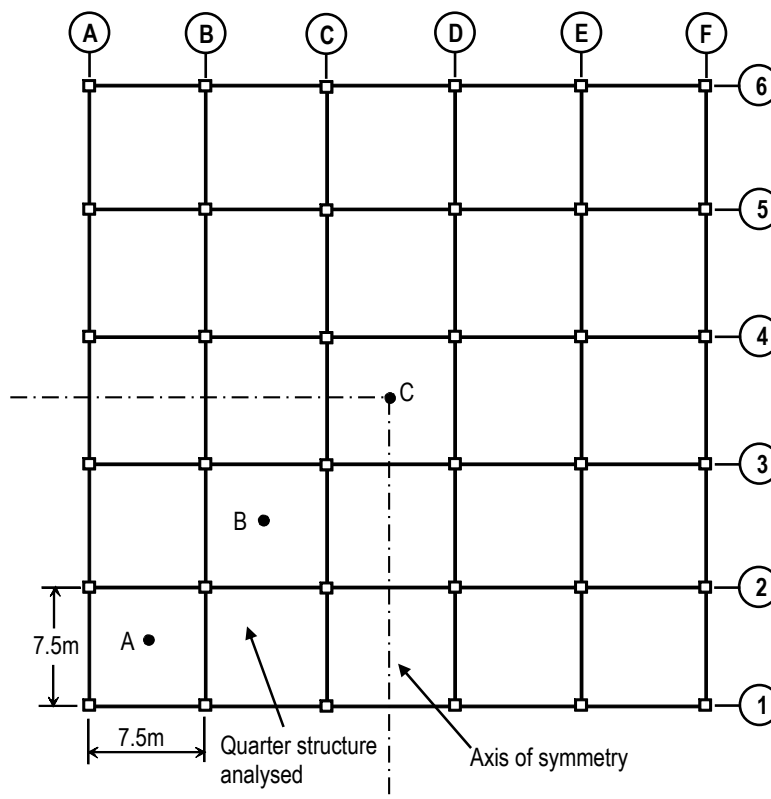


Fig. 2 - Concrete structure layout for whole ground floor heated by the ISO384 fire.

Therefore, at the fire limit state, the total design load on the structure is 10.75 kN/m² when the partial safety factor of 0.5 is applied to the imposed load. This loading is used throughout the example. The characteristic strength of concrete and reinforcing steel are assumed to be 45MPa and 460MPa, respectively. It is also assumed that two hours' fire resistance is required for the building. Therefore the nominal covers of beams, slabs and columns for the required fire resistance are 30mm, 25mm and 25mm respectively¹⁴. According to Eurocode 2¹³ each floor slab is nominally 250mm thick and designed as a flat slab. The dimensions of

the cross-sections of beams and columns are 500mm x 350mm and 350mm x 350mm respectively. Fig. 3 shows the cross-section details of beams and columns.

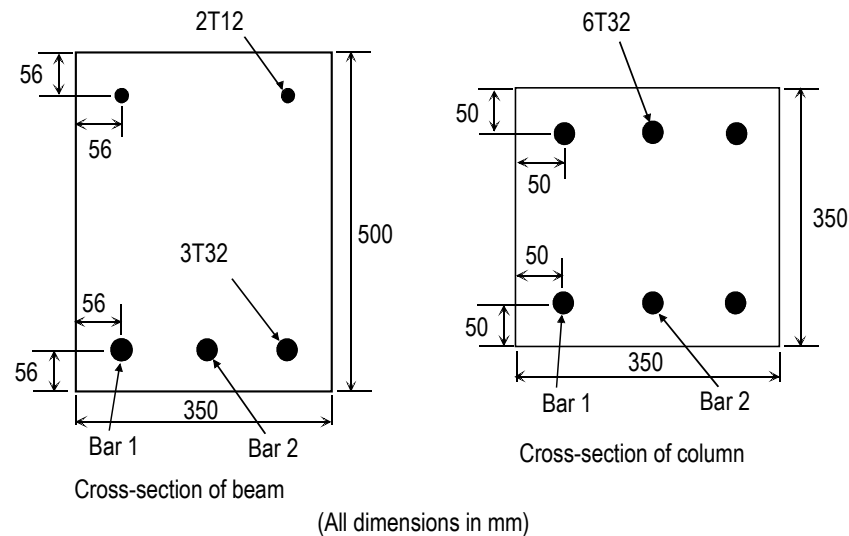


Fig. 3 - Cross-sectional details of beams and columns.

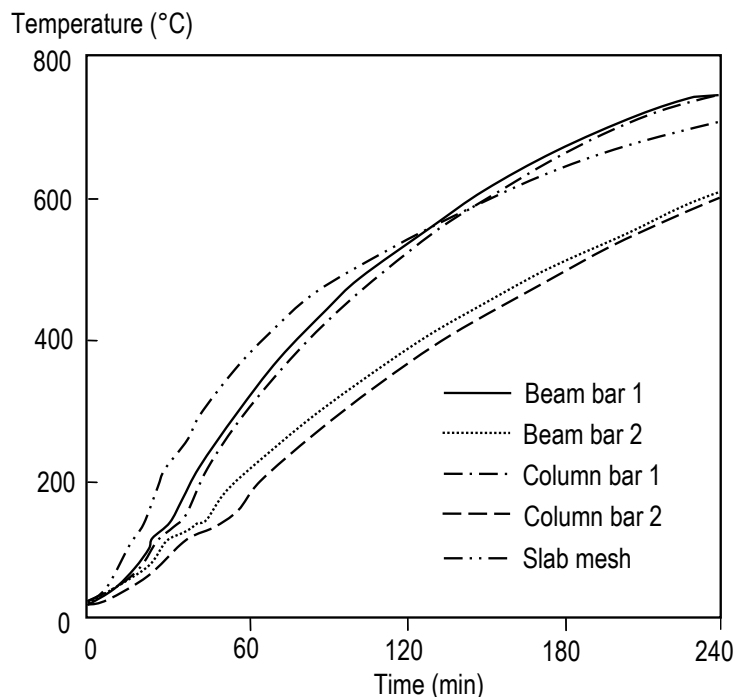


Fig. 4 - Predicted temperatures of main reinforcement for beams, columns and slabs.

In this case it is assumed that the whole ground floor of the building is engulfed in fire. Because of the inherent symmetry of the case, only a quarter of the structure is modelled. The first step is to perform a thermal analysis using *Vulcan*. The temperature histories of the main reinforcing steel bars in the beam and column sections, and the reinforcing mesh in the slab are shown in Fig. 4. The maximum temperatures of reinforcement at 120min and 180min are about 530°C and 660°C respectively. It is obvious that the concrete covers provide very good thermal insulation to the reinforcement during the fire. In this thermal analysis it is assumed that no concrete spalling happens in the fire condition.

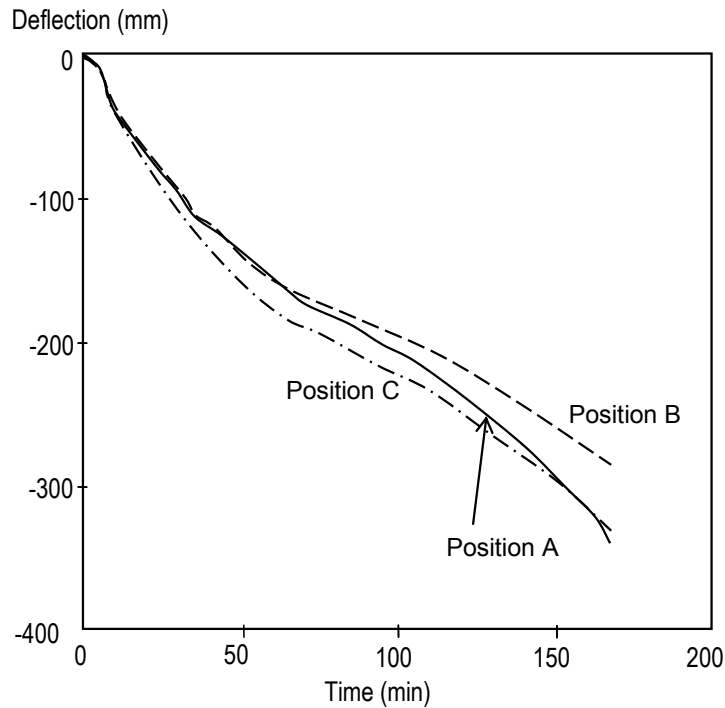


Fig. 5 - Predicted deflections at key positions of the concrete floor.

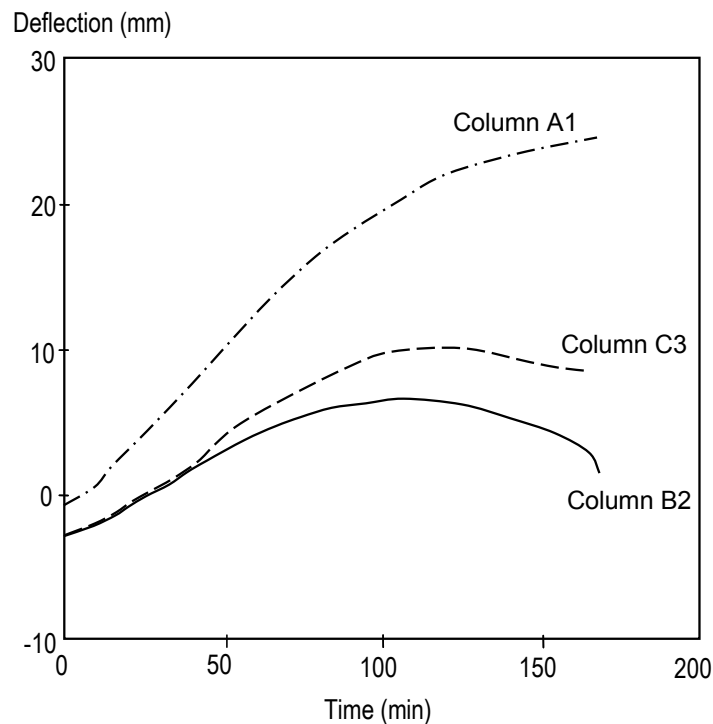


Fig. 6 - Predicted vertical deflections at the tops of three ground floor columns, A1, B2 and C3.

In other words, it is assumed that all the reinforced concrete cross-sections remain intact. The temperatures of the cross-sections of the members, generated by thermal analysis, are then used to carry out the structural analysis. The deflections of some key positions (see Fig. 2) within the structure analysed are presented in Fig. 5. It is evident that the maximum deflection of the floor slabs at 120min is about 250mm, which is $span/30$. Fig 6 shows the

vertical deflections at the tops of three ground floor columns, A1, B2 and C3. It is evident that the columns initially extend upwards due to thermal expansion, then downwards after about 110min because of the reduction of the strength and stiffness of their concrete. The analysis was finally stopped due to buckling of Column B2. It is very clear that, as in composite structures, some fire protection of columns within reinforced concrete buildings is crucial for the extended survival of such structures in fire conditions. For reinforced concrete columns it is also essential to prevent spalling from the column faces in order to avoid direct exposure of the reinforcement to the fire.

Fig. 7 shows the deflection profile of the structure modelled at 150min. A vector plot of the distribution of principal membrane tractions (forces per unit width of slab) at the Gauss points of the slab elements at 150min is shown in Fig. 8. In this plot, the lengths of the vectors are proportional to their magnitudes; thin vector lines denote tension and thick lines denote compression. The figure shows repeated patterns clearly indicating tension fields in the central region of each floor panel, together with the peripheral compression 'rings' which are characteristic of tensile membrane action. It is obvious that the area in tension is rather smaller than the compression region. This is because the deflections are relatively small, less than $span/30$, so tensile membrane action is not very significant.

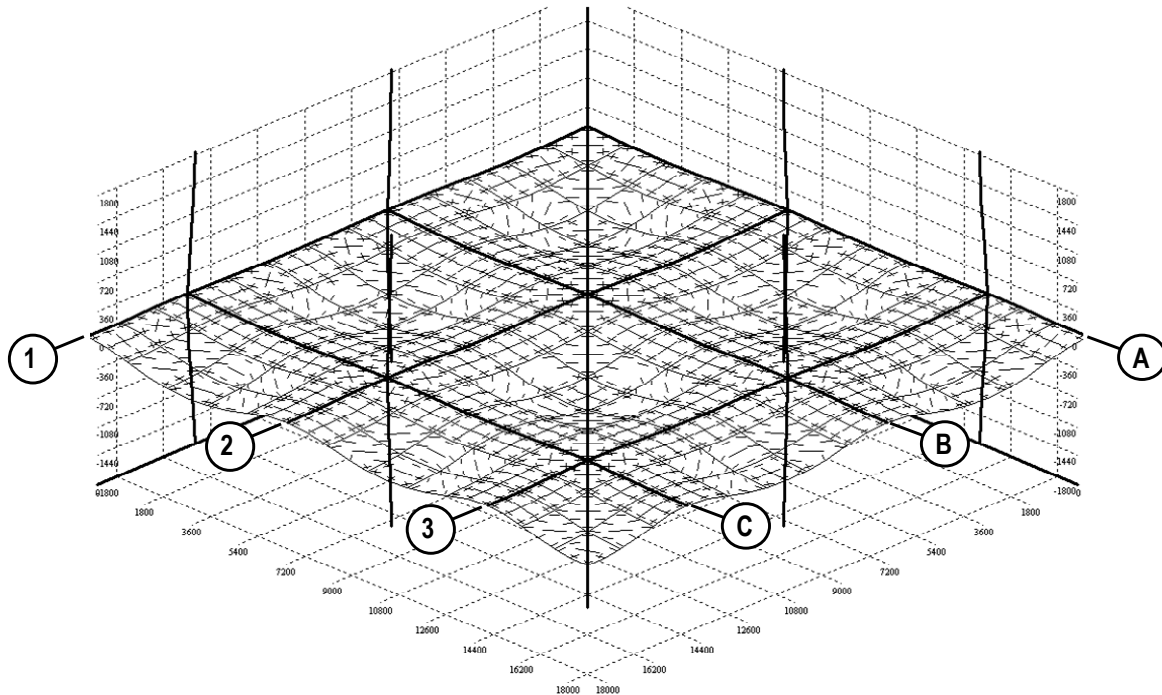


Fig. 7 - Deflection profiles at 150min, with cracking patterns of bottom layer of floor slab.

On detailed inspection of the compression and tension forces across the cut-lines (see Fig 8) it is clear that the compressive membrane forces are much larger than the tensile membrane forces. Hence, in order to maintain the equilibrium at this advanced stage of the fire, the reinforced concrete beams should probably carry tensile forces, since it is unlikely that the whole resultant of the slab forces is balanced by column shear. Fig. 9 shows the change with time of the axial forces of the concrete beams at three key positions shown in Fig 8. It can be seen that at ambient temperature the beams are all subject to resultant tension force. During the first 30min of the fire the tensile forces within the beams increase dramatically, to about three times the ambient-temperature value. Since concrete is very weak in tension the tensile forces within the beams are predominantly carried by the main

reinforcing bars. It is evident from the figure that even after 150min the tensile forces of the beams are about twice their values at ambient temperature. Hence the possibility of tensile failure of the beam reinforcement in the initial stages of the fire is quite high, depending on the type of fire and dimensions of cross-sections of the beam and slabs.

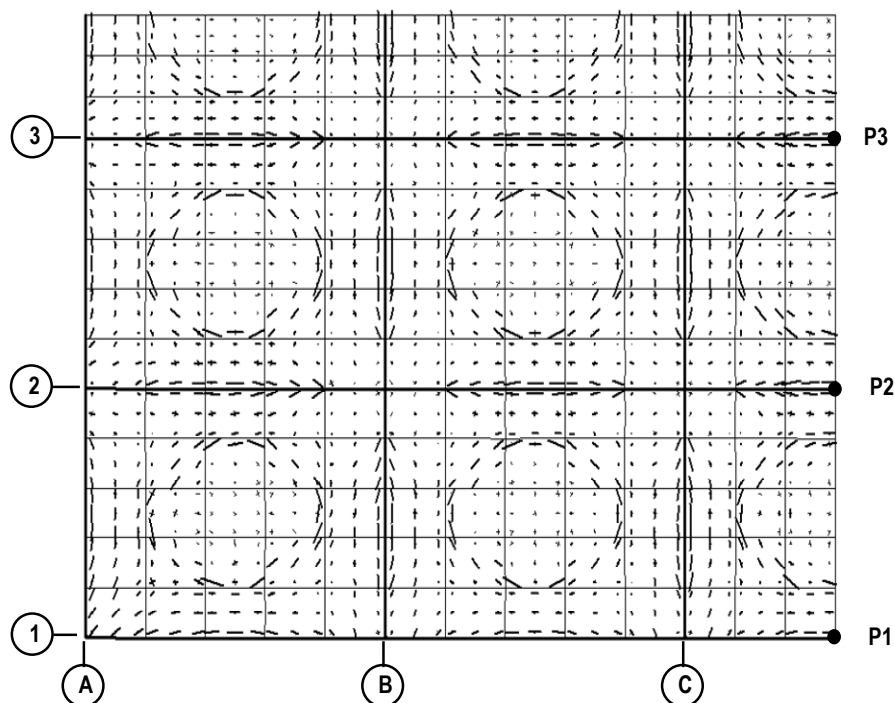


Fig. 8 - Distribution of principal membrane tractions at 150min (thick line=compression; thin line=tension).

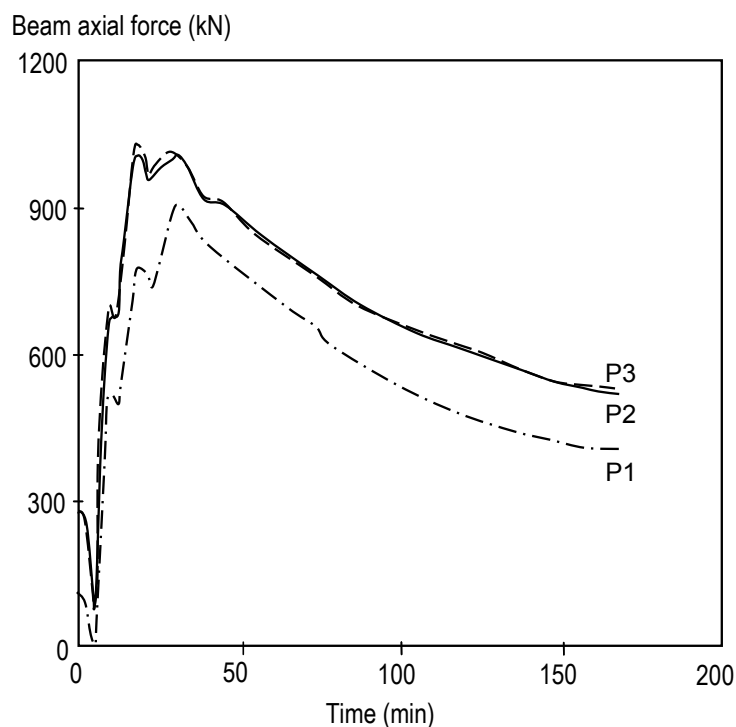


Fig. 9 - Tensile axial forces of beams at key positions.

4. STRUCTURAL BEHAVIOUR WITH FIRE COMPARTMENTS IN DIFFERENT LOCATIONS

In order to study the interactions between the cool and hot zones of the structure, a series of analyses has been carried out for different extents and positions of localised fire compartments. Three different locations are modelled, as indicated in Fig. 10. The temperature distributions for the structural members within the fire compartment are assumed to remain the same as above. The structure beyond the fire compartment is assumed to remain at 20°C.

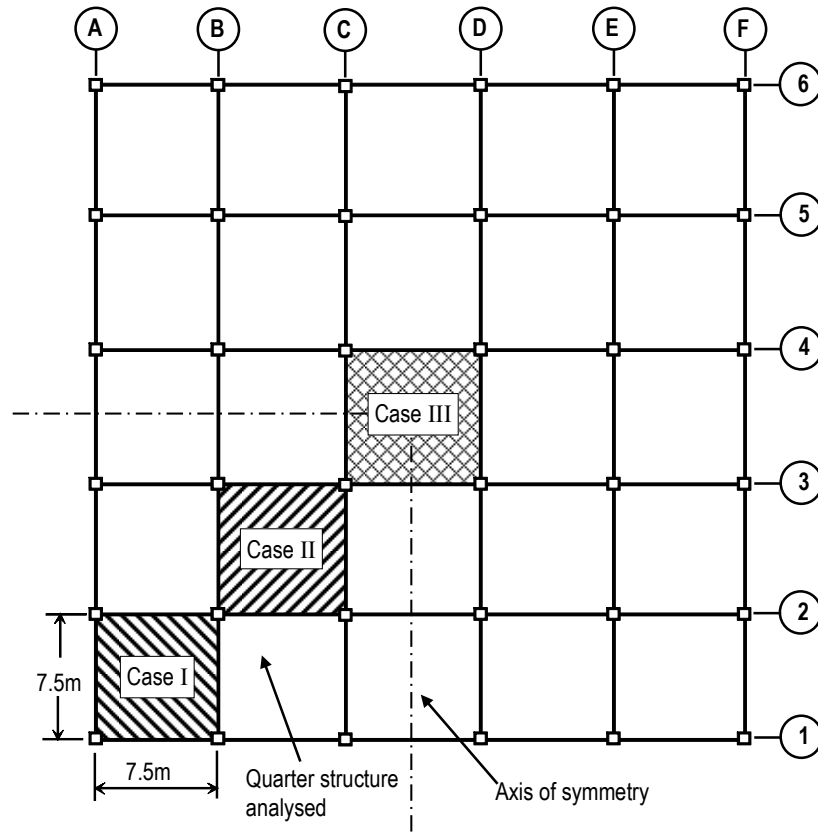


Fig. 10 - Concrete structure layout, with different fire compartment positions marked.

Fig. 11 shows the increase in deflection, at the centre of the fire compartment, with time for the three different cases. The time at which the deflection reaches 220mm is about 50min more for Case III (fire in an internal bay) than for Case I (fire in the corner bay). The structural behaviour within each compartment is clearly different, especially at high temperatures. This is because of the extent of restraint, from the adjacent cool structure and continuity of the floor slabs, which is greater for the internal bays than for the corner bays.

Figs. 12 to 14 show the distributions of the principal membrane tractions in the slab at 150min for Cases I, II and III. It is evident that no tensile membrane forces are formed for Cases II and III within the fire compartment, and that even for Case I only a very small portion of area within the fire compartment experiences tensile membrane forces.

It is clear from the above analyses that the presence or absence of adjacent cool slab areas has significant influence on the behaviour of the structure within the fire compartment. The restraint and continuity from this cool structure provide some benefits in increasing the fire resistance of the structure within the fire compartment. All analyses were eventually

terminated due to buckling of heated columns. Once again, these confirm that prevention of column failure is most important in designing reinforced concrete structures for high fire resistance periods.

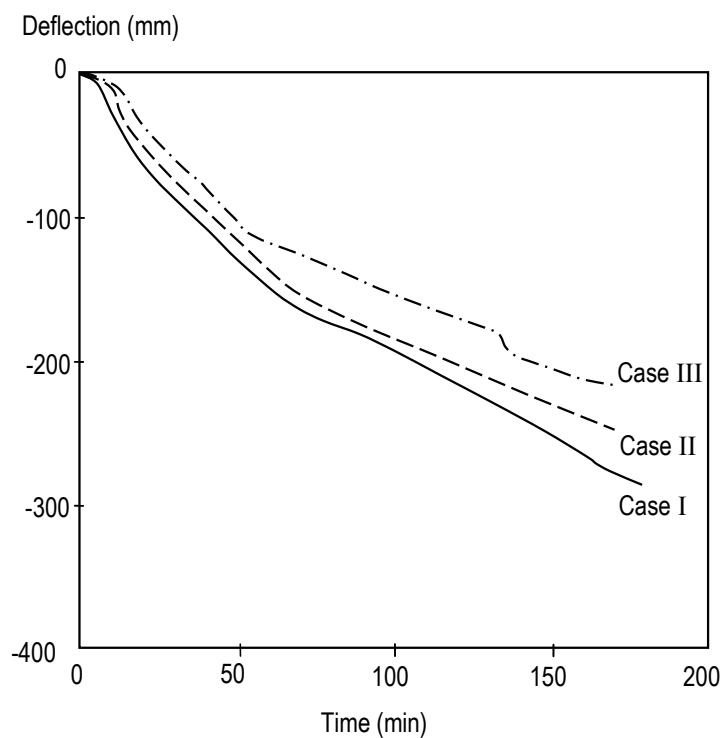


Fig. 11 - Comparison of predicted central deflections for different fire compartment positions.

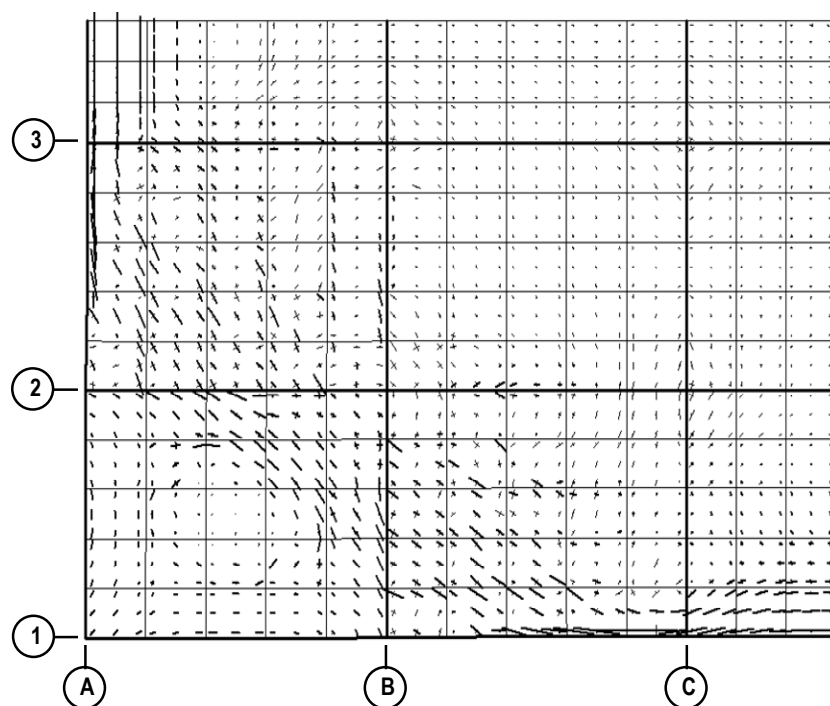


Fig. 12 - Case I: distribution of the principal membrane tractions at 150min (thick line=compression; thin line=tension).

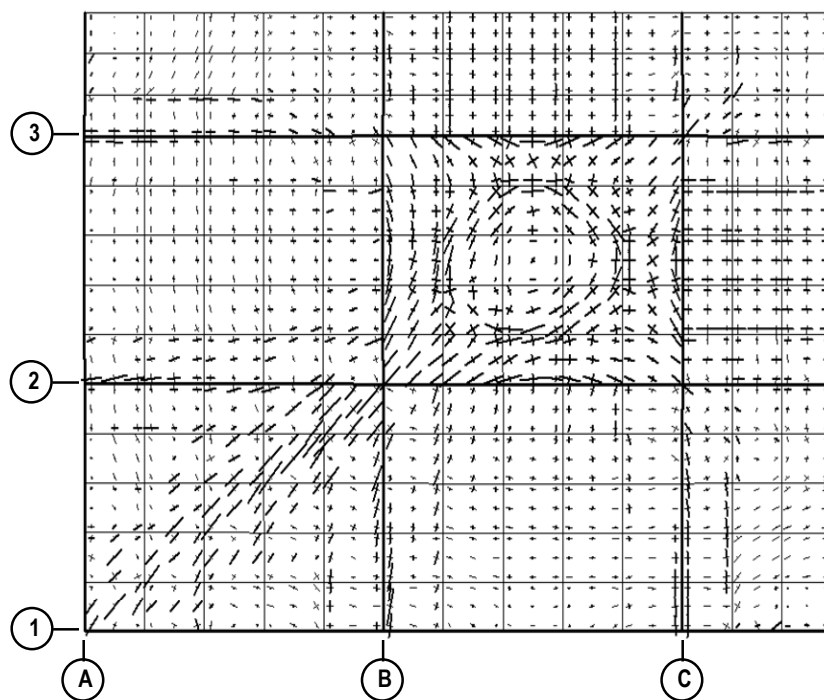


Fig. 13 - Case II: distribution of the principal membrane tractions at 150min (thick line=compression; thin line=tension).

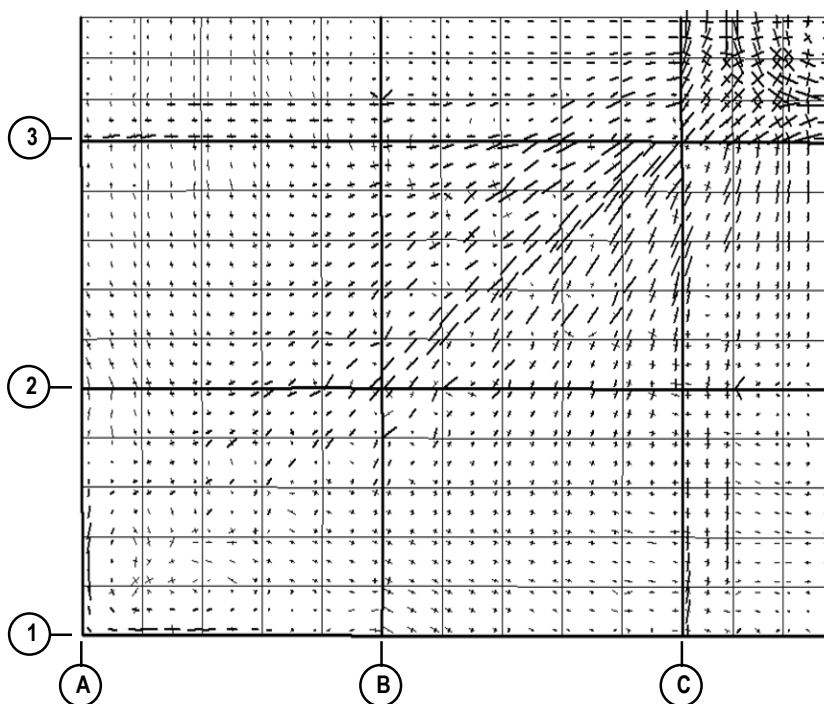


Fig. 14 - Case III: distribution of the principal membrane tractions at 150min (thick line=compression; thin line=tension).

5. CONCLUSIONS

In this paper a series of analyses has been carried out by using the computer program *Vulcan* on a generic reinforced concrete structure subject to the ISO834 standard fire. It is obvious that structural frame behaviour could be well represented through such FE analysis,

which can provide information for rational design of reinforced concrete structures in fire. It is clear that adjacent cool structure provides restraint and continuity, increasing the fire resistance of the structure within the fire compartment. It is also clear from this study that relatively small areas of tensile membrane force were formed within the concrete slabs, and large areas of the slabs were subject to compressive membrane force during the fire. As a result the downstand concrete beams were subjected to enhanced tension during the fire, especially in the initial stages, and these tensions were mainly carried by their tensile reinforcement. It is therefore very important to keep the temperature of the reinforcement within certain limits.

The covers to reinforcement specified in current design codes seem reasonable provided that concrete spalling does not occur during the fire. Designers should therefore pay attention to measures to prevent concrete spalling, in order to enable structures to satisfy their fire resistance requirements. As for composite structures, the fire resistance of columns is vitally important for reinforced concrete buildings. In all cases analysed in this paper the eventual structural failures were due to buckling of the heated columns.

6. REFERENCES

- [1] EN 1992-1-2, "Eurocode 2, Design of concrete structures, Part 1-2: General rules - Structural fire design", Commission of the European Communities, Brussels, 2004.
- [2] EN 1993-1-2, "Eurocode 3, Design of steel structures, Part 1-2: General rules-Structural fire design", Commission of the European Communities, Brussels, 2005.
- [3] International Organisation for Standardisation, "ISO 834: Fire Resistance Tests - Elements of Building Construction," 1985.
- [4] Swinden Technology Centre, "The Behaviour of multi-storey steel-framed buildings in fire: A European joint research programme", British Steel plc, Rotherham, UK, 1999.
- [5] Ellingwood, B., and Lin, T.D., "Flexure and shear behaviour of concrete beams during fires", *Journal of Structural Engineering, ASCE*, **117** (2), pp.440-458, 1991.
- [6] Huang, Z., and Platten, A., "Non-linear finite element analysis of planar reinforced concrete members subjected to fire", *ACI Structural Journal*, **94** (3), pp.272-282, 1997.
- [7] Lie, T.T., and Celikkod, B., "Method to calculate the fire resistance of circular reinforced concrete columns", *ACI Material Journal*, **88**(1), pp.84-91, 1991.
- [8] Najjar, S.R., and Burgess, I.W., "A non-linear analysis for three-dimensional steel frames in fire conditions", *Engineering Structures*, **18** (1), pp.77-89, 1996.
- [9] Huang, Z., Burgess, I.W., and Plank, R.J., "Modelling membrane action of concrete slabs in composite buildings in fire. Part I: Theoretical development", *Journal of Structural Engineering, ASCE*, **129** (8), pp.1093-1102, 2003.
- [10] Huang, Z., Burgess, I.W., and Plank, R.J., "Modelling membrane action of concrete slabs in composite buildings in fire. Part II: Validations", *Journal of Structural Engineering, ASCE*, **129** (8), pp.1103-1112, 2003.
- [11] Huang, Z., Burgess, I.W., and Plank, R.J., "A Non-linear Beam-column Element for 3D Modelling of General Cross-sections in Fire", Research Report DCSE/03/F/1, Department of Civil & Structural Engineering, University of Sheffield, 2003.
- [12] Bathe, K.J., "Finite Element Procedures in Engineering Analysis", Prentice-Hall Inc., New Jersey, 1982.
- [13] EN 1992-1-1, "Eurocode 2: Design of Concrete Structures, Part 1: General Rules and Rules for Buildings", Commission of the European Communities, Brussels, 2004.
- [14] British Standards Institution, "BS8110: Structural Use of Concrete, Part 1: Code of Practice for Design and Constructions", London, 1997.



FACTORS GOVERNING THE FIRE PERFORMANCE OF HIGH STRENGTH CONCRETE SYSTEMS

V.K.R. KODUR¹ and L. PHAN²

ABSTRACT

High strength concrete (HSC), is being increasingly used in a number of building applications, where structural fire safety is one of the major design considerations. Many research studies clearly indicate that the fire performance of HSC is different from that of normal strength concrete (NSC) and that HSC may not exhibit same level of performance (as NSC) in fire. This paper discusses the material, structural and fire characteristics that influence the performance of HSC under fire conditions. Data from earlier experimental and numerical studies is used to illustrate the impact the concrete (material) mix design and structural detailing (design) has on fire performance of HSC systems. An understanding of various factors influencing fire performance will aid in developing appropriate solutions for mitigating spalling and enhancing fire resistance of HSC members.

Keywords: fire resistance, high strength concrete, governing factors, reinforced concrete columns, spalling

1. INTRODUCTION

In recent years, the construction industry has shown significant interest in the use of high strength concrete (HSC), in applications such as bridges, offshore structures, and high-rise buildings. This is due to significant economic, architectural, and structural advantages HSC can provide compared to conventional, normal strength concrete (NSC). One of the major uses of HSC in buildings is for structural framing consisting of beams and columns, which are the primary load-bearing components, and hence, the

¹ Professor, Civil and Env. Eng., Michigan State University, East Lansing, MI.

² Research Structural Engineer, Building and Fire Research Laboratory, National Institute of Standards Technology, Gaithersburg, MD.

provision of appropriate fire safety measures is a main safety requirement in building design. With the increased use of HSC, concern has developed regarding the behaviour of such concrete's in fire. In particular, the occurrence of spalling at elevated temperatures, as observed in studies carried out in a number of laboratories, was a reason for this concern¹⁻⁶.

Building codes generally specify fire resistance requirements for structural members. In North America, concrete structures are to be designed in accordance with the ACI standard⁷ in USA and the CSA standard⁸ in Canada. The recent edition of the standards contains detailed specifications on the design of HSC structural members; however, there are no guidelines for the fire resistance design of HSC structural members either in CSA standard⁸ or the ACI standards^{7,9}.

Generally, concrete structural members (mainly NSC) exhibit good performance under fire situations. However, results from a number of studies^{1-6, 10-12} have shown that there are well-defined differences between the properties of HSC and NSC at high temperatures. Further, concern has developed regarding the occurrence of explosive spalling when HSC is subjected to rapid heating, as in the case of a fire^{4,5,11}.

Tracing the fire response of HSC structural system requires the use of accurate numerical models that properly account for material characteristics (including spalling) and structural response under real fire exposure scenarios. In the last few years there has been limited number of studies on the fire behaviour of HSC. Most of these studies focused on either material response – on small scale HSC cylinders tests, or on structural response – mainly on HSC columns. There have been no studies that integrated the material and structural response of HSC. In this paper, based on a detailed literature review, the fire behaviour of HSC is examined from material level to structural level. A discussion on the various factors that influence spalling and fire endurance of HSC members is presented. The effect of various factors on fire performance will help in developing solutions for mitigating spalling and enhancing fire endurance of HSC structural members. Such solutions are very critical for updating design standards including ACI 216⁹.

2. CONCRETE AND FIRE

Structural members are to be designed to satisfy the requirements of serviceability and safety limit states for various environmental conditions. Fire represents one of the most severe conditions and hence the provision of appropriate fire safety measures for structural members is a major safety requirement in building design. The basis for this requirement can be attributed to the fact that, when other measures for containing the fire fail, structural integrity is the last line of defence.

Generally, concrete structural members (traditionally used to be made of NSC) exhibit good performance under fire situations. Studies show, however, that the performance of HSC is different from that of NSC and may not exhibit good performance in fire. Further, the spalling of concrete under fire conditions is one of the major concerns due to the low porosity (permeability) in HSC. The spalling of concrete exposed to fire has been observed under laboratory and real fire conditions^{2,5,11,13}. Spalling, which results in the rapid loss of concrete during a fire, exposes deeper layers of concrete to fire temperatures, thereby increasing the rate of transmission of heat to the inner layers of the member, including the reinforcement.

Spalling is theorized to be caused by the build-up of pore pressure during heating. HSC is believed to be more susceptible to this pressure build-up because of its low permeability compared to NSC. The extremely high water vapour pressure, generated during exposure to fire, cannot escape due to the high density of HSC and this pressure often reaches the saturation vapour pressure. At 300°C, the pressure

reaches about 8 MPa. Such internal pressures are often too high to be resisted by the HSC mix having a tensile strength of about 5 MPa².

Data from various studies^{10, 11, 14} show that the fire behaviour of HSC, in general, and spalling in particular, is affected by a number of factors. However, in many of the earlier studies, the focus is entirely based either on material characteristics or on structural considerations. In this paper, a holistic approach is used to discuss the effect of various parameters on the fire performance of HSC members.

3. FACTORS GOVERNING FIRE PERFORMANCE

The fire resistance of a structural member is dependent on the geometry, the materials used in construction, the load intensity and the characteristics of the fire exposure itself. Fire endurance of HSC members depend not only on the extent of spalling but also on the rate of loss of strength in concrete. Further, achieving required fire endurance in HSC member through improved design, rather than through external fire protection, will enhance the cost-effectiveness and aesthetics of the overall structural system.

A review of the literature indicates that the main aim of many researchers was to explore measures for mitigating spalling in HSC^{2, 4, 5, 6, 10}. Often, these measures were based on very limited fire tests on small-scale specimens^{2, 10}. The focus of the current paper is to compile information from previous studies and to evaluate the overall fire endurance of HSC members, which depends not only on the extent of spalling but also on the overall behaviour of HSC member in fire.

Data from various studies carried out in a number of organizations world-wide^{3-6, 12-14}, clearly show that fire performance of HSC, in general, and spalling in particular, is complex and is affected by a number of factors. However, to achieve an optimum design a holistic approach has to be adapted where in the behaviour at both material and structural levels have to be considered. With this approach in mind, and based on the analysis of model predictions, test data, and the visual observations made during and after the fire tests, the factors that influence the fire performance of HSC structural members can be broadly classified into 3 categories: namely, fire characteristics, material characteristics and structural characteristics. These factors are briefly discussed below.

3.1 Fire Characteristics

The type of fire, the fire size and heat output, has significant influence on the fire performance of a concrete structural system. The high rate of temperature rise can induce spalling in concrete members. This is mainly due to high temperature gradients that develop within a cross-section, which in turn increases the pore pressure generated in the concrete. This effect can lead to significant spalling in HSC members. In many of the fire tests, undertaken under hydrocarbon fires, high rate of spalling was observed and this spalling started within the first few minutes of fire exposure^{4, 5}. This can be explained to the fact that the temperatures attained in the hydrocarbon fire is about 815 °C in the first 3 minutes of fire exposure, as opposed to about 490 °C in typical ASTM E-119 fire. Thus, higher temperature gradients develop under hydrocarbon fires very quickly once the fire starts.

Much of the current fire provisions contained in codes and standards are based on (standard ASTM-E119 or similar) fire scenarios, which represents typical building fires. These provisions may not be directly applicable to fires resulting in infrastructure projects such as offshore structures, and tunnels due to a wide range of differences in fire characteristics. These fires, often referred to as hydrocarbon fires, typically represented by ASTM-E1529 Standard fire, are much more severe (than building fires) and are characterized by fast heating rates or high fire intensities. In Fig. 1, the time-temperature curves from two standard tests and a typical building fire based on temperature measurements acquired in experiments involving office furnishing conducted by DeCicco, et al.¹⁵, is compared. Temperature development in a

fire, where hydrocarbon fires might present, is likely to be closer to the ASTM E-1529 curve. Thus, the fire in infrastructure projects is likely to be much more intense than typical building fires and can reach very high temperatures within the first few minutes of fire exposure. Hence, proper attention should be given to spalling mitigation techniques when HSC structural members are used in applications involving scenarios where hydrocarbon fire might result.

3.2 Material Characteristics

The behaviour of a concrete structural member exposed to fire is dependent, in part, on thermal and mechanical properties of concrete of which the member is composed. Similar to other materials the thermo-physical and mechanical properties of concrete change substantially within the temperature range associated with building fires. These properties vary as a function of temperature and depend on the composition and characteristics of concrete. The strength of concrete has significant influence on the properties of HSC at both room and high temperatures. This variation of properties at elevated temperatures is more pronounced for mechanical properties, which are affected by strength, moisture content, density, heating rate, amount of silica fume and porosity. Based on the review of previous fire resistance studies, the following factors have significant influence on the fire performance of HSC.

Concrete Strength: Results from a number of fire resistance tests show that strength of concrete has significant influence on fire performance of concrete members. The higher the strength, or the associated lower permeability, the higher will be the probability of spalling. Further, the loss of strength with temperature is higher for HSC as compared to NSC. A comparison of the variation of strength for HSC and NSC is shown in Fig. 2 as a function of temperature¹. It can be seen that the rate of loss of strength is higher (and significant) for HSC over the entire temperature range. In addition, the fire induced spalling of HSC is significantly higher than that for NSC. Based on full-scale fire tests on loaded columns, the spalling performance of NSC columns has been compared with that of HSC columns in a number of studies^{11, 13}. In majority of these studies, the spalling was quite significant in the HSC columns as compared to NSC columns. While it is hard to specify the exact strength range, based on the available information, concrete strengths higher than 70 MPa are more susceptible to spalling and may result in lower fire resistance.

Silica Fume: Results from fire endurance tests on HSC columns¹⁶ clearly indicate that silica fume, and associated concrete strength, has an influence on fire endurance. Based on fire resistance tests, while for NSC columns (concrete strength of about 40 MPa) a fire endurance of about 6 hours was obtained³, for HSC columns (concrete strength of about 114 MPa), with similar confinement, fire endurance of only about 4 hours was obtained^{11, 16}. In these tests, the extent of spalling was very significant in columns with high silica fume content (about 15%). The higher silica fume, and associated compressive strength, increases the extent of spalling, due to increased compactivity, and leads to decreased fire endurance. This could be attributed to the fact that the addition of silica fume appears to reduce the permeability of the concrete, restricting the loss of moisture during curing, drying, and the fire test. Further research is needed to quantify the exact extent of silica fume on spalling and fire endurance of HSC members.

Concrete Moisture Content: The moisture content, expressed in terms of relative humidity (RH), influences the extent of spalling. Higher RH levels lead to greater spalling. Fire-resistance tests on full-scale HSC columns and HSC blocks have shown that significant spalling occurs when the RH is higher than 80%^{5, 11}. The time required to attain an acceptable RH level (below 75%) in HSC structural members is longer than that required for NSC structural members because of the low permeability of HSC. In some cases, such as in offshore structures, RH levels can remain high throughout the life of the structure and should therefore be accounted for in design⁵.

Concrete Density: The effect of concrete density was studied by means of fire tests on normal-density (made with normal-weight aggregate) and lightweight (made with lightweight aggregate) HSC blocks⁵. The extent of spalling was found to be much greater when lightweight aggregate is used. This is mainly because the lightweight aggregate contains more free moisture, which creates higher vapour pressure under fire exposures.

Fibre Reinforcement: Studies show that the addition of polypropylene fibers minimizes spalling in HSC members under fire conditions^{4, 6, 13}. One of the most accepted theories on this is that by melting at a relatively low temperature of 170°C, the polypropylene fibres create "channels" for the steam pressure within the concrete to escape, thus preventing the small "explosions" that cause spalling. The amount of polypropylene fibres needed to minimize spalling is about 0.1 to 0.15% (by volume)^{4, 5, 6, 17}. In some studies, addition of steel fibres was found to be beneficial in enhancing fire endurance of HSC column¹³. The presence of steel fibres increases the tensile strength of concrete, at high temperatures, and thus reduces spalling and enhances fire resistance^{13, 17}.

Type of Aggregate: Of the two commonly used aggregates, carbonate aggregate (predominantly limestone) provides higher fire resistance and better spalling resistance in concrete than does siliceous aggregate (predominantly quartz). This is mainly because carbonate aggregate has a substantially higher heat capacity (specific heat), which is beneficial in preventing spalling. This increase in specific heat is likely caused by an endothermic reaction that occurs due to dissociation of the dolomite in the carbonate concrete. In general the fire endurance of HSC columns made with carbonate aggregate concrete is about 10% higher than HSC columns made with siliceous aggregate concrete^{11, 12, 13}.

3.3 Structural Features

The structural behaviour of concrete under fire conditions can be gauged from various fire resistance tests on reinforced concrete (RC) columns. Fig. 3 illustrates the typical structural behaviour of an HSC column as compared to NSC column³. In this figure the variation of axial deformation with time is compared for NSC and HSC columns. It can be seen from the figure that the behaviour of the HSC column was different from that of the NSC column and the fire resistance of HSC column to be lower than that of NSC column. There is significant contraction in the NSC column leading to gradual ductile failure. However, in the case of the HSC column the deformation is significantly lower than that of the NSC column and the contraction of the HSC column is much lower. This can be attributed to the fact that HSC becomes brittle at elevated temperatures and the strain attained at any stress level is lower than that attained in NSC for any given temperature^{3, 11}. Data from previous studies is used to quantify the structural features that contribute to spalling and to the overall fire resistance of HSC members.

Specimen Dimensions: A review of the literature shows that the risk of explosive thermal spalling increases with specimen size. This is due to the fact that specimen size is directly related to heat and moisture transport through the structure, as well as the capacity of larger structures to store more energy. Therefore, careful consideration must be given to the size of specimens when evaluating the spalling problem; fire tests are often conducted on small-scale specimens, which can give misleading results. However, when spalling mitigation measures are incorporated, the risk of explosive spalling decreases and fire resistance increases with the size of the members. Also, similar cover thickness to reinforcement, as in the case for NSC columns, based on structural (corrosion) considerations should be provided for HSC columns.

Lateral Reinforcement: Results from fire resistance studies clearly show that the layout of ties and confinement of columns have an influence on the fire performance of HSC columns. Higher fire endurance in HSC columns can be achieved by providing improved tie configuration (provision of bent ties at 135° back into the core of the column and increased lateral reinforcement) and with closer tie

spacing (at 0.75 times that required for NSC columns). Fig. 4 shows a conventional and modified tie configuration for HSC column. The provision of cross ties also improves fire endurance^{11, 16}. These improved tie provisions also minimise the extent of spalling in HSC columns. This increased fire endurance and reduced spalling are mainly due to ties holding the longitudinal rebars, firmly in place, under fire exposure conditions. This mechanism helps to minimise the movement and buckling of longitudinal bars which in turn reduces the strains induced in concrete.

Fig. 5 show photographs of the column specimens, with conventional and improved tie configuration, after the fire resistance test as reported by Kodur and McGrath¹¹. The extent of spalling in columns, with bent ties configuration, was relatively less compared to that in columns without bent tie configuration. Columns containing only 90° ties would typically lose a significant portion of the columns section upon failure. Columns using 135° ties would exhibit the classic pyramid compression failure section with the failed section being confined locally to one or two tie spacing.

Degree of Restraint: The degree of restraint, during fire exposure conditions, influences the extent of spalling and fire endurance to some extent. The analysis of the test results shows that increasing the degree of restraint increases the generation of forces in the column¹⁴. However, the forces generated are not very significant when compared to overall column strength. Further, the generated restraint forces in HSC columns were very close to those generated in NSC columns.

Load Intensity and Type: The type of load and its intensity have significant influence on spalling and the resulting fire resistance. The fire endurance of a reinforced concrete column increases with a decreasing load. A higher load intensity leads to lower fire resistance, since the loss of strength with a rise in temperature is greater for HSC than for NSC. This has been confirmed through number of fire tests where a loaded HSC structural member was more susceptible to higher spalling than an unloaded member^{11-14, 16}. This is specially true in columns with conventional tie configuration and subjected to loads greater than service loads. This occurs because a loaded structural member is subjected to stresses due to load in addition to the pore pressure generated by steam. Further, the extent of spalling is higher if the load is of an eccentric (or bending) type since this will induce additional tensile stresses.

4. DESIGN IMPLICATIONS

High-strength concrete is a high-performing material that offers a number of advantages. In recent years significant research has been undertaken to study the fire behaviour of HSC members and to quantify the factors influencing their spalling and fire endurance. However, eve-to-date there are no specific guidelines in codes and standards for the fire resistance design of HSC structural members.

As illustrated above, enhancing fire performance of HSC requires proper measures to be considered in the mix-design and in structural design stages. By adopting appropriate measures both at material and structural level, spalling in HSC can be minimised and fire endurance can be enhanced even for concrete strength as high as 110 MPa. While this has been shown through limited fire tests, at present there is no understanding or broad guidelines on the measures needed to address fire problems of HSC. Development of fire resistance design guidelines for HSC members requires detailed numerical modelling studies and quantification of the extent of influence of various factors on spalling and fire resistance. Such models should account for many of the above mentioned factors in tracing the fire performance of HSC members.

5. SUMMARY

High strength concrete is a high-performing material and offers a number of benefits over normal strength concrete. However, there is a concern on the occurrence of spalling and lower fire endurance of HSC (as compared to NSC). The fire characteristics, concrete mix properties and structural design features have an influence on the fire performance (both spalling and fire endurance) of HSC columns. The fire intensity, fire size and heat output, and rate of heating influence the degree of spalling and fire endurance duration of HSC members. The main parameters that influence fire performance of HSC at material level are: concrete strength, silica fume, concrete moisture content, concrete density, fibre reinforcement, and type of aggregate. At the structural level, tie spacing, confinement, tie configuration, load levels and size of the members play an important role in determining fire endurance. By adopting proper guidelines, both at material and structural levels, spalling in HSC members can be minimized to a significant extent and fire endurance can be enhanced. Adding polypropylene fibres to concrete mix is much more effective in minimising spalling in HSC under hydrocarbon fires. Similarly, under building fire exposure, using bent tie configuration for lateral reinforcement in HSC columns is very effective in minimizing spalling and enhancing fire endurance.

6. REFERENCES

- [1] Phan, L.T. "Fire Performance of High-Strength Concrete: A Report of the State-of-the-Art", National Institute of Standards and Technology, Gaithersburg, MD, pp. 105, 1996.
- [2] Diederichs, U.; Jumppanen, U.M., Schneider, U. "High Temperature Properties and Spalling Behaviour of HSC", Proceedings of 4th Weimar Workshop on HPC, HAB Weimar, Germany, pp. 219-235, 1995.
- [3] Kodur, V.R., Sultan, M.A. "Structural behaviour of high strength concrete columns exposed to fire" Proceedings: International Symposium on High Performance and Reactive Powder Concrete, Vol. 4, 217-232, Sherbrooke, Quebec, 1998.
- [4] Danielsen, Ulf. "Marine Concrete Structures Exposed to Hydrocarbon Fires", Report, SINTEF – The Norwegian Fire Research Institute, pp. 56-76, 1997.
- [5] Bilodeau, A; Kodur V.R.; Hoff, G.C. "Optimization of the type and amount of polypropylene fibres for preventing the spalling of lightweight concrete subjected to hydrocarbon fire", Cement and Concrete Composites Journal, 26(2), pp. 163-175, 2004
- [6] Hertz K.D. "Limits of Spalling of Fire-Exposed Concrete", Fire Safety Journal 38 (2003) pp 103-116 National Research Council of Canada, National Building Code of Canada, Ottawa, ON, 1995.
- [7] ACI Committee 318, "Building Code Requirements for Reinforced Concrete" (ACI 318-02), American Concrete Institute, Detroit, 2002.
- [8] Canadian Standards Association, Code for the Design of Concrete Structures for Buildings. CAN3-A23.3-M02, Rexdale, ON, 2002.
- [9] ACI Committee 216, "Standard Method for Determining Fire Resistance of Concrete and Masonry Construction Assemblies", American Concrete Institute, Detroit, 1997.
- [10] Phan, L.T. and Carino, H.J. "Effects of Test Conditions and Mixture Proportions on Behavior of High-Strength Concrete Exposed to High Temperatures", ACI Material Journal v.00(1) , pp. 54-66, 2002.
- [11] Kodur, V.R.; and McGrath, R.C. "Fire endurance of high strength concrete columns", *Fire Technology – Special Issue*, Vol. 39: No. 1, pp. 73-87, 2003.
- [12] Kodur, V. R., Wang T.C.; and Cheng, F.P. "Predicting the fire resistance behaviour of high strength concrete columns", Cement and Concrete Composites Journal, 26, pp. 141-153, 2004.
- [13] Kodur V.K.R., Cheng F.P. and Wang T.C. "Effect of strength and fiber reinforcement on the fire resistance of high strength concrete columns", ASCE Journal of Structural Engineering, 129(2), pp. 253-259, 2003.

- [14] Ali, F.A., Nadjai, A., Glackin, P., Silcock, G., "Outcomes of a major research on fire resistance of concrete columns", Fire Safety Journal, 39, pp. 433-445, 2004.
- [15] DeCicco, P.R. and Cresci, R.J., and Correale, W.H., "Fire Tests, Analysis and Evaluation of Stair Pressurization and Exhaust in High Rise Office Buildings," Brooklyn Polytechnic Institute, 1972.
- [16] Kodur V.K.R.; and McGrath, R. "Effect of silica fume and confinement on fire performance of high strength concrete columns" in Press: Canadian Journal of Civil Engineering; pp 24, 2006.
- [17] Kodur, V.R. "Fiber reinforcement for minimizing spalling in HSC structural members exposed to fire", Innovations in Fibre-Reinforced Concrete for Value, ACI Special Publication SP: 216, pp. 221-236, 2003.

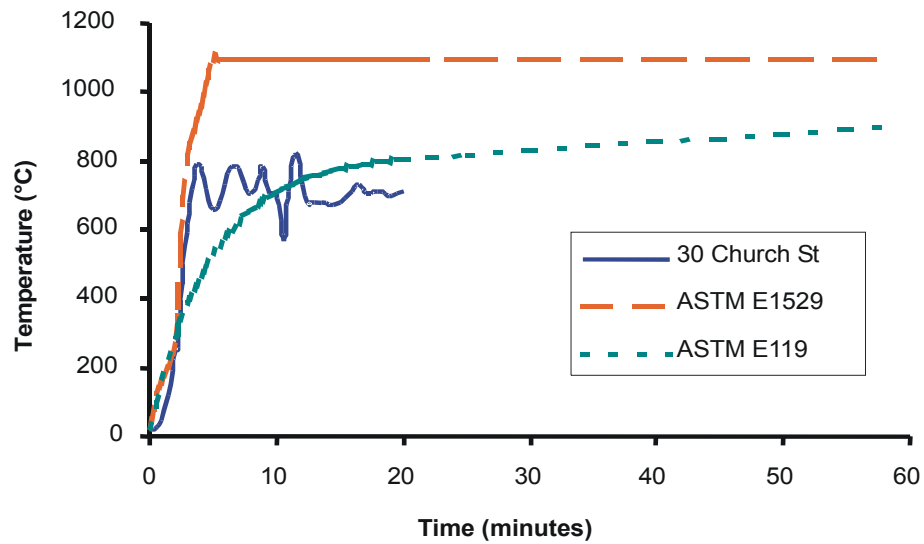


Fig. 1- Time-Temperature Curves from two Standard Tests and Temperature Measurements in a Typical Building¹⁵

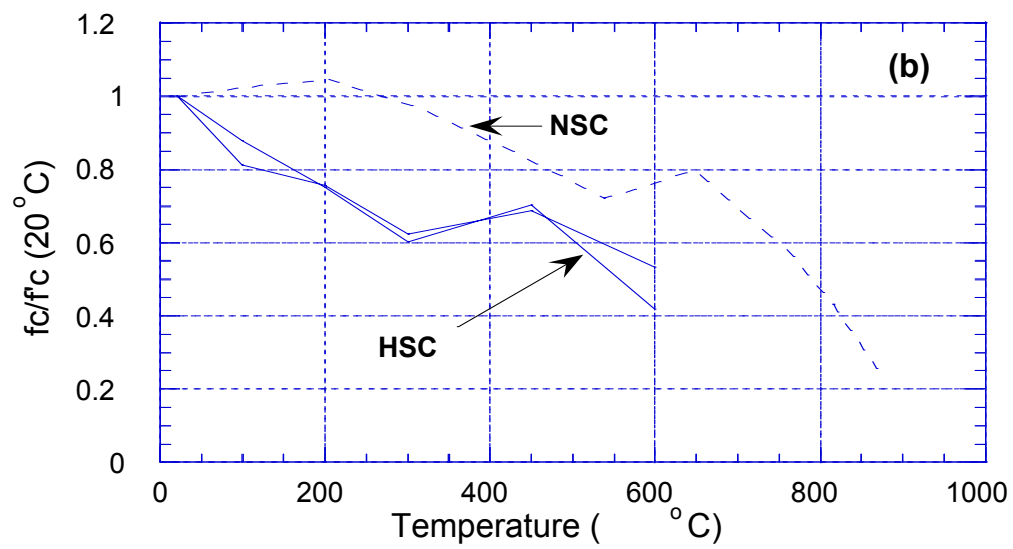


Fig. 2- Variation of Strength as a Function of Temperature for NSC and HSC¹

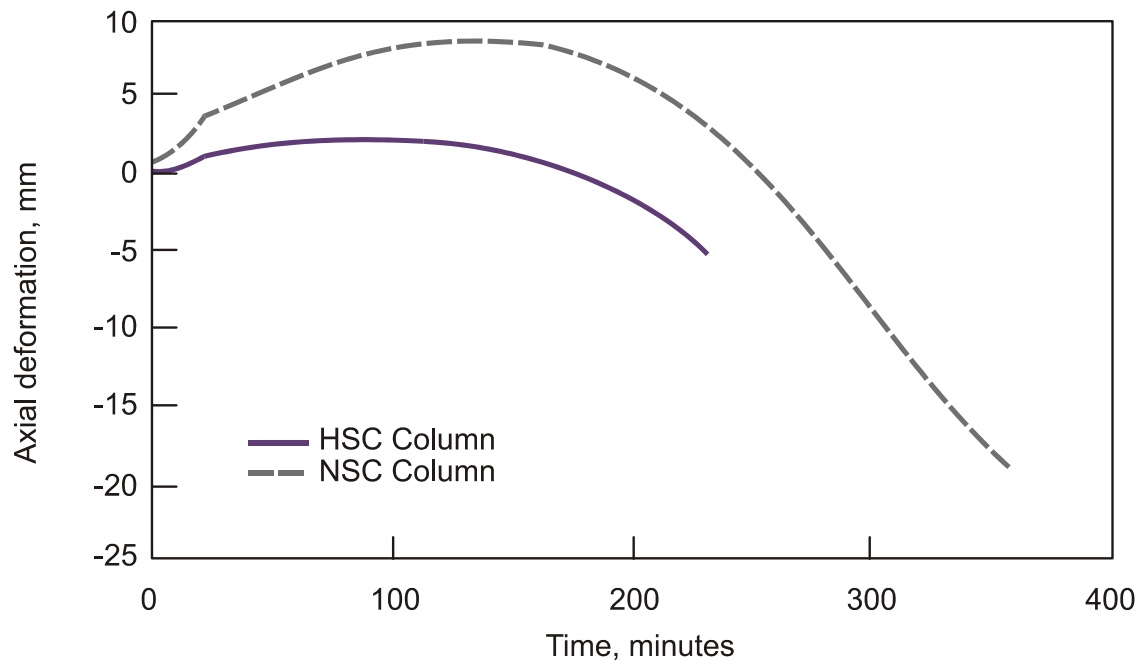
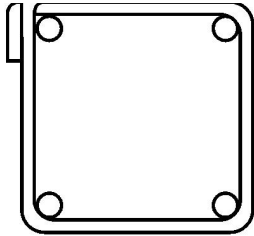
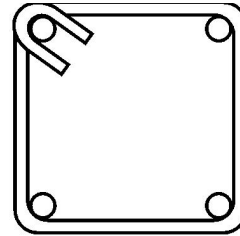


Fig. 3- Axial Deformation for HSC and NSC Columns³



(a) Conventional Tie Configuration



(b) Modified Tie Configuration

Fig. 4- Conventional and Modified Tie Configuration for Reinforced Concrete Columns¹²



Conventional Tie Configuration



Modified Tie Configuration

Fig 5- Comparison of Spalling in HSC Columns after Fire Resistance Tests¹¹



FIRE PERFORMANCE OF HPLWC HOLLOW CORE SLABS

Marco BRECCOLOTTI¹, Annibale Luigi MATERAZZI² and Ilaria VENANZI³

ABSTRACT

In this paper are presented experimental and numerical investigation carried out to evaluate the fire behaviour of high performance lightweight concrete (HPLWC) hollow core slabs.

In particular, a series of full-scale furnace tests was performed to assess the slabs' load bearing capacity under fire conditions along with the characteristics of the thermal field.

Numerical simulations of the heat diffusion process were also carried out using a finite element model of the panel cross section. The ultimate strength was evaluated according to the advanced calculation methods suggested by the Eurocodes, using decay laws of the mechanical properties found in literature.

The comparison between the experimental and numerical investigation gave insight into the fire performance of HPLWC hollow core slabs and enlightened on the phenomena governing their fire resistance.

1. INTRODUCTION

Pre-stressed concrete hollow core slabs have been manufactured for several years using normal weight-normal strength concrete (NSC).

The flexural behaviour of pre-stressed NSC hollow core slabs under fire conditions has been deeply investigated in the last few years and can be considered satisfactory if the onset of torsion moments is prevented through suitable design provisions.

Some doubts still stand about the shear strength, as remarked by Van Hacker [1] and Fellingner [2] who developed extensive surveys on this topic. Both Authors highlighted the role of the connections details on the full-scale fire behaviour and recommended to pay special

¹ Research Fellow, University of Perugia, Department of Civil and Environmental Engineering, 06125 Perugia, Italy, email: breccolotti@strutture.unipg.it

² Professor, University of Perugia, Department of Civil and Environmental Engineering, 06125 Perugia, Italy, email: materazzi@unipg.it

³ Research Fellow, University of Perugia, Department of Civil and Environmental Engineering, 06125 Perugia, Italy, email: ilaria.venanzi@strutture.unipg.it

attention, during the organization of furnace tests, on the boundary restraints, in order to simulate accurately the conditions usually met in the real structures.

During the last years the use of high performance lightweight concrete (HPLWC) has been considered to manufacture these structural components. In fact the characteristics of lightness, relatively high strength and superior durability make this material suitable for many structural applications.

The low thermal diffusivity of this material, due to the low density of the aggregates and to the latent heat of the free water, as highlighted in [3,4], may be considered, in principle, a favorable property in case of exposure to fire. In the specific case of hollow core slabs, which have no transverse reinforcement, these characteristics may lead in some cases to the onset of cover spalling, due to the high thermal gradients and the internal pore pressures.

However the information on the mechanical and thermal properties of the HPLWC and, in particular, on the fire resistance of HPLWC structural components is still incomplete. The research mainly dealt with the fire behaviour of light weight concrete, considering small size samples, paying special attention to the study and the prevention of the phenomenon of the spalling through the addition of various types of fibres (Sullivan & Sharshar in 1992 [5], Hertz in 1984 [6] and 1991 [7], Hammer in 1995 [8], Felicetti et al. in 2002 [3] and Felicetti and Gambarova in 2003 [4]), even though some interesting studies on beams are available (Hansen & Jensen in 1995 [9] and Sullivan in 2000 [10]).

The present paper is aimed at giving a contribution to the understanding of the fire behaviour of HPLWC hollow core slabs, presenting and critically discussing the results of full scale furnace tests. The experimental results are analysed with the support of a numerical simulation of the thermal field, carried out applying the finite element method and using data on the thermal properties of the high performance light weight concrete taken from the available literature.

2. FURNACE TESTS

Two full-scale furnace tests were carried out on a total of four HPLWC hollow core slabs.

To highlight the effect of concrete maturity on the possible onset of spalling, the second test was carried out almost one year after the first one.

During each test, two panels, simply supported on the furnace walls, were simultaneously heated following the ISO 834 thermal program. One of them was loaded following a four point bending scheme, while the other one was left unloaded during the heating and was used to assess the residual strength after cooling.

Fig. 1 shows a picture representing the experimental set up

The slabs were 4.3 m long with a cross section of 1.2 x 0.2 m, made from C48/58 N/mm² concrete and had a unit weight of 1.9 kN/m³. The pre-stressing reinforcement was made up of seven 3/8" strands per slab. The mix design of the concrete used for the slabs is listed in Table 1.

Additional shear reinforcement was placed at both ends of each slab by cutting the concrete over two cores, setting in place steel stirrups and casting concrete to fill the holes.

The thermal boundary conditions at the slabs ends varied between the two tests. In fact, while during the first test the holes were left open, during the second test they were closed, using mineral wool to prevent air circulation. The holes insulations are visible in the picture of Fig. 1.

The specimens were built on the 29th of June 2002 and were stored in the factory under the same curing conditions used for the everyday production until September 23rd,

2004, when the first furnace test was carried out. The second furnace test was performed the 12th of October 2005. During the period between the first and the second test the panels were stored near the furnace, in extremely dry conditions, further contributing to the maturity of concrete and to the reduction of free water content.

Table 1. Mix design of the HPLWC.

Material	Quantity
Cement	380 kg/m ³
Water	100 kg/m ³
T8 expanded clay	578 kg/m ³
Fine sand	526 kg/m ³
Sand	279 kg/m ³
Slurry	41 kg/m ³



Fig. 1. Experimental set up of the 2nd test.

2.1 Experimental set-up

During each furnace test, two slabs were used: one was loaded during the furnace tests following a four point bending scheme, while the other was only heated and submitted to an analogous four point bending test after cooling, to estimate the residual strength after exposure to fire. The value of the vertical load was selected to cause a bending moment at the mid-span section equal to 60% of the corresponding value in service conditions. In particular, the total load of 40 kN (20 kN at each point), corresponding to a bending moment of 33.7 kNm, was applied.

The vertical deflections of the loaded slabs were monitored for the whole duration of the tests.

Both slabs have been fitted with thermocouples placed at different locations and depth (Fig. 2).

The thermocouples have been installed inside the hardened concrete by drilling holes and using insulating material to close them. It was decided to use insulating material instead of cement mortar to avoid possible measurement inaccuracy due the evaporation of the residual moisture of the sealing material.

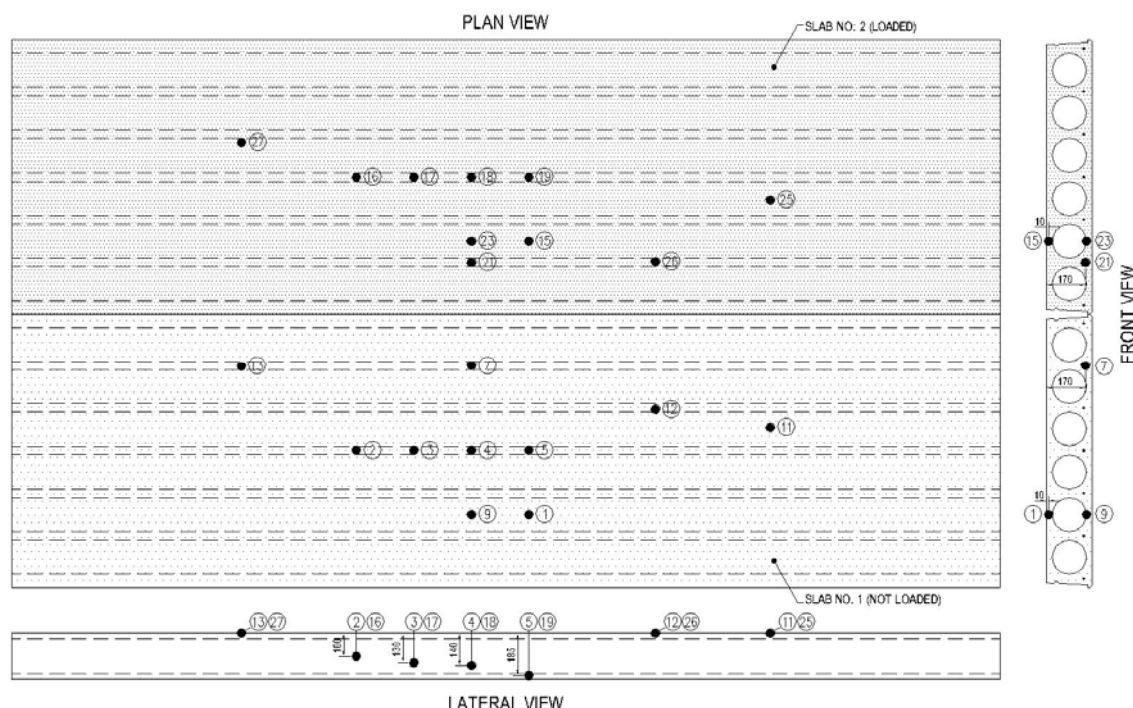


Fig. 2. Temperature sensors location.

2.2 Experimental results

The experimental results are presented in Figures 3 to Fig. 5. In particular, Figures 3 and 4 represent the deflection and the deflection speed of the loaded slabs during the two furnace tests.

During the 1st test a brittle collapse in shear of the loaded slab occurred after 76 minutes and is clearly visible in Fig. 3. It was anticipated at the 40th minute by the formation of a pass-through vertical hole, which allowed the hot gases to escape and by several concrete cover spalling that seriously damaged the loaded slab. The pass-through hole was closed on the spot with insulating material to continue the test until failure.

During the 2nd test no cover spalling and no brittle failure occurred. The loaded slab was assumed to collapse, according to the UNI-EN 1363-1 [11], when the deflection speed reached the limiting value expressed by:

$$v = \frac{dz}{dt} = \frac{L^2}{9000 \times d} \text{ (mm / min)}$$

(1)

where L is the net length of the test specimen and d is the specimen design height. In our case the limiting deflection speed was equal to:

$$v = \frac{4000^2}{9000 \cdot 200} = 8.89 \text{ mm/min} \quad (2)$$

As depicted in Fig. 4 the overcoming of this threshold value occurred at 90 min, time at which the collapse was considered to have occurred.

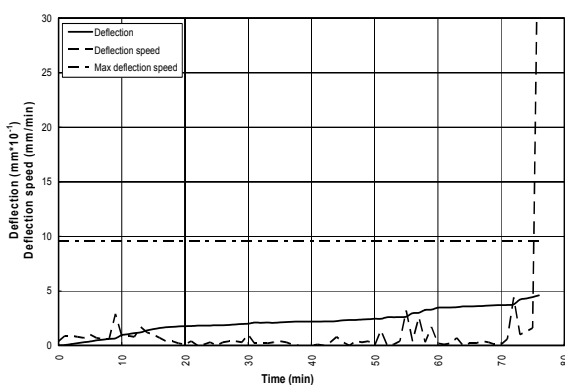


Fig. 3. Deflection D and deflection speed dD/dt of the loaded slab during the 1st furnace test.

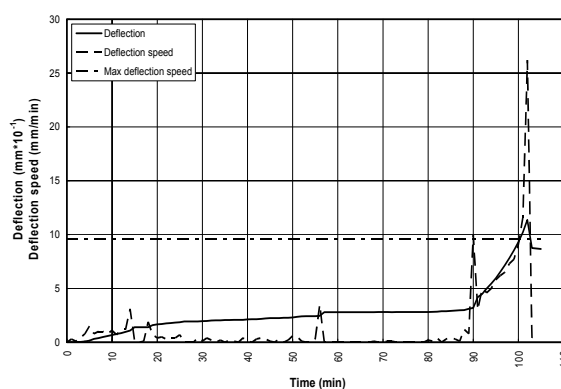


Fig. 4. Deflection D and deflection speed dD/dt of the loaded slab during the 2nd furnace test.

In Fig. 5 are represented the temperature histories in the loaded slabs measured during the 1st and the 2nd furnace tests. Their values represent the increments with respect to the ambient temperature. In the 1st picture relating to the thermocouples no. 15 are also shown the furnace temperature histories, together with the target heating programme ISO 834. In each case the actual furnace temperature was matched quite precisely by the target furnace temperature.

A good agreement between data for the 1st and the 2nd tests was generally exhibited.

Some irregularities in the temperature time histories of the 1st test can be seen at the sensors no. 18, 21, 23 and 26, most likely due to the effect of the spalling, which occurred during the test. Visual checks during the execution of the test confirmed that the areas where the thermocouples 18, 21, 23 and 26 had been installed were subjected to explosive spalling.

Almost the totality of the thermocouples installed in the unloaded slabs exhibited a good agreement between the results of the experimental tests.

The presence of insulating material at the ends of the holes did not affect the temperature inside the slabs. This behaviour can be ascribed to the low amount of heat that the slabs exchange with the external atmosphere by convection, as the hole axes are horizontal.

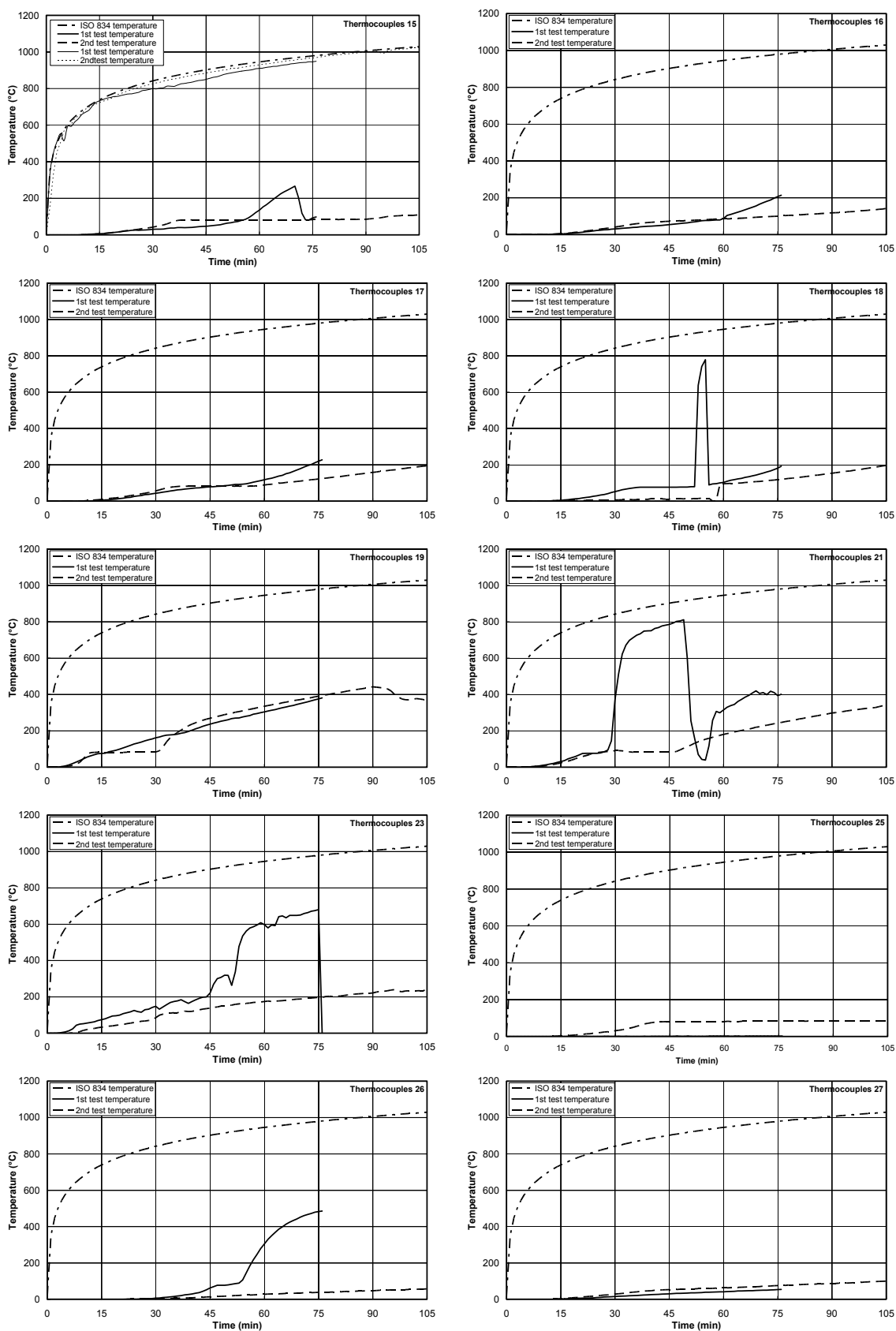


Fig. 5. Temperatures recorded by the thermocouples during the 1st and the 2nd tests.

2.3 Residual strength

The load bearing capacity after cooling of the slabs that were not loaded during the furnace tests was evaluated by means of additional 4 points bending tests. In the evaluation of the results, one must keep in mind that the duration of the second test was longer than that of the first one: the first fire test lasted 75 minutes, while the second one was interrupted after 105 minutes.

The moments that caused the collapse of the slabs were 51.17 kNm and 54.08 kNm including a bending moment of 5.75 kNm due to the self-weight, respectively for the slab of the 1st and the 2nd test.

The small difference (roughly a 5%) between the ultimate moments measured during the tests is evidently due to experimental fluctuations.

Two aspects of these results can be highlighted.

First of all the residual strength of the heated slabs is quite small in comparison with the ultimate bending moment of the undamaged slabs, which is equal to 101.5 kNm. The reduction of the load bearing capacity after cooling the slabs due to fire exposure is approximately equal to 50%, for both 75 and 105 minutes ISO 834 fire exposure.

Furthermore, the data demonstrated that the residual mechanical properties of the slabs heated during the first and the second test are almost the same, apart from their age and water content of concrete, and that the different duration of the fire exposures has a negligible effect.

3. NUMERICAL ANALYSIS OF THE FIRE RESISTANCE

The analytical evaluation of the load bearing capacity under fire of the slabs was carried out assuming the commonly adopted hypothesis that the thermal and the mechanical problems can be studied as uncoupled.

3.1 Analysis of the thermal field

The analysis of the time variant temperature field inside the slabs cross sections was carried out using the finite element code FIRES T3 [12].

As thermal properties of HPLWC, the experimental data provided by Felicetti and Gambarova [3,4] in 2002 were used in the analysis of the thermal field. Fig. 7 is shown the thermal diffusivity D_c defined as:

$$D_c = \frac{\lambda}{\rho c} \quad (3)$$

with ρ = density, c = specific heat and λ = thermal conductivity of the material.

Such data regards a concrete almost identical to that used for the production of the hollow core slabs of the present study. It was assumed a constant density value of 1900 Kg/m³ and a constant specific heat value of 840 J/Kg°K as suggested by the Eurocode 4 [13] for the lightweight concrete. The thermal conductivity was computed in order to give, together with the previous properties, the thermal diffusivity taken from the literature.

The lower surface of each slab was considered exposed to the ISO 834 standard fire and a two dimensional analysis was performed, assuming the temperature field as constant along the slab's longitudinal axis. Taking advantage of the slab symmetry with respect to a vertical plane, only half of the section was modelled.

In a previous investigation by the Authors [14] it was observed that the temperature of the air in contact with the upper surface of the cross section only slightly affects the ultimate strength of the slab, while the actual temperature of the air inside the holes has a great influence on the fire resistance of the slab and therefore must be accurately modelled. Since the time histories of the air temperature inside the holes can not be determined, a priori, the simplified hypothesis of constant temperature inside the holes has been adopted and a parametric analysis, considering four different constant values of this temperature (100, 200, 300 and 400 °C), was performed.

In Fig. 6 the temperature recorded by particular thermocouples during the two experimental tests compared with the corresponding temperature foresaw by the numerical simulation are depicted. The 1st picture relates to thermocouples no. 7, placed close to one of the strands; the 2nd one is related to the thermocouples no. 9, placed in the lower point of the inner surface of a hole; the 3rd regards to a point at the extrados of the unloaded slab and the last one a point placed at mid height of the loaded slab.

3.2 Evaluation of the load bearing capacity under fire

The bending load bearing capacity has been calculated taking into account the pre-stressing of the hollow core slabs and the degradation of the constitutive materials' properties due to exposure to fire.

Knowing the cross-section geometry, the initial pre-stress (74.1 kN per strand), the area of the 3/8" strands (52 mm²), and the actual stress – strain relationship of the pre-stressing steel, the initial value of steel's stress and strain before the cut of the strands has been evaluated.

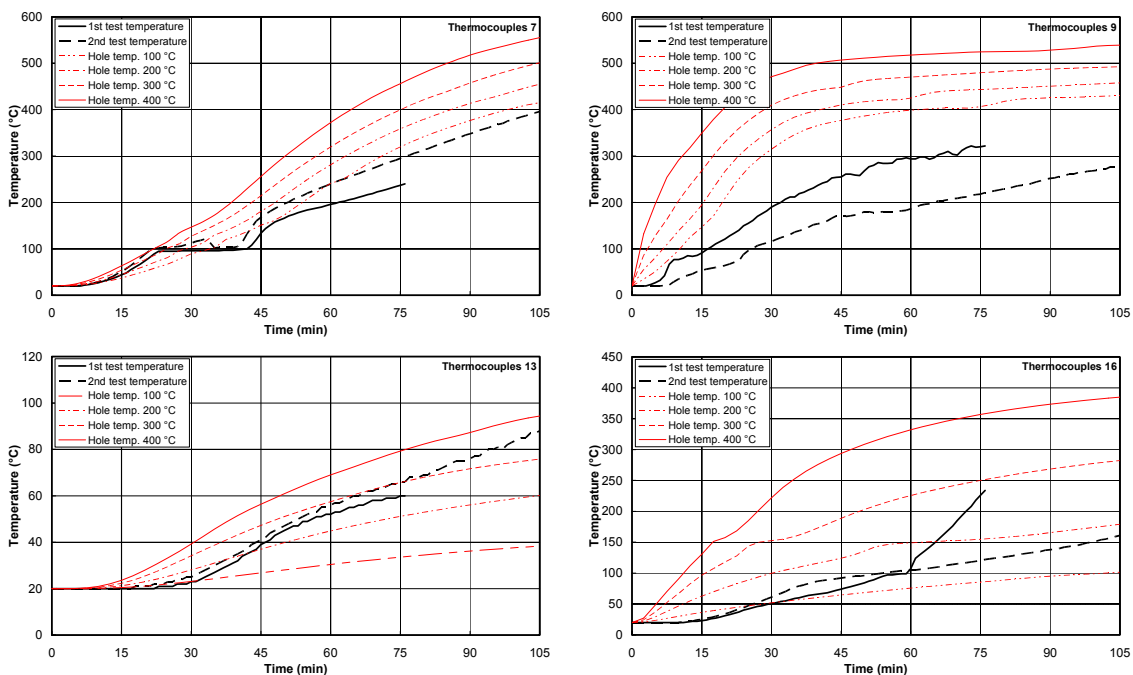


Fig. 6. Comparison of the experimental and numerical temperatures of the thermocouples no. 7, 9, 13 and 16.

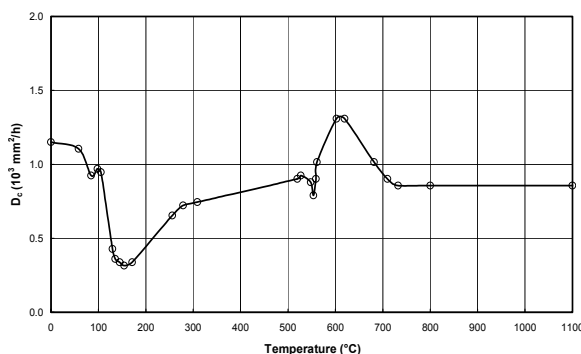


Fig. 7. Concrete diffusivity [3,4].

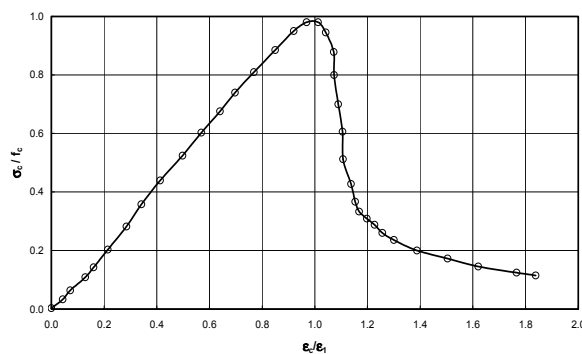


Fig. 8. Concrete stress-strain curve at 20°C [3,4].

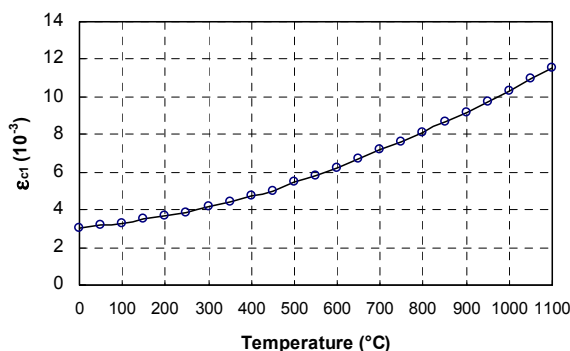


Fig. 9. Variation of ϵ_{cl} for HPLWC with temperature [3,4].

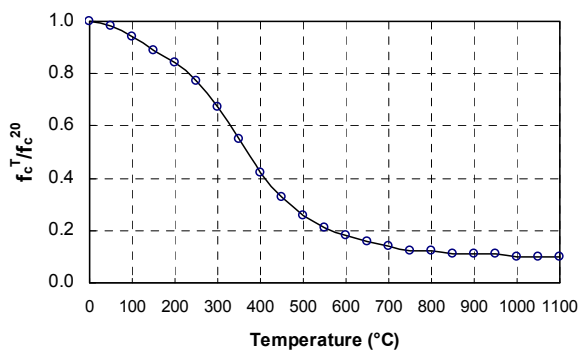


Fig. 10. Variation of f_c for HPLWC with temperature [3,4].

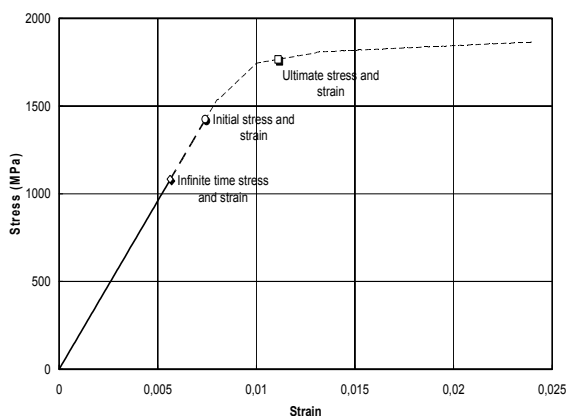


Fig. 11. Effective stress – strain curve for pre-stressing steel.

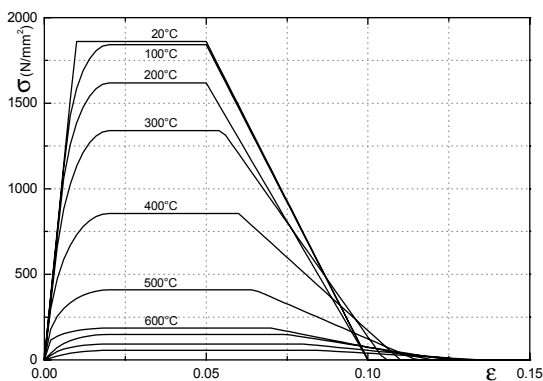


Fig. 12. Stress-strain curves for pre-stressing steel [2].

Later on, assuming a pre-stress loss at infinite time equal to 24%, the corresponding values of stress (σ_{op}) and strain (ϵ_{op}) have been calculated. Stating that the cross section remains in a plain, a first tentative strain diagram across the section, defined by the position of the neutral axis and by the value of the curvature $1/R$, was assumed.

The corresponding compressive force C_1 acting on the concrete was determined from the stress-strain law taken from the results of the experimental tests reported in [3,4], using the proper values of the temperature-dependent parameters ϵ_{cl} and f_c and setting the partial safety

factors to 1. In Fig. 8 the stress-strain law for the HPLWC at the ambient temperature is depicted. Figs. 9 and 10 show the variation of ε_{cl} and f_c with temperature.

For determination of tensile force T_I in pre-stressing strands the value of the total strain:

$$\varepsilon_{tot} = \varepsilon_{op} + \varepsilon_I \quad (4)$$

was first determined, where ε_{op} is strain of the strands for time equal to infinite and ε_I the increase of the strain corresponding to the application of the external moment (Fig. 11). The stress corresponding to this strain value has been taken from the Eurocode 2 [15] (Fig. 12).

The condition $C_I = T_I$ indicates that the tentative strain diagram is correct and that the internal moment can be calculated as

$$M = C_I \times z = T_I \times z \quad (5)$$

with z equal to the lever arm of the internal forces. If $C_I \neq T_I$ the computation has to be repeated assuming different values for the position of the neutral axis until the equilibrium is reached. Repeating this procedure for different values of the curvature $1/R$ allows the construction of a Moment – Curvature diagram, whose maximum value can be assumed as the ultimate bending moment for the corresponding fire exposure duration (Fig. 13). The procedure was repeated again for different fire exposure durations and for the 4 different thermal boundary conditions considered in the parametric analysis. The results of such investigation are summed up in Fig. 14, along with the value of the external applied moment. The time of collapse for the 1st and the 2nd test are also highlighted.

4. COMMENTS ON THE EXPERIMENTAL AND NUMERICAL RESULTS

Observing the results of the experimental tests, a general good agreement can be found between the results of the numerical modelling of the thermal field and the values of the temperature recorded by the thermocouples.

The comparison of the experimental and the numerical results of the temperature values in the concrete generally shows a better agreement in the cases where the temperature inside the holes has been assumed equal to 100 and 200 °C (see Fig. 6).

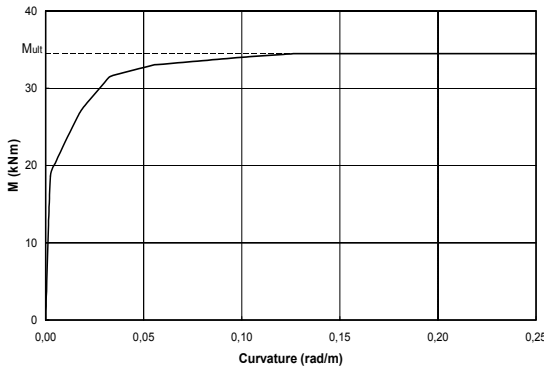


Fig. 13. Example of the Moment – Curvature relationship.

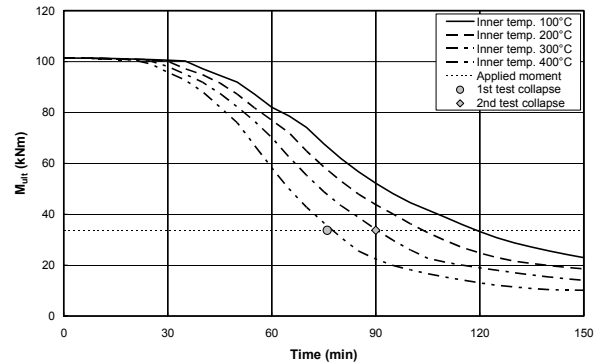


Fig. 14. Ultimate moment for different boundary condition.

From this point of view the influence of the water contained in the concrete in modifying the temperature time histories has to be highlighted. For instance, thermocouples no.5, 7, 19 and 21 for several minutes during the 1st or the 2nd test recorded a constant temperature equal to about 100°C, which is the water's ebullition temperature, event unpredictable by the model adopted for the numerical analysis of the thermal field. Aside, this fact testifies the presence of water, which is responsible for the onset of the spalling phenomena.

The comparison between the experimental and numerical data for the load bearing capacity presents more difficulties. During the 1st test, the fact that the occurrence of spalling greatly reduced the load bearing capacity of the slab, aspect this latter that can not be easily taken into account in the numerical evaluations.

However in the 2nd test, since the collapse of the slab occurred for the overcoming of the threshold deflection speed value, no clear comparison between numerical and experimental data can be done, even if it is evident from Fig. 14 that the decay of the load bearing capacity of the slab for the case of temperature inside the holes equal to 200 °C reaches the external applied moment at 90 minutes, duration at which the experimental test was considered to be completed.

5. CONCLUSIONS

In the present study the fire behaviour and residual strength after a fire of pre-cast hollow core slabs made of high performance light weight concrete have been investigated, by means of experimental tests and numerical simulations.

The tests were carried out in a furnace on full-scale specimens using the ISO 834 standard fire.

The tests showed that the exposition of the concrete elements to a dry environment, after a preliminary and adequately long hardening phase, heavily reduces the amount of water entrapped in the concrete pores, thus decreasing the risk of spalling. In this case a good structural performance of the elements exposed to fire has been revealed, comparable with those currently manufactured using normal-weight normal-strength concrete. On the contrary, when the spalling occurs, the degradation of the load bearing capacity can be so relevant to cause the collapse for values of the external loads well below the expected theoretical ones.

The tests performed on the slabs left unloaded during the heating showed a considerable reduction (around 50%) of the load bearing capacity after cooling if compared with the theoretical values.

The comparison between the numerical and the experimental tests showed that the numerical model used in the present study can be reliably applied to evaluate the temperature fields and the load bearing capacity of the hollow core slabs, if realistic mechanical and thermal materials properties are used in the analysis and if no concrete spalling occurs during the fire tests.

6. ACKNOWLEDGEMENTS

The Authors gratefully acknowledge the logistic support of the firm Generale Prefabbricati S.p.A. of Perugia (Italy) for having kindly manufactured and supplied the test slabs and the financial support from the Association of the Italian Producers of Concrete, which was granted through the "Ulisse" Project, Subproject "High-Performance Light-Weight Concrete".

7. REFERENCES

- [1] Van Acker A., "Shear resistance of prestressed hollow core floors exposed to fire", *Structural Concrete*, Vol. 4, No. 2, pp. 65-74, 2003.
- [2] Fellingner, GHH., "Shear and Anchorage Behaviour of Fire Exposed Hollow Core Slabs", Delft University Press, 2004.
- [3] Felicetti R., Gambarova PG, Silvia M, Vimercati M., "Thermal Diffusivity and Residual Strength of HPLWC Exposed to High Temperature". Proc. of the 6th Int. Symp. on Utilization of HSC/HPC, Leipzig, Germany, pp. 935-948, June 2002.
- [4] Felicetti R., Gambarova PG., "High-Performance Light-Weight Concrete: Material and Sectional Properties during and after Fire". Proc. Int. Conf. on Advances in Concrete and Structures – ICACS 2003, Xuzhou, China, September 2003.
- [5] Sullivan P.J.E., Sharshar R., "Performance of concrete at elevated temperatures (as measured by the reduction in compressive strength)", *Fire Technology*, August 1992.
- [6] Hertz K., "Heat induced Explosion of Dense Concretes", Report No. 166, Institute of Building Design, Technical University of Denmark, 1984.
- [7] Hertz K., "Danish investigations on Silica Fume Concrete at Elevated Temperatures", ACI 1991 Spring Convection, Boston, MA, March 1991.
- [8] Hammer T.A., "High-Strength Concrete Phase 3, Compressive Strength and E-Modulus at Elevated Temperatures", SP6 Fire Resistance, Report 6.1, SINTEF, Structures and Concrete, SFT70 A95023, February, 1995.
- [9] Hansen P.A., Jensen J.J., "High-Strength Concrete Phase 3, Fire Resistance and Spalling Behaviour of LWA Beams", SP6 – Fire Resistance, report 6.3, SINTEF NBL-Norwegian Fire Research Laboratory, STF25 A95004, March 1995.
- [10] Sullivan P.J.E., "Deterioration and explosive spalling of high strength concrete at elevated temperature", International RILEM Workshop on Life Prediction and Aging Management of Concrete Structures, Cannes, France, 16-17 October 2000.
- [11] UNI EN 1363-1, "Fire resistance tests – General requirement". July 2001.
- [12] Iding R., Bresler B., Nizamuddin Z., "Fires T3 - A Computer Program For The Fire Response Of Structures", University of California at Berkeley, 1977.
- [13] Eurocode 4: Design of composite steel and concrete structures - Part 1-2: General rules - Structural fire design, prEN 1994-1-2, 2003.
- [14] Materazzi AL, Breccolotti M. "Fire behaviour of HPLWC hollow core slabs: full scale furnace tests and numerical modelling". Proc. of the workshop Fire Design of Concrete Structures: What now? What next? Milan, Italy, December 2-4, 2004.
- [15] Eurocode 2: Design of concrete structures – Part 1-2: General rules – Structural fire design, prEN 1992-1-2, 2004.



ASSESEMENT OF DAMAGE IN CONCRETE STRUCTURES EXPOSED TO FIRE. MICRO AND MACROSTRUCTURAL ANALYSIS

C. ALONSO¹

ABSTRACT

The assessment of the integrity of a concrete structure in a post fire situation involves addressing the damaged of each component. It is important to differentiate if the concrete is affected by chemical or physical deterioration and to identify the penetration of the damage. In present paper the assessment of damage of concrete and reinforcements in two post-fire concrete structures suffering different scenarios of fire are considered. In-situ inspection and laboratory tests have been performed.

Results indicate that the measurement of the level of dehydration of CSH is a simple method and good indicator to asses the penetration of heat able to induce chemical damage in cement paste. The no presence of portlandite can lead to erroneous interpretations in the case that carbonated concrete exists. The distribution of cracking is needed to assess the penetration of physical damage in concrete components, the BS microscopy has resulted a good technique to asses this type of damage. Explosion does not necessarily results with chemical alteration of materials but produces an extensive damage due to cracking.

1. INTRODUCTION

Fire is considered one of the most serious potential risks for buildings and structures. But concrete is generally considered to have an acceptable resistance to fire in comparison with other construction materials, such as wood or steel

When concrete remains exposed for long time to high temperatures, mechanical losses of its properties take place. Laboratory experiences show that in case of concrete not protected the mechanical properties decrease drastically for temperatures above 300°C. They are attributed to

¹ C. Alonso, Rs.Prf., PhD Sc, Institute of Construction Science Eduardo Torroja. c/ Serrano Galvache, 4, 28033 Madrid, Spain.
mcalonso@ietcc.csic.es

the microstructure transformations occurring in cement paste and aggregates, and the volume changes induced by thermal stresses [1-8].

After fire the assessment of deterioration of the structure is needed in order to identify the level of damage induced by the chemical transformation and the cracking, both contributing to losses in mechanical strength [9].

In-situ non-destructive techniques are widely employed for distinguishing between damage and apparently non affected areas of concrete, as resilience, hammer-tapping, ultrasonic pulse [10-13]. However, the determination of the penetration of the damage and to differentiate between the types of damage is important to ascertain the consequences of the thermal gradients, which requires the use of concrete cores for laboratory analysis, usually for mechanical strength and petrography analysis and thermal alteration of cement paste. More feasible methods are being adopted as for instance infra-red thermal imaging, digital camera colorimetry [14-16]. Chemical analysis of cement paste, as TG and DRX tests are also employed in order to determine the presence of portlandite as indicator of the penetration of the heat, as this component decomposes at temperatures above 450°C when mechanical strength has been lost [17]. Also attempts have been made at the assessment of cracking using petrography thin sections and SEM [1, 18-21].

However, the isolated use of any method does not give very reliable results because of the gradient and in-homogeneity of damage that cause differences in the external and internal strength, [16]. The assessment of post-fire reinforced concrete structures is complex due to the overlapping of chemical and physical phenomena inducing different damages.

The aim of present paper is to contribute to the identification of indicators of damage to assess the RC structures affected by the fire. The chemical alteration in the cement paste due to the effect of high temperatures and physical damages in concrete components induced by thermal stresses are considered in order to identify the thickness of the affected concrete cover.

2. EXPERIMENTAL SET UP

Tunnel and building post-fire concrete structures that suffered different scenarios of fire are considered.

- 1) The tunnel structure has a height and wide of 4.55m by 10.5m. It was built with mass concrete of HA-25 of 30 cm thickness without reinforcement. It has also a roof of 18 cm with a ventilation chamber made of reinforced concrete of HA-35. The surface of the concrete was covered with a non-reflecting paint. The fire was initiated due to the combustion of the cabin of a truck, and lasted 20 minutes.
- 2) The building was an underground electricity station with three basements. The roof of the first basement was built with prestressed beams. A reinforced concrete slab of 3m was constructed between the second and third basement. Each floor has columns of different dimensions, 250x30x35 and 250x30x50, separated every 4 to 5 m. Some crossing concrete beams of 35x30 complete the structure. The fire was initiated in the first basement and got down to the second and third basements. The duration of the active fire in the third basement took 2 days.

The damage produced by the fire in both structures was assessed. A visual in-situ inspection and ultrasonic measurements were made. Set of laboratory tests were performed in cores taken from the structures: 1) Stereoscope Microscopy, 2) Backscattering Electron Microscopy, 3) Thermo-gravimetry, 4) Porosimetry, 5) Mechanical strength and 6) Micro-hardness.

3. ASSESMENT OF POST-FIRE LEVEL OF DAMAGE IN THE TUNNEL

The fire produces in the concrete of the walls some local explosions, as noticed in figure 1. The depth of the explosion was 1-1.5cm. Combustion of the painting was also detected.



Figure 1. Local explosions in the concrete walls of the tunnel after fire.

Table 1 summarises the results for compressive strength, porosity, weight losses, carbonation depth and micro-hardness from the concrete and cement paste.

The compressive strength tests in cores were not able to discriminate with respect to the damage induced by the fire, in fact, the strength was above the characteristic compressive strength required in the specifications of the structure. Total porosity indicates an increase in the zone affected by the fire in a depth of 1 cm. After looking at the distribution of pore size, given in figure 2, the increase in porosity was noticed in the region from 0.1 to 1 μm and that above 10 μm .

Table 1. Properties of the concrete of the tunnel after fire

Sample	Compressive strength (N/mm ²)	Porosity %	Micro-hardness (Vickers) 0-1.5 cm	% water in CSH	% water from Portlandite	Carbonation depth (cm)
Non affected concrete	44.5	6.81	61.5 \pm 8.5	1.13	0.31	0.2
Affected with explosion concrete	-	9.15	75.0 \pm 8.0	-	-	0.0
Affected without explosion	46.5	13.11	55.5 \pm 8.3	1.28	0.34	0.3

The carbonation of the paste was not significant and also the CSH and portlandite analysis indicate that the effect of the heat was not enough to affect the chemical properties of the paste. This was further confirmed with the results from micro-hardness, the values obtained are similar and within the scatter, included in the standard deviation of the mean values.

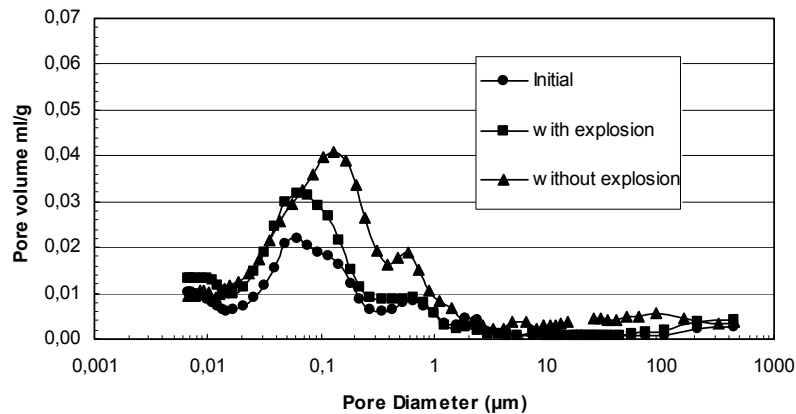


Figure 2. Pore size distribution of concrete tunnel up to 1cm depth in non and affected cores.

In order to identify physical damages in the concrete components, backscattered microscopy results, given in figure 3, indicate that the fire only affects the painting and less than 1mm of the external concrete in zones not affected by the explosion, which appear more porous. However, microcracks inside the concrete crossing the paste and aggregates were observed in the affected concrete samples. This microcracking extends up to 1.2 cm, but the paste is not chemical altered.

From these results it can be concluded that the level of damage in tunnel after fire is not due to chemical transformation of concrete component but cracks appears as consequence of the explosion, which is attributed to thermal and pore pressure stresses inside the first cm of the concrete cover. As the CSH is not altered suggests that the maximum temperature of exposure should be below 200°C.

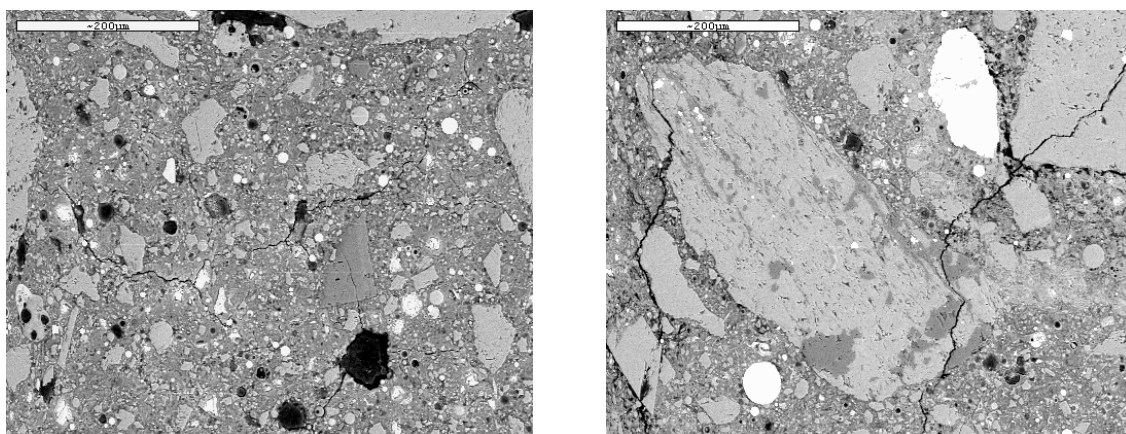


Figure 3. Left, initial aspect of cement paste. Right, cracks due to the explosion of concrete in affected zone, x 200. Depth 1.2 cm depth.

4. ASSESMENT OF POST-FIRE LEVEL OF DAMAGE IN UNDERGROUND BUILDING

The in-situ inspection of the damage after the fire indicates that apparently the structure was seriously affected, as indicate the numerous damages in the different components of the structure, as may be observed in figure 4. Local Concrete explosions occurred on the ceiling of the slab of the third floor up to 2-3 cm depth, leaving the rebars exposed to the atmosphere. The reinforcement showed general oxidation, with brown and black colour, which is typical of corrosion induced at high temperature.

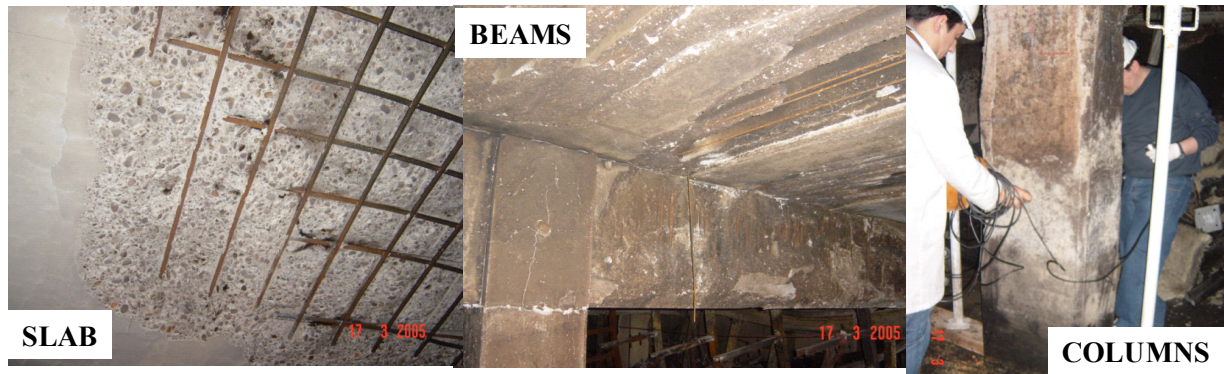


Figure 4. Damages observed in different elements of the structure: Slab, beams and columns.

The pretressed beams of the ceiling of the first floor showed explosions that had destroyed partial or total the beams, even prestressed wires were broken. Probably the damage induced by the explosion took place in several stages: a) first a concrete explosion due to thermal and pore pressure stresses that leaves the wires exposed directly to the fire, b) followed by a sudden increase of the temperature of the wire, and c) broken of some wires due to loss in ductility of the steel. This last fact can be confirmed in the laboratory with strain tests. The structural reinforced concrete beams, showed explosion of the concrete at the corners and around the ribs.

The structural beams of the third floor showed an increase in deformation and cracking at the central length. The columns shown heterogeneous damages even within the same floor, some columns did not show apparent damages, while others shown heavy cracking and explosion of concrete at the corners.

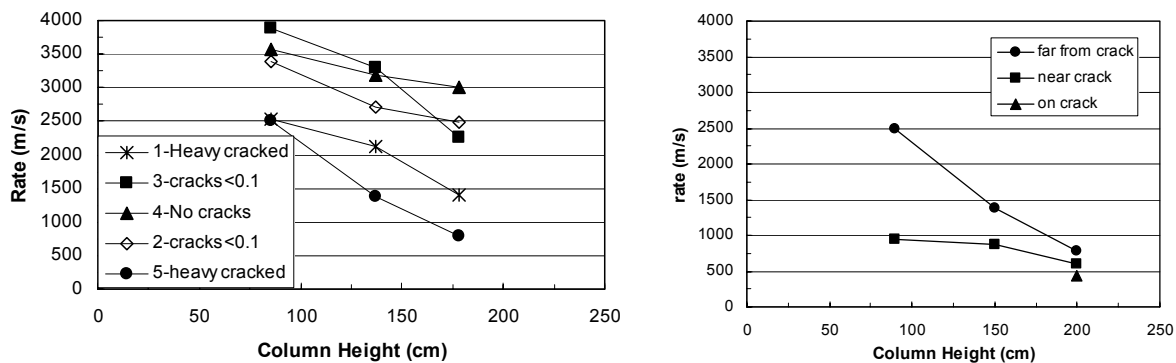


Figure 5. Variation of ultrasound rate of damaged columns. Influence of height and cracking

The ultrasound pulse test performed on the columns point out the heterogeneities in the damage within each column and between columns, as shown in figure 5. The ultrasound rate varies with: a) the height of the column, showed by a decrease, b) the presence and size of the cracks and c) the distance to the crack. This last case put in evidence, that on a same column sharp variations in cracking intensity damage are identified, that correspond well with the ultrasound rate measurements. However, the penetration of the damage can not be deduced from this technique.

Concrete cores were taken in column 1 and 2 showing different cracking at the surface and ultrasound rates, as shown in figure 6. In column 1, left in the figure, a crossing core from one to other face (30 cm) was extracted. The cores resulted broken into pieces during the extraction. In the holes it was observed the penetration of the cracks, in column 1 up to 7-8 cm, while in column 2, small cracks were only observed up to a depth of 4 cm. Some concrete samples from the corners of the columns, showing or not explosion, were taken in order to analyse the damage of the concrete in the laboratory.



Figure 6. cores and holes taken from column1, left, and column 2 right.

Table 2 shows the results from carbonation depth in columns and beams, the results show carbonation up to a depth of 1.5 cm. This test was performed in order to discriminate with the identification of decrease of portlandite content, not to be attributed to fire action. The strength could only be determined in the centre of column 2, the value showed a low residual strength of the inner concrete.

Table 2. Carbonation depth and residual strength of concrete

Sample	Compression (N/mm ²) centre 15 cm	Carbonation depth (cm)
Column 1	-	1.5
Column 2	17	1.5
beam	-	1-1.5
corner	-	0.5-1

The tests performed in the laboratory indicate that the level and origin of the damage varies for each type of element. The concrete of the prestressed beams showed low porosity and no differences could be detected at the different depths studied, 1, 3 and 5 cm (rebar level). In the case of the columns, the porosity is higher in column 1 showing a small decrease at depths above 7 cm, as can be observed in figure 7-left.

The micro-hardness test, in right of figure 7, was able to identify variations between the different concretes (beams or column); however changes with the depth of the core in the hardness of the paste were not detected, the measurements are within the scatter. However, differences in the hardness of the two columns were determined, in accordance with the differences of the cracking observed in the inspection.

To address the changes in cement paste the TG test have contribute in two ways, through the determination of dehydration of CSH and the dehydration of portlandite. In the case of the concrete of the prestressed beam no significant changes were noticed for CSH; figure 8-left, while the portlandite content, figure 8-right, only shows decrease up to 1.5 cm. This change can not be attributed only to the action of the fire, as the concrete was already carbonated at that depth. The above results have allowed interpreting that the temperature reached by the concrete of the prestressed beams was below 300°C to allow a mechanical strength decrease due to chemical changes, although the damage showed a severe cracking due to the explosion.

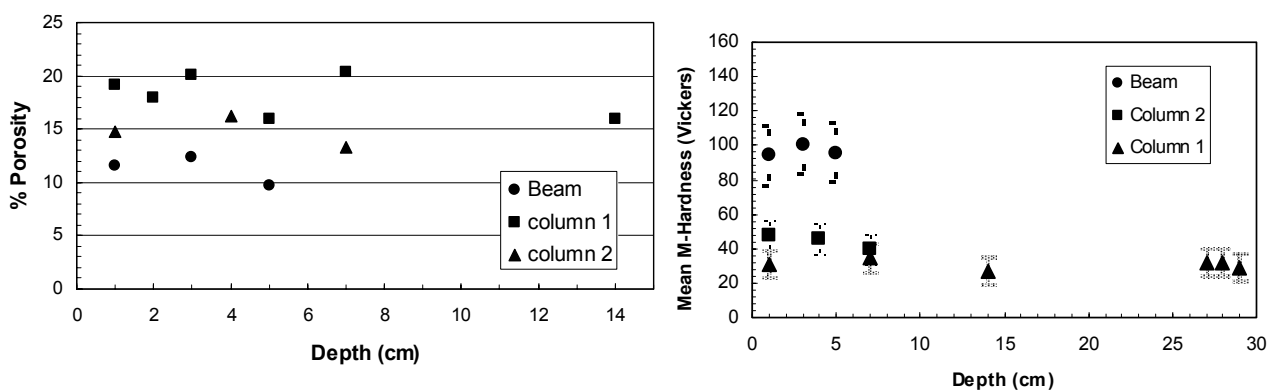


Figure 7. Variations in porosity and micro-hardness of prestressed beams and columns.

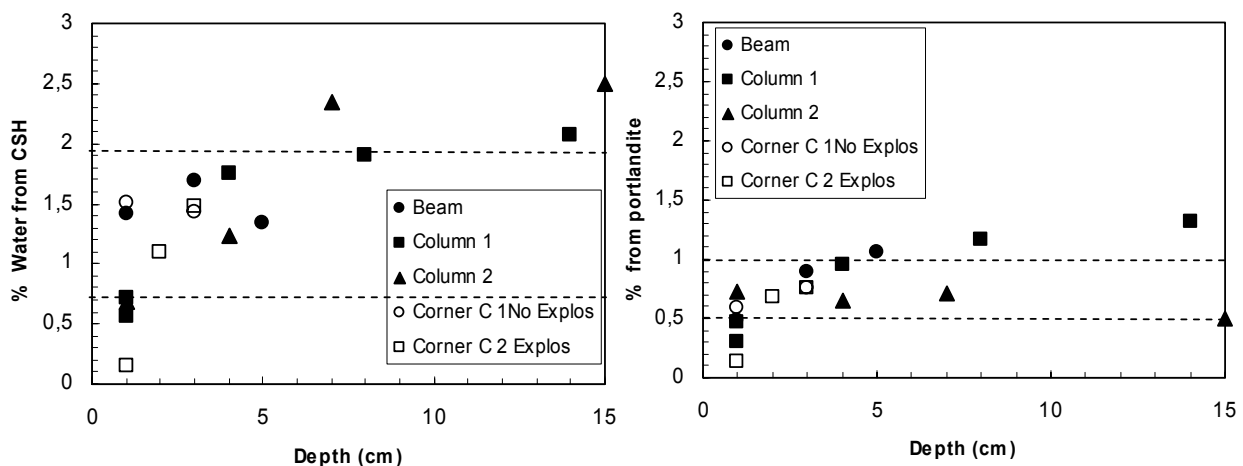


Figure 8. CSH and Portlandite content of concretes from prestressed beams, columns and corners.

The paste of the columns shows changes in CSH dehydration up to at least 7 cm. This result does not correspond always with an increase in portlandite inside the concrete. This apparent contradiction has been attributed to handling during preparation of samples for TG test, which has a risk of carbonation at the atmosphere and disappearance of subsequent portlandite. The dehydration of CSH identified in the TG test as weight loss between 100 to 350°C does not take place at ambient temperature.

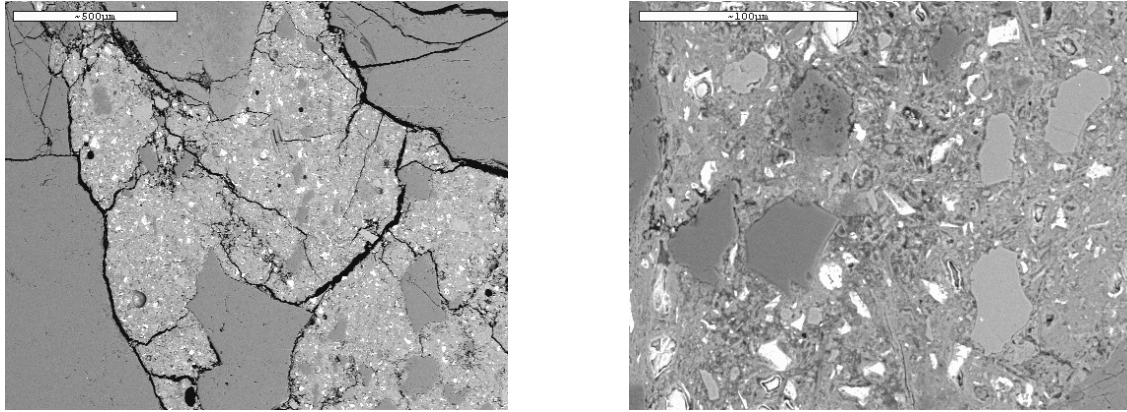


Figure 9. Aspect of cement paste and cracking in prestressed concrete beam, x 500.

Finally Backscattering Microscopy was used to confirm the type of damage. In the case of the concrete from the prestressed beams it was observed an intense micro cracking in the bulk of the concrete, both in aggregates and paste, figure 9-left. However the paste does not show chemical alteration, figure 9-right. The damages observed in the concrete of the prestressed beams is attributed to the explosions due thermal and pore pressures accumulated inside the concrete. The compression of the concrete has resulted in more severe explosion risk during initial stages of fire.

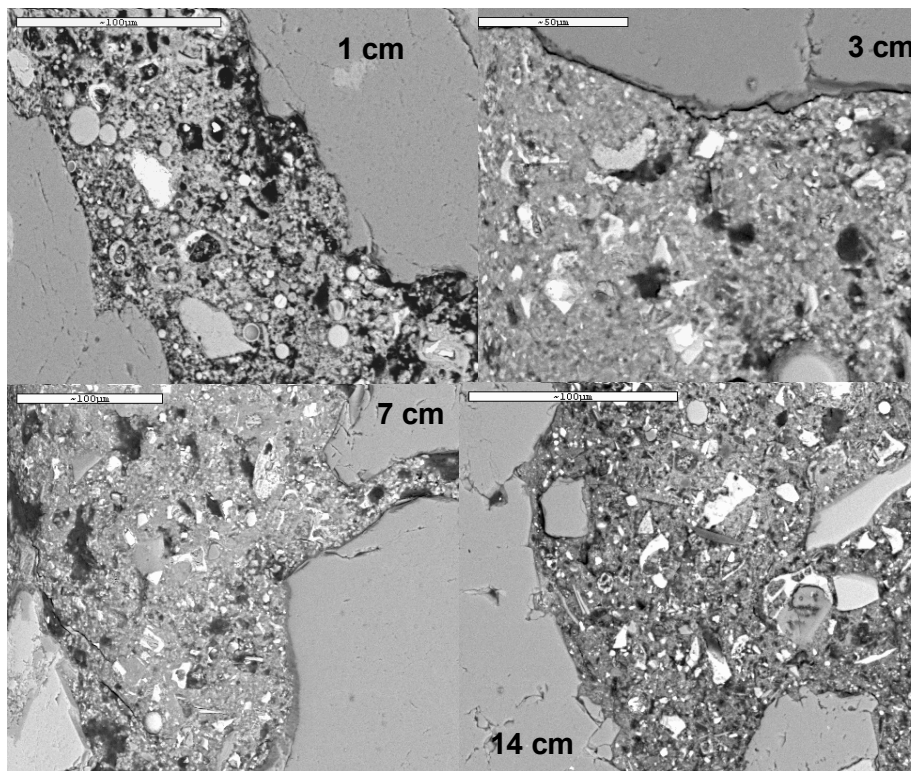


Figure 10. Cement paste and aggregate interface at different depths, x 500

The concrete of the columns was very affected by the heat, as can be seen in figure 10. The paste shows low consistency and high porosity in the depths 1 and 3 cm. At 8 and 14 cm depth the paste is also porous but the alteration is heterogeneously distributed. The aggregates

are altered and broken in some places and a lot cracking is observed up to 7 cm depth, figure 11.

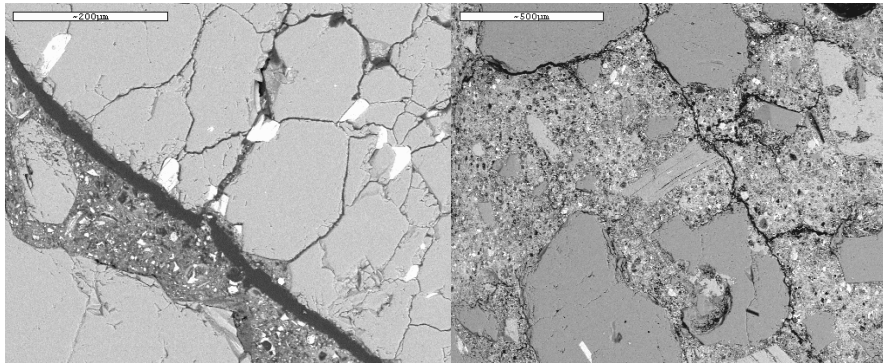


Figure 11. Alteration of siliceous aggregates, x 200, and Cracking, x 75.

The effect of the heat in the prestressed steel wires produces a decrease in ductility and in some cases brittle failures. Results are given in figure 12 and table 3.

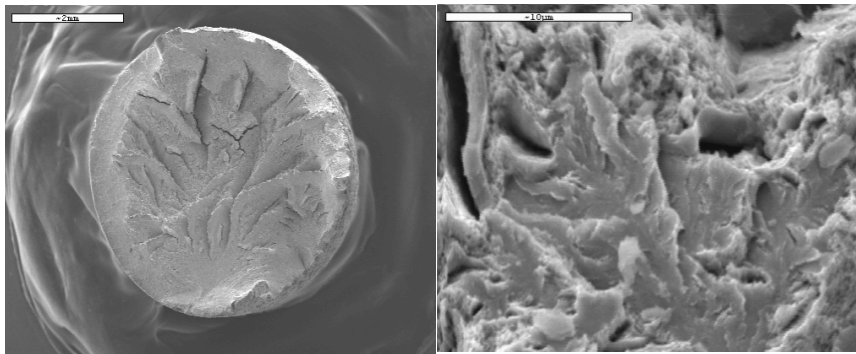


Figure 12. Brittle failure of prestressed wire

Table 3. Mechanical properties of steel wires after fire

Elastic limit (MPa)	Max Load (MPa)	Load to break (MPa)	Young Modulus	Area reduction (%)	Deformation (mm)
1884.1	1889	1796	0.0076	19.00	0.0096
1435.6	1610	1430	0.00625	16.60	0.0362
1101	1224	1093	0.00253	17.06	0.0242
759.66	780	613	0.00502	31.00	0.0110
1265.48	1425	1425	0.00662	11.61	0.0270
1304.3	1468	1467	0.00685	15.15	0.0250
1311.77	1414	1379	0.00644	2.16	0.0157

5. DISCUSSION

The analysis of post-fire concrete structures is a complex matter as chemical and physical phenomena are acting simultaneously. The fire induces stresses due to thermal deformation of components, paste and aggregates during heating and cooling, the heat has produced water vapour and in consequence increase in pore pressing and finally the high

temperatures, in the region of temperatures between 100 to 300 °C has produced the decomposition of CSH, that represents more than 70% of cement paste and the real responsible of the mechanical strength.

The type of structure, buildings or tunnels, reinforced or prestressed concretes, respond in a different way to fire. Besides, the scenarios of fire and the duration are fundamental in the level of the damage.

The suitable assessment of post-fire concrete structures implies to answer some relevant uncertainties, as for instance: 1) the maximum penetration of the temperature able to produce chemical alteration in the components of the concrete, paste and aggregates, 2) The penetration of the cracks, and 3) the loss of mechanical strength, in order to give data for the further evaluation of the residual load bearing capacity of the structure. To properly address this, adequate indicators of the damage have to be identified.

The action of the heat in the concrete creates a gradient of degradation which depends on the material properties and the intensity and duration of the fire. Due to the gradient of damage the identification of the mechanical strength decay related to the damage is not always possible and mean values are obtained, that in many cases mask within the bulk of the concrete depending on the depth of the altered zone. Other indirect techniques are possible in order to approach to the assessment of the residual strength.

Different techniques and tests have been employed to identify the depth of damage; however, the use a unique method is not possible to address the damage, a combination of test is more accurate. Depending on the type of damage to asses, chemical or physical parameters, the recommended test may vary.

The chemical alterations in cement paste components are adequately identified with TG tests. However the isolate determination of portlandite transformation level, as indicator of mechanical strength loss, is affected by the carbonation of the concrete cover due to the interaction during the preparation of the powdered sample with the CO₂ of the atmosphere. Besides, the portlandite represents less than 20% of total OPC cement paste, and with pozzolan cements is consumed during pozzolanic reaction. Portlandite is not stable at temperatures above 450°C and dehydrates. On the other hand, the CSH initiates its transformation at $T^a > 100^{\circ}\text{C}$, and resulted fully decomposed at 350°C, with loss of cementitious properties (strength). Besides, the CSH represent more than 75% of total cement paste, been more sensitive to identify the changes in its content.

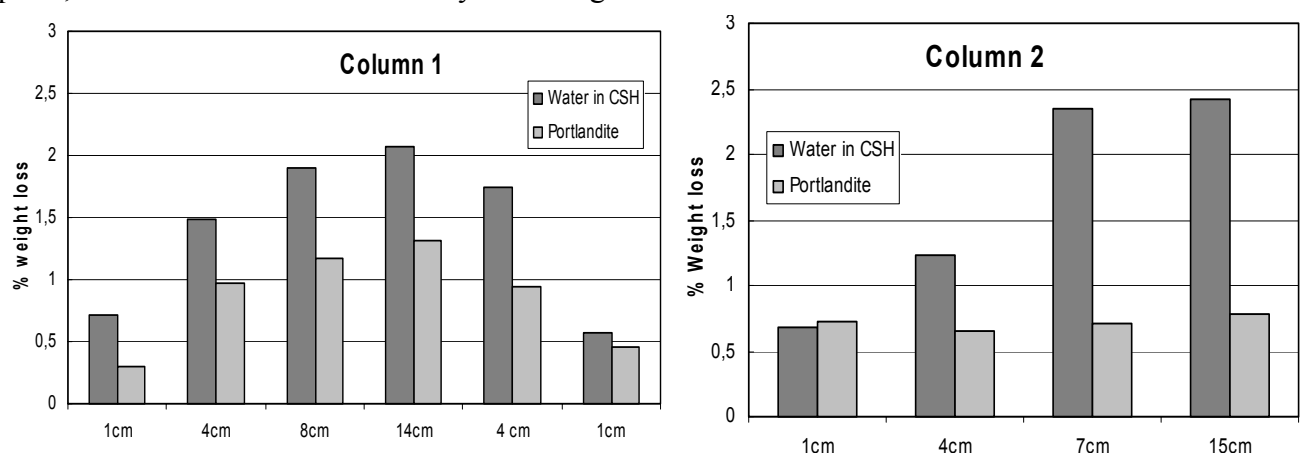


Figure 13. Variation of CSH and portlandite due to the penetration of the chemical damage.

In present paper the determination of CSH dehydration level has allowed to differentiate between sound concretes and total or partial alteration of cement paste. The TG results of columns 1 and 2 represented in figure 13 indicate the gradients of CSH within the

concrete. While the portlandite in one column 2 shows no profile and appears similar to the external part that was carbonated; the CSH content shows a gradient.

The ultrasound has the advantage of NDT that can be applied in-situ. In present work, this technique has been able to differentiate at a macro-level the presence of cracking; however, it has not been able to differentiate respect the origin and depth of the cracks, as a consequence of thermo-mechanical stresses due to the gradients of temperature or due to the chemical degradation of hydrated cement paste. The Backscattering Microscopy technique has been able at a micro-level to identify the origin and the severity of cracking and degradation of cement paste and aggregates. The Micro-hardness has differentiated between different damaged and quality of concretes. The porosity has also contributed although in less extent to differentiate between levels of damage.

The assessment methodology used has allowed differentiating levels of damage of the two structures exposed to different scenarios of fire. The low level of the damage in the case of the tunnel recommends repairing, while the extension of the damage in the case of the building has suggested the decision of demolishing.

6. CONCLUSIONS

The use of a set of tests allows differentiating between several levels of damage and to identify indicators of damage in post-fire structures:

1. The use of ultrasound as a non destructive technique allows identifying the damaged part of the structure, but does not inform on the penetration of the damage.
2. The TG test is an accurate method to determine the chemical degradation of the cement paste, although the identification of the degradation of CSH is more accurate than the determination of portlandite.
3. The microscopy of back-scattering is able to differentiate between sound and altered zones due to heating of cement paste and is a good method to identify the presence of cracking and its distribution in the bulk of the concrete. The penetration of the damage is possible with this technique.
4. Porosity and micro-hardness in present work have resulted in methods that contribute to assess the damage. In particular micro-hardness has demonstrated to be a method that could contribute to identify the loss of mechanical strength in the cement paste, but more intensive studies are needed in order to address more accurately the sensitivity of the technique.

7. ACKNOWLEDGEMENTS

The author wish acknowledge to Unidad de Carreteras de Huesca del Ministerio de Fomento, in particular to Mr. Angel Hernandez del Cura for the accessibility of the tunnel and to DETECSA, for the possibility to study the post-fire damage of the building.

8. REFERENCES

- [1] Z.P. Bazant and M. F. Kaplan. Concrete at high temperatures: Material properties and mathematical models. Logman Grp. Ltd. , England (1996).
- [2] Piasta, Z. Sawicz, and L. Rudzinski, Changes in structure of hardened cement pastes due to high temperature, *Mater. Struct.* **17** (1984) 291-295.
- [3] S. Y. N. Chan, X. Luo, and W. Sun, Effect of high temperature and cooling regimes on the compressive strength and pore properties of high performance concrete, *Construction and Building Materials* **14** (2000) 261-266.
- [4] G. A. Khoury, Compressive strength of concrete at high temperatures: a reassessment., *Magz of Conc Rs.* **161** (1992) 291-309.
- [5] H. Malhotra, The effect of temperature on compressive strength of concrete., *Magz. of Conc. Rs.* (1956) 85-94.
- [6] F. Rostasy, C. Ehm, and K. Hinrichsmeyer, "Structural alterations in concrete due to thermal and mechanical stresses," presented at the Pore Structure and Contruction Materials Properties, Versailles, France, 1987.
- [7] X. Fu, and D. Chung, Reversible decrease of the flexural dynamic modulus of cement pastes up on heating., *Cemt. and Conc. Rs.* **27** (1997) 839-844.
- [8] H. Sugiyama, M. Abe, and H. Maeda, Pore size distribution and strength development of concrete exposed to high temperature, *Semento, Konkurito Ronbunshu* **50** (1996) 122-127.
- [9] D. C. Tay and C.T. Tam, In situ investigation of the strength of deteriorated concrete, *Construction and building materials*, **10**, n1, February (1996) 17-26.
- [10] A. Benedetti. On the ultrasonic pulse propagation into fire damaged concrete, *ACI structural journal*, **95**, n 3 May (1998).
- [11] A. Benedetti and E. Mangoni, Damage assessment in actual fire situations by means of non-destructive techniques and concrete tests, *Fire design of concrete structures: what now?, what next?*, edt P. Gambarova, R. Felicetti, A. Meda and P. Riva, (2004) 231
- [12].R. Fellicety, The drilling resistance test for the assessment of the thermal damage concrete. *Fire design of concrete structures: what now?, what next*, edt P. Gambarova, R. Felicetti, A. Meda and P. Riva, (2004) 241.
- [13] J. Calavera, J.M. Izquierdo et al, Fire in the Windsor building. Survey of the fire resistance and residual bearing capacity of the structure after the fire. NIT INTEMAC, dec (2005).
- [14] R. Fellicety, Digital camera colorimetry for the assessment of fire- damaged concrete *Fire design of concrete structures: what now?, what next?*, edt P. Gambarova, R. Felicetti, A. Meda and P. Riva, (2004) 211.
- [15] N Short and J. Purkiss. Petrographic analisis of fire damaged concrte, *Fire design of concrete structures: what now?, what next?*, edt P. Gambarova, R. Felicetti, A. Meda and P. Riva, (2004) 221.

- [16] X. Zhang, HX Du, B Zhang and D.V. Philips, assessment of fire damage of concrete by using infrared thermal imaging method, Concrete for extreme conditions, Edt R. K. Dhir, M. J. McCarthy and M D. Newlands, (2002)59-604.
- [17] C. Alonso and L. Fernandez Municio, Dehydration and rehydration processes of cement paste exposed to high temperature environments, *J. Mater. Sci.* 39 (2004) 3015.
- [18] M.A. Rilley, Possible new method for assessment of fire-damaged concrete, Magazine of concrete research, vol43, (1991) 87-92
- [19]. J. Piasta. Heat deformation of cement phases and microstructure of cement paste, Materials and Structures, v. 17, (1984) 415-420
- [20] P. Cioni, P. Croce and W. Salvatore. Assessing fire damage to R/C elements, Fire Safety Journal, vol 36 (2001) 181-199.
- [21] C. Alonso, C. Andrade, E. Menendez and E. Gayo. Microstructure changes in high and ultra high concrete exposed to high temperature environments. Quality of concrete structures and materials and testing. ACI, SP-229-19, edt Lindsay K. Kennedy (2005) 289-302.



PERFORMANCE OF CARBON FRP REINFORCED CONCRETE BEAMS

Muhammad Masood RAFI¹, Ali NADJAI², Faris ALI³ and Didier TALAMONA⁴

ABSTRACT

The fire resistance of concrete members reinforced with fibre reinforced polymer (FRP) rebars is extremely crucial area that needs to be investigated prior to implementing FRP composite materials in buildings. This paper presents the results of an experimental investigation undertaken to evaluate the performance of reinforced concrete (RC) with Carbon FRP (CFRP) bars/ steel bars under ambient temperature and elevated temperatures. Four typical RC beams with CFRP/steel were tested under monotonic loading at ambient temperature up to failure. Three similar beams were tested under fire conditions using ISO834 curve subjected to 40% of their ultimate load. The results obtained from the cooling and the fire test regarding load, deflection, failure mode and cracking pattern are discussed in this study.

1. INTRODUCTION

Worldwide interest in the use of Fibre Reinforced Polymer (FRP) reinforcement in concrete structures as an alternative to a traditional structural material such as steel reinforcement has increased significantly in recent years. FRP reinforcement has an advantage over steel in that it has high corrosion resistance and a high strength to weight ratio. For example, in the UK and European Union countries alone, the annual cost of repair and maintenance of the infrastructure, as a result of problems associated with corrosion, is around £20 billion¹. Most existing solutions for the improvement of structural durability are expensive or complicate initial construction. It is generally expected that the use of FRP rebars, as opposed to steel, will reduce these maintenance costs by over 80% in the long-term¹. Furthermore, the use of composites in the rehabilitation of existing structures reduces the overall costs (including time for execution) by over 25%.

¹ PhD Student, University of Ulster at Jordanstown, FireSERT, 27B16, Shore Road, BT37 0QB
Email: rafi-m@ulster.ac.uk

² Professor, University of Ulster at Jordanstown, FireSERT, 27B16, Shore Road, BT37 0QB

³ Lecturer, University of Ulster at Jordanstown, FireSERT, 27B16, Shore Road, BT37 0QB

⁴ Research Fellow, University of Ulster at Jordanstown, FireSERT, 27B16, Shore Road, BT37 0QB

While FRP reinforcement is mainly used in bridges, there is enormous economic potential for its use in multi-storey buildings, parking garages and industrial structures. However, before FRP can be used to reinforce concrete members in buildings, the stability of these members to meet stringent fire resistance requirements must be established. Although it was found that the behaviour of FRP reinforced concrete structures at ambient temperatures is satisfactory²⁻¹³ information regarding the behaviour of FRP reinforced concrete members at high temperatures is still lacking. The behaviour of FRP bar reinforced concrete under fire exposure is quite different from conventional steel reinforced concrete. When embedded in concrete, the lack of oxygen will inhibit the burning of FRP reinforcement, but the resin will soften. The critical time will occur when the resin on the surface of the FRP bar reaches its glass transition temperature. At this point, the resin will no longer be able to transfer stresses from the concrete to the fibre, i.e. the bond will fail. Locally this may result in increased crack width hence increased deflections. Collapse will occur when the temperature of the fibre reaches the level at which it starts to degrade. The fire resistance of concrete reinforced with FRP rebars depends on the change in mechanical properties of FRP and concrete due to fire exposure. The effect of fire on the mechanical properties of concrete is well documented where it has been shown that high temperature decreases the modulus of elasticity and the compressive strength of concrete. A serious matter relating to the use of FRP's in structural applications is the lack of design codes and specifications. However, data of the effect of high temperatures on the FRP is limited. The behaviour of these composites when subjected to fire is complex and not sufficiently well understood.

The aim of this study is a directive preliminary investigation comparing the fire performance of RC beams with CFRP compared with steel reinforced beams.

2. EXPERIMENTAL SETUP

A typical specimen of cross-section 120x200mm with an overall length of 2000mm and a clear span of 1750mm was used as shown in Fig. 1. The tensile reinforcement consisted of 2 x 9.5mm CFRP bars or 2T10 steel bars to provide similar area of reinforcement. The beams were tested under 4-point loading as shown in Fig. 1. The load was applied by means of a 200 kN hydraulic jack and transmitted to the beam using a spreader beam.

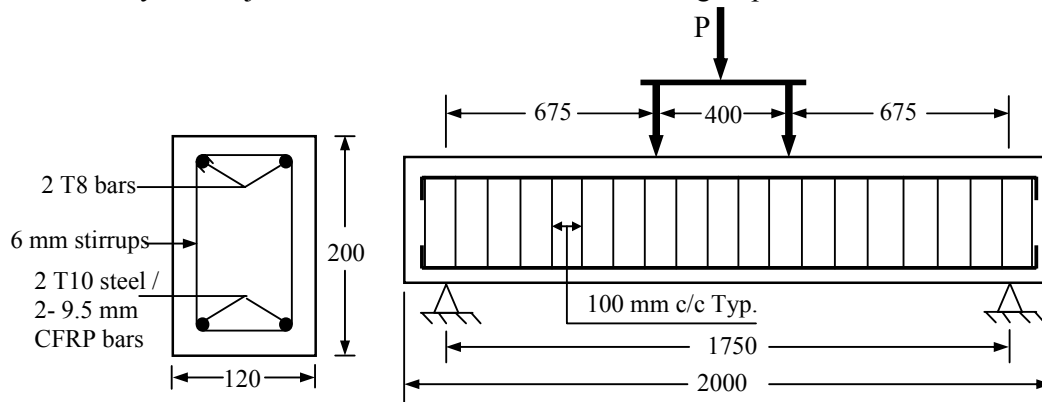


Fig. 1 - Experimental setup.

2.1 Material properties

Identical concrete mixes of 325 Kg/m³ ordinary Portland cement, 1001 Kg/m³ of graded crushed stone, 853 Kg/m³ of sand and 216 litres/m³ of water were used. The maximum aggregate size was 10 mm. The exact amount of water varied depending on the moisture contents of aggregates. The compressive strength of the concrete on the day of the testing is shown in Table 1. Each beam tested is defined by letters comparing its reinforcing material and testing conditions. The notation of beams is as: the first letter (B) stands for beam; the second letter indicates the testing temperature: R for room temperature and E for elevated temperature; the third letter represents the type of tension reinforcing bar material: S for steel and C for CFRP bars. These notations have been consistently followed throughout the rest of the text. The material properties of steel and CFRP rebars i.e ultimate strength, ultimate strain and elastic modulus are given in Table 2.

Table 1 Cylinder strength of concrete at the day of test

Beam	Compressive Strength (MPa)
BRS1	46.52
BRS2	44.64
BES1	30.45
BRC1	42.55
BRC2	41.71
BEC1	35.89
BEC2	33.22

Table 2 - Mechanical properties of tensile reinforcement

Bar Type	Nominal Ultimate Strength (MPa)	Ultimate Strain	Elastic Modulus (GPa)
CFRP – 9.5mm	1676	0.0145	135.9
Main Steel - 10mm	530*	0.0048*	201
Top Steel - 8mm	566*	0.0049*	194
Stirrup Steel - 6mm	421*	0.0041*	200

* parameters corresponding to 0.2% offset yield stress for steel bar

3. EXPERIMENTAL RESULTS

3.1. Room temperature tests

The beams were at least 2 months old at the time of testing. The specimens were tested under increasing load up to failure. The load was applied in small increments (5kN for FRP and 2.5kN for steel) and was kept constant for 3 minutes in order to spot any cracks and take a record of them. The initial cracking loads (P_{cr}) for each beam are independent of reinforcing material type as shown in Table 3.

Table 3 - Load, deflection and modes of failure

Beam	P_{cr} (kN)	P_u (kN)	Deflection at P_u (mm)	Modes of failure
BRS1	7.8	41.9	29.16	Steel Yielding
BRS2	7.5	40.1	27.78	Steel Yielding
BRC1	7.1	88.9	35.26	Shear Compression
BRC2	7.1	86.5	35.50	Compression

Figure 2 shows the repeatability of the load versus deflection of the beams tested at ambient temperatures. It can be seen that the two types of beams exhibited the same behaviour before cracking. Beyond the initial cracking the beams reinforced with steel were stiffer than the beams reinforced with CFRP. The steel yielded at early stage (around 39kN) with a deflection equal to 8mm. The maximum load achieved by the carbon fibres beams is much higher (around 89kN) compared to the steel reinforced beams, which is around 40kN. Table 3 summarise the failure modes of each tested beam. Figure 3 illustrates the cracking pattern.

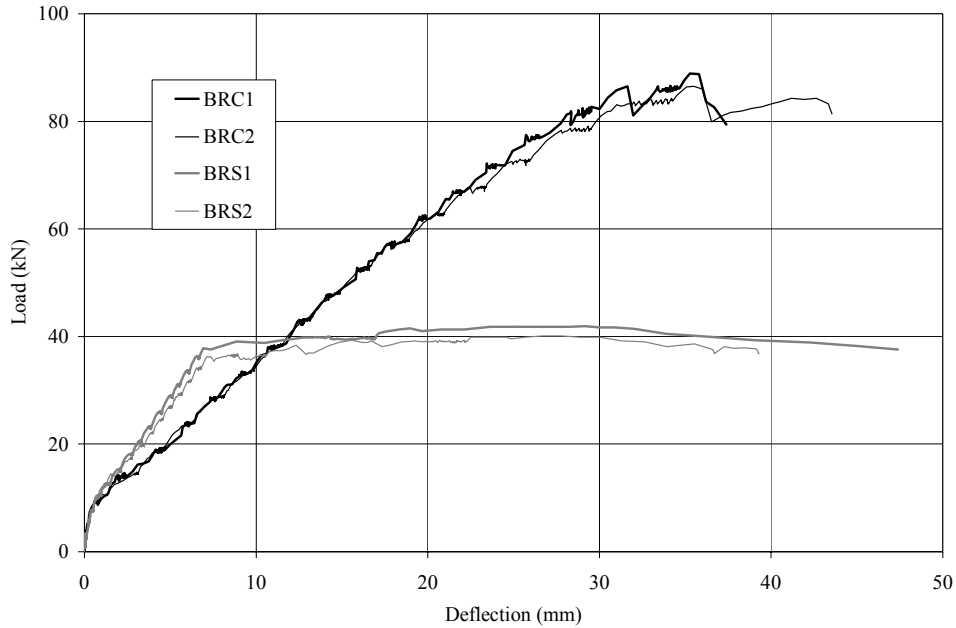


Fig. 2 - Load - deflection diagram.

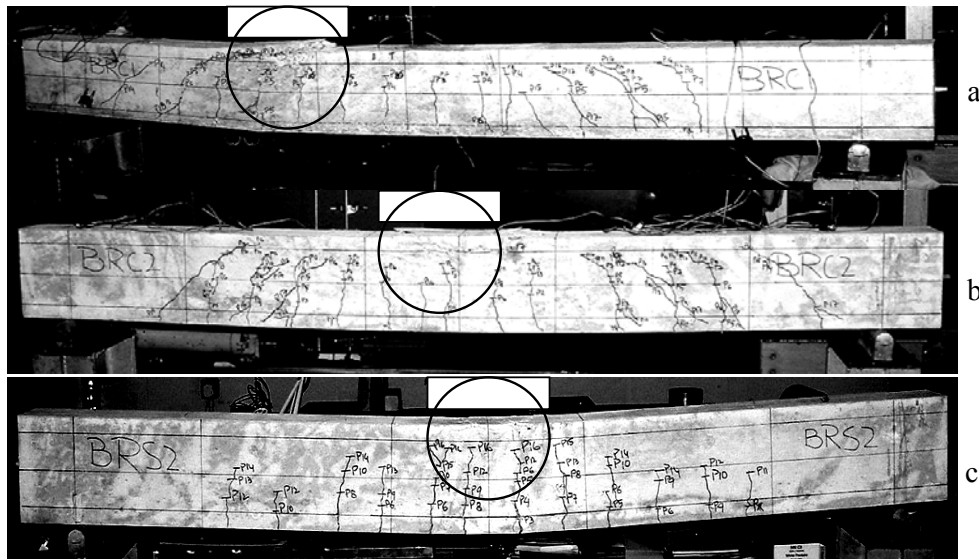


Fig. 3 - Cracking pattern of beams at failure.

3.2. Fire Tests

The beams were at least 3 months old at the time of testing. The load applied was 40% of the capacity of each beam and kept constant for the entire duration of the test. The furnace started after at least 30 minutes of load application with the ISO834¹⁴ heating fire curve. The total length exposed to the heat was measured as 1550mm.

The load applied on the BEC and BES RC beams was 30kN and 15.5kN, respectively. Figure 4 shows beam BEC1 in the furnace before (Figure 4a) and after (Figure 4b) fire. It can be seen in Figure 4a that the specimen beam (BEC1) severely cracked before fire started. These cracks provided an access to the heat, which degraded material properties of FRP bars. Figure 4b shows that one of the cracks, which was at a stirrup location, opened up and eventually caused failure in the beam due to crushing of concrete on top of this crack. The fibres of the bars were seen cut at this crack location after the cooling stage as shown in Figure 5.



Fig. 4 - CFRP specimen in the furnace before and after testing.

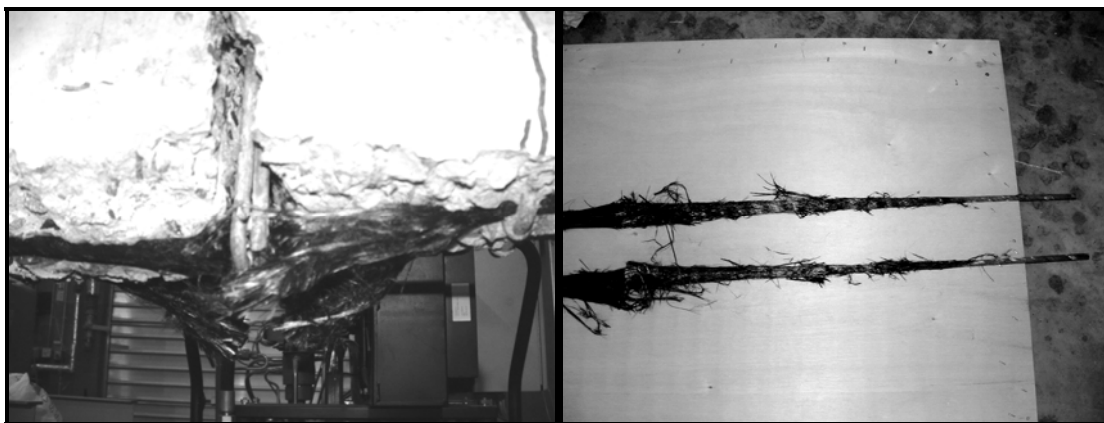


Fig 5 – CFRP bars after testing.

Figure 6 shows the time-deflection diagram. The initial deflection due to the applied load was not included on this diagram. Both type of beams experienced different behaviour under fire conditions.

The steel reinforced beam deflection increased linearly during the duration of the fire test and the rate of deflection became non-linear (in the last 10 minutes) before failure occurs. The CFRP reinforced beams deflection rates were less than the BES1 beam and the rate of deflection increased sharply before failure (within the last 2 minutes).

The failure has been considered when the deflection at mid-span of the beam exceeded $L/30^{15}$. The fire resistance recorded for the beams is given as follows:

Beam BEC1	-	63 minutes
Beam BEC2	-	51 minutes
Beam BES1	-	79 minutes

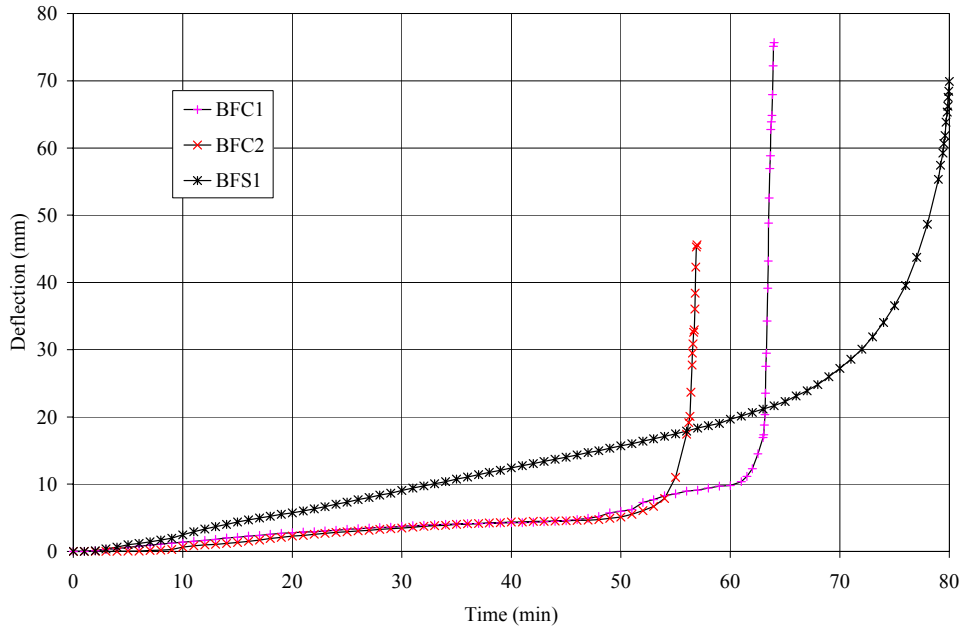


Fig 6 – Time deflection diagram.

Figure 7 and 8 show the temperature evolution for beam BEC1 and BEC2, respectively. The thermocouple TC1 recorded the temperature on one of the CFRP bars. The supplier provided the glass-transition temperature (T_g) of resin as 96°C , which corresponds to the bar softening. It can be seen that this temperature was reached after around 12 minutes of fire exposure. The bond between concrete and FRP bars is the first mechanism likely to be affected by temperatures beyond T_g and FRP bars could loose around 80 to 90% of bond strength in the temperature range of $200\text{--}250^{\circ}\text{C}^{16}$. The polymer, however, controls the properties in the transverse direction only. The fibres control the properties in the longitudinal direction. The anchorage to the bar was provided at the cooler ends of the beam. Close to the failure both bars slipped at the end close to the crushing point of beam. The examination of the bars revealed that the surface layer is stripped from the core, which exposed the longitudinal fibres. It was evident that all resin in the part of the beam exposed to the heating evaporated and residues of the burnt bars were seen on the broken concrete.

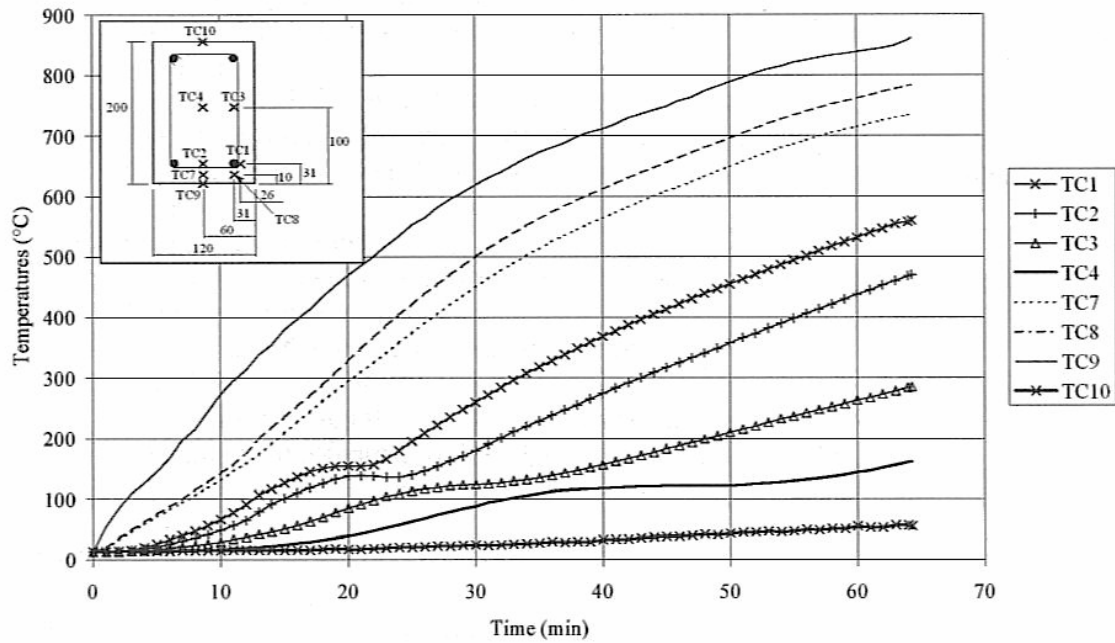


Fig. 7 – Temperatures in specimen BEC1.

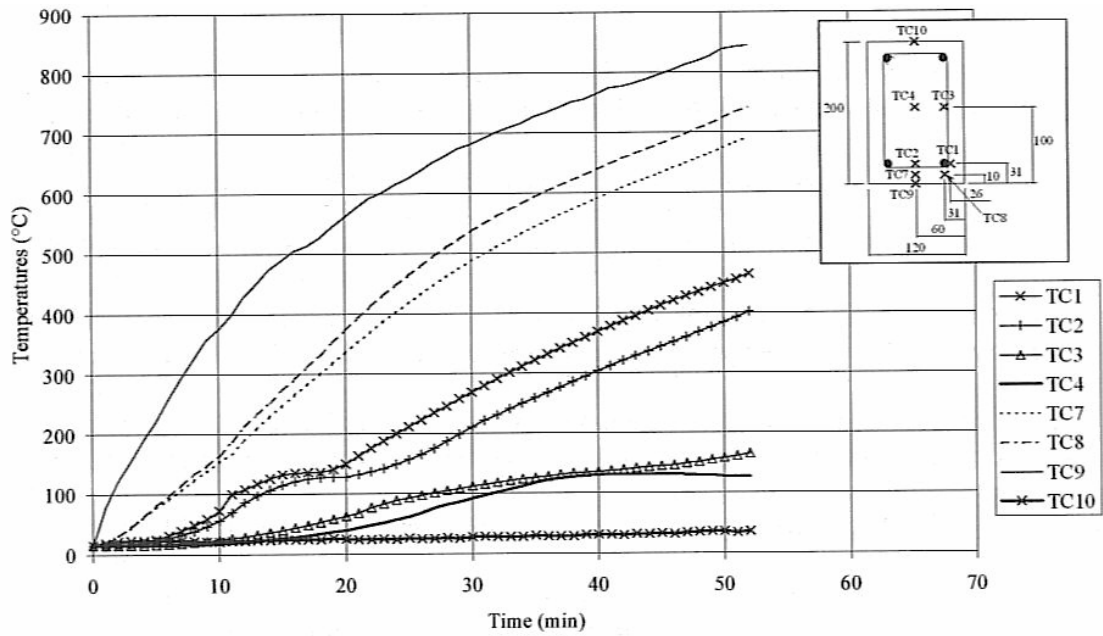


Fig 8 - Temperatures in specimen BEC2.

4. CONCLUSIONS

This paper presented a comparison of fire resistance tests between typical RC beams reinforced with different reinforcing materials (steel and FRP). The results obtained showed that failure mechanisms did not change between ambient and elevated temperatures. It was also evident that the steel reinforced beam is more ductile both at ambient and elevated temperatures compared to the CFRP reinforced beam (Figure 2 and Figure 6). The CFRP reinforced beams (Figure 6) was found to be stiffer compared to the steel RC beams at elevated temperature contrary to ambient temperature (Figure 2). The only reason is the concrete strength on the CFRP beams is more than the steel beam (Table 1) in addition to the cooler protected part of the beam played a role as anchorage to the bars. Preparations for the further beam tests are in progress.

5. REFERENCES

- [1] Balafas, IG., Burgoyne, CJ., Economic Viability of FRP in Concrete Structures, ConFibreCrete, Web-ste: www.shef.ac.uk, 2001
- [2] Burgoyne, C.J., "Should FRP be Bonded to Concrete." Fiber-Reinforced-Plastic Reinforcement for Concrete Structures: International Symposium, Detroit: American Concrete Institute, pp. 367-380, 1993
- [3] Aiello, M.A. and Ombres, L., "Structural Performances of Concrete Beams with Hybrid (Fibre-Reinforced polymer-Steel) Reinforcements." Journal of Composites for Construction, Vol. 6, No. 2, pp. 133-140. 2002.
- [4] Saafi, M., "Effect of Fire on FRP reinforced Concrete Members", Composite Structures, 58, No. 1, pp. 11-20, 2002
- [5] Somboonsong, W., Ko, F. K., and Harris, H. G., "Ductile hybrid fiber reinforced plastic (FRP) rebar for concrete structures: design methodology," ACI Materials Journal, 1998.
- [6] Abu-Tair, A.I., Nadjai, A., New Method for Evaluating the Surface Roughness of Concrete for Repair or Strengthening, International Journal of Construction and Building Materials, V.14, 171-176, 2000.
- [7] Talamona, D, Nadjai, A, Ali, F., Determination of the bending moment capacity of RC beams at ambient and elevated temperatures, Journal of Applied Fire Science, Vol. 11(1), 75-90, 2003.
- [8] Fujisaki T., Research and Development of Grid Shaped FRP Reinforcement. Nanni A, Dolan C, editors. Int. Symposium on Fiber Reinforced Plastic Reinforcement for Concrete Structures. ACI SP-183, pp. 177-92, 1993
- [9] Nakagawa H. Application of three-dimensional fabrics reinforced concrete to building panel. Nanni A, Dolan C, editors. Int. Symposium on Fiber Reinforced Plastic Reinforcement for Concrete Structures, SP-183, pp. 211-32, 1993
- [10] Tanan H., Fire resistance of continuous fiber reinforced concrete. Taerwe L, editor. Non-metallic (FRP) reinforcement for concrete structures. RILEM Proceedings 29, pp. 368-75, 1995
- [11] Sakashita M., Deflection of continuous fiber reinforced concrete beams subjected to loaded heating. Non-metallic (FRP) reinforcement for concrete structures, Japan Concrete Institute, vol. 2, pp. 51-58, 1997
- [12] Wang YC, Wong, PMH, and Kodur, V., Mechanical Properties of fibre Reinforced Polymer Reinforcing Bars at Elevated Temperatures, Designing Structures in Fire, Baltimore, USA, October 2003.
- [13] Eurocode 2: Design of concrete structures, 1992. ENV EC2.

- [14] ISO-834, Fire Resistance Tests, Elements of Building Construction. International Standards Organization, Geneva, 1975.
- [15] BS476-20, Fire Test on Building Materials and Structures, British Standards Institution, 1987, London.
- [16] Katz A, Berman N, Bank LC. Effect of High Temperature on Bond Strength of FRP Rebars. J Composites for Construction, 3(2), 1999, pp. 73-81.
- [16]



ANALYSIS OF HOLLOWCORE CONCRETE FLOOR SLABS UNDER FIRE

Jeremy CHANG¹, Andrew H. BUCHANAN², Rajesh DHAKAL³ and Peter J. MOSS⁴

ABSTRACT

The aim of this paper is to provide recommendations to designers, and to propose a simple method for designers to model the structural behaviour of hollowcore concrete floor slabs in fire. The proposed finite-element model incorporates a grillage system using beam elements to capture the thermal expansion of the precast units in both directions, with the topping concrete over several precast units modelled by shell elements. The research reported herein compares the proposed model with various fire test results of hollowcore concrete slabs. The simulation outcomes show good agreement with the experimental results.

Several hollowcore concrete slab flooring systems tested previously at the University of Canterbury for seismic purposes were simulated using this modelling scheme. Various supporting schemes have been considered, and the results show that different arrangements of axial and rotational restraint at the supports can significantly influence the fire performance of the concrete slab floors.

¹ PhD candidate, University of Canterbury, Department of Civil Engineering, Private Bag 4800, Christchurch, New Zealand, email: clc45@student.canterbury.ac.nz

² Professor, University of Canterbury, Department of Civil Engineering, Private Bag 4800, Christchurch, New Zealand, email: andy.buchanan@canterbury.ac.nz

³ Senior Lecturer, University of Canterbury, Department of Civil Engineering, Private Bag 4800, Christchurch, New Zealand, email: rajesh.dhakal@canterbury.ac.nz

⁴ Associate Professor, University of Canterbury, Department of Civil Engineering, Private Bag 4800, Christchurch, New Zealand, email: peter.moss@canterbury.ac.nz

1. INTRODUCTION

Precast prestressed hollowcore concrete (HC) floor systems have become very common in New Zealand and in many other countries. HC floor systems consist of several HC slabs with or without a layer of reinforced concrete (RC) topping. The benefits of using HC floor system are the low onsite labour cost, low self-weight, consistent quality, and economical use of concrete.

The structural behaviour of a HC floor system under fire is complicated, and precise computer models for simulating the structural behaviour of HC slabs under fires have been developed to improve the understanding of this behaviour¹. There are many existing studies investigating this behaviour with different approaches^{1,2,3,4,5,6,7}. However, very detailed finite element analyses for modelling the structural fire behaviour of HC slabs are too time-consuming to apply in the day-to-day design process. At the other end of the spectrum, simplistic approaches using a simple code rules are insufficient to capture the thermal expansion across the units or the effects of the support conditions. This paper aims to propose a simple yet sufficiently accurate method for designers to model the structural fire behaviour of HC slabs, and then based on the simulation results to provide some recommendations on the fire design of HC floor systems.

2. BACKGROUND

It is widely recognised that the behaviour of HC slabs under fire is more complicated than that of solid slabs. The cavities at the centre of the slabs cause discontinuity of the thermal transfer, and the thermal gradient needs to be addressed correctly to accurately model the temperature induced mechanical strains in the webs². The support conditions also have significant influence on the structural behaviour of floors⁸, this is especially so in HC floor system^{1,2,9}, and the effect of the support conditions should be considered in design. The presence of prestressing stress has been proven to also considerably influence the predicted overall structural performance¹⁰ as the HC units have no reinforcing and the resistance to tensile stresses comes from the prestressing tendons. Therefore, the fire design of the HC floor system needs to be able to accommodate different support conditions in different buildings, and the designers must recognise the fact that prestressed structural members demonstrate different behaviour to ordinary members.

There are three design methods for concrete members outlined in the Eurocode 2¹¹, namely tabulated data, simple calculation methods and advanced calculation methods. The tabulated data from the Eurocode 2, or the NZ Concrete Structures Standard NZS3101¹², do not consider the unique thermal gradient of the HC slabs nor does it take into account the influence of the surrounding structural members. Simple calculation methods cannot

accurately predict the thermal gradient, or include the effect of support conditions. Due to the rapid development in computation in recent years with advanced modelling methods, commercial finite element analysis [FEA] programs could be used to design HC floor systems based on the fundamental physical behaviour with due consideration to the effects from the surrounding structure. This fits into the category of “advanced calculation methods”.

This research uses the commercially available non-linear FEA program SAFIR¹³. The program was developed for analysing steel or composite structures, but the shell element in SAFIR has been proven to also accurately predict the fire behaviour of RC slabs¹⁴. A previous study showed that SAFIR can successfully predict the structural behaviour of *hibond* slabs (proprietary composite slabs) using a combination of shell and beam elements¹⁵, which is the basic idea behind the proposed model in this study.

The grillage analogy has been used for a long time and proved to be reliably accurate in bridge designs¹⁶. Grillages by definition have straight longitudinal and transverse beams rigidly connected together, each beam with its bending and torsional stiffness, and at each junction the deflection and slope is calculated^{17,18}. This grillage analogy became the alternative option.

Previous study has demonstrated that two-way supported RC slabs have better fire resistance than one-way supported slabs due to the membrane action¹⁴. Besides, restraint due to the surrounding structure has been proven to have a favourable effect on the performance of HC floor system in fire. After introducing the new model, this research uses it to explore the possibility of increasing fire resistance in the HC floor systems through membrane action.

3. MODEL DESCRIPTION

The aim of this model is to simulate the behaviour of the entire floor system including the surrounding structural members such as columns and beams. Detailed descriptions are shown in elsewhere¹⁹, but a summary of the key features is reported here. The final proposed model as shown in Fig. 1 uses beam grillages for the HC units, and shell elements to model the topping RC slab. Shell elements in SAFIR require less discretisation and are suitable for large displacements, but the thermal gradient is one directional and perpendicular to the element. Beam elements are more complex, requiring more computational effort, but can capture the thermal gradient more accurately and allow for prestressing.

The grillage system allows the model to capture the thermal expansion in both lateral directions, so that the effects of the restraints on lateral displacements from the surrounding structure can be well captured. In the grillage, all degrees of freedom except warping of the longitudinal and transverse beams are shared at the intersection points. The topping is modelled using shell elements which join the grillage system at these points and share these degrees of freedom. The longitudinal beams are used to address the thermal gradient around

the voids correctly and include the effect of the prestressing tendons. This prestress effect is accounted for when the stress equilibrium in the cross-section is calculated at the first time step. The transverse beams comprise only the top and bottom flanges and span only within the width of each HC unit, thus accounting for the thermal expansion of each unit in the lateral direction, which may affect the structural behaviour of the HC floor system especially when there are restraints on the sides. Therefore, the effects of the restraints on lateral displacements from the surrounding structure can be included. Examples of the thermal gradients in a longitudinal and transverse beam are shown in Fig.2 (a).

Some details need to be overlooked to reduce the complexity of the model. Shear and anchorage failures as well as bond failures are not considered in this model due to the complexity and the computational effort needed when simulating the entire structure. Spalling may cause problem as observed in experiments before¹⁴ but is not considered here, as the possibility of spalling depends on the curing period and the age of the building, and introducing these factors would make the results specific and not representative. Currently, no FEA program incorporates this effect on account of the uncertainties and lack of specific experimental data.²⁰

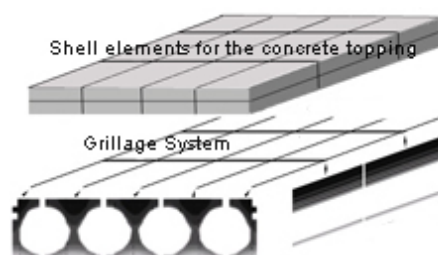


Fig. 1 – Schematic drawing for modelling of HC floor system



Fig. 2. – Temperature distribution of SP265 Ergon after 2hr. of ISO fire from (a) longitudinal beam (b) transverse beam

4. MODEL VALIDATION

This section shows the comparison between the test data carried out by various institutes and the simulation results.

4.1. Universities of Ghent and Liège

Four tests were carried out in the Universities of Ghent and Liège in 1998 focusing on the influence of detailing and of restraint conditions on the shear capacity of HC slabs⁹. Detailed descriptions and the explanations of the designs are given in the test reports.^{21,22} Each test had two 2.4m wide floor (2 HC units) spanning 3m and supported on three beams as shown in Fig. 3 (a). Each floor was independent. The floors had self weight of 3kN/m^2 , a line load of 100kN in the middle of each of the two spans, and were exposed to 2 hours of ISO fire. Afterwards, extra load was applied to check the remaining load capacity. The parameters studied in the four tests are shown in Table 1. Only half of the floor was simulated (one 1.2m wide floor span of 3m) as shown in Fig. 3 (b). The filling of the voids at the ends was included in the model, but the peripheral ties and the detailed anchorage were not.

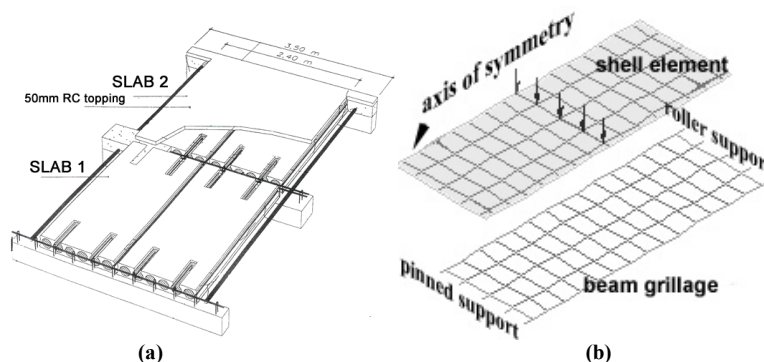


Fig. 3 – (a) Detailing of Test 1 in 1998 SSTC tests⁹ (b) illustration of the simulation model

Table 1 Studied parameters in 1998 tests in University of Ghent²¹

Parameters	Test 1	Test 2	Test 3	Test 4
HC section (type)	SP200 Ergon	VS20 Echo	VS20 Echo	SP265 Ergon
Height of HC section	200mm	200mm	200mm	265mm
Peripheral ties	none	exists	exists	none
Reinforced topping	50mm	none	none	30mm

Test 4 has been simulated using SAFIR with a different approach before². The differences between the old and new models are the presence of the transverse beams and the location of dividing the units. The new method recognises that the bottom flange is more likely to split than the web. Therefore, it is more reasonable to divide the units at the thinnest point of the flange as shown in Fig.2(a) rather than at the middle of the web. The previous

study showed that the heat transfer through the cavities in SAFIR is properly calculated and the thermal gradient given by the simulation was similar to the experimental results. Hence, the thermal gradient in the new model must also be accurate.

In all the tests, the compressive strength of the concrete in the HC units was around 45MPa, and the strands strength was 1.85GPa. The results from Tests 1 and 4 with RC topping slabs are shown in Fig.4 and 5. The level of prestressing was assumed to be 75% of the strand strength.

To check if the transverse beams increase the stiffness of the slab, the transverse beams were removed in one simulation. Fig.4 (b) shows that the presence of transverse beams has no influence on the vertical displacement in this case where the slab consists of only two units. It confirms the idea the transverse beams should only contribute to the transverse displacement, or become effective when the slab consists of multiple units over the width or the support condition at the sides become important.

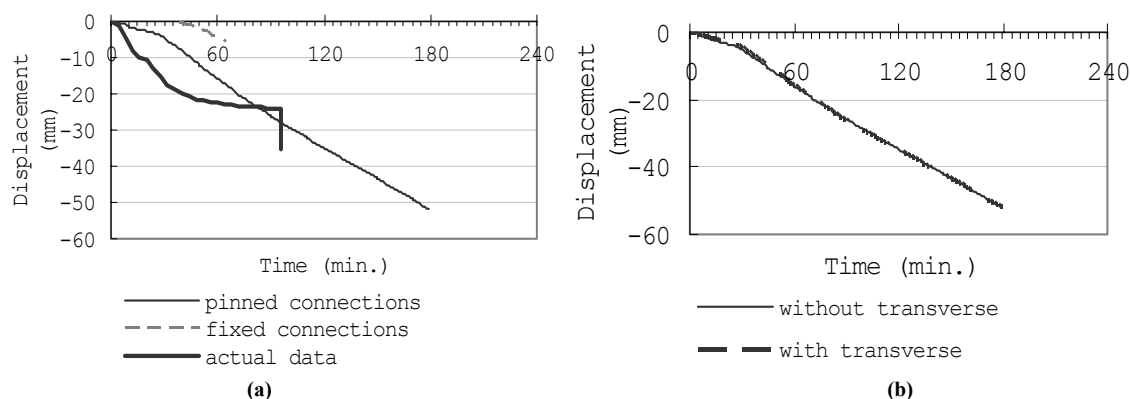


Fig. 4 – Simulation results from Test 1 (a) different support condition against actual result (b) effect of transverse beams

In Test 1, the simulation run with no rotational restraints at the ends predicted that the slab had more than 3 hours of fire resistance, but this reduces to 1 hour if there are full rotational restraints. However, in reality the support condition is one of partial rotational restraint, and the slab withstood 83min. of the fire. Fig.4(a) shows that the simulation result was not close to the experimental data²². The maximum difference between the maximum deflections obtained from simulation and the test data was 10mm. During the experiment, shear cracking was observed 7min. from the start of the experiment, and vertical cracking was observed at 12min.²². This explained the rapid increase in midspan deflection in the experiment at the early stage of the fire. The simulation model could not predict the shear displacement or failure, as shear effects are not included in the computer software used.

In Test 4, the HC unit is changed from SP200 Ergon with circular voids to SP265 Ergon with oval shaped voids, and the number of voids changed from six to five, but the applied load and other mechanical values were the same as in Test 1. The experimental result

in Fig. 5 showed that the slab could sustain up to 2 hours of ISO fire. The failure from the actual data was caused when the fire was stopped after 2 hours and more loading was added at the midspan to check the capacity. There was no shear failure or substantial shear displacement during the fire test. Therefore the simulation result matched the test data reasonably well up to 120min.. The maximum difference between the two deflections was around 5mm.

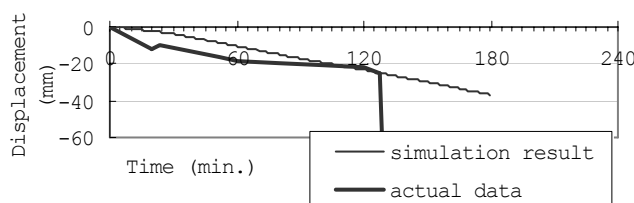


Fig. 5 – Simulation results of Test 4

4.2. Danish Prefab Concrete Association (Betonelement-Foreningen, BEF)

Three fire tests with HC slabs were conducted by BEF in 2005⁵. The purpose of these tests was to confirm if after exposing to the ISO fire for 60min., the HC slabs could still resist at least 65% of the ultimate design shear capacity in cold condition derived from the DS411 Danish Standard²³. Therefore, the applied shear force in these tests was higher than expected in a normal fire design. In these tests the fire curve followed only 60min. of the ISO fire and then stopped, and the tests continued for a further 60 to 90min. with the constant applied load. The tested specimens were 265mm thick, with no topping, spanning 3.27m as shown in Fig. 6(a) the simulation model is shown in Fig. 6(b). The HC unit in the test as shown in Fig. 7(a) was discretised as shown in Fig. 7(b).

Three load levels, 65%, 75% and 80% of the ultimate shear capacity (91.6kN/m) were used in the test. The dead weight of the HC slabs is 3.65kN/m² including joint castings.

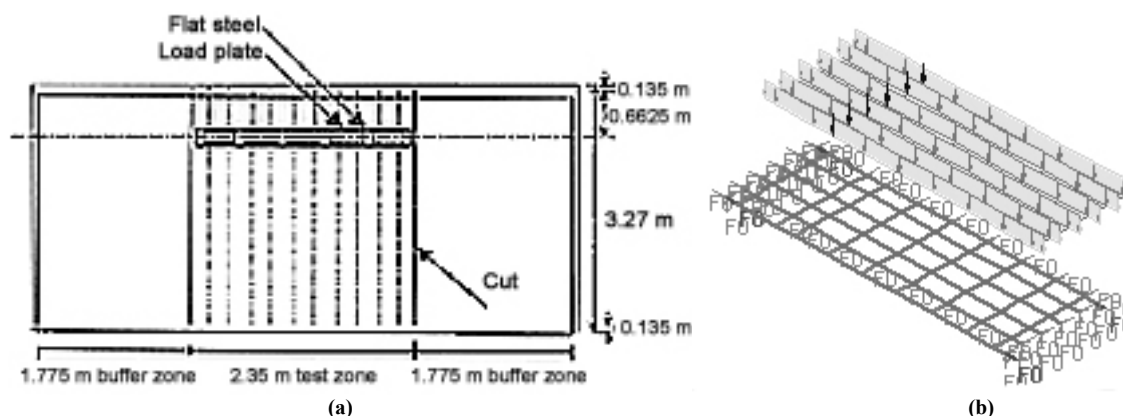


Fig. 6 – (a) original test layout² (b) SAFIR grillage model and loads for BEF 2005 tests

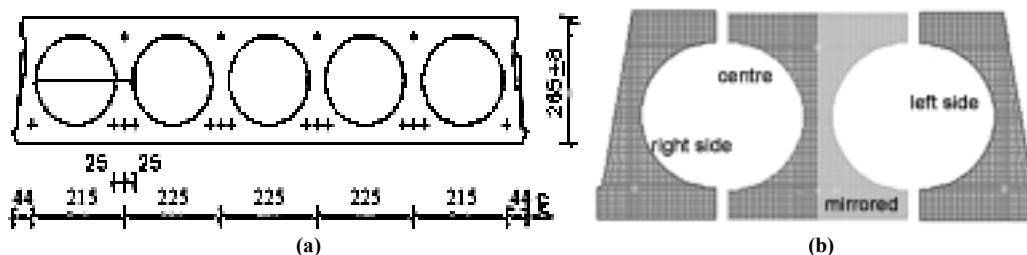


Fig. 7 – (a) HC dimension for BEF test⁵ (b) discretised model (right, web, left)

The test results showed that the HC slabs have good shear resistance under elevated temperature. The comparison between the analytical prediction and experimental results in Fig. 8 shows that the vertical displacements calculated from the simulation are close to the test data. The difference between the vertical deflection at the centre and the side of the unit in the simulations is almost the same as that from the tests. The difference between the predictions and the test data is presumed caused by shear deformation. In the case with an applied load equal to 80% of the slab's shear capacity, the slab had a shear failure after 45 minutes of ISO fire exposure. The model could not foresee the shear failure and therefore it continued to provide results after this time. The large shear force was not captured in the analysis, and the model underestimated the deflection. Nevertheless, in normal practice such high level of shear force is never designed for.

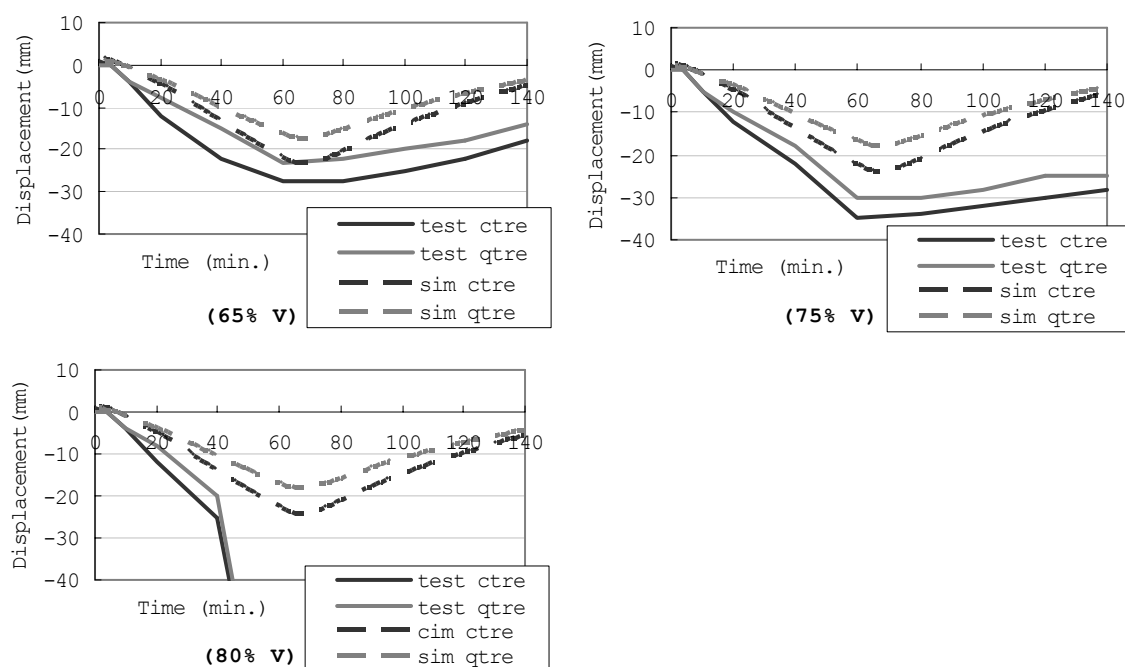


Fig. 8 – Comparison between the vertical displacements at midspan (ctre) or at the location of the point load (qtire) from simulation (sim) and test (test) results

5. STRUCTURAL SIMULATION

Currently University of Canterbury is developing several new designs to increase the earthquake resistance of HC floor systems^{24,25,26}. The proposed model is being used to check their fire resistances. The simulation shown here is based on one structure previously tested for the seismic purposes²⁵, consisting of 300mm thick HC units (300Dycore) and 75mm thick RC topping. The dimensions of the tested floor are shown in Fig. 9(a). One of the simulation models is shown in Fig. 9(b). The tested floor was 6.1m wide, but by using symmetry about one side, the total width it represented was 12.2m. The span length was also 12.2m. The surrounding beams were 400mm wide by 750mm deep. A 200mm thick in-situ RC slab was added at the side between the first HC unit and the side beam to ensure smooth transition of deformation from the flexible side beam to the rigid HC floor units²⁴.

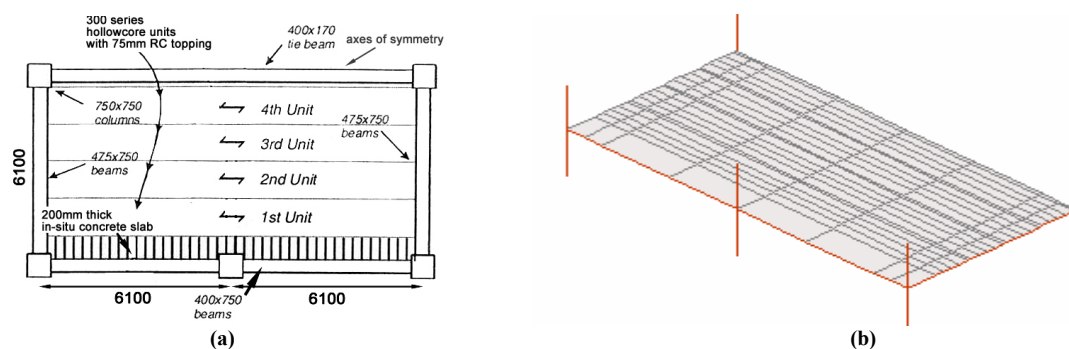


Fig. 9 – Half of the floor plan of simulated test (a) from the drawing²⁵ (b) in simulation

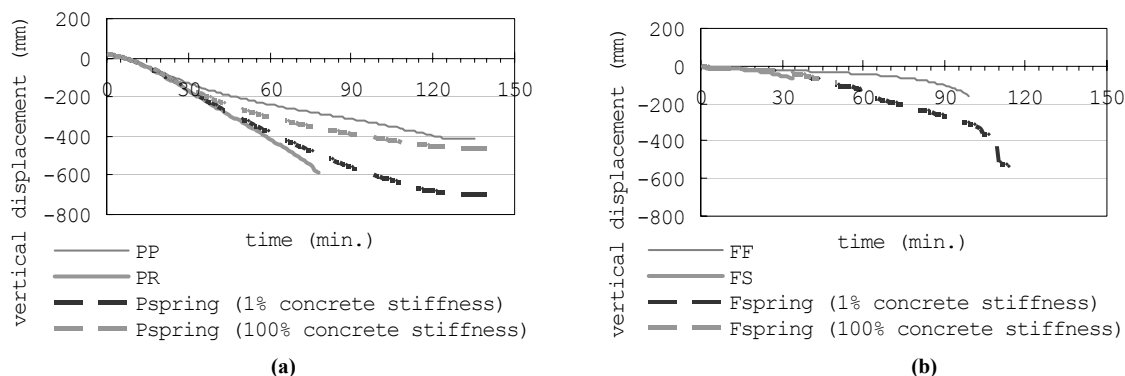


Fig. 10 – Midspan vertical displacements at the centre of the slab with different connection types: (a) without rotational restraints (b) with rotational restraints

Two parameters are studied here: the connection type at the ends of the units, and the vertical supports at the sides of the floor. Previous studies have shown that providing axial restraints can improve the fire resistance^{1,2,8,9}, and the latest experimental study in the University of Canterbury on seismic behaviour of HC floor system showed that providing rotational restraints at the ends enhances seismic performance. To study the effect of the end supports, six different support conditions were simulated: pin-pin ('PP'), pin-roller ('PR'),

pin-pin and a spring ('Pspring'), fix-fix ('FF'), fix-slide ('FS'), and fix-fix and a spring ('Fspring'). In this first set of analyses, supports at the side were not considered, and the piece of in-situ RC slab at the side was ignored. The results are shown in Fig. 10. Both Fig. 10(a) and (b) highlight the benefit of providing even just a little axial restraint, as the cases with no axial restraint fail much earlier than the other cases. By comparing the PP and FF cases these two figures, it is observed that providing rotational restraint will reduce the overall deflection, however, the fire resistance will also be reduced.

The idea behind the second set of simulations was that the membrane action inherent in two-way slabs can be taken into account if vertical supports are provided at the sides of the HC floors. The in-situ RC topping slab was included in this set of analyses. Six different situations were studied to see the effect of the vertical supports at the sides: (1) no supports at the side but fixed at the ends ('one-way supported'), (2) fixed at all four sides ('all fixed'), (3) pinned at all four sides ('all pinned'), (4) two ends fixed and sides rigidly connected to beams which are fixed at the two extremes ('with two beams'), (5) floor rigidly connected to beams at all four sides with the four corners fixed ('with all beams'), and (6) the beams connected to columns at the four corners with fixed base ('with clmn.'). The maximum vertical displacements in the slab are shown in Fig. 11.

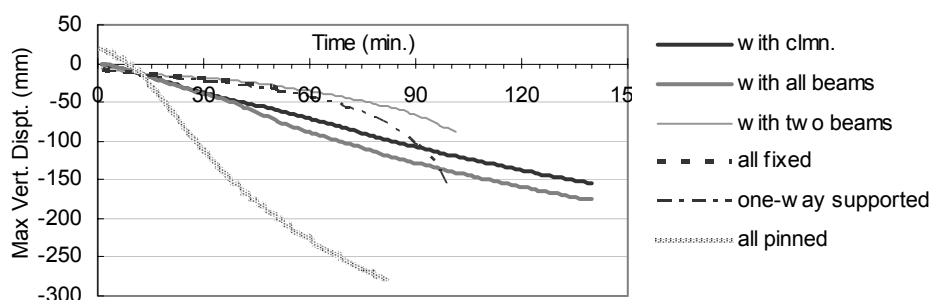


Fig. 11 – Maximum vertical displacements in the slab with different support conditions

The results confirm the finding from the previous set of simulations. Only in the case with all four sides fixed is the predicted fire resistance less than 1 hour. The cases closer to the reality showed (i.e. 'with clmn.' and 'with all beams' cases) higher than 2 hours of resistance. The graph also shows that the vertical displacement at the centre of the 'with clmn.' case is less than that of the 'with all beams' case. This is because the presence of columns allows the corners to move away thereby resulting in horizontal outward movement of the side beams. The 'all pinned' case failed earlier than the 'PP' case from Fig. 10. Further investigation has shown that this is caused by a numerical problem in the program, and it is not an indication of the real failure time.

From the results here it can be said that the best fire resistance is provided when there are partial restraints on rotational and axial deformation at all sides. The worst fire resistance is from the case with fixation at all sides (which has fire resistance of 50min. as shown in Fig.

11) Note that fully fixed support condition is also not recommended from the seismic design point of view²⁶. By comparing the ‘one-way supported’ and the ‘with two beams’ cases, the results indicate that providing vertical support along the sides reduces the maximum displacement significantly, but only slightly increase the fire resistance of the HC floor system.

6. CONCLUSIONS AND FUTURE STUDIES

A new modelling scheme is proposed to simulate the behaviour of HC floor system under fire. The new scheme uses a grillage system to model the HC unit, and a layer of shell elements to model the RC topping slab. The advantage of the new scheme is that it recognises the effects of thermal expansion in the transverse direction, and it can also model the membrane action through the topping layer.

The new model can predict the fire performance of HC slabs well, on the condition that no shear failure or significant shear displacements are present. It is expected that this new model could work better in actual building design than in the simulating test results, because shear failure or displacement is likely to be significantly reduced with the presence of axial restraints.

From the preliminary study on the HC floor design, axial restraints at the end supports are strongly recommended, but restraining rotation at the sides has little benefit on improving fire resistance. Future studies will include more detailed connections, and also investigate whether an intermediate beam to reduce the width of bay is necessary for fire safety.

7. REFERENCES

- [1] Fellingner, J.H.H., *Shear and Anchorage Behaviour of Fire Exposed Hollow Core Slabs*, DUP Science, Delft, Netherlands, 2004.
- [2] Dotreppe, J-C. and Franssen, J-M., “Precast hollow core slabs in fire: numerical simulations and experimental tests”, *3rd International Workshop “Structures in Fire”*, Ottawa, Canada, May 2004, paper S5-1
- [3] Materazzi, A. L. and Breccolotti, M., “Fire behaviour of HPLWC hollow core slabs: full scale furnace tests and numerical modelling”, *fib Task Group 4.3*, Milan, Italy, Dec, 2004
- [4] Micelli, F., Mariacongedo, P. & De Lorenzis, L. *Resistenza al Fuoco di Pannelli Cavi in Calcestruzzo Precompresso*, Internal Report, Università degli Studi di Lecce, Italy, 2005
- [5] *Bef. Hollow Core Slabs and Fire – Documentation on Shear Capacity*, Birch & Krogboe A/S, Denmark, 2005.
- [6] Andersen, N. E. and Lauridsen, D. H. *Danish Institute of Fire Technology Technical Report X 52650 Part 2 - Hollow core Concrete Slabs*, DIFT, Denmark, 1999.
- [7] Lennon, T., “Precast Hollowcore slabs in fire”, *Structural Engineer* Vol. 81 No. 8, pp.

30-35, 2003

- [8] Buchanan, A.H. *Structural Design for Fire Safety*. John Wiley & Sons, Chichester, 2001
- [9] Dotreppe, J-C., and Van Acker, A., “Shear resistance of precast prestressed hollow core slabs under fire conditions”, *1st fib Congress*, Japan, pp.149-158, 2002.
- [10] Chang, J., *Performance of Concrete Flooring under Fire in Modern Building System*, PhD Thesis, University of Canterbury, NZ, 2007 (in progress)
- [11] ENV 1992-1-2, *Eurocode 2: Design of concrete structures. prEN 1992-1-2: General rules- Structural fire design*, European Committee for Standardization, Brussels, 2002
- [12] NZS 3101: Part 1:1995, *The Design of Concrete Structures*, SNZ, Wellington, NZ, 1995
- [13] Franssen, J-M, Kodur, V.K.R. and Mason, J., *User's Manual for SAFIR2001 Free: A Computer Program for Analysis of Structures at Elevated Temperature Conditions*, University of Liège, Belgium, 2002.
- [14] Lim, L., *Membrane action in fire exposed concrete floor systems*, PhD Thesis, University of Canterbury, NZ, 2003
- [15] Lim, L., Buchanan, A. H. and Moss, P. J., “Numerical modelling of two-way reinforced concrete slabs in fire”, *Engineering Structures*, Vol.26, pp. 1081-1091, 2004
- [16] Hambly, E.C., *Bridge Deck Behaviour*, 2nd Ed., E & FN Spon, London, 1991
- [17] West, R., *The Use of a Grillage Analogy for the Analysis of Slab and Pseudo-Slab Bridge Decks*, research report 21, Cement and Concrete Association, Bristol, England, 1973
- [18] Livesley, R.K., *Matrix Methods of Structural Analysis*, Pergamon Press, Oxford, 1964
- [19] Chang, J., “Simple method for modelling hollowcore concrete slabs under fire”, *19th Australasian Conference on Mechanics of Structures and Materials*, Christchurch, NZ, Nov. 2006.
- [20] Franssen, J-M., “Structures in fire, yesterday, today and tomorrow”, *8th International Symposium on Fire Safety Science*, Beijing, China, pp.21-35, Sept. 2005
- [21] Fib, *Résistance au Cisaillement de Dalles Alvéolées Précontraintes*. Studiecommissie SSTC. University of Liège, Belgium, 1998
- [22] Fib, *Résistance au Cisaillement de Dalles Alvéolées Précontraintes (Partie 1) –Annexes*. Studiecommissie SSTC. University of Ghent, Belgium, 1998
- [23] Danish Standards: DS411 *Norm for betonkonstruktioner*. Dansk Standard. Charlottenlund 1999
- [24] Lindsay, R., *Experiments on the Seismic Performance of Hollow-Core Floor Systems in Precast Concrete Buildings*, ME Thesis, University of Canterbury, NZ, 2004
- [25] Matthews, J., *Alternative Load Paths for Floor Diaphragm Forces Following Severe Damage to the Supporting Beams*, PhD Thesis, University of Canterbury, NZ, 2004
- [26] MacPherson, C., *Seismic Performance and Forensic Analysis of a Precast Concrete Hollow-Core Floor Super-Assemblage*, ME Thesis, University of Canterbury, NZ, 2005

SIF'06

MODELLING MEMBRANE ACTION OF MODEL-SCALE SLABS AT AMBIENT AND ELEVATED TEMPERATURES

S. J. FOSTER¹, I. W. BURGESS² and R. PLANK³

ABSTRACT

This paper presents the results from a series of numerical studies conducted on unrestrained reinforced slabs, of relatively high span/depth ratio, at large displacements. Previous experimental work involved a series of tests carried out on thin model-scale slabs at ambient and elevated temperatures. The purpose of the studies reported here was to investigate the influence of the following parameters, at both ambient and elevated temperatures, on the degree of mobilisation of membrane action within the model scale slabs:

- Thermal gradient;
- Bond strength;
- Distribution and cross sectional area of reinforcement;
- The influence of concrete tension;

The more detailed issues being studied include the major factors influencing the development of the tensile membrane forces within the slabs at both ambient and elevated temperatures. Numerical and experimental results are compared with the well known BRE Method, which is based on a simplified representation of tensile membrane action. The results of these comparisons show that the latter is generally conservative, although the approach is an upper-bound one and may not be applicable under all circumstances.

KEYWORDS: Tensile membrane action, concrete, slabs, large displacements, high temperature experiments, fire performance, yield line theory.

¹ Ove Arup Ltd, 30 Barkers Pool, Sheffield, S1 3HB, UK; samantha.foster@arup.com

² Department of Civil & Structural Engineering, University of Sheffield, Sheffield, S1 3JD, UK; ian.burgess@sheffield.ac.uk

³ School of Architectural Studies, University of Sheffield, S10 2TN, UK; r.j.plank@sheffield.ac.uk

1. INTRODUCTION

There has been a great deal of work in the last decade in modelling full-scale composite frames in fire conditions. However, there has been limited investigative work carried out on the structural behaviour of floor systems at large displacements at both ambient and elevated temperatures. Early investigative work on large displacement of slabs was undertaken in the late 1960s, and this showed that at ambient temperature reinforced concrete slabs perform better than is conventionally thought. The increased load capacity of the slab was attributed to in-plane forces which are created due to the boundary conditions and resultant displacements. The slab becomes a self equilibrating system. This mechanism is known as Tensile Membrane Action as the slab is resisting the loads by diaphragm action.

Work has been undertaken to investigate the degree of mobilisation of tensile membrane action within a slab at both ambient and elevated temperatures due to a number of parameters:

- Bond strength,
- Distribution and cross sectional area of reinforcement,
- The influence of concrete tension,
- Influence of thermal gradient.

Some comparisons have been made with the well known BRE Method, which is based on a simplified representation of Tensile Membrane Action [1].

2. MODEL SET-UP

Modelling of the behaviour of the slabs at ambient and elevated temperature was undertaken using the finite element software *Vulcan*. This software has been extensively validated over the years with experimental data collated from the full-scale tests carried out at Cardington. *Vulcan* models the complex factors that arise in fire conditions, such as thermal expansion of the elements, change of material properties with temperature and concrete cracking and crushing. Fig. 1 shows how the slab elements are configured.

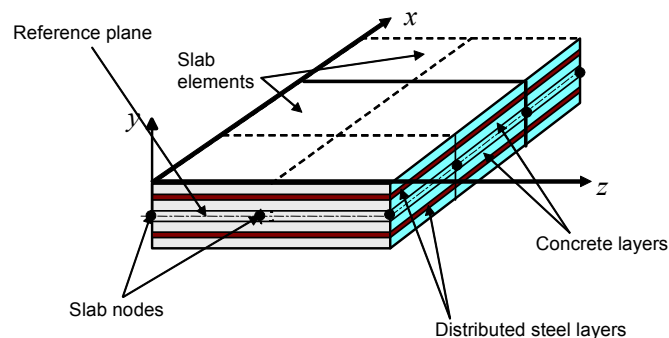


Fig. 1 – The distribution of slab elements

The main features of the program are not discussed here but further details are given in references [2, 3].

2.1 Validation of Model

The model-scale slabs were representative of tested slabs that have been tested at both ambient and elevated temperatures. The models were created using an assemblage of finite

plate elements using a quadrilateral 9-noded element. The elements were divided into several layers representing the concrete and reinforcing steel (Fig. 1). The tested slabs were horizontally unrestrained with edges simply supported. In order to check that the boundary conditions of modelled slabs were representative of the tested slabs, crack patterns for the bottom layer of the slab (Figs. 2(a) and 2(b)) were analysed. The critical load intensity in tests was approximately 3.3kN/m^2 , which compared well to the 3.6kN/m^2 predicted by *Vulcan* for the initiation of cracking. Beyond this stage it can be seen that the crack patterns show a developing yield-line mechanism.

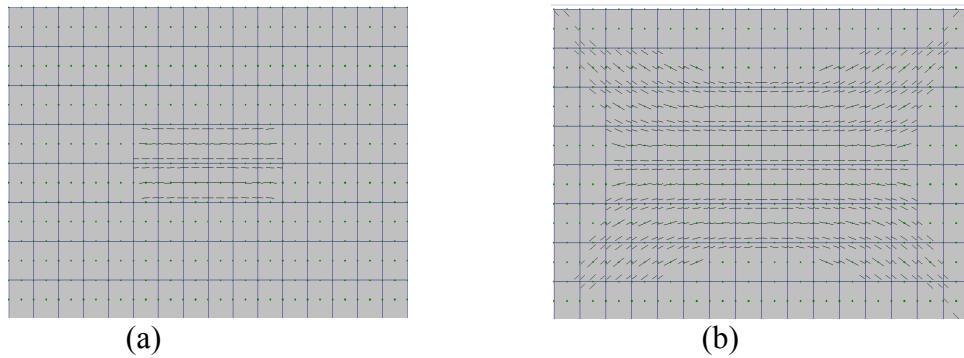


Fig. 2 - Crack patterns for bottom layer of full slab for load (a) 3.74kN/m^2 and (b) 4.96kN/m^2

3. PARAMETRIC STUDIES AT AMBIENT TEMPERATURE

Several experimental studies were undertaken at ambient temperature to investigate the influence of the following parameters on the load capacity of the slab:

- Bond strength
- Development of membrane forces

Further parametric studies were conducted using *Vulcan* to study the influence of concrete tension and reinforcement yield strength on the slab behaviour. The influence of concrete tension could not be evaluated experimentally. The experimental and numerical results were also compared with the BRE Simple Design Method.

The model scale slabs in the ambient tests had a total reinforcement of 0.3% of the slab cross-sectional area. In order to investigate the influence of the bond strength on the overall load carrying capacity of the slab, the tested slabs were reinforced with two types of wire; smooth and deformed wire. The tested ductility was 20% for the smooth wire and 11% for the deformed wire. Table 1 shows a comparison of two tested slabs and the material data collected. The tests are identical in that the slabs have the same aspect ratio and arrangement of reinforcement. The main difference between these two tests is the reinforcement type, Test 1 was reinforced with smooth wire, and Test 2 with deformed wire. These slabs had isotropic reinforcement in that they had the same steel area in both the short and long spans.

Table 1. Isotropic slabs of aspect ratio 1.55

Test	Size (mm)	t(mm)	$f_y(\text{N/mm}^2)$	$f_c(\text{N/mm}^2)$	$f_t(\text{N/mm}^2)$	Yield line capacity(kN/m^2)
1 <i>smooth wire</i>	850x550	19.5	256	28	1.76	2.54
2 <i>Deformed wire</i>	850x550	16	248	25	1.66	1.99

The load carrying capacities of the two slabs are shown in Fig. 3, and are shown as enhancements above yield-line capacity to illustrate the development of tensile membrane action within the slabs. The experimental results have also been compared with theoretical predictions by the simplified approach; which are shown in Fig. 3 by the two straight lines. The load carrying capacity of the two slabs quickly increases with increasing slab displacement up to a vertical displacement of 30mm, beyond which the actual capacity of the slab in Test 2 decreases. The reason for this reduction in capacity was fracture of the deformed wire. Both slabs had suffered cracking, but the slab reinforced with smooth wire was still integral when removed from the loading rig whereas for that with deformed wire the fracture of the reinforcement was clearly seen.

The test results of the slab with the smooth wire compare well to the theoretical predictions, since, due to their lower bond strength and greater ductility, the wires did not fracture. The test results of the slab with deformed wire did not compare well to theory, as the analysis predicted an ever-increasing load capacity, because the method does not take into consideration the decrease in load due to fracture of reinforcement.

Comparison of the test results with *Vulcan* is also shown in Fig. 3. The numerical results in which concrete tensile strength is accounted for show predictions in the region of 1.6 times the experimental initial peak, followed by massive amounts of simultaneous cracking which causes the apparent “plateaux” in the strength of these very lightly reinforced slabs. For comparison purposes it is more instructive to inspect the modelling without including concrete tension. These curves show good agreement with both the simplified method and the tests.

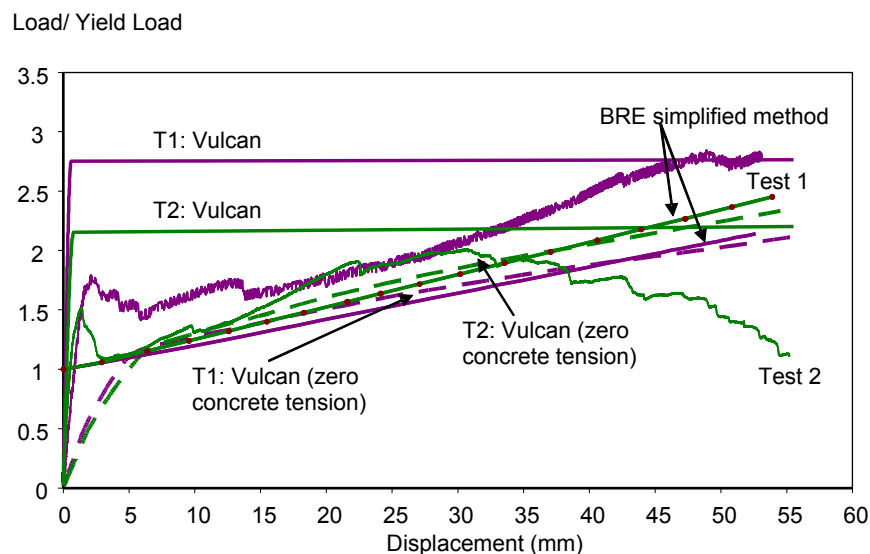


Fig. 3 - Comparison of Test 1 and Test 2 with *Vulcan* and simplified method

A study was undertaken to investigate the effect of variation of the yield strength of reinforcement and the compressive and tensile strengths of concrete. A range of concrete strengths were investigated, from very low ($F_c=6\text{N/mm}^2$) to the strength measured on the day of the test. The influence of zero concrete tensile strength was investigated. The results of this study are presented in Fig. 4. The study showed that;

- In initial deflection behaviour, the concrete tensile strength is very important,
- At large deflections, the tensile strength of the reinforcement is important in determining the load capacity of the slab.

The load-displacement curves for various concrete strengths shown in Fig. 4 converge at large displacement, indicating that concrete strength does not affect the enhancement factor.

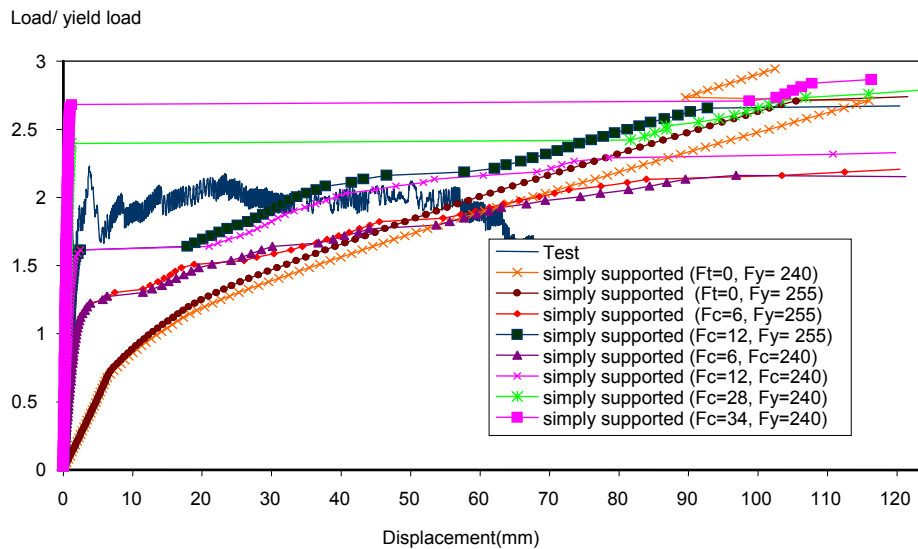


Fig. 4 - Investigation of the influence of the yield strength and concrete compressive for slab of aspect ratio 1.55

The development of membrane forces within an isotropic slab (Test 1) at a mid-span displacement of 33mm and load of 3kN/m^2 is shown in Fig. 5. Compression forces are seen to form in the central zone of the quarter-slab, parallel to the short span (indicated by the blue vectors). The edges parallel to the long span move inwards, and as the slab displaces these compressive forces start to develop in the central zone as the slab starts to 'jam'. The zone of pure tension is represented by the thin red lines.

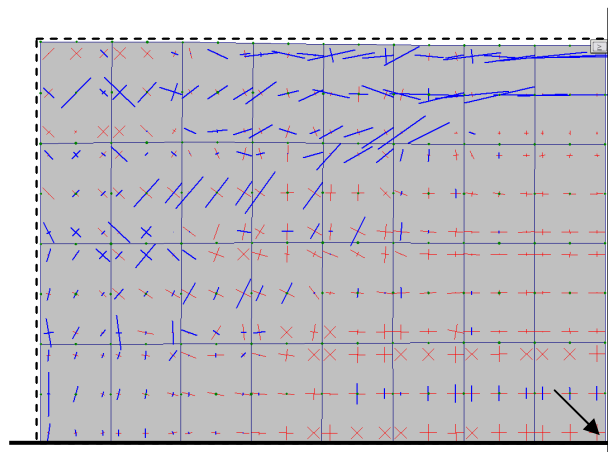


Fig. 5 - Membrane tractions for quarter-slab at 33mm deflection for a load of 3kN/m^2 and zero concrete tensile strength

This 'jamming' of sections of the slab was observed during testing, and therefore the predictions by *Vulcan* seem to tie in well to the observed slab behaviour. However, the simplified method does not consider the development of compressive forces within the central

zone. Further investigations have been undertaken to assess the sensitivity of the enhancement of load capacity to these forces, but this is difficult to quantify as it occurs once the slab has formed its yield line mechanism and is at large displacement.

Numerical studies were also performed to investigate the slab's response to increased areas of total reinforcement and to compare this with the simplified design method. Investigations were undertaken on model slabs with cross-sectional areas of reinforcement varying from 0.05% to 0.7% whilst other variables remained constant. The enhancements predicted by the simplified method are shown in Fig. 6 and by numerical analysis in Fig. 7.

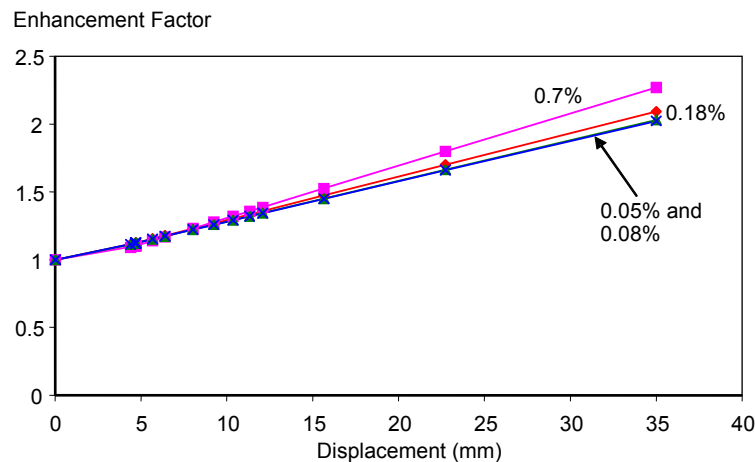


Fig. 6 -Enhancements predicted by the Simple Design Method for various reinforcement percentages.

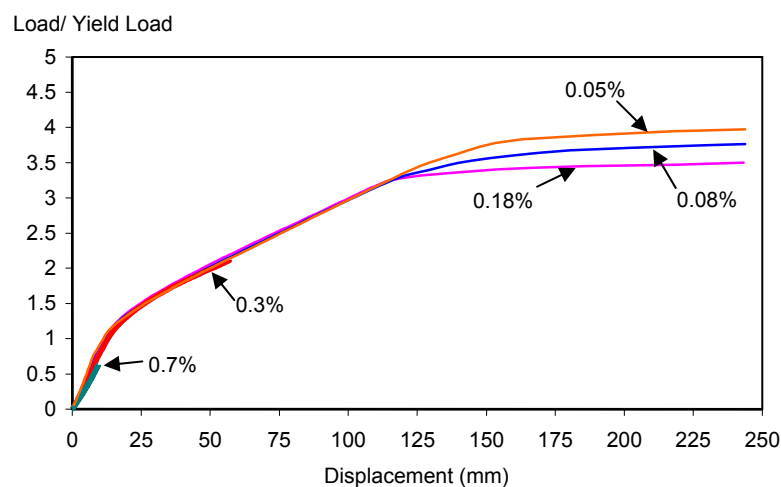


Fig. 7-Enhancements predicted by *Vulcan* without concrete tension.

The results highlight the fact that the numerical predictions do not follow the same pattern as the Simplified Method's predictions. The latter limits the amount of reinforcement to 0.7%, because of the stress block adopted. The approach is based on yield line theory, and so slabs must have high span/depth ratios, have low reinforcement percentages and be designed as 'under-reinforced'. Cross-sections must be ductile, and limitations have been put on the percentage of reinforcement, with 0.75% being the maximum allowable for yield line design [4].

3. PARAMETRIC STUDIES AT ELEVATED TEMPERATURES

A number of experimental studies were undertaken at elevated temperatures to investigate the influence of the following parameters on the load capacity of the slab:

- Bond strength,
- Thermal gradient,
- Reinforcement area ,
- Development of membrane forces .

Further parameters were studied using *Vulcan*. These included the influence of concrete tension and the development of membrane forces within the slab at elevated temperatures. The experimental and numerical results were also compared with the Simplified Design Method.

The crack patterns on the bottom surface of the slab were plotted at various temperatures (see Fig. 8). It can be seen that the crack initiation is different from that at ambient temperatures, with cracks developing at the corners of the slab followed by transverse cracking across the short span of the slab at higher temperatures.

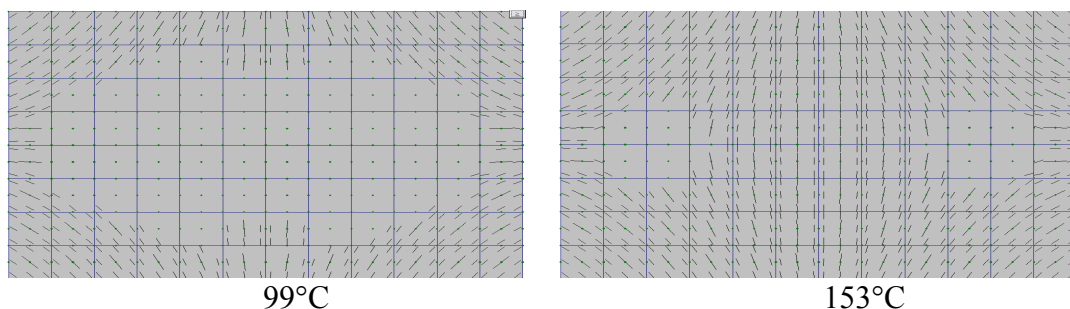


Fig. 8 - Crack patterns for full slab at different bottom surface temperatures.

The influence of bond strength was investigated experimentally by using smooth and deformed wires within the slab. Fig.9 shows comparisons between two tests with identical conditions apart from the reinforcement type. Test 4 was reinforced with smooth wire and Test 3 with deformed wire. The slabs had a total reinforcement percentage of 0.15% and load ratio of 1.7. The *Vulcan* predictions for both tests showed a good degree of accuracy, with slight discrepancies at temperatures in excess of 600°C. The *Vulcan* predictions towards the end of Test 4 are in close agreement with the measured mid-span displacements. However towards the end of Test 3, the *Vulcan* predictions diverge from the test results. Further studies indicated that bond between the reinforcement and concrete as being lost at this stage. *Vulcan* can not at present model this effect.

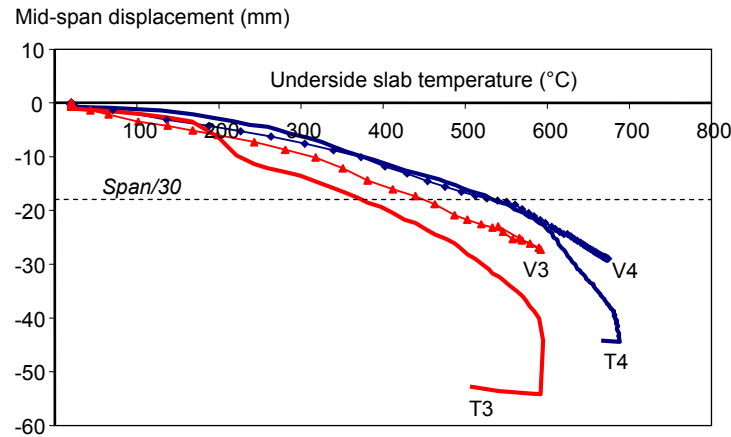


Fig. 9 -Comparison of mid-span displacements for Tests 3 and 4 with *Vulcan* predictions.

Numerical studies were undertaken to investigate the effects of temperature profile on the membrane action of the slabs. The test data is shown in Table 2.

Table 2: Test 5 parameters.

Test 5	Reinf.Area(%)	F_c (N/mm ²)	Yield Capacity (kN/m ²)	Load Ratio Q/W_u
Smooth Wire	0.15	44	2.21	2.8

Fig. 10 shows the resulting vertical displacements, assuming different linear temperature gradients across the slab depth.

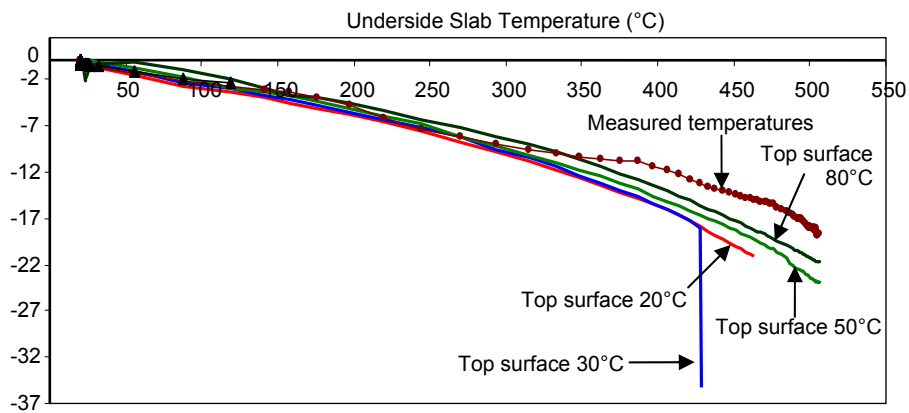


Fig. 10 - Comparison of mid-span displacements with *Vulcan* predictions for various linear temperature gradients.

For lower surface temperatures in the range 20°C-300°C, the rates of displacement for all temperature profiles were similar. Above 300°C the rate of displacement for the measured temperature profile decreased compared to the other temperature profiles. At the beginning of a test, high thermal gradients are created through the depth at a time when strength and stiffness are reasonably intact. These gradients reduce as the top surface temperature of the slab increases, as lower surface stiffness and strength is becoming considerably degraded.

Studies were carried out on the effects of reinforcement area on slab performance. The results indicated that slabs reinforced with lower reinforcement performed better than those with high percentages. Fig.11 shows the test results and Fig.12 shows a comparison with the BRE Simplified Design Method.

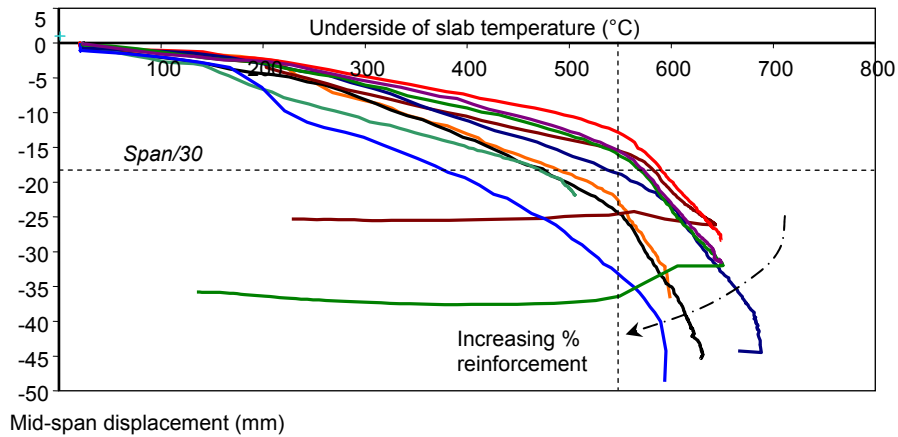


Fig. 11- Comparison of Test results with increasing slab reinforcement areas.

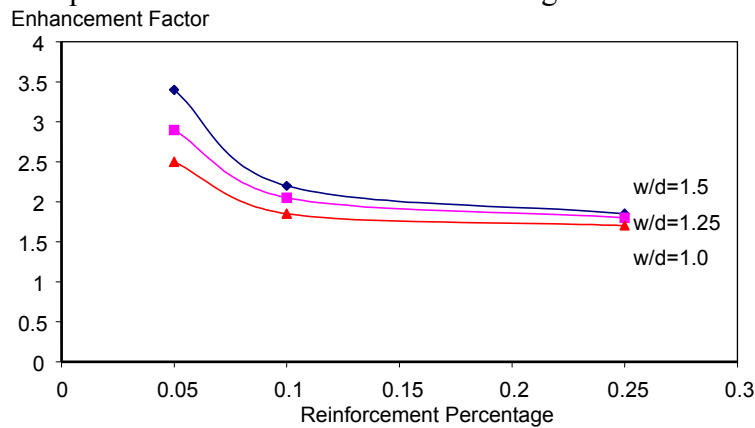


Fig. 12- Comparison of the applied load/yield load ratio with percentage reinforcement with displacement/effective depth (w/d)

Observing the development of membrane forces shows that for slab displacements between 10-15mm, compressive forces are seen to develop across the short span of the slab, and these are then relieved at larger displacements as the slab develops membrane action, with tensile forces within the central zone and a compressive peripheral ring around the edges of the slab. The compressive band seems to be influenced by the area of reinforcement. Figs. 13(a) and 13(b) compare the membrane traction plots for slabs which have different reinforcement percentages. The development of membrane forces at high temperatures is different from that at ambient temperature. Further investigations have identified that the geometry of the slab also influences the development of membrane forces.

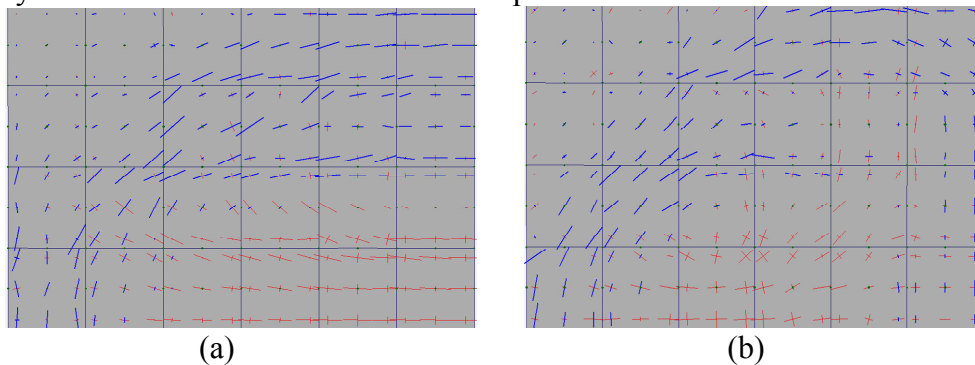


Fig. 13 - Membrane traction plots for (a) slab reinforced with 0.5% reinforcement at 221°C and (b) 0.1% reinforcement at 341°C (bottom surface temperatures).

Studies were undertaken to investigate the slab behaviour with no contribution from concrete tensile strength or stiffness. This is one of the most important factors in determining the overall slab behaviour and is probably the hardest part to quantify. Slabs which have undergone extensive cracking will have little contribution from concrete in tension. However, slabs which have undergone little or no cracking will gain some strength contribution from concrete in tension. Fig. 14 shows that the influence of concrete in tension does not become significant until after 200°C, and that the thermal gradient is the most influential factor in initial displacements. Fig. 15 illustrates that as the percentage of reinforcement increases the influence of concrete in tension diminishes.

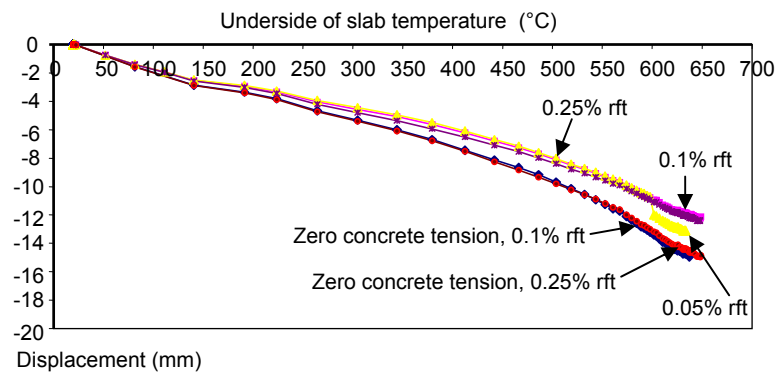


Fig. 14 - Numerical study comparing the displacements of models with varying amounts of reinforcement at zero applied load.

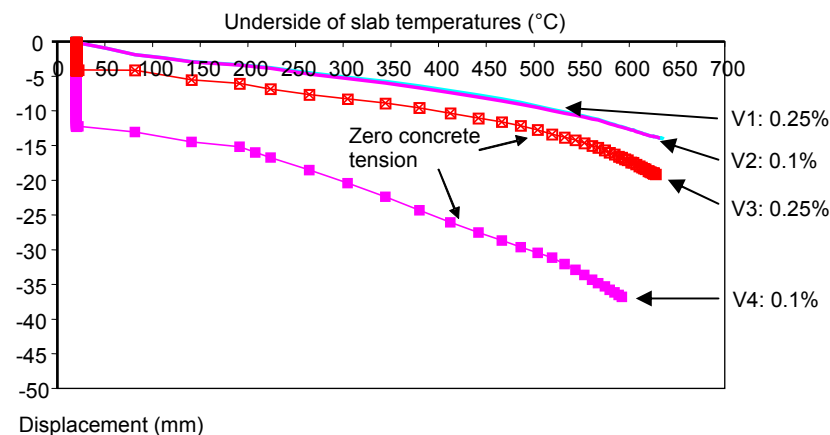


Fig. 15 - Numerical study comparing loaded slabs with varying areas of reinforcement with and without concrete tension.

5. COMPARISONS OF SLAB BEHAVIOUR AT AMBIENT AND ELEVATED TEMPERATURES WITH DIFFERENT FACTORS

From the detailed investigations undertaken the performance of loaded reinforced concrete slabs is seen to differ at elevated temperatures from that at ambient temperature. At ambient temperature, the main mechanisms that develop are:

- Development of yield line cracks, with the reinforcement yielding along these cracks.
- Concrete strength is not a significant factor at high displacements, but the strength and type of rebar used significantly affects the load capacity of the slab.
- The BRE Simplified Design Method is only applicable for slabs with low reinforcement percentages and high span/depth ratios.
- The tensile strength of concrete is significant at low deflections, but is very difficult to determine. The BRE Simplified Design Method does not consider the contribution of concrete tension within its approach.
- The simplified approach does not consider the effects of bond and fracture of reinforcement. It predicts continuously increasing linear enhancements.
- The work has highlighted the fact that *Vulcan* is currently unable to model reinforcement bond slip, and a criterion will need to be developed.

The high-temperature testing and numerical work on loaded reinforced concrete slabs has shown that slabs perform differently under heated and ambient-temperature conditions. The main mechanisms that develop at high temperatures are:

- At low displacements, thermal bowing of the slab is a significant factor in the slab displacements.
- At large displacements, concrete tensile strength is the main factor in the contribution of the slabs' resistance to the applied load.
- There was a difference in load-carrying capacity of slabs reinforced with smooth and deformed wire. However, this may not be entirely due to the reinforcement type as its influence is difficult to isolate.
- The development of membrane forces at high temperatures is different from their development at ambient temperature, and seems to be dependent on the aspect ratio and percentage of reinforcement.

At ambient temperature, the influence of concrete tension contributed to the initial load carrying capacity of the slab. The results from the high-temperature tests showed that up to 200°C, the thermal gradient and expansion of the slab is the main dominant factor. Above 200°C there is an increasing contribution by concrete tensile strength.

6. CONCLUSIONS

From the studies undertaken it has been shown that the performance of slabs at ambient temperature is very different from that at elevated temperatures. Some of main factors influencing the slab's performance at ambient and elevated temperatures are:

- Bond strength and type of reinforcement within the slab,
- Concrete tensile strength,
- Thermal bowing,
- Reinforcement percentage,
- Aspect ratio of the slab.

It is apparent from the tests that there is a lack of published test data for heated reinforced concrete slabs. The tests undertaken were limited to simple support conditions, and further testing is required on different floor systems and boundary conditions.

7. REFERENCES

1. Newman, G.M., Robinson, J.T. and Bailey, C.G., *SCI-P288: Fire Safe Design, A new approach to multi-storey steel framed buildings*, Steel Construction Institute, (2000).
2. Huang, Z., Burgess, I.W. and Plank, R.J., "Modelling membrane action of concrete slabs in composite buildings in fire. Part I: Theoretical development", *Journal of Structural Engineering, ASCE*, **129** (8), (2003), pp1093-1102.
3. Huang, Z., Burgess, I.W. and Plank, R.J., "Modelling membrane action of concrete slabs in composite buildings in fire. Part II: Validations.", *Journal of Structural Engineering, ASCE*, **129** (8), (2003), pp1103-1112.
4. May, M. and Lodi, S. H., "Deficiencies of the normal moment yield criterion for RC slabs", *Proceedings of the Institution of Civil Engineers, Structures and Buildings*, **158**, Issue SB6, (2005), pp371-380.



BEHAVIOUR OF PRECAST R.C. ELEMENTS UNDER FIRE CONDITIONS

Alberto MEDA¹ and Paolo RIVA²

ABSTRACT

The behaviour in fire conditions of three prestressed concrete elements typical of the precast production is numerically analysed herein. A thin-webbed element, a TT element and an I beam were considered under fire scenarios. The analyses were performed by means of a fibre-model implemented on a commercial Finite Element code. The results show the vulnerability of these structures, typical of Italian industrial buildings, to a fire exposure.

1. INTRODUCTION

The Italian precast production is dominated by prestressed concrete elements for industrial buildings. Typically, thin-webbed or TT elements are used for roof construction while TT beams are used as floor elements. These two kinds of elements are usually simply supported on prestressed concrete main girders having a I section.

These structures are often subjected to fire due to industrial production accidents or to burning of stored materials, resulting, at least Italy, in the buildings with the highest fire risk. These elements are designed by adopting small thickness in order to reduce the dead load, which involves a high cost in the production process. In fact, the reduction of the transportation costs is an important parameter in making economical a precast construction.

The afore-mentioned small thickness induces a high vulnerability of these structures under fire. Low level fire analysis, such as the tabular or sectional methods, cannot be useful for these structures and more accurate fire analyses have to be performed.

In the present paper the three typical members described before are analysed by adopting a fiber-element model¹ implemented on a commercial Finite Element code².

The elements were considered exposed to fire on different sides, by attempting to represent the typical fire scenarios that can be found in a industrial precast building. The

¹ Associate Professor, University of Bergamo, Department of Engineering Technologies and Design, 24044 Dalmine (BG), Italy, email: alberto.meda@unibg.it.

² Professor, University of Bergamo, Department of Engineering Technologies and Design, 24044 Dalmine (BG), Italy, email: paolo.riva@unibg.it.

analyses have been performed by using the fire scenario and material models suggested by Eurocode-1³ and Eurocode-2⁴ respectively.

The results show that the elements are able to sustain the design 120' of ISO-834³ fire exposure with the exception of the TT element, which collapses after 112'.

2. PRECAST ELEMENT PROPERTIES

Figure 1 shows the geometry of the elements analysed:

- the thin webbed open section element (a) has an open shape cross-section with a horizontal slab, having thickness of 70 mm and two 64 mm thick wings inclined by 30° to the horizontal. The total depth is 700 mm while the length is 20 m with a clear span of 19.80 m. The element is reinforced with 16 prestressed 0.5" strands;
- the TT element (b) has a section with two webs having a thickness of 180 mm and a flange with a thickness of 55 mm. The depth is 650 mm while the length is 15.10 m with a clear span of 14.95 m. An in situ concrete topping is added, with a thickness of 60 mm. The element is reinforced with 12 prestressed 0.6" strands;
- the I beam (c) has two flanges having the same width but different thickness (32 mm the upper and 12 mm the lower) and a 30 mm thick web. The total depth is 1400 mm while the length is 14.95 m with a clear span of 14.75 m. The element is reinforced with 23 prestressed 0.5" strands in the lower part and 2 0.5" strands in the upper part.
- all the elements have a 120' fire design strength (R120).

All the strands are considered as having an initial tension after prestress losses equal to 1050 MPa. Only the prestressing reinforcement has been considered in the analyses, while the ordinary reinforcement (transverse and longitudinal) was neglected. In fact, the aim of the analysis is to study the flexural behaviour of the elements, while the shear bearing capacity is not considered herein. Furthermore, it is observed that the contribution to the element strength of the ordinary longitudinal reinforcement is very small.

The characteristics of the materials at 20°C are summarized in Table 1

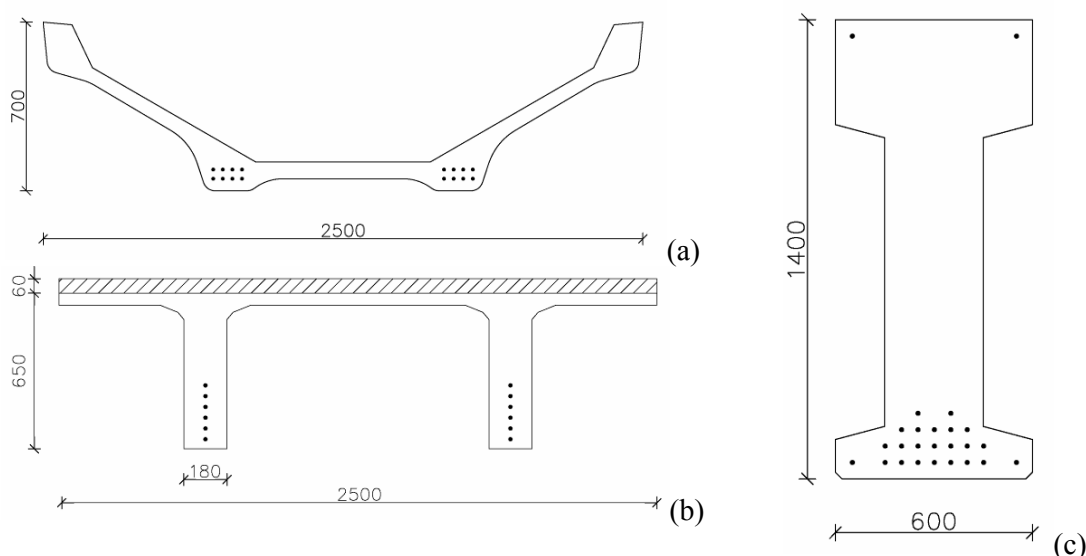


Fig. 1 – Analysed element sections: thin-webbed open section (a), TT (b) and I (c).

Tab. 1 – Material properties

Concrete		
Compressive strength	f_{ck}	45 MPa
Tensile strength	$f_{ctk,0.05}$	2.7 MPa
Young's modulus	E_{cm}	36 000 MPa
Prestressing steel		
Ultimate strength	f_{pk}	1 860 MPa
Nominal yield strength	$f_{py}=0.9 f_{pk}$	1 674 MPa
Young's modulus	E_{pm}	195 000 MPa

3. MODELLING

The behaviour of the precast elements exposed to fire is here investigated by Finite Element analysis, adopting a fiber-element model¹, developed within the commercial FE code ABAQUS².

In the developed model (Fig. 2), a beam is subdivided into elements of length equal to the smaller of either the stirrup spacing, or the beam depth. Each beam element is divided into non-linear fiber sub-elements, characterised by monoaxial behaviour only. The Navier-Bernoulli hypothesis is enforced on the element faces, thus enabling the element to represent bi-axial bending and axial force. Shear and torsion are transferred between each element by means of a set of linear springs, representing the elastic shear and torsion stiffness. Hence, axial forces and bending moments are uncoupled from shear forces and torsion.

Any mechanical and thermal constitutive law could be adopted for concrete and reinforcing steel fiber sub-elements.

The structural response of RC beam and frames under fire conditions is computed based on a fiber sub-elements temperature history, determined by means of an uncoupled FE transient thermal analysis adopting a mesh consistent with the stress analysis model (i.e. the number of elements and the position of their centroid for both thermal and mechanical analysis coincides). In case of a constant fire scenario over an entire structural element (i.e. a beam or a column) of constant section, the thermal analysis may be greatly simplified, by performing a 2D analysis on the cross-section, and assuming the same temperature distribution for the entire structural element.

For the analyses herein presented, the mechanical properties of the concrete and reinforcing steel sub-elements as a function of temperature have been taken from Eurocode-2⁴, as shown in Fig. 2.

Concerning concrete behaviour in tension, the post cracking behaviour has been modelled by means of a cohesive crack model, by assuming a crack spacing equal to the element length (i.e. stirrup spacing), a tensile strength decreasing with temperature according to EC 2, and a constant fracture energy, independent of temperature. Finally, a small residual strength, equal to 5% the tensile strength has been assumed, for numerical stability purposes. It is anyway observed that the assumed behaviour in tension has a limited influence on the overall structural behaviour in bending of RC structures.

The thermal analysis is performed adopting the material properties (concrete density, specific heat and thermal conductivity) suggested by Eurocode-2⁴ (Fig. 3), while the standard ISO-834³ temperature versus time curve is used (Fig. 3) for the fire scenario. Finally, the presence of reinforcement has been neglected in the thermal analysis, and the reinforcement temperature has been assumed as equal to the concrete temperature.

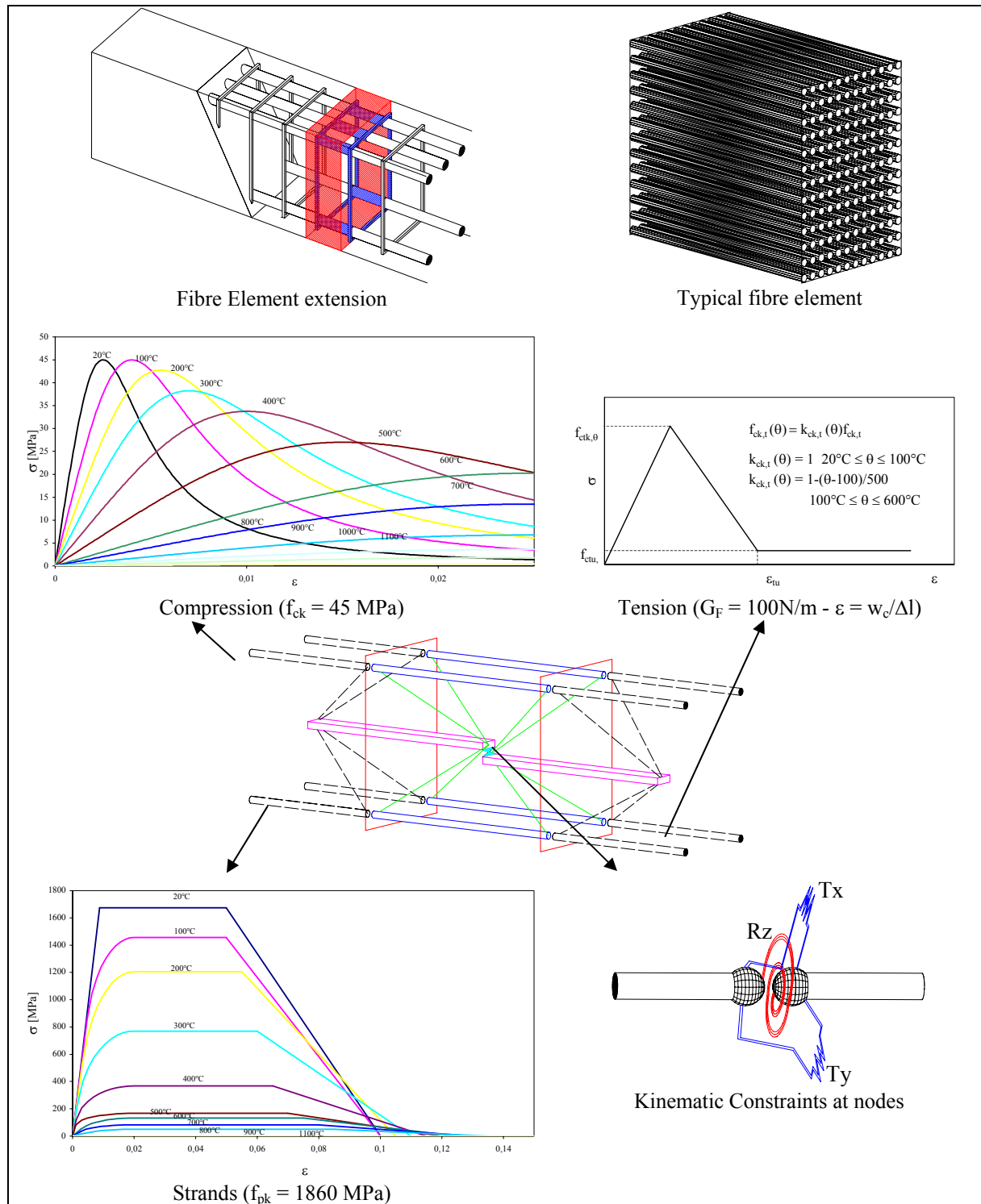


Fig. 2 – Fiber-Element Model

The analysis procedure may be summarized as follows:

- given the structure, the FE mesh for both thermal and static analyses is defined;
- a transient thermal analysis is performed using the given fire scenario and the temperature in the structure is determined at fixed time intervals (2 minutes in this case);
- the initial static conditions at ambient temperature (20°C) are determined by static analysis under the acting loads ($\gamma_{GA} G_k + \gamma_P P_k + \psi_{1,1} \gamma_Q Q_{k,1} = G_k + P_k + 0.5 Q_{k,1}$ according to EC 1³);
- the structural response under fire conditions is derived, by applying the temperature history and distribution previously determined. The analysis is carried out until either the desired

time of exposure to fire (for instance 120 min) or the structural collapse is reached (i.e. when the equilibrium conditions are no longer satisfied or the analysis integration procedure does not converge any longer).

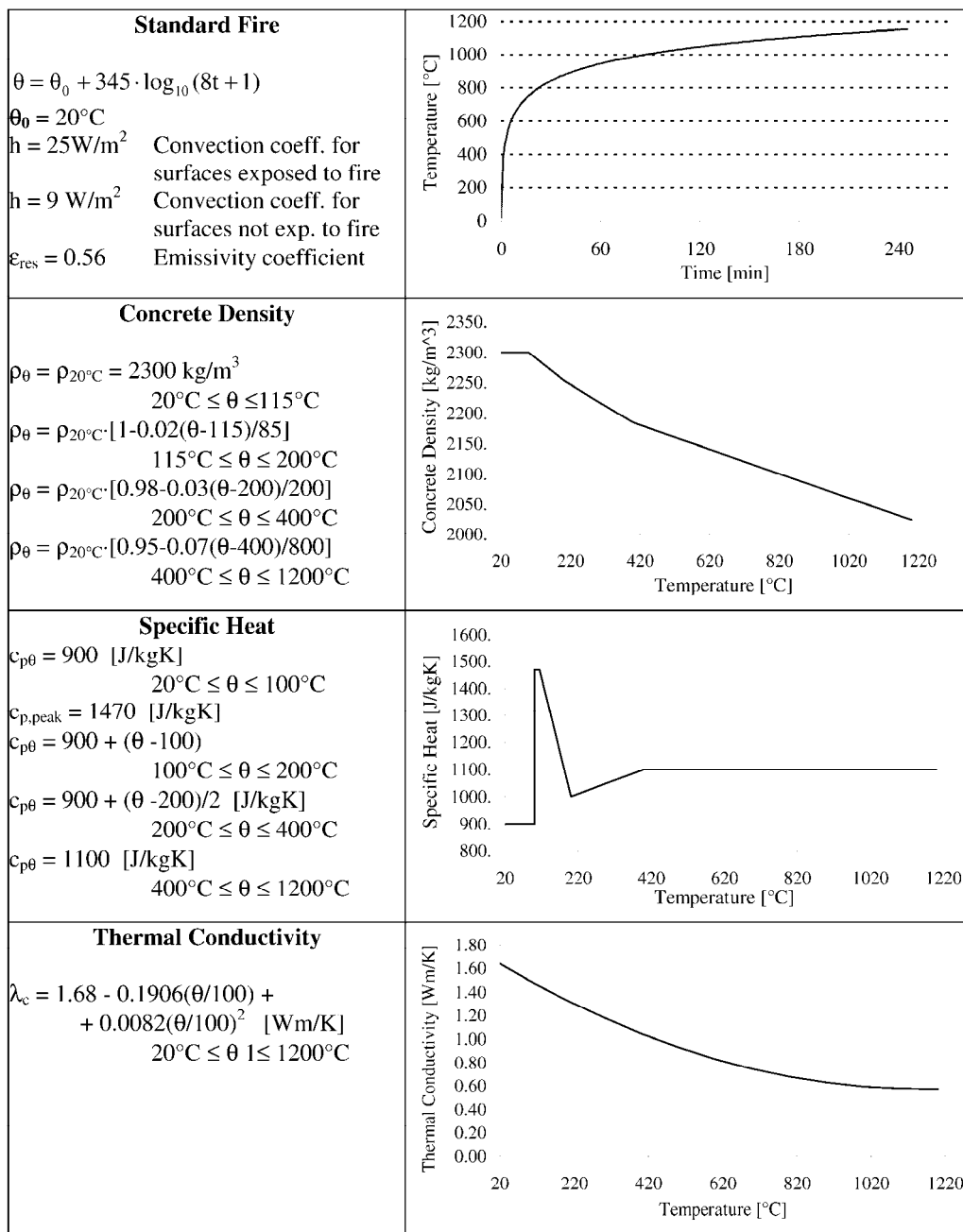


Fig. 3 – Fire curve and concrete thermal properties.

4. RESULTS

The analyses were carried out both by neglecting or considering the second order effects. This has a particular relevance in the deflection response.

The results are presented in the following for the three different elements.

4.1 Thin-webbed open section element

The element was modelled by using fiber elements spaced every 150 mm. A permanent load due to the dead and finishing loads equal to 7.70 kN/m and a live snow load equal to 4.55 kN/m (multiplied by 0.5 for the fire load combination) were considered.

The element was considered as subjected to the fire from the bottom side while a of 20°C air temperature was imposed to the upper part. This is a typical scenario for a roof element in an industrial building.

The temperature distribution at 30' intervals is shown in Fig. 4. It is possible to note the relatively good behaviour of the concrete bulbs, protecting the reinforcement from the heat flow.

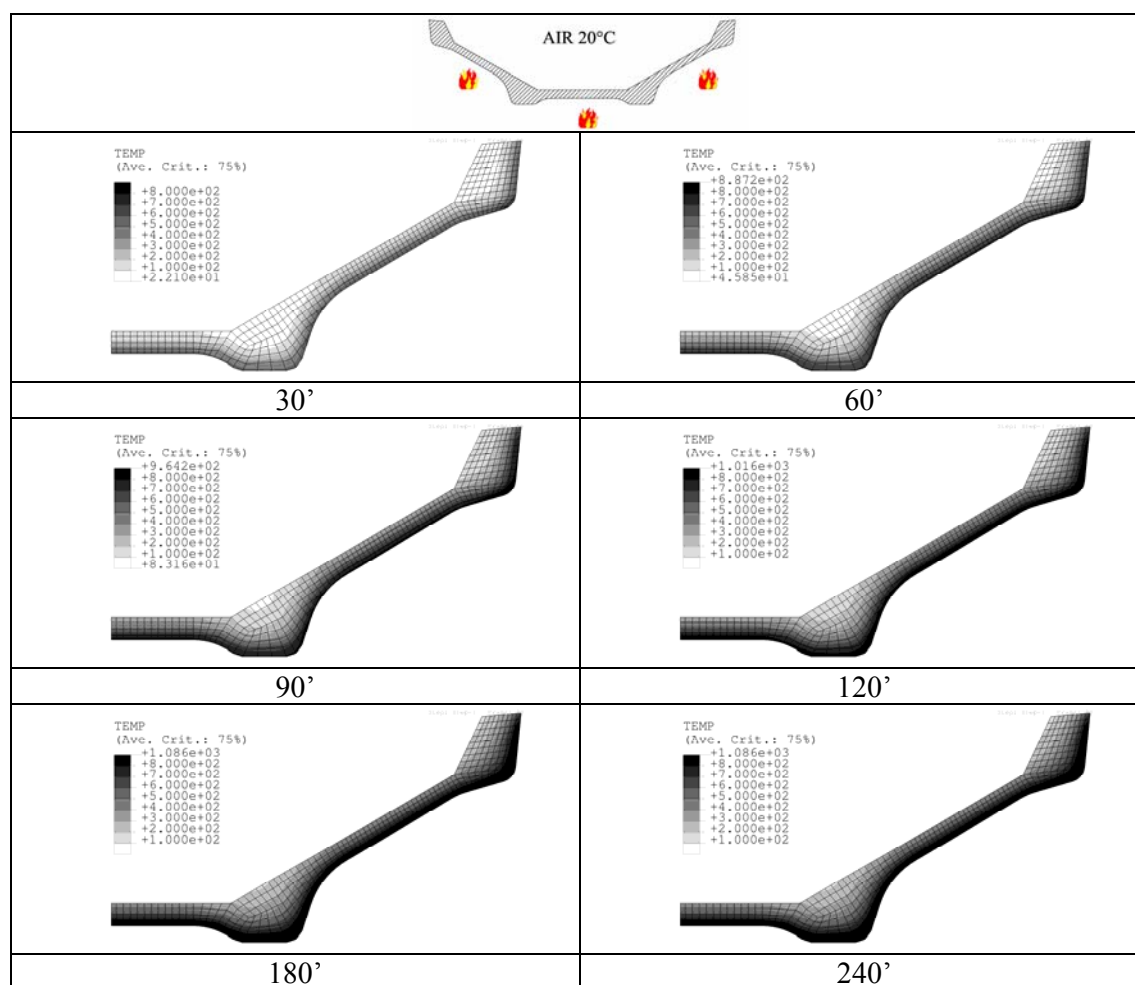


Fig. 4 – Temperature distribution for the thin-webbed element.

The collapse occurred after 143' of fire exposure with a midspan displacement of 1800 mm and 1600 mm for the first and second order analysis (Fig. 5a,b,c), respectively. The smaller vertical displacement observed for the second order analyses is due to the arch effect of the displaced prestressing strands.

A considerably different horizontal displacement was obtained in the two different analyses (Fig. 5d): with the second order analysis the displacement at the support is limited to 50 mm and tends to become null at the collapse whereas for the first order analysis the maximum horizontal displacement is equal to 180 mm.

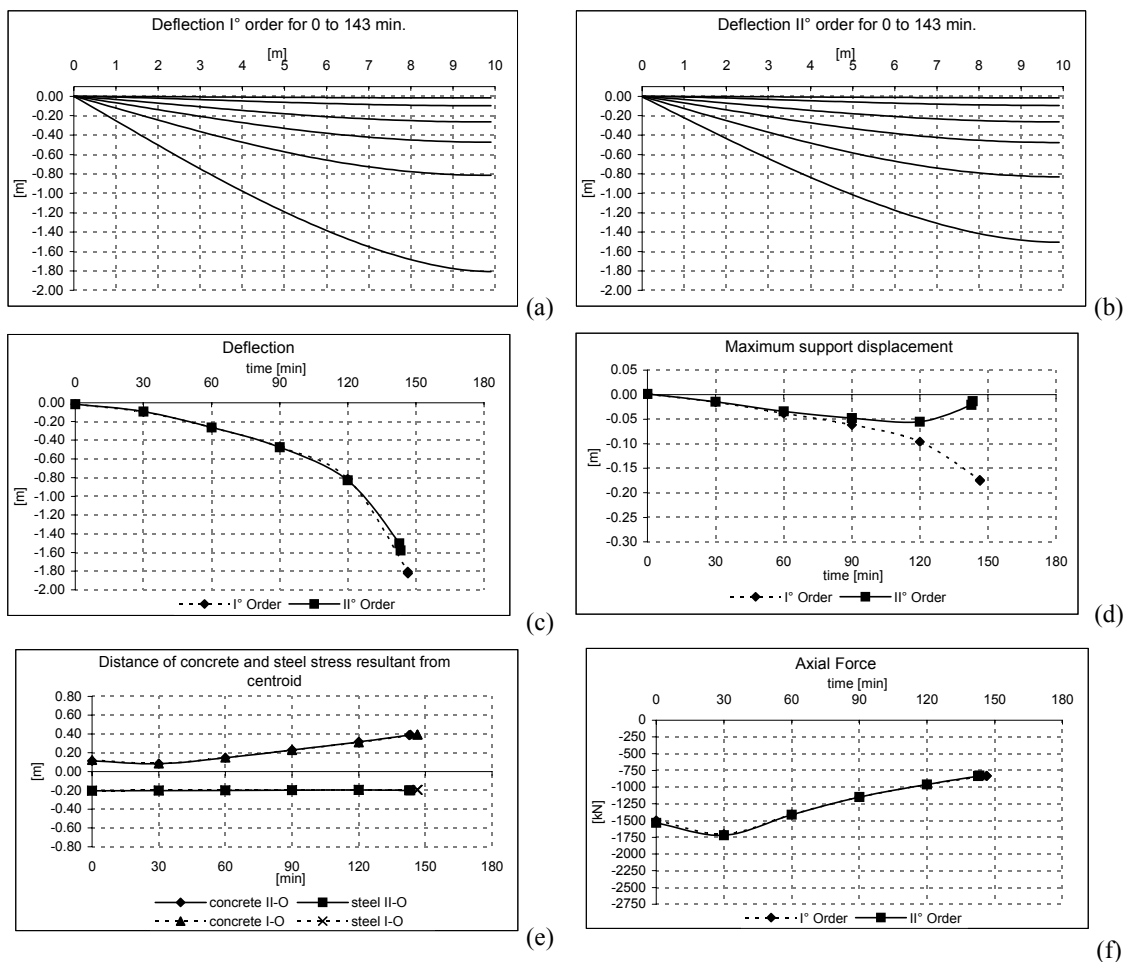


Fig. 5 – Response of the thin webbed open section element.

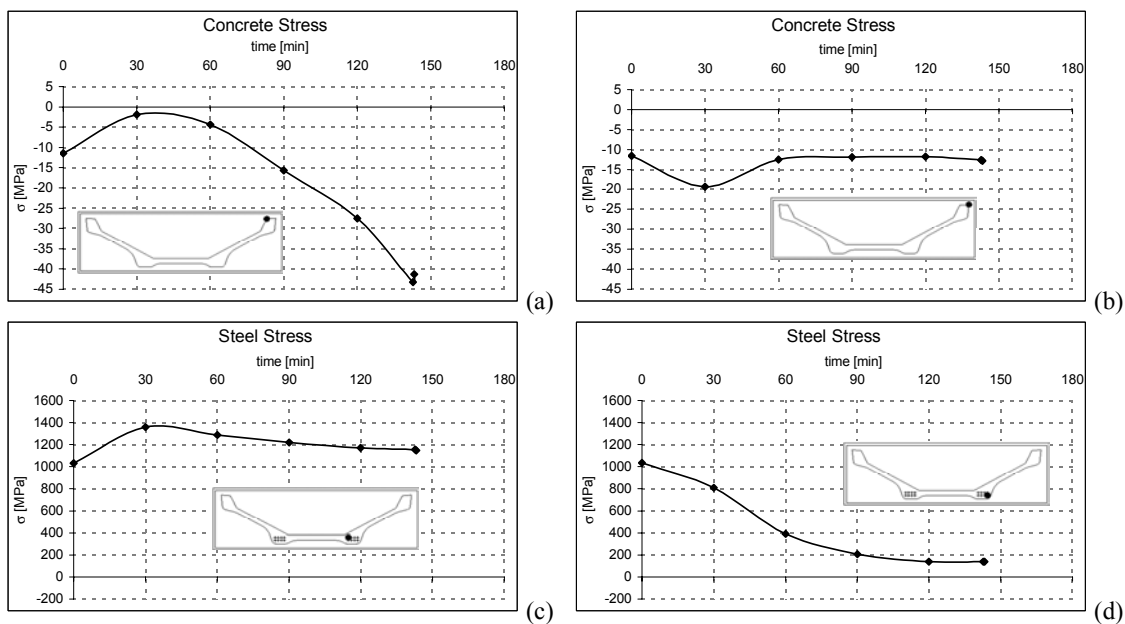


Fig. 6 – Concrete and prestressing steel stress in the thin webbed open section element.

Fig. 6 illustrates the concrete and steel stress development with time in the most significant fibres. The results show that in the first 30' of fire exposure, due to the thermal gradient, the compression stress in the “cold” concrete fibres shows an initial decrease, whereas for concrete fibres next to the exposed surface an initial increase is observed. After approximately 60', the compression stress in the concrete next to the exposed surface stabilizes at a constant stress value, whereas in the “cold” fibres it increases up to collapse. As for the prestressing steel, an initial stress increase for the strands far from the exposed surface is observed, whereas for strands closer to the exposed surface a decrease in the stress is noted from the fire start. The colder strands show an approximately constant stress up to collapse, whereas the effective stress in the hotter strands tends to zero with time.

4.2 TT element

The element was modelled by using fiber elements spaced at 150 mm. A permanent load due to the dead load, the in-situ cast topping and the finishing equal to 20 kN/m and a live load equal to 5 kN/m (multiplied by 0.5 for the fire load combination) were considered.

The element was considered as subjected to the fire from the bottom side while a of 20°C air temperature was imposed to the upper part. This is a typical scenario for a floor element in an industrial building.

The temperature distribution at 30' intervals is shown in Fig. 7. It is possible to note a critical behaviour: the thin webs reach relatively soon high temperatures and are not able to adequately protect the prestressing strands.

The collapse occurred after 112' of fire exposure with a midspan displacement of 1400 mm and 1000 mm for the first and second order analysis (Fig. 8a,b,c), respectively. Likewise the open section element, a considerably different horizontal displacement was observed in the two analyses (Fig. 8d): with the second order analysis, the maximum displacement at the support is equal to 50 mm, and tends to 0 towards collapse, whereas for the first order analysis it is equal to 18 mm.

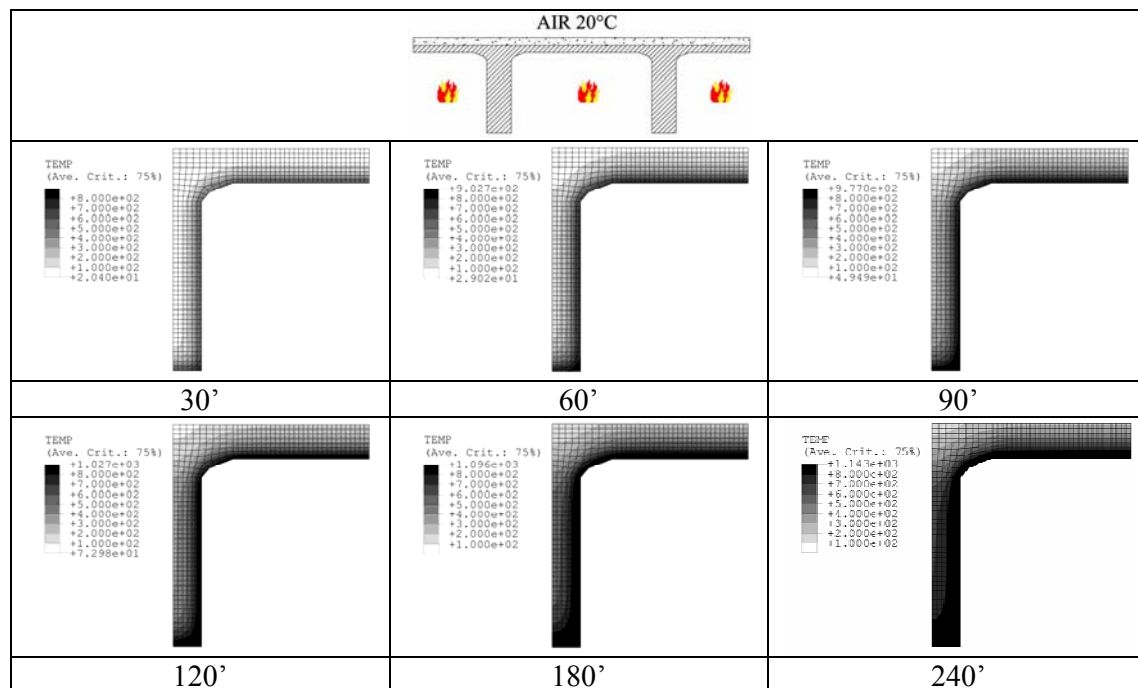


Fig. 7 – Temperature distribution for the TT element.

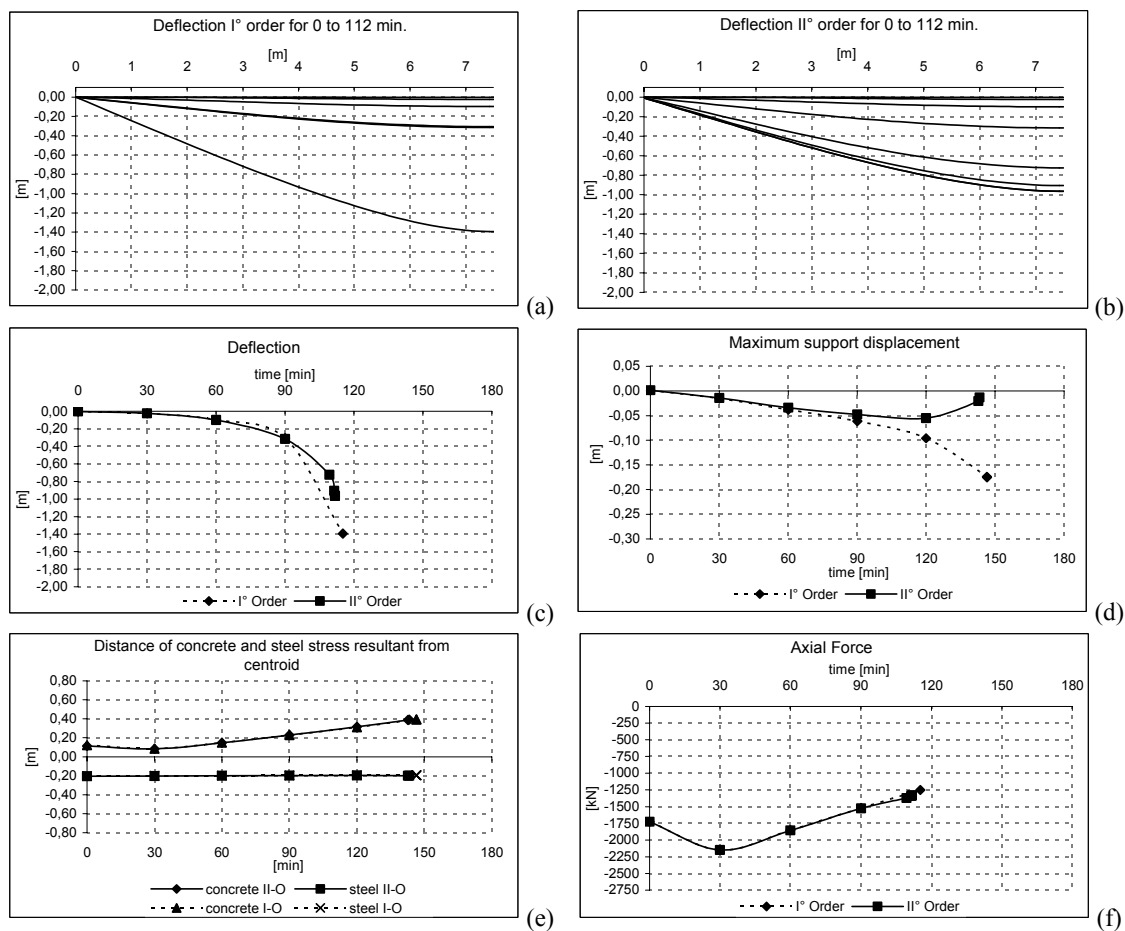


Fig. 8 – Response of the TT element.

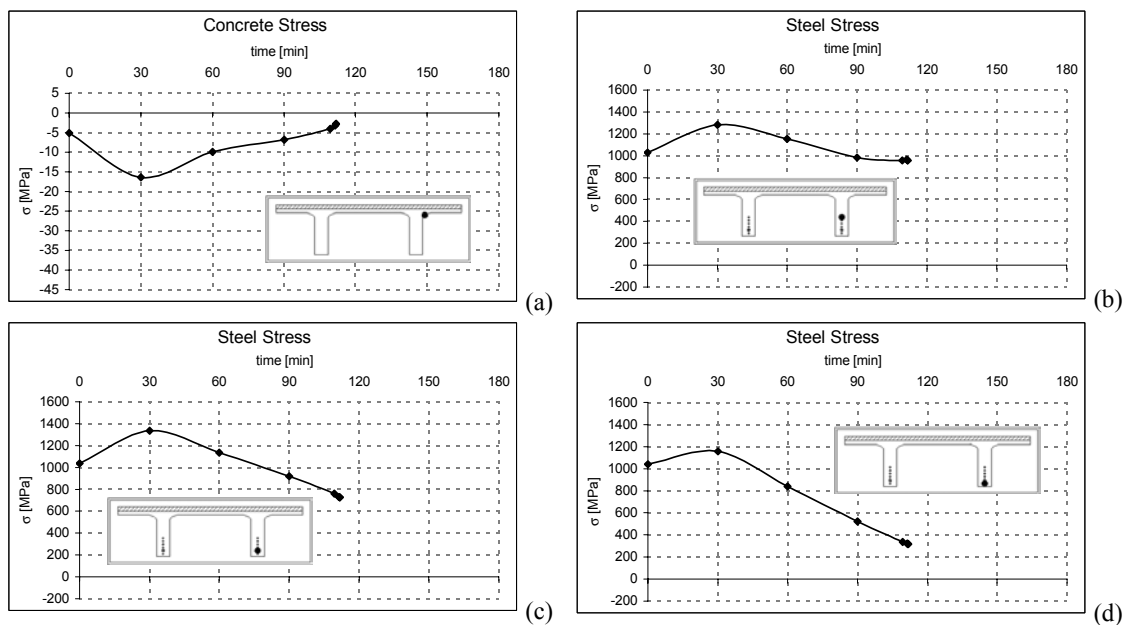


Fig. 9 – Concrete and prestressing steel stress in the TT element.

Fig. 9 illustrates the concrete and steel stress development with time in the most significant fibres. The results show that in the first 30' of fire exposure, due to the thermal gradient, the compression stress in the concrete fibres exhibit an initial increase, after which progressively decreases until the section collapses. As for the prestressing steel, an initial stress increase is observed for all strands. After the first 30', the colder strands show a small stress decrease until, eventually, the stress stabilizes to the initial value, whereas the effective stress in the hotter strands decreases with time and tends to zero for the strands close to the bottom surface.

4.2 I element

The element was modelled by using fiber elements spaced at 200 mm. A dead load due to the self and the roof weight, equal respectively to 14.105 kN/m and 48.90 kN/m, and a live snow load equal to 23.10 kN/m (multiplied by 0.5 for the fire load combination) were considered. The element was subjected to fire on all sides. This is a typical scenario of main roof girder element in industrial buildings.

The temperature distribution at 30' intervals is shown in Fig. 10. The temperature distribution shows that the concrete effectively protects the prestressing strands with the exception of the two edge strands on the lower flange.

The collapse occurred after 139' of fire exposure, with a midspan displacement of 470 mm and 370 mm for the first and second order analysis, respectively (Figs. 11a,b,c). The maximum horizontal displacement is equal to 120 mm for both analyses (Fig. 11d).

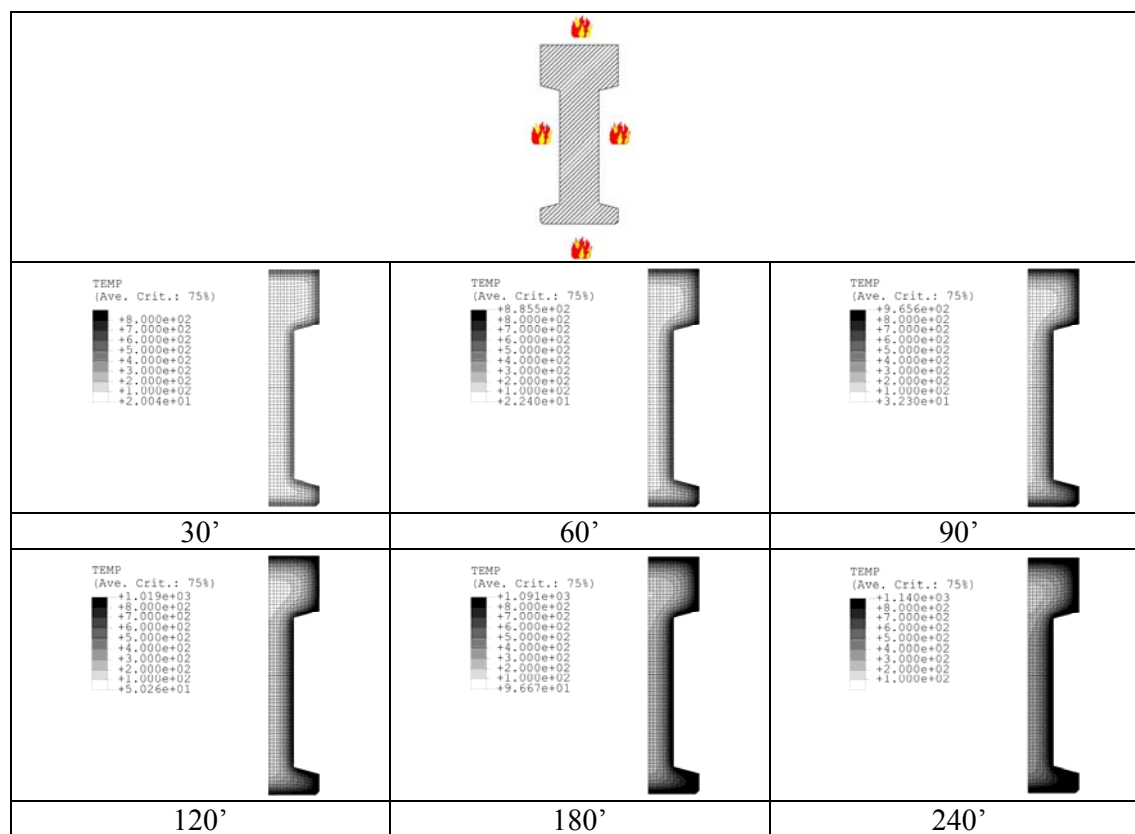


Fig. 10 – Temperature distribution for the I-beam.

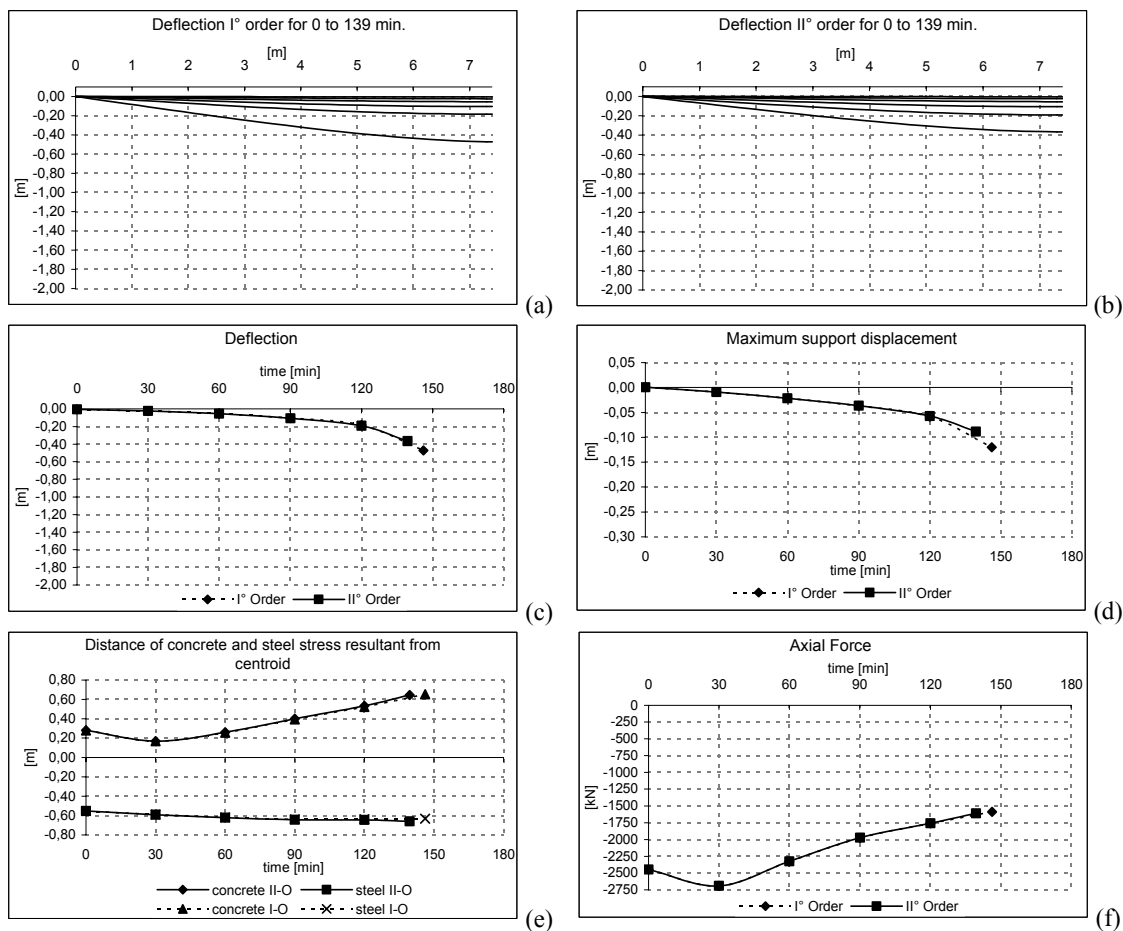


Fig. 11 – Response of the I-beam.

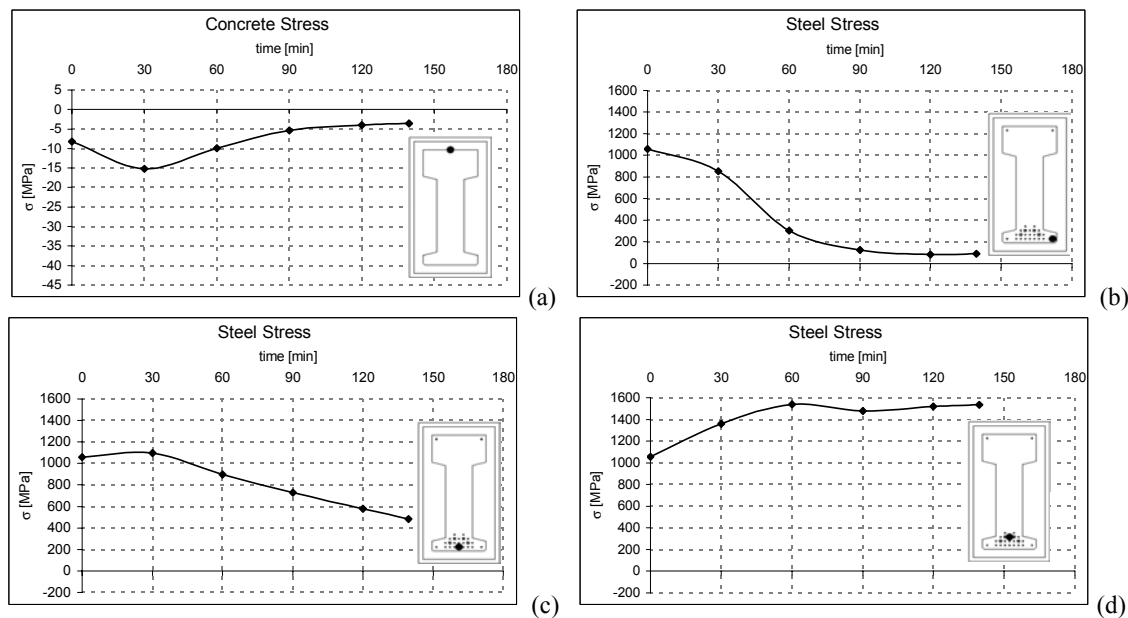


Fig. 12 – Concrete and prestressing steel stress in the I-beam.

Fig. 12 reports the concrete and steel stress development with time in the most significant fibres. The results show that in the first 30' of fire exposure the compression stress in the concrete fibres exhibit an initial increase, after which progressively decreases until the section collapses. As for the prestressing steel, the stress in the strand next to the bottom edge of the section decrease rapidly, reaching a value of approximately 100 MPa after 90' of fire exposure. The stress in the strands next to the centre of the exposed surface exhibits an initial increase followed by a progressive decrease. Finally, the stress in the colder strands, which are effectively protected from fire, show a progressive increase during the first 60' of fire exposure, when an almost constant stress value equal to 1500 MPa is reached.

5. CONCLUSIONS

The following remarks can be drawn from the analyses presented in this study:

- although the code verification of the TT element, based on sectional analysis, allows a R120 rating, the non-linear analyses show that the actual resistance is equal to 112', due to an insufficient fire insulation of the prestressing strands. This result demonstrate that sectional analysis not always leads to conservative results and that a non-linear analysis should be carried out when dealing with TT elements;
- both the open section and the I-beam elements showed a satisfactory behaviour, both of them collapsing after approximately 140' of ISO 834 fire exposure;
- in all cases, second order analysis leads to considerably smaller displacements than the first order analysis, due to the arch action of the displaced prestressing strands;
- the maximum vertical displacement at collapse is approximately equal to $L/15$ for the open section and TT elements, while it is equal to $L/40$ for the I-beam, where L is the element length. Large displacements comparable to those found with the analyses are often observed after real fires of industrial building.

6. ACKNOWLEDGEMENTS

The analyses were carried out by Mr. Stefano Ferrari in partial fulfilment of his Civil Engineering Master Thesis. The assistance of Mr. Marco Manzoni of Magnetti Building S.p.A. in providing the details of actual commercial P.C. elements is gratefully acknowledged.

7. REFERENCES

- [1] Riva P., "Nonlinear and Plastic Analysis of RC Concrete Beams," Proceedings of the workshop: Fire Design of Concrete Structures: What now? What next?, Milano, 2-4 December 2004, Starry Link Editore, 2005.
- [2] HKS, "ABAQUS V.6.5 Theory and Users Manuals," Providence, Rhode Island, 2004.
- [3] EN 1991-1-2:2002, "Eurocode 1: Actions on structures. Part 1.2: General actions – Actions on structures exposed to fire," 2002.
- [4] EN 1992-1-2:2004, "Eurocode 2: Design of Concrete Structures – Part 1-2: General rules – Structural fire design", 2004.



EXPERIMENTAL EVALUATION OF COMPRESSION RESISTANCE OF HC-FST COLUMNS AFTER FIRE

Audronis Kazimieras KVEDARAS¹ and Žygimantas BLAŽEVIČIUS²

ABSTRACT

There are only a few analytical methods to estimate the post-fire resistance of composite column and there are a large amount of different geometrical and physical parameters, which influence on the post-fire resistance. Experimental investigation is the way to find out the influence of different parameters and to develop or to revise the analytical formulas that evaluate the known influences.

There are not too much researches carried out on the post-fire behaviour of concrete-filled steel tubular columns. In this paper there are presented data of the experimental investigation of post-fire behaviour of axially loaded HC-FST (hollow concrete-filled steel tubular) columns with a wide range of different parameter measuring. Behaviour of such columns, which were used without a fire protection, after their exposure to fire, similar to standard¹² fire, has been experimentally investigated in conditions of normal ambient temperature. The experimental values of post-fire resistance were measured and failure mode was determined for 4 axially loaded HC-FST columns. For the comparison with post-fire investigation results the testing of axially loaded columns under the normal ambient conditions were performed and these results are presented. These tests included: 4 HC-FST columns, 8-th HC-FST and 4 HCT (hollow concrete tubular) stub columns.

1. INTRODUCTION

The presence of load bearing concrete core within a hollow steel column has a beneficial effect on the fire and post-fire resistance of the steel section. A great effect is tangible if even there is a hollow concrete core inside of steel section. In many cases we can find some methods to estimate the fire resistance of composite column, but there are only few of analytical methods such as given in¹, that determinate the resistance of C-FST (Concrete-Filled Steel Tubular) columns after exposure to fire. Following the usual methods for fire resistance calculations of steel and composite steel-concrete structures it is possible

¹ Professor, Vilnius Gediminas Technical University, Saulėtekio al. 11 Vilnius, Lithuania, e-mail: akve@st.vtu.lt

² Post-graduate student, Vilnius Gediminas Technical University, Saulėtekio al. 11 Vilnius, Lithuania, e-mail: zygiui@centras.lt

suggesting the way for defining the post-fire resistance of the C-FST columns by two steps: 1) calculating the temperature distribution in the cross-section of the column during the fire; 2) calculating the axial buckling load of the column previously affected by elevated temperatures. The temperature distribution for the elements of HC-FST cross-section could be finding by using the FEM programmes. The buckling capacity of the column previously affected by fire should be calculated by estimating different deformation and strength indices of the materials (steel and concrete). There is a lot of information about the thermal and physical properties of steel and concrete at elevated temperatures, for instance^{2,3,4}, but not too much data about their properties after exposing to fire⁵. Therefore, the need for deeper investigation of behaviour of the HC-FST columns as they were exposed to fire exists.

The main objectives of the research presented in this paper are: first, to carry out a series of tests on HC-FST columns after exposure to standard fire⁶ under axial load with discovering their behaviour, second, to develop a mechanical model for HC-FST columns after exposure to the fire.

2. THE OBJECT OF EXPERIMENTAL STUDIES

The object of the experimental studies is an appraisal the compressive capacity of HC-FST columns under ambient conditions and their residual capacity (post-fire resistance) after exposing to fire temperatures.

Due to complexity of tests with HC-FST and HC columns under fire, their studies (involving natural-size building structures) are carried out quite seldom in the Lithuania and in the neighbouring countries. Pursuant to the study programme 20 HC-FST and HC (hollow concrete) specimens (Fig. 1) have been tested under natural conditions and after exposing them to fire temperatures. The specimens were manufactured by cutting long columns which age was 15 years by keeping them under the outdoor conditions without additional protective measures against steel corrosion and concrete erosion. Long columns consisted of the spirally welded steel tubes, inside which a hollow concrete cores were formed by centrifuging the mix. The outer diameter of the steel tube was $d_e = 219$ mm, and the wall thickness was about $t_a = 1.6$ mm. The wall thickness of the centrifuged concrete core of the HC-FST and HC columns varied $t_c = 17\text{--}46$ mm.

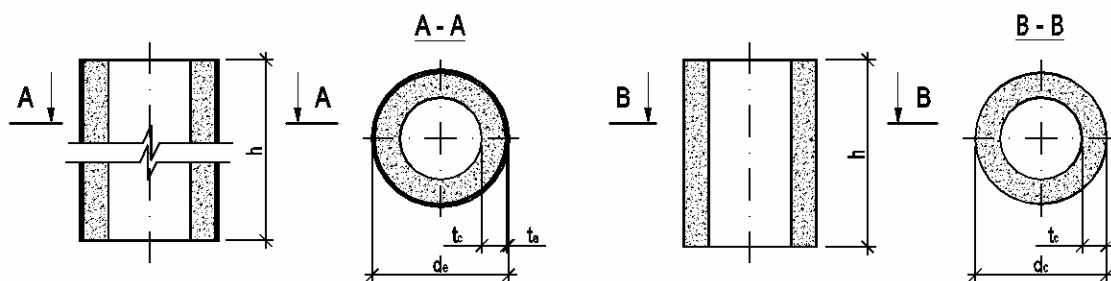


Fig. 1 – HC-FST and HC specimens.

12 short ($h = 300$ mm) and 8 long ($h = 2000$ mm) HC-FST elements were fabricated by cutting them from the elements of initial 5.5 m length. It was intended to test 4 long HC-FST specimens for defining of their compressive capacity under ambient conditions and 4 long HC-FST specimens for defining of their residual compressive capacity after exposing to fire temperatures. 8 short HC-FST specimens were used to determine their axial compressive capacity, whereas other 4 were used to make the concrete rings, which were tested to define concrete compressive strength.

3. PREPARATION OF SPECIMENS

The cutting machine (Fig. 2) with a special abrasive discs was used for cutting the HC-FST elements from the initial length to the shorter ones. During the cutting process, the HC-FST elements of the initial length were laid on cylindrical guides, which rotated the tubular element round its axis in respect to the rotating cutting disc. Above mentioned equipment ensured the perpendicularity of the ending cross-section.



Fig. 2 – Cutting machine used for preparing of the specimens.

Disparities on the specimen edges remaining after cutting were removed by grinding with an abrasive disc until even bearing surfaces (with a tolerance of ± 0.2 mm) were formed.

In order to determine the mechanical characteristics of steel, 16 standard steel specimens were prepared and tested for tension strength. The standard specimens were made from the steel shell of the HC-FST elements, from which it was taken off manufacturing the HC specimens. The making and testing of the specimens were carried out in compliance with the requirements given in³ and applicable for such kind of tests.

In order to determine the mechanical characteristics of concrete, 4 short HC specimens were manufactured by removing the steel shell from HC-FST elements and cutting them to the length that was foreseen. The geometrical parameters of HC-FST and HC specimens and intended type of testing are given in Table 1.

4. TEST EQUIPMENT AND PROCEDURES

All specimens were prepared, and the tests were carried out in the laboratories of the Faculty of Civil Engineering of Vilnius Gediminas Technical University. The longitudinal load on the HC-FST and HC specimens was created in the press with its hydraulic jack of 500 tons capacity. The fire conditions were created in the electrical furnace “Utena” designed and manufactured specifically for tests on combustibility and fire resistance of building structures with natural geometrical parameters. The furnace chamber has a floor area of 400 mm x 400 mm, and it is 1400 mm in height. The interior faces of the chamber are lined with the insulating material - kaolin wool plates. The electric spiral collars are embedding in vertical plates of kaolin with the interval of 5 cm beside the surface that is closer to furnace chamber. The furnace temperature was measured with the aid of three inner platinum-rhodium thermocouples, which were also embedded in the kaolin insulation of chamber. According to defined programme and the indication of inner thermocouple, the temperature regime was

Table 1 – Geometrical parameters of HC-FST and HC specimens

No.	Type of the specimen cross-section	Code of the specimen	h [mm]	t_a [mm]	$t_{c,mean}$ [mm]	Type of the test
1	HC-FST	1I1	2004.0	1.65	20.10	I
2	HC-FST	2I2	1992.0	1.60	28.90	I
3	HC-FST	3I2	2000.0	1.60	31.90	I
4	HC-FST	5I1	1999.0	1.63	24.875	I

5	HC-FST	0T1	295.0	1.60	15.65	I
6	HC-FST	1T1	300.0	1.65	23.60	I
7	HC-FST	2T1	298.0	1.60	15.90	I
8	HC-FST	2T2	298.5	1.60	25.50	I
9	HC-FST	3T1	298.0	1.60	16.15	I
10	HC-FST	3T2	298.0	1.60	16.55	I
11	HC-FST	4T1	298.0	1.63	19.025	I
12	HC-FST	5T1	296.0	1.63	24.375	I
13	HC	0TB2	296.5	1.60	21.90	I
14	HC	1TB2	296.0	1.65	21.60	I
15	HC	4TB2	300.0	1.63	20.875	I
16	HC	5TB2	300.0	1.63	20.375	I
17	HC-FST	1I2	1997.0	1.65	28.60	II.1
18	HC-FST	3I1	1999.0	1.60	32.40	II.1
19	HC-FST	4I1	1998.0	1.63	25.125	II.2
20	HC-FST	5I2	1998.0	1.63	23.125	II.1

Notes:

- The meanings of the markings in the Table columns: h – element length; t_a – steel shell thickness; $t_{c,mean}$ – mean thickness of the concrete ring of the element;
- Test type marking and test type description accordingly are:
 - „I“ – determination the compressive strength of the whether HC-FST, or HC specimen axially loaded under normal ambient conditions;
 - „II.1“ – determination the compressive strength of the HC-FST specimens at ambient conditions following the 45 minutes heating and loaded with an 180 kN axial load;
 - „II.2“ – determination the compressive strength of the HC-FST specimens at ambient conditions following the 45 minutes heating and loaded with an 120 kN axial load;

maintained and automatically adjusted with the aid of heating controller PROTERM 100. The heating controller capacities to regulate temperature regime in three levels of furnace chamber: top, middle height and bottom levels. The temperatures measured by three inner thermocouples were averaged automatically and the average temperature was used as the criterion for controlling the furnace temperature.

4.1 Test under normal ambient conditions – Type I test

4.1.1 Equipment for Type I test

4 short HC, 4 short HC-FST and 4 long HC-FST specimens were prepared for Type I test and tested. The ends of the specimens were rested against rigid steel press plates 50 mm thick, fixed in the press body via hinged support. Between the ends of a specimen and the press plates, the aluminium spacers were placed, which were cut from the medium-hard aluminium sheet 1 mm thick. The specimen supporting scheme ensured the articulating of the support and uniform application of the pressure to the relatively evenly ground bearing cross-section of the element.

For strain measuring, 8 PKB-type, 50-mm basis length strain-gauge transducers each were attached to the outer surface of the HC and HC-FST specimens in the middle part of the height. 4 transducers each were attached to the specimen in the vertical direction for measuring the longitudinal strains, and 4 transducers each – in the horizontal direction for measuring the transversal strains. The transducers were connected to the universal data acquisition system ALMEMO 5590-2. For measuring the horizontal displacements of the middle part of the HC-FST specimens, the electronic displacement indicators were used. They were fixed independently from the specimen and the press and also connected to the universal data acquisition system ALMEMO 5590-2. The specimen fixing scheme is given in Fig. 3.

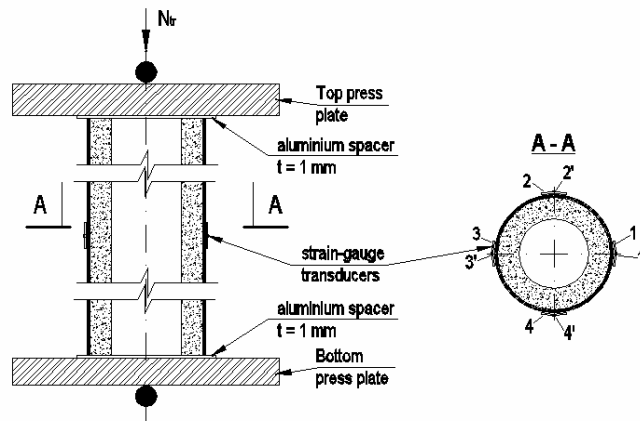


Fig. 3 – The specimen fixing scheme for Type 1 test.

4.1.2 The Process and Measuring of Type I test

In respect of every specimen, the concentricity of the load was checked before applying the breaking load to the specimen. The centring of the specimens was effected by applying a load equal to up to 30 % of the expected failure capacity and by comparing the readings of the strain-gauge transducers. In case of large differences in the readings of strain-gauge transducers attached at the opposite sides of the element, the specimen supporting point was adjusted accordingly. After centring the specimen, the load was increased, and the measuring was carried out from the beginning (at the load value of 0–5 kN). The average speed of loading was 34 kN/min. The load was increased gradually in 30 kN stages, whereas the readings of the strain-gauge transducers and displacement measuring devices were recorded at every stage of the load. Under the conditions of a load next to the strength limit of the specimen, the readings of the strain-gauge transducers and the shear measuring devices were recorded every 5–10 kN. All the specimens were subjected to testing until their failure. The main test parameters of the Type I and II specimens are given in Table 2.

The standard steel specimens were tested in the 250 kN capacity tension machine available at the laboratory of the Department of Steel and Timber Structures of VGTU.

The compressive strength of concrete was determined from the tests of 4 short HC specimens.

4.1.3 Experimental results and specimen behaviour during the test under ambient conditions

Failure of the HC specimens occurred after forming of the longitudinal cracks in the hollow concrete core. The failure mode of both short and long HC-FST specimens is quite similar. The specimens lost their load-bearing capacity because local buckling of the thin-walled steel shell and the hollow concrete core at the ends of the specimen at one of the press plates. As the failure criterion for the test under ambient conditions was taken the load bearing

Table 2 – Main parameters of the test

No.	Type of the specimen cross-section	Code of the specimen	Type of the tests	N_{ue} [kN]	t_{max} [°C]	T [min]
1	HC-FST	1I1	I	625	-	-
2	HC-FST	2I2	I	690	-	-
3	HC-FST	3I2	I	745	-	-
4	HC-FST	5I1	I	725	-	-
5	HC-FST	0T1	I	605	-	-
6	HC-FST	1T1	I	980	-	-
7	HC-FST	2T1	I	860	-	-

8	HC-FST	2T2	I	940	-	-
9	HC-FST	3T1	I	755	-	-
10	HC-FST	3T2	I	550	-	-
11	HC-FST	4T1	I	860	-	-
12	HC-FST	5T1	I	810	-	-
13	HC	0TB2	I	635	-	-
14	HC	1TB2	I	370	-	-
15	HC	4TB2	I	300	-	-
16	HC	5TB2	I	542	-	-
17	HC-FST	1I2	II.1	(180) 330	960	45.0
18	HC-FST	3I1	II.1	(180) 385	918	30.0
19	HC-FST	4I1	II.2	(120) 270	964	45.0
20	HC-FST	5I2	II.1	(180) 265	990	45.0

Notes:

1. The meanings of the markings of the Table columns: N_{ue} – the trial load-bearing capacity for axially loaded specimen (the value in brackets means the value of the axial load during the preheating of the specimen); t_{max} – the maximum temperature of the furnace reached during the Type 1 test 1st stage, T – the duration of preheating of the specimen during the Type 1 test 1st stage.

capacity at the moment when an irreversible decreasing of load carrying capacity in the specimens begins. The specimens 5T2 (with parameters $L \times t_c \times t_a - 296 \times 24.4 \times 1.63$ mm), 4T1 (with parameters $L \times t_c \times t_a - 298 \times 19.1 \times 1.63$ mm) and 1I1 (with parameters $L \times t_c \times t_a - 2004 \times 20.1 \times 1.65$ mm) are selected to demonstrate the typical failure mode of the specimens tested under ambient conditions (in Fig. 4).

The measuring of the horizontal displacements of the long HC-FST specimens in their middle height fixed very small displacements even just before specimens failing. Measured displacements could not be related with the beginning of the overall buckling of the specimen. The values of the longitudinal and transversal strains measured at the surface of the steel shell of the HC-FST specimens in relation to N_{tr}/N_u are given in Fig. 5.

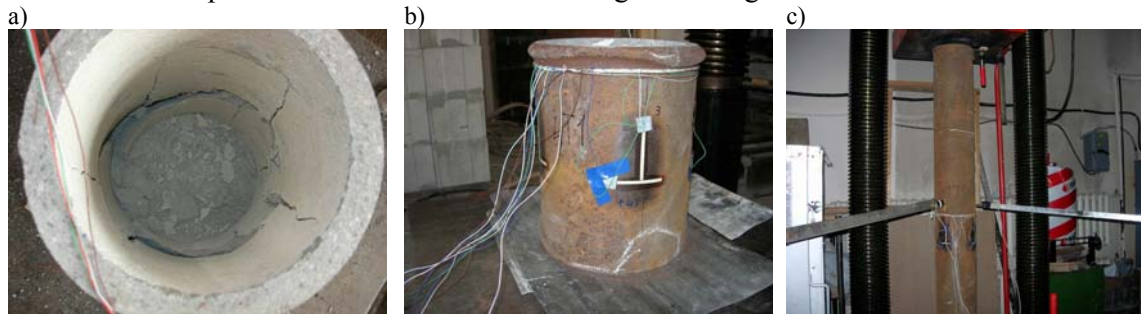


Fig. 4 – Specimens of Type I test: a) HC-type specimen after testing; b) short HC-FST-type specimen after testing; c) long HC-FST-type specimen during the test.

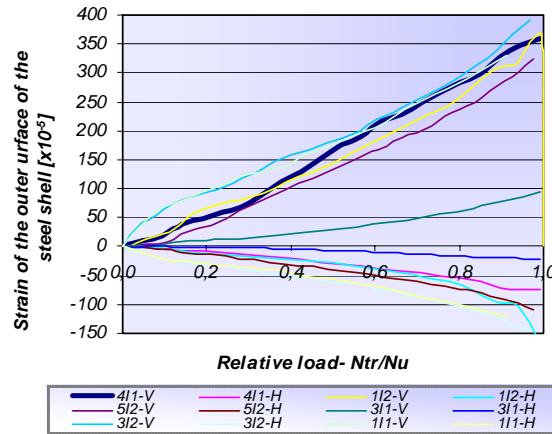


Fig. 5 – Longitudinal and transversal strains of the steel shell in relation to the relative load N_{tr}/N_u of the HC-FST, measured during the test under ambient conditions

The recorded mean values of ultimate normal stresses of the HC specimens – $\sigma_{u,m} = 45.44$ MPa. The mean of ultimate normal stresses have been calculated from the equation: $\sigma_{cr} = N_{cr} / A_c$, where: N_{cr} – critical experimental load applied to the specimen; A_c – the cross-section area of the hollow concrete core of the specimen. According to^{8,9}, the ring strength of the concrete can be equated with specific compressive prism strength of concrete – $f'_{c,m}$.

The mean value of the trial steel yield strength was $f_{y,m} = 318.3$ MPa, whereas the mean value of the steel ultimate strength was $f_{u,m} = 358.3$ MPa.

4.2 Determination of residual resistance – test of type II

4 long HC-FST specimens were prepared for the in-place test. The purpose of the test was to determine the residual resistance of the structures after their pre-heating. During the 1st stage of the test it was foreseen to subject an axial load on the specimens, and at the same time to heat them. The duration of heating was 45 minutes for three of HC-FST specimens and 30 minutes for one of them. During the 2nd stage it was foreseen to apply an axial load on the pre-heated specimens cooled until normal (20°C) temperature and increase load until they failure.

4.2.1 Equipment for post-fire resistance test

The test equipment was prepared for the testing as it was possible in pursuance of the requirements given in^{10,11}. The air pressure in the chamber of the furnace was not measured, and the heating agent was the electrical spirals but not the gas burners as it is prescribed in requirements mentioned above. The fixing scheme applied during the 1st stage of the post-fire resistance test allowed to heat the middle part of the HC-FST specimens. The specimens were put into the special electric furnace in the vertical position. For the purpose of avoiding additional heat losses through non-insulated points of the specimen and obtaining a more uniform distribution of temperature along the structure, the ends of the specimen protruding from the heating chamber of the furnace (both at the top and at the bottom) were covered with a 50 mm in thick mineral wool mat. At one end of the specimens, notches were made, which formed openings with cross-section area – 0.25 cm^2 . The function of the openings was to let escape water steam that got formed in the inner cavity of the specimen and in the concrete of the core during the heating. The scheme of the installation of the specimens is given in Fig. 6.

The temperature in the furnace was measured by stationary platinum-rhodium thermocouples and using a portable furnace thermocouple connected to universal data acquisition system ALMEMO 5590-1. Three stationary furnace thermocouples were installed in the heat-insulating layer of kaolin wool in one of the walls of the heating chamber (at the

upper, middle and lower zones of the heating chamber). The measuring accuracy of the stationary furnace thermocouples was 5°C within the measuring range over 300°C . The measuring accuracy of the portable thermocouple was 0.1°C within the measuring range from 0 to 1200°C .

The trial temperature regime of the furnace was maintained using a 3-channel programmable temperature controller “PROTERM-100”. The function of the temperature controller is to maintain the trial temperature regime uniform within all the levels of the furnace (lower, middle and upper). During the tests the temperature regime was maintained as close as possible to the standard fire curve stated in¹³.

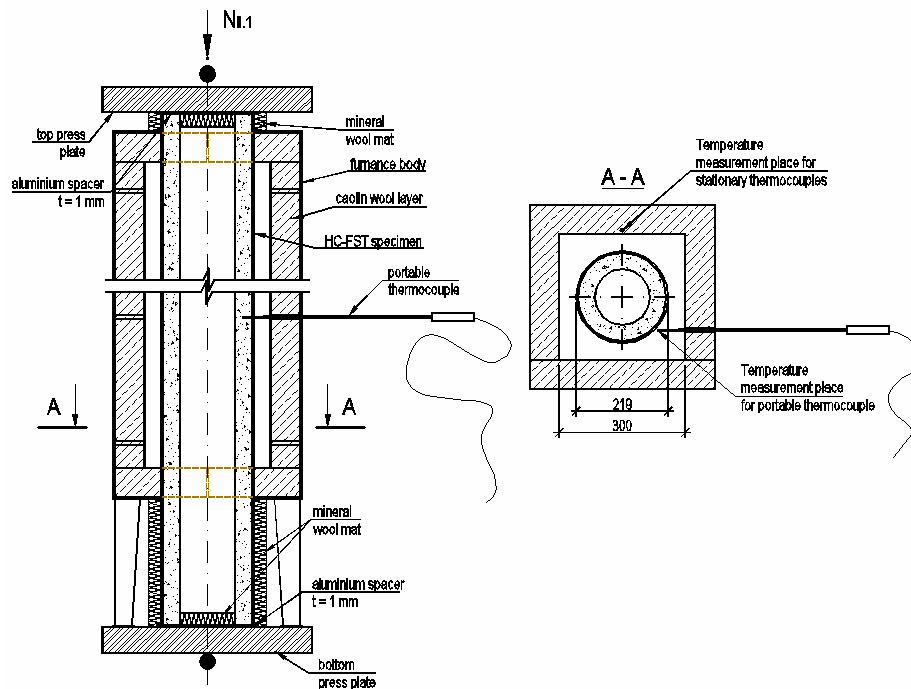


Fig. 6 – The scheme of the installation of the specimens for post-fire resistance test 1st stage

Before the beginning of the 2nd stage of the test type II strain-gauge transducers were attached to the outer surface of HC-FST elements (8 per each). All test equipment used in the test was the same to the equipment used for testing during the Type I tests.

4.2.2 The process and measuring of Type II test

The process and measuring during the 1st stage of the Type II test were the similar to ones during the Type I test. Throughout the heating period, the temperature was periodically measured by stationary and portable furnace thermocouples, and the behaviour of the specimens was monitored. The specimens during the test and after it are shown in Fig 7. The curves of the temperature regime applied during the 1st stage of Type II test are given in Fig. 8. The curves with code names of the specimens were traced on the basis of temperature measuring data in the heating chamber of the furnace in its hottest point or its vicinity during the testing of the corresponding specimen. The curves given in the diagram show that after approximately 7 min. the temperature in the furnace was slightly higher than the temperature according to the standard fire curve. The specimen that had been subjected to heating for 45 minutes were removed from the furnace and allowed to cool for 2 full days (48 hours).

a)

b)

c)

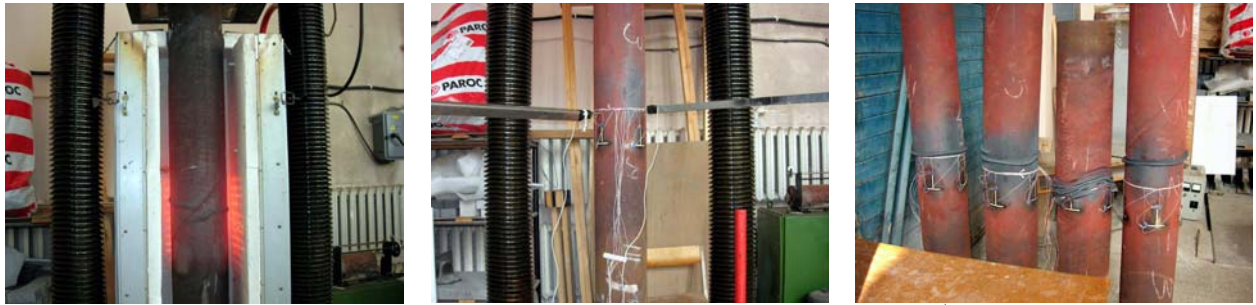


Fig. 7 – Views on the test specimens: a) HC-FST specimen after Type II 1st stage test; b) HC-FST specimen before Type II 2nd stage test; c) HC-FST specimens after Type II test.

The process and the measuring during the 2nd stage of the test are similar to those performed during Type I tests. The following parameters were recorded during every stage of the load application: the quantity of the load, the strain of the surface of the steel shell and the horizontal deformation of the middle part of the specimen. The experimental load-bearing capacity of the specimen was taken as the maximum load recorded during the compression test.

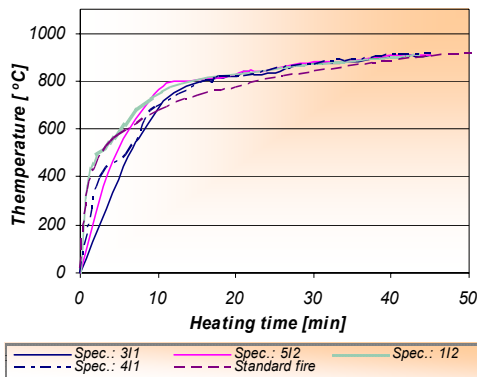


Fig. 8 – Furnace heating regime during the 1st stage or the Type II test.

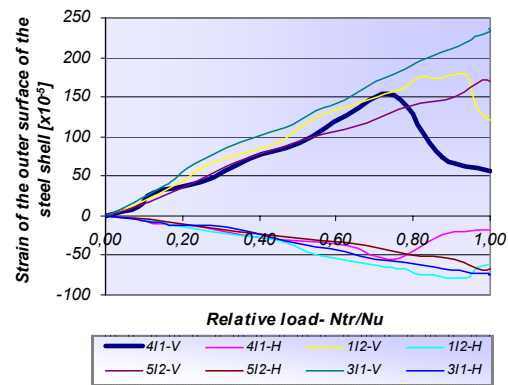


Fig. 9 – Longitudinal and transversal strain of the steel shell in relation to the relative load N_{tr}/N_u of the HC-FST specimens of the 2nd stage of the Type II test.

4.2.3 Experimental results and behaviour of the specimens exposed to fire

As the failure criterion for the post-fire resistance test was taken the maximum load reached during the test. The maximum temperature in the heating chamber of the furnace reached during the test was as high as 990°C. The failure mode of the specimens was similar to the one noted during the Type I test: the loss of the load-bearing capacity of specimens was a local buckling of the thin-walled steel shell and partial failure of the concrete core. All the specimens buckled locally at the points, which had been more heated during the 1st stage of the test, or in their vicinity. The measuring of the horizontal displacements of long HC-FST specimens in their middle height showed a very small their values, which could not be related with the beginning of the overall buckling of the specimen. The observed failure mode of the Type II test specimens indirectly endorses the attitude of the¹² for possibility to decrease substantially the effective length of C-FST columns behaving in fire in comparison with those behaving under the normal conditions.

The dependency of the transversal and longitudinal strains on the surface of the steel shell of the specimens tested for residual resistance to the relative load N_{tr}/N_u is given in Fig. 9. The principal parameters recorded during their test are given in Table 2.

4.2.4 *The behaviour of the specimens after recording their maximum load-bearing capacity*

The fact, that the specimens did not buckle like column element, but failed locally in the cross-section of the element most affected by heat and were still able to keep some load, prompted us to study the residual load-bearing capacity of the column previously heated during 45 min and after recording their maximum load-bearing capacity. For this purpose, one Type II test specimen (112 – in Table 2) was subjected to further axial compression after the maximum load (330 kN) was already recorded. The element, with the initial geometrical length of 1997 mm, was further tested until its length decreased to 1700 mm. The minimal resisting force of the specimen, recorded during this particular test was 85 kN, i.e. 25.8 % of the maximum experimentally determined its load-bearing capacity. After the minimal load value was reached, axial load-bearing force during further testing raised up to 175 kN. At the end of the test (when that element had lost 300 mm of its initial geometrical length) the load-bearing force of the HC-FST specimen made up 105 kN.

Observation of the specimen behaviour under axial compression after pre-heating under partial loading and after recording its maximum load-bearing capacity showed the further possibility to resist some portion of load. That may be important expecting particular service of HC-FST columns before their final failure.

5. ESTIMATION OF THE STUDY RESULTS

The residual (post-fire) compressive resistance of the specimen determined during the Type II tests (after a 45 minutes pre-heating regime) on average makes up 41 % of the trial load-bearing capacity of specimens tested under normal conditions, and approximately 134 % of the mean load value, which was applied during heating. According to obtained trial value (41 %) of load-bearing capacity of HC-FST columns in post-fire conditions and taking into account that according to¹³ the design load applied on the structures in analysis of the most civil buildings under fire conditions makes up approximately 40 % of the design load under normal ($t = 20^{\circ}\text{C}$) conditions it can be assumed that the load bearing capacity of the HC-FST columns (with geometrical parameters similar to those of tested columns) is the almost very similar for the pre-heated as well as for the pre-heated and then cooled columns (with the duration of heating – 45 min.).

Calculation of temperature distribution in the section of the column under testing presented in¹⁴ showed the temperature magnitude of concrete core 10-15 percent less than temperature inside the furnace chamber during the heating. It is seen, that the calculated value of the temperature distribution (neglecting the water existence within the concrete core) is not well adequate with the experimental data as the water steam was clear observed for 30 minutes from the beginning of the heating. The calculated by FEM modelling temperature distribution in the cross-section of HC-FST column after 30 min. and after 45 min. from the beginning of the standard¹³ fire showed in Fig. 10 and Fig. 11.

In⁵ it is given that the design residual strength of concrete (after its pre-heating to the 500°C and higher temperatures) conservatively can be neglected (although it may amount the 30 % of initial strength) but the residual (cooled after pre-heating) strength of the steel (with the characteristic values of strength in tension equal 375 MPa and less) makes up 100% of its strength in normal conditions. Hence, we would be able to assume the post-fire resistance of HC-FST column (after its pre-heating until steel shell and concrete core had reached 500°C and higher temperature) consisting of only the compressive resistance of the steel shell.

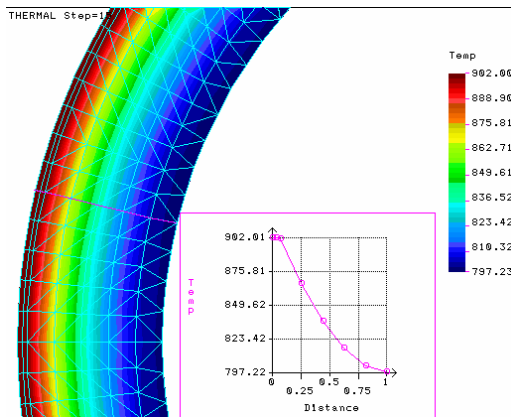


Fig. 10 – Temperature distribution in the cross-section of the HC-FST column after 45 min from the beginning of the standard fire.

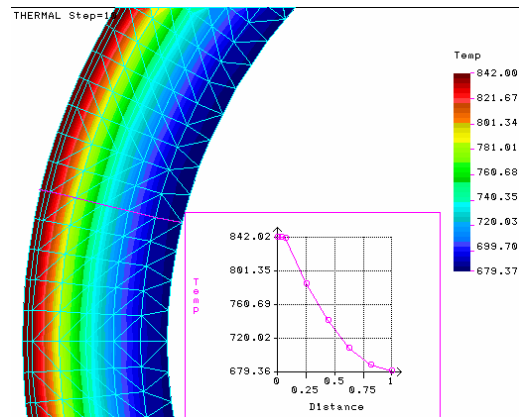


Fig. 11 – Temperature distribution in the cross-section of the HC-FST column after 30 min from the beginning of the standard fire.

Compressive resistance of the CHS columns (with the mean geometrical and mechanical properties of steel shell of the tested HC-FST specimens) under the ambient conditions was determined from calculations according to¹⁵ and¹⁶ and makes up – 302.6 kN. This value obtained by calculation is just a little lower than mean trial value of HC-FST specimens' post-fire resistance (312.5 kN).

The compressive resistance of the HC-FST column with geometrical parameters of the tested specimens (from Table 1) in ambient temperatures calculated according to¹⁷ makes up 635 kN and is quite close to the experimental mean value 696 kN.

As well the analysis of the compressive resistance of the same CHS column under fire conditions was made. Compressive resistance of the CHS column in fire conditions after 45 min. of heating was obtained as the result of calculation according to¹⁸ and makes up only 18.02 kN. It's 10 times less then the axial load (180 kN) applied on the HC-FST specimens during the pre-heating stage of post-fire resistance tests.

From the analysis of experimental results and calculation results it can be stated, that the greater portion of the load applied to the HC-FST column is taken by concrete core in fire situation (or during the pre-heating) and by the steel shell – when pre-heated HC-FST column is cooled to normal temperature.

6. CONCLUSIONS

1. The influence of temperature on the compressive resistance of HC-FST specimens is immense. According to the test data residual (post-fire) compressive resistance of HC-FST specimens makes up about 41 % of the resistance of those elements under ambient conditions. This experimentally obtained utilization level value of HC-FST columns in post-fire conditions is very close to the usually taken level (40%) of design load for fire analysis of structures.

2. On the basis of the analysis of tests results, it can be stated, that after the exposing to fire temperatures with duration 45 min, the residual compressive resistance of the HC-FST columns is not sufficient for further normal use of the structures, but allows expecting particular safe use during small period of time. In the buildings with statically indeterminate frameworks after the fire it is believable redistribution of internal forces between HC-FST columns due to their plastic failure mode and ability to take relatively great (in comparison with their post fire resistance) the post-failure load.

3. Observation of the behaviour of the HC-FST specimens under axial compression and previously affected by fire temperatures, let us expecting not sudden failure mode via the

overall buckling of HC-FST columns but the failure mode that could be described as local buckling of the thin-walled steel shell and local failure of the hollow concrete core.

4. From the water steam emission observation it can be stated, that temperature distribution in the section of columns during testing is substantially influenced by availability of free and chemically combined water in the concrete core of HC-FST element. Water inside the concrete should be always estimated in analysis of temperature distribution through the cross section of the HC-FST column under heating.

5. The concrete core takes the greater part of the axial load applied to the CH-FST column during the fire, but is not well resisting in post-fire situation. The steel shell takes the greater part of the axial load acting on the pre-heated and then cooled CH-FST column but is not well resisting the normal stresses in fire.

7. REFERENCES:

- [1] Han, L-H. and Huo, J-S. Concrete-Filled Hollow Structural Steel Columns After Exposure to ISO-834 Fire Standard. *Journal of Structural Engineering*. 2003, Vol. 129, No 1, p. 68-78.
- [2] Colina, H., Moreau, G. and Cintra, D. Experimental Study of Transient Thermal Creep and Other Phenomena of Concrete at High Temperature. *Journal of civil engineering and management*. Vilnius. 2004, Vol. X, No 4, p. 255-260.
- [3] Bednarek, Z. The influence of the temperature increase on the steel strength properties used for the appraisal of the fire safety of the reinforced concrete structures. Dissertation for habilitation. Technical sciences, Civil Engineering (J7). Vilnius: "Technika", 1996, (In Russian).
- [4] Bednarek Z. and Kamocka R. Analysis of thermal strain of structural steels in variable thermal field. *Journal of civil engineering and management*. Vilnius: 2004, Vol. X, Suppl. 1, p. 19-22.
- [5] Mosalkov, I. L., Pliusina, G. F. and Frolov, A. J. Fire resistance of building structures. Moscow: "LEIDYKLA", 2001. (In Russian).
- [7] LST EN 10002-1:2003 – Metallic materials. Tensile testing. Part 1: Method of test at ambient temperature.
- [8] Vadlūga, R. and Kudzys, A. On the compressive strength of the centrifuged concrete. Transactions of KPI. *Researches on the reinforced concrete structures*. Vol.1. Vilnius: "Mintis", 1966. p. 111-116.
- [9] Kudzys, A. Reinforced concrete structures of annular cross-section. Vilnius: "Mintis", 1975. (In Russian).
- [10] EN 1363-1. Fire resistance tests - Part 1: General requirements. August 1999.
- [11] EN 1365-4. Fire resistance test of load bearing elements - Part 4: Columns. August 1999.
- [12] EN 1994-1-2. Eurocode 4 – Design of composite steel and concrete structures – Part 1-2: General rules – Structural fire design.
- [13] EN 1991-1-2:2002 Eurocode 1: Actions on structures. Part 1-2: General actions. Actions on structures exposed to fire.
- [14] Blaževičius, Ž. and Šaučiuvėnas, G. The course of an experimental research on the fire resistance of HC-FST columns and the results of their calculation. In: Proceedings of the republican conference in Vilnius, Lithuania „Building Constructions. The Development of Building Structures during Integration to the space of Eurocodes” (In press).
- [15] STR 2.05.08:2005. Design of steel structures. General rules. Vilnius: "Rekona", 2005.
- [16] EN 1993-1-1. Eurocode 3: Design of steel structures - Part 1-1: General rules and rules of buildings.
- [17] EN 1994-1-1. Eurocode 4 – Design of composite steel and concrete structures – Part 1-1: General rules and rules for buildings.
- [18] EN 1993-1-2. Eurocode 3: Design of steel structures – Part 1-2: General rules – Structural fire design.



EFFECTS OF THERMAL GRADIENTS ON MEMBRANE STRESSES IN THIN SLABS

Anthony K. ABU¹, Ian W. BURGESS² and Roger J. PLANK³

ABSTRACT

The Building Research Establishment (BRE) of the United Kingdom has developed a simple design method for the determination of the capacity of composite slabs in fire. The method, based on ambient temperature large-deflection plastic theory, predicts the capacity by calculating the enhancement added by tensile membrane action to the theoretical yield-line load of the slab. Tensile membrane action is a load-carrying mechanism experienced by thin slabs undergoing large vertical deflections, where stretching of the midplane produces a central area of tensile force balanced by a peripheral ring of compressive force. The use of this mechanism in structural fire engineering introduces safety and economy, as a large number of floor beams can be left unprotected. The method, developed on the assumption that the slabs are simply-supported, also assumes that the development of the tensile membrane mechanism is maintained at elevated temperatures. An analytical procedure for the determination of this membrane capacity has recently been developed by the University of Edinburgh. It argues that the development of tensile membrane action at elevated temperatures differs from that at ambient temperature, and that the tensile forces developed in the centre of the slab can only be balanced by sufficient anchorage along the slab's boundaries. Experimental investigations on large-deflection behaviour of simply-supported slabs at ambient and elevated temperatures, conducted at the University of Sheffield, have confirmed the variation in the mechanism at ambient and elevated temperatures, but have identified that the load-carrying capacity can be effectively developed without the horizontal anchorage along the slab's boundaries.

These observations have led to the belief that thermal gradients, acting alone through the depth of the slab, can induce considerable amounts of tensile membrane action. This paper therefore investigates this phenomenon in simply-supported thin slabs. It examines

¹ Research Student, Dept. of Civil & Structural Engineering, University of Sheffield, Sheffield S1 3JD, UK
Email: cip04aka@sheffield.ac.uk

² Professor, Dept. of Civil & Structural Engineering, University of Sheffield, Sheffield S1 3JD, UK
Email: ian.burgess@sheffield.ac.uk

³ Professor, School of Architectural Studies, University of Sheffield, Sheffield S1 3JD, UK
Email: r.j.plank@sheffield.ac.uk

displacements and stresses developed at ambient and elevated temperatures, using the Rayleigh-Ritz approach. Good comparisons are made with finite element analyses.

1. INTRODUCTION

Real building fires and full-scale fire tests on steel-framed structures have shown that buildings possess inherent fire resistance far greater than their perceived capacities. The survival of buildings such as the uncompleted 14-storey building construction in Broadgate, London in 1990 and the Cardington fire tests of the 1990s have led to the understanding that conventional methods of protecting all steel members are very conservative¹. In fire, if compartmentation is maintained and composite slabs are allowed to undergo large vertical deflections and two-way bending, then slabs generate a higher self-sustaining load-carrying capacity through a mechanism known as tensile membrane action. This mechanism, which increases its load capacity with increasing vertical deflection, develops as the mid-plane of the slab is stretched to produce a central area of tensile force balanced by a peripheral ring of compressive force. The effective utilisation of this capacity in structural fire engineering provides sufficient safety and economy, as a greater number of beams in a floor slab can be left unprotected². Subsequent to the Cardington tests, the BRE developed a simple design method to predict the load-carrying capacity of composite slabs in fire incorporating tensile membrane action^{3,4}. The method calculates the enhancement membrane action provides in addition to the traditional flexural capacity of the slab, by considering ambient temperature conditions. Failure is based on the formation of a full-depth crack across the shorter span of the slab^{3,4}. It is assumed that the mechanism at ambient temperature is maintained at elevated temperatures³, and an SCI design guide has been produced to facilitate the use of the method¹.

To use the BRE Membrane Action Method in the design of composite slabs in fire, a floor plate is divided into square or rectangular panels, as shown in Fig. 1. Within a panel, the

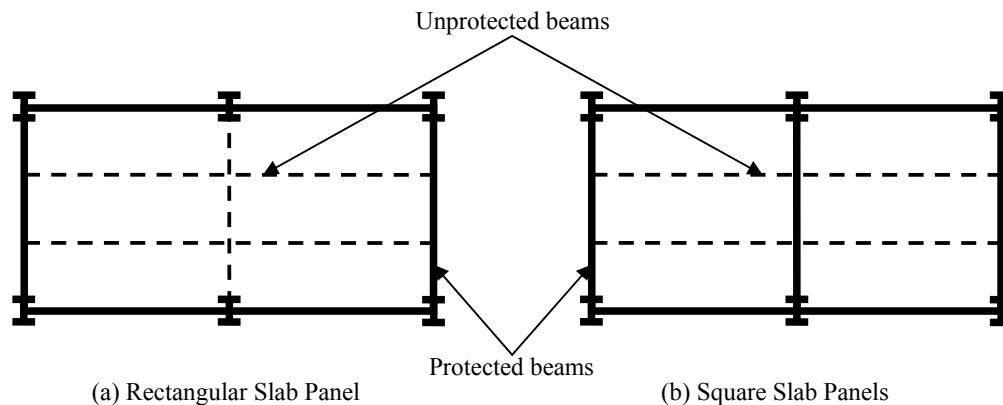


Fig. 1: Rectangular and Square Slab Panels

beams are left unprotected with protected beams on the perimeter². The method, which refers to observations at Cardington, assumes that the reinforcement across the perimeter of the panel fractures, due to large hogging moments³. The slab panel is therefore treated as a simply supported slab on edges that resist vertical deflection. At elevated temperatures the lower layers of composite slabs are at high temperatures. Because of the low resistance of steel to heat, the contribution of the steel deck to the capacity of the concrete slab is negligible. Tests have also shown that the steel deck de-bonds from the concrete at elevated temperatures. As a result, the effective slab depth providing the necessary tensile membrane

capacity is represented as a flat slab³, as in Fig. 2 below. In the figure, a is the longer span, b is the shorter span and h is the thickness.

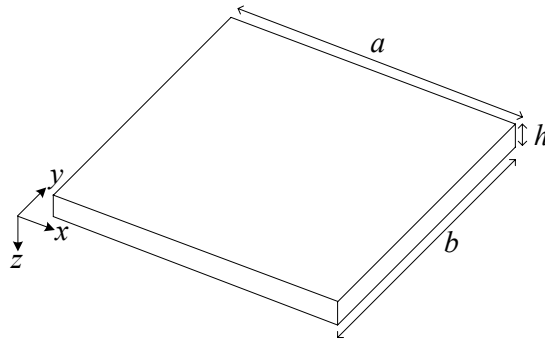


Fig. 2: Flat Slab with its dimensions

Cameron and Usmani^{5, 6} have proposed a new design method to determine the membrane capacity of composite floors in fire. Their analytical method, developed from classical large-deflection theory, is a 3-step process that generates a temperature distribution through the slab; consisting of a mean temperature increase and a thermal gradient, then determines the vertical deflection and stress-strain distribution due to the thermally induced strains and, using an energy method, calculates the membrane capacity of the slab. The method assumes that the tensile forces developed in the slab can only be balanced by the provision of anchorage along the slab boundary. It assumes that this horizontal anchorage will be provided by the adjacent slabs, where an interior slab is concerned, but proposes that the design of composite beams on the edges of buildings and their connections should account for the required lateral restraint to the slabs in addition to the vertical restraint they provide.

Tests by Foster et al.^{7, 8} on small-scale simply-supported flat slabs at the University of Sheffield have shown that the mode of failure of concrete slabs in fire differs from what is observed at ambient temperature. At elevated temperatures, thermal bowing of the slab induces double-curvature bending which generates full-depth cracking across the shorter span of the slab, which may lead to an eventual yield-line type of failure mechanism^{7, 8}. The observations and the magnitudes of vertical deflections reached in these small-scale tests have suggested that thermal gradients acting alone through the depth of the slab can cause significant amounts of tensile membrane action in simply-supported slabs. Contrary to the suggestion by the Cameron and Usmani^{5, 6}, it does not seem to be necessary to provide horizontal edge restraint to sustain this load-carrying mechanism.

The research reported here, as part of a larger investigation into the analytical quantification of membrane capacity of simply-supported composite slabs in fire, looks at an initial investigation into the effects of these thermal gradients on the development of tensile membrane action and the associated stresses, using the variational Rayleigh-Ritz Method. The development of tensile membrane action at ambient and elevated temperatures is considered, and good comparisons are made with the finite element package *Vulcan*⁹⁻¹⁰, developed over the years at the University of Sheffield.

2. LARGE DEFLECTION PLATE THEORY

Classical plate theory for medium-thick plates assumes that:
the deflection of the mid-surface is small compared with the thickness of the plate
the mid-plane remains unstrained subsequent to bending

lines initially normal to the mid-surface remain normal to that surface after bending and stresses normal to the mid-plane are small compared with those in the plane of the plate and may therefore be neglected¹¹

For thin plates undergoing large deflections, the first two assumptions in medium-thick plate theory are modified to account for the straining of the mid-surface, due to stretching of the plate and the contribution of the out-of-plane deflection¹². The governing equations for large deflection theory of plates are defined as¹²:

$$\frac{\partial^4 F}{\partial x^4} + 2 \frac{\partial^4 F}{\partial x^2 \partial y^2} + \frac{\partial^4 F}{\partial y^4} = E \left[\left(\frac{\partial^2 w}{\partial x \partial y} \right)^2 - \frac{\partial^2 w}{\partial x^2} \frac{\partial^2 w}{\partial y^2} \right] \quad (1)$$

$$\frac{\partial^4 w}{\partial x^4} + 2 \frac{\partial^4 w}{\partial x^2 \partial y^2} + \frac{\partial^4 w}{\partial y^4} = \frac{h}{D} \left(\frac{q}{h} + \frac{\partial^2 F}{\partial y^2} \frac{\partial^2 w}{\partial x^2} + \frac{\partial^2 F}{\partial x^2} \frac{\partial^2 w}{\partial y^2} - 2 \frac{\partial^2 F}{\partial x \partial y} \frac{\partial^2 w}{\partial x \partial y} \right) \quad (2)$$

F is a stress function such that:

$$N_x = h \frac{\partial^2 F}{\partial y^2}, \quad N_y = h \frac{\partial^2 F}{\partial x^2}, \quad N_{xy} = -h \frac{\partial^2 F}{\partial x \partial y} \quad (3)$$

and N_x , N_y and N_{xy} are the forces per unit length in the directions x , y and xy , with w , q and D being the vertical deflection, the load per unit area and the flexural rigidity of the plate respectively. For a plate whose origin of co-ordinates is at a corner, as in Fig. 2, exact solutions to the governing equations of large deflection theory can be obtained if the following functions are defined as¹²:

$$w = \sum_{m=1}^{\infty} \sum_{n=1}^{\infty} w_{mn} \sin \frac{m\pi x}{a} \sin \frac{n\pi y}{b} \quad (4)$$

$$q = \sum_{m=1}^{\infty} \sum_{n=1}^{\infty} q_{mn} \sin \frac{m\pi x}{a} \sin \frac{n\pi y}{b} \quad (5)$$

$$F = \frac{P_x y^2}{2bh} + \frac{P_y x^2}{2ah} + \sum_{m=0}^{\infty} \sum_{n=0}^{\infty} f_{mn} \cos \frac{m\pi x}{a} \cos \frac{n\pi y}{b} \quad (6)$$

However, approximate solutions for the plate load-deflection behaviour are obtained if the variational Rayleigh-Ritz Method is employed¹². The method requires that the mechanical strain energy of the plate, considering both stretching and bending, is obtained, and the amplitudes of any shape functions used in the generation of the strain and potential energies are determined by minimising the total potential energy. The coefficients determined can then be used to approximate the deflected shapes and stresses in the plate. The total strain energy and the strains at any point in the slab are given by:

$$V = \frac{E}{2(1-\nu^2)} \iiint \left[\varepsilon_x^2 + \varepsilon_y^2 + 2\nu \varepsilon_x \varepsilon_y + \frac{1-\nu}{2} \gamma_{xy}^2 \right] dx dy dz \quad (7)$$

$$\begin{aligned} \varepsilon_x &= \frac{\partial u}{\partial x} + \frac{1}{2} \left(\frac{\partial w}{\partial x} \right)^2 - z \frac{\partial^2 w}{\partial x^2}, \quad \varepsilon_y = \frac{\partial v}{\partial y} + \frac{1}{2} \left(\frac{\partial w}{\partial y} \right)^2 - z \frac{\partial^2 w}{\partial y^2} \\ \gamma_{xy} &= \left(\frac{\partial u}{\partial y} + \frac{\partial v}{\partial x} \right) + \frac{\partial w}{\partial x} \frac{\partial w}{\partial y} - 2z \frac{\partial^2 w}{\partial x \partial y} \end{aligned} \quad (8)$$

To use the Rayleigh-Ritz Method functional expressions are defined for the displacements in the x , y and z directions, such that these expressions satisfy the geometric and natural boundary conditions. For the analyses, the origin is set in the centre of the plate (Fig. 3) and, given the symmetry of the problem, quarter-sections are modelled.

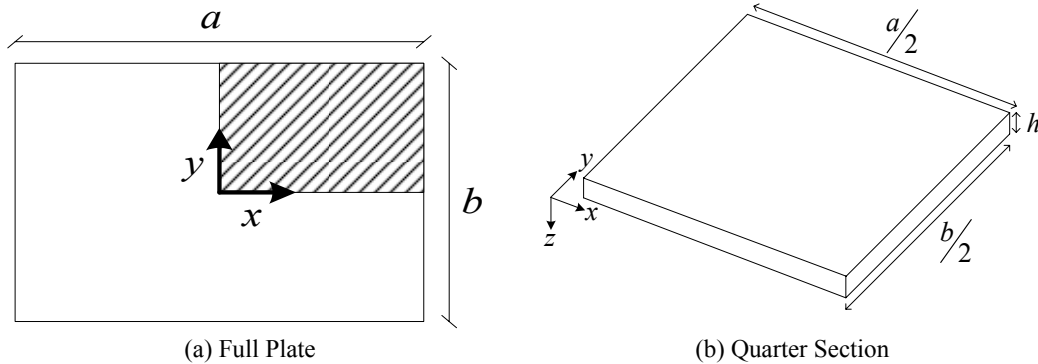


Fig. 3: Typical plate with its dimensions

The geometric and natural boundary conditions are:

$$N_x = 0, \quad x = \pm \frac{a}{2} \quad M_x = 0, \quad x = \pm \frac{a}{2} \quad N_y = 0, \quad y = \pm \frac{b}{2} \quad M_y = 0, \quad y = \pm \frac{b}{2}$$

$$w = \frac{\partial^2 w}{\partial x^2} = \frac{\partial^2 w}{\partial y^2} = 0 \quad \text{on } x = \pm \frac{a}{2} \text{ and } y = \pm \frac{b}{2}$$

3. SOLUTION OF THE LARGE-DEFLECTION PROBLEM

3.1 Research on Solutions of Large-Deflection Plate Problems

Attempts have been made by a number of researchers to approximate vertical deflections and stresses of thin plates under large deflections using the principle of minimum potential energy. Berger¹³ proposed a strain energy equation that ignored the second invariant of the mid-surface strains. However, subsequent research established the ineffectiveness of this equation for plates with movable boundaries¹⁴. Banerjee and Datta¹⁵ proposed a method that linearised the total potential energy with an expression, in terms of a factor and the vertical deflection, which gave good results if the right factor was chosen. However, there could be no physical justification for the selection of specific values for the factor. Boresi and Turner¹⁶ proceeded by maintaining the non-linear energy equations and defining functional expressions for the in-plane strains in the x and y directions, and for the vertical deflection. Odd-numbered double Fourier series expressions were used for the strains and the vertical deflections.

3.2 Solution Adopted

For large deflection of plates, the mid-surface strains depend on the stretching of the mid-surface and the contribution of vertical deflection. Preliminary finite element analysis and observations from tests show that, for simply supported slabs subjected to large deflections, the edges (including the corners) are pulled-in. However, the expressions proposed by Boresi and Turner¹⁶ artificially keep the corners fixed in position, preventing the slab from attaining appreciable magnitudes of displacement. The expressions are modified to

suit the observations. The in-plane strain expressions therefore require the use of the full Fourier series instead of just the odd-numbered terms. The strains are thus defined as:

$$\varepsilon_x = \sum_{m=1}^{\infty} \sum_{n=1}^{\infty} A_{mn} \cos \frac{m\pi x}{a} \cos \frac{n\pi y}{b}, \quad \text{where } m, n = 1, 2, 3, \dots \quad (9)$$

$$\varepsilon_y = \sum_{m=1}^{\infty} \sum_{n=1}^{\infty} B_{mn} \cos \frac{m\pi x}{a} \cos \frac{n\pi y}{b}, \quad \text{where } m, n = 1, 2, 3, \dots \quad (10)$$

with the out-of-plane deflection as:

$$w = \sum_{m=1}^{\infty} \sum_{n=1}^{\infty} W_{mn} \cos \frac{m\pi x}{a} \cos \frac{n\pi y}{b}, \quad \text{where } m, n = 1, 3, 5, \dots \quad (11)$$

4. AMBIENT AND ELEVATED-TEMPERATURE RAYLEIGH-RITZ ANALYSES

Tensile membrane action is deemed to have developed in a thin plate when vertical displacements are of the order of the thickness of the plate. Thus, regardless of the type of action imposed on the plate, the development of the mechanism can be observed once the magnitudes of vertical deflections are about the thickness of the plate.

The analyses were carried out on quarter-sections of horizontally unrestrained linear-elastic plates of dimensions 5000mm×5000mm×100mm. The plates had a modulus of elasticity of 18000N/mm² and a Poisson's ratio of 0.25. The software used for the analytical study was MAPLE 9.5 (by Waterloo Maple Inc.). Comparisons were made with the geometrically non-linear finite element analysis program *Vulcan*⁹⁻¹⁰, but a linear-elastic material was used. For membrane tractions and stresses, results were taken at Gauss points and compared with those obtained from the analytical solution. The comparisons were made with results along 3 lines in the plate. These were along the centre-line, the edge and mid-way between these lines (see the legends in Figs. 7 and 13).

4.1 Ambient Temperature Analysis

A 100kN/m² (0.1N/mm²) load was placed on the plate. The displacements and subsequent strains and stresses were determined. The horizontal displacements (u and v) in the x and y directions are given by:

$$u = \frac{a}{\pi} \sum_{m=1}^{\infty} \sum_{n=1}^{\infty} \frac{1}{m} A_{mn} \sin \frac{m\pi x}{a} \cos \frac{n\pi y}{b} - \frac{\pi^2}{8a^2} \sum_{m=1}^{\infty} \sum_{n=1}^{\infty} m^2 W_{mn}^2 \left(x - \frac{a}{2m\pi} \sin \frac{2m\pi x}{a} \right) \left(1 + \cos \frac{2n\pi y}{b} \right) \quad (12)$$

$$v = \frac{b}{\pi} \sum_{m=1}^{\infty} \sum_{n=1}^{\infty} \frac{1}{n} B_{mn} \sin \frac{n\pi y}{b} \cos \frac{m\pi x}{a} - \frac{\pi^2}{8b^2} \sum_{m=1}^{\infty} \sum_{n=1}^{\infty} n^2 W_{mn}^2 \left(y - \frac{b}{2n\pi} \sin \frac{2n\pi y}{b} \right) \left(1 + \cos \frac{2m\pi x}{a} \right) \quad (13)$$

Resulting plate deflections, membrane tractions and stresses are given in Figs. 4-9. In the figures that follow, the continuous lines represent the results from the analytical model while the broken lines represent the results from the *Vulcan* finite-element analysis, as shown in

Fig. 4. A legend for each plot is given in Fig. 7 ((a) for vertical displacements, (b) for mid-plane horizontal displacements, (c) for membrane tractions and (d) for stresses).

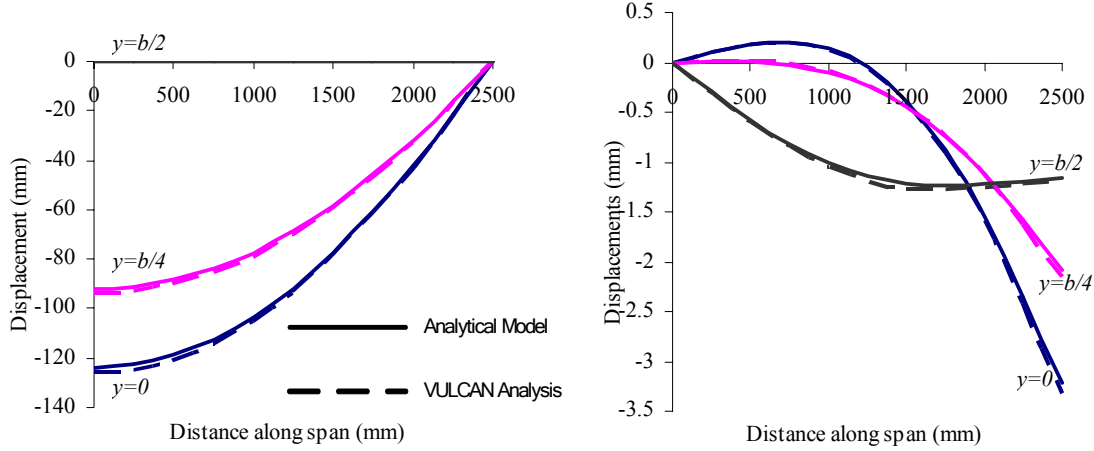


Fig 4: Ambient-temperature vertical displacements

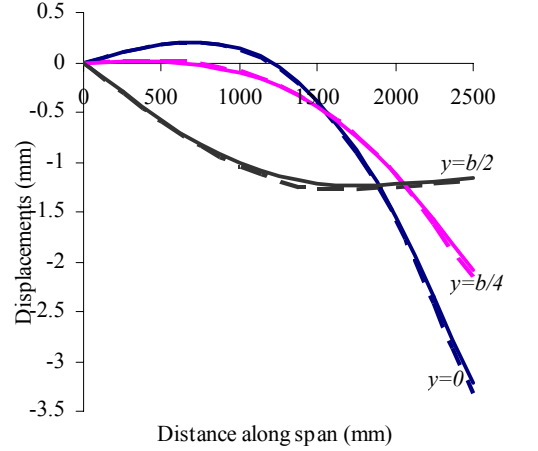


Fig 5: Ambient-temperature in-plane Displacements

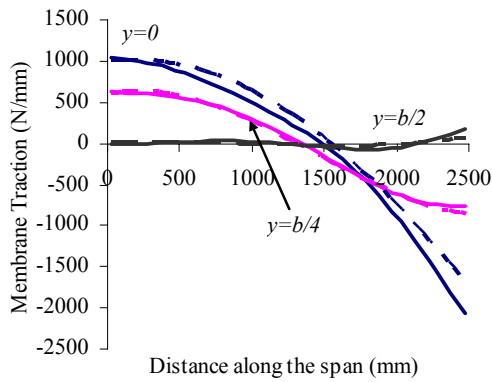


Fig 6: Ambient-temperature membrane tractions across span

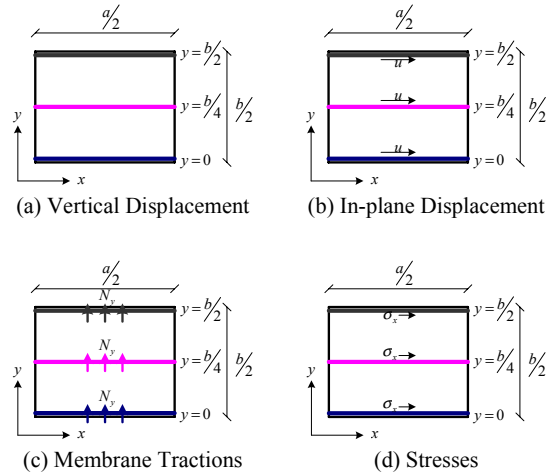


Fig 7: Ambient-temperature Legends

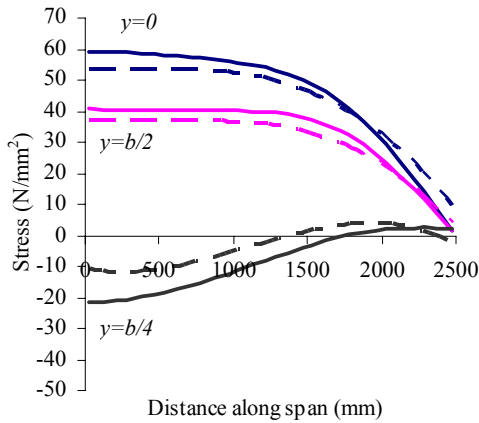


Fig 8: Ambient-temperature bottom layer stress distribution

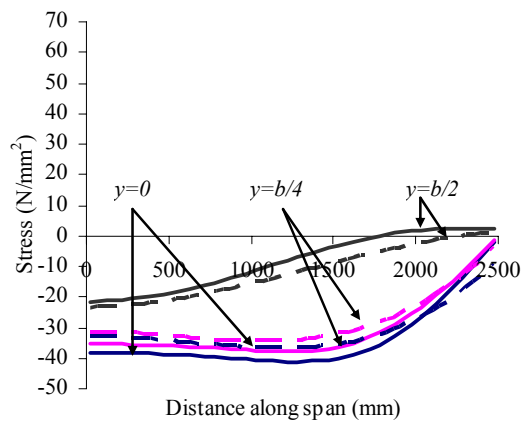


Fig 9: Ambient-temperature top layer stress distribution

4.2 Elevated Temperature Analysis

At elevated temperatures the thermal strain given by $\varepsilon_t = \alpha \Delta T$ (where α is the coefficient of thermal expansion and $\Delta T = T - T_0$ is the change in temperature at the depth being considered) influences the mechanical strains developed in the plate. For the analysis α is kept constant at $10 \times 10^{-6}/^\circ\text{C}$. As the aim is to investigate the effects of thermal gradients only, steady state conditions are used and a version of the *Vulcan* software which maintains room-temperature material properties is used for the comparison. The Young's modulus of the material is therefore kept at 18000 N/mm^2 in all layers, regardless of the imposed temperature gradient. No loads are imposed on the plate for the elevated-temperature analysis. The linear temperature variation between temperatures T_2 on the bottom face and T_1 on the top face is defined as¹⁷:

$$T = T_m + Z \frac{(T_2 - T_1)}{h}, \quad \text{where } T_m = \frac{T_1 + T_2}{2} \quad (14)$$

Therefore the mechanical strain at any point in the slab is obtained as:

$$\begin{aligned} \varepsilon_x &= \frac{\partial u}{\partial x} + \frac{1}{2} \left(\frac{\partial w}{\partial x} \right)^2 - \alpha \Delta T - z \frac{\partial^2 w}{\partial x^2}, \quad \varepsilon_y = \frac{\partial v}{\partial y} + \frac{1}{2} \left(\frac{\partial w}{\partial y} \right)^2 - \alpha \Delta T - z \frac{\partial^2 w}{\partial y^2} \\ \gamma_{xy} &= \left(\frac{\partial u}{\partial y} + \frac{\partial v}{\partial x} \right) + \frac{\partial w}{\partial x} \frac{\partial w}{\partial y} - 2z \frac{\partial^2 w}{\partial x \partial y} \end{aligned} \quad (15)$$

The in-plane displacements thus become:

$$\begin{aligned} u &= \frac{a}{\pi} \sum_{m=1}^{\infty} \sum_{n=1}^{\infty} \frac{1}{m} A_{mn} \sin \frac{m\pi x}{a} \cos \frac{n\pi y}{b} \\ &\quad - \frac{\pi^2}{8a^2} \sum_{m=1}^{\infty} \sum_{n=1}^{\infty} m^2 W_{mn}^2 \left(x - \frac{a}{2m\pi} \sin \frac{2m\pi x}{a} \right) \left(1 + \cos \frac{2n\pi y}{b} \right) + \alpha \Delta T x \end{aligned} \quad (16)$$

$$\begin{aligned} v &= \frac{b}{\pi} \sum_{m=1}^{\infty} \sum_{n=1}^{\infty} \frac{1}{n} B_{mn} \sin \frac{n\pi y}{b} \cos \frac{m\pi x}{a} \\ &\quad - \frac{\pi^2}{8b^2} \sum_{m=1}^{\infty} \sum_{n=1}^{\infty} n^2 W_{mn}^2 \left(y - \frac{b}{2n\pi} \sin \frac{2n\pi y}{b} \right) \left(1 + \cos \frac{2m\pi x}{a} \right) + \alpha \Delta T y \end{aligned} \quad (17)$$

Similarly, the displacements and subsequent strains and stresses can be determined. Results for plate deflections, membrane tractions and stresses are given in Figs. 10-15 for a thermal gradient of 7°C/mm . The continuous lines in the subsequent figures represent the results from the analytical model, while the broken lines represent the results from the *Vulcan* finite-element analysis, as shown in Fig. 10. Legends for the plots are given in Fig. 13 ((a) for vertical displacements, (b) for mid-plane horizontal displacements, (c) for membrane tractions and (d) for stresses).

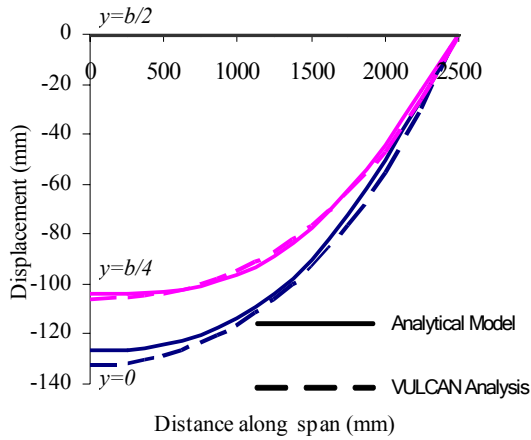


Fig 10: Elevated temperature vertical displacements

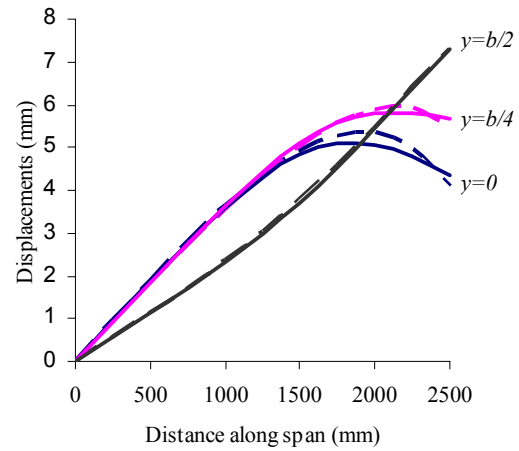


Fig 11: Elevated temperature in-plane displacements

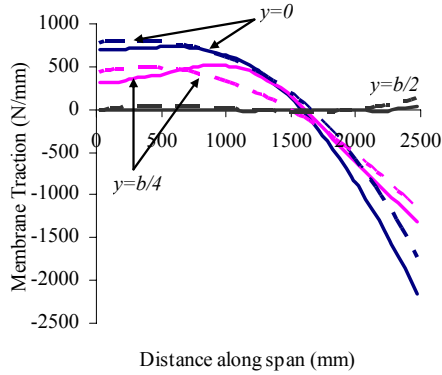


Fig 12: Elevated temperature membrane tractions across the span

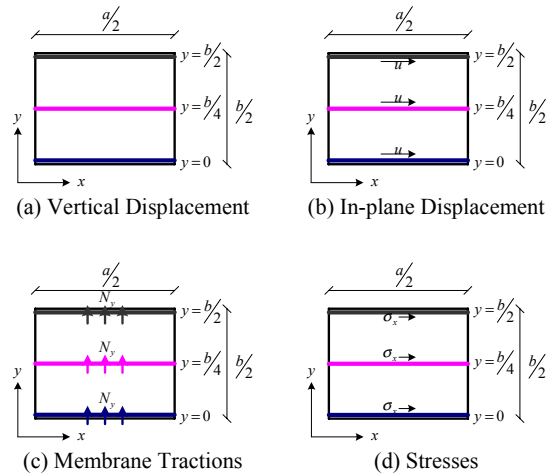


Fig 13: Elevated temperature legends

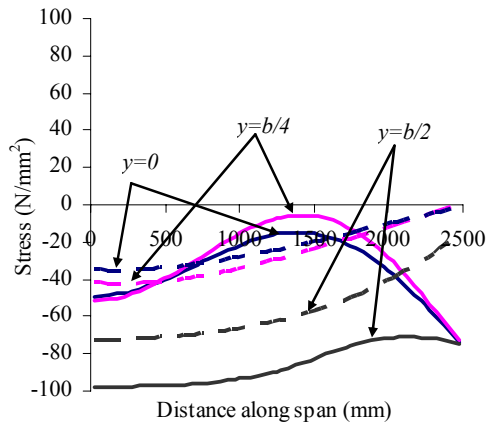


Fig 14: Elevated temperature bottom layer stress distribution

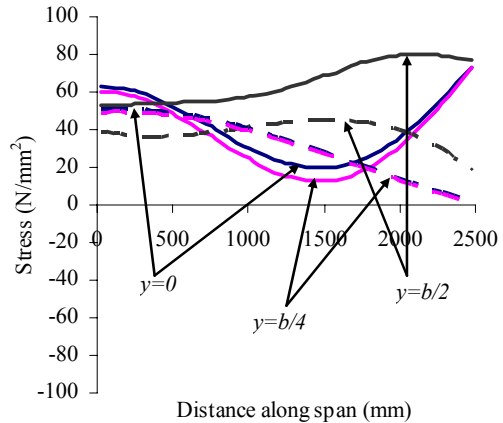


Fig 15: Elevated Temperature Top Layer Stress Distribution

5. DISCUSSIONS

The analytical solutions and the *Vulcan* results are in very good agreement. Fig.4 shows the ambient-temperature central vertical deflection as 124mm, which is greater than the thickness of the slab, confirming the tensile membrane mechanism. The horizontal displacements (Fig. 5) emphasize the existence of a tensile area with a surrounding ring of compression. The central portion of the plate is stretched, but the edges and corners are pulled-in towards the centre of the slab, creating the ring of compression. A plot of membrane forces per unit length across the span is shown in Fig. 6. Tensile forces are observed in the middle of the slab, and these decrease in magnitude and eventually become compressive forces towards the edge. Across the boundary, membrane tractions are zero in accordance with the set boundary conditions. Fig. 8 and Fig. 9 confirm the presence of tensile and compressive stresses, in the bottom and top layers respectively, of a plate loaded at ambient temperature. It also shows the compressive stresses that develop along the mid-section of the edge due to the inward movement of the edge; this stress reduces in magnitude along the edge, towards the corners.

The through-depth temperature expression used (Equation 14) combines a mean temperature increase with a thermal gradient. The thermal gradient induces vertical deflections, and as Fig. 10 shows, the central deflection from the elevated-temperature analysis (126mm) also exceeds the thickness of the plate, indicating the presence of tensile membrane action. A uniform thermal expansion would have produced horizontal displacements of 8.75mm along the edge of the plate, but stretching of the mid-regions of the plate and the corresponding inward movement of the edges and corners generate the displacements shown in Fig. 11. In similar fashion to the ambient-temperature case, membrane tractions are plotted in Fig. 12. These also show the presence of tensile forces in the centre of the plate with compressive forces along the periphery. When an unloaded slab is exposed to heat on its bottom surface, thermal expansion of hotter lower layers against cooler upper layers creates compressive stresses in the lower layers and tensile stresses in the upper layers (Fig. 14 and Fig. 15).

For the central region of the plate, where tensile membrane forces are present, the method gives a good prediction of the stresses, but fails to do so for the area where in-plane stresses are controlled by the presence of the compressive ring. An investigation into this behaviour, conducted on uniformly heated plates, revealed that, due to the limitations of the Rayleigh-Ritz approach, complete convergence was only attainable with excessively high numbers of strain and vertical displacement expressions. An automatic solution procedure has proved very difficult to implement, as the procedure could not be transformed into a numerical process.

6. CONCLUSION

The method has shown that differential thermal expansion through the depth of a simply-supported slab can induce a considerable amount of tensile membrane action. It has also proved that it is not necessary to design edge beams and their connections to provide lateral restraint as the compressive ring develops, irrespective of the horizontal restraint along the boundary. The next step in the project is to investigate the influence of these thermal gradients and restraints along the boundary on the development of membrane action. It is hoped that this research will help establish the true mechanism of tensile membrane action in composite slabs at high temperatures, so that the necessary steps can be taken to harness this self-sustaining load-carrying mechanism.

7. REFERENCES

- [1] Newman, G. M., Robinson, J. T., Bailey, C. G. "Fire Safe Design: A New Approach to Multi-Storey Steel-Framed Buildings." SCI Publication P288 (2000)
- [2] Bailey C. G. "Membrane of slab/beam composite floor systems in fire". Engineering Structures 26 (2004), pp1691-1703
- [3] Bailey C. G. "Design of Steel Structures with Composite Slabs at the Fire Limit State. Final Report prepared for the Department of the Environment, Transport and the Regions, and the Steel Construction Institute, Report No. 81415." The Building Research Establishment (2000)
- [4] Bailey C. G. "Membrane action of unrestrained lightly reinforced concrete slabs at large displacements." Engineering Structures 23 (2001), pp470-483
- [5] Cameron N. J. K., Usmani A. S., "New design method to determine the membrane capacity of laterally restrained composite floor slabs in fire. Part 1: Theory and method." The Structural Engineer 83 (2005), pp28-33
- [6] Cameron N. J. K., Usmani A. S., "New design method to determine the membrane capacity of laterally restrained composite floor slabs in fire. Part 2: Validation." The Structural Engineer 83 (2005), pp34-39
- [7] Foster S. J., Bailey C. G., Burgess I. W., Plank R. J. "Experimental behaviour of concrete floor slabs at large displacements." Engineering Structures 26 (2004), pp1231-1247
- [8] Foster S. J., Burgess I. W., Plank R. J. "Investigation of Membrane Action in Model scale slabs subjected to high temperatures." Proceedings of the 4th International conference of Advances in Steel Structures, Vol. II, Shanghai, China (2005), pp933-940
- [9] Huang Z., Burgess I. W., Plank R. J. "Modelling Membrane Action of Concrete Slabs in Composite Buildings in Fire. I: Theoretical Development." ASCE Journal of Structural Engineering 129 (8) (2003), pp1093-1102
- [10] Huang Z., Burgess I. W., Plank R. J. "Modelling Membrane Action of Concrete Slabs in Composite Buildings in Fire. II: Validations." ASCE Journal of Structural Engineering 129 (8) (2003), pp1103-1112
- [11] Park, R. and Gamble, W. L. "Reinforced Concrete Slabs." Second Edition, John Wiley and Sons Ltd. (2000)
- [12] Timoshenko, S. and Woinowsky-Krieger S. "Theory of Plates and Shells." International Student Edition, Second Edition, McGraw-Hill Book Company, Inc. (1959)
- [13] Berger, H. M. "A New Approach to the Analysis of Large Deflections of Plates." Journal of Applied Mechanics, Volume 22 (1955), pp465-472
- [14] Nowinski, J. L. and Ohnabe, H. "On certain inconsistencies in Berger equations for large deflections of elastic plates." International Journal of Mechanical Sciences, volume 14 (1958), pp165
- [15] Banerjee, B. and Datta, S. "A new approach to an analysis of large deflections of thin elastic plates." International Journal of Non Linear Mechanics, volume 16 No. 1 (1981), pp47-52
- [16] Boresi, A. P. and Turner, J. P. "Large Deflections of Rectangular Plates." International Journal of Non Linear Mechanics, volume 18 No. 2 (1983), pp125-131
- [17] Johns, D. J. "Thermal Stress Analyses." Pergamon Press Ltd. (1965)



BEHAVIOUR OF THE UHPFRC BSI[®] AT HIGH TEMPERATURES

J.C. MINDEGUIA ¹, M. DHIER SAT ², A. SIMON ³ and P. PIMIEN TA ⁴

ABSTRACT

This paper presents the results of an experimental study carried out at high temperatures on an industrial Ultra High Performance Fiber Reinforced Concrete, the BSI[®], developed by the firm Eiffage TP. This material reaches a compressive strength of about 150 MPa thanks to optimized techniques of formulation.

Tests of determination of the thermal properties were carried out at temperatures from 20°C to 914°C. We present the procedure of these tests as well as the evolution with the temperature of thermal diffusivity, thermal conductivity and the specific heat of material.

Hot compression tests were carried out thanks to an original equipment developed at the CSTB. We present the results obtained for temperatures going from 20°C to 600°C. We analyze the stress/strain curves, the evolution of compressive strength and modulus of elasticity with temperature. We also present the curves of thermal strain of the material, highlighting the original behaviour of this particular concrete with the temperature.

Lastly, we present the methods and the results of fire tests carried out on samples of various geometries. These tests show the good behaviour of material with temperature.

1. INTRODUCTION

The recent developments in the field of superplasticizers, the improvement of mixture methodology and the use of new fillers have led to a spectacular evolution of concrete performances. As result of this progress, UHPFRC (Ultra High Performance Fibre Reinforced Concrete) makes it possible to change the methods of structures design. UHPFRC differs

¹ PhD Student, University of Pau et des Pays de l'Adour, LaSAGEC², 64600 Anglet, France,
email: jc.mindeguia@cstb.fr

² Civil Engineer, Eiffage TP, 93330 Neuilly S/ Marne, France,
email: mdhiersat@construction.eiffage.fr

³ Project Manager, Eiffage TP, 93330 Neuilly S/ Marne, France,
email: asimon@construction.eiffage.fr

⁴ PhD, Vice Division Manager, Centre Scientifique et Technique du Bâtiment, 77447 Marne la Vallée, France,
email: pimienta@cstb.fr

from High and Ultra High Performance Concrete by his higher compressive strength ($\geq 150\text{MPa}$), and by the systematic use of fibres which ensures that the material is not brittle, modifying by the way the conventional requirements for passive and/or active reinforcement [1], [2]. The mixture of UHPFRC consists in high binder content and in special selection of aggregates.

Sudden exposure to high temperatures strongly modifies the behaviour of concrete. To increase the level of safety for concrete structures in the event of fire, design calculations have to take the dependence of the thermo-mechanical properties with temperature into account. Furthermore, a lot of researches have shown that concrete could present a risk of thermal instability with fast rise in temperatures. This phenomenon is commonly called spalling. Moreover, high strength concretes seem to have an increased susceptibility to this instability [3]. Nowadays, big scale fire tests are still the most reliable way to predict the risk of spalling.

This paper presents the results of an experimental study on the temperature-dependant behaviour of the BSI®, an industrial UHPFRC developed by the company EIFFAGE. A particular formula of this material has been studied, consisting in a hybrid mixture of steel fibres and organic fibres (polypropylene fibres) [4].

Thermal properties have been determined on prismatic samples of dimension $165\text{ mm} \times 100\text{ mm} \times 40\text{ mm}$. The testing equipment is inspired by the hot wire method, which is frequently used in the field of dense refractory products. This type of test gives us hot thermal properties, more representative than residual properties. We present the temperature-dependence of the different thermal properties (thermal conductivity $\lambda(T)$, thermal diffusivity $a(T)$ and volumetric heat capacity $\rho C(T)$) for temperatures going from 20°C to 914°C .

An original equipment based on a high-temperature furnace and a system of strain measurement has been used. It allowed us to carry out uniaxial compressive tests on $104\text{ mm} \times 300\text{ mm}$ cylindrical samples at temperatures from 20°C to 600°C [5]. The samples have been maintained at high temperature during the test. We present the evolution of the stress/strain curves, the compressive strength and the modulus of elasticity with temperature. The difference between the samples weight before and after the test, gives us the evolution of the density with temperature. The equipment made it possible to measure the free thermal strain of the concrete up to a temperature of 600°C . By this way, we have observed an unusual thermal dilatation of concrete, i.e. non monotonic.

At last, samples of different shapes and dimensions have been exposed to fire test. The high rate of heating applied was the one of the HCM curve (Hydrocarbon Modified). This type of curve, which is representative of a tunnel fire, allowed us to reach a temperature of 1300°C in a few minutes. During tests, none of the exposed samples showed spalling and the visual appearance of the concrete remained the same up to temperature of about 950°C . At higher temperatures, we observed a brown colouration of steel fibres.

2. SAMPLES PREPARATION

In order to obtain a Ultra High Performance concrete that is able to resist to severe thermal solicitations (ISO fires, HC, HCM, RWS) the nominal formula of the BSI® was derived by incorporating polypropylene fibres. A formula called "fire" was defined for the present study and its mix proportions are given in table 1.

Tab. 1 : Mix proportions of BSI®.

Compound	[Kg/m ³]
CERACEM® Premix	2355
Superplasticizer SIKA	44.6
Water	216
Steel fibres 20/0.3	195
Polypropylène fibres	3

For this study, a SKAKO mixer of capacity 125 liters was used to make the following samples:

Thermal properties tests

2 prismatic samples of 165mm x 100mm x 40mm, stored at 20°C and 50%HR.

Mechanical properties tests

- 12 cylindrical samples of Ø10.4 cm x 30 cm, stored at 20°C and 50%HR, for the hot compressive tests.
- 3 cylindrical samples of Ø11 cm x 22 cm stored in water (French standard) for the 28 days compressive strength at 20°C ($R_{c28moy} = 153$ MPa and $E_{i28moy} = 55.2$ GPa).
- 3 cubic samples of 10x10x10 cm³ stored in water at 20°C, for the 28 days compressive strength at 20°C.

HCM180 Fire test

- 8 cylindrical samples of Ø11 cm x 22 cm
 - 4 placed in a tight envelope from unmoulding and stored at 20°C
 - 4 stored at 20°C and 50%HR and subjected to a heat treatment
- 12 cubic samples of 10x10x10 cm³
 - 6 placed in a tight envelope from unmoulding and stored at 20°C
 - 6 stored at 20°C and 50%HR and subjected to a heat treatment

The heat treatment evoked above is divided in three stages: a first stage of rise in temperature of 20°C until 80°C at a heating rate of 20°C/h, a second stage of maintain at 80°C during 48h and finally a natural cooling until 20°C. During these three stages the samples are maintained in a wet envelope in order to avoid their natural desiccation with 20°C. At the end of cooling the samples are stored again at 20°C and 50%HR.

The pre-heating aims to accelerate the maturation of the concrete. Fire tests on the dried and wet samples allow us to study the fire behaviour of concrete structure in different conditions of humidity.

3. EXPERIMENTAL SETTINGS

3.1 Thermal properties

The procedure of these tests are inspired from the norm NF EN 993-15 “Methods of dense shaped refractory products – Part 15: Determination of thermal conductivity by the hot-wire (parallel) method”.

The hot-wire method is a method of dynamic measurement based on the determination of the rise in the temperature according to time in a given point and a specified distance of a linear thermal source placed between two prismatic samples of 165 mm x 100 mm x 40 mm.

The samples are heated in a furnace (fig. 1) and are maintained at this temperature. A later local heating is provided by a linear electric conductor (the hot wire) embedded in the sample. This conductor transports an electrical current of stable known power in the time and over the entire length of the sample. A thermocouple is placed at a specified distance of the hot wire, the branches of the thermocouple being parallel with the wire.

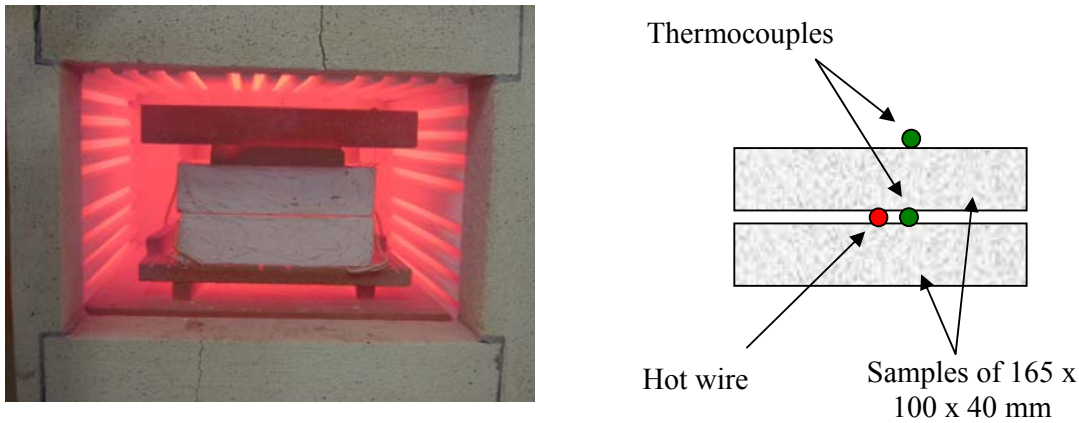


Fig. 1 – Hot thermal tests apparatus.

Thermal conductivity $\lambda(T)$ and thermal diffusivity $a(T)$ are assessed by inverse methods from the expression of the heating production by the hot wire and from the heat transport equation in the sample. As we can determine the density of the concrete ρ before and after the different test, we are able to calculate the specific heat $C(T)$ thanks to the equation (1).

$$a = \frac{\lambda}{\rho \cdot C} \quad (1)$$

Thermal properties have been assessed at the following temperatures: 23°C, 150°C, 302°C, 451°C, 602°C and 914°C. At the time of the tests, the samples were 49 days old.

3.2 Mechanical properties

The testing apparatus is composed of a cylindrical electric furnace which can contain cylindrical samples of 104 mm x 600 mm (fig. 2). The heating is ensured by 3 radiant rings laid out along the longitudinal axis of the furnace. These rings are controlled independently by means of 3 thermocouples (type K) in order to reduce as well as possible the heat gradient inside the furnace. The unit is controlled electronically, which makes it possible to fix the heating rate of the samples.

The longitudinal strains of the sample are determined thanks to an extensometer equipped with three LVDT sensors.

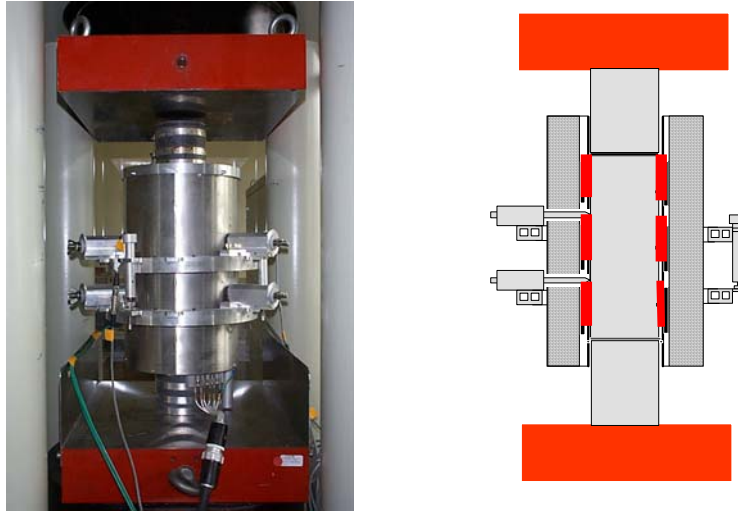


Fig. 2 – Hot mechanical tests apparatus.

The tests are inspired by the RILEM recommendations [7]. Samples were heated at a rate of 1°C/min until the following temperatures: 90°C, 150°C, 300°C, 450°C and 600°C. Once the test temperature reached, samples are maintained at this temperature during one hour (2 hours for 90°C) in order to insure a good homogeneity of the thermal field in the sample. During the heating phase, the thermal strain of the samples was measured.

At the end of the stabilization stage of temperature, the samples were compressed until rupture by the plates of the press. We deduced from these tests the stress/strain curves and the compressive strength of material according to the temperature.

3.3 HCM Fire test

We tested the fire behaviour of samples of various dimensions in a gas-burners furnace of the CSTB. This furnace, of dimensions 3 m x 4 m x 2 m, makes it possible to reproduce the HCM curve of rise in temperature. This thermal scenario, fixed by the equation (2), reaches the temperature of 1000°C in only 2 minutes (Fig. 3).

$$T = 1280(1 - 0,325e^{(-0,167t)} - 0,675e^{(-2,5t)}) + 20 \quad (2)$$

T: temperature in °C.

t: time in min.

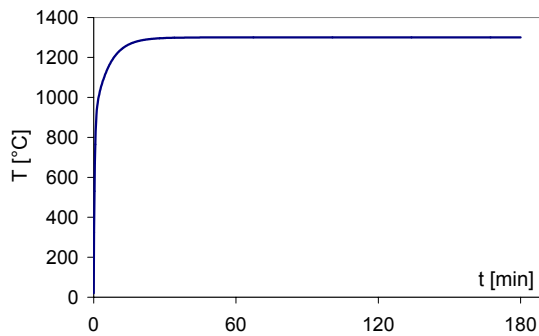


Fig. 3 – HCM curve and global view of the gas-burners furnace.

The 20 samples were divided in two identical series and each one was exposed to a HCM180 fire, with an 8 days interval. This measure was adopted in order to check the repeatability of the results.

4. RESULTS AND DISCUSSION

4.1 Density

First of all we present the results of density. The density at 20°C was given by measuring the mass of 11 x 22 cm samples. The same samples were weighed after HCM test to determine their density at 1300°C. Thanks to the hot compression tests, we were able to calculate the density of the cylindrical samples at the various temperatures (after compression test). On figure 4, we present the evolution of the densities according to the temperature as well as the evolution of the relative densities with the temperature in comparison with the values of the Eurocode 2 [8]. We precise that the thermal expansion of the samples was not taken into account for the calculation of the densities.

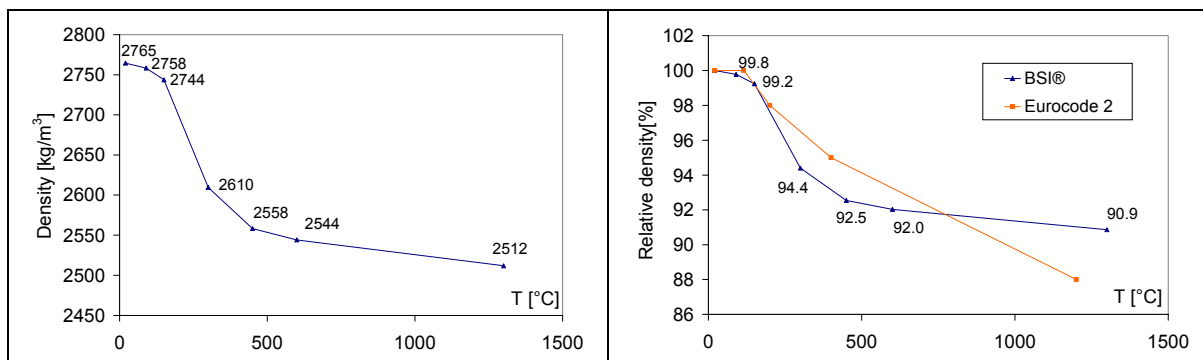


Fig. 4 – On the left, evolution of the densities according to temperature. On the right, evolution of the relative densities according to temperature.

The density at 20°C is relatively high. This material has a very compact matrix and thus has a high density. Between 90°C and 450°C, the loss of density is approximately 8% because of the important water departure in this range of temperature. Between 600°C and 1300°C, the density decreases only of 1% because practically all the water of material has already evaporated. The evolution of the relative density with the temperature is relatively close to that defined by Eurocode 2.

4.2 Thermal properties

We present on figure 5 the results of the thermal properties tests. The results are presented in the form of curve of evolution with the temperature. On each figure, we present the values defined by the Eurocode 2 and the by the French Technique Document DTU 92-701 [9]. The specific heat was given thanks to the values of density coming from the fire and mechanical tests. The value at 914°C was calculated by linearly extrapolating the values between 600°C and 1300°C.

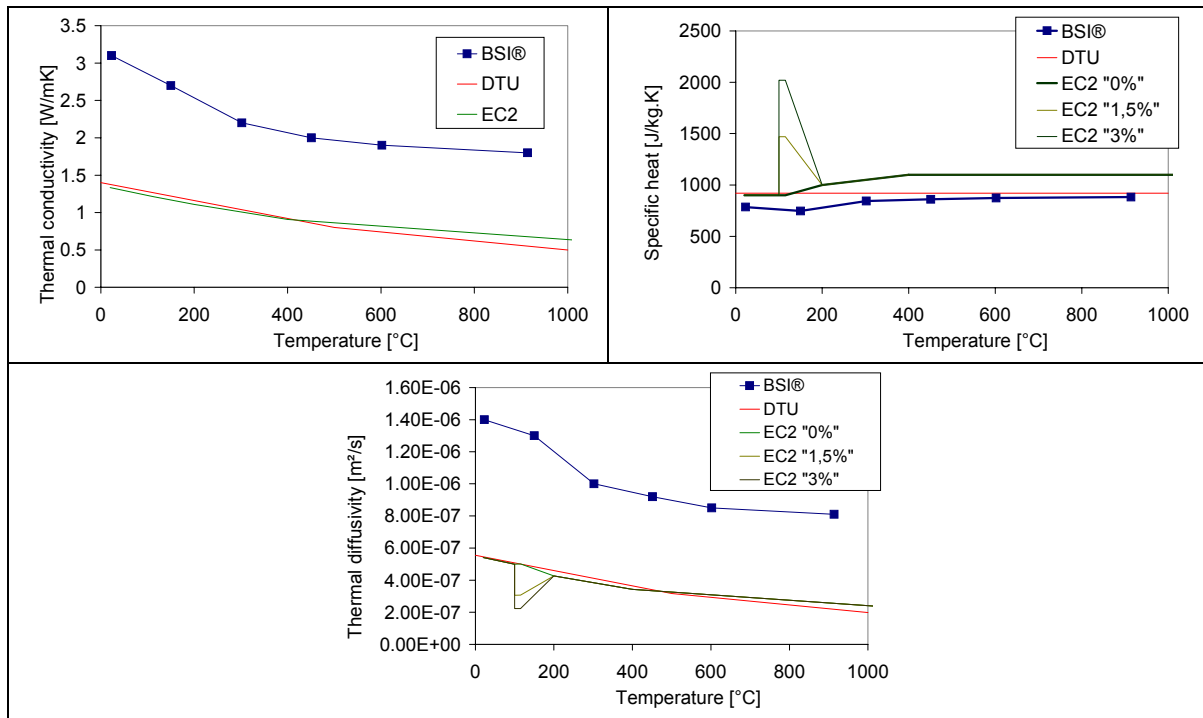


Fig. 5 – Evolution of the thermal properties according to temperature.

According to the results of figure 5, we can note that the material has a thermal conductivity 2 times higher than the values defined by the normative documents. Two reasons can explain this: the presence of steel fibres in this concrete (the thermal conductivity of steel is approximately 50 times higher than that of a traditional concrete) and the strong compactness of material. The evolution of the thermal conductivity of material with the temperature seems to follow the same law as the evolution of the normative documents.

The specific heat of material is comparable with the values defined by the normative documents. However, it does not have a peak of values close to 100°C, as it is defined in the standards. This peak corresponds to the important consumption of energy by water evaporation. This behaviour can be explained by the very small quantities of interstitial water present in this material. It is to note that the various samples lost only approximately 0,5% of their mass after a heating at 80°C during 48h.

Finally, we notice that this material diffuses twice more heat than an ordinary concrete, thus reducing the heat gradients within material during the heating.

4.3 Mechanical properties

We present in the table 2 the values of the compressive strengths obtained at 20°C on cylindrical samples of dimensions 110 x 22 mm and 104 x 300 mm and on cubic samples of 100 x 100 x 100 mm. The last column of the table presents the ratios of the different compressive strength that we obtained in comparison with the values obtained on the 110 x 220 mm samples. The modulus of elasticity was only calculated on the cylindrical samples.

Tab. 2 : compressive strength and modulus of elasticity at 20°C.

$f_{c20^{\circ}\text{C}}$ [MPa]	n°1	n°2	n°3	Mean	Ratio / 110x220 mm
110 x 220mm	151,82	151,35	155,26	152,81	1
104 x 300mm	147,45	148,40	/	147,93	0,97
100 x 100 x 100mm	156,30	176,42	160,32	164,35	1,08
$E_{20^{\circ}\text{C}}$ [GPa]	n°1	n°2	n°3	Mean	Ratio / 110x220 mm
110 x 220mm	54,34	55,72	55,53	55,20	1
104 x 300mm	50,22	50,18	/	50,20	0,91

Results of the hot compression tests carried out on the 104 x 300 mm cylinders are presented on figure 6. Two samples were tested at each temperature. The figure shows the curves presenting the evolution of the strains according to the stress applied to the sample for the various temperatures.

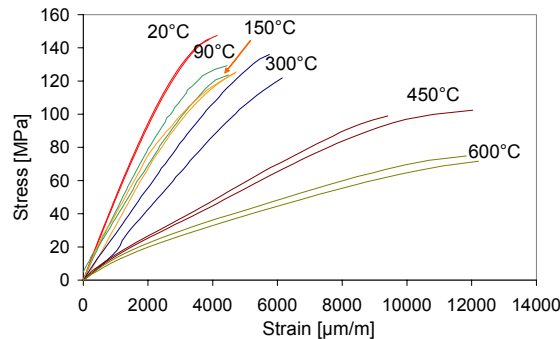


Fig. 6 – Stress/strain curves for the different temperatures.

We can observe that the rigidity of material decreases with the rise in temperature. However, at 150°C, the material is as rigid as at 90°C. In addition, we note that the strain reached at rupture grows with the rise in temperature. This can be explained by additional induced strain by crack closing. These cracks are generated during the heating phase because of the thermal incompatibilities between the cement paste and the aggregates..

The compression tests were carried out until rupture of the sample. We measured the stress applied to the sample at the instant of the failure. That allows us to present on figure 7

the compressive strength of the material according to temperature. Absolute values and relative values are gathered in table 3.

Tab. 3 : compressive strengths and relative strengths obtained at the different temperatures.

f_{cT} [MPa]	n°1	n°2	Mean	Mean relative value $f_{cT} / f_{c20^{\circ}\text{C}}$ [%]
20°C	147,45	148,40	147,93	100,00
90°C	129,39	124,11	126,75	85,68
150°C	126,75	125,82	126,29	85,37
300°C	138,50	123,95	131,23	88,71
450°C	100,96	102,47	101,72	68,76
600°C	75,60	72,64	74,12	50,10

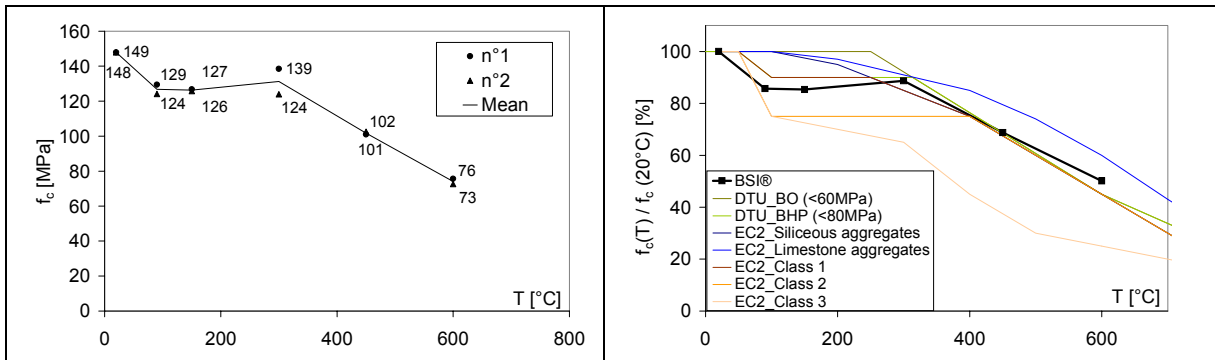


Fig. 7 – On the left, evolution of the compressive strengths according to temperature. On the right, evolution of the relative strengths according to temperature and comparison with normative documents.

We observe on figure 7 a weak dispersion of the results of compressive strengths. The strength of material at 20°C is about 150 MPa, which is a main property of the UHPFRC. Then the strength presents a 15% decrease at 90°C. Between 90°C and 300°C, compressive strength does not decrease and presents even a light increase of about 5%. From 300°C, compressive strength decreases in a linear way with the rise in temperature. At 600°C, the material lost half (50%) of its initial compressive strength.

We present on figure 7 the evolution of relative strengths according to temperature. These relative strengths are defined as the ratio between the value obtained at the test temperature and the initial value (20°C). In spite of its high initial strength, the material is in good accordance with the values defined by the standards. The values are located between the values defined by Eurocode for a class 1 concrete ($f_c=60$ MPa) and a class 2 concrete ($f_c=80$ MPa) until the temperature of 300°C. Beyond 300°C, its behaviour meets the values defined by the DTU.

From the curves of figure 6, we calculated the modulus of elasticity of material at the different temperatures. We defined the modulus of elasticity as the ratio between the stress and the strain of the sample, for a load corresponding to 30% of the hot compressive strength. It is to note that this ratio can only be considered as an "apparent" modulus of elasticity because the mechanical behaviour of the concrete at high temperature is not elastic linear. The values of modulus of elasticity and relative modulus obtained at the various temperatures are gathered in table 4.

Tab. 4 : modulus of elasticity and relative modulus obtained at the various temperatures.

E_T [GPa]	n°1	n°2	Mean	Mean relative values $E_T / E_{20^\circ\text{C}}$ [%]
20°C	50,22	50,18	50,20	100,00
90°C	41,72	37,21	39,47	78,62
150°C	40,70	32,70	36,70	73,11
300°C	27,86	20,97	24,42	48,64
450°C	12,95	12,03	12,49	24,88
600°C	11,11	9,61	10,36	20,64

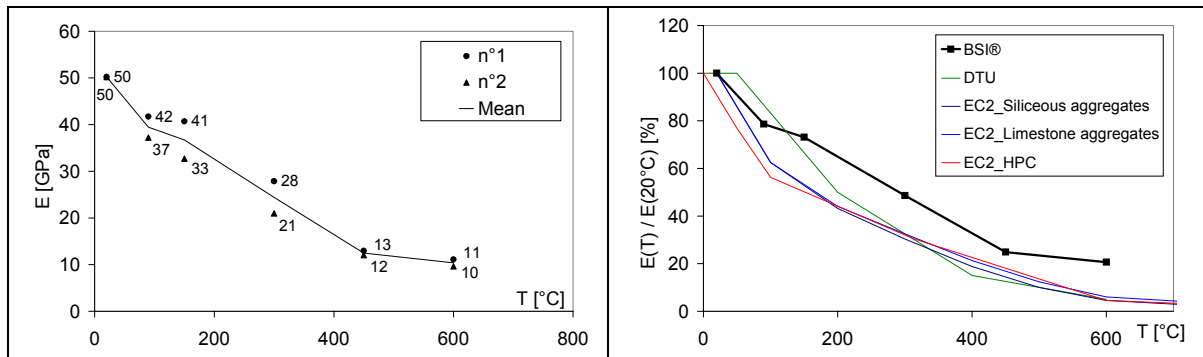


Fig. 8 – On the left, evolution of the modulus of elasticity according to temperature. On the right, evolution of the relative modulus of elasticity according to temperature and comparison with normative documents.

Figure 8 shows that the modulus of elasticity decreases in a relatively linear way with the rise in temperature. At 20°C, the modulus of elasticity is about 50 GPa and reaches at 600°C the value of 10 GPa, which represents a loss of rigidity of material of about 80%.

We also notice that in spite of the high strength of the material, the loss of rigidity with temperature is less important than the loss defined by the standards.

During the heating phase before each compression test, we measured the thermal strain of the samples. We present on figure the 9 curves obtained at the various temperatures of test. We also present the comparison of the mean thermal strain curve with the values envisaged by the normative documents.

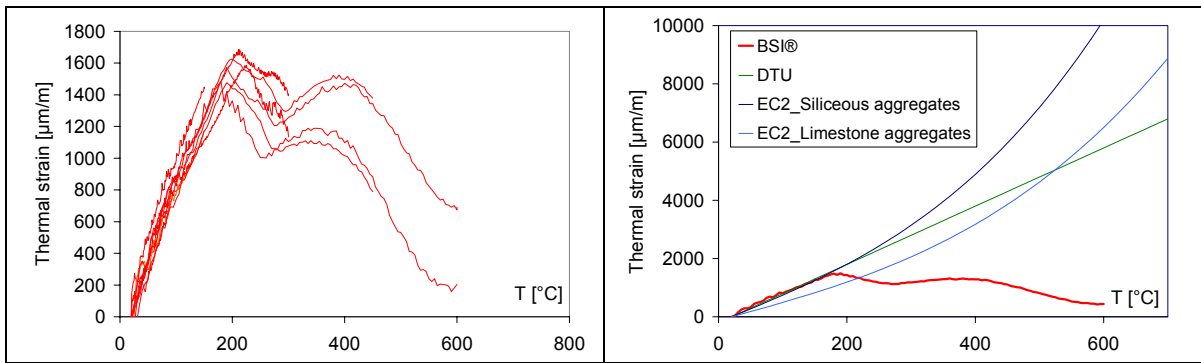


Fig. 9 – On the left, thermal strain during the heating phase of the hot compression tests. On the right, comparison of the mean curve with the normative documents curves.

We observe an original thermal behaviour. Indeed, the material first of all expands in a relatively linear way until 190°C. Beyond this temperature, the material behaviour brutally changes and the concrete shrinks until 275°C before expanding again between 275°C and 390°C. At last, the material behaviour changes once again and the concrete shrinks until the temperature of 600°C.

This behaviour is in good accordance with thermal strain defined by the standards until the temperature of 190°C. Beyond this temperature, the measured thermal strains strongly deviates from standards values because of the original behaviour previously described.

4.4 HCM Fire test

On figure 10, we present the visual aspect of one of the samples tested with HCM180 fire. Visual observations of the samples after HCM180 tests bring the following remarks:

- all the samples surfaces present a very marked brown colouration (fig. 10). This colouration appears at a temperature near 950°C,
- none of the samples that were pre-heated in oven for accelerated maturation showed any effect of spalling,
- some local fractures appear on certain 28 days samples which were stored in water,
- a great majority of steel fibres disappeared from the surface of the samples leaving only the print of their volume (fig. 10).

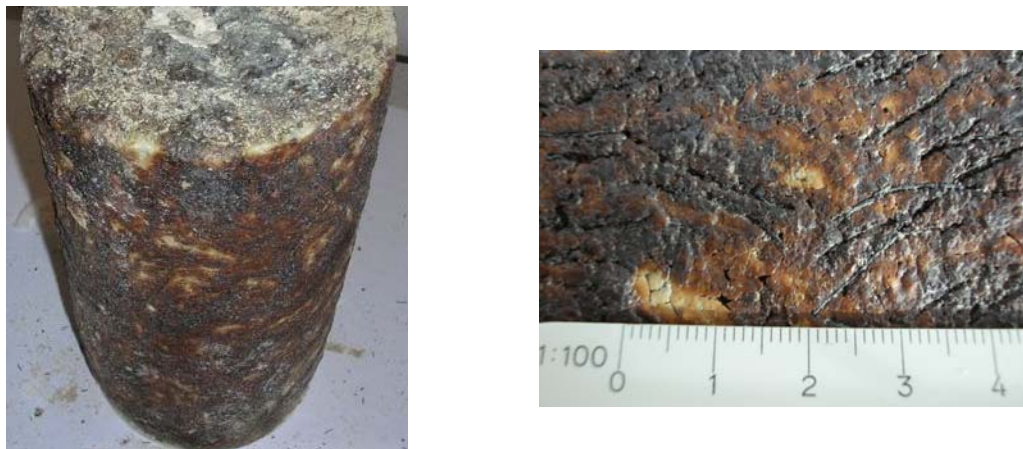


Fig. 10 – On the left, global view of a sample after HCM test. On the right, zoom on the sample surface.

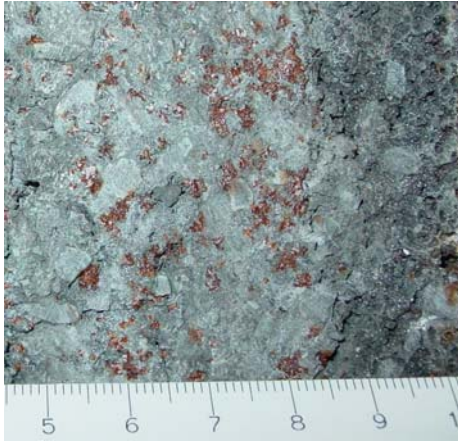


Fig. 11 – View of half of a vertically sawn sample.

To try to understand the origin of the surface colouration, which closely looks like corrosion, a cylinder was sawn vertically (fig. 11). We could observe that this colouration appears only at the sample surface, that the steel fibres had disappeared on a depth from approximately 20mm and that on this same layer the concrete had a similar porous morphology as a volcanic rock.

Beyond this superficial layer, the concrete keeps a dense structure and fibres are always present. It should be noted that the colouration of fibres is here undoubtedly the fact of sawing under water.

All the samples were weighed before and after the fire test. This reveals that on average, an 11x22 mm cylinder with accelerated maturation loses 9.10% of its mass during HCM180 fire. After the period of maturation, this cylinder had already lost 0.45% of its mass. Those stored in water lost on average 10.7% of their mass after HCM180 test.

5. CONCLUSIONS

The present study allowed us to determine several characteristics of concrete BSI® at high temperature and to check its stability under HCM fire.

This UHPFRC is a material with strong compactness and thus presents a high density at 20°C. The loss of density with temperature, because of the departure of the water, is comparable with the values defined by the standards.

Concerning thermal properties, the particularity of this material is to have a very high thermal conductivity because of its strong compactness and of the presence of steel fibres in its composition. Its specific heat and its evolution with the temperature are very close to those defined by the standards. Nevertheless, the low free water content of the material does not involve peak of specific heat around 100°C. Finally, thermal diffusivity is much more important than the one of the ordinary concretes.

The material has a very high compressive strength at 20°C. The evolution of strength and modulus of elasticity with the temperature is in good agreement with the standards. Contrary to traditional concretes, the free thermal strain of this material is non monotonous and presents sudden changes of behaviour according to the temperature. This phenomenon, still not explained today, should be analysed more deeply. This property could be favourable to the integrity of a structure subjected to fire. Indeed, the zone exposed to the fire will induce smaller strains to the rest of the structure.

Several samples of various geometries were exposed to HCM180 fire. No spalling was observed on the pre-heated samples. Certain samples stored in water presented some local fractures. For temperatures higher than 950°C, we observed on the samples surface a very marked brown colouration.

6. REFERENCES

- [1] Thibaux T., Hajar Z., Simon A., Chanut S., “Construction of an ultra high performance fiber reinforced concrete shell for the tollgate of Millau viaduct”, 6th RILEM symposium on fibre reinforced concrete, BEFIB 2004, Varenna, Italy, Septembre 2004.
- [2] Hajar Z., Simon A., Lecoindre D., Petitjean J., “Design and construction of the first ultra high performance concrete road bridges”, International symposium on ultra high performance concrete, Kassel, Germany, Septembre 2004.
- [3] Khoury G.A., "Spalling", *Course on Effect of Heat on Concrete*, International Centre for Mechanical Sciences (CISM), Udine, Italy, 9-13 June 2003.
- [4] Genes P., Alexandre F., Novarin M., Simon A., “Restructuration d’un immeuble parisien”, Revue TRAVAUX n°813, France, Novembre 2004.
- [5] Hager I., Pimienta P., "Transient thermal strains of High Performance Concretes", *Key note for Concreep7, International conference on creep, shrinkage and durability of concrete and concrete structures*, Nantes, France, 12-14 Septembre 2005.
- [6] NF EN 993-15, "Methods of dense shaped refractory products – Part 15 : Determination of thermal conductivity by the hot-wire (parallel) method", September 1998.
- [7] RILEM, "Compressive strength for service and accident conditions", Materials and structures. 28, p.410-414. 1995.
- [8] EN 1992-1-2, "Eurocode 2 : Design of concrete structures – Part1-2: General rules – Structural fire design", December 2004.
- [9] NF P 92-701, "Méthode de prévision par le calcul du comportement au feu des structures en béton", December 1993.



EXPERIMENTAL STUDY OF TRANSIENT THERMAL STRAIN AND CREEP OF AN ORDINARY CONCRETE AT HIGH TEMPERATURES

J.C. MINDEGUIA ¹, P. PIMIENTA ², I. HAGER ³, C. LABORDERIE ⁴ and H. CARRÉ ⁵

ABSTRACT

This paper presents the results of an experimental study carried out on an ordinary concrete. An original equipment allowed us to carry out compression tests at high temperatures by measuring the longitudinal and radial strains of the samples.

A first series of hot compression tests allowed us to determine the stress/strain curves of the material at the various temperatures as well as the evolution of compressive strength with the temperature.

Short-term creep tests were carried out at various temperatures. The recovery of material was also measured. The influence of certain parameters was studied: heating rate and preheating.

At last, Thermal Strain Under Load tests allowed us to calculate the Transient Thermal Strains (TTS) of the material. The influence of certain parameters on the TTS was studied: heating rate, preheating.

¹ PhD Student, University of Pau et des Pays de l'Adour, LaSAGeC², 64600 Anglet, France,
email: jc.mindeguia@cstb.fr

² PhD, Vice Division Manager, Centre Scientifique et Technique du Bâtiment, 77447 Marne la Vallée, France,
email: pimienta@cstb.fr

³ PhD, Lecturer, Cracow University of Technology, Kraków, Poland,
email : mailto:hager@imikb.wil.pk.edu.pl

⁴ PhD, Professor, Director of laboratory, University of Pau et des Pays de l'Adour, LaSAGeC², 64600 Anglet, France, email : christian.laborderie@univ-pau.fr

⁵ PhD, Lecturer, Director of Engineer School ISA-BTP, University of Pau et des Pays de l'Adour, 64600 Anglet, France, email : helene.carre@univ-pau.fr

1. INTRODUCTION

Concrete is a material commonly used in structures which present high risks of blaze: tunnels, nuclear plants, nuclear waste storage zones or tall buildings. Sudden exposure to high temperatures strongly modifies the behaviour of concrete, and happens even at low heating rates. At micro-scale level, many physico-chemical phenomena take place: internal micro-cracking related to thermal mismatch between hardened cement paste and aggregates, dehydration of C-S-H and C-H, phase change of some types of aggregates (e.g. quartz), mass transfer (liquid water, vapour and dry air), heat transfer, ...[1] At macro-scale level, these fully coupled mechanisms involve a progressive loss of the material stiffness with the temperature and a non-linear temperature-dependence of the compressive strength. Furthermore, a lot of researches have shown that concrete structures could present a risk of thermal instability with fast rise in temperatures. This phenomenon is commonly called spalling [2]. Thus, induced thermal damage can seriously affect the stability of the structure. Therefore, good understanding of the concrete behaviour with high temperatures is needed in order to increase the level of safety for concrete structures in the event of fire.

Among the properties of concrete at high temperatures, Transient Thermal Strain (TTS) seems to be an important mechanism of the structural behaviour when exposed to fire. This phenomenon occurs in conditions very close to those of a structure during blaze. Indeed, we only observe it when the temperature is applied on mechanically loaded elements (e.g. column or wall). TTS is an additional strain which appears during non-stationary heating of concrete maintained at a constant load. In certain cases, TTS, which compensates the free thermal strain, can relax mechanical stresses induced by temperature increase. According to several authors, total strain in a concrete element can be written as the sum of different components : stress-dependant strain, which must take into account the loss of stiffness of the material with temperature, free thermal strain, creep strain, which is mostly activated at high temperatures, and Transient Thermal Strain [3], [4], [5], [6]. Different studies have shown that the TTS is dependent on several parameters: loading rate, nature of aggregates, free water content, heating rate and heating scenario. Moreover, the irreversibility of the phenomenon has been observed, i.e. it does not appear during the cooling phase [7].

This paper presents the results of an experimental study on the temperature-dependant behaviour of an ordinary concrete (compressive strength of about 30 MPa). An original equipment based on a high-temperature furnace and a system of strain measurement has been used. It allowed us to carry out tests on 104 mm × 300 mm cylindrical hot samples. The technique of measuring was inspired by the RILEM recommendations [8] and is completed by a new system of radial strains measurement.

A first series of hot compression tests has been carried out. We present the evolution of the stress/strain curves and the compressive strength with temperature from 20°C to 600°C. During the heating phase, the equipment made it possible to measure the free thermal strain of the concrete up to a temperature of 600°C.

Steady-state creep tests have been carried out at different temperatures (from 20°C to 400°C) at a constant load of 40% of the compressive strength. It confirmed the fact that creep is rapidly activated at high temperatures. The influence of the heating rate and the heating scenario on the creep strain activation has been studied. During these tests, creep recovery has been assessed.

Afterwards, samples were heated under constant load of 40% of their compressive strength. It allowed us to measure Transient Thermal Strain up to a temperature of 400°C. The influence of the heating rate and the heating scenario on TTS has been studied.

2. SAMPLES PREPARATION

We chose to carry out this experimental study on ordinary concrete samples of dimensions 104 mm x 300 mm. The length on diameter ratio was selected to reduce the end effects (particularly cooling of the sample). The samples were grounded in order to guarantee a good orthogonality of their end surfaces with the vertical axis.

E/C concrete ratio was equal to 0.54 and G/S ratio to 1.24 in order to obtain an ordinary concrete. The aggregates used were limestone. 28 days compression strength, assessed on 16 mm x 32 mm cylinders stored in water, reached the value of 45.4 MPa. The density of this concrete is equal to 2300 kg/m³.

The 104 mm x 300 mm samples were stored according to the RILEM recommendations [8]: storing one day in their mould before being placed 7 days in sealed bags at 20°C. The samples are then stored at 20°C and 50% of relative humidity until the date of the tests. Tests were carried out on samples at ages between 97 and 402 days.

3. EXPERIMENTAL SETTINGS

An original experimental device has been developed at the CSTB during these last years [7]. The testing apparatus consists in a cylindrical electric furnace which can contain cylindrical samples of 104 mm x 300 mm (fig. 1). The heating is ensured by 3 radiant rings laid out along the longitudinal axis of the furnace. These rings are controlled independently by means of 3 thermocouples (type K) in order to reduce as well as possible the heat gradient inside the furnace. These thermocouples are fixed on the sample surface. It is to note that the measured temperatures are surface temperatures and not core temperature as it is specified in the RILEM recommendations [8]. The unit is controlled electronically, which makes it possible to fix the heating rate of the samples. The longitudinal strains of the sample are determined thanks to an extensometer equipped with three LVDT sensors.

A new system of radial strains measurement has been developed for this study. This system consists in measuring the radial strains in three points of the sample surface thanks to three INVAR[®] rods connected to three LVDT sensors (fig. 2).

The device composed by the furnace, the measurement system (longitudinal and radial) and the sample can be placed between the plates of a hydraulic press. By this way, the various compression tests can be carried out at high temperatures.

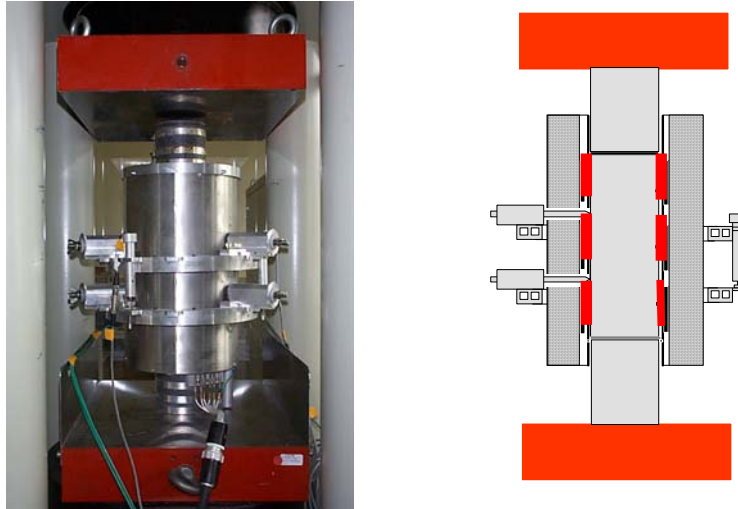


Fig. 1 – Hot mechanical tests apparatus and longitudinal strain measurement.



Fig. 2 – Hot mechanical tests apparatus with radial strain measurement.

4. EXPERIMENTAL PROGRAM

Three series of hot mechanical tests were carried out. Figure 3 illustrates the testing conditions for the three series.

I Series: hot compression tests. The samples are heated at the heating rate of $1^{\circ}\text{C}/\text{min}$ until the temperatures of 120°C , 250°C and 400°C . After a one hour stabilization stage of the temperature (2 hours for 120°C), the sample is compressed until rupture. These tests allow us to determine the stress/strain curves at various temperatures as well as the evolution of compression strength with the temperature. During the heating phase, free thermal strain of the sample is measured. Two samples were tested at each temperature.

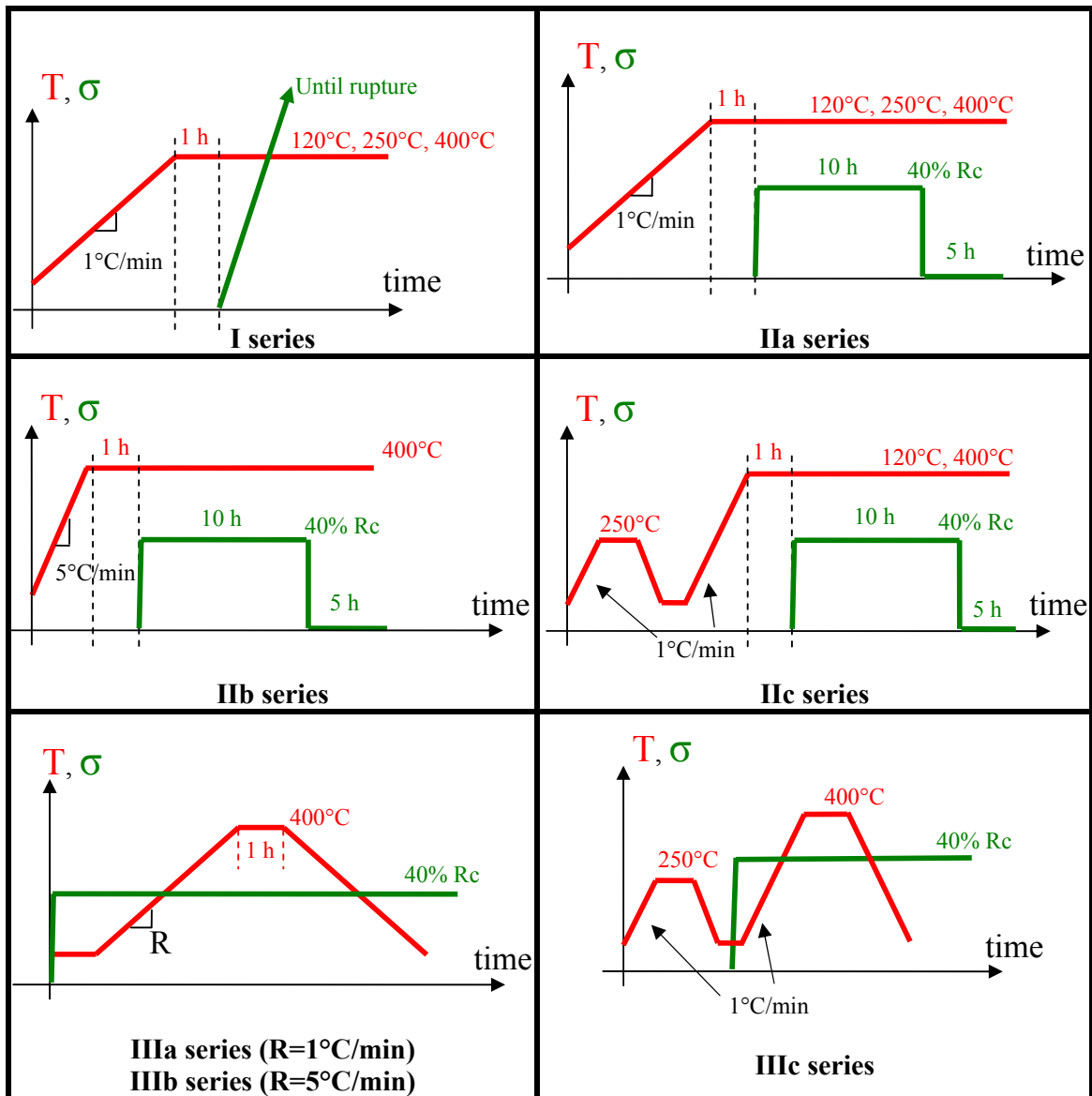


Fig. 3 – Experimental program.

IIa series: hot creep tests. The samples are heated at the heating rate of 1°C/min until the temperatures of 120°C, 250°C and 400°C. Free thermal strain of the samples is measured during this phase. After a one hour stabilization stage of the temperature, we apply during 10 hours a load of 108 kN. This load corresponds to 40% of the compression strength obtained at 20°C on the 104 mm x 300 mm samples. Following the return-to-zero loading, measurements were continued during 5 hours. One sample was tested for each temperature.

IIb series: hot creep test at 400°C in the conditions of the IIa tests after a heating phase of 5°C/min heating rate.

IIc series: hot creep tests after thermal preheating at 250°C. The samples are first heated at 250°C at the heating rate of 1°C/min then slowly cooled to 20°C. The same samples are then heated at the temperatures of 120°C and 400°C at the heating rate of 1°C/min before being tested with the IIa tests conditions.

IIIa series: thermal strain under load test. We apply a compression load of 108 kN (40% of $R_{c20^{\circ}\text{C}}$) to a sample at 20°C . Then the sample is heated at the heating rate of $1^{\circ}\text{C}/\text{min}$ under mechanical load until the temperature of 400°C . After a one hour stabilization stage of the temperature, the sample is slowly cooled to 20°C .

IIIb series: idem but with a heating rate of $5^{\circ}\text{C}/\text{min}$.

IIIc series: thermal strain under load tests after preheating at 250°C . A sample is heated with 250°C at the heating rate of $1^{\circ}\text{C}/\text{min}$ then slowly cooled with 20°C . The same sample is then tested under the IIIa test conditions.

IV series: free thermal strain test was carried out: a sample was heated until the temperature of 400°C at the heating rate of $1^{\circ}\text{C}/\text{min}$ then slowly cooled after a one hour stabilization stage of temperature.

5. RESULTS

5.1 Free thermal strain (I, II and IV series)

Figure 4 presents the various free thermal strain curves of the material recorded during the heating and cooling phases of I, II and IV series. From these results, we determined an average thermal strain curve for the heating phase and another for the cooling phase. A technique of optimization by least squares was used in order to approach these average curves with a 6th degree polynomial. The analytical curves are presented in bold line in figure 4. We can observe that longitudinal and radial strains are very close. The thermal gradient along the sample radius could explain the fact that longitudinal strains are slightly more elevated than radial strains.

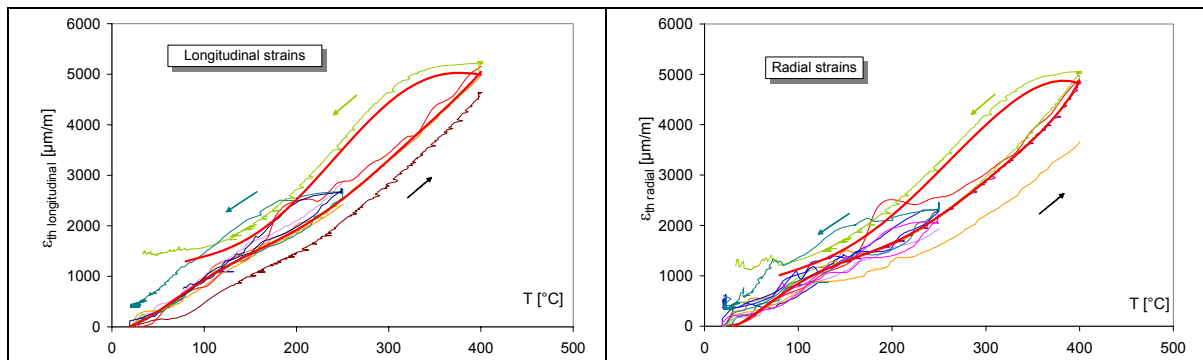


Fig. 4 – Free thermal strain. On the left, longitudinal strains. On the right, radial strains. Mean calculated thermal curves are represented by a bold line.

5.2 I series: hot compression tests

Figure 5 presents the stress/strain curves obtained at the various temperatures.

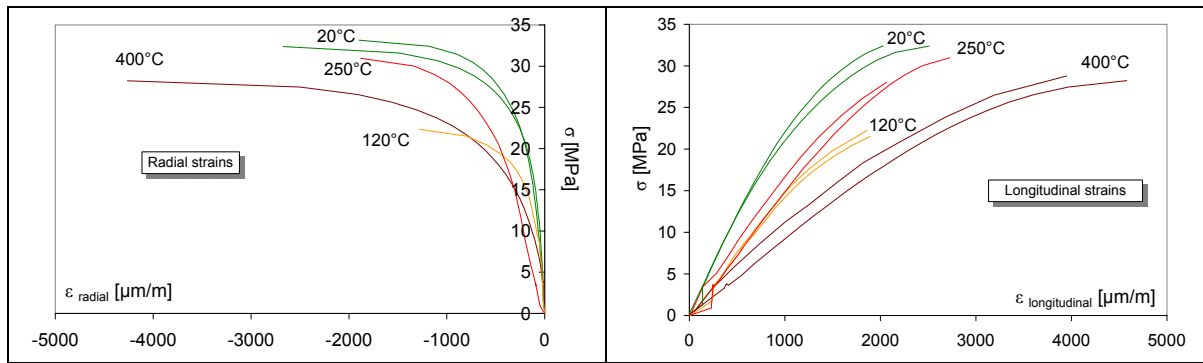


Fig. 5 – Stress/strain curves at different temperatures. On the left, radial strains. On the right, longitudinal strains.

In the two directions, we note a reduction in the stiffness of the material, caused by thermal damage. In the longitudinal direction, we observe that the strain reached at rupture increases with temperature. That can be explained by cracks closing. These cracks are generated during the heating stage because of the matrix dehydration from 100°C and by the thermal strain mismatch between cement paste and aggregates. This tendency is not observed in the radial direction due to the extension of the material in this direction. Indeed, the radial strain reached at rupture is higher at 120°C and 250°C than the rupture strain at 20°C. We observe that the mechanical behaviour of the concrete is strongly nonlinear, especially in the radial direction. This nonlinearity intensifies with the increase of the temperature.

Figure 6 presents compressive strengths obtained at the various temperatures. Between 20°C and 120°C strength reaches approximately 80% of initial strength. That can be explained by the CSH surface bonds reduction due to the fluidity increase and the water dilation around 100°C [9]. At 250°C, the concrete reaches its initial strength. This can be explained by the water departure which brings closer the CSH layers [9]. Strength decreases until 400°C to reach 87% of the initial strength.

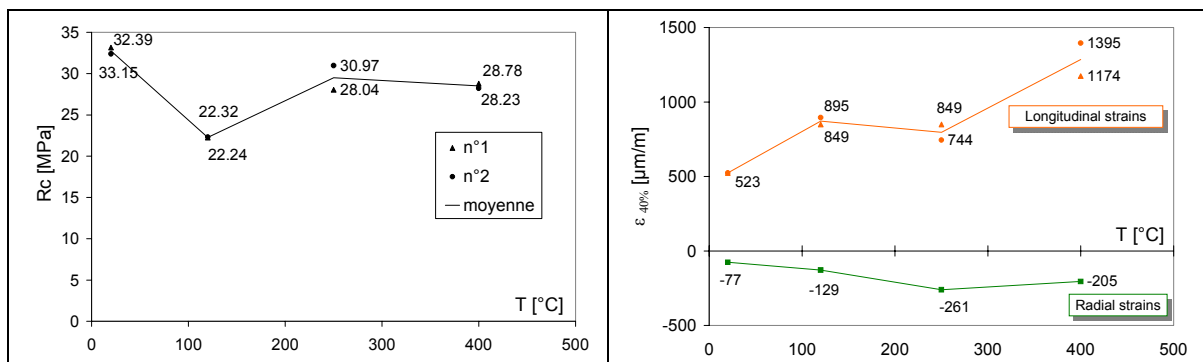


Fig. 6 – On the left, compressive strength evolution with temperature. On the right, evolution with temperature of the strain reached at 40% of the initial strength.

In order to compare the elastic strains with the creep and transient thermal strains, we assessed the elastic strain of the material that is reached at a load corresponding to 40% of the initial strength (≈ 13 MPa). Figure 6 shows the evolution of this strain with temperature.

5.3 II series: short-term creep tests

Figure 7 presents the results of creep tests in the longitudinal and radial directions. Figure 8 presents the results of recovery strains in the both directions.

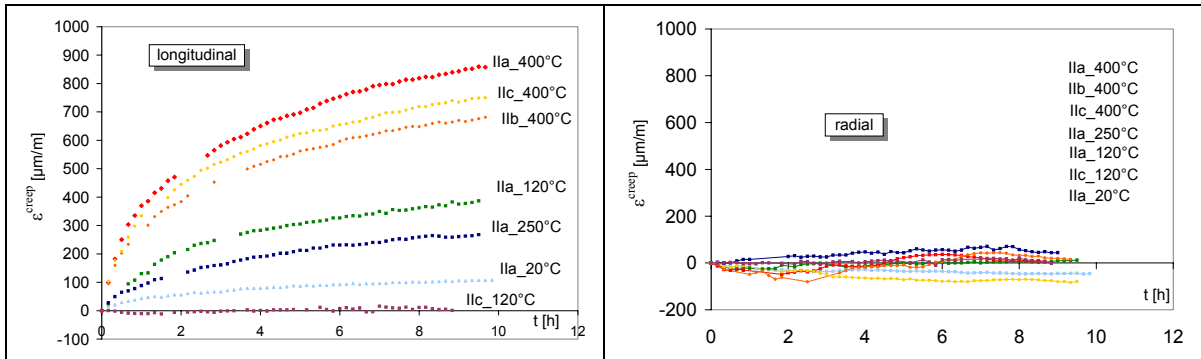


Fig. 7 – On the left, longitudinal creep strains. On the right, radial creep strains.

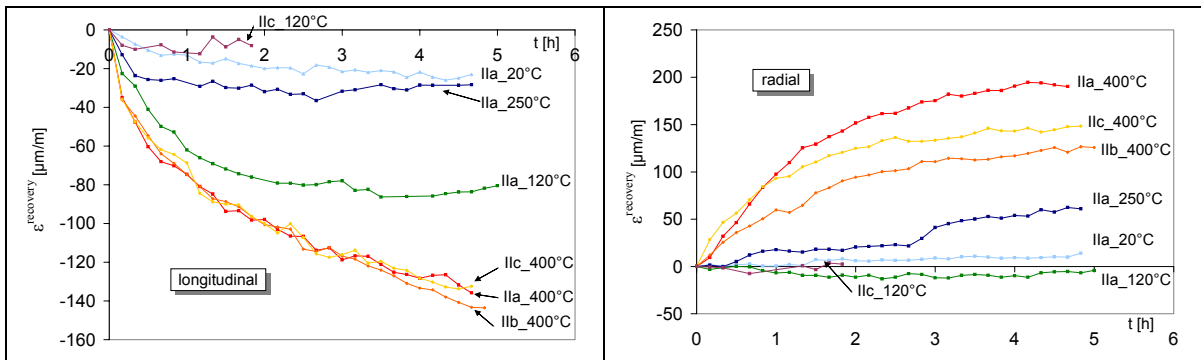


Fig. 8 – On the left, longitudinal recovery strains. On the right, radial recovery strains.

In the longitudinal direction, we can note that creep is activated from the first hours of the loading. That can be explained by the important level of mechanical loading. We note that higher is the temperature, higher and faster is the creep activation. These results are in good agreement with the thermally activated rupture of the microstructure bonds as assumed by Dias & Al. [10]. We can note that creep is more activated at 120°C than at 250°C. The results of figure 6 had shown us that the strength at 120°C point was lower. At this temperature, the microstructure bonds seem to be then weaker and creep could be then more activated.

By comparing the IIa_400°C and IIb test results, we observe that the creep carried out after a fast heating (5°C/min) is less important than the one carried out after a slow heating (1°C/min). For the moment, we have no explanation to this phenomenon. However, we can presume that it can be explained by the different hydric conditions of these two tests. Indeed, according to Bažant [11], the presence of water in material reduces the energy of activation and increases the mobility of the solid particles, facilitating the creep activation.

By comparing the IIa_400°C and IIc_400°C tests, we note that the creep carried out after a preheating at 250°C is slightly lower than the one carried out without preheating. On the other hand, by comparing the IIa_120°C and IIc_120°C tests, we note that creep is not activated for the sample that has been preheated. By preheating the sample at 250°C, we break microstructure bonds. If the sample is once again heated at 120°C, all the bonds being able to activate creep were already broken during the preheating [10]. On the other hand, by exceeding the temperature of 250°C, as for the IIc_400°C test, new bonds are broken and creep can be activated.

The thermally activation process is observed during the recovery phase too. On the other hand, there is no difference in behaviour between the Ila_400°C, I Ib and I Ic_400°C tests. We propose to explain this result by assuming that after 10 hours at 400°C, the state of the concrete is not influenced anymore by his thermal history.

In the radial direction, we can observe that the creep curves do not seem to follow a particular tendency. The order of magnitude of the measured strains is negligible compared to the longitudinal creep strains. On the other hand, the radial recovery is activated with the temperature and exceeds the values of longitudinal recovery.

Several mathematical creep laws exist in the literature [12]. We chose to approximate the longitudinal creep strains by a power law (1).

$$\epsilon^{creep}(T, t) = K(T).t^{\frac{1}{n}} \quad (1)$$

In order to approach the value of n , we plotted the curves of $\log(\epsilon^{creep})$ according to $\log(t)$. An acceptable slope for the whole tests is 1 per 3. After having fixed n at 3, we determined K by plotting the curves of ϵ^{creep} according to $t^{1/3}$ (fig. 9a). The slope of the different curves gives us the values of K according to the test series. The various results are presented on figure 9b.

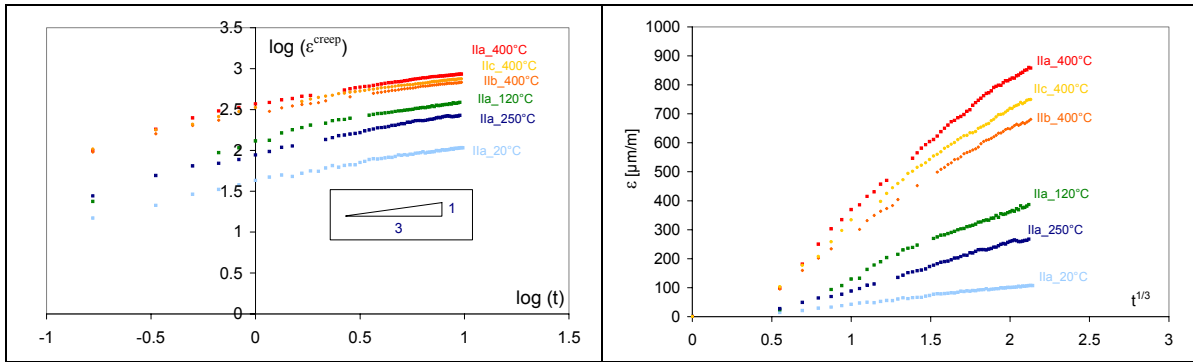


Fig. 9a – Determination of the power law parameters.

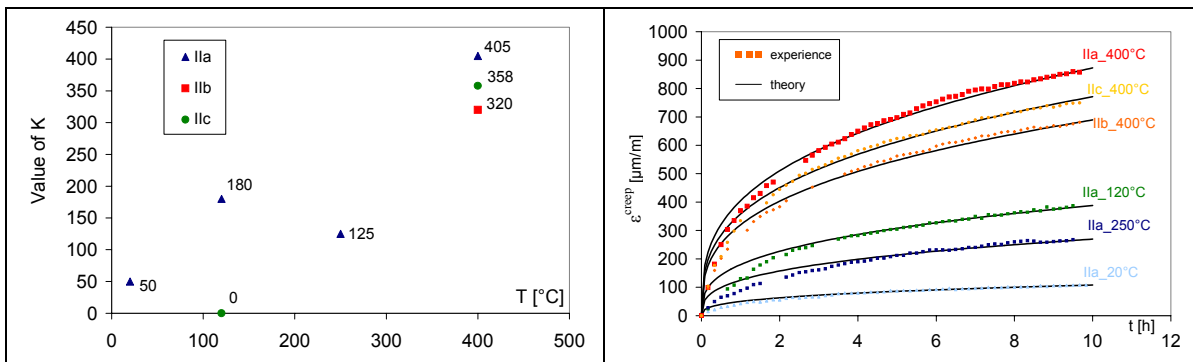


Fig. 9b – Determination of the power law parameters. On the right, calculated curves compared to experimental points.

The approximation of the creep curves by this power law is in good accordance with the short-term creep experimental results. Fixing n to 3 seems to be a good estimation for concrete. On the other hand, K depends on the concrete type but it gives us useful information about the creep activation.

5.4 III series: Thermal Strain Under Load

Figure 10 presents the curves of thermal strain under load (this strain will be called Total Strain, or TS for the rest of the paper) obtained for the IIIa, IIIb and IIIc series. We separated the longitudinal strains and the radial strains. For the two directions, the expansion of material is counted like positive.

In the longitudinal direction, we observe that the material is expanding during the test. The behaviour of material for the IIIb test (5°C/min) is very close to the IIIa test (1°C/min). The important difference in heating rate between the two tests (ratio of 5) does not seem to influence the TS. On the other hand, preheating to 250°C (IIIc test) generates from 100°C a TS much higher than the tests without preheating.

In the radial direction, material also expands during TS test. On the other hand, the various test conditions do not seem to influence the TS.

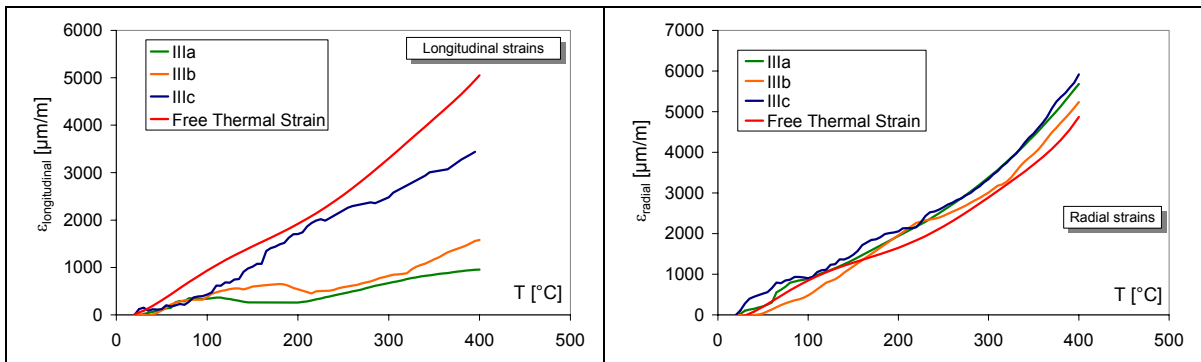


Fig. 10 – On the left, longitudinal total strain curves. On the right, radial total strain curves.

We calculated the transient thermal strain (TTS) according to the expression (2). This expression commonly met in the literature proposes a simplified definition of the total strain (TS) based on the theory of superposition.

$$\text{Total strain (TS)} = \text{Free thermal strain} + \text{TTS} \quad (2)$$

TTS were calculated according to the results of figure 10 (TS) and according to the analytical expression of free thermal strain (fig. 4). The TTS obtained for the different tests are presented in the figure 11.

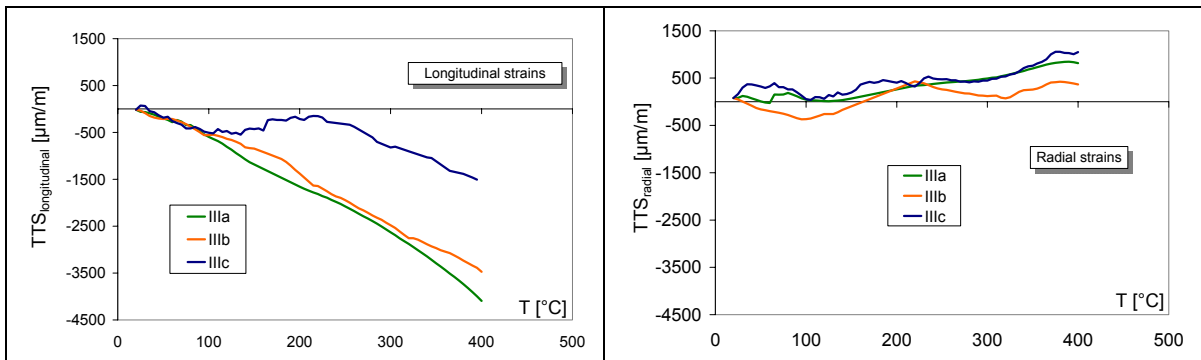


Fig. 11 – On the left, longitudinal TTS curves. On the right, radial TTS curves.

In the longitudinal direction, we can note that for the IIIa and IIIb tests, the TTS is relatively linear and appears from 20°C. The heating rate does not seem to influence the TTS as already found by several authors [5].

Until 100°C, IIIc test presents the same TTS that the tests without preheating. This result is different that the one observed by [7]. These authors found that Total strain after preheating was very close to the free thermal strain until the preheating temperature.

Between 100°C and 250°C, the slope of the TTS changes. At around 250°C, there is no TTS anymore. Between 250°C and 400°C, the TTS decreases linearly according to the same slope that the IIIa and IIIb tests. Preheating the material strongly influences the TTS. Until 250°C, the TTS is less important than the tests without preheating. Beyond the preheating temperature, the TTS is the same that the tests without preheating. That can be explained by a "thermal memory" of the material, which is most probably related to the free water movement, the level of matrix dehydration and the thermo-chemical damage that happens during the preheating [7].

In the radial direction, the calculated TTS are very weak compared to the longitudinal TTS. TTS appears only from 150°C. The various test conditions do not seem to influence the TTS appearance. In the radial direction, material is in extension (by Poisson effect). So we can suppose that TTS does not appear when the material is in extension. We can compare this result with thermal strain under direct tension. In those tests, the authors do not observe any TTS [13].

6. CONCLUSIONS

A complete study of the mechanical properties at high temperatures was carried out on an ordinary concrete. In particular, it enabled us to distinguish the various strain components leading to the total strain of material under the effect of temperature increase.

We determined the free thermal strain curves of the material, during heating and cooling. We could note that the longitudinal and radial thermal strains were relatively close.

The stiffness of material decreases with the temperature. This can be explained by the thermal damage of material caused by the matrix dehydration and the thermal mismatch between the cement paste and the aggregates. Compressive strength of the material decreases to 120°C. This can be due to the fluidity and the dilation of water. The material strain at rupture and the strain under a load corresponding to 40% of the 20°C compressive strength increases with temperature.

The creep of material is quickly activated in the longitudinal direction with the rise in the temperature. The creep is not activated when the sample is preheated at a higher temperature. The activation of the recovery of material in the longitudinal direction follows the same laws as for creep. In the radial direction, creep is practically not activated. On the other hand, the radial recovery is activated with the temperature and exceeds the values of longitudinal recovery. A power law allowed us to analytically approach the longitudinal short-term creep curves.

From the tests of Thermal Strain Under Load (total strain), we calculated the TTS of material. In the longitudinal direction, TTS appears from 20°C before following a linear evolution with temperature. The heating rate does not seem to influence the appearance of the

TTS. On the other hand, preheating the sample strongly reduced the TTS until the temperature of preheating. In the radial direction, TTS is very weak and appears only from 150°C. In this direction, the heating rate and the preheating do not influence the TTS.

7. ACKNOWLEDGEMENTS

The authors wish to thank the Aquitaine French region for their financial support and Mr Philippe RIVILLON, division manager at the CSTB, for his precious technical support.

8. REFERENCES

- [1] Schrefler B.A., Khoury G.A., Gawin D., Majorana C.E., "Thermo-hydro-mechanical modelling of high performance concrete at high temperatures", Engineering Computations, vol. 19, n° 7-8, 2002, p. 787-819.
- [2] Khoury G.A., "Spalling", Course on Effect of Heat on Concrete, International Centre for Mechanical Sciences (CISM), Udine, Italy, 9-13 June 2003.
- [3] Li L.Y., Purkiss J., "Stress-strain constitutive equations of concrete material at elevated temperatures", Fire Safety Journal, v 40, n 7, October, 2005, p 669-686.
- [4] Jumppanen U.M., Diederichs U., Hinrichsmeyer K., "Materials properties of F-concrete at high temperatures", Technical Research Centre of Finland, Research Reports 452, Espoo, 1986.
- [5] Schneider U., "Behaviour of concrete under Thermal Steady State and Non-Steady State Conditions", Fire and Materials, v 1, n 3, Sep, 1976, p 103-115.
- [6] Anderberg Y., Thelandersson S., "Stress and deformation characteristics of concrete at high temperatures. 2, Experimental investigation and material behaviour model", Bulletin 54, University of Lund, Sweden, 1976.
- [7] Hager I., Pimienta P., "Transient thermal strains of High Performance Concretes", Key note for Concreep7, International conference on creep, shrinkage and durability of concrete and concrete structures, Nantes, France, 12-14 September 2005.
- [8] RILEM, "Compressive strength for service and accident conditions", Materials and structures. 28, p.410-414. 1995.
- [9] Khoury G.A., "Compressive strength of concrete at high temperatures: a reassessment", Magazine of concrete research, vol. 44, n°161, 1992, p 291-309.
- [10] Dias W.P.S., Khoury G.A., Sullivan P.J.E., "Basic creep of unsealed hardened cement paste at temperatures between 20°C and 725°C", Magazine of concrete research, vol. 39, n° 139, June 1987, P. 93-101.
- [11] Bažant Z.P., "Mathematical model for creep and thermal shrinkage of concrete at high temperature", Nuclear Engineering and Design, vol. 76, n 2, Nov, 1983, p 183-191.
- [12] Gillen M., "Short-term creep of concrete at elevated temperatures", Fire and Materials, vol. 5, n°4, 191, p. 142-148.
- [13] Hager I., Pimienta P., "Mechanical properties of HPC at high temperatures", Workshop fib, Fire design of concrete structure : What now? What next? Milan, Italy, December 2-4, 2004.



EXPERIMENTAL BEHAVIOUR OF CONCRETE FLOOR SLABS AT AMBIENT AND ELEVATED TEMPERATURES

Colin G. BAILEY¹ and Wee Siang TOH²

ABSTRACT

This paper presents a series of 22 tests at ambient temperature (ambient tests), and 15 tests at elevated temperatures (fire tests) on horizontally unrestrained small-scale concrete slabs with an aspect ratio of 1.0 or 1.55. The slabs were reinforced with either mild steel or stainless steel mesh reinforcement of different grades, ductility, sizes and bar spacing.

All the ambient tests supported a load well above the theoretical yield-load showing that membrane action occurred. Two distinct modes of failure were observed in the ambient test, which were governed by the reinforcement ratio, aspect ratio and reinforcement ductility. The first mode of failure, generally for lightly reinforced slabs, comprised fracture of the reinforcement across the shorter span of the rectangular slabs or across one of the spans of the square slabs. The other mode of failure, generally for heavily reinforced slabs or slabs with high ductility reinforcement, comprised compressive failure at the corners of the slabs.

The fire tests consisted of the same slab geometry adopted in the ambient tests, in which 15 tests have been completed and presented in this paper. The tests showed that membrane action occurs, with compressive and tensile membrane action occurring around the perimeter and at the centre of the slabs, respectively. The mode of failure, for all reinforcement ratios and ductility, comprised of fracture of reinforcement. The slabs also clearly showed that they deformed as rigid plates when approaching the failure point. No compression failure was observed.

Comparison between the simple design approach shows good correlation with the test results both at ambient and elevated temperatures. However, the tests have allowed some of the assumptions within the original design method to be addressed, particularly compressive failure experienced in the ambient tests, which was previously impossible due to lack of test data.

¹ Professor, University of Manchester, School of Mechanical, Aerospace and Civil Engineering, PO Box 88, Pariser Building, Sackville Street, Manchester M60 1QD, U.K., email: colin.bailey@manchester.ac.uk

² Research Associate, University of Manchester, School of Mechanical, Aerospace and Civil Engineering, PO Box 88, Pariser Building, Sackville Street, Manchester M60 1QD, U.K., email: s.toh@manchester.ac.uk

1. INTRODUCTION

Tensile membrane action in concrete (or steel-concrete composite) slabs has shown to occur in full-scale fire tests and in real buildings following actual fires. A simple design method, developed by Bailey, was published in 2000^[1] and 2001^[2]. This method has recently been updated in 2006^[3] to include more efficient reinforcement patterns and the practical use of natural fires.

The method developed by Bailey still has a number of conservative assumptions which can only be addressed by extensive testing. This led to a programme of work, which is currently being carried out by the authors, looking at the tensile membrane action of horizontally unrestrained slabs at both ambient and elevated temperatures, incorporating mesh reinforcement.

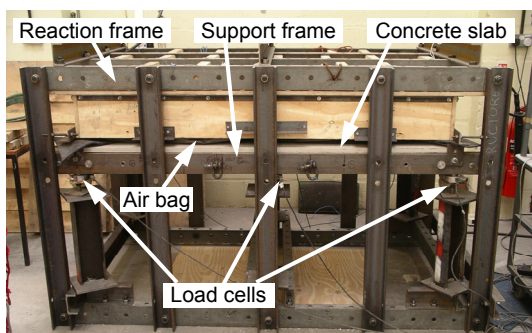
The results from the tests have led to a refinement of the original design method, which is discussed in this paper.

2. AMBIENT TESTS

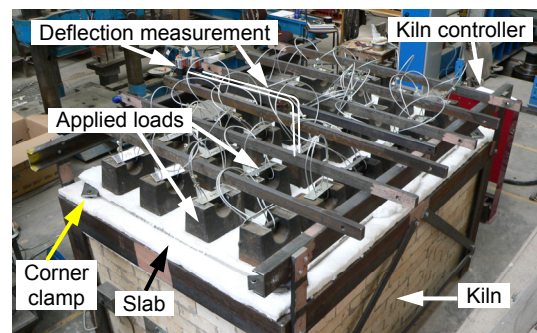
A series of 22 small-scale reinforced concrete slabs were tested at ambient temperature at the University of Manchester from Nov 2004 to July 2005. The slabs had a size of 1.2m×1.2m or 1.8m×1.2m with a target thickness of 20 mm and a concrete cover of 5 mm. The slabs were supported vertically on 50 mm wide angles, resulting in a clear span of 1.1m×1.1m or 1.7m×1.1m, giving an aspect ratio of 1.0 or 1.55. The corners of the slabs were lightly clamped, with rollers between the clamps and slabs, allowing free horizontal movement. There was no horizontal restraint provided to the slab's perimeter (see Fig. 1(a)).

The proportions of the concrete mix comprised 44% Granno aggregate (maximum size 6 mm), 30% sand, 20% cement and 6% water. The reinforcement consisted of either mild steel or stainless steel wire mesh of different grades, ductility, diameter and bar spacing. Tables 1 and 2 summarise the details of the tests together with the calculated yield loads and maximum recorded test loads.

All the slabs supported a load well above the theoretical yield-line load showing that membrane action occurred. Table 1 shows that the maximum test load P_{test} (including self-weight of the slabs) ranged from 1.45 to 2.43 above the yield-line load P for the slabs with mild steel mesh, whereas the enhancement P_{test}/P varied from 1.44 to 3.52 for the slabs with stainless steel mesh as shown in Table 2.



(a) Ambient test



(b) Fire test

Fig. 1 – Typical experimental tests set-up.

Observations from the slab tests with mild steel mesh showed two distinct modes of failure, which were found to be dependent on the reinforcement ratio, aspect ratio and ductility of the reinforcement. Considering a constant aspect ratio it was found that the first mode of failure, for lightly reinforced slabs, comprised fracture of the reinforcement across the shorter span of the slabs (see Fig. 2(a)). The other mode of failure, for heavily reinforced slabs, comprised compressive failure at the corners of the slabs (see Fig. 2(b)). Due to the high ductility of stainless steel it was found that all slabs finally failed by compressive failure at the corners.



(a) Fracture of reinforcement along short span



(b) Compressive concrete failure at corners

Fig. 2 – Two typical modes of failure for test slabs at ambient temperature.

Table 1 – Details of mild steel slab tests at ambient temperature.

Test	Size (m×m)	Depth (mm)	Reinforcement					f_{cu} (MPa)	P (kN/m ²)	P_{test} (kN/m ²)	$\frac{P_{test}}{P}$	Δ (mm)	P_{limit} (kN/m ²)	$\frac{P_{limit}}{P_{test}}$
			\varnothing (mm) for span		Spacing (mm)	f_y (MPa) for span								
			long	short		long	short							
M1	1.8×1.2	18.2	2.42	2.42	50.8	734	759	41.3	8.54	20.74	2.43	44.05	15.50	0.75
M2	1.2×1.2	19.1	2.42	2.42	50.8	734	759	38	13.83	26.99	1.95	28.50	20.31	0.75
M3	1.8×1.2	22	1.53	1.49	25.4	451	454	35.3	6.35	12.28	1.93	34.53	9.13	0.74
M4	1.2×1.2	20.1	1.53	1.49	25.4	451	454	35.3	8.17	18.29	2.24	22.34	11.91	0.65
M5	1.8×1.2	18.9	1.47	1.48	12.7	406	435	37.9	8.69	17.92	2.06	32.76	12.72	0.71
M6	1.2×1.2	21.6	1.47	1.48	12.7	406	435	38.6	15.72	27.03	1.72	21.20	21.19	0.78
M7	1.8×1.2	20.4	0.84	0.85	12.7	599	604	41.6	5.11	8.65	1.69	39.79	7.68	0.89
M8	1.2×1.2	19	0.84	0.85	12.7	599	604	42.9	6.68	10.70	1.60	25.75	10.08	0.94
M9	1.8×1.2	22	0.66	0.68	6.35	450	402	37.6	5.07	7.35	1.45	34.49	7.16	0.97
M10	1.2×1.2	19.7	0.66	0.68	6.35	450	402	37.3	6.36	9.89	1.56	22.32	9.13	0.92

Table 2 – Details of stainless steel slab tests at ambient temperature.

Test	Size (m×m)	Depth (mm)	Reinforcement					$\frac{f_u}{f_{0.2p}}$		f_{cu} (MPa)	P (kN/m ²)	P_{test} (kN/m ²)	$\frac{P_{test}}{P}$	Δ (mm)	P_{limit} (kN/m ²)	$\frac{P_{limit}}{P_{test}}$
			\varnothing (mm) for span		Spacing (mm)	$f_{0.2p}$ (MPa) for span										
			long	short		long	short	f_1	f_2							
S1	1.8×1.2	19	2.99	3	50.8	639	614	1.39	1.40	40.6	10.59	17.14	1.62	41.42	16.55	0.97
S2	1.2×1.2	20.4	2.99	3	50.8	639	614	1.39	1.40	41.2	18.65	26.81	1.44	26.59	25.43	0.95
S3	1.8×1.2	21	2.51	2.51	50.8	569	555	1.50	1.53	50	9.20	17.31	1.88	38.61	15.67	0.91
S4	1.2×1.2	19	2.51	2.51	50.8	569	555	1.50	1.53	50.7	11.71	22.78	1.94	25.38	21.06	0.92
S5	1.8×1.2	17.6	1.55	1.53	25.4	344	447	2.13	1.65	49.8	4.46	13.35	2.99	31.23	7.70	0.58
S6	1.2×1.2	20.6	1.53	1.55	25.4	447	344	1.65	2.13	49.8	8.15	26.78	3.28	22.42	13.21	0.49
S7	1.8×1.2	20.5	1.58	1.58	12.7	265	271	2.18	2.16	41.9	7.59	19.48	2.57	26.62	11.64	0.60
S8	1.2×1.2	19.3	1.58	1.58	12.7	265	271	2.18	2.16	43	10.22	35.98	3.52	17.85	16.48	0.46
S9	1.8×1.2	19.7	0.97	0.97	8	293	287	2.29	2.38	37.1	4.78	14.26	2.98	27.83	7.77	0.54
S10	1.2×1.2	18.8	0.97	0.97	8	293	287	2.29	2.38	37.2	6.53	20.18	3.09	18.01	10.80	0.54
S11	1.8×1.2	18.9	0.8	0.76	6.35	329	557	2.14	1.41	45.7	5.90	16.23	2.75	29.49	8.58	0.53
S12	1.2×1.2	22.3	0.76	0.8	6.35	557	329	1.41	2.14	48.2	10.34	31.53	3.05	24.83	16.88	0.54

3. FIRE TESTS

A similar experimental programme at elevated temperatures, consisting of the same slab geometry adopted in the ambient tests and adopting the similar support conditions, is currently being carried out with 15 tests having been completed and presented herein. The details of the tests are given in Tables 3 and 4.

All tests were carried out under transient heating state, with a predefined working load uniformly applied on the top surface of the slab by using the dead weights as shown in Fig. 1(b). The electric kilns, located beneath the slabs, provided a heating rate of 300°C per hour up to a maximum temperature of 900°C or 1000°C, and the maximum temperature was thereafter maintained. The kiln, bottom and top surface temperatures of the slabs, as well as the reinforcement temperature at three locations at the centre of the slabs were recorded during the tests. Fig. 3 shows the typical temperature recording for a test slab.

All the tests showed that membrane action occurs, with compressive membrane action occurring around the perimeter and tensile membrane action occurring at the centre of the slab. The observed mode of failure for all the slabs consisted of fracture of reinforcement across the shorter span of the rectangular slabs or across one of the spans of the square slabs (see Fig. 4). No compression failure, as identified in the ambient tests (Fig. 2b), was observed.

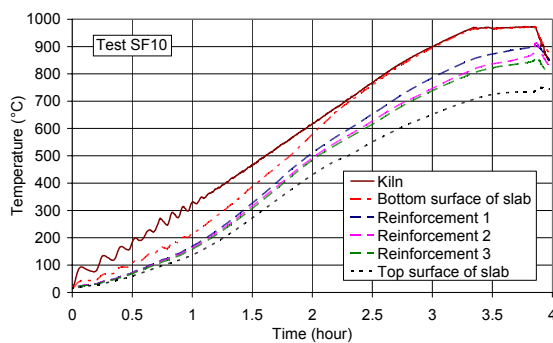


Fig. 3 – Typical temperatures recorded in fire tests.



Fig. 4 – Mode of failure for test slabs at elevated temperatures.

The slabs also clearly showed that they deformed as rigid plates when approaching the failure point. However, it was observed that the mild steel slabs normally collapsed in a more sudden manner, whereas the stainless steel slabs' collapse was gentler, mainly due to the difference in the ductility of the meshes. As a result, two different ways were adopted to define the failure points for both types of slabs in the analyses. The failure point of the mild steel slabs refers to the start of the runaway phenomenon. The failure point of the stainless steel slabs refers to the start of significant rupture of the reinforcement. The failure points, represented by the critical temperatures T_c and critical displacements Δ_c , for all the slabs are shown in Tables 3 and 4.

Table 3 – Details of mild steel slab tests at elevated temperatures.

Test ¹	Size	Depth	Reinforcement					f_{cu}	P	P_{test}	$\frac{P_{test}}{P}$	Start of runaway		Predicted T_s based on Δ_c	$\frac{T_s}{T_c}$
			\varnothing (mm) for span		Spacing	f_y (MPa) for span						T_c	Δ_c		
	(m×m)	(mm)	long	short	(mm)	long	short	(MPa)	(kN/m ²)	(kN/m ²)		(°C)	(mm)	(°C)	
MF1	1.8×1.2	19.6	2.43	2.41	50.8	722	695	43.2	9.36	5.280	0.56	764	211	786	1.03
MF2	1.2×1.2	23	2.41	2.43	50.8	684	780	43.3	18.87	5.519	0.29	694	114	805	1.16
MF3	1.8×1.2	18.9	1.54	1.54	25.4	360	348	39.1	4.13	3.655	0.89	727	157	656	0.90
MF4	1.2×1.2	19.6	1.54	1.54	25.4	311	350	39	6.03	5.429	0.90	685	122	632	0.92
MF6	1.2×1.2	19.3	1.51	1.52	12.7	402	467	38.5	18.37	7.900	0.43	760	133	688	0.91
MF7	1.8×1.2	18.8	0.86	0.83	12.7	409	471	43.8	3.36	4.460	1.33	556	114	557	1.00
MF8	1.2×1.2	20.7	0.86	0.83	12.7	409	471	43.5	5.58	4.646	0.83	650	110	630	0.97

¹ MF5, MF9 and MF10 to be tested.

Table 4 – Details of stainless steel slab tests at elevated temperatures.

Test ^a	Size (m×m)	Depth (mm)	Reinforcement properties	f_{cu} (MPa)	P (kN/m ²)	P_{test} (kN/m ²)	$\frac{P_{test}}{P}$	Fracture of mesh		Predicted T_s based on Δ_c (°C)	$\frac{T_s}{T_c}$
								T_c (°C)	Δ_c (mm)		
SF2	1.2×1.2	20.4	Same as Table 2	38.5	21.94	7.92	0.36	885	153	991	1.12
SF4	1.2×1.2	18.6		45.7	11.06	5.41	0.49	825 ^b	113 ^b	- ^b	-
SF6	1.2×1.2	18.7		46.5	8.64	5.41	0.63	903	160	916	1.01
SF8	1.2×1.2	22		41.2	14.84	7.97	0.54	879	122	907	1.03
SF9	1.8×1.2	19.8		40.4	4.84	3.68	0.76	885	166	901	1.02
SF10	1.2×1.2	22.5		39.7	10.66	7.98	0.75	873	132	890	1.02
SF11	1.8×1.2	19.8		40.8	6.29	5.29	0.84	826	163	827	1.00
SF12	1.2×1.2	23.1		41.7	13.53	8.00	0.59	835	110	825	0.99

^a SF1, SF3, SF5 and SF7 to be tested.

^b Test stopped before failure.

4. SIMPLIFIED METHOD AT AMBIENT TEMPERATURE

The simplified design method originally developed by Bailey^{[1]-[6]}, and recently extended by Bailey and Toh^[6] to include a more precise in-plane stress pattern, is used to predict the load-displacement response of the tested slabs. The method which includes membrane action is based on the fundamental principles of rigid plastic behaviour with change of geometry. The following assumptions are incorporated into the method:

1. Based on a predefined yield-line pattern, the in-place forces increase with increase in vertical displacement and rotation of rigid plates about yield-lines.
2. The self-equilibrium in-plane forces comprise compressive membrane action around the perimeter of the slab and tensile membrane action in the central area of the slab.

- Based on the in-plane stress distributions, as shown in Fig. 5, the in-plane forces along the rigid plates are defined by the constants 'k' and 'b' or 'v' depending on the stress pattern.
- One possible mode of failure is by fracture across the shorter span, with the tension force across the assumed fracture line (prior to actual fracture) being balanced by perimeter triangular compressive stress blocks over a length of ml (see Fig. 6).
- When the applied load on the slab exceeds a certain limit, the fracture of the reinforcement across the central crack will initiate at the slab's centre and gradually propagate towards its edges. For simplicity, the tensile stress of reinforcement across the crack is assumed to vary linearly from its yield stress (f_y) near the edge of the slab to its ultimate stress ($f_u = f_2 \times f_y$) at the slab centre, as shown in Fig. 6.
- Two modes of failure are considered, comprising fracture of reinforcement across the shorter span of the slab (as explained in assumptions 4 and 5 above) and compression failure of concrete in the corners of the slab.

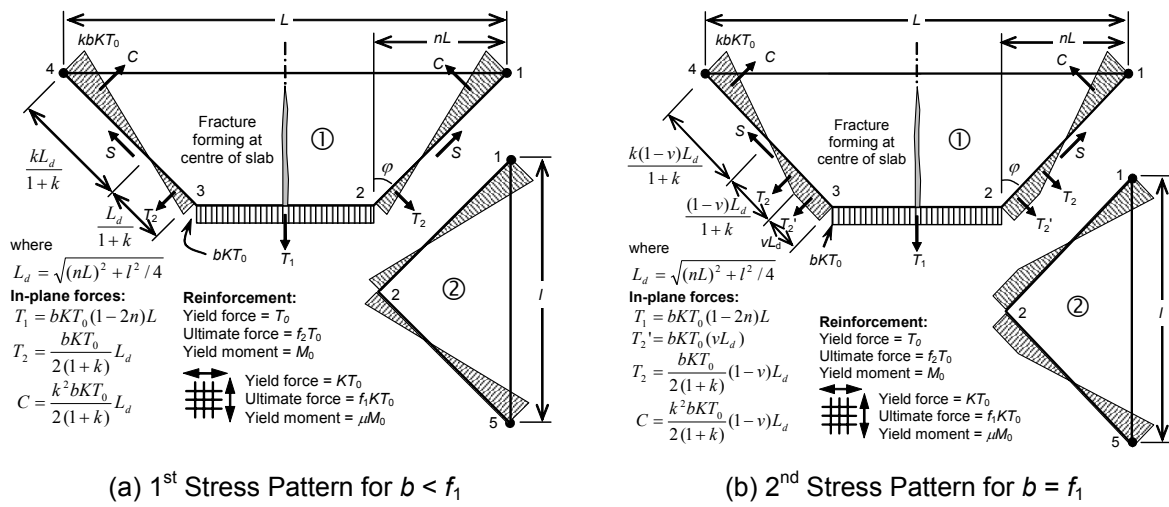
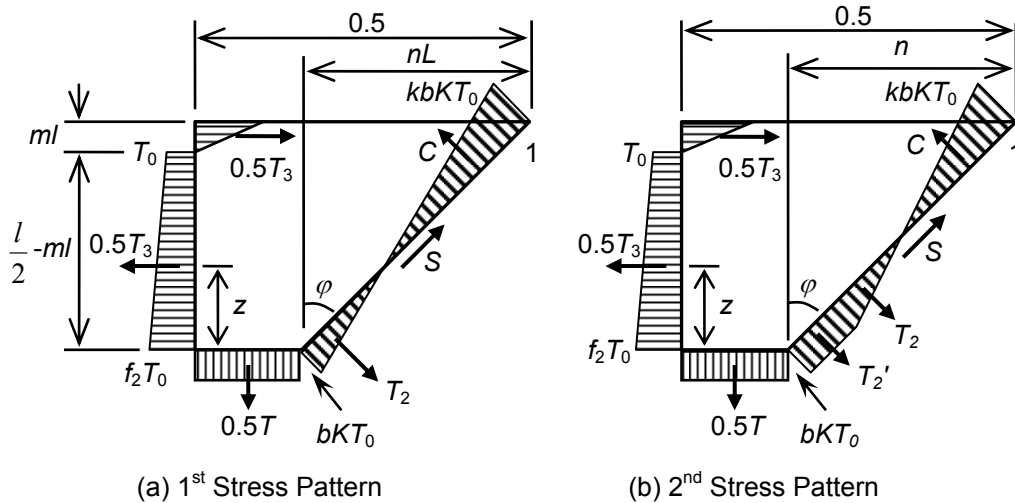


Fig. 5 – In-plane stress distribution patterns.



$$\text{The in-plane level arm } z \text{ is given by } z = \frac{2 + f_2}{3(1 + f_2)} \left(\frac{l}{2} - ml \right)$$

Fig. 6 – In-plane stress distribution.

The basic equations for the simplified design method are presented below.

4.1. YIELD LINE PATTERN

The in-plane stress distributions are based on an assumed yield line pattern determined by the factor 'n' (see Fig. 5), given by,

$$n = \frac{1}{2\sqrt{\mu a^2}} \left[\sqrt{3\mu a^2 + 1} - 1 \right] \quad (1)$$

where a = aspect ratio of the slab and is given by L/l .

For a square slab, with isotropic or orthotropic reinforcement, the 'shorter' span of the slab is defined by the span with the smaller moment capacity so that the moment capacity ratio ' μ ' is always less than, or equal to, unity. By substituting the value of ' μ ' into Eq. (1), it can be proved that the factor 'n' is always smaller than, or equal to, 0.5 leading to a physical possible yield-line pattern.

4.2. 1ST STRESS PATTERN

For the failure mode of reinforcement fracture across the shorter span, the in-plane stress distribution is defined by the constants 'k' and 'b', as given by (Fig. 5a),

$$k = \frac{4na^2(1-2n)}{4n^2a^2+1} + 1 \quad (2)$$

$$b = \frac{1}{K(A+B)}(1-2m) \left(\frac{1+2f_2+2m}{3} \right) \leq f_1 \quad (3)$$

in which $A = (1-4n^2)a^2$; $B = \frac{2-k}{3}[(2na)^2+1]$.

Considering a triangular compressive stress block (ml) at both ends of the assumed fracture line with the full slab depth ' H ' being in compression and the contribution of the reinforcement in compression ignored, the width factor ' m ' can be determined from the equilibrium of the in-plane horizontal forces across the full central fracture line as follows,

$$m = \frac{1}{2} \left(1 + \frac{0.8f_{cu}H}{(1+f_2)T_0} \right)^{-1} \quad (4)$$

Substituting the value of ' m ' from Eq. (4) into Eq. (3), the constant 'b' can be calculated. If the constant 'b' is less than or equal to ' f_1 ', the 1st Stress Pattern (Fig.5a) is valid and the load carrying capacity for a given displacement can be calculated. If however the constant 'b' is greater than ' f_1 ', the 2nd Stress Pattern (Fig. 5b) must be used.

Once the in-plane stresses are defined, the load carrying contribution from the membrane forces and the increase in bending resistance, due to the in-plane compressive forces, are represented separately by the enhancement factors above the yield-line load as follows,

1. Enhancement due to membrane forces for Elements 1 and 2 (Fig. 5(a)):

$$e_{1m} = \frac{4b}{3+g_1} \frac{w}{d_1} \left(1-2n + \frac{n(2-k)}{3} \right) \quad (5)$$

$$e_{2m} = \frac{2bK}{3+g_2} \frac{w}{d_2} \left(\frac{2-k}{3} \right)$$

2. Enhancement due to the effect of in-plane forces on the bending capacity for Elements 1 and 2 (Fig. 5(a)):

$$e_{1b} = 2n \left[1 + \frac{\alpha_1 b}{2} (k-1) - \frac{\beta_1 b^2}{3} (k^2 - k + 1) \right] + (1-2n)(1 - \alpha_1 b - \beta_1 b^2) \quad (6)$$

$$e_{2b} = 1 + \frac{\alpha_2 bK}{2} (k-1) - \frac{\beta_2 b^2 K}{3} (k^2 - k + 1)$$

in which $\alpha_{i=1,2} = \frac{2g_i}{3+g_i}$; $\beta_{i=1,2} = \frac{1-g_i}{3+g_i}$

where g_1 and g_2 are defined in Fig. 7.

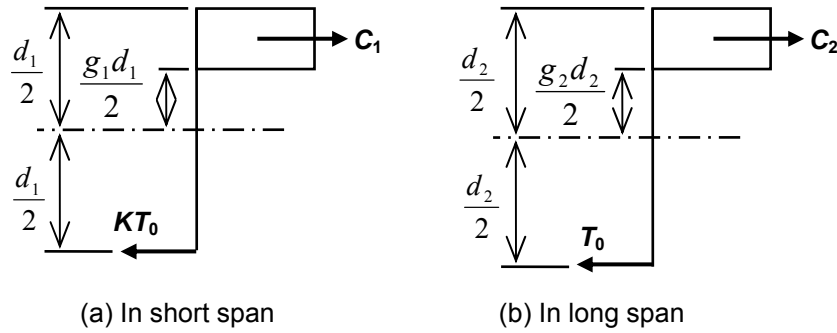


Fig. 7 – Calculation of moment resistance.

3. Net enhancement for each element:

$$e_1 = e_{1m} + e_{1b} \quad (7)$$

$$e_2 = e_{2m} + e_{2b}$$

4. Overall enhancement:

$$e = e_1 - \frac{e_1 - e_2}{1 + 2\mu a^2} \quad (8)$$

5. The enhancement shown in Eq. (8) is applied to the yield line load P , which for a square or rectangular slab subjected to a uniformly distributed load, is given by:

$$p = \frac{24\mu M}{l^2} \left[\sqrt{3 + \frac{1}{(a')^2}} - \frac{1}{a'} \right]^{-2} \quad (9)$$

where $a' = \sqrt{\mu} a$.

4.3. 2ND STRESS PATTERN

When, according to Eq. (3), the constant 'b' is greater than the factor between ultimate and yield stress (f_i), the in-plane forces should be derived based on the 2nd Stress Pattern as shown in Fig. 5(b).

The constants 'k' and 'v', defining the in-plane stress distribution for the failure mode of reinforcement fracture across the shorter span, are given by,

$$k = \frac{4na^2(1-2n) + (1+v)(4n^2a^2 + 1)}{(1-v)(4n^2a^2 + 1)} \quad (10)$$

$$v = \frac{\frac{1}{K}(1-2m)(1+2f_2+2m)-1-3a^2+4na^2}{2+4na^2} \quad (11)$$

The enhancement above the yield-line load due to membrane action and the effect of in-plane forces on the bending capacity, is given by,

1. Enhancement due to membrane forces for Elements 1 and 2 (Fig. 5(b)):

$$\begin{aligned} e_{1m} &= \frac{4b}{3+g_1} \frac{w}{d_1} \left(1 - \frac{n}{3} (4+k-(1+k)(2v-v^2)) \right) \\ e_{2m} &= \frac{2bK}{3+g_2} \frac{w}{d_2} \left(\frac{2-k+(1+k)(2v-v^2)}{3} \right) \end{aligned} \quad (12)$$

2. Enhancement due to the effect of in-plane forces on the bending capacity for Elements 1 and 2 (Fig. 5(b)):

$$\begin{aligned} e_{1b} &= 2n(1-v) \left(1 + \frac{\alpha_1 b}{2} (k-1) - \frac{\beta_1 b^2}{3} (k^2-k+1) \right) + (1-2n+2nv)(1-\alpha_1 b - \beta_1 b^2) \\ e_{2b} &= (1-v) \left[1 + \frac{\alpha_2 bK}{2} (k-1) - \frac{\beta_2 b^2 K^2}{3} (k^2-k+1) \right] + v(1-\alpha_2 bK - \beta_2 b^2 K^2) \end{aligned} \quad (13)$$

Similarly, the net enhancement for each element can be obtained by Eq. (7) and the overall enhancement is given by Eq. (8).

4.4. COMPRESSIVE FAILURE OF CONCRETE

For the compressive failure of concrete as shown in Fig. 2(b), assuming that the concrete compressive strength is limited to $0.45d$, where d is the average effective depth of the reinforcement in both orthogonal direction, the constant 'b' is given by^[6],

$$b = \frac{1}{kKT_0} \left(0.67f_{cu} - 0.45 \left(\frac{d_1+d_2}{2} \right) - T_0 \left(\frac{K+1}{2} \right) \right) \quad (14)$$

In case of the 1^{st} Stress Pattern, the constant 'b' is the minimum value given by Eqs. (3) and (14); while in case of the 2^{nd} Stress Pattern, the constant 'b' is the minimum value of 'f₁' or that given by Eq. (14).

4.5. MAXIMUM DISPLACEMENT

The simple method cannot predict the maximum displacement at which actual fracture of the reinforcement, or crushing of the concrete, occurs. A very simplified and conservative prediction of the maximum vertical displacement Δ at ambient temperature proposed by Bailey^[4] is given by,

$$\Delta = \sqrt{\left(\frac{0.5f_y}{E} \right) \frac{3L^2}{8}} \quad (15)$$

where 'E' is the Young's modulus of the reinforcement in the longer span. The maximum allowable displacement (Δ) and corresponding load capacity (P_{limit}) is shown in Tables 1 and 2 for all slabs.

5. SIMPLIFIED METHOD AT ELEVATED TEMPERATURES

The simplified method discussed in Section 4 can be easily adopted for analysing the concrete slabs at elevated temperatures. The equations from (1) to (14) may be applied incorporating the thermal effects on the material properties. In this study, the reduction factors at elevated temperatures for mechanical properties of mesh reinforcement and concrete were taken from EN1992-1-2^[7] and EN1993-1-2^[8].

The design procedure, at elevated temperatures, is briefly discussed as follows:

1. Assign a temperature increment scheme for the slabs. In this study, it was assumed that the temperature of the reinforcement increases monotonically from 20°C to 1000°C, and the temperature of concrete is 20% lower than the reinforcement.
2. At each reinforcement temperature, determine the corresponding yield-line load. Plotting the computed yield-line loads versus the temperatures will generate the solid thick curve in Fig. 8, taking the Test SF12 as example.
3. For a series of vertical deflections (e.g. $w = 40, 80, 120$ and 160 mm), determine the enhancement factors over the range of temperatures specified in Step 1.
4. Compute the load carrying capacity by multiplying the yield-line loads from Step 2 by the enhancement factors from Step 3. Plotting the obtained load carrying capacities versus the temperatures for each value of w will generate the four dash lines in Fig. 8.
5. For a given constant working load, extract the corresponding temperatures for the yield-line load and various values of w . The calculated temperature/displacement response can then be compared with the test results, as illustrated in Fig. 9.

The above design procedure can be easily conducted using a standard spreadsheet.

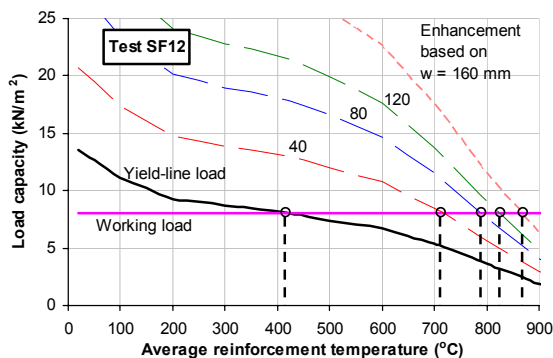


Fig. 8 – Variation of load carrying capacity of slab with deflection and temperature.

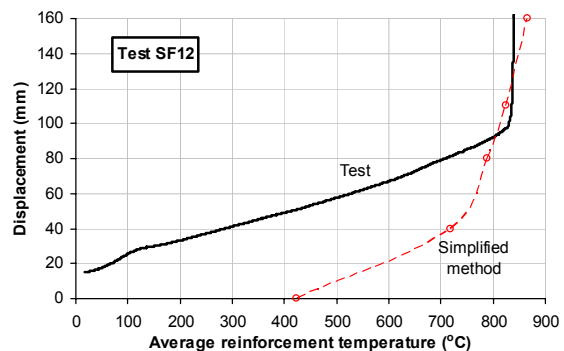


Fig. 9 – Comparison of simplified method with test.

6. COMPARISON BETWEEN TEST RESULTS AND SIMPLE ANALYSES

When compared against the twenty-two ambient tests, the simplified design method tends to give conservative predictions. Based on the maximum allowable displacement (Δ) given by Eq. 15, it was found that the ratio of the predicted allowable load to the maximum test load $P_{\text{limit}}/P_{\text{test}}$ ranged from 0.97 to 0.65 for the mild steel slabs and 0.96 to 0.44 for the stainless steel slabs.

Comparison of the predicted displacement/temperature response (based on the principle of rigid plastic behaviour with change of geometry) and the test results, of the seven mild steel reinforced slabs at elevated temperatures, is shown in Fig.10. The predictions for MF2 and MF6 do not correlate very well with the test results. It was found that these slabs

had a low load ratio (refer Table 3) and further investigation is required to understand the poor correlation. The predicted displacement/temperature response and the test results, for the stainless steel reinforced slabs, are shown in Fig. 11. In general the predictions are very good except for slabs SF2 and SF4, which again had a low load ratio (refer Table 4).

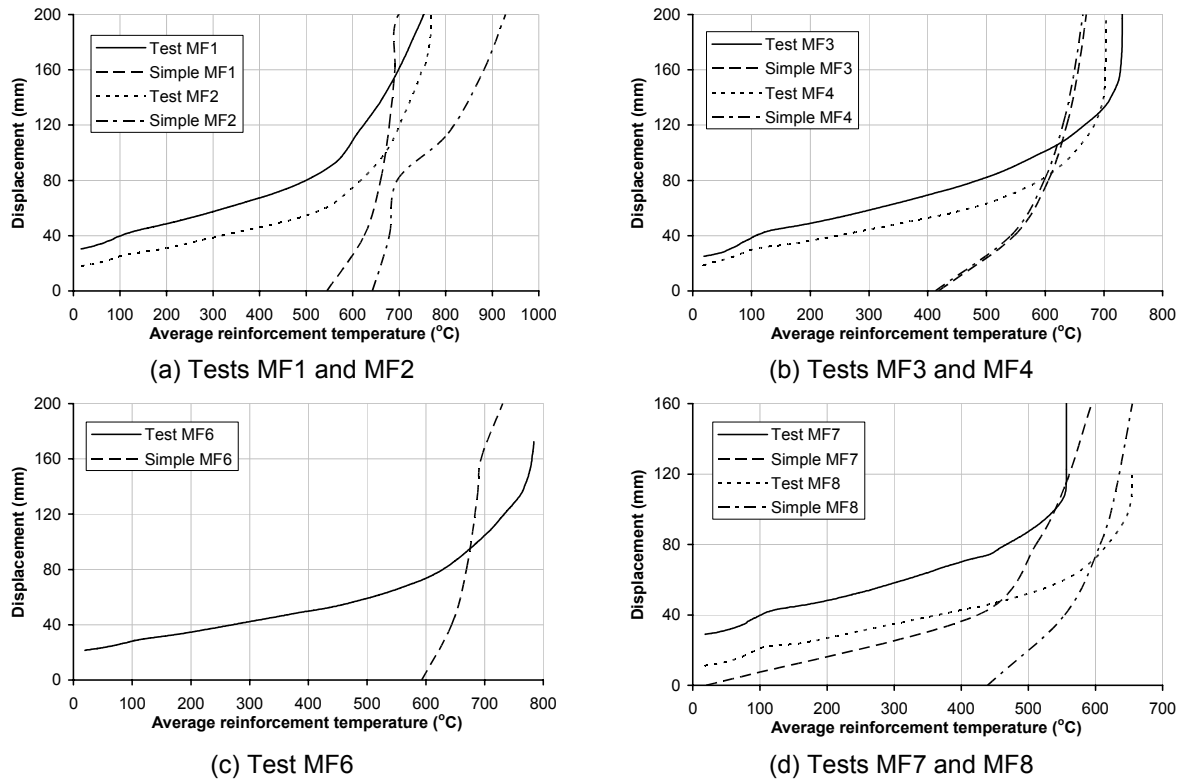


Fig. 10 – Slabs with mild steel mesh at elevated temperatures.

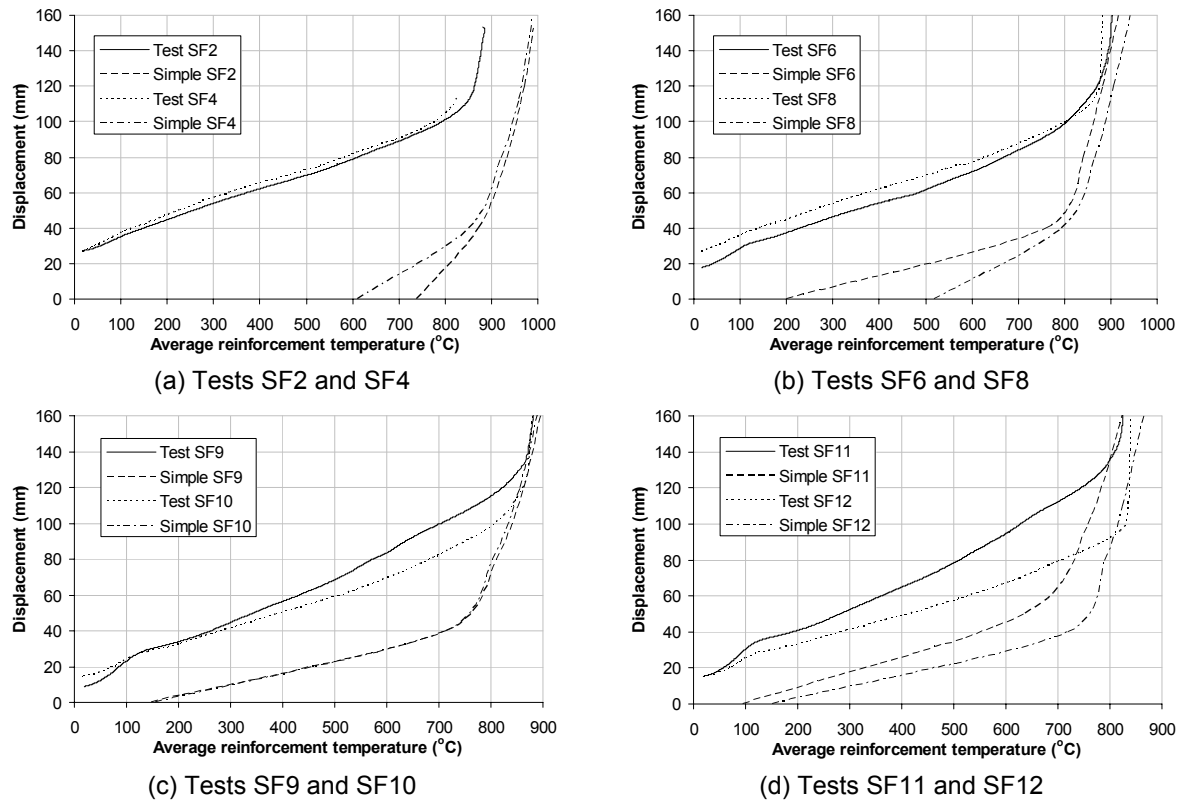


Fig. 11 – Slabs with stainless steel mesh at elevated temperatures.

7. CONCLUSIONS

This paper presents the experimental results from 22 tests of horizontally unrestrained concrete slabs at ambient temperature with 15 of the ambient tests repeated at elevated temperature. The tests comprised of mild steel or stainless steel mesh reinforcement with varying bar diameter, spacing and ductility. Observations from the tests showed that two modes of failure were observed at ambient temperature comprising fracture of the reinforcement or crushing of the concrete at the corners of the slab. At elevated temperatures all the tests failed by fracture of the reinforcement.

Results from the tests allowed refinement of the original design method, developed by Bailey, to predict the membrane behaviour of unrestrained slabs. This consisted of including a procedure for predicting the crushing behaviour of concrete at the corners, together with a more accurate representation of the in-plane stress distribution.

The simple design method produced excellent predications at ambient temperature and good predictions at elevated temperature. In some cases, where the load ratio was low, the prediction for the response at elevated temperatures was not so good. The reason for the discrepancy between the prediction and test results for these cases is currently under investigation.

8. REFERENCES

- [1] Newman G.M., Robinson J.T. and Bailey C.G., *Fire Safe design: A New Approach to Multi-Storey Steel-Framed Buildings*. SCI Publication P288. The Steel Construction Institute, Ascot. 2000. ISBN 1 85942 120 2.
- [2] Bailey C.G. Steel Structures supporting composite floor slabs: design for fire. BRE Digest 462. December 2001. ISBN 1 86081 527 8.
- [3] Newman G.M., Robinson J.T. and Bailey C.G., *Fire Safe design: A New Approach to Multi-Storey Steel-Framed Buildings (Second Edition)*. SCI Publication P288. The Steel Construction Institute, Ascot. 2006. ISBN 1 85942 169 5.
- [4] Colin G., Bailey, Membrane action of unrestrained lightly reinforced concrete slabs at large displacements, *Eng. Struct.*, 23(5), pp. 470-483, 2001.
- [5] Colin G., Bailey, Efficient arrangement of reinforcement for membrane behaviour of composite floor slabs in fire conditions, *J. Constr. Steel Res.*, 59(7), pp. 931-949, 2003.
- [6] Colin G., Bailey and Wee Siang, Toh, New simplified membrane design method for concrete floor slabs, *J. Struct. Eng. – ASCE*. [Under Review]
- [7] Eurocode 2: Design of concrete structures. Part 1.2: General rules - structural fire design, EN1992-1-2, British Standard Institution, 2004.
- [8] Eurocode 3: Design of steel structures. Part 1.2: General rules - structural fire design, EN1993-1-2, British Standard Institution, 2005.



NEW NDT TECHNIQUES FOR THE ASSESSMENT OF FIRE DAMAGED CONCRETE STRUCTURES

Matteo COLOMBO¹ and Roberto FELICETTI²

ABSTRACT

An extensive research programme has been performed at Politecnico di Milano in order to identify quick and easy methods for the assessment of the thermal damage experienced by reinforced concrete structures in consequence of a fire. As a result, three new investigation techniques have been proposed, which allow to assess the whole thermal damage profile in one single test: a simplified interpretation technique for the indirect Ultrasonic Pulse Velocity method, an affordable approach to concrete colorimetry and the real-time monitoring of the drilling resistance.

In this paper, the pros and cons of the proposed techniques are pointed out, as revealed by laboratory tests. The actual in situ viability of each method is then discussed, after the investigations conducted on two full-scale structures: a precast R/C industrial building surviving a real fire and a concrete tunnel submitted to hydrocarbon-pool fire tests.

1. INTRODUCTION

Concrete is known to exhibit a good behaviour at high temperature, thanks to its incombustible nature and low thermal diffusivity, which guarantee a slow propagation of thermal transients within the structural members. As a consequence, very strong thermal gradients are experienced by the reinforcement cover during a fire and the material thermal damage rapidly decreases from a maximum to nil within a few centimetres depth. Only in the cases of quite long fire duration and relatively thin cross sections the exposure to high temperature is expected to sizeably impair the bearing capacity of the structural members [1]. One important exception is the occurrence of explosive spalling, i.e. the sudden expulsion of concrete chips prompted by the vapour pressure build-up, which has the effect of exposing deeper layers of concrete to the maximum fire temperature, thereby increasing the rate of

¹ MSc, Politecnico di Milano, DIS - Dept. of Structural Engineering, p.za L. da Vinci 32, 20136 Milan, Italy
email: mcolombo@stru.polimi.it

² Professor, Politecnico di Milano, DIS - Dept. of Structural Engineering, p.za L. da Vinci 32, 20136 Milan, Italy
email: roberto.felicetti@polimi.it

transmission of the heat. This phenomenon usually takes place at relatively low temperature ($< 400^{\circ}\text{C}$) and the remaining material might have not experienced a significantly high temperature (as in the case of the Channel tunnel fire).

The outcome of heating is a series of chemo-physical transformations occurring in the concrete at increasing temperature [2]: the physically combined water is released above 100°C ; the silicate hydrates decompose above 300°C and the portlandite will be dehydrated above 500°C ; some aggregates begin to convert or to decompose at temperatures above 600°C (α - β SiO_2 -conversion, decomposition of limestone). The mechanical response of the material is weakened concurrently and the compressive strength is expected to be reduced slowly below 450 - 500°C and rapidly above 500°C . This irreversible decay can significantly depend on the mix design, on the heating and cooling conditions and on the structural effects of thermal gradients (self-stresses, cracking). Then, no fixed relationship can be found between the maximum temperature and the residual concrete strength. Nonetheless, concrete structures frequently survive the fire with no significant member collapse and the problem of assessing their residual capacity become of prime interest for designing possible strengthening and repair interventions.

Concerning the other mechanical parameters, a more marked decrease of the Young's modulus is usually observed, whereas the tensile strength exhibits the most temperature sensitive behaviour [3]. Other physical properties are more or less affected by the high temperature exposure, such as density, porosity (total volume and average size of pores), concentration of microcracks, colour, electric conductivity, etc. This extensive series of transformations casts the base for the Non-Destructive material assessment, although the traditional testing techniques are generally not suitable for the inspection of such a highly heterogeneous layered and fractured material.

The possible approaches to this problem (Table 1) generally involve the inspection of the average response of the concrete cover [4, 5], a point by point analysis of small samples taken at different depths [6, 7, 8] or some special techniques for the interpretation of the overall response of the concrete member [8, 9, 10]. However, the majority of these methods are generally not very practical for in situ applications, being either fast but sketchy (e.g. the rebound hammer) or accurate but time consuming (e.g. the point by point analyses).

In order to overcome these limitations, an extensive research programme has been performed at Politecnico di Milano in the framework of UPTUN, an European Research Project focused on the innovative upgrading methods for fire safety in existing tunnels (Technical Task 4.3 - *Innovative damage assessment, repair, recovery and retrofitting*).

Table 1 - Possible approaches to the ND assessment of fire damaged concrete structures.

Average response of the concrete cover	Point by point response of small samples	Special interpretation techniques
Schmidt rebound hammer	Small scale mechanical testing	UPV indirect method
Windsor probe	Differential Thermal Analysis (DTA)	Impact echo
Capo test	ThermoGravimetric Analysis (TGA)	Sonic tomography
BRE internal fracture	Dilatometry (TMA)	Modal Analysis of
Ultrasonic Pulse Velocity	Thermoluminescence	Surface Waves (MASW)
	Porosimetry	Ground-Penetrating Radar
	Colorimetry	Electric Resistivity
	Micro-crack density analysis	
	Chemical analysis	

The twofold objective was to check the viability of some well-established NDT techniques and to propose quick and easy methods for the assessment of the damage experienced by reinforced concrete structures in consequence of a fire [11]. To this latter goal, three new investigation techniques have been proposed, which allow to assess the whole thermal damage profile in one single test, even being based on inexpensive devices and not requiring demanding laboratory analyses. The main features of the proposed test methods and the outline of the experimental programme performed for their calibration and verification are illustrated in the following. Then, their in-situ practicability is discussed, following the investigations conducted on two RC structures surviving a real fire.

2. LABORATORY BENCHMARKS FOR FIRE DAMAGE ASSESSMENT

The main aspect to be considered in any experimental investigation on the response of thermally damaged concrete is the temperature field reached during the heating phase, that is a function of both the heating rate and the following spell at the maximum temperature. The maximum temperature experienced by the material at each point is usually of prime interest, being the mechanical decay almost totally irreversible and less affected by the cooling process. In order ascertain the performances of the proposed techniques and to cover the whole range from the material characterization under homogeneous damage conditions to the strong gradients ensuing from real fires, a series of three testing conditions has been considered in the preliminary part of this research programme.

2.1 Homogeneously damaged concrete cubes for calibration tests

An ordinary concrete and a structural lightweight concrete (NC and LWC, average cubic strength $R_{cm} = 50 \text{ N/mm}^2$ - max aggregate size = 16 mm - cube size = 150 mm) have been tested in compression as they were or after a slow thermal cycle up to $T_{max} = 200, 400, 600$ and 800°C (heating rate = 0.5°C/min , 1 hour spell at T_{max} , cooling rate = 0.2°C/min). These concretes exhibited very similar compressive strength decays (Fig. 1), with a significant loss at temperatures higher than 400°C , in accordance with Eurocode 2 for siliceous concrete (EN 1992 Part 1.2: General rules – Structural fire design, 2004).

The same cubes have been used to calibrate the response of a series of different NDT methods, in order to ascertain their intrinsic sensitivity to the thermally induced strength loss. The results concerning some well established techniques (Schmidt's rebound hammer and Ultrasonic Pulse Velocity) showed a remarkable dispersion, compared to like results available in the literature [7, 12]. This evidence is probably ascribable to a number of differences in the operational parameters (specimens size, experimental procedure, material porosity and initial moisture content), revealing the need for standardized calibration procedures.

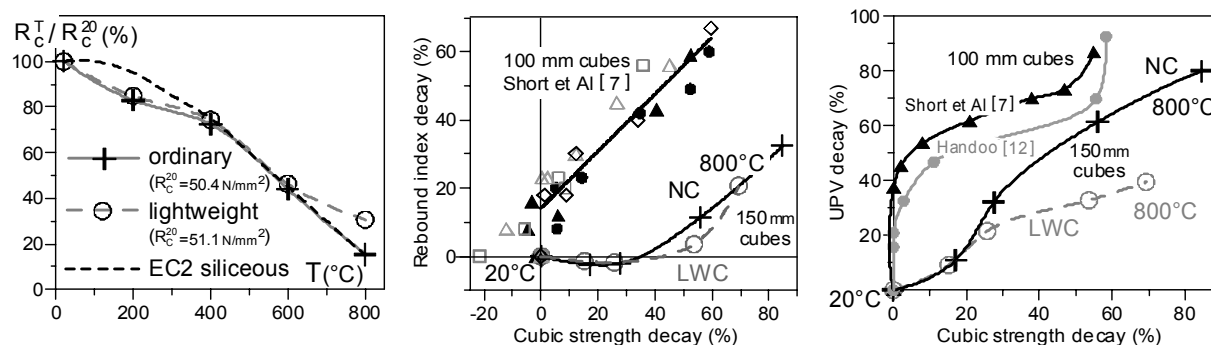


Fig. 1 - Residual strength decay of the uniformly damaged concrete cubes and concurrent relative decay of the Schmidt's rebound hammer and of the Ultrasonic Pulse Velocity.

2.2 Concrete panels under a constant temperature gradient

The same two concretes adopted for calibration tests were used to prepare as many small panels (275x550x80 mm) which have been exposed to a marked thermal gradient ($> 5^{\circ}\text{C}/\text{mm}$) by heating them on the one side ($T_{\max} = 750^{\circ}\text{C}$) while keeping cold the opposite side with a fan (Fig. 2). These specimens are intended as a first, well controlled benchmark for checking the reliability of the proposed test methods in the assessment of the damage gradient within a concrete member. Then, the maximum temperature profile within the panels has been determined by means of three embedded thermocouples. From the temperature at each point and after the plots of the strength decay (see Fig. 1) the profiles of the relative residual strength R_c^T/R_c^{20} have been also worked out, in order to better illustrate the expected mechanical response through the specimen thickness.

2.3 Concrete wall submitted to a ISO 834 standard fire

A more realistic benchmark for the effect of thermal gradients has been provided by a standard fire test on a concrete duct for electric cabling protection in railway tunnels (ISO 834 fire curve, 90 min duration - Fig. 3). The test was run in a vertical furnace, after closing the specimen in a low-grade reinforced-concrete box ($R_{cm} \cong 30 \text{ N}/\text{mm}^2$). As a consequence, the 0.2 m thick concrete wall on the back of the duct was partly exposed to the burners and partly protected by the tested specimen itself. Even not being the object of the fire test, this wall is an interesting example of the possible not uniform damage pattern resulting from a severe fire. A first evidence of this aspect is provided by the plot of the average rebound index at different heights on the back wall (Fig. 3).

In view of the following studies, the temperature of the exposed portion (lines A-C) has then been monitored on both faces and at half thickness and the experimental temperature field has been modelled and fitted numerically, allowing to plot the continuous diagram of the maximum temperature experienced by this concrete member (including the cooling phase). It has to be remarked that in the case of a strong thermal transient, that is the rule in real fires, the temperature of the inner material of a structural member keeps rising during the early cooling phase. This is due to the heat stored in the external hot layer, which flows towards the colder part of the member regardless of the stage of the fire load. As in the previous case, the profiles of the expected residual strength ratio f_c^T/f_c^{20} have been also worked out, based on the standard decay curve for siliceous concrete (EC2 in Fig. 1).

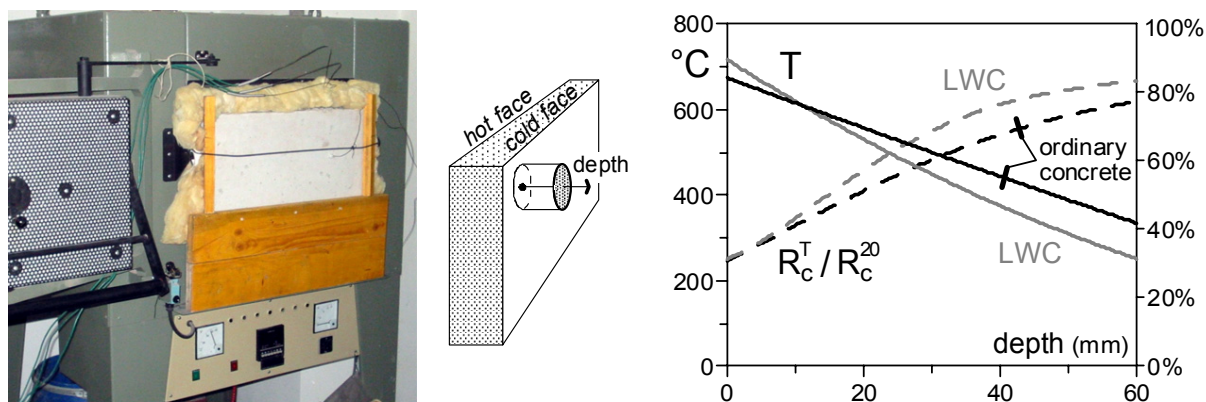


Fig. 2 - Concrete panel positioned as a replacement for the furnace door and exposed to a thermal gradient; ensuing maximum temperature and residual strength profiles through the panels thickness.

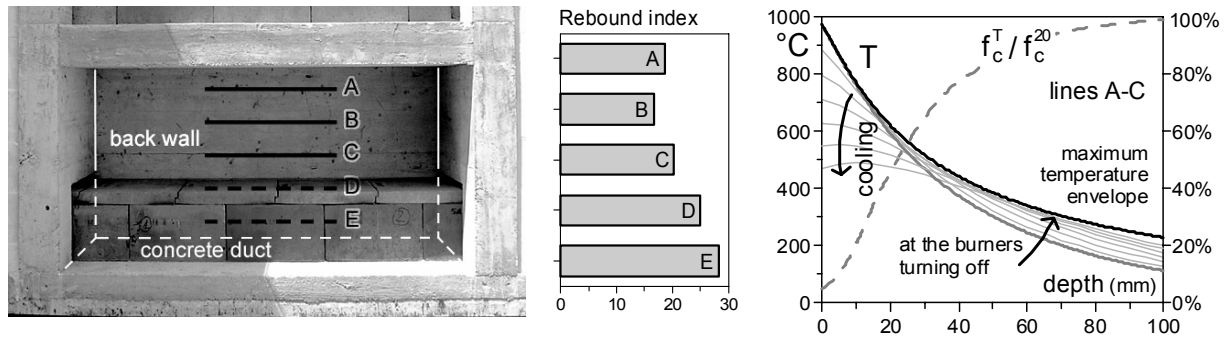


Fig. 3 - Fire-test setup including the concrete duct to be tested and the back wall which has been the object of ND testing; rebound hammer response of the wall after testing and maximum temperature envelope in the exposed part of the wall.

3. NEW NON-DESTRUCTIVE INVESTIGATION TECHNIQUES

As already stated, the main objective of the present research programme is to identify quick and easy methods which could allow to assess the whole thermal damage profile. The outcome consists of three proposals, which are herein briefly illustrated.

3.1 Simplified interpretation of the indirect Ultrasonic Pulse Velocity test results

As it is generally recognized, the velocity of sound in concrete is strongly affected by the thermal damage, thanks to the drying of pores and to the pronounced temperature sensitivity of the Young's modulus (Fig. 1). However, detecting the velocity profile within a member submitted to strong temperature gradients is quite a difficult task. Useful information on the damage depth and severity can be provided via the indirect UPV technique. In this method the measurement of the pulse arrival time is performed by applying both the emitting and the receiving probes on the same face of the investigated element (Fig. 4). Under the assumption that the material velocity rises at increasing depth (that is the rule after a fire), the path of sound waves corresponding to the minimum travel time is the best compromise between reducing the covered distance and exploiting the faster deep layers. Then, the actual depth of the material involved in this pulse propagation is governed by the distance between the probes. A number of repeated measurements of the pulse arrival time T at increasing distance X allows then to investigate deeper and deeper material layers. The outcome of the test series is a plot on the X - T axes whose interpretation has been the object of different numerical methods proposed in the literature [9].

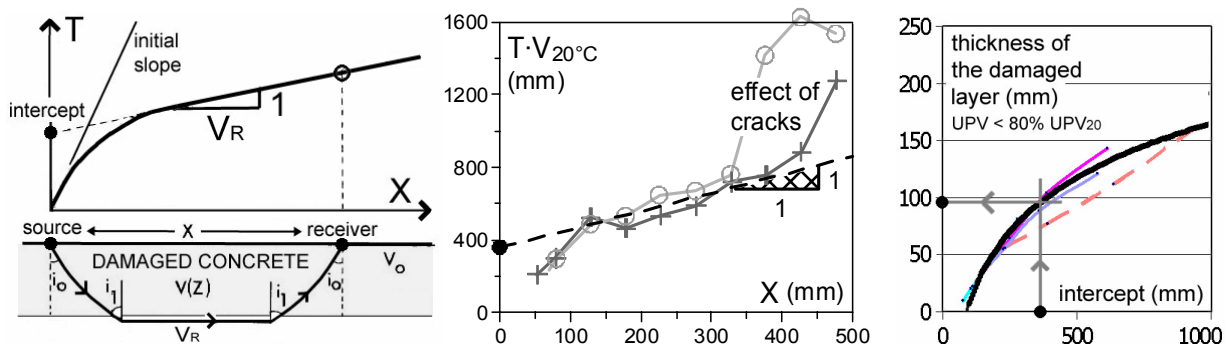


Fig. 4 - Minimum travel-time path and shape parameters of the X - T curve; experimental X - $T \cdot V_{20^\circ C}$ curves obtained from the concrete wall of Fig. 3 (lines B-C) and assessment of the damage thickness (≈ 100 mm) via the intercept of the final asymptote (≈ 360 mm).

The method herein proposed is based on the sketch on the $X-T$ plot of the line corresponding to the final asymptote, whose slope is generally known, being the reciprocal of the velocity $V_{20^\circ\text{C}}$ in the pristine material (in case of thick members and short fire duration). The intercept of this line at $X = 0$ proved to be strongly related to the thickness of the sizably damaged concrete [11]. A series of numerical simulations of different thermal transients involving a broad range of concrete mixes revealed the scarce influence on this relationship of the heating conditions and of the inherent material sensitivity to high temperature. Then, no preliminary information on the member under investigation are needed for the application of this method. Other correlation curves are available in case the whole member thickness is somewhat affected by thermal damage (thin members, long fire duration) and for detecting less stringent damage thresholds.

The reliability and viability of this procedure have been tested by analyzing the concrete wall exposed to a 90 min ISO 834 fire (Fig. 4). The results highlight the good sensitivity of the method, which allows to detect a relatively small velocity decay (see the profile of the maximum temperature in Fig. 3). Nonetheless, it has to be noted that the recording of each $X-T$ plot is generally a demanding task, especially in the presence of cracks, which could more or less noticeably delay the pulse arrival time and impair the convexity of the curve. Moreover this test requires a flat surface and is therefore not appropriate for shotcrete or in the occurrence of spalling.

3.2 Digital camera colorimetry

The colour of concrete is known to change at increasing temperature, generally from normal to pink or red ($300-600^\circ\text{C}$), whitish grey ($600-900^\circ\text{C}$) and buff ($900-1000^\circ\text{C}$). The pink-red discolouration ensues from the presence of iron compounds in the fine or coarse aggregate, which dehydrate or oxidise in this temperature range. The strength of this colour change depends on the aggregate type and it is more pronounced for siliceous aggregates and less so for calcareous and igneous aggregates [13]. Detecting this first colour alteration is of great interest because its appearance usually coincides with the onset of a significant loss of concrete strength as a result of heating.

In this research programme a simplified approach to colorimetry has been formulated, based on the analysis of the side picture of a concrete core, taken via a commonly available low-cost digital camera [14]. The starting point of this method is that digital pictures are usually not very accurate by the colorimetric point of view, but they still allow to recognize slight colour variations among different points on the same sample. Moreover, the considerable amount of data available in a single digital image (many thousands of pixels) allows to separately analyse the cement mortar and the aggregate and to outline some statistical trends ascribable to the inherent heterogeneity of the material.

The analysis of the cores taken from the uniformly heated concrete cubes allowed to recognize the main features of the colour variation on the CIE 1931 xy chromaticity diagram (Fig. 5) and to define a well suited scalar measure of the colour variation for the problem at issue (the difference $x - y$).

Concerning the assessment of damage gradients, 4 + 4 concrete cores have been taken from the cited small concrete panels. The colour variation profiles clearly reveal up to which depth the material has been significantly affected by high temperature. For both the concretes herein investigated, the onset of chromatic alteration corresponds to a 470°C maximum temperature and a 35% decay of the residual strength. These thresholds are slightly higher compared to the UPV technique, but they seem still adequate to the purpose of the structural assessment after a fire. The only limitation of this method is that a core has to be cut from the member, precluding the systematic analysis of thin structural elements.

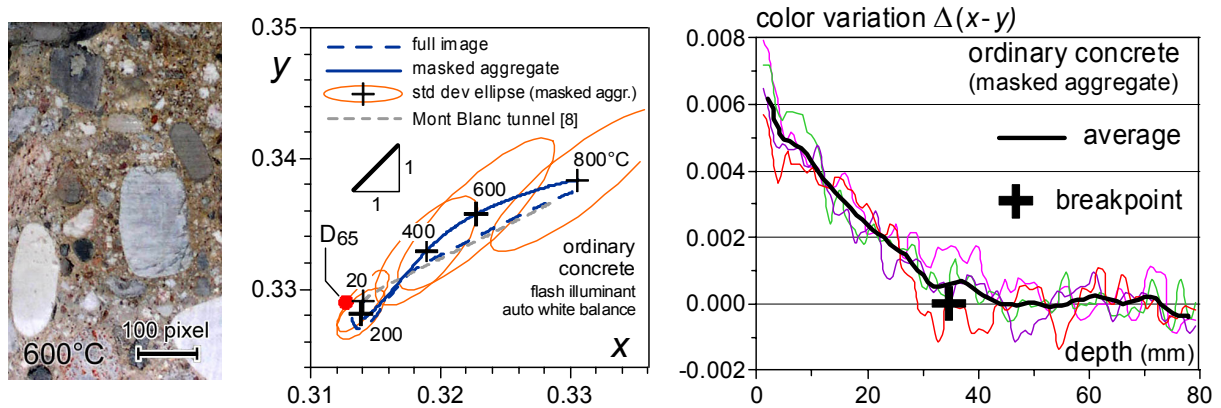


Fig. 5 - Digital image of a uniformly heated concrete core and effect of high temperature on the chromaticity of ordinary concrete; colour variation profiles within one small panel submitted to a constant thermal gradient (see Fig. 2).

3.3 Drilling resistance

The measurement of the drilling resistance appears to be a promising and fast technique to continuously "scan" any strongly layered materials at increasing depth. Some examples of this kind of approach are available in the literature, mainly based on the measurement of either the thrust to be exerted to drill the material at a constant feed rate [15] or the work dissipated to drill a unit deep hole (J/mm - [16]). Concerning the application to fire damaged concrete structures, the thickness to be inspected usually extends to several centimetres and a hammer drill is generally recommended to prevent an excessive bit wearing and overheating. In this case, the sensitivity to the exerted thrust is largely masked by the hammering action and the specific dissipated work (the "drilling resistance" hereafter) appears to be the most promising indicator of the material soundness. Once a constant drill bit performance is guaranteed via the hammering action, the most interesting feature of this technique is that the deep virgin material is inspected in the final stage of the drilling process. Hence, a reference drilling resistance is available for each test and no special calibration curves should be needed for the evaluation of the thickness of damaged concrete.

In this research programme, the drilling resistance has been measured by modifying a common battery hammer-drill (Hilti TE 6-A fitted with 10 mm bits) in order to monitor the electrical power consumption, the bit rotation and the hole depth (Fig. 6, [17]). After proper transformation and analog filtering, the electrical signals are acquired by a laptop computer and processed by a dedicated software, which allows to display the test results in real-time.

The sensitivity of this method to the thermal damage has been preliminarily ascertained by testing the uniformly damaged concrete cubes. Due to the counteracting effect of the increasing material deformability and nearly constant fracture energy, which initially fosters more dissipative penetration mechanisms, only a sizeable thermal damage can be detected via the drilling resistance technique ($T \geq 400-550^{\circ}\text{C}$, $R_c^T \leq 0.5 \div 0.7 R_c^{20^{\circ}\text{C}}$). However, similar damage levels are considered in the popular "Reduced cross-section method" for the design of concrete structures under thermal loads and for the evaluation of the residual capacity after a fire (critical temperature = 500°C).

As regards the assessment of thermal gradients, the drilling tests clearly reveal their effect on the mechanical response of a member (Fig. 6), albeit the result is partially masked by the inherent material heterogeneity ascribable to the aggregate. However, owing to the random nature of this disturbance, it can be easily cleaned out by averaging the results of a few repeated tests. In the case of the concrete wall submitted to a ISO 834 fire, the average

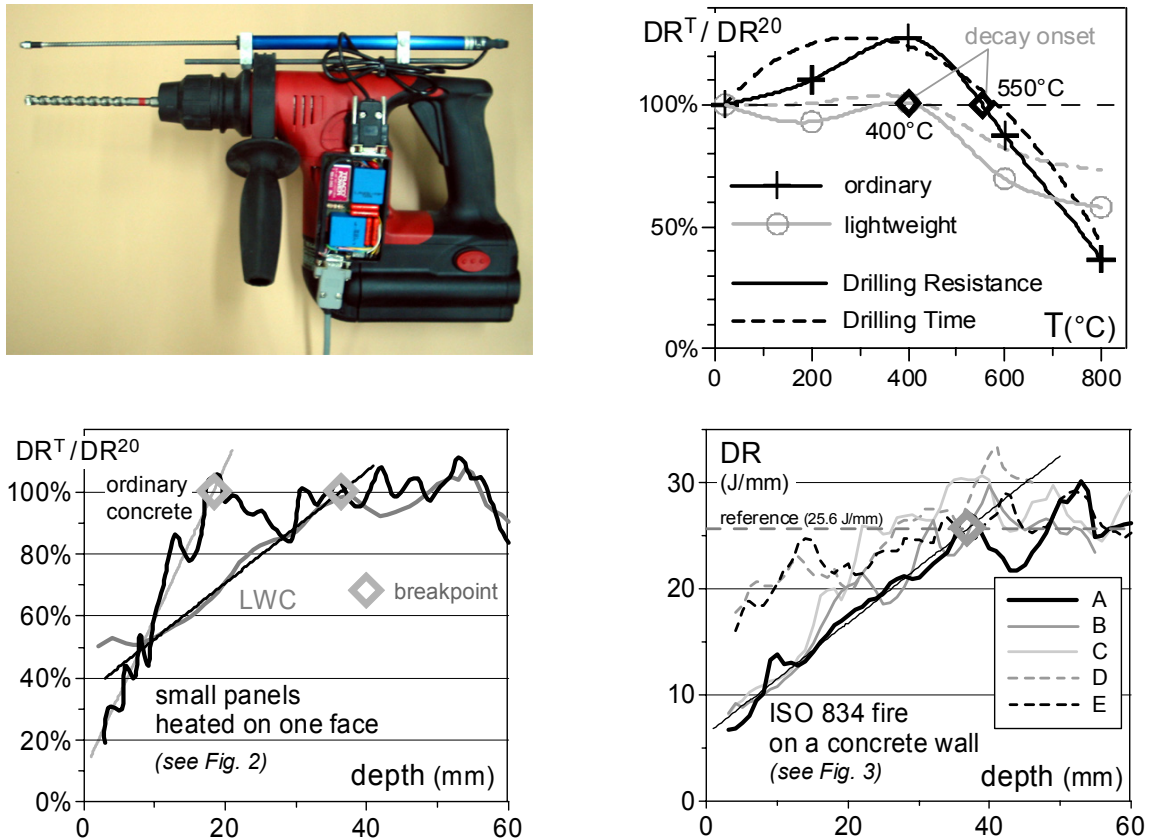


Fig. 6 - The battery hammer drill fitted with the electronic circuits and the displacement transducer; sensitivity to high temperature of the drilling parameters and average profiles of the drilling resistance through the concrete panels submitted to strong thermal gradients.

diagrams pertaining to different areas clearly reveal which part of the structure went through a severe thermal exposure (lines A-C) and which one was only marginally impaired during the fire test (lines D-E). It is worth to note that only about 5 minutes were needed in this latter case to perform the whole series of tests and the results were immediately available for the interpretation thereafter. These are definitely the main benefits of this kind of NDT technique.

4. REAL FIRE IN A PRECAST RC STRUCTURE

The occasion for a first check on the viability of the cited NDT techniques in the case of a real fire has been provided by the thorough analysis of an industrial building surviving a 4 hour fire. The original grade of this concrete is typical of precast RC structures ($R_{cm} \cong 55 \text{ N/mm}^2$). Despite the actual thermal load experienced by each member is unknown, this case allowed to compare a number of investigation techniques in terms of sensitivity to the thermal damage, time needs for the implementation and in situ practicability (Table 2).

Among them, the well-known rebound hammer technique confirmed to be of valuable help for a first, quick monitoring of the severity of the effect of fire on each member. In the case of a severely damaged column (0.45 x 0.45 m - Fig. 7), the simple inspection of the rebound index itself allowed to recognise the most impaired parts of the member, with no need for specific correlations with the residual strength. However, this parameter provides just an estimate of the surface hardness, but no information on the damage depth. Hence, the drilling resistance profile has been evaluated on the two most severely exposed sides of the column, by performing three repeated tests on each face. The results clearly show that

Table 2 - Summary of the techniques utilized for the assessment of the precast RC structure.

structural element	parameter	method
main beams of the roof	residual deflection 1 st mode frequency (torsional) shrinkage cracks opening rebound index Ultrasonic Pulse Velocity drilling resistance	laser theodolite accelerometer microscope Schmidt's hammer indirect UPV modified drill
thin webbed roof elements	residual deflection rebound index	digital image analysis Schmidt's hammer
columns	rebound index Ultrasonic Pulse Velocity drilling resistance	Schmidt's hammer indirect UPV modified drill

different damage depths actually correspond to the same response at the member surface.

Similar conclusions have been drawn by means of the indirect Ultrasonic Pulse Velocity method, though at the price of a more demanding test procedure and under the possible influence of cracks within the concrete cover, which may lead to an overestimation of the damage depth (the first branch of the X-T curve in Fig. 7 is not convex and the intercept value appears too large). This is a common structural effect of strong thermal gradients, which makes the ultrasonic inspection difficult to be performed but has no practical consequences on either the implementation and the results of the drilling test.

No colorimetric analyses have been performed in this case, in order to prevent the further damage of cutting the cores from the investigated members.

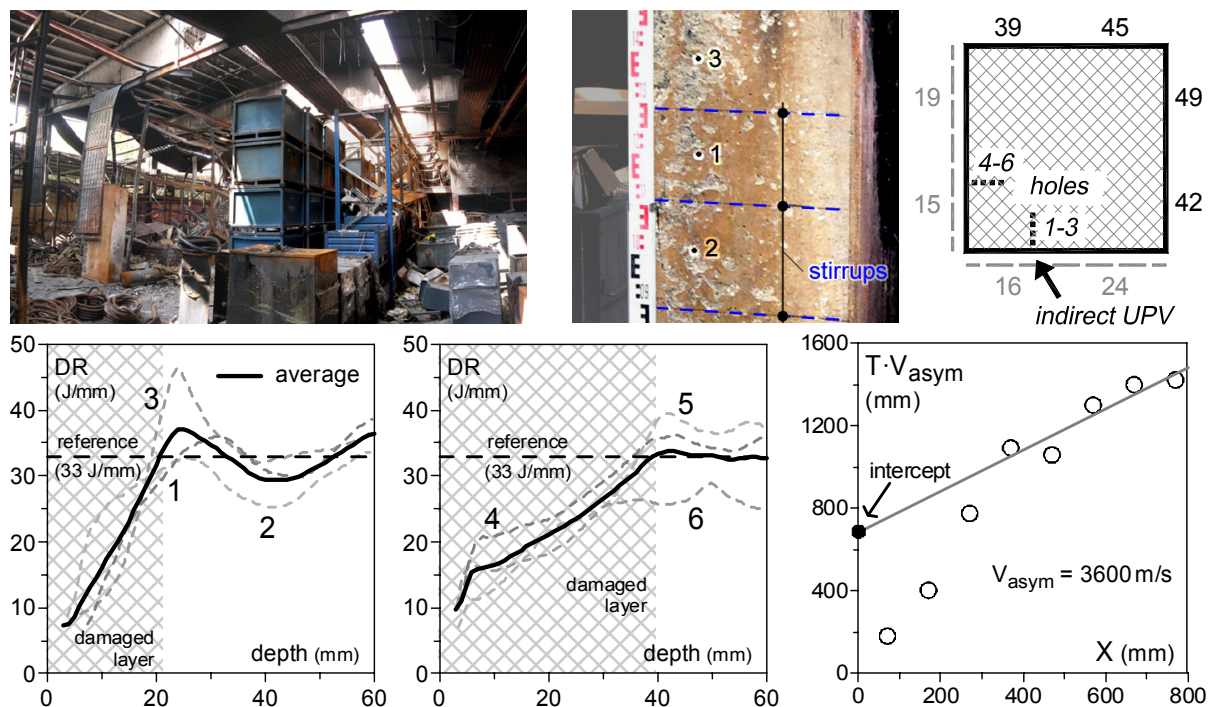


Fig. 7 - View of the precast RC structure after the fire; detail of a significantly damaged column and rebound index around its cross-section; results of the drilling resistance and indirect UPV tests (asymptotic velocity = 3600 m/s, intercept \cong 700 mm).

Table 3 - Material properties of the 6 shotcrete mixes for tunnel lining renewal.

id	fc (MPa)	fct (MPa)	Ec (GPa)	rebound index	std dev
A	34.8	4.7	18.4	35	3.7
B	49.0	4.3	28.3	19	5.0
C	13.5	1.1	6.9	20	1.8
D	85.5	3.0	35.5	31	3.6
E	37.0	7.6	22.6	33	2.7
F	3.7	1.1	2.5	13	0.83

Table 4 - Geometry and ultrasonic velocity of the lining materials tested in the mini-tunnel (1.0 x 1.0 m panels).

panel #	thickness (mm)	base panel thickness (mm)	UPV (m/s)
1	45	50	2840
2	50	100	4530
3	40	50	1580
4	40	50	1620

5. HYDROCARBON FIRE TESTS IN A MOTORWAY TUNNEL

The second verification case considered in this programme is connected again to the tasks of the UPTUN Project (Workpackage 6 - *Fire effects and tunnel performance: system response*). Taking advantage of the lining renovation works in progress in the north channel of the Virgolo tunnel (Bolzano - Italy), the Brennero Motorway management decided to run a series of real-scale tests on different active and passive fire protection systems and to compare the performance of six different shotcrete mixes for lining repair (Table 3 - [18]). The fire load was provided by the diesel oil stored in a series of stainless steel tubs arranged next to the side wall of the tunnel (three tests - 10 to 30 MW pool fires). Both the environment temperature (28 points) and the concrete lining temperature (92 points at 5, 25 and 50 mm depth) were accurately monitored during the tests. A further small scale test has been also conducted in a concrete box (the "mini-tunnel"), where a series of protective lining materials laid on concrete supports have been exposed to a very severe fire (Table 4). The available data on the mechanical properties and the results of some preliminary ND tests highlight the wide assortment of the materials at issue, ranging from lightweight insulating mixes (C, F, 3 and 4) to high performance micro-concrete (D and 2).

Besides the intriguing figures of this experimental programme, a severe verification of the in-situ viability of different NDT techniques has been possible, including the limitations due to a number of operational difficulties to be faced (roughly finished shotcrete surface, hard to approach test points, interfering research teams, short time available for testing). Concerning the results of the main tunnel test, it can be observed that the gas temperature in

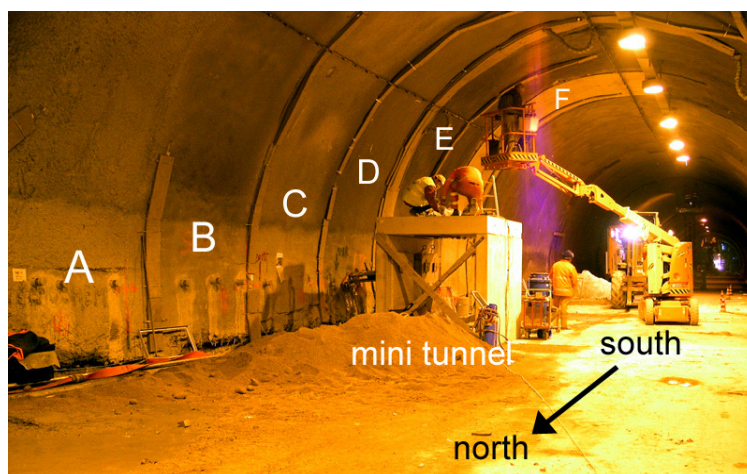


Fig. 8 - The north channel of the Virgolo tunnel covered with six different lining systems and the "mini-tunnel" containing four concrete panels during the hydrocarbon-pool fire test.

the upper part of the tunnel section reached the value of 250-300°C for about 15 min, leading to a temperature in the range 50-200°C at 5 mm depth in the shotcrete samples, depending on their closeness to the oil tubs and on the ventilation conditions (Fig. 9). Due to the surface roughness, it was not feasible to perform the UPV tests and the rebound index itself has been measured only after smoothing some spots on the lining. The time limitations and the not easily accessible vault precluded cutting any core from the lining.

On the opposite, the drilling resistance tests were easy and fast to perform and about 40 holes have been drilled in 7 minutes at 3 m height with only aid of a ladder. The average drilling resistance profiles pertaining to the six shotcrete samples can be summarized in a few damage parameter (the damage depth and the minimum drilling resistance at the surface), by simply normalizing the whole profile on the final, almost constant reference value (Fig. 10).

It has to be noted that, despite the relatively low temperature recorded within the lining, a sizeable damage has been recognized in the first 10-15 mm via the drilling technique. This result is consistent with the visual observation of the vault after fire (extensive delamination and buckling of sample B and microcracking of sample D) and can be probably explained as the outcome of the self-stress ensuing from the thermal gradient.

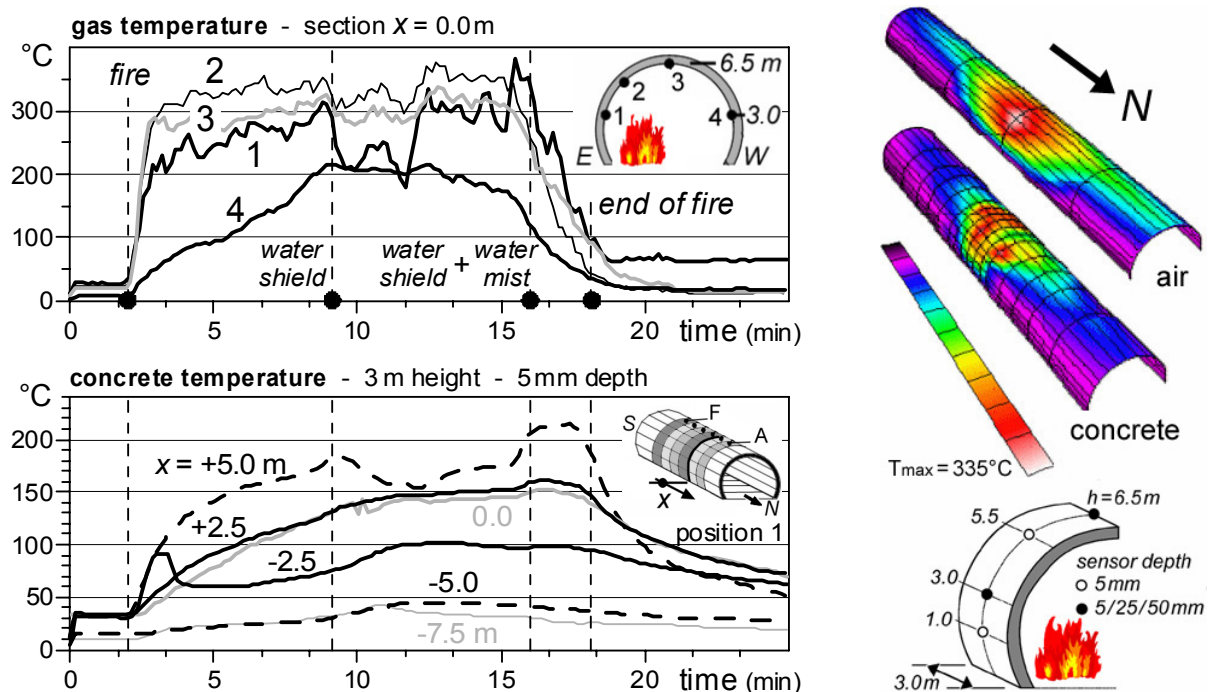


Fig. 9 - Gas and concrete temperature during the 30 MW fire test in the Virgolo tunnel [18].

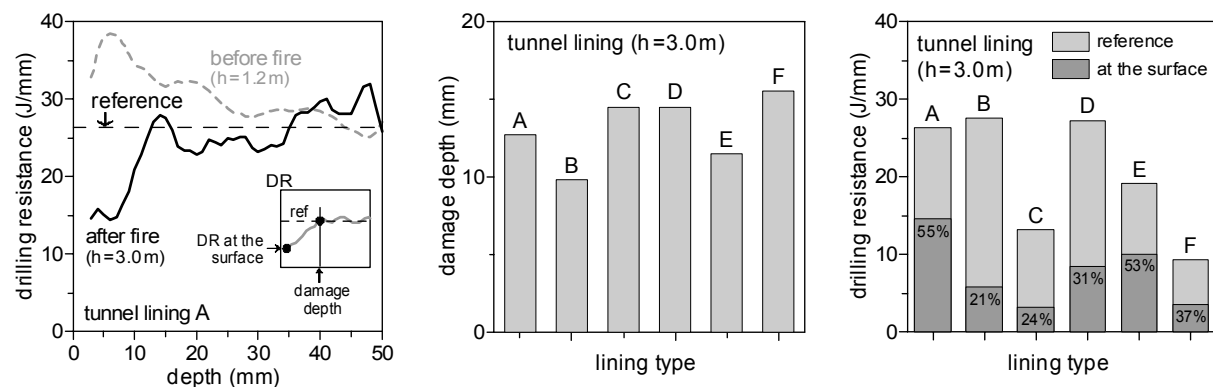


Fig. 10 - Drilling resistance profile in the first shotcrete sample and histograms of the damage depth and maximum damage at the surface for the six samples.

More severe heating conditions have been recorded in the mini-tunnel test, although the short fire duration considerably smoothed the effects at depth exceeding 10 mm (Fig. 11). The results also draw attention to the strong effect of thermal diffusivity, which can halve the maximum temperature undergone by concrete in the case of lightweight mixes.

Concerning the assessment of the damaged materials, much better operational condition have been managed in this case and the smooth face of the tested panels allowed to perform the indirect UPV tests. However, the presence of a stiff base panel and the possible effect of the lining delamination took the lion's share in determining the final asymptote of X - T curve, especially for soft insulating materials. Just in the case of the high performance concrete (panel #2), the effect of fire exposure can be clearly detected, with a 15% decay of the asymptotic velocity (as a possible effect of drying) and a 150 mm intercept (Fig. 12).

The colour variation profiles have been assessed as well, taking advantage of the holes remaining after cutting some small diameter cores. In the case of sample #2, the discolouration onset is determined at about 5 mm depth, which seems to be in good agreement with the temperature recorded during the test and in consideration of the sensitivity of the method. It has to be noted that this colour alteration was hardly noticeable with the naked eye.

Finally, the drilling resistance method confirmed its good reliability and viability, allowing to detect the damage depth, the maximum damage at the surface and the interface between the protective lining material and the harder concrete support (Fig. 13). The results show again that the mechanical weakening seems to exceed the simple chemo-physical effects of heating, probably because of the strong thermal gradients induced by this severe fire.

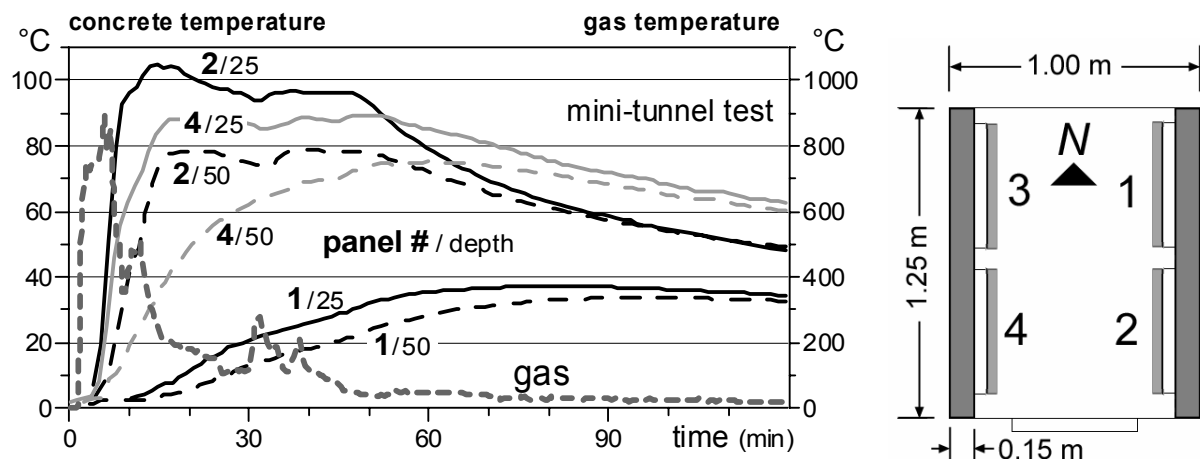


Fig. 11 - Temperature of gas and concrete (25-50 mm depth) in the mini-tunnel fire test [18].

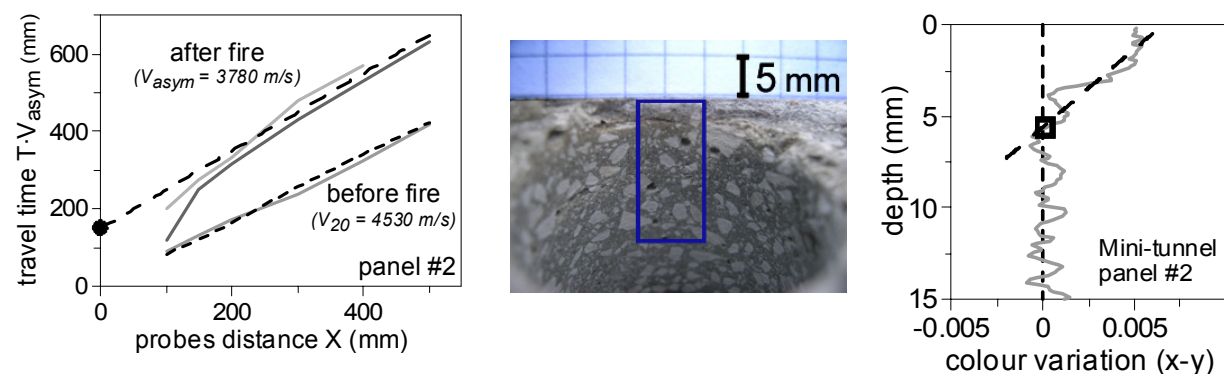


Fig. 12 - Indirect UPV X - T curves measured on the mini-tunnel panel #2 and assessment of the colour variation profile on the face of a micro-core hole via the digital image analysis.

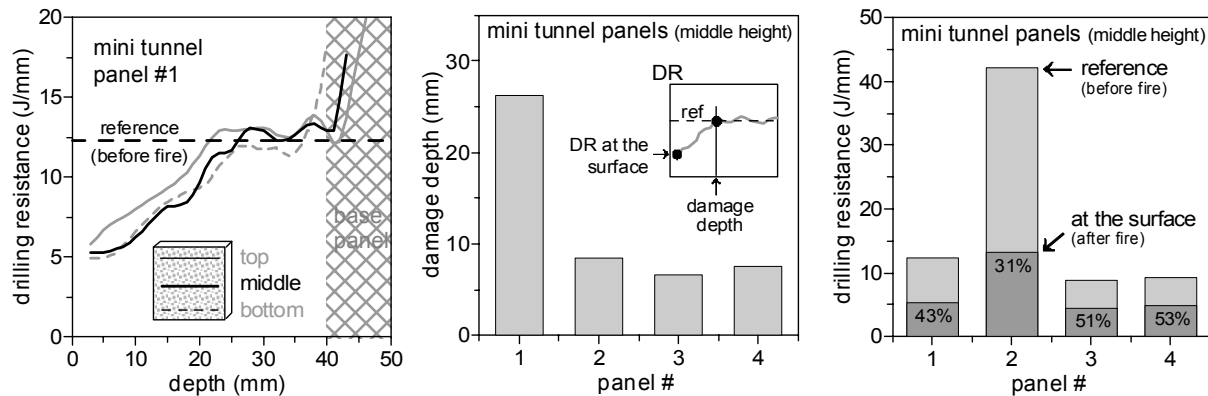


Fig. 13 - Drilling resistance profile within the mini-tunnel panel #1 and histograms of the damage depth and maximum damage at the surface for the samples at issue.

6. CONCLUSIONS

In this paper three innovative NDT methods for the assessment of fire damaged concrete structures have been presented, following the promising results of some preliminary laboratory tests. The viability of these methods in case of real fires and actual in-situ operational conditions has then been checked with reference to a precast RC structure and a motorway tunnel, allowing to formulate the following set of conclusions:

The indirect Ultrasonic Pulse Velocity method proved to be quite sensitive, thanks to the prompt effect of heating on the dynamic modulus and moisture content of concrete. The application of this technique is rather time consuming (≈ 15 min/test) and requires an almost flat surface, which makes it generally not appropriate for shotcrete or in the occurrence of spalling. The proposed procedure allows to considerably speed up the interpretation of the results with no need for a preliminary calibration for the specific material properties. However, the possible influence of cracks, delaminations and presence of distinct layers could markedly affect the results and a careful check on both their repeatability and consistency is recommended, regardless of the interpretation procedure.

The proposed simplified approach to colorimetry proved to be a powerful tool for releasing the evaluation of the well known colour alteration of heated concrete from the need for an expert judgment. Compared to a common colorimeter, the considerable amount of data available in a single digital image (many thousands of pixels) allows to separately analyse the cement mortar and the aggregate and to outline some statistical trends ascribable to the inherent heterogeneity of the material. Moreover, a scalar measure of the colour variation has been expressly defined in to order to simplify the assessment of the material. The in-situ application to the real fire cases confirmed the viability of this method, with the only limitation of the permanent damage produced by cutting the concrete cores to be analysed.

The continuous monitoring of the drilling work dissipated by a common hammer drill confirmed to be a reliable method for assessing the severe damage gradients occurring in concrete structures during a fire. In the case of in situ applications this technique proved to be very fast and easy to be implemented, with no influence of cracking, surface roughness and spalling. The evaluation of the material response relative to the inner undamaged layer allows to release the results from the availability of specific calibration curves and from the repeatability of the testing conditions (bit wearing, stiffness and mass of the tested member, average thrust). The immediate availability of the results confirmed to be of valuable guidance in the assessment of concrete structures surviving complicated fire scenarios.

7. ACKNOWLEDGEMENTS

The author wishes to acknowledge the financial support of CTG - Italcementi Group, in the framework of the European Communities Project UPTUN on the upgrading of existing tunnels. A grateful acknowledgement goes to all the students who lively cooperated to the development of the NDT techniques in partial fulfilment of their MS degree requirements: M. Bondesan and G. Pizzigoni (drilling tests), G.A. Basilico and D. Cabrini (concrete colorimetry), A. Faccoli and L. Marzorati (indirect UPV interpretation). A particular acknowledgement goes to prof. K. Bergmeister (BOKU University - Vienna - Austria) for his factual support to the experimental activities in the Virgolo tunnel.

8. REFERENCES

- [1] CIB W14 Report, "Repairability of Fire Damaged Structures", Drysdale D. and Schneider U. (eds), Fire Safety Journal, V. 16, pp. 251-336, 1990.
- [2] Khoury G. A., "Effect of Fire on Concrete and Concrete Structures", Progress in Structural Engineering Materials, V. 2, pp. 429-447, 2000.
- [3] Felicetti R., Gambarova P.G. and Meda A., "Expertise and assessment of structures after fire", in Fib Task Group 4.3.2 "Guidelines for the Struct. Design of Concrete Buildings Exposed to Fire", Chapter 10, 43 pp. (in publication).
- [4] Tay D.C.K. and Tam C.T., "In situ investigation of strength of deteriorated concrete", Construction and Building Materials, V. 10, n. 1, pp. 17-26, 1996.
- [5] Cioni P., Croce P. and Salvatore W., "Assessing fire damage to R/C elements", Fire Safety Journal, V. 36, pp. 181-199, 2001.
- [6] Short N.R., Purkiss J.A. and Guise S.E., "Assessment of Fire-Damaged Concrete", Proc. of the Concrete Communication Conference, British Cement Association, pp. 245-254, 2000.
- [7] Short N.R., Purkiss J.A. and Guise S.E., "Assessment of Fire-Damaged Concrete Using Crack Density Measurements", Structural Concrete, V. 3, pp. 137-143, 2002.
- [8] Laboratoire Central des Ponts et Chaussées, "Présentation des techniques de diagnostic de l'état d'un béton soumis à un incendie", Report ME 62, 114 p., 2005.
- [9] Benedetti A., "On the ultrasonic pulse propagation into fire damaged concrete", ACI Structural Journal, V. 96, n. 3, pp. 257-271, 1998.
- [10] Abraham O. and Dérobert X., "Non-destructive testing of fired tunnel walls: the Mont-Blanc Tunnel case study", NDT&E International, V. 36, pp. 411-418, 2003.
- [11] Felicetti R., "New NDT techniques for the assessment of fire damaged RC structures", Technical Report, Dept. of Structural Engrg. (DIS), Politecnico di Milano, 26p., 2005.
- [12] Handoo S.K., Agarwal S. and Agarwal S.K., "Physicochemical, Mineralogical and Morphological Characteristics of Concrete Exposed to Elevated Temperatures", Cement and Concrete Research, V. 32, pp. 1009-1018, 2002.
- [13] Short N.R., Purkiss J.A. and Guise S.E., "Assessment of Fire-Damaged Concrete Using Colour Image Analysis", Construction and Building Materials, V. 15, pp. 9-15, 2001.
- [14] Felicetti R., "Digital-Camera Colorimetry for the Assessment of Fire-Damaged Concrete", Proc. Int. Workshop on "Fire Design of Concrete Structures: What now? What next?" - *fib* Task group 4.3, P.G. Gambarova, R. Felicetti, A. Meda and P. Riva (editors), Milan (Italy), pp. 211-220, 2005.
- [15] Chagneau F. and Levasseur M., "Contrôle des matériaux de construction par dynamostratigraphie", Materials and Structures, V. 22, pp. 231-236, 1989.
- [16] Gucci N. and Barsotti R., "A non-destructive technique for the determination of mortar load capacity in situ", Materials and Structures, V. 28, pp. 276-283, 1995.
- [17] Felicetti R., "The Drilling Resistance Test for the Assessment of Fire Damaged Concrete", Journal of Cement and Concrete Composites, special issue on NDT in Concrete, (in publication) 2006.
- [18] Bergmeister K., "Real Scale Fire Tests - Virgolo Tunnel", Test Report Nr. 875-05-004, Dept. of Struct. Engrg. and Natural Hazards, BOKU University, Vienna (Austria), Rev. 1.3, October 2005, 180p.

SiF'06

TRANSIENT THERMAL STRAIN OF SELF-COMPACTING CONCRETE – WITH AND WITHOUT POLYPROPYLENE FIBRES

Bertil PERSSON¹

ABSTRACT

This article outlines a theoretical and an experimental investigation on the transient thermal strain of Self-Compacting Concrete. For this purpose more than about 100 laboratory experiments at high temperature on the deformation both with and without loading were performed involving normal, High-Performance and Self-Compacting Concrete, with and without polypropylene fibres. The theoretical background for the transient thermal strain is described. The result indicates much lower thermal expansion coefficient and lower transient thermal strain for Self-Compacting Concrete with polypropylene fibres than for Self-Compacting Concrete without polypropylene fibres. The experiments in a way clarify the functioning of polypropylene fibres in Self-Compacting Concrete at high temperature, i.e. the moisture is prevented from moving inward in Self-Compacting Concrete with fibres and thus moves outward and leaves the Self-Compacting Concrete. For Self-Compacting Concrete without fibres high pressure is instead built up by moisture moving inward in the Self-Compacting Concrete with the temperature gradient. The work was performed at Lund University, Lund, 2003–2005.

1. INTRODUCTION

The interest in using of Self-Compacting Concrete, SCC, and High-Performance Concrete, HPC, is increasing rapidly in order to solve modern work-environmental conditions and construction moisture problems. At present SCC covers 50% of the precast market in Sweden, and in some factories as much as 100%. About 7 million m² of HPC flooring have been cast in the last decade, also a way to achieve site speed since moulds may be removed earlier with HPC than with normal concrete, NC. For both SCC and HPC the fire spalling resistance is of great importance since fire spalling resistance is required in both tunnels and dwelling houses.

¹ Lund University, Div. Building Materials, P.O. Box 118, SE-221 00 Lund, Sweden, e-mail: bertil.persson@byggtek.lth.se

One way to solve the fire spalling resistance seem to be to introduce polypropylene fibres, ppf, in the mix proportions [1]. Another factor invoked to justify the use of ppf for mix proportions is a potential increase of durability in severe conditions or possible effect on shrinkage [2,3]. Recent research shows that transient thermal strain, TTS, increases with HPC compared to NC. TTS is defined as the difference between thermal deformation with loading and thermal without loading, other parameters being held constant [4,5]. TTS for HPC and SCC may be larger than for NC due to more cement paste in both HPC and SCC than in NC [6]. The objective of the work was to establish fundamental values of TTS for SCC both with and without ppf and to compare the results with TTS of NC.

2. PREVIOUS RESEARCH

Analysis and experimental results show clearly that TTS of HPC is superior to that of NC, even though TTS is larger for concrete with siliceous aggregate than for concrete based on limestone aggregate [6]. Comparisons were made between TTS of NC with limestone aggregate and CEM II (cement content: 350 kg/m³, water content: 181 kg/m³, w/c = 0.52, and 28-day strength of 37 MPa), HPC with limestone aggregate and CEM I (cement content: 377 kg/m³, silica fume: 38 kg/m³, water content: 124 kg/m³, w/c = 0.33, water-binder ratio, w/b=0.30, and 28-day strength of 113 MPa), and, finally, HPC with siliceous aggregate and CEM I (cement content: 450 kg/m³, silica fume: 45 kg/m³, water content: 148 kg/m³, w/c = 0.33, w/b=0.30, and 28-day strength of 92 MPa). Dry HPC (pre-heated and dried at 105 °C) exhibits lower thermal expansion coefficient than 2.5%-moistured HPC. Therefore TTS of dry HPC became higher than that of 2.5%-moistured HPC since the reduction of the total deformation due to thermal expansion was larger for 2.5%-moistured HPC than for dry HPC [6]. TTS mainly consists of creep since the deformation remains after the concrete is cooled. However, TTS of NC is more stress-related than creep, which shows little stress effect up to 40% of ultimate loading [7]. TTS is about twice as large at 40% stress level as at 20% stress level [6]. It is also clarified that TTS only exists during the first temperature cycles [6]. Once the hydrated water in the concrete is dried out no more moisture movements take place in the cement gel and thus no TTS, which is moisture-related [6]. Experiments on TTS of cement paste demonstrate that expansion takes place up to 150 °C and thereafter contraction, which indicates that TTS mostly takes place in the cement paste [6]. At tension no TTS seems to exist [6]. It has also been shown that the permeability development related to high temperature may be an explanation for the behaviour of ppf in concrete [8,9], Fig. 1. Fig. 1 shows the intrinsic permeability versus heating temperature [9]. Traditional tunnel with CEM I (cement content: 260 kg/m³, fly ash: 60 kg/m³, water content: 157 kg/m³, w/c = 0.60, w/b=0.49, and 28-day strength of 52 MPa) was studied. The ppf was of 18 µm diameter and 6 mm in length. At low temperature ppf expand or melt and then lower the permeability compared with concrete without ppf – at higher temperature ppf evaporates leaving free space for the water to leave the concrete externally without any critical pressure building up [8-10]. From the theoretical point of view a hollow cylinder is preferred to measure TTS, since the temperature then stabilises more rapidly during the heating [5,11]. On the other hand pressure built up in the surface of the concrete during the heating is not realistic with a hollow cylinder as with a massive one, Fig. 2 [8,9,12]. Fig. 2 shows the concrete vapour pressure versus depth during heating of full-scale slabs, 0.5x1.4x1.8 m [8,9]. Maximum pressure at about 25 mm depth is typical of concrete in which depth spalling occurs. Simulations slightly underestimate the transient thermal strain which is estimated from total strain deducted with the strain without loading [13-15], Fig. 3.

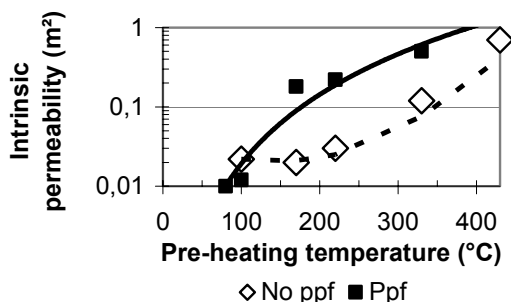


Fig. 1 - Intrinsic permeability vs heating temperature [9].

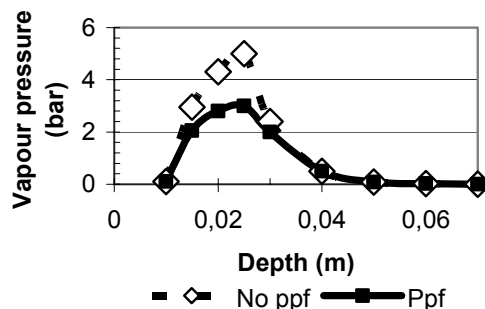


Fig. 2 - Vapour pressure vs depth during heating of full-scale concrete slabs, 0.5x1.4x1.8 m [8,9].

3 EXPERIMENTAL

3.1 Materials

Appendix 1 shows chemical and physical properties of the cements used [16]. The aggregate was quartzite or gneiss with an elastic modulus of 61 GPa and compressive strength 330 MPa (quartzite) or 230 MPa (gneiss). Appendices 2–3 show the mix proportions of studied concrete [16,17]. Compulsive mixing was used with water, additives and admixtures added to dry materials and mixed for 3 min. From the fresh concrete 100-mm cylinders, 200 mm long, were cast. Thermocouples were cast-in at 20-mm depth in the cylinders. For strength tests 100-mm cubes were cast. After demoulding the specimens were cured at relative humidities of either 30%, 60% or 90% until testing.

3.2 Methods

Testing took place between 3 and 14 months' age in a high-temperature oven, Fig. 4.

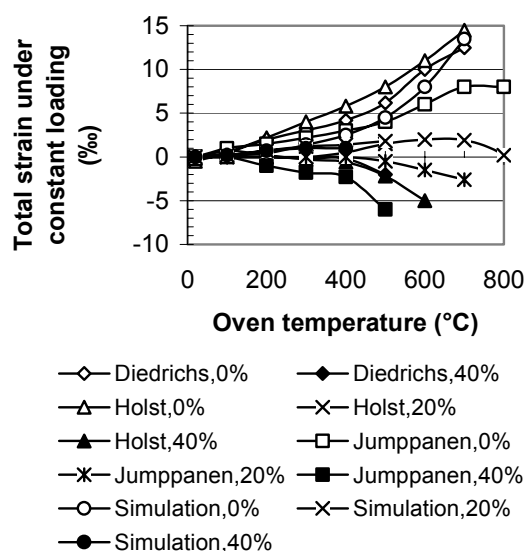


Fig. 3 - Strain with 40% of ult. loading at 20 °C during temperature increase [13-15].



Fig. 4 - Electrical oven with LVDTs and cooling equipment.

The concrete temperature rise was held constant at 7.5 °C/min. [18], i.e. the temperatures at 20-mm and 50-mm depths are given in Fig. 5 and described with the equations:

$$T_{20} = 3.78 \cdot \exp(0.00663 \cdot U) \quad \{200 < U < 600 \text{ °C}\} \quad (1)$$

$$T_{50} = 1.11 \cdot \exp(0.00778 \cdot U) \quad \{200 < U < 600 \text{ °C}\} \quad (2)$$

With ppf the following temperatures were obtained (°C):

$$T_{20} = 6.7 \cdot \exp(0.00555 \cdot U) \quad \{200 < U < 800 \text{ °C}\} \quad (3)$$

$$T_{50} = 6.15 \cdot \exp(0.00525 \cdot U) \quad \{200 < U < 800 \text{ °C}\} \quad (4)$$

where U denotes the oven temperature (°C), T_{20} and T_{50} temperature at 20-mm and 50-mm surface depth (°C). Testing continued until explosion, which was the case for most of the specimens without ppf, or until about 950 °C oven temperature, Fig. 5. Measurements were taken at 20 °C outside the oven with two LVDTs placed between water-cooled stainless steel supports in the oven. Before concrete testing the deformations were calibrated. The pressure was adjusted to a constant level, ± 0.1 kN, with a newly developed high-accuracy computer-steered hydraulic system (in order to avoid unbalanced deformations a constant loading of 0.5 kN was applied as a minimum loading).

4. RESULTS AND DISCUSSION

4.1 Thermal expansion and shrinkage

Figs 6 (oven start temperature: 20 °C) and 7 (start temperature: 225 °C) show deformations without loading of SCC and NC with CEM I. Fig. 8 (start temperature: 20 °C) shows deformations without loading of SCC and NC with CEM II. Figs 9 (CEM I) and 10 (CEM II) show summaries of the coefficient of thermal expansion (with shrinkage), μ (‰/°C). It was observed that μ increased with higher RH before the heating. More moisture in the concrete before heating caused more expansion than in concrete with lower moisture content. Larger expansion due to higher moisture content was not compensated for by larger shrinkage due to larger evaporation. For concrete with ppf about 30% lower μ was obtained than for concrete without ppf since moisture then evaporated to the surface of the concrete and thus did not build up internal pressure in the concrete. With ppf the concrete was impregnated at lower temperatures, preventing moisture transports, and at higher temperature canalised with ppf. At higher temperatures higher permeability was obtained in concrete with ppf than in concrete without ppf [2,10] The following equation was obtained for μ (‰/°C) [16,17]:

$$\mu = k_{ppf} [0.014 \cdot (w/c)^2 - 0.011 \cdot w/c + 0.0022] \cdot RF - 0.97 \cdot (w/c)^2 + 0.76 \cdot w/c - 0.133 \quad \{0.30 < w/c < 0.50; 30\% < RH < 90\} \quad (5)$$

where $k_{ppf} = 0.67$ with ppf and $k_{ppf} = 1$ otherwise.

4.2 Thermal transient strain, TTS

Deformations, with and without loading, were measured and TTS calculated for loading levels varying between 0 and 45% of the ultimate one at 20 °C. TTS is dependent on the temperature increase excluding thermal expansion and shrinkage. The temperature increase of the SCC and NC described with the equations (1)–(4). The deformation of the SCC and NC was more or less linear with the temperature of the SCC and NC up to about 600 °C. Thereafter SCC and NC without loading exhibited an increasing thermal expansion while SCC and NC exhibited a decreasing expansion with increasing loading. At about 50% loading of the ultimate loading contraction was obtained. This in turn was dependent on strain in the cement paste which was dependent on the loading level. In these tests the total deformation first of all was reduced by the deformation due to thermal expansion and shrinkage.

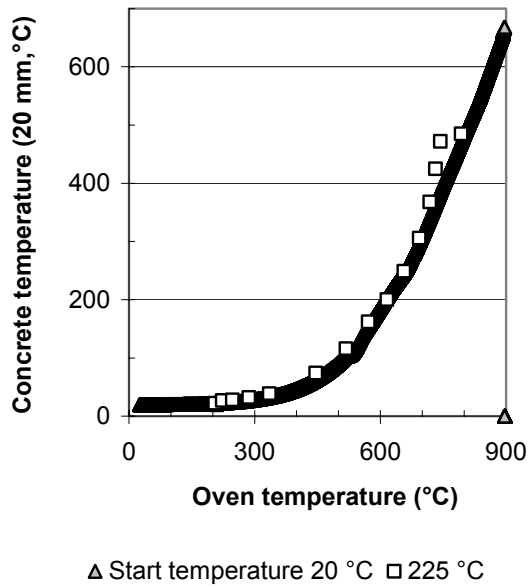


Fig. 5 – Concrete and oven temperature.

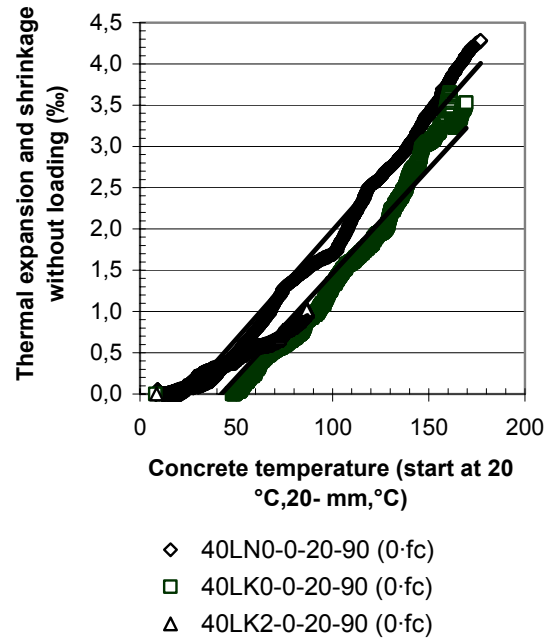


Fig. 6 – Deformations with CEM I (no load).

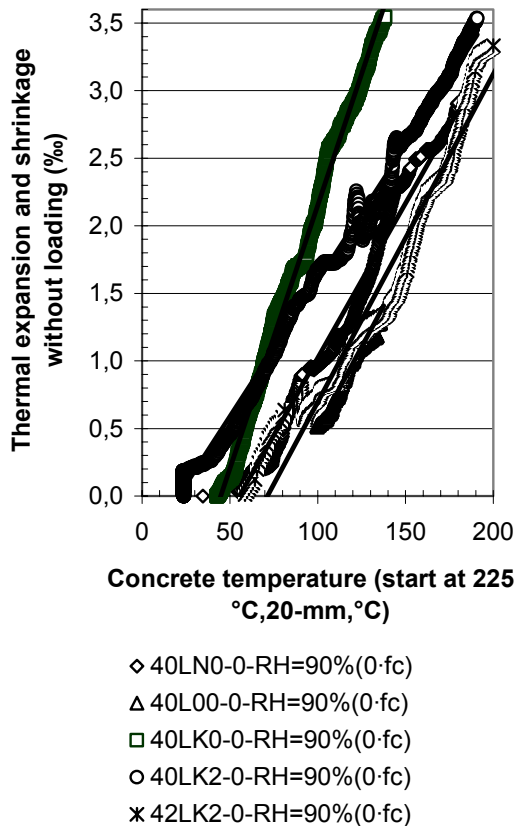


Fig. 7 – Deformations from 225 °C with CEM I without loading.

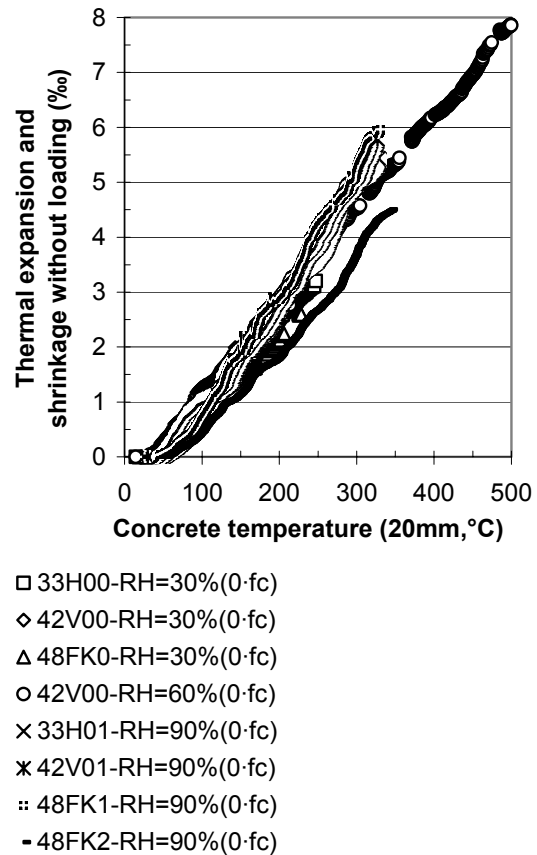


Fig. 8 – Deformations with CEM II without loading.

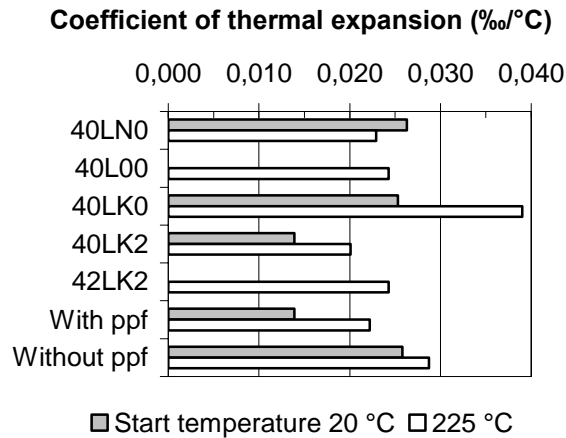


Fig. 9 - Thermal expansion coeff. (CEM I).

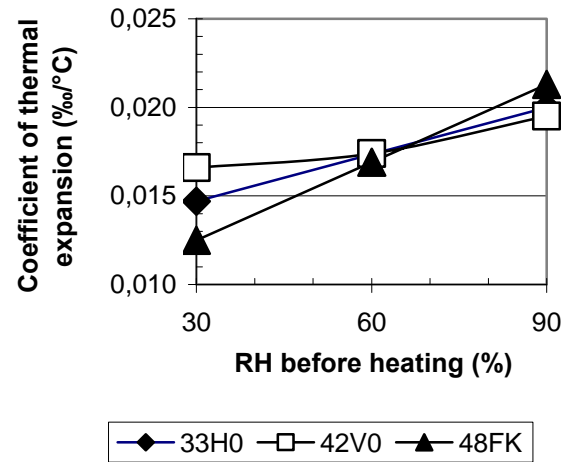


Fig. 10 – Thermal expansion coeff. (CEM II)

Thereafter the resulting deformation was divided by the stress in order to obtain the specific transient thermal strain, J_{TTS} , which besides stress was dependent on the loading level and the temperature increase, Figs 11–18. J_{TTS} were related to the temperature development, dJ_{TTS}/dT , at the temperature development of 450 °C/h up to 500 °C concrete temperature, i.e. more or less the highest temperature that is of interest for concrete structures. With knowledge of dJ_{TTS}/dT it is possible to estimate deformations after fire of SCC and NC dependent on loading level, the ppf content, temperature and w/c. In order to further facilitate these comparisons dJ_{TTS}/dT was related to the elastic deformation, δ_{el} , at 20 °C as shown in Appendices 2–3:

$$\varphi = (\delta_T - \delta_{el}) / \delta_{el} \quad (6)$$

where δ_{TTS} denotes deformation due to TTS. For concrete without ppf the relative TTS, $d\varphi/dT$, increased with the loading level and, in contrast to concrete with ppf, $d\varphi_{TTS}/dT$ decreased with increasing loading level, Figs 19–20. The following equations were obtained (up to 250 °C for concrete without ppf and up to 500 °C for concrete with ppf):

$$d\varphi/dT_{no\ ppf} = (-0.22 \cdot (\sigma/fc) - 0.011) \cdot vct + 0.127 \cdot (\sigma/fc) + 0.0173 \{0.3 < vct < 0.5; 0.15 < \sigma/fc < 0.45\} \quad (7)$$

$$d\varphi/dT_{ppf} = (-0.53 \cdot (\sigma/fc) + 0.265) \cdot vct + 0.238 \cdot (\sigma/fc) - 0.0868 \{0.3 < vct < 0.5; 0.15 < \sigma/fc < 0.45\} \quad (8)$$

σ/fc denotes the loading level of ultimate loading before testing. The total deformation relative to the elastic deformation at a specific temperature increase is thus obtained by multiplication by the temperature increase in the concrete, preferably up to 250 °C for concrete without ppf since more or less all concrete without ppf exploded. For concrete with ppf TTS at a temperature increase up to 500 °C is well documented. With ppf in the concrete lower TTS and thus less difference in deformation between the surface of the concrete and the inner of the concrete was observed than in concrete without ppf. This means that less shear forces between the surface and the inner of the concrete exist in concrete with ppf than in concrete without ppf. This observation of different TTS of concrete with ppf and without ppf is probably the explanation for the function of ppf to prevent fire spalling in concrete [16,17]. High moisture content in concrete at high temperatures without ppf gives large TTS. If the moisture instead moves out of the concrete the moisture content in the concrete will be lower and therefore also TTS.

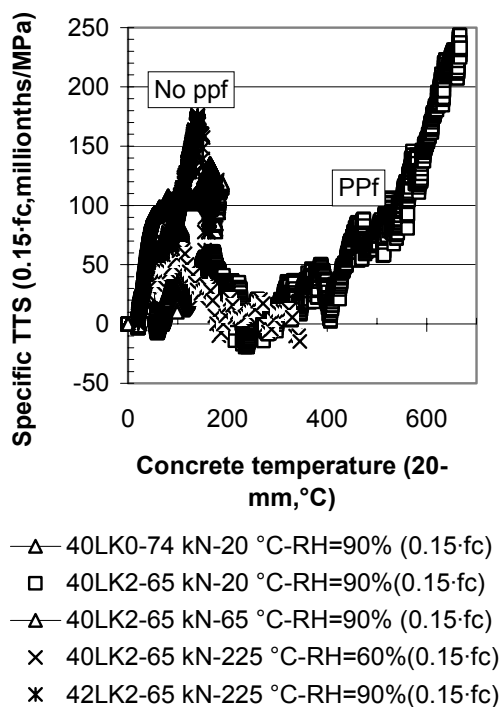


Fig. 11 – Specific TTS, CEM I, at 15% loading level.

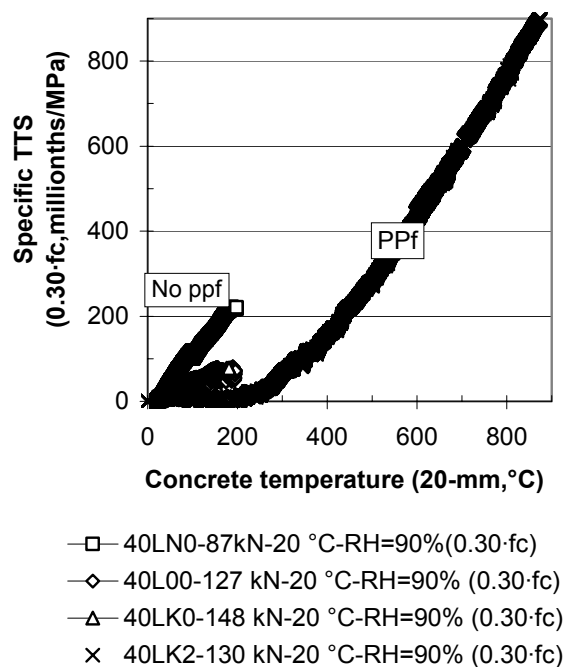


Fig. 12 – Specific TTS, CEM I, at 30% loading level.

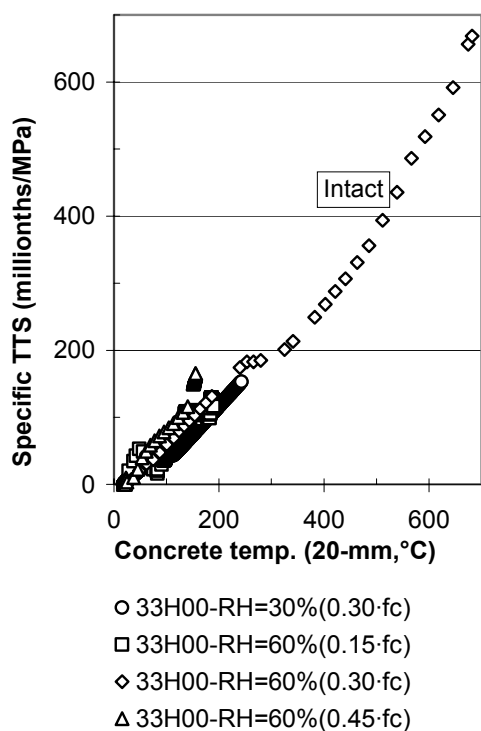


Fig. 13 – Specific TTS, concrete 33H00.

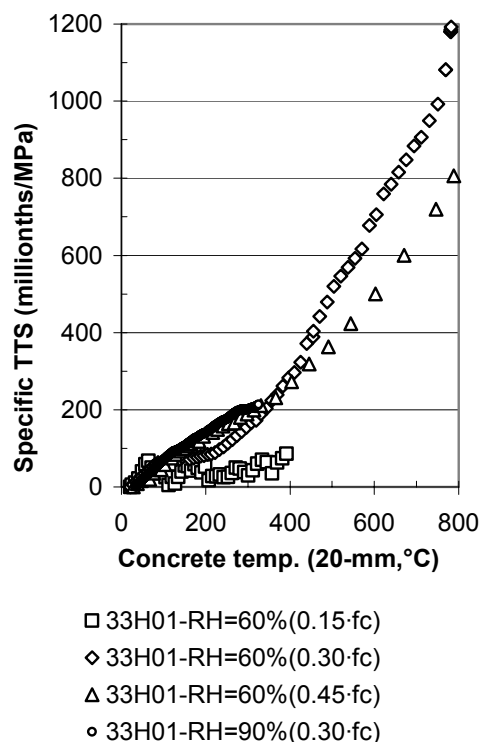


Fig. 14 – Specific TTS, concrete 33H01.

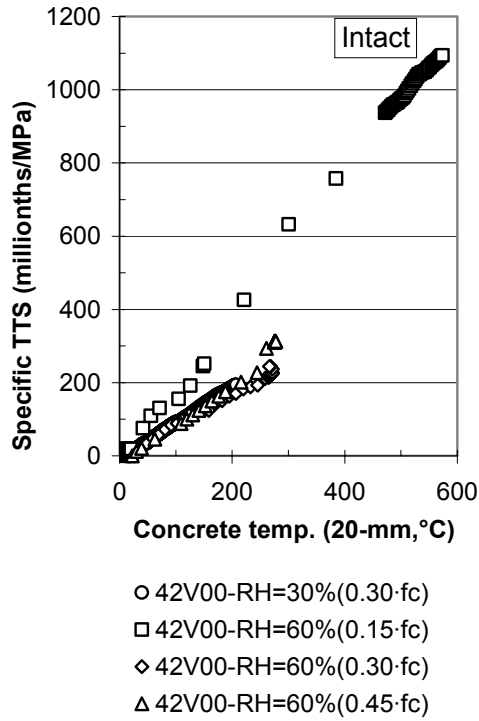


Fig. 15 – Specific TTS, concrete 42V00.

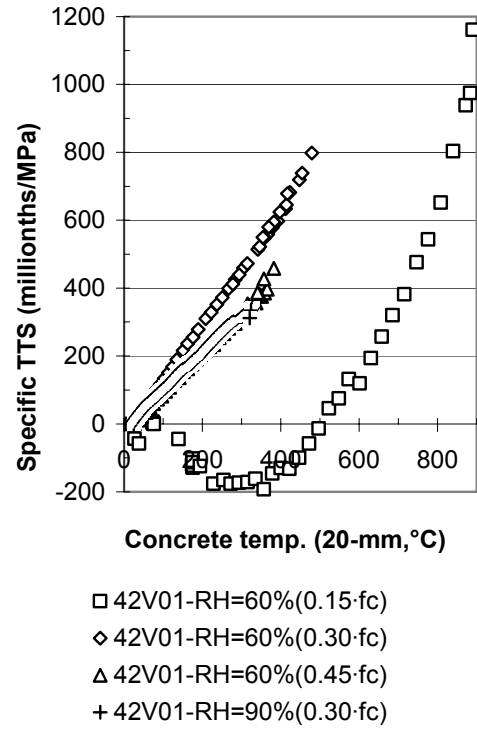


Fig. 16 – Specific TTS, concrete 42V01.

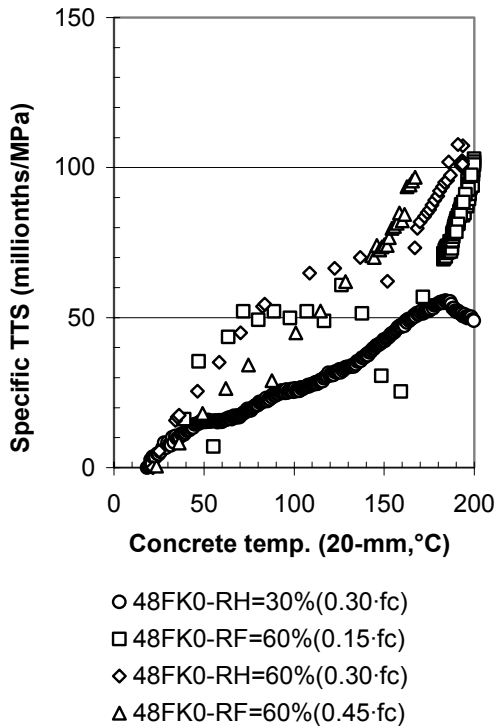


Fig. 17 – Specific TTS, concrete 48FK0.

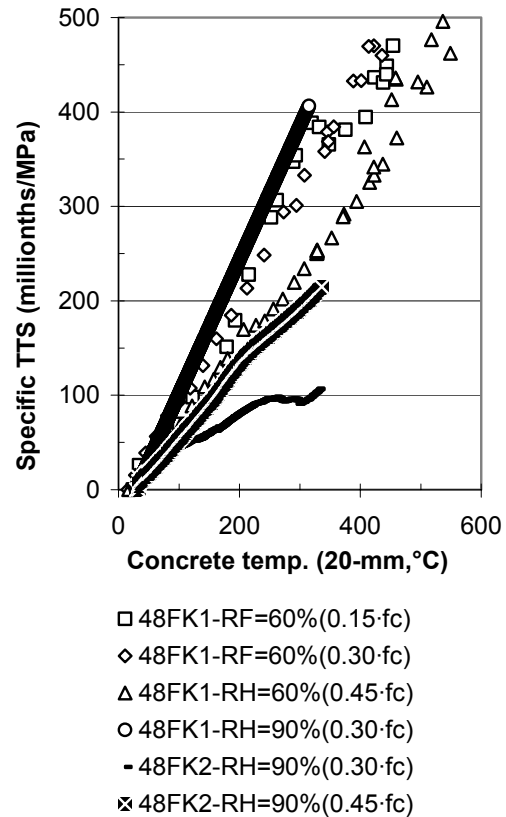


Fig. 18 – Specific TTS, concrete 48FK1.

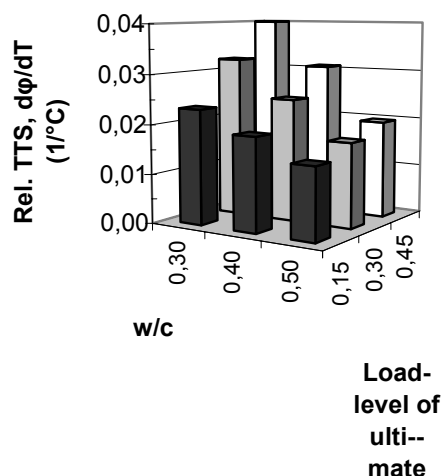


Fig. 19 – Relative TTS without ppf to elastic strain.

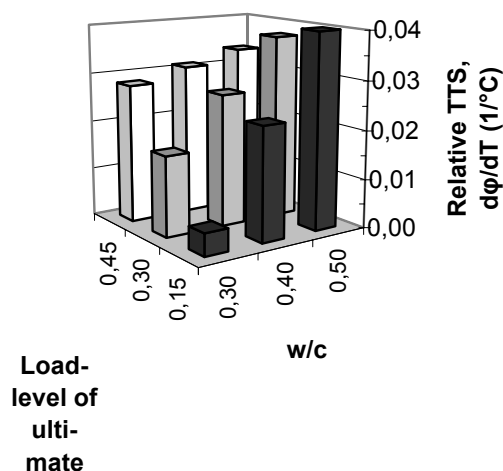


Fig. 20 – Relative TTS with ppf to elastic strain.

5. CONCLUSIONS

This article outlines extensive studies of transient thermal strain of Self-Compacting Concrete. Small difference were found between normal and Self-Compacting Concrete as related to the transient thermal strain. Almost all specimens without ppf exploded independent of loading and moisture level. Almost all specimens with ppf withstood explosive spalling at rapid heating. Polypropylene fibres in the mix proportions had more pronounced effect on transient thermal strain, i.e. lower transient thermal strain in concrete with polypropylene fibres than in concrete without polypropylene fibres. The coefficient of thermal expansion was smaller in concrete with polypropylene fibres than in concrete without polypropylene fibres. Both observations were probably explained by lower moisture content at high temperatures in concrete with polypropylene fibres than in concrete without polypropylene fibres. The moisture of the concrete probably moves out of concrete with polypropylene fibres instead of inward into the concrete, which was the case for concrete without polypropylene fibres.

6. ACKNOWLEDGEMENT

Financial support from Abetong Ltd, Heidelberg Cement Group, Växjö, and the Swedish Road Administration is acknowledged. I am also most grateful to Professor S. Thelandersson and Senior Lecturer Y. Anderberg for advice.

7. REFERENCES

1. Diedrichs, U., Jumppanen, U.-M., Schneider, U., "High Temperature Properties and Spalling Behaviour of High Strength Concrete". Weimar. Eds.: F.H. Wittmann and P. Schwesinger. Freiburg and Unterengstringen, 1995, 129-143.
2. Persson, B., "Fire Resistance of Self-Compacting Concrete, SCC", *Materials and Structures*, Vol. 37, No. 273, 2004, 575-584.
3. Persson, B., "Durability of Self-Compacting Concrete with Ppf", *Nordic Concrete Research*, 2005, 9 pp.
4. RILEM, "Thermal Strain", Recommend. Part 6, *Materials and Structures*, 1997, 17-21
5. RILEM, "Transient Thermal Creep for Service and Accident Conditions", Recommendations Part 7, *Materials and Structures*, 31, 1998, 290-295.
6. Hager, I., Pimienta, P., "TTS of HPC", CONCREEP 7, Nantes, Eds.: Pijaudier-Cabot, G., Gérard, B., Acker, P., 2005, 461-472.
7. Persson, B., "Quasi-instantaneous and Long-term Deformations of HPC with Sealed Curing", *Advanced Cement Based Materials* 8, 1998, 1-16.
8. Lackner, R., Zeiml, M., Leithner, D., Mang, H., "Concrete tunnel linings under fire loading. From Material Characterization to Structural Safety", CONCREEP 7, Nantes, Ed.: Pijaudier-Cabot, G., Gérard, B., Acker, P., 2005, 479-490.
9. Kusterle, W., et al., "Brandbeständigkeit von Faser-, Stahl- und Spannbeton", Bundesministerium für Verkehr, Innovation und Technologie in Zusammenarbeit mit der Eisenbahn - Hochleistungsstrecken AG. Stressenforschung. Heft 544. ISSN 0379-1491. Bundesstrassensverwaltung. Stubenring 1, A-1010 Wien. 2004, 221 pp.
10. Alonso, C., Andrade, C., Menedez, E., Gayo, E., "Microstructural Changes in High and Ultra High Strength Concrete Exposed to High Temperature Environment", Fourth ACI/Canmet congress on the quality of concrete structures and latest progress on concrete materials and testing methods, ACI special report SP 229, Eds.: Helene, P., Figueiredo, E.P., Holland, T., Bittencourt, R., 2005, 289-302.
11. Sabeur, H., Colina, H., Thevenin, G., "Transient Thermal Creep of HPC at High Temperatures under Accidental Conditions", CONCREEP 7, Nantes, Eds.: Pijaudier-Cabot, G., Gérard, B., Acker, P., 2005, 503-508.
12. Zeiml, M., Lackner, R., Mang, H., "Coupled analysis of heat and multiphase mass transport in concrete subjected to fire loading", Proc. Conference Computational Methods, Barcelona, Eds.: Papadrakis, M., Oñate, E., Scheffler, E., 2005, 1-23.
13. Mounajed, G., Boussa, H., Grondin, F., "Transient Thermal Creep" of Concrete: Intrinsic Behaviour or Structural Effect?" CONCREEP 7, Nantes, Eds.: Pijaudier-Cabot, G., Gérard, B., Acker, P., 2005, 509-514.
14. Mounajed, G., et al, "Multi-scale Approach of Thermal Damage: Application to Concrete at High Temperature", Proc. 5th Conference on Fracture Mechanics, Colorado, 2004, 513-520.
15. Holst, F., "Mechanical Properties of HPC at High Temperatures", HPC Interim report M7:2, Div. Building Materials, Lund, 1994.
16. Persson, B., "Durability of Self-Compacting Concrete with polypropylene fibres", TVBM-7183, ISBN-91-631-6150-8, Lund University, Lund, 2005, 73 pp.
17. Persson, B., "Self-Compacting Concrete without Filler – Explosive Spalling at High Temperature", TVBM-7179, ISBN 91-631-6150-8, Lund, 2004, 54 pp.
18. Persson, B., "Self-Compacting Concrete at Fire Temperatures", TVBM-3110. ISBN 91-631-3301-6, Lund, 2003, 200 pp.

Appendix 1 - Chemical composition and physical properties of cements (%) [16].

Cement	CEM I 42.5 BV/SR/LA	CEM II/A -L 42.5 R
CaO	65	63.4
SiO ₂	21.6	19.4
Al ₂ O ₃	3.5	3.5
Fe ₂ O ₃	4.4	2.6
K ₂ O	0.58	1.4
Na ₂ O	0.05	0.30
MgO	0.78	2.9
SO ₃	2.07	3.4
Ignition losses	0.47	7.0
CO ₂	0.14	4.4
C ₂ S	21	12.6
C ₃ S	57	51
C ₃ A	1.7	7
C ₄ AF	13	6
Water demand (%)	25	28.2
In. setting time (min.)	145	151
Density	3214 kg/m ³	3065 kg/m ³
Spec. surface (m ² /kg)	305	475

Appendix 2 – Mix proportions and properties of SCC with CEM I [16] (kg(m³))

Concrete	40LN0	40L00	40LK0	40LK2	42LK2
Crushed 11-16	471	496	474	450	450
Crushed 8-11	139	146	189	208	208
Sand 0-8	1000	1053	912	990	990
Limestone filler 40 µm			92	97	97
CEM I	441	464	430	450	450
Ppf				1.4	1.4
Air-entr. ag.	0.13	0.09	0.09	0.13	0.23
Viscosity ag.		2.3			
Superplast.	2.2	4.6	5.6	32.4	33.7
Water	176	186	172	180	193
Slump (mm)	180	620	640	600	600
Test age (months)	3	3	3	3	3
Cyl. str. (MPa)	37	54	63	55	55
E-modulus (GPa)	29	35	37	35	35
E-def. (mill.)	35	29	27	29	29
Moisture (%)	5.6	5.6	5.5	5.4	5.4
Test age (months)	12	12	12	12	12
Cyl. str. (RF=60%,MPa)	40	58	70	70	65
E-modulus (GPa)	30	36	39	39	38
E-def. (millionths)	34	28	26	25	27
Moisture (RF=60%,%)				3.1	
Cyl. str. (RF=90%,MPa)	41	61	72	74	68
Elastic modulus (GPa)	30	37	40	40	39
Elastic deformation (millionths)	33	27	25	25	26
Moisture (RF=90%,%)	5.3	5.6	5.3	5.0	

N = NC, 2 = 1.4 kg/m³ 18 µm ppf, 40 = w/c.

Appendix 3 – Mix proportion and properties SCC with CEM II [17] (kg(m³))

Concrete	33H00	33H01	42V00	42V01	48FK0	48FK1	48FK2
Crushed 11-16			557	557			
Crushed 8-11	809	803			700	697	694
Crushed 4-8			222	222			
Sand 0-8	969	962	893	892	1050	1045	1041
Limestone filler 40 µm					20	20	23
CEM II	456	453	426	426	387	385	389
Ppf		0.7		0.7		0.7	1.4
Air-entr. ag.			0.14	0.14			
Viscosity ag.			1.8	1.8			
Superplast.	5.4	5.4	4.3	4.3	3.2	3.8	3.8
Water	150	156	177	177	185	188	187
w/c	0.33	0.34	0.42	0.42	0.48	0.49	0.48
Slump(flow)	720	670	650	600	680	630	600
Test age (months)	8	8	10	10	10	10	10
Strength (MPa)	62	57	38	43	49	50	48
Cube str. (MPa)	87	80	53	59	68	70	67
Test age (months)							
RH = 30%	12	-	14		14		
RH = 60%	10	10	12	12	12	12	
RH = 90%		13		15		15	15
Moisture (%)							
RH = 30%							4.1
RH = 60%	3.1	3.6	3.8	3	3.7	3.1	3.2
RH = 90%							2.7
Elastic modulus (GPa)	37	36	29	31	33	33	33
Elastic deformation (millionths)	27	28	35	33	30	30	31

Notations: K = limestone filler, RH = relative humidity, 1 = 0.7 kg/m³ 18 µm ppf, 33 = w/c.



LIQUID/STEAM PRESSURE MEASUREMENT INSIDE CONCRETE EXPOSED TO FIRE

Robert JANSSON¹

ABSTRACT

In order to investigate the mechanism of fire spalling, and obtain experimental data on the liquid/steam pore pressure inside concrete exposed to fire, a pressure measurement system containing oil as the pressure carrier has been used.

The liquid/steam pressure inside a fire tested self compacting concrete was measured at different ages, load levels and specimen sizes. The results do not show any clear relationship between age and pressure development in the fire situation. A conclusion from the tests performed is that it is unlikely that the pore pressure is the main reason for fire spalling of the investigated concrete.

1. INTRODUCTION

The high density and the thermal properties of concrete are advantageous when concrete is exposed to fire. Heat transport is in most cases a slow and well known process which depends largely on the aggregate that is used and the concrete quality [1]-[3]. The slow nature of this process leads to the formation of a very steep temperature gradient in the concrete element exposed to the fire, especially in the early stages of exposure to a flashed over fire. Therefore, the temperature dependant degradation of the material is limited to a relatively thin layer which grows slowly with the time of exposure. This makes the explosive spalling of the concrete, which occurs under certain circumstances, particularly onerous to the fire resistance, as the advantageous insulation function of the outer material is lost. In certain specific instances the whole cross-section may collapse.

Fire spalling is a poorly understood phenomenon that occurs due a complex interplay between numerous parameters in the material and/or structure. Some of the main factors that are known to influence the risk of fire spalling are the moisture level, aggregate type, permeability, cross section and speed of heating. For the past 40 years or more, two main

¹ Project manager, PhD-student, Fire Resistance, Swedish National Testing and Research Institute, Fire Technology, email: robert.jansson@sp.se

theories have traditionally been used to explain the origin of fire spalling of concrete, i.e., thermally triggered forces and steam pressure from the water present in the concrete.

In 1965, Harmathy [4], [5] presented a theory that explained spalling as a moisture phenomenon i.e. moisture clog spalling. Concrete is a porous material and, according to this explanation, desorption of water in the early stages of fire exposure starts when heat begins to penetrate the concrete. A major part of the desorbed vapour then moves to colder regions of the concrete and is adsorbed into the colder concrete matrix. When the drying front moves further into the concrete, this phenomena leads to the formation of a fully saturated layer in front of the vapour, a so called moisture clog. This moisture clog acts as an obstruction to the vapour and the vapour is forced to find release through the fire exposed side of the concrete. Finally, at some point in time, as the heat increases, the hot side of the moisture clog itself will begin to evaporate and the steam pressure will begin to rise. Indeed, the formation of a moisture clog where the concrete matrix is saturated with liquid is supported by fire test data as in many cases when concrete is fire tested with a single side of exposure, liquid water can be seen, literally pouring out of the non-exposed side, as illustrated in figure 1.



Fig. 1 Liquid water on the non-(fire)-exposed side of 200 mm thick concrete slabs.

The other explanation, presented for example by Bazant [6], relates to “brittle fracture and delamination buckling caused by compressive biaxial thermal stresses parallel to the heated surface”. Bazant also point out the moisture clog alone cannot cause spalling. When a crack, produced by pore pressure, starts to open, the available volume for the water vapour and liquid increases drastically and the pressure drops. Thus, Bazant [6] concluded that the pore pressure can only act as a trigger for the spalling phenomenon. Once the pore pressure has triggered the crack, its growth and the resulting explosive spalling will depend on the thermal stresses.

These theories point out that the internal pressure of water and vapour in any concrete element is an important factor in understanding the phenomenon of explosive spalling. Several models have been developed to describe the underlying physics of heat and mass transfer (sometimes coupled to mechanical properties) of concrete at high temperatures [7]-[9]. Indeed,

in recent years, developments in computational capacity and numerical codes have lead to the construction of more and more refined, constitutive relations between the properties of matter in concrete. In light of this, there is a need for more experimental data for the validation of these models. Therefore, measurements of the internal liquid/steam pressure in concrete exposed to fire, such as those presented in this paper, are of fundamental interest.

2. EXPERIMENTAL DESCRIPTION

2.1 Pressure measurement

A variety of methods used to measure the pressure inside heated concrete can be found [10]-[15]. Direct measurements with embedded electrical sensors have been conducted by Phan [10], Consolatio et al. [11] and Dal Pont and Ehrlacher [12]. One problem with this type of measurement is the size effect, i.e., the size of the sensor must be small to minimize the influence of the sensor on the thermal field in the concrete. Further, the temperature range where the pressure sensor is functional can be a limiting factor. Naturally, sophisticated pressure gauges can be used which have a broad temperature range but no such sensors exist that can survive a standard fire test. The fact that pressure gauges in these type of tests are sacrificial are limiting their use in extensive test programs.

Indirect measurement can also be used. In this approach the pressure is conducted out of the specimen in a small pipe so that the pressure can be measured outside of the sample. In this case the pipe is open ended with one end inserted into the sample and the other end connected to the external pressure gauge. This is a more cost effective method of measurement because the pressure sensor can be reused and the working conditions for the sensor are more stable. The actual measurement can be made as a vapour pressure measurement, using an empty pipe [13], [14]; or as a fluid pressure measurement, using oil as the pressure conductor [15].

In the experiments presented in this paper, oil has been used as the pressure carrier. The advantage of oil as a pressure carrier is largely due to its minimal compressibility. The disadvantage of using oil, however, is that oil is subject to thermal expansion in the pipe when exposed to elevated temperatures. This thermal expansion could potentially be misinterpreted as a pressure rise. Preliminary investigations of the effect of such expansion on the pressure measurements in experiments, in which the concrete is exposed to an ISO 834 curve, indicate that this effect will be minimal. This is due to the fact that the ISO 834 curve will give rise to high temperature gradients in the concrete, and only the top of the oil filled pipe will be heated in the initial stages of the fire exposure. As the main purpose of these measurements is to measure the pressure up to the point of first explosive spalling, it is expected that this method will provide sufficiently accurate results up to this point. A simple experiment where 5 cm of a plugged oil pipe was exposed to an environment at 200 °C, indicates that the thermal expansion is in an acceptable range, i.e. only a minor overestimation of the pressure will be made with this system.

2.2 Test setup

During casting of the concrete test specimens, thin steel pipes with an inner diameter of 2 mm and wall thickness of 0.2 mm were inserted into the concrete, see figure 2. One end of each steel pipe was placed near the surface to be fire tested. The pipe extended from the measurement point through the test specimen, exiting on the cold side. To ensure that no concrete, i.e. cement paste, would fill the pipes, thin welding bars were inserted into the pipes

during casting. Figure 2 shows a pressure measurement station with three steel pipes and one thermocouple. The struts placed at each of the four corners of the measurement station are used to position the whole apparatus correctly in the concrete specimen. The steel pipes are (from left to right) 10, 20 and 30 mm shorter than the four struts. This setup is then placed in the casting mould with the struts placed on the surface which is to be exposed to the fire, ensuring that each pressure measurement is made 10, 20 and 30 mm from the surface exposed to fire.

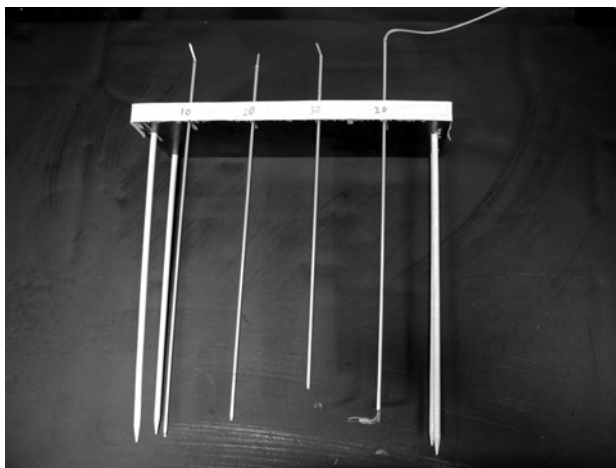


Fig. 2 The oil pipes and one thermocouple

When the fire tests were conducted the welding bars inside the steel pipes were removed and the pipes were filled with high temperature silicone oil, Sil 300, produced by Haake. Filling of the pipes was conducted by inserting a thin injection needle and carefully injecting oil from the bottom of the pipe to ensure that no air was trapped. Outside the concrete the steel pipes were connected to a pressure gauge using a T-junction (see Figure 3). The pressure gauges that were used were of the type P8AP/100bar from Hottinger Baldwin Messtechnik GmbH.

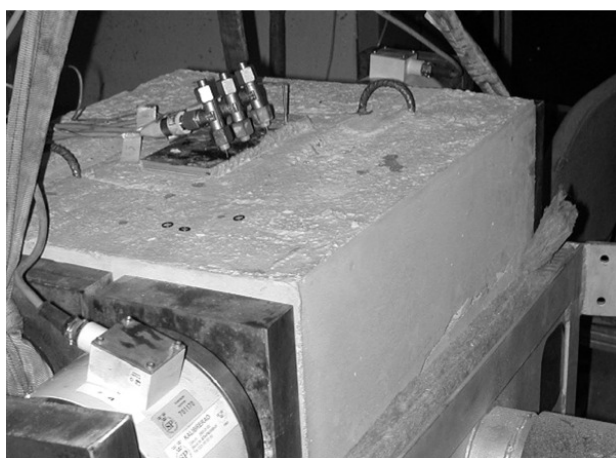


Fig. 3 The pressure gauges connected to the small pipes with angle tees.

Two sizes of test specimens were used in this experimental series: concrete slabs with dimensions $600 \times 500 \times 200 \text{ mm}^3$ and $1800 \times 1200 \times 200 \text{ mm}^3$. All specimens were equipped with both pressure gauges and type K thermocouples. Each specimen was equipped with

thermocouples at a minimum of 3 different depths: 10, 20 and 40 mm in the small slabs and 10, 20, 25, 40, 80 and 120 mm in the larger test slabs.

The small slabs were tested on a small scale furnace with an opening area of 500 x 400 mm². During most of the tests a compressive load was applied with a loading system consisting of 36 mm post tensioning bars inside aluminium pipes. Load cells were applied to measure the load during the test. One such load cell can be seen in the left hand corner of figure 3. The large slabs were tested on the horizontal furnace with an opening area 3 x 5 m², with the same type of loading system as the small slabs. The test on the horizontal furnace was made in accordance with EN 1363-1 which means that plate thermometers were used to control the furnace temperature. The use of type K thermocouples during the test on the small furnace and plate thermometers on the horizontal furnace made the thermal exposure somewhat different. Thus, the large slabs tested according to the EN 1363-1 standard experienced a slightly higher thermal exposure.

2.3 Test specimens

The material used in these tests was self-compacting concrete with limestone filler. All test specimens were produced at the same time and stored in indoor climate before the fire tests. More details of the composition and properties are shown in table 1.

Table 1 - Concrete admixtures and characteristics.

Water	230
Cement (CEM II)	355
Limestone filler (Limus 25)	105
Plasticizer (Sikament 20HE)	2,4
Stabilizer (Sika Stabilizer 100)	4,0
Aggregate 0-8 mm	1029
Aggregate 8-16 mm	554
w/c	0,65
w/p	0,50
Air (%)	1,8
Slump	620
Compressive strength (28 days)	37
Moisture (% , 3 month old)	5.3
Moisture (% , 6 month old)	5.0

The name of the test specimens is for example “A, 3 month, 5%”. This means Specimen A tested at the age 3 month with an external load level of 5 % of the compressive strength. The A and B letters are used when two equal tests have been carried through. All the load levels refer to the strength at 3 month, which was 39,4 MPa.

3. RESULTS

The temperatures measurements from a typical test specimen tested on the small furnace during 60 minutes are shown in figure 4. This test specimen, which was tested with a

load level of 5 % of the ultimate compressive strength at 3 months, started to spall after 16 minutes. Figure 5 shows the size of some of the first material spalled off in these test. The sound of the spalling in these experiments is a mix of loud bangs and quiet plops. Further results and discussion focussing on the amount of spalling, can be found in the article “Spalling of self compacting concrete” by Boström and Jansson also presented at this workshop.

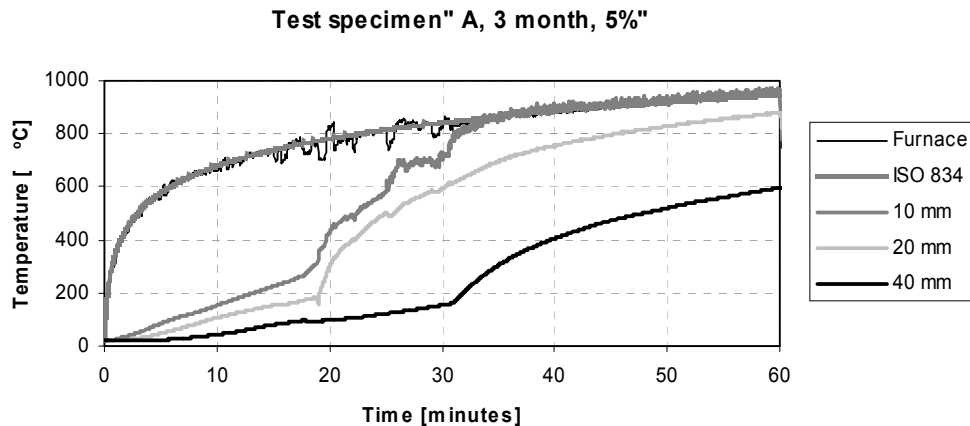


Fig. 4 Temperature vs. time for a test specimen tested using the small furnace. This specimen started to spall at 16 minutes.



Fig. 5 This is some of the material spalled of form specimen “A, 3 month, 5%”.

To obtain a clearer picture, all graphs from pressure measurements shown in this report show the pressure development until the time of the first spalling, which means that when the pressure curve is ended, spalling has occurred. In figure 6 the measured pressures at the depth of 10 mm are shown, for concrete of different ages. The plot shows the pressure development to the time of spalling. Of the specimens tested, two did not spall during the fire tests: “B, 6 month, 0%” and “B, 3 month, 10%”. All other specimens did spall.

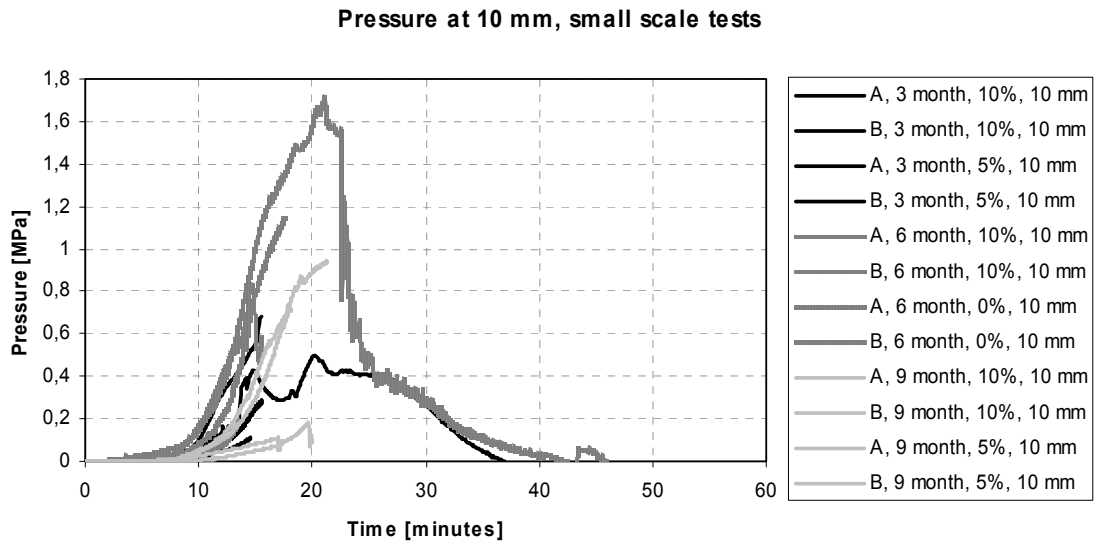


Fig. 6 Pressure vs. time at different ages for the measurements at the depth of 10 mm.

The measured pressures at the depth of 20 mm are shown in figure 7. Note that in this figure the pressure in specimen “B, 3 month, 10 %” rises rapidly. The pressure is actually higher than all other of the measurements at the depth of 10 mm.

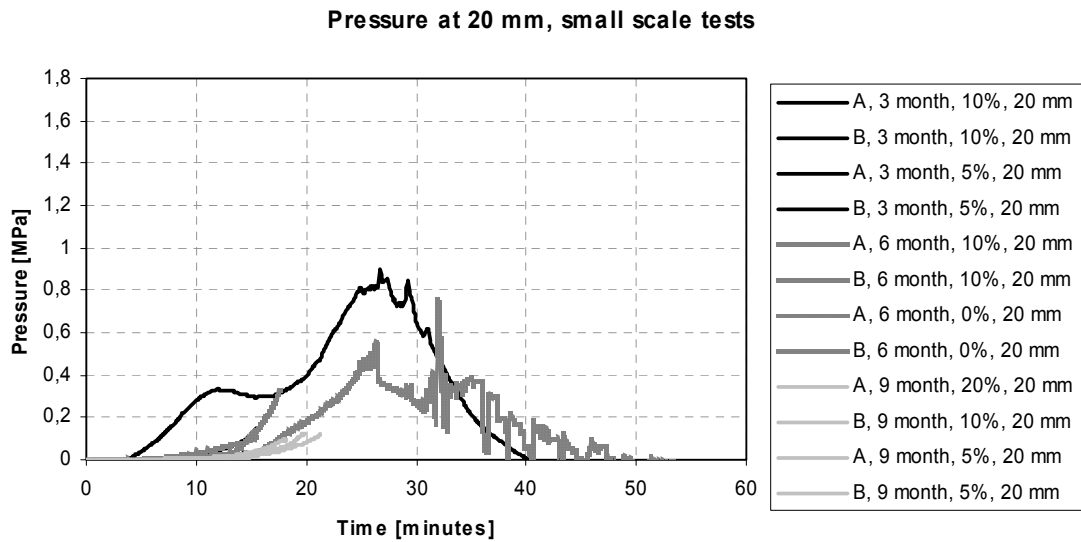


Fig. 7 Pressure vs. time at different ages for the measurements at the depth 20 mm.

At the depth of 30 mm only small pressures were built up before the spalling occurred, see figure 8. The highest pressure was measured in specimen “B, 3 month, 10 %”, as found at the depth of 20 mm.

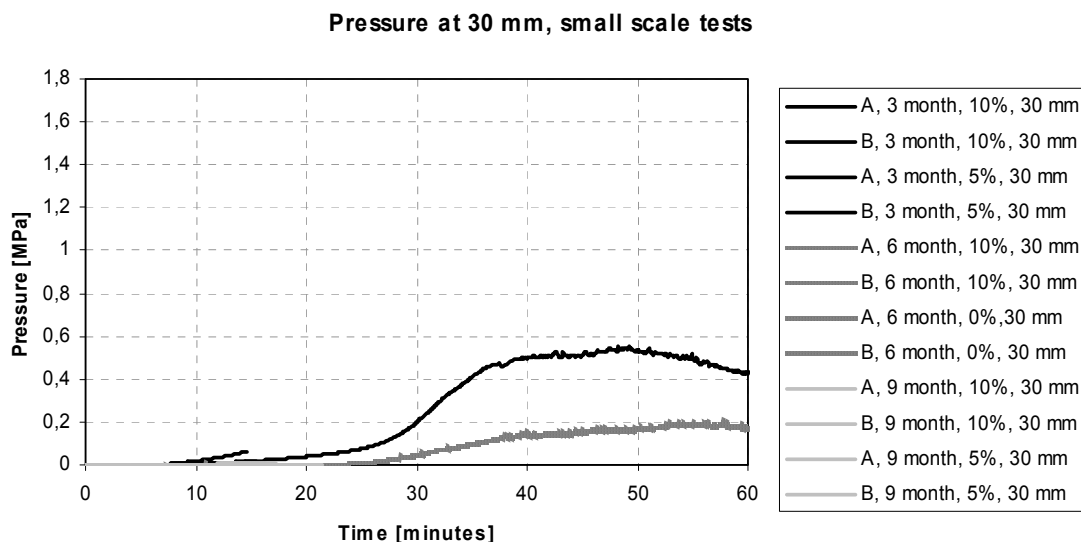


Fig. 8 Pressure vs. time at different ages for the measurements at the depth 30 mm.

Pressure measurements were also conducted during tests of large slabs of the same quality of concrete, on the horizontal furnace. Four large slabs were tested with pressure measurements being taken at depths of 10, 20, 30, 40 and 50 mm. During these tests, two of the slabs were loaded in compression with 10% of the 3 month compressive strength and two slabs were unloaded. During these tests the concrete started to spall after 10 minutes and during that time the highest pressure recorded in one of the 20 pressure gauges was 0.3 MPa. Due to limited space in this article and the fact that these results provide no further insight into the discussion below, graphical results are not presented here.

4. DISCUSSION AND CONCLUSIONS

A self compacting concrete was tested at different ages, 3, 6 and 9 month, and load levels, 0, 5 and 10 % of the compressive strength at 3 month, on a small scale furnace. The results do not show any clear relationship between the age and the pressure development in the fire exposed concrete. The highest pressure measured, 1.8 MPa, was at the depth of 10 mm, in a specimen that was not spalling. All of the specimens, but two, spalled when they were exposed to an ISO 834 curve.

Previous tests have provided results in the same range of pressures as those presented in this paper. As a comparison, even though the concrete mixes and the placement of the pressure gauges are different, experiments conducted by Harada and Terai [15] with ISO 834 thermal exposure resulted in a maximum pressure of 0.2 MPa. Similarly, in the experiments conducted by Kusterle et al. [14], with the extremely tough LT1 “Lainz 180” temperature curve, the maximum pressure measured was 1 MPa. The highest pressures recorded in tests of this type on concrete have been made by Phan [10] who measured 2.1 MPa in moist, cured, high strength concrete cylinders that spalled.

The maximum pressure measured, in the tests presented here, before spalling is low compared to the normal tensile strength of concrete. This supports the explanation for explosive spalling that Bazant [6] has proposed, i.e., that the pore pressure alone cannot cause explosive spalling. If the pore pressure is involved, the role may be only as a trigger, i.e. the

pressure leads to a slight deformation that initiates the process of thermal stress promoted brittle fracture. This conclusion is further supported by the fact that, although the concrete exhibited significant spalling, the maximum pressure recorded during the large scale test on the horizontal furnace was only 0.3 MPa. The obvious conclusion to be drawn from this fact is that the pore pressure cannot be the sole explanation for the spalling behaviour seen in the concrete investigated, and may not even be an important factor.

The results presented in this paper give no definitive proof of the role of pore pressure (or indeed, whether there is any role) in the spalling of concrete. Before general conclusions can be drawn concerning spalling behaviour in concrete, further results are needed from other concrete mixes and geometries. Such tests will be the subject of future work.

5. REFERENCES

- [1] Eurocode 2: Design of concrete structures - Part 1-2: General rules - Structural fire design, prEN 1992-1-2, final draft, December 2003
- [2] Flynn D. R., "Response of High Performance Concrete to Fire Conditions: Review of Thermal Property Data and Measurement Techniques", Metsys Report No. 98-01-101 December 1998, NIST
- [3] Jansson R., "Measurement of Concrete Thermal Properties at High Temperature" Proceedings of FIB Task Group 4.3 Workshop, Fire Design of Concrete Structures: What now? What next?, Milan, Italy, pp 101-107, 2004
- [4] Harmathy, T. Z., "Effect of moisture on the fire endurance of building materials", Moisture in Materials in Relation to Fire Tests, ASTM Special Technical Publication No. 385, pp 74-95, 1965
- [5] Harmathy, T. Z., "Fire Safety Design & Concrete", Concrete Design & Construction Series, Longman Group UK Limited pp. 1-412, 1993
- [6] Bazant, Z. P., "Concrete Creep at High Temperature and its Interaction with Fracture: Recent Progress", Concreep-7 Conference: Creep, Shrinkage and Durability of Concrete and Concrete Structures, pp 449-460, 2005
- [7] Tenchev R. , Purnell P., "An application of a damage constitutive model to concrete at high temperature and prediction of spalling" International Journal of Solids and Structures 42 (2005) 6550–6565
- [8] Gawin D., Pesavento F., Schrefler B. A., "Modelling of hygro-thermal behaviour of concrete at high temperature with thermo-chemical and mechanical material degradation" Comput. Methods Appl. Mech. Engrg. 192 (2003) 1731–1771
- [9] Alnajim A., "Modelisation et simulation du comportement du beton sous hautes temperatures par une approche thermo-hygro-mecanique couplee. Application a des situations accidentelles." PhD thesis, Universite de Marne la Vallee U.F.R de Sciences et Technologies, pp. 1-183, 2004

- [10] Phan T. L., “High-Strength Concrete at High Temperature – An Overview” Utilization of High Strength/High Performance Concrete, 6th International Symposium. Proceedings. Volume 1. June 2002, Leipzig, Germany, Konig, G.; Dehn, F.; Faust, T., Editor(s), 501-518 pp, 2002.
- [11] Consolazio, G. R.; McVay, M. C.; Rish, J. W., “Measurement and Prediction of Pore Pressure in Cement Mortar Subjected to Elevated Temperature” NIST SP 919; September 1997. International Workshop on Fire Performance of High-Strength Concrete. Proceedings, pp.125-148, 1997.
- [12] Dal Pont S., Ehrlacher A., “Numerical and experimental analysis of chemical dehydration, heat and mass transfers in a concrete hollow cylinder submitted to high temperatures” International Journal of Heat and Mass Transfer 47 (2004) pp. 135–147
- [13] Kalifa P., Menneteau F.D., Quenard D., “Spalling and pore pressure in HPC at high temperatures” Cement and Concrete Research 30 (2000) pp.1915-1927
- [14] Kusterle W. et al. “Brandbeständigkeit von Faser-, Stahl- und Spannbeton” Heft 544, Bundesministerium für Verkehr, Innovation und Technologie, Wien, pp.1-221, 2004
- [15] Harada, K.; Terai, T., “Heat and Mass Transfer in the Walls Subjected to Fire”, U.S./Japan Government Cooperative Program on Natural Resources (UJNR). Fire Research and Safety. 13th Joint Panel Meeting. Volume 1. March 13-20, 1996, Gaithersburg, MD, Beall, K. A., Editor(s), pp 423-435, 1997.



SPALLING OF SELF COMPACTING CONCRETE

Lars BOSTRÖM¹ and Robert JANSSON²

ABSTRACT

The first results of an experimental research program on spalling of self compacting concrete are presented. Twelve different concrete qualities for house building applications have been fire tested with a fire exposure in accordance with ISO 834. The general result is that there is a high probability for spalling of self compacting concrete if no precautions are taken such as addition of polypropylene fibres or thermal insulation. The present results show, once more, that polypropylene fibres give a good protection against fire spalling. In addition to polypropylene fibres, filler of polypropylene has been tested. The results show clearly that fibres are needed and that filler does not prevent spalling.

1. INTRODUCTION

Self compacting concrete reached the market 20 years ago, although the production was quite low. The interest continuously increases for self compacting concrete because of its favourable characteristics in the fresh state. No energy is needed to compact the concrete so the reinforcement is covered or the mould is filled out, i.e. no vibration is needed. Thus the work environment is better and casting of more complex structures can be done. The use of finer fractions of the ballast in self compacting concrete as well as super plasticizers are the main differences compared to conventional concrete. This gives the self compacting concrete its flowing characteristics in the fresh state, but it also makes the concrete less permeable. Regarding durability the low permeability is favourable, but for fire resistance it may lead to problems. An experimental study was therefore carried out in 2001 where some different qualities of self compacting concretes as well as conventional vibrated concretes were fire tested [1]. The results showed clearly that the self compacting concrete spalled severely and the conventional concrete did not. Due to the problems with spalling it was decided that a more extensive study was needed in order to establish guidelines on the use of self compacting

¹ Manager, SP Fire Technology, Fire Resistance, Box 857, SE-501 15 Borås, Sweden,
email: lars.bostrom@sp.se.

² Research assistant, SP Fire Technology, Fire Resistance, Box 857, SE-501 15 Borås, Sweden,
email: robert.jansson@sp.se

concretes when fire resistance is required. These guidelines should show when extra protection such as thermal insulation or use of polypropylene fibres are needed for the different qualities of self compacting concretes that are actual in practice.

The first step in the study was to develop a reliable and economical test methodology. The best reliability would be obtained by full scale testing, but that would be very expensive and time consuming. Therefore a small scale test was preferred together with a few full scale tests for verification. The methodology has been published in [2]. The second step, which is still in progress, was to manufacture a range of different qualities of self compacting concretes. In all around 70 different qualities shall be studied. Up to now 30 qualities have been casted and are now curing and under conditioning.

The present paper will focus on the experimental studies made at SP and no comparison is made with results from other studies. A lot of work has been done at other institutes and universities on the fire resistance of self compacting concrete. It is, however, difficult to compare results since different test methods are used, different concrete qualities tested and different measurement techniques are adopted for measurement of spalling.

2. TEST SPECIMENS AND MATERIALS

A total of 12 qualities of concrete have been examined so far in the presented project, if the tests performed for examination of the test methodology are dismissed. The examined concrete qualities and the admixtures are presented in table 1. All concrete qualities were self-compacting concretes, with a slump flow of more than 600 mm, see table 1.

Tab 1 - Concrete admixtures and characteristics.

	Concrete quality											
	1	2	3	4	5	6	7	8	9	10	11	12
Water	198	198	198	200	212	230	212	212	230	230	230	199
Cement	380	380	500	390	410	355	410	410	355	355	355	280
Filler	80	160	-	110	122	105	122	122	105	105	105	82
Plasticizer	2,2	3,0	2,2	3,0	3,8	2,4	3,6	3,8	2,3	2,4	2,5	2,2
Stabilizer	-	-	-	-	-	-	-	-	-	4,0	4,0	2,8
Fiber 1	-	-	-	0,5	-	-	1,0	-	-	-	0,5	-
Fiber 2	-	-	-	-	1,0	-	-	1,5	-	-	-	-
Fiber 3	-	-	-	-	-	5,0	-	-	10,0	-	-	-
0-8 mm	1059	1003	1031	917	882	1037	883	885	1020	1029	1026	1096
8-16 mm	622	589	605	721	693	559	694	695	549	554	552	643
w/c	0,52	0,52	0,40	0,51	0,52	0,65	0,52	0,52	0,65	0,65	0,65	0,71
w/p	0,43	0,37	0,40	0,40	0,40	0,50	0,40	0,40	0,50	0,50	0,50	0,55
Air (%)	1,7	2,4	2,1	1,7	1,7	1,2	1,7	1,5	1,7	1,8	1,9	2,3
Slump	690	690	605	630	670	610	650	630	650	620	650	680
Strength	52	50	51	45	47	35	44	45	34	37	40	34

Only one type of cement (CEM II) has been used in these concretes. This cement is mainly used for housing applications in Sweden. Other concrete qualities are presently being manufactured where also qualities for tunnel constructions will be studied. A total of approximately 70 different concrete qualities will be examined experimentally, most of them self compacting concretes. The filler used is designated Limus 25 and is a limestone filler. The plasticizer is designated Sikament 20HE and the stabilizer is designated Sika Stabilizer 100.

Two different polypropylene fibres (Fiber 1 and Fiber 2 in table 1) and polypropylene filler (Fiber 3) have been used. Fiber 1 is designated Sika Crackstop and has a diameter of 18 μ m and a length of 6 mm. Fiber 2 is designated Sika Crackstop and has a diameter of 32 μ m and a length of 12 mm. Fiber 3 is designated Sika IgniFill and is a polypropylene filler. The compressive strength shown in table 1 is the 28 days strength measured on cubes in accordance with EN 137010. The value is a mean of three tests.

Three different types of test specimens have been manufactured. Most of the specimens have been small slabs with the dimensions 600 x 500 x 200 mm³. These specimens have been used for the main study. In addition to the small slabs, large slabs as well as large beams has also been used. The large slabs had the dimensions 1800 x 1200 x 200 mm³, and the beams 3600 x 600 x 200 mm³. There has not been any reinforcement in the small slabs. In the large specimens some reinforcement were used in order to ensure safe handling of the specimens.

In all specimens aluminium tubes were placed on half the height along the major axis. In the tubes were 32 mm diameter post-tensioning bars placed for loading. With these bars a total compressive stress of approximately 20 MPa could be achieved and in the small slabs the possible compressive stress was around 24 MPa. In the large slabs a total of 6 bars were mounted and in the small slabs were three bars mounted. The beam specimens were loaded with external actuators in bending.

3. TEST METHODS

Tests have been carried out on two different furnaces, a large horizontal furnace for full scale testing and a small furnace. One test has been performed on the large furnace at which a total of eight specimens were placed on the furnace, six slabs and two beams. All specimens were exposed on one surface, i.e. a one-sided fire exposure. The test set-up is shown in figure 1. The heating was made in accordance with EN 1363-1, i.e. the standard time-temperature curve (ISO 834). Plate thermometers were used for measurements on the furnace temperatures.

The small slabs were all tested on a small furnace. They were also fire exposed on one surface only. The exposed area was 500 x 400 mm². The test set-up is shown in figure 2. In these tests a conventional thermocouple was used for measuring the furnace temperature. The furnace was in all tests controlled in accordance with the standard time-temperature curve (ISO 834). Since the size of the furnace is so small and the temperature was measured with a conventional thermocouple the heat exposure is lower compared to the full scale test.

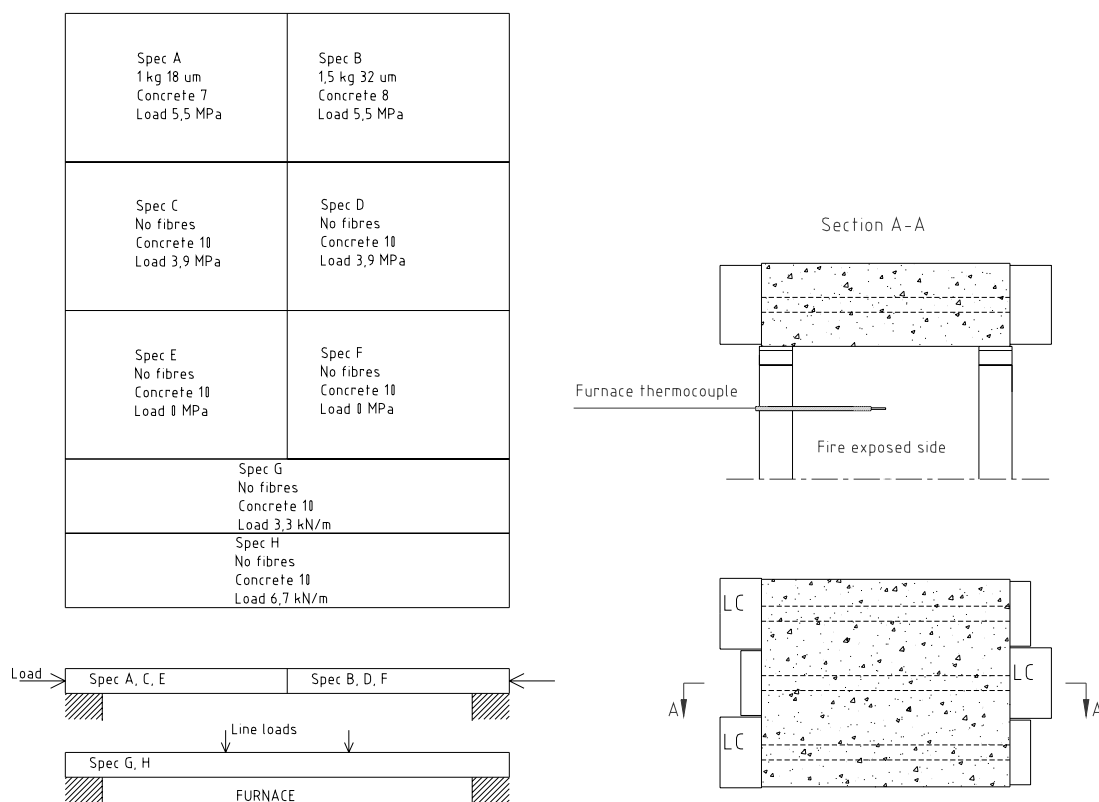


Fig 1 - Test set-up of the full scale test to the left, and the small scale test to the right.

4. RESULTS

The test results obtained with the small slabs are presented in table 2. In table 3 are the results from the tests with large slabs and beams assembled. For some specimens no values are given on the moisture content and the reason for this is that the fire tests has been done very recently and the moisture content measurements was not ready when this paper was written. The load level given in the table is the compressive stress applied, except for the beam specimens where the load level is the maximum bending stress on the fire exposed surface (tension stress). Two different values on the spalling is presented. One is the maximum depth recorded on the fire exposed surface. The other measure is a mean spalling depth calculated from 20 measurements evenly distributed on the fire exposed surface.

Tab 2 - Test results from the small slab tests.

Concrete	w/p	w/c	Filler	Fibres			Age	Moisture (%)	Load (MPa)	Spalling	
				Type	Amount	Length				Max	Mean
1	0,43	0,52	Lime	-	-	-	6	4,5	6,3	43	20
1	0,43	0,52	Lime	-	-	-	6	4,5	6,3	40	20
2	0,37	0,52	Lime	-	-	-	6	4,1	6,2	62	32
2	0,37	0,52	Lime	-	-	-	6	4,1	6,2	36	18
3	0,40	0,40	Cement	-	-	-	6	5,1	6,0	51	33
3	0,40	0,40	Cement	-	-	-	6	5,1	6,0	46	33
4	0,40	0,51	Lime	18 m	0,5	6	3	-	0	0	0
4	0,40	0,51	Lime	18 m	0,5	6	6	4,3	5,8	0	0
4	0,40	0,51	Lime	18 m	0,5	6	6	4,3	5,8	0	0
5	0,40	0,52	Lime	32 m	1,0	12	6	4,9	5,9	0	0
5	0,40	0,52	Lime	32 m	1,0	12	6	4,9	5,9	0	0
6	0,50	0,65	Lime	Filler	5,0	-	3	-	0	0	0
6	0,50	0,65	Lime	Filler	5,0	-	6	4,6	4,6	35	18
6	0,50	0,65	Lime	Filler	5,0	-	6	4,6	4,6	45	20
7	0,40	0,52	Lime	18 m	1,0	6	6	4,8	5,3	0	0
7	0,40	0,52	Lime	18 m	1,0	6	6	4,8	5,3	0	0
8	0,40	0,52	Lime	32 m	1,5	12	6	5,7	5,8	0	0
8	0,40	0,52	Lime	32 m	1,5	12	6	5,7	5,8	0	0
9	0,50	0,65	Lime	Filler	10,0	-	6	5,0	4,2	43	26
9	0,50	0,65	Lime	Filler	10,0	-	6	5,0	4,2	55	27
10	0,50	0,65	Lime	-	-	-	3	5,3	2,0	56	15
10	0,50	0,65	Lime	-	-	-	3	5,3	2,0	43	25
10	0,50	0,65	Lime	-	-	-	3	5,3	3,9	0	0
10	0,50	0,65	Lime	-	-	-	3	5,3	3,9	30	21
10	0,50	0,65	Lime	-	-	-	6	5,0	0	24	3
10	0,50	0,65	Lime	-	-	-	6	5,0	0	0	0
10	0,50	0,65	Lime	-	-	-	6	5,0	3,9	31	19
10	0,50	0,65	Lime	-	-	-	6	5,0	3,9	43	19
10	0,50	0,65	Lime	-	-	-	9	-	2,0	34	18
10	0,50	0,65	Lime	-	-	-	9	-	2,0	36	17
10	0,50	0,65	Lime	-	-	-	9	-	3,9	38	24
10	0,50	0,65	Lime	-	-	-	9	-	3,9	66	26
11	0,50	0,65	Lime	18 m	0,5	6	6	-	4,8	0	0
11	0,50	0,65	Lime	18 m	0,5	6	6	-	4,8	33	14
12	0,55	0,71	Lime	-	-	-	6	-	0	28	13
12	0,55	0,71	Lime	-	-	-	6	-	0	37	13
12	0,55	0,71	Lime	-	-	-	6	-	4,1	43	24
12	0,55	0,71	Lime	-	-	-	6	-	4,1	54	29

Tab 3 - Test results from the large slab and beam tests.

Concrete	w/p	w/c	Filler	Fibres			Age	Moisture (%)	Load (MPa)	Spalling	
				Type	Amount	Length				Max	Mean
7	0,40	0,52	Lime	18 m	1,0	6	8	4,8	5,5	0	0
8	0,40	0,52	Lime	32 m	1,5	12	8	5,7	5,5	0	0
10	0,50	0,65	Lime	-	-	-	6	5,0	0	104	40
10	0,50	0,65	Lime	-	-	-	6	5,0	0	69	35
10	0,50	0,65	Lime	-	-	-	6	5,0	3,9	117	55
10	0,50	0,65	Lime	-	-	-	6	5,0	3,9	87	41
10	0,50	0,65	Lime	-	-	-	6	5,0	$0,5 \cdot 10^{-3}$	32	8
10	0,50	0,65	Lime	-	-	-	6	5,0	$1,0 \cdot 10^{-3}$	37	6

5. DISCUSSION AND CONCLUSIONS

5.1 Effect of filler

Concretes 1, 2 and 3 contained different amount of limestone filler (0, 80 and 160 kg/m³). In concrete 3 the filler was replaced with cement, i.e. the amount of cement increased from 380 to 500 kg/m³. At the time of testing, after 6 months curing, the moisture content was different ranging from 4,1 % of concrete 2 (with 160 kg/m³ filler) to 5,1 % of concrete 3 where the limestone filler had been replaced with cement. All these concretes had the same amount of water when casting. There is a slight difference in the observed spalling depths indicating that increased amount of filler increases the amount of spalling. Another observation made is that the concrete without limestone filler where the amount of cement had been increased seemed to spall more compared with a concrete with limestone filler with the same water-powder ratio (w/p).

5.2 Effect of polypropylene fibres and filler

All specimens with polypropylene fibres except one did not spall. The specimen that spalled had high w/p as well as w/c ratio and should therefore be less susceptible compared to the other qualities. On the other hand another specimen of the same quality was also tested and it did not spall. A relatively low amount of fibres were used (0,5 kg/m³) which probably is on the lower limit to avoid spalling.

Another polypropylene product, a filler, was included in the study. The advantage with this filler is that it does not affect the characteristics of the fresh concrete as the fibres do. The test results show clearly that the polypropylene filler does not give the searched effect on the spalling. Even so large amounts as 10 kg/m³ did not reduce the spalling. This indicates that the form of the polypropylene is important. It is not only the creation of voids in the concrete but also the form of the voids that are crucial.

Two different types of polypropylene fibres were examined. One smaller fibre with a diameter of 18 m and length 6 mm, and one larger with a diameter of 32 m and length 12 mm. Different amount of fibres were used 0,5 and 1,0 kg/m³ for the smaller fibres (concrete 4 and 7) and 1,0 and 1,5 kg/m³ for the larger fibres (concrete 5 and 8). None of these specimens spalled indicating that for that quality of concrete a relatively small amount of fibres is needed and both types of fibres works well.

Concrete 7 and 8, i.e. concrete with polypropylene fibres, were also tested in full scale. The results were the same as in the small scale test, no spalling occurred.

5.3 Effect of load level

Concretes 10 and 12 have been tested with different load levels. From these results it is difficult to say whether the load level has an effect or not on the spalling. The tests on concrete 12 show a larger amount of spalling on the loaded specimens compared with the unloaded. Concrete 10 have been tested at three different ages, 3, 6 and 9 months, and the results are different. At the age 3 months the spalling is slightly smaller when loaded to 2,0 MPa compressive stress compared to the higher loading of 3,9 MPa. At 6 months age the tests were made unloaded and with a load of 3,9 MPa compressive stress. In these tests the loaded specimens spalled more than the unloaded specimens. At 9 months age there is a small difference in the amount of spalling. The specimens with higher stress spalls slightly more.

Concrete 10 was also tested in full scale, both slab specimens and beams. Two load levels were used on both the slabs and the beams. The slabs were either unloaded or loaded to 3,9 MPa compressive stress. The beams were loaded in bending to a bending stress of 0,5 and 1,0 kPa, i.e. a very low bending stress. The specimens were tested at an age of 6 months. All slab specimens spalled. The loaded slabs spalled slightly more compared with the unloaded slabs, but the difference is very small. Although, when comparing the spalling depth between the full scale slabs and the small ones tested on the small scale furnace, the large slabs spalled significantly more. It is currently not possible to point out a specific reason for this. One explanation can be that the heat exposure is different. In the small scale furnace is the furnace temperature measured with a conventional thermocouple and the distance from floor and walls to the specimen is small. In the full scale test was the furnace temperature controlled with plate thermometers. This leads to a more severe heat exposure in the large furnace compared with the small one. Another difference is of course the size of the specimens. There may be boundary effects that affect the amount of spalling.

The beam specimens showed the same type of spalling that have been observed in earlier studies [2], i.e. the spalling takes place where the tensile stress is smallest and the shear stress largest close to the supports, see figure 3. The stress levels used were very small and no difference in spalling depth between the two specimens could be observed.

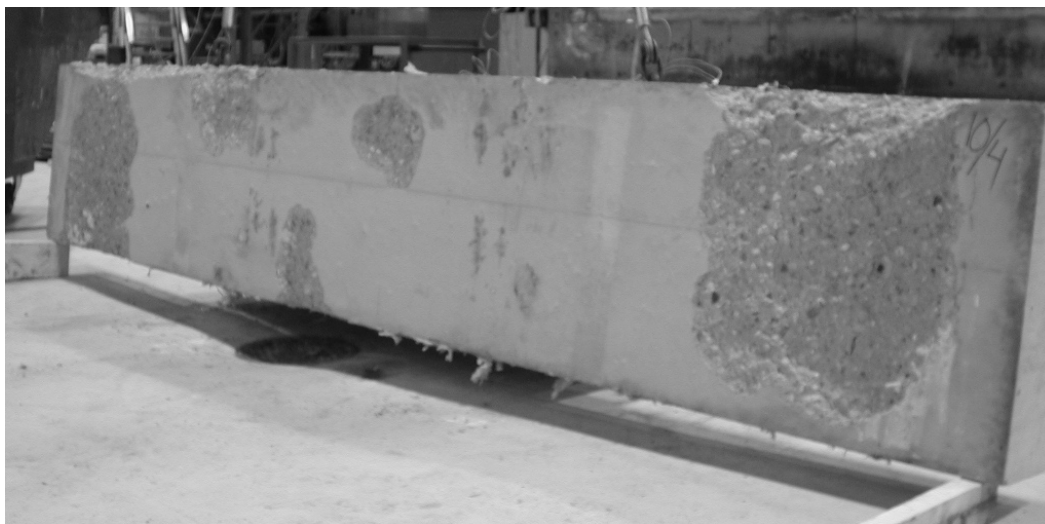


Fig 3 – Beam specimen after fire test.

5.4 Effect of water-powder ratio

Concretes 1, 2, 10 and 12 have all different water-powder ratios. In figure 4 are the results presented for both loaded and unloaded specimens. These tests were made at an age of 6 months. These results do not indicate any effect of the water-powder ratio on the spalling depth. This was not expected since an addition of fine materials (cement and filler) gives a denser concrete which normally have a higher risk for spalling.

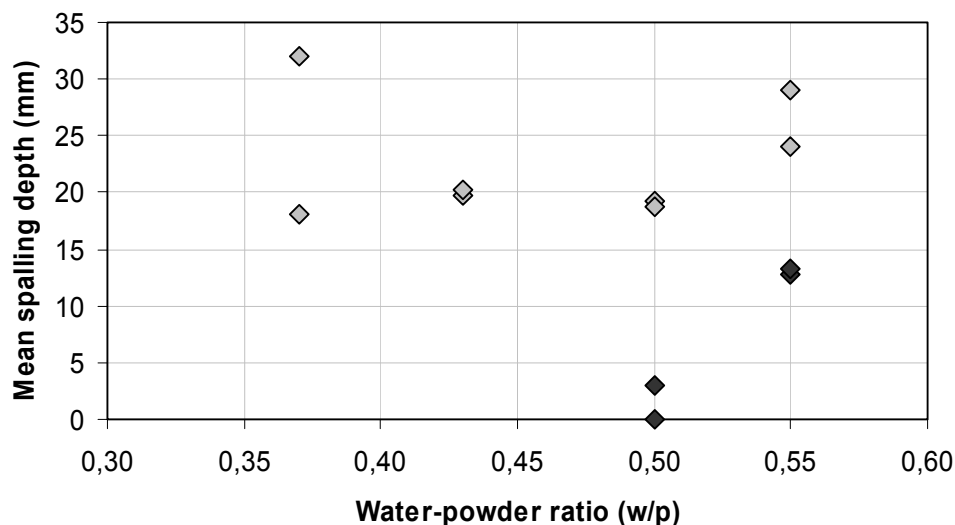


Fig 4 – Effect of water-powder ratio on the mean spalling depth

5.5 Effect of age

Concrete 10 has been tested at different age from 3 months up to 9 months. The results are presented in figure 5. The moisture content of the concrete was at age 3 months $u = 5,3 \%$. At 6 months the moisture content was $u = 5,0 \%$. No results on the moisture content at age 9 months were available at the time of writing this paper. Nevertheless, it is known that the drying of these dense concretes is a very slow process so no dramatic change in moisture content would be expected at the age 9 months.

There is no effect due to age in the present results. For the specimens with a higher load level there is a tendency of increasing spalling with age, but this is not the case for the specimen with a lower load level. Hence it is difficult to draw any conclusions from these results.

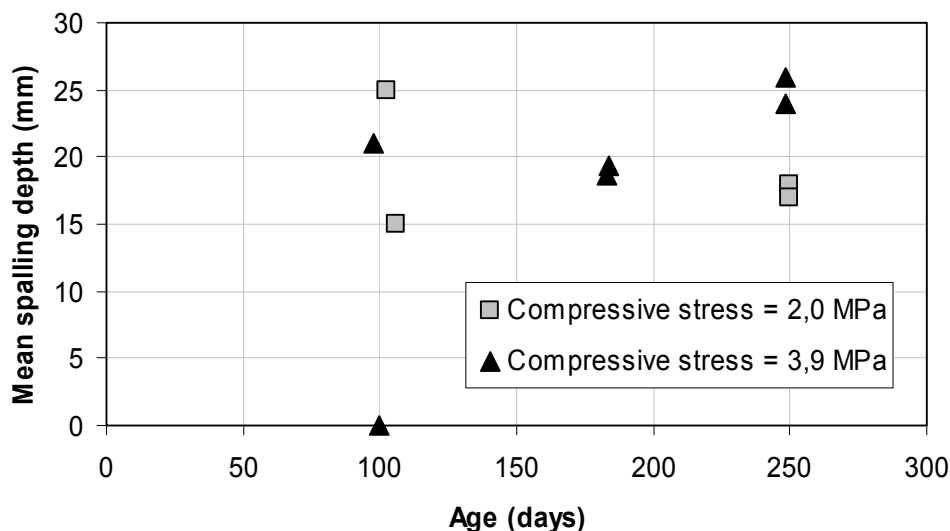


Fig 5 – Effect of age on the mean spalling depth

5.6 Comparison with a previous study

A general observation is that the spalling depth was much smaller than expected from earlier experience [2]. The geometry of the test specimens and the fire exposure were the same in the previous study as in the present. In figure 6 are some results from the previous study shown together with results from the present one. In both studies self compacting concrete was used. A difference was the age when tested, in the previous study the age was months compared to six months in the present study. The moisture content was roughly the same, around 5 %. The load was lower in the previous study. The compressive stress was 2,5 MPa only. Even so the amount of spalling was much higher in the previous tests. One difference between the two test programs is how the load was applied. In the previous study an external cradle was used to apply the load, i.e. there were no tubes going through the specimens, and thus the load level was kept during the whole test. If the load is applied within the specimen, such as it was done in the present study, the load may be lost if the post tension bars get heated and loses its modulus of elasticity. In the present study the load level was measured with load cells during the fire tests and also the temperature within the specimens at different depths from the exposed surface. These measurements showed that the load level was kept during the tests. Thus the difference in spalling is not due to the different methods of loading. Another explanation to the difference in spalling may be the influence by the tubes casted into the specimens. These may act as channels for the water vapour to migrate out of the specimen and thus the vapour pressure decreases.

In [2] also full scale tests were performed. In these tests the loading was made through pre-stressed wires. The concrete used was from the same batch as for the small scale slabs. The results show that the spalling was much less in the full scale tests compared with the small slabs. Although, the mean spalling depths measured were between 40-50 mm which coincides well with the results from the present measurements.

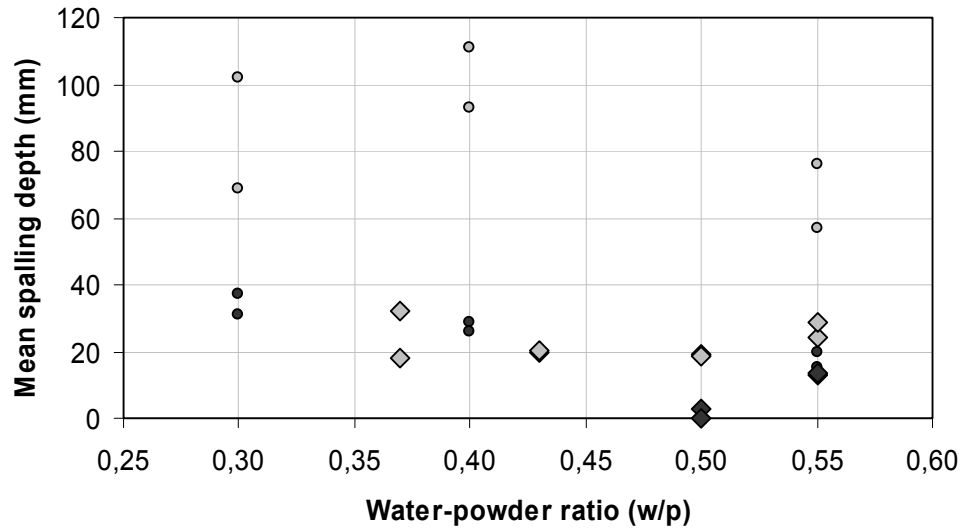


Fig 6 – Effect of water-powder ratio on the mean spalling depth. The filled symbols show the results from unloaded specimens. The large symbols are the results from the present study and the small symbols from the previous study [2].

6. REFERENCES

- [1] Boström L. The performance of some self compacting concretes when exposed to fire. SP Report 2002:23, Borås, Sweden, 2002
- [2] Boström L. Innovative self compacting concrete – development of test methodology for determination of fire spalling. SP Report 2004:06, Borås, Sweden, 2004



RESIDUAL STRENGTH OF R.C. BEAMS AFTER FIRE

Simona COCCIA¹ and Zila RINALDI²

ABSTRACT

The paper faces the problem of the evaluation of the residual strength of simple reinforced concrete schemes after fire. At this aim an analytical model, already developed by the authors, is extended and upgraded in order to account for the damages induced by the fire actions. A conventional temperature-fire curve is considered and proper constitutive relationships for the materials after cooling are chosen, according to experimental data available in literature and to European code suggestions. The residual bending moment-mean curvature relationships of cracked elements are obtained and implemented for the analysis of beams.

1. INTRODUCTION

The modelling of the behaviour of r.c. structures subjected to fire is still considered a difficult topic, mainly due to the great amount of parameters playing a role in the solution of the problem. Furthermore, for safety and economical reasons, it is not very simple to carry out experimental tests on full-scale elements, or on simple structures. Anyway, due to the topical interest on this matter, simplified analytical and numerical models are available in literature, often based on limit-state analysis or finite-element procedures^{1,2,3}. Even in the European code EC2⁴ a section devoted to the “structural fire design” (Part 1.2) is introduced.

The study of a structure under fire should include two different states, related to the fire resistance and to the residual resistance. In the first case the structure is analysed during the fire time, while the second aspect is related to the bearing capacity after cooling.

This last case, of fundamental importance for the choice of maintenance or demolition of a construction, is analysed in this work.

Aim of the paper is the evaluation of the residual strength of simple beam schemes after fire characterised by different durations. The analyses are carried out with a simplified non linear model, already developed by the authors and now extended to post-fire response of r.c.

¹ PhD, University of Rome “Tor Vergata”, Department of Civil Engineering, 00133 Rome, Italy,
email: coccia@ing.uniroma2.it.

² Professor, University of Rome “Tor Vergata”, Department of Civil Engineering, 00133 Rome, Italy,
email: rinaldi@ing.uniroma2.it.

elements. The basic model accounts for the non linear behaviour of the materials and the tension stiffening effects through the introduction of the bond-slip relationship at the steel-concrete interface. In order to analyse the behaviour of elements after fire, the concrete and steel constitutive laws and the decay of bond resistance are assigned according to experimental and numerical results available in literature. The main outcome of the model is the definition of the bending moment-mean curvature relationship for a prefixed axial load level, to be implemented for the analysis of statically determined and undetermined structures. A preliminary analysis is devoted to the study of the mean behaviour of a reference element in order to deepen the understanding of the response after fire, both in terms of strength and deformability. Finally the proposed model is applied for the analysis of a simple beam scheme and its residual behaviour is studied.

2. ANALYTICAL MODEL

2.1 Analytical model without fire

The evaluation of the residual capacity of a simple structure after fire is carried out with an analytical model, already developed by the authors and suitably modified in order to account for fire effects.

The basic model, described and validated by Grimaldi and Rinaldi⁵, allows obtaining the relationship between bending moment and mean curvature of a reference element, accounting for the cracking, the non-linear behaviour of the materials and the bond-slip relationship at the concrete-rebar interface.

The procedure and the main hypothesis of the model are here briefly summarised. The non linear behaviour of a reference r.c. element, whose length is equal to the crack distance (λ), is studied by increasing the strain in the concrete in the cracked section, and following all the phases, from cracking to steel yielding, up to the failure. The failure is defined by the reaching of the ultimate strain in one of the materials.

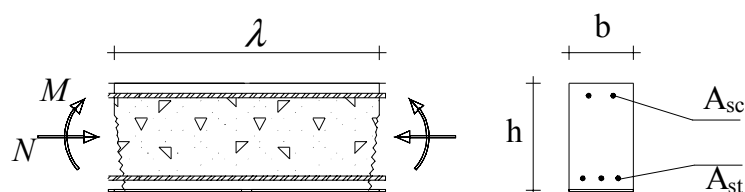


Fig. 1. Reference element model

Whatever constitutive relationship of the materials can be adopted in the model; in this study we assume the Park & Paulay law for concrete in compression, while a brittle linear elastic behaviour is considered in tension. The steel is simulated with a linear elastic relationship with hardening and the bond-slip law is rigid-plastic (limit value σ_b) with degradation (limit value σ_d) (Fig. 2).

The Bernoulli's hypothesis of plane section is valid in the cracked section only, while it is removed in the other sections of the element. The model procedure starts with the solution of the cracked section in which, with the assumed hypothesis of plane section and with the further assumption of cracked concrete (null tensile stresses), the equilibrium equations and constitutive relationships give the unknown values of the neutral axis and stress in the steel rebar.

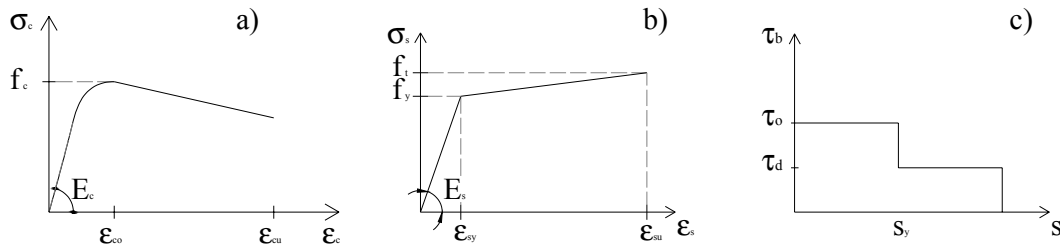


Fig. 2. Constitutive relationships: a) concrete in compression; b) steel; c) bond-slip

After the concrete cracking a slip along the whole element occurs and, with the adopted bond-slip law (Fig. 2) the steel distribution is linear along the element.

A simple equilibrium equation at the concrete-rebar interface allows determining the value of the steel stress in each section, in particular in the symmetrical one, located in the middle of the element. In this section, in which no strain linearity is imposed between steel and concrete, the stress in the tensile concrete is assumed equal to the maximum one. This hypothesis corresponds to the maximum crack distance. It is worth mentioning that the complete procedure, described in detail by Grimaldi and Rinaldi⁵, does not require the definition of the limit value τ_o , as this parameter appears in all the equations in the coupled form:

$$\tau^* = \tau_o \frac{\lambda}{\Phi} \quad (1)$$

being λ the crack distance and Φ the rebar diameter. The value of τ^* can be determined with equilibrium condition at the steel rebar interface in the cracking stage, and can be considered a constant function with the increasing loads⁵.

In particular the procedure can be summarized as follows:

- 1) analysis of the cracked section: evaluation of the stress distribution by solving equilibrium equations;
- 2) evaluation of the τ^* factors by equilibrium condition of the steel bar at the first crack formation;
- 3) analysis of the symmetrical cross section: evaluation of the stress distribution by solving equilibrium equations;
- 4) analysis of intermediate sections (for example the one in which the steel rebar strain is equal to the yield one: evaluation of stress distribution by solving equilibrium equations).

Once known the stress and strain distribution along the element the mean curvature ρ_m can be evaluated:

$$\rho_m = \frac{1}{\lambda} \int_0^\lambda \rho(z) dz; \quad \rho = \frac{\epsilon_c + \epsilon_s}{d} \quad (2)$$

being ρ the local curvature, related to a section, ϵ_c the maximum strain in compressive concrete, ϵ_s the stress in the tensile rebar, d the depth of the this section and z the longitudinal axis of the reference element.

Finally the bending moment mean curvature relationship can be drawn.

2.2 Residual behaviour after fire

The residual behaviour of the reference element after fire is evaluated with the above described model, by varying the constitutive relationship of the material in order to account for the damage and decay provided by the exposure to the fire.

The fire is described by the standard ISO-834 temperature-time curve (Fig. 3a), and the section thermal analysis is performed with the FE program Thermocad⁶. The relationships between the temperature and concrete decay (both in compression and tension) are chosen according to the EC2 curves (Fig. 3b, c), in the hypothesis, accepted by many authors, that the hot and residual mechanical properties of the concrete coincide.

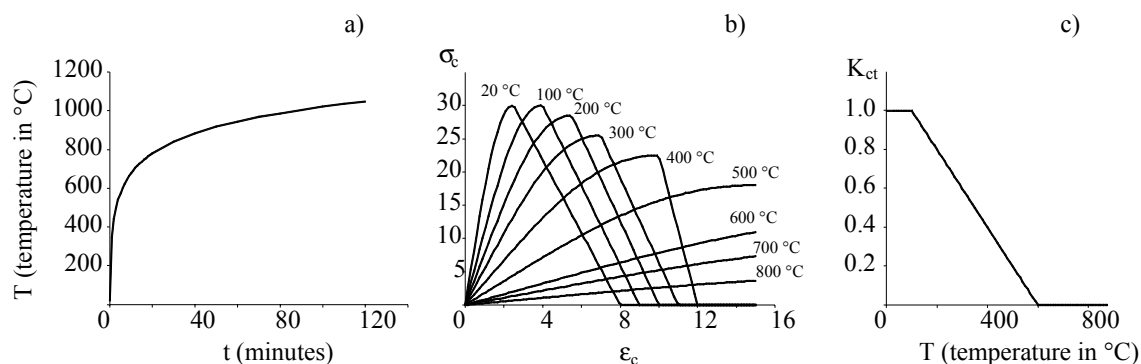


Fig. 3. a) Standard fire curve (ISO-834); b) constitutive laws of concrete in compression under fire (EC2); c) decay parameter of concrete in tension (EC2).

As a matter of fact, the cross-section is considered a “composite” one constituted by subsections. Each subsection is defined by a constant temperature and then by a proper constitutive relationship of the concrete, related to the reached temperature value (Fig.4).

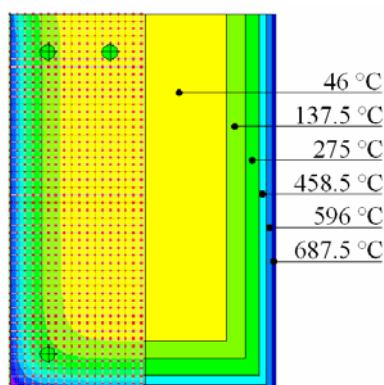


Fig. 4. Temperature distribution and section modelling

In particular for concrete in compression both the decrease of the peak strength and the increase of the ultimate strain is provided; furthermore the reduction of the tensile strength is given according to the EC2 in the “un-cracked” sections of the model, through the factor K_{ct} (Fig. 3c).

The equilibrium equations, necessary to the model development, consist in integrations of different constitutive equations of concrete, according to the reached temperature, inside the section.

Recent studies, carried by Felicetti and Meda⁷, have shown the influence of the type of steel (Carbon, Tempocore, hot rolled, cold formed bars) on its response after fire. In particular for usually adopted European Tempocore rebars the authors highlight a significant sensitivity to

temperature higher than 550°. According to these results, it is assumed the yielding and ultimate decay of the steel after cooling as reported in Fig 5.

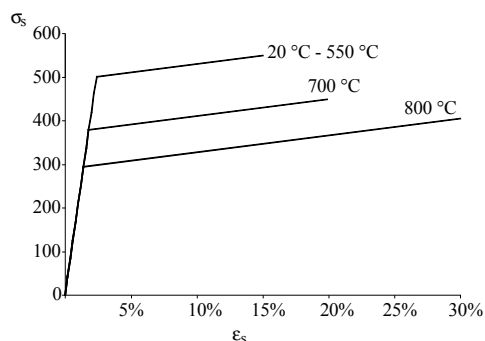


Fig. 5. Steel constitutive laws after cooling

Finally the influence of the fire exposure on the bond-slip relationship is considered. This aspect is not well assessed in literature and more studies are needed in order to deepen the knowledge on this topic. Pull-out tests carried out by Haddad and Shannis⁸ on high strength concrete specimens with reinforcing steel showed severe reductions of bond strength of about 25% and 70% at temperatures of 600° and 800°, respectively. Substantial decrease in bond strength was also experimentally found by Chiang and Tsai⁹, if the exposure temperature exceeded 200°. On the basis of these results, in the same paper, the authors suggested a procedure for the prediction of the residual bond strength after fire.

The effect of fire on bond, after cooling, is simulated in our model by reducing the limit values σ_o and σ_d through a function of the temperature (T) . In this paper this parameter is assumed equal to K_{ct} (decay coefficient for tensile stress, Fig. 3c).

3. RESIDUAL BEHAVIOUR AFTER FIRE OF THE REFERENCE R.C. ELEMENT

The residual behaviour of a r.c. element after fire, is described through bending moment-mean curvature relationships obtained with the proposed model.

The geometry of the analysed element is reported in Fig. 6.

The fire is applied on three sides and three different values of duration are considered (30', 60', 120'); positive and negative bending moments are considered as load parameters.

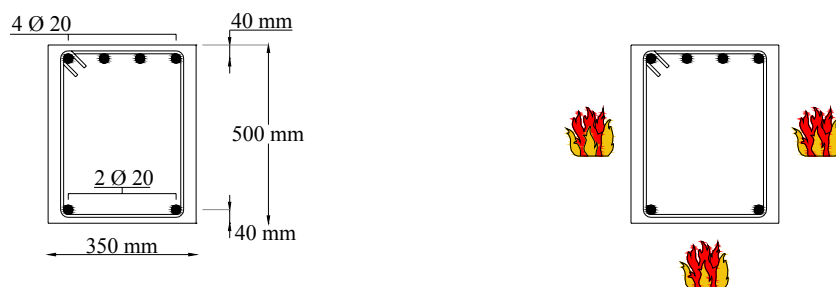


Fig. 6. Geometry of the analysed cross-section

Some remarks can be address on the basis of the obtained results. As expected, for the considered boundary conditions, the influence of the fire on the local strength is significant when the element is subjected to positive bending moment (Fig. 7). In this case, in fact, the tensile reinforcement is subjected to the highest temperature and its residual strength can be

strongly reduced. In agreement with the assumed decay relationship of the steel rebars (recover of the original stresses for temperatures below 700°) the residual yielding and ultimate bending moment are strongly affected by exposure times higher than 60'.

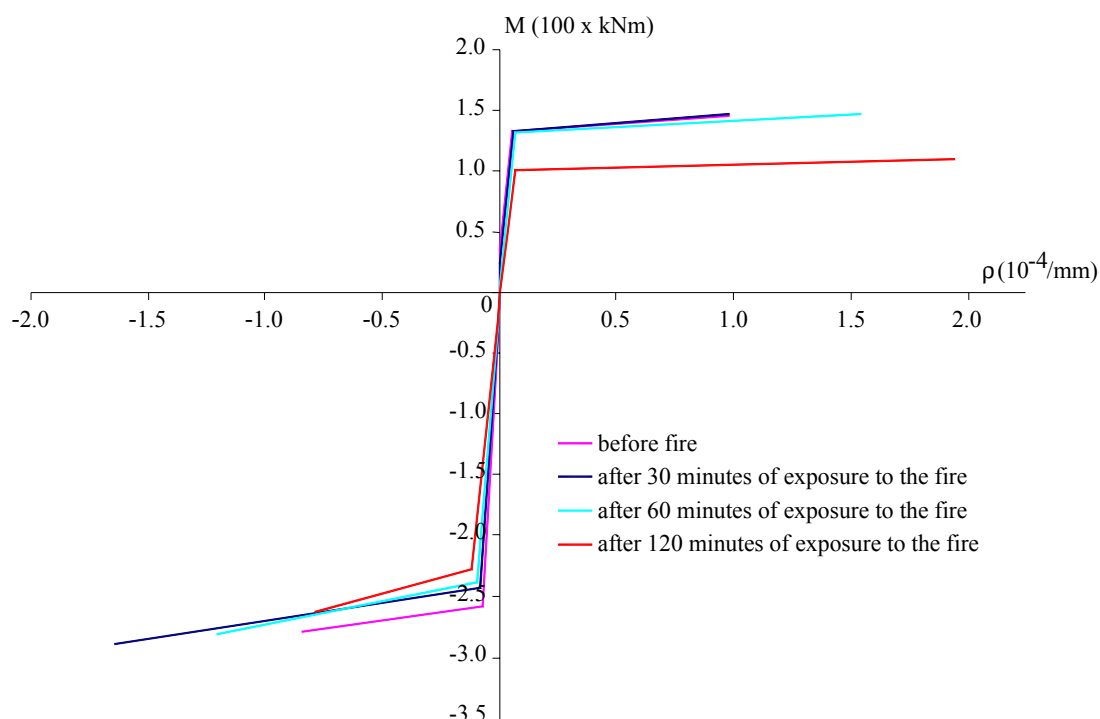


Fig. 7. Positive and negative bending moment-mean curvature relationships

In particular, in this conditions, an almost linear moment reduction occurs, as highlighted in Fig. 8, where the ratio between the moment at a given exposure time and the moment at room temperature, related to the yielding and ultimate stages, are plotted.

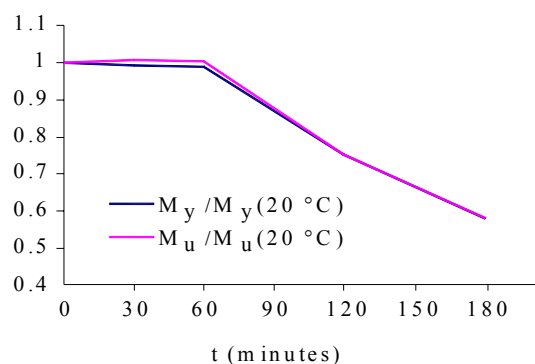


Fig. 8. Positive bending moments: residual non-dimensional yielding and ultimate bending moment vs. exposure time

The effect of fire on the reference element ductility is further analysed. Due to the rapid degradation of the concrete in tension, the “cracked section” governs the deformability aspects, at least for exposition times higher than 30'. In this case tension-stiffening effects and slip phenomena, related to bond decay also, can be neglected and the mean curvature is almost coincident with the local one. This aspect is clearly highlighted in Fig. 9a where the ratios

between the mean and local curvatures (ρ_m and ρ_l), at the yielding and ultimate stages, are plotted versus different fire durations.

It can be clearly observed that, while in the undamaged element differences between local and mean curvatures can be significant, (mean ultimate curvature is about $\frac{1}{2}$ of the local one), after fire these characteristics tend to be similar and to coincide for exposure time of 120 minutes.

The mean ultimate and yielding residual curvatures are plotted versus the exposure time in Fig. 9b, together with the ductility index μ , defined as the ratio between the mean ultimate and yielding curvatures ($\mu = \rho_u / \rho_y$).

The increase of the mean ultimate curvature with the fire duration is obviously related to the above-said phenomenon: while the local curvature is almost constant with the temperature (for positive bending moments the concrete ultimate strain is less affected by the fire) the mean curvature tends to the local one when the fire duration increases.

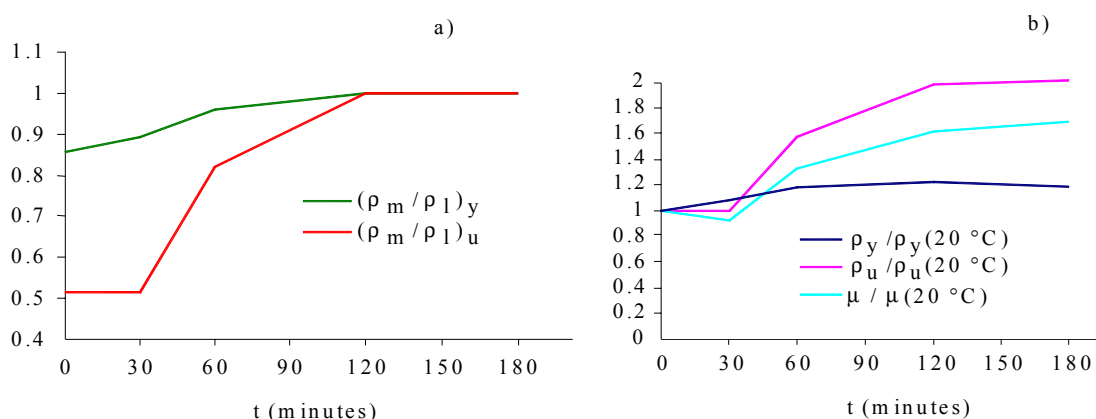


Fig. 9. Positive bending moments: a) ratio between mean and local curvatures at yielding and ultimate stages vs. exposure time; b) residual non-dimensional

A different behaviour is exhibited by the element subjected to negative moment. In this case, according with the boundary conditions, the tensile reinforcement is less affected by the fire, being close to the adiabatic surface. For this reason the bending moment reduction is less sensitive to the fire durations. In particular, even if the peak concrete stress is reduced with the temperature, a slight increase of the ultimate moment occurs after 30' of exposure time. This phenomenon is due to the increase of the ultimate concrete strain, that governs the local failure. For higher values of the exposure times the bending moments decrease very slightly with the temperatures, with the pattern highlighted in Fig. 10.

Contrarily to the above-analysed positive bending moments, in this case the reduction of bond and tensile stress in the concrete, due to the fire, plays a significant role in the definition of the mean curvature of the element.

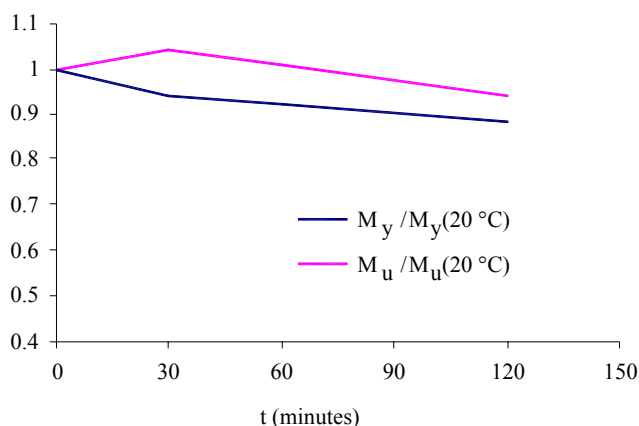


Fig. 10. Negative bending moments: residual non-dimensional yielding and ultimate bending moment vs. exposure time

As highlighted in Fig 11, where the ratios between mean and local values of the yielding and ultimate curvatures are reported, it appears more proper to adopt mean curvatures, instead of local ones, for deformability analysis. In this case, in fact, not negligible differences between them occurs with a decrease of the mean ultimate curvature up to about 40% respect to the local one (Fig. 11a).

Finally the mean values of the yielding and ultimate curvatures, together with the ductility index are reported in non-dimensional form respect to the room temperature in Fig 11b. The increase of the mean ultimate curvature and ductility index, up to about 30' of exposure time is due to the increase of the ultimate concrete strain in the exposed surface. For higher temperatures the effect of the stress reduction in compressed concrete governs the behavior, the neutral axis depth is higher and the mean curvature reduces.

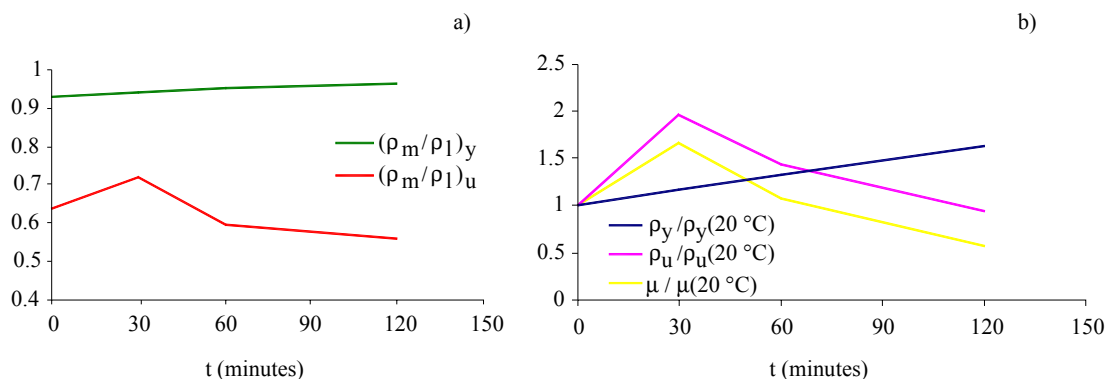


Fig. 11. Negative bending moments: a) ratio between mean curvature influence of the mean curvature residual non-dimensional yielding and ultimate bending moment vs. exposure time

In order to check the effectiveness of the procedure the ultimate values of the bending moment ($M_{u,m}$) are compared with the ones obtained by applying the simplified method of the “effective section” ($M_{u,eff}$), allowed by the EC2. In particular, for each analysed fire duration, the concrete with temperature higher than 500° is assumed not to contribute to the load bearing capacity, while the residual concrete cross-sections is characterised by the constitutive relationship related to room temperature. The steel decay after fire is assumed as reported in the previous paragraph, in agreement with the hypothesis of the analytical model. The obtained results for both positive and negative moments show, as assessed in literature³, that

the effective section method catches well the ultimate strength, at least in the case of pure flexure.

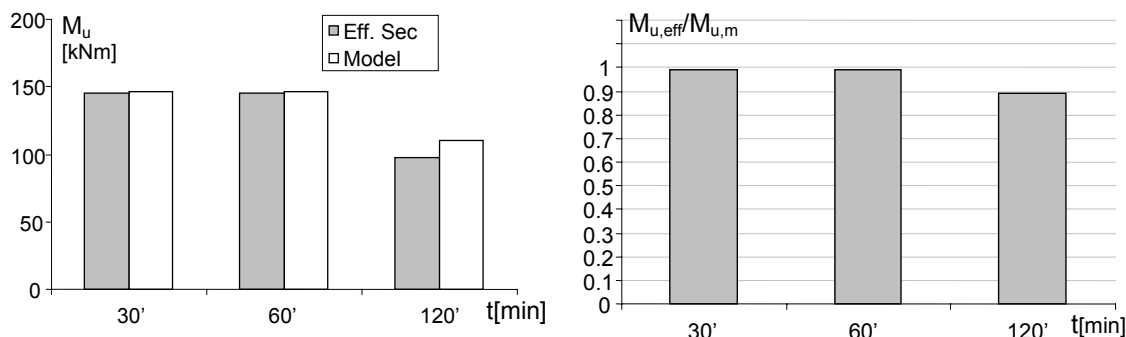


Fig. 12. Positive bending moment: comparison between ultimate moment obtained with the section effective method $M_{u,eff}$ and with the model $M_{u,m}$

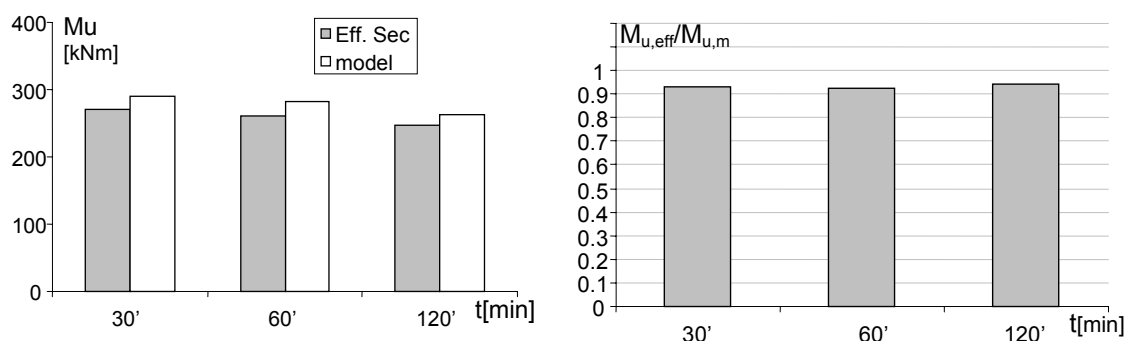


Fig. 13. Negative bending moment: comparison between ultimate moment obtained with the section effective method $M_{u,eff}$ and with the model $M_{u,m}$

Very low scatter values (less than 10%) are found and anyway the simplified method is always on the safe side.

4. RESIDUAL BEHAVIOUR AFTER FIRE OF R.C. BEAM

The residual behaviour after fire of a reference statically undetermined scheme is studied with the above described analytical model. In particular the beam sections are characterised by the bending moment-mean curvature relationship obtained with the analytical model, which accounts for the average non-linear behaviour of an element between two subsequent cracks. The displacements (v) of the schemes are obtained through integration of the mean curvatures along the beam length, for each value of external generalised load q :

$$v(q) = \int_z \rho(z, q) \cdot z \cdot dz \quad (3)$$

As an example the beam geometry reported in Fig.13 is here studied in order to evaluate the residual strength and ductility characteristics. The fixed end scheme is subjected to uniform distributed load increased up to the failure, and it is characterised by rectangular 30x55 cm²

cross-sections, whose behaviour is analysed in the previous section. Different fire durations are considered equal to 30', 60', 90' and 120'.

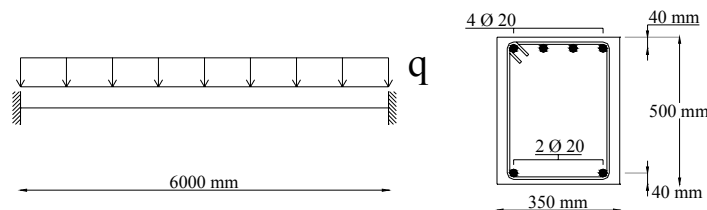


Fig. 13. Reference beam scheme

The obtained results are summarised through load-midspan displacement relationships, reported in Fig. 14.

A reduction of the global stiffness can be observed after cooling. In particular the increase of the deformability occurs both in the elastic and plastic ranges. For exposure times higher than 60' a reduction of the yielding and ultimate bending moment (of about 20%) also occurs.

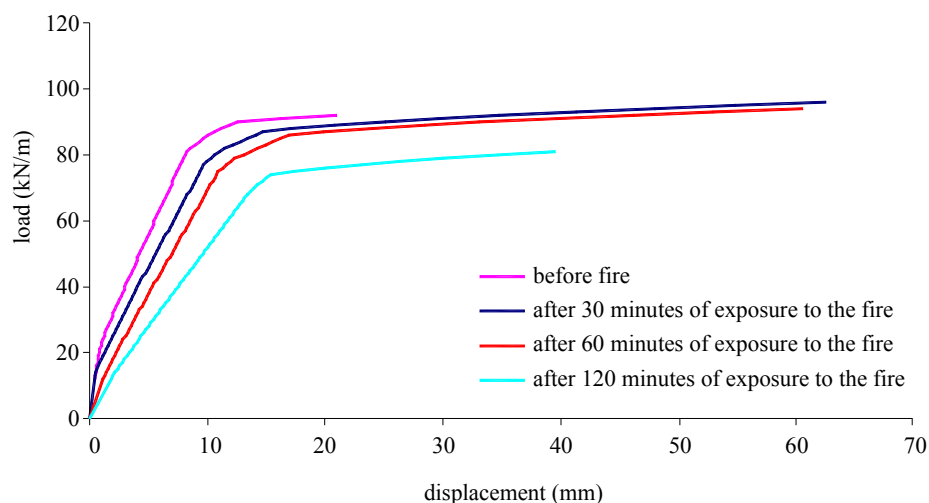


Fig. 14. Load-midspan relationships

6. CONCLUSIONS

A simplified analytical model developed by the authors is applied for the analysis of the residual strength of beam schemes after fire acting on three sides of the cross-sections.

Both the ultimate and service states are considered and studied for elements subjected to positive and negative bending moments.

According to the boundary conditions, and to the hypothesis of the residual behaviour of the material and bond after cooling, the following conclusions can be drawn:

- in sections subjected to positive bending moments the sharp reduction of strength is obviously related to the steel decay; for high exposure times mean and local curvature are almost coincident and bond decay and tension-stiffening effects can be neglected. For this reason the deformability of the scheme is increased with the exposure time.
- in section subjected to negative bending moment the bearing capacity is less sensitive to the fire, on the contrary the influence of the bond and concrete decay is more significant in the framework of deformability analysis.

7. REFERENCES

- [1] Dotreppe J., C, Franssen J., M, Vanderzeypen Y. "Calculation Method for Design of Reinforced Concrete Columns under Fire Conditions". ACI Structural Journal, 1999; 96(1): 9-18
- [2] Terro M.J., "Numerical modeling of the behavior of concrete structures in Fire". ACI Structural Journal, 1998; 95 (2): 183-193
- [3] Meda A., Gambarova P. G., Bonomi M. "High-Performance Concrete in Fire-Exposed Reinforced Concrete Sections" ACI Structural Journal, Vol. 99. No. 3, May/June 2002
- [4] Eurocode 2; UNI EN 1992-1-2: Design of concrete structures- Part 1-2: General rules- Structural fire design. 2005
- [5] Grimaldi, A., Rinaldi, Z.,: "Influence of the steel properties on the ductility of r.c. structures"; Proc. 12WCEE World Conference on Earthquake Engineering, Auckland New Zealand, 2000
- [6] Thermocad - User Manual Concrete s.r.l.
- [7] Felicetti, R. and Meda, A. "Residual behaviour of reinforcing steel bars after fire" fib symposium "Keep concrete attractive" Budapest 2005
- [8] Haddad, R., H and Shannis, L., G. "Post-fire behaviour of bond between high strength pozzolanic concrete and reinforcing steel", Construction and Building Materials, 18 pp. 425-435, Elsevier. 2004
- [9] Chiang, C-H., and Tsai, C-L. "Time-temperature analysis of bond strength of a rebar after fire exposure", Cement and Concrete Research, 33 pp. 1651-1654, Pergamon. 2003

SIF'06

PERFORMANCE OF CONCRETE IN FIRE: A REVIEW OF THE STATE OF THE ART, WITH A CASE STUDY OF THE WINDSOR TOWER FIRE

Ian FLETCHER¹, Audun BORG, Neil HITCHEN and Stephen WELCH²

ABSTRACT

This paper provides a “State of the Art” review on current research into the effects of fire exposures upon concrete. The principal effects of high temperature in concrete are loss of compressive strength and spalling, the forcible ejection of concrete from a member. Though a lot of information has been gathered on both phenomena, there remains a need for a broader understanding of the response of concrete structures to different heating regimes and the performance of complete concrete structures subjected to realistic fire exposures.

There is a lack of information derived from large-scale tests on concrete buildings in natural fires. Besides undertaking further fire tests, lessons can also be learnt from real fires and the University of Edinburgh has embarked upon detailed studies of the serious fire in the Windsor Tower, Madrid. In order to properly characterise the fire and the performance of the structure a data-gathering exercise has been undertaken and computer modelling tools are being applied in order to obtain better insights into the structural response. Initial results suggest that the observed behaviour is fully in accordance with what might be expected for a structure of this type, under the conditions prevailing at the time of the fire when significant refurbishment work was underway; in particular, the lack of fire protection of certain parts of the steelwork was a major reason for the partial collapse of the building and the particular nature of the glazed curtain walling may have played its part in facilitating upward fire spread.

1. INTRODUCTION

In order to advance the understanding of the performance of concrete-framed structures during a fire it is important to establish the scope and conclusions of earlier studies

¹ PhD Student, University of Edinburgh, School of Engineering and Electronics, Edinburgh, EH9 3JL, UK
e-mail ian.fletcher@ed.ac.uk

² Lecturer, University of Edinburgh, School of Engineering and Electronics, Edinburgh, EH9 3JL, UK
e-mail s.welch@ed.ac.uk

and to highlight research gaps. This paper examines the current “state of the art” of our understanding of concrete in fire and overviews notable areas of recent research.

Gaining an improved understanding of concrete in fire is also greatly aided by the examination of experimental measurements and data obtained from real-world fires. Concerning the latter, a detailed assessment is underway on the fire in the Windsor Tower in Madrid, which occurred in February 2005, with advanced modelling tools being used to assess the fire development and structural response of this mainly concrete-framed structure. Having adequately characterised the actual fire and the performance of the structure, establishing a well-defined case study, the modelling tools will then be used to examine sensitivities to a range of parameters of interest, generalising the conclusions to other possible fire scenarios and structural arrangements.

2. AREAS OF RESEARCH EXAMINED

2.1 Chemical responses of concrete to fire

When subjected to heat, concrete responds not just in instantaneous physical changes, such as expansion, but by undergoing various chemical changes. This response is especially complex due to the non-uniformity of the material. Concrete contains both cement and aggregate elements, and these may react to heating in a variety of ways.

First of all, there are a number of physical and chemical changes which occur in the cement subjected to heat^[1,2]. Some of these are reversible upon cooling, but others are non-reversible and may significantly weaken the concrete structure after a fire. Most porous concretes contain a certain amount of liquid water in them. This will obviously vaporise if the temperature significantly exceeds the moisture plateau range of 100-140°C or so, normally causing a build-up of pressure within the concrete. If the temperature reaches about 400°C, the calcium hydroxide in the cement will begin to dehydrate, generating further water vapour and also bringing about a significant reduction in the physical strength of the material. Other changes may occur in the aggregate at higher temperatures, for example quartz-based aggregates increase in volume, due to a mineral transformation, at about 575°C and limestone aggregates will decompose at about 800°C. In isolation, the thermal response of the aggregate itself is more straightforward but the overall response of the concrete due to changes in the aggregate may be much greater. For example, differential expansion between the aggregate and the cement matrix may cause cracking and spalling.

These physical and chemical changes in concrete will have the effect of reducing the compressive strength of the material. Generally, concrete will maintain its compressive strength until a critical temperature is reached, above which point it will rapidly drop off. This generally occurs at around 600°C. This is only a little higher than critical temperatures for steel, but because of the much lower conductivity of concrete the heat tends not to penetrate very far into the depth of the material, meaning that the structure as a whole normally retains much of its strength (timber is similar in being able to retain strength in its depth once surface layers have been attacked by fire).

2.2 Spalling

One of the most poorly understood processes in the reaction of concrete to high temperatures or fire is that of ‘explosive spalling’^[3]. This is the process whereby chunks of concrete break off and are ejected from the surface of the concrete slab, often at fairly high velocities. The phenomenon is generally assumed to occur at high temperatures, yet it has also

been observed in the early stages of a fire^[4] and at temperatures as low as 200°C^[5]. If severe, spalling can have a deleterious effect on the strength of reinforced concrete structures, due to enhanced heating of the steel reinforcement. Spalling may significantly reduce or even eliminate the layer of concrete cover on the reinforcement bars, thereby exposing the reinforcement to high temperatures, leading to a reduction of strength of the steel and hence a deterioration of the mechanical properties of the structure as a whole.

The mechanism leading to spalling is generally thought to involve large build-ups of pressure within the porous material which the structure of the concrete is not able to sufficiently dissipate, so fractures occur and chunks of the material are forced suddenly outward. While still in its early stages, modelling of spalling is beginning to show promise^[3].

The main prerequisites for spalling are relatively well established, these being moisture content of at least 2% and most importantly steep temperature gradients within the material. A value of 5K/mm is a rough minimum and at 7-8K/mm spalling is very likely^[6]. Temperature gradients are dependent not only on gas-phase temperatures but also heating rates, so that it is not possible to define a threshold temperature per se. However, these values may be affected by the type of concrete, including the strength of the material and the presence of fibres, as described below.

There has been a large amount of recent research on the potential for inclusion of various types of fibres into concrete to mitigate the effects of spalling. Some studies^[7,8,9,10] have included polypropylene fibres into the concrete matrix. The theory is that when the concrete is subjected to heat, the polypropylene will melt, creating pathways within the concrete for the exhaust of water vapour and any other gaseous products, which will thereby reduce the build-up of pressure within the concrete. There has been some debate as to whether mono-filament or multi-filament fibres are better able to mitigate spalling^[11]. It has also been suggested that the melted polypropylene fibres can form a barrier to the transport of moisture further into the concrete, preventing pressure build-up at greater depth and forcing the moisture to escape instead^[8]. The same report suggests that the polypropylene fibres may provide a mechanism for cracking deeper within the concrete, which may mitigate spalling at the surface, but may have adverse structural consequences. Clearly, more work needs to be done in this area. Other studies have added steel fibres to concrete systems^[11]; the theory behind this is that the steel will increase the ductility of the concrete and make it more able to withstand the high internal pressures. Results are, so far, inconclusive^[11].

Recently there has been increasing use of 'high strength concrete'. This material typically has considerably higher compressive strength than normal strength concrete, however it is also considerably less porous and moisture absorbent. While this generally reduces the water content of the cement, it is also harder for water vapour to escape during heating. Spalling has been suggested to be relatively more common in high strength concrete, due to the lower porosity of high strength concrete and hence the increased likelihood of high pressure developing within the concrete structure^[7,1]. However, some recent research has shown that this is not necessarily the case, with testing showing higher spalling resistance in high strength concrete than in normal strength^[8,2].

An aspect of concrete behaviour in fire that has not been revealed by testing based on standard fire curves is the post-fire cooling stage. The importance of a cooling-off phase in the assessment of a sample's resistance to heat was demonstrated during a test of some concrete structural elements at Hagerbach test gallery, Switzerland. During the test a concrete sample resisted temperatures of up to 1600°C for two hours without collapsing, but half an hour into the cooling-off phase the sample collapsed explosively^[12].

2.3 Cracking

The processes leading to cracking are believed to be essentially the same as those leading to spalling. Thermal expansion and dehydration of the concrete due to heating may lead to the formation of fissures in the concrete rather than, or in addition to, explosive spalling. These fissures may provide pathways for direct heating of the reinforcement bars, possibly bringing about more thermal stress and further cracking. Under certain circumstances the cracks may provide pathways for hot combustion products to spread through the barrier to the adjoining compartment, but this has not been the subject of significant research^[12].

Geogali & Tsakiridis^[13] have made a case study of cracking in a concrete building subjected to fire, with particular emphasis on the depths to which cracking penetrates the concrete. It was found that this relates to the temperature of the fire, and that generally the cracks extended quite deep within the concrete member. Major damage was confined to the surface near to the fire origin, but the nature of cracking and discolouration of the concrete suggested that the material around the reinforcement had reached about 700°C. Cracks which extended more than 3cm into the depth of the structure were attributed to a short heating/cooling cycle due to the fire being extinguished.

2.4 Spalling containment

Research has also been undertaken on the effects of wrapping a concrete member in a variety of fabrics in order to assess any improvement of spalling resistance that this may provide^[14]. It was found that a metal fabric had a beneficial effect on spalling resistance, with less effect being produced by carbon fibre and glass fibre fabrics. All tests were noted to have a reduction or absence of spalling when polypropylene fibres were added to the concrete mixture^[9]. Steel fabric reduces spalling by providing lateral confinement pressure to the concrete member which is greater than the internal vapour pressure causing the spalling. The reduced effect of carbon and glass fibre fabrics is due to the bond strength of these materials reducing at high temperatures and therefore the ability of the fabric to provide confinement being suppressed. It does not appear that the wrapping these concrete members in fabric induces cracking deeper within the structure.

2.5 Effects of reinforcement bars

The performance of steel during a fire is understood to a higher degree than the performance of concrete, and the strength of steel at a given temperature can be predicted with reasonable reliability. It is generally held that steel reinforcement bars need to be protected from exposure to temperatures in excess of 250-300°C. This is due to the fact that steels with low Carbon contents are known to exhibit 'blue brittleness' between 200 and 300°C. Concrete and steel exhibit similar thermal expansion at temperatures up to 400°C; however, higher temperatures will result in significant expansion of the steel compared to the concrete and, if temperatures of the order of 700°C are attained, the load-bearing capacity of the steel reinforcement will be reduced to about 20% of its design value.

Reinforcement can have a significant effect on the transport of water within a heated concrete member, creating impermeable regions where water can become trapped. This forces the water to flow around the bars, increasing the pore pressure in some areas of the structure and therefore potentially enhancing the risk of spalling. On the other hand, these areas of trapped water also mitigate the heat flow near the reinforcement, thereby reducing the temperatures of the internal concrete^[15]. A large area of current study is targeted at the effects of using reinforcement constituted by glass or carbon fibres, rather than steel, in concrete^[16,17,18,19,20]. Much of this research is motivated by the relative lack of information on Fibre Reinforced Plastic (FRP) reinforcement at high temperatures, and concern over

thermally-induced failures. However, most of the testing indicates that with sufficient cover to the reinforcement, FRP reinforcement will have perfectly adequate fire endurance.

2.6 Structural Stability and modelling

After a fire, changes in the structural properties of concrete do not fully reverse themselves, as opposed to a steel structure, where cooling will generally restore the material to its original state. This is due to changes in the physical and chemical properties of the cement itself. The non-reversibility of these processes has led to an interesting line of research which aims to assess the severity of a fire (i.e. the maximum temperature to which the structure was exposed) by examination of the state of the concrete structure after the fire^[21]. It should be noted that, in some circumstances, a concrete structure may be considerably weakened after a fire, even if there is no visible damage.

Several models are available for the mechanical behaviour of concrete at elevated temperatures. A number of these are reviewed by Li & Purkiss^[22], including the model suggested by Schneider^[23], in order to produce a model which may be used in finite element analysis of a structure. It is noted that these models break the strain imposed on the concrete into four different types: the “free thermal strain”, caused by the change in temperature, “creep strain”, caused by the dislocation of microstructures within the material, the “transient strain”, caused by changes in the chemical composition of the concrete and the “stress-related strain”, caused by externally applied forces.

The models examined by Li & Purkiss each handle these strains differently^[22]. “Free thermal strain” is solely a function of the temperature of the concrete member; however creep, transient and stress-related strains are all functions of the temperature, time and stress, making it difficult to separate which particular strains are being influenced during a given experiment. In order to reduce this level of complication, some of the models gather two or even all three of these strains together into one term. Typically, this is the “transient creep strain”, incorporating the creep strain and transient strain together.

Based on the results of these models, Li & Purkiss created a new model and used it to demonstrate the significance of transient strain^[22]. It was shown that models that do not include transient strain are unconservative for high temperatures, though at low temperatures transient strain appears to have less effect. It was also noted that “it is evident that the full stress-strain curves provided in EN 1992-1-2^[24] for higher temperatures are unconservative”.

While it is important to understand the performance of individual concrete members during a fire, the behaviour of the same members within the context of a complete structure can depart widely from their independent responses. This is due to a variety of factors – for example, thermal expansion of members which have been subjected to heating may lead to forces being exerted upon the cooler members due to differential expansion, and upon the hotter members due to restraining forces provided by the rest of the structure. The effects of thermal expansion have long been recognized with steel and composite members^[25], but little research is available for concrete structures.

Modelling has largely been undertaken of the effects of increased temperature on individual concrete elements, for example concrete columns^[26]. These have been used in particular to compare predictions with the structural Eurocodes and validate against the behaviour of real concrete columns during full-scale fire testing. Further fire testing has been carried out on concrete columns, for example by Benmarce *et al*^[27]. This study examines the boundary conditions of the column as well as the effects of heating on the concrete itself, and hence has a closer approximation to the effects of fire on a whole structure. This is important, as the behaviour of a structural member must be related to the structure it is in, rather than being examined in isolation, in order for it to be useful; it is also necessary in considering the effects of the member on rest of the structure. The study concluded that this is an area that has

not been examined sufficiently^[26], but the tests determined that the additional forces generated were low, around 15% of the design load of the columns. However, the columns tested were 125mm x 125mm cross section x 1.8m high with 108 N/mm² high strength concrete, which is very small for a concrete section. Hence it is uncertain whether this data would be scalable to larger members or applicable to members with normal strength concrete.

The main reports on the effects of fire on whole structures have been produced as a result of tests carried out at Cardington by the Building Research Establishment (BRE)^[4,28,29]. One of the structures built at Cardington is a concrete building, consisting of high strength concrete columns and normal strength concrete flat slabs. The fire test on this structure, using wooden cribs to provide the fire loading rather than a furnace, was not entirely successful due to problems with the data collection; however it did indicate that a concrete column exposed to a real fire situation was unlikely to fail. Also, large amounts of spalling were induced in the concrete floor slabs. However, these remained intact, which was attributed largely to the “compressive membrane action” as the expansion of the concrete slab was restrained due to the presence of cold surrounding areas of structure, and therefore load was supported by the compressive strength of the concrete. This mechanism differs from “tensile membrane action”, where the reinforcement in a concrete slab restrains the slab as it suffers displacement. Compressive membrane action can only take place at relatively small displacements; however it does not rely on the reinforcing bars retaining their strength at high temperatures, as tensile membrane action does. In the case of the Cardington test the reinforcing bars are unlikely to have retained large amounts of strength due to being directly exposed to high temperatures as a result of the significant spalling in the concrete cover.

It is also worth considering that while an individual concrete member may fail, the overall structure may well remain intact, due to the fact that redundancy of the structure allows members to redistribute the loads previously carried by failed members. This is a common phenomenon in composite structures.

The Cardington data has been used to provide input values for a finite element model which made a large number of assumptions with respect to the performance of concrete in fire (for example, the effects of spalling were neglected)^[10]. Further study of the effects of fire upon a whole-frame structure would be extremely useful. It is hoped that the examination of the effects of fire upon the Windsor Tower (c.f. section 3 below) will go some way towards developing a better understanding of the effects of a fire upon complete structures, without the necessity of carrying out further expensive large-scale fire tests.

2.7 Composite Structures

A common form of construction for floor slabs is known as “Composite Construction”. In this method, a concrete slab is cast upon steel beams. The formwork for this slab is a profiled metal sheet, known as decking, which spans between the beams. “Shear studs” are welded to the top of the steel beams, through this profiled decking. These studs allow a mechanical bond to be formed between the concrete and the steel member, and therefore allow the beam and the slab to act as a single member with an increased strength. The steel decking is left permanently in place after the concrete has been cast. Steel reinforcement is typically added above the profiled decking.

There has been a significant amount of work carried out on composite steel and concrete structures, for example the Cardington project carried out full-scale fires on a steel-framed building with composite concrete decking floor slabs^[27]. These structures have been found to have considerable resistance to fire^[30]. This is in part due to the concrete floor having capacity to act as a tensile membrane, allowing the load to redistribute through the structure when the mechanical properties of steel are reduced. This can lead to a reduction in

the requirement for fire protection on the steel areas of the structure, a fact that has been recognised in recent design guidance and is increasingly reflected in engineering design.

3. WINDSOR TOWER FIRE CASE STUDY

The Windsor Tower in Madrid was involved in a major fire, of duration 18-20 hours, on 12-13 February 2005, which caused extensive structural damage to the upper floors of the building. Due to the nature of the building's construction, a largely concrete frame with steel perimeter columns, this fire has provoked intense interest amongst researchers hoping to better understand the performance of concrete structures in fire. In general, the concrete structure appears to have performed very well, and the most severely affected areas of the building appear to be those where the structural steelwork had not yet received fire protection, which was being installed in the building at the time when the fire broke out.

Analysis of records of the fire, together with data gathered on the construction details, has enabled establishment of computer models of the fire development and structural response. These provide a means of characterising the fire and assessing the actual performance of the structure under these heating conditions. However, it is not intended that this be a purely "forensic" exercise, but rather the modelling tools will be used to examine sensitivities to parameters of interest, such as glazing failure, compartmentation failure, external fire spread, fuel source distribution and progressive burnout.

The areas of the building where most damage occurred were the upper storeys above the strong transfer floor (T2), i.e. floors 17-28. The major structural failures can be very simply attributed to the fact that the perimeter steel columns over this height were not fire protected; once they had lost significant strength, then much of the concrete perimeteric flooring was unable to support itself as a cantilever and suffered progressive collapse, with failure of a large section on the north-east corner of the building at 01:15hrs. There were some variations in this behaviour though, with no collapse in regions adjacent to the new fire escape, on the west face, presumably due to the additional support for the floor, but some failure of a further section of floor slab together with the supporting concrete portal frame towards the north façade. It is also of interest that there was no significant collapse of the floor slab on floor 9, which also sustained a fully flashed over fire for a period after 06:00hrs in the morning, and for which there was no fire protection applied to the steel-work on two of the sides; the steel columns here showed severe buckling, but the overall stability of the structure was maintained due to load sharing – with support coming from the protected steel columns both above and below.

Initial studies indicated that it will be quite challenging to model the thermal and structural response of the floor slabs themselves due to their complex method of construction. This utilises a type of clay permanent formwork to create a "waffle slab" profile. As this clay remains in place during the life of the building, there are areas of the concrete which have an additional layer of insulation against fire. This may complicate the analysis as the addition of two layers of insulation to the reinforcing steel, both which will have different thermal properties and one of which is believed to possess no permanent structural properties, will add a large number of variables to any model created. However, it is believed that little work has previously been carried out to examine the effects of fire on this type of concrete slab, and as it is believed to be a widespread form of construction in Spain, at least historically, it may provide a useful precedent for analysis of this form of construction.

Defining the development of the fire is also a very challenging exercise, but necessary in order to facilitate modelling of the structural response. It is fairly well-established that the fire broke out on the 21st floor, in office 2109 at approximately 23:05hrs and was detected at 23:08hrs; a 50cm flame was reported to have been seen there at 23:18hrs, consistent with a hypothesised waste-paper basket fire source, and the fire brigade were called at 21:21hrs; by

23:35 the fire on this floor was fully flashed over^[31]. Simulations of fire development have been performed using the FDS^[32] and SOFIE^[33] CFD codes but the biggest uncertainty is the time of glazing failure, which has a dominant influence on the fire development. The strategy adopted to overcome this is to run a number of different simulations, each with different glazing failure temperatures, in order to bound the possible behaviours. An initial finding is that if there is no glazing failure at all within the growth period of the fire then the model predicts a decay and eventual extinction; in order to generate a realistic representation of the real fire, a major glazing failure is required in the first 10 minutes or so.

Having established itself on one floor, there is a great interest in the mechanism of fire spread to other parts of the building. Significant effort has gone into defining the rate of floor-to-floor fire spread, in order to determine the thermal exposure boundary conditions on the rest of the structure, at least in approximate terms. Initial reports indicated that the rate of upward fire spread had been “very rapid”, with some suggestion, mainly via news reports and anecdotal evidence, that the fire had reached the top of the building by 00:00hrs. However, more careful investigation indicates that this is probably a significant overestimate. A number of subsequent studies have now reported more precise estimates floor-to-floor fire spread rates, varying from an average of 6.5 minutes per floor (INTEMAC report^[34]) to 15 minutes per floor (Japanese study^[35]). The latter report provides a detailed time breakdown of the estimated burning histories on each floor; it suggests that the initial upward spread to the 22nd floor took 40 minutes, progress to the 23rd & 24th floors took a further 70 minutes and that the fire reached the top of the building (28th floor) after a further 30 minutes. A time-stamped photograph of the east face, where the room of fire origin - office 2109 - was located, taken at 00:50hrs, is consistent with this, showing obvious external flaming on only 3 or 4 floors, though at this stage there has apparently not been any significant break-out of the fire through the façade on the south face. This suggests that the progress rate upwards from one floor to the next was not indeed that rapid up until this point. Downward spread commenced with involvement of floor 20 at 01:00hrs and then a very steady progression of about 20 minutes per floor, down to floor 12 at 05:40hrs, interrupted only by a long delay of 80 minutes in passing the transfer floor T2. It is interesting to note that on average this downward spread rate actually exceeds that for progress up the building, indicating that a different mechanism was involved (most likely involving inflamed molten solids or liquids physically transferring the fire as they flowed through openings between the floors).

Further to these studies, the report of the National Scientific Police has also provided another estimate of the rate of upward spread which averages approximately 10 minutes per floor^[31]. In trying to reconcile this figure with the others quoted it should be noted that there are a number of uncertainties in defining the fire location. Most of the photographic evidence pertains only illustrates what conditions had evolved on the perimeter of the building; had there been internal openings in the floor slabs deeper into the building, e.g. for service ducts, it is possible that the fire may have been spreading more rapidly internally than was apparent from the external footage. It is certainly very clear from the video and photographic evidence that the fire was unevenly distributed around the perimeter of the building, i.e. it does not break-out of the façade on all sides of each floor simultaneously. Initial upward spread seems to have been fastest on the east face, above the room where the fire initial broke out, suggesting that floor-to-floor spread was predominantly occurring in the region of the façade, rather than internally. Together with the possibility of significant fire spread away from the façades this non-uniformity might be part of the reason for the remaining discrepancy in the estimates of the rate of upward spread; another aspect could be terminological differences in defining when a floor is “on fire” (which might vary from having sustained a small localised ignition, to full flashover engulfing the whole floor). Further work is underway to try to establish more clearly the precise course of the fire development throughout the structure.

In conjunction with this, modelling studies have been undertaken in order to examine various hypotheses about the mechanism of floor-to-floor fire spread. Field modelling using FDS^[32] and SOFIE^[33], together with the Law external flaming model^[36] as adopted in Eurocode 1 (Annex B)^[37], suggested that flame temperatures near the glass on the floor above the fire might have been of the order of 850°C. Analyses using the computer package BREAK1^[38] reveal that on this basis the time to cracking of a single pane of glass would have been of the order of 250-300 seconds. However, as part of a facelift operation a glazed curtain wall had been added to the building in recent years, so that there was effectively a double skin on the building with a fully glazed external wall and an internal façade consisting of alternating Aluminium (lower) and glass (upper) panels on each floor. Hence, it is insufficient to predict time to failure of the glass, and it is also necessary to estimate time for the glass to fall out, thereby exposing the internal glass to more intense heating and causing it to fail too. Weather reports for the dates of the fire were analysed and it was found that the wind was very light at the time, with hourly averages in the range 0 to 7 km/h during the first 7 hours (averaging 2.7 km/h, and direction varying from N to W, averaging NW); video and photographic evidence is also in accordance with the fact that the direction of the wind had a westerly component at the height of the building. The low velocities mean that once the external glazing had cracked, with the internal partition still intact, then relatively small pressure differences might be expected between its surfaces. This would be consistent with an average time to failure, i.e. glazing dropping out, being at least a factor of two longer than the time to cracking, since there would be relatively small unbalanced forces on the cracked glass.

A useful overview of the mechanisms of fire spread in multi-storey buildings with glazed curtain wall façades is provided by Morris & Jackman^[39]. For example, this mentions that the observed vertical spread mechanism for the fire in the 62-storey First Interstate Bank fire, Los Angeles, California, in 1988^[40], was via flames “breaking out of the external skin followed by break-in on the floor above, supplemented by failure of the fire-stopping between the floor slab and the curtain wall system over a gap of approx. 100mm”. Two other cases are identified in which multi-floor fires developed: the office block fires in a 38-storey tower in Philadelphia, Pennsylvania^[41] and a 12-storey building in Basingstoke, UK^[42] (both 1991). There is some evidence that the equivalent fire stopping in the Windsor Tower was not fully installed at the time of the fire (it is believed to have been missing in many places). Hence an alternative to the above described external spread scenario might be that fire broke into the cavity within the curtain walling and propagated directly to the floor above via this internal space followed by failure of the original inner skin glazing and entry of the fire into the next compartment. However, if the glazing of the inner skin extends only over the upper half of the floor height then the internal pane might actually have been more robust to cracking than the larger external panes in the curtain wall. To what extent the internal cavity could have generated a “chimney effect” remains uncertain, as it is not clear how hot gases might have escaped from the top. However, considering the lack of any evidence to the contrary, the presumption must be that this space does not provide a well-ventilated high temperature combustion region until such as time as the façade opens up properly via failure of the external glazing; at this point, the situation is similar again to a purely external spread route and there seems to be no reason to assume that spread via this mechanism would be particularly rapid. Hence it is debatable whether a route via an internal cavity in the curtain wall would in practice speed up the rate of spread in the current case, and indeed evidence from the fire reported above suggests that spread rates were not particularly rapid even when this mechanism was of relevance.

Morris & Jackman draw attention to the fact that there some inherent structural weaknesses in glazed curtain walling systems, which have a tendency to allow fire to spread from storey to storey by a variety of mechanisms^[39]. This view is supported by observations

from measured failure times in special fire tests on multi-storey buildings, which included glazed curtain walling. Failure times of between 5 and 13 minutes were reported for the tests with glazed façades, with a big influence of the fire load. With fire resisting panels instead of glass these times were more than doubled; however, the comparison is not strictly correct for the current case because standard glazing was not tested. Though there is no reason to suspect that fires are any more likely to develop in buildings with glazed façades the tendency for substantially greater consequential losses per fire are a concern to insurers; this fact is clearly exacerbated when such fires lead to structural failures of major parts of a building, as occurred in the Windsor Tower, with the costs of repair greatly increased. It is hoped that by better understanding these types of fires, and the behaviour of concrete structures, these types of losses could be minimised in the future.

4. CONCLUSIONS

In general the behaviour of concrete in fire is not very well characterised at present, and further research is required in almost every aspect of this field. Specifically the mechanism and causes of spalling, currently one of the greatest concerns for those interested in concrete building safety in fire and high temperatures, are not adequately understood. There is a need for more systematic studies which examine the effects of varying heating conditions, both on spalling behaviour and more generally.

The majority of past research work on the response of concrete to fire (or, more frequently, high temperatures) has looked at the effects of fire upon individual structural members, and most commonly when subjected to heating from standard fire tests. There is a great need for development of models which consider the effects of fire on the whole structure under more realistic heating regimes. There is also a fundamental requirement for further large-scale testing of concrete structures, to observe the behaviour of complete concrete structures in real fires and also for validation of advanced computer modelling tools.

The University of Edinburgh are working towards filling some of the knowledge gaps by the detailed examination of the effects of fire upon the Windsor Tower, gathering data and applying modelling tools to bound and characterise the behaviour. Initial results suggest that the observed response was well within the bounds expected for a structure of this type; the lack of fire protection of certain parts of the steelwork was a major reason for the partial collapse of the building and whilst the particular nature of the glazed curtain-walling may have permitted upward fire spread, this might not have been any worse than performance of a building lacking an additional façade skin.

5. REFERENCES

- 1 Bazant, Z.P. & Kaplan, M.F. "Concrete at High Temperatures" Longman, 1996. ISBN 0-5820-8626-4.
- 2 Carvel, R. "Fire protection in Concrete Tunnels" in The Handbook of Tunnel Fire Safety (Ed. A. Beard & R. Carvel) Thomas Telford, London, 2005. ISBN 0-7277-3168-8.
- 3 Tenchev, R. & Purnell, P. "An application of a damage constitutive model to concrete at high temperature and prediction of spalling". International Journal of Solids and Structures, 2005. 42(26): 6550.
- 4 Canisius, T.D.G., Waleed, N. & Matthews, S.L. "A preliminary study of the Cardington Concrete Building under a compartment fire", Proceedings of Structural Faults and Repair Conference 2003, July 2003, London

- 5 Both, C., van de Haar, P., Tan, G. & Wolsink, G. "Evaluation of passive fire protection measures for concrete tunnel linings". Proc. Int. Conf. on Tunnel Fires and Escape From Tunnels, Lyon, France, 5-7 May 1999. Organised by Independent Technical Conferences Ltd. ISBN 1 901808 12 2. 95-104.
- 6 Schneider, U. & Lebeda, C. (2007) "Baulicher Brandschutz", Bauwerk Verlag, Berlin, Germany, 400 pp.
- 7 Hertz, K.D. & Sorensen, L.S. "Test method for spalling of fire exposed concrete". Fire Safety Journal, 2005. 40(5): 466.
- 8 Ali, F., et al. "Outcomes of a major research on fire resistance of concrete columns". Fire Safety Journal, 2004. 39(6): 433.
- 9 Han, C.-G., et al. "Performance of spalling resistance of high performance concrete with polypropylene fiber contents and lateral confinement". Cement and Concrete Research, 2005. 35(9): 1747.
- 10 Steinert, C. "Brandverhalten von Tunnelauskleidungen aus Spritzbeton mit Faserzusatz" (Fire Behaviour in Tunnel Linings made of Shotcrete with added Fibres) MFPA Leipzig, April 1997.
- 11 Shuttleworth, P. "Fire protection of concrete tunnel linings". Proc. 3rd Int. Conf. on Tunnel Fires and Escape From Tunnels, Washington DC, USA, 9-11 October, 2001. Organised by Tunnel Management International. ISBN 1 901808 18. pp. 157-165.
- 12 Wetzig, V. "Destruction mechanisms in concrete material in case of fire, and protection systems" Proc. 4th Int. Conf. on Safety in Road and Rail Tunnels (SIRRT), Madrid, Spain, 2-6 April 2001.
- 13 Georgali, B. & Tsakiridis, P.E. "Microstructure of fire-damaged concrete. A case study". Cement and Concrete Composites, 2005, 27, 255-259
- 14 Bisby, L.A., Green, M.F., & Kodur, V.K.R. "Modeling the behavior of fiber reinforced polymer-confined concrete columns exposed to fire". Journal of Composites for Construction, 2005, 9(1): 15-24.
- 15 Chung, J.H. & Consolazio, G.R. "Numerical modeling of transport phenomena in reinforced concrete exposed to elevated temperatures". Cement and Concrete Research, 2005. 35(3): 597.
- 16 Abbasi, A. & Hogg, P.J. "Fire testing of concrete beams with fibre reinforced plastic rebar". Composites Part A: Applied Science and Manufacturing. In Press, Corrected Proof.
- 17 Williams, B., et al., "Fire insulation schemes for FRP-strengthened concrete slabs". Composites Part A: Applied Science and Manufacturing, 2005. In Press, Corrected Proof.
- 18 Abbasi, A. & Hogg, P.J. "A model for predicting the properties of the constituents of a glass fibre rebar reinforced concrete beam at elevated temperatures simulating a fire test". Composites Part B: Engineering, 2005. 36(5): 384.
- 19 Wang, Y.C. & Kodur, V. "Variation of strength and stiffness of fibre reinforced polymer reinforcing bars with temperature". Cement and Concrete Composites, 2005. 27(9-10): 864.
- 20 Abbasi, A. & Hogg, P.J. "Temperature and environmental effects on glass fibre rebar: modulus, strength and interfacial bond strength with concrete". Composites Part B: Engineering, 2005. 36(5): 394.
- 21 Alarcon-Ruiz, L., et al. "The use of thermal analysis in assessing the effect of temperature on a cement paste". Cement and Concrete Research, 2005. 35(3): 609.
- 22 Li, L.-y. & Purkiss, J. "Stress-strain constitutive equations of concrete material at elevated temperatures". Fire Safety Journal, 2005. 40: 669.
- 23 Schneider, U. "Concrete at High Temperatures – A General Review". Fire Safety Journal, 1988, 13: 55-68

- 24 Eurocode 2: Design of concrete structures Part 1.2: general rules, structural fire design. EN 1992-1-2, Brussels: European Committee for Standardisation/British Standards Institution; 2003.
- 25 Usmani, A.S., Rotter, J. M., Lamont, S., Sanad, A.M. & Gillie, M. "Fundamental principles of structural behaviour under thermal effects", Fire Safety Journal, 2001, 36: 721-744.
- 26 Bratina, S., Cas, B., Saje, M. & Planinc, I. "Numerical modelling of behaviour of reinforced concrete columns in fire and comparison with Eurocode 2". International Journal of Solids and Structures, 2005, 42: 5715-5733.
- 27 Benmarce, A. & Guenfoud, M. "Behaviour of axially restrained high strength concrete columns under fire". Construction and Building Materials, 2005. In Press.
- 28 Lennon, T. "Whole building behavior - results from a series of large scale tests". Proceedings of the CIB-CTBUH International Conference on Tall Buildings, 8-10 May 2003.
- 29 Bailey, C. "Holistic behaviour of concrete buildings in fire". Proceedings of the Institute of Civil Engineers: Structures and Buildings, 152, Issue 3 (2002): 199-212.
- 30 Fakury, R.H., et al. "Design of semi-continuous composite steel-concrete beams at the fire limit state". Journal of Constructional Steel Research, 2005. 61(8): 1094.
- 31 National Scientific Police report, Windsor Tower fire investigation seminar, University of Cantabria, Spain, 31 March 2006 (per Portilla, D.A. – personal communication)
- 32 McGrattan, K.B. (ed.) "Fire Dynamics Simulator (Version 4) - Technical Reference Guide", National Institute of Standards and Technology Special Publication 1018, 94 pp., March 2006.
- 33 Lewis, M.J., Moss, J.B., Rubini, P.A. (1997) "CFD modelling of combustion and heat transfer in compartment fires", in Proc. of the 5th Int. Symp. on Fire Safety Science, Elsevier, 463-474.
- 34 Calavera, J., González-Valle, E., Díaz-Lozano, J., Fernández-Gomez, J., Ley, J. & Izquierdo, J. M. "Fire in the Windsor Building, Madrid, Survey of the fire resistance and residual bearing capacity of the structure after the fire", Notas de Información Técnica NIT-02 (05), December 2005, INTEMAC, Spain, ISSN 1885-4575.
- 35 Kono, M. et al. "The Madrid city Windsor building fire inspection report", The Madrid city Windsor building fire investigation committee (BCS, JSCA et al), 1 July 2005, 133 pp. (In Japanese).
- 36 Law, M. "Design guide for fire safety of bare exterior structural steel - Designers manual", AISI, Washington/Ove Arup & Partners, London, January 1977.
- 37 Eurocode 1: Basis of design and actions on structures, Part 1.2: Actions on structures - actions of structures exposed to fire, EN 1991-1-2, European Committee for Standardisation/British Standards Institution, November 2002.
- 38 Joshi, A.A. and Pagni, P.J., "Users' Guide to BREAK1, The Berkeley Algorithm for breaking window glass in a compartment fire", National Institute of Standards and Technology Report No. NIST-GCR-91-596, Gaithersburg, MD, 1991.
- 39 Morris, B. & Jackman, L.A. "An examination of fire spread in multi-storey buildings via glazed curtain wall façades", The Structural Engineer, 81(9), 22-26, 6 May 2003.
- 40 Morris, J. "The First Interstate Bank fire – what went wrong?", Fire Prevention, No.226, January/February 1990, 20-26.
- 41 Klem, T. J. "High-rise fire claims three Philadelphia fire fighters", NFPA Journal, September/October 1991, 64-67, 89.
- 42 FPA Casebook of Fires, Offices, Fire Prevention No.242, September 1991, pp. 30-31.



PERFORMANCE IN FIRE OF INSULATED FRP-WRAPPED REINFORCED CONCRETE COLUMNS

Ershad U. CHOWDHURY¹, Luke A. BISBY², Mark F. GREEN³
and Venkatesh K.R. KODUR⁴

ABSTRACT

Research has demonstrated that fibre-reinforced polymers (FRPs) can be used efficiently and safely in strengthening and rehabilitation of reinforced concrete (RC) structures. However, the use of FRPs in buildings has been limited because relatively little is known about the behaviour in fire of RC structural members that have been strengthened with FRP systems. This paper presents the recent results of an ongoing experimental study of the fire performance of FRP-wrapped RC circular columns. The results of fire tests on two columns are presented, one of which was tested without supplemental fire protection, and one of which was protected by a supplemental fire protection system applied to the exterior of the FRP strengthening system. The primary objective of these tests was to compare the fire behaviour of the two FRP-wrapped columns and to investigate the effectiveness of the supplemental insulation system. The thermal and structural behaviour of the two columns are discussed. The results show that though FRP systems are sensitive to high temperatures, satisfactory fire endurance ratings can be achieved for RC columns that are strengthened with FRP systems by providing adequate supplemental fire protection. In particular, the insulated FRP-strengthened column in this study was able to resist elevated temperatures during the fire tests for at least 90 minutes longer than the equivalent uninsulated FRP-strengthened column.

¹ Graduate Student, Queen's University, Department of Civil Engineering, Kingston, ON, Canada, K7L 3N6
email: chowdhury@civil.queensu.ca

² Assistant Professor, Queen's University, Department of Civil Engineering, Kingston, ON, Canada, K7L 3N6
email: bisby@civil.queensu.ca

³ Professor, Queen's University, Department of Civil Engineering, Kingston, ON, Canada, K7L 3N6
email: greenm@civil.queensu.ca

⁴ Formerly a Senior Research Officer at the Fire Research Program, National Research Council of Canada, Ottawa, ON, Canada, K1A 0R6 email: kodur@egr.msu.edu

1 INTRODUCTION

Fibre reinforced polymers (FRPs) are becoming more widely accepted in the construction industry as materials to prolong the service life and decrease the cost of maintenance and repair of our infrastructure systems. Numerous studies have shown that circumferential wraps of FRP on the exterior of reinforced concrete (RC) columns can significantly increase the strength and ductility of these members. Hence, the use of FRPs has been widespread in repair and restoration of RC columns in existing bridges. The application of FRP wraps in buildings, however, has been hindered due to uncertainties regarding their behaviour in fire. The matrix components of currently available FRPs are combustible, raising concerns as to the fire performance of FRP-strengthened RC columns in buildings, where fire is one of the primary design considerations.

An ongoing research project is currently underway at Queen's University, Canada, in collaboration with the National Research Council of Canada (NRC) and industrial partners, to begin to address this knowledge gap. The project involves both experimental and numerical studies of the fire performance of FRP-wrapped reinforced concrete columns and externally FRP-strengthened reinforced concrete slabs and beams. Based on these studies, design recommendations and rational guidance is being developed for FRP-strengthened concrete structures with respect to fire safety considerations. This paper presents a recently conducted portion of the overall experimental study. Specifically, results of tests conducted on two full-scale FRP-wrapped reinforced concrete circular columns subjected to a sustained axial load and the ASTM E119 standard fire are presented.

2 RESEARCH SIGNIFICANCE

The reluctance of many engineers to use FRPs in buildings is due, in part, to the relative lack of knowledge of their performance during fire^{1, 2}. Based on the limited available information^{3, 4, 5}, there are a number of risks associated with structural uses of FRPs in fire, such as smoke generation, toxicity, flame spread, etc. Furthermore, the polymer resins of FRPs degrade rapidly above their glass transition temperatures⁶, thus raising potential concerns regarding the structural integrity of FRP-strengthened RC columns during fire. As no specific information is currently available on the critical temperature at which currently available FRPs lose their structural integrity and/or bond to concrete, the American Concrete Institute⁶ suggests that the strength contribution from FRPs should be ignored in FRP-strengthened concrete structures during fire, that is, the RC structure alone must be able to endure the fire for the required duration.

Based on limited information available in the literature^{7, 8}, FRP-strengthened RC structures with adequate supplemental fire protection can endure in excess of 4 hours of fire exposure. However, the performance of FRP-strengthened concrete columns without any supplementary fire protection has not yet been explored. This paper investigates the fire endurance of FRP-strengthened RC circular columns with and without fire protection, and also investigates the effectiveness of a new supplementary fire protection system.

3 EXPERIMENTAL PROCEDURE

3.1 Column Specimens

The portion of the experimental program presented in the current paper involved fire tests on two FRP-wrapped circular columns, one of which was insulated for fire protection with a new system that was developed by an industry partner. As these test specimens were part of an ongoing study, the FRP-wrapped column without protection was designated as Column 3, and FRP-wrapped and insulated column as Column 4. Other than the presence of supplemental fire protection on Column 4, both columns were identical, with 400 mm diameter and 3810 mm length from end plate to end plate. The cross-sectional dimensions and reinforcement details of the columns are given in Figure 1. The longitudinal steel reinforcement in the columns consisted of eight 19.5 mm diameter deformed bars, which were symmetrically placed with 40 mm clear cover to the spiral reinforcement. The lateral reinforcement for the columns consisted of 11.3 mm diameter deformed steel spiral with a center-to-centre pitch of 50 mm. The longitudinal reinforcing bars and the steel spiral had measured yield strengths of 456 MPa and 396 MPa, respectively.

Both columns were fabricated with siliceous (granite) aggregate concrete. The mix proportions for the concrete are provided in Table 1. The average 28-day compressive cylinder strength of the concrete was 32.7 MPa and the corresponding compressive strength on the day of the fire test was 32.9 MPa.

Prior to fire testing, two layers of carbon FRP were bonded to the exterior of the two circular columns using an epoxy saturant/adhesive. The carbon FRP had an ultimate tensile strength of 3800 MPa and tensile elastic modulus of 227 GPa (based on of the nominal thickness of 0.165 mm as suggested by the manufacturer). Column 4 was provided with a unique spray-applied cementitious mortar-based fire protection system developed by an industry partner. After installation of the insulating material, using a shotcreting rig, the average thickness of the insulation was measured to be 53 mm. Details of the FRP-wrap and insulation systems are provided in Table 2. The FRP-strengthening system theoretically increased the axial design capacity of the columns by 63.5% based on ACI 440 guidelines⁶.

3.2 Fire Endurance Test Conditions and Procedure

Prior to testing, the columns were instrumented with chromel-alumel (Type-K) thermocouples and electrical resistance strain gauges at their mid-height. Figure 3 shows the location and number of the sensors in the columns, with some minor differences noted for Column 3 since it was not protected with supplemental fire insulation.

The column specimens were fire-tested in the full-scale column furnace at the National Research Council of Canada (NRC), Ottawa. This test furnace was designed to expose the column specimens to a standard time-temperature fire curve and to subject the columns to a sustained concentric axial load during the fire test, as prescribed by ASTM E119⁹ or CAN/ULC S101¹⁰. The end plates of the column specimens were bolted to the test frame loading head at the top and hydraulic jack at the bottom, resulting in a fixed-fixed end condition. Both columns were subjected to a concentric axial applied load of 2635 kN, which represents 56% of the ultimate strengthened design capacity according to ACI 440⁶. This load was held constant throughout the fire tests, until the hydraulic jack could not maintain the load, at which point the columns were assumed to have failed and the test was stopped. If the column specimen did not fail under the sustained axial load during the first 5 hours of the test, the load was steadily increased until the column failed, at which point the test was stopped.

4 RESULTS AND DISCUSSION

Table 2 gives a summary of the results of the fire endurance tests. Column 3, which was not protected by supplementary insulation, resisted the sustained concentric load of 2635 kN for 210 minutes, at which point sudden failure occurred. Prior to failure of Column 3, spalling of the concrete was observed from the view ports along the walls of the furnace leading to the sudden crushing of the concrete core. There was no obvious buckling of the longitudinal reinforcing bars or deformation of the spirals in Column 3 (refer to Figure 3). The insulated Column 4, on the other hand, was able to maintain the applied load for 300 minutes, after which time the load was gradually increased to induce failure, which occurred in a non-violent manner by apparent crushing of the concrete core at about 4575 kN. The supplemental insulation system remained intact for the entire duration of the fire test and even after failure of Column 4 (refer to Figure 4). However, minor cracks, not more than 5 mm wide by the end of the test, developed and widened during the fire test. Comparing the fire performance of the two column specimens, the 53 mm of the supplemental insulation provided at least an additional 90 minutes of fire endurance to the FRP-strengthened column.

4.1 Thermal Behaviour

Figure 5 shows the recorded temperature-time curve at the level of the FRP wraps, insulation and reinforcing bars during the fire tests of Columns 3 and 4. Early in the fire test, the FRP-wrap on Column 3 ignited causing the temperature to rise rapidly within the FRP and demonstrating the sensitivity of FRP to combustion. Since concrete has a relatively low thermal conductivity, the temperature of the longitudinal reinforcing steel, which was 50 mm within the concrete, was much lower than the temperature recorded at the FRP/concrete interface. The highest temperature recorded on the longitudinal reinforcing steel during the Column 3 fire test (prior to failure) was about 517 °C. However, the highest temperature recorded on the steel reinforcement during the fire test of Column 4 was significantly lower, which was about 280 °C. Even though Column 4 was thermally insulated, the temperature at the FRP/concrete interface reached the glass transition temperature of the FRP, which was 71 °C for the carbon FRP system used in this study, at about 34 minutes into the fire test. This indicates that the insulation system used in this study would likely not be able to protect the FRP system, which is widely thought to degrade at temperatures beyond its glass transition temperature⁶, for the entire duration of the fire test. However, since the insulation system remained intact for the entire period of the fire test, it was impossible to precisely identify the temperature at which the FRP system lost its mechanical properties and/or bond to the concrete surface. The insulation system was, however, successful in maintaining low internal temperatures within the column (refer to Figure 6), such that it essentially retained its room temperature unwrapped strength for the full duration of the fire. Column 4 was thus able to resist the sustained fire test load for more than 300 minutes, unlike the uninsulated Column 3, which failed under the sustained fire test load after 210 minutes of fire exposure.

The recorded temperature-time curves at various locations within the concrete of Columns 3 and 4 are shown in Figure 6. As expected, the internal concrete temperatures were considerably lower in Column 4 than in Column 3. The temperatures recorded within the concrete increased at a steady rate until they reached 100 °C, after which point the temperatures increased at a lower rate for a small period of time. This reduced rate of temperature increase has been observed previously and is attributed to moisture movement and evaporation within the concrete. Column 3 failed by spalling of the concrete cover leading to crushing of concrete core. However, this spalling occurred after several hours of

fire exposure, and it therefore does not appear that the FRP wrap significantly increased the propensity for cover spalling in the FRP-strengthened columns.

4.2 Structural Behaviour

Figure 7 shows the axial deformations of Columns 3 and 4 during the preload and fire test phase. Both columns experienced an initial load of about 350 kN from the weight of the hydraulic jack prior to the start of the preload phase. This is obvious in Figure 8, where the recorded strains in the reinforcing steel during the preload phase are shown. Examination of Figure 7 shows that Column 3 failed under the sustained fire test load of 2635 kN after 210 minutes, whereas Column 4 resisted the sustained fire test load for more than 300 minutes, after which point when the load was gradually increased to 4583 kN. For both columns, the temperature at the level of the FRP exceeded the glass transition temperature of the epoxy resin/adhesive relatively early on in the fire exposure. Thus, it can be conservatively assumed that the FRP wraps were rendered structurally-ineffective by the end of the fire tests. However, even though the FRP-strengthening system was presumed to have been rendered ineffective by the end of the fire tests, the loss of strength of the two columns was significantly different. In the case of Column 3, the tested strength of the column was lower than the factored design strength of an equivalent unwrapped column, which was 2882 kN when calculated according to ACI 318 design standard¹¹. This indicates that Column 3, without supplementary fire protection, had experienced significant loss of strength during the fire exposure. However, Column 4 failed after 300 minutes of fire exposure at a load 59% higher than the factored strength of an equivalent unwrapped column. Clearly, Column 4 failed at a higher applied load than Column 3 because its internal temperatures were maintained at low values by the supplemental insulation system.

The observed axial deformations of the columns were the result of a combination of load effects and thermal expansion. During the preload phase of the fire test, Column 3 had an axial deformation of 8.8 mm from the sustained applied load of 2635 kN and Column 4 had 6.56 mm axial deformation. Examining Figure 7, Column 3 began experiencing increasing axial deformations beyond about 100 minutes of fire exposure, around which time the average temperatures of its reinforcing steel was 297 °C (refer to Figure 5) and the internal temperature of concrete 50 mm within the column was 276 °C (refer to Figure 6). Concrete begins to lose its room temperature compressive strength at temperatures above 200 °C and its room temperature elastic modulus at temperature above 50 °C¹². At temperatures close to 300 °C, reinforcing steel loses about 20% of its initial room temperature yield strength¹³. At failure, Column 3 had an axial deformation of about 32 mm. On the other hand, Column 4 maintained a constant axial deformation value under the sustained applied load for the initial 300 minutes of exposure (because the internal temperatures of its reinforcing steel and compressive concrete were relatively low as compared to Column 3). Column 4 began experiencing axial deformation again after 300 minutes from the increasing applied load. At failure, Column 4 had an axial deformation of about 22 mm.

Figure 8 shows the tensile strains of the reinforcing steel recorded by the strain gauges (SGs) located at the column mid height in the configuration shown in Figure 2. Strain gauges on both Columns 3 and 4 recorded similar strains during their preload phases, except for strain gauge SG1 in Column 4, which malfunctioned and did not record any strain values from the start of the test. Also, the strain gauges in both columns were effective only during the preload phase (the first 45 minutes or so of the test) and approximately 60 minutes into the fire tests. No obvious explanation for the loss of the strain gauges during the fire tests has yet been suggested.

5 SUMMARY AND CONCLUSIONS

Based on the results of full-scale fire endurance tests on two FRP-wrapped (confined) reinforced concrete circular columns presented herein, the following conclusions can be derived:

- FRP materials can be used in buildings. By providing appropriate fire insulation, reinforced concrete columns that have been confined with FRP-wraps can endure elevated temperatures of fire under strengthened service loads for more than 300 minutes.
- The supplemental fire protection system used herein was able to maintain low temperatures in the concrete and reinforcing steel during the fire test, thus enabling the concrete and steel to retain most of their room temperature strength during the fire endurance tests.
- Although the insulation system used in this research was an effective fire protection system for the reinforced concrete column, the insulation system was not able to protect the FRP system during the fire endurance tests by maintaining the temperature of the FRP system below its glass transition temperature. The temperature of the FRP system remained below its glass transition temperature for about 34 minutes with about 53 mm of insulation.
- Further research, particularly on FRP-strengthened RC square columns, is needed to accurately identify the performance of FRP-strengthened RC structures in fire. Numerical models are currently being developed that can simulate the behaviour of FRP-strengthened RC structural members at elevated temperatures. Once validated, these models can be used to develop design recommendations and guidelines for the safe use of FRP materials in buildings.

6 ACKNOWLEDGEMENTS

The research presented herein was conducted in collaboration with National Research Council of Canada (NRC), Intelligent Sensing for Innovative Structures (ISIS Canada), Queen's University and industrial partners – Fyfe Co. LLC and Degussa Building Systems. The authors would like to acknowledge these organisations for their support and participation in this research. The authors would also like to thank the NRC Technical Officers (J. Latour, P. Leroux, J. Hum, J. Henrie, R. Rombough and R. Monette), Queen's University Technical Staff (Paul Thrasher, Neil Porter and Dave Tryon) and Degussa Corporation Specialists (R. J. Ewanko Jr. and M. Urbas).

7 REFERENCES

- [1] Harries, K.A., Porter, M.L. and Busel, J.P., "FRP Materials and Concrete – Research Needs", ACI Concrete International, **25**(10), pp. 69-74, 2003.
- [2] Karbhari, V.M., Chin J.W., Hunston, D., Benmokrane, B., Juska, T., Morgan, R., Lesko, J.J., Sorathia, U., and Reynaud, D., "Durability gap analysis for fiber-reinforced composites in civil infrastructure", Journal of Composites for Construction, **7**(3), pp. 238-247, 2003.

- [3] Kodur, V.K.R., “Fire resistance requirements for FRP structural members,” Proceedings of the Annual Conference of the Canadian Society for Civil Engineering, Regina, Saskatchewan, pp. 83-95, 2001.
- [4] Kodur, V.K.R., and Baingo, D., “Fire resistance of FRP reinforced concrete slabs”, IRC Internal Report No. 758, National Research Council of Canada, Ottawa, 37 pp., 1998.
- [5] Bisby, L., Williams, B., Kodur, V.R., Green, M., and Chowdhury E., “Fire Performance of FRP systems for Infrastructure: A State-of-the-Art Report”, Research Report, Institute for Research in Construction, National Research Council Canada, RR 179, 2005 (IRC-IR-179).
- [6] ACI, “ACI 440.2R-02: Guide for the Design and Construction of Externally Bonded FRP Systems for Strengthening Concrete Structures”, American Concrete Institute, Farmington Hills, Michigan.
- [7] Bisby, L.A., Kodur, V.K.R., and Green, M.F., “Fire Endurance of Fiber-Reinforced Polymer Confined Concrete Columns”, ACI Structural Journal, **102**(6), pp. 883-891, 2005.
- [8] Williams, B.K., “Fire Performance of FRP-Strengthened Reinforced Concrete Flexural Members”, PhD thesis, Department of Civil Engineering, Queen’s University, Kingston, Ontario, Canada.
- [9] ASTM., “ASTM E119-01: Standard Methods of Fire Test of Building Construction and Materials”, American Society for Testing and Materials, West Conshohocken, P.A., 2001
- [10] ULC., “CAN/ULC-S101-M04: Standard Methods of Fire Endurance Tests of Building Construction and Materials”, Underwriters’ Laboratories of Canada, Scarborough, ON, 2004.
- [11] ACI, “ACI 318-95: Building Code Requirements for Structural Concrete”, American Concrete Institute, Farmington Hills, MI., 1995.
- [12] Schneider, U., “Concrete at High Temperatures – A General Review”, Fire Safety Journal, **13**, pp. 55-68, 1988.
- [13] Lie, T.T., “Structural Fire Protection”, American Society of Civil Engineers Manual and Reports on Engineering Practice No. 78, ASCE, New York, NY, U.S.A, 1992.

Table 1: Concrete mix proportions of column specimens

Mix Parameter	Columns
Aggregate Type	Crushed Granite (Siliceous)
Maximum Aggregate Size	14
Type 10 Cement (kg/m ³)	280
Coarse Aggregate (kg/m ³)	1020
Fine Aggregate (kg/m ³)	980
Water (kg/m ³)	152
Slump (mm)	Max 150
Water-cement Ratio	0.54
Specified 28-day Strength	32.7
Test day Strength	32.9

Table 2: Summary of fire endurance tests on columns 3 and 4

Column No.	Layers of FRP ^a	Insulation Thickness ^b (mm)	Unwrapped Design Resistance ^c (kN)	Wrapped Design Resistance ^d (kN)	Fire Test Load Ratio ^e	Failure Load (kN)	Fire Endurance (min.)
3	2	0	2882	4712	0.56	2635	210
4	2	53	2882	4712	0.56	4583	>300

^a Carbon FRP system had a nominal thickness of 0.165 mm per layer.

^b Insulation System was used in this portion of the research

^c Design capacity of the unwrapped column was determined based on ACI 318 design code¹¹

^d Design capacity of the FRP-wrapped column was determined based on ACI 440 design guidelines⁶

^e Fire test load ratio is equivalent to applied load over factored resistance. The applied load was determined in accordance with ULC S101¹⁰

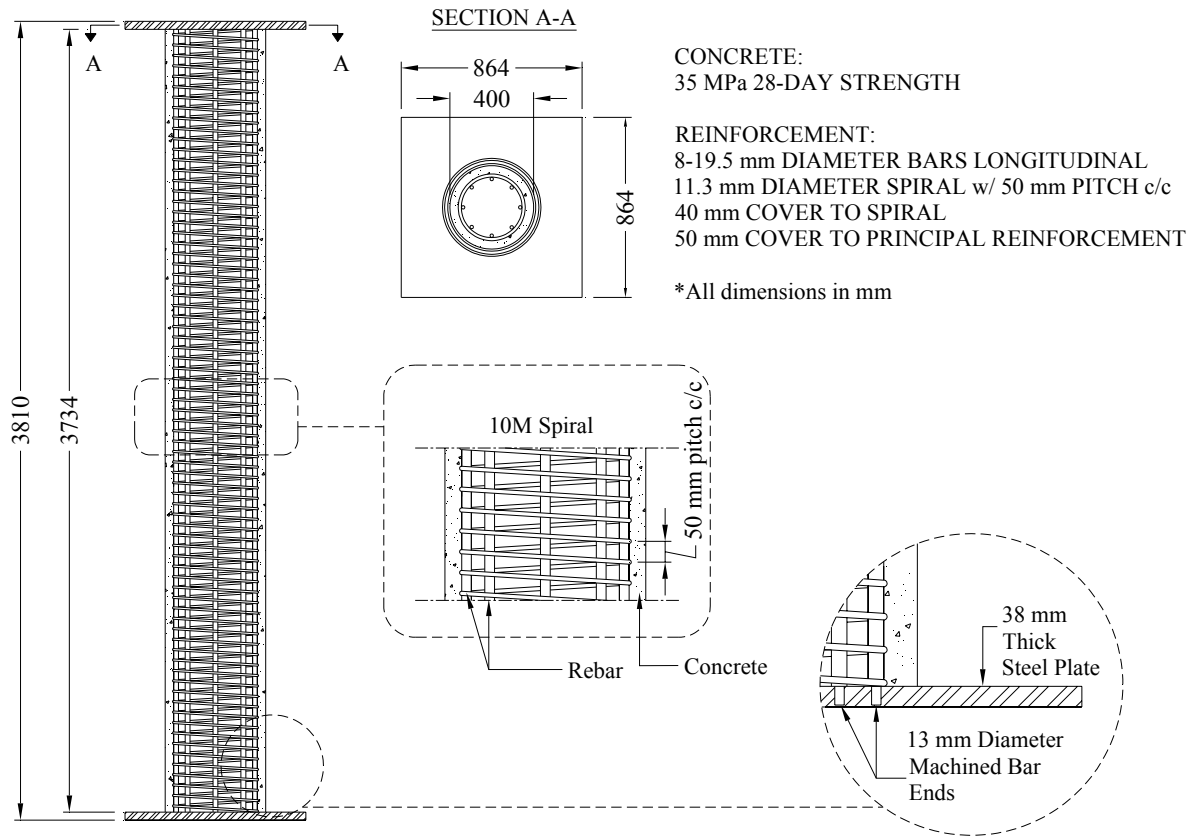


Fig. 1 – Elevation and cross-sectional details of Column 3 and Column 4 prior to strengthening

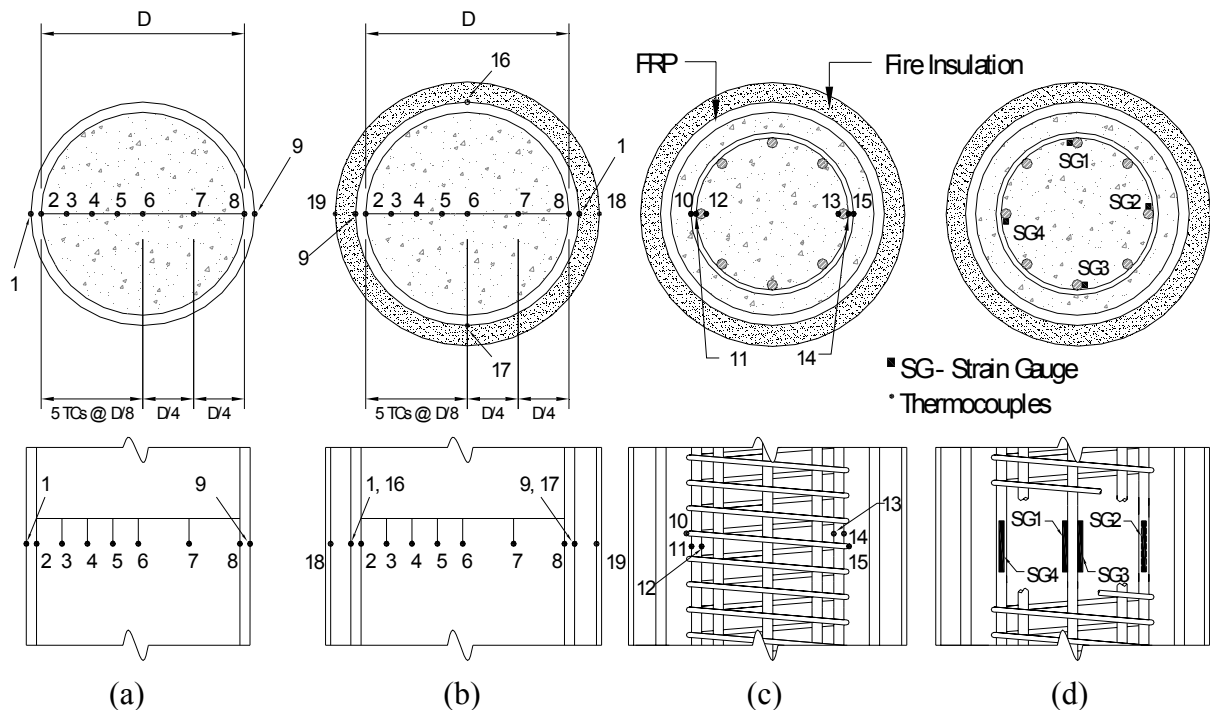


Fig. 2 – Location and numbering of thermocouples and strain gauges at mid-height: (a) Thermocouples within the concrete and on FRP surface of Column 3, (b) Thermocouples within the concrete and on FRP surface of Column 4, (c) Thermocouples on the reinforcing steel of Columns 3 and 4, and (d) Strain gauges on the reinforcing steel on Columns 3 and 4

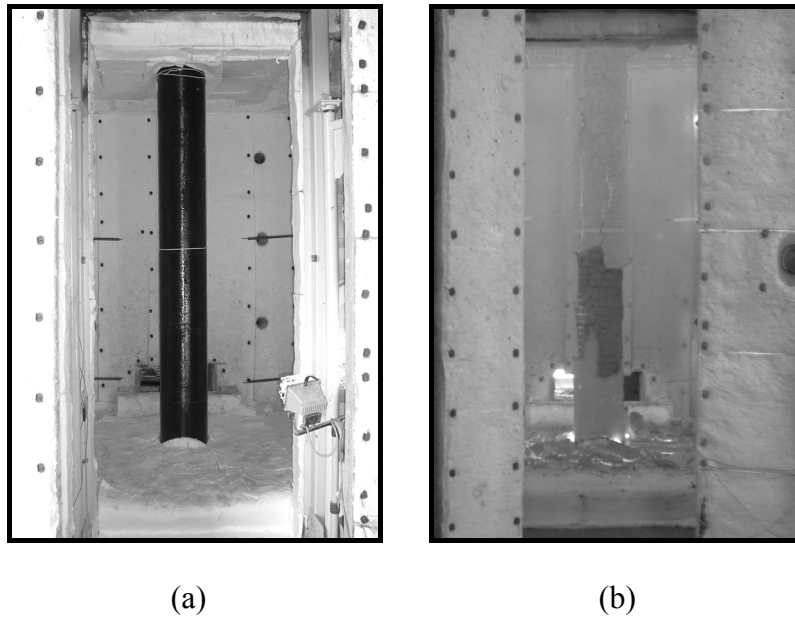


Fig. 3 – Column 3: FRP-wrapped Concrete Column (a) before fire test, and (b) immediately after fire test

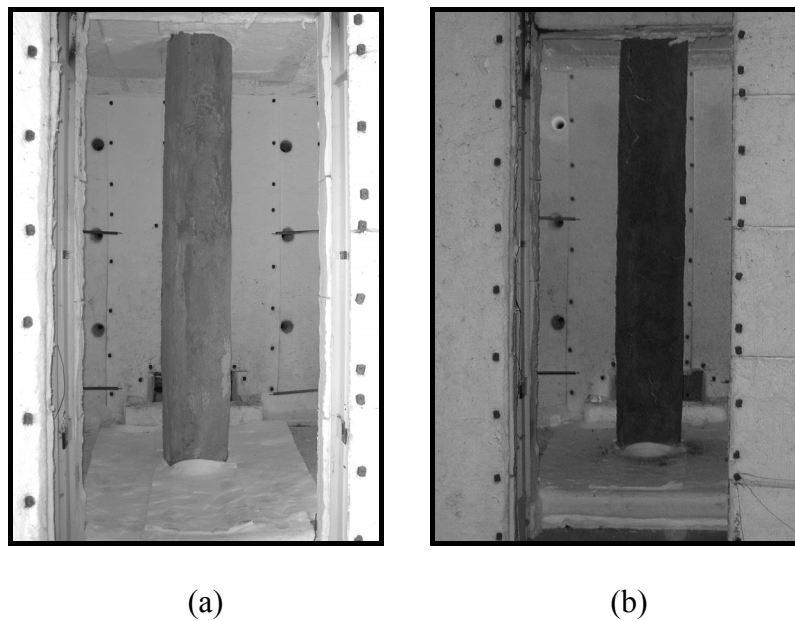


Fig. 4 – Column 4: FRP-wrapped and Insulated Concrete Column (a) before fire test, and (b) immediately after fire test

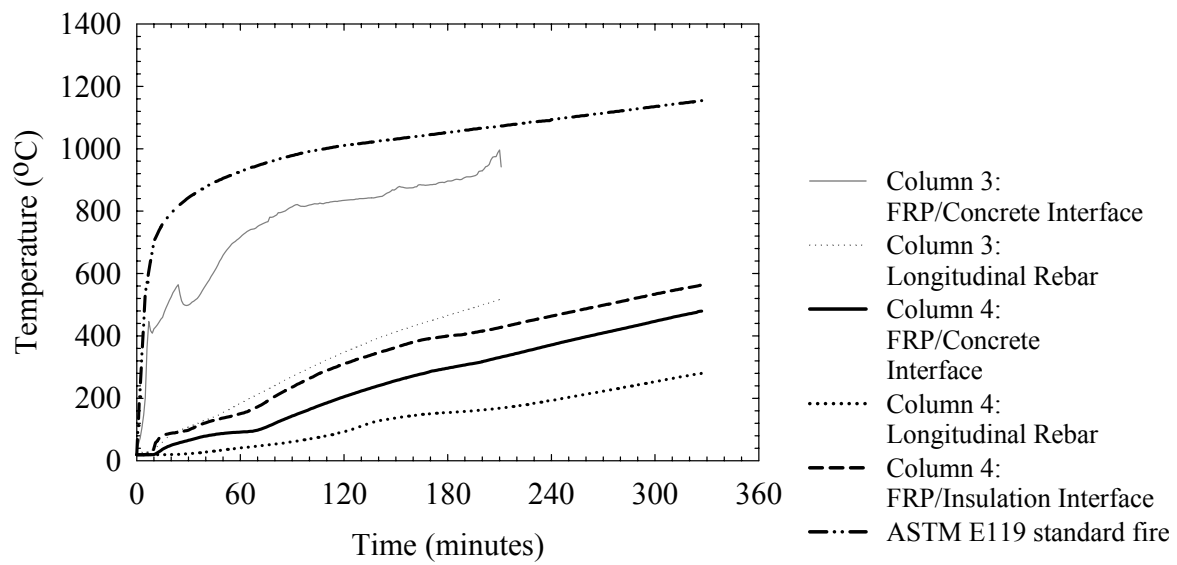


Fig. 5 – Temperatures at the FRP, insulation and reinforcing bars within Columns 3 and 4.

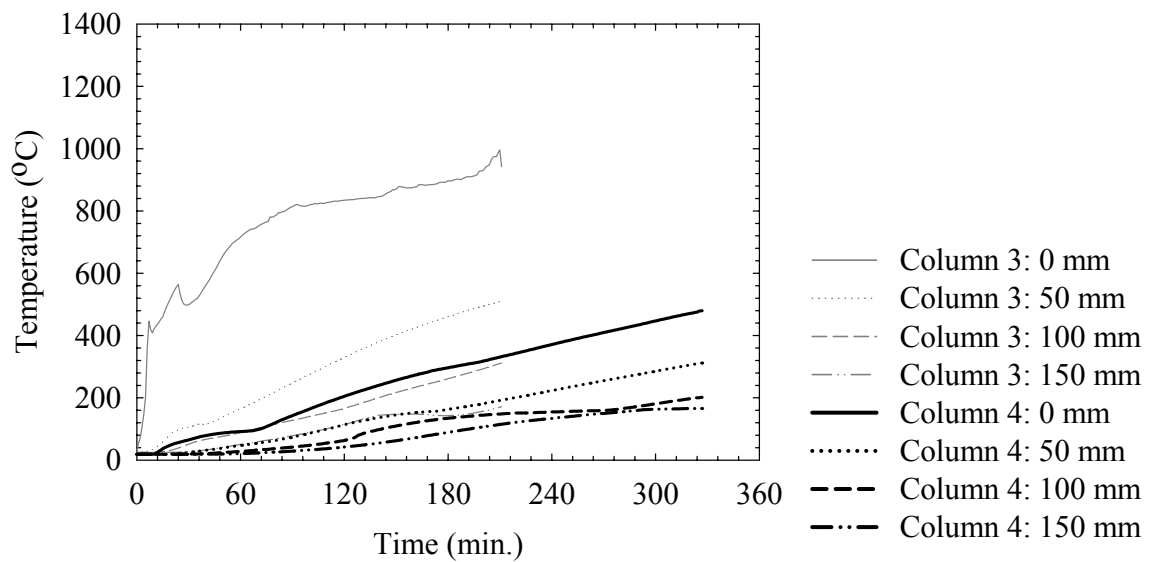


Fig. 6 – Temperatures in concrete at various depth of Columns 3 and 4

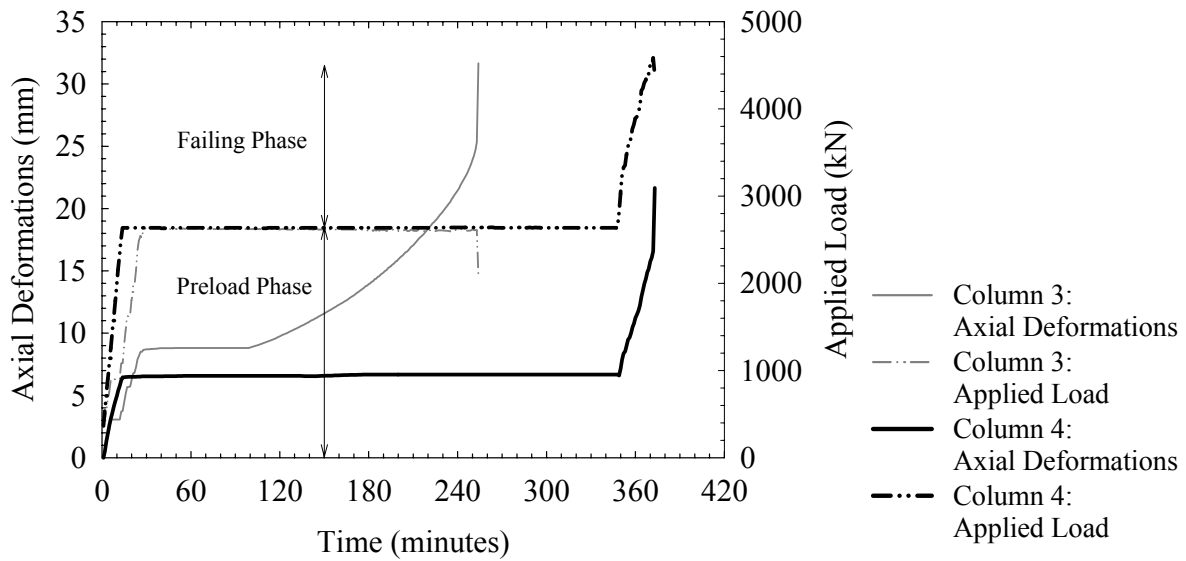


Fig. 7 – Axial deformations and load applied during the fire tests of Column 3 and Column 4

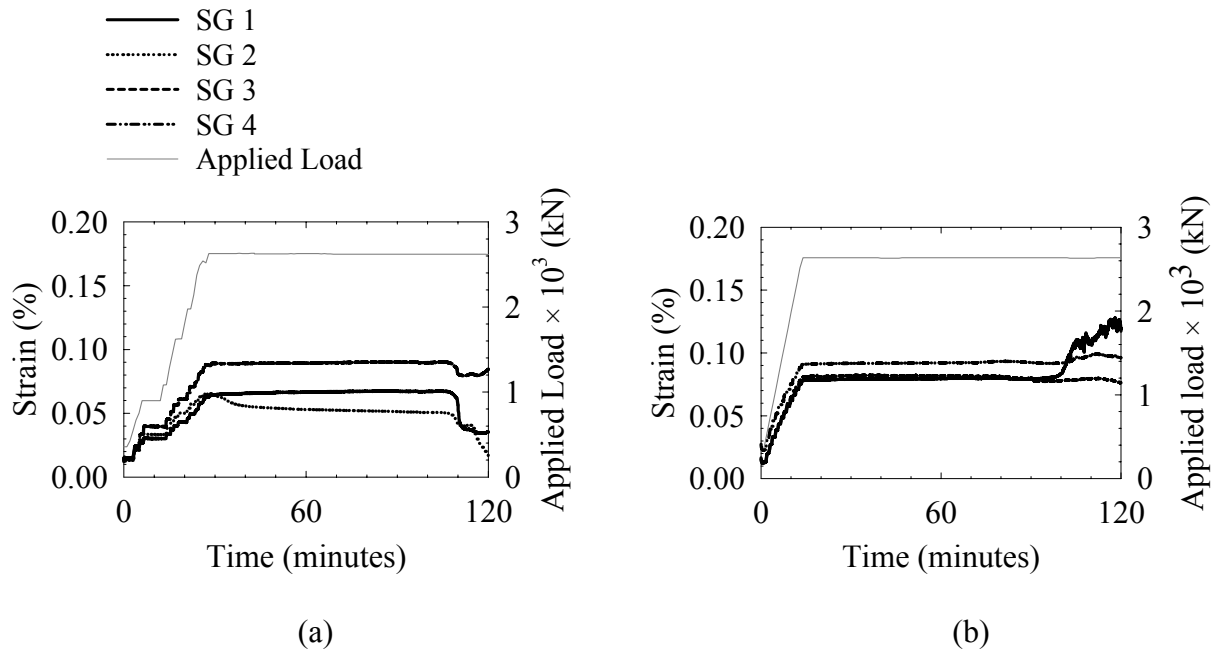


Fig. 8 – Tensile strains recorded by strain gauges (SG) on longitudinal reinforcing steel of (a) Column 3, and (b) Column 4.

Composite Structures



GENERIC MODEL FOR A COMPOSITE T-BEAM AT ELEVATED TEMPERATURE

Mark A. BRADFORD¹

ABSTRACT

This paper presents a generic modelling of a composite beam at elevated temperature, by isolating the member from a structural assemblage and developing the nonlinear equations of its equilibrium state under thermal loading. It allows for a description of the structural response that is transparent, in deference to many advanced numerical schemes in which the influence of the governing parameters is not clear. The analysis herein is restricted to the pre-yielded state, and it is important for the obtaining the service response of a composite flexural member in a compartment when subjected to fire. The formulation is demonstrated with an example that illustrates the prowess of the technique.

1. INTRODUCTION

Recent sophisticated methods of numerical analysis in the discipline of structural fire engineering have provided valuable theoretical predictions of structural behaviour at elevated temperature. These numerical techniques allow for a wide variety of end conditions, gravity loading regimes and the like for structural elements; either in isolation or as part of a structural framework.

A common difficulty with sophisticated numerical techniques is in the translation of problem-specific results to more general predictive rules that form the basis for codification of the research findings. This difficulty can be profound in fire engineering, and the quest for rational performance-based designs is reliant on being able to find a rational prediction to the structural behaviour for a particular loading and fire scenario. So as to better understand the structural behaviour, it is essential to have a generic model for the problem in which the underlying parameters that govern the structural response can be identified.

Several analyses of composite beams in frame structures have been proposed, based on modelling the steel, concrete, steel sheeting, reinforcement and shear connection with

¹Scientia Professor, The University of New South Wales, School of Civil & Environmental Engineering, UNSW, Sydney, NSW 2052, Australia.
Email: m.bradford@unsw.edu.au

finite elements. Perhaps the most-used software for this is the ABAQUS package [1]. Hitherto, these techniques are still considered to be research tools and their results have not yet distilled directly down into design codes. Because of the complexity of describing a composite beam and of the elevated temperature response of the constituent materials, the underlying “feeling” for the structural response can be lost and this structural response is described by the results of often one-off finite element analyses. This is not altogether familiar to structural engineers who tend to use concepts of engineering and of engineering mechanics to explain and even to “validate” the results of a finite element study, rather than using the results of a numerical analysis to try to explain the structural concepts as often seems the case in fire engineering. Nevertheless, elevated temperature structural mechanics is not widely understood by many engineers, and so it is useful to be able to provide a rational, mechanics-based explanation for the results of finite element studies.

This paper attempts to provide a generic, albeit fairly simplistic, representation of a composite beam in a compartment subjected to fire. At this stage, the beam is modelled as a steel I-section with a flat reinforced concrete slab with which it has full shear interaction [2]. The ends of the member may have longitudinal or rotational springs to allow for semi-rigid construction [3] and for the restraining effects of the cooler parts of the structure. The principle of virtual work is used to determine the deformation of the member by deriving the differential equations of its response and the static and kinematic boundary conditions, and a procedure is described to determine the equation of equilibrium of the member. The technique is then illustrated by a numerical example.

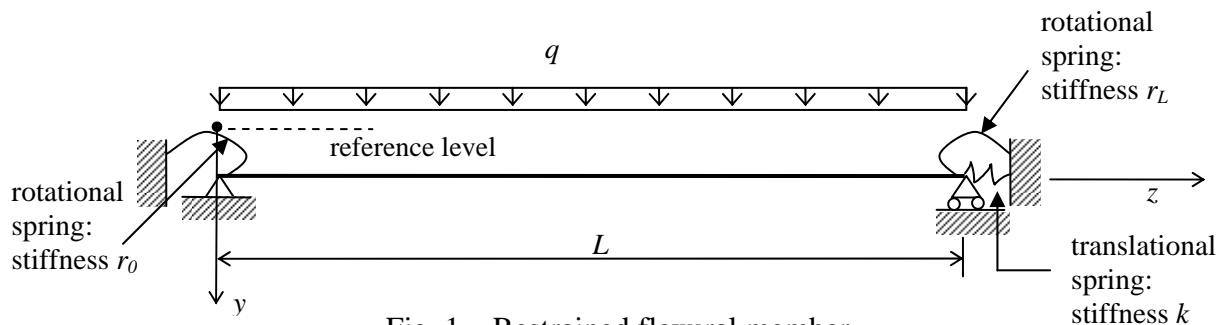


Fig. 1 – Restrained flexural member

2. DEFORMATIONS

Figure 1 shows a composite beam at the early stages of thermal loading when the material properties are pre-yield. The thermal state is defined by a temperature field $\mathfrak{T} = \mathfrak{T}_c \cup \mathfrak{T}_r \cup \mathfrak{T}_s$, where c denotes the concrete, r the steel reinforcement in the slab and s the steel joist, and \mathfrak{T}_ω ($\omega = c, r, s$) denotes the component temperature field. Each of these temperature fields results in a non-mechanical thermal strain $\varepsilon_{T_\omega}(y)$, where y is arbitrarily measured from the reference level located at the top of the cross-section, so that for a temperature $T_\omega(y)$ within the appropriate component ω , this strain is $\varepsilon_{T_\omega}(y) = \alpha_\omega T_\omega$ where α_ω is the coefficient of thermal expansion for component ω . The elastic modulus of the material $E_\omega(y)$ depends on the temperature field \mathfrak{T} and is given by empirical relationships in design data and elsewhere [4]. It is assumed that the reinforcement is fully bonded to the slab and full shear interaction exists between the slab and joist components [3]. The composite flexural member is supported against vertical deflection at both ends ($v_0 = v_L = 0$) and has a rotational linear spring at each end of stiffnesses r_L and r_L and a linear translational spring of stiffness k located at end L . The

thermal regime is assumed to be one for which the temperature field and material properties are constant along the member.

The nonlinear representation of the total strain in each component can be decomposed into the mechanical and non-mechanical components according to

$$\varepsilon_{\omega} = w' + \frac{1}{2}v'^2 - yv'' = \varepsilon_{m\omega} + \varepsilon_{T\omega} \quad (\omega = c, r, s), \quad (1)$$

and so the stress induced by the mechanical strains in each component is

$$\sigma_{\omega} = E_{\omega} \left(w' + \frac{1}{2}v'^2 - yv'' - \varepsilon_{T\omega} \right) \quad (2)$$

in which $() = d()/dz$ and w is defined as the axial deformation of the top reference fibre.

The statement of the principle of virtual work for the member shown in Figure 1 is

$$\int_{vol_{\omega}} \sum_{\omega} [\delta \varepsilon_{\omega} \cdot \sigma_{\omega} d(vol_{\omega})] + r_0 v'_0 \delta v'_0 + r_L v'_L \delta v'_L + k w_L \delta w_L = \int_0^L q \delta v dz \quad (3)$$

for all kinematically admissible variations of the displacements v , w , v and w , in which vol denotes the volume of component ω . Substituting Equations (1) and (2) into Equation (3) produces

$$\int_{vol} \left\{ \left[\overline{EA} \left(w' + \frac{1}{2}v'^2 \right) - \overline{EB}v'' - \overline{EF} \right] \delta w' + v' \delta v' + \left[-\overline{EB} \left(w' + \frac{1}{2}v'^2 \right) + \overline{EG} + \overline{EI}v'' \right] \delta v'' \right\} dz + r_0 v'_0 \delta v'_0 + r_L v'_L \delta v'_L + k w_L \delta w'_L = 0, \quad (4)$$

in which the cross-sectional properties are

$$\overline{EA} = \int_{A_c} E_c dA_c + \int_{A_s} E_s dA_s + E_r A_r \quad (5)$$

$$\overline{EB} = \int_{A_c} E_c y dA_c + \int_{A_s} E_s y dA_s + D_r E_r A_r \quad (6)$$

$$\overline{EI} = \int_{A_c} E_c y^2 dA_c + \int_{A_s} E_s y^2 dA_s + D_r^2 E_r A_r, \quad (7)$$

and the elasto-thermal cross-section parameters are

$$\overline{EF} = \int_{A_c} E_c \varepsilon_{Tc} dA_c + \int_{A_s} E_s \varepsilon_{Ts} dA_s + \varepsilon_{Tr} E_r A_r \quad (8)$$

$$\overline{EG} = \int_{A_c} E_c y \varepsilon_{Tc} dA_c + \int_{A_s} E_s \varepsilon_{Ts} y dA_s + \varepsilon_{Tr} D_r E_r A_r, \quad (9)$$

in which D_r is the depth of the reinforcement below the reference axis. Defining the reference strain as

$$\varepsilon_{rf} = w' + \frac{1}{2}v'^2 - \overline{EF}/\overline{EA} \quad (10)$$

produces the statement of the principle of virtual work as

$$\int_0^L \left\{ \overline{EA} \left(\epsilon_{rf} + \frac{\overline{EF} \overline{EG}}{\overline{EA}} \right) \delta w' + \overline{EA} \left(\epsilon_{rf} + \frac{\overline{EF} \overline{EG}}{\overline{EA}} \right) v' \delta v' + \left(\overline{EI} v'' - \overline{EB} \epsilon_{rf} - \frac{\overline{EF} \overline{EG}}{\overline{EA}} \right) \delta v'' \right\} dz + r_0 v'_0 \delta v'_0 + r_L v'_L \delta v'_L + k w_L \delta w'_L = 0. \quad (11)$$

The differential equations for the axial (w) and transverse (v) deformations of the member under thermal actions, as well as the boundary conditions, can be obtained directly by integrating Equation (11) by parts. This produces, after some manipulation

$$\begin{aligned} & \left(\overline{EA} \epsilon_{rf} - \overline{EB} v'' \right) \delta w \Big|_0^L + k w_L \delta w_L + v' \left(\overline{EA} \epsilon_{rf} - \overline{EB} v'' \right) \delta v \Big|_0^L + \left(\overline{EI} v'' - \overline{EB} \epsilon_{rf} - \frac{\overline{EF} \overline{EG}}{\overline{EA}} \right) \delta v' \Big|_0^L \\ & + r_0 v'_0 \delta v'_0 + r_L v'_L \delta v'_L + k w_L \delta w'_L \\ & + \int_0^L \left[\left(\overline{EI} v'' - \overline{EB} \epsilon_{rf} - \frac{\overline{EF} \overline{EG}}{\overline{EA}} \right)' - v'' \left(\overline{EA} \epsilon_{rf} - \overline{EB} v'' \right) - v' \left(\overline{EA} \epsilon_{rf} - \overline{EB} v'' \right)' - q \right] (\delta v) \\ & - \left(\overline{EA} \epsilon_{rf} - \overline{EB} v'' \right)' (\delta w) \Big] dz = 0. \end{aligned} \quad (12)$$

The deformations w in Equation (12) are arbitrary, and so

$$\left(\overline{EA} \epsilon_{rf} - \overline{EB} v'' \right)' = 0, \quad (13)$$

which produces

$$\overline{EA} \epsilon_{rf} - \overline{EB} v'' = \text{const} = N. \quad (14)$$

The deformations v in Equation (12) are also arbitrary, leading to

$$v^{iv} - \mu^2 v'' = \frac{q}{EI}, \quad (15)$$

in which

$$\mu^2 = \frac{N}{EI} \quad \text{with} \quad \overline{EI} = EI - \frac{\overline{EB}^2}{EA}. \quad (16)$$

Equation (12) also contains the boundary conditions for the member. These are given by

$$\left[v' \left(\overline{EA} \epsilon_{rf} - \overline{EB} v'' \right) \right]_L \delta v_L = 0 \quad \text{and} \quad - \left[v' \left(\overline{EA} \epsilon_{rf} - \overline{EB} v'' \right) \right]_0 \delta v_0 = 0, \quad (17)$$

$$\left(\overline{EI} v'' - \bar{\rho} + r_L v' \right)_L \delta v'_L = 0 \quad \text{and} \quad \left(-\overline{EI} v'' + \bar{\rho} + r_0 v' \right)_0 \delta v'_0 = 0, \quad (18)$$

$$\left(\overline{EA\epsilon_{rf}} - \overline{EBv''} + kw\right)_L \delta w_L = 0 \quad \text{and} \quad \left(\overline{EA\epsilon_{rf}} - \overline{EBv''}\right)_0 \delta w_0 = 0, \quad (19)$$

in which the constant $\bar{\rho}$ is

$$\bar{\rho} = \frac{N \overline{EB} + \overline{EF} \cdot \overline{EG}}{\overline{EA}} = \frac{\phi^2}{\bar{\lambda}^2} \overline{EB} + \frac{\overline{EF} \cdot \overline{EG}}{\overline{EA}}, \quad (20)$$

where

$$\phi = \mu L, \quad \bar{\lambda} = \frac{L}{\bar{r}}, \quad \bar{r}^2 = \frac{\overline{EI}}{\overline{EA}}, \quad (21)$$

with μ being an axial force parameter, \bar{r} a transformed radius of gyration and $\bar{\lambda}$ being a transformed slenderness ratio.

Each of the six equations (17) to (19) can be written as $[]_0 ()_0 = 0$ or $[]_L ()_L = 0$. The kinematic boundary conditions are represented by $() = 0$, and the dual static boundary conditions by $[] = 0$ whenever $() \neq 0$. The solution of Equation (15), if q is taken as constant with respect to z , can be written in vector notation as

$$v = \mathbf{m}_c^T \mathbf{q}_c + \frac{qL^2 z^2}{2EI\phi^2} \quad (N \leq 0) \quad \text{or} \quad v = \mathbf{m}_t^T \mathbf{q}_t + \frac{qL^2 z^2}{2EI\phi^2} \quad (N \geq 0), \quad (22)$$

in which

$$\mathbf{m}_c = \langle \cos(\mu z) \quad \sin(\mu z) \quad 1 \quad z \rangle^T, \quad \mathbf{m}_t = \langle \cosh(\mu z) \quad \sinh(\mu z) \quad 1 \quad z \rangle^T, \quad (23)$$

$$\mathbf{q}_c = \langle A_{1c} \quad A_{2c} \quad A_{3c} \quad A_{4c} \rangle^T, \quad \mathbf{q}_t = \langle A_{1t} \quad A_{2t} \quad A_{3t} \quad A_{4t} \rangle^T, \quad (24)$$

with the subscript $()_c$ indicating the axial force being compressive and $()_t$ indicating it being tensile. The vectors containing the four constants of integration \mathbf{q}_c or \mathbf{q}_t can be determined from the four Equations (18) and (19), which for the flexural member shown in Figure 1 are the two kinematic boundary conditions that

$$v_L = v_0 = 0, \quad (25)$$

and the two static boundary conditions that

$$\overline{EI}v_L'' - \bar{\rho} + r_L v_L' = 0 \quad \text{and} \quad -\overline{EI}v_0'' + \bar{\rho} + r_0 v_0' = 0. \quad (26)$$

3. EQUILIBRIUM

Because N is constant and so $\frac{1}{L} N dz = N$, Equations (10) and (14) produce

$$N = \frac{\phi^2 \overline{EI}}{L^2} = \frac{\overline{EA}}{L} \int_0^L (w' + \frac{1}{2} v'^2) dz - \frac{\overline{EB}}{L} \int_0^L v'' dz - \overline{EF} \quad (27)$$

where $\int_0^L w' dz = w_L$. Since

$$\int_0^L w' dz = \int_0^L dw = w_L, \quad (28)$$

and from Equations (14) and (19)

$$kw_L = -N = -\phi^2 \overline{EI} / L^2, \quad (29)$$

the equation for the equilibrium of the member shown in Figure 1 is

$$\begin{aligned} \phi^2 \left(\frac{1}{\bar{\lambda}^2} + \frac{1}{\bar{k}} \right) + \frac{\overline{EF}}{\overline{EA}} + \frac{qL^2}{\phi^2} \cdot \frac{\overline{EB}}{\overline{EA EI}} + \frac{q^2 L^6}{3\phi^4} \frac{1}{\overline{EI}^2} + \frac{\overline{EB}}{\overline{LEA}} \left(\int_0^L \mathbf{m}''^T dz \right) \mathbf{q} \\ - \frac{2}{L} \left(\int_0^L z \mathbf{m}'^T dz \right) \mathbf{q} - \frac{1}{L} \mathbf{q}^T \left(\int_0^L \mathbf{m}'^T \mathbf{m}' dz \right) \mathbf{q} = 0 \end{aligned} \quad (30)$$

in which $\mathbf{m} = \mathbf{m}_c$ and $\mathbf{q} = \mathbf{q}_c$ if the member is in compression and $\mathbf{m} = \mathbf{m}_t$ and $\mathbf{q} = \mathbf{q}_t$ if it is in tension, and where

$$\bar{k} = \frac{kL^3}{\overline{EI}}. \quad (31)$$

Equation (30) represents a (scalar) nonlinear equation in the axial force parameter whose form can be established for the particular case of the boundary conditions (represented by \mathbf{q}_c or \mathbf{q}_t). An analytic formulation for this equation in closed form is cumbersome since general expressions for the constants A_1, \dots, A_4 are not straightforward, but the equation is solvable by mathematical packages such as Maple [5]. It can be seen from Equation (30) that the solution for the axial force depends on the dimensionless slenderness ratio $\bar{\lambda}$, on the dimensionless modified translational spring stiffness \bar{k} and on the dimensionless load parameters $qL^2 \overline{EB} / (\overline{EA EI})$ and qL^3 / \overline{EI} , as well as on the dimensionless thermal parameter $\overline{EF} / \overline{EA}$.

4. ILLUSTRATION

In order to illustrate the afore-described procedure, consider a 10 m long composite beam whose cross-section is shown in Figure 2 for which the (unreinforced) slab is 3500 mm wide and 130 mm deep, the steel joist is an Australian 360 UB 57 [5] (depth = 359 mm, flange width = 172 mm, flange thickness = 13 mm, web thickness = 13 mm), with the

temperature and elastic modulus being assumed to vary as shown in the figure. Using the top of the cross-section as the reference level, the section elastic and thermal/elastic properties can be determined, with a coefficient of thermal expansion for both materials taken as $= 10 \cdot 10^{-6} / ^\circ\text{C}$ as $\overline{EA} = 12.393 \cdot 10^9 \text{ N}$, $\overline{EB} = 1.01686 \cdot 10^{12} \text{ Nmm}$, $\overline{EI} = 160.842 \cdot 10^{12} \text{ Nmm}^2$, $\overline{\overline{EI}} = 77.4075 \cdot 10^{12} \text{ Nmm}^2$, $\overline{EF} = 26.3993 \cdot 10^6 \text{ N}$, $\overline{EG} = 2.67742 \cdot 10^9 \text{ Nmm}$, $\overline{r} = 113.92 \text{ mm}$ and $\overline{\lambda} = 87.78$. For simplicity it is assumed that the sustained external load $q = 0$ and that the beam has “pin” supports so that $r_0 = r_L = 0$.

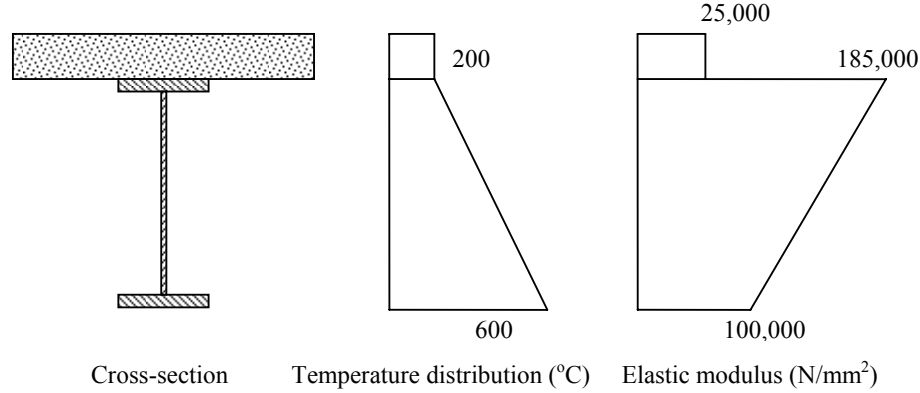


Fig. 2 – Composite beam example

For this example, the boundary conditions are $v_0 = v_L = 0$ and $v_0 = v_L = \overline{\rho} / \overline{\overline{EI}}$ so that

$$v = \frac{\overline{\rho} L^2}{\phi^2 \overline{\overline{EI}}} \left[1 - \cos(\mu z) + \left(\frac{\cos \phi - 1}{\sin \phi} \right) \sin(\mu z) \right] \quad (32)$$

in which, using Equation (20),

$$\overline{\rho} = 131.971 \times 10^6 (\phi^2 + 0.04322) \text{ Nmm}. \quad (33)$$

The equation of equilibrium in (30) then reduces to

$$\left(129.78 + \frac{1}{\bar{k}} \right) \phi^2 - \frac{1.7049(\phi^2 + 0.04322)(1 - \cos \phi)}{\sin \phi} \bullet \left[170.49(\phi^2 + 0.04322) \left(\cos \phi - \frac{\phi}{\sin \phi} + 2 \sin^2 \phi \right) + \frac{164.10}{\phi} \right] + 236.6 = 0. \quad (34)$$

For a dimensionless spring stiffness $\bar{k} = 10 \cdot 10^3$, the solution of Equation (32) is $= 1.1545$, corresponding to an axial force $N = 1031 \text{ kN}$ and to a value of the parameter $\overline{\rho} = 181.61 \cdot 10^6 \text{ Nmm}$. The mid-span deflection is therefore $v = 34.01 \text{ mm}$ and the mid-span mechanical strain at the bottom of the steel fibre can be determined from Equation (2) with y

= 489 mm as 0.00072, which is less than the yield strain at $T = 600^{\circ}\text{C}$ and so the steel joist would be elastic at the temperature regime shown in Figure 2.

5. CONCLUSIONS

This paper has presented a generic technique, based on a rational mechanics-based approach using virtual work, to derive the equation for the equilibrium of a composite flexural member in a sub-assembly that also allows for the deflections and mechanical strains in the member to be determined. It identified the parameters on which the deformations and stresses in the member are based. The method can be programmed using simple packages instead of more sophisticated finite element software, so that generic solutions can be determined. This allows for the governing parameters to be identified, as was shown in the example.

6. ACKNOWLEDGEMENT

This work was supported by the Australian Research Council through a Federation Fellowship awarded to the author.

7. REFERENCES

- [1] ABAQUS *Theory Manual, Version 6.4*. Hibbit, Karlsson and Sorensen Inc., Pawtucket, Rhode Island, 2005.
- [2] Ranzi, G., Bradford, M.A. and Ansourian, P. "Behaviour of composite steel-concrete beams with longitudinal and transverse partial interaction in fire. *III European Conference on Computational Mechanics Solids, Structures and Coupled Problems in Engineering*, Lisbon, Portugal, June 2006 (submitted).
- [3] Trahair, N.S., Bradford, M.A. and Nethercot, D.A. "*The Behaviour and Design of Steel Structures to BS5950*", 3rd edition (UK), Spon Press, London, 2001.
- [4] Standards Australia. "*AS4100 Steel Structures*", Standards Australia, Sydney, Australia, 1998.
- [5] Waterloo Maple Inc. "*Maple 10 User Manual*", Maplesoft, Waterloo, Canada, 2005.
- [6] BHP *Hot Rolled and Structural Steel Products*. BHP Co. Pty Limited, Melbourne, Australia, 1998.



PERFORMANCE OF CELLULAR COMPOSITE FLOOR BEAMS AT ELEVATED TEMPERATURES

Ali NADJAI¹, Olivier VASSART², Faris ALI, Didier TALAMONA,
Ahmed ALLAM and Mike HAWES

ABSTRACT

This paper describes an experimental study at ambient and elevated temperatures on the behaviour of full scale composite floor cellular steel beams. A total of four specimens, comprising two different steel geometries and loading conditions were tested under monotonic loading and at elevated temperatures. All beams were designed for a full shear connection between the steel beam and the concrete flange using shear studs. The beams were designed to fail by web buckling, which was observed in all the tests. Failure temperature observed in the fire tests indicated that failure by web post buckling of cellular beams in fire cannot simply be estimated by applying temperature dependent reduction factors on stiffness, as given in codes. A finite element model is then established with both material and geometrical non-linearity using shell elements to compare the experimental results. The comparison between the finite element prediction and actual tests results are quite good in terms of failure modes, load deflection behaviour and ultimate loads.

1. INTRODUCTION

The widespread use of CBs as structural members has prompted several investigations into their structural behaviour. Early studies concentrated on in-plane response in both the elastic [1-2] and plastic [3,6] ranges. Extensive measurements were made of the stress distributions across the cross-section, and these were compared with the predictions of various theoretical studies employing a Vierendeel analogy [7], finite difference techniques [8-10], various finite element schemes [11], and a complex variable analytical method [12]. As a result of various

¹ Professor, University of Ulster, School Built Environment, FireSERT, Belfast BT37 OQB, UK
email:a.nadjai@ulster.ac.uk

²Senior Manager, Arcelor Profil Luxembourg S.A Research Centre, L-4009 Esch-sur-Alzette email:
Olivier.vassart@arcelor.com

series of tests a number of different failure modes have been observed [13-16]. The main failure modes are a Vierendeel collapse mechanism in which plastic hinges form at the section touching the four reentrant corners of a castellation, buckling of a web-post, and web weld failure. Several collapse mechanisms have been proposed [17-19] and the lateral buckling of the web posts has been analysed; however only limited investigations of composite floors using cellular steel beams at ambient temperature have been conducted [20]. These beams have been used widely in roof and composite construction without having been rigorously investigated under fire conditions.

A composite concrete floor-slab has the effect of significantly increasing the flexural resistance of a steel section; however its effect on shear resistance is more complex. Investigation of the behaviour of composite beams with isolated web openings in otherwise solid webs has shown that the slab significantly increases the shear-carrying capacity beyond that of the steel beam alone. This is due to the enhanced flexural and shear capacity of the upper part of the beam across an opening, although an unsupported web-post is more susceptible to buckling. In fire, the temperature distribution across a composite member is non-uniform, since the web and bottom flange have thin cross-sections and a greater exposed perimeter than the top flange. The deterioration of the material properties of the web will therefore become an important effect on the overall performance of the member in the event of fire.

The fire resistance of CBs has been very controversial in recent years, with most of the debate being concerned with their requirements for intumescent protection. A rather illogical prescriptive “rule” [21] for beams with web openings, requiring 20% extra coating thickness compared with solid-web beams, has recently been subjected to much criticism on the basis of thermal tests on beams coated with specific intumescent products. The previous mentioned document [21] was followed by a most recent publications [22-24] justifying the traditional prescriptive fire protection rules, based on understanding of the mechanics of structural behaviour in fire.

The experimental and numerical aspects of this project have the potential to provide essential data in several areas currently lacking systematic research. It will underpin the current lead in expertise which is held by European fire engineering designers, and will assist European-based fabricators who have made cellular beams the most popular long-span system in current construction. The Purpose of these tests is not to evaluate the intumescent performance but to provide data on the structural web post failure temperature. Figures 1 & 2 summarizes the test beams configurations, and Table 1 identifies the detailing information for each beam test.

2. EXPERIMENTAL TEST PROGRAM

The tests was carried out on four full-scale composite cellular steel beams using span lengths of 4500mm subjected to one point load and two-point loadings using two types of beams:

- a- Symmetrical composite beams (Test A1): The beam for Test A1 has been produced on the basis of UB 406X140X39 as a top tee section and of UB 406X140X39 as a bottom tee section having a finished depth of 575 x 140 CUB 39 kg/m
- b- Asymmetric Composite beams (Test B1): The beam for Test B1 has been produced on the basis of UB 406X140X39 as a top tee section and of UB 457X152X52 as a bottom tee section having a finished depth of 630 x 140/152 ACUB 46kg/m

Each beam was tested: 1- at ambient temperature up to failure, 2-at elevated temperatures under load derived from cold test.

The concrete slabs were all nominally 150 mm thick and 1200 mm wide using normal-weight concrete (Grade 35 N/mm²). The slab reinforcement consisted of welded wire mesh reinforcement A142 having yield strength of 460N/mm². Full interaction between the slab and beam was ensured in all specimens by the use of a high density of shear connectors of 19mm diameter studs at height 120 mm. The shear studs have been equally distributed in one row with a distance of 150 mm over the beam length. A Holorib sheets HR 51/150 with a thickness of 1.25 mm have been used as sheeting. The measured yield stress from a tensile yield stress from a tensile test was $F_y = 327 \text{ N/mm}^2$. Concrete compressive strength was determined at different stages of time: after 2 weeks, 28 days and during the testing days giving an average of 35N/mm² using a compressive strength calibrated machine at the University of Ulster.

Table 1. Steel Cellular beams detailing.

Top T	Bot T	a_o (mm)	W (mm)	W/ a_o	$a_o/t_w \epsilon$	e (mm)	e/ a_o	d/ t_w	A_{fB}/A_{fT}
UB406X140X39 S355	UB406X140 X39/ S355	375	125	0.33	59.60	500	1.33	83.9	1
UB406X140X39 S355	UB457X152 X52/ S355	450	180	0.4	59.21 70.31	630	1.4	84.3	1 1.43

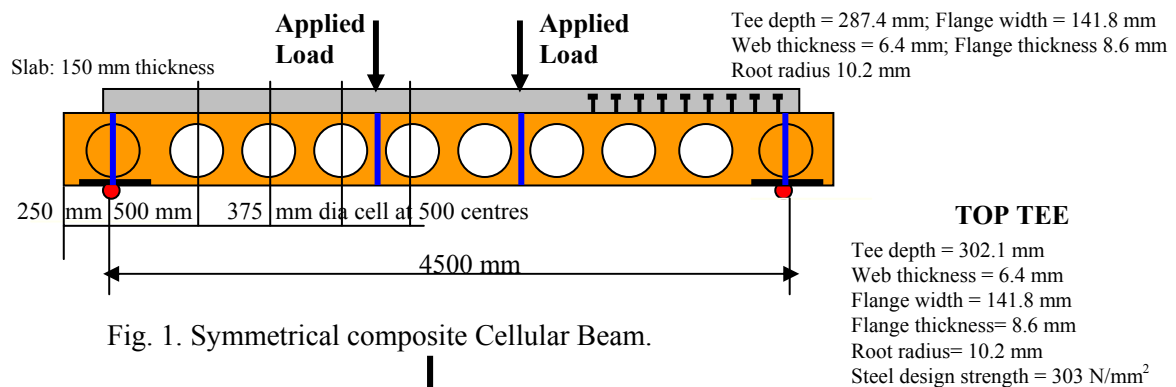
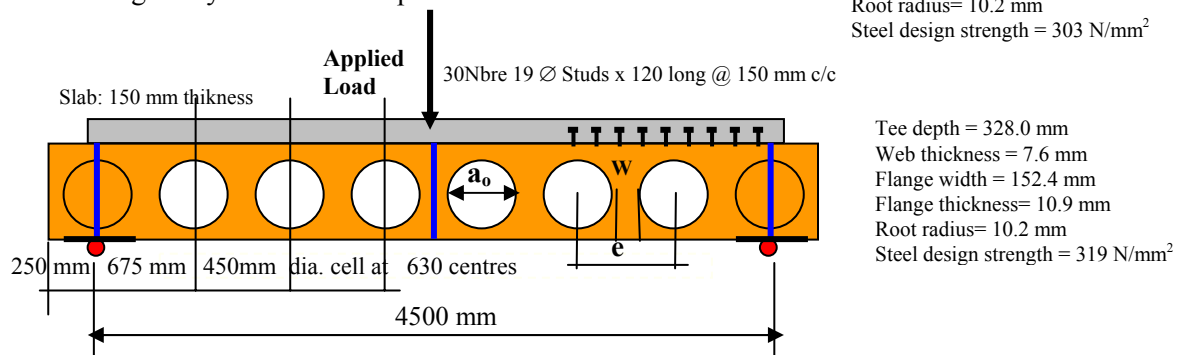


Fig. 1. Symmetrical composite Cellular Beam.

Fig. 2. Detailing of Asymmetric Composite Cellular Beam:
406x140UB39 Top & 457x152UB52 Btm Tee.

3. TESTING PROCEDURE OF THE COOLING TESTS

Both tests 1A and 1B were conducted using portal frames with a capacity of 160 Tones loading system. The composite beam specimen was simply supported at both ends. A 600 KN Hydraulic jack was used to apply the monotonic load. The load was applied to the top concrete flange through a distribution beams exhibited in Figure 3 for two point loadings. Figure 3 demonstrates the equipment used to record the experimental data: load versus deflections and strain gauges readings.

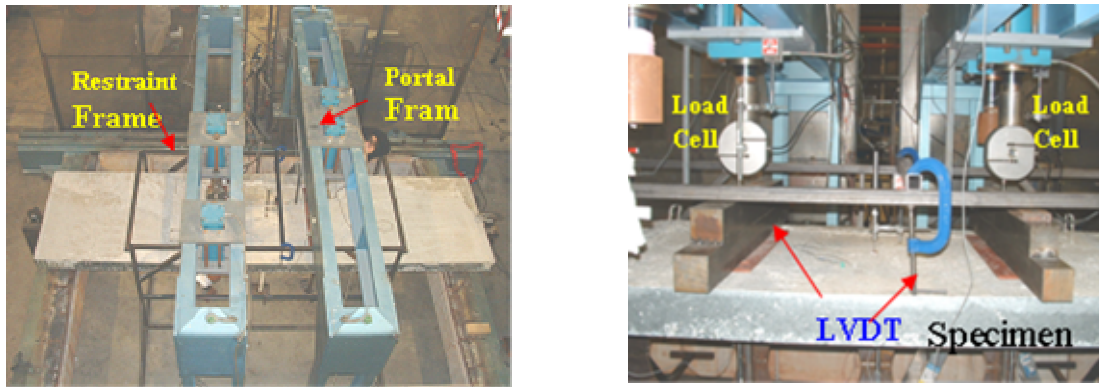


Fig. 3: Experimental Set up / Load Introduction of Test 1A

For both test A1 and B1 load cycles at a load level of 20% and 60% of the pre-design load have been applied to avoid slippage of the load introduction and supports as well as friction in the shear joint and the structure. All the load cells used for the experimental were calibrated before testing procedure took place. Twenty percent of the pre-design load used by Westok software has been kept for one-hour time before load has been increased. Each load step with a value of 10 kN/ step was kept for 3 minutes intervals.

Both Ultimate failures of the specimens were associated with web-post buckling, and study of various measures of buckling load led to the conclusion that this maximum load represented the web buckling load. Variation of central deflection with load is shown in Figure 4. In each case the buckling mode comprised double curvature bending of the post (see Figure 4). Before this occurring high strains had developed following tensile yield of the lower part of the steel beam. Tensile strains developed above the opening indicating that the neutral axis was close to or in the slab.

After the post web buckling took place the beam was then followed by hinges around the openings making the webs to buckle in form S shape. BS 5950: Part 1 specifies that the maximum deflection under factored load for a beam of this type should not exceed: span/200. The maximum deflection in both test beams just before failure was 10 mm, which is well within British Standards recommendations. Diagrams of the measurements as well as photographs of the failure mechanism are given in the following figures.

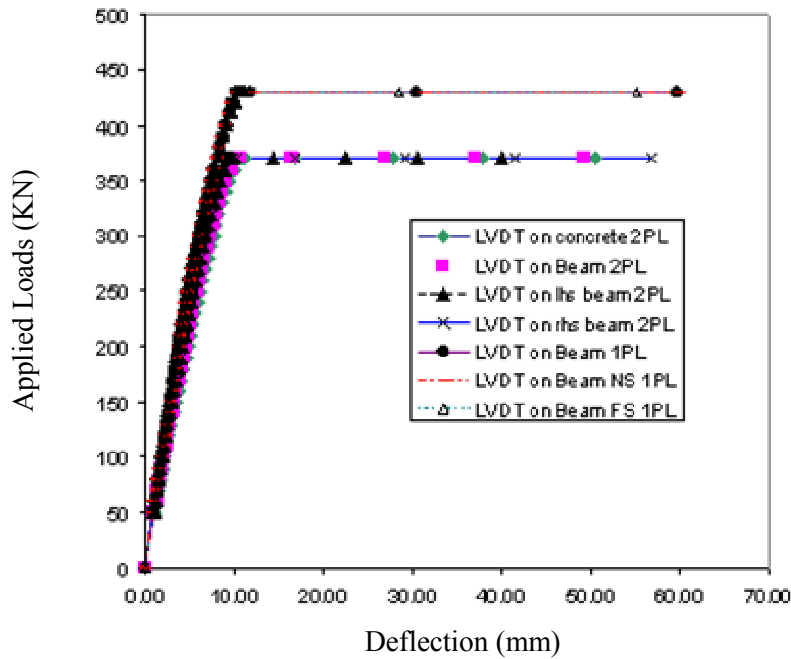


Fig. 4. Load vs. deflection for Tests A1 and B1 at ambient temperature



Post web buckling mode failure A1



Post web buckling mode failure B1

4. EXPERIMENTAL RESULTS TESTS AT ELEVATED TEMPERATURES

The composite cellular steel beam tests A2 and B2 were tested under the same fire curve shown in Figure 5. This fire curve was set up in order to produce lower peak temperatures but of longer duration sufficient to permit significant heat conduction, which may produce a large build up of vapour pressure and the creation of significant thermal expansion producing a restraint force coming from the concrete slab. The applied loads for tests A2 and B2 are calculated as 180 kN and 210 kN respectively from $0.5 \times$ failure load obtained from the cold tests A1 and B1. Both beams A2 and B2 were kept loaded to its respective applied load for duration over an hour time before the furnace started functioning. The positions of the thermocouples (Figure 6) were located at each web post along its depth of the section and also around the openings.

Figures 7 and 8 demonstrated that a linear elastic response with almost equal deflections in both beams can be seen in the time deflection curves at 30 minutes time when the temperature is equal to 320°C . Beam A2 starts to show loss in stiffness at time 40 min when the temperature is 432°C while beams B2 still with no sign of weakness. At 60 min time the deflection is increasing in both beams and stiffness decreasing at a temperature equal to 634°C . Between 60 and 70 min both beams deflection are becoming larger with less stiffness and strength in the member when the temperature achieved 712°C . After that time the beams tried to become a live just for a short time due to the presence the reinforced concrete slab on the top of the steel members. This instability of the beams is due to the rapid loss of web post

capacity relative to the loss of capacities in the Tee-sections. This failure mechanism is known as web post buckling and a typical form can be seen in Figure 9.

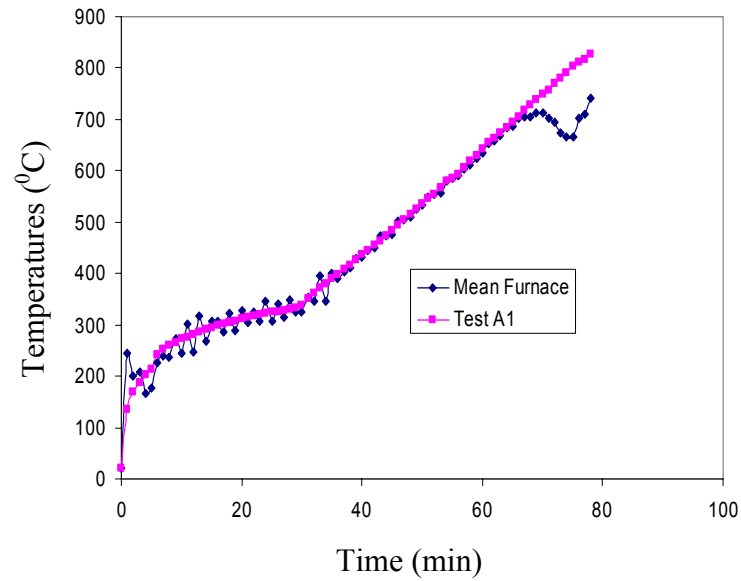


Fig. 5. Furnace temperature time curve used in the experimental study

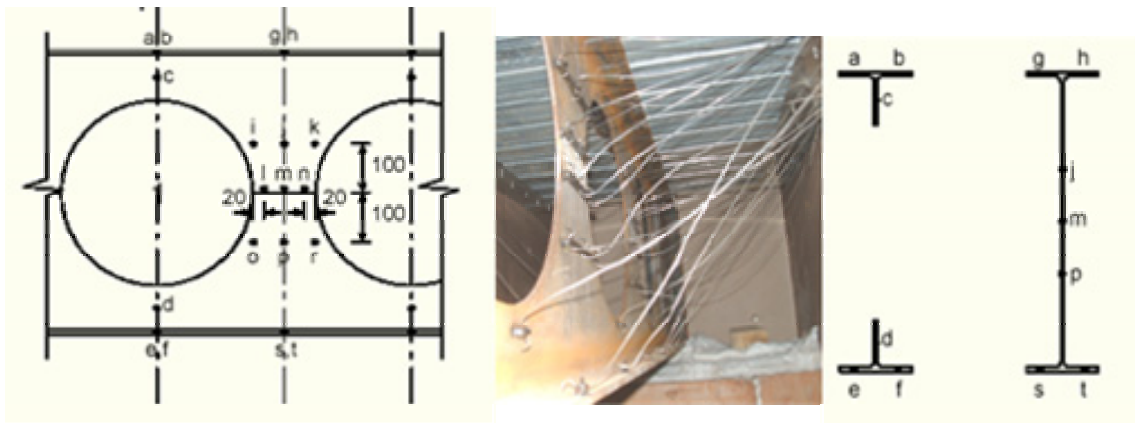


Fig. 6. Typical Thermocouples locations



Fig. 9. Web post buckling failure mechanism

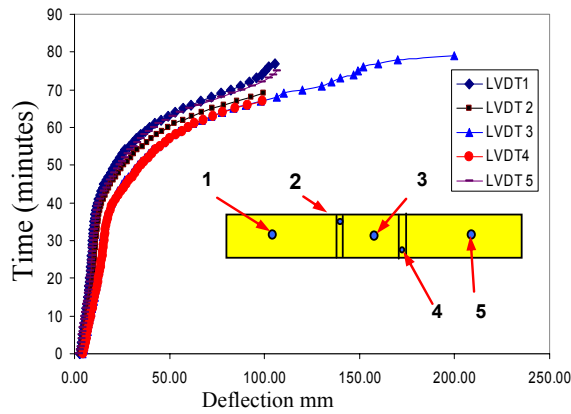


Fig. 7. Time versus deflection of test A2.

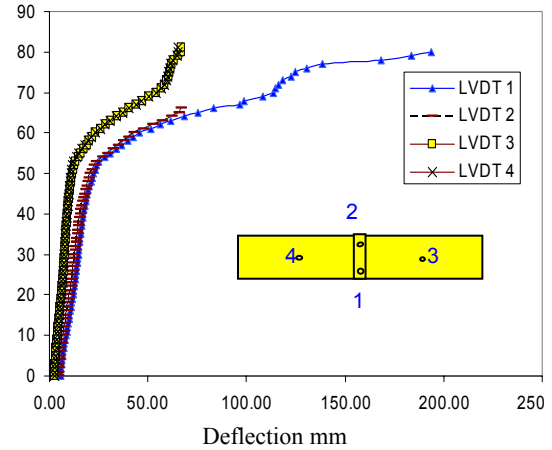


Fig. 8. Time versus deflection of test B2.

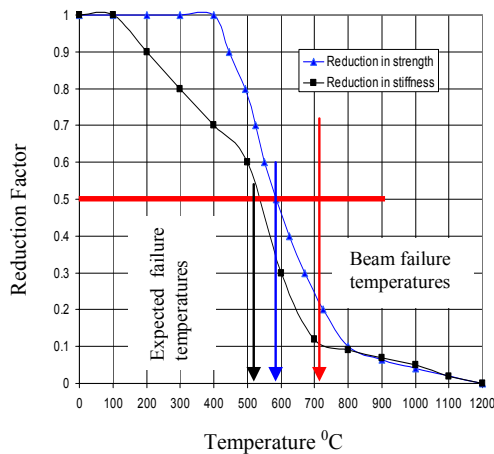


Fig. 10. Temperature versus reduction factor.

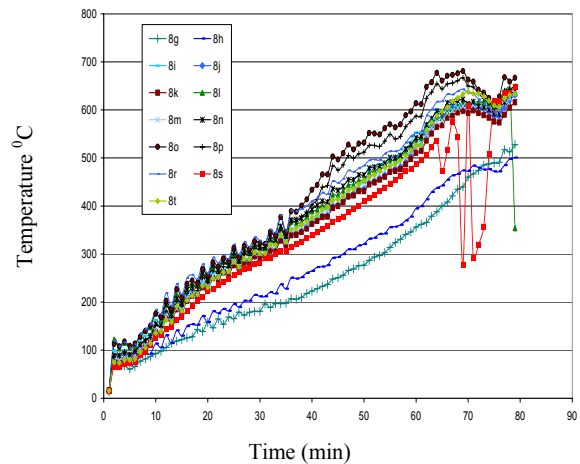


Fig. 11. Time versus deflection of test A2.

Figure 10 demonstrates that the stiffness and strength are expected to fail at temperatures given respectively 540 °C and 600 °C. In comparison with the experimental results the beams failed beyond the expected time at temperature equal to 650 °C while the furnace temperature was around 740 °C. We may conclude that from Figure 10 that the Young modulus decreases quicker than the steel strength limit and so we have a web-post buckling. The difference between the temperature of the top and the bottom (as shown in figure 11) tee is not relevant for the web-post buckling.

5. FINITE ELEMENT MODEL AND COMPARISONS

A finite element model was built in the software SAFIR, University of Liege, Belgium, in order to simulate the complete behaviour of Cellular Beams taking into account local instabilities. This model was calibrated on a lot of different cold tests performed during the last years [25, 26]. This model was used to simulate the behaviour of Cellular beams in case of fire. The following Figures 12-13 show the shell finite element model built to simulate the tests A and B:

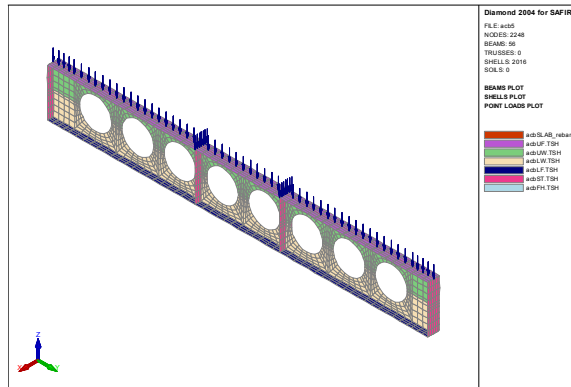


Fig. 12 : FEM Model of Test A

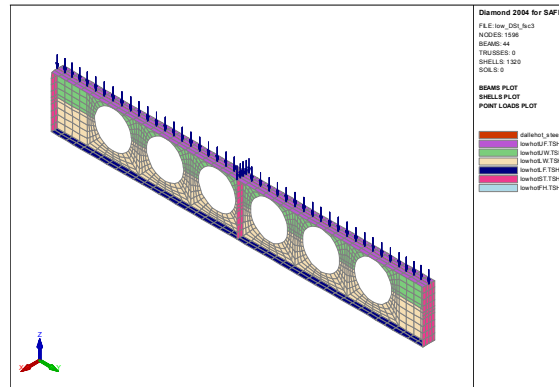


Fig. 13 : FEM Model of Test B

Exactly the same model was used to simulate the cold tests and the tests at elevated temperature. Comparison between FEM Model and tests at ambient temperature for the variation of central deflection with load is shown in Figure 14-15.

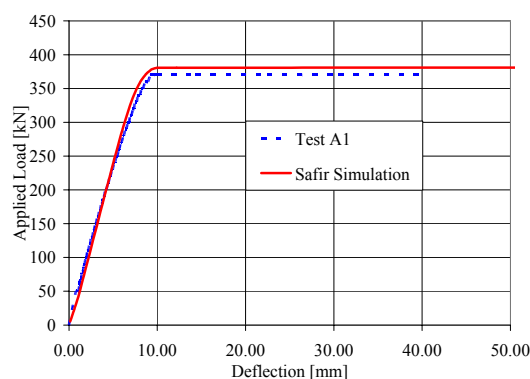


Fig. 14 : FEM Vs Test A1

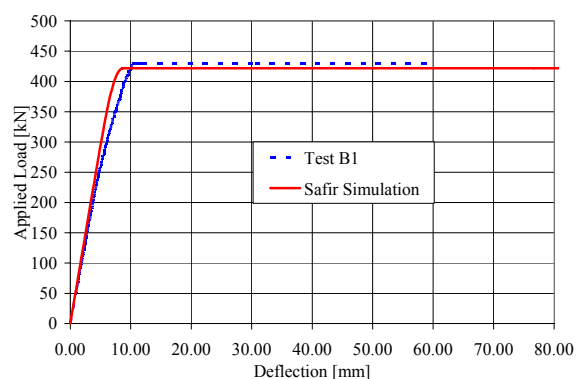


Fig. 15 : FEM Vs Test B1

The different temperatures measured during the two tests at elevated temperature were directly introduced in the FEM model to simulate the behaviour of the cellular beams in hot conditions. But, as shown on the Figure 11, the evolution of the temperature along the beam is not constant for a given section. So, an average value for the temperature was taken for each geometrical property, different Time/Temperature curves were introduced for the bottom flange, web, upper flange and concrete slab. The next Figures 16-17 show the repartition of the stresses in the steel section of the Cellular beam for the test B2:

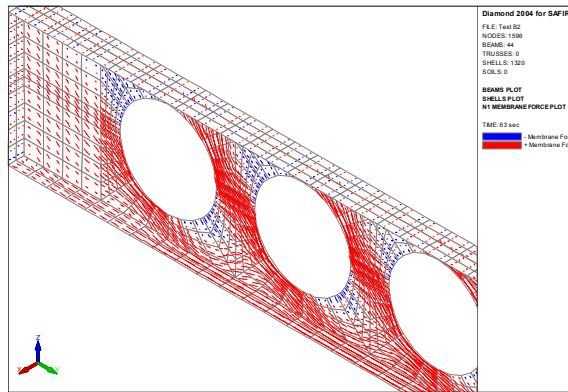


Fig. 16 : Membrane force in tension

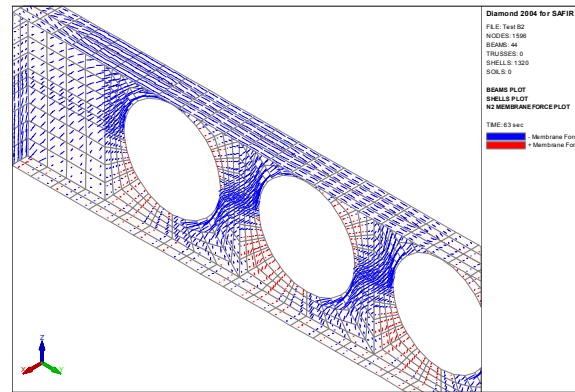


Fig. 17 : Membrane force in compression

The deformation (without amplification) in function of time is given at some relevant steps for the test at elevated temperature B2 in the following Figures 18-20:

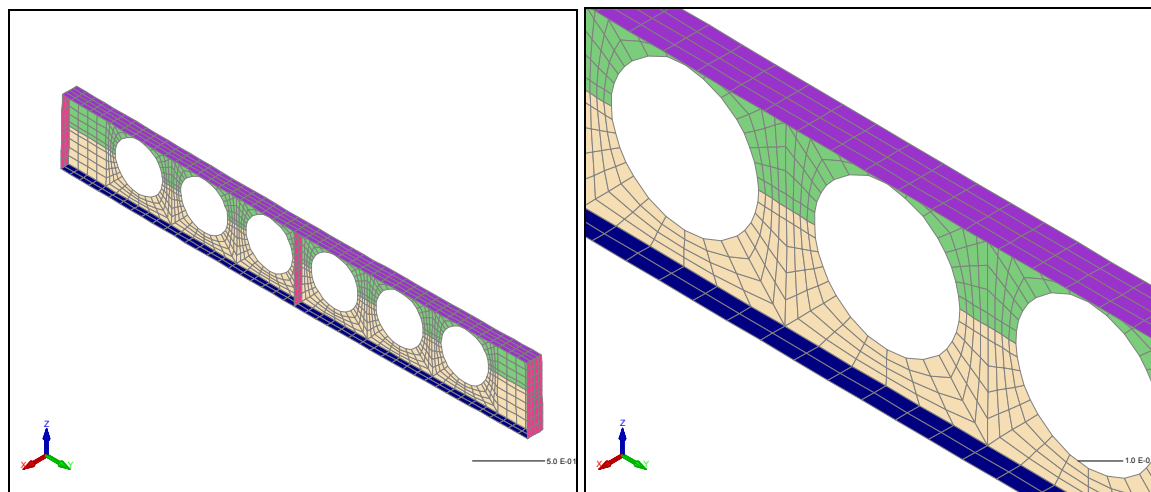


Fig. 18: Displacements after 3000 sec of heating

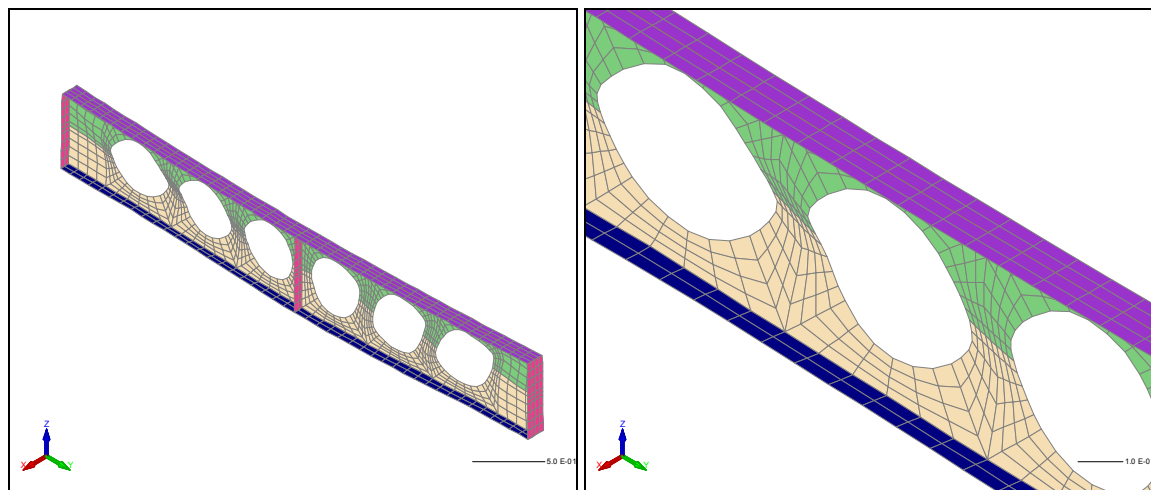


Fig. 19: Displacements at the beginning of the web post buckling

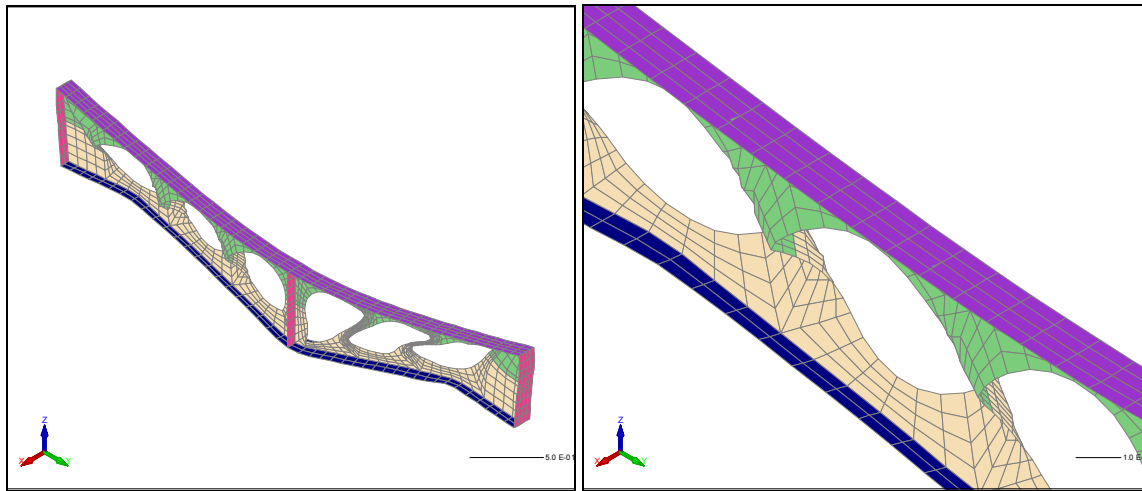


Fig. 20: Displacements at the end of the test

The next Figures 21-22 show the comparison between displacements at mid span between the tests (A2 and B2) and the FEM model in SAFIR:

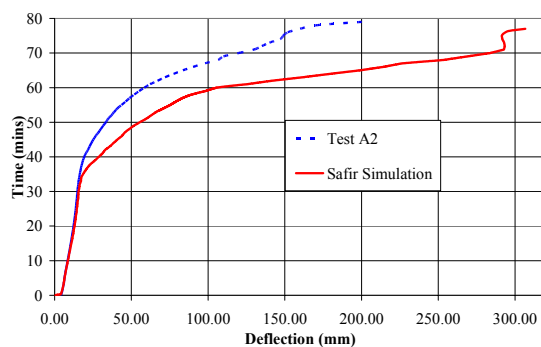


Fig. 21 : FEM Vs Test A2

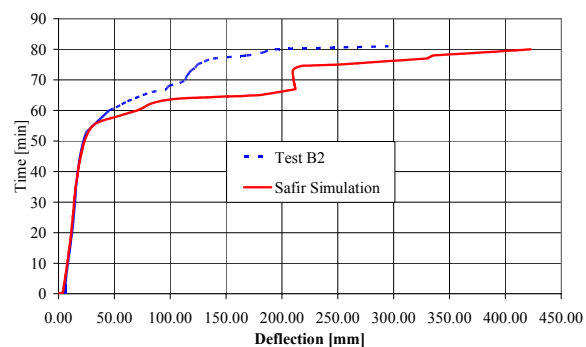


Fig. 22 : FEM Vs Test B2

6. CONCLUSION

This paper describes an experimental and analytical study of the behaviour of composite floor cellular steel beams in fire conditions conducted at the FireSERT, University of Ulster. The study suggests the following:

- The two beams failed due to web post buckling and the instability resulted in sudden loss of stiffness and strength in the beams
- The experimental data has compared well with the results from the Finite Element Modelling, giving confidence that it can be used for further parametric studies.
- The numerical model is capable to simulate the mechanical behaviour of composite Cellular beam sections in both cold and at elevated temperature conditions with a relatively high accuracy.

7. ACKNOWLEDGEMENT

The principal author wishes to acknowledge Mr. Mike Hawes (Westock LTD, Wakefield, England WF4 5ER) for the support funding of this research project.

8. REFERENCES

- [1] “Properties and strength of castellated beams. Consideration of previous tests”, Report D.GE. 71/262, The United Steel Companies Ltd, Swinden Laboratories, Rotherham, (1957).
- [2] Gibson & Jenkins, The Structural Engineer, 35 (12), (1957) pp467-479.
- [3] Sherbourne, Proc. 2nd Commonwealth Welding Conference, Institute of Welding, London, C2 (1966) pp1-5.
- [4] R. Delesques : Stabilité des montants de poutres ajourées, revue Construction métallique n°3-1968, CTICM, 1968, p.26-33
- [5] A. Bazile et J. Texier, Essais de poutres ajourées, revue Construction métallique n°3-1968, CTICM, 1968, p.12-25.
- [6] Hosain & Speirs, J. American Welding Society, Welding Res. Supp., 52 (8), (1973) pp329-342.
- [7] Mandel et al., J. Structural Division, ASCE, 97 (ST7), (1971) pp1947-1967.
- [8] Shoukry, J. American Welding Society, Welding Res. Supp., 44 (5), (1965) pp231-240.
- [9] RG Redwood, Analyse et dimensionnement des poutres ayant des ouvertures dans les âmes, revue Construction métallique n°3-1978, CTICM, 1978, p.15-27
- [10] D. Mateesco et G. Mercea, Un nouveau type de poutres ajourées, revue Construction Métallique, n°3-1981, CTICM, 1981, p.3-14
- [11] Srimani, & Das, Computers and Structures, 9, (1978) pp169-174.
- [12] Gotoh, Trans. JSCE, 7, (1976) pp37-38.
- [13] Nethercot & Rockey, The Structural Engineer, 49 (7), (1971) pp312-330.
- [14] Nethercot & Trahair, The Structural Engineer, 54 (6), (1976) pp197-204.
- [15] Kerdal & Nethercot, J. Construct. Steel Research, 4, (1984) pp295-315.
- [16] Okubo & Nethercot, Proc. Instn. Civ. Engrs., Part 2, (79), (1985) pp533-557.
- [17] Knowles, Proc. Instn. Civ. Engrs., Part 1, 90, (1991) pp521-536.
- [18] Dougherty, J. South African Institution of Civil Engineers, 35 (2), (1993) pp12-20.
- [19] Zaarour & Redwood, Journal of Structural Engineering, (1996) pp860-866.
- [20] Megharief & Redwood, Proc. Annual conference, Canadian Society for Civil Engineering, (1997) pp239-248.
- [21] “Fire Protection for Structural Steel in Buildings”, Second Edition, ASFP/SCI/FTSG, (1992).
- [22] Bailey C.G. Indicative Fire Tests to Investigate the Behaviour of Cellular Beams Protected with Intumescent Coatings. *Fire Safety Journal. Fire Safety Journal.* 39 2004 pp 689-709.
- [23] “RT1006 Version 02: Fire Design of Cellular Beams with Slender Web Posts”, SCI, Ascot, (2004).
- [24] Newman G.M., Robinson J.T. and Bailey C.G., Fire Safe design: A New Approach to Multi-Storey Steel-Framed Buildings (Second Edition). SCI Publication P288. The Steel Construction Institute, Ascot. 2006.
- [25] D. Bitar, T. Demarco, P.O. Martin, Steel and non composite cellular beams – Novel approach for design based on experimental studies and numerical investigations, brochure EUROSTEEL, june 2005
- [26] Large web Openings for service integration in composite floor, ECSC contract 7210-PR-315, 2004



THERMAL AND STRUCTURAL BEHAVIOUR OF ORTHOTROPIC SLABS IN FIRE

Xinmeng YU¹, Zhaohui HUANG², Ian W. BURGESS³ and Roger J. PLANK⁴

ABSTRACT

When an orthotropic composite slab cast on steel decking is subjected to fire attack, there is a decreasing temperature gradient from the bottom surface to the top surface. In addition, the temperature within the continuous upper portion of the slab varies in the horizontal sense due to the presence of the ribs. This makes it different from a flat slab.

In this study, using a layered 9-noded iso-parametric slab element and a 3-noded beam element, an orthotropic slab element is developed to model orthotropic slabs in fire. The element is assembled from a solid slab element which represents the continuous upper portion of the profile, and a special beam element which represents the ribbed lower portion. An equivalent width for the cross-section of this beam element is determined according to the dimensions of the cross-section of the ribbed profile, and the beam shares the nodes of the solid slab element. Slight modifications are applied to the slab and beam models. The temperature within each layer of the slab element can vary between adjacent Gauss integration points so as to reflect the temperature gradients in the horizontal plane. It is reasonable to ignore the torsional resistance of the beam element, because it actually represents the equivalent of a group of ribs rather than one individual rib.

Two fire tests on composite slabs have been modelled to validate the approach. Cases of orthotropic slabs with wide range of parameters defining the ribbed profile have been studied, which show that the orthotropic slab model is robust and effective in reflecting the influence of the shape of ribs on the thermal and structural performance of the slabs in fire. The study shows the influence of decking shape on the temperature distribution in the slab.

¹ PhD Student, University of Sheffield, Department of Civil Engineering, S1 3JD, UK;
email: x.m.yu@sheffield.ac.uk.

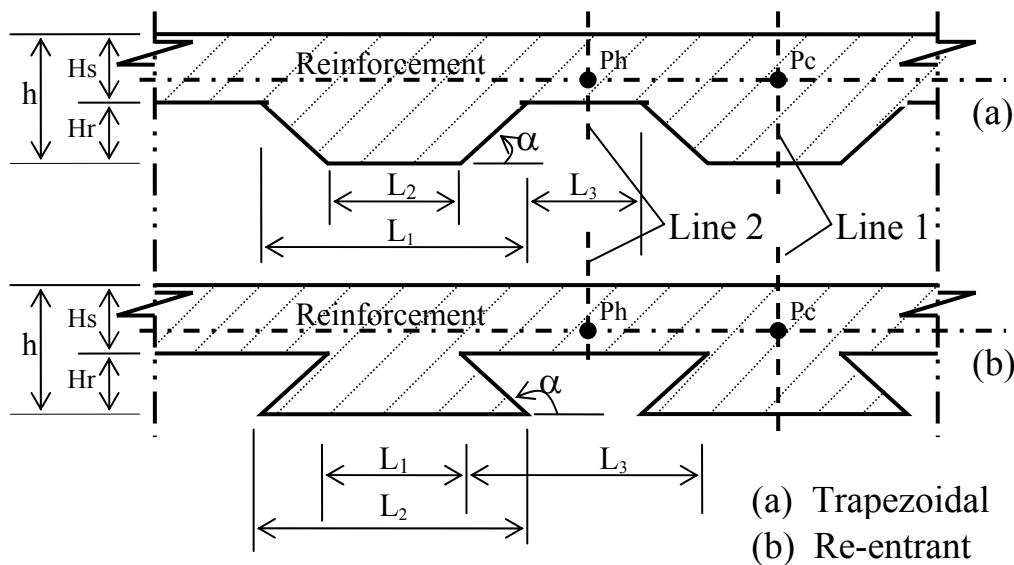
² Lecturer, University of Sheffield, Department of Civil Engineering, S1 3JD, UK;
email: z.huang@sheffield.ac.uk.

³ Professor, University of Sheffield, Department of Civil Engineering, S1 3JD, UK;
email: ian.burgess@sheffield.ac.uk.

⁴ Professor, University of Sheffield, School of Architecture, S10 2TN, UK;
email: r.j.plank@sheffield.ac.uk

NOTATION

Decking Geometric Parameters



Symbols

h	Slab depth	A45	$\alpha=45^\circ$; similarly for A90, A120, etc.
H_{eff}	Effective depth (defined in EC4)	P_h	Reinforcement position in the thinner parts of the slab
H_s	Concrete slab depth	P_c	Reinforcement position in the thicker parts of the slab
H_r	Height of steel decking (rib depth)	T_h	Temperature at P_h
L	Span	T_c	Temperature at P_c
L_0	Average of L_1 and L_2	T_{ec4}	Reinforcement temperature of an orthotropic slab at effective depth
L_1	Distance between two upper flanges	ϕ_{tf}	View factor at top flange of the decking
L_2	Width of the lower flange	ϕ_{web}	View factor at web of the web of the decking
L_3	Width of the upper flange		
RWR	Rib width ratio = $L_0/(L_1+L_3)$		
α	Angle between lower flange and web of decking		

1. INTRODUCTION

Orthotropic metal-decked composite slabs have been widely used in recent decades. These composite slabs consist of a cold-formed profiled thin-walled (typically, 0.6-1.2mm) steel decking, and concrete which is cast on top of this. Normally, the concrete is reinforced with a light anti-crack mesh, and may also contain individual bars, usually placed within the ribs. The profiles can be classified into trapezoidal and re-entrant types as shown above; trapezoidal decking may occasionally be used over long spans using extra-deep ribs which contain individual bars. However, the decking acts as a reinforcement, being bonded to the slab surface through indentations in the profile, and the composite slab itself has a very low centre of reinforcement compared to a conventionally reinforced slab. Due to the intrinsic efficiency of composite construction and the displacement of concrete by the profile shape,

considerably less concrete is used than in conventional reinforced concrete construction¹. Another advantage of an orthotropic slab over a flat one is that it saves construction time. Trapezoidal decking slabs are more popular than re-entrant ones because of ease of casting of concrete.

When the concrete is subjected to fire, the chemically bound water in the cement gel releases by dehydration into the liquid phase as free water, and the free water converts to the vapour phase. The water phase (solid, liquid or gaseous), the dimension of the structure, the mixture type, and the heating history all affect the temperatures in the slab in fire^{2,3}. Another complex feature comes from the coupled thermo-hydral-mechanical processes in the heated concrete. It is obvious that modelling of heat and mass transfer within concrete in fire is very complicated. Therefore, in this study, for simplicity, Huang's model⁴ is adopted to predict temperature distribution within the cross section of the composite slab. In this model, the thermal properties of concrete and steel are considered as temperature-dependent and the effects of moisture evaporation within the concrete are taken into account.

Thermal analyses show that, when an orthotropic slab is subjected to fire attack, the temperature within its continuous upper portion varies in the horizontal plane due to the presence of the ribs. The thinner part is subject to higher temperatures than the thicker part. The Cardington fire tests⁵ also show that the reinforcement temperature in the thinner portion is much higher than in the thicker portion. This issue should be taken into account in the development of orthotropic slab model to analyse ribbed slabs in fire.

In Eurocode 4⁶ (EC4), orthotropic slabs are treated as equivalent solid slabs with an effective depth (H_{eff}) and the steel decking is ignored in fire conditions. This method is not applicable to deep-deck slabs with rebar in the ribs. For these fire resistance is usually expressed in standard classes, ranging from 30 to 120 minutes (and beyond) in 30-minute intervals. Only exposure from below is considered, which in practical cases will always be decisive. These rules are highly empirical in nature, and lack a fundamental scientific basis⁷. As stated above, the presence of the rib makes orthotropic slabs different from flat ones in both thermal and structural behaviour.

A number of models have been developed for modelling of orthotropic composite slabs in fire. In the first phase of an ECSC research project⁷, a special-purpose model was developed for simulation of the mechanical behaviour of fire-exposed composite slabs. In order to obtain reasonable agreement between numerical and experimental results for the continuous decking slab, a full continuous horizontal crack separating the ribs from the concrete plane was assumed and explicitly taken into account. This was done simply by ignoring the contribution of the ribs and the steel decking to the stiffness.

Elghazouli and Izzuddin⁸ developed a model in which the composite slab was treated as an orthogonal elasto-plastic grillage of beam-column elements, and temperature variations were introduced across the two orthogonal cross-section directions as well as along the element length. The deflections were obtained from the integration of the orthogonal beam-column elements. The shortcoming of this model is that the realistic slab behaviour cannot be modelled properly in this way, since the effects of in-plane shear and Poisson's Ratio are ignored. Membrane action, which may cause a considerable reduction of displacements⁹ of slabs deforming in double-curvature due to two-way support conditions. Gillie *et al.*¹⁰ described a method of modelling composite floor slabs using a stress-resultant approach. A drawback of this method is that the model does not allow stresses to be output from the analysis.

In the University of Sheffield's software, *Vulcan*, an effective-stiffness model¹¹ was developed in which the orthotropic slab was treated as a solid slab with different orthogonal stiffnesses and layered temperatures which are uniformly distributed horizontally. The effective-stiffness factors obtained from cross-section bending stiffnesses at ambient

temperature are applied as constants to modify the material stiffness of the layered concrete slab throughout the fire stage. In fact, the effective-stiffness factors change at elevated temperatures, due to the degradation and failure of the materials. In Lim *et al.*'s model^{12,13}, the solid part of the ribbed slab was modelled as assembly of brick-like shell elements, and each individual rib was modelled using beam elements. It is obvious that a large number of elements are needed for modelling composite slabs of practical dimensions in this way, and computation is extremely expensive.

In this study a more robust procedure will be developed to model orthotropic slabs subject to fire conditions, taking into account more realistic temperature distributions.

2. NON-LINEAR PROCEDURE FOR MODELLING OF ORTHOTROPIC COMPOSITE SLABS

2.1 Orthotropic slab element

The software *Vulcan* has been developed at the University of Sheffield for three-dimensional analysis of composite and steel-framed buildings in fire. The program is based on a 3D non-linear finite element procedure in which a composite building is modelled as an assembly of beam-column, spring, shear connector and slab elements. The beam-column line element is three-noded, and its cross-section is divided into a matrix of segments to allow for variation of temperature, stress and strain through the cross-section¹⁴. Slabs are modelled using nine-noded layered plate elements based on Mindlin-Reissner theory, in which each layer can have different temperature and material properties⁹. Both material and geometric non-linearities are considered in beam-column and slab elements.

As shown in Fig. 1 the current orthotropic slab element is based on the previous beam and solid slab elements in *Vulcan*. The element is assembled from a solid slab element which represents the continuous upper portion of the profile and an equivalent special beam element which represents the ribbed lower portion. It is assumed that the reference axis of the beam element coincides with the mid-plane of the slab element. An equivalent width for the cross-section of this beam element is determined according to the cross-sectional dimensions of the ribbed slab, and it shares the 3 middle nodes of the solid slab element on the reference plane. The previous non-linear formulations of both the solid slab and beam elements are employed. The temperature of each layer of the slab element can vary between adjacent Gauss integration points. The cross-section of the beam element uses its segmented nature to represent different temperatures and materials within the ribs. In this model the beam element is used to represent a group of ribs of the composite slab, and hence the width of the beam element is an equivalent width calculated from the RWR and the width of the solid slab element. It is therefore reasonable to assume that the beam element has only uniaxial properties without torsional resistance.

The stiffness matrix of an orthotropic slab element \mathbf{K}_{orth} is assembled from the stiffness matrices of a nine-noded solid slab element \mathbf{K}_{slab} and a three-noded beam element \mathbf{K}_{beam} :

$$\mathbf{K}_{orth} = \mathbf{K}_{slab} + \mathbf{K}_{beam} \quad (1)$$

The internal forces of the orthotropic slab element \mathbf{F}_{orth} can be obtained from those of the solid slab element \mathbf{F}_{slab} and the equivalent beam element \mathbf{F}_{beam} as:

$$\mathbf{F}_{orth} = \mathbf{F}_{slab} + \mathbf{F}_{beam} \quad (2)$$

The detailed formulations of K_{slab} , K_{beam} , F_{slab} , and F_{beam} can be found in References 9 and 14.

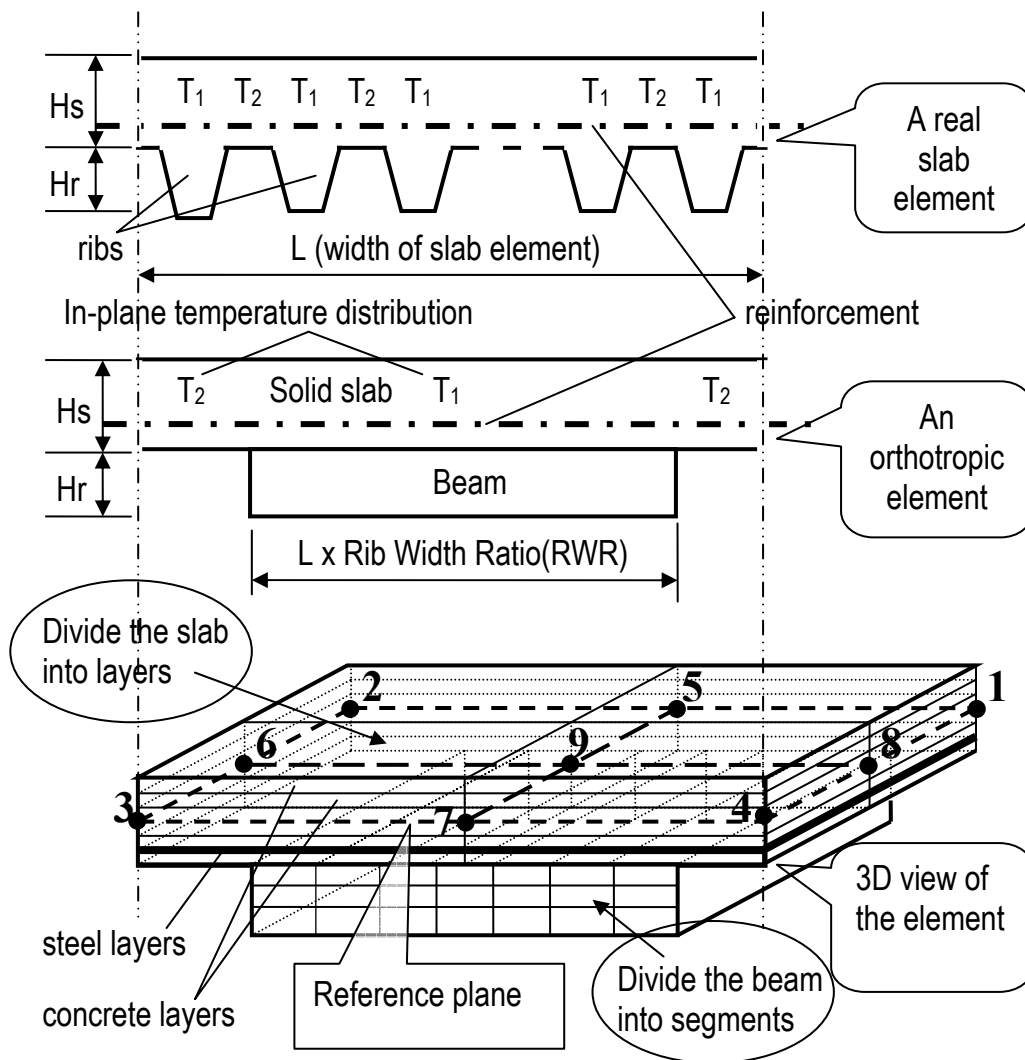


Fig. 1 - An orthotropic slab element model.

2.2 The simplified temperature distribution within each layer of the solid slab element

Due to the presence of the ribs, the temperature distribution within any layer of the solid slab element is non-uniform. In order to take into account this factor within the model a simplifying assumption was made; the temperatures within a layer are divided into three zones at the Gauss Integration Points (see Fig. 2). The higher temperatures at the axis of symmetry, Line 2, are applied to six Gauss Integration Points (1,2,3,7,8,9) and the cooler temperatures at the axis of symmetry, Line 1, are used for three Gauss Integration Points (4,5,6). The temperature distribution within the rib part at Line 2 is used to represent the temperature distribution of the cross-section of the beam element. This is a reasonable representation of the real temperature distribution within a ribbed slab. Hence, at each Gauss Integration Point, the material stiffness, strength, and thermal expansion is calculated according to the corresponding temperature.

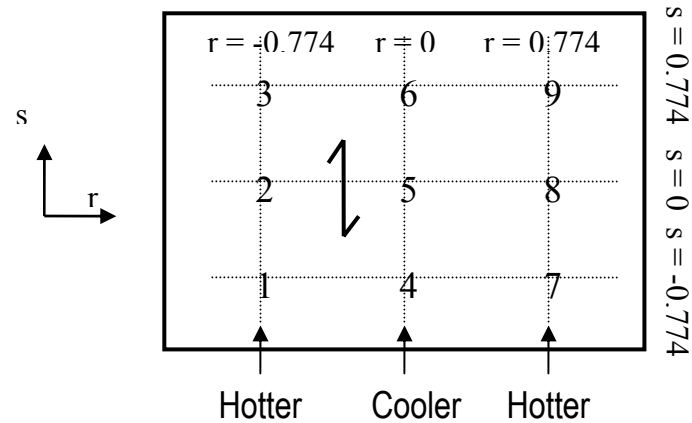


Fig. 2 – Temperature distribution at Gauss Integration Points within a layer of orthotropic slab element.

3. MODEL VALIDATION

3.1 Modelling of the TNO fire test

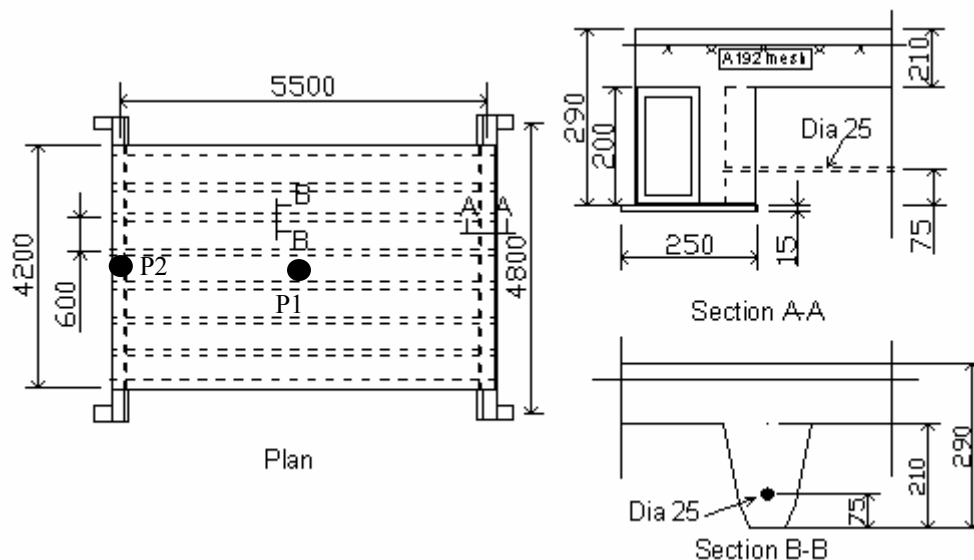


Fig. 3 - Details of TNO fire test.

A major fire test was carried out at TNO in the Netherlands in September 1996 as part of an ECSC research project¹. The specimen tested consisted of a single span of deep-deck normal-weight concrete slab with two RHS edge beams, simply supported at four corners. Fig. 3 shows the details of the test. The overall dimensions of the test specimen were 5.6m x 4.6m, with the edge beams spanning in the shorter direction. The overall depth of the slab was 290mm. The test load including self-weight was 6.65 kN/m^2 , a typical office building load intensity. The slab was unrestrained against thermal expansion, but the RHS edge beams were torsionally restrained at both ends. The edge beams were designed to achieve at least 60 minutes' fire resistance, and the composite slab was reinforced to achieve 120 minutes' fire resistance. In this numerical study, the tested material properties of structural steel, concrete and reinforcement were used. Further details are available from Reference 1. In order to

model the test, a thermal analysis was conducted to predict the temperature distributions within the cross-sections of the beams and ribbed slabs using *Vulcan*. The tested loads, and predicted temperature data were used in the structural modelling.

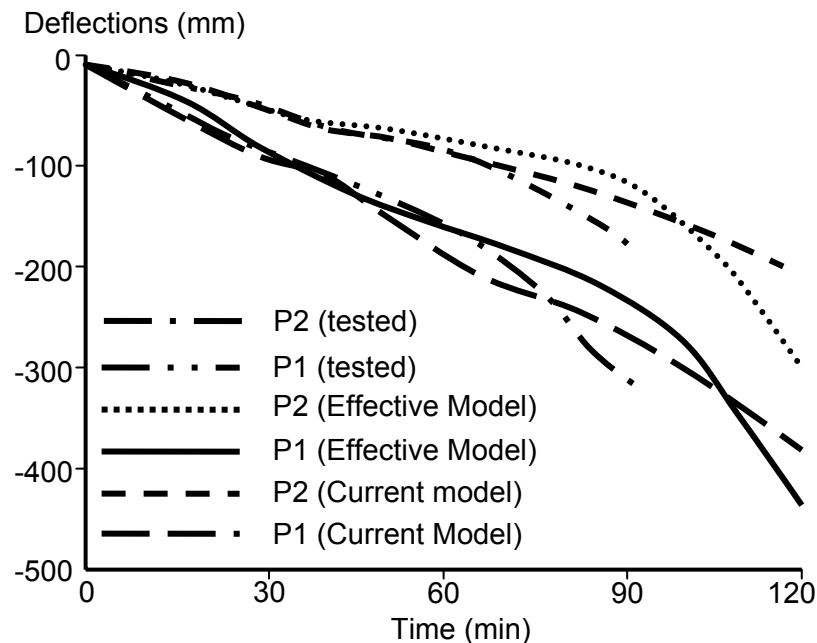


Fig. 4 - Comparison of predicted deflections with test results in TNO Fire Test.

Fig. 4 shows a comparison of predicted deflections using the current model and the previous effective-stiffness model at two key positions P1 and P2 (see Fig. 3), together with the test results. It can be seen that the curves predicted by the current model agree well with test results up to 70 minutes into the test. It is evident that the structural behaviour predicted by the two models differs.

3.2 Modelling the BRANZ fire test on a two-way simply supported decking slab

A series of full-scale fire tests conducted at the Cardington in the UK have shown that the fire resistance of unprotected composite floor structures is much better than standard furnace fire testing suggests. The composite concrete slabs may play an important role in increasing the fire resistance of the structure due to tensile membrane action, and so it is important to model the composite slabs correctly. Recently, six two-way simply supported concrete slabs were tested at the BRANZ fire test furnace in New Zealand. One of the tests, carried out on the 1st July 2002¹⁵, was on a Hibond orthotropic ribbed slab. The tested slab had the dimensions 4.3x3.3x0.130m, and was made of normal-weight concrete with 30MPa compressive strength. The slab was subject to a uniformly distributed live load of 3.0 kN/m^2 during the fire test.

The test was modelled as part of this study. The distribution of temperatures within the cross-section of the slab was predicted by *Vulcan*, and these temperatures were applied in the structural analysis.

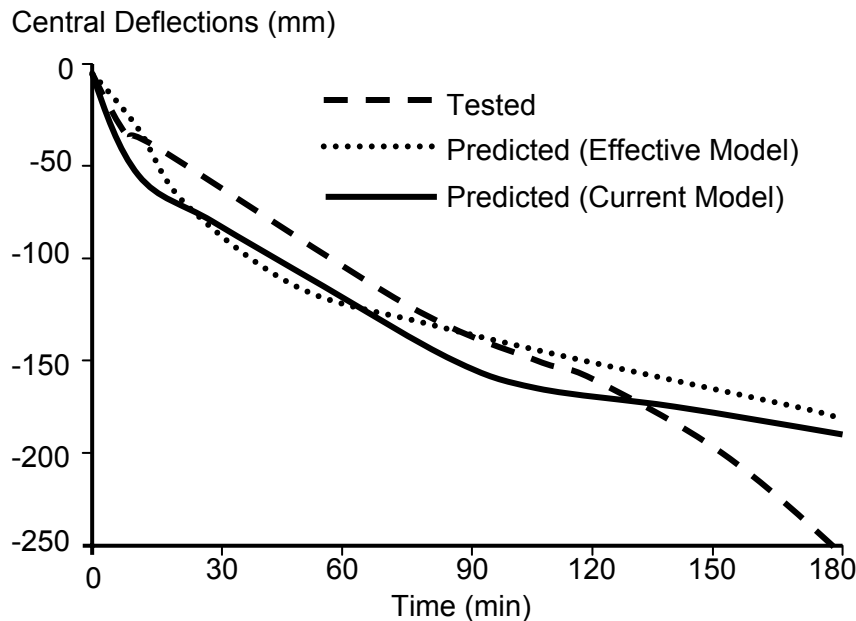


Fig. 5 – Comparison of predicted deflections with test results in BRANZ Fire Test.

Fig. 5 shows a comparison of central deflections predicted by the current orthotropic model and the effective stiffness model with test results. In the effective stiffness model the average temperature between the thinner and thicker parts was applied because the model assumed that each layer had uniform temperature distribution. Reasonable agreement was achieved by both models with the test results before 130 min test time. After that time the test deflections accelerated, but the predictions from both models were more stable. The reason for the difference between test and prediction may be due to the large cracks formed in the middle of test slab. The observations in the test¹⁵ support this: (a) Flames penetrated through the discrete crack in the middle of the slab in the later stage of the test; (b) Significant corner cracks formed during the test.

4. THE INFLUENCE OF RIB SHAPES OF ORTHOTROPIC SLABS IN FIRE

4.1 Decking shape parameters

Reference 7 lists a number of decking types with trapezoidal and re-entrant shapes. The different deckings were sorted and grouped according to the depth (H_r) and average width (L_0) dimensions of ribs. By considering the popularity and the rib width ratio (RWR) of existing deckings, the parameters of these groups were selected and are listed in Table 1.

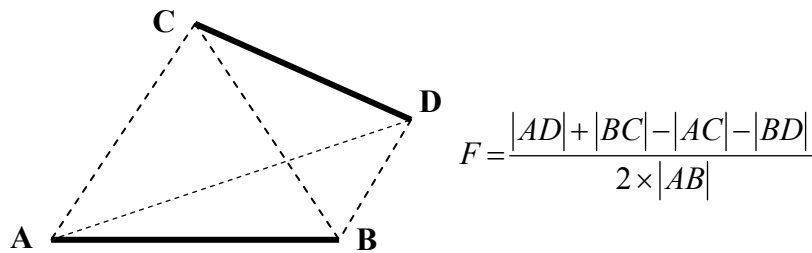
While an orthotropic slab is subjected to fire, the fire radiation which acts on the bottom surface of the decking differs with shape and distance. The view factor is used to quantify this relationship. In this study, a simplified model was adopted to address this factor:

(1). Unit view factor was assumed at bottom of the rib, as the reference level.

(2). The view factors at the top flange (ϕ_{tr}) and web (ϕ_{web}) of the indented surfaces of the slab were assumed to be uniform and determined according to Fig. 6. This approximation was developed by Wickstrom *et al.*¹⁶ in 1990 and accepted by Eurocode 4².

Table 1: Orthotropic slab deckings used in the parametric study

Groups	L(mm)	L ₀ (mm)	H _s (mm)	RWR	$\alpha(^{\circ})$					
					45	60	75	90	105	120
1	200	40	60	0.2	√	√	√	√		
2	200	60	40	0.3	√	√	√	√		
3	250	80	80	0.32	√	√	√	√		
4	200	120	40	0.6	√	√	√	√	√	√
5	200	120	60	0.6	√	√	√	√	√	√
6	250	175	60	0.7	√	√	√	√	√	√
7	300	210	40	0.7	√	√	√	√	√	√

Fig. 6 – Determination of view factor, F , in 2-dimensional cases (radiation from $|CD|$ to $|AB|$).

4.2 Influences of shapes of decking on the thermal and structural behaviours

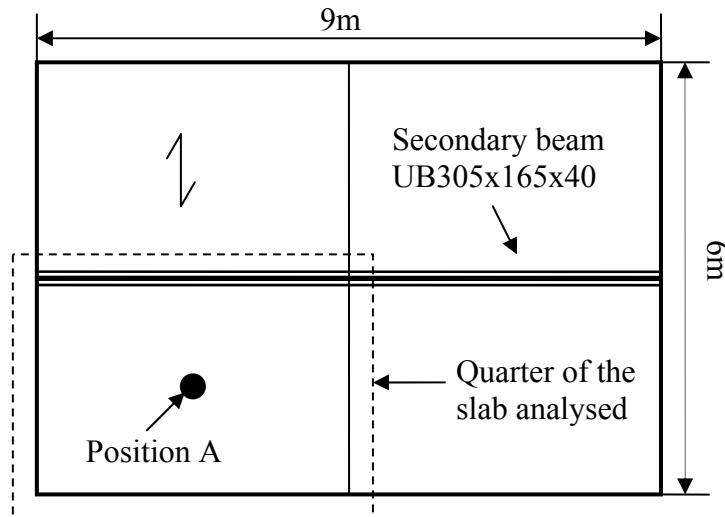


Fig. 7 – Two-way simply supported composite floor subject to ISO834 fire.

A two-way simply supported 9mx6m composite floor with a secondary beam in the middle of the shorter span (see Fig. 7) subject to an ISO834 fire was selected for this study. The secondary beam was assumed to be protected so that the bottom flange and web temperature linearly increased to 620°C at 180 minutes. Using the inherent symmetry only a quarter of the structure needed to be analysed. The thickness of the continuous thinner portion was 70mm. A142 mesh was located 20mm above the top flange of the decking. The uniformly distributed load was 5kN/mm². The compressive strengths of both the normal-weight concrete (NWC) and the light-weight concrete (LWC) at ambient temperature were

30N/mm². The study focused on the influence of the shape of the decking on the thermal and structural behaviour of the composite floor in fire.

The thermal analyses were conducted using *Vulcan*, again based on Huang's model⁴ and the structural behaviour was predicted by the new model. Eighty-six cases were modelled for both NWC and LWC in this study, including slabs treated as solid with nominal effective thicknesses obtained according to EC4.

Fig. 8 shows the temperature histories of the reinforcement in a typical group of profiled slabs (Group 6). Some general conclusions about the temperatures of reinforcement can be drawn from this study:

- For the slabs with $RWR \leq 0.32$ (Group 1-3), the shape of the rib has little influence on T_h , but considerably influences T_c . The greater the angle α , the lower T_c becomes. Deeper ribs (with greater H_r) also affect the influence of the angle α on T_c . For those with RWR over 0.6 (Group 4-7) the shape of rib does not influence T_c very much, especially when α is greater than 90°, but decreases T_h by over 100°C.
- After 180min of the ISO834 fire, for NWC slabs T_h is in the range 650°C-750°C and T_c in the range 450°C-650°C; for LWC slabs T_h is in the range 600°C-700°C and T_c in the range 350°C-650°C.
- If a profiled slab is treated as solid, with an effective thickness obtained according to EC4, the reinforcing mesh temperature is close to T_c . This gives the slab a better fire resistance than the real ribbed slab, especially in the later stages of the fire.

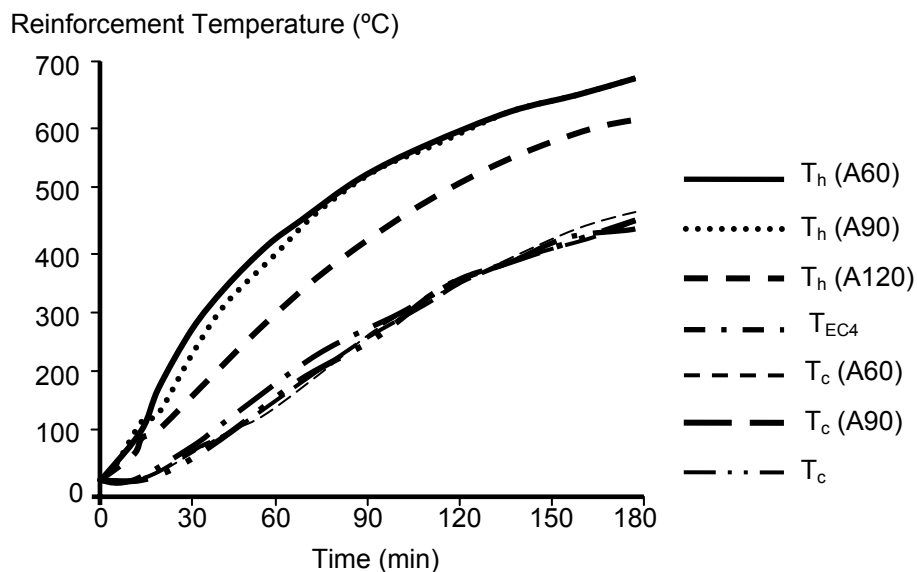


Fig. 8 - Reinforcement temperatures at thin and thick sections of the NWC slab (Group 6) in an ISO834 fire.

Fig. 9 shows the deflections at Position A (see Fig. 7) of the same group of profiled slabs. Some general conclusions concerning the structural behaviour of composite slabs in fire can be drawn, as follows:

- NWC slabs with $H_r \geq 80$ mm (Groups 3 and 7) or $RWR \geq 0.7$ (Groups 6 and 7) have better fire resistance than NWC slabs with $H_r < 80$ mm and $RWR \leq 0.6$ (Groups 1, 2, 4 and 5).
- LWC slabs have better fire performance compared to NWC slabs with the same compressive strength.

- Slabs with $\alpha = 90^\circ$ have higher deflection than those with other angles, for the same rib depth.
- For slabs with $RWR \geq 0.6$ (Groups 4-7), the shape has little influence on the deflection, except for those with $\alpha = 120^\circ$, which have the smallest deflection.
- Slabs with $H_r = 60\text{mm}$ show smaller deflection than those with H_r of 40mm and 80mm.
- For slabs with $RWR \leq 0.32$, there is a significant discrepancy in deflections between the orthotropic model and the equivalent solid slab with EC4 effective thickness.

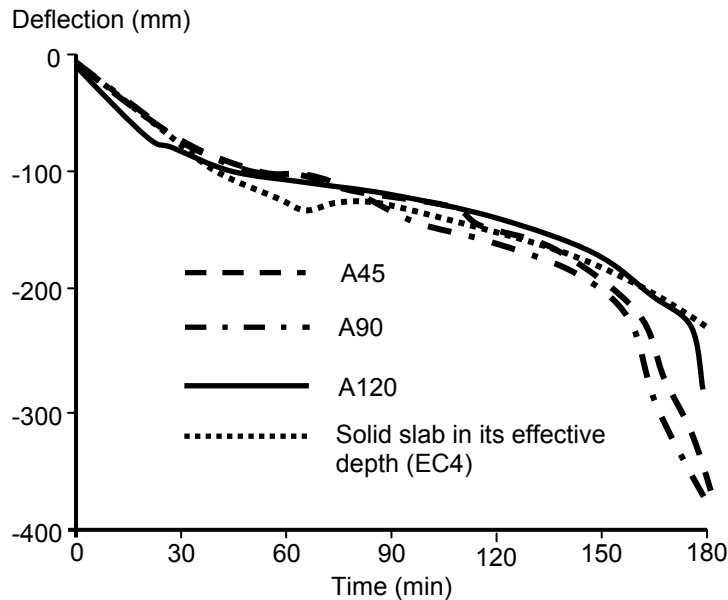


Fig. 9 – Deflections at Position A (see Fig. 6) of the NWC slab (Group 6) in the ISO834 fire.

5. CONCLUSIONS

In this paper the development of an orthotropic slab model to model ribbed slabs in fire has been described. The model is based on the slab and beam element formulations within the software *Vulcan* developed at the University of Sheffield. The two main new features of the model are:

- (1) The continuous top part of the ribbed slab is represented by solid slab elements, and the rib in the lower part is modelled as an equivalent beam element with uniaxial properties. Both the orthotropic character and membrane actions of ribbed slabs are taken into account in a logical manner. This approach also allows the modelling of deep-deck slabs.
- (2) The model allows non-uniform temperature distribution within each layer of the solid slab element. Hence, the temperature distribution across the cross-section of the profiled slabs can be represented more accurately. This overcomes the drawbacks of the previous effective-stiffness model, in which uniform average layer temperatures are used. In particular, better representation of reinforcement temperatures at the thin and thick sections of the cross-section of the ribbed slab is achieved by the current model.

A series of parametric studies using various decking shapes has been carried out. It shows that the current model can sensitively reflect the influence of shape on the thermal and structural behaviour. It also shows that the simplified method in EC4, which treats the orthotropic slab as an equivalent solid slab with an effective thickness, is not conservative

when RWR is around 0.3, especially at the later stages of the fire; however for LWC slabs with $RWR \geq 0.6$, the agreement is very good. This discrepancy in performance mainly derives from the thermal properties of concrete and the temperatures of the reinforcement, which are respectively hotter and cooler in the thinner and thicker portions of the slabs.

6. REFERENCES

- [1] Corus Construction Centre website: <http://www.corusconstruction.com>.
- [2] Bazant, Z.P. and Kaplan, M., “Concrete at High Temperatures”, ISBN 0-582-08626-4, Longman Group Limited, 1996.
- [3] Tenchev, R.T., Li, L.Y., Purkiss, J.A. and Khalafallah, B.H., “Finite element analysis of coupled heat and mass transfer in concrete when it is in a fire”, *Magazine of Concrete Research*, **53** (2), (2001) pp117-125.
- [4] Huang, Z., “The Analysis of Thermal And Fire Performance of Cementitious Building Components”, PhD thesis, University of Central Lancashire, 1995.
- [5] ECSC Project Report, “Behaviour of a Multi-Storey Steel-Framed Building Subject to Natural Fires”, Document Ref. : S423/2/Part T2, 1996.
- [6] Draft prEN1994-1-2: “Eurocode 4 - Design of composite steel and concrete structures”. Final Draft (Stage 34), 2003.
- [7] Both, C., “The Fire Resistance of Composite Steel-Concrete Slabs”, ISBN 90-407-1803-2-Y / CIP, Delft University Press, 1998.
- [8] Elghazouli, A.Y. and Izzuddin, B.A., “Analytical Assessment of the Structural Performance of Composite Floors Subject to Compartment Fires”, *Fire Safety Journal*, **36**, (2001) pp769-793.
- [9] Huang, Z., Burgess, I.W. and Plank, R.J., “Modelling Membrane Action of Concrete Slabs in Composite Buildings in Fire. Part I: Theoretical development”, *Journal of Structural Engineering, ASCE*, **129** (8), (2003) pp1093-1102.
- [10] Gillie, M., Usmani, A., Rotter, M. and O'Connor, M., “Modelling of Heated Composite Floor Slabs with Reference to the Cardington Experiments”, *Fire Safety Journal*, **36**, (2001) pp745-767.
- [11] Huang, Z., Burgess, I.W. and Plank, R.J., “Effective Stiffness Modelling of Composite Concrete Slabs in Fire”, *Engineering Structures*, **22**, (2000) pp. 1133-1144.
- [12] Lim, L.C.S., “Membrane Action in Fire Exposed Concrete Floor Systems”, PhD thesis, University of Canterbury, New Zealand, 2003.
- [13] Lim, L., Buchanan, A., Moss, P. and Franssen, J.M., “Numerical Modelling of Two-Way Reinforced Concrete Slabs in Fire”, *Engineering Structures*, **26**, (2004) pp1081-1091.
- [14] Huang, Z., Burgess, I.W. and Plank, R.J., “3D Modelling of Beam-Columns with General Cross-Sections in Fire”, *Paper S6-5, Third International Workshop on Structures in Fire, Ottawa, Canada*, pp323-334, 2004.
- [15] Lim, L.C.S. and Wade, C., “Experimental Fire Tests of Two-Way Concrete Slabs”, Fire Engineering Research Report 02/12, University of Canterbury, New Zealand, September 2002.
- [16] Wickström, U. and Sterner, E., “TASEF-Temperature Analysis of Structures Exposed to Fire-User's Manual”, Swedish National Testing Institute, SP Report 1990:05.



FIRE RESISTANCE OF HIGH-STRENGTH CONCRETE-FILLED STEEL COLUMNS

Peter SCHAUMANN¹, Venkatesh KODUR² and Oliver BAHR³

ABSTRACT

At ambient temperature, the load-bearing capacity of Hollow Structural Section steel columns can be improved by using high strength concrete as filling. However, it is difficult to predict the behavior of high strength concrete in case of fire because of complex phenomena like micro cracking and spalling. A numerical investigation with the computer program BoFIRE, verified by comparison to test data, was undertaken to investigate if the high strength concrete material properties given by the North American and European codes lead to a reliable prediction of the fire resistance period. Different types of high strength concrete-filling are considered. Furthermore, Eurocode 2 provides a simplified approach for the determination of the fire resistance period of concrete-filled Hollow Structural Section steel columns. Since it is restricted to normal strength concrete-filling, it is examined if the range of application can be extended to high strength concrete-filling.

1. INTRODUCTION

The filling of Hollow Structural Section (HSS) steel columns with high strength concrete (HSC) offers many advantages over traditional columns at room temperature. The enhanced load-bearing capacity allows minimized dimensions of the cross-section and hence more usable space in buildings. In contrast to this, the filling with HSC may cause problems at elevated temperatures in case of fire. Due to its reduced porosity, which is equal to small and less interconnected pores, HSC is sensitive to rising temperatures since water cannot evaporate. The build-up of steam-pressure may lead to micro cracks and spalling because of the low tensile strength of concrete. This results in a sharply reduced fire resistance period.

¹ Professor, University of Hannover, Institute for Steel Construction, Hannover, Germany,
email: schaumann@stahl.uni-hannover.de.

² Professor, Michigan State University, Department of Civil and Environmental Engineering, East Lansing, USA, email: kodur@egr.msu.edu.

³ Research Assistant, University of Hannover, Institute for Steel Construction, Hannover, Germany,
email: bahr@stahl.uni-hannover.de.

A numerical study is performed using the Finite Element-based computer program BoFIRE to investigate the behavior of HSS steel columns filled with HSC at elevated temperatures. The European¹ and North American^{2,3} code provisions for material properties and load computations are implemented in the computer program. The validity of the material properties is established by comparing predictions from the model with test data published in the literature. It included three different types of filling with plain HSC, steel fiber reinforced HSC and bar reinforced HSC.

2. TESTING PROGRAM

A review of literature indicates that there is very limited fire tests on HSC-filled HSS columns exposed to fire^{4,5}. The main objective of the reported tests was to determine the fire resistance of HSS steel columns filled with different types of HSC. The tests, that were undertaken on HSS columns, included plain HSC-filling (columns C-46 and C-47), HSC with steel fibers (columns C-36 and SQ-11) and HSC with 4×15 mm reinforcement bars (column SQ-14), and is presented in Figure 1. Full details of the fire tests are documented in references [4] and [5].

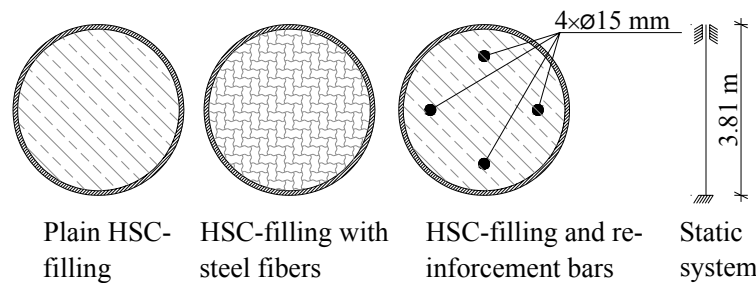


Fig. 1 – Cross-section and static system of circular HSC-filled HSS columns.

The tested HSS columns were 3.81 m long with fixed-fixed end conditions and filled with calcareous (limestone) HSC. After the load was applied, the columns were exposed to heating according to the Canadian code CAN/ULC-S101-M89⁶ until failure occurred. This fire is equivalent to ASTM E-119 or ISO-834 standard fire. The fire resistance period of some of the tested columns (selected from literature) is calculated with the computer program BoFIRE. This allows verification of material properties given by the North American and European codes. Moreover, it facilitates to study the influence of the concrete filling on the fire resistance. The material properties for steel fiber reinforced HSC-filling are taken according to the published data by Kodur & Sultan⁷, which is reproduced in the appendix. The test data of the different columns, taken from references^{4,5,17}, is summarized in Table 1, where the ‘C’ in the column denotes circular cross-section and ‘SQ’ square cross-section.

Tab. 1 – Summary of fire resistance test data on HSC-filled HSS columns^{4,5,17}.

Tube filling	Column	Cross-section	Test load in kN	Concrete strength in MPa	Fire resistance in minutes
Plain HSC	C-46	273.1 x 6.35	1,050	82.2	48
	C-47	273.1 x 6.35	1,050	107.0	51
Steel fibers	C-36	219.1 x 4.78	600	98.1	174
	SQ-11	203.2 x 6.35	900	99.5	128
Reinforcement bars	SQ-14	203.2 x 6.35	1,150	81.7	89

3. SIMPLIFIED APPROACH ACCORDING TO EUROCODE 2, PART 1-2¹

The Eurocode 4, part 1-2⁸ is relevant for the design of composite structures. However, this code only provides tabular data for the fire design of concrete-filled HSS columns. The corresponding annex also offers the possibility of computing the residual load-bearing capacity in case of fire. For this purpose it is necessary to determine the temperature field which is elaborate. Apart from these two methods, this code refers to the Eurocode 2, part 1-2¹ for fire design of concrete structures. Provided that the steel tube is neglected, it is allowed to use the so-called simplified Method A from the latter code. The advantage is that this method is based on a simple formula. However, the equation is restricted to normal strength concrete. A comparison of fire resistance predictions from the Eurocode equation with test results (see Table 1) is undertaken to investigate if the scope of application can be extended to HSC-filled HSS columns.

It should be noted that the studied columns C-46, C-47, C-36 and SQ-11 are not within the scope of application since a minimum of four reinforcement bars is required which they do not have. Therefore these columns were assumed to have four bars. Yet this does not result in higher fire endurance according to Method A. The concrete cover was set to 25 mm, leading to a negative impact on the fire resistance so that the result can be seen as conservative. As regards the columns SQ-11 and SQ-14, it has to be stated that the restriction of the parameter 'b' is not kept. Since the discrepancy is rather small, these columns were also examined with the simplified approach. The outcome of the investigation is presented in Figure 2.

With respect to the columns C-46 and C-47 with mere HSC-filling, the fire resistance period calculated by the simplified Method A is close to the corresponding test result. This is in as far astonishing as these columns do not provide the reinforcement bars which is a precondition for the use of the simplified approach.

For the HSS steel columns C-36 and SQ-11, with steel fiber reinforced concrete filling, the approach computes very conservative results, which is underlined by Figure 2. This can be attributed to the fact that Method A does only take conventional reinforcement into account, but not the beneficial effect of steel fibers. The result for the column SQ-14 with reinforcement bars is conservative, too.

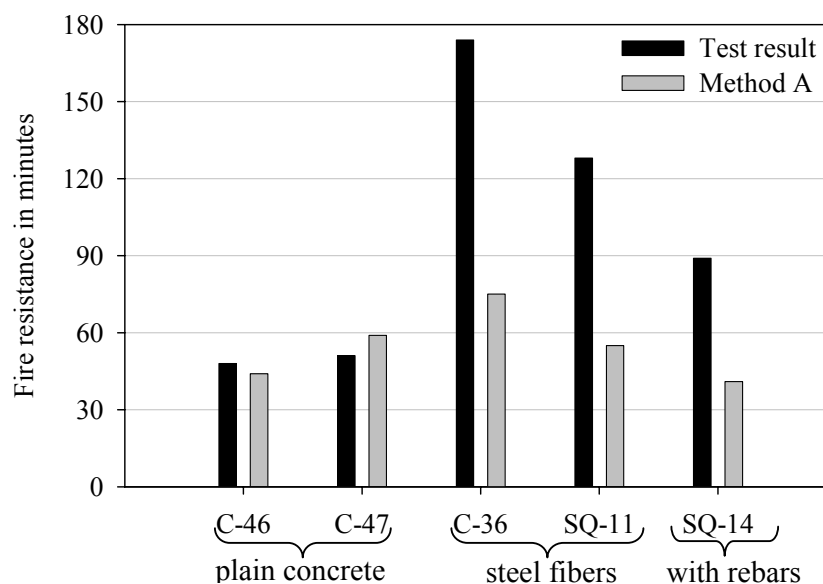


Fig. 2 – Comparison between tested and calculated fire resistance.

4. PRESENTATION OF THE USED FEM-PROGRAM BOFIRE

All parametric studies were carried out using the transient, non-linear, incremental computer code BoFIRE. This program was written by Schaumann⁹ and further developed by Upmeyer¹⁰ and Kettner¹¹. It is capable of predicting thermal and structural behavior of both steel and composite structures exposed to fire. The program is based on the following principle:

$$R(t) \geq S(t) \quad (1)$$

where $R(t)$ = resistance at time t ; $S(t)$ = effect of mechanical action at time of fire exposure t .

The load-bearing capacity of structures $R(t)$, which are charged by a mechanical load $S(t)$ while exposed to fire, depends on the modification of the material properties, such as decreasing of strength and elastic modulus affected by heat. Thus, the procedure for determining the remaining load-bearing capacity of structures is based on a numerical calculation model coupling the thermal and mechanical response at various time steps. At first, the thermal response takes place. In this stage, the fire temperature and the temperature distribution of the cross-section are computed. According to the temperature distribution, the modification of the material properties caused by temperature can be computed. Subsequently, the mechanical response is calculated where deformation and remaining strength of the members are determined. These results are compared to the applied load on the column and it is verified whether the structure still has sufficient load-bearing capacity. This procedure is repeated for various time steps until the resistance of the member is less than the applied load, which represents failure of the column. The duration to failure is taken as the fire resistance period of the column.

4.1 Thermal response

In BoFIRE, the temperature field is calculated using the Fourier differential equation for heat conduction:

$$-div(\lambda \times grad \theta) + c \times \rho \times \dot{\theta} - f = 0 \quad (2)$$

where λ = thermal conductivity; θ = temperature; c = heat capacity; ρ = density; $\dot{\theta}$ = derivation of temperature with respect to time; f = heat source.

Caused by the modifications of material properties due to heat exposure, the differential equation becomes transient since the temperature field gets inhomogeneous. Thus, that equation has to be solved numerically. In the following, the basis of that method will be described according to Kettner¹¹. A mathematical transformation of Equation (2) results in the weak formulation of the differential equation:

$$\int_{\Omega} \lambda \times grad \theta : grad \delta \theta dA + \int_{\Gamma} q \times \delta \theta \times n dS + \int_{\Omega} \rho \times c \times \dot{\theta} \times \delta \theta dA = 0 \quad (3)$$

where A = area; Γ = boundary of considered area; q = heat flux; n = normal vector on the boundary.

For the solution of the weak form, bi-linear shape functions on a four node isoparametric element according to Equation (4) are used.

$$N_i = \frac{1}{4} \times (1 \pm \eta) \times (1 \pm \xi) \quad (4)$$

The approach is presented on the left side of Figure 3. An example for mesh generation with BoFIRE is shown at the right side of Figure 3. Moreover, the computer program BoFIRE also recognizes different material properties as a function of temperature including that of fire protection materials.

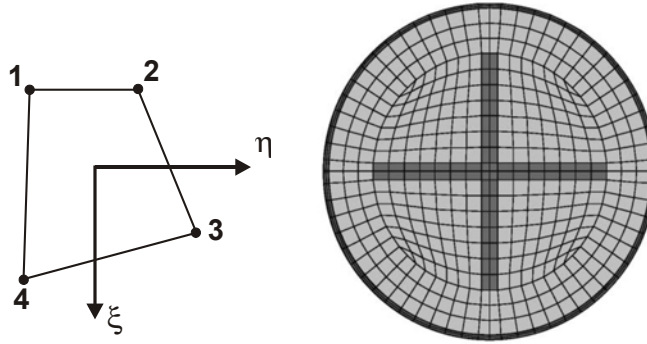


Fig. 3 – Four node isoparametric element (left) and mesh for a concrete-filled HSS column with embedded X-shape profile (right).

4.2 Mechanical response

It is possible to calculate all types of cross-sections and linear structures as beams, columns or plane frames taking second order theory into account. The calculation is based on the Bernoulli hypothesis for plain state of strains. Shear deformations are not considered. Due to the nonlinear material properties, cross-sectional values and internal forces depend on the temperature field and strains into the cross-section. The strains are calculated by the balance of internal and external forces. The solution of the incremental system equation is given by Schaumann⁹:

$$\Delta \underline{S}_L - \Delta \underline{S}_{th} = (\underline{K}_t^I - \underline{K}_{t0}^I) \times \underline{v}_{t0} + \Delta \underline{K}^{II} \times \underline{v}_{t0} + (\underline{K}_t^I + \underline{K}_t^{II}) \times \Delta \underline{v} \quad (5)$$

where \underline{S}_L = difference between external forces per time increment; \underline{S}_{th} = difference between thermal strains per time increment; $(\underline{K}_t^I - \underline{K}_{t0}^I) \times \underline{v}_{t0}$ = difference of system matrix stiffness (elastic portion); $\underline{K}^{II} \times \underline{v}_{t0}$ = difference of system matrix stiffness (geometric portion according to second order theory); $(\underline{K}_t^I + \underline{K}_t^{II}) \times \underline{v}$ = difference of deformations per time increment.

At first, the internal force variables and deformations caused by the external forces \underline{S}_L are computed in one or more increments. In a parallel calculation the temperature field is established as previously described. Because of the incremental procedure it is possible to linearize the influence of non-linear material behavior and temperature distribution.

5. COMPARISON BETWEEN TESTED AND COMPUTED FIRE RESISTANCE

The tested and calculated fire resistance period of the different columns can be seen in Figure 4. A moisture content of 10% was considered in the computer program BoFIRE. Regarding the numerical results for HSS columns filled with plain HSC it is obvious that the fire resistance is overestimated to a great extent. This is true for both the North American and the European HSC material properties. With respect to the circular HSS columns C-46 and C-47 it is obvious that the gap between the tested and calculated fire endurance becomes greater with increasing concrete compressive strength. However, the results for both numerical models are conservative for HSC-fillings with additional steel fibers (columns C-36 and SQ-11) and reinforcement bars (column SQ-14).

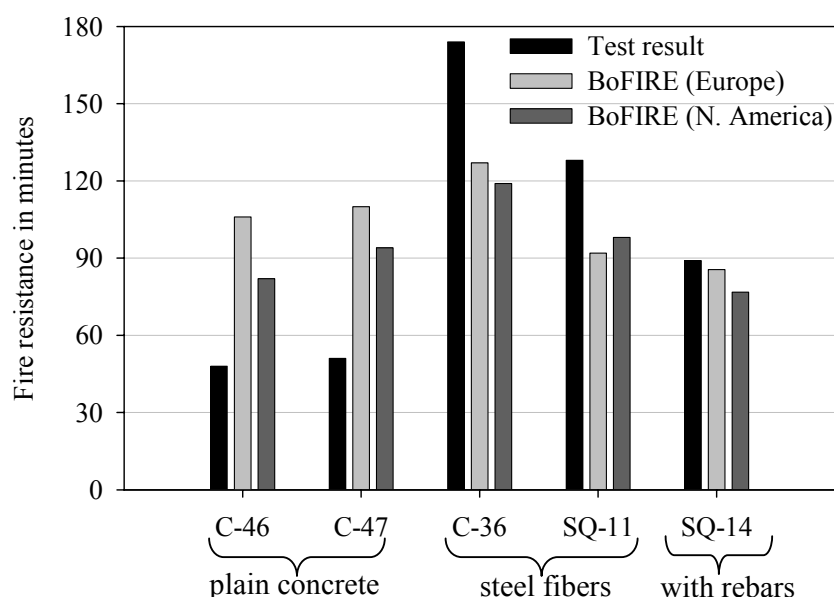


Fig. 4 – Comparison between tested and calculated fire resistance.

The divergence between computed and recorded fire resistance period for mere HSC-filling is attributed to local failure of the columns. Due to cracking of the concrete, the cross-sectional load-bearing capacity is significantly decreased, which causes failure. As the program BoFIRE does not take such effects into account, it might be reasonable to establish a three-dimensional model for this problem in future. Nevertheless, by comparison to the recorded test data it is examined if the distribution of temperatures derived from the computer program BoFIRE is sufficient.

For this purpose, the points at which temperatures are measured in BoFIRE are arranged according to the location of the test thermocouples. At the example of column C-46 with plain HSC-filling, the measured and calculated temperatures according to the HSC material properties defined in the Eurocode 2, part 1-2¹ are presented in Figure 5. A moisture content of 10% of the concrete weight is taken. The comparison ends after 48 minutes since the column fails. Concerning measure point MP 2, the resulting BoFIRE temperatures stand in good agreement with the recorded temperatures. As regards MP 1 in the center of the column, a maximum difference between computed and measured temperatures of approximately 29°C has to be noticed. However, these slight differences cannot be seen as the reason for the high overestimation of the fire resistance of the HSS steel columns with mere HSC-filling.

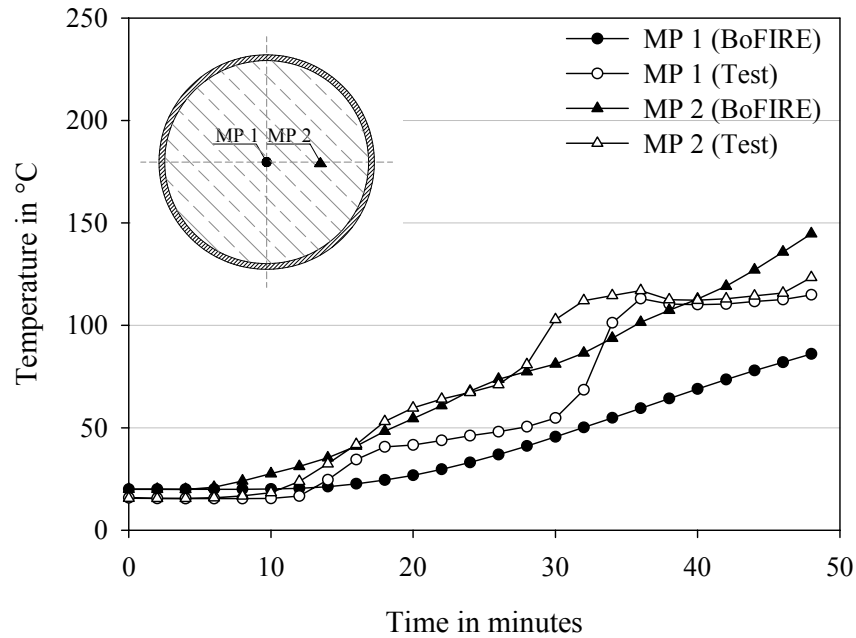


Fig. 5 – Recorded and calculated temperatures for column C-46 according to material properties defined in Eurocode 2, part 1-2¹.

Moreover, it is interesting to study the influence of the moisture content u on the temperature field and the fire resistance period. It is evident from Figure 6 that the computed temperatures for MP 1 decrease with an increasing moisture content u . The difference between ratios of $u=0\%$ and $u=10\%$ already totals to about 120°C after 48 minutes and hence influences the fire resistance period. For example, the fire resistance periods for $u=0\%$ and $u=10\%$ are 89 minutes and 110 minutes, respectively. The results for the moisture content of $u=10\%$ stand in best accordance with the measured temperatures.

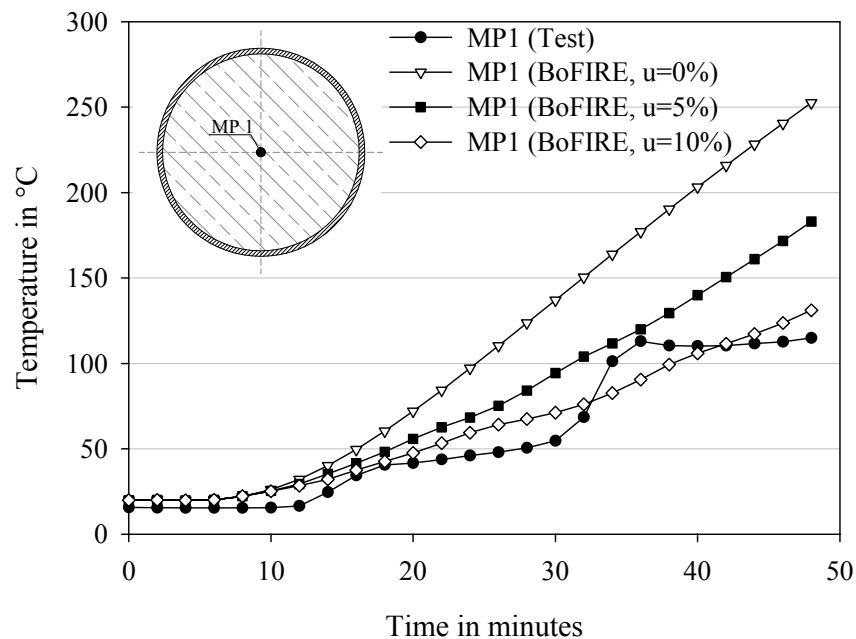


Fig. 6 – Recorded and calculated temperatures for column C-46 with varying moisture content u (calculated with material properties defined in Eurocode 2, part 1-2¹).

For a comparison between the European and North American material properties, the computed temperatures for column SQ-14 (reinforced with bars) are presented in Figures 7 and 8. It becomes clear that the use of the European material properties leads to more realistic cross-sectional temperatures for this example. In addition, the prediction of the fire resistance period stands in very good accordance with the real fire endurance.

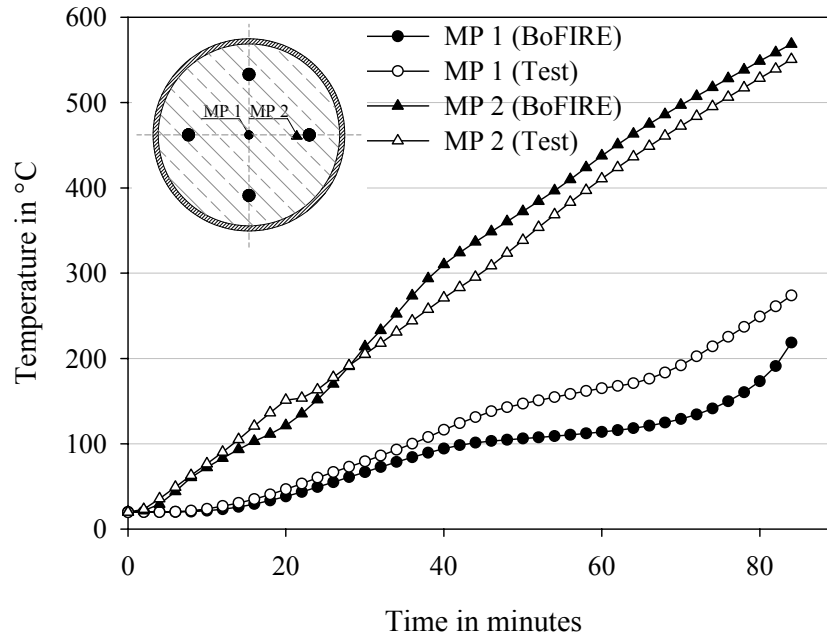


Fig. 7 – Recorded and calculated temperatures for column SQ-14 according to material properties defined in Eurocode 2, part 1-2¹.

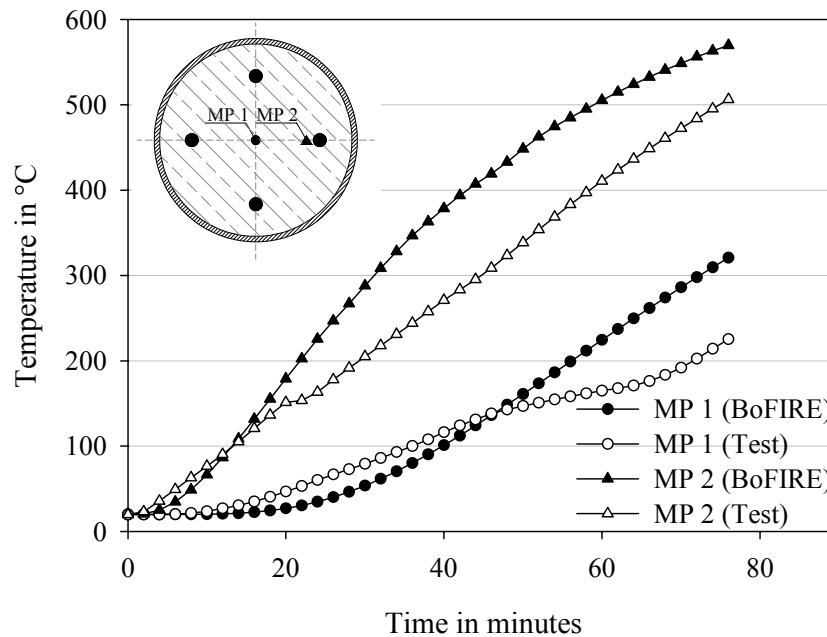


Fig. 8 – Recorded and calculated temperatures for column SQ-14 according to North American material properties^{2,3}.

On the whole, it can be concluded that the calculation of the temperature field with the program BoFIRE is appropriate. Therefore the great difference between tested and computed fire resistance period of plain HSC-filling must be due to micro cracking (which leads to faster loss of strength with temperature) and to spalling. To clarify this question, a comparison of the tested axial deformations between the column with plain HSC-filling C-46, the bar reinforced HSS steel column SQ-14 and the fiber reinforced column SQ-11 is drawn in Figure 9.

Apparently, the general load-bearing behavior is the same for these columns: In the early stages of fire exposure, the load share of the steel part increases significantly since it expands faster than the concrete core. After approximately 20 minutes, the load has to be carried by the concrete core in order of the decreased yield strength of the steel part leading to contraction of the whole column and finally to failure⁴. As it can be seen in Figure 9, the type of concrete-filling influences the contraction phase. The decline is more gradual for both reinforced columns, namely SQ-11 and SQ-14, whereas the failure occurs suddenly for column C-46 with plain HSC-filling. The latter is due to the missing reinforcement resulting in cracks in the concrete core in the local buckling zone. In case of load eccentricities, the load cannot be carried any more¹².

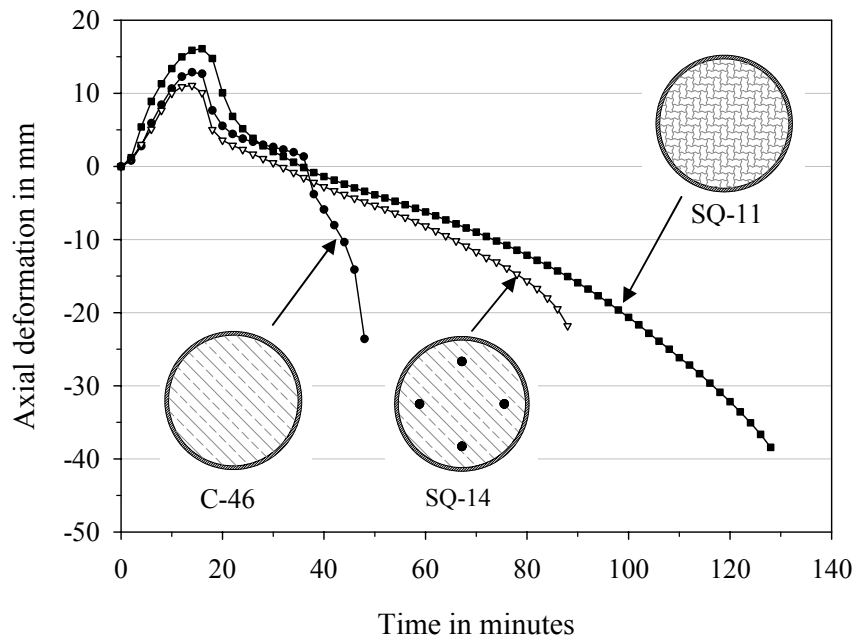


Fig. 9 – Axial deformations recorded in test for specimens C-46, SQ-11 and SQ-14.

Apart from the former investigation, the results of the numerical simulation with the program BoFIRE are also compared to the results derived from the simplified Method A. It is clear that the latter is in particular advantageous for HSS steel columns with mere HSC-filling, given by the specimens C-46 and C-47, as the results stand in far better accordance with the test results than the results calculated with BoFIRE. Contrary to this, the BoFIRE results are more realistic for the other specimens with steel fibers (columns C-36 and SQ-11) and reinforcement bars (column SQ-14).

6. CONCLUSIONS

The temperature field established on the basis of implemented material properties can be seen as sufficient. However, the carried out investigations show that current North American and European material properties are not reliable in predicting the fire resistance period of HSS columns with mere HSC-filling. The divergence between computed and tested fire resistance can be attributed to cross-sectional failure resulting from micro cracks and spalling. The use of additional steel fibers or reinforcement bars significantly reduces these phenomena, which results in conservative computation of the fire endurance with the computer program BoFIRE.

Investigations on the simplified Method A provided by the advanced Eurocode 2, part 1-2¹ show that the scope of application might be extended to HSC. In addition, it could be worthwhile to take the beneficial effect of HSC-filling with steel fibers into account to gain a more realistic prediction of the fire resistance period. Nevertheless, the investigation is based on a limited number of cross-sections and should be extended to other testing programs. As it is difficult and elaborate to consider phenomena like spalling in numerical programs, simplified approaches like Method A are in particular interesting for HSS steel columns with mere HSC-filling. Based on further fire tests and numerical studies, Method A would provide an efficient and economic engineering device for calculating the fire resistance period.

7. REFERENCES

- [1] European Committee for Standardization (CEN), prEN 1992-1-2 (Eurocode 2), “Design of concrete structures, Part 1-2: General rules – Structural fire design”, 2002.
- [2] Canadian Standards Association, “Code for the Design of Concrete Structures for Buildings (CAN3-A23.3-M94)”, Rexdale, 1994.
- [3] Canadian Standards Association, “Limit States Design of Steel Structures (CAN/CSA-S16-01)”, 2001.
- [4] Kodur, V.K.R., “Performance of high strength concrete-filled steel columns exposed to fire”, Canadian Journal of Civil Engineering 25, pp. 975–981, 1998.
- [5] Lie, T.T. and Kodur, V.K.R., “Fire resistance of steel columns filled with bar-reinforced concrete”, Journal of Structural Engineering 122(1), pp. 30-36, 1996.
- [6] Canadian Standards Association, “Standard Methods of Fire Endurance Tests of Building Construction and Materials (CAN/ULC-S101-M89)”, 1989.
- [7] Kodur, V.K.R. and Sultan, M.A., “Effect of temperature on thermal properties of high-strength concrete”, Journal of Materials in Civil Engineering 15(2), pp. 101-107, 2003.
- [8] European Committee for Standardization (CEN), prEN 1994-1-2 (Eurocode 4), “Design of composite steel and concrete structures, Part 1-2: General rules – Structural fire design”, 2004.
- [9] Schaumann, Peter, “Computation of steel members and frames exposed to fire” (in German: “Zur Berechnung stählerner Bauteile und Rahmentragwerke unter Brandbeanspruchung”), Technisch-wissenschaftliche Mitteilungen Nr. 84-4, Institut für konstruktiven Ingenieurbau, Ruhr-Universität Bochum, Germany, 1984.
- [10] Upmeyer, Jens, “Fire design of partially encased composite columns by ultimate fire loads” (in German: “Nachweis der Brandsicherheit von kammerbetonierten Verbundbauteilen über Grenzbrandlasten”), Institute for Steel Construction, University of Hannover, Issue 19, 2001.

- [11] Kettner, Florian, “Investigations on the load-bearing behavior of composite columns under fire conditions”, Institute for Steel Construction, University of Hannover, 2005 (<http://www.stahlbau.uni-hannover.de/en/veroeffentlichungen> → publications → 2005).
- [12] Kordina, Karl and Klingsch, Wolfram, “Fire resistance of composite columns and of solid steel columns – part I”, Studiengesellschaft für Anwendungstechnik von Eisen und Stahl e.V., Project 35, 1983.
- [13] Cheng, F.-P., Kodur, V.K.R. and Wang, T.-C., “Stress-strain curves for high strength concrete at elevated temperatures”, Journal of Materials in Civil Engineering 16(1), pp. 84-94, 2004.
- [14] Kodur, V.K.R. and Lie, T.T, “Fire performance of concrete-filled hollow steel columns”, Journal of Fire Protection Engineering 7(3), pp. 89-98, 1995.
- [15] Kodur, V.K.R. and McGrath, R., “Fire endurance of high strength concrete columns”, Fire Technology 39(1), pp. 73-87, 2003.
- [16] Kodur, V.K.R., “Fire resistance design guidelines for high strength concrete columns”, ASCE/SFPE Specialty Conference of Designing Structures for Fire, Baltimore, 2003.
- [17] Kodur, V.K.R., “Solutions for enhancing the fire endurance of steel HSS columns filled with high strength concrete”, in Press, AISC Steel Construction Journal, pp. 1-22, 2006.

8. APPENDIX

The following formulae describe the material behavior of HSC with steel fibers at elevated temperatures according to Kodur & Sultan⁷ and are referred to as North American material models, for HSC, in the main text:

8.1 Stress-strain relationship

$$f_c = f'_c \times \left[1 - \left(\frac{\epsilon_{\max} - \epsilon_c}{\epsilon_{\max}} \right)^H \right] \quad \text{for: } \epsilon_c \leq \epsilon_{c,\max}$$

$$f_c = f'_c \times \left[1 - \left(\frac{30 \times (\epsilon_{\max} - \epsilon_c)}{(130 - f'_{c0}) \times \epsilon_{\max}} \right)^2 \right] \quad \text{for: } \epsilon_c > \epsilon_{c,\max}$$

Where:

$$H = 2.28 - 0.012 \times f'_{c0}$$

$$\epsilon_{\max} = 0.0018 + (6.7 \times f'_{c0} + 6 \times \theta + 0.03 \times \theta^2) \times 10^{-6}$$

And:

$$f'_c = f'_{c0} \times (1.0625 - 0.003125 \times (\theta - 20)) \quad \text{for: } \theta < 100^\circ\text{C}$$

$$f'_c = 0.75 \times f'_{c0} \quad \text{for: } 100 \leq \theta < 400^\circ\text{C}$$

$$f'_c = f'_{c0} \times (1.33 - 0.00145 \times \theta) \quad \text{for: } \theta \geq 400^\circ\text{C}$$

Such that:

$$0 \leq f'_c \leq f'_{c0}$$

Unit: MPa

8.2 Thermal capacity

The specific heat is the product of thermal capacity and density. A value of 2,535 kg/m³ is assumed for the density of HSC with calcareous aggregates.

$\rho_c \times c_p(\theta) = 3.81 \times 10^6$	for $0^\circ\text{C} \leq \theta \leq 400^\circ\text{C}$
$\rho_c \times c_p(\theta) = (-0.0165 \times \theta + 10.41) \times 10^6$	for $400^\circ\text{C} < \theta \leq 475^\circ\text{C}$
$\rho_c \times c_p(\theta) = (0.0079 \times \theta - 1.182) \times 10^6$	for $475^\circ\text{C} < \theta \leq 625^\circ\text{C}$
$\rho_c \times c_p(\theta) = (0.2333 \times \theta - 142.06) \times 10^6$	for $625^\circ\text{C} < \theta \leq 700^\circ\text{C}$
$\rho_c \times c_p(\theta) = (-0.1800 \times \theta + 147.25) \times 10^6$	for $700^\circ\text{C} < \theta \leq 800^\circ\text{C}$
$\rho_c \times c_p(\theta) = 3.25 \times 10^6$	for $800^\circ\text{C} < \theta \leq 1000^\circ\text{C}$

8.3 Thermal conductivity

$\lambda_c = 1.80 - 0.0016 \times \theta_c$	for $0^\circ\text{C} \leq \theta \leq 500^\circ\text{C}$
$\lambda_c = 1.20 - 0.0004 \times \theta_c$	for $500^\circ\text{C} < \theta \leq 1000^\circ\text{C}$

8.4 Thermal elongation

$\varepsilon_c(\theta) = -2.00 \times 10^{-4} + 9 \times 10^{-6} \times \theta$	for $0^\circ\text{C} \leq \theta \leq 700^\circ\text{C}$
$\varepsilon_c(\theta) = -3.45 \times 10^{-2} + 58 \times 10^{-6} \times \theta$	for $700^\circ\text{C} < \theta \leq 870^\circ\text{C}$
$\varepsilon_c(\theta) = 1.60 \times 10^{-2}$	for $870^\circ\text{C} < \theta \leq 1000^\circ\text{C}$

8.5 Variation of density

$\rho(\theta)/\rho(20^\circ\text{C}) = 1.003 - 6 \times 10^{-5} \times \theta$	for $0^\circ\text{C} \leq \theta \leq 700^\circ\text{C}$
$\rho(\theta)/\rho(20^\circ\text{C}) = 2.214 - 1.79 \times 10^{-3} \times \theta$	for $700^\circ\text{C} < \theta \leq 785^\circ\text{C}$
$\rho(\theta)/\rho(20^\circ\text{C}) = 0.817 - 1.00 \times 10^{-5} \times \theta$	for $785^\circ\text{C} < \theta \leq 1000^\circ\text{C}$



NUMERICAL MODELLING OF LATERAL TORSIONAL BUCKLING FOR PARTIALLY ENCASED STEEL BEAMS AT ELEVATED TEMPERATURES

P.A.G. PILOTO¹; L.M.R MESQUITA² and Ana Ramos GAVILÁN³

ABSTRACT

Partially encased beams are composed structural elements widely used for industrial and commercial buildings with increasing significance. Composite beams may be designed for service load conditions without the collaborative contribution of slabs. Instability problems may occur because concrete may not have the age to resist and also because the concrete may slip over steel, crack or crush. Lateral torsional buckling is an instability phenomenon that may occur in these situations.

This paper presents a material and geometric non linear finite element model for determining lateral torsional buckling resistance of partially encased beam without encasement reinforcement in fire conditions. The steel part of the composed section will be modelled by finite shell element, concrete part by three dimensional finite solid elements and the bond contact with finite non linear spring elements, from Ansys. Elevated temperatures will be applied in both four sides of the cross section along the beam, based on the ISO834 standard fire curve.

Failure of concrete will also be predicted when subjecting partially encased beams to fire conditions.

1. INTRODUCTION

Steel beam with partial encasement represents a composite section with two different materials, with distinct mechanical behaviour, being usually used in construction for increasing fire resistance, see figure 1.

¹ Coordinator Prof., Polytechnic Institute Bragança, Dep. Applied Mechanics, 5300 Bragança, Portugal,
e-mail: ppiloto@ipb.pt

² Research Assistant, Polytechnic Institute Bragança, Dep. Applied Mechanics, 5300 Bragança, Portugal,
e-mail: lmesquita@ipb.pt

³ Research Assistant, EPSZ – University of Salamanca, Dep. of Mechanics, 49022 Zamora, Spain,
e-mail: aramos@usal.es

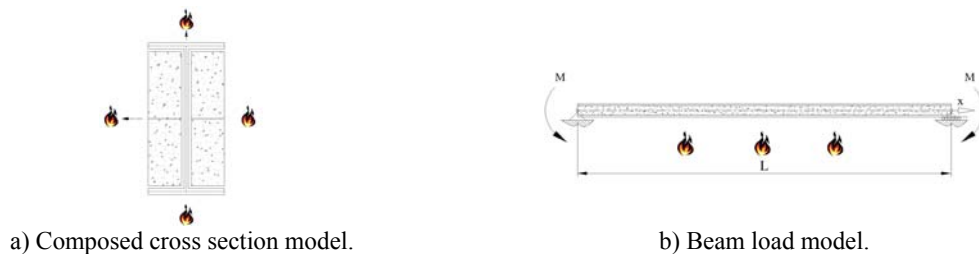


Fig. 1 – Partially encased steel beam with concrete.

Concrete slabs may not transmit the stabilizing effect to prevent lateral torsional buckling (LTB) of partially encased beams. Also, concreting the steel beam within 7 or 8 days provides less torsional stiffness than after 28 days ^[1]. This instability phenomenon is responsible for a simultaneous lateral displacement and cross-section rotation. This means that bending around the minor axis and torsion about the longitudinal axis of the element are involved.

Experimental tests conducted at room temperature were presented by the Technical University of Berlin ^[2] and other experimental and numerical results were presented during the European research project for technical steel research, at CTICM and LABEIN ^[3]. This work intends to be the preliminary phase of a full scale test program in fire conditions, complemented with numerical research and intends to deal with the interaction between concrete and steel, finding failure of concrete that may occur during instability, in these conditions.

Non linear numerical results of partially encased concrete beams at room temperature and in fire conditions will be presented for the case of uniform bending load, see figure 1.

Incremental mechanical load will be applied at room temperature conditions to determine design buckling resistance.

A transient non-linear thermal analysis will be subsequently followed by a non linear static analysis to address the ultimate limit state. Beams will be subjected to constant mechanical load (50% of the plastic resistant moment) in fire conditions.

2. LATERAL TORSIONAL BUCKLING (LTB)

Accidental fire conditions reduce the load bearing capacity and increase the risk of failure by lateral instability. The partial concrete protection may not be sufficient to provide stabilizing effect during the increase of steel temperature. Ultimate LTB resistance must be checked in the designing phase in order to get the assurance that structures are appropriately safe and resistant with regard to accidental loading conditions.

2.1 Critical moment

The ideal behaviour of a perfectly straight simply supported beam with perfectly elastic material behaviour, subjected to bending about major axis and prone to LTB is characterized with elastic critical moment (M_{cr}). This value corresponds to the load level at equilibrium bifurcation ^[3].

For LTB, the critical moment may be determined assuming the validity of the elastic theory (energy method) and some assumptions regarding the concrete strength contribution. Torsion constant and the moment of inertia may be calculated for the composed section based

on the characteristic values of steel part and based on the reduced characteristic values of concrete part, as represented in the next expressions ^[2].

$$\begin{aligned} J &= J_a + J_{c,red} \\ I_z &= I_{za} + I_{zc,red} \end{aligned} \quad (1)$$

where J and I_z represent the torsion constant and the moment of inertia of the composed section. $J_{c,red}$ and $I_{zc,red}$ represent the reduced torsion constant and the reduced moment of inertia of concrete, while J_a and I_{za} represent the torsion constant and the moment of inertia of steel. The concrete part is accounted for by reducing this part to an equivalent steel part, $J_{c,red}$ and $I_{zc,red}$, using equation 2.

$$\begin{aligned} I_{zc,red} &= I_{zc} E_c / E_a \\ J_{c,red} &= J_c G_c / G_a \end{aligned} \quad (2)$$

Taking into consideration only the compressive part of concrete, see figure 2, both geometric properties may be determined according to the plastic compressive zone, defined by e_{pl} .

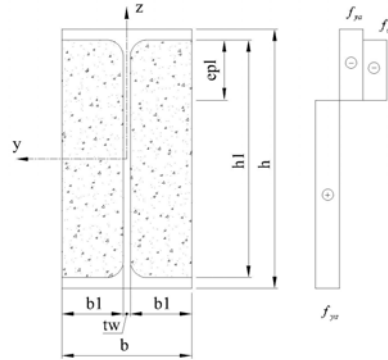


Fig. 2 – Notation for material plastic section.

$$e_{pl} = \frac{2f_{ya} t_w h_l / 2}{2f_{ya} t_w + 2b_l \beta_R} \quad (3)$$

where f_{ya} and β_R represent the design strength of steel and concrete.

The geometric properties of concrete may be determined according to the previous expression.

$$\begin{aligned} \alpha &= [1 - 0.63 e_{pl} / (b - t_w)] / 3 \\ J_c &= (b - t_w) e_{pl}^3 \alpha \\ I_{z,c} &= e_{pl} (b - t_w)^3 / 12 \end{aligned} \quad (4)$$

Assuming constant stiffness values along the beam length, considering the influence of the warping restrain small, the influence of moments of inertia much smaller than the

influence of torsion constant, assumptions may be used to calculate the critical moment. The warping constant of the concrete part is neglected and a symmetric section may be considered [2].

Flexural and torsional stiffness are determined in accordance to the previous equations. Critical moment may be determined taking into account the loading conditions, the moment distribution and the lateral restraints. For uniform bending moment and simple supported beams the critical moment is defined by equation (5).

$$M_{cr} = \frac{\pi}{L} \sqrt{(EI_z) \left(GJ + \frac{\pi^2 EI_w}{L^2} \right)} \quad (5)$$

2.2 Plastic moment

The full plastic moment is well known for the case of steel beams. For partially encased beams only the plastic compression zone of concrete will be considered, in accordance to the represented model to determine plastic moment without rebar reinforcement [2].

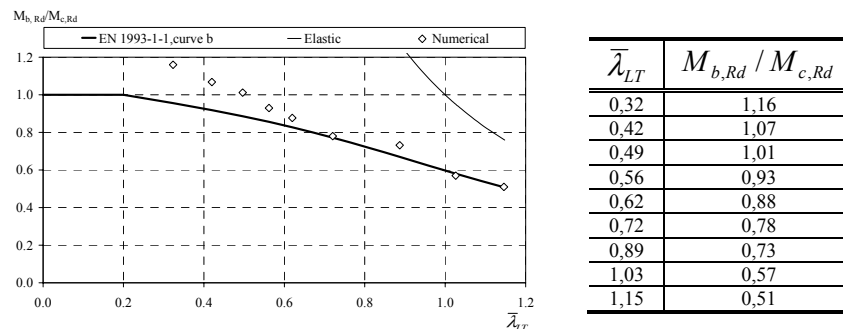
$$M_{pl} = M_{pl,a} - \frac{2f_{ya}t_w(0.5h_1 - e_{pl})^2}{2} + \beta_R 2b_1e_{pl}(0.5e_{pl} + 0.5h_1 - e_{pl}) \quad (6)$$

$M_{pl,a}$ represents the full plastic moment for the steel section.

2.3 Design buckling resistance at room temperature

The real behaviour of partially encased steel beams is significantly different from the ideal. Buckling develops since the very beginning of the loading by equilibrium divergence. The ultimate LTB moment resistance ($M_{b,Rd}$) corresponds to the maximum load bearing capacity. The non-dimensional beam slenderness, $\bar{\lambda}_{LT}$, is the governing parameter for LTB. The larger slenderness of a beam corresponds to a smaller ultimate LTB resistance. The reduction factor χ_{LT} should be derived from a specific buckling curve. No allowance for LTB will be considered for non-dimensional slenderness smaller than $\bar{\lambda}_{LT,0} = 0.2$.

Figure 3 represents the design buckling resistance for partially encased steel S235 IPE200 beams with C20/25 concrete, using the simplified method presented in Eurocode 3. Numerical results, obtained at room temperature, are also presented for specific beam lengths.



a) Design buckling resistance curve. b) Numerical results.
Fig. 3 – Lateral torsional buckling design for partially encased steel with concrete.

3. THERMAL NUMERICAL MODEL

Partially encased beam will be subjected to fire conditions, according to the standard fire nominal curve, ISO 834. Convective heat flux will be applied to the composite member, depending on the bulk temperature and constant convective coefficient $\alpha_c = 25 [W / m^2 K]$. Radiative heat flux will depend on the assumed configuration factor, resultant emissivity, $\varepsilon_{res} = 0.7$, considered for both exposed steel and concrete surfaces, and on the radiation temperature, considered equal to the bulk nominal temperature [4].

The procedure for determining the temperature development in this type of composite members may be based on advanced calculation models. Non linear transient analysis will be used, based on a full incremental time procedure. All the heat flux exchanges, between concrete and steel, consider both materials in perfect contact.

3.1 Numerical model

Three dimensional model based on ANSYS shell131, solid70 and combine39 finite elements were used to simulate thermal behaviour of partially encased steel beams with concrete in fire conditions, see figure 4.

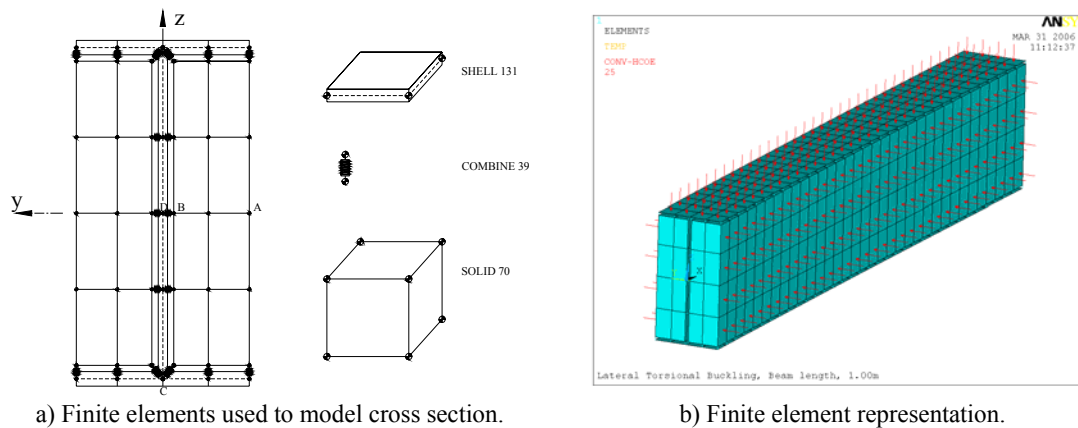


Fig. 4 – Cross section and mesh representation for thermal model.

Finite shell element (shell131) is a three-dimensional layered shell with four nodes having in-plane and thru-thickness thermal conduction capability. The conducting shell element is applicable to three dimensional transient thermal analyses. Shell131 generates temperatures that can be passed to structural shell elements in order to model the thermo – mechanical behaviour. The shape functions are linear for in-plane interpolation with 2x2 integration scheme, while for thickness (assuming no temperature variation) the shape functions are assumed constant with 1 integration point.

Finite solid element (solid70) has a three-dimensional thermal conduction capability. This element has eight nodes with a single degree of freedom (temperature at each node). The element is used to model concrete three dimensional transient thermal analyses and must be replaced by an equivalent structural element to model thermo-mechanical behaviour. The shape functions are linear in each orthogonal direction and possess a 2x2x2 integration scheme.

Finite combine element (combine39) is a unidirectional finite element defined by two nodes with nonlinear generalized temperature variation – heat flux capability. The element behaviour is defined by the generic curve temperature versus heat flux. The element has no mass or thermal capacitance. The full contact area of steel and concrete was modelled by this non linear spring element, connecting node to node, between steel finite shell element and concrete finite solid element. The bond thermal model considers perfect contact, allowing for all thermal flux to pass throughout the interface in both directions. The heat flux – temperature variation curve is defined constant and does not input any thermal resistance across interface.

3.2 Material behaviour

Non-linear unsteady state analysis requires the knowledge of steel conductivity and specific heat variation with temperature. According to EC3 - part 1.2 ^[5], for carbon steel these properties vary with temperature, as represented in figure 5. Specific mass is assumed to be constant and equal to 8750 [kg/m³].

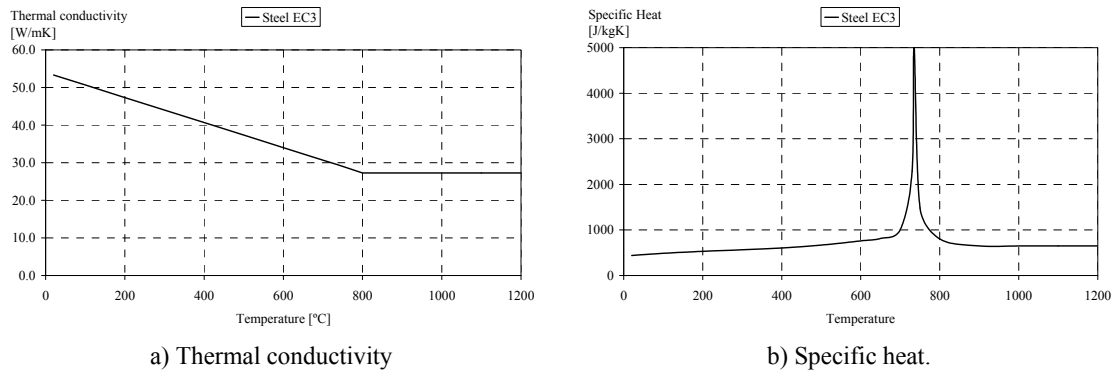


Fig. 5 – Thermal behaviour of carbon steel S235.

Thermal conductivity of concrete, λ_c , may be obtained from Eurocode 2 ^[6], between lower and upper limit values. The lower limit of thermal conductivity for normal weight concrete was adopted.

Specific heat, $C_p(\theta)$ of dry concrete ($u = 0\%$), depends on temperature and was obtained from the siliceous aggregates ^[6], according to figure 6.

The variation of the specific mass of concrete with temperature is influenced by water loss during the heating process and is defined as follows ^[6].

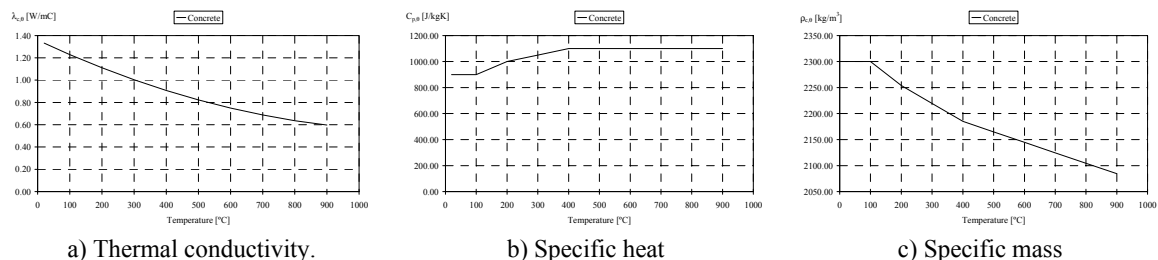


Fig. 6 - Thermal properties of concrete C20-25.

3.3 Results

Results may be presented in time domain. Figure 7 represents the temperature variation across the partially encased section. The steel web receives heat, principally, from both steel beam flanges and less from the adjacent encased concrete.

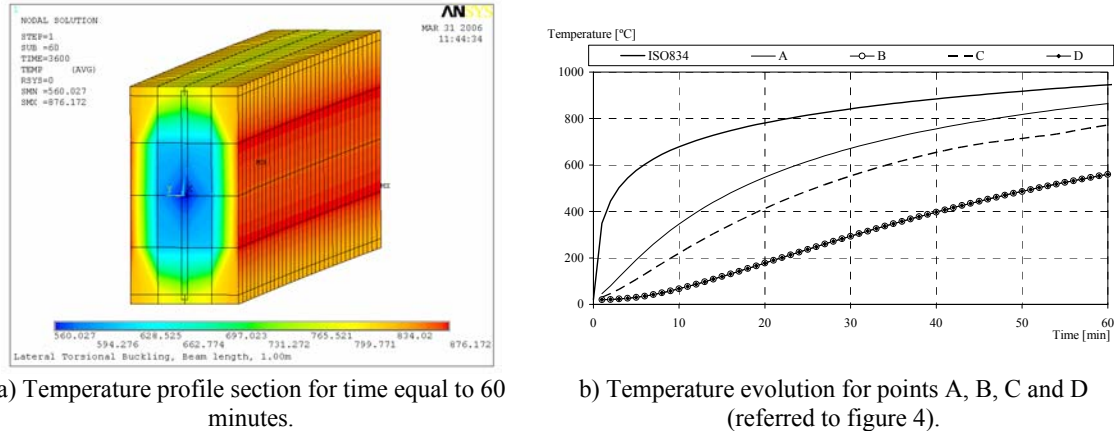


Fig. 7 – Finite element thermal transient results.

4. THERMO-MECHANICAL NUMERICAL MODEL

4.1 Numerical model

Three dimensional model based on ANSYS shell181, solid65 and combine39 finite elements were used to simulate thermo-mechanical behaviour of partially encased steel beams with concrete in fire conditions, see figure 8.

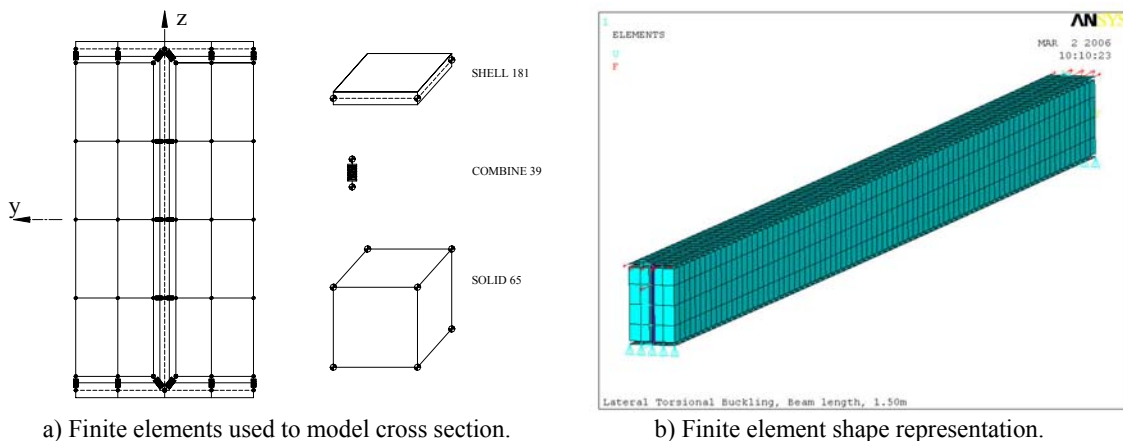


Fig. 8 – Cross section and mesh representation for thermo-mechanical model.

Finite shell element is suitable for analyzing thin to moderately-thick shell structures. It is a 4-node element with six degrees of freedom at each node: translations in the x, y, and z directions, and rotations about the same axis. This element is also well-suited for material and geometric non-linear applications. Bilinear elements, when fully integrated (2x2, in plane), are too stiff for in-plane bending, nevertheless, full integration scheme was adopted because this element uses the method of incompatible modes to enhance the accuracy in

bending-dominated problems ^[7]. This element is associated with linear elastic and elasto-plastic material properties, being the von Mises isotropic hardening plasticity model used with multilinear isotropic hardening.

Finite solid element is used to model concrete and is capable of cracking in tension and crushing in compression. The element is defined by eight nodes having three degrees of freedom at each node: translations in the nodal x, y, and z directions. This element presents linear shape functions with an integration scheme of 2x2x2.

The non linear spring is a uniaxial element defined by two nodes with nonlinear generalized force-deflection capability with large displacement. Figure 9 represents the behaviour of the bond model between concrete and steel, representing the force versus relative displacement. The longitudinal option is an uniaxial tension-compression element with up to three degrees of freedom at each node: translations in the nodal x, y, and z directions. No bending or torsion is considered. The full contact area of steel and concrete was modelled by this non linear spring element, connecting node to node finite shell element and finite solid element. The bond mechanical model was considered equal to the behaviour of the push out tests obtained for concrete –filled steel tubes ^[8]. When the last data point force is exceeded, the previous slope is maintained.

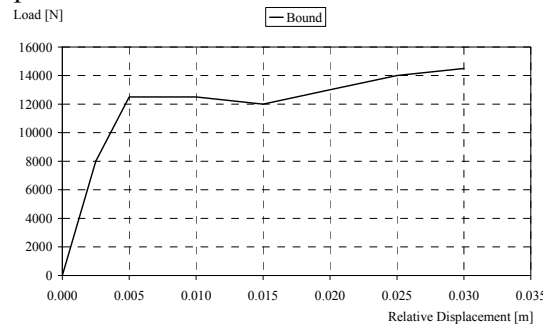


Fig. 9 – Bond interface between concrete and steel.

The assumption of this bond model ensures that once the peak level force is reached, concrete will travel along the steel with practically no increase in force (curve almost parallel to horizontal axis). This approach may be questionable due to the fact that bond behaviour may be considered different in tension compared to the compression zones of the flexural member. The element behaviour follows the represented curve in tension and in compression.

Structural elements always present initial imperfections due to fabrication processes, transportation, storage and construction methods. The initial out-of-straightness imperfection causes a secondary bending moment as soon as any compression load is applied, which in turn leads to further bending deflection and a growth in the amplitude of this bending moment. Stable deflected shape equilibrium can be established until the internal compression forces do not exceed the internal moment resistance. The numerical model was implemented with an initial out-of-straightness represented by a harmonic function with $L/400$ of maximum amplitude, to account for global imperfections.

A constant mechanical bending moment is applied, corresponding to 50% of the section plastic moment, and thermal load resulting from fire conditions applied for each time step. A non linear static analysis was undertaken to address the ultimate limit state.

4.2 Material behaviour

Steel stress-strain relation is based on an elastic- elliptic -plastic model ^[5], see figure 10. The yield stress at room temperature was considered equal to the characteristic value of steel S235. The elasticity modulus varies with temperature as represented.

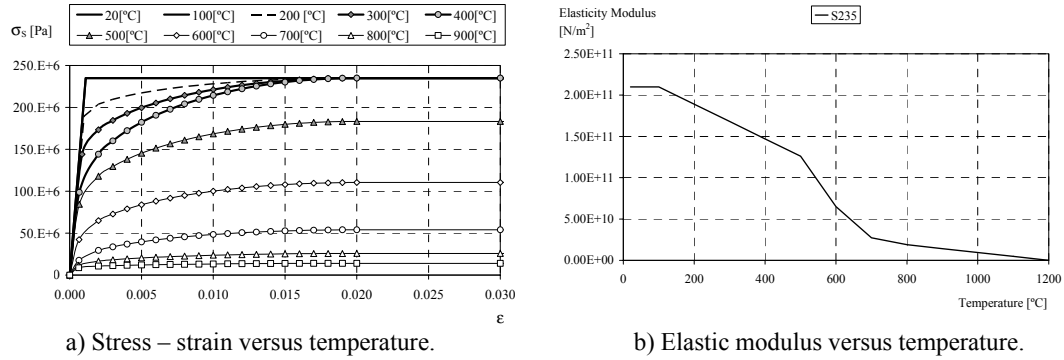


Fig. 10 – Mechanical behaviour of steel S235.

The concrete material is capable of directional integration point cracking and crushing besides incorporating plastic behaviour. Cracking is allowed in three orthogonal directions at each integration point. If cracking occurs at an integration point, the cracking is modelled through an adjustment of material properties which effectively treats the cracking as a “smeared band” of cracks, rather than discrete cracks. In addition to cracking and crushing, the concrete may also undergo plasticity, with the Drucker-Prager failure surface being most commonly used. In this case, the plasticity is verified before the cracking and crushing checks occurs. This material model predicts either elastic behaviour, cracking behaviour or crushing behaviour. If elastic behaviour is predicted, the concrete is treated as a linear elastic material. If cracking or crushing behaviour is predicted, the stress-strain elastic matrix is adjusted for each failure mode. The concrete material is assumed to be initially isotropic.

The presence of a crack failure mode at an integration point is represented through modification of the stress-strain relations by introducing a plane of weakness in a direction normal to the crack face. If stress relaxing is considered in tension, the secant modulus works with adaptive descent and diminishes to 0.0 as the solution converges, see figure 11. A multiplier coefficient of 1.0 was used for determining the amount of tensile stress relaxation.

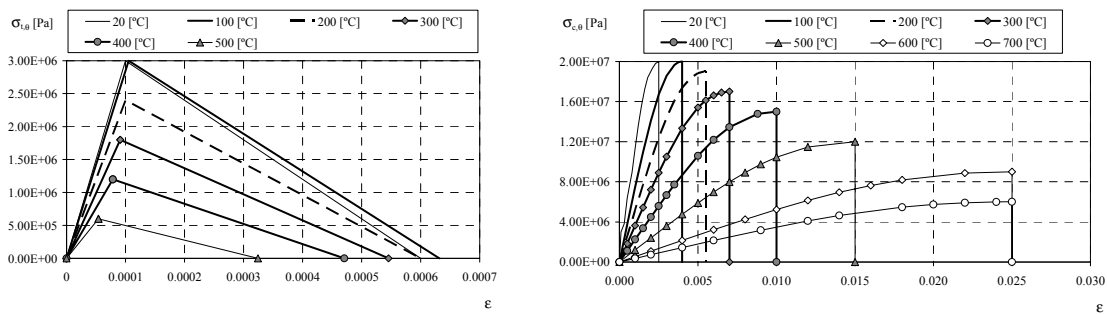


Fig. 11 - Strength for concrete material.

The presence of a crushing failure mode at an integration point is defined as the complete deterioration of the material structural integrity. Under these conditions, material strength is assumed to have degraded to an extent such that the contribution to the stiffness of an element at the integration point can be ignored.

4.3 Results

The fire resistance time will be determined for the last time increment, which a small temperature increment produces a large displacement and is possible to sustain the equilibrium. As represented in figure 12, concrete cracks after the mechanical load is applied and a progressive failure is verified as the temperature rise.

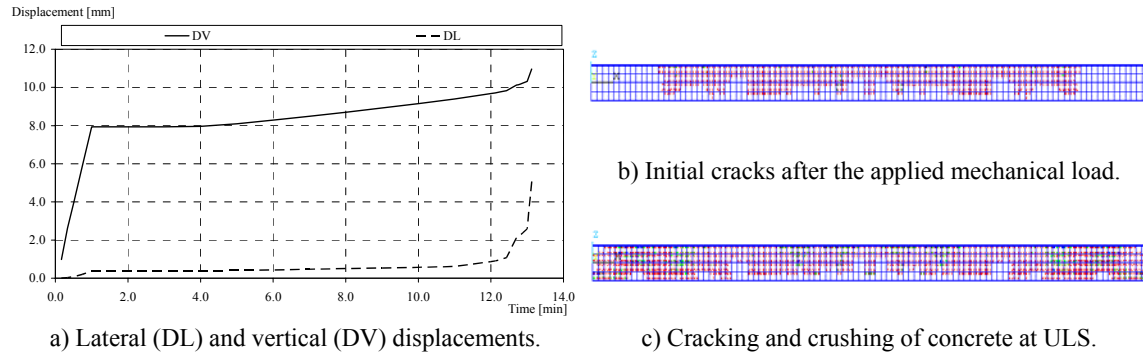


Fig. 12 – Results for a beam length of 3 [m].

In figure 13, the fire resistance time is presented for different beam slenderness values. Fire resistance decreases as the beam slenderness increase, for the same initial mechanical load.

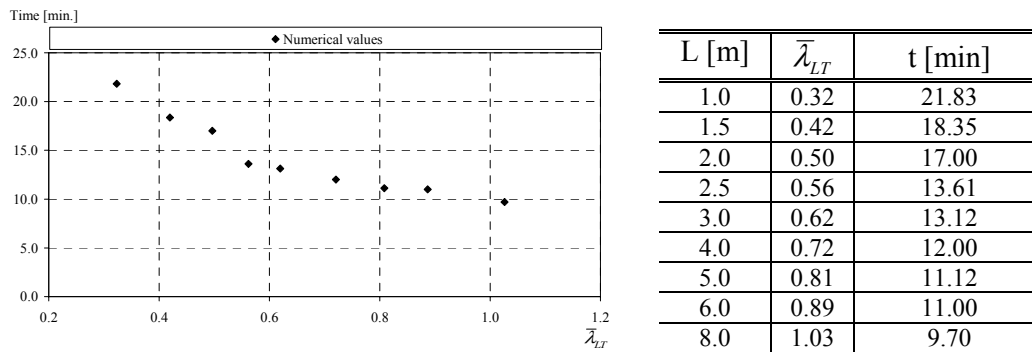


Fig. 13 – Numerical values of fire resistance time.

5. CONCLUSIONS

A non linear finite element model for determining lateral torsional buckling resistance of partially encased beams in fire conditions was presented. A special attention was considered to the bond model between concrete and steel. The model predicts the concrete failure by cracking and crushing. Fire resistance of partially encased beams subjected to a constant uniform bending moment and to an increasing temperature has been determined.

The results have shown that, with the same mechanical load, as the beams slenderness increases the fire resistance time decreases.

6. REFERENCES

- [1] – Boissonade, N.; Jaspart, J.P.; Maquoi, R.; “Development of a general model for lateral torsional buckling check in the erection phase. Application to partially encased beams, including the restraining effect of metal sheeting”; University of Liège, Department M&S; July 2004.
- [2] – Lindner, Joachim; Budassis, Nikos; “Lateral torsional buckling of partially encased composite beams without concrete slab”; conference proceeding of composite construction in steel and concrete IV, May 28-June 2 of 2000; pp. 117-128, ASCE, 2002.
- [3] - European commission, “Lateral torsional buckling in steel and composite beams”; ISBN 92-894-6414-3; Book 1,2 and 3; Technical steel research final report EUR 20888 EN; August 2002.
- [4] – CEN; EN 1991-2-2; “Eurocode 1, Actions on structures – Part 1-2: General actions - Actions on structures exposed to fire”; November 2002.
- [5] – CEN; EN 1993-1-2; “Eurocode 3, Design of Steel Structures – Part 1-2: General rules, Structural fire design”; April 2005.
- [6] – CEN; EN 1992-1-2, “Eurocode 2: Design of concrete structures - Part 1-2: General rules - Structural fire design”; December 2004.
- [7] - J. C. Simo and F. Armero, "Geometrically nonlinear enhanced strain mixed methods and the method of incompatible modes," IJNME, Vol. 33, pp. 1413-1449, 1992).
- [8] – Brahmachari, Koushik; “Connection and flexural behaviour of steel RHS filled high strength concrete”; Ph.D. thesis presented at the University of Western Sidney, December 1997.



THE EFFECT OF EDGE BEAM PROTECTION ON COMPOSITE STRUCTURES IN FIRE

S. LAMONT¹, M. GILLIE² and A.S. USMANI³

ABSTRACT

The structural behaviour of a steel-concrete composite frame subject to a natural fire is analysed using a numerical model. The behaviour is compared when fire protection is applied to only the external beams and when no beams are fire protected. The behaviour of the structure in the two cases is significantly different. When the edge beams are unprotected, the columns displace inwards towards the end of the fire indicating the possibility of imminent runaway collapse. Conversely, an instability in the primary beam occurs at much lower temperatures when the edge beams are protected. In the later stages of the fire mechanical strains in the reinforcement of the concrete slab are found to be higher, on average, when fire protection is applied to the edge beams. It is concluded fire protecting the edge beams has a number of effects on the fire resistance of the structure, some beneficial, some detrimental. On balance, fire protecting edge beams provides a small increase in fire resistance.

1 INTRODUCTION

Historically, fire resistance design of structures has been based on the behaviour of single structural elements in Standard Fire Tests. Engineers have long recognized that whole-frame structural behaviour in fire cannot be described by a test on a single element and, further, that the Standard Fire Test is not representative of the temperatures that occur in compartment fires. However, it is only in recent years that researchers have begun to investigate and understand the behaviour of complete structures in response to real fires. This new understanding has come about largely as the result of a series of full-scale fire tests conducted on a steel-concrete composite structure at Cardington, UK¹ in the mid-1990s, and subsequent numerical modelling and theoretical work.

¹ Dr S Lamont B.Eng, PhD Arup Fire, San Francisco
Susan.Lamont@arup.com

² D M Gillie B. Eng, PhD School of Engineering, University of Edinburgh,
M.Gillie@ed.ac.uk

³ Dr A S Usmani BE, MS, PhD School of Engineering University of Edinburgh,
Asif.Usmani@ed.ac.uk

The Cardington tests led to progress in three areas. The fundamental mechanics of heated structures were elucidated by Rotter *et al*² and Usmani *et al*³. Secondly, numerical modelling of the Cardington structure by a number of authors produced a detailed understanding of the Cardington frame in fire⁴⁻⁷. Thirdly, some progress has been made in translating these analytical developments in to design advice by Bailey⁸ and Cameron⁹. Lamont *et al*¹⁰ extended the understanding developed from the Cardington tests by considering the behaviour of a generic steel-concrete composite structure under various fire scenarios. It was established that, from a structural point of view, a well-ventilated ("short hot") fire was most detrimental. Study of the same generic structure¹¹ also identified possible instabilities in structural behaviour when the end conditions of composite beams effectively changes from fixed to pinned as a result of heating.

These developments have demonstrated that composite steel-framed structures may survive fire exposure even when all internal beams are left unprotected. Internal beams in the Cardington Frame achieved temperatures far in excess of the critical temperatures for collapse predicted by the Standard Fire Test (typically around 550°C). However, in the Cardington Tests the edge beams were nearly always protected and subsequent analytical work has always assumed that the edge beams in structures have been fire protected. Therefore, it has not yet been determined what effect unprotected edge beams might have on structural behaviour. This question is significant from both structural and practical standpoints. Many interpretations of structural behaviour in fire have relied on some form of lateral restraint to floor slabs being present in order for collapse to be avoided. If edge beams are unprotected, loss of stiffness due to heating may significantly reduce the available lateral restraint. In practice omitting fire protection from all the steel beams including the edge beams is desirable because this speeds up construction and reduces initial build costs as well as costs associated with maintenance of the fire protection material over the life of the building. Moreover it increases the sustainability of the steel frame and reduces health and safety risks associated with installation and maintenance.

This paper takes Lamont's¹⁰ previous study of a generic frame as a starting point and examines the effects of removing fire protection from the edge beams of the structure

2 NATURE OF THE STUDY

The aim of this study was to compare the behaviour of composite structures with no fire protection applied to the edge beam with the behaviour when edge beams were fire protected. To do this, a generic structure that is typical of many low-medium rise office structures designed for efficiency was considered. The generic structure studied and the approach to the associated numerical modelling have been described in detail in an earlier paper¹⁰ so only brief details are given here.

The structure was designed according to EC4 Part 1.1 and consisted of profiled concrete-metal deck floor slabs acting compositely with a steel frame. It was of 5-storeys with an identical floor plan at each level (Fig. 1). It was assumed that only one floor of the building would be affected by fire and that the fire compartment would encompass the entire floor. Lamont's earlier paper established that the form of compartment fire that resulted in the largest forces and strains in the structure was a well-ventilated, or "short-hot" fire. Consequently, atmosphere temperature-time curves were specified according to Pettersson's¹² fire curves with an opening factor of $0.08\text{m}^{1/2}$. The fire load was taken as 250MJ/m^2 and the vertical gravity and live loading taken as (a relatively high) 7.25kN/m^2 .

The temperatures in the concrete and protected beams were calculated using the adaptive finite element heat transfer research code HADAPT and the unprotected steel

temperatures obtained from EC3 Part 1.2¹³. Temperature time curves for various elements of the structure are shown in Fig. 3. The mechanical behaviour of the heated structure was determined using the commercially available Abaqus¹⁴ finite element software, coupled with the specifically developed FEAST¹⁵ code for analysing the behaviour of the concrete floor slabs.

In this study the behaviour of the structure was considered in two fire scenarios: when only edge beams had fire protection, and when there was no fire protection on any beams. In both cases the columns were protected to their full height. The results from the analyses are largely plotted as a variable against temperature. In each case the temperature is that of the hottest part of the structure (the unprotected secondary steel beams) -- not the atmosphere temperature. Temperature rather than time has been chosen as the variable of comparison as there are no time-dependent phenomena represented in the models. During this study reference will be made to individual beams in the frame and so a grid system has been adopted. For example, referring to Fig. 1, the secondary beam running between locations B1 and B2 will be identified as beam B12.

3 DEFLECTION RESPONSE

The deflection patterns seen in the structure will be described in this section and then explained in the light of the force patterns in the various structural elements which are detailed in the next section. The deflection responses of various beams in the structure are plotted against temperature in Figs 4-7. In each figure a comparison is made between the deflections of beams when fire protection was, and was not, present on the edge beams. The *x*-axes, therefore, run positive in both directions. The *y*-axes measure vertical deflections at mid-span, with downward deflections taken as negative.

It is clear that in all cases the deflections increase when fire protection is removed from the edge beams. The phenomenon is most apparent for the edge beams themselves (Figs 6 and 7), which deflect little when protected. This general observation, however, disguises a more significant phenomenon: the relative deflections between the various parts of the structure alter when fire protection is removed from the edge beams. For example, the deflections of secondary edge beam AB1 and internal beam AB2 when fire protection is applied are in a ratio of about 1:10 (Figs 4 and 6). However, when the fire protection is removed the relative deflections are in a ratio of only about 1:4. Comparison of contour plots of the deflection patterns of the structure (Figs 8 and 9) with the different degrees of fire protection also clearly show this effect. It is apparent from these figures that when the edge beams are fire protected, the concrete slab and associated beams behave as a membrane and deflect in to a "bowl" shape that has curvature in both directions. When the edge beams are unprotected the deflection pattern is much more one way with the slab behaving more as a catenary structure between beams 1 and 4.

The deflections of column B1 (which are typical) are shown in Figs 10 and 11, where horizontal displacements over the height of the column are plotted for various temperatures for both scenarios. In each case the column is initially pushed out by the thermally expanding beam and slab. When the edge beams are fire protected the outward deflections peak at 90°C and then again at 600°C. When the edge beams are not fire protected deflection peaks are still present but now at 90°C and 400°C. In this case the sign of the deflections reverses in the final stages of the fire. When columns are pulled back through their original position this typically indicates impending structural failure because the column receives little or no lateral support from the floor and consequently its effective length increases. This in combination with an increasing P-Delta moment on the column will eventually result in failure by buckling

or plastic bending. For this reason the frame may have slightly less fire resistance as a whole when the edge beams are unprotected. The behaviour of the column is closely related to both thermal expansion in the structure and the effect of a primary beam instability, a phenomenon that was mentioned above and which will be discussed in more detail below.

4 FORCES IN THE STRUCTURE

4.1 Forces in the Beams

The forces in primary beam B14 are shown in Fig. 12. The plot is of a similar form to those for deflections and compares the force patterns for the two fire scenarios on the same plot. The most striking feature of this plot is that there is a sudden drop in the axial force in the beam at about 90°C in the unprotected case and at around 430°C in the protected case. The cause of the drop in both cases is a primary beam instability of the form previously identified by Lamont and Usmani¹¹. In the early stages of the fire the primary beam rapidly develops large compressive forces due to restrained thermal expansion. At the same time the bending moments in the beam are increasing due to thermal gradients and the vertical components of the forces in the secondary beams that frame in to the beam (Fig. 15). This combination results in yielding in the beam B14 and a plastic hinge forming at the interior support. As a consequence the effective end restraint of the composite beam-slab section changes from a close-to-fixed condition to a close-to-pinned condition. This in turn results in a rapid increase in deflections (Fig. 5) and a consequent rapid loss of compression in the primary beam as forces are relieved by its increasing length.

The instability occurs much earlier when the edge beams are protected because there is more restraint to expansion of the primary beam and relative displacements between the edge of the structure and the primary beam are higher and so the vertical components of the forces in the secondary beams are greater. The instability has consequences for much of the rest of the structure and this is shown in many of the figures presented here as a step, or rapid, change in the variable being plotted.

The forces in beam B14 after the instability are very similar for both the protected and unprotected cases. This results from the beam being close to a fully plastic state and gradually losing capacity as the material properties decay with increasing temperature. The forces in both cases are limited by its material strength rather than by the loading or geometry of the structure.

Plots of the forces in edge primary beams A14 and A46 are shown in Figs 13 and 14. In both cases the forces in the beams when unprotected follow the expected pattern of rapid increases in compressive forces due to restrained thermal expansion followed by a plateau once the yield strength is reached and then gradual decay due to loss of material properties with temperature. In the unprotected case beam A14 has superimposed on these general trends a sharp fall in axial force around 430°C that corresponds to the primary beam instability discussed above. When these beams are fire protected the forces in them are much more stable although the effects of restrained thermal expansion are still clearly apparent.

Axial forces in secondary beam AB2 are plotted in Fig 15. The force patterns follow the characteristic pattern of forces in a restrained heated beam for both the protected and unprotected cases. The forces in the protected edge beam case are slightly lower due to the bigger difference in deflections between beams A14 and B14 allowing more thermal expansion to be relieved by geometrical lengthening of the beam.

For the protected edge beams parallel to the secondary beams (Figs 16 and 17) the forces are compressive near the interior columns but tensile near the edges of the frame.

Although much cooler than the unprotected beams, the protected beams are still heated to around 300°C (Fig. 3) and so the compression results from thermal expansion restrained by the cooler composite slab that acts compositely with the beams and the hogging moment over the continuous support as a result of the temperature gradient through the composite. At the edges of the structure the beam can't develop any hogging moment because there is no slab on the other side but instead acts like a "barrel strap", restraining the expanding composite slab.

4.2 Slab Forces and Reinforcement Strains

The slab membrane forces are plotted along a line 4.2m from grid-line 1 for both scenarios in Figs 18 and 19. At ambient temperature the slab behaves as a continuous beam spanning over an interior support. In both cases this initial force pattern is rapidly swamped as the thermal expansion in the heated secondary beams produces large tensions in the relatively cool slab. These tensions are smaller near the edge of the structure where the beam expansion can be relieved by lateral expansion (Figs 10 and 11). The difference in magnitude and pattern of the forces in the slab when fire protection is and is not present on the edge beams is small. Slightly reduced forces result when fire protection is present due to the smaller secondary beam forces discussed above.

Slab forces along a line 0.6m from grid-line 1 are shown in Figs 18 and 19. The response here is complicated by the proximity of the stiff column at B1. When the edge beams are protected, the force distribution at ambient temperature is rapidly lost as large compressive forces result from a "compressive ring" forming around the edge of the structure. When the edge beams are not fire protected Fig. 22, tension is seen in the early stages of the fire as the slab restrains the expanding edge beams. Later compression results as compression ring forms to resist the greater deflection in the interior of the structure.

The mechanical strains in the slab reinforcement at 950°C are plotted in Figs 22 and 23. These strains have had free thermal expansion strains removed and so indicate how close the reinforcement is to failure. The mechanical strains at yield and rupture of reinforcing steel depend on both the grade of reinforcement and its temperature. Typical values at ambient temperature are 0.2% for yield and 0.6% for rupture; both of these rise with increasing temperature. Both scenarios create large areas of yield parallel to the secondary beams but those in the protected case are somewhat less extensive. The strains in this direction are largely due to compatibility requirements between the cool slab and the hot secondary beams. As the beams expand they are restrained by the slab and tensile strains result in the reinforcement.

The strains parallel to the primary beams are largely compressive or only slightly tensile when no fire protection is present (Fig. 23b). Here the imposed curvature on the slab that results from thermal gradients within its depth and eccentric forces from the primary beams acting compositely results in the reinforcement, which is above the neutral axis, being compressed. At locations distant from the primary beams the neutral axis is higher in the slab and this accounts for the small tensile strains seen in these areas. When the edge beams are fire protected the curvature of the slab is much less and so not sufficient to counteract the tension imposed by the expanding beams and tension strains result.

5 DISCUSSION

The results have shown that the effects of removing fire protection from the edge beams of a structure are not straightforward. It is clear however that no runaway failure occurs in either scenario that has been considered and this suggests that preventing structural

collapse is not critically dependent on the presence of edge beam fire protection in this particular case. However with no fire protection on the edge beams column B1 is pulled back through its original position and is thus likely to fail earlier than when the edge beams are protected.

The forces and deflections that develop in the structure in the two cases are significantly different but it is not immediately clear that one set is more detrimental to the structure than the other. The primary beam instability is the most significant structural event that occurs in the initial stages of the fire and this is triggered at an earlier point when fire protection is present. To date¹¹, this form of instability has only been studied numerically. If future experimental testing suggests that significant dynamic forces can result from such an instability, then it would be desirable to ensure that it occurs as late as possible in the fire. In this case it would appear that applying fire protection to edge beams could in fact be detrimental to the structure since the protection could result in an instability occurring very early in the fire. A more in depth study of the probability and likely consequences of dynamic behaviour of structures in fire is needed to settle this question.

If the instability is found not to be of great consequence in regard to structural stability, then the most important aspect of the structural behaviour would be the column stability as discussed above and the mechanical strains in the reinforcement of the slab. The slab provides an alternative load carrying mechanism once the material properties of the steel beams have decayed to the point at which they no longer provide significant structural strength. In order to resist increasing tensile forces the steel mesh in the reinforcement must not rupture. It has been shown that the presence of edge beam fire protection reduces the area of tensile strains in the reinforcement parallel to the secondary beams and thus the structure may have slightly greater reserves of strength later in the fire when the edge beams are protected. However, this effect is small and is more likely to depend on the exact structural and loading arrangements of a given structure than to occur generally.

6 CONCLUSIONS

By leaving all the beams unprotected the deflection response of the composite slab is much greater, however, the relative displacement between the edges of the frame and the primary beam is reduced.

When the edge beams were unprotected the slab behaved as if supported on only the 12m beams and deflected in a 1D manner (like catenary action in a beam) rather than two dimensionally in tensile membrane action, as was the case when the edge beams were fire protected.

The timing of the primary beam instability was affected by the presence or otherwise of fire protection on the edge beams.

Greater differential deflections between the edge primary beams and internal primary beams result in the instability occurring earlier in the fire.

The very large deflections of the frame when the edge beams were unprotected resulted in the columns being pulled in towards the centre of the building near the end of the heating regime. This is an indication of impending failure.

The greatest areas of tensile mechanical strains in the reinforcement of the concrete slab occur when fire protection is present.

It can not be said that applying fire protection to edge beams of composite frame structures is either always beneficial or always detrimental to their behaviour in fire. For certain situations it may be possible to omit fire protection on edge beams and still achieve the required fire resistance of such structures. However,

applying fire protection to edge beams appears to be a robust solution and allows for greater lateral support to columns in the later stages of fires

7. REFERENCES

- [1] Bravery P.N.R. Cardington large building test facility. Technical Report, Building Research Establishment, 1993
- [2] Rotter J.M., Sanad A.M., Usmani A.S., Gillie M. Structural performance of redundant structures under local fires. In *Proceedings of Interflam '99*, volume 2, Scotland, 1999
- [3] Usmani A.S., Rotter J.M., Lamont S., Sanad A.M., Gillie M. Fundamental principles of structural behaviour under thermal effects. *Fire Safety Journal*, 36(8):721-744, 2001
- [4] Gillie M., Usmani A.S., Rotter J.M. A structural analysis of the first Cardington test. *Journal of Constructional Steel Research*, 56(6):581-601, 2001
- [5] Gillie M., Usmani A.S., Rotter J.M. A structural analysis of the Cardington British Steel Corner test. *Journal of Constructional Steel Research*. 58(4) 427-442, 2002
- [6] Bailey C.G. The behaviour of full-scale steel-framed buildings subject to compartment fires. *The Structural Engineer*, 77(8):15-21, 1999
- [7] Huang Z., Burgess I.W., Plank R.J. Non-linear modelling of three full-scale structural fire tests. In J-M Franssen, editor, *Structures in Fire – Proceedings of the First International Workshop*, pages 53-70, 2000
- [8] Bailey C.G. *Structural Fire Design of Unprotected Steel Beams Supporting Composite Floor Slabs* University of Manchester, 2002
- [9] Cameron N. *The Behaviour and Design of Composite Floor Systems in Fire*. PhD thesis, University of Edinburgh, 2004.
- [10] Lamont S., Usmani A.S., Gillie M. Behaviour of a small composite steel frame structure in a “long-cool” and a “short-hot” fire. *Fire Safety Journal*, 39(5):327-357, 2004
- [11] Lamont S., Usmani A.S. Possible ‘panel instability’ in composite deck floor systems under fire. *Journal of Constructional Steel Research* 59:1397-1433, 2003
- [12] Pettersson S.E., Magnusson S.E., Thor J. *Fire Engineering Design of Steel Structures*, Swedish Institute of Steel Construction, Publication 50, Stockholm, 1976.
- [13] ENV Eurocode 3 Design of Composite Steel and Concrete Structures, 1994
- [14] Hibbet, Karlson and Sorenson, Providence, Rhode Island, USA. *Abaqus Users' Manual, Vols I to III, Ver 5.8*, 1998.
- [15] Gillie M., Usmani A.S., Rotter J.M. Modelling of heated composite floor slabs with reference to the Cardington experiments. *Fire Safety Journal* 36(8):745-767, 2001

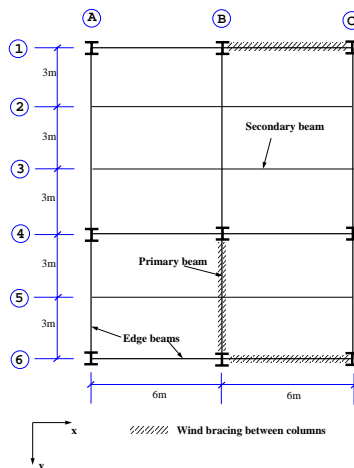


Figure 1 Schematic plan view of the generic frame

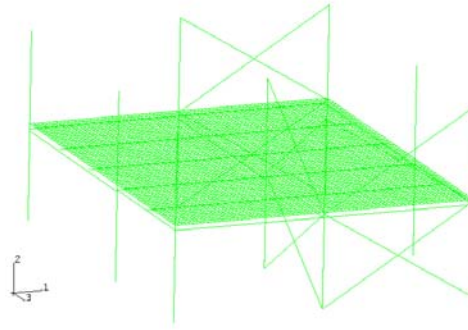


Figure 2 Finite element mesh of the generic frame

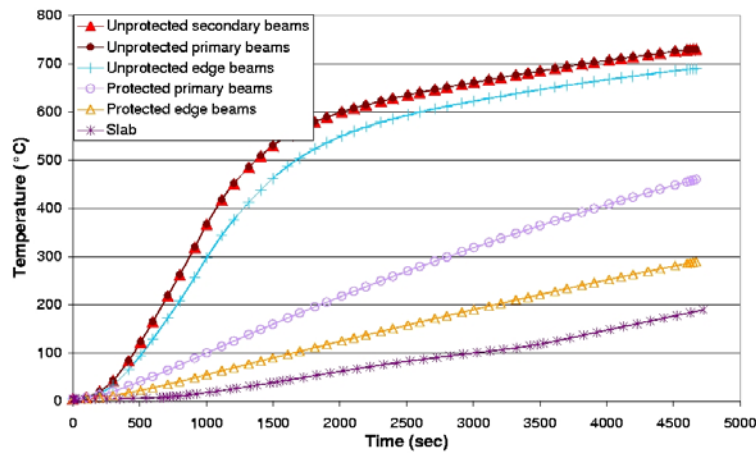


Figure 3 Temperature-time curves for the structure

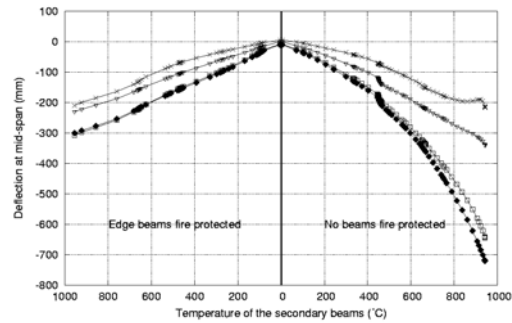


Figure 4 Deflections of the internal secondary beams

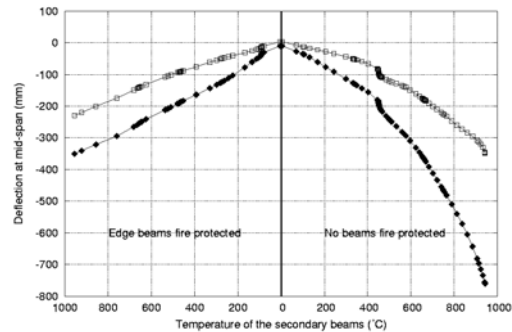


Figure 5 Mid-span deflections of the internal beams

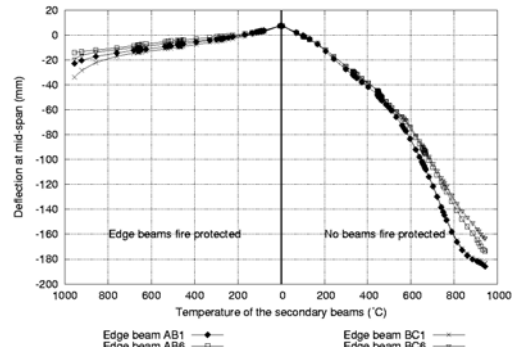


Figure 6 Mid-span deflections of secondary edge beams

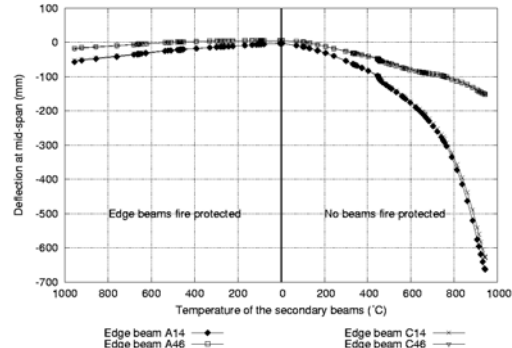


Figure 7 Mid-span deflections of the primary edge beams

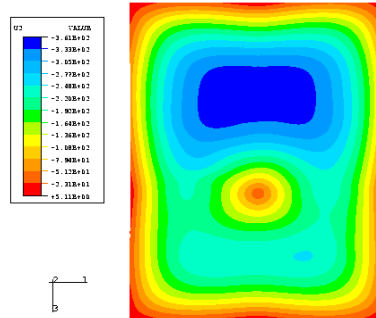


Figure 8 Contour plot of vertical deflections, edge beams fire protected

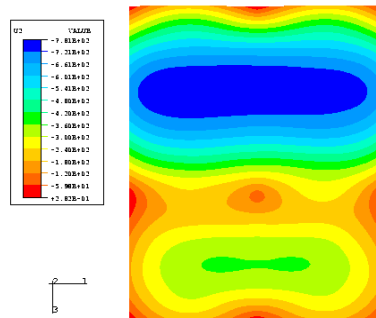


Figure 9 Contour plot of vertical deflections, no beams fire protected

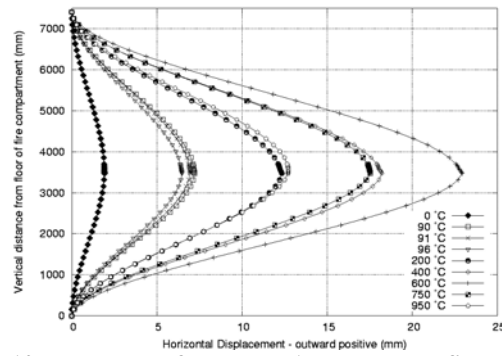


Figure 10 Movement of column B1, edge beams fire protected

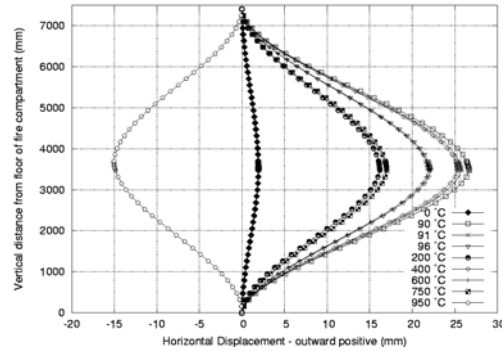


Figure 11 Movement of column B1, no beams fire protected

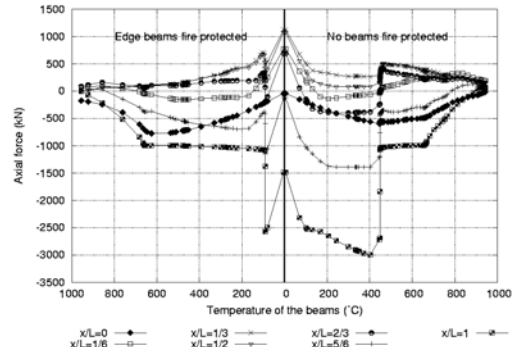


Figure 12 Primary beam B14: Axial force against beam temperature

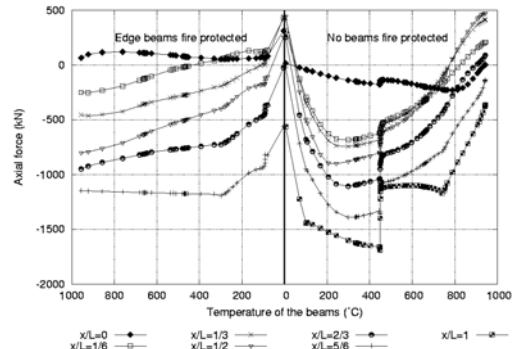


Figure 13 Edge primary beam A14: Axial force against beam temperature

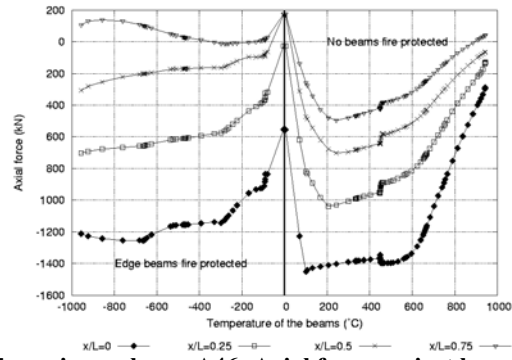


Figure 14 Edge primary beam A46: Axial force against beam temperature

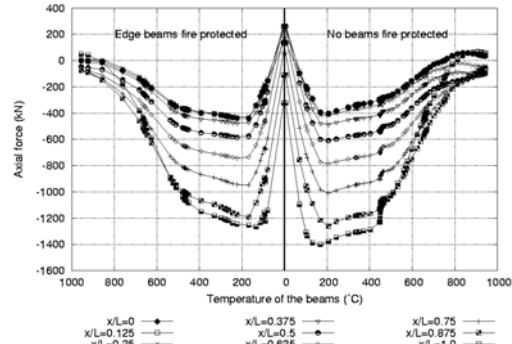


Figure 15 Secondary beam AB2: Axial force against beam temperature

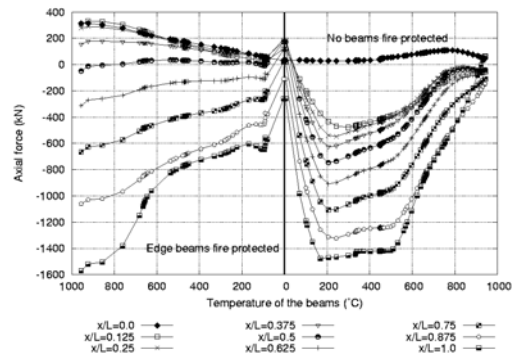


Figure 16 Edge secondary beam AB1: Axial force against beam temperature

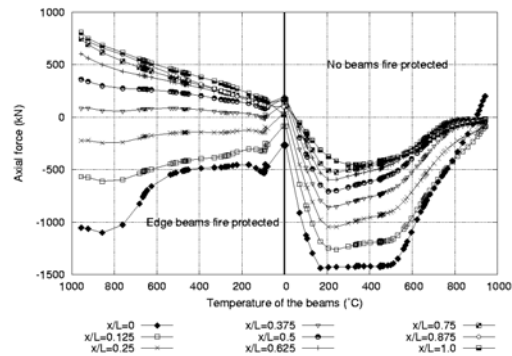


Figure 17 Edge secondary beam BC1: Axial force against beam temperature

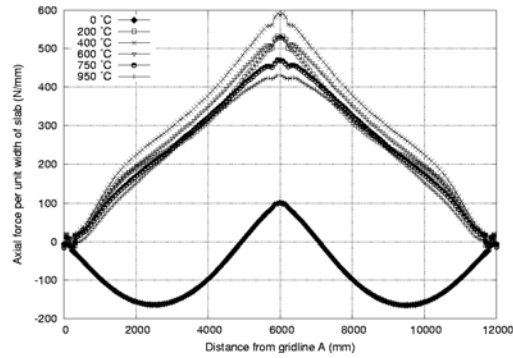


Figure 18 Force in the thin direction of the slab 4200mm from gridline 1, edge beams fire protected.

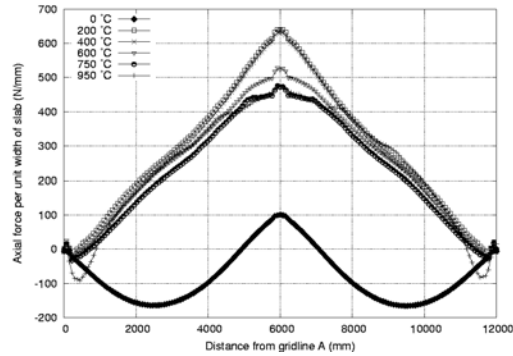


Figure 19 Force in the thin direction of the slab 4200mm from gridline A: no beams fire protected

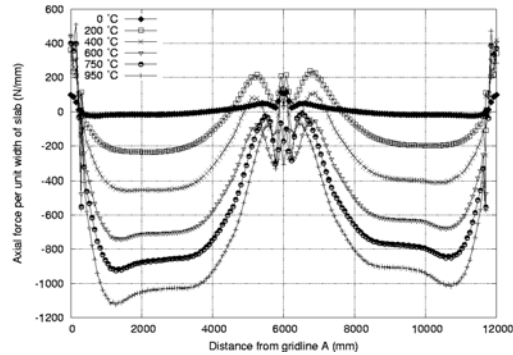


Figure 20 Axial force in the thin direction of the slab 600mm from gridline 1, edge beams fire protected

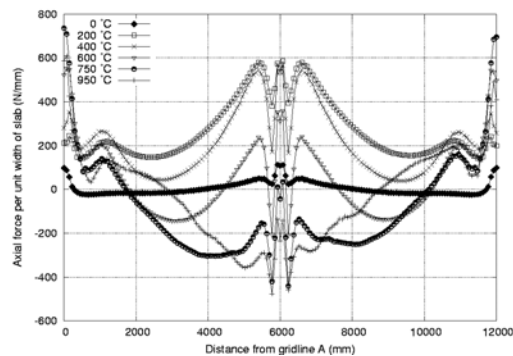


Figure 21 Axial force in the thin direction of the slab 600mm from gridline 1, no beams fire protected.



A PERFORMANCE BASED DESIGN METHODOLOGY FOR COMPOSITE FLOOR SLABS IN FIRE

David LANGE¹, Asif USMANI², Neil CAMERON³,
Wolfgang WINKLER⁴ and Jose TORERO⁵

ABSTRACT

The design of steel and composite structures worldwide is moving away from a prescriptive approach to a performance based approach. This approach is less easily implemented in structural design for fire resistance due to the inherent computational difficulties in any performance based framework for design for fire resistance, including complex structural calculations and the difficulties and restrictions imposed by defining a 'design' fire. New numerical and analytical techniques, however, can be implemented in order to attempt to address these difficulties, and when embedded in a performance based design framework, offer the designer some initial step towards a truly performance based approach for fire engineering.

Work previously carried out at the University of Edinburgh has gone some way to providing a greater understanding of the effects of heating on structural elements, as well as addressing the issue of how load is carried during fire, yet these new analysis techniques have yet to be presented in a comprehensive design methodology.

This paper offers a performance based design methodology for fire resistance demonstrated for reinforced and composite concrete 1 and 2 way spanning slabs by building on previous work^(1,2) undertaken to assess the load carrying capacity of these members by catenary and membrane action. All structures in fire research has shown that floor systems are the most important members in enabling a building to maintain its stability during and after fires by employing membrane mechanisms which are more readily available because of the imposed thermal strains. The method presented in references 1 and 2 is based upon the detailed understanding developed at the University of Edinburgh during the analysis of the

¹ MEng, School of Engineering & Electronics, University of Edinburgh, email: david.lange@ed.ac.uk

² Senior Lecturer, School of Engineering & Electronics, University of Edinburgh, email: asif.usmani@ed.ac.uk

³ PhD, SKM Anthony Hunts, Edinburgh, email: NCameron@skm.co.uk

⁴ Dipl. Ing., ILF Innsbruck, Austria email: wolfgang.erich@gmx.de

⁵ Professor, School of Engineering & Electronics, University of Edinburgh, email: jltorero@staffmail.ed.ac.uk

Cardington fire tests and uses no empirical factors or correlations in its derivation. It has also been validated by satisfactory predictions of the floor slab behaviour in four Cardington tests. This work however was restricted to assessing the limit capacity of relatively thin composite floors found in steel frame structures dominated by membrane resistance. This has been extended to thicker slabs where deflections may be small and flexure remains the dominant mechanism.

The method is presented in a framework which offers an initial step towards a performance based design methodology. It provides a means of assessing the limits of applicability of the main load carrying actions and provides guidelines as to when fire resistant design should rely entirely on membrane action, on bending or on some combination of the two.

1. INTRODUCTION

The use of the concepts of risk and reliability is inevitable for the development of performance based design on a proper scientific basis. The application of the concept of performance based methodology to actual design is not simple because of the large ranges of probability and consequences of events which exist. This is compounded by the infinite number of different actions that can be taken to reduce the probabilities of the events and also the magnitude of the consequences, which is essentially the goal of design.

Clearly while the use of this concept poses major challenges, it also offers enormous opportunities because of the element of choice inherent in the concept. The designer using these concepts has numerous choices to address his design problem to enable him to arrive at a solution for which the risk is acceptable.

The basic elements of a performance based design framework are defined in such a way as to allow the user freedom to compose any solution to the problem, allowing also the freedom to employ new techniques and technology as they become available. The design objectives must be clearly stated at the outset of the project, and any design solution which fulfils these objectives whilst still adhering to the performance targets of the design framework should be permitted. It should be noted that although the targets in terms of life, property and business protection may remain similar to those prescribed in prescriptive design codes, these targets should remain independent to the prescriptive building code performance goals.

Concerning the actual composition of the solution to the problem, there has been a number of methods proposed for the determination of ultimate capacities of floor slabs in fire. For example, a membrane action enhanced yield line analysis, as proposed by Bailey (3) for composite floor slabs in fire; to the energy method proposed by Cameron (1,2). Both of these methods deal with composite concrete floor systems, normally subjected to large deflections in fire, but neither of the methods give any limits of applicability for the lower limit of deflection at which they become useable. Although the assumption that membrane capacity is the final load carrying capacity in fire depends upon there being large displacements, which are not necessarily present in every definable fire scenario for every possible arrangement of slab, in particular, slabs with low span/depth ratios are far less likely to experience large enough displacements to allow membrane capacity to take place than slabs with high span/depth ratios.

As demonstrated by both the Broadgate fire in London and the Cardington tests, buildings subjected to fire attack adopt large displacements as a means of transferring the load from one load carrying action to another, implying that the effect of heating on the geometry of a structure is of greater importance than the effect of heating on the material properties.

This suggested that fire protection measures as they stand currently are perhaps unnecessary and definitely unscientific in their application.

Traditional fire resistance tests involve placing the member to be tested unrestrained in a furnace and subjecting the element to some standard fire by programming the furnace to control the heating to follow the temperature time curve prescribed(4). This method of testing is, however, unrealistic, as it fails to take account of the restraint imposed on the element by the surrounding structure and because the standard fire curves originally date from 1916 and were based upon ad hoc measurements of temperatures of wood cribs burning.

Concerning the surrounding structure, the analytical method proposed in (1) assumes lateral but no rotational restraint from the surrounding structure and is therefore selected over other methods for the determination of the membrane capacity.

Although this paper makes no attempt to address the issue of a design fire, it proposes a methodology for the design of floor slabs given some design fire.

2. MEMBRANE CAPACITY

The analytical method employed for determining the tensile membrane capacity of a slab subjected to heating has three stages, all explained in more detail in (1):

1. Calculation of the temperature distribution through the depth of the member
2. Calculation of the deflected shape of the member, based upon the gross cross-sectional area, and the thermal stresses and strains in the rebars associated with this deflected shape and temperature distribution
3. Calculation of the limiting deflection and the internal and external work done to move from the thermal deflection to the limiting deflection, based on the reinforcement only.

The 1st step above, calculating the temperature distribution through the slab, can be carried out using many different methods, required as output is only the equivalent temperature distribution as an idealised uniform mean temperature, ΔT , and an idealised temperature Gradient, T_y , as defined in (5). It is currently calculated using a 1-Dimensional Finite Element Mesh for heat transfer, as described in (6).

Thermal loading is presented in two components, both related to the temperature distribution: as a thermal force caused by the thermal expansion of the member being heated acting against lateral restraint; and as a thermal moment caused by the temperature gradient present in the member.

Because the deflected profile of any member is a function of this thermal loading, which in turn is a function of the slab depth and the thermal gradient in the member, the tensile membrane capacity for two members of different depth will vary for any given fire.

Comparison of the membrane capacity of thin and thick one way spanning slabs, one of 100 and one of 250 mm depth, spanning 7 metres, and subjected to a 120 minute British Standard Fire(Fig. 1a); and of 2 way spanning slabs, again, spanning 7 metres square, of 100mm and 200mm depths and subjected to a 120 minute British Standard fire, (Fig. 1b) illustrates this fact and raises the issue that tensile membrane action is not suitable as an ultimate load carrying capacity for thicker slabs.

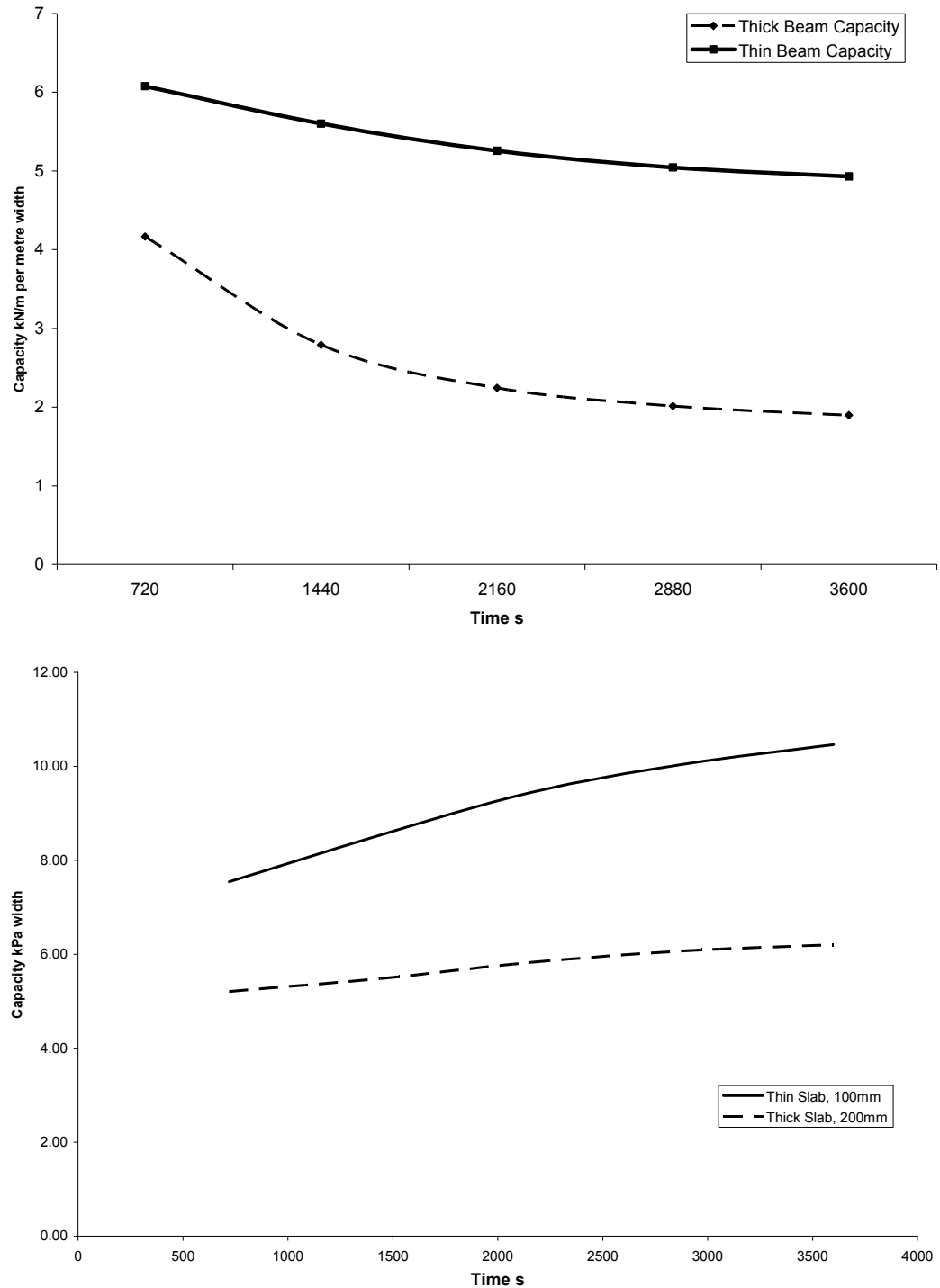


Fig. 1 a, - Comparison of tensile membrane capacity of two 1 way spanning slabs, one of 100 and one of 250 mm depth, spanning 7 metres, and b - of two 2 way spanning slabs, 7 metres square, of 100mm and 200mm depths. All subjected to a 120 minute British Standard Fire.

This difference between the capacity of thick and thin slabs can be explained by looking at the tensile membrane capacity of a single reinforcement bar at varying initial deflections, each representing a different thermal deflection.

Looking, first of all, at a 1 dimensional element, with no physical thickness (or which is thermally thin), assuming no temperature difference between the upper and lower surface, and full lateral restraint but no rotational restraint, we have an imposed thermal strain in the member equal to:

$$\varepsilon_T = \alpha \Delta T \quad (1)$$

Because of the lack of rotational restraint, this increase in length causes some initial thermal deflection in the member, equal to:

$$\delta = \frac{2l}{\pi} \sqrt{\varepsilon_T + \frac{\varepsilon_T^2}{2}} \quad (2)$$

In the method employed for determining the membrane capacity of slabs and beams, the failure criteria are based upon some limiting strain in the steel reinforcement. For example, the deflection, δ , caused by the thermal strain in a single reinforcement bar increases the capacity of the bar by reducing the tensile strain which it is subjected to for a given load, thus increasing the size of load which it can carry before the failure strain is reached.

Since the reinforcement bars in a slab are embedded in the concrete and are not able to deform based on their own thermal expansion, but follow the deformed shape of the concrete in which they are embedded, the ultimate capacity calculated by this method is related to the deformed shape of the concrete member, which is a function of slab depth, thermal force and the thermal moment which induces some curvature in the member due to the difference in the thermal forces in the upper and lower fibres of the member. This thermal moment is greatly dependant on the depth of the slab, and it can be shown that a thick slab or beam deforms less for a given fire than a thin slab. Also, since the steel reinforcement is embedded in insulating concrete, and rarely reaches temperatures greater than 400°C, it is implied that the geometric effects of heating on these members has a dominant effect on the choice of load-carrying mechanism when compared to the material degradation of the member due to the increased temperature. By proper selection of the load carrying mechanism to be designed for, unnecessary overlap in design criteria can be avoided by providing a more realistic assessment of the ultimate load carrying capacity and thus reducing the need for alternative fire protection measures.

3. FLEXURAL CAPACITY

The application of thermal force to any member causes some compression in the section. Since this increases the area in compression it effectively moves the neutral axis for bending down a distance corresponding to the increased area in compression (Fig. 2 – Effect of thermally induced forces on the neutral axis for bending in a rectangular cross-section). This drop in the neutral axis can be calculated and the increased bending capacity can be determined, assuming a balanced steel ratio (Fig. 3).

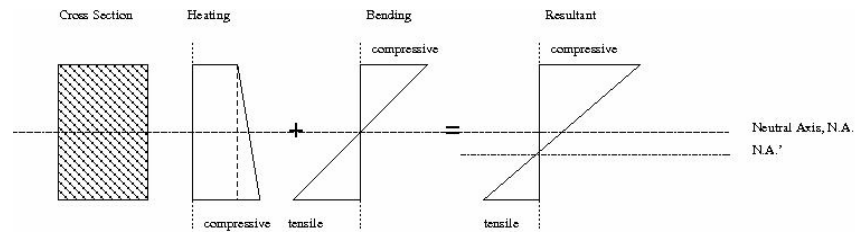


Fig. 2 – Effect of thermally induced forces on the neutral axis for bending in a rectangular cross-section

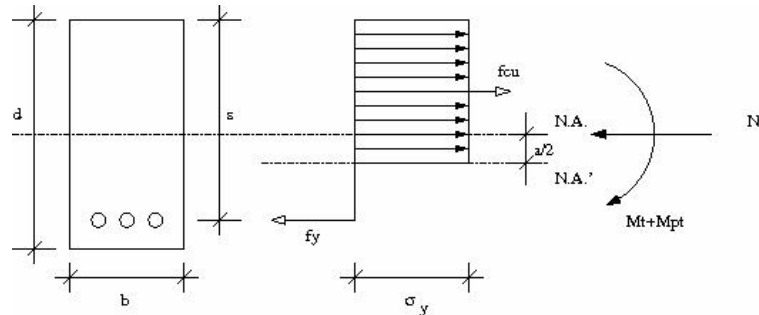


Fig. 3 – Forces acting on member cross section during heating at the plastic moment

$$a = \frac{N^T}{b\sigma_y} \quad (3)$$

$$M_{pt} = \sigma_y \cdot b \cdot \left(\frac{d}{2} + \frac{a}{2} \right)^2 + \sigma_{ys} \cdot A_s \cdot \left(s - \frac{d}{2} - \frac{a}{2} \right) - M^T \quad (4)$$

The flexural capacity of slabs increases with their depth and with the thermal forces present in the member. This is shown in (Fig. 4), for 100mm wide beams of varying depth subjected to a thermal force and gradient equivalent to an upper surface temperature of 20°C and a lower surface temperature of 1200°C. Comparison between the capacities both with and without thermal loading shows only a very small difference – the drop in the neutral axis in this case is equivalent to only a few tenths of a millimetre and therefore makes only a few tenths of a percentage difference to the plastic moment of the section. This will not necessarily be the case for every fire, and in fact it depends upon the shape of the temperature time curve. A large ΔT , resulting from a long and hot temperature time curve, will produce a larger thermal strain in the beam and therefore move the plastic neutral axis further down away from the geometric neutral axis.

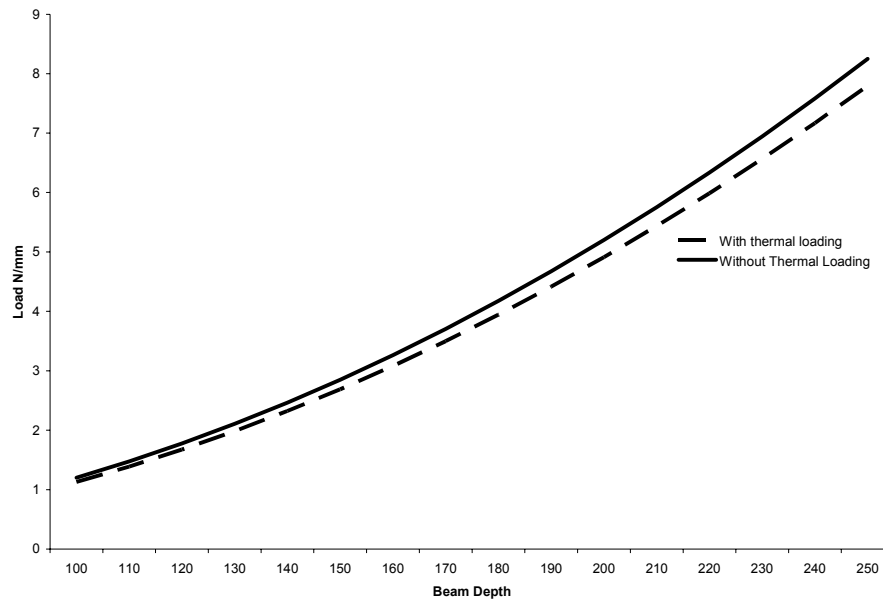


Fig. 4 - Plastic moment of simply supported beams of length 5m and width 100mm, one without the effects of thermal expansion, with temperature dependant material properties, and the other exposed to a lower surface temperature of 1200°C and an upper surface temperature of 20°C with varying depths

4. PROPOSED DESIGN METHODOLOGY

Based on the relation between flexural capacity and slab depth, and membrane capacity and thermal deflection, it is apparent that the depth and initial deflection of a beam or slab should be considered before a load carrying mechanism is selected as the dominant mechanism under fire. For very high deflections, or thin members, the membrane capacity is clearly dominant over the flexural capacity, whereas for very low deflections and thick members the flexural capacity is dominant; there is also some middle ground where the two mechanisms act together, where the steel is under large strain due to the temperature but where the concrete is not cracked through its depth due to the large deflections and still has some compressive capacity.

This gives three design options for horizontal members as shown in (Table 1).

Region	Dominant Mechanism
A	Flexural only
B	Flexural and Membrane
C	Membrane only

Table 1 – Design options and their load carrying mechanisms

Analysis example is a series of 1 way spanning slabs of varying length and depth, exposed on the lower surface to an exponential temperature time curve (7).

$$T(t) = T_0 + (T_{\max} - T_0)(1 - e^{-at}) \quad (5)$$

Where: T_{max} is the maximum compartment temperature, T_0 is the initial temperature, and a is an arbitrary parameter relating to the rate of heating.

In this case, the fire was of duration 3600 seconds, maximum temperature 1200 degrees, and with a growth rate, a , of 0.005. The beams span was varied from 3000mm to 10000mm, while the depth was varied between 100 and 200 mm, with a constant width of 100mm. Steel reinforcement was provided in the form of 8 bars of diameter 8mm, at 25mm from the base of the beam. During the flexural calculation concrete properties were kept constant, since it was assumed that the area in compression was relatively cool; whereas for the membrane calculation concrete properties followed the reduction factors given in the Eurocodes. The cover to reinforcement was kept the same in each case to ensure that the temperature of the reinforcement bars was kept the same from beam to beam. Concrete properties were:

Modulus of Elasticity, E	12500 N/mm ²
Coefficient of thermal expansion, α	$14 \times 10^{-6}/K$

Table 2 – Properties of Concrete for Analysis

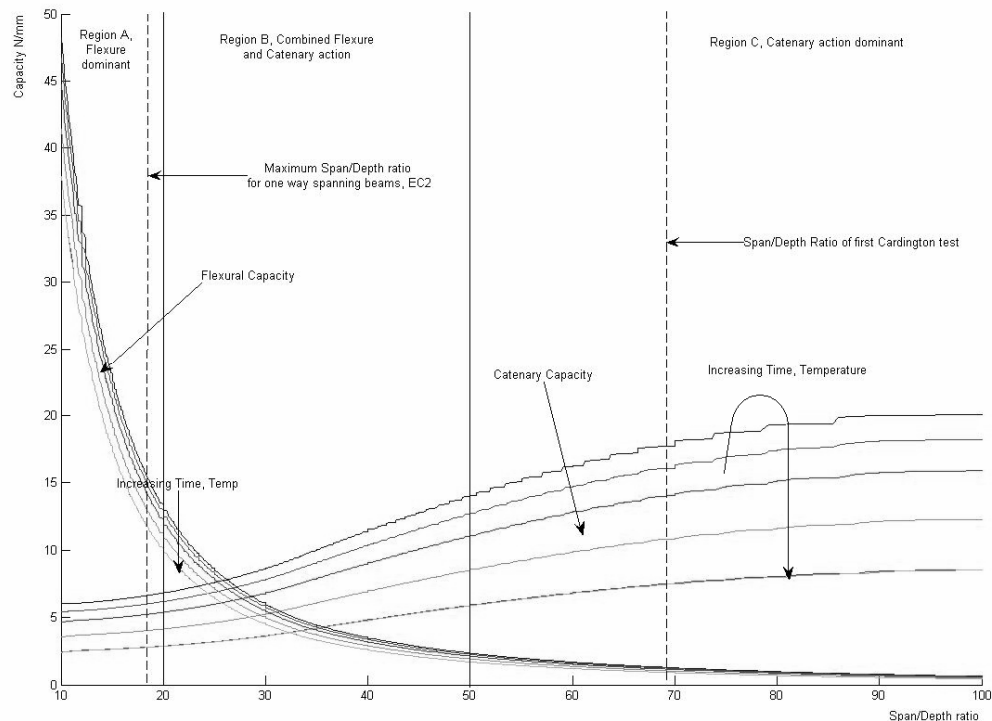


Fig. 5 – Flexural and membrane capacities of a series of 1 way spanning slabs of varying length and breadth

Fig. 5 shows these three regions quite clearly, and shows them to conform well to common design methodologies for beams. Region A encompasses the Span/Depth ratios for a simply supported reinforced concrete beam as given by both BS8110 (8) and Eurocode 2. Region C, for reference, also quite clearly encompasses the Span/Depth ratio of the first Cardington test (5).

For the middle region where both flexure and membrane capacity contribute to the members' ultimate strength design for either would provide a conservative estimate of the members' strength.

Fig. 6 shows the same graph, capacity against span/depth ratio, alongside the deflection/depth ratio plotted against the span/depth ratio. This clearly shows that an increase in the deflection of the slab corresponds with a transition from one load carrying capacity to another. It also shows the relationship between the deflection due to fire and the span/depth ratio. As discussed earlier, lower span/depth ratio, higher deflection; and a higher deflection implies higher membrane capacity and therefore more suitability of this load carrying action as an ultimate load carrying action during fire attack. In the given example, membrane action becomes more important at a deflection/depth ratio of around 0.5, and it becomes the main load carrying action at deflection/depth ratios of greater than 0.75.

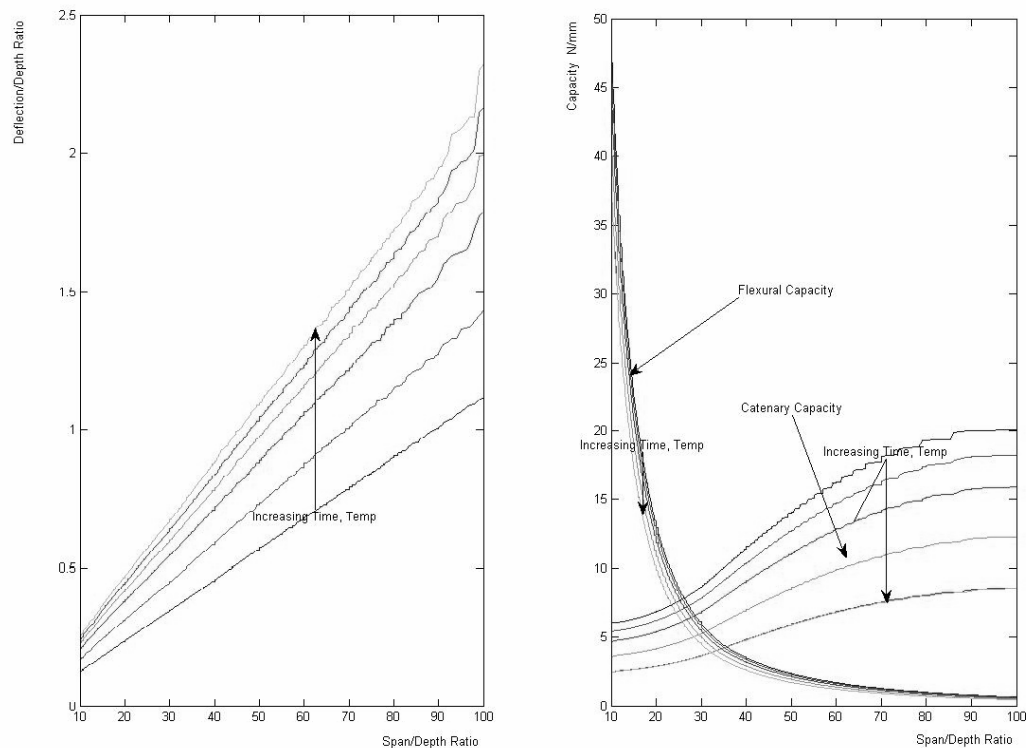


Fig. 6 – Deflection/Depth against Depth/Length, and membrane and flexural capacity for a series of beams of varying length and depth (3-10m, 100-300mm)

Fig. 7 and Fig. 8 show the same analysis for a square 2 way spanning slab of varying size exposed on the lower surface to the same Exponential Fire as the 1 way spanning slab example was. The slabs length and breadth was again increased from 3000mm to 10000mm, while the depth was varied between 100 and 200 mm. Steel reinforcement was provided in the form of an A142 mesh 50mm from the base of the slab. Concrete properties were: modulus of Elasticity, 12500 N/mm²; coefficient of thermal expansion, $14 \times 10^{-6}/K$. The flexural capacity was calculated using a simple yield-line analysis.

Fig. 7 shows the flexural and membrane capacity of the slabs plotted alongside their span/depth ratios, from a span/depth ratio of 30 to 100:

For span/depth ratios of less than 30, the flexural capacity is very much larger than any available membrane capacity.

The three regions for selection of load carrying mechanism are very clearly visible, flexural dominant, membrane dominant and some combination of the two.

The span/depth ratios of the first Cardington test and the Span/Effective Depth ratio for two way spanning continuous slabs, as recommended by the I.S.E in their manual for the design of RC structures, fall within their relevant regions at the earlier times in the fire.

It is clear that as the fire progresses and more energy is transferred to the slab, the three regions move toward the vertical axis, i.e. as the fire continues, the span/depth ratio at which the membrane capacity becomes dominant decreases, and the size of the region where flexural action is more important decreases.

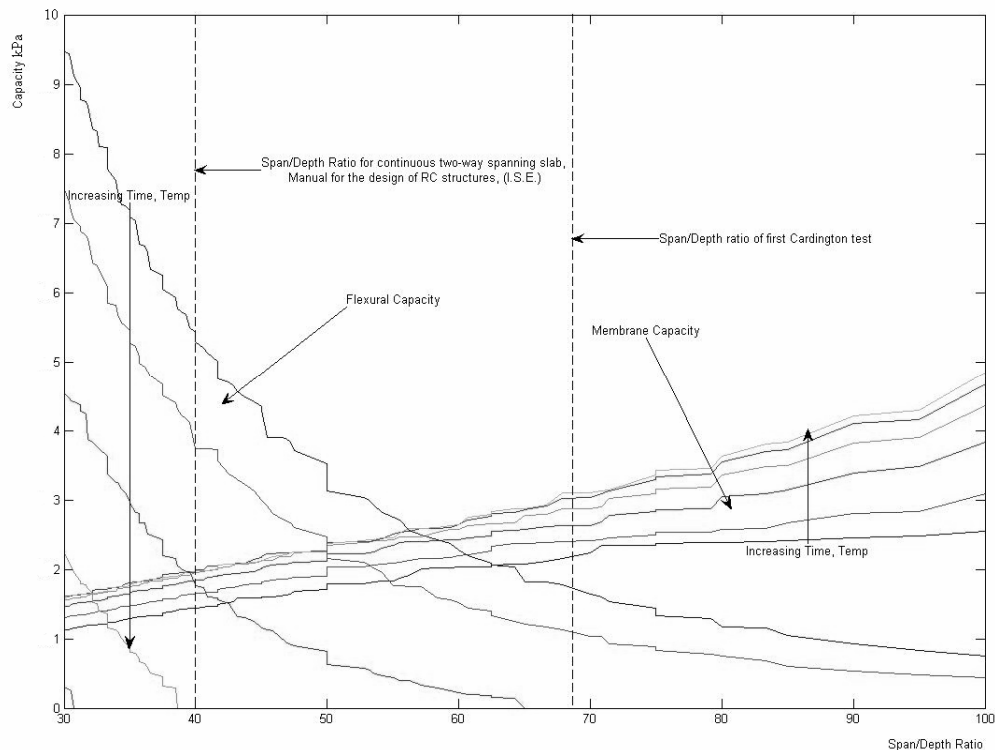


Fig. 7 – Deflection/Depth against membrane and flexural capacity for a series of 2 way spanning slabs of varying length and breadth (3-10m square, 100-300mm)

Fig. 8 shows again the same graph, plotted alongside the deflection/depth against the span/depth ratios for the same slabs. In both one and two dimensional examples, the membrane capacity increases with the thermal deflection. However in the one dimensional example, this stops increasing after an amount of time and begins to decrease. Whereas in the two dimensional example the capacity plateaus on the graphs. This difference is perhaps due to the compatibility of the reinforcement bars running orthogonal to each other, since they double the calculated capacity for square 2 way spanning slabs. In cases where the slab has an aspect ratio larger than 1.5 (1), the one-dimensional model will give a more accurate,

although still conservative, determination of the ultimate capacity. Because the membrane capacity actually increases as the fire continues, the transition from flexural action dominant to membrane action dominant is much clearer, and occurs at a deflection/depth ratio of about 0.7 at all of the times during the fire looked at.

This clear definition between the regions of flexural and membrane dominance allow for an easy selection of the load carrying capacity to be checked for in fire design.

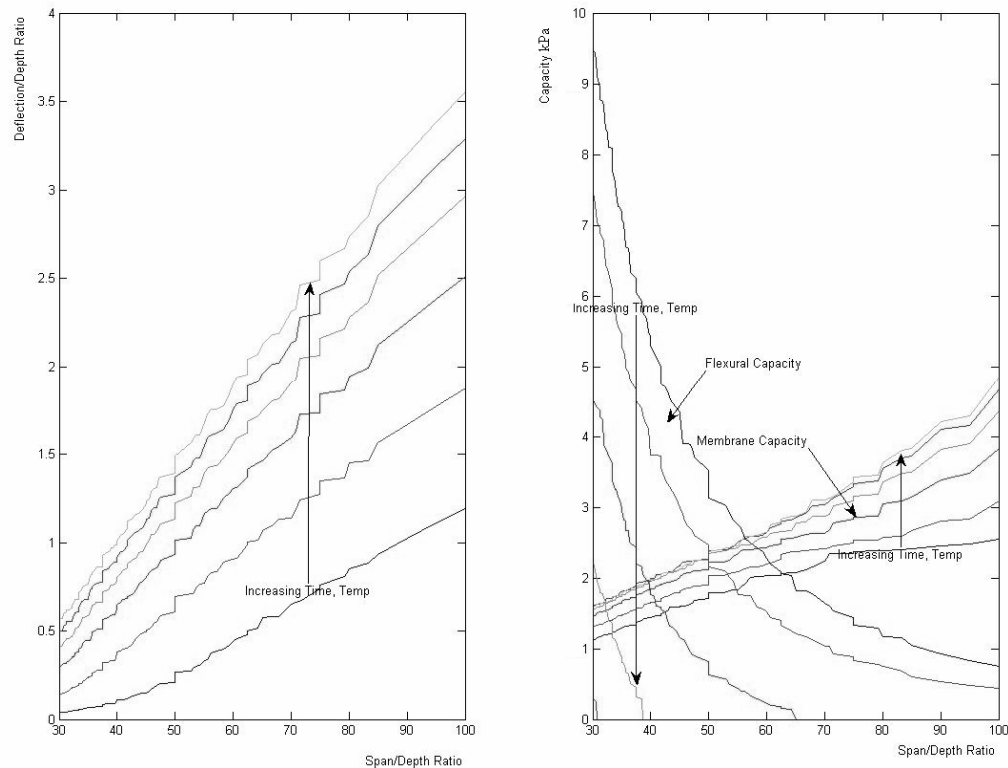


Fig. 8– Deflection/Depth against Depth/Length, and membrane and flexural capacity for a series of 2 way spanning slabs of varying length and depth (3-10m, 100-300mm)

4. CONCLUSIONS

A method of selecting and assessing the ultimate load carrying capacity of reinforced and composite concrete floor slabs and beams subjected to fire attack has been presented. Although it has only been presented for one fire scenario, it can be easily adapted for any number of fire scenarios and slabs, and simple design curves can be developed for a quick assessment of the ultimate capacity of any slab subjected to fire attack, at any time after the heating regime has begun.

This methodology will hopefully speed up and simplify the process of designing structures for fire safety and help to eliminate the application of unnecessary and unscientific protection measures.

Although presently there is no provision made for cooling in the methods employed or the results presented, conservative estimates of the capacity during cooling can be made by

assuming a permanent deflection after heating and recalculating the capacity of the slab retaining the final deflection for the slab as the thermal strain in the rebars is reduced.

In all of the 2 dimensional analyses carried out, an A142 reinforcing mesh was assumed. In the 1 dimensional analyses an 8mm bar diameter was assumed with a spacing of 100mm centre to centre. Obviously the membrane and flexural capacity will depend greatly upon the reinforcement ratio, and further work needs to be done to show design curves for different steel ratios as well as different fires and slabs.

5. REFERENCES:

¹ N. Cameron and A.S.Usmani. A new design method to determine the membrane capacity of laterally restrained composite floor slabs in fire. Part 1: Theory and method. *The Structural Engineer*, 83(19):28-33, 2005

² N. Cameron and A.S.Usmani. A new design method to determine the membrane capacity of laterally restrained composite floor slabs in fire. Part 2: Validation. *The Structural Engineer*, 83(19):34-39, 2005

³ Bailey C.G, Membrane action of unrestrained lightly reinforced concrete slabs at large displacements, *Engineering Structures*; 23 (2001) 470-483

⁴ Drysdale, D., An Introduction to Fire Dynamics, Second Edition; 1998; John Wiley & Sons, 0-471-97291-6

⁵ A.M. Sanad, S. Lamont, A.S.Usmani, and J.M. Rotter. Structural behaviour in fire compartment under different heating regimes – part 1 (slab thermal gradients). *Fire Safety journal*, 2000.

⁶ Huang HC, Usmani AS. Finite element analysis for heat transfer – theory and software. London: Springer-Verlag; 1994.

⁷ A.S. Usmani*, Y.C. Chung, J.L. Torero; How did the WTC towers collapse: a new theory. *Fire Safety Journal* 38 (2003) 501–533

⁸ BS8110-1:1997 Concrete Design, Section 3. Design and detailing: reinforced concrete



NUMERICAL ANALYSIS OF THE EFFECT OF LOCALISED FIRES ON COMPOSITE STEEL CONCRETE BUILDINGS

Jean-Marc FRANSSSEN¹, Dan PINTEA² and Jean-Claude DOTREPPE³

ABSTRACT

Fully developed fires in a compartment are considered to be represented accurately enough by a one zone situation which means that the conditions in term of gas temperatures or incident heat flux to the structure and to the boundaries of the compartment are uniform. Yet, at the early stage of every fire and, if the fire size is small compared to the size of the compartment, the fire is localized and its effects on the structure depend of various parameters such as the fire size, the rate of heat release, but also from the distance of each structural element from the fire. The methodologies that are used for analysing the behaviour of the structure when it is subjected to a uniform situation cannot be applied in these conditions.

The concept of "zoning" can be applied: the structure is arbitrarily divided into several zones in which the situation is approximated as uniform. It will be shown in this paper that this division leads to spurious forces in the structure, especially in shell finite elements.

The structural code of the author has been adapted in a way to accommodate a continuous spatial variation of the fire environment. In the beam finite elements, a series of uncoupled 2D thermal analyses is performed, one in each longitudinal point of integration. Similarly, in the shell finite elements, a series of 1D thermal analyses is performed across the thickness of the slab, one at each point of integration in the plane of the element.

After a discussion of the concept and the particularities dictated by the continuous thermal environment, the methodology utilised will be explained and will be shown in an example consisting of a composite steel concrete 30 by 40 m² car park subjected to a localised fire of the "Hasemi" type as given in EN 1991-1-2. If time permits, the car park tested in Vernon by CTICM will also be analysed. A similar methodology could be used if the fire conditions would be described by a C.F.D. analysis.

¹ Ass. Professor, University of Liege, Department M&S, 1, Chemin des Chevreuils, 4000 Liege, Belgium,
email: jm.franssen@ulg.ac.be

² Prof., University of Liege

³ Dr ir, University of Liege

1. INTRODUCTION

When structural elements are testing against fire in a furnace, every precaution is taken in order to have a uniform spatial distribution of the temperature in the furnace or, more precisely, to have a uniform thermal attack on the elements. In real buildings, the fully developed fire that usually develops in the compartment is considered to be represented accurately enough by a one zone situation, which means that the conditions in term of gas temperatures or incident heat flux to the structure are uniform.

This uniform situation has direct consequences on the numerical simulations that are performed to model the behaviour of the structure. The temperature distribution in the flat elements such as walls, floors and ceilings is essentially uniaxial, with a gradient only across the thickness of the slab. In linear elements such as beams and columns the temperature distribution is essentially 2D with no variation along the length of the elements. This is of course taken into account in the analyses and, in beams for example, as long as the cross section remains the same, the same temperature distribution can be considered for every longitudinal point of integration. The same holds in the slabs for every point of integration in the plane of the elements. The temperature distribution can have a 2D (for slabs) or 3D (for beams) pattern near the edges of the compartment because of the influence of the adjacent cold compartments, but this effect is strongly localised.

There are yet some situations when the thermal attack from the fire is inherently variable in space. This is in fact the case, with very few exceptions, at the beginning of every fire; any fire is localised in the compartment before it turns to a fully developed fire. This preliminary phase is usually disregarded for the analysis of the structural behaviour because the low temperatures associated to this phase are considered to have negligible effects on the structure. In some cases, even this localised fire may be a threat for the structure. On example is a localised fire under a statically determinate steel truss girder. Losing the one member of the truss that is located just above the fire leads to the loss of the whole girder.

Some fires keep a localised character during the entire duration. This can be the case if the fire area is localised within the compartment, for example if a ticket counter is the only engulfed area in an otherwise much larger entrance hall of a railway station or if a few cars burn in a large car park. In these cases, even if the structure is statically indeterminate, a proper analysis of the structural behaviour must take into account the spatial variability of the thermal boundary conditions.

This paper discusses some of the aspects related to this spatial variability and gives some indications how they can be incorporated in a numerical analysis in a cost effective way. Two points are essentially discussed: the three-dimensional character of the temperature distribution and the proper consideration of the temperature distribution in the finite elements.

2. THERMAL PROBLEM

If the thermal boundary conditions vary along the two planar co-ordinates of a slab and if the slab is thermally thick enough to create thermal gradients across the thickness of the slab, which is the case except in very thin steel sheets, then the temperature distribution shows a 3D pattern in the slab. If the thermal boundary conditions vary along the longitudinal co-ordinate of a beam and if the cross section of the beam is thermally thick enough to create thermal gradients in the section, which is the case except in very small steel bars, then the temperature distribution shows a 3D pattern in the beam.

Does it mean that this 3D temperature distribution has to be explicitly taken into account and that it can be determined only by a full 3D thermal analysis? If this is the case,

the cost in term of time required to build the model, in term of memory allocation and in term of computing time would be prohibitive for any structure of s significant size. Two different aspects of the question have to be considered: the variability of the temperature at the joints between adjacent structural members and the variability of the temperature along each member.

2.1 Variability at the joints

The joint between adjacent beam type members is a geometrically complex object, especially if more than two members meet at the joint and these members are of different sizes. Flush end plates, stiffeners, angles, bolts or welds and gaps of different sizes are commonly present in these joints and they all influence the temperature distribution and the heat flow from one member to the other. The exact representation of the thermal situation in the joint can only be made by means of a multitude of 3D finite elements for each joint. Such analyses have been done in the past, usually with the aim of analysing the temperature distribution in detail in a single joint, without any subsequent structural analysis being made on the model. In these thermal analyses, the thermal boundary conditions are either uniform, or they vary in a discrete manner from one to the other side of the joint. For example, the part of a column that is located below the joint is submitted to a standard fire whereas the part of the column that is located above the joint is in a room temperature environment. Even in these cases of stepwise variation of the boundary conditions, it has been observed that the perturbation of the 2D temperature distribution that prevails away from the joint is limited to a short distance from the joint, see **Figure 1**. This means that it can be considered as an acceptable simplification to perform the 3D thermal analysis of each beam member separately, neglecting the local influence of the joint.

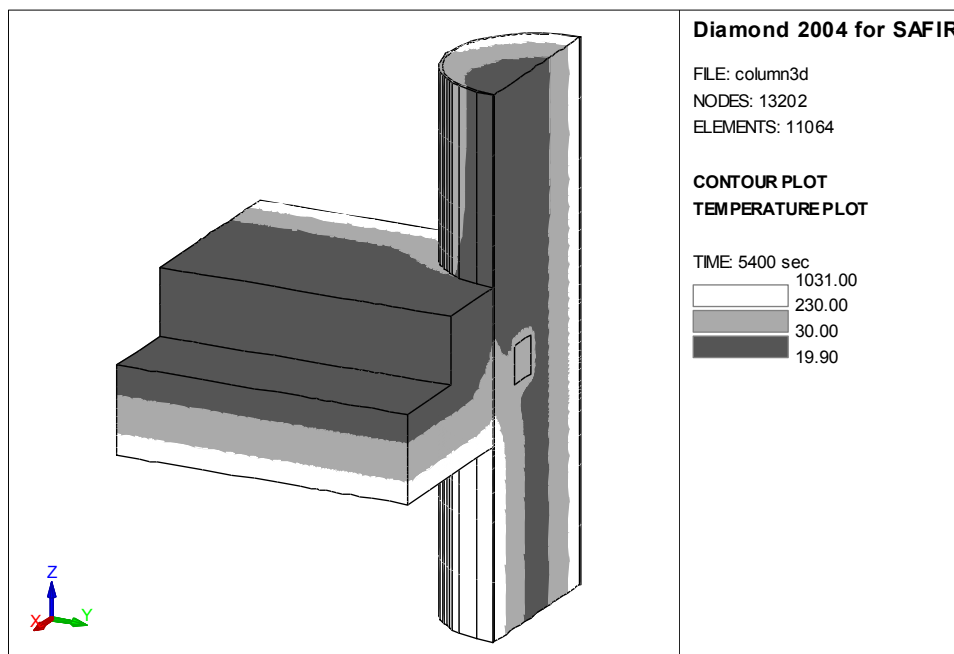


Figure 1: isotherms in a joint between a composite column and a concrete slab

It has to be mentioned that the subsequent structural analysis that will be made of the structure normally relies on oriented finite elements such as beam elements because a structural analysis of a complete building based on 3D solid elements is unfeasible. These oriented elements don't have the capability to take into account the real 3D stress distribution

that prevails in the joints. Some simplifications are also made near the joints when using these elements. In other words, the richness of a full 3D temperature distribution that could eventually be calculated in the joints cannot be exploited by the oriented elements used in the structural analysis.

Thus, instead of a full 3D thermal analysis of the complete structure, it is acceptable to perform a series of 3D thermal analyses, each one in a defined structural member, a slab, a wall, a beam, a column or a member in a truss. This reduces the unfeasible problem into a series of problems of reasonable size.

2.2 Variability along the members

The question examined here is how a variation of the boundary conditions along the axis of a member is reflected in the temperature distribution. In order to investigate this question, a steel member has been analysed because steel has a higher thermal conductivity than concrete and is the material that will have the highest capability to transmit a heat flux along the elements.

The most severe variation of the boundary condition is a stepwise variation, quite unlikely to occur in reality. The situation considered here is an incident flux of 100 kW/m^2 on one part of a steel member and a sudden drop to 0 for the other part of the member. This value of 100 kW/m^2 has been chosen because it is the highest possible incident flux according to Annex C of Eurocode 1 [1]. A frontier with air at 20°C was imposed on the entire length of the plate, for simulating the environment to which the structure re-radiates. The temperature variation along the length of the plate will be examined.

The temperature on the cross section of a steel member is quite uniform. The problem has been analysed as a 2D situation as would be relevant, for example, for a plate (web or flange) of a steel profile; one dimension is the longitudinal axis of the steel member and the other dimension is across the thickness of the plate, see **Figure 2**.

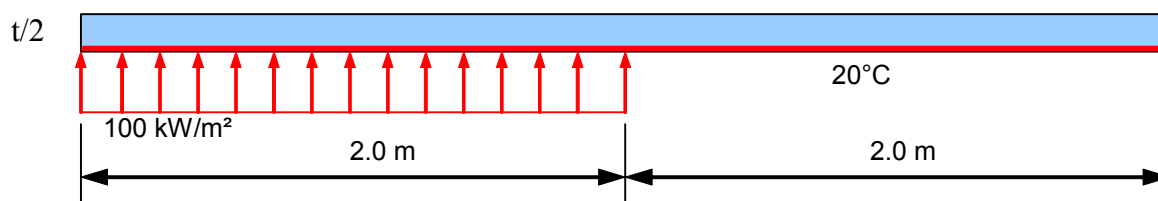


Figure 2: steel bars with a stepwise variation of the boundary conditions

Four values of the section factors A_m/V have been analysed, namely 40, 80, 250 and 400 m^{-1} , that is plate thicknesses of 50, 25, 8 and 5 mm have been considered, with the fire applied on both sides (1/2 of the thickness considered in the analyses owing to symmetry).

Each plate has been analysed as unprotected and also as thermally on each face by 20 mm of a hypothetic product with $\lambda = 0.08 \text{ W/mK}$ and $c\rho = 170 \text{ kJ/Km}^3$ (no water content). Thermal properties of steel and boundary conditions are from Eurocode 3 [2].

A 100 mm thick concrete slab has also been submitted to the same discontinuous boundary conditions.

The results can be seen in terms of isotherms at a given time, see Figure 3, or in terms of temperature evolution along the plate at various times, see Figure 4.

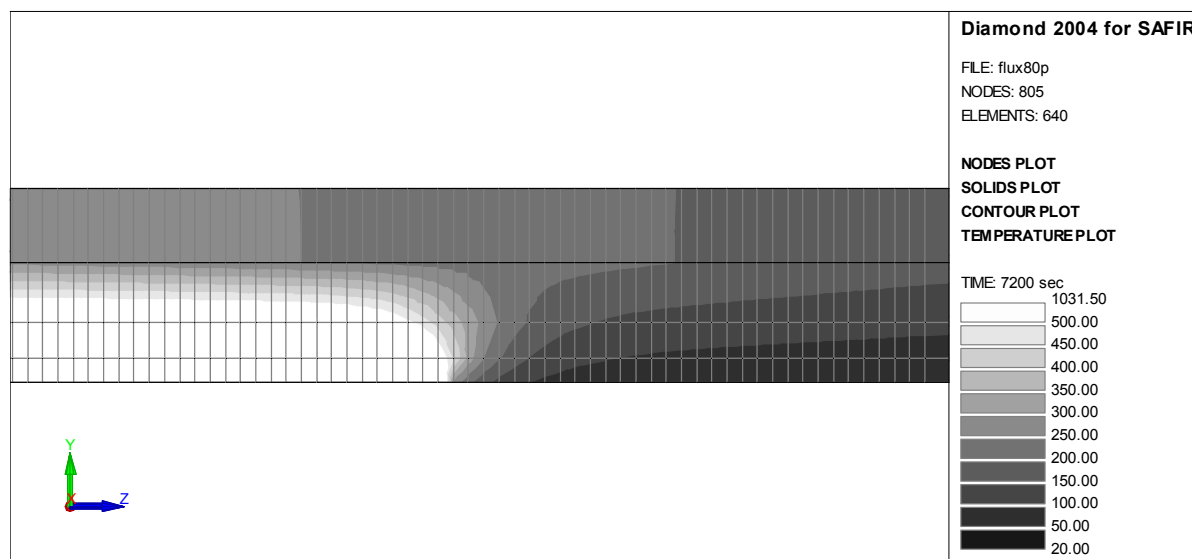


Figure 3: isotherms after 2 hours in a protected 80 mm plate

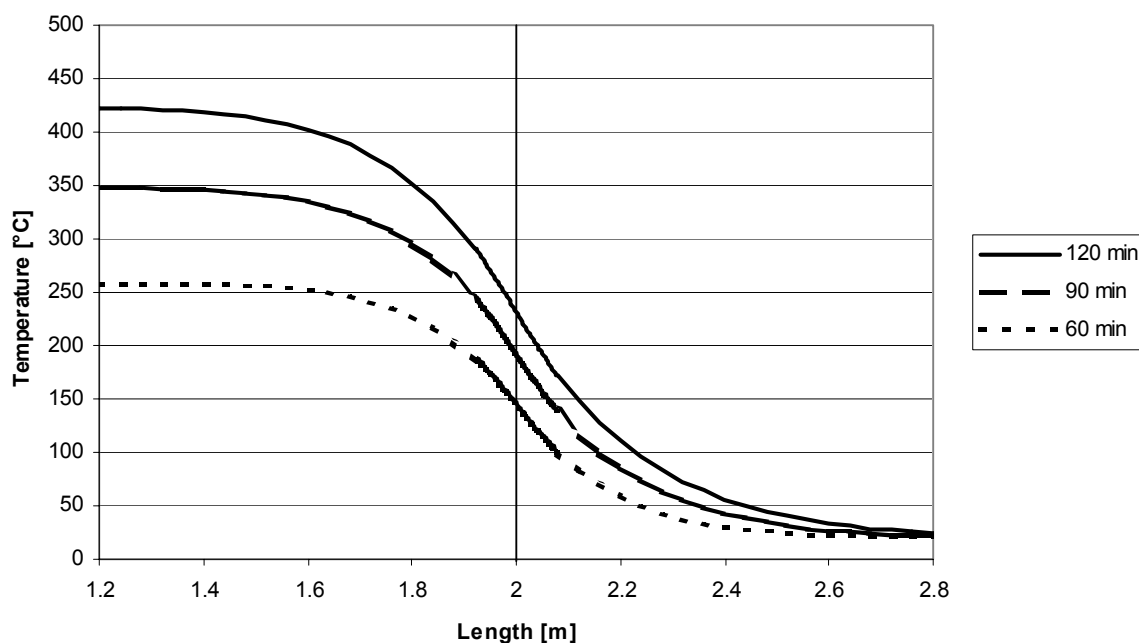


Figure 4: evolution of the temperature along the protected 80 mm plate

The results of all calculations can be summarised in Table I that gives the interface length L_i defined as the distance from midpoint to the point along the plate where the steel temperature changes by less than 10°C to the left (Hot zone) and to the right (Cold Zone) compared to the values at the end of the plate, where the perturbation has no influence. For the concrete slab, the interface length is evaluated on the exposed surface.

Table I: interface length L_i in various situations

t [mm]	Protection	Time [min]	L_i Hot Zone [mm]	L_i Cold Zone [mm]
40	No	10	158	215
40	No	20	165	336
40	No	30	221	429
25	No	10	108	237
25	No	20	156	357
25	No	30	143	444
8	No	10	78	259
8	No	20	71	354
8	No	30	70	411
5	No	10	57	256
5	No	20	56	331
5	No	30	56	364
40	Yes	60	293	328
40	Yes	90	405	463
40	Yes	120	497	580
25	Yes	60	345	400
25	Yes	90	445	539
25	Yes	120	522	655
8	Yes	60	352	466
8	Yes	90	406	585
8	Yes	120	393	674
5	Yes	60	322	464
5	Yes	90	266	563
5	Yes	120	405	633
Concrete	No	60	41	119
Concrete	No	90	46	152
Concrete	No	120	49	178

It can be observed that the interface length:

- is longer in protected sections than in unprotected sections,
- is longer in massive sections than in thin sections,
- increases with time but tends toward a constant value (because the problem tends toward a steady state situation),
- is longer in the cold part than in the heated part,
- is significantly smaller in the concrete slab than in steel plates.

In all situations, the interface length is rather limited: not more than two times the thickness in the concrete slab and not more than 0.5 meter in the steel members. These values have been obtained with a variation in the boundary conditions that is quite extreme and unrealistic. It can be inferred from this analysis that if the temperature in the bars or in the slabs has a tendency to go back to the undisturbed values at a rather short distance of the perturbation when this perturbation is so severe, then this would be the case for even much shorter distances if the perturbation is less severe, for example in the case of a continuous variation of the boundary conditions along the length of the member.

It has indeed been observed [3] that in a IPE600 steel beam submitted to the highly localised fire model of Eurocode 1, the temperature in the sections is very similar when it is calculated either as a series of 2D calculations in different sections, that is without any consideration for the longitudinal heat flows, or as a single 3D calculation in the complete beam.

2.3 Conclusion of section 2

As a conclusion of the above discussion, it seems to be a sufficiently good approximation to calculate the temperatures in a structure subjected to a localised fire as a series of uncoupled uniaxial calculations in the slabs and walls, and as a series of uncoupled 2D calculations in beams in columns. The effect of the variation of the longitudinal boundary conditions on the temperatures that is not considered is negligible. The effect at the joint between adjacent members is more significant but a structural analysis based on oriented members such as beam or shell finite elements is anyway not capable of taking the true temperature field in the joints into account.

3. STRUCTURAL PROBLEM

The question examined here is the influence that the degree of precision in the representation of the temperature distribution has on the stress distribution in finite elements. Only the influence of a longitudinal variation of temperature will be examined here because this is the typical consequence of a localised fire. The question is examined separately for the beam and for the shell finite elements.

3.1 In beam finite elements

If the temperature is varying along the length of an otherwise unstressed beam, this temperature variation should not generate any stress in the beam. What kind of representation of this variation has to be taken into account for not generating spurious stresses in beam finite elements?

If the **average** temperature along the length of the element is taken into account, the thermal strain ε_{th} is a constant. If the longitudinal field of displacement $u(x)$ is a linear function of the longitudinal co-ordinate x (with is typical in elements with 2 nodes), then the strain $\varepsilon = \partial u(x)/\partial x$ is also a constant and the element can find a position, in fact a thermal elongation, leading to no mechanical strains $\varepsilon_m = \varepsilon - \varepsilon_{th}$ and hence to no stresses.

If a linear variation of the temperature along the length is taken into account, the thermal strain $\varepsilon_{th}(x)$ is a linear function of x .

- If the longitudinal field of displacement $u(x)$ is linear, then the strain $\varepsilon = \partial u(x)/\partial x$ is a constant and the mechanical strain will be linear whatever the thermal elongation of the member because $\varepsilon_m(x) = \varepsilon - \varepsilon_{th}(x)$. The element will share the thermal elongation between the longitudinal points of integrations, creating spurious compression stresses in some points and spurious tensile stresses in others.
- If the longitudinal field of displacement $u(x^2)$ is a second order function of x , then the strain $\varepsilon(x) = \partial u(x^2)/\partial x$ is linear the element can find a position leading to no mechanical strains $\varepsilon_m = \varepsilon(x) - \varepsilon_{th}(x)$ and hence to no stresses. The software SAFIR [4] has a non linear longitudinal displacement field owing to a 3rd central node that bears the non linear component of the longitudinal displacement. It is thus capable of representing linear temperature distributions whereas most common elements with only 2 nodes are not.

Figure 5 shows the diagram of axial force in a hypothetical 10 meters long cantilever beam subjected to a localised fire located 2.5 meters under the supports (on the left of the

Figure). The beam finite element of SAFIR has been forced to be linear in this application. After one minute, the uniform temperature in element 2, for example is 488°C at the first longitudinal point of integration and 276°C at the second point of integration. The axial force at these integration points is +82 and -82 kN which, for this IPE80 section, leads to spurious stresses of 107 N/mm². When the longitudinal displacement in the elements is allowed to be a second order function of the longitudinal co-ordinate, the axial force at the same instant drops to less than 10⁻⁴ Newton.

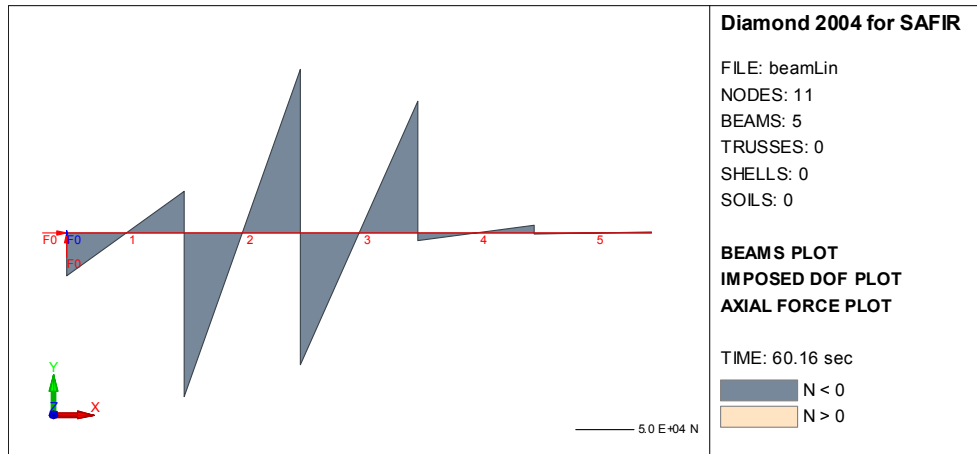


Figure 5: axial force diagram in a linear beam element

3.2 In shell finite elements

When a fire is localised, the thermal gradients in the plane of a shell are radial around a point that is the foot of the normal from the fire source to the plate. If the gradient in the radial direction is linear and there is no gradient in the circumferential direction, a shell finite element in which the membrane displacement is a linear function of the two planar co-ordinates will generate spurious stress in the radial direction, but none in the circumferential direction. A finite element in which the membrane displacement field is a second order power of the planar co-ordinates is required to represent the linear gradient without any spurious stresses.

Because the shell element in SAFIR is linear, the spurious radial stresses cannot be avoided and their influence will have to be evaluated.

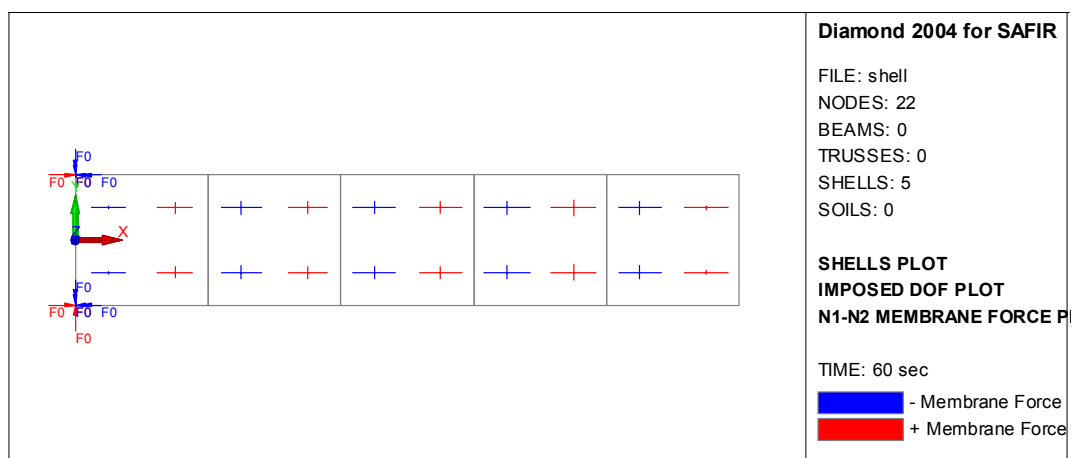


Figure 6: membrane forces in a steel plate with uniaxial gradient

Figure 6 shows the membrane forces in a hypothetical 1 x 5 m² cantilever beam made of a 20 mm thick steel plate in which a thermal gradient of -100°C/m after 60 seconds has been introduced in the X direction. It can be observed that the most important spurious stresses are in the direction of the thermal gradient (in the order of 85 N/mm²), with smaller stresses also observed in the transverse direction (in the order of 30 N/mm²).

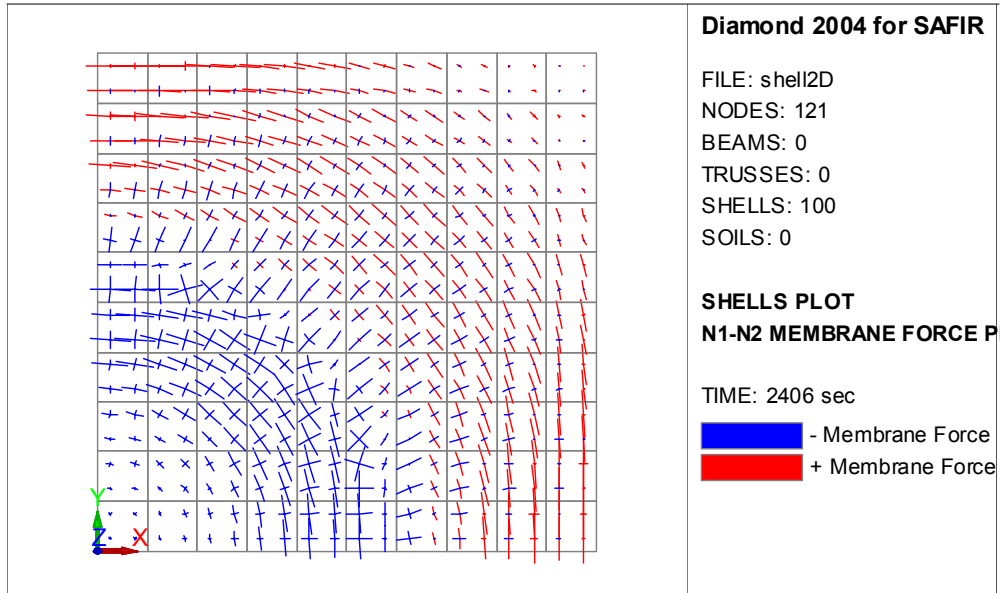


Figure 7: membrane forces in a steel plate with radial thermal gradient

Figure 7 shows the membrane forces distribution in a steel plate subjected to a localised fire in the centre (1/4 only represented). Although the theoretical solution to this problem is not available (all material properties are non linear), the stress distribution fits with common sense and is quite continuous which seems to be an indication that spurious stresses are of a lower order of magnitude than the true stresses.

4. ALGORITHMIC MODIFICATIONS

Various algorithmic modifications are required because the temperature distribution in the beams, for example, is no longer the same in all sections (the same holds for shells). Much more information has to be stored in the data structure. This data structure has been adapted in order to limit the increase of memory requirement.

The first modification was the division of the matrix where all the parameters related to the constitutive model are stored for each point of integration of the structure. This is because the number of parameters required for the uniaxial models used in the beams is significantly smaller than the number of parameters required for the plane stress models used in the shell. Utilisation of a single matrix for all integration point would thus spoil a lot of memory cells (in the integration points with uniaxial laws). There is now a matrix for the integration points with uniaxial laws and another matrix for the points with 2D laws.

The other big modification is linked to the thermal calculations. Instead of a single 2D calculation for a beam member, two 2D calculations are performed for each beam finite element that make the beam member. In these 2D thermal analyses, the boundary conditions are highly dependent on the location of the analysed section in the beam element with respect to the localised fire in the compartment. This means that the structural model has to be created before the thermal calculations are performed and the thermal module must have access to

this structural file in order to determine this position of the analysed section. If the size of the section is small with respect to the size of the compartment, it is sufficient to represent the position of the section by the position of one characteristic point, le centre of gravity for example.

If a localised fire has to be analysed in SAFIR, two 2D thermal analyses are performed in each beam finite element (one at each of the longitudinal point of integration of the beam element) and four 1D thermal analyses are performed in each shell finite element (one at each of the planar point of integration of the shell element).

5. APPLICATION

An example is presented here as an application of the previous concepts and as a validation of the algorithmic modifications. In order to eliminate the complexity of the problems linked to the CFD file, the localised fire is taken according to the localised model presented in Annex C of Eurocode 1 [1].

The structure is part of an open car park, see **Figure 8**. In the X direction, the 15 cm slabs has 7 spans of 5.4 m, i.e. a total length of 37.8 m. In the Y direction, the columns are spaced at 15 m, which makes a total length of 30 m. The external columns are made of HE300AA, the central columns are made of HE500A and the beams of IPE500 sections. The beams extend only in the Y direction. The concrete slab is linked to the steel beams which generates a composite behaviour. The Figure shows different colours in the shells because the reinforcing bars are different in the spans and on the supports.

The fire source is created by four cars located side by side at $Y = 27$ m, i.e. near one of the longitudinal side of the car park. The first car burning is at $X = 18.9$, i.e. in the centre of span 3. Cars 2, 3 and 4 are at $X = 21.6$, 24.3 and 27 m respectively. There is a delay of 12 minutes for the fire to propagate from each car to the next one, with car one being first ignited. The maximum heat release rate for each car is 9.8 MW, 30 minutes after ignition.

Approximately one third of the car park is supposed to be affected by the fire, whereas the rest is supposed to remain at room temperature.

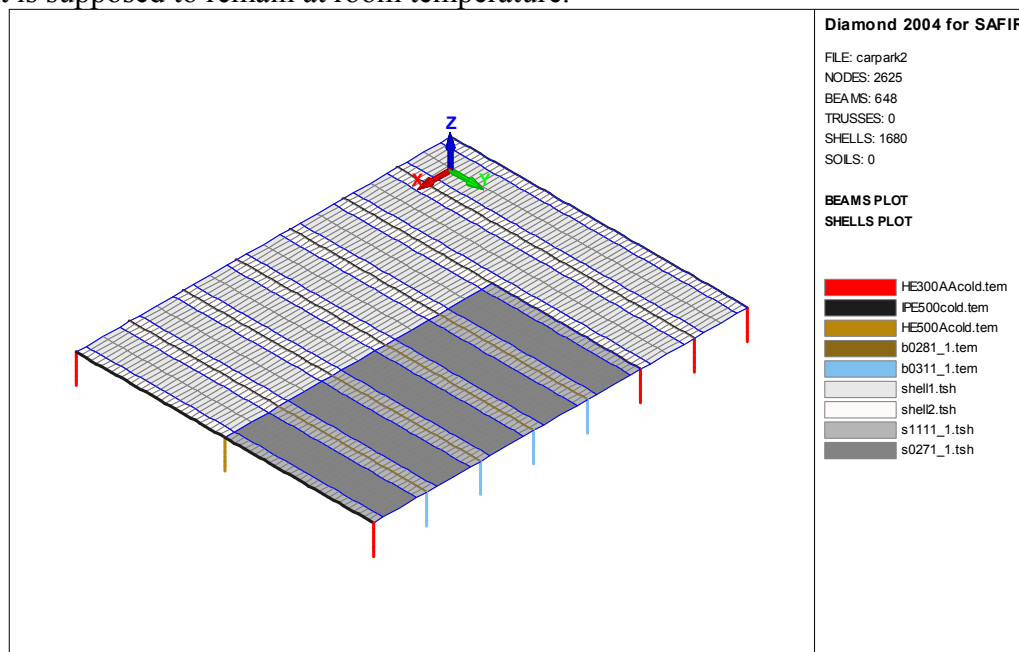


Figure 8: car park subjected to a localised fire

Figure 9 shows the vertical displacements in the slab after 20 minutes of fire. At this moment, cars 1 and 2 are on fire. The displacement pattern is continuous but this is inherent to the formulation of these displacement based elements. It would be the case also with spurious stresses.

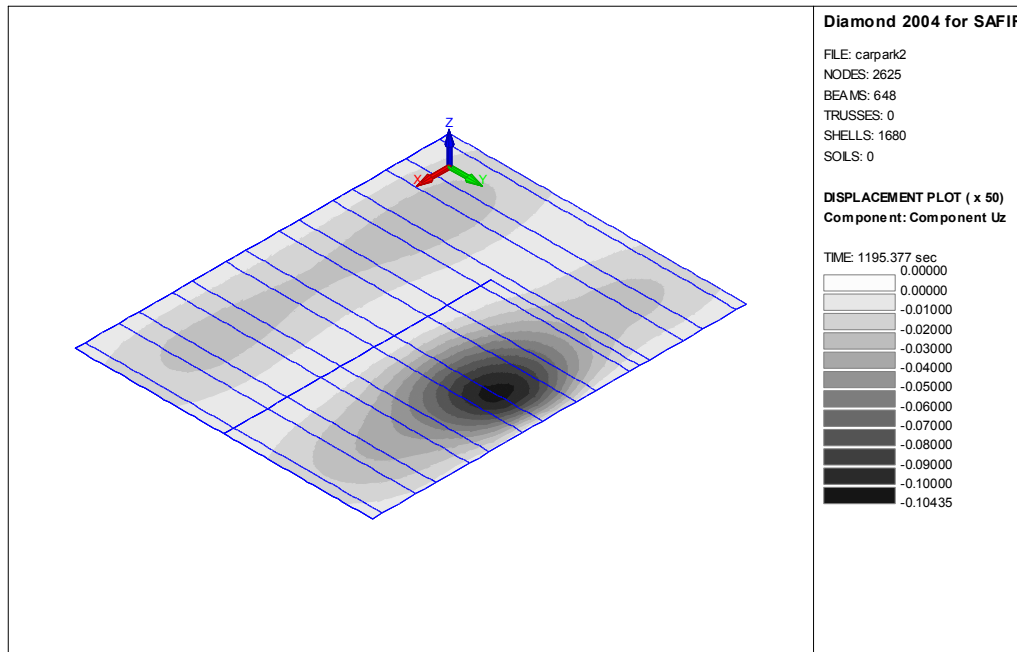


Figure 9: vertical displacements after 20 minutes

Figure 10 is more interesting because it shows how continuously distributed are the bending moments, notwithstanding the local character of the fire and the rather high aspect ratio of 3.4 for some elements.

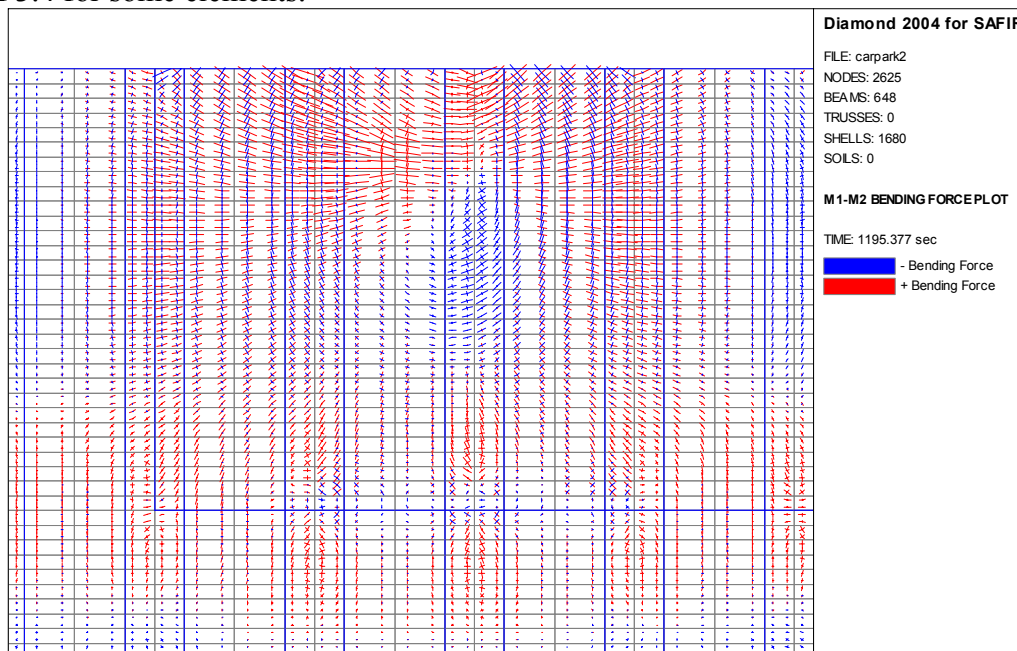


Figure 10: bending moments after 20 minutes of fire

6. CONCLUSIONS

The basic concepts for considering a localised fire into a numerical structural model have been highlighted. The application of these concepts requires significant modification in the algorithmic structure of the software. The relevant modification have been implemented into the software SAFIR and the applicability has been shows for a particular case in which the localised fire was based on Annex C of Eurocode 1.

The route has been paved for analysing a structure for which the thermal environment would be determined by a CFD software.

7. REFERENCES

- [1] *Eurocode 1: Actions on structures – Part 1-2: General actions – Actions on structures exposed to fire*, EN 1991-1-2, November 2002, CEN, Brussels.
- [2] *Eurocode 3: Design of steel structures – Part 1-2: General rules – Structural fire design*. ENV 1993-1-2; CEN, Brussels, 1995.
- [3] *Effect of localised fires on continuous steel beams*, Gens F, Franssen J-M & Dotreppe J-C, EUROSTEEL 2005, 4th European Conf. on Steel and Composite Structures, Hoffmeister B. & Hechler O. ed., Aachen (2005), 85-92
- [4] *SAFIR. A Thermal/Structural Program Modelling Structures under Fire*, Franssen J-M, Engineering Journal, A.I.S.C., Vol 42, No. 3 (2005), 143-158

Timber Structures



THERMO- MECHANICAL MODELLING OF THE TIMBER CONNECTION BEHAVIOUR UNDER FIRE

Patrick RACHER¹, Karine LAPLANCHE² and Dhionis DHIMA³

ABSTRACT

As timber is a combustible material, fire safety is a significant obstacle for the use of the timber in buildings. Among the various structural components, the connections are often the weakest elements in a timber construction. In fire situation as well as in normal condition, they govern the load-carrying capacity of the structure and its safety. However, the lack of knowledge was pointed out for a general joint design when setting new rules as the Eurocode 1995-1.2^[1].

In this paper, a three-dimensional finite element approach is developed to investigate the performance of timber dowelled joints in fire. In a first part, the three-dimensional finite element model is presented. The thermo-physical modelling of the components is described. For the mechanical simulation, the plasticity is considered using the Von Mises criterion for the steel components and the Hill criterion for timber.

In a second stage, a validation of the proposed model is achieved considering experimental results in normal and fire situations. This evaluation is made for the thermal and the mechanical parts of the model. Then, the first stage of the general research program on the fire performance of timber connections is described. The analysis is focused on the steel to timber fastener behaviour in fire. With fasteners of 12 to 20 mm in diameter, the simulations are done to evaluate the influence of the timber thickness. Slip modulus and load-carrying capacity of the fasteners are evaluated with time exposure in fire.

¹ Assistant Professor, Blaise Pascal University Clermont, Civil Engineering Laboratory, 63174 Aubiere, France; Email: patrick.racher@lgc.univ-bpclermont.fr.

² PhD student, Blaise Pascal University Clermont, Civil Engineering Laboratory, 63174 Aubiere, France; Email: karine.laplanche@lgc.univ-bpclermont.fr.

³ Engineer, CSTB, Safety, structures and fire Department, 77421 Champs sur Marne, France, Email: DHIMA@cstb.fr.

1. INTRODUCTION

Due to the combustibility of the timber, research was focused on the reaction to fire and the charring rate of wood products. The structural analysis of timber in fire was mainly addressed to the behaviour of beams and columns ^[2]. Only limited works were carried out to evaluate the fire performance of timber connections and time-to-failure ^[3, 4, 5]. The most significant results were related to the load-carrying capacity of nailed connections ^[6].

As performance-based approach is now widely introduced in the national regulations, the needs arise for modelling the joint behaviour under fire. Like in normal condition, connections are often the governing components of the timber structure behaviour. Their performances are particularly important for safety analysis. To date, several works are dedicated to the analysis of dowelled connections ^[7, 8]. Investigations for an analytical model are based on the Johansen's yield theory ^[9] using an embedding strength reduction with temperature.

Nevertheless, optimisation of the joint performance in fire requires a large amount of experiments. Thus, the development of a suitable numerical model is necessary to evaluate many non linear effects such as the load distribution among the fasteners, the internal stresses in the reduced timber elements, the properties of components, so as the heat transfer. At the material scale, both problems are complex when considering the effects of anisotropy and moisture movement. The present study of timber connections exposed to fire is addressed at the meso-scale in order to define not only the failure level but the whole range of the behaviour. The overall objective of this research is to provide the connection properties needed as inputs for a performance based approach at the structural scale.

In a first stage, standard fire conditions are considered. The thermal field within the connected elements and the fasteners is defined by a simplified thermal analysis based on thermal properties of timber given in EN1995-1.2 ^[2]. Taking into account the variation of the timber characteristics with temperature, the mechanical response of the connection is obtained from a non-linear finite element analysis. Both models are working with constant three-dimensional meshing of the joint area. This thermo-mechanical modelling was first validated on test results for steel to timber joints in normal and fire conditions ^[10]. Then, simulations are performed for single and multiple fasteners in order to investigate the effect of the joint geometry on the time to failure.

2. FINITE ELEMENT MODELLING

When timber joints are exposed to high temperatures, thermal and mechanical problems interact. Depending on the joint pattern, the heat transfer results in stiffness variation of the components which modifies the internal behaviour of the timber joint. Induced by the heating of the steel parts and the charring of the timber, these variations govern the joint slip in fire and the time to failure which is mainly reached in shear.

In our approach, the thermal and mechanical responses are calculated using successively two three dimensional finite element models. The calculations are done at the same time increment with the same meshing of the connection. This modelling approach was implemented in the finite element code MARC, using quadratic elements with 20 nodes.

2.1 Thermal model

At each time increment, the calculation of the temperature field inside the components

is based on the theory of heat transfer considering the given thermal flux. A main assumption is that no internal sources are considered.

For the thermal properties of the materials, the well-known properties of steel are taken into account as defined in the EN1993-1.2 rules^[11]. At this stage, the main difficulty is linked to the pyrolysis modelling of the timber. From the works done in this area, three models (figure 1) were preliminary evaluated on previous experiments^[12, 13, 14, 15].

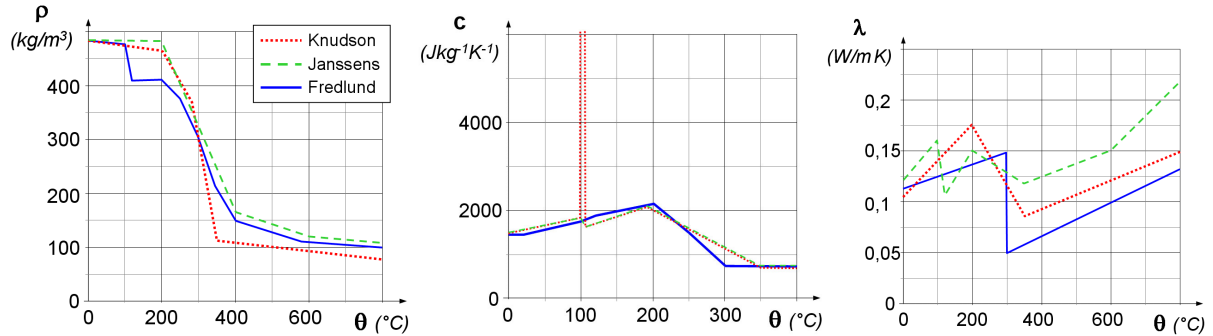


Fig. 1 - Variation of the thermal properties for softwood timber.

When considering timber sizes as encountered for structural elements, this analysis shown that better results are obtained using the Fredlund model. This model was considered in the thermal calculations.

2.2 Structural model

To describe the load-carrying capacity as well as the stiffness of the timber connections, the model has to take into account the local plastic behaviour of the material beneath the fasteners. This local behaviour of the timber is of main importance for the simulated result as it governs the load distribution on the fasteners and the timber stress interactions in the joint area^[16].

Then, elastic-plastic behaviour is considered for the steel components while the timber is assumed as an non-linear orthotropic material. With the hypothesis of transverse isotropy, the elastic strain-stress relation is given by $\{\epsilon_{ij}\} = [S_{ij}]\{\sigma_j\}$ with the compliances :

$$S_{11} = \frac{1}{E_0}, S_{22} = S_{33} = \frac{1}{E_{90}}, S_{44} = S_{55} = \frac{1}{G} \quad (1)$$

where E_0 and E_{90} are the elastic modules parallel and perpendicular to the grain,

G is the shear modulus.

The Hill criterion was considered for the plasticity of the timber. It was expressed by:

$$\sigma^2 = a_1(\sigma_y - \sigma_z)^2 + a_2(\sigma_z - \sigma_x)^2 + a_3(\sigma_x - \sigma_y)^2 + a_4\tau_{zx}^2 + a_5\tau_{yz}^2 + a_6\tau_{xy}^2 \geq 1 \quad (2)$$

$$\text{with :} \quad a_1 = \frac{1}{\sigma_{c,90}^2} - \frac{1}{2\sigma_{c,0}^2} \quad a_2 = a_3 = \frac{1}{2\sigma_{c,0}^2} \quad a_4 = a_5 = a_6 = \frac{1}{\tau_v^2} \quad (3)$$

where σ_i and τ_{ij} are the timber stresses,

$\sigma_{c,0}$ and $\sigma_{c,90}$ are the compressive yield strength parallel and perpendicular to the grain,

τ_v is the shear yield strength of the timber.

Furthermore, a Mohr-Coulomb criterion is introduced at the interface between the timber and the fasteners. This point is important in order to take into account the contact and the friction effects on the timber stresses beneath the fastener. For standard bolts or dowels, the friction coefficient is set equal to 0,3.

With these assumptions, the calculations are achieved considering the mechanical properties of the materials for the given thermal field. As shown on the figure 2, the properties are modified with the temperature using the coefficients $k_{\theta,w}$ for timber and $k_{\theta,a}$ for steel defined in the EN1993-1.2 ^[11] and EN1995-1.2 ^[1] rules. In complement, the friction remains constant along the resisting part of the timber in contact with fasteners.

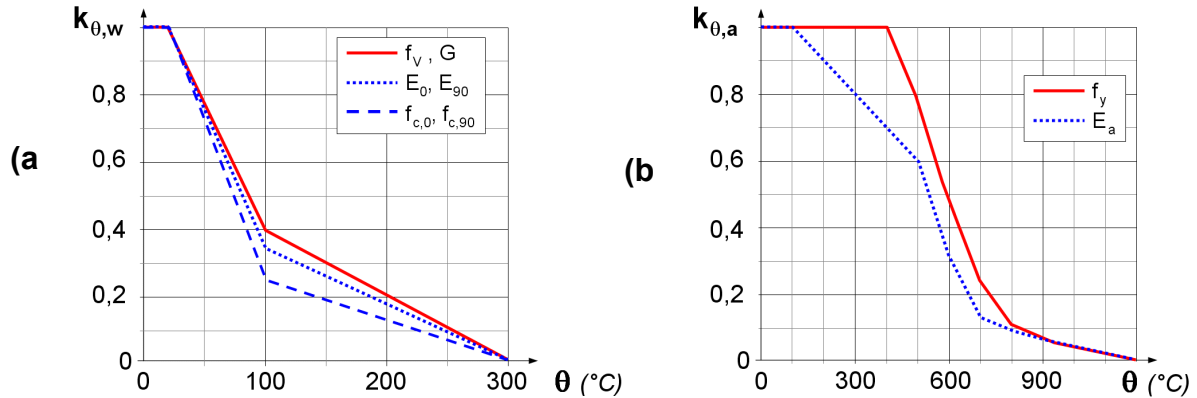


Fig. 2 - Variation of the mechanical properties with temperature: a) timber, b) steel.

3. EXPERIMENTAL VALIDATION

A number of fire tests on timber connections were carried out in France ^[10, 17]. The results obtained in normal and fire conditions for steel to timber and timber to timber joints are used for validation of the modelling (figure 3 and table 1). With glued laminated members of strength class GL24h, the theoretical reference capacity is calculated from the Johansen and the block shear formulations ^[9, 18].

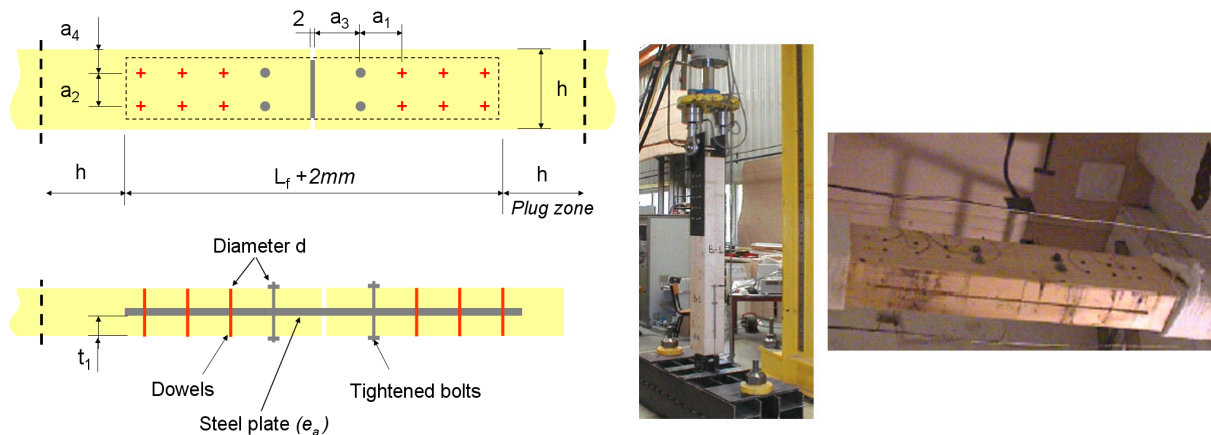


Fig. 3 - Geometry of the steel to timber connections and configuration of normal and fire test.

Table 1 - Geometry (in mm) and theoretical load-carrying capacity R_j of the joint.

d	t_1	h	$a_1=a_3$	a_2	a_4	e_a	R_j (kN)	
							Johanssen	Block shear
16	75	160	112	64	48	8	342	351

For comparison of the model and experimental results, it was taking into account the material properties defined in the table 2. Two set of properties were considered for the timber as only embedding tests were carried out.

The finite element sensitivity was examined during initial simulations. Then, a two-stage validation was carried out.

Table 2 - Material properties of the timber and steel components.

	E_0	E_{90}	G	ν	$f_{c,0}$	$f_{c,90}$	f_v
Timber	10 000	333	625	0,41	21,8	5,2	2,8
	12 000	400	750	0,41	27,8	6,2	3,5

	E	G	ν	f_y
Fastener	210 000	5 000	0,33	300
Steel plate	210 000	5 000	0,33	355

In a first stage, the model and test results are compared for normal conditions. The plastic behaviour of the fastener was only obtained for test 3, otherwise brittle shear failures were observed (figure 4-b). The mean value of the load-carrying capacity was equal to 335 kN. Comparatively to the tests, the figure 4-a shows the ability of the model to predict the behaviour of the connection. A more accurate estimation of the joint stiffness requires a better estimation of the timber modulus by tests or identification. At the yield level ($F=260\text{kN}$), the figure 4-c presents the shear stress distribution in the timber. The stress concentration along the row is in accordance with the observed failure.

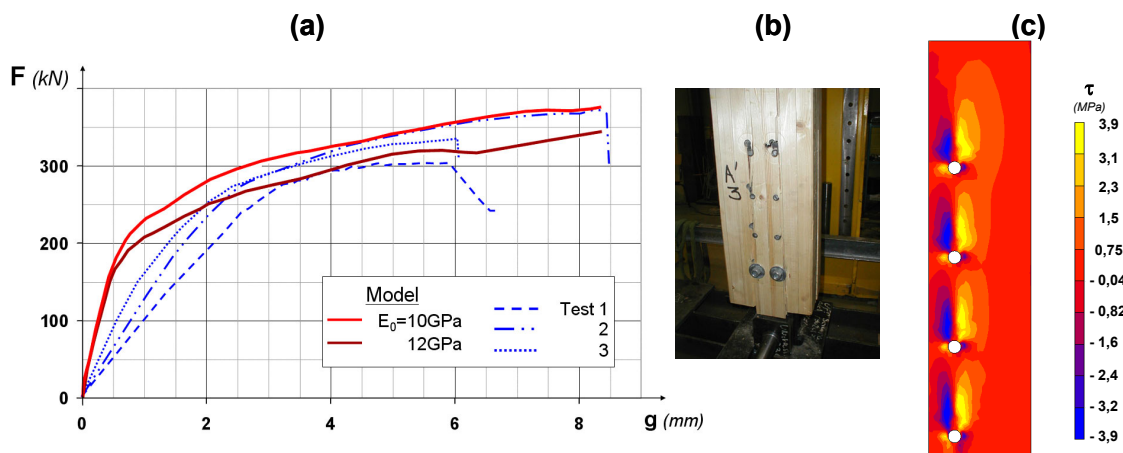


Fig. 4 - Load-slip behaviour (a), failure mode (b) and timber shear stresses (c, $E_0=12\text{ GPa}$).

The second stage of validation is conducted for fire exposure of the joints. The tests were carried out at the CTICM fire station for loading ratio η_{fi} of 10 and 30% and a standard fire exposure. With two replications, the joints reached an average time to failure t_{fi} respectively equal to 55,5 and 36 minutes. For these conditions, the two step thermo-mechanical model leads to the following predictions: $t_{fi} = 56,5$ minutes for $\eta_{fi} = 10\%$ and $t_{fi} = 40$ minutes for $\eta_{fi} = 30\%$. For the calculated joints, the deviation is about 10% in predicted time to failure.

Furthermore, the temperature profiles are compared with the thermocouples measurements. The figure 5 gives the temperatures for the timber element and the dowels at the load level of 10%. The figure shows that the increase of the temperature inside the components is almost linear with time. As the heat flux is limited through the dowels, their properties are very little affected. The main changes taken into account during the simulation

are related to the timber properties.

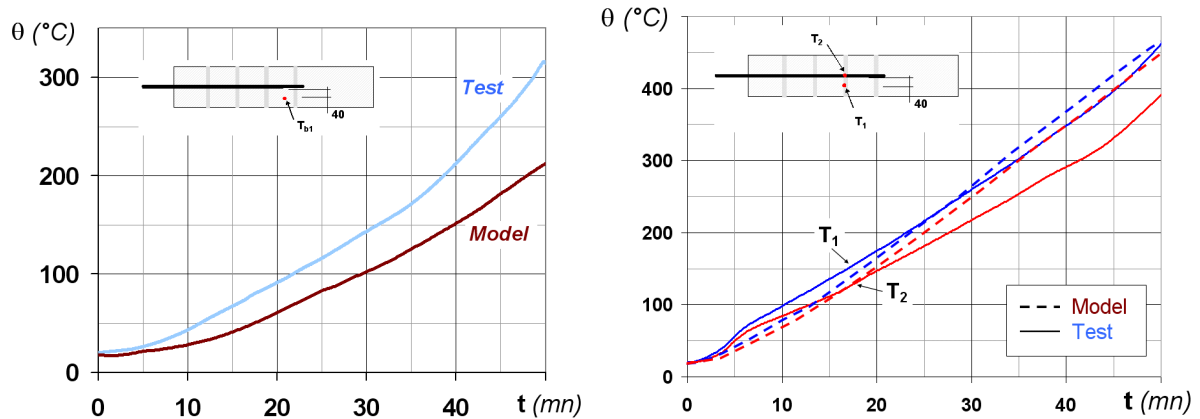


Fig. 5 - Temperature in the timber and in the dowels under standard fire.

From these results, the proposed approach is in good agreement with the experiments. This validation is actually extended to all the connection tested to estimate the robustness of the model which is demonstrated by the first results on the simulated time to failure (table 3).

Table 3 - Experimental and simulated time to failure for different load ratio η_{fi} .

Connection type	t_1 (mm)	t_1 or e_a (mm)	d (mm)	η_{fi} (%)	t_{fi} (mn)		Error (%)
					Tests	Model	
Timber to timber	64	64	16	10	59,5	60,5	2
				20	45,5	46,5	2,2
				30	39,5	36	8,9
Steel to timber	75	75	16	10	55,5	56,6	1,9
				30	36	40	11
	95	95	20	10	90	80	11

4. BEHAVIOUR OF SINGLE FASTENER JOINT

For the analysis of the strain and the stress interactions in the joint area, the effect of the main parameters needs to be first investigated on single fastener joint. For steel to timber connections, the main parameters are the thickness of the outside timber member and the heat flux through the steel plate. They affect the thermal transfer as well as the variation of the relative stiffness between components. Both effects control the mechanical part of the response.

For dowel of 16mm in diameter, simulations were carried out for timber thickness t_1 varying from 50 to 250 mm. With a given joint geometry, the thermal field is first calculated for a time of exposure equal to 30, 60 or 90 minutes. Then the load-slip curve of the heated joint is simulated. The figure 6 gives the calculated load-slip curves for thicknesses t_1 equal to 200 and 125mm.

As mentioned previously, the fire behaviour of the timber joint is clearly affected by the reductions of the timber properties more than those of the fasteners properties. But for the steel to timber connection, a specific parameter is related to the relative stiffness variation of the steel plate and timber elements in fire exposure. For unprotected steel plates, the reductions of stiffness and bearing strength result in increased rate of the load-carrying capacity reduction with smaller timber thickness t_1 (figure 6).

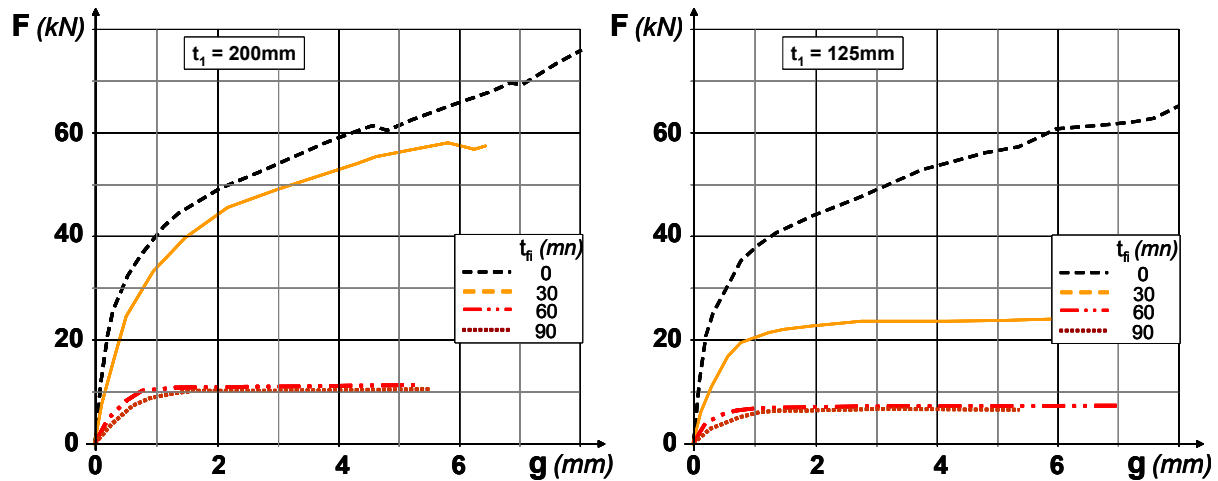


Fig. 6 - Load-slip behaviour of the joint for various time of fire exposure.

In the apparent linear domain, the variation of the slip modulus with time of fire exposure depends on the thickness t_1 . The figure 7 gives the relative reduction coefficient k_g . For a required fire resistance R30, timber structures could take benefit of a more precise definition for the conversion factor η_f defined in the Eurocode 5 ($\eta_f=0,13$ for nails and 0,44 for dowels). From these results, the values given in the design rules correspond to a fixed thickness t_1 about 60mm for nails and 130mm for dowels.

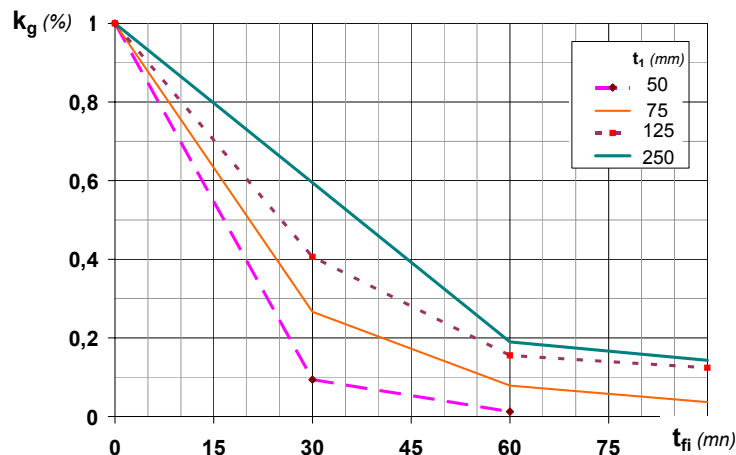


Fig. 7 - Reduction of slip modulus with time of fire exposition.

At the yield load level, Noren^[6] and Povel^[8] have shown the applicability of the analytical model defined by Johanssen^[9] for nailed or dowelled timber to timber joints. In order to extend the use of this calculation method to the steel to timber dowelled joints, comparison with the finite element results were carried out.

From the simulated temperature profile, average temperatures θ_f for dowel and θ_t for timber were considered to define the reduced properties of the joint components. Facing to the lack of available data on the embedding strength at elevated temperatures, the reduction of embedding is assumed to be the same as for the timber compressive strength. This assumption agreed with the thermo-mechanical simulations as shown on the figure 8.

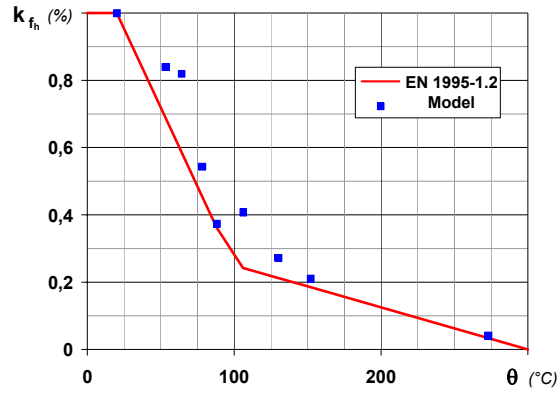


Fig. 8 - Reduction coefficient for the timber embedding strength with temperature.

Then, the fastener capacity $R_{1,fi}$ for an exposure time t_{fi} is defined as:

$$R_{1,fi} = \min \left[\frac{f_{h,\theta_t} t_{1,fi} d}{f_{h,\theta_t} t_{1,fi} d \left[\sqrt{2 + \frac{4 M_{y,\theta_f}}{f_{h,\theta_t} t_{1,fi}^2 d}} - 1 \right]}, \frac{2 \sqrt{M_{y,\theta_f} f_{h,\theta_t} d}}{2 \sqrt{M_{y,\theta_f} f_{h,\theta_t} d}} \right] \quad (4)$$

where: f_{h,θ_t} is the embedding strength at the temperature θ_t ,

M_{y,θ_f} is the fastener yield moment for θ_f ,

$t_{1,fi}$ is the effective timber thickness after a time exposure t_{fi} .

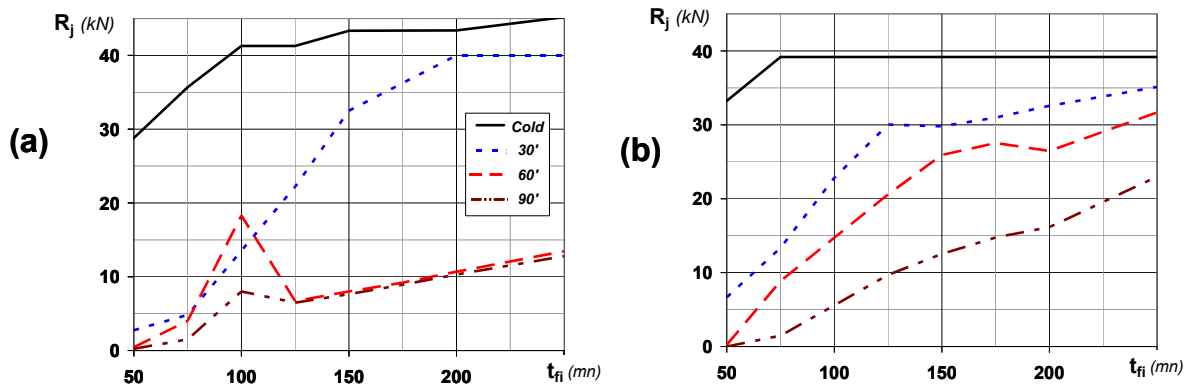


Fig. 9 - Yield load level predictions: a) model results, b) Johanssen theory.

The figure 9 shows the simulated and the calculated values of the yield load for time exposure varying from 0 to 90 minutes. If the changes are quite similar up to 30 minutes, large discrepancy is obtained in the predicted values by the analytical method. This indicates that the use of the Johanssen theory needs a better estimation of the temperatures in fastener and in the timber. For larger time and thickness, the fastener capacity is no more governed by the bending of the dowel and the timber embedding, but by the plate behaviour.

To state an approach simpler than FEM model, the calculation method for fire joint design could be based on a time dependant reduction capacity $k_{1,fi}$. Including a thickness effect, this factor will be applied to the fastener capacity in normal conditions R_1 .

$$R_{1,fi} = k_{1,fi}(t_1) R_1 \quad (5)$$

From the previous results for a 16 mm dowel, the figure 10 gives a preliminary estimation of the coefficient $k_{j,fi}$ with time exposure and timber thickness.

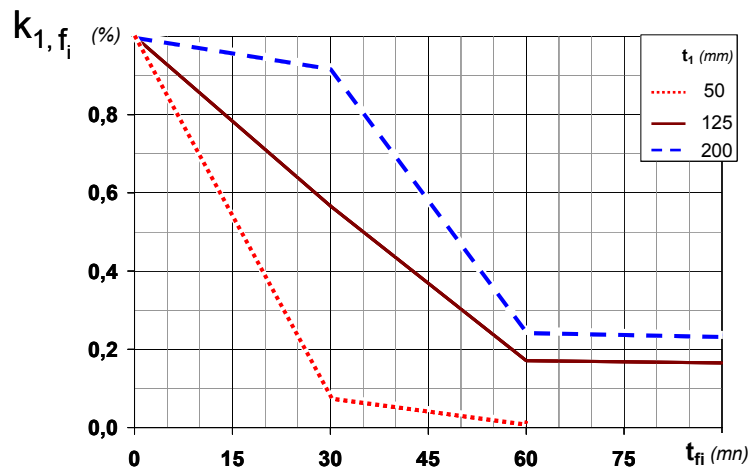


Fig. 10 - Reduction coefficient for the steel to dowel fastener capacity with time of exposure.

5. CONCLUSION

In this paper, a three-dimensional finite element approach is proposed to evaluate the performance of steel to timber dowelled joints in fire. The model was validated on the experimental results obtained on dowelled timber to timber and steel to timber joints. Differences between measured and predicted time to failure are less than 10%. The thermal simulations are also in agreement with thermocouples data.

Aiming to develop a general and simple approach which can be used easily for the design, a first step of analysis is focused on the fastener capacity in steel to timber joint. The conclusion is that the Johansen theory cannot be extended to the calculation of heated steel to timber joints whereas its use was demonstrated for timber to timber connections. A proposal is made for an analytical calculation which can be defined for the both type of connection.

Further simulations can give a precise definition of the time dependant reduction coefficient for the fastener capacity. Then, the study of the fire performance of timber joints will be extended at the connection level. At this level, a large analysis is required as the effective number and the block shear failure mode are to be considered.

5. REFERENCES

- [1] CEN TC250-SC5, "EN1995-Part 1.2: Design of timber structures - General rules Structural fire design", Brussels, 2004.
- [2] Schaffer, Erwin L. and al, "Strength validation and fire endurance of glued laminated timber beams", Research paper FPL 467, Forest Prod. Lab., Wisconsin, USA, 1986
- [3] Buchanan, Andrew H., "Fire performance of timber construction", Progress in Structural Engineering and Materials, pp 278-289 (2), 2000.

- [4] König, Jürgen and Fontana, Mario, “The performance of timber connections in fire-test results and rules of Eurocode 5”, Proceeding RILEM Symposium Joints in Timber Structures, Stuttgart, pp 639-648, 2001.
- [5] Fornather, Jochen, Bergmeister, Konrad and Hartl, Hans, “Fire behaviour of steel and fasteners in wood composites”, RILEM Symposium Joints in Timber Structures, Stuttgart, pp 619-628, 2001.
- [6] Noren, Joakim, “Load-bearing of nailed joints exposed to fire”, Fire and Materials. 1996; Vol. 20, pp 133-143, 1996.
- [7] Frangi, Andrea and Mischler, Adrian, “Fire tests on timber connections with dowel-type fasteners”, CIB W18, paper 37-16-2, Meeting XXXVII, Edinburgh, 2004.
- [8] Povel, Daniel, “Tragfähigkeit von Holzverbindungen mit stabförmigen Verbindungsmitteln im Brandfall“, PhD Thesis, Technical University Berlin, 2002.
- [9] Johansen, K.W., “Theory of Timber Connections”, Forest Products Journal, Vol.25, N°2, pp 249 -262, 1949.
- [10] Racher, Patrick and al, “Fire behaviour of joints in timber structure” (in French), Final report, FFB-IRABOIS, Paris, May 2004.
- [11] CEN TC250-SC3, “EN1993-Part 1.2: Design of steel structures - General rules Structural fire design”, Brussels, 2003.
- [12] Laplanche, Karine ; Dhima, Dhionis and Racher, Patrick, “Predicting the behaviour of dowelled connections in fire : Fire tests results and heat transfer modelling”, 8th World Conference of Timber Engineering, Lahti, Finland, Vol. 2, pp 335-341, 2004.
- [13] Janssens, Marc, “Modelling the thermal degradation of structural wood members exposed to fire”, Fire and Materials; Vol. 28, pp 199-207, 2004.
- [14] Fredlund, B., “Modelling of heat and mass transfer in wood structures during fire”, Fire safety journal, Vol.20, pp 39-69, 1993.
- [15] Knudson, R.M., Schniewind, A.P., “Performance of structural wood members exposed to fire”, Forest Products Journal, Vol. 25, N°2, pp23-32, 1975.
- [16] Racher, Patrick, Bocquet, Jean-François, “Non-linear analysis of dowelled timber connections: a new approach for embedding modelling”, E-Journal of structural engineering, N°5, pp 1-9, 2006.
- [17] Kruppa, Joel and al, “Fire resistance tests of timber connections” Final report, CTICM N°187/JK/NB, Paris, 2000.
- [18] Racher, Patrick, “Mechanical timber joints – General” Timber Engineering STEP1, Centrum Hout , Netherlands, 1995.



PREDICTING THE STRUCTURAL FIRE PERFORMANCE OF SOLID WOOD-FRAMED FLOOR ASSEMBLIES

Noureddine BÉNICHOU¹

ABSTRACT

An analytical model for predicting the fire resistance of gypsum protected, wood-joint floor assemblies is presented. The model is a structural response model that uses the temperature profile, inside the wood-joint floor, produced from experimental data. The structural model, based on bending theory and experimental observations, calculates the deflection of the wood joists and the predicted time to structural failure of the assembly. The model produces structural fire resistance failure time and deflection predictions that are comparable with the experimental data. This paper also presents future developments of the model and challenges associated with modelling wood-framed assemblies.

1 INTRODUCTION

Lightweight wood-framed assemblies, commonly used in the construction of walls and floors of residential buildings, are required to have adequate fire resistance so that the fire is contained within the compartment of fire origin for a specified duration of time. This containment delays fire spread to other compartments and provides for safe evacuation and rescue operations. Traditionally, fire resistance has been determined using:

- Test methods in accordance with procedures outlined in standards or

- Reference to ready-to-use tables found in building codes or

- Design procedures, such as the component additive method, often found in building codes.

Alternatively, fire resistance can be evaluated using validated numerical models, which are becoming available with the application of more performance-based designs. In this case, to simulate the fire resistance behaviour of wood-frame assemblies, it is essential to evaluate their thermal and structural responses when exposed to fires. The thermal response gives estimates of the temperature distribution in the assembly. The structural response calculates the structural failure of an assembly, based on this temperature distribution.

¹ Senior Research Officer, Fire Research Program, National Research Council of Canada, Ottawa, ON, Canada, email: noureddine.benichou@nrc.gc.ca

The National Research Council of Canada (NRC) has developed an analytical model to predict the structural fire response of lightweight wood-joist floor assemblies exposed to fires. This model is based on experimental observations from tests carried out at NRC over the past decade. It also uses the equations of strength of materials and the effects of temperatures on the mechanical properties.

First this paper describes briefly the test results that have led to the development of the fire resistance model. The paper then describes, in detail, the theoretical framework of the structural response model, which predicts the time to failure and deflection of floor assemblies. Finally, the paper presents a simulation displaying how good the agreement is between the experimental results and the model predictions.

2 EXPERIMENTAL STUDIES

To determine the effects of various parameters on the fire resistance of wood-framed assemblies, a detailed experimental study was undertaken. The experimental program consisted of full-scale fire tests on 19 floors. The systems tested were replicates of floor assemblies commonly used in North America and listed in the National Building Code (NBC) of Canada¹. As shown in Fig. 1, typical floor assemblies are constructed with materials that include:

Wood joists representing the framing and spaced at 400 mm o.c. or 600 mm o.c.

Layers of fire rated (Type X) gypsum board (GB), 12.7 or 15.9-mm thick, fixed to either resilient channels (RC) or joists using screws. RCs are usually used to improve the acoustic performance.

Insulation within the cavities including glass fibre, rock fibre or cellulose fibre.

Subfloor attached to the framing from the top using screws or nails.

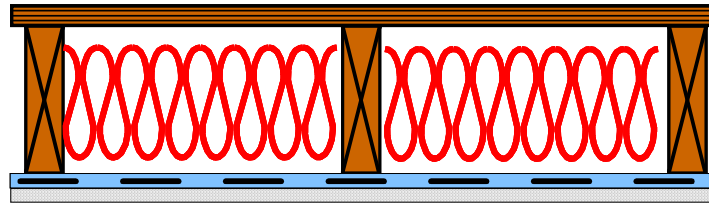


Fig. 1 - Typical wood-joist floor assembly

The full-scale floor tests were carried out by exposing one side of the assemblies to heat in a propane-fired horizontal furnace using gas fuel burners, in accordance with the CAN/ULC-S101-M89 standard². The assemblies were sealed at the edges against the furnace using ceramic fibre blankets to minimize heat leakage. The furnaces can accommodate floor assemblies that are 4.8 m long by 3.9 m wide. Type K chromel-alumel thermocouples were used for measuring temperatures at a number of locations throughout an assembly. For the loading, the furnace has a loading device and the load is transmitted through hydraulic jacks to simulate vertical structural loads. Loads on the assemblies were calculated based on the material characteristics of the assembly in accordance with CAN/ULC-S101-M89². The furnace temperature was measured by nine shielded thermocouples in accordance with CAN/ULC-S101-M89² and the average of the required nine-thermocouple temperatures was used to control the furnace temperature. In addition, the deflection at the unexposed surface was measured at different locations. During the tests, the furnace and assembly temperatures, deflections and the gauge pressure of the loading system were recorded at 1-minute intervals. Complete details on the construction of the floor assemblies, instrumentation location test procedures and results are given in references^{3, 4 and 5}. The time to failure is based on failure

criteria derived from CAN/ULC-S101-M89², i.e.: a) Thermal failure; b) Integrity failure; or c) Structural failure - loss of load-bearing capacity or excessive deflection of assemblies.

The results^{3, 4 and 5} have shown that the main factors that affected the performance of assemblies are the attachment of gypsum board, type of insulation, and the number of gypsum board layers. The results have also shown that key design trends can be summarized as follows:

Assemblies with screws located further away from board edges (38 mm versus 10 mm) provide higher fire resistance.

In assemblies with wood joists and a single-layer gypsum board ceiling finish, glass fibre insulation reduces the fire resistance while rock and cellulose fibre increased the fire resistance compared to a non-insulated assembly. In assemblies with a double-layer of gypsum board finish, the glass, rock and cellulose fibre all reduce the fire resistance compared to a non-insulated assembly.

For floor assemblies with wood-I-joists and finished with a double-layer of gypsum board, the glass fibre reduces the fire resistance while rock fibre increases the fire resistance compared to a non-insulated assembly.

Assemblies with two layers of gypsum board with staggered joints provide a significant increase in the fire resistance compared to an assembly with one layer of gypsum board.

For wood-I joist floor assemblies with glass fibre insulation and a double-layer of gypsum board, the effects of joist spacing and resilient channel spacing (406 mm o.c. and 610 mm o.c.) are significant.

An increase in structural load decreases fire resistance.

As fire design of floor assemblies is usually carried out by reference to standard fire tests, the results of this study were used as the basis for updating the tables of Appendix A of NBC¹ including generic fire resistance ratings of hundreds of assemblies. Designers can use the table for their designs, but the user can also choose from any other acceptable source.

3 DEVELOPMENT OF FIRE RESISTANCE MODELS

Although very beneficial, fire resistance test methods have drawbacks, including high costs and time, limitations of specimen geometry and loading, and to a lesser degree repeatability. Calculation methods offer one way of overcoming some of these problems when attempting to assess the fire resistance of lightweight-framed assemblies. The calculation methods also aid in designing an experimental program, improve products manufacturing, and assist the industry in taking full advantage of the opportunities offered by performance-based codes, as these methods would facilitate a faster design process. In the following sections, a model for predicting the fire resistance of wood-framed floor assemblies is presented.

3.1 Behaviour of Wood-Joist Floors under Fire Exposure

In order to develop a fire resistance model for floor assemblies that replicate test results, the fire resistance behaviour from the experimental program must be carefully observed. Test results, carried out at NRC over the past years, have shown that the behaviour of wood-joist floors, when exposed to fire, depends on several key factors: the layers of gypsum board separating the wood joists from the flames, the insulation between the joists, the material properties of the wood joists, and the temperatures to which the assembly is subjected.

The test results have shown also that, when wood-joist floors are exposed to fire, the temperature will increase in the gypsum first, followed by an increase in the joists. At

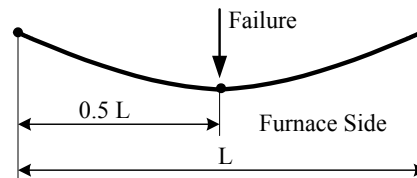
temperature levels ranging between 280 C and 300 C, the wood will begin to char, causing deflection towards the fire. This will cause gaps in the gypsum board joints to form, allowing even more heat to reach the joists. As the wood chars further and the cross-section of the joists decreases, the deflection will increase until the overall assembly fails. Fig. 2 shows the behaviour and failure mode of a wood-joist floor assembly.

3.2 Description of the Wood-Joist Floor Fire Resistance Model

Following the same logic underlying the behaviour observed in the experimental studies, the fire resistance of a wood-joist floor assembly is determined by the thermal and structural performance of the floor when exposed to fire. In this model, the thermal response is predicted by input of the temperature profile as measured from experimental tests (no calculation yet). The structural response model determines the degradation of the mechanical properties of joists at elevated temperatures, cross-section reduction, the deflection of the joist, and the time to structural failure of the assembly. Structural failure, which usually governs failure of floor assemblies, occurs when the stresses caused by the applied load exceeds the physical resistance of the joist, or when the span/deflection ratio drops below a certain value (usually < 30). In the latter case, it is said that the joist has failed due to deflection.



a) Wood joist assembly at the end of a test



b) Schematic representation of the behaviour of a wood joist assembly

Fig. 2 - Behaviour and failure mode of a wood-framed assembly

To perform the structural response calculation, the joist cross-section is divided into a number of elements in both directions (see Fig. 3). The calculation of mechanical properties, inertia, moments and deflection are described in the following sections.

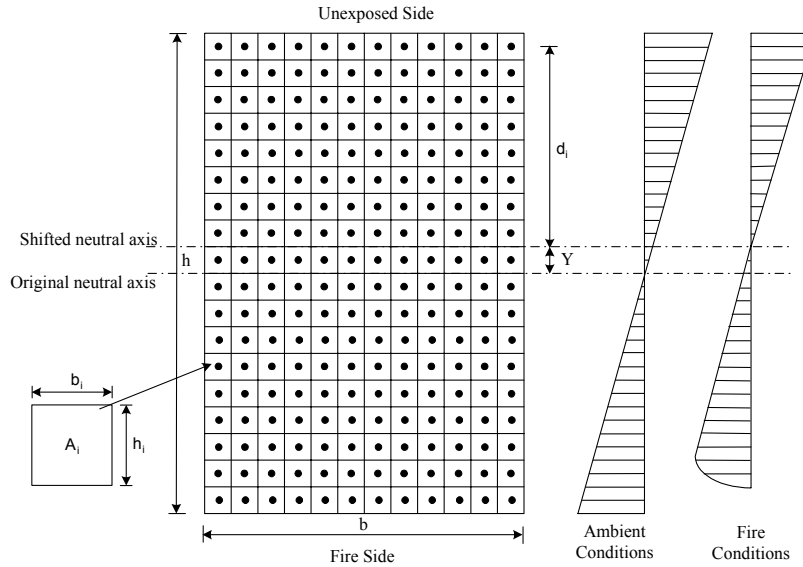


Fig. 3 - Cross-section division diagram and stress diagrams

3.3 Moment Applied on the Joist

Assuming that the joist is a simply supported member with a uniform distributed load, the bending moment applied to the joist can be calculated using the following equation:

$$M(x) = \frac{wLx}{2} - \frac{wx^2}{2} \quad (1)$$

Where $M(x)$ is the applied moment, w is the uniform distributed load, L is the length of the joist, and x is the current position along the length. The midpoint on the joist is the weakest location because the applied moment is the greatest. At $L/2$:

$$M_{\max} = \frac{wL^2}{8} \quad (2)$$

3.4 Resisting Moment of the Joist

The internal forces of the wood-joist allow it to resist an applied moment up to a certain value. The magnitude of the resisting moment is dependent on the yield stresses in both tension and compression. When loaded from above, the joist will be in tension below the neutral axis and in compression above the neutral axis. Since the corresponding yield stresses run in the axial direction of the joist, and in opposite directions, they create a couple around the neutral axis. The following equations govern the resisting moment relationship:

$$M_{RT} = \left| \sum_{i=1}^m \sigma_{Ti} * A_i * d_i \right| \quad (3)$$

$$M_{RC} = \left| \sum_{i=1}^m \sigma_{Ci} * A_i * d_i \right| \quad (4)$$

$$M_R = M_{RT} + M_{RC} \quad (5)$$

Where M_{RT} is the resisting moment due to tensile stresses, σ_{Ti} is the element tensile yield stress, M_{RC} is the resisting moment due to compressive stresses, σ_{Ci} is the element compressive yield stress, A_i is the element area, and d_i is the distance from the centroid of the element to the neutral axis. The value of d_i for each element changes with time and is determined by computing the shift Y (distance from the original neutral axis to the current neutral axis) at every time step.

3.4.1 Yield stresses for the current time step

Wood-joint assemblies are commonly subjected to both tensile and compressive forces, and consequently there are tensile and compressive stresses that can be found internally in the joist. Yield stress is the point when the forces loading the member exceed the elastic range, and will cause permanent deformation. The tension and compression yield stresses are affected by temperature. Fig. 4 shows the curve describing both tensile and compressive yield stresses of wood as a function of temperature. These data were obtained from various sources^{6, 7, and 8}. These properties are used in the model predictions.

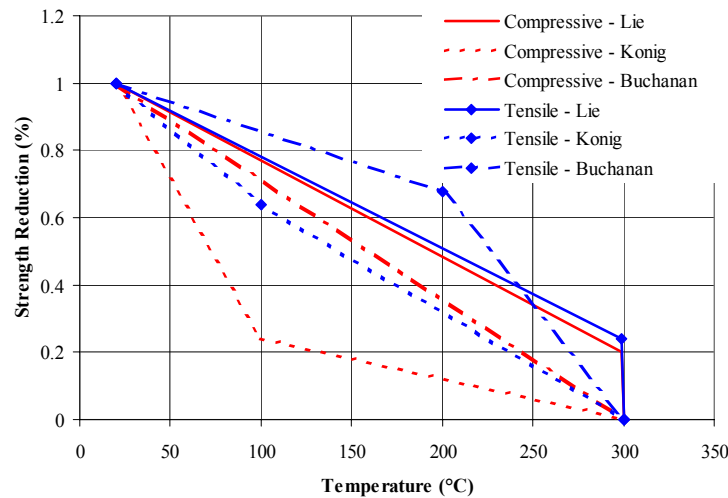


Fig. 4 - Yield stress of wood as a function of temperature

3.4.2 Position of the neutral axis for the current time step

Once wood elements begin to char, the neutral axis of the joist will change position (moves up provided that the exposure is from below). The new position of the centroid can be calculated with the following equation:

$$\sum_{i=1}^m (\sigma_{Ti} + \sigma_{Ci}) * A_i = 0 \quad (6)$$

Once the location of the neutral axis is found, the value of the distance Y (see Fig. 3) can be determined.

3.5 Deflection of the Joist

There are two main factors that affect the deflection of the beam (joist): loading and eccentricity of the surface of the joist.

3.5.1 Deflection due to load

For a typical joist, the overall deflection due to a uniform distributed load is:

$$y(x) = \frac{w}{24EI} * (-x^4 + 2Lx^3 - L^3x) \quad (7)$$

Where $y(x)$ is the deflection, w is the distributed load, E is the modulus of elasticity (defined below), I is the moment of inertia (defined below), x is the position on the joist and L is the length of the beam (joist). The midpoint on the joist is the location of the maximum deflection. At $L/2$:

$$y_{\max} = \frac{5 w L^4}{384 EI} \quad (8)$$

3.5.2 Modulus of elasticity for the current time step

The modulus of elasticity is a function of temperature, so in order to calculate the corresponding overall E value, the temperature-dependent value is taken for each remaining element of the cross-section of the joist.

$$E = \frac{\sum_{i=1}^m E_i * A_i}{\sum_{i=1}^m A_i} \quad (9)$$

Where E is the average modulus of elasticity of the cross-section, A_i is the area of a single element, and E_i is the modulus of elasticity of a single element at temperature T , as depicted in Fig. 5. These properties will be used in the model predictions.

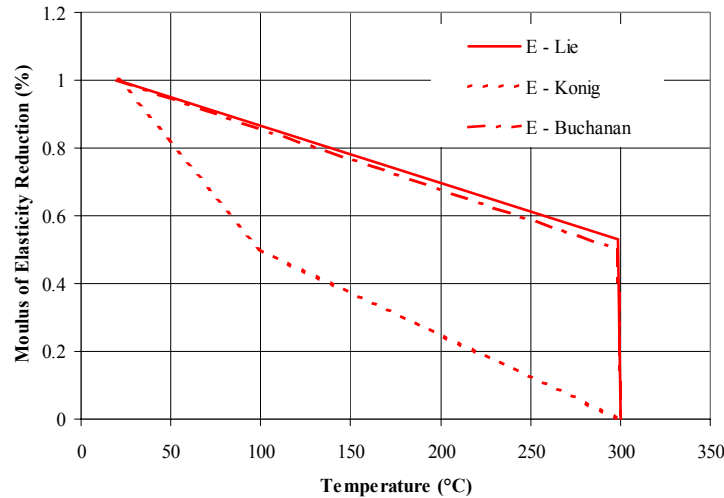


Fig. 5 - Modulus of elasticity of wood as a function of temperature

3.5.3 Moment of inertia and rigidity for the current time step

The moment of inertia is dependent on the geometry of the cross-section of the joist. Once elements begin to char, the neutral axis of the joist will change position, affecting the value of the moment of inertia. The value of the moment of inertia can then be calculated using the following equation:

$$I = \sum_{i=1}^m \left(\frac{1}{12} * b_i * h_i^3 + d_i^2 * A_i \right) \quad (10)$$

Where I is the moment of inertia, b_i is the width of each element, and h_i is the height of each element. The distance d_i denotes the vertical distance from the element centroid to the neutral axis, and A_i represents the area of each element. The model calculates the rigidity (product of the modulus of elasticity and the moment of inertia), for each joist in the floor, as follows:

$$EI = \sum_{i=1}^m \frac{b_i * h_i^3}{12} E_i + \sum_{i=1}^m [(b_i * h_i)(d_i)^2] E_i \quad (11)$$

Where b_i is the element width, h_i is the element depth, d_i is the distance from the element centroid to the neutral axis, and E_i is the temperature-dependent modulus of elasticity of the element.

3.5.4 Deflection due to initial joist surface eccentricity

In addition to the deflection due to the loading, the eccentricity of the surface of the wood affects the deflection of the joist. In general, the eccentricity can be expressed with a sinusoidal equation:

$$y_e = e * \sin\left(\frac{\pi x}{L}\right) \quad (12)$$

Where y_e is the magnitude of the deflection due to eccentricity, e is the maximum eccentricity, x is the position along the joist, and L is the length of the joist.

3.5.5 Overall deflection

The overall deflection of a joist can be described as the sum of the deflections due to load and eccentricity. If the downward direction is assumed to be positive, then the load and eccentricity will cause positive deflections. Consequently, the overall deflection at any given point can be expressed as:

$$\Delta = y_{max} + y_e \quad (13)$$

4 MODEL PREDICTIONS AND COMPARISON WITH EXPERIMENTAL DATA

In order to verify the validity of the model, it is necessary to compare the predictions with experimental data. At this stage, one test was used to evaluate the predictions by the fire resistance model. Details of the wood-joist properties are shown in Table 1. Using these properties, the model will determine the time to failure and the deflection at each time step,

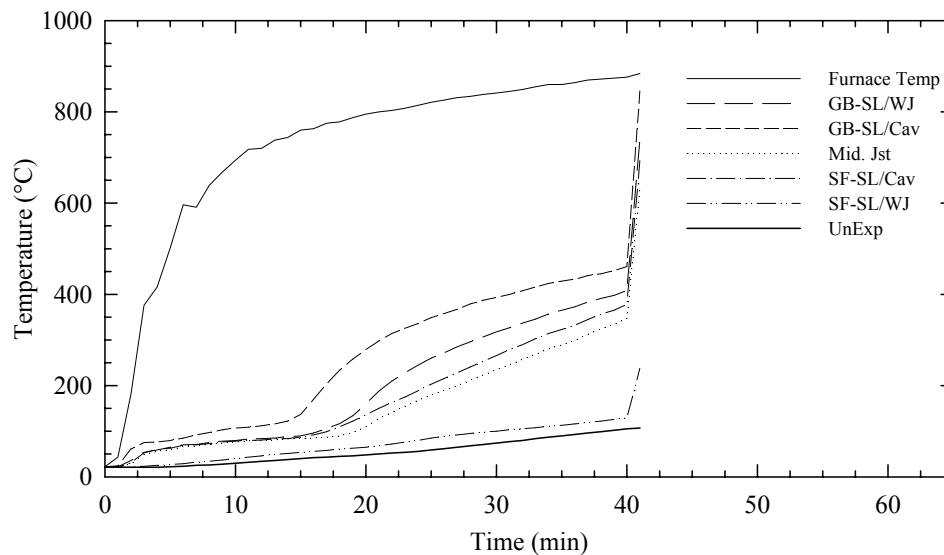
which can then be compared to the experimental results. For this test, temperatures on the unexposed sides did not reach the temperature failure criterion, as the assembly failed structurally at 41 min.

Table 1 - Wood joist properties

Property	Assumed value
Width	38 mm
Height	235 mm
Length	3874 mm
Load (per joist)	2080 N/m
Charring Temperature	300 C
Initial Maximum Eccentricity	1 mm
Ambient Modulus of Elasticity	7000 MPa
Ambient Tensile Strength	25 MPa
Ambient Compressive Strength	25 MPa

4.1 Experimental Time-Temperature Data⁴

Fig. 6 shows the average time-temperature curves obtained from the experimental tests at different locations (as indicated on the figure). The temperatures start gradually increase and once they reach about 100°C a plateau is formed corresponding to the dehydration of the gypsum board. This lasts for about 15 min after which the temperatures start increasing again at a faster rate. At 40 min, the temperatures show a rapid increase at all points except on the unexposed side. This is an indication that gypsum board has completely fallen off and the flames are impinging directly on the wood. Temperatures on the unexposed sides did not reach the insulation failure criterion, as the assembly failed by structural instability at 41 min.



Legend

SL - Single Layer GB - Gypsum Board WJ - Solid Wood Joist Cav - Cavity Mid.Jst - Middle Joist
UnExp - Unexposed Side SF - Subfloor

Fig. 6 - Temperature distributions for tested floor

4.2 Charring of the Section of Different Time Steps

The joist begins charring as soon as a single element reaches the charring temperature. While there is still wood physically present in the element after charring occurs, the material properties are said to have reached a point where that element no longer adds to the strength of the joist, and can therefore be disregarded in calculations. Fig. 7 shows a diagram depicting typical charring in a cross-section of the joist at 29 and 40 min, respectively, based on the input temperatures from the experimental data.

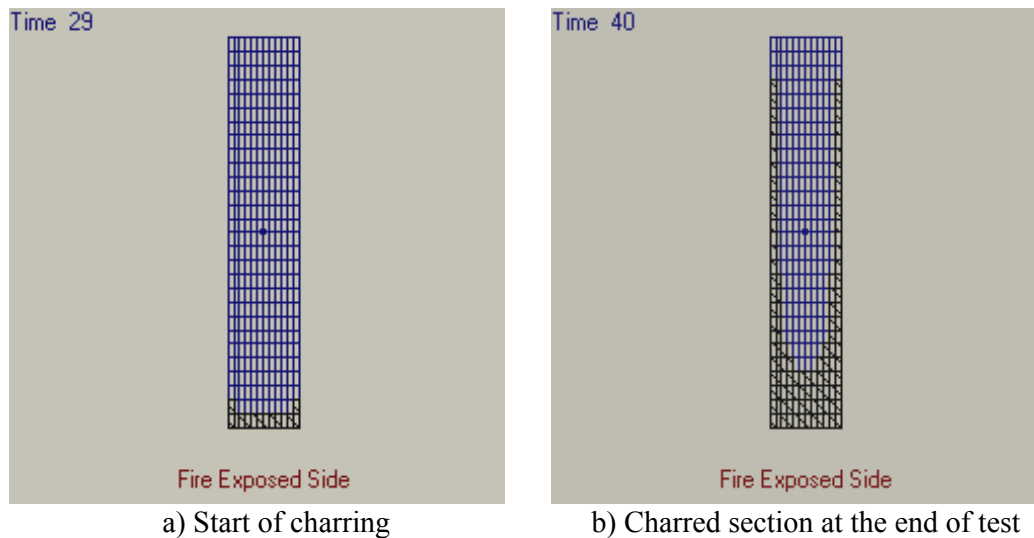


Fig. 7 - Charring diagram of the joist

4.3 Moment Resistance of Joist

To measure the performance of the structural response model, the predictions of the structural fire resistance and deflection at mid-length are evaluated. Fig. 8 illustrates the moment resistance versus time as predicted by the structural response model, based on the mechanical properties shown in Fig. 4 and Fig. 5. The fire resistance decreases with increasing time because the value of the mechanical properties decreases with time and the cross-section of the joists reduces after charring. The intersection of the horizontal line, at the level of the applied moment, with the moment resistant curve, represents the theoretical time to structural failure of the wall. The time-to-structural failure of the assembly is about 26, 36 and 37 minutes using the properties from König, Buchanan and Lie, respectively, while the time to structural failure measured experimentally is 41 min. As expected the definition of mechanical properties has a large effect on the model predictions. The difference between the analytical and experimental failure is 36 % to 10% on the conservative side.

4.4 Deflection of the Joist

Fig. 9 illustrates the maximum mid-length deflections plotted against the time for both the analytical predictions and the test results, and based on the mechanical properties shown in Fig. 4 and Fig. 5. As shown in the figure, the deflection is very small in the first 20 to 25 min. After this point, the model predictions and the test measurements start increasing at a faster rate (higher for König's properties compared to the others due to the definition of the properties). In general the trend in the rate of increase in the model predictions is similar to that of the test results. The difference in the predictions may be due to the definition of change of mechanical properties with temperature and the nominal values of the mechanical

properties, which could be different than the actual value of the joists tested. The model also checks to see if the joist fails due to excessive deflection, which is set to occur when the span/deflection < 30 ($L/y < 30$). For this test, the values for L/y before and after the joist fails are greater than 30. Consequently, this indicates that the joists failed due to load first, and not due to deflection.

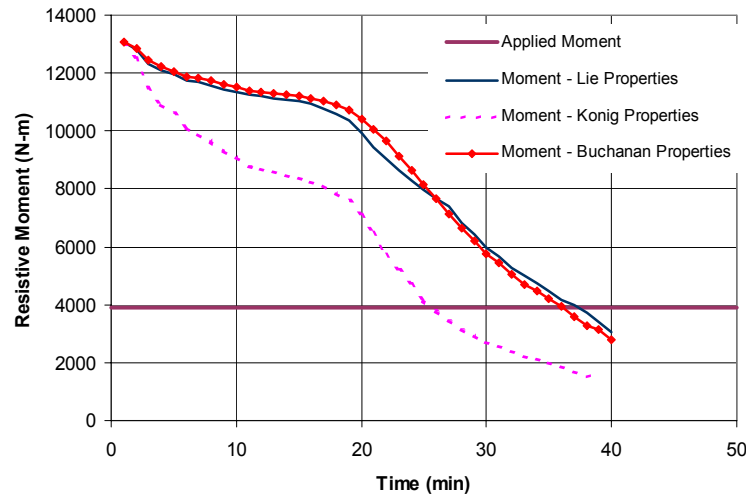


Fig. 8 - Predicted resistive moments

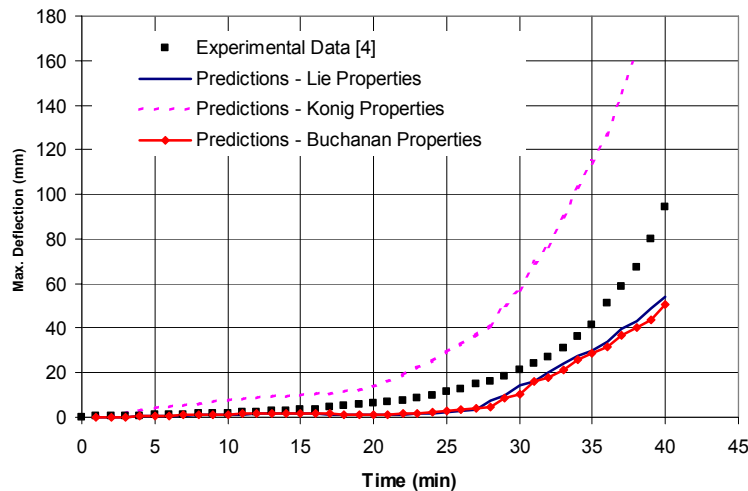


Fig. 9 - Predicted and measured maximum deflection

5 CONCLUSIONS, FURTHER WORK AND CHALLENGES

This paper described a model for the prediction of the fire resistance of lightweight wood-frame floor assemblies exposed to standard fires. As this stage of the development, the model deals only with the structural response, while the temperature profiles are input using data obtained from experimental studies. The structural response model is based on experimental observations for tests carried out at NRC over the past decade and uses the bending equations to evaluate the moment resistant and deflection assuming the assembly as a simply supported beam. The model predicts the time to structural failure of assemblies, taking into account the reduction in mechanical properties with elevated temperatures, as well

as the shift of the neutral axis towards the cooler region of the cross section with time. It also calculates the deflection along the joists, taking into account the change in flexural rigidity with elevated temperatures. Comparison of the structural failure time and the deflection as predicted by the model, with the results of one experimental full-scale floor standard test exposed show that model predictions are conservative and depend greatly upon how the mechanical properties versus temperature are defined.

To improve the current model, a thermal response model will be developed to predict the temperatures instead of using temperatures obtained from experimental data. The thermal response model will be coupled with the structural response model, and will form the new fire resistance model. The predictions of the new fire resistance model (temperatures, deflections and time to failure) will be validated against an extensive set of standard fire test data obtained from experimental programs carried out at NRC. The model also requires validation in non-standard fires. An experimental program is planned to expose structural wood-framed assemblies to design fires (non-standards fires) likely to occur in residential occupancies. The material properties, as an important factor for predicting the fire performance, will be incorporated into the model using existing and new data. The new data will be obtained by carrying tests on the different component of wood-framed assemblies.

Although the current fire resistance model can provide some prediction and may be suitable to assess the time to failure of load-bearing wood-frame floor assemblies for practical applications, there are still some challenges with the modelling of floor assemblies. These include:

The definition of non-standard fires, especially for the decay phase.

How to move from modelling a single joist to a whole floor system and the issues of load redistribution.

Accounting for the effect of continuity and restraint (isolated element vs. part of system).

The reliability of the data depicting the material properties.

6 REFERENCES

- [1] Canadian Commission on Building and Fire Codes, National Building Code of Canada, IRC, NRC, Ottawa, Canada, 1995.
- [2] CAN/ULC-S101-M89, Standard Methods of Fire Endurance Tests of Building Construction and Materials, Underwriters' Laboratories of Canada, Scarborough, Canada, 1989.
- [3] Bénichou, N. and Sultan, M.A.; Design considerations for fire resistance performance of lightweight-framed assemblies; CSCE 2003 Annual Conference, Moncton, NB, pp. 567-1 - 567-10, 2003.
- [4] Sultan, M.A., Séguin, Y.P., and Leroux, P., Results of Fire Resistance Tests on Full-Scale Floor Assemblies; Internal Report No. 764, Institute for Research in Construction, National Research Council of Canada, Ottawa, ON, Canada, 1998.
- [5] Sultan, M.A. and Bénichou, N., Fire Resistance Performance of Lightweight Floor Assemblies; Designing Structures for Fire Conference, Baltimore, MD, U.S.A., pp. 203-214, 2003.
- [6] Lie, T.T., (Editor), Structural Fire Protection, American Society of Civil Engineers, Manuals and Reports on Engineering Practice No. 78, 1992.
- [7] König, J. and Walleij, L., Timber frame assemblies exposed to standard and parametric fires. Part 2: a design model for standard fire exposure, Report No. I 0001001. Tratek, Swedish Institute for Wood Technology Research, Stockholm, Sweden, 2000.
- [8] Buchanan, A.H., Structural Design for Fire Safety, John Wiley & Sons, 2001.



IN-DEPTH TEMPERATURE MEASUREMENTS OF TIMBER IN FIRES

Pedro RESZKA¹ and Jose L.TORERO²

ABSTRACT

Modern construction relies more and more on metallic connectors. Their failure during fires is related to the glass transition of the lignin matrix at around 100°C. Based on this information, a series of tests were carried out exposing a wood specimen to various heat fluxes in a Cone Calorimeter. The aim of this research is to develop a sound temperature measurement methodology in wood samples exposed to high heat fluxes and to build a database in order to evaluate different wood pyrolysis models. The experiments yielded highly repeatable results that are seldom achieved with wood.

1. INTRODUCTION

Fire resistance of timber has been the subject of numerous studies and a number of guidelines have been proposed for the design of wooden structures on the basis of their resistance to fire^{[1][2]}. The effect of fire on timber is separated in two distinctive processes, the loss of section due to burning and charring and the loss of strength of the un-charred section. This paper deals with the latter phenomenon, which has become an important issue in modern timber building design.

The physical properties of each of the polymers that make up wood evolve with temperature, being lignin the one that shows the most significant mechanical property changes at the lowest temperatures. Lignin is an amorphous polymer that cements the cells together, thus providing resistance to compression and shear^{[3][4]}. Lignin attains its glass transition at temperatures as low as 60°C when saturated with water^[5], leading to a loss of binding strength between the fibres. The attainment of the glass transition has important effects on the modulus of elasticity and on thus on the mechanical behaviour of wood^{[5][6]}. Previous research^{[6][7]} has shown that lignin experiences a significant loss of its mechanical strength around 100°C. Despite the uncertainty of the glass transition temperatures, it is clear

¹ PhD Student, School of Engineering and Electronics, The University of Edinburgh, Edinburgh EH9 3JN, UK, email: pedro.reszka@ed.ac.uk

² Professor, School of Engineering and Electronics, The University of Edinburgh, Edinburgh EH9 3JN, UK, email: jltorero@staffmail.ed.ac.uk

that they are lower than the temperatures affecting other processes linked to strength reduction, like charring, which occurs on the vicinity of 300°C^[8]. Another important characteristic of the process of lignin vitrification is that the heat required for this endothermic process is low compared to the latent heat of evaporation of water; Irvine reports changes in the specific heat of lignin of around 0.3 – 0.36 J/g·K during the process. This transition is therefore relatively weak, and can be blurred by any loss of moisture^[5].

Metallic connectors have a widespread use in modern timber construction. Their presence leads to an increase in the impact of the role of shear stress in the failure of timber structures during fires. Failure by shear stress is generally not related to fibre strength or loss of cross section, but mostly to the failure of the lignin matrix^[4]. Thus, the performance of metallic connectors will be affected by property changes of this nature.

When a timber element is exposed to the heat-flux from a fire, it gradually heats up creating a temperature gradient within the wood. The in-depth propagation of the heat by conduction ultimately dictates the failure mode of the element. Thus, the analysis of the timber failure in fires requires a proper prediction of the transient in-depth temperature distributions.

Numerous models and experiments have been carried out in the past to understand and predict the behaviour of wood subjected to high heat fluxes^{[9][10][11]}, but they have been mainly centred on addressing the problems of its ignition and pyrolysis. Low temperature loss of strength has been considered only as a correction^{[2][12]}. In-depth temperature measurements on wood have been carried out, exposing samples to constant heat fluxes or to furnace tests^{[4][11][13][14][15][16][17][18][19][20]}. The former have been used mainly to validate mathematical models, while the latter have been largely employed to generate equations that predict temperature as a function of depth.

The limitations of standard furnace testing are described by Drysdale^[21], and include furnace-dependent results and variable imposed heat fluxes which are difficult to quantify. The temperature-depth equations^{[12][16][18]} also have some weaknesses, like the fact that some of them only account for the non-charred part of the wood, use fixed charring rates or are independent of the imposed heat flux (they assume a standard furnace exposure): Nevertheless, they are valid and useful tools and were applied as a background for the development of design methods in Eurocode 5^{[16][18]}.

$$T(x) = T_i + (T_p - T_i) \cdot \left(1 - \frac{x}{a}\right)^2 \quad (1)$$

where

T = wood temperature [°C]

T_i = initial wood temperature [°C]

T_p = char front temperature, generally assumed to be 300°C

x = depth measured from the char front [mm]

a = thermal penetration depth, usually taken as 40 mm

The use of a standard furnace represents a significant limitation to the definition of these in-depth temperature profiles. The main reason is that the imposed heat flux does not only vary with time but is also difficult to define because it will be the result of the overall thermal conductivity of the sample. Therefore, generalization of these in-depth temperature distributions to realistic fires to assess performance under fire might induce errors that have yet to be quantified.

This paper reports on a series of measurements of in-depth temperatures on wood specimens subjected to constant heat fluxes. The use of constant heat fluxes provides a thermal boundary condition on the samples that can be quantified with greater precision, thus

facilitating the validation of analytical and numerical models. The aim of this research is to develop a methodology for reliable measurement of temperature distributions in wood samples exposed to fire-like heat fluxes and to build a sound data-base of temperature measurements in order to evaluate different models that predict the evolution of these temperature profiles. Surprisingly, these measurements cannot be found in the literature.

2. EXPERIMENTAL PROCEDURE

A series of tests were carried out in a Cone Calorimeter exposing a wood specimen to heat fluxes between 10 and 60 kW/m². The experiments carried out were performed in two stages. The initial stage consisted of measuring the temperature profiles of wood samples exposed to various heat fluxes, while during the next step mass loss measurements were done using the same heat fluxes as in the previous phase. This was done to avoid interference of the thermocouples in the mass loss rate measurements. However, this report only presents the results of the first stage of the research.

The specimen was tested in a vertical configuration (i.e. the exposed face is in a vertical position), with no piloted ignition source. The type of wood used during the experiments was Redwood Pine (*Pinus sylvestris*). The sample dimensions were ~100 x 97 x 67 mm. The selected heat fluxes were 10, 18, 25, 40 and 60 kW/m². These heat fluxes represent a wide set of exposures that is unusual for structural type analyses, nevertheless given the low temperature of the lignin glass transition it was deemed necessary to study exposures typical of the early stages of fire growth.

In each experiment, five thermocouples were placed in 2 mm diameter holes drilled perpendicular to the exposed surface, from the back (unexposed) side of the specimen. One hole was drilled on the centre of the sample face, while the remaining four holes were drilled on a 20 mm radius circle around the first hole. The thermocouple junctions were placed at depths of 5, 10, 15, 20, 25, 30, 35 and 40 mm from the exposed surface. The thermocouples utilised were N-type with fibreglass insulation. The fibreglass insulation allows the thermocouple to reach temperatures as high as 540°C without sustaining considerable damage. The tip of the thermocouples was cut off after each test and a new junction was welded in order to ensure the total integrity of the device.

An aluminium block (31 mm thick) was attached to the back of the sample as a means of providing a well defined back-end boundary condition. For all tests an extra thermocouple was fitted at the interface between the sample and the aluminium block to track the evolution of its temperature. Measurements showed that the aluminium block had a constant temperature along its depth. Each experimental condition (i.e. heat flux and thermocouple depth) was repeated three times, with a total of 120 tests carried out.

The specimens were acquired kiln dried, and they were kept in a room where the maximum and minimum temperature and relative humidity were recorded each day for about a month before the experiments commenced. It was found that the temperature and humidity variations were not significant, with less than 10°C difference between the highest and lowest recorded temperatures in 82 days, and a variation in the moisture content of air always lower than 35% RH in the same period. The average moisture content of the samples was of about 11%. Prior to each experiment, the specimen was weighed and its dimensions measured.

During the first series of tests only the temperatures were recorded, with no mass loss measurements or gas analysis performed. Measurement of the ambient temperature in the Cone Calorimeter was also carried out. A few tests with mass loss and temperature measurements were conducted to demonstrate consistency. Mass loss measurements were discarded for those experiments.

The duration of the tests was determined by the temperature of the back of the sample. The experiments would continue until the heat losses at the back of the specimen were significant (i.e. greater than 10%) compared to the incoming heat flux from the Cone Calorimeter.

3. EXPERIMENTAL RESULTS

The experiments yielded highly repeatable results that are seldom achieved with wood. The results were averaged for each thermocouple depth and heat flux. In most of these averaged results, a plateau is unmistakably identified in the vicinity of 100°C, clearly showing the effect of the evaporation of the moisture contained within the wood. No plateau is observed that can be attributed to the glass transition of lignin.

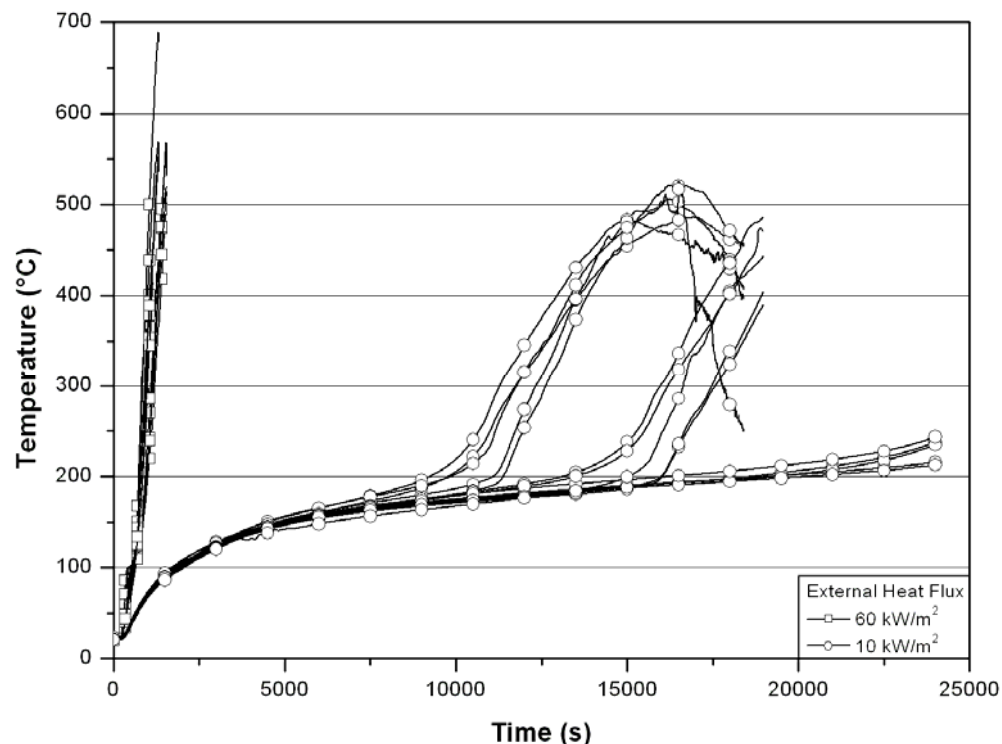


Fig. 1 – Raw thermocouple readings for two different heat fluxes, 10 and 60 kW/m² at a depth of 15 mm.

A weaker repeatability was found in the lower heat fluxes, with some tests showing faster heating rates than others. Figure 1 shows all the thermocouple readings taken at a depth of 15 mm from the exposed surface for imposed heat fluxes of 10 and 60 kW/m². While all the measurements for the 60 kW/m² case follow a general trend, the three repetitions done at 10 kW/m² show different heating patterns. The samples reached 200°C all at different times, with a difference of about 10,000 seconds between the extreme cases.

A sample of the averaged results is presented in Figure 2. As it can be seen, Figure 2 shows the average temperature histories for 8 thermocouples. All thermocouples show the presence of a plateau at approximately 100°C. This plateau becomes less obvious for deeper thermocouples. Temperatures have all been truncated at the point where the regression front

reached the thermocouple. This point is generally characterized by very unstable measurements obtained from the thermocouple. The data obtained beyond this point was deemed to be unusable.

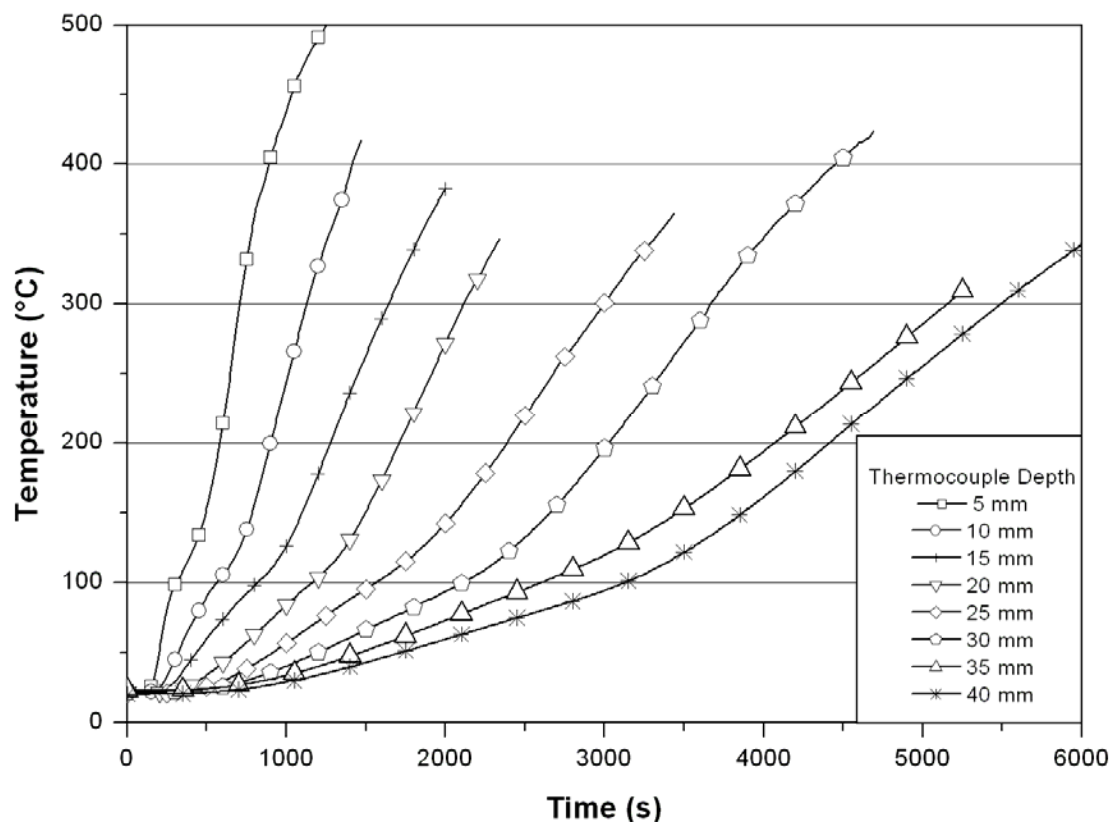


Fig. 2 – Average temperature readings for an imposed heat flux of 25 kW/m² for various thermocouple depths.

4. SIMPLIFIED HEAT TRANSFER MODEL

A semi-infinite heat transfer model that treats the material as an inert solid was used to establish characteristic values for the different parameters of the problem^[22]. These characteristic values were used to non-dimensionalize time, depth and temperatures. This analysis was done as a baseline exercise to establish departures from an inert heating solution. The non-dimensional variables are the following:

$$t^* = \frac{t}{t_c} \quad (2)$$

$$x^* = \frac{x}{x_c} \quad (3)$$

$$\theta^* = \frac{T - T_\infty}{T_c - T_\infty} \quad (4)$$

The characteristic variables are showed below:

$$T_C = \frac{a\dot{q}_e''}{h_{TOT}} \quad (5)$$

$$x_C = \frac{k}{h_{TOT}} \quad (6)$$

$$t_C = \frac{k \cdot \rho \cdot c}{h_{TOT}^2} \quad (7)$$

where

t = time [s]

x = depth from exposed surface [m]

T = wood temperature [°C]

T_∞ = initial wood temperature [20°C]

a = wood absorptivity [0.88]

\dot{q}_e'' = external (imposed) heat flux [W/m²]

h_{TOT} = total heat transfer coefficient (convection and radiation) [35 W/m²·K]

k = thermal conductivity of wood [0.105 W/m·K]

ρ = wood density [524.21 kg/m³]

c = wood specific heat [2200 J/kg·K]

The temperature distribution for the heating of an inert solid with constant heat flux is given by the following expression:

$$\theta(x,t) = T_C \cdot \left[\operatorname{erfc}\left(\frac{n}{\sqrt{4t}}\right) - e^{(mn+m^2t)} \cdot \operatorname{erfc}\left(m\sqrt{t} + \frac{n}{\sqrt{4t}}\right) \right] \quad (8)$$

with

$$\theta = T - T_\infty \quad (9)$$

$$n = \frac{x}{\sqrt{\alpha}} \quad (10)$$

$$m = \frac{h_{TOT}}{\sqrt{k \cdot \rho \cdot c}} \quad (11)$$

$$\alpha = \frac{k}{\rho \cdot c} \quad (12)$$

5. ANALYSIS OF RESULTS

Figure 3 represents the non-dimensional temperature distribution for thermocouples placed at 5 mm from the surface for heat fluxes of 10, 25 and 60 kW/m². Also included is the inert heating temperature history per equation (8). This corresponds to the inert heating case, and a comparison of this curve with the other temperature profiles establishes how much they depart from this behaviour. It can be stated that the initial behaviour of wood is inert. The samples subjected to higher heat fluxes depart in the first place from the non-burning behaviour (for the 60 kW/m² case, this occurs at a non-dimensional time of around 2.0; for 25 kW/m² this happens at around 2.6). This departure is originated by the commencement of the evaporation of the moisture contained in the wood, which due to its endothermic nature, slows down the heating. Since the samples subjected to lower heat fluxes have been heated for a “longer” non-dimensional time without any fall in the intensity of the heat flux, their non-dimensional temperatures continue to rise above the temperatures of the samples in which the loss of water has already started. The higher heat fluxes later catch-up with the other samples, because the heating rate of latter has already been hindered by the onset of the moisture evaporation. Another retard in the heating rate occurs when the samples reach the temperatures that mark the beginning of the process of pyrolysis (another endothermic reaction). This happens at a non-dimensional time of about 3.5 for 60 kW/m² and at around 6.0 for 25 kW/m². The fact that the non-dimensional temperature of the 60 kW/m² sample does not rise above that of the 25 kW/m² one is attributed to the non-dimensionalisation: the real temperatures are divided by $T_C - T_\infty$, and the terms in T_C are the same for all the heating scenarios, except for the value of the imposed heat flux.

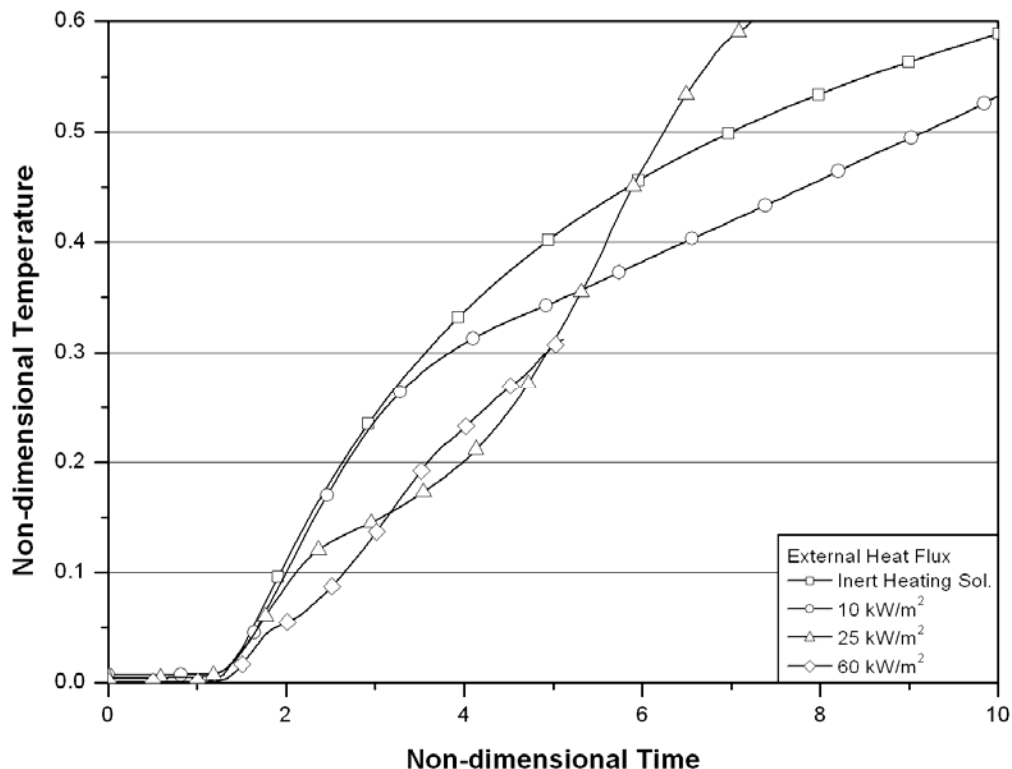


Fig. 3 – Non-dimensional temperature curves for various heat fluxes at a thermocouple depth of 5 mm.

It is interesting to note that for the heat fluxes below the accepted critical heat flux for ignition of wood (12 kW/m^2 [21]), the wood behaved very much like an inert material. No 100°C plateau was observed in those cases, probably due to the fact that the heating was slower than the migration of the moisture into deeper parts of the specimen. However, the curve does depart from the inert solution when this temperature is reached (occurring at a non-dimensional time of 5.00 for 10 kW/m^2 ; see Figure 3). This indicates the onset of endothermic reactions at approximately 10 kW/m^2 .

In the deeper regions, the heating rate is slower than at shallower regions. This is because the incoming heat flux to the deeper regions is attenuated by the diffusion of the heat through the solid. Figure 4 shows the non-dimensional temperature curves for a depth of 30 mm. A change in the gradient is observed for 60 and 25 kW/m^2 when the sample reaches a temperature of 100°C , at non-dimensional times of 12.6 and 18.6 respectively. For 10 kW/m^2 , this occurs at a time of 80.6, falling off the scale of the graph. The evaporation of the moisture is not associated with a temperature plateau in this case, but with a steep increase in the heating rate. The difference between the three different curves is reduced as the thermocouple depth increases. The 60 kW/m^2 curve quickly becomes the one with the highest non-dimensional temperature, due to the effect of the increased imposed heat flux caused by the burning of the sample. At a non-dimensional time of 18.9, the 60 kW/m^2 specimen reaches the pyrolysis temperature; this can be observed in the graph as a slight change in the gradient.

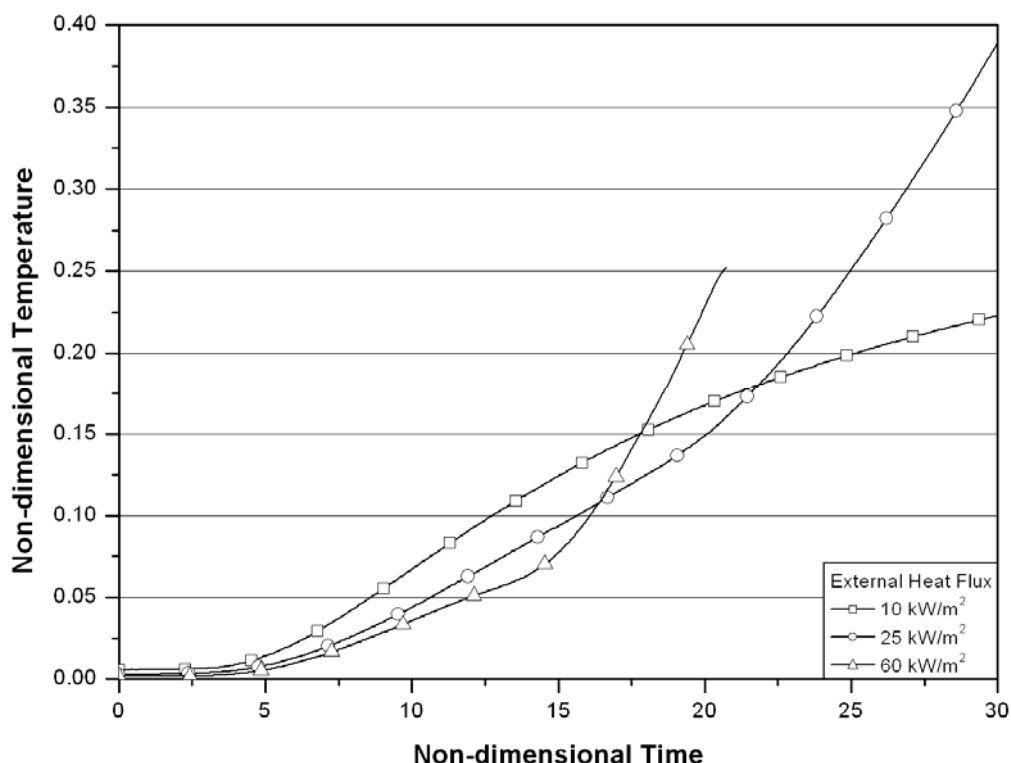


Fig. 4 – Non-dimensional temperature curves for various heat fluxes at a thermocouple depth of 30 mm.

6. CONCLUSIONS

Temperature measurements carried out in wood specimens subjected to various fixed heat fluxes yielded results that are highly repeatable, something seldom achieved with wood. A reliable methodology for measuring these temperatures was developed, and a considerable data-base temperature profiles was built. The results show the effect of the evaporation of the moisture contained in the sample, but showed no clear consequence of the vitrification of lignin, confirming that this process does not require much heat input to take place. The start of the pyrolysis reactions is also marked by a change of gradient in the temperature-time curves. Weaker repeatability was observed for the lower heat fluxes.

An analysis was carried out to determine the departures in the behaviour of the samples exposed to different heat fluxes from that of an inert solid. This analysis established that wood behaves almost like an inert material when heated with low heat fluxes. The onset of the pyrolytic behaviour is at about 10 kW/m². The differences between the curves of samples heated at different imposed heat fluxes diminish as the depth increases, but there is still a marked distinction between the lower and higher heat fluxes.

7. REFERENCES

- [1] CEN (2004) "Eurocode 5: Design Of Timber Structures - Part 1-2: General - Structural Fire Design". EN 1995-1-2, European Committee For Standardization, Brussels.
- [2] White, RH (2002) "Analytical Methods for Determining Fire Resistance of Timber Members", in *SFPE Handbook of Fire Protection Engineering*, 3rd Edition (eds. PJ DiNemmo *et al*), pp. 4-257 – 4-273. Society of Fire Protection Engineers, Boston.
- [3] Kollmann, FF and Cote, WA (1968) *Principles of Wood Science and Technology*. George Allan & Unwin Ltd, London.
- [4] Dias de Moraes, P (2003) "Influence de la Temperature sur les Assemblages Bois". PhD Thesis, Universite Henri Poincare, Nancy 1.
- [5] Irvine, G (1984) "The Glass Transitions of Lignin and Hemicellulose and Their Measurement by Differential Thermal Analysis". *Tappi Journal*, Vol. 67, No. 5, pp. 118 – 121.
- [6] Schaffer, EL (1973) "Effect of Pyrolytic Temperatures on the Longitudinal Strength of Dry Douglas-Fir". *Journal of Testing and Evaluation*, Vol. 1, No. 4, pp 319 – 329.
- [7] Young, SA and Clancy, P (2001) "Compression Mechanical Properties of Wood at Temperatures Simulating Fire Conditions". *Fire and Materials*, Vol. 25, pp. 83 – 93.
- [8] White, RH and Dietenberger, MA (1999) "Fire Safety", in *Wood Handbook – Wood as an Engineering Material. Gen. Tech. Rep. FPL-GTR-113*.
- [9] Atreya, A (1998) "Ignition of Fires". *Phil. Trans. R. Soc. Lond.*, Vol. 356, pp. 2787 – 2813.
- [10] Babrauskas, V (2001) "Ignition of Wood: A Review of the State of the Art". *Interflam 2001*, pp. 71 – 88. Interscience Communications Ltd., London.
- [11] Janssens, ML (2004) "Modelling of the Thermal Degradation of Structural Wood Members Exposed to Fire". *Fire and Materials*, Vol. 28, pp. 199 – 207.
- [12] Schaffer, EL (1984) "Structural Fire Design: Wood" *Wood Res. Pap. FPL 450*.
- [13] Spearpoint, MJ and Quintiere, JG (2000) "Predicting the Burning of Wood Using an Integral Model". *Combustion and Flame*, Vol. 123, pp. 308 – 324.
- [14] Schaffer, EL (1967) "Charring Rate of Selected Woods – Transverse to Grain". *US Forest Service Research Paper FPL 69*.

- [15] Fredlund, B (1992) “Modelling of Heat and Mass Transfer in Wood Structures During Fire”. *Fire Safety Journal*, Vol. 20, pp. 39 – 69.
- [16] Frangi, A and Fontana, M (2003) “Charring Rates and Temperature Profiles of Wood Sections”. *Fire and Materials*, Vol. 27, pp. 91 – 102.
- [17] Tran, HC and White, RH (1992) “Burning Rate of Solid Wood Measured in a Heat Release Rate Calorimeter”. *Fire and Materials*, Vol.16, pp. 197 – 206.
- [18] Janssens, ML and White, RH (1994) “Short Communication: Temperature Profiles in Wood Members Exposed to Fire”. *Fire and Materials*, Vol. 18, pp. 263 – 265.
- [19] Tsantaridis, LD and Ostman BA (1998) “Charring of Protected Wood Studs”. *Fire and Materials*, Vol. 22, pp. 55 – 60.
- [20] Mikkola, E (1991) “Charring of Wood Based Materials”. *Fire Safety Science – Proceedings of the Third International Symposium*, pp. 547 – 556. Interscience Communications Ltd., London.
- [21] Drysdale, DD (1998) *An Introduction to Fire Dynamics*, 2nd Edition. John Wiley & Sons, Ltd., Chichester.
- [22] Long, RT, Torero, JL, Quintiere, JG, Fernandez-Pello, AC (1999) “Scale and Transport Considerations on Piloted Ignition of PMMA”. *Fire Safety Science – Proceedings of the Sixth International Symposium*, pp. 567 – 578. Interscience Communications Ltd., London.

SiF'06

USING COMMERCIAL FEA SOFTWARE PACKAGES TO MODEL THE FIRE PERFORMANCE OF EXPOSED GLULAM BEAMS

B.L. BADDERS¹, J.R. MEHAFFEY², and L.R. RICHARDSON³

ABSTRACT

This paper describes the results of a study to explore the use of packaged finite element analysis (FEA) programs to model structural fire performance of exposed wood members. Copies of four FEA programs commonly used to predict the response of structures exposed to elevated temperature were acquired. Either the full version of the program was purchased or, if available, a demonstration version was acquired. A glulam beam with known ASTM E 119 test data was modeled in two-dimensions to assess each program.

The programs used were COMSOL, FIRES-T3, SAFIR, and TASEF. The density, thermal conductivity, and specific heat for wood and char were derived from the computer model CROW, previously developed by Janssens[1].

All FEA programs are reasonably consistent with each other; however, the predicted heat transfer through the beam section is lower than measured in the test. The input data and boundary conditions had to be adjusted to account for changes in thermal properties as a function of temperature, moisture evaporation, and migration and char contraction. The effect of the flame on the heat transfer to the surface was initially ignored.

Each program has advantages and disadvantages to both use and appropriateness. This paper discusses some of the advantages and disadvantages of each FEA program for the specific application of modeling exposed wood members.

COMSOL was selected for a more detailed analysis, due to some of the unique features it offers. One of the unique features of COMSOL is the ability to create variable sub-domain boundaries that can be set up as a function of a dependent variable, such as time or temperature.

¹ Group Leader, Engineering and Research Section, Department of Fire Technology, Southwest Research Institute®, San Antonio, Texas, USA, email: barry.badders@swri.org

² Ph.D., Forintek Canada Corp., Ottawa, ON, Canada, email: jim.mehaffey@ott.forintek.ca

³ Ph.D., Forintek Canada Corp., Ottawa, ON, Canada, email: les.richardson@ott.forintek.ca

This made it possible to simulate the different sub-domain layers and the thermal feedback from flame to the wood.

1. INTRODUCTION

Modeling the structural fire performance of wood is complicated by exothermic heating, moisture evaporation and migration, and the formation of char. Finite element analysis (FEA) models have been difficult to use for structural fire performance of wood because the methods do not handle well the complicated physics of wood degradation in fire. However, by using apparent material properties and appropriate boundary conditions, commonly used FEA programs can provide reasonable predictions. To demonstrate this, four commercially available programs were selected and the produced results were compared to known data.

2. FINITE ELEMENT ANALYSIS SOFTWARE PACKAGES

Demonstration versions or full versions of four FEA programs were acquired. The programs used were FIRES-T3, SAFIR, TASEF, and COMSOL. Each program provided its own set of unique advantages and disadvantages.

2.1 FIRES-T3

A full-functioning version of FIRES-T3 was already on hand. FIRES-T3 was written to specifically model the thermal response of structures in fire. The user is required to define the mesh nodes and elements, provide data on the material density, specific heat and thermal conductivity, define the fire exposure conditions, and input the constants for the heat conduction equation. The program does allow for temperature-dependent properties. Only limited knowledge of partial differential equations is required.

The program lacks a graphical user interface, requires manual input of a test file, and is particular to the location and order of text within the input file, making a single error difficult to trace. However, the documentation for creating the input file is easy to follow. FIRES-T3 can be obtained from the Department of Fire Protection Engineering at the University of Maryland at College Park.

2.2 SAFIR

A demonstration version of SAFIR was acquired. The demonstration version was limited to 500 nodes, 500 elements, two-dimensional analysis, and other limitations, which did not affect the work associated with this paper. SAFIR is similar to FIRES-T3, in that it is specifically written to model the thermal response of structures in fire. SAFIR will also model the structural response in combination with the thermal response. The program provides some pre-defined materials and defined fire conditions, including the ISO 834 and ASTM E 119 time-temperature curves. The user can provide temperature-dependent thermal properties and define a different exposure condition.

A third party graphical user interface is available and easy to use. At least for the demonstration version, the user is required to modify the input file to include the user defined material properties and run the simulation from a DOS environment. SAFIR can be obtained from J.-M. Franssen, 1, Chemin des Chevreuils, 4000 Liege 1, Belgium, jm.franssen@ulg.ac.be.

2.3 TASEF

A demonstration version of TASEF was acquired. The demonstration version was only limited to a specified period of evaluation. TASEF is similar to FIRES-T3 and SAFIR in that it is specific to simulating the thermal response of materials and assemblies when exposed to fire. TASEF allows the user the same flexibility in defining material properties and fire conditions; some material thermal properties are pre-defined, or they can be specified by the user.

A third party graphical user interface is available but was not used in generating the input file. TASEF provides a DOS application for generating the input file, which makes it a simple systematic process. Once the input file is generated, changes to the model are easily made directly in the text input file, or the DOS application can be used to modify the input file. TASEF can be obtained from SP Swedish National Testing and Research Institute.

2.4 COMSOL

A full version of COMSOL 3.2 was already on hand. COMSOL is not written specific to a particular application. The program is capable of solving a heat conduction equation with temperature-dependent thermal properties and user-defined boundary conditions, both of which can be entered in tabular or equation form. The structural response can be coupled to the thermal response for modeling structures under load.

COMSOL comes complete with a graphical user interface and a postprocessor. The program is relatively intuitive to use but requires a greater understanding of partial differential equations and FEA methods than FIRES T3, SAFIR, and TASEF. COMSOL can be obtained through www.comsol.com.

COMSOL has a parameterized geometry function that allows boundaries to be varied as a function of other parameters. This feature is of particular interest to modeling wood because shrinkage due to drying and char formation can be accounted for. This feature was set up in COMSOL for the model, but the work is not complete and will be reported at a later date.

3. MATERIAL AND THERMAL PROPERTIES

A glued laminated (glulam), two-dimensional cross section of a 2400F-V4 Douglas fir beam was selected for the models. The dimensions of the cross section were 222×419 mm. This wood beam was chosen, because in 1997, the American Forest and Paper Association conducted a series of tests at Southwest Research Institute with documented results[2]. The data from these tests is available for comparison to the model simulations. Four tests were conducted as part of this program at 0%, 25%, 50%, and 100% of design load. Only the data for the non-loaded beam was selected for comparison.

An important aspect to effectively modeling the thermal response of any material is using appropriate thermal properties. The thermal response of wood presents some unique obstacles presented by moisture evaporation and migration, char formation, exothermic reaction, and mass transfer.

Table 1 – Douglas fir Properties as a Function of Temperature.

T (°C)	ρ (kg/m ³)	c_p (J/kg-K)	k (W/m-K)
20	474	1518	0.1027
40	474	1615	0.1093
60	474	1712	0.1157
80	474	1809	0.1220
100	474	1906	0.1280
120	460	1622	0.1403
140	460	1699	0.1468
160	460	1777	0.1534
180	460	1854	0.1599
200	460	1931	0.1665
250	438	2029	0.1729
300	416	1955	0.1956
350	393	1774	0.2477
400	371	1675	0.3004
600	282	1782	0.3020
800	258	1869	0.3624
1000	258	1865	0.4506
1200	258	1708	0.5577

Janssens[1] developed a model referred to by the acronym CROW (Charring Rate of Wood) that models the char rate in one dimension. CROW accounts for the dry density of the wood, moisture content of the wood, lignin content of the wood and char contraction, which are the four major factors that affect the thermal degradation in a fire event. CROW was used to determine the thermal properties of Douglas fir used in the models. **Table 1** presents the Douglas fir properties.

The property input into TASEF requires a specific volumetric enthalpy as a time integration of the density and specific heat product. To account for the moisture evaporation, the heat of vaporization for water is added to the specific volumetric enthalpy at 120°C, and TASEF performs a linear interpolation from 100 to 120°C.

SAFIR allows the moisture content to be entered as a percentage. SAFIR adds the heat of vaporization as a constant to the specific heat between 100 and 115°C and then linearly decreases from 115 to 200°C. Alternatively, the moisture can be accounted for manually by adding the heat of vaporization to the specific heat. The former was used in the simulations presented in this paper.

FIRES T3 and COMSOL only account for the moisture through the specific heat values. For both these programs, the heat of vaporization was accounted for by increasing the specific heat between 100 and 120°C.

4. MODEL RESULTS AND COMPARISON TO TEST DATA

In comparing the results of the simulations to the test data, only the temperatures at 300°C and below are considered since the 300°C isotherm represents the char front[3]. **Figure 1** is a graphical illustration of the test data and model simulation data.

The results of the models are all consistent. The char front location, as a function of time, is in good agreement less the 10% difference between the test data and model simulation data up to 60 min. See **Table 2**. Beyond 60 min, the data begins to deviate significantly from the model results. None of the models account for the effect of flaming on the surface and how the boundary conditions change as a result. It is expected that if the surface flaming were accounted for at the boundary conditions, the results beyond 60 min would be significantly better.

The thermocouple data from the test report is not completely axi-symmetric. This is to be expected due to the property variations inherent in wood. The thermocouple locations and model nodal temperatures correspond for the measurements represented, but other thermocouple measurements on the symmetric axis will vary.

Table 2 – Comparison of Char Front Times to Thermocouple Locations.

Thermocouple Horizontal Location From Face of Beam (mm)	Time Char Front Reaches Thermocouple Location (min)								
	Test Data	FIRES T3	Percent Difference	SAFIR	Percent Difference	TASEF	Percent Difference	COMSOL	Percent Difference
16	16.0	17.1	6.6%	16.5	2.8%	14.9	6.7%	16.2	1.1%
32	36.3	39.8	9.8%	38.2	5.3%	37.0	2.0%	38.3	5.5%
48	59.8	69.4	16.1%	68.4	14.5%	65.9	10.3%	68.8	15.1%
67	78.3	105.9	35.4%	106.2	35.7%	102.0	30.4%	107.1	36.9%
79	118.5	NA	-	NA	-	NA	-	NA	-
111	NA	NA	-	NA	-	NA	-	NA	-

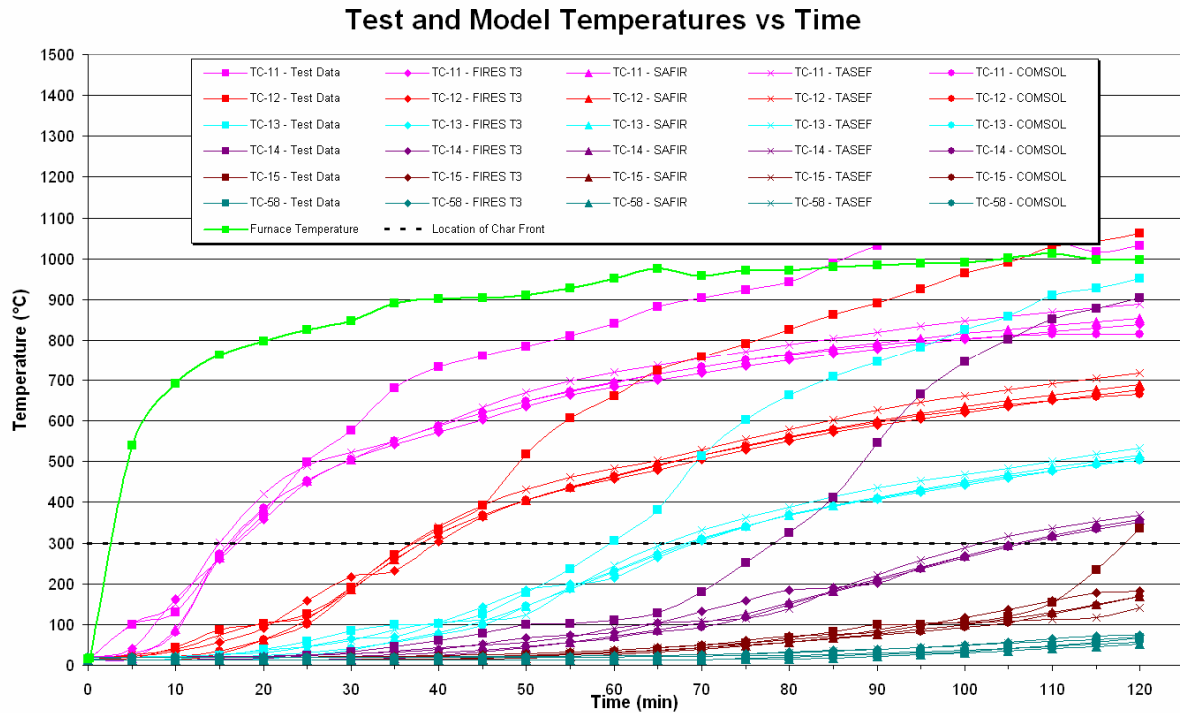


Figure 1 – Graphical Representation of Test and Model Simulation Data.

The location of the char front (300°C isotherm) indicates how much load carrying capacity wood remains. **Figure 2** illustrates a wood beam exposed to fire on three sides. Structural failure occurs when the full strength cold core and reduced strength heated zone are no longer capable of supporting the load. The char has no strength. Eurocode 5, Part 1.2 [3] provides the best recommendation based on available data for the bending strength of heated wood. See **Figure 3**.

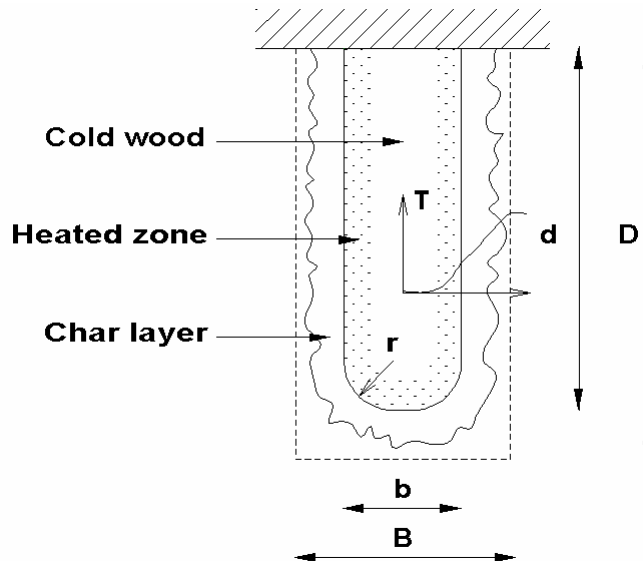


Figure 2 – Wood Beam with Three-sided Fire Exposure After Some Time.

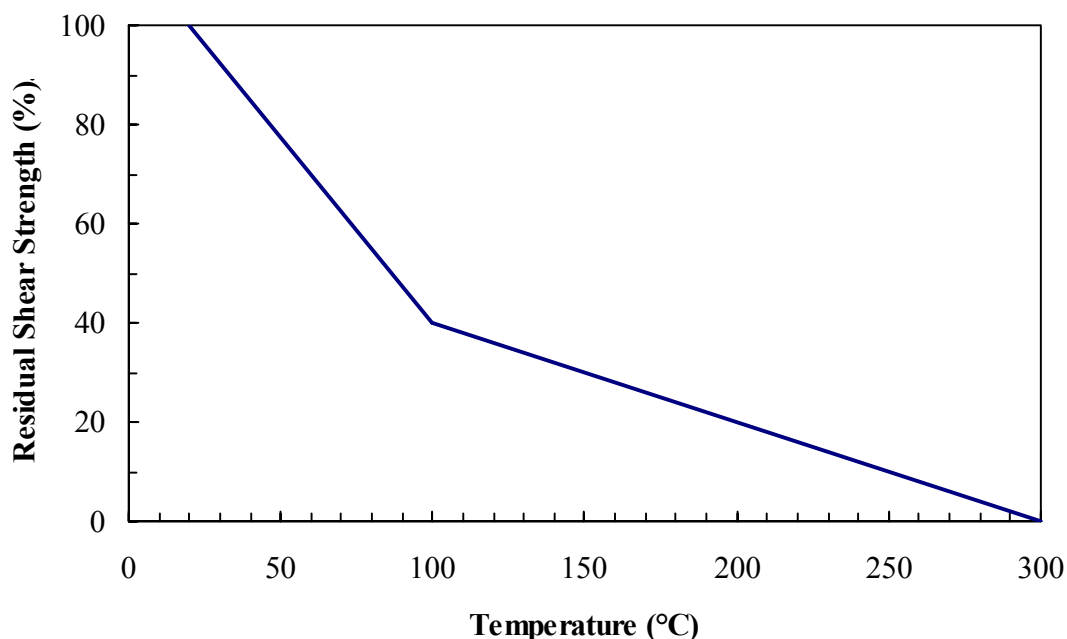


Figure 3 – Residual Strength of Wood as a Function of Temperature.

5. CONCLUSION

The combustion and reaction of wood exposed to fire conditions is a complex issue with many physical and chemical phenomena occurring. The structural fire performance of wood can be modeled with commonly used packaged finite element analysis programs, by using appropriately selected material properties to account for the physics that the programs do not directly address and applying the appropriate boundary conditions. Users should be cautious with the selection of these properties and the range of application of the results. Although some basic knowledge is required, FIRES-T3, SAFIR, and TASEF do not require great experience in partial differential equations or finite element modeling, and therefore, are good programs for the practicing engineer. COMSOL provides the most flexibility and is best suited for users with advanced experience in partial differential equations and finite element analysis modeling.

6. REFERENCES

1. Janssens, M.L., *Modeling of the Thermal Degradation of Structural Wood Members Exposed to Fire*. Fire and Materials, 2004. 28: p. 199-207.
2. Garabedian A. Janssens, M.L., *Evaluation of the Effect of Load on the Fire Resistance of Glulam Beams*. 1997, Southwest Research Institute: San Antonio.
3. CEN, "EN 1995-1-2:2003: Eurocode 5 - Design of Timber Structures - Part 1-2: General - Structural Fire Design," European Committee for Standardization, Brussels, Belgium, 2003.



PREDICTING THE FIRE RESISTANCE OF LIGHT-FRAME WOOD FLOOR ASSEMBLIES

Steven CRAFT¹, George HADJISOPHOCLEOUS¹, Burkan ISGOR¹ and Jim MEHAFFEY²

ABSTRACT

Models are available to predict the fire-resistance ratings of wood-frame assemblies protected by gypsum board. These models treat calcination of gypsum as occurring over a fixed temperature range or as characterized by apparent specific heat data generated at one fixed heating rate. In wood, moisture movement is neglected and pyrolysis is treated the same way as calcination of gypsum. These models are able to predict the performance of assemblies conditioned to a prescribed temperature and moisture content, and then exposed to a standard fire test in which temperatures increase monotonically.

Performance-based design and risk assessment approaches, however, require simulation of the response of assemblies for a variety of design fires under a variety of initial conditions (including seasonal variations in the moisture content of wood). For scenarios that differ from standard fire tests, such as those with a rapid heating phase followed by a cooling phase, better representations of the performance of gypsum board and wood are required.

This paper includes a discussion of ongoing attempts to derive a better description of the calcination of gypsum board and pyrolysis of wood. Thermal gravimetric analyses (TGA) were conducted on gypsum board and wood at several heating rates that are likely to be encountered in fires. Arrhenius rate constants have been computed for the calcination of gypsum and the pyrolysis of wood. Preliminary results suggest that previously-developed models are poorly equipped to deal with the rapid heating rates often observed in real fires.

1. INTRODUCTION

Traditionally, the fire-resistance rating of an assembly has been determined by subjecting a replicate of the assembly to the fire-resistance test ASTM E119¹. Computer models^{2, 3, 4, 5} have been developed as an alternative for predicting the ratings of wood-frame

¹ Department of Civil and Environmental Engineering, Carleton University 1125 Colonel By Drive, Ottawa, Ontario K1S 5B6 Canada, email: george_hadjisophocleous@carleton.ca

² Forintek Canada Corp., Suite 4100 CTTC, 1125 Colonel By Drive, Ottawa, Ontario K1S 5R1 Canada, email: jim.mehaffey@ott.forintek.ca

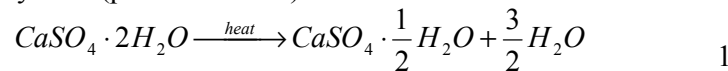
assemblies protected by gypsum board. These models treat calcination of gypsum and pyrolysis of wood as occurring over a fixed temperature range, by including the energetics associated in the apparent specific heats or enthalpies of the materials. In both gypsum board and wood, moisture movement is accounted for only through calibration of material properties (particularly in the thermal conductivity). Therefore, these models accurately predict the performance of assemblies exposed to a standard fire test in which the temperature increases monotonically at a specific rate. However, the calibration limits the use of the models in simulating realistic fires.

With the increasing use of performance-based design, computer models are more commonly used to assess designs. Risk assessment models, however, simulate the response of assemblies for a variety of design fires. For scenarios that differ from the standard fire test, such as those with a rapid heating phase followed by a cooling phase, better representation of the thermal degradation of gypsum board and wood are required in order to accurately model the performance of these assemblies.

The objective of this paper is to present models for the thermal degradation of gypsum board and wood that predict their response regardless of the heating rate, initial conditions and configuration. These degradation models will be used in a heat and mass transfer model in order to predict the failure of light-frame wood assemblies.

1.1 Gypsum Board

Gypsum board's excellent fire resistance derives from the fact that gypsum contains 21 percent by mass chemically bound water. A vast amount of energy is required to release and evaporate this chemically bound water. The release of this water, called calcination, is a two step process. The first reaction converts the calcium sulphate dihydrate (gypsum) to calcium sulphate hemihydrate (plaster of Paris).



The second step is the conversion of calcium sulphate hemihydrate to calcium sulphate anhydrate.



Both reactions are endothermic and produce liquid water, which requires a large amount of additional energy to evaporate.

As gypsum board is exposed to fire, the paper burns off within the first few minutes. As heat is conducted into the board the gypsum begins undergo calcination. The rate of release of the chemically bound water is a function of temperature. In fire exposures, calcination is usually complete by 200°C. Another reaction occurs at temperatures above 600°C. This reaction is believed to be decarbonation of calcium carbonate (Calcite) to form calcium oxide and carbon dioxide.

1.2 Wood

Wood undergoes thermal degradation when exposed to elevated temperatures. At temperatures above 100°C, chemical bonds begin to break. Between 100°C and 200°C, primarily non-combustible products, such as carbon dioxide, traces of organic compounds, and water vapour are produced. The rate at which the bonds are broken increases with

increasing temperature and contributes to mass loss. Above 200°C cellulose breaks down, producing tars and flammable volatiles. Above 450°C, all volatiles have been released, leaving behind activated char that can be oxidized to carbon dioxide, carbon monoxide, and water vapour, if oxygen is present⁹.

2. METHODOLOGY

2.1 Materials

Two materials have been tested: gypsum board and wood. In order to gain some insight into the variability of gypsum board, samples were taken from four different products from two manufacturers. Table 1 summarizes the gypsum board products obtained for tests.

Table 1. Gypsum board products tested.

Manufacturer	Product	Density (kg/m ³)
Manufacturer A	12.7 mm (1/2") Fire-rated	740
Manufacturer A	15.9 mm (5/8") Fire-rated	690
Manufacturer B	15.9 mm (5/8") Fire-rated	720
Manufacturer A	12.7 mm (1/2") regular	620

The wood sample chosen was spruce since it is the most common species in the spruce pine fir (SPF) species group, the main species group for construction grade lumber in eastern and central Canada.

In total, 11 TGA tests were conducted at the National Research Council of Canada. The distinguishing factors of each test are provided in Table 2. Note that tests 3 and 10 are identical to tests 2 and 9 in order to evaluate repeatability.

2.2 Modelling Mass Loss

An Arrhenius expression was used to model the mass loss of both gypsum board and wood when exposed to elevated temperatures. In the Arrhenius equation (Equation 1), two constants need to be determined, the pre-exponential factor A in 1/s and the activation energy E_A in J/mol.

$$\frac{dm}{dt} = -m A e^{-E_A/RT} \quad 1$$

where m is unit mass in kg/m³, t is time in seconds, R is the universal gas constant, and T is temperature in Kelvin. In order to solve for the pre-exponential factor and the activation energy, the following rate constant, k, was introduced.

$$\frac{dm}{dt} = -m k \quad 2$$

The rate constant k was then calculated for each data point generated in the TGA tests, based on the rise in temperature and the decrease in mass. The values of k are used to plot ln(k) vs. 1/RT. Since k is defined as

$$3 \quad k = A e^{-E_A/RT}$$

so that

$$4 \quad \ln(k) = \ln(A) - \frac{E_A}{RT}$$

The y-intercept on the graph is equal to $\ln(A)$ and the slope is equal to negative E_A .

Table 2. List of tests completed.

Test	Material	Heating Rate (°C/min)	Atmosphere
1	Manufacturer A 12.7 mm (1/2") Fire-rated	20	Air
2	Manufacturer A 12.7 mm (1/2") Fire-rated	5	Air
3	Manufacturer A 12.7 mm (1/2") Fire-rated	5	Air
4	Manufacturer A 15.9 mm (5/8") Fire-rated	5	Air
5	Manufacturer B 15.9 mm (5/8") Fire-rated	5	Air
6	Manufacturer A 12.7 mm (1/2") Regular	5	Air
7	Manufacturer A 12.7 mm (1/2") Fire-rated	2	Air
8	Spruce	20	Nitrogen
9	Spruce	5	Nitrogen
10	Spruce	5	Nitrogen
11	Spruce	2	Nitrogen

3. RESULTS AND DISCUSSION

3.1 Gypsum Board

As summarised in Table 2, seven TGA tests were completed using gypsum board. In Figure 1, a comparison is presented of the mass remaining as a function of temperature for each of the four products when heated at 5°C/minute (tests 2, 4, 5, 6). The initial drop in the mass loss below 100°C is due to the free water contained in the sample. The presence of free water is due to the conditioning of the samples prior to testing (50 percent relative humidity at 23°C). There is a large difference between the 15.9 mm fire-rated manufacturer A sample which lost 0.83 percent by 80°C and the 15.9 mm fire-rated manufacturer B sample which lost 0.34 percent. However, these are relatively close to the published values of 0.4 and 1 percent for sorption and desorption measurements respectively⁶. The calcination of gypsum takes place in the range of 80°C to 160°C for all four samples heated at 5°C/minute. After calcination takes place there is a small linear decrease in mass with temperature between 160°C and 600°C. It is not known at this time what causes this mass loss. Between 600°C and 730°C, each sample shows varying evidence of another reaction taking place. It is believed that this reaction is the decarbonation of calcium carbonate (CaCO₃). Differential scanning calorimetry (DSC) tests completed using Portland cement which shows a similar reaction above 600°C which was reported as decarbonation of calcium carbonate⁷. Also, TGA results for pure calcium carbonate are reported to match nicely with the reaction past 600°C seen below⁸. The 15.9 mm fire-rated sample from manufacturer A shows very little mass loss in this range (approx. 0.5 percent), while the 12.7 mm regular sample from manufacturer A shows substantial mass loss (approx. 7.5 percent).

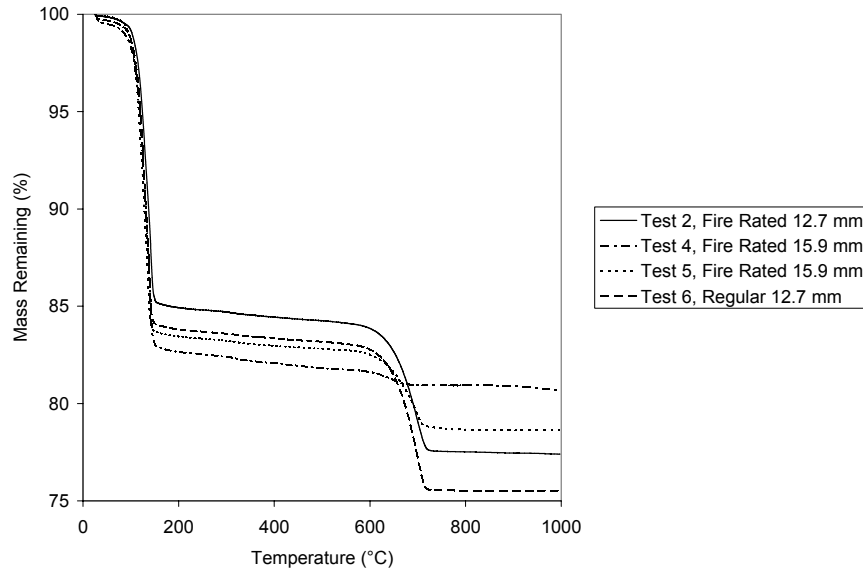


Figure 1 - Comparison of mass loss with a heating rate of 5°C/minute among four different gypsum board products from two manufacturers.

To estimate the percentage of gypsum in each sample, the mass loss due to calcination was estimated. Knowing that 21 percent of mass is released from gypsum as liquid water during calcination, the initial gypsum content can be estimated. Table 3 provides an estimation of the gypsum content of each sample.

Table 3. Comparison of gypsum content for each gypsum board product.

Product	Density (kg/m ³)	Estimated Gypsum (%)	Estimated Gypsum/ Unit Surface Area (kg/m ²)
Manufacturer A Fire-rated 12.7 mm	740	69.5	6.53
Manufacturer A Fire-rated 15.9 mm	690	79.0	8.67
Manufacturer B Fire-rated 15.9 mm	720	76.9	8.80
Manufacturer A Regular 12.7 mm	620	74.4	5.86

According to manufacturer A's material safety data sheet, the minimum gypsum content is 75 percent by weight for both regular and fire-rated boards. The 12.7 mm fire-rated board from manufacturer A seems to have approximately 5 percent less than the 75 percent suggested by the manufacturer. This may mean that the method used above underestimates the gypsum content or the plaster of Paris used in the manufacturing of the gypsum board is not fully hydrated by the time the gypsum board enters the driers.

In Figure 2, a comparison is presented of the mass loss as a function of temperature for 12.7 mm fire-rated gypsum board from manufacturer A when tested at three different heating rates. Table 4 shows the temperature range within which calcination takes place for each heating rate.

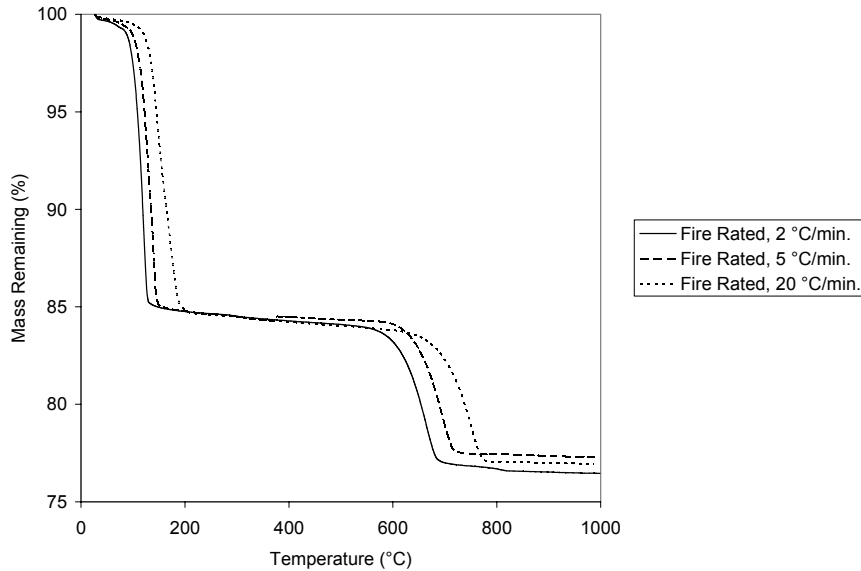


Figure 2 - Mass loss of 12.7 mm fire-rated gypsum board at heating rates of 2, 5, and 20°C/minute.

Table 4. Comparison of temperature range in which calcination occurs for three heating rates.

Product	Heating Rate (°C/min.)	Estimated Temp. at Start of Calcination	Estimated Temp. at End of Calcination
Fire-rated 12.7 mm	2	60°C	135°C
Fire-rated 12.7 mm	5	75°C	155°C
Fire-rated 12.7 mm	20	100°C	205°C

It is clear from Figure 2 and Table 4 that the more rapid the rise in temperature, the higher the temperature range where calcination takes place. This is one of the main shortfalls in the current models for calcination; they do not account for the rate of heating.

In determining the constants for the Arrhenius equation for each sample and heating rate, a linear regression analysis has been completed. The results of $\ln(k)$ versus $1/RT$ is plotted in Figure 3 for 12.7 mm fire-rated gypsum board from manufacturer A heated at 5°C/minute. Table 5 provides a summary of the constant values determined.

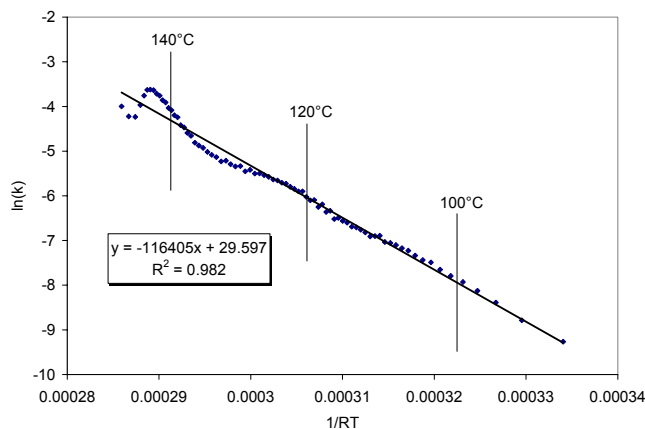


Figure 3 - Plot of $\ln(k)$ versus $1/RT$ for 12.7 mm fire-rated gypsum board from manufacturer A heated at 5°C per minute.

Table 5. Summary of results for the calcination mass loss model.

Test	Material	Heating Rate (°C/min)	Pre-exponential Factor (A) (1/s)	Activation Energy (E_A) (J/mol)
1	Man. A 12.7 mm Fire-rated	20	6.7×10^7	80 000
2	Man. A 12.7 mm Fire-rated	5	7.1×10^{12}	116 000
3	Man. A 12.7 mm Fire-rated	5	4.3×10^{12}	115 000
4	Man. A 15.9 mm Fire-rated	5	7.1×10^{11}	109 000
5	Man. B 15.9 mm Fire-rated	5	2.0×10^{12}	111 000
6	Man. A 12.7 mm Regular	5	3.2×10^{12}	113 000
7	Man. A 12.7 mm Fire-rated	2	8.0×10^{14}	130 000

There is significant variability in the pre-exponential factor. This is partly caused by the fact that the pre-exponential factor is equal to e , the base of the natural logarithm, raised to the power of the y-intercept. Therefore a small change in the y-intercept causes a significant difference in the pre-exponential factor. The variability in the pre-exponential factor between heating rates is also partly because the Arrhenius function does not model the reaction perfectly. Therefore, there is some dependence of the Arrhenius function's constants on heating rate. This is also evident from the activation energy. For the tests carried out at the 5°C/minute heating rate, the maximum difference in activation energy is 6 percent, but between the 2°C/minute heating rate and the 20°C/minute heating rate there is 38 percent difference.

In order to predict the mass loss during calcination at any heating rate for the gypsum board from manufacturer A, the values from the two 5°C/minute tests were used (tests 2 and 3). Therefore, the model used a pre-exponential factor of 5.7×10^{12} and an activation energy of 115,500 J/mol. A comparison between the models predicted mass loss and the experimental mass loss is shown in Figure 4. The model predicts the mass loss at 2°C/minute and 5°C/minute quite closely, however at 20°C/minute the model predicts calcination happening much sooner than experiment shows. However, since the heating rate seen in the bulk of the gypsum board during fire exposure is believed to be between 2 and 5°C/minute, this model is considered adequate. In modelling the mass loss for each sample, the percent gypsum and percent of free water were taken from the mass loss data and used as inputs to using the Arrhenius function. Therefore, in order to model calcination using this model, these material properties are needed.

The same method that was used to determine the constants for the Arrhenius equation to model calcination was used to model decarbonation. The constants were determined only for the 12.7 mm fire-rated gypsum board from manufacturer A, heated at 5°C/minute. The pre-exponential constant and the activation energy were found to be 2.4×10^{13} /s and 291000 J/mol, respectively.

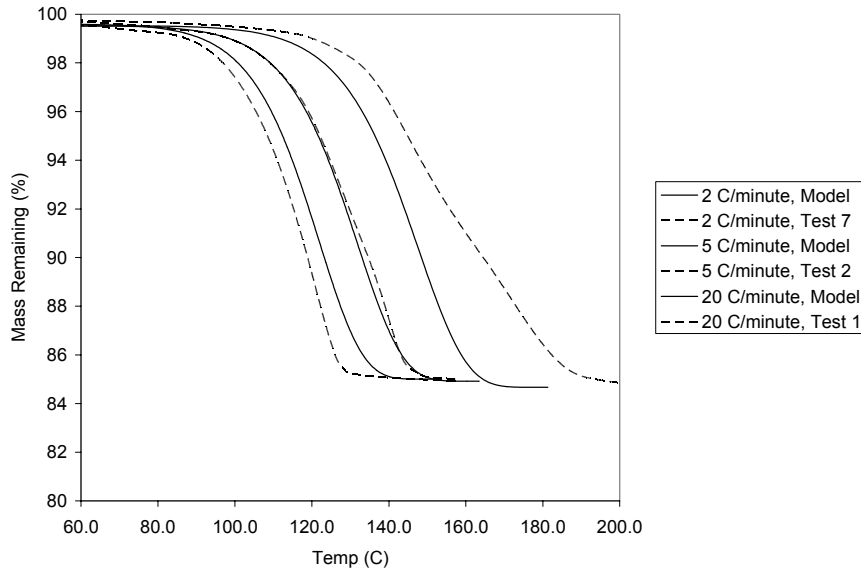


Figure 4 - Comparison between calcination model for 5°C/minute used to model heating rates at 2, 5, and 20°C/minute for 12.7 mm fire-rated gypsum board from manufacturer A.

3.2 Wood

Four TGA tests were completed on spruce in a nitrogen atmosphere. Three tests were completed at 2, 5, and 20°C/minute heating rates and the results for mass loss are shown in Figure 5. The initial mass loss up to approximately 110°C corresponds to the loss of the bound moisture. According to the wood handbook⁹, the equilibrium moisture content at 23°C and 50 percent relative humidity is 9.2 percent. This is very close to the approx. 9.5 percent mass loss up to 100°C. There is very little mass loss between 90°C and 200°C at a heating rate of 2°C/minute and between 135°C and 250°C at a heating rate of 20°C/minute. Pyrolysis occurs between 200°C and 360°C when heated at 2°C/minute and between 250°C and 405°C when heated at 20°C/minute. Once pyrolysis is complete, there is approximately another 10 percent mass loss up to 600°C. There seems to be very little mass loss above 600°C with approximately 15 percent mass remaining at 1000°C. The sample heated at 2°C/minute seems to experience more mass loss above 600°C than the other two samples. It is not known why this occurred. One possibility could be that the rate of nitrogen released into the chamber containing the sample may not be high enough to ensure that no oxidation takes place.

The same method to determine the Arrhenius constants as that used for gypsum was used for spruce. A summary of the constant values determined is provided in Table 6.

Table 6. Summary of test results for wood in nitrogen mass loss model.

Test	Material	Heating Rate (°C/min)	Pre-exponential Function (1/s)	Activation Energy (J/mol)
9	Spruce	20	4.5×10^6	105 000
12	Spruce	5	4.8×10^7	117 000
13	Spruce	5	3.2×10^7	119 000
15	Spruce	2	4.6×10^6	109 000

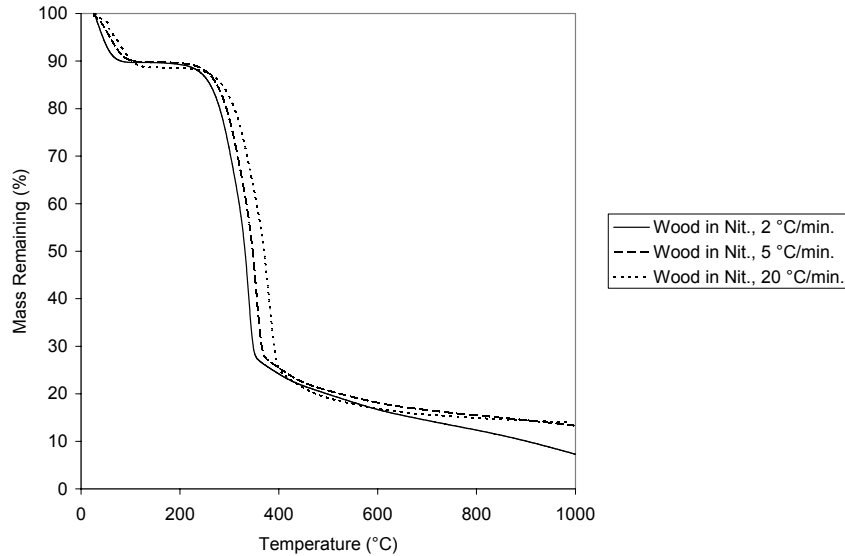


Figure 5 - Comparison of mass loss of spruce with increasing temperature at three different heating rates in a nitrogen atmosphere.

The values above compare favourably to previously published values. Moghtaderi¹⁰ found typical values for activation energy and pre-exponential factor values for pyrolysis of wood are in the order of 10^5 J/mol and 10^8 /s, respectively.

In order to predict the mass loss during pyrolysis at any heating rate, the constants from the 5°C/minute were used. The model used a average pre-exponential function and activation energy of 4.0×10^7 /s and 118,000 J/mol respectively. Figure 6 compares the results of the model to experiment data for the three heating rates. It is apparent that by using one Arrhenius function to model the rate of pyrolysis, the beginning of pyrolysis is underestimated and the later stages of pyrolysis are overestimated. However, the model shown is an improvement over models previously used in heat transfer analyzes for light frame assemblies.

The model for pyrolysis based on the 5°C/minute data is compared in Figure 7 to three published models for pyrolysis that have been reported in Moghtaden¹⁰.

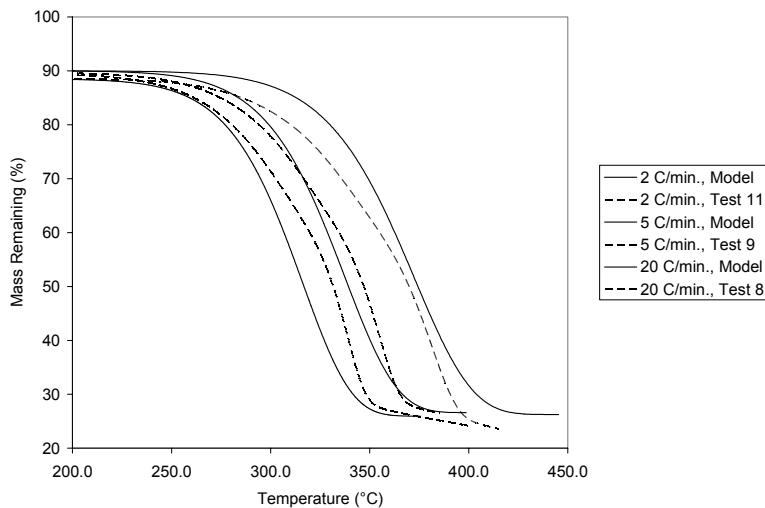


Figure 6 - Comparison between model for pyrolysis of wood in nitrogen based on average constant values at 5°C/minute and experimental mass loss data.

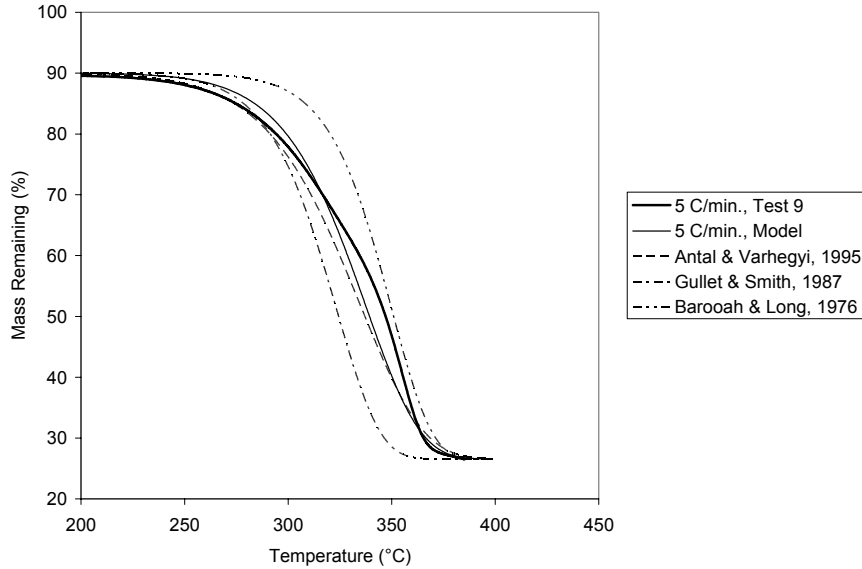


Figure 7 – Comparison between model for pyrolysis of wood in nitrogen based on average constant values at 5°C/minute, experimental mass loss data, and models published by Moghtaderi.¹⁰

4. HEAT AND MASS TRANSFER MODEL

The work presented in this paper is part of an ongoing effort to model the heat and mass transfer in a light-frame wood floor assembly. The heat and mass transfer model is based on work completed by Fredlund¹¹ who developed a one-dimensional heat and mass transfer model for wood. The following partial differential equations represent the energy balance and the mass balance used in the model.

$$5 \quad \frac{\partial}{\partial x} \left(k \frac{\partial T}{\partial x} \right) - \dot{m}'' c_v \frac{\partial T}{\partial x} + \dot{Q}''' = \rho c \frac{\partial T}{\partial t}$$

where k is thermal conductivity, T is temperature, x is spatial co-ordinates, \dot{m}'' is mass flux, c_v is specific heat of the water vapour and or pyrolysis products, \dot{Q}''' is the source term which accounts for the energy associated with evaporation, pyrolysis and calcination, ρ is density, c is specific heat, t is time.

$$6 \quad \frac{\partial}{\partial x} \left(\frac{D_x}{v} \frac{\partial P}{\partial x} \right) + \frac{V_p M_{\text{eff}}}{RT^2} \frac{\partial T}{\partial t} P + \dot{Q}''' = \frac{V_p M_{\text{eff}}}{RT} \frac{\partial P}{\partial t}$$

where D_x is the permeability, v is the kinematic viscosity, P is the pressure, V_p is the pore volume, M_{eff} is the effective molecular weight, R is the gas constant, \dot{Q}''' is the source term which accounts for the generation of water vapour and pyrolysis products.

The heat transfer model has been used to predict the results of an experiment involving four layers of 12.7 mm fire-rated gypsum board stacked together and exposed to the ASTM E119¹ temperature-time curve, with plans to include mass transfer in the near future. Material properties and experimental data are taken from Takeda and Mehaffey³ with the exception of the apparent specific heat. The heat transfer analysis uses the model for calcination of gypsum board presented in this paper. A comparison between results from the

heat transfer analysis and the experiment is shown in Figure 8. There is excellent agreement between the model's predictions and the experimental data with respect to the time and temperature at which the effect of calcination is complete.

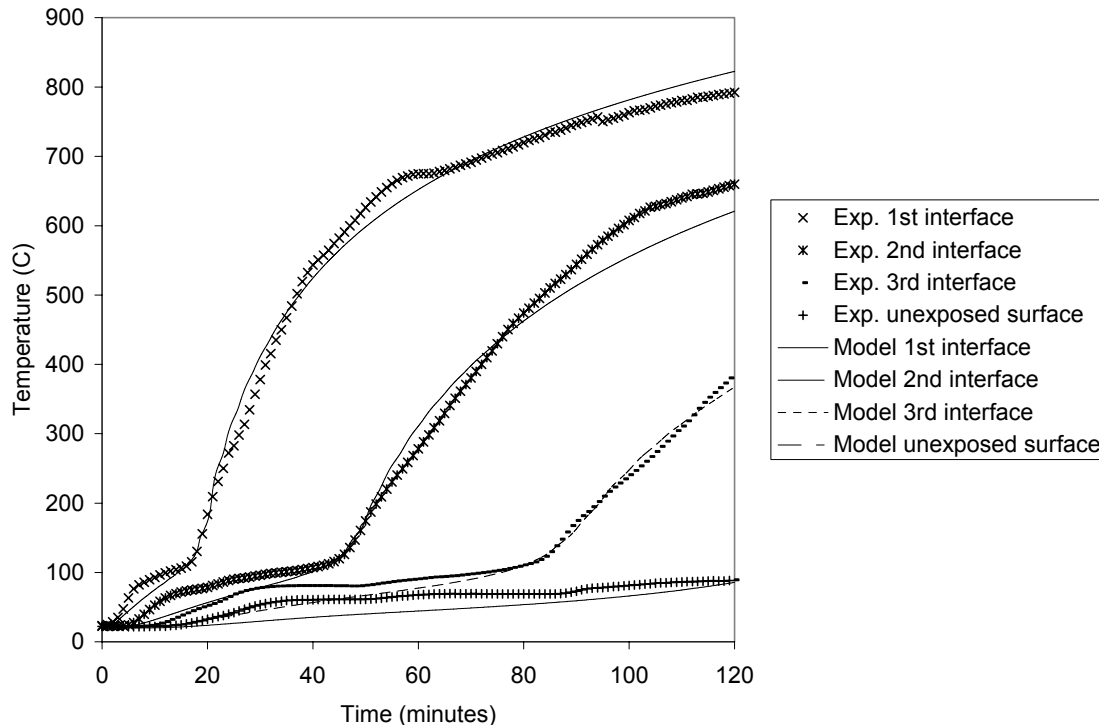


Figure 8 – Comparison between heat transfer analysis using calcination model and experiment consisting of four layers of 12.7 mm fire-rated gypsum board.

5. CONCLUSIONS

Models based on an Arrhenius expression have been developed to predict mass loss during calcination and decarbonation in gypsum board as well as pyrolysis in wood.

To use these models, the mass loss at the start and end of each process needs to be known. In gypsum board, the amount of free water, gypsum content, and calcium carbonate content need to be known. In wood, the bound moisture and the density of char need to be known.

The Arrhenius model derived in this paper accurately predicts mass loss of gypsum due to calcination at lower heating rates of 2 and 5°C/minute with less accuracy at 20°C/minute. However, since the bulk of the gypsum sees these lower heating rates, this model is expected to give good results when used in a heat and mass transfer analysis.

Pyrolysis in nitrogen has successfully been modelled using an Arrhenius expression. The constants derived from the 5°C/minute heating rate gave good predictions of mass loss for the 2 and 20°C/minute heating rates. This model will improve the predictions for temperature and the rate of charring over the previous method used in heat transfer models of light-frame wood assemblies.

6. ACKNOWLEDGEMENTS

Forintek Canada Corp. would like to thank its industry members, Natural Resources Canada (Canadian Forest Service), and the Provinces of British Columbia, Alberta, Saskatchewan, Québec, Nova Scotia, New Brunswick and Newfoundland for their guidance and financial support for this research.

The authors would also like to take Nouredine Benichou and Malgosia Kanabus-Kaminska from the National Research Council of Canada for there ongoing support in this research.

7. REFERENCES

1. Standard Test Methods for Fire Tests of Building Construction and Materials, ASTM E119, Annual Book of ASTM Standards, Vol. 04.07, ASTM, Philadelphia, pp. 331-51 (2001).
2. Mehaffey, J.R., Cuerrier, P., and Carisse, G. 1994. A Model for Predicting Heat Transfer through Gypsum-Board/Wood-Stud Walls Exposed to Fire. *Fire and Materials* (18), pp. 297-305.
3. Takeda, H. and Mehaffey, J.R. WALL2D: a model for Predicting Heat Transfer through Wood-Stud Walls Exposed to Fire. *Fire and Materials* 22, 133-140 (1998).
4. Clancy, P. 1999. Time and Probability of Failure of Timber Framed Walls in Fire. PhD Thesis, Victoria University of Technology, Victoria, Australia.
5. Thomas, G.C. 1997. Fire Resistance of Light Timber Framed Walls and Floors. PhD Thesis, School of Engineering, University of Canterbury, Christchurch, New Zealand.
6. Kumaran, M.K., Lackey, J.C., Normandin, N., Tariku, F. and Reenen, D.V. 2002. A Thermal and Moisture Transport Property Database for Common Building and Insulating Materials. National Research Council Canada. 229 p. Available from: National Research Council
7. Sha, W., O'Neill, E.A. and Guo, Z. 1999. Differential Scanning Calorimetry Study of Ordinary Portland Cement. *Cement and Concrete Research* (29), pp. 1487-1489.
8. Kanabus-Kaminska, Malgosia. 2005. National Research Council Canada, Ottawa, ON, Canada. Personal communication.
9. Schniewind, Arno P., ed. Concise Encyclopedia of Wood and Wood-Based Materials. 1st Edition. Elmsford, NY. Pergamon Press. 271-273.
10. Moghtaderi, B. 2006. The State-of-the-art in Pyrolysis Modelling of Lignocellulosic Solid Fuels. *Fire and Materials* (30), pp. 1-30.
11. Fredlund, B. 1993. Modelling of Heat and Mass Transfer in Wood Structures During Fire. *Fire Safety Journal* 20, pp. 39-69.



MODELLING RESISTANCE OF WOODEN I-JOISTS EXPOSED TO FIRE

Jürgen KÖNIG¹ and Bo KÄLLSNER²

ABSTRACT

A numerical study is being conducted with the objective to determine cross-sectional and strength and stiffness properties of I-shaped joists and studs subjected to charring under ISO 834 standard fire exposure. The objective of this paper is to give the relevant design parameters in terms of Eurocode 5 (EN 1995-1-2) for I-joists in bending where the tension flange is on the fire exposed side of the joist; these are the time of start of charring, notional charring depths and modification factors for strength. The I-joists are assumed to be integrated in floor assemblies consisting of joists, linings made of gypsum plasterboard or wood-based panels, cavities completely filled with batt-type rock or glass fibre insulation, and a decking. Heat transfer analyses were performed using SAFIR. This software permits to study the effect of the lining falling off at specified times that are known from full-scale testing or using the criterion of insufficient penetration length of fasteners into unburned wood. For the determination of the notional charring depth in the flange and the modification factors of the whole cross-section, a computer program, written as a Visual Basic macro embedded in Excel, was developed, using the temperature output from the heat transfer calculations and relative strength and stiffness values given by EN 1995-1-2, i.e. compressive strength, tensile strength and moduli of elasticity in compression and tension. The notional charring depth is calculated such that the notional residual cross-section of the flange remains rectangular and the section modulus of the I-section is unchanged. The effect of various parameters on the notional charring rate is shown, such as charring phases (i.e. a distinction is made whether the I-section is initially unprotected, protected by a lining, or unprotected after failure of the lining), flange dimensions and depth of cross-section. Modification factors are shown as functions of the notional charring depth for different charring phases. In order to simplify these relationships, simple expressions are proposed for increased user-friendliness and code specification.

¹ Senior Research Scientist, SP Trätekt, Stockholm, Sweden,
email: juergen.koenig@sp.se

² Adjunct Professor, SP Trätekt, Stockholm, and School of Technology and Design, Växjö University, Sweden,
email: bo.kallsner@sp.se

1. INTRODUCTION

Wooden I-shaped joists and studs, consisting of flanges made of solid timber or LVL and a web made of wood-based panels (such as particle board, fibreboard or OSB), are increasingly used in timber frame construction. While design models for fire exposed timber frame construction with solid timber joists and studs are available, e.g. in Eurocode 5 (EN 1995-1-2¹), there is still a need to develop corresponding rules for timber frame assemblies with I-shaped joists and studs. For the time being, fire resistance classification is normally done by fire testing of floor and wall assemblies.

The normal design procedure of timber members exposed to fire consists of several steps:

- Determination of action effects (internal forces and moments);
- Determination of the residual cross-section of the member taking into account the effect of fire protective claddings (thermal analysis) on the charring depth;
- Determination of the degradation of strength and stiffness properties, e.g. by modification factors or the use of an effective residual cross-section where applicable;
- Calculation of the mechanical resistance of the member.

The goal of the study presented here is to derive simple, easy-to-use expressions for the following parameters:

- Time of start of charring;
- Charring rates;
- Modification factors for the reduction of strength and stiffness parameters (such as bending strength, shear strength and modulus of elasticity).

The design model should also be applicable where failure times of fire protective claddings must be determined by testing.

The constructions dealt with in this paper consist of floor joists with a lining and a decking (generally called as fire protective claddings) and cavities that are completely filled with batt-type rock or glass fibre insulation. The glass fibre insulation is assumed to provide protection to the I-joists as long as the fire protective cladding remains attached to the structure. This paper only deals with I-joists in bending where the tension flange is on the fire exposed side of the floor assembly.

2. METHODOLOGY

The charring and mechanical properties of I-joists are determined in two steps. The charring properties are determined using the residual cross-section from the thermal analysis, assuming that all parts of the cross-section with temperatures greater than 300°C have undergone charring. The notional charring depth, $d_{\text{char},n}$, of the fire exposed flange is determined, assuming that

- the notional residual cross-section of the fire exposed flange is rectangular and the flange width is equal to the original flange width b ;
- the section modulus of notional residual cross-section, W_r , is equal to the residual cross-section obtained by the thermal analysis.

The modification factor for the reduction of bending strength, $k_{\text{mod,fi,fi}}$, is determined from

$$k_{\text{mod,fi,fi}} = \frac{M_{\text{fi}} W}{M W_r} \quad (1)$$

where:

M is the bending moment resistance under ambient conditions;

M_{fi} is the bending moment resistance in the fire situation;

W_r is the section modulus of the residual cross-section of the I-joist;

W is the section modulus of the original cross-section of the I-joist.

A typical cross-section of an I-joist is shown in Figure 1a. Most calculations were conducted for an I-joist (H200) with $h = 200$ mm, $b = 48$ mm, $h_{\text{fl}} = 48$ mm and $b_w = 8$ mm. Thereafter the flange width was varied from 36 to 88 mm and the depth of the cross-section was increased to 300 mm. With respect to the web properties some simplifying assumptions were made. The flanges of I-joists and studs are produced using solid timber or engineered wood products such as LVL, while the web is normally made of wood-based panels (particleboard, OSB or wood fibreboard). Since the effect of the web is small on both temperature development in the web and the resistance of the cross-section, see Figure 2, (the modulus of elasticity of the web is between 20 and 50 % of the modulus of elasticity of the flanges), the modulus of elasticity of the web was taken equal to zero in the bending resistance analysis, see Figure 1b, while thermal properties of wood were assumed for the web in the thermal analysis, see Figure 1c. Also, determining the notional charring depth, the web was disregarded.

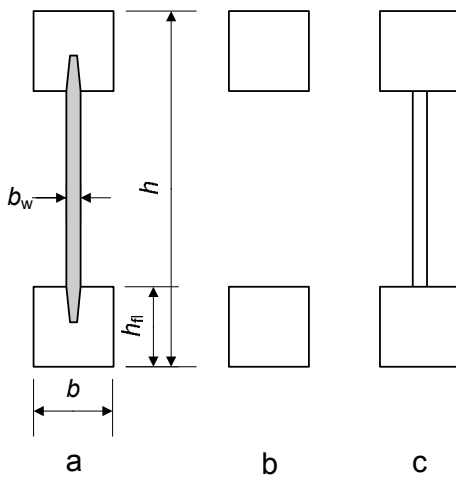


Figure 1 – a) Dimensions of I-shaped section, b) Cross-section for mechanical analysis (bending) and determination of notional charring depth, c) Cross-section for thermal analysis

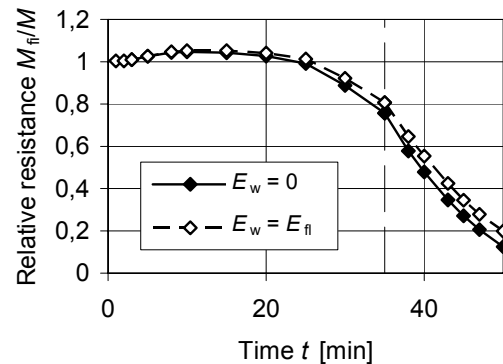


Figure 2 – Example of effect of web properties on relative bending resistance

Although floor and wall assemblies always include claddings on the fire exposed side, calculations were also conducted on assemblies consisting of an I-joist plus the cavity insulation (without cladding). The results of these calculations were used for studying the effect of some parameters, e.g. the flange width.

For application of the results from the thermal and mechanical analyses in a simplified design model, the following goals were set up:

The design model should be easy to use and available to all designers; it was not the purpose to create a design tool that could be felt as a “black box”;

Charring and strength parameters should be given as linear expressions;

The charring model should be consistent with testing and be modified where other species or engineered wood with different charring performance is used;

The model should also be applicable by using specific data determined by testing, e.g. failure times of fire protective claddings.

Following the format of EN 1995-1-2¹, the notional charring rate is determined as the one-dimensional charring rate multiplied by a number of coefficients taking into account the influence of various parameters such as the shape of the cross-section and the charring phase (protected or after failure of cladding). Strength and stiffness parameters are multiplied by modification factors for bending strength, $k_{mod, fm, fi}$, and for modulus of elasticity, $k_{mod, E, fi}$.

3. THERMAL ANALYSIS

3.1 Software and discretisation

The thermal analysis was executed using the software SAFIR 2004. This version of SAFIR permits modelling the failure of claddings at specific times, e.g. when a pre-defined failure criterion has been reached (a specific temperature on the unexposed side of gypsum plasterboard linings, or pull-out failure of fasteners, or a value known from full-scale fire tests), by using the temperature field from the first run as start temperature field in the following calculation without the cladding that is assumed to have fallen off.

For the thermal analysis a grid was used with element sizes from 2 mm × 2 mm to 8 mm × 8 mm, see Figure 3.

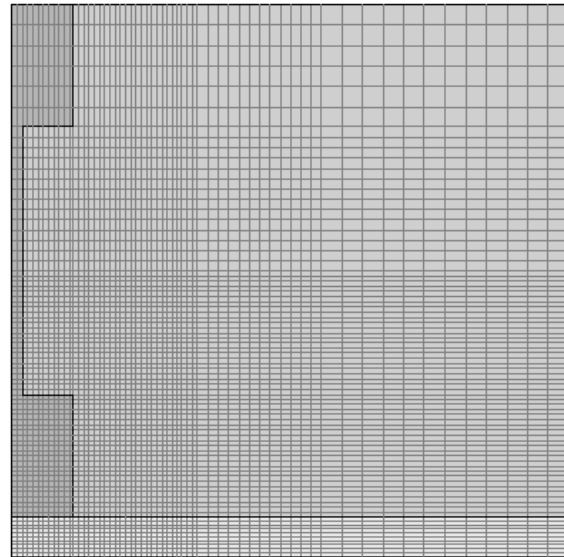


Figure 3 – Discretisation for the thermal analysis: I-joist with $h = 200$ mm, $b_{fl} = 48$ mm, $h_{fl} = 48$ mm, $b_w = 8$ mm and cladding $h_p = 15,4$ mm. The cladding on the ambient side was neglected

3.2 Thermal properties

In the heat transfer calculations, the thermal properties of timber were taken from EN 1995-1-1¹, based on König and Walleij². The heat capacity values of gypsum plasterboard were taken from Sultan³, whereas the thermal conductivity values were modified to fit the test results by König and Rydholm⁴ on 95 mm thick timber slabs protected by Swedish gypsum plasterboard of types A or F in accordance with EN 520⁵, see Figure 4. For the insulation material the thermal properties were taken from Källsner and König⁶.

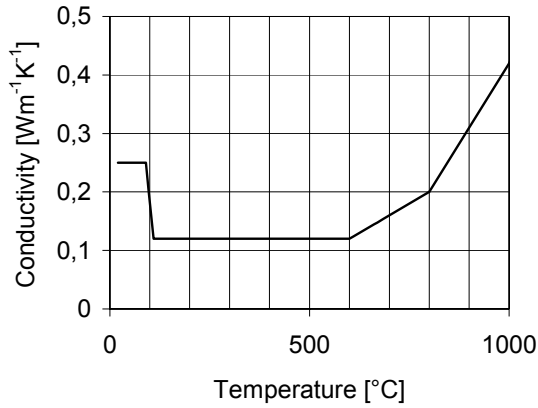


Figure 4 – Thermal conductivity of gypsum plasterboard

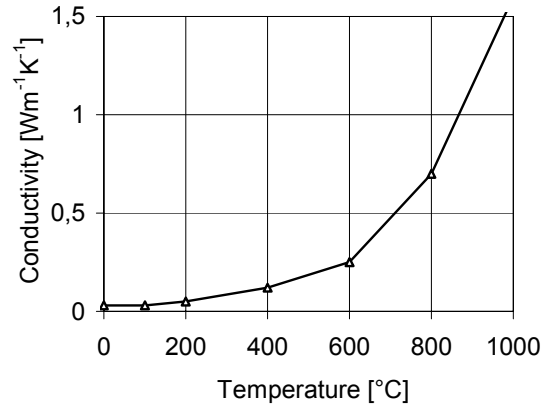


Figure 5 – Thermal conductivity of insulation

An example of typical results of the thermal analysis is shown in Figure 6. The graph indicates a rounded shape of the residual cross-section of the fire exposed flange; the char-line of which is defined as the location of the 300°C isotherm. Of special interest is the charring depth in the middle of the flange (axis of symmetry of the cross-section), $d_{char,m}$. The char development for the I-shaped section H200 is shown below, see 5.2.

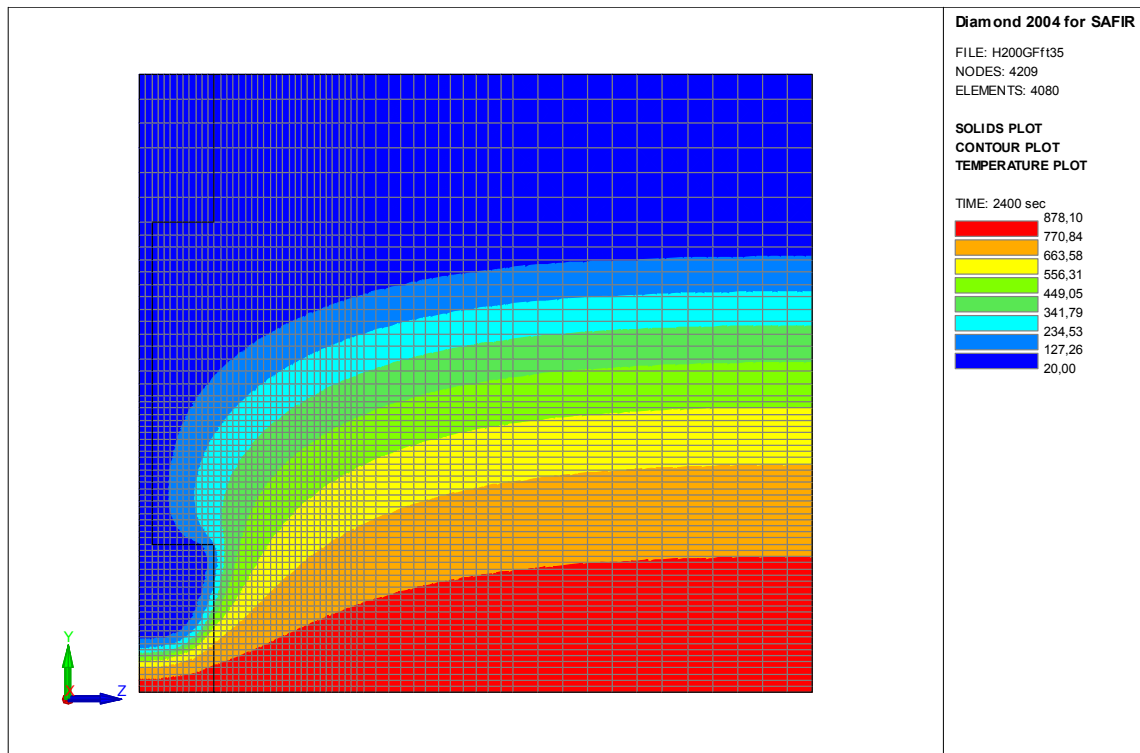


Figure 6 – Example of temperature field of assembly at 40 minutes, 5 minutes after failure of fire protective cladding

4. STRUCTURAL ANALYSIS OF CROSS-SECTION

4.1 Software

For the structural analysis, a computer program CSTFire, written as a Visual Basic macro embedded in Excel, was developed, using the temperature output from the heat transfer calculations and the relative strength and stiffness values given by EN 1995-1-2¹, i.e. compressive and tensile strengths, f_c and f_t , and moduli of elasticity in compression and tension, E_c and E_t . These values are given as bi-linear functions of temperature from 20 to 300°C with breakpoints at 100°C, also taking into account the effects of transient moisture situations and creep, see Figure 7. The software takes into account the possibility of permitting ductile behaviour of wood under elevated temperature. Contrary to ambient conditions where failure on the tension side of a beam is brittle, in the fire situation tensile failure of the outermost fibres won't cause immediate collapse of the member since a redistribution of internal stresses will take place as long as equilibrium is maintained.

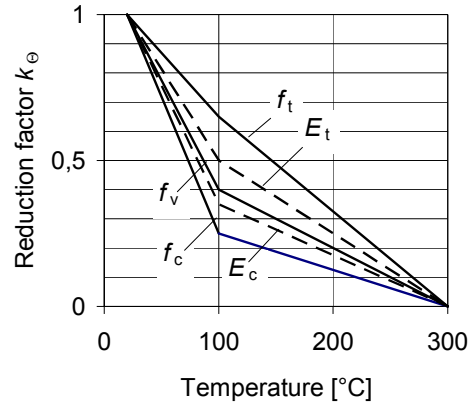


Figure 7 – Reduction factors for strength and stiffness properties according to EN 1995-1-2¹

Since the reduction of strength and stiffness properties is different for tension and compression, CSTFire uses an iteration process, increasing the curvature of the member until the maximum moment resistance is reached. The element size used for the structural analysis was chosen as 1 mm × 1 mm. Since a coarser grid was used in the thermal analysis, intermediate temperature values were determined by linear interpolation.

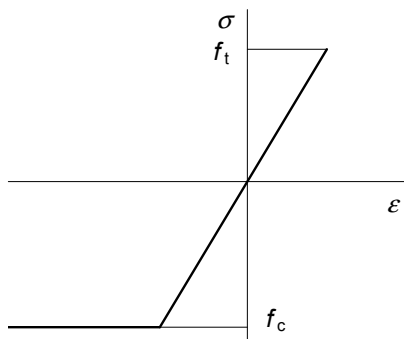


Figure 8 – Stress-strain relationships of wood

4.2 Material properties

The calculations were conducted assuming material properties that are representative for I-shaped sections used in practice, using the stress-strain relationship shown in Figure 8. Since the values of tensile and compressive strength of solid timber given in design or product standards, e.g. EN 338⁷, are values of the whole cross-section and were determined on the assumption of a linear relationship between stress and strain until failure, the use of these values in a finite element analysis would not be correct. Therefore, compressive strength values were determined using the data from Thunell⁸ giving the compressive strength of clear pine wood (*pinus sylvestris*) for different moisture contents and dry densities up to 350 kg/m³. These values can be expressed⁹ as:

$$f_c = 0,114 \rho_{0,12} - 9 \quad (2)$$

where $\rho_{0,12}$ is the dry density of wood in kg/m^3 , based on the volume of the wood at a moisture content of 12 %. For the I-joists assumed here with solid timber flanges of a quality slightly better than strength class C30 according to EN 338⁷, the producer declared a bending strength f_m of 27 N/mm^2 . For strength class C30 the characteristic density including 12 % moisture is 380 kg/m^3 , that is the dry density is 339 kg/m^3 and, with expression (2), the compressive strength is $29,7 \text{ N/mm}^2$. In the calculations the rounded value of $f_c = 30 \text{ N/mm}^2$ was used. Since $f_c > f_m$, the bending stresses over the depth are linearly distributed. Therefore we can assume $f_t = f_m = 27 \text{ N/mm}^2$. For I-joists with the tension flange on the fire exposed side, the calculations below showed, that there is no influence of compressive strength on the results as long as it is greater than the tensile strength.

5. RESULTS AND MODELLING

5.1 Resistance

Calculations were made of an I-shaped section H200, see Section 2, with a fire exposed tension flange and various gypsum plasterboard claddings and failure times of the claddings. In all cases the cavities were completely filled with rock fibre insulation. In Figure 9 the results of the calculations are shown as relative resistances versus time. Case 1 is shown as a reference scenario to demonstrate the effect of the claddings. For the effect of the flange width b and the depth of the joist h , see Figure 10 and Figure 11 (the effect of flange depth is not shown here). In all cases 1, 2, 3 and 4, the resistance increases initially above the values at ambient temperature since the wood on the fire exposed tension side becomes ductile at elevated temperatures, permitting the redistribution of internal stresses utilizing that the compressive strength is larger than the tensile strength and/or the material is assumed as elastic-plastic in compression, see Figure 8.

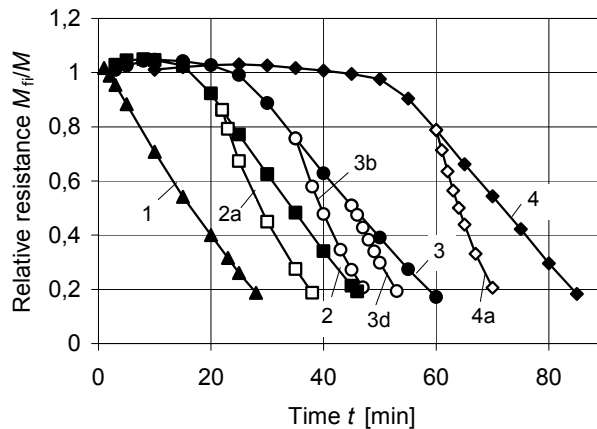


Figure 9 – Relative resistance of I-joist H200 with different gypsum plasterboard claddings and different failure scenarios assumed for claddings, see Table 1

Table 1 – Assemblies and failure scenarios of claddings

Case	Cladding	Failure time of cladding t_f min
1	none	
2	12,5 mm GA	none
2a	12,5 mm GA	21
3	15,4 mm GF	none
3a	15,4 mm GF	32
3b	15,4 mm GF	35
3c	15,4 mm GF	40
3d	15,4 mm GF	45
4	12,5 mm GA + 15,4 mm GF	none
4a	12,5 mm GA + 15,4 mm GF	60
4b	12,5 mm GA + 15,4 mm GF	70

5.2 Temperatures and charring

Relationships of charring depth in the middle of the flange versus time are shown in Figure 12. Most curves correspond to the cases shown in Figure 9. Again case 1 (initially

unprotected by a cladding) serves as the reference scenario. In cases without failure of the cladding, after some time charring starts at time t_{ch} , initially at a lower rate than in case 1 (charring phase 1), but later on with an increasing rate, see also Figure 13. When the cladding fails at time t_f , an immediate increase of the charring takes place, however after a few minutes the charring rate has slowed down and stabilized (charring phase 3), but it is greater than the charring rate during charring phase 1. For simplification, the non-linear relationships were replaced by secant values for $d_{char,m} = 20$ mm. When the charring has reached that value, the relative resistance is about 0,3. Thus secant values give slightly conservative results at load levels that are common in practice and slightly non-conservative values for lower resistances.

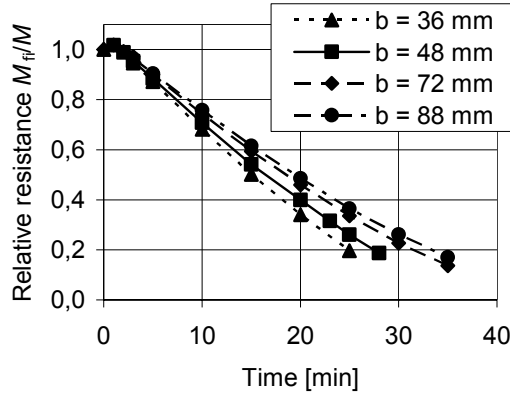


Figure 10 – Effect of flange width on relative resistance ($h = 200$ mm)

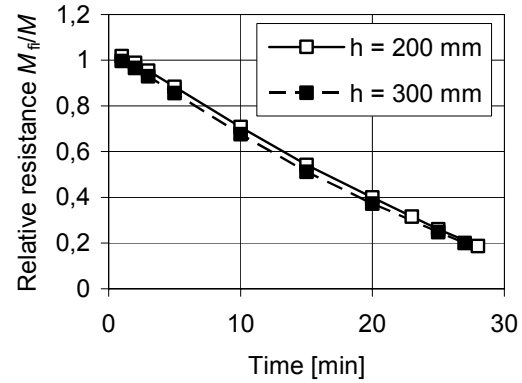


Figure 11 – Effect of depth on relative resistance ($b = 48$ mm)

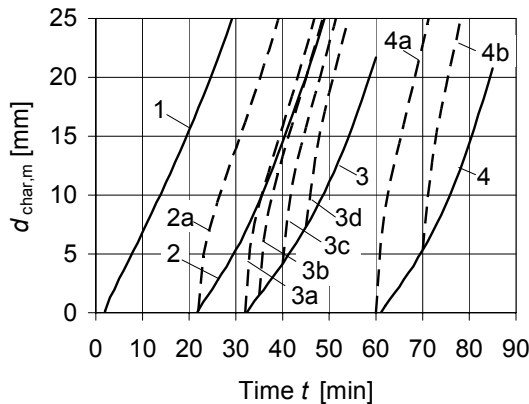


Figure 12 – Charring depth vs. time in the middle of the flange

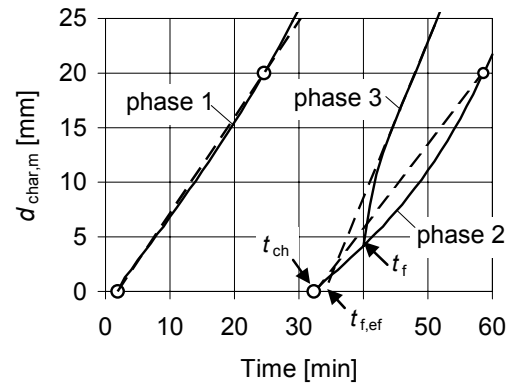


Figure 13 – Modelling of charring depth by linearization at different charring phases 1, 2 and 3

For charring phase 3 after failure of the cladding, the best fit was obtained by introducing an effective failure time of the panel (see Figure 13), determined as 90 % of the actual failure time (see Figure 14). With $k_2 = \frac{\beta_{char,m,2}}{\beta_{char,m,1}}$ and $k_3 = \frac{\beta_{char,m,3}}{\beta_{char,m,1}}$, where the figures

1, 2 and 3 in the subscripts refer to the corresponding charring phases, k_2 was determined as approximately 1 (not shown) and k_3 as shown in Figure 15.

The influence of the flange width on the charring depth in the middle of the flange, $\beta_{\text{char,m}}$, is shown in Figure 16 and 17 for charring phase 1. Again, the corresponding charring rates were determined as the secant values for $d_{\text{char,m}} = 20$ mm. The ratio k_b shown in Figure 17, is defined as $k_b = \frac{\beta_{\text{char,m}}}{\beta_{\text{char,0}}}$, where $\beta_{\text{char,0}} = 0,65$ mm/min, that is the one-dimensional charring rate of a semi-infinite wood slab, given by EN 1995-1-2¹.

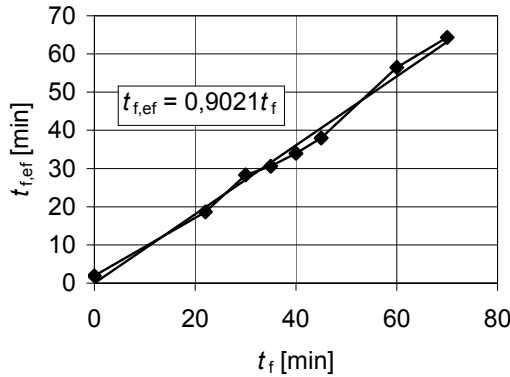


Figure 14 – Determination of effective failure time of cladding

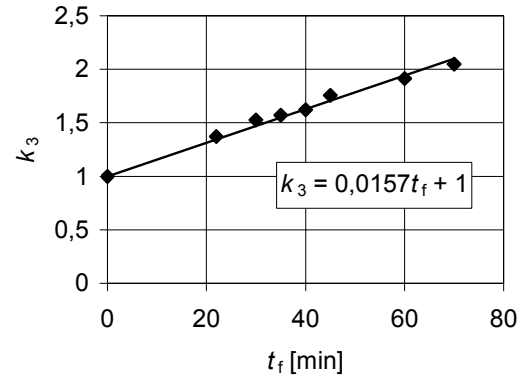


Figure 15 – Determination of k_3 for charring rate after failure of cladding (phase 3)

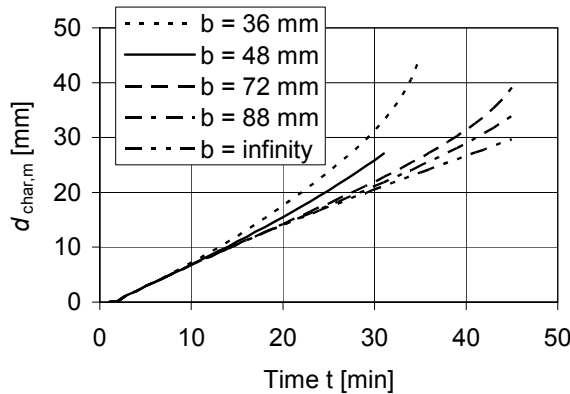


Figure 16 – Effect of flange width on charring depth in the middle of the flange (charring phase 1)

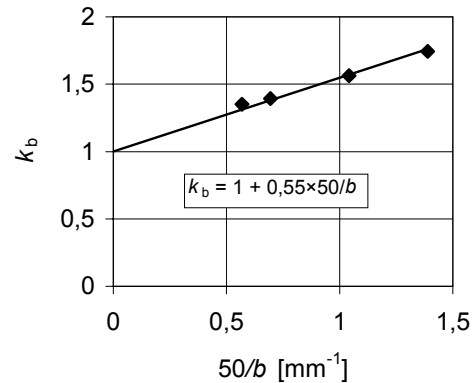


Figure 17 – Determination of flange width factor (and charring rate β_m)

5.3 Notional charring depth

Using the above mentioned software CSTFire, from the section modulus of the residual cross-section, for various time steps the notional charring depths $d_{\text{char,n}}$ were determined and compared with the charring depth in the middle of the flange, $d_{\text{char,m}}$, denoting

$$k_n = \frac{d_{\text{char,n}}}{d_{\text{char,m}}} \quad (3)$$

Relationships of k_n versus $d_{\text{char,m}}$ are shown in Figure 18. For small charring depths $d_{\text{char,m}}$ the values of k_n are greater when the flange is protected by a cladding, since the

residual cross-section of the flange is smaller, see Figure 19, however for resistances relevant in practice, the differences are small. As a reasonable approximation, $k_n = 1,6$ should be used in all cases.

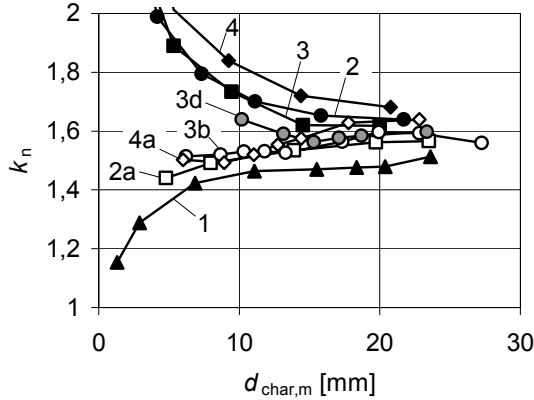


Figure 18 – Relationship of $k_n = d_{char,n}/d_{char,m}$ vs. $d_{char,m}$

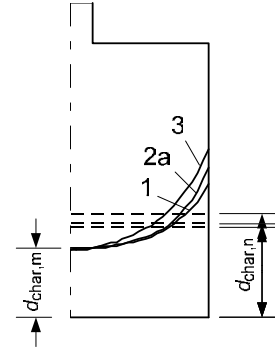


Figure 19 – Real and notional charring depths in flange for charring phases 1 (curve 1), 2 (curve 3) and 3 (curve 2a); for curve numbering see Table 1

Using the coefficients derived above, the charring rates for charring phases 2 and 3 can be determined as

$$\beta_n = \beta_0 k_b k_2 k_n \quad (4)$$

$$\beta_n = \beta_0 k_b k_3 k_n \quad (5)$$

where β_0 is the one-dimensional charring rate. The charring depth can easily be determined using the expression for the start of charring, t_{ch} , given in EN 1995-1-2¹, and the failure time of the cladding.

5.4 Bending strength

Since the designer will always determine the notional charring depth, $d_{char,n}$, the modification factors for bending, $k_{mod, fm, fi}$, are also presented as functions of $d_{char,n}$, see Figure 20, where the different curves refer to the cases of Table 1. Comparing curves 1, 2, 3 and 4, we can see that there is a greater strength reduction during charring phase 2 than charring phase 1, the greatest strength reduction for claddings consisting of several layers (case 4). After failure of the cladding, a fast (within 3 minutes) recovery of strength takes place with modification factors even greater than for curve 1. An explanation of this effect is that the temperature gradient largely depends on the charring rate: at smaller charring rates as during charring phase 2 greater parts of the flange are affected by elevated temperature, and vice versa, at very large charring rates, the temperature affected zone is small, see Figure 21 showing temperature profiles below the char-line for $d_{char,m} = 12$ mm.

For I-joists used as floor joists, gypsum plasterboard claddings will normally fall off the floor due to thermal degradation of the cladding, or due to pull-out failure of fasteners. Therefore the most frequent scenario would be charring phase 3 (cases 2a, 3a, 3b or 4a, see Figure 9). For design, the following expression, obtained by fitting to curve 1, can be used:

$$k_{mod, fm, fi} = 1 - 0,015 d_{char,n} \quad (6)$$

The effect of the flange width, see Figure 22, that, although being small, can be taken into account by introducing a coefficient $k_{b,kmod}$ given by

$$k_{b,kmod} = \frac{10,5}{b} + 0,8 \quad (7)$$

and

$$k_{mod,fi,fi} = 1 - 0,015 k_{b,kmod} d_{char,n} \quad (8)$$

An example of stresses and strength distributions along the symmetry axis of the cross-section is shown in Figure 23. It can be seen that tensile failure has occurred in a zone close to the char-line.

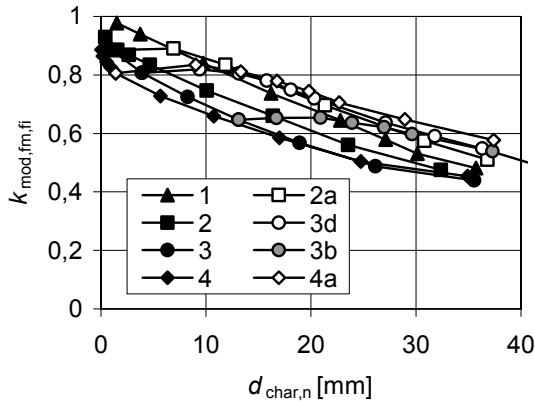


Figure 20 – Modification factors for bending strength vs. notional charring depth

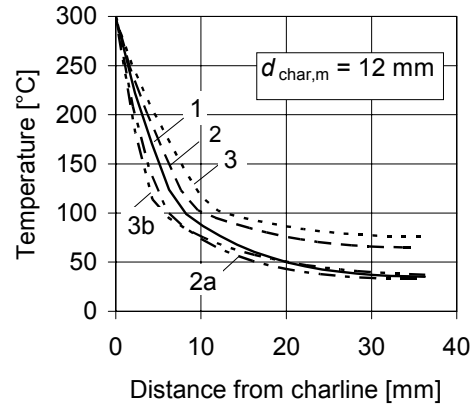


Figure 21 – Temperature profiles below char-line along axis of symmetry

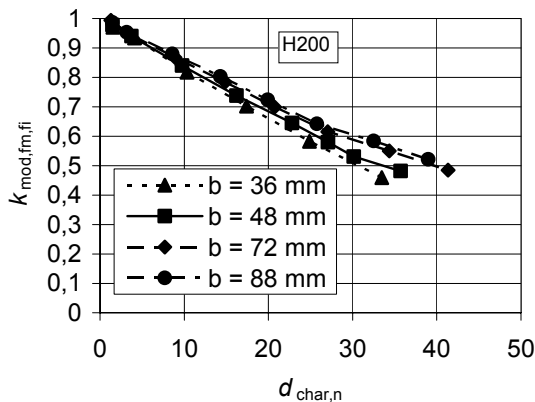


Figure 22 – Effect of flange width on modification factor for bending strength

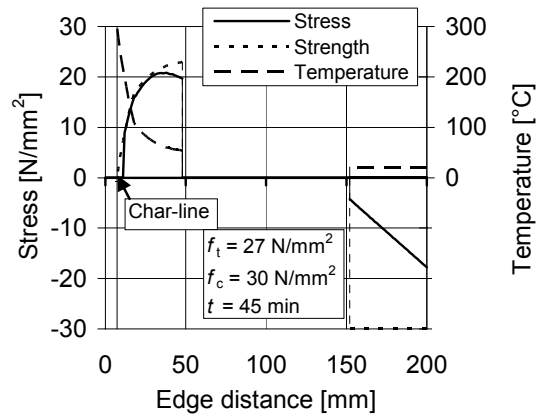


Figure 23 – Example of stress distribution along axis of symmetry of cross-section

5.5 Shear failure

A check of shear resistance close to supports should be done by determining shear strength at locations of the web with maximum temperature elevation. From Figure 6 can be seen that maximum web temperatures are reached at a distance of about 20 mm from the upper edge of the fire exposed flange. For some cases modification factors $k_{mod,fi,fi}$ were

determined by multiplying the web temperature in that zone by k_{Θ} for shear strength according to Figure 7 and plotted as functions of $k_b \times d_{char,n}$, see Figure 24. Considering phase 3 after failure of panels as the most relevant failure scenario, the curves can be fitted by a linear expression given by

$$k_{mod,fv,fi} = 1,53 - 0,022 k_b d_{char,n} \quad (7)$$

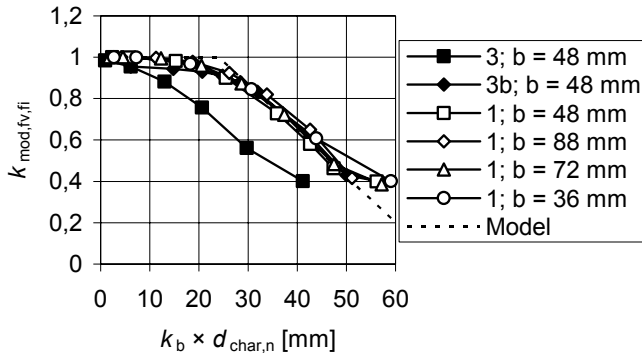


Figure 24 – Modification factor for shear strength vs. notional charring depth

Web temperatures of 100°C (that is $k_{mod,fv,fi} = 0,4$) are reached when $k_b \times d_{char,n} = 60$ and the relative bending resistance is about 0,3 or smaller. Therefore, in normal cases, shear resistance should not be decisive in the design of I-joists.

6. ACKNOWLEDGEMENT

The investigation described in this paper was funded by Nordic producers of I-shaped joists and studs, NICE – Nordic Innovation

Centre, and Vinnova – Swedish Agency for Innovation Systems.

7. REFERENCES

- [1] EN 1995-1-2:2004 Eurocode 5: Design of timber structures – Part 1-2: General – Structural fire design.
- [2] König, J. and Walleij, L., 1999, One-dimensional charring of timber exposed to standard and parametric fires in initially protected and non-protected fire situations. Träteknik – Swedish Institute for Wood Technology Research, Report No. I 9908029.
- [3] Sultan, M. A., 1996, A model for predicting heat transfer through noninsulated unloaded steel-stud gypsum board wall assemblies exposed to fire. Fire Techn., Third Quarter, 1996, 239-259.
- [4] König, J. and Rydholm, D., 2003, Small-scale fire tests of heavy timber components. Träteknik – Swedish Institute for Wood Technology Research, Report No. P 0310036.
- [5] EN 520:2004, Gypsum plasterboards – Definitions, requirements and test methods. European Committee for Standardization, Brussels.
- [6] Källsner, B. and König, J., 2000, Thermal and mechanical properties of timber and some other materials used in light timber frame construction. Proceedings of CIB W18, Meeting 33, Delft, Lehrstuhl für Ingenieurbau, University Karlsruhe, Karlsruhe, Germany.
- [7] EN 338:2003, Structural timber – Strength classes. European Standard. European Committee for Standardization, Brussels.
- [8] Thunell, B., 1941, Hållfasthetsegenskaper hos svenskt furuvirke utan kvistar och defekter. Royal Swedish Institute for Engineering Research, Proceedings No. 161, Stockholm.
- [9] König, J. and Källsner, B., 2001, Cross-section properties of fire exposed rectangular timber members. Proceedings of CIB W18, Meeting 34, Delft, Lehrstuhl für Ingenieurbau, University Karlsruhe, Karlsruhe, Germany.



FIRE BEHAVIOUR OF TIMBER BLOCK WALLS

Andrea FRANGI¹ and Mario FONTANA²

ABSTRACT

A comprehensive research project on the structural behaviour of timber block walls has been recently completed at the ETH Zurich. In addition to a large number of investigations at normal temperature under static and dynamic loading, the fire behaviour of timber block walls was experimentally analysed with 6 large-scale fire tests. All fire tests were based on ISO-fire exposure. The paper describes the main results of the fire tests. Particular attention is given to the analysis of different structural wall modifications used in order to improve the buckling behaviour of the block wall in fire.

1. INTRODUCTION

In the last years the construction industry has drawn attention to new construction methods based on building systems. Wood particularly fits the requirements of the idea “built with system” because of its easy manufacturing possibility. An example of a new successful construction system is the timber block wall system called STEKO that has been developed together with the Institute of Structural Engineering at the ETH Zurich and has become increasingly popular not only for residential but also for office buildings in Switzerland and abroad. STEKO is a rapid construction system that uses large hollow timber blocks that simply slot together (see fig. 1). The main advantages of this new building system are:

- prefabrication of the timber blocks,
- simple and rapid construction,
- no glue or other fixings are needed to complete a load-bearing wall construction,
- no drying-out time is required

¹ PhD, Senior research associate, Institute of Structural Engineering - Steel, Timber and Composite Structures, IBK HIL D35.1, ETH Zurich, 8093 Zurich, Switzerland, email: frangi@ibk.baug.ethz.ch

² Professor, Institute of Structural Engineering - Steel, Timber and Composite Structures, IBK HIL D36.1, ETH Zurich, 8093 Zurich, Switzerland, email: fontana@ibk.baug.ethz.ch

Further electrical services can be run in an easy way within the vertical voids of the finished wall. The voids can be filled with insulation which is dry injected into the cavity and permits to satisfy high thermal requirements.



Fig. 1 – STEKO basic hollow timber block made from cross-glued boards (left), timber block with base plate and top plate (center) and schematic timber block wall construction (right).

STEKO hollow timber blocks are made from cross-glued boards of spruce and have horizontal and vertical interlocking parts. The basic timber block has dimensions of $B \times H = 16 \text{ cm} \times 32 \text{ cm}$ and is available with lengths of 16, 32, 48 and 64 cm. Figure 2 shows the geometry of the typical timber block $16 \times 32 \times 48 \text{ cm}$. Starting from a level timber base plate, the blocks are simply stacked on top of each other row by row, each block locating accurately onto the blocks below by means of integral locating dowels (see figure 1 right). A top plate finishes the wall construction. Specially designed blocks accommodate for corners, wall ends and to line windows and door apertures.

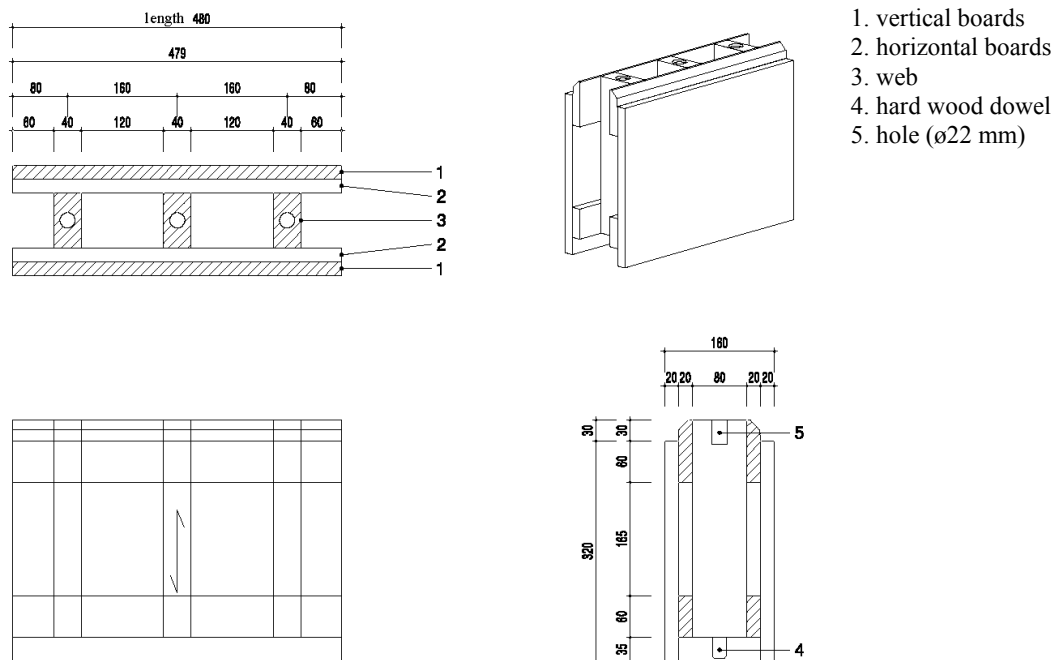


Fig. 2 – Geometry of STEKO basic hollow timber blocks made from cross-glued boards.

Timber is a combustible material. If wood is subjected to sufficient heat a process of thermal degradation (pyrolysis) occurs, producing combustible gases, accompanied by a loss in weight and cross-section. A surface char layer is then formed, which because of its low thermal conductivity protects the interior of the timber cross-section against heat¹. The time

dependent thermal degradation of wood is called charring rate and is defined as ratio between the distance of the char-line from the original wood surface and the fire duration time. The charring of wood is the main parameter to describe the fire behaviour of timber constructions^{2,3}. In a typical fire test, load-bearing timber walls tend to deform away from the furnace and fail by buckling in that direction⁴. The load-bearing behaviour of timber block walls is very sensitive to vertical loads acting eccentrically. In case of fire, after the outer layer exposed to fire is completely charred, the residual cross-section is eccentrically loaded leading to large horizontal deformations and global buckling of the wall system. It is therefore of primary importance to take into account the stability of the wall exposed to fire.

In addition to a large number of investigations at normal temperature under static and dynamic loading⁵, the fire behaviour of the timber block wall system was experimental analysed with large-scale fire tests. The objectives of the tests were to enlarge the experimental background of timber block walls in fire and to establish design models for the fire resistance of the timber block wall system. This paper describes the main results of the fire tests. Particular attention is given to the analysis of different structural wall modifications used in order to improve the buckling behaviour of the block wall in fire.

2. TEST PROGRAMME

The fire behaviour of the timber block wall system was experimental analysed with 6 large-scale fire tests. All fire tests were based on ISO-fire exposure⁶ and performed on the 3x3 m vertical furnace at the Swiss Federal Laboratories for Materials Testing and Research in Dubendorf. Starting from a typical timber block wall following test parameters were varied:

- vertical timber studs were inserted in the vertical voids (wall 1 and 3)
- the timber block wall was protected by gypsum fibreboards (wall 4 and 6)
- the timber blocks were filled with concrete (wall 2 and 5)

The objective of these structural wall modifications was the improvement of the buckling behaviour of the block wall in fire. Table 1 gives an overview of the fire tests performed. For walls 1 and 3 timber blocks with vertical grooves and plywood clips inserted in the grooves were used (see figure 3).

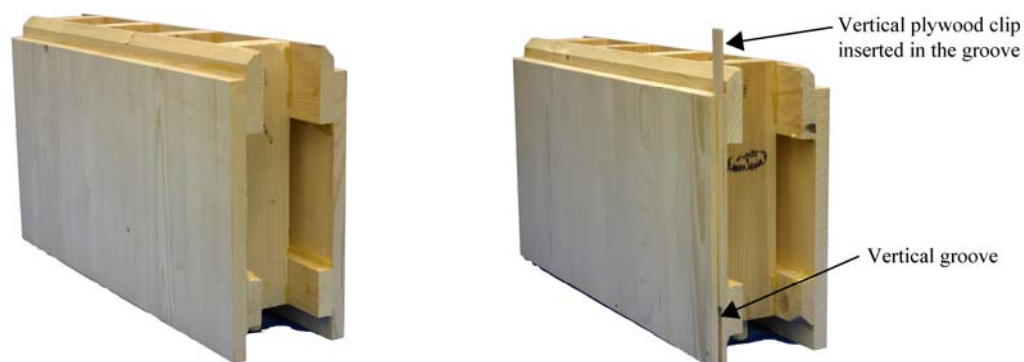
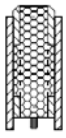
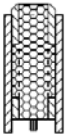
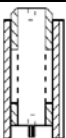
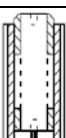
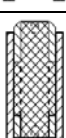
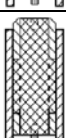


Fig. 3 – Timber block without vertical grooves (left) and with vertical groove and plywood clip inserted in the groove (right).

During the fire tests, the timber block wall was loaded with a constant static load $q = 30 \text{ kN/m}$ that simulated the typical load in residential buildings up to 3 storeys. For these

buildings the Swiss fire regulations usually require a fire resistance of 30 minutes. For residential timber buildings with 4 up to 6 storeys a fire resistance of 60 minutes is required. As the fire test performed with the timber block wall 2 filled with concrete aimed at a fire resistance of 60 minutes, wall 2 was loaded with a constant static load $q = 60 \text{ kN/m}$ that simulated the typical load in residential buildings up to 6 storeys.

Table 1 – Overview of the fire tests performed with the STEKO timber block wall.

	Wall	Description of the timber block wall	Load level
	1	STEKO blocks with vertical plywood clips Vertical studs 40/77 mm with spacing $e = 960 \text{ mm}$ Timber blocks filled with isofloc cellulose	30 kN/m
	3	STEKO blocks with vertical plywood clips Vertical studs 77/77 mm with spacing $e = 480 \text{ mm}$ and 320 mm , respectively Timber blocks filled with isofloc cellulose	30 kN/m
	4	STEKO blocks without vertical plywood clips Vertical studs not used; Timber blocks without filling Fire exposed wall side protected by 10 mm thick Fermacell gypsum fibreboards	30 kN/m
	6	STEKO blocks without vertical plywood clips Vertical studs not used; Timber blocks without filling Both wall sides protected by 10 mm Fermacell gypsum fibreboards	30 kN/m
	2	STEKO blocks without vertical plywood clips Vertical studs not used Timber blocks filled with concrete	60 kN/m
	5	STEKO blocks without vertical plywood clips Vertical studs not used Timber blocks filled with reinforced concrete	30 kN/m

3. TEST SPECIMENS

The six different timber block walls were manufactured by the Swiss firm STEKO Holz-Bausysteme AG, Kesswil and tested under the ISO-standard fire exposure. Figure 4 shows the cross-section of all timber block walls and figure 5 illustrates as example the geometry of the timber block wall 1. The specimens consisted of hollow timber blocks made from precisely machined off-cuts of common solid timber (spruce) grade C24 according to EN 338⁷. The density of the timber blocks was about 450 kg/m^3 and the moisture content about 10%. The timber base plate as well as the top plate consisted of glued laminated timber (spruce) grade GL24h according to EN 1194⁸.

For the timber block walls 1 and 3 vertical timber studs made of common solid timber (spruce) grade C24 according to EN 338 were inserted in the cavities. The timber studs were 2 mm smaller than the wall cavity, so that they were not subjected to vertical loading. Further the timber blocks were filled with isofloc cellulose type LM. Isofloc cellulose fibre insulation

is made of recycled newsprint and boric salt. The mean density of the isofloc cellulose fibre insulation used for the specimens 1 and 3 was 65 kg/m^3 and the moisture content about 10%.

The timber block walls 4 and 6 were protected by 10 mm thick Fermacell gypsum fibreboards which were attached to the timber block wall using common staples with a length of 19 mm, a diameter of 1.5 mm and a spacing of about 140 mm. The mean density of the gypsum fibreboards was 1150 kg/m^3 . The gypsum fibreboards were about 40 mm smaller than the wall height, so that they were not subjected to vertical loading.

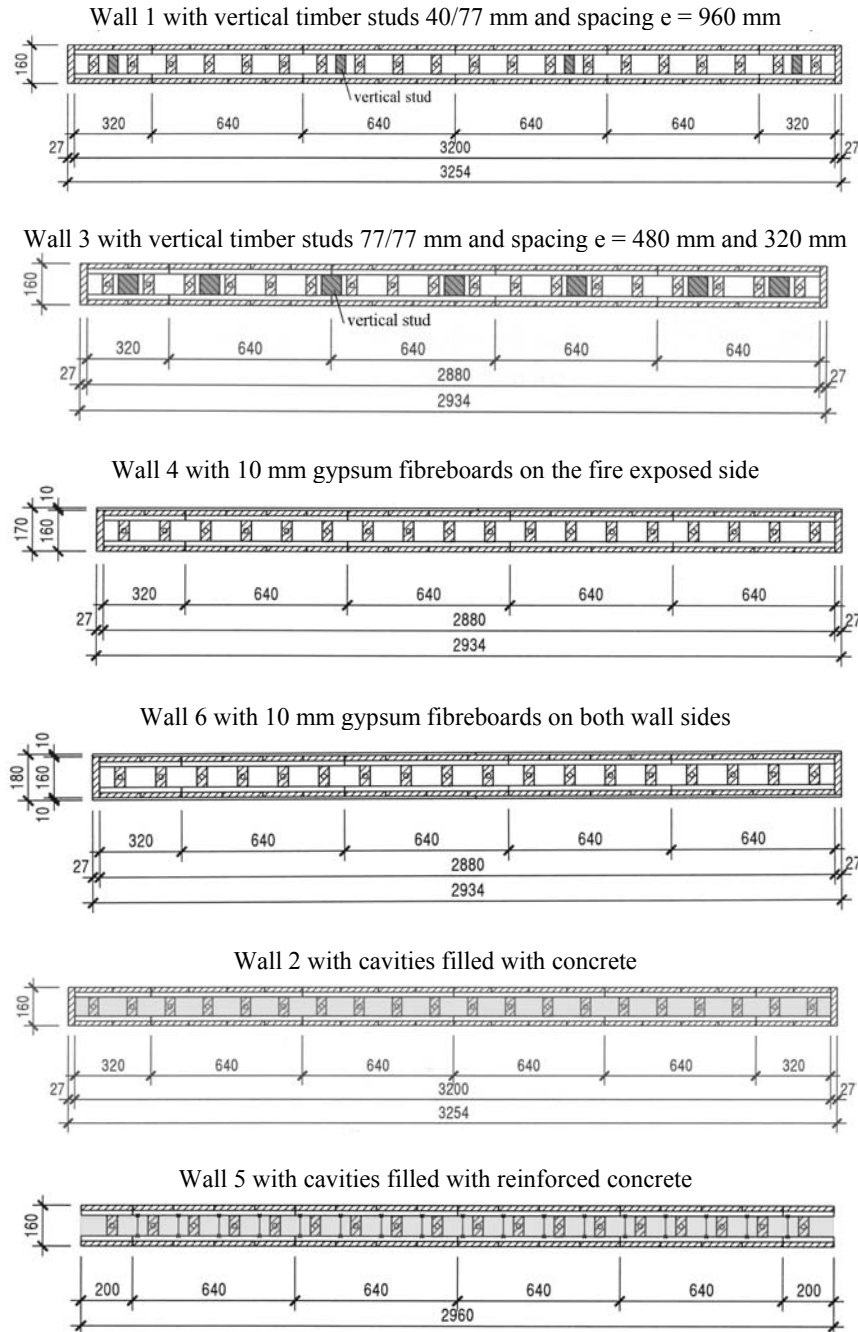


Fig. 4 – Cross-sections of the timber block walls tested under ISO-fire exposure.

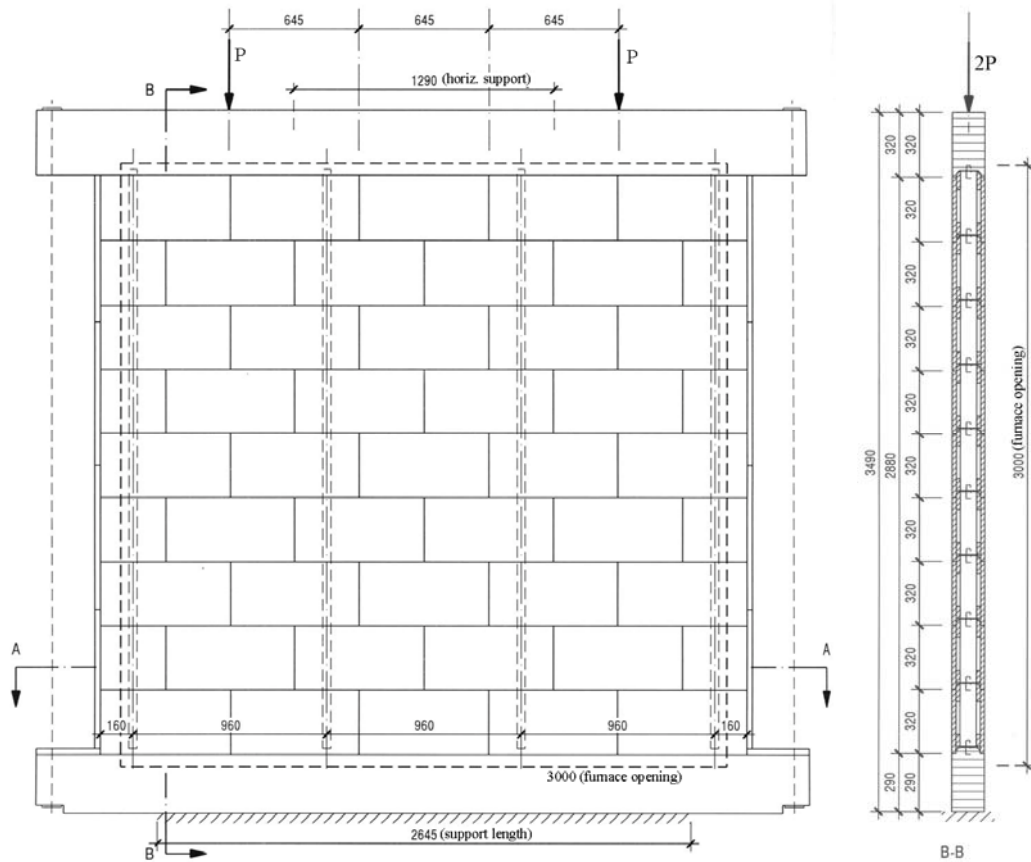


Fig. 5 – Geometry of the timber block wall 1.

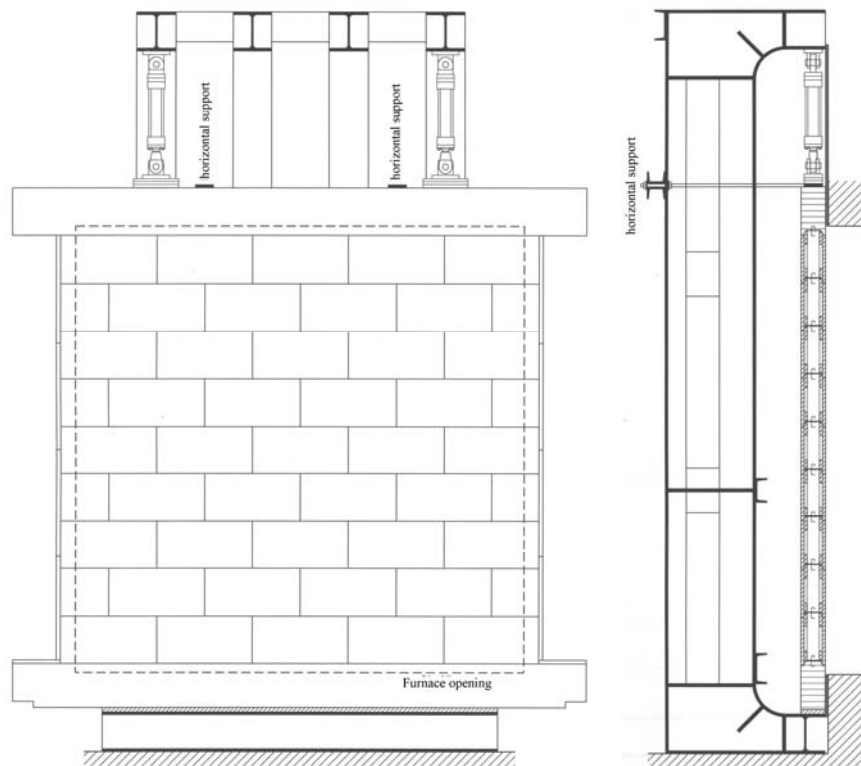


Fig. 6 – Test set-up for the fire tests with timber block walls.

The timber blocks of walls 2 and 5 were filled with concrete (self compacting concrete with a water-cement ratio of about 0.55 and a cement content of about 350 kg/m³). The measured mean concrete cube compressive strength was 33 N/mm² and the mean concrete density 2200 kg/m³. In addition the concrete of wall 5 was reinforced with a Murinox reinforcing mesh (2 vertical bars with $\varnothing \approx 10$ mm and spacing of 80 mm) made of stainless steel (DIN 1.4016, yield strength ≈ 520 N/mm²) which is often used for masonry.

4. TEST ARRANGEMENT

All fire tests were based on ISO-fire exposure and carried out on the 3x3 m vertical furnace at the Swiss Federal Laboratories for Materials Testing and Research in Dübendorf. During the fire tests, the timber block wall was loaded with a constant static load. The wall was already loaded about 20 minutes before the start of the fire test. Figure 6 shows the test set-up.

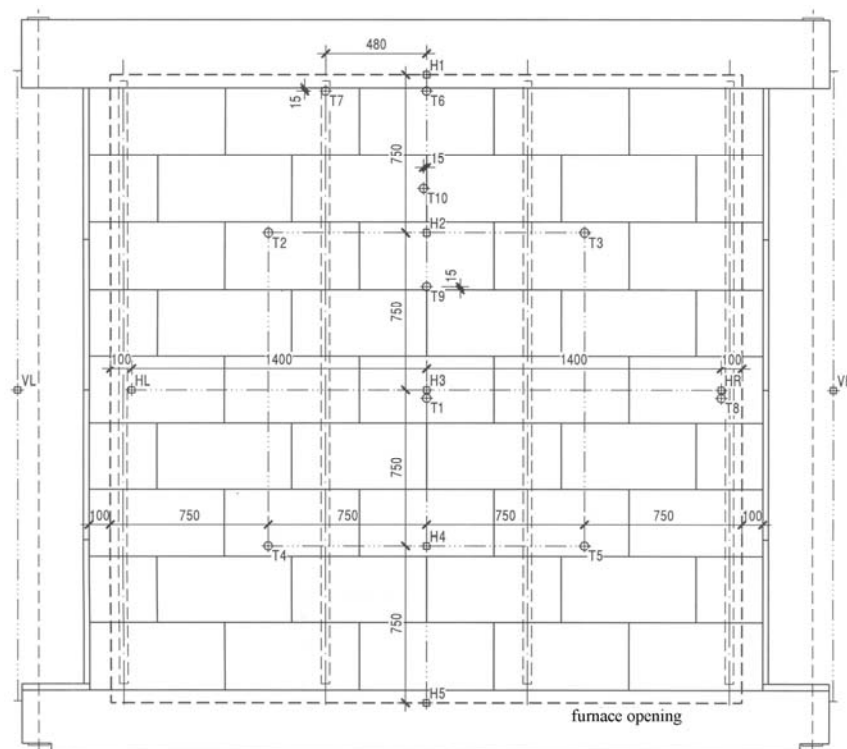


Fig. 7 – Position of the measurement equipment.

During the tests the horizontal deformation of the timber block wall was measured in 7 points (H1 to H5, HL and HR) using linear voltage displacement transducers (LVDTs). Five LVDTs (H1 to H5, see fig. 7) were attached in the middle of the wall and uniformly placed along the wall height. Further the vertical deformation of the timber block was measured in 2 points using LVDTs (VL and VR, see fig. 7). During the tests, the temperature was measured at selected locations on the fire unexposed side and recorded every minute with thermocouples of chromel-alumel, type K. At the end of the fire tests, the burners were immediately turned off, the wall was removed and the fire was extinguished with water. Figure 7 shows as typical example the position of the LVDTs as well as the thermocouples for the timber block wall 1.

5. TEST RESULTS

5.1 Walls 1 and 3

Walls 1 and 3 were filled with isofloc cellulose. Further vertical timber studs were inserted in the wall cavities. Figure 8 shows the measured horizontal deformation H3 (see fig. 7) and the vertical deformation V (as average between VR and VL) as a function of the time for both fire tests. The start of the fire test is indicated with time zero. A positive horizontal deformation indicates a deformation in the direction of the fire unexposed side of the timber block wall. A negative vertical deformation means a compression of the timber block wall.

Charring of the fire exposed outer layer of the timber walls began after about 3 min. In the case of the wall 1 a strong increase of the horizontal and vertical deformation was observed after about 20 minutes, when the fire exposed outer layer of the timber block wall was almost completely charred and started falling down into the furnace. Wall 1 finally failed after 26 minutes. After the fire test visual observations of the timber block wall confirmed that the fire exposed outer layer was completely charred. On the other hand the horizontal boards on the fire exposed wall side were only partially charred (the residual cross-section was about 10-15 mm) and the webs of the timber block wall as well as the studs inserted in the cavities were completely intact. Figure 9 left shows the timber block wall after the fire test. The fire test showed that number and dimensions of the vertical studs used in this test were not able to guarantee the stability of the wall and confirmed that the fire resistance of the timber block wall was reached as soon as the fire exposed outer layer was completely charred.

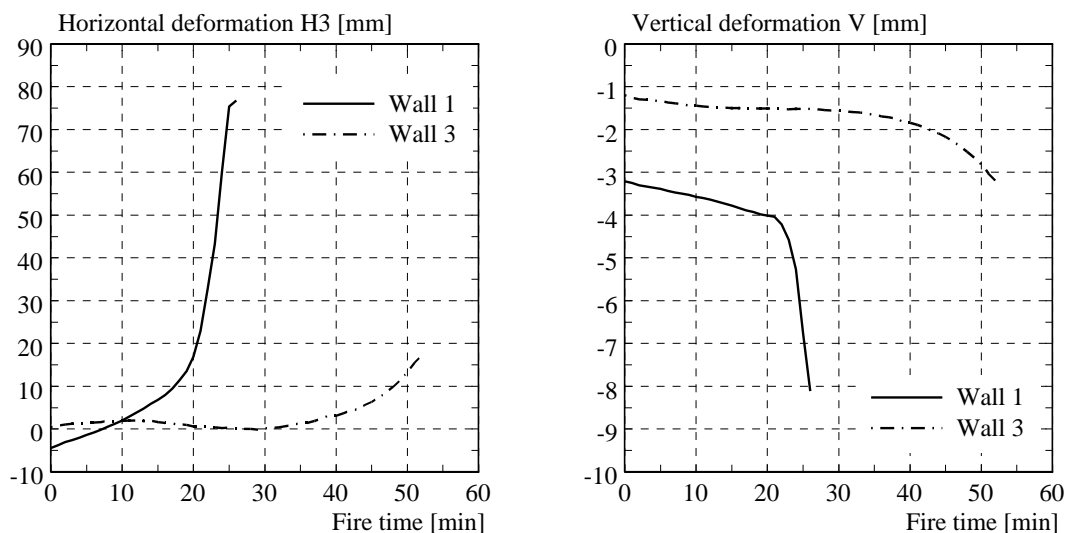


Fig. 8 – Horizontal deformation H3 and vertical deformation V as a function of the time for the fire tests with the walls 1 and 3 with timber studs inserted in the wall cavities.

After about 20 minutes the fire exposed outer layer of the timber block wall 3 was almost completely charred and started falling down into the furnace as already observed in the case of wall 1. Unlike wall 1 an increase of the horizontal and vertical deformation was first observed after about 40 minutes. After 43 minutes the horizontal boards were completely charred and started falling down into the furnace. The fire test was finally stopped after 51 minutes as the failure of the wall was expected due to the measured increase of the horizontal and vertical deformation. Visual observations of the timber block wall after the fire test confirmed that the fire exposed outer layer as well as the horizontal boards were completely

charred. The webs of the timber block wall as well as the studs inserted in the cavities were only partially charred (the residual cross-section was about 50-60 mm). Further it was observed that the isofloc cellulose insulation did not fall into the furnace, so that charring occurred mainly on the narrow side of the webs and studs, while the wide sides were more or less protected by the insulation (see figure 9 right). Thus one-dimensional charring can be assumed for the webs and studs. The fire test showed that number and dimensions of the vertical studs used in this test were able to guarantee the stability of the wall and permitted to improve significantly the fire resistance of the timber block wall in comparison to wall 1, which failed after 26 minutes as the fire exposed outer layer was completely charred.



Fig. 9 – Left: wall 1 after the fire test with the fire exposed outer layer completely charred. Right: Detail of wall 3 after the fire test showing a web and a stud partially charred. The isofloc cellulose insulation did not fall into the furnace and protected the wide sides of the webs and studs from charring.

5.2 Walls 4 and 6

Walls 4 and 6 were protected by 10 mm gypsum fibreboards. Figure 10 shows the measured horizontal deformation H3 (see fig. 7) and the vertical deformation V (as average between VR and VL) as function of the time. Like walls 1 and 3 the increase of the horizontal deformation occurred in the direction of the fire unexposed side of the timber block wall.

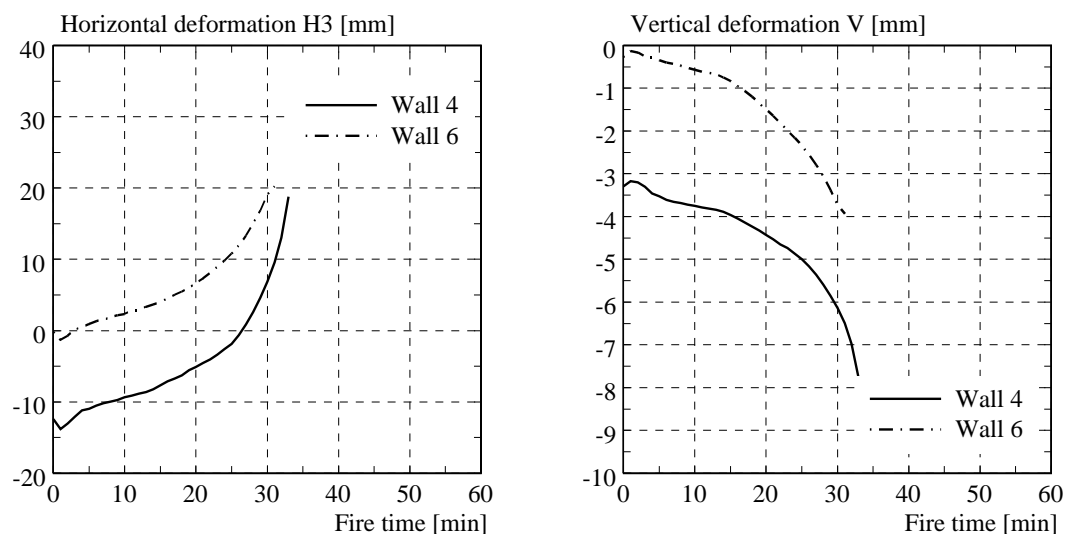


Fig. 10 – Horizontal deformation H3 and vertical deformation V as function of the fire time for the fire tests with the walls 4 and 6 protected by 10 mm gypsum fibreboards.

The first crack in the gypsum fibreboard was observed after 10 minutes in the case of wall 4 and after 13.5 minutes for wall 6. In the following more cracks were observed in the gypsum fibreboards during both tests. Large pieces of the gypsum fibreboards first started falling down after 18 minutes for wall 4 and 3 minutes later in the case of wall 6, so that after about 25 minutes most of the outer layer of the timber block walls was directly exposed to fire. At the same time a strong increase of the horizontal deformation was observed. The fire test on wall 6 was stopped after 30 minutes as the wall failure was expected due to the measured increase of the horizontal and vertical deformation. This assumption is confirmed by the fire test on wall 4 which failed after 33 minutes. After the fire test visual observations of the timber block walls showed that the fire exposed outer layer was completely charred. On the other hand the horizontal boards were only partially charred and the webs more or less completely intact. Figure 11 shows the timber block wall 4 during and after the fire test. The fire tests demonstrated that a fire resistance of 30 minutes can be achieved by protecting the timber block wall with 10 mm gypsum fibreboards. Further it was confirmed that the wall failure occurred as soon as the fire exposed outer layer was completely charred.

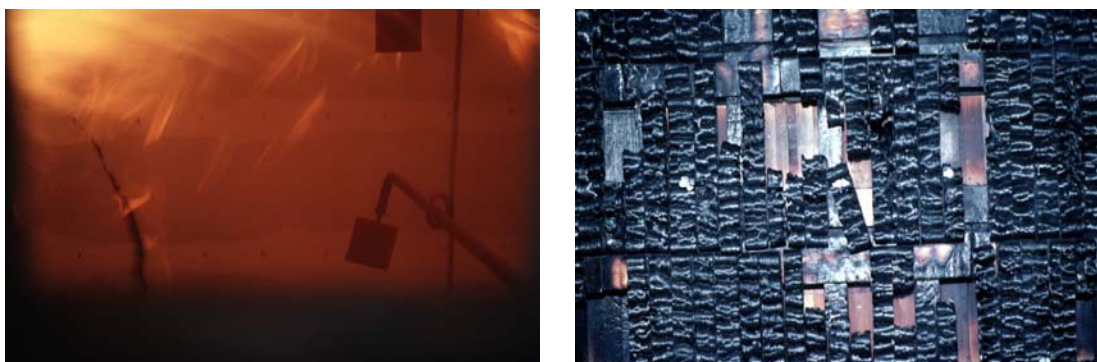


Fig. 11 – Cracking in the gypsum fibreboard of wall 4 (left) and fire exposed side of wall 4 after the fire test (right).

5.2 Walls 2 and 5

Walls 2 and 5 were filled with concrete. Figure 12 shows the measured horizontal deformation H_3 (see fig. 7) and the vertical deformation V as a function of the time for both fire tests. Unlike the other walls the increase of the horizontal deformation occurred in the direction of the fire exposed side of the timber block wall. Further it can be seen that the vertical deformation of the timber block wall measured at the beginning of the fire test was partially compensated by the thermal expansion of the concrete.

Charring of the fire exposed outer layer of the timber walls began after about 3 minutes. Unlike walls 1 and 3 the fire exposed outer layer of the timber block wall started falling down into the furnace after 26 minutes for wall 2 and 30 minutes for wall 5 (i.e. about 6-10 minutes later than in walls 1 and 3). Thus the concrete causes the fire exposed outer timber layer to heat more slowly, possibly partially reducing the charring rate of the timber. Spalling of concrete was first observed after 33-35 minutes. The webs of the timber block walls were directly exposed to fire after 46-47 minutes; the horizontal boards started falling down after 56-57 minutes. A significant increase of the horizontal deformation was observed after about 60 minutes. The fire test on wall 2 was finally stopped after 76 minutes, the fire test on wall 5 after 90 minutes. In both cases no wall failure was observed.

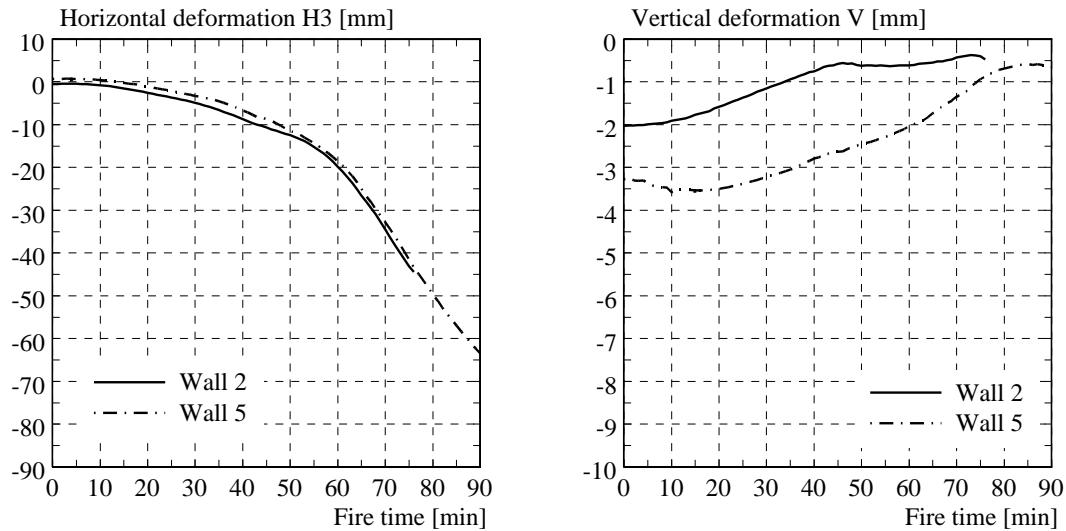


Fig. 12 – Horizontal deformation H3 and vertical deformation V as function of the fire time for the fire tests with the walls 2 and 5 filled with concrete.

Visual observations of the timber block wall after the fire test confirmed that the fire exposed outer layer as well as the horizontal boards were completely charred. Due to the protection by the concrete charring of the webs of the timber block walls occurred only on the edge in contact with the fire exposed wall side (see fig. 13 right). The residual cross-section of the webs was about 40-50 mm; in some locations it was about 30 mm due to large and deep spalling of concrete. Figure 13 shows the timber block wall 5 after the fire test. It can be seen that the horizontal concrete layers located between the horizontal timber boards and formed by casting the concrete in the cavities were partially intact after the fire test, protecting the timber webs from fire. The fire tests demonstrated that timber block walls with cavities filled with concrete show excellent fire behaviour and a fire resistance of 90 minutes can be achieved.



Fig. 13 – Fire exposed side of wall 5 after the fire test (left) and detail of one-dimensional charring of the timber webs between the concrete (right).

6. SUMMARY AND CONCLUSIONS

A comprehensive research project on the structural behaviour of the timber block wall system STEKO has been recently completed at the ETH Zurich. STEKO is a rapid construction system that uses large hollow timber blocks that simply slot together. In addition to a large number of investigations at normal temperature under static and dynamic loading, the fire behaviour of the timber block wall system was experimental analysed with 6 large-scale fire tests. All fire tests were based on ISO-fire exposure and performed on the 3x3 m vertical furnace at the Swiss Federal Laboratories for Materials Testing and Research in Dübendorf. During the fire tests, the timber block wall was loaded with a constant static load that simulated the typical load in a residential building. The fire tests enlarge the experimental background of timber block walls in fire and permit to establish design models for the fire resistance of the timber block wall system.

The fire tests showed that after the fire exposed outer layer is completely charred, the residual cross-section of the timber block wall is eccentrically loaded leading to large horizontal deformations and global buckling of the wall system. Typical timber block walls without structural wall modifications have fire resistance less than 30 minutes. An efficient modification in order to improve the buckling behaviour of the block wall in fire is the use of vertical timber studs inserted in the vertical voids. This modification permitted to increase significantly the fire resistance of the wall system. Another possibility is to fill the timber blocks with concrete. Timber block walls with cavities filled with concrete showed excellent fire behaviour and a fire resistance of 90 minutes was achieved. Finally the timber block wall can be protected by additional boards. By protecting the wall system with 10 mm gypsum fibreboards a fire resistance of more than 30 minutes was achieved.

7. REFERENCES

- [1] Frangi, A and Fontana, M., “Charring rates and temperature profiles of wood sections”, Fire and Materials, Volume 27, Issue 2, March/April 2003.
- [2] König, J., “Structural fire design according to Eurocode 5 - Design rules and their background”, Fire and Materials, Volume 29, Issue 3, May/June 2005.
- [3] EN 1995-1-2 (Eurocode 5), “Design of timber structures, Part 1-2 General rules-Structural fire design”, Final Draft, CEN, Brussel, December 2003.
- [4] Buchanan, H., “Fire performance of timber construction”, Progress in Structural Engineering and Materials, Volume 2, Issue 3, 2000.
- [5] Steurer, A and Fuhrmann, C., „Grundlagen der Berechnung und Bemessung zur STEKO-Bauweise“, Institute of Structural Engineering IBK, ETH, Zurich, 2001.
- [6] ISO 834-1, “Fire-Resistance Tests-Elements of Building Construction-Part 1: General Requirements”, International Organization for Standardization, 1999.
- [7] EN 338, “Structural timber – Strength classes”, CEN, Brussel, April 2003.
- [8] EN 1194, “Timber structures – Glued laminated timber – Strength classes and determination of characteristic values”, CEN, Brussel, April 1999.



EFFECT ON THE CHARRING RATE OF WOOD IN FIRE DUE TO OXYGEN CONTENT, MOISTURE CONTENT AND WOOD DENSITY

Magdalena CEDERING¹

ABSTRACT

An experimental study on the charring rate of wood exposed to fire, has been carried out. Within the study 287 timber studs have been exposed to fire in a test furnace. The objectives of the study were to examine how the charring rate is affected by the oxygen content in the furnace, the moisture content in the wood and the wood density. The experimental results indicate that the oxygen content has an effect on the charring rate. Increased oxygen content increases the charring rate. Further, the moisture content in the wood has an effect on the charring rate, a higher moisture content results in a lower charring rate. Both these effects are, however, very small. From the result of the study, it is not possible to say whether or not the wood densities tested have an influence on the charring rate.

1. INTRODUCTION

The charring rate of wood is an important factor in many different applications. The charring rate is crucial when fire testing different structures such as wooden fire doors or windows. Furthermore the fire design of wooden structures is generally based on the charring rate. When the charring rate is known, the amount of unaffected wood in the structure can be calculated. A compilation of charring rates from previous studies has been done by Babrauskas [1] and is between 0,5 and 0,8 mm/min for massive wood with a density between 400 and 550 kg/m³.

In design codes the charring rate is assumed to be constant and thus not affected by the oxygen content, moisture content or the density. Although, studies made on small samples have shown significant effects on the weight loss due to these factors. A study made by Ohlemiller et al. [2] showed that an environment with higher oxygen content gives rise to a higher charring rate on small wood samples. Mikkola [3] has derived from previous studies that the charring rate is inversely proportional to the density.

¹ Research Assistant, SP Swedish National and Research Institute, Fire Technology, Sweden, email: magdalena.cedering@sp.se.

In some tests made by a manufacturer of wooden doors a significant difference was obtained when comparing the test results from different laboratories. The only known difference between the laboratories was the oxygen content in the furnaces. Today the European standard EN 1363-1 on fire resistance testing of building products requires a minimum oxygen content of 4 % in the furnaces but there is no upper limit. Therefore an experimental test series was carried out in order to determine the effect of oxygen content, moisture content and wood density on the charring rate.

2. TEST SPECIMENS AND MATERIALS

For each experiment a wall was made of timber studs. The timber was Norwegian spruce (*Picea abies*) with dimensions (width x depth x height) 40 x 140 x 1000 mm. Each wall was built up of between 55-60 studs with varying density and moisture content. The studs were joined with four nails each and were pressed together in a supporting wall. Wider joints between the studs due to irregularities in the studs were sealed with stone wool insulation, to prevent fire exposure from more than one side. In total three timber walls were prepared. Figure 1 shows a wall ready for testing.

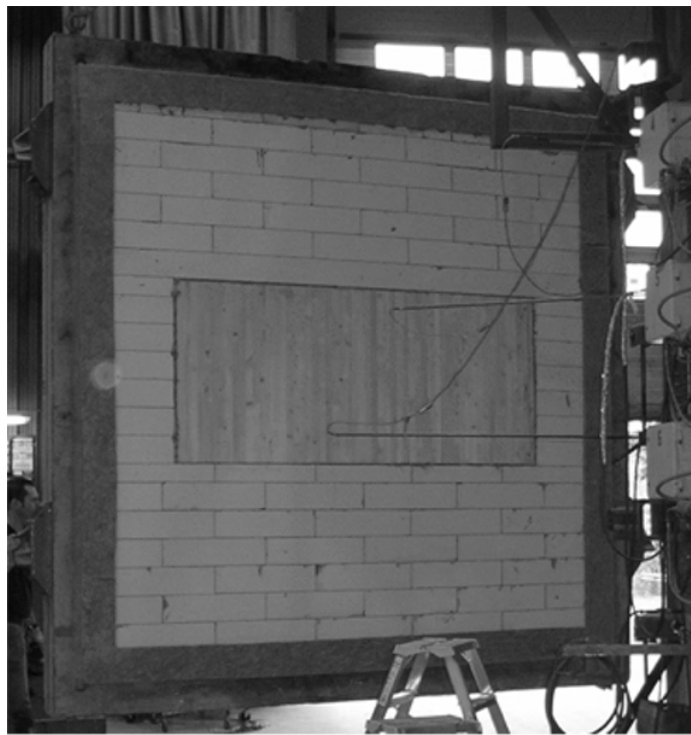


Fig. 1 - Test wall in the supporting wall.

Three solid timber walls were tested in different oxygen content: 4 %, 7 % and 10 %, respectively. The studs in each wall were divided into three parts and each part had its own moisture content: 6 %, 12 % and 18 %, respectively. To attain the moisture contents of 6 % and 12 % the studs were dried and placed in a climate chamber. The studs with 18 % moisture content were placed directly in a climate chamber. The mean moisture contents in

each part of the walls are shown in table 1. A schematic drawing of the timber walls is shown in figure 2.

Table 1 - Moisture content of the walls

Oxygen content in which the wall was tested in	Mean value of the moisture content in the studs (%)		
4 %	6,3	11,7	20,3
7 %	6,2	11,8	19,1
10 %	6,4	11,3	17,9

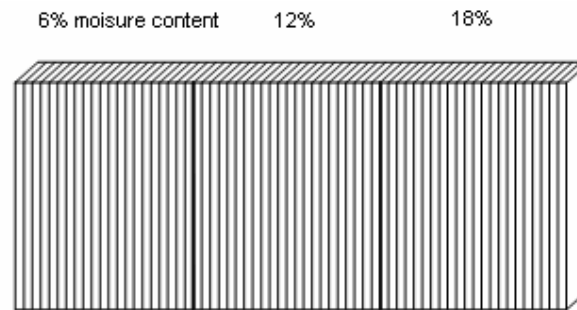


Fig. 2- Timber wall (2,6 m x 1 m) containing standing cross bars of dimension (140 mm x 40 mm)

The dry density of the timber studs varied between 321 kg/m^3 and 454 kg/m^3 . The studs were selected so that the three parts in each wall had almost the same density variation. In each part the studs with the lowest density were placed in one end, the second lowest next to it i.e. the density rising towards the other side.

3. TEST METHODS

The walls were tested in accordance with EN 1363-1, i.e. the temperature curve was in accordance with ISO 834. The fire exposure was obtained for 60 minutes and thereafter the wall was removed from the furnace and quickly cooled down.

Two samples, each of 100 mm length, were sawn from each timber stud. The position on the studs where the pieces were taken varied depending on knots and other irregularities. Also the areas nearest the ends were avoided. The remaining cross sectional area after the char layer had been removed, figure 3, was analyzed and the mean charring rate was calculated.

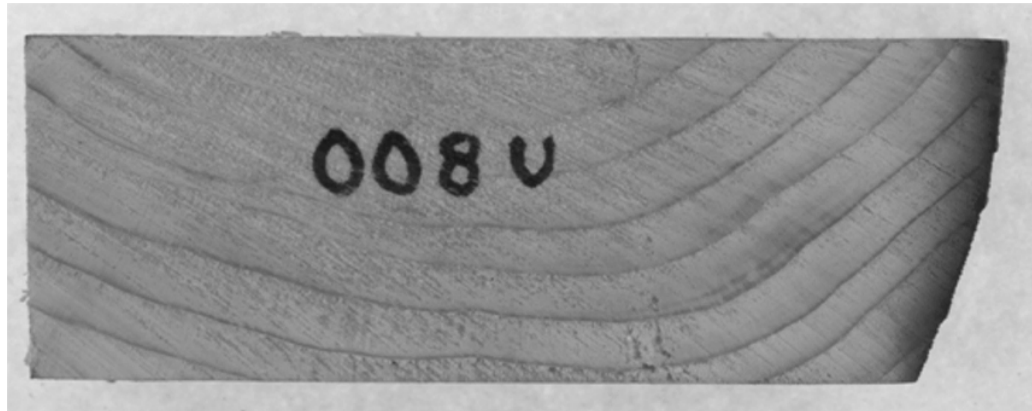


Fig. 3- A cross section after the fire test.

4. RESULTS

4.1 Effect of oxygen content on the charring rate

The results of the present study show a charring rate between 0,53 and 0,87 mm/min. Both the mean and the median value were 0,67 mm/min. This coincides well with the interval from Babrauskas[1]. The measured charring rates are plotted in a histogram, see figure 4, and the result is close to a normal distribution.

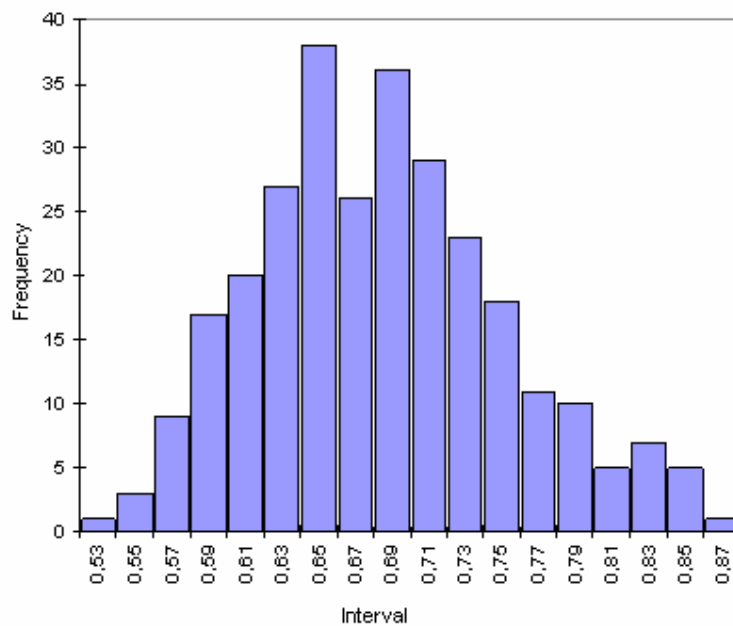


Fig. 4- Histogram on the charring rate fore all test specimens.

The charring rate from the fire testes with different oxygen content were compared by t-tests. In this t-test all specimens were included, i.e. no differentiation was made between

different moisture content and density. Table 2 illustrates the result and shows that there is only a very small effect of the oxygen content on the charring rate, although a significant difference (the p-value < 0,05). The largest difference is 0,05 mm/min which corresponds to an increased charring of 3 mm after 60 minutes.

Table 2- Comparison of mean values for different groups.

Compared oxygen content	Mean value 1	Mean value 2	p-value	Difference, mean value
4 % and 7 %	0,65	0,68	0,00	0,03
4 % and 10 %	0,65	0,70	0,00	0,05
7 % and 10 %	0,68	0,70	0,01	0,02

4.2 Effect of moisture content on the charring rate

The effect of the moisture content was also compared using a t-test and the results are shown in table 3. An increased moisture content results in a decreased charring rate. The difference is statistically significant between the groups and the effect of the moisture content is also very small.

Table 3– Comparison of mean values for different groups.

Compared moisture content	Mean value 1	Mean value 2	p-value
6 % and 12 %	0,70	0,68	0,01
6 % and 18 %	0,70	0,64	0,00
12 % and 18 %	0,68	0,64	0,00

4.3 Effect of moisture content and oxygen content on the charring rate

In table 4, the mean values are shown as a function of both oxygen content and moisture content and the different oxygen contents are compared. At lower moisture contents the p-value indicates that there is a statistically significant difference between the groups. The largest difference is 0,09 mm/min, which gives a charring rate of 5,4 mm after an hour. The table also shows that at a higher moisture content there is no significant difference between the groups.

Table 4– Comparison of mean values for different groups.

Moisture content	Compared oxygen content	Mean value 1	Mean value 2	p-value
6 %	4 % and 7 %	0,67	0,69	0,06
	4 % and 10 %	0,67	0,76	0,00
	7 % and 10 %	0,69	0,76	0,00
12 %	4 % and 7 %	0,63	0,69	0,00
	4 % and 10 %	0,63	0,71	0,00
	7 % and 10 %	0,69	0,71	0,15
18 %	4 % and 7 %	0,64	0,65	0,51
	4 % and 10 %	0,64	0,64	0,78
	7 % and 10 %	0,65	0,64	0,69

In table 5 the mean values are also shown as a function of both oxygen content and moisture content; but here the different moisture contents are compared. Here one can see that there is a statistical significant difference between all groups, apart from those between 12 % and 18 % tested in 4 % oxygen content and between 6 % and 12 % in 7 % oxygen content.

Table 5– Comparison of mean values for different groups.

Oxygen content	Compared moisture content	Mean value 1	Mean value 2	p-value
4 %	6 % and 12 %	0,67	0,63	0,01
	6 % and 18 %	0,67	0,64	0,02
	12 % and 18 %	0,63	0,64	0,57
7 %	6 % and 12 %	0,69	0,69	1,00
	6 % and 18 %	0,69	0,65	0,01
	12 % and 18 %	0,69	0,65	0,02
10 %	6 % and 12 %	0,76	0,71	0,01
	6 % and 18 %	0,76	0,64	0,00
	12 % and 18 %	0,71	0,64	0,00

A mean value graph of the charring rates for the groups with different moisture and oxygen content is shown in figure 5. The small figure illustrates the mean value of the group and the line illustrates the 95 % distribution of the charring rate. The graph shows that the effect of moisture content of the charring rate is more pronounced at higher oxygen contents. At 4 % oxygen content there is almost no difference between charring rates due to different moisture contents and at 10 % oxygen content the difference is significant. The graph also shows that the effect of the oxygen content is negligible at higher moisture content and significant at lower moisture content.

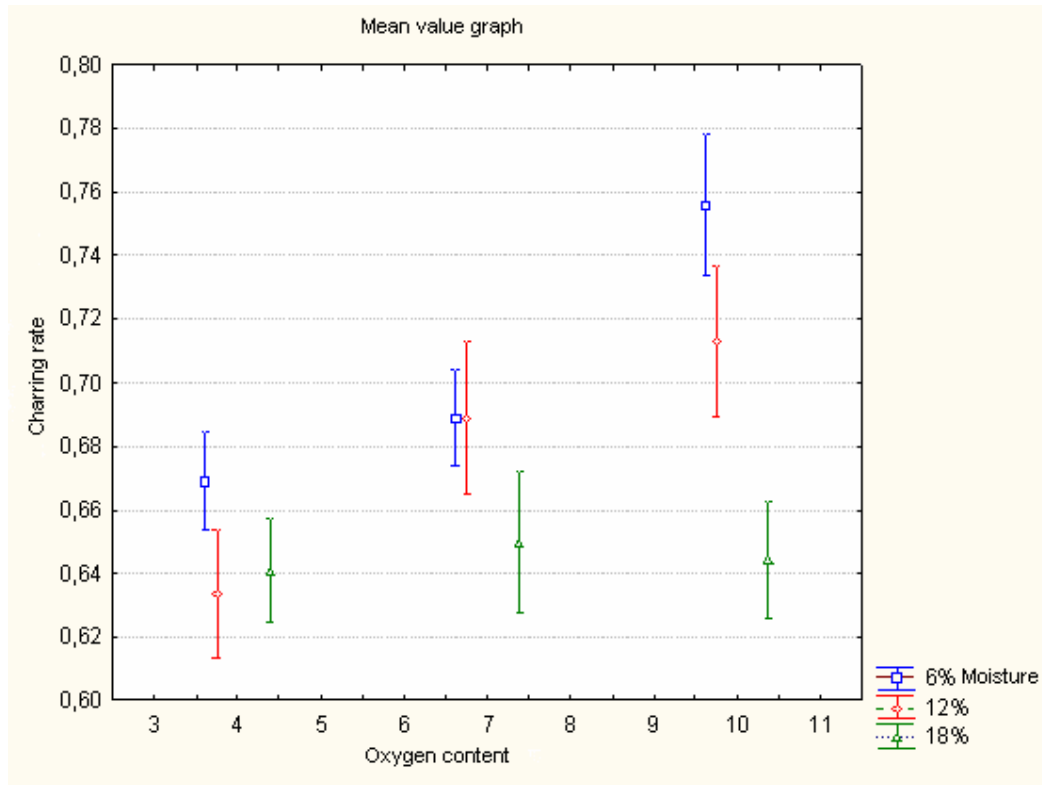


Fig. 5- Charring rate (mm/min) for different oxygen content

4.4 Effect of wood density on the charring rate

The charring rate for different wood density is shown in figure 6. The values in the graph are spread and there is no significant variation on the charring rate for different wood density.

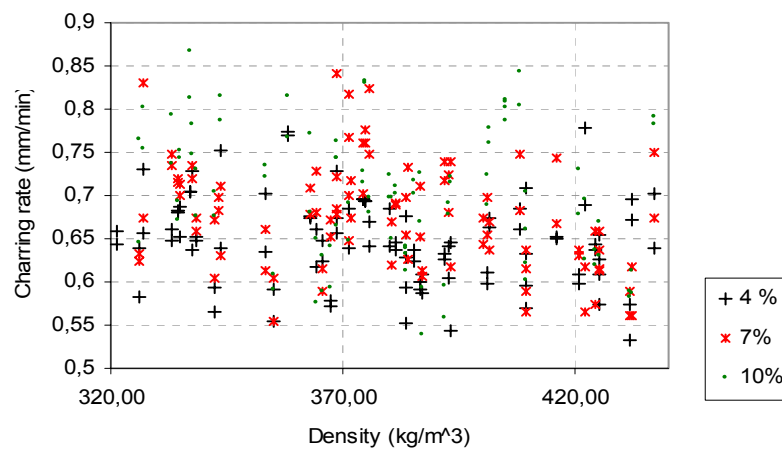


Fig. 6 – Charring rate at different density.

5. DISCUSSION AND CONCLUSIONS

The results from this study demonstrate that there is an effect, although a very small effect, on the charring rate of the oxygen content in the furnace and that the effect is statistically significant. This difference is very small, giving an increase of the charring rate of 0,05 mm/min when the oxygen content increases from 4 % to 10 % and the wood is exposed to the standard time-temperature curve (ISO 834) during 60 minutes.

The results also show that the effect of the oxygen content on the charring rate is dependent on the moisture content in the timber. At low moisture content in the timber the charring rate increases when the oxygen content increases. Although, at low moisture content there is no effect on the charring rate due to the oxygen content.

Further, the moisture content has an effect on the charring rate. But this effect is also very small, around 0,06 mm/min. One question is whether this effect is lower in this study because timber with different moisture content was tested at the same time. During the test the moisture vaporizes and mixes in the furnace and the surface of all studs are exposed to gas with the same humidity.

In this study no effect could be observed of the density on the charring rate. The values exhibited significant spread and it was not possible to say whether the density had any influence on the charring rate. One reason could be that the density in a stud varies very much for different parts. The calculated density used in this study is a mean value for the whole stud and not the actual density for the analyzed parts.

6. REFERENCES

- [1] Babrauskas V. Charring rate of wood as a tool for fire investigations. *Interflam 2004*, Vol 2, pp 1155-1170.
- [2] Mikkola, E Charring of wood, Research Report. Technical research centre of Finland, Nr. 689, Espoo, Finland, 35pp., 1990
- [3] Ohlemiller, T.J, Kashiwagi, T., Werner, K.: Wood gasification at fire level heat fluxes. *Combustion and flame* 69, pp 155-170., 1987



SIMULATION OF CROSS LAMINATED TIMBER BOARDS UNDER FIRE EXPOSURE

J. SCHMID¹, J. KÖNIG², J. FORNATHER³ and K. BERGMEISTER⁴

ABSTRACT

The aim of this study [1] was to verify rules given in EN 1995-1-2 [2] for structural fire design for solid timber panels by applying the reduced cross section method (RCSM). The RCSM introduces a zero strength layer of 7 mm to compensate material reduction due to temperature load. Software written by Trätekt based on fundamental mechanical relationships was upgraded and used to run studies with solid timber panels. Studies covered fire exposure to the tension as well as the compression side of samples in bending, different material characteristics and different cross sections. Furthermore, two different material reduction functions were compared. They were derived in previous studies of Trätekt (Stockholm) and BOKU (University of Natural Resources and Applied Life Sciences, Vienna).

For comparison purposes, simulations with solid cross sections without cross layers but with infinite dimensions in width (solid timber) were performed. The results of this study, which consider the standard fire load according to ISO 834 [3] show that the zero strength layer is first and foremost very sensitive to the location of fire exposure. Furthermore, dependence on the material reduction function as well as on the material characteristics can be observed. Fire exposure on the compression side leads to comparatively high values of the zero-strength layer (non-conservative results), while results of exposure on the tension side show a better concurrence with existing rules. The constant depth of a zero-strength zone of 7 mm given in EN 1995-1-2 [2] is exceeded in almost all cases depending on the time of fire exposure and tested build-up.

¹ MSc, Student – University of Technology, Vienna, Austria
email: joachim.schmid@gmx.at.

² PhD, Swedish National Testing and Research Institute-SP Trätekt/Wood Technology, Stockholm, Sweden
email: juergen.koenig@sp.se.

³ PhD, Austrian Standards Institute, Vienna, Austria
email: jochen.fornather@on-norm.at.

⁴ Professor, University of Natural Resources and Applied Life Sciences, Department of Civil Engineering and Natural Hazards, Vienna, Austria
email: konrad.bergmeister@boku.at.

1. INTRODUCTION

For the design of solid timber panels at ambient conditions different methods are available: the composite theory, the theory of elastic combined structures and the method of shear analogy [4, 5]. Rules for design at elevated conditions are very rare. While the RPM (Reduced property method) of the Eurocode can not be used for panels, it is obvious to use the RSCM [6]. In practice engineers consider the residual cross section until the char layer reaches a cross layer. Then the remaining cross section is reduced to a panel of odd layers again, the cross layer is neglected, compare black line and black arrows in Fig. 1 of a five-layer solid timber panel with a total thickness $h = 85$ mm. By means of the simulated bearing capacity (chain dotted line) a corresponding cross section can be derived (dotted line) which lead to a different design. Grey marked areas show zones where design according to the reduced cross section (black line) would lead to a too optimistic design. Appearing maxima of these zones are donated with Δ_i .

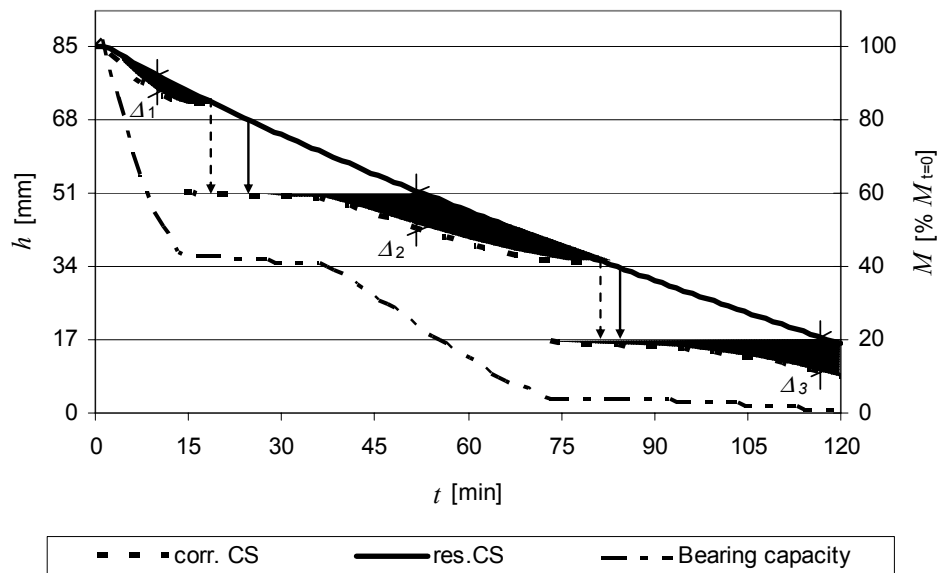


Fig. 1 – Procedure to apply the RSCM on a five-layer solid timber panels.

2 SIMULATIONS

Simulations base on the theory of combined structures and were run according to derived one-dimensional temperature distributions according to standard fire exposure of ISO 834 [3]. Solid timber and solid timber panels were simulated as single span girder since joints between single panels may not be considered under fire exposure. Hence, the fire exposure is situated on one side of the panel with infinite dimension in width.

2.1 Software

Simulations were run with software developed by Trätek [7] which was upgraded as well as applied to solid timber panels for this study. Temperature distributions used by the software are derived by TCD 5.0 [8] according to ISO-standard fire exposure.

The calculation model of the software is based on general rules of solid mechanics with combined structures and uses the Euler hypotheses of plane cross sections. As its first step the material properties are established: For each single simulation step the defined geometry matrix is divided in areas of 0,5 x 0,5 mm dimension which are associated with a defined material (E, f_t, f_c). Depending on the allocated temperature and the chosen type of temperature characteristics of the material the defined input values are determined for every area of the cross section. According to the material behaviour of wood a two-linear stress-strain relationship with a constant plateau in compression is used. Hence, in a second step with the maximum strain of a fibre at an edge an appropriate strain distribution for the cross section is derived. With Hooke's law the according tensions and hence the bearing capacity are calculated for any fire exposed cross section at any time between $t = 0$ and 120 minutes. A proving loop exists to ensure that weakened areas on the side of fire exposure don't limit the bearing capacity.

This procedure leads to a bearing capacity at specific points in time, $M(t)$. Results were used to derive a corresponding cross section at ambient conditions using the bending strength f_b and a linear stress-strain distribution. The result is a corresponding high $h_{corr}(t)$ of a cross section with an equal bearing capacity. By means of the 300°C-line, which limits the residual cross section at elevated conditions is described by $h_{res}(t)$. Using $h_{corr}(t)$ and $h_{res}(t)$ the value of the zero-strength layer (t) can be derived.

2.2 Simulated Serials

For simulations different cross sections with different symmetrical build-ups with three to nine layers ($d = 17, 20$ and 32 mm), different material qualities and two different material reductions under temperature load were used. The simulated cross sections are typical build-ups available from some producers and are exposed on the side in tension (zzw) and compression (dzw).

The sensitivity study on material properties cover variation of tensile strength f_t , variation of compression strength f_c as well as variation ENb, compare Table 1. The latter includes classes C14 to C50 according to EN 338 [9]. While EN 1995-1-2 [2] oblige the use of 20% fractile values 5% fractile values were used, hence evaluated differences in results for the derived zero-strength layer are under 1,0 mm. For ENb studies the compression strength f_c was derived by means of Thunell's formula [10] which expresses the relation of density and compression strength.

Table 1 – Material properties for sensitivity studies.

Material Number i		1	2	3	4	5	6	7	8	9	10	11	12
Sensitivity Study	Property [N/mm ²]												
Variation f_t	f_t	25	30	35	40	45	50	55	60	-	-	-	-
	f_c	44	44	44	44	44	44	44	44	-	-	-	-
Variation f_c	f_t	37,5	37,5	37,5	37,5	37,5	37,5	37,5	37,5	-	-	-	-
	f_c	30	35	40	45	50	55	60	-	-	-	-	-
Variation ENb	f_b	14	16	18	20	22	24	27	30	35	40	45	50
	f_c	32	34,3	35,5	36,6	37,7	38,9	41,2	42,3	44,6	46,9	49,1	51,4

While variation f_t and variation f_c uses f_t and f_c as input for the simulations, simulating variation ENb need a previous step to define an appropriate value for f_t . The sensitivity study on type of material reduction covers functions which were derived in previous studies of Trätek [7] and BOKU [11]. These functions, shown in Fig. 2, define the reduction of tensile strength (k_{ft}), of compression strength (k_{fc}) and of modulus of elasticity in tension (k_{Et}) as well as compression (k_{Ec}).

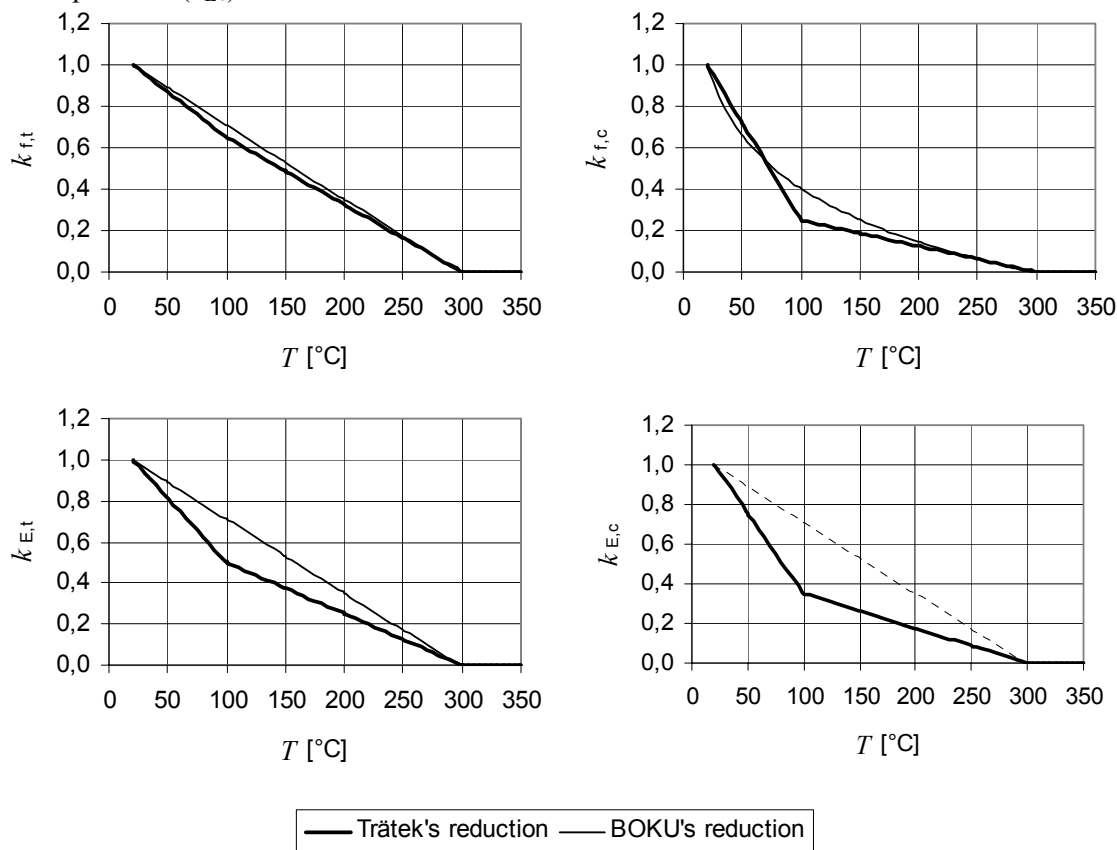


Fig. 2 – Material reduction functions due to temperature load.

The used software does not consider the mass flow due to vapour inside the cross section or phenomena such as creep, discussed by [12]. These Phenomena can be considered by manipulating the thermal conductivity, density as well as the heat capacity [13]. Material reduction functions of Trätek are calibrated to fire experiments to cover appearing

phenomena. Functions according to studies of BOKU do not include these effects; they were derived in tension and compression test of samples which were heated by heating plates. Different heating methods (fire exposure and oven tests) lead to significant differences of the moisture and temperature distributions. Experiments with fire exposure can be compared with oven heated experiments only in a limited way; it can be assumed, that differences in test results for eg. shear strength may result from the moisture concentration gradient, the temperature gradient and a total pressure gradient [14].

3 RESULTS

Simulation results show that solid timber panels as well as solid timber are first and foremost very sensitive to the location of fire exposure. Results for the zero-strength layer δ_i as well as $t_{=120}$ were evaluated to derive characteristic values for every build-up of solid timber boards. Fig. 3 shows curves for the characteristic values of δ_i (5% fractile values) for simulated solid timber panels. While the 7 mm-limit of fire exposure on the side in tension is exceeded moderately, almost no result for exposed side in compression is situated beneath the limit of EN 1995-1-2 [2], see Fig. 3. Appropriate envelope curves are indicated as dotted line.

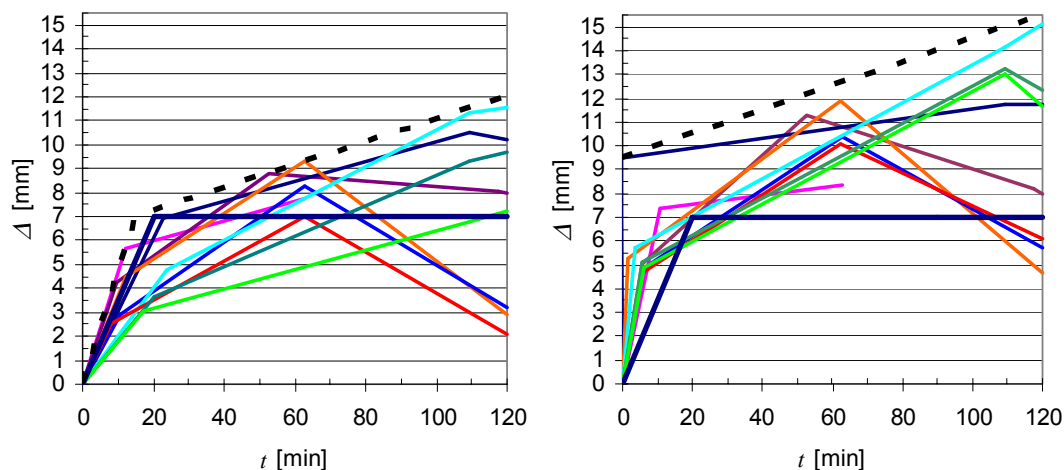


Fig. 3 – Characteristic results for solid timber panels 3 to 9 layers (ENb-study). Exposed side in tension (left) and compression (right).

While BOKU reduction functions for tensile strength and modulus of elasticity are equal, Trätekt reduction allow comparatively high strain on the side of tension. Thus, fire exposure on side of tension allows a clear redistribution of load to the side of compression. While samples according to Trätekt reduction functions show a significant initial peak of bearing capacity at the beginning of fire exposure, see Fig. 1, this can not be observed for BOKU reduction functions. This phenomenon leads to a certain positive displacement of the bearing capacity. While the BOKU envelop curve for exposed side in tension is situated above Trätekt curve, for exposed side in compression a reversal can be observed due to more optimistic material reductions according to BOKU, see Fig. 4.

The value of δ_1 is variable in time as well as in depth of the zero-strength zone; the evaluated samples show the following tendency: the more layers a solid timber panel with constant total thickness h consists of, the earlier and the lower is the value for δ_1 . This can be observed also for solid timber panels with constant layer thickness d and increasing number

of layers n for exposed side in tension. The appearance of Δ_2 is clearly related to the single layer thickness d , it is observed when the char reaches a load bearing layer, when char reaches a depth of $2d$. Values for Δ_i do not follow a general tendency for both, exposed side in tension and compression respectively; it is not possible to give general statements of any order of solid timber panels in view of the depth of the zero-strength layer.

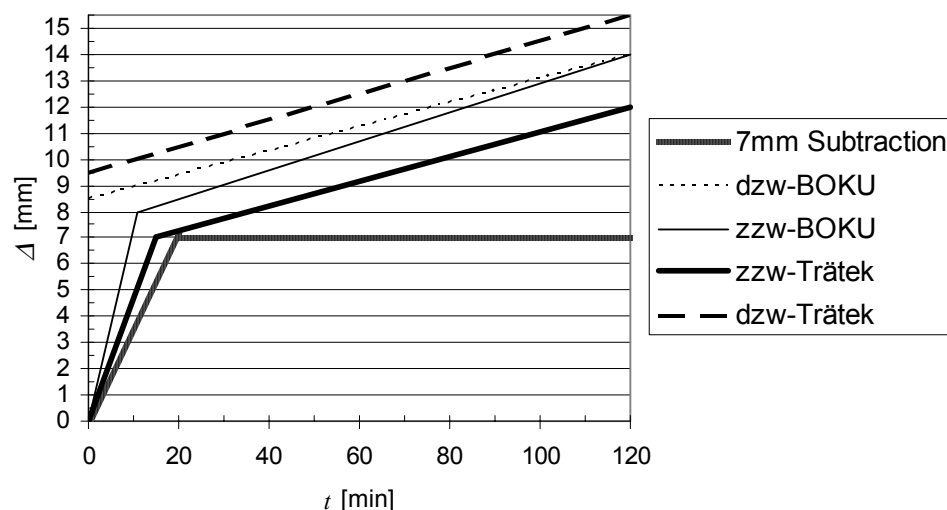


Fig. 4 – Characteristic envelope curves for zero-strength values for solid timber panels.

Characteristic results for solid timber with $h = 45, 95, 140$ and 200 mm (solid timber panels without cross layers) show different results. Deviating from EN 1995-1-2 [2] regulations a one-dimensional charring was simulated.

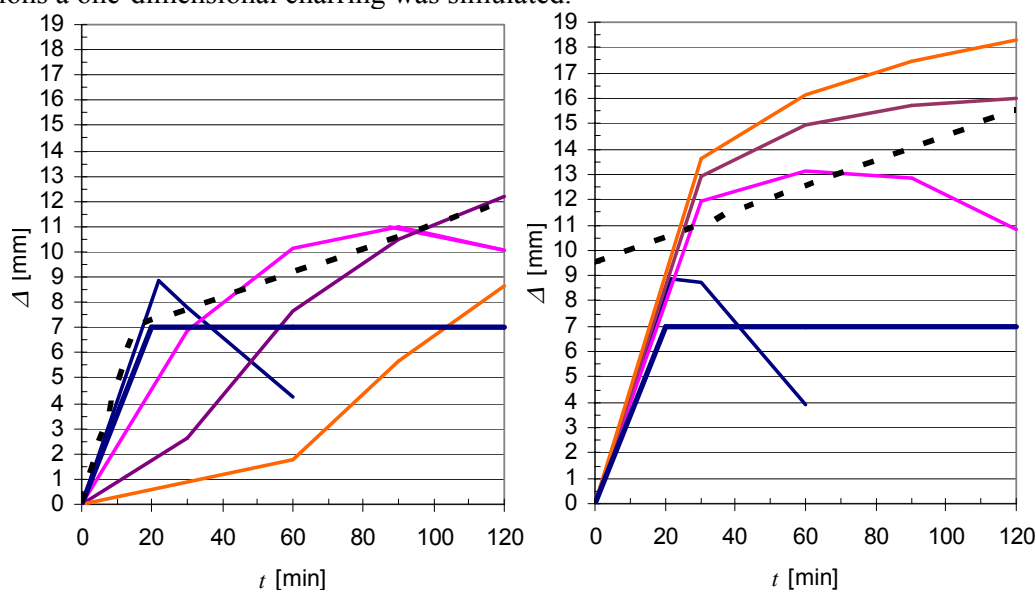


Fig. 5 – Characteristic results for solid timber (ENb-study). Exposed side in tension (left) and compression (right).

Fig. 5 shows results for simulated solid timber and enclosing curves presented for solid timber panels. For exposed side in compression curves for characteristic values exceed clearly defined envelop curve.

Due to the fact that producers tend to leave voids between elements of cross layers, a higher charring rate for these elements seems to be appropriate.

4 SUMMARY

Simulations were based on standard fire load according to ISO 834 [3]. The software used did not consider the cross layers, neither for their proportion of bearing capacity, nor for their sensitivity to deflection. Samples were simulated as single span girder due to the lack of appropriate joints between panels within the span. Simulations covered a practical range of solid timber panels from 3 to 9 layers with a layer thickness of 17, 20 and 32 mm.

Clear differences between simulations, depending on the location of fire exposure, were observed; The simplified bilinear stress-strain relationship of wood and solid timber panels respectively and the possibility of strain on high values of strain on the side in tension potentate remarkable load redistribution to the side of compression during the temperature loading, which is not possible with fire exposure on side of compression. This fact leads to a high sensitivity to this parameter. The difference of simulated material reduction types due to temperature load (TräteK and BOKU) has its origin in the way the primary experiments were carried out and the functions derived.

According to a proposed applied RSCM the resultant functions for characteristic values for the compensating zero-strength zone were compared with the existing rules given in the Eurocode. Comparisons show that the depth of a zero-strength layer of 7 mm is exceeded in almost all cases. Envelope curves for exposed side in tension and compression according to BOKU differ less, but effects such as creep are not considered here. TräteK envelope curves show differences of approximately 3,5 mm between those for fire exposure on side in tension and compression, envelope curves according to BOKU lie between these curves. It is not possible to give a general order of solid timber panels with different build-up.

Additionally fire exposure of solid timber samples with a thickness of 45 to 200 mm was simulated. A one-dimensional charring leads to characteristic results that exceed the limit of 7 mm of the Eurocode. As expected, results for exposed side in compression show higher values for a zero-strength zone to compensate material reduction due to temperature load.

5 REFERENCES

-
- [1] J.Schmid, J.König, J.Fornather, K.Bergmeister, "Simulation of cross laminated timber boards under fire exposure", Master Thesis, University of Technology, Vienna, Austria, 2006.
 - [2] EN 1995-1-2, Eurocode 5 – Design of timber structures – Part 1-2 – General – Structural fire design, Brussel, Belgium, 2004.
 - [3] ISO 834-1, Fire-resistance tests - Elements of building construction - Part 1: General requirements, 1999.
 - [4] H. Blaß, R. Görlacher, Brettsperrholz – Berechnungsgrundlagen Holzbau Kalender 2003, pp. 580 – 598, Bruderverlag, Köln, Germany, 2003.
 - [5] H. Blaß, P. Fellmoser, "Bemessung von Mehrschichtplatten" (Design of solid wood panels with cross layers), Bauen mit Holz, Bruderverlag, Köln, Germany, 08-2003 and 09-2003.
 - [6] J. König, "Structural fire design according to Eurocode 5 –design rules and their background", Fire and Materials, John Wiley & Sons, Ltd., Chichester, UK 2004
 - [7] J. König, L. Walleij, "Timber frame assemblies exposed to standard and parametric fires - Part 2: A design model for standard fire exposure", TräteK Report, Stockholm, Sweden, 2000.
 - [8] TCD 5.0, "User's Manual for TCD 5.0 with Tempcalc. Fire Safety Design", Lund, Sweden 1999.
 - [9] EN 338– Structural timber – Strenth Classes, Brussel, Belgium, 2003.
 - [10] B. Thunell, "Strength Properties of Swedish Pine-Wood as Determined from Small clear Specimens", Generalstabens Litografiska Anstaltsförlag, Stockholm, Sweden, 1941.

-
- [11] G.Reden, J.Fornather, K.Bergmeister, W.Luggin, H.Hartl, Ch.Stöffler, Z.Giertlová, „VERSUCHSBERICHT, Mittelbrandversuchsserie – MBV 1, Brandversuche unter Zug- und Druckbelastung“, FFF - Forschungsprojekt „Brandschutz im Holzbau“, Vienna, Austria 2002.
- [12] F. Yong and P. Clancy, Compression properties of wood as function of moisture, stress and temperature, Fire and Materials, John Wiley & Sons, Ltd., Chichester, UK, 2004.
- [13] J. König, Effective thermal actions and thermal properties of timber member in natural fires, Fire and Materials, John Wiley & Sons, Ltd., Chichester, UK, 2006.
- [14] A. Mischler, A. Frangi, “Pull-out tests on glued-in rods at high temperatures”, Swiss Federal Institute of Technology, Zurich, CIB-W18 Meeting 34, Venice, Italy 2001.

Fire Safety Engineering



SEGMENTATION OF ANALYSIS/DESIGN LEVELS FOR STRUCTURAL FIRE ENGINEERING

Nestor IWANKIW¹

ABSTRACT

Various levels/types of analysis and design methods for structural fire engineering exist, similar to those in other areas of structural engineering (seismic and wind) and in construction material design resistance. These differences entail distinct idealization assumptions, limitations, degrees of complexity, advantages and disadvantages, and applicability to certain classes of problems. Hence, the structural fire engineering methods can range from the simple derivatives of standard fire test results and prescriptive ratings to the most advanced, nonlinear finite element analyses of an entire structural frame subjected to localized natural fire. The selection of the analysis/design approach could influence its results and conclusions.

Current building codes and standards cite certain structural fire engineering methods in an indirect manner, with most emphasis on the easiest and traditional prescriptive methods. A more complete and transparent segmentation of the full spectrum of analysis/design alternatives is desirable to enable further progress in performance-based structural (PBD) fire design, through better identification of the inherent assumptions and limitations of each approach. This paper presents a classification system for structural fire engineering work, highlighting the key constituent factors and variables for any construction material. Major gaps in structural fire design are identified as research needs. This hierarchy is expected to be of practical value to researchers, practitioners, standards developers, regulators, owners, and the public in more explicitly identifying the relative suitability of alternative approaches to the solution of fire design problems.

¹ PhD, PE, SE, Senior Engineer, Hughes Associates, Inc., 5953 N. Oconto Ave., Chicago, IL 60631, USA, email: niwankiw@haifire.com

1. INTRODUCTION

Standard fire tests, prescriptive building code ratings and their convenient empirical correlations represent the base level of general knowledge in the field from which better design accuracy and applicability can be attained with more refined, higher-level engineering. The latter has become also generically identified as performance-based design (PBD). However, it should be clearly recognized that there is not one PBD approach, but rather different hierarchies of engineering refinement that can be attained within this advanced PBD domain. This paper overviews the non-prescriptive fire engineering methods and highlights their pertinent similarities and differences.

2. GENERAL SEGMENTATION LEVELS FOR PBD

As with other types of analyses and design, structural fire engineering can be addressed at various levels of sophistication. The associated engineering costs and time are usually directly proportional to the level of refinement employed. Figure 1 accordingly illustrates 4 groupings of advanced structural fire engineering alternatives, their estimated improvements in solution accuracy and the commensurate expense of increased engineering effort and complexity. Since the fundamental base layer of standard fire resistance ratings (prescriptive design) is considered to be generally conservative, more refined design will often result in savings of fire protection costs, or at least a rational re-allocation of the available project budget among the various passive and active fire safety measures. Sometimes, the nature of the building project is beyond the scope of the elementary code provisions (such as exposed steel members in required protected construction), and the only recourse is a more advanced analysis. Its project value will depend on fire protection material savings and/or other fire safety enhancements compared to the additional engineering costs incurred. Thus, the incentive for transcending the minimum criteria of the prescriptive code can be economic, functional, or both.

A thermal-only analysis for a natural/real fire, in place of the standard ASTM E119 or ISO 834 exposure, with critical material temperature limits could provide a marginally better solution with only potentially slightly more work. However, because the important loading and structural response features are not included in such, it is a solution of rather marginal value. The four remaining advanced engineering options relate to the breadth of the structural model used in determining if any failure(s) will occur under load during a fire:

1. single member
2. subassembly
3. frame-initial failure
4. frame-progressive failure

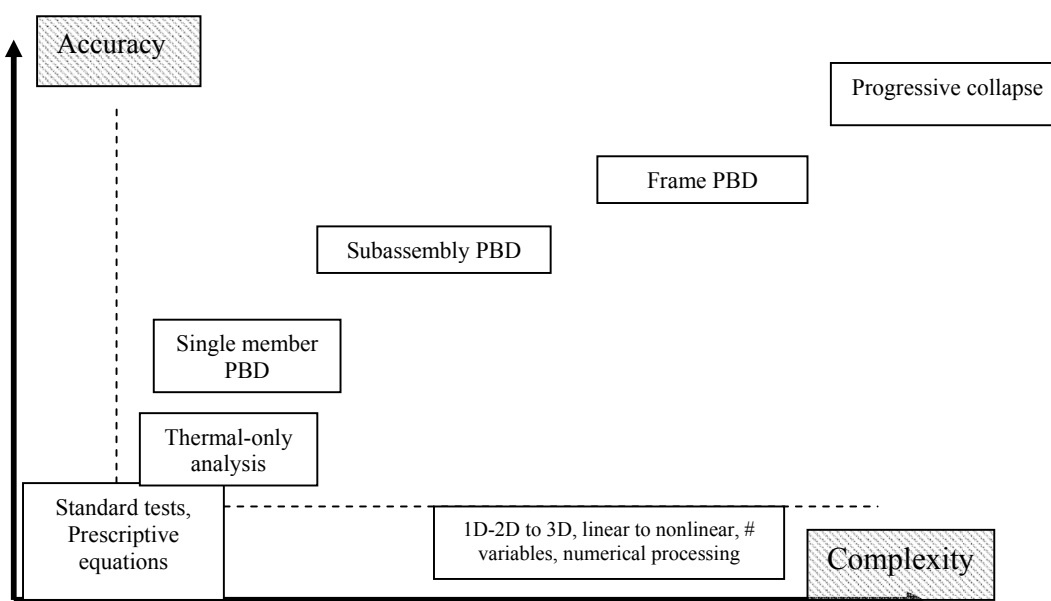


Figure 1 Advanced Structural Fire Engineering Alternatives

The primary objective of structural fire resistance design is to avoid collapse during a fire exposure. Collapse can be broadly classified as either local or global. Local collapse is failure of a single member, connection, or limited frame subassembly, while global or progressive (disproportionate) collapse produces a major cascading series of related failures triggered by the original local failure. The latter is the much more dangerous and destructive in terms of both public safety and property loss. Use of the single member, sub assemblage, or full frame structural/fire analyses will identify the source and type of any initial failure. Ordinarily, avoidance of this first structural limit state will suffice for compliance with the minimum safety requirements of the building codes. This is often referred to as member-based or element-by-element design. However, with more recent concerns about terrorist attacks, there is an increased awareness of the risks of disproportionate collapse, particularly for taller monumental buildings and other critical facilities. As subsequently discussed, progressive failure analysis is yet not well developed or established for common structural design applications.

3. CHARACTERIZATION OF ALTERNATIVES

It is important to not only be aware of the different levels of advanced structure fire resistance, but to also understand what each embodies in terms of solution benefits and limitations, and of the expected complexity of the undertaking. Analogous to structural analysis/design at ambient conditions, PBD must provide not only for the primary collapse prevention objective, but also suitable performance/serviceability. The latter limit state under fire exposures should assess affects of the following for purposes of fire containment, if they are not directly included in the model:

- deflections,
- wall or floor slab cracking,
- separation openings or
- fire protection fall-off/damage
- other damage, and
- temperatures on unexposed surfaces

A flow-chart of the PBD process, as illustrated in Figure 2, will frequently be iterative, both for redesign to prevent collapse and for situations when the modeling results are inconsistent with its initial assumptions (eg, fire compartment boundaries are likely to be breached or expected protection damage will alter structural response).

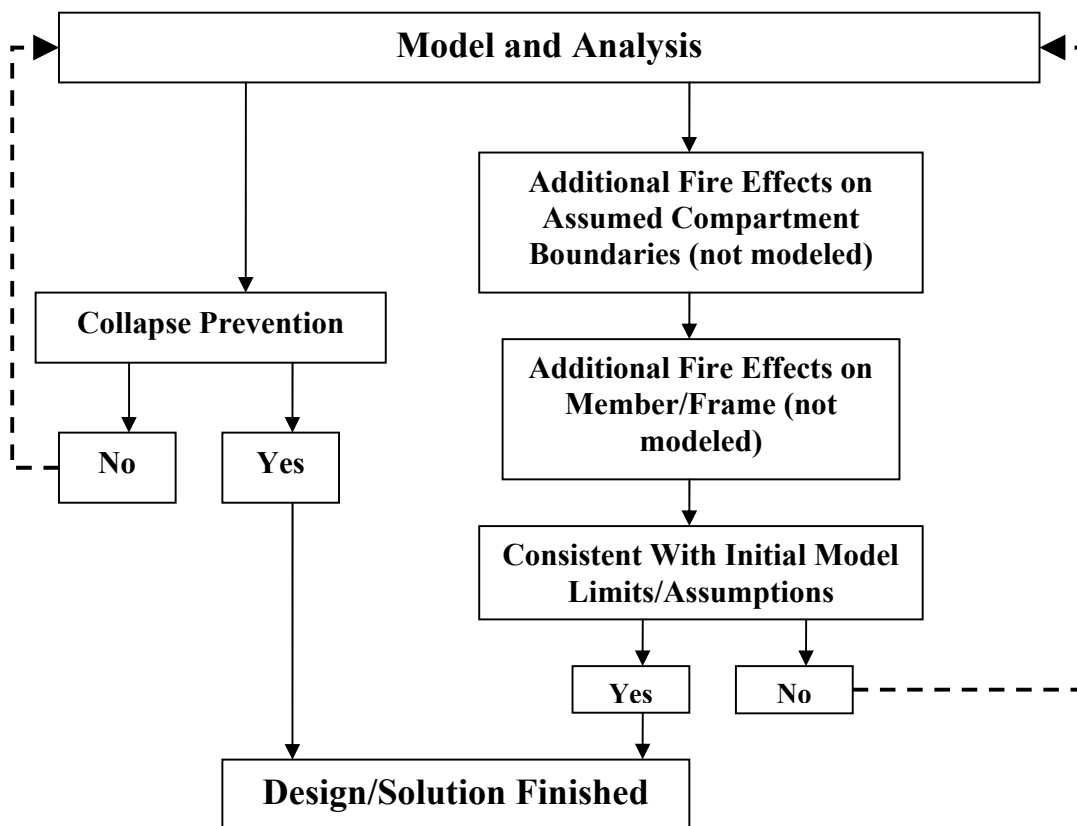


Figure 2 Fire Engineering Objectives and Process

Tables 1a and 1b summarize the key attributes of the single member, subassembly, and full-frame alternatives. The key characteristics are considered to be the

1. fire exposure
 - a. standard fire curve (ASTM E119 or ISO 834)
 - b. natural/real fire
 - i. parametric curve
 - ii. zone
 - iii. CFD

2. model boundary conditions (thermal restraint)
3. thermal strain formulation
4. connection fire response model
5. heat transfer idealization
6. member, or framing system, ultimate strength
7. deflection/damage/thermal assessment

A rational assessment of these seven characteristics can estimate the relative positioning of each alternative in Figure 1, using the prescriptive, standard fire resistance ratings as the baseline in the two-dimensional space of accuracy and complexity. In R&D, robustness and accuracy of the analytical simulation is often the principle single constraint. However, the fiscal and scheduling realities of engineering practice must regularly balance trade-offs between potential design benefits of additional refinements and their costs. The relative merits for selection of a particular approach within this context will be greatly project dependent. The more advanced techniques will be driven by special needs.

Table 1a Key Characteristics of Single Member Analysis

Compartment Fire-Single Member Analysis		
Fire		
Standard (E119 or ISO834)	Natural	
	Parametric Curves	Simulation Models – zone or CFD
Thermal Restraint – none or approx.		
Thermal Strains – none or approx.		
Connection fire response effects – none or grossly idealized		
Heat Transfer		
1D (lumped mass)	2D	3D
Concurrent Loads ^{1,2}		
Max. Design		Expected Load Combination
Member Strength		
Temperature-modified normal design provisions		Other rational mechanistic model
Integrity Assessment		
Determine safety or ultimate failure mode of member		
Performance Assessment		
Did large deflection/distortion lead to breach of adjacent fire barrier(s) or other induced failure(s) ? And/or check standard test limits.		

¹ If no applied loads are assumed, maximum temperature solution attained does not require any further structural analysis

² Load effects on given member determined from usual ambient structural analysis

While the fire modeling side of this problem is only peripherally addressed in this presentation, one basic recommendation in this regard is made. The imposed fire exposure can range from a standard fire curve to the most sophisticated CFD simulation of a natural fire. It would typically be greatly incongruent and of no technical solution benefit to pair the most simple fire or structural model with its most advanced counterpart for a given problem, as illustrated in Figure 3. The refinement level of the fire model

Table 1b Key Characteristics of More Advanced Analyses

Single/Multiple Compartment Fires- Subassembly or Full Frame Analysis					
Fire					
Standard (E119)		Natural			
		Parametric Curves		Simulation Models – zone or CFD	
Thermal Restraint – included					
Thermal Strains – included					
Connection fire response effects – modeled					
Heat Transfer					
1D (lumped mass)		2D *		3D *	
Concurrent Loads ¹					
Max. Design			Expected Load Combination *		
Structural Analysis					
Linear elastic		2 nd order elastic *		Fully nonlinear (geometry and material) *	
No stability effects		Elastic member/frame buckling		Elastic and inelastic buckling: local, member, and frame	
2D	3D	2D	3D	2D	3D
Member Strength					
Temperature-modified normal design provisions		Temperature-modified normal design provisions		Directly computed	
Integrity Assessment					
Determine safety or initial structural failure mode					
				Continue thru possible progressive failure mechanisms	
Deflection/Damage/Thermal Check					
Did deflections cause any additional damage and fire spread consequences beyond those directly modeled? (fire barrier cracking, openings, etc., temperatures on unexposed surfaces)					

¹ If no applied loads are assumed, maximum temperature solution attained has no need for further structural analysis

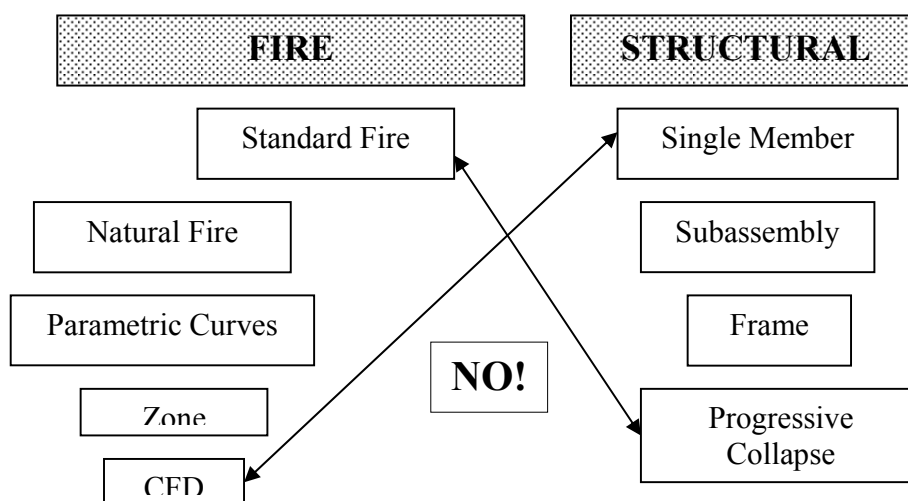


Figure 3 Matched Refinement of Fire and Structural Models

should be similar to that of the structural for overall consistency of the problem idealization.

4. KEY STRUCTURAL MECHANISMS FOR ADVANCED ANALYSES

Table 1b lists several modeling/response attributes possible for the more advanced structural-fire solutions. Unless one performs the most intricate 3-D, highly discretized and nonlinear analysis, some degree of modeling simplification with assumptions will normally be advantageous. The highest analysis level will ordinarily be employed only in research or forensic studies of major events. In design practice, the relative importance and prudent selection of the PBD method should be heuristically guided by the scope of the particular project and nature of expected results. Past experience and knowledge in the field will be extremely useful in reducing large complex problems to much more manageable proportions. However, if an important performance attribute is ignored or incorrectly modeled, the final analysis results could be substantially erroneous. The following sections conceptually outline several such higher-order considerations:

4.1 Thermal Strains/Restraint

Often, an essential element for the fidelity of a structural-fire model is adequate representation of the thermally-induced strains and forces, particularly in the floors, and their affects on the frame. Two recent papers^{1,2} on analyses of the 9/11 World Trade Center (WTC) collapses and the NIST 2005 Report³ have demonstrated the great importance of properly including this behaviour, that is usually not considered under ambient conditions. Deflections of floors with reduced heat-affected stiffness will arise from both the existing vertical loads and thermal gradients (bowing). Furthermore, the expansion restraint of the heated floor by the adjacent columns will induce compression and incremental curvatures, as shown in Figure 4. These high temperature affects will not only reduce the strength of the horizontal members acting as beam-columns, but more critically, the overall stability of the main building columns for which they provide lateral bracing. These columns, due to the horizontal displacements/flexibility and sag of the fire floor(s), now have longer unbraced lengths, along with new demands for floor reaction support, that reduce their strength for carrying the other imposed superstructure loads. A frame or subassembly model would be necessary to explicitly capture this type of behaviour. More discussion of these WTC and other advanced studies is provided subsequently.

4.2 Catenary Action

A floor slab and beam may change from pure bending resistance at ambient temperatures to combined bending and axial compression due to restraint of thermally-induced expansion; finally, after further thermally-induced bowing to produce the large vertical deflection during the high temperature stages of a fire exposure, it will experience the combined bending and axial tension mechanism (catenary or membrane action). This redistribution of the load-carrying capabilities of a typical steel-concrete composite floor system in a building from simple flexure under service conditions to catenary action at ultimate is schematically illustrated in Figure 5. This floor mechanism is naturally related to the thermal expansion affects discussed previously. As vividly demonstrated in the Cardington research, catenary action of a floor system can provide additional reserve strength beyond its primary bending resistance, if its cross-section, end

connections and boundary conditions are amenable to formation of this mechanism. Ordinarily, special formulation provisions must be included to capture this response mode in a single member or subassembly-type solutions.⁴

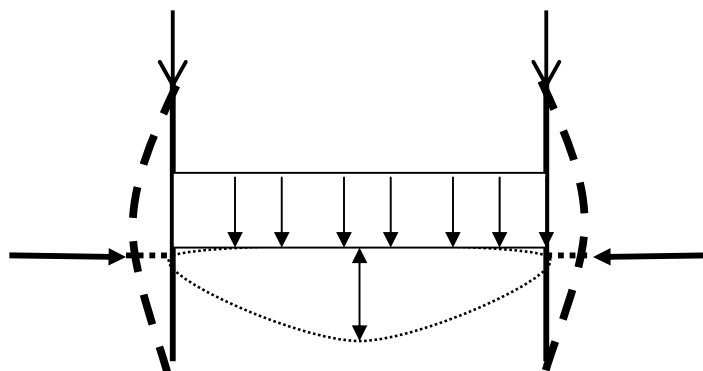


Figure 4 Affects of Floor Thermal Expansion on Columns

4.3 Progressive Failure

Most of the structural-fire analyses are considered to be static in nature, unless dynamic affects of blast, impact or seismic actions are involved. Static problems usually enable relatively easier solutions. However, the analytical determination of whether an initial local/member failure can propagate to further global or disproportionate structural instabilities may be difficult, or impossible, for most finite element software operating in a static analysis mode. Numerical solution convergence for any subsequent catastrophic and complex global collapse mechanisms can be much more easily achieved if the nonlinear software processes the analysis (with resulting large deformations, member failures, singularities, etc.) as a dynamic, rather than static equilibrium problem, with an appropriate time step.⁵

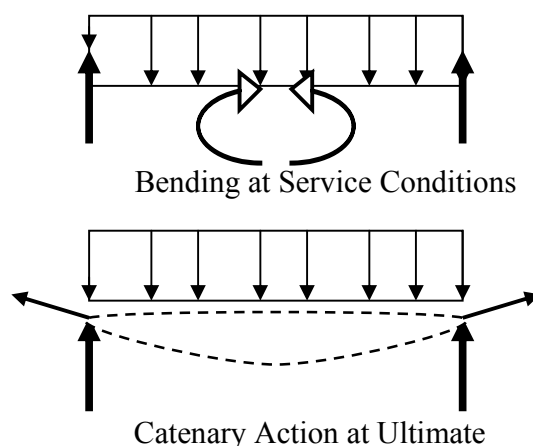


Figure 5 Changes in Structural Resistance of Floor Beams
From Primary Bending to Catenary Action

In addition, it may be necessary to conduct such simulations in full three-dimensional space, with adequate and appropriate discretization of the potentially affected members, i.e. many more model nodes and elements, to reach the best response fidelity. Such intricate simulations will require extensive computing resources, expertise, time and effort to accomplish. More

research on progressive collapse is needed. At the current time, most structural design problems do not mandate consideration of such global failure.

5. COMPARATIVE REVIEW OF SELECTED ADVANCED STUDIES

Since the 9-11 tragedies, much work, many papers and reports have been written to explain how the WTC collapses happened and their causes. The references cited earlier^{1,2,3} and four other papers^{4,6,7,8} provide further insights into several advanced modelling perspectives, and the requisite engineering judgment to simulate a complicated failure under fire exposures. The Table 2 summary shows that the analytical results and conclusions can vary, depending on the assumptions and methods employed.

Table 2 Summary of Selected Advanced Studies

Reference	Building	Fire Model	Structural Model	Results
6	WTC	Parametric	Single member (floor truss)	Effects of protection thickness - floor failure initiated collapse
8	Multi-story steel frame (One Meridian Plaza)	Parametric	2-D subassembly, nonlinear, w/floor beams or slab	Effects of horizontal expansion at floor beams on columns
1	WTC	Parametric	2-D subassembly, nonlinear	Perimeter column collapse due to floor truss failure
2	Parking garage	Temperatures from full-scale fire test	3-D, nonlinear	Validation with test results, demonstrate column response to horizontal slab expansion and vertical deflections
7	WTC	special	3-D, non-linear	Simulate damage, core and perimeter column collapses
3	WTC	CFD	3-D, fully nonlinear	Simulate damage & perimeter column collapses
4	Steel floor system (Cardington)	empirical	subassembly	Catenary action strength mechanism

6. RESEARCH NEEDS

Some future research needs to help enhance this practical application framework for fire PBD are:

- further experimental validation of models
- calibration/validation of simpler models by means of the more advanced ones
- better understanding of progressive collapse and its mitigation
 - i. fire and structural effects that breach compartment walls to facilitate horizontal fire spread
 - ii. fire and structural effects that breach horizontal separations to facilitate vertical fire spread
 - iii. fire effects on damaged structures (terrorist or seismic)
 - iv. real-time predictions to guide emergency evacuations

7. CONCLUSIONS

Several distinct choices for analytical models are possible for a variety of structural-fire interaction problems. Expertise and good engineering judgment are invaluable to selection of the best PBD approach for a given technical issue within the context of a particular construction, forensic, or research Project. This paper outlined the various alternatives available for this type of structural modelling, along with their limitations, which should provide a helpful guidepost to general practitioners and regulatory building officials who are not intimately familiar with these subjects.

The prevalent time and budget constraints of Projects will often preclude regular application of the most advanced fire PBD approaches in practice. Thus, the simple or intermediate complexity models are expected to be generally favored. However, the inherent assumptions and limitations of such solutions must be duly recognized. Since the analytical results can differ with modelling approach and assumptions employed, it is important to use the appropriate level of refinement for the given project objective(s). Much like standard fire tests of limited size assemblies, single member or subassembly models are incapable of resolving broader frame interaction and stability issues.

The greatest practical benefit of the most advanced, nonlinear, 3-D solutions, in combination with suitable experimental and actual performance data, is to broaden understanding of the collapse phenomena involved, further validate and serve as calibrations tools for the simpler methods that will be the most frequently used. In some form, they could also eventually serve as real-time predictors of the severity of a given ongoing structural-fire event relative to building evacuations.

8. REFERENCES

- [1] Usmani, A.S., Chung, Y.C., and Torero, J.L., "How did the WTC Towers collapse: a new theory", *Fire Safety Journal* 38 (2003), 501-533, Elsevier
- [2] Li, Y., Hirshima, T., Uesigi H., and Wakamatsu, T., "An Analytical Method of Deflection Behavior Concerning Three-Dimensional Steel-Frame Exposed to Fire which takes Account of the Thermal Expansion of a Floor Slab", *Fire Science and Technology*, Vol. 24, No. 4 (2005), 211-236
- [4] Bailey, C., "Membrane Action of Composite Floor Systems in Fire", *SiF'04, Structures in Fire, Proceedings of the 3rd International Workshop*, NRC-CNRC, IRC Ottawa, Canada, (2004) , pgs. 335-352

- [3] NIST NCSTAR 1, Federal Building and Fire Safety Investigation of the World Trade Center Disaster – Final Report on the Collapse of the World Trade Center Towers”, Sept., 2005
- [5] Franssen, J.M., and Gens, F., “Dynamic Analysis Used to Cope with Partial and Temporary Failures”, *SiF’04, Structures in Fire, Proceedings of the 3rd International Workshop*, NRC-CNRC, IRC Ottawa, Canada, (2004) , pgs. 297-310
- [6] Quintiere, J.G., di Marzo, M., and Becker, R., “A suggested cause of the fire-induced collapse of the World Trade Towers”, *Fire Safety Journal* 37, (2002), 707-715, Elsevier
- [7] Abboud, N., Levy, M., Tennant, D., et al, “Anatomy of the World Trade Center Collapses “A Structural Engineering Investigation”, *Proceedings of Designing Structures for Fire Conference*, Sept. 30-Oct. 3, 2003, Baltimore MD, SEI and SFPE
- [8] Garlock, M. and Quiel, S., “Effect of Slab and Fireproofing on Perimeter Columns in a Steel Building Under Fire”, submitted for publication in *AISC Engineering Journal*



APPLICATION OF FSE TO AN INDUSTRIAL BUILDING

Nicolas TAILLEFER, Dhionis DHIMA AND Philippe FROMY¹

ABSTRACT

Fire security in industrial plants is a major concern for both employees and the environment. That is why, for this type of buildings, French regulation requires ensuring the fire stability of the structure and preventing the spread of the fire from one part of the building to another or to the outside. This article deals with a case study which illustrates a method that can satisfy both stability and containment criteria. It deals with a nuclear plant building. The main structure consists in steel frames. Inside and outside walls are constituted of the concrete blocks infill of the steel frames. The final purpose of the study is to propose fire protection measures, if needed, in order to satisfy fire safety requirements.

Assessing the impact of a potential fire is the central point of the study. In comparing Fire Safety Engineering (FSE) approach with conventional ISO fire results, the paper demonstrates one of the major advantages of more accurate methods to describe fire risk. Indeed, taking into account the localization of the potential fire, the amount and type of fuel load in each part of the building, and the available air supply, led to define fire scenarii which are much more realistic than ISO fire. Consequently, corresponding thermal actions were defined according to fire engineering correlation formula or using a 2 zones model program. Then using SAFIR finite element program, the impact of different thermal actions (ISO or natural fire type) on the structure's elements has been analyzed and it was possible to assess the effect of potential fire on the stability of the building and on the risk of loss of containment. In some cases, conventional ISO fire proved to be too severe, whereas in other cases it underestimated the risk.

Containment requirement consists in preventing the spread of the fire outside the compartment where the fire first started. As separating walls are made of concrete blocks infilling steel frames, it is necessary to ensure that the frames remain stable and that the deformations of the beams sustaining the masonry walls do not cause the collapse of the concrete blocks. An acceptability criterion for the walls deformations has been defined from

¹ Engineers. Centre Scientifique et technique du Bâtiment, DSSF/ISTA/Fire section, 84, avenue Jean Jaurès, Champs sur Marne, BP 02, F-77421, Marne La Vallée Cedex 2
email : nicolas.taillefer@cstb.fr, d.dhima@cstb.fr, fromy@cstb.fr

ISO fire test results about similar walls. Finally, the calculated beam deformations are compared to this criterion in order to conclude about containment requirement.

The study points out that realistic fire scenarii lead to the collapse of the building and loss of containment for only two cases, corresponding to two different fire locations. The fire stability of other compartments of the building indeed proved to be satisfied without specific protection.

The last point of the study concerns fire protection measures needed to satisfy French fire security regulation. The use of FSE approach allows an optimization of the protection. The chosen protection consists in gypsum layers. The optimization involves the material layer thickness and the number of elements protected. Since most of the real thermal actions in the building compartments are not very severe for the structure, the protection is limited to the most vulnerable parts of the building. Based on an accurate assessment of the thermal action on steel elements, the gypsum layer thickness was adjusted.

This case study clearly demonstrates the interest of FSE approach especially for buildings where thermal actions are not uniform. Such an approach can improve the security level of this type of building and also optimize protection measures. Therefore, the article could probably contribute to make this interesting approach known and encourage industrial building owners to consider it as a good alternative to more conventional methods, when assessing the security level of their plant.

1. INTRODUCTION

The aim of this study is to investigate the fire behaviour of an existing nuclear building in order to optimise the fire protection of the main structure and to fulfil fire safety requirements.

The former French regulation concerning the fire resistance of buildings was modified in March 22nd, 2004 [1] and now enables the use of FSE approach by taking into account real thermal actions while determining fire stability. The fire scenarii, for this type of thermal actions, must be defined in agreement with a local safety commission. According to the French regulation, the fire stability of this building under the ISO fire is 2 hours.

As a consequence, the use of FSE for the industrial buildings allows, simultaneously, taking the most relevant actions, in order to ensure fire stability, and reducing the costs of these measures, with respect to safety requirements.

This study consists in assessing the stability of the structure submitted to standard ISO-R834 fire in the first part, and to a natural fire in the second part. Indeed, in the case of a natural fire, if the fuel elements are consumed and if the structure is still steady, it can be concluded that stability is ensured without time limitation. Compared to ISO-fire, a natural fire takes into account more realistic parameters for the fire development, such as fire load, fire location, dimensions of the compartment and opening factor, which proved to have a great influence on the development and the impact of fire in a building.

Depending on the compartment where fire may take place, the thermal actions are determined either using correlation formulas of fire engineering for local type fires, or using a 2 zones model (FISBA [2]) for fully developed fire types. The analysis of the mechanical behaviour of the structure as well as calculations of heating are carried out with SAFIR [3]. It is a non-linear finite elements program which takes into account the evolution of thermal and mechanical properties as a function of the temperature and calculates heat gradients and great displacements.

Acceptability criteria for concrete blocks walls stability are deduced from ISO fire tests. This criterion has been used to determine relevant protection of steel structure so as to restrain the walls displacements. This study allowed to optimise such a protection and to satisfy the French safety requirements for this type of building. The different stages of this study consist in determining:

- initial fire sources and realistic fire scenarii,
- thermal actions to which the structure will be subjected for each scenario,
- heating of each structure element,
- stability of the structure and building containment,
- optimized protection, if needed in order to fulfill safety requirements.

The purpose of this study is:

- firstly, to demonstrate the advantages of FSE approach in the analysis of fire behavior of industrial building with respect to fire safety,
- secondly, to encourage the use of a scientific approach like FSE, in order to optimize the costs of the protection measurements for the structure.

2. DESCRIPTION

The building is a 42 m long, 12 m width and 8.5 m high. Figure 1 shows an upper view of the building. Except the frame of file 57 all the others are infilled steel frame structure. The building is divided in 6 major volumes. Some of these volumes contain intermediate floors. Steel frames are linked together through steel beams at the top of the roof and by two edge beams. All frames are made of IPE450 columns and IPE400 beams. The intermediate beams (supporting intermediate levels) are made of IPE500 steel section. Purlins and ridge beams of the roof consist in IPE240 type beams. In file 57 frame, there is no intermediate beam and consequently the volume between file 56 and 58 is a single great compartment. This compartment is a weak point of the building, so, it will be analysed with more details further in this paper.

All the walls of the building are made of 150 mm thick concrete blocks. They are coated on each side with a 5 mm thick layer of cement or gypsum. The clamping of these walls is ensured by the intermediate beams and ridge beams of the steel frame. The function of these walls is to ensure the integrity and the insulation of the building, so as the containment between two compartments simultaneously. Inside the building, 2 hours fire resistant doors are inserted in the concrete block walls. The roof, directly supported by steel frame, is made of 100 mm thick SIPOREX panels covered by aluminium sheets and tarlined paper.

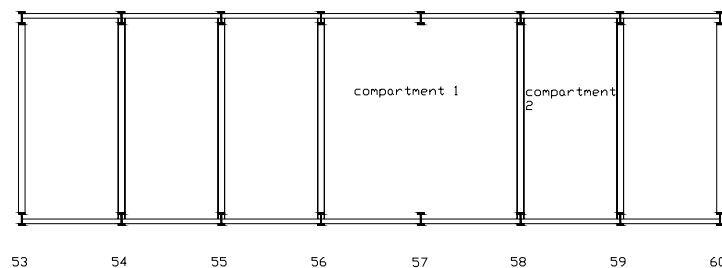


Fig. 1 - Steel frame of the building.

Containment is not required for the two lateral exterior walls of the control room, located at the ground floor between files 58 and 59. Consequently, the windows and doors inserted in these walls can be opened. The separating walls, however, has to prevent the spread of the fire to another compartment. The 2nd floor of this compartment is made of a concrete slab supported by steel beams. These beams are fixed on the intermediate beams of the steel frame of files 58 and 59.

3. FIRE SCENARI

In order to study the building's structure fire behavior it is essential to know the thermal actions with a good precision. French fire safety regulation allows two approaches:

- prescriptive approach based on ISO R834 curve (conventional fire),
- approach based in a natural fire safety concept.

This second approach enables realistic fires to be considered in order to assess the fire stability of the building. Since thermal loads are really different from one compartment to another, this approach becomes much more interesting, not only for fire stability and containment criteria, but also while optimizing fire protection needed to fulfil safety requirements.

After having studied the fuel quantities located in this building, it was clear that potential fires that would take place in the great compartment between files 56 and 58 or in the control room between file 58 and 59 are simultaneously the most dangerous for the structure and most representative of the potential fires. That is why this paper will focuses on the behaviour of the building submitted to these types of fires.

Potential combustible in these parts of the building are:

- electric cables,
- plastics materials,
- cellulose materials.

Different fire scenarii are defined according to fuel elements type and the position of the structure targets affected by the fire. This paper focuses on the most dangerous scenarii for fire resistance of the building.

3.1 Fires scenarii in the compartment between files 56 and 58 (compartment 1)

Two fires scenarii are taken into account: a local fire and a fully developed fire.

First scenario simulates a fire of electric cables fixed on columns of the frames. The second scenario takes into account the ignition of all cables located in this volume. This situation would give a relatively severe and generalized fire. Even if the probability for such a scenario to actually occur is very low, it has mainly been considered because of the strategic importance of the building. It is of course a catastrophic (extreme) case.

3.2 Fires scenarii in the control room between files 58 and 59 (compartment 2)

In the control room (ground floor) between files 58 and 59, there are a large quantity of cellulose products and electric cables that could easily lead to a generalised fire. In order to take into account the influence of openings of this room, two scenarii are investigated.

Scenario 3: all the doors are closed, but window glasses are broken very quickly after initial fire started. Because of the large quantity of combustible (mainly cables), HRR is limited by the air flow entering by the windows. The maximum HRR produced is 4,5 MW (S3).

Scenario 4: the room doors leading outside the building are open when fire starts and window glasses blow out very quickly. The opening rate is greater than in scenario 1. Then, a large amount of combustible may burn simultaneously, since a greater quantity of air enters in the compartment. The maximum HRR produced by this scenario is 9 MW (S4). Figure 2 illustrate the heat realise rate for these two scenariis.

The heat release rate (HRR), calculated for these two scenariis, are given on figure 2. The studied compartment is 12 m long, 6 m large and 3 m high.

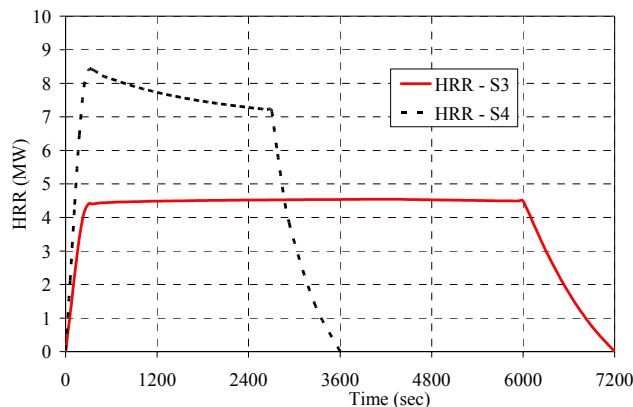


Fig. 2 - Heat realise rate in the control room for two scenariis (scenario 3 and scenario 4)

4. THERMAL ACTIONS APPLIED TO THE STRUCTURAL

4.1 Fire calculation model and results

The calculation of the thermal actions S1 is based on the engineering correlation formula. The estimated duration of this fire is 20 minutes. Given that the target (the column) is in contact with flames (parietal flame of the cables), it is supposed to be directly affected by the average temperature of the flame, considered equal to 800°C on 3,5 m high.

The thermal action S2 is calculated using a mono-volume 2-zones model developed at CSTB, named FISBA [2]. In the volume, lower and upper layers, flame and plume zones are described using engineering correlations and differential equations derived from principles of conservation for mass, energy and species. The model predicts the gas temperatures for each zone, the interface height, the mass flux through openings, the pressure inside the volume, the heat fluxes, the temperatures profile in the walls, etc. Radiation is taken into account. Ventilation is also considered, either natural (vertical and/or horizontal openings, building leakages) and/or mechanical (fans and ducts). Combustion in upper layer can be considered. The chosen chemical species are unburned fuel, O₂, CO₂. Concentration of CO can be predicted if the source term is given as a production law. Options exist concerning entrainment laws and conductive thermal transfer. Gas entrainment through openings is also considered. More details about this model can be find in [2].

In each gas zone, at a given moment, all the fire characteristics (temperature, chemical composition, attenuation coefficient of the light) are uniform in each point of the zone, but they vary with time. These two zones exchange to one another chemical mass, energy and species, in particular through flames and thermal plume. The model considers that the "upper gas zone" is spread out over the whole surface of the ceiling.

Thermal action S2 given in figure 3 represents the gas temperature of the upper zone of the compartment between files 56 and 58. Thermal actions S4 and S5 given in figure 3 represents the gas temperature of the upper zone in the control room, for two scenarii described in section 3.2. For these three thermal actions, as well as for S1, it is assumed that all structure elements of the compartment affected by fire are heated by gas temperature.

4.2 Gas temperatures for each scenario

The elements of the structure of the building (targets) are affected according to one of the following thermal actions:

- ISO: thermal actions according to ISO R834 curve (compartment 1 and 2),
- S1: thermal action defined for the localised fire scenario 1 (compartment 1),
- S2: thermal action defined for the generalized fire scenario 2 (compartment 1),
- S3: thermal action defined for the generalized fire scenario 3 (compartment 2),
- S4: thermal action defined for the generalized fire scenario 4 (compartment 2)

Fig.3 compares the gas temperatures in the different scenarii considered in this paper.

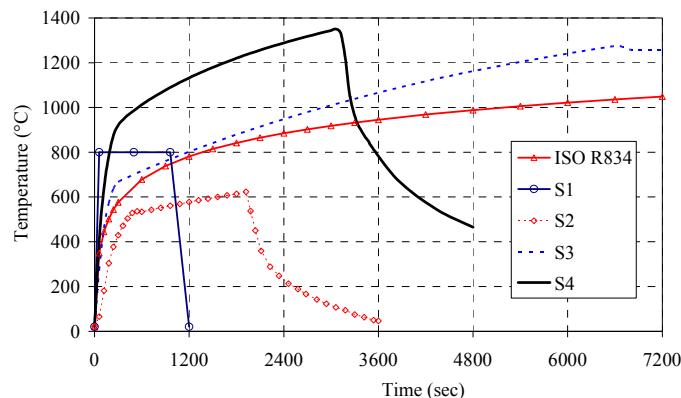


Fig. 3. Different types of thermal actions, described in terms of gas temperature.

5. THERMO MECHANICAL BEHAVIOUR OF THE BUILDING STRUCTURE

As far as the containment of the building is concerned, the stability of the concrete block walls is very important. The limiting value of displacements acceptable for the concrete block walls, used as acceptability criterion, was based on standard test results. These tests simulated thermal actions given by ISO R 834 curve.

The thickness of the walls tested and of the real walls are the same. Loaded and unloaded walls, with 3 m width and 3 m height, were tested, in the same time. Analysing all the results, it was decided to set the maximum acceptable deformation for a 3,5 m high wall to 50 mm. At this level of displacement, the stability, insulation and integrity requirements of the walls can still be satisfied.

The mechanical behaviour of the steel frame of the building has been studied for the whole structure. This method permitted to assess the risk of chain failure in case one part of the structure proved to be weaker than the others.

5.1 Design assumptions

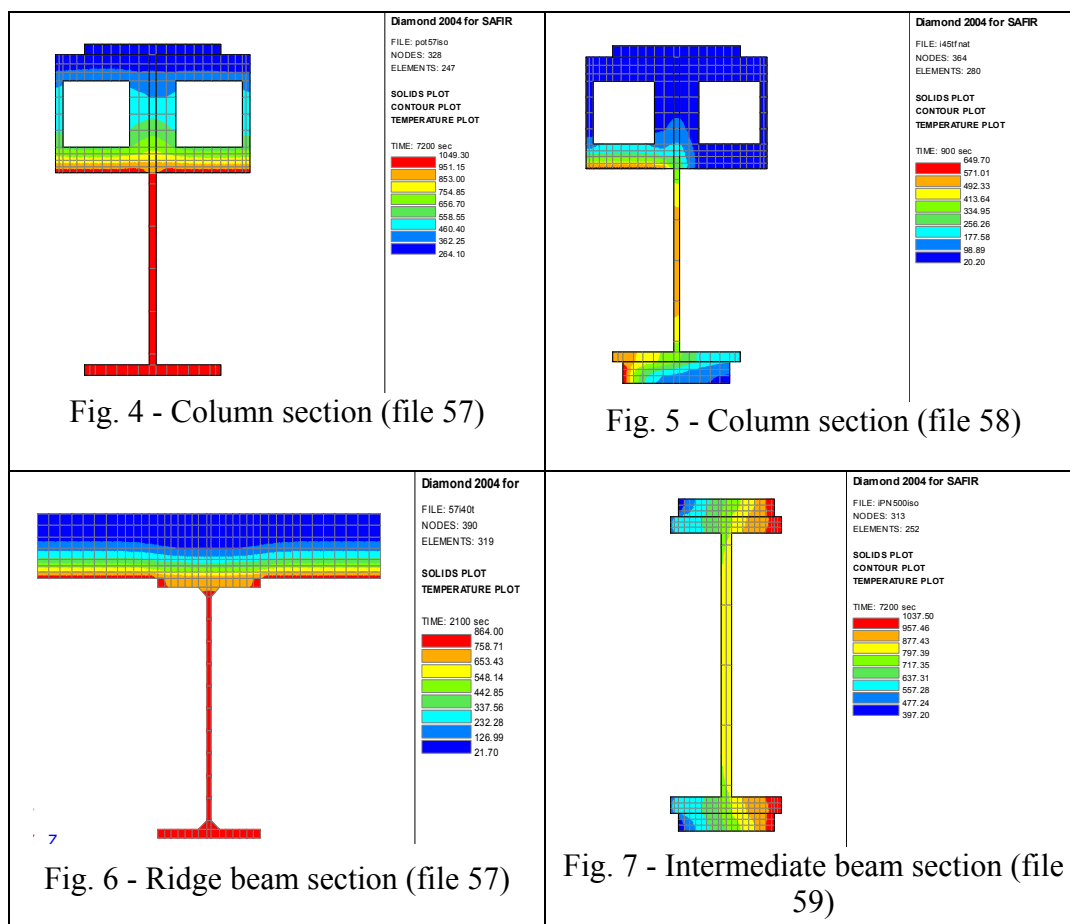
1. The thermal actions are defined according to §4.
2. The mechanical loads applied to the modelled structure are calculated according to Eurocode 0 [7].
3. The thermo physical and mechanical properties of all the steel and concrete elements are those given in Eurocodes 2 and 3 fire part 1.2 [5], [6].
4. The heat exchange coefficients used for the calculation of heating of the various elements are those given in Eurocode 1 fire part 1.2. [7]
5. The columns of steel frame are supposed restrained at ground level.
6. The assumption of Bernoulli is considered valid in fire situation.

5.2 Heat transfer and structural model

The thermal and mechanical analysis in this study are realised with a non-linear finite element program (SAFIR) developed by Franssen and al [3]. Thermal analysis calculations are realised using a 2D model and mechanical analysis used a 3D model. This thermo-elastic-plastic finite elements programme takes into account the great displacements and transversal thermal gradient in mechanical calculation. Figures 4 to 7 represent the principal sections' meshes used to calculate the temperatures of heating of the columns and the beams of the studied building (temperatures calculated for ISO fire).

5.3 Results of heating calculations

Figures 4 to 7 show the temperature fields calculated at a chosen moment for ISO. These temperatures vary with time according to thermal actions. Then they are taken into account in the structural model. The use of an integrated thermal and structural model as SAFIR, which takes into account in the structural model all the temperatures calculated by the thermal model is a real advantage, not only for the precision of the results, but also for the time saved during calculations.



5.4 Results of mechanical calculations

In order to present a clear analysis of the study, this paragraph only releases a minimum of results on the behavior of selected parts of the steel frame. Figure 8 shows the mechanical model of the building. Compartment 2 intermediate floor beams are represented.

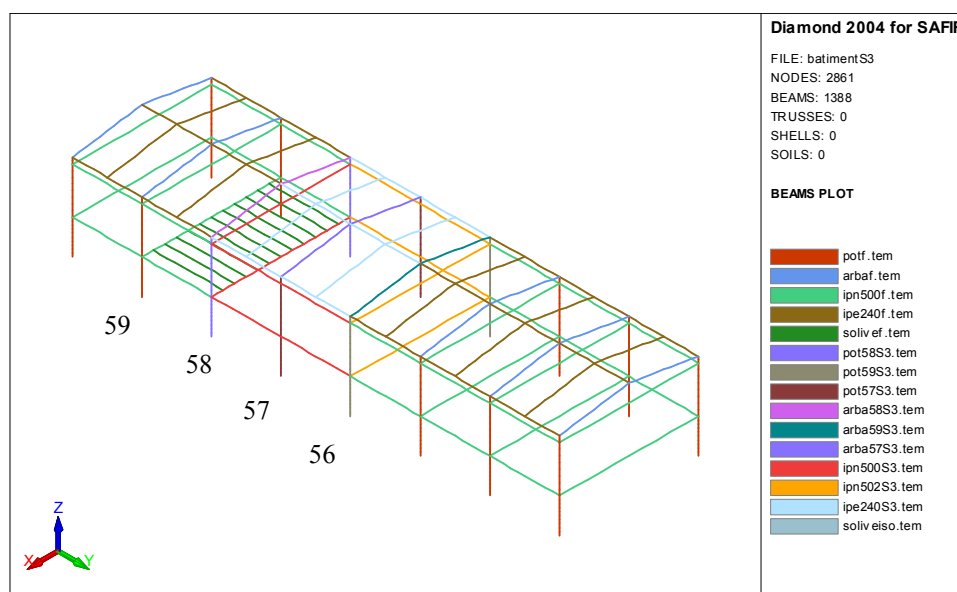


Fig. 8 - Overview of the structure

A – Fire occurs in the volume located between files 56 and 58.

The thermal actions supposed to affect the structure of this compartment are ISO, S1 and S2. The most dangerous effect in thermal action S2 (local fire) tackles the file 57 frame. Consequently, the thermal action is taken into account only for this frame.

Thermal action S1 is applied at one column of this frame. Fire stability and containment of the building are not affected, due to the fact that deformations remain small during the whole fire time. Comparison between previous 2D and 3D structural models reveals good similarities in the results. 3D model leads to a better assessment of lateral restraints due to real structures elements. On the contrary, 2D model was based on a total symmetry in the plane of the frame and assumes lateral beams contributions can be neglected. According to the results, the assumptions of the 2D simulation prove to be relevant in this case.

Thermal actions ISO and S2: figure 9 shows the vertical displacement of node 41, in the top of the file 57 frame. For ISO, the slope of vertical displacement and its value increase very quickly, just before the collapse of the frame. For S2 the maximum displacement is less than 60 mm. Experience showed that the roof materials are able to comply with this displacement pattern and consequently keep their integrity. It is important to note that applying ISO fire temperature curve in this volume is completely unrealistic. Indeed, the volume of the compartment is great whereas the effective fuel load is small. The fire stability of the structure reaches 36 minutes for ISO and 2 hours for S1 and S2 (natural fires). However, if the containment criterion is considered, lateral displacements of intermediate beams (IPN500) of frame 56 and 58 exceed the acceptable displacement for masonry walls in the case of S1 and S2. So, in these cases, the failure of the masonry walls occurs first, much before the structure collapses, which drastically reduces the security level of the structure. It can be noticed that S2 and ISO are very severe thermal actions. That is why protection was not designed according to these extreme cases. S2 simulation shows that lateral walls remain stable (small displacements), but walls separating compartment 1 from the others could fail in case of very severe fire. Moreover, S2 results make evidence that chain failure is avoided even for this type of fire.

It can therefore be concluded that if a fire occur in the unprotected compartment, security requirements are satisfied for local fires. For generalised fire, stability is granted but containment between the compartment in fire and the others is not sure. This is a risk with little probability, and it has been proved that fire would not extend outside the building since lateral walls are stable. The occurrence of such a fire assumes that all other security measurements have failed. It was finally decided not to protect this compartment.

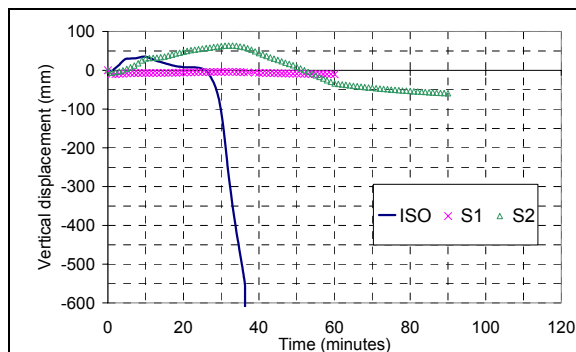


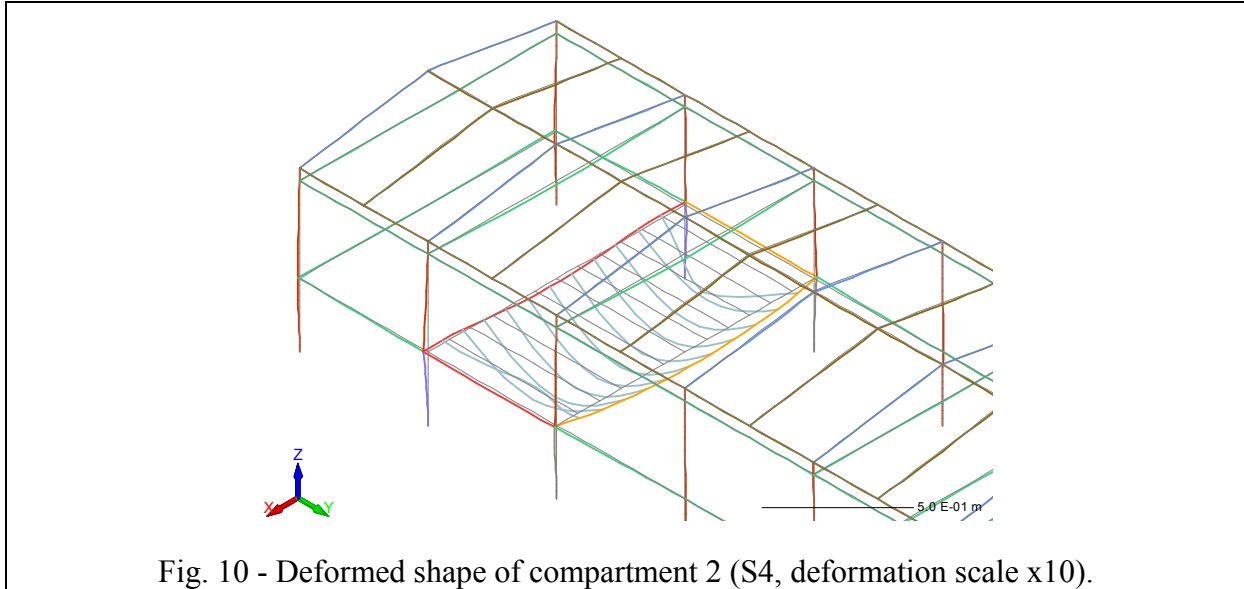
Fig. 9 - Evolution vertical displacement of the top of the frame.

Element	Max top displacement [mm]		
	ISO	S1	S2
Separating walls	625	2	445
Lateral walls	29	11	28

Table 1 - Maximum deformation of beams supporting masonry walls.

B – The fire occurs in volume between files 58 and 59 (control room).

The fire stability of the unprotected structure reaches 22 for ISO and S3 and 19 minutes for S4. As a result, the structure collapses before the fire stops. In order to satisfy the safety requirements in case of fire in this compartment, a fire protection is needed. Figure 10 shows the deformed shape of the compartment for S4, just before collapse occurs.



Failure seems to occur because of the buckling of the floor beams located near to lateral walls. It is due to great normal forces, which are generated because the dilatation of steel floor beams is blocked by the local rigidity of the join between the intermediate beams and the column.

6. PROTECTION OF LOAD BEARING STRUCTURE OF THE CONTROL ROOM

In case a fire would take place in the control room, the fire protection of the steel structures is needed in order to ensure the safety requirements of the building (both stability of the intermediate floor and containment requirements). This protection limits heating of the structure and consequently the deformation of the structure as well as the deformation of the concrete back walls. It is worth noting that the protection layers fire behavior has to be compatible with the protected structure displacements. Therefore, buildings options like fixing modes play a major role in the protection reliability.

For the control room structure, the protected elements are the intermediate beams of the frame of files 58 and 59, the edge beams, at the same level, as well as the purlins support of the floor and the floor itself. The protection of these elements is realized with gypsum plaster boards as shown in figures 11 for the floor and 12 for the intermediate beams.

As first trial, only purlins were protected. Fire stability for S4 increased (30 minutes when purlins are protected and 19 minutes if not protected), but was still not satisfactory. Fire protection of both purlins and intermediate beams enabled to reach stability and containment criteria. The proposed protection system (plaster board) is rather simple and limited to a small number of elements.

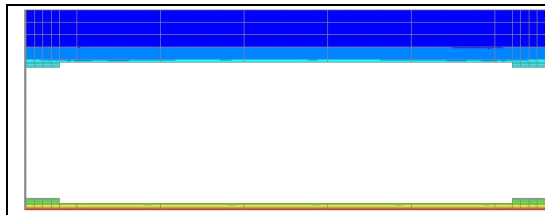


Fig.11 - Temperature field of protected floor modeled section, S4.

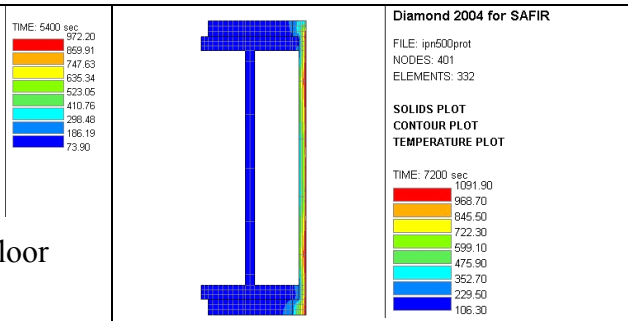


Fig.12 - Temperature field of protected intermediate beams, S4.

Figures 13 shows lateral displacement of masonry walls. Protection of intermediate beams reduce the horizontal displacement of the intermediate wall at 2nd floor level to less than 20 mm, which prove to be compatible with acceptable displacements of masonry walls. As shown on figure 14, purlins deflection quickly increases for ISO and S4 when the structure is not protected. This evolution is due to buckling of purlins which are submitted to large axial forces due to restrained thermal elongation. The fire protection reduces purlins temperatures and axial forces remain compatible with purlins resistance. Moreover, this resistance is not much affected by temperature in the case where purlins are protected.

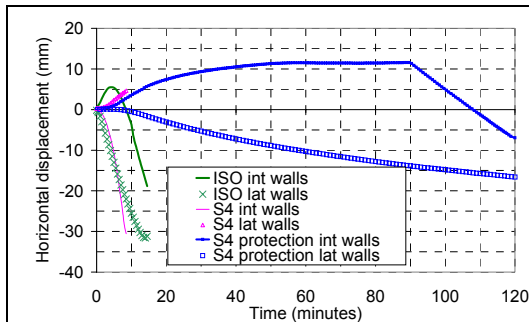


Fig. 13 – Horizontal displacement of intermediate and edge beams (mid span)

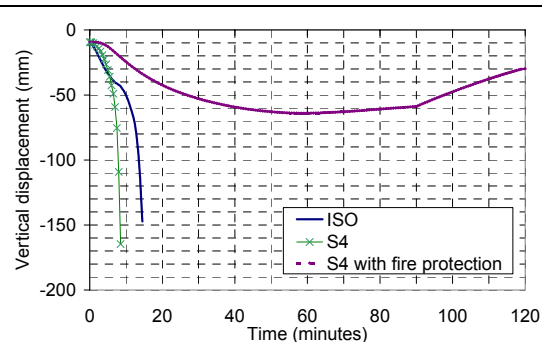


Fig. 14 - Vertical displacement at mid span of purlins

7. CONCLUSION

This study analyzed the fire behavior of an industrial building according to a prescriptive approach with a standard fire (ISO 834) and a FSE approach with more realistic thermal actions. The comparison of the results clearly illustrates the advantages of FSE approach, which enabled to limit fire protection to well-identified and restrained areas. This approach is particularly adapted for building where the quantity of the combustible in each compartment is well identified and remains unchanged throughout the life of the building.

The first very important conclusion is that the real thermal actions can be more dangerous than conventional ISO fire. Consequently, the prescriptive approach is not always safe. On the contrary, for compartments where the real thermal actions are rather low, this approach could be considered as an unnecessary severe method. In case fire protection is designed according to Standard fire, protection measurements can be very expensive without satisfying safety requirements for all potential fires in the building. On the other hand, the application of a FSE approach makes an optimization of protection measures costs possible.

Nevertheless, relevant assessment of fire scenarios is of major concern in ensuring a satisfying security level for buildings.

Secondly, the acceptability criterion about the masonry walls deformations which ensure the containment of the building is defined by conventional tests. This criterion is used to design the fire protection needed for steel frame elements in order to limit the displacements of the concrete blocks inserted between them. The containment requirement has proved to be more severe than the structural stability of the frames.

8. REFERENCES

- [1] "Arrêté du 22 Mars 2004 relatif à la résistance au feu des produits, éléments de construction et d'ouvrages" - *Ministère de l'intérieur, de la sécurité intérieure et des libertés locales, France* – 2004
- [2] Curtat M. - "Modélisation du feu de local - Contribution du CSTB à l'action FIS : le logiciel FISBA (Feu et Incendie Simulés dans un Bâtiment)" - *Revue générale de Thermique* (now *International Journal of Thermal Science*) - tome 27 n°:315-316 - 1988
- [3] Franssen, J-M., Kodur, V.K.R. and Mason, J. "User's Manuel for SAFIR : A computer Program for Analysis of structures Submitted to Fire", *International Report SPEC/2000_03*, 2000, University of Liege, Ponts et Charpentes, Belgium, 2000.
- [4] Eurocode 0 Part 1.1: Basis of Structural Design, prEN 1993 1-1, July 2001.
- [5] Eurocode 2: Design of concrete structures, Part 1.2: General rules structural fire design", prEN 1993 1-2, mars 2004
- [6] Eurocode 3: Design of steel structures, Part 1.2: General rules structural fire design, prEN 1993 1-2, June 2004.
- [7] Eurocode 1: Actions on structures, Part 1.2: General actions – Actions on structures exposed to fire, EN 1991-1-2.



FIRE SAFETY ENGINEERING ANALYSIS OF A SINGLE STOREY FRAMED BUILDING BASED ON STRUCTURAL GLOBAL BEHAVIOUR

J. de LA QUINTANA¹, J. GRIJALVO², F. REY³, and J. UNANUA⁴

1. INTRODUCTION

A new regulation for fire safety in industrial buildings came into force in Spain in January 2005. This regulation prescribes high periods of fire resistance for structures resulting necessarily in the need to protect steel structures with passive protection systems. This fact renders the steel structures less competitive than concrete for industrial buildings. FSE may be a mean to overwhelm the difficulties posed to steel structures by providing information about structural behaviour in case of fire.

LABEIN-Tecnalia has developed a FSE study for a steel industrial hall producer, PRADO T.M., with the aim of analysing the behaviour of their model structure in case of fire.

2. CASE STUDY

A real representative steel industrial hall was chosen for the FSE analysis. The hall is a single storey framed building without beams for a bridge crane; the distance between frames is 10 meters. The frames are pinned on their connection with the foundations and are composed of class 4 variable sections. The connections of the beam and the columns are welded/ built in ones. Secondary structural elements play an important role in the structural stability of the frames (purlins, bracing system and

¹ Head of Fire Safety Engineering and Steel structures dept., LABEIN-Tecnalia, C/ Geldo – Edificio 700. Parque Tecnológico de Bizkaia, E – 48160 Derio, Spain
email: jq@labein.es

² Research Assistant, Fire Safety Engineering and Steel structures dept., LABEIN-Tecnalia, C/ Geldo – Edificio 700. Parque Tecnológico de Bizkaia, E – 48160 Derio, Spain

³ Research Assistant, Fire Safety Engineering and Steel structures dept., LABEIN-Tecnalia, C/ Geldo – Edificio 700. Parque Tecnológico de Bizkaia, E – 48160 Derio, Spain

⁴ Research Assistant, Fire Safety Engineering and Steel structures dept., LABEIN-Tecnalia, C/ Geldo – Edificio 700. Parque Tecnológico de Bizkaia, E – 48160 Derio, Spain

tension members used to connect the purlins with the compressive flange of the beams in the hogging bending moment length).

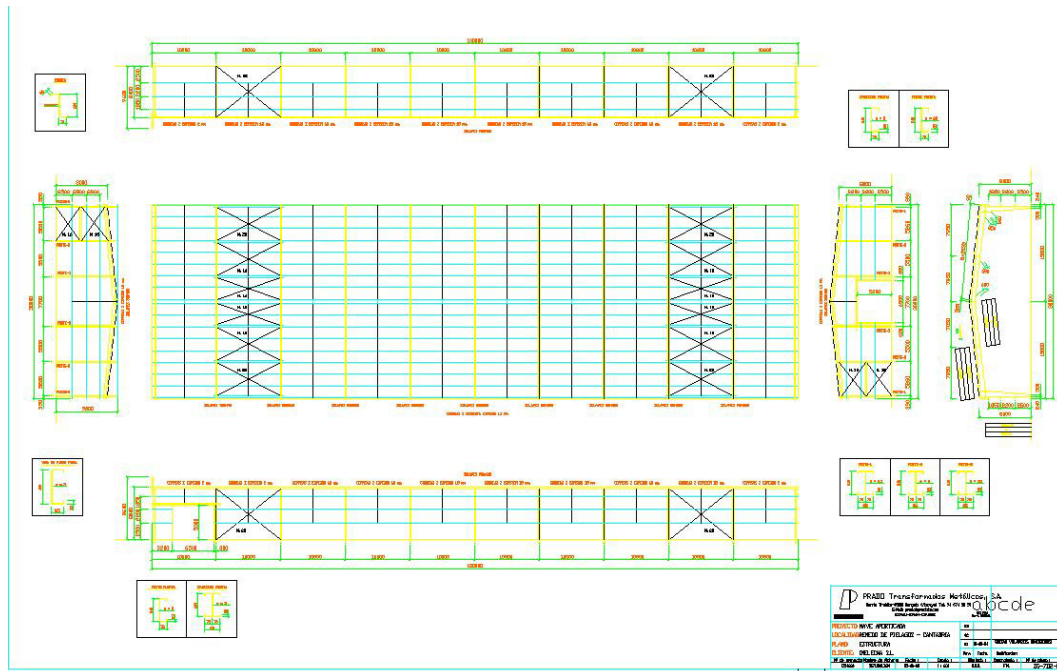


Fig. 1 General drawing of the PRADO T.M. industrial hall.

The structure was conceived to support wind, snow and dead loads. There is no live load to be supported by the steel structure. The wind and snow loads were not considered to verify the structural response in case of fire as the Eurocodes propose; therefore, the only action considered is the dead load.

Some steps were done to reach the final goals of the project. Firstly an analysis of the structural response under standard exposure (ISO curve) was carried out, and later it was also analyzed the structural response under natural fire conditions. The structural response was analyzed with the non-linear finite element code Abaqus. In both cases, firstly an analysis of a single frame was done to obtain information about potential failure modes and later a simulation of the whole structure (ten frames and secondary elements) to ascertain the global behaviour of the hall.

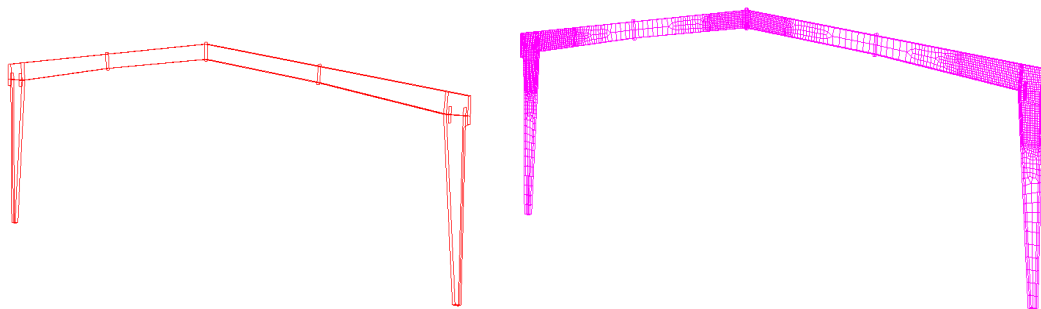


Fig. 2 Modelling of structure members.

As the frames are composed of class 4 sections, they were modelled with shell elements. The density of the mesh was not uniform and it was enhanced in the regions of the frame likely to develop hinges

due to local buckling failures. The secondary members were modelled with 3D beams and in case of the bracing members with truss elements.

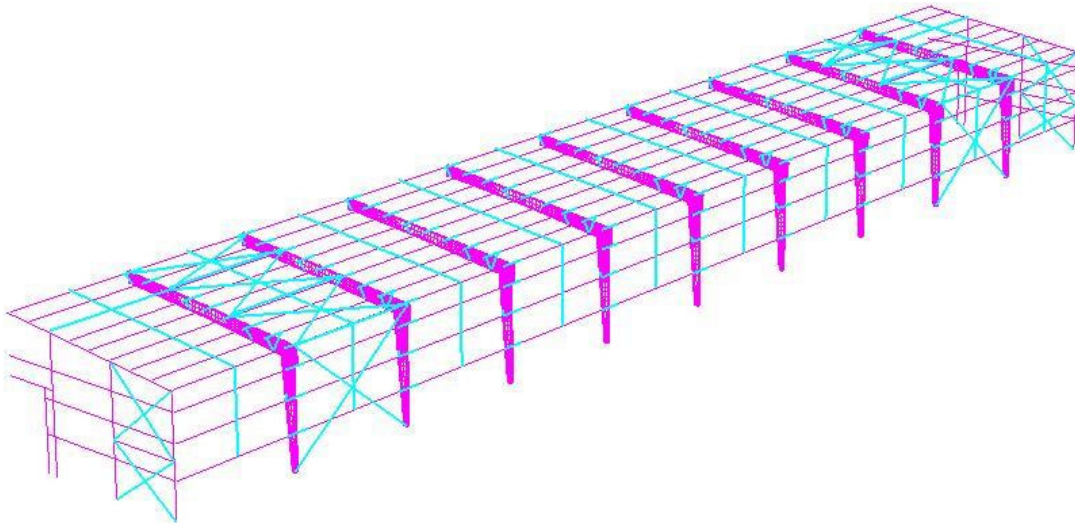


Fig. 3 Modelling of 3D structure.

2.1 Analysis of the structure submitted to the standard exposure curve.

A single frame was analyzed. The temperature rise within the structure was obtained solving the conduction within the steel sections in the shell model of the frame; the standard time – temperature curve was given as a boundary condition.

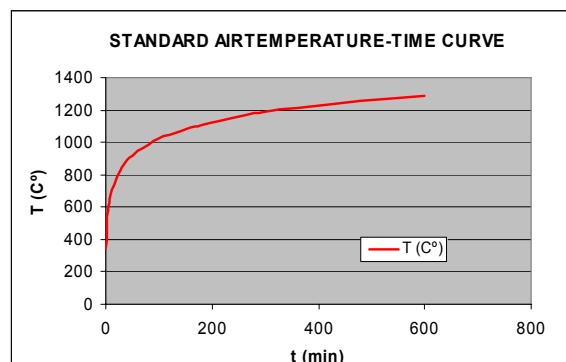


Fig. 4 ISO curve. Temperature – time.

In a first simulation, they were introduced global and local imperfections, and later one simulation was performed neglecting them and another one considering only half a frame with symmetry boundary condition and without imperfections. As the results did not differ too much, it was decided to neglect

in the model the imperfections; their effect is negligible by comparison with the thermal induced actions. This conclusion matches with some references of other FSE studies.

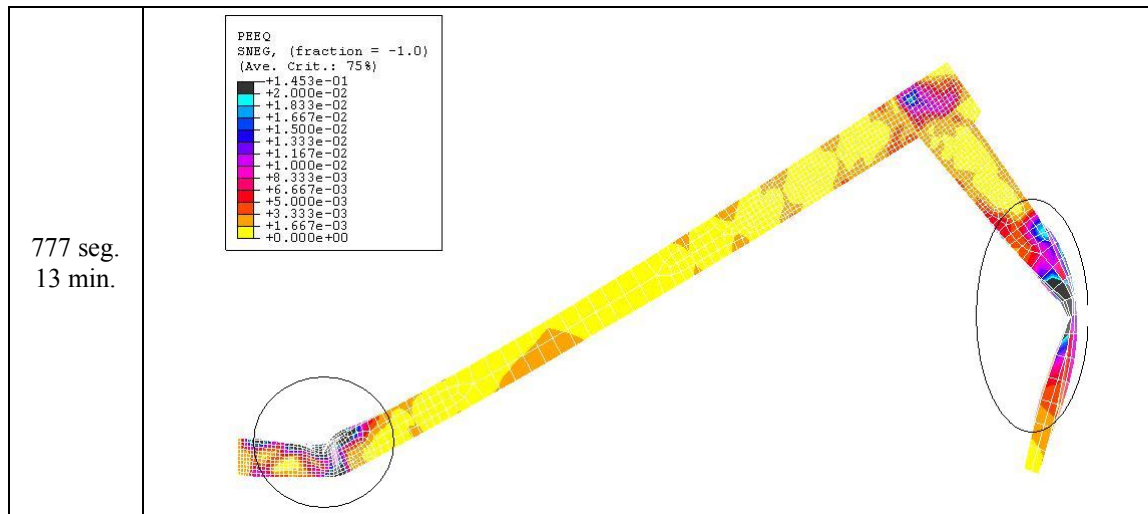


Fig. 5 Failure time and mode. Structure submitted to ISO curve fire.

2.2 Analysis of the structure submitted to natural fire.

The structure was analyzed considering thermal action due to natural fire. Two different fire scenarios were considered depending on the origin of the fire, in one case, fire was ignited far from the façade and in other case fire was developed near the façade, engulfing directly a column. In the case of the fire beginning by the centre of the hall, the zone model Ozone was used to calculate fire evolution.

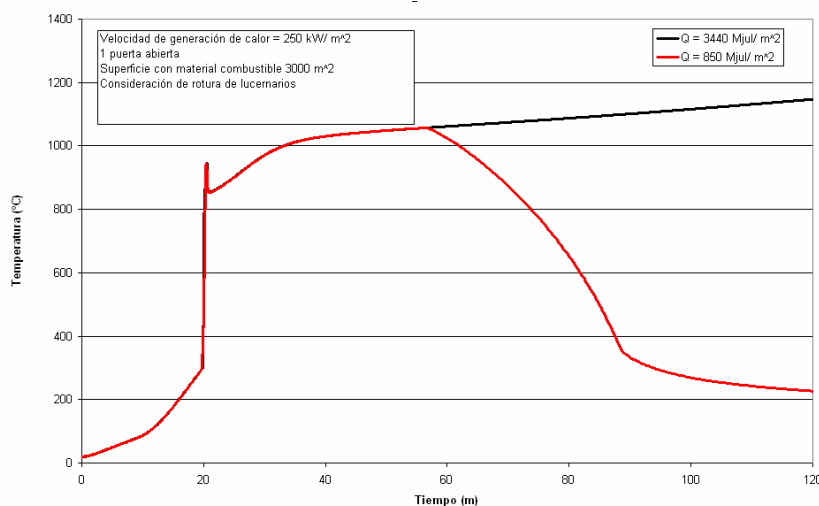


Fig. 6 Gas temperature.

During the first stage of the fire, it was considered to create a two layer distribution in the hall, a hot upper one representing the smoke accumulated under the ceiling heating beams and upper parts of the column and a cold lower one affecting the lower part of the columns. In case of fire near a column, the temperature evolution within the steel sections was calculated considering localized effect of the flame on the column.

In case of fire beginning in the centre of the hall, the collapse occurred after the onset of flash – over. Two different growing phase velocities were simulated. It was concluded that, although the structure collapses, it happens in safe conditions, when collapse occurs, the environment inside the hall is untenable neither for occupants nor firemen and the failure mode is inwards, preventing firemen outside the building from being trapped by debris.

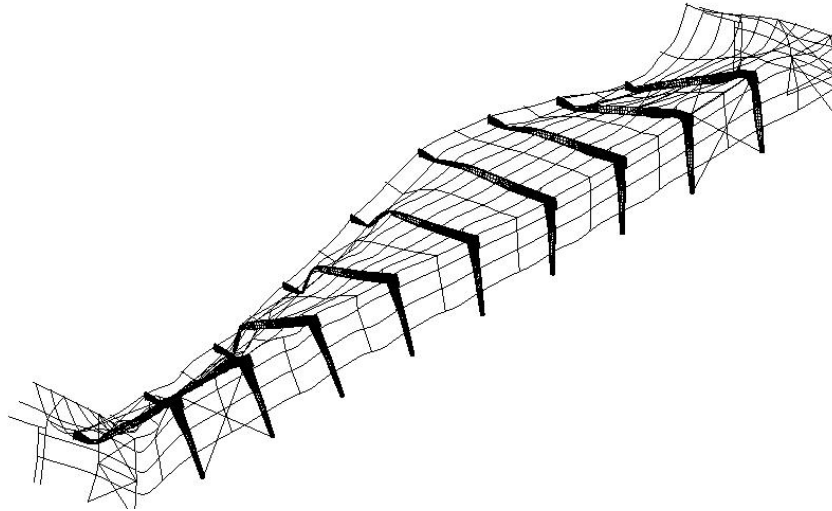


Fig. 7 3D structure failure mode. Submitted to natural fire.
A real fire in a similar industrial hall occurred accidentally showing exactly this predicted behaviour.



Fig. 8 Real case fire in a similar industrial hall.

In case of localized fire in the column, only one frame was simulated. In this case, the collapse of the frame occurred before the onset of flash – over, and it was outwards, endangering the people outside the building. It was recommended to protect columns with passive protection systems to prevent that failure mode because it is a common practice in industrial halls to accumulate significant fire load leaning on the façade.



Fig. 8 Local collapse of un-protected column.

3. CONCLUSIONS

In conclusion, this analysis shows that the considered steel structure provides an acceptable level of safety on the basis of a performance based approach if localized passive protection is applied rather than the costly protection prescribed by the regulation.

This way the resultant safety of the building has been assessed in a technical and cost-effective way resulting in gaining a good competitive position for the product.



A REAL FIRE IN SMALL APARTMENT – A CASE STUDY

Valdir Pignatta e SILVA¹, Ricardo Hallal FAKURY²,
Francisco Carlos RODRIGUES² and Fabio Domingos PANNONI³

ABSTRACT

Although natural fire is allowable by Brazilian standards of the fire safety design, there are not any specifications to appliance to the ordinary buildings constructed with the typical construction and structural materials from Brazil. This paper describes the behavior of a cold formed steel framed structure in response to a real fire occurred in a residential apartment, on 3rd January, 2002. A set of residential buildings that constructed in 1995 in Limeira city, State of Sao Paulo, Brazil, is composed by four identical four-storey blocks of eight apartments per floor housed by poor people; each apartment has 44.3 m² of total area, including two bedrooms, one living room, bathroom and kitchen. The structure and masonry were built, respectively, by cold formed steel and ordinary bricks. The Brazilian Code allows this type of buildings be neglected from structural checking in fire situations.

The fire has started in a little Christmas tree into an apartment on the fourth floor. Although the fire had been developed without any restraint, nothing spread to the neighboring apartments occurred, and not even the damaged structure presented risks of global or partial collapse. In this case study, a real fire in a residential apartment was modeled, as well the structural fire resistance; the maximum fire temperature reached during the burning on the structural material was assessed by metallographic tests and computational modelling, to the further comparative analysis between the theoretical and actual results.

¹ Professor, Polytechnic School of the University of Sao Paulo, Department of Structural and Geotechnical Engineering, Av. Prof. Almeida Prado, trav2, n271, CEP 05508-900, Sao Paulo, Brazil
email: valpigss@usp.br

² Professor, Federal University of Minas Gerais, Department of Structural Engineering, Av. Contorno, n842, 2º andar, CEP 30110-060, Belo Horizonte, MG, Brazil
email: fakury@dees.ufmg.br, francisco@dees.ufmg.br

³ Specialist Engineer, Ph.D.. Gerdau Acominas S.A., Rua Cenno Sbrighi, 170, 2º andar, Ed. II, CEP 05036-010, Sao Paulo, SP, Brazil
Email: fabio.pannoni@gerdau.com.br

A CFD scenario, representative from the actual building geometry, materials and fire behavior was modeled by means of the software SMARTFIRE. Details of the fire scenario as actual fire load, material composition and location of the furniture imputed to the modeling were obtained from the apartment's owner and measurements taken during the site inspection; after that, a steel thermal analysis in fire situation was conducted by means the software Supertempcalc, and the structural analysis of the steel frame was performed according to the expressions recommended by the Brazilian Standard for design of cold formed steel for room temperature, similar to AISI/USA, but using the strength reduction factors recommended by Eurocode 3 part1.2.

1. INTRODUCTION

Although the Brazilian population density is not to be big (180 million inhabitants for 8,5 million m²), it experiences a massive people migration to the biggest cities, in the search for a job. Most part of these people, due to their very poor economic conditions, join or create what we call “favela” (shantytown). An alternative to reduce this situation is the construction of low-cost buildings. The cost reduction is gotten in detriment of requirements as comfort and safety, but, still, such requirements are sufficiently superior to those found in the “favela”. The Brazilian regulation allows that, buildings of social interest, with limited total area and height, can dispense structural verification in fire situation. These residential buildings are, most of all, an assemblage of small area apartments, separated by concrete or ceramic blocks. The inherent low fire load, the structure partial protection against fire and compartmentation, while imperfect, allows intuit that the safety is not very harmed in these cases.

The four storey steel framed building “Conjunto Habitacional Juscelino Kubitschek” (Fig. 1), conceived as of social interest, was erected in 1988, in Limeira city (State of Sao Paulo). It constitutes four identical blocks, two by two. Each block has four floors, with eight apartments per floor. These apartments are very simple, have 44.29 m² total area, and contain two bedrooms, a living room, kitchen, a bath-room and a small service area. The building has a steel cold formed structure (Fig. 2).



Fig. 1 – Conjunto Habitacional Juscelino Kubitschek.



Fig. 2 – Column and beams view.

In January 2002, a fire started in the fourth floor apartment, and despite the fire not had been effectively controlled, even so, the fire didn't spread to other apartments. The fire destroyed all living room furniture and covering. The family who slept in the bedrooms was saved, and part of all inner masonry was demolished in the after fire due to small cracks and fissures. The fire didn't damage the steel structure. This real fire allowed to the authors to face a more scientific evaluation of the fire effects. This paper describes the analysis

conducted and presents the main conclusions, taking as reference the real situation found at the end of the fire after.

2. THE BUILDING STRUCTURE

As seen on Fig.3, cold formed steel were used for columns and beams (i.e., box-sections). Columns, 200 mm high x 100 mm width were constructed using two U shapes (200 x 50 x 30 x 5,0), fillet welded all around the sections. All the beams had the same external dimensions, and were constructed with two U shapes (200 x 50 x 15xt, welded the same way. The structural elements didn't use any traditional fire protection, but they can be considered partially protected by a 100 mm masonry (concrete blocks plus a mortar-based cover), according Fig. 4. A concrete/ceramic composite slab was used, with 70 mm thickness + 50 mm top cover + 20 mm undercover, resulting in a 140 mm composite deck.

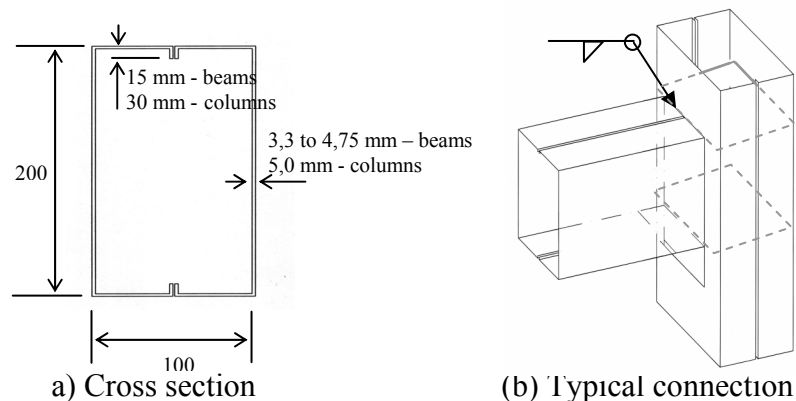


Fig. 3 – Beams and columns.

3. THE FIRE AND ITS CONSEQUENCES

The building plant can be seen on Fig. 4, and gives an idea of the furniture arrangement, and the place where the fire started, as assumed by the Firemen Dept. Report⁽¹⁾. The composite slab started to degrade just close where the fire initiated (Fig. 5). The steel structure didn't collapse and showed any visible damage. Masonry cover showed some local spalling, as can be seen on Fig. 5, but, in general, there were no cracks or fissures on the walls neither on the slabs, so, compartmentation was maintained. The fire didn't spread to bedrooms or bath-room, however, the smoke production was intense; the reason was due to compartmentation, although imperfect, was efficient.

4. METALLOGRAPHIC ANALYSES

The original structural design was not found, then samples (300 mm x 60 mm) were taken off from living room's column and beams, for metallographic and tensile tests. The objectives were to obtain steel's chemical composition and follow any tensile reduction. One sample, A1, is representative of cold regions (it was protected by walls in four sides, and the original paint was intact after wall demolition) and served as a reference to the others (Figs. 6 and 7).

Table I gives the sample's chemical composition, and Table II shows the measured tensile properties. It can be shown that it was used a high strength low alloy steel containing Copper and Chromium, that is, a weathering steel.

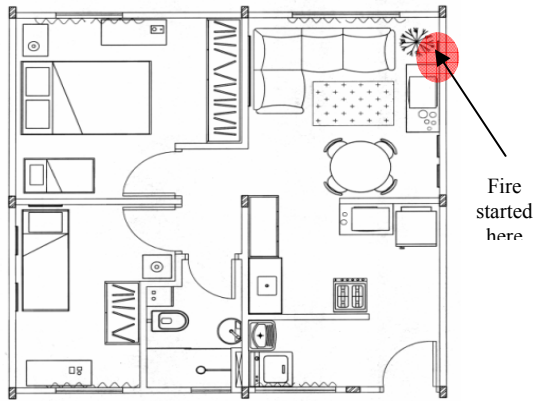


Fig. 4 – Apartment's plant with furniture, Fig. 5 – Composite slab damage detail.
showing where the fire started.

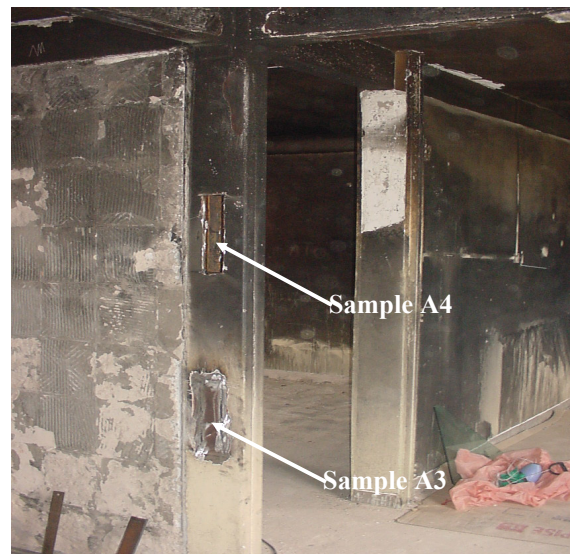
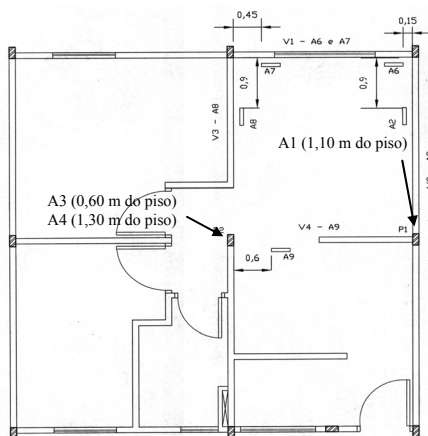


Fig. 6 – Samples positioning.

Fig. 7 – Central column .

The micrographs reveal a perlitic-ferritic structure, very typical for a structural grade steel. It can be seen a very thin layer of decarburized steel, caused by the reducing atmosphere along the fire. For most hot rolled shape production, final rolling occurs when the steel is about 870°C or higher, depending the mill procedures. Austenite is the metallographic structure, that is transformed into ferrite and pearlite along cooling to ambient temperature.

The Iron-Carbon diagram can be used to foresee the steel phases changes. The diagram has three invariant points of witch only one is relevant to the present study. This is known as the eutectoid point and occurs at 0,8% carbon and 723°C. At this stage austenite will begin to transform to a constituent known as pearlite which consists of alternate plates or lamellae of ferrite and cementite.

The temperatures at which transformations take place are known as the critical temperatures. Thus, the eutectoid temperature, A1, is 723°C. If the steel temperature doesn't exceed, for some time, this temperature, we expect that steel mechanical properties will be acceptable.

Table 1 – Sample's chemical composition.

Element	A1 (cold)	A2	A3	A4	A6	A7	A8
%C	0,119	0,117	0,108	0,112	0,114	0,106	0,106
%Mn	0,432	0,398	0,394	0,398	0,398	0,395	0,386
%P	0,094	0,096	0,099	0,104	0,096	0,093	0,086
%S	0,012	0,008	0,013	0,014	0,008	0,007	0,006
%Si	0,453	0,437	0,480	0,493	0,435	0,426	0,415
%Al	0,045	0,060	0,056	0,057	0,060	0,059	0,058
%Nb	0,013	0,015	0,015	0,015	0,015	0,015	0,014
%V	0,006	0,005	0,006	0,006	0,005	0,005	0,005
%Ti	<0,005	<0,005	<0,005	<0,005	<0,005	<0,005	<0,005
%Cu	0,204	0,200	0,219	0,215	0,199	0,200	0,201
%Cr	0,869	0,848	0,890	0,896	0,844	0,841	0,830
%Mo	<0,005	<0,005	<0,005	<0,005	<0,005	<0,005	<0,005
%B	0,0001	0,0001	0,0001	0,0001	0,0001	0,0001	0,0001
%Ni	0,013	0,013	0,012	0,012	0,013	0,013	0,013

Table 2 - Tensile properties for the test specimens.

Sample	Properties				
	Yield strength (MPa)	Ultimate Strength (MPa)	Elongation, % (200 mm)	Decarburizing thickness (μm)	Grain size (ASTM)
1	402	529	30	50	11
2	394	517	29	200	11
3	400	525	32	120	11
4	389	507	31	120	11
6	444	557	27	40	11
7	445	558	27	Nil	11
8	406	533	28	150	11

The residual mechanical properties, after cooling to ambient temperatures, will be the same as in the pre-fire condition. Smith et al⁽²⁾ and Kirby et al⁽³⁾ give experimental data for structural steels submitted to different heating – cooling cycles. Any temperature rise between 720 °C and 870 °C has a low impact on steel's mechanical properties after cooling to ambient temperatures. Any heating beyond these values will cause a permanent transformation, resulting in a grain growth, and, sometimes, in hardening that, with the cooling, will affect adversely the residual mechanical properties. Tests carried on seven samples didn't reveal any significant change on microstructure; the same is valid for the tensile properties. This permits us to affirm that structural components were not heated to temperatures up to 870°C. It was clear the existence of an original adherent mill scale on the central column, a strong indication that temperatures were below 550°C. Samples took from beams showed a much more rougher surface, indicating a temperature range from 650°C up to \approx 720°C.

5. COMPUTATIONAL FLUIDS DYNAMICS BASED ON THE SOFTWARE SMARTFIRE

An educational version of the SMARTFIRE V4.0⁽⁴⁾ software, developed by the Fire Safety Engineering Group at the University of Greenwich, was used to perform the fire simulations in this study, with a special feature developed particularly for this project. This

included a simultaneous capture of temperatures data from selected control volumes specially positioned along the structure.

SMARTFIRE is an open architecture CFD environment written in C++; it has four major components: a CFD numerical engine, a graphical user interface, an automated meshing tool and an intelligent control system. It permits to simulate a fire, in a fast and confident way. It uses three-dimensional unstructured meshes, enabling complex irregular geometries to be meshed without the recourse of cruder methods such as the stepped regular meshes or body-fitted meshes. The first step was to introduce the scaled apartment ambient that is materials, fire characteristics, etc. Walls, slabs, apertures, fuels, were all introduced in the model. Some control volumes were introduced, in a way of capture the gas temperatures (along time) facing the samples we took for analysis (Fig. 8). In the following, it was created a CFD mesh with more than 105,000 tetrahedron elements. We started the fire on the TV rack (as proposed by the Fire Dept. Report), propagating to a Christmas tree and, then, to a sofa. Some items were not included (as the living room curtain), for simplicity. The peak heat output inputs were 15.65 MJ for the sofa, 7.84 MJ for the Christmas tree, and 5.37 MJ for the TV rack; details were presented before by Pannoni et al.⁽⁵⁾. Objects burns were triggered, so some trigger volumes were constructed to activate the other fire, and so on. We created two trigger condition to ignite the fire: 573K OR maximum radiation Y negative flux greater than 22000W/m^2 (the radiant flux down onto the object from the hot gases, in the ceiling layer – the most common mechanism for remote objects to be ignited). It was assumed the six-flux radiation model, and for turbulence, the K-Epsilon model. Simulation results are represented, synthetically, in Fig. 9 and 10. Maximum temperatures were obtained in the control volume located over the steel sample located at V1, that is, in the top of window. Minimum temperatures were obtained in the control volume close to sample A3, that is, in the lower part of the central column. In a general way, higher temperatures were obtained with times around 25 – 26 minutes from the fire beginning.

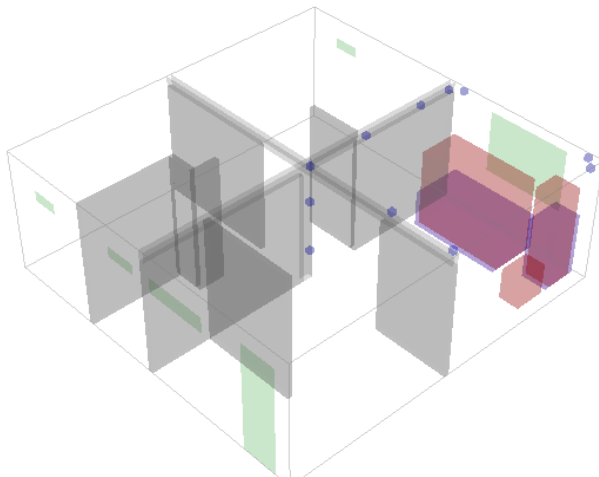


Fig. 8 – SMARTFIRE graphical interface, showing volume controls.

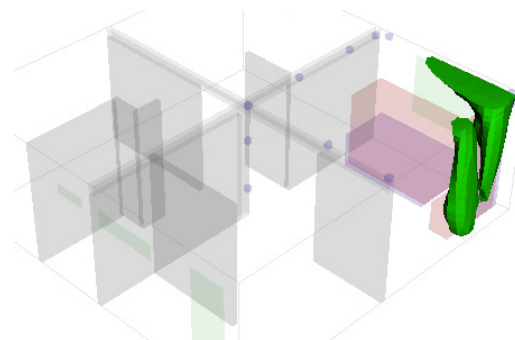


Fig. 9 – SMARTFIRE fire scenario after 2 minutes.

It is important to point out that, while the inner doors were all opened, compartmentation was very effective. Fig. 11 shows a plane for a 5 minute scenario; temperatures around 190°C were obtained inside the bedroom ($\approx 2\text{ m}$ height). Fig. 12 shows the gas temperatures close the central column and beam (the most heated one).

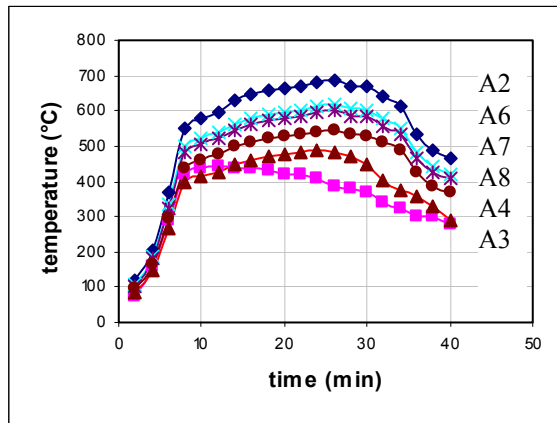


Fig. 10 – CFD temperature estimate, using specific control volumes.

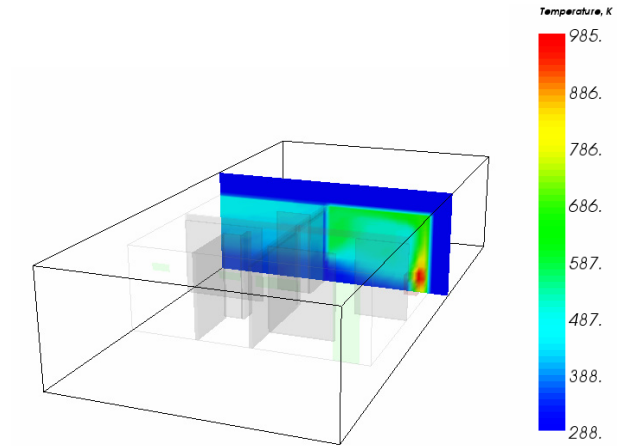


Fig. 11 – Compartmentation effect over temperature distribution, 5 min scenario.

If it was used traditional method, ISO-Fire⁽⁶⁾, the section factors would be 147 m^{-1} and 208 m^{-1} , respectively, for column and beam, or approximately 600°C and 655°C for 15 min and 780°C and 815°C for 30 min.

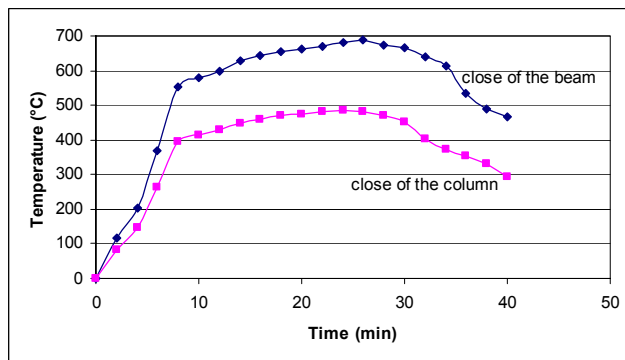


Fig. 12 - Gases temperature based on the SMARTFIRE.

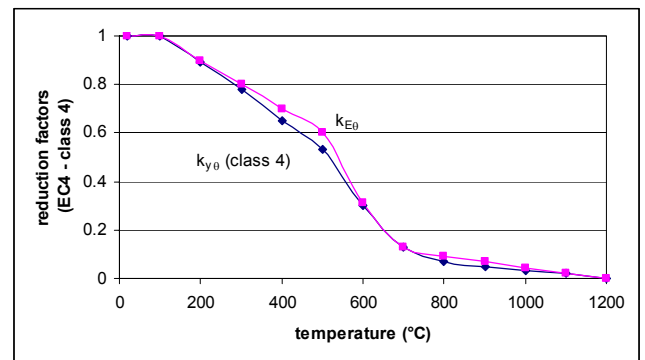


Fig. 13 – Reduction factors of the steel.

6. THERMAL ANALYSES BASED ON THE SOFTWARE SUPERTEMPCALC

The reduction factors of the steel for strength and modulus of elasticity were presented in the Fig. 13. The total emissivity for steel, concrete or masonry was considered as 0.7. The density for masonry and concrete, were considered, respectively, as 1600 and 2300 kg/cm^3 . It was considered moisture content of 1.5 % of concrete weight; other thermal parameters from EC 2⁽⁷⁾, EC 3⁽⁸⁾ and OZONE⁽⁹⁾.

Column and a 10 cm thick normal brick temperatures (facing one side) were obtained using the software Supertempcalc⁽¹⁰⁾ (for convection, radiation and conduction) with ISO and Natural fires, based on item 5, Fig 12 (Figs. 13 and 15). The equivalent temperature is the uniform temperature that causes the same resistance to normal force (Figs. 14 and 16 and Table 3).

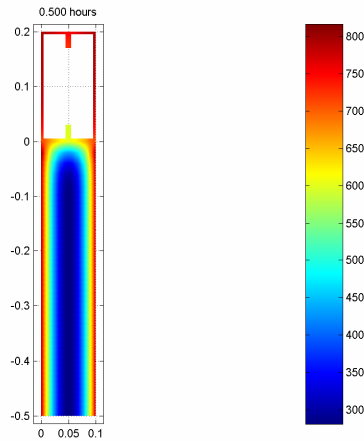


Fig. 13 - Temperature at 30 min on the central column and wall (ISO-Fire).

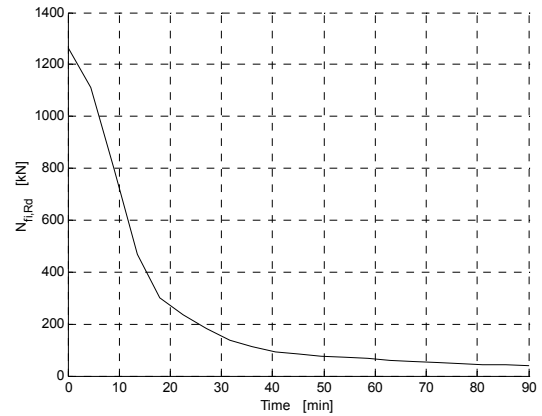


Fig. 14 - Resistance to normal force vs. time on the column with wall, where $N_{fi,Rd} = A f_y k_{y,\theta}$ (ISO-Fire).

Table 3 - Equivalent temperature for the column – ISO-Fire

Time (min)	$k_{y,\theta}$	Equivalent temperature (°C)
0	1	20
4.56	0.881642	207.86
9	0.632318	415.82
13.56	0.372497	588.98
18	0.239644	613.68
22.56	0.185231	629.94
27	0.145084	661.73
31.56	0.109844	715.99
36	0.088712	765.90
40.56	0.073862	810.99
45	0.065033	842.34

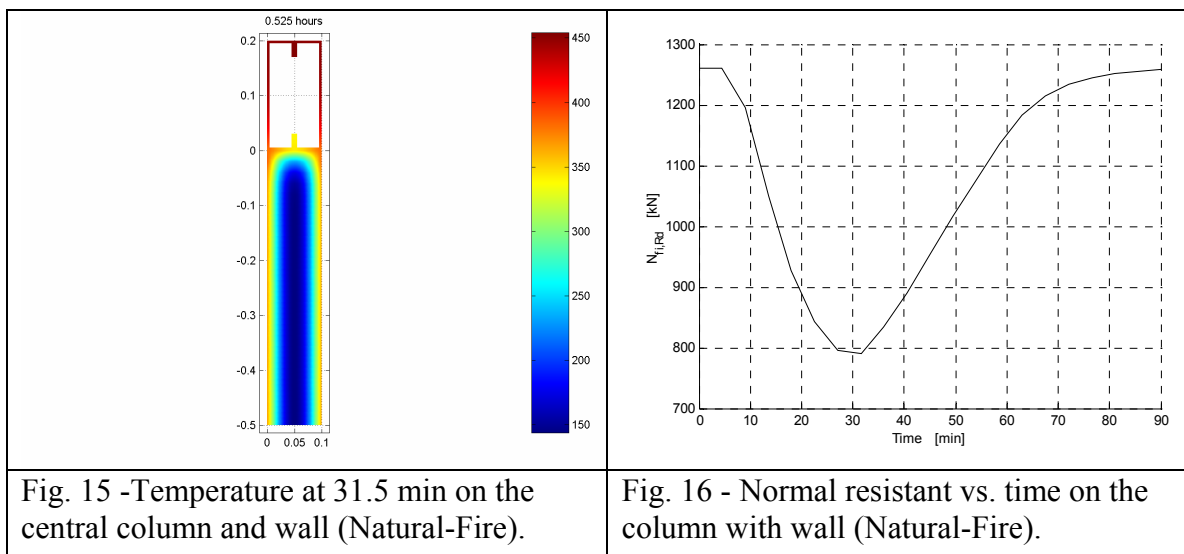


Fig. 15 -Temperature at 31.5 min on the central column and wall (Natural-Fire).

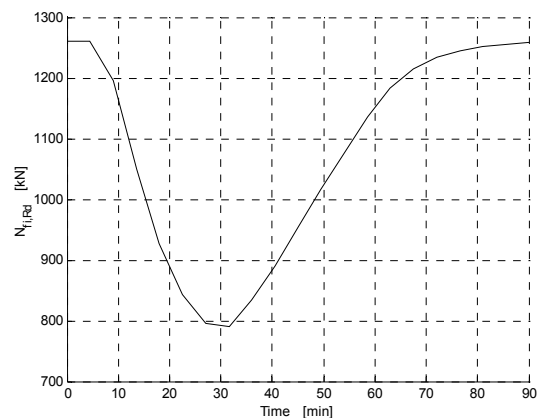


Fig. 16 - Normal resistant vs. time on the column with wall (Natural-Fire).

At 31.5 min the steel temperature that causes the same resistance to a normal force is equivalent to a uniform temperature 382.5 °C (reduction factor equal 0.675).

The temperatures of the beam under the slab (Figs. 17 and 19) were determined by thermal analyses using the software Supertemcalc (convection, radiation and conduction) with ISO and Natural fires. The equivalent temperature is the uniform temperature that causes the same resistance to bending moment (Figs. 18 and 20, and Table 4).

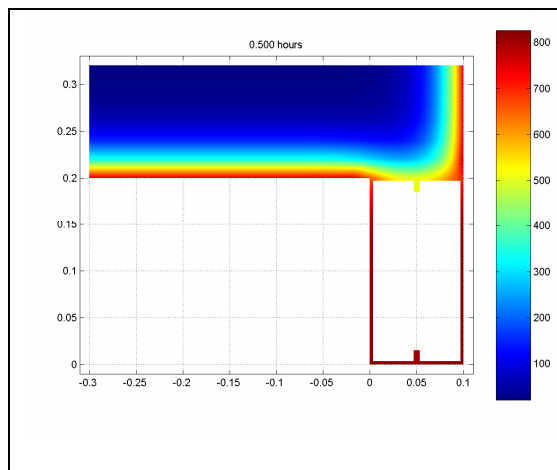


Fig. 17 - Temperature at 30 min on the beam under a slab (ISO-Fire).

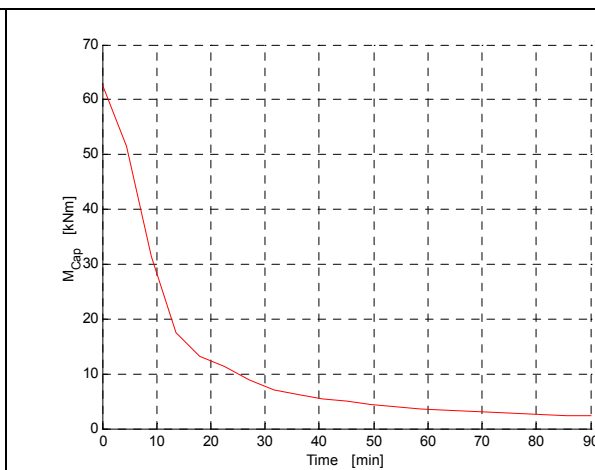


Fig. 18 –Resistance to bending moment vs. time on the beam under a slab (ISO-Fire).

Table 4 - Equivalent temperature for the beam – ISO-Fire

Time (min)	Reduction factor	Equivalent temperature (°C)
0	1	20
4.56	0.82	267.07
9	0.5	518.04
13.56	0.279	608.81
18	0.211	619.86
22.56	0.18	632.79
27	0.143	664.12
31.56	0.114	707.88

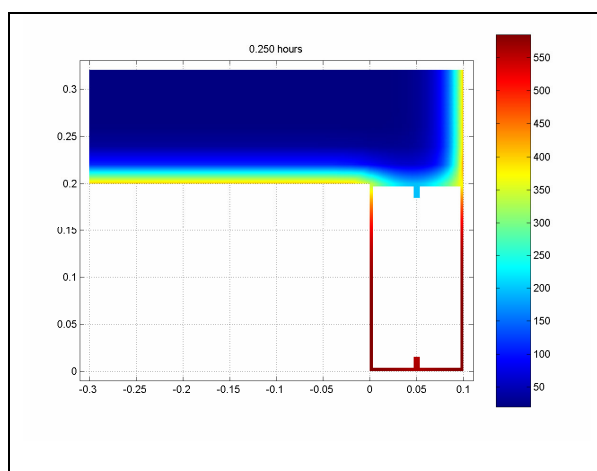


Fig. 19 - Temperature at 30 min on the beam under a slab (Natural-Fire).

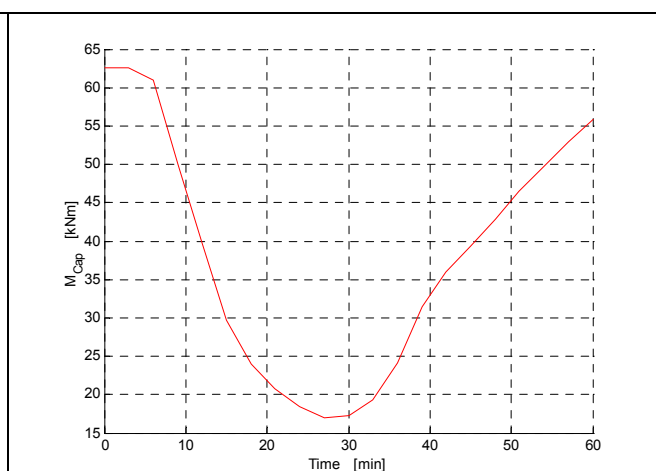


Fig. 20 – Resistance to bending vs. time on the beam under a slab (Natural-Fire).

At 27 min the steel temperature that causes the same bending moment resistant is equivalent to a uniform temperature 610 °C (reduction factor equal 0.27).

7. STRUCTURAL ANALYSES

The complete tri-dimensional building structure was modeled including all 4-blocks, slabs simulated as diaphragm with infinite stiffness in its plane, and with zero stiffness in the perpendicular plane. All connections between columns and beams and foundations were considered fixed in both directions. (Figs. 2 and 3). The structural analysis was done using the software SAP 2000⁽¹¹⁾, with accidental combination of loads recommended by NBR 14323^(12, 13):

$$F_{fi,d} = \sum_{i=1}^n \gamma_{gi,fi} F_{Gi,fi,k} + F_{Q,exc} + \psi \sum_{j=1}^m \gamma_{qj,fi} F_{Qj,fi,k} \quad (1)$$

Where:

$F_{fi,d}$ – design value of action in fire

$F_{Gi,fi,k}$ – characteristic value of permanent action i in fire

$F_{Qj,fi,k}$ – characteristic value of variable action j in fire

$F_{Q,exc.}$ – characteristic value of thermal (exceptional, accidental) action, generally equal zero in the presence of gravitational load and ISO-Fire

$\gamma_{gi,fi} = 1,2$ - partial safety factor for permanent action i in fire

$\gamma_{qj,fi} = 1,0$ - partial safety factor for variable action j in fire

$\Psi = 0.2$ for places where there is neither predominance of weights of equipment that remains fixed for long periods of time, nor of people concentration.

$\psi = 0.0$ for wind loads

The dead loads were pre-casted slab concrete/ceramic 120 mm thick and wall with normal brick 100 mm thick. The considered live loads were 1.5 kN/m² on the floor, 0.5 kN/m² on the ceiling and 3.0 kN/m² on the stairs.

The cold formed steel was verified based on the NBR 14762⁽¹⁴⁾, similar to AISI⁽¹⁵⁾, adapted for the fire situation. This adaptation consisted in including the reduction factors $k_{y,\theta}$ and $k_{E,\theta}$ for class 4 elements from Eurocode 3 – Part 1.2⁽⁸⁾. Besides that, other equations (p. ex. eqs. 2 and 3) recommended by NBR 14323^(12, 13), based on the old Eurocode 3 – Part 1.2⁽¹⁶⁾, were verified using a simplified software developed by Soares⁽¹⁷⁾:

$$\varphi_E = \frac{N_{fi,Sd}}{N_{fi,Rd}} + \frac{M_{x,fi,Sd}}{\left(1 - \frac{N_{fi,Sd}}{N_{ex,fi}}\right) W_{el,x} k_{y\theta} f_y} \leq 1,0 \quad \text{and} \quad \varphi_R = \frac{N_{fi,Sd}}{A k_{y,\theta} f_y} + \frac{M_{x,fi,Sd}}{W_{el,x} k_{y\theta} f_y} \leq 1,0 \quad (2)$$

$N_{fi,Sd}$ - design value of the compression in fire

$N_{fi,Rd}$ - design value of the compression resistance of the gross cross-section, in fire

$M_{x,fi,Sd}$ - design value of the bending moment in fire

$W_{el,x}$ - plastic section modulus

$N_{ex,fi}$ - value of elastic buckling load

A – area

$k_{y,\theta}$ - yield strength reduction factor

f_y – characteristic value of yield strength

$$N_{fi,Rd} = \frac{\rho_{\theta} A_{eff} k_{y,\theta} f_y}{(1 + \lambda_{0,\theta})} \text{ for } 0 \leq \lambda_{0,\theta} < 0.2 \text{ or } N_{fi,Rd} = \frac{\rho_{\theta} A_{eff} k_{y,\theta} f_y}{1.2} \text{ for } \lambda_{0,\theta} \geq 0.2 \quad (3)$$

where:

A_{eff} – area effective of cross section including local buckling effects

ρ_{θ} - reduction factor for flexural buckling for a temperature θ

$\lambda_{0,\theta}$ - reduced slenderness in fire

The compartmentation efficiency and the heat transfer between steel and slab or wall lead to a thermal gradient in the structural elements. That gradient and, consequently, the efforts were not considered in this structural analysis. The actions from the axial deformation and the little minor inertia bending moment were also not considered. By other hand, we used the maximum temperatures from metallographic or thermal analysis as a uniform distribution.

In this paper, we studied the central column with one face protected by a wall and the beam close the window, the hottest region. The column buckling lengths were 2.92 m e 3.68 m. One adopted $f_y = 390$ MPa, minimum value from metallographic.

The column temperature was considered below 550 °C, and it is based on the metallographic tests. As shown by SMARTFIRE and Supertempcalc, the medium temperature was below 400 °C. At this level of temperature, the columns of the 1st and 4th floor have φ_E and $\varphi_R \leq 1.0$, then, there is structural safety based on the hypothesis of this paper. It is possible to notice *in loco* that no failure, global or local, occurred with the column.

The hottest beam temperature ranged 650°C to 723 °C, following metallographic observation. Based on the SMARTFIRE and Supertempcalc, the beam reached a medium temperature of 610°C. For that level of temperature, $\varphi_R \leq 1.0$, i. e., the structures are in fire safety. By simplified design method no collapse would happen, confirmed by actual facts.

Using the curve ISO 834⁽⁶⁾, and determining the equivalent temperature on the beam, based on the Supertempcalc, the beam fire resistance is approximately 30 min, i. e., $\varphi_R \leq 1.0$ for FR = 30 min.

8. CONCLUSION

A small apartment real fire scenario was analyzed. A steel structure, without any fire protection showed inherent resistance. The compartmentation, while imperfect, was made evident. Thermal and structural analysis, by using software (SMARTFIRE, Supertempcalc and others) and metallographic tests were performed. It was concluded by metal analysis that steel components were heated up to temperatures below 550°C for the central column, and around 650°C for the hottest beam. Computational modeling shows “medium” temperatures about 380°C in central column and 610°C along beam. Based on these results, and applying simplified structural analysis, it can be observed acceptable safety levels.

The sequence of this work is already in progress, that is, the study of the inherent fire safety of low-cost, residential buildings, without the traditional application of fire protection products.

9. REFERENCES

- [1] Corpo de Bombeiros da Polícia Militar do Estado de São Paulo (State of Sao Paulo Firemen Dept.). Certidão de Sinistro n.015/130/03, expedido pelo 16º GB – 1º SGB – 3º/4º PB, Limeira, State of Sao Paulo. Brazil. 2003.
- [2] Smith, C.I., Kirby, B.R., Lapwood, D.G., Cole, K.J., and Cunningham, A.P., “The Reinstatement of Fire Damaged Steel Framed Structures”, British Steel Corporation, Teeside Laboratories. United Kingdom. 1980.

- [3] Kirby, B.R., Lapwood, D.G. and Thomson, G., “The Reinstatement of Fire Damaged Steel and Iron Framed Structures”, British Steel Corporation, Swinden Laboratories. United Kingdom. 1986.
- [4] Ewer, J., Jia, F., Grandison, A., Galea, E. and Patel, M., “SMARTFIRE V4.0 User Guide and Technical Manual”, Fire Safety Engineering Group, University of Greenwich, UK, 2004.
- [5] Pannoni, F.D., Silva, V.P., Fakury, R.H., and Rodrigues, F.C., “Simulation of the Dynamics of the Fire at 41 Angelo Perillo Road, Limeira, Brazil, 2002”, Proc. XXVI Iberian Latin-American Congress on Computational Methods in Engineering – CILAMCE 2005, Guarapari, ES, Brazil, 19th – 21th October 2005.
- [6] International Standardization for Organization - Fire-resistance tests - Elements of building construction. ISO 834. Genève, 1994.
- [7] European Committee for Standardization. Eurocode 2: Design of concrete structures - Part 1-2: General rules - Structural fire design part 1.2. Brussels. 2004.
- [8] European Committee for Standardization. Eurocode 3: Design of steel structures - Part 1-2: General rules - Structural fire Design. Brussels. 2005.
- [9] Cadorin, J. F; Franssen, J. M. Software OZONE V 2.2. Liège. 2002.
- [10] Anderberg Y. SUPER-TEMPCALC. A commercial and user friendly computer program with automatic FEM-generation for temperature analysis of structures exposed to heat. Fire Safety Design. Lund; 1991. and TCD 5.0. User’s Manual. Fire Safety Design. Lund. 1997.
- [11] SAP 2000 Nonlinear. Version 8.2.7, Computers and Structures, Inc., Berkeley, CA, USA. 2003.
- [12] NBR 14323. Dimensionamento de Estruturas de Aço de Edifícios em Situação de Incêndio (Steel fire design) ABNT - Associação Brasileira de Normas Técnicas (Brazilian Standard). Rio de Janeiro. 1999.
- [13] Silva, P. V.; Fakury, R. H., “Brazilian standards for steel structures fire design”, Fire Safety Journal 37. Elsevier, 2002.
- [14] NBR 14762. Dimensionamento de Estruturas de Aço Constituídas por Perfis Formados a Frio (Cold formed steel design). ABNT - Associação Brasileira de Normas Técnicas (Brazilian Standard), Rio de Janeiro, 2001.
- [15] American Iron and Steel Institute, “Cold Formed Steel Design”, AISI. USA, 1996.
- [16] European Committee for Standardization. Eurocode 3 – Part 1.2. Design of Steel Structures-Structural Fire Design, Brussels, 1995.
- [17] Soares, C. H., “Dimensionamento de estruturas de aço constituídas por perfis formados a frio em situação de incêndio”, (Cold formed steel design – Master Degree), UFMG, Belo Horizonte, 2002.

10. ACKNOWLEDGEMENTS

To CBCA – Brazilian Center of Steel Construction for supporting this research, to COSIPA – Companhia Siderurgica Paulista for all lab. tests, to FIPAI/EESC-USP, to Dr. John Ewer from the University of Greenwich, and Mrs. Marcia Olivieri Silverio Pannoni – MyDeWi.



ACCURACY IN PREDICTING THE TEMPERATURE EVOLUTION IN COMPARTMENT FIRES

Antonín UHLÍŘ¹, Tomáš BAIERLE² and František WALD³

ABSTRACT

The paper presents a sensitivity study of the influence of the thermal properties of the enclosures to the temperature evolution in compartment fires. The parametric curve in the document EN 1993-1-2:2005 is evaluated on the measured data during the fire test on the steel structure in the Cardington BRE laboratory. The accuracy in predicting the temperature evolution by the parametric fire curves is discussed and compared to the zone model OZONE 2.2.

1. INTRODUCTION

The temperature development in the fire compartment is affected by the amount of the fire load, the ventilation conditions, the rate of heat release, the boundary elements of the compartment, and the active fire protection. The boundary of enclosure of the fire compartment is acting by its thermal permeability, capacity and emissivity of its surface. The simplest models of fire are nominal fire curves, which is the pore time temperature ratio. The parametric fire curves are modifying the time temperature curve by effective time. The modification allows to take into account the ventilation by opening factor and the surfaces of enclosure by boundary factor, which is representing the lost of heat at the surfaces by convection, radiation and conduction. The factor may be expressed as

$$b = \sqrt{\rho c \lambda} \quad (1)$$

in $\text{J m}^{-2} \text{s}^{-0.5} \text{K}^{-1}$, where ρ is density of boundary of enclosure in kg m^{-3} , c is specific heat in $\text{J kg}^{-1} \text{K}^{-1}$ and λ is thermal conductivity in $\text{W m}^{-1} \text{K}^{-1}$, see [1]. The factor may be varied on

¹ Research assistant, Czech Technical University in Prague, Dept. S&TS, CZ166 29 Praha, Czech Republic
email: antonin.uhlir@fsv.cvut.cz

² Research assistant, Czech Technical University in Prague, Dept. S&TS, CZ166 29 Praha, Czech Republic
email: tomas.baierle@fsv.cvut.cz

³ Professor, Czech Technical University in Prague, Dept. Steel & Timber Struct., CZ166 29 Praha, Czech Rep.
email: wald@fsv.cvut.cz

boundaries $100 \leq b \leq 2\,200$. The reference factor was chosen as $b_{ref} = 1160 \text{ J m}^{-2} \text{ s}^{-0.5} \text{ K}^{-1}$, which is close to enclosure of a light weight concrete. The factor is combined with ventilation factor O , which is modifying the equivalent time,

$$\Gamma = (O/O_{ref})^2 / (b/b_{ref})^2 = (O/0.04)^2 / (b/1160)^2 = (O/b)^2 / (0.04/1160)^2 \quad (2)$$

For $\Gamma = 1.0$ predicts the parametric fire curve the temperatures close to the standard nominal fire curve till about 1300°C . The zone models, the oldest descriptions of fire curve [2], are introducing the quality of surfaces by global expression of by discrete manner for one/two zones, which are taken into account. The finite element models of fluid dynamics CDF are taking the quality of the surfaces by discrete manner, see [3]. The temperature development in the fire compartment influences the fire design of structures. During the different stages of fire design is the information about the structural surfaces précising. Under pre-design the designer / fire specialist is assuming the values, which will be known afterwards. This contribution is devoted to the influence of prediction of the quality of the surfaces for the parametric fire curves and zone models.

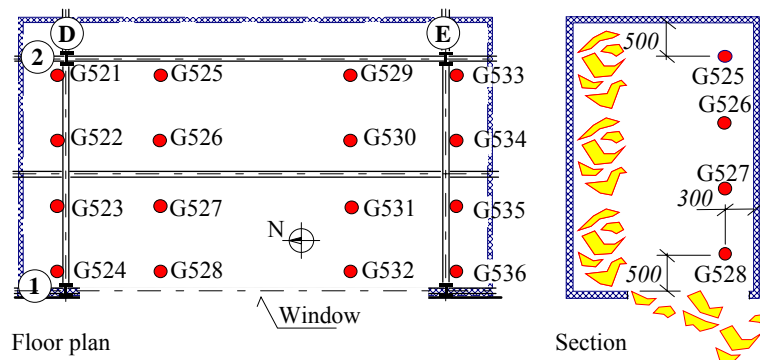


Fig. 1 – Location of the thermocouples in fire compartment in Cardington January 16, 2003

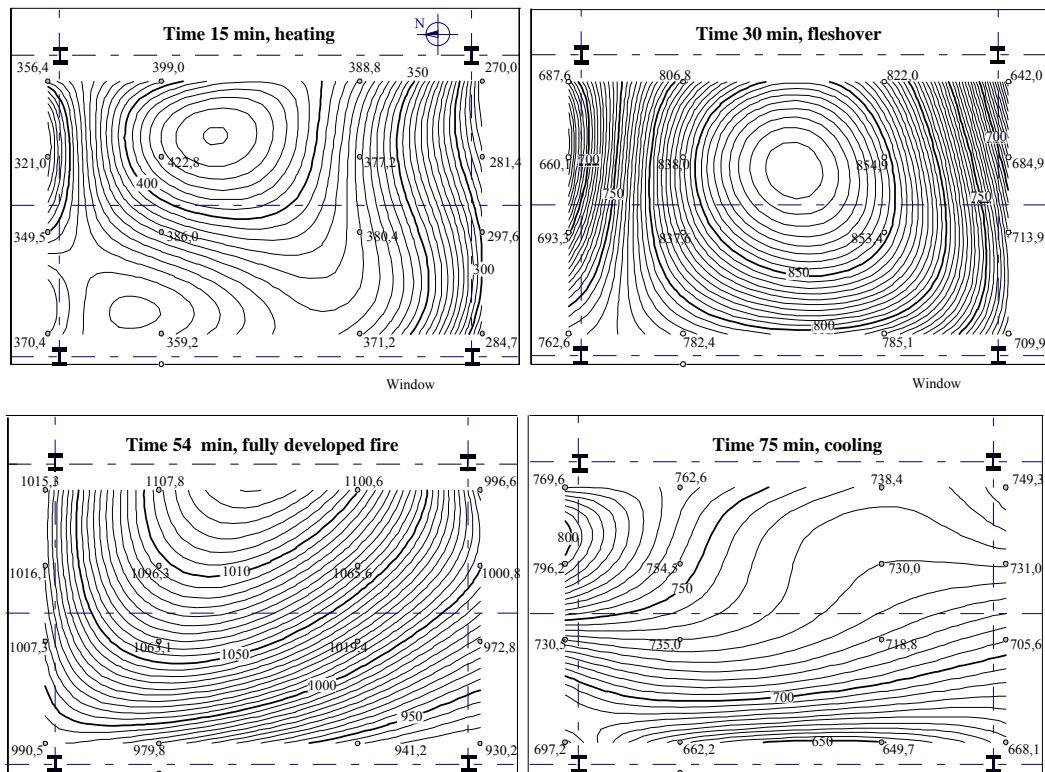


Fig. 2 – Isotherms during the fire test in Cardington January 16, 2003

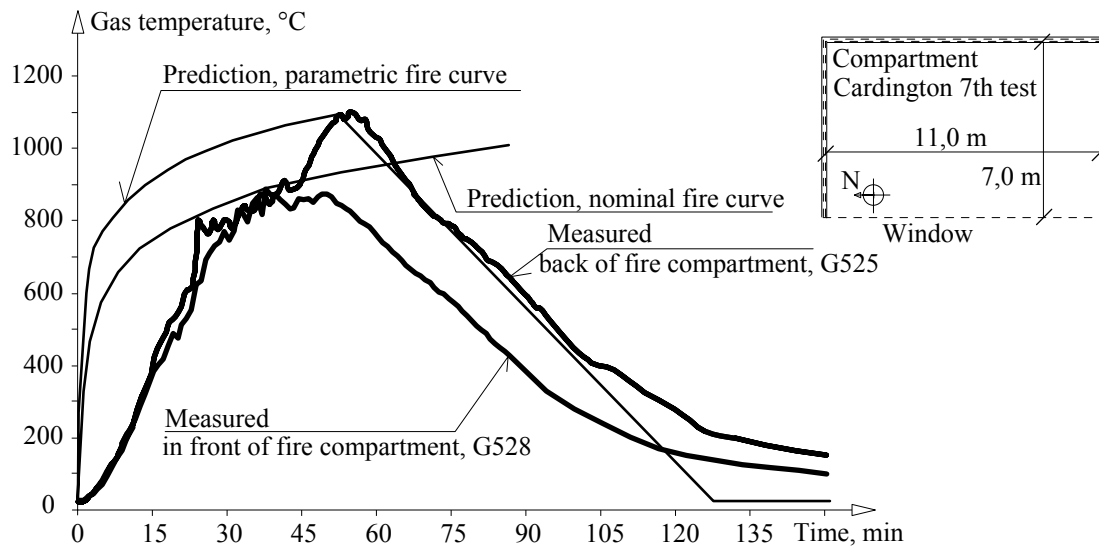


Fig. 3 – Comparison of the prediction of temperature by the parametric and nominal fire curve to the seventh large experiment in Cardington BRE laboratory

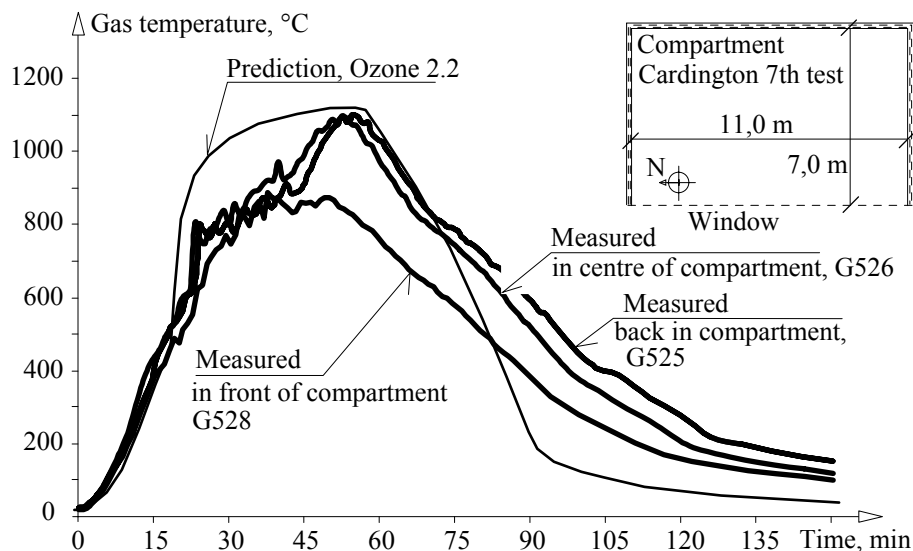


Fig. 4 – Comparison of the prediction of temperature by zone model to the seventh large experiment in Cardington BRE laboratory

2. CARDINGTON EXPERIMENT

The seventh large fire test in of Building Research Establishment's Cardington laboratory, which was performed January 16, 2003 and focussed on behaviour of connection, allows checking the accuracy of the prediction of the reached temperature as well. The fire compartment was built at the fourth floor 11 m long and 7 m depth, see Fig. 1 (for details [4]), which is summarising the thermocouples measured gas temperature. The mechanical and fire load and openings were optimize to reach the highest temperatures in the fire compartment and forces in the connections and composite slab. The fire load was represented by the timber cribs as 40 kg/m^2 , which represents the fire load of the administrative building today. The window opening under ceiling size $1,27 \times 8,7 \text{ m}$ allowed the fast development of the temperature in fire compartment. The homogeneity of the gas temperature is demonstrated on

Fig. 2 by isotherms. The gas temperature difference were less than 120 °C. The temperature development by parametric fire curve and by two zone model Ozone 2.2, see (Franssen, 2004), is summarised in Fig. 3, respectively Fig. 4. The comparison shows a good prediction of maximal temperature and the conservatism of the estimation of the natural fire. The zone model is rather accurate related to the beginning of the heating phase and maximal temperature. The parametric curve is conservative under heating and accurate in predicting of the in highest temperature and in the cooling phase.

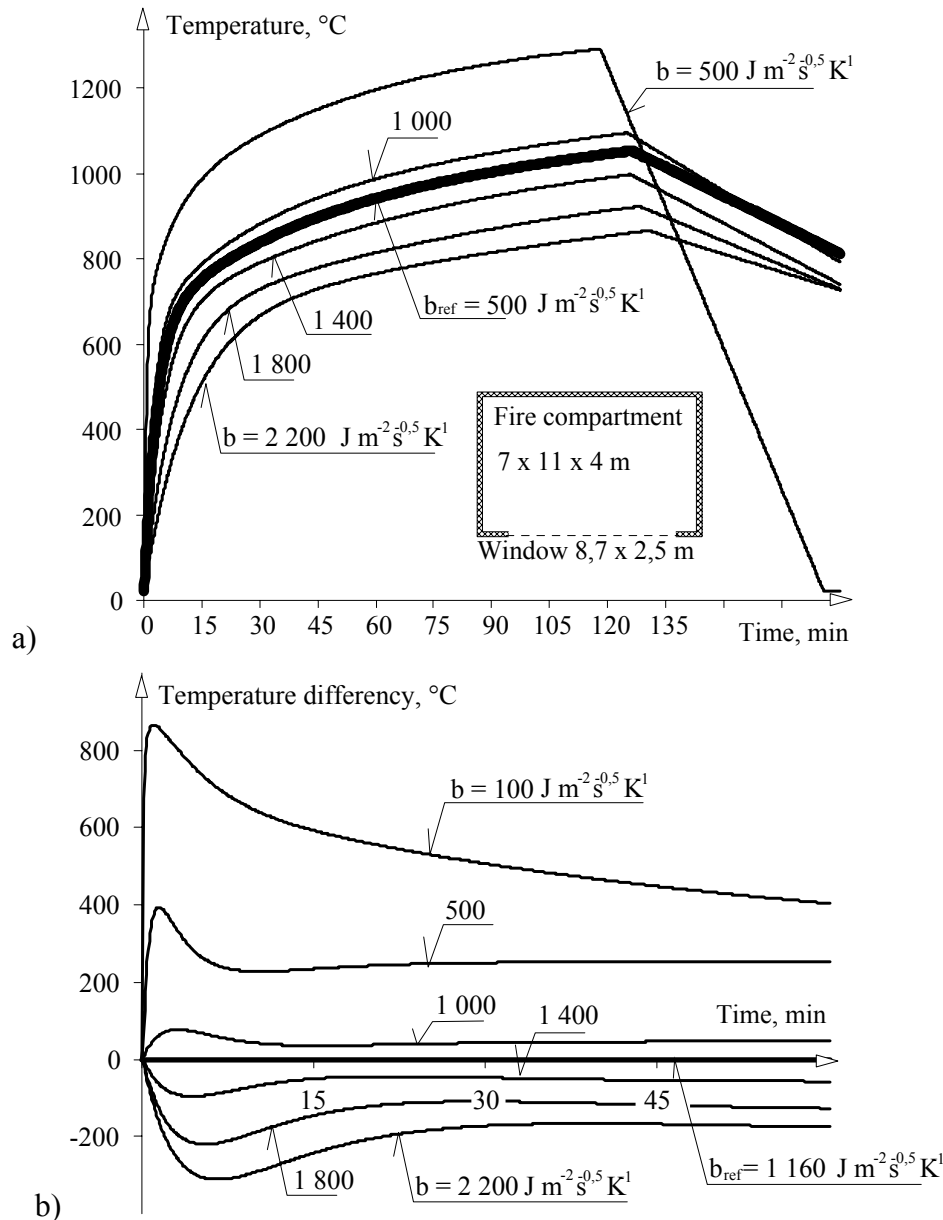


Fig. 5 – Influence to boundary factor b ; a) shape of the parametric curves; b) expressed in temperature difference against the temperature reached with the reference factor $b_{ref} = 1160 \text{ J m}^{-2} \text{ s}^{0.5} \text{ K}^1$

3. SENSITIVITY IN PREDICTION OF ENCLOSURES

The influence of the quality of boundary of enclosure was studied by the parametric fire curve and checked by the zone model under different ventilation conditions as well as fire load. Fig. 5 shows on the influence to boundary factor b expressed in temperature difference

against the temperature reached with the reference factor that the influence of boundary of enclosure affects more the beginning of curve till about 15 min of fire. Fig. 6 shows the prediction of temperature development by parametric fire curve for fire compartment with total area of vertical openings $A_v = 16 \text{ m}^2$; total area of enclosure $A_t = 360 \text{ m}^2$ including openings, weighted average of window heights on its walls $h_{eq} = 2,0 \text{ m}$; and opening factor $O = 0,0627 \text{ m}^2$ and fire load for a classroom of school $q_{fk} = 347 \text{ MJm}^{-2}$ [4], see annex For the simulation shown at Fig. 7 was for concrete taken $c_b = 1000 \text{ J kg}^{-1} \text{ K}^{-1}$, $\rho_b = 2300 \text{ kg m}^{-3}$, $\lambda_b = 1,6 \text{ W m}^{-1} \text{ K}^{-1}$, for masonry $c_z = 840 \text{ J kg}^{-1} \text{ K}^{-1}$, $\rho_z = 1600 \text{ kg m}^{-3}$, $\lambda_z = 0,7 \text{ W m}^{-1} \text{ K}^{-1}$ and plasterboard $c_s = 1000 \text{ J kg}^{-1} \text{ K}^{-1}$, $\rho_s = 900 \text{ kg m}^{-3}$, $\lambda_s = 0,25 \text{ W m}^{-1} \text{ K}^{-1}$. The maximal reached temperatures are summarised on Fig. 7. The predicted temperature varies from 776°C in office building for an enclosure of the normal concrete to 1308°C in case of dwelling with plasterboards.

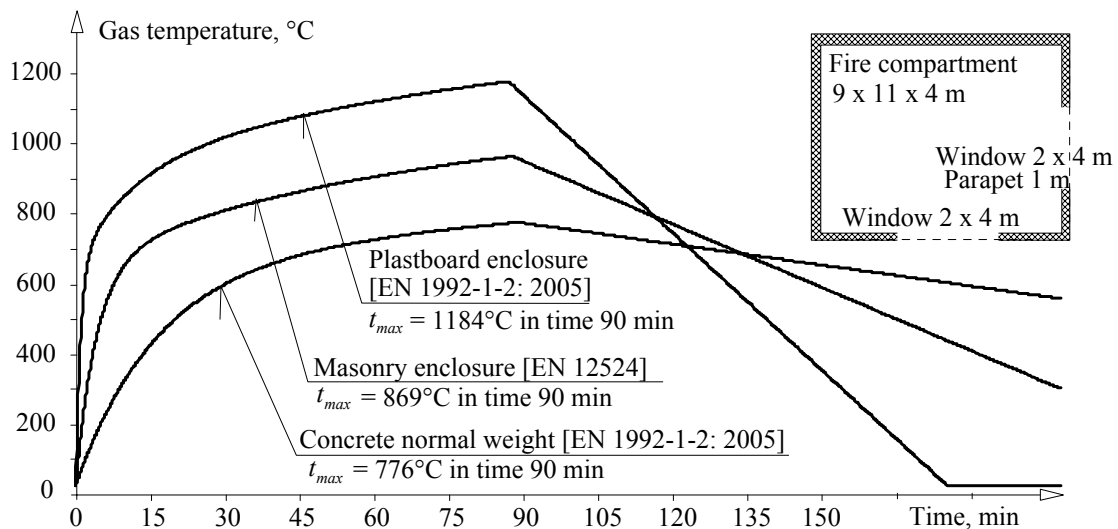


Fig. 6 – Influence of the different materials of enclosure to the parametric fire curves

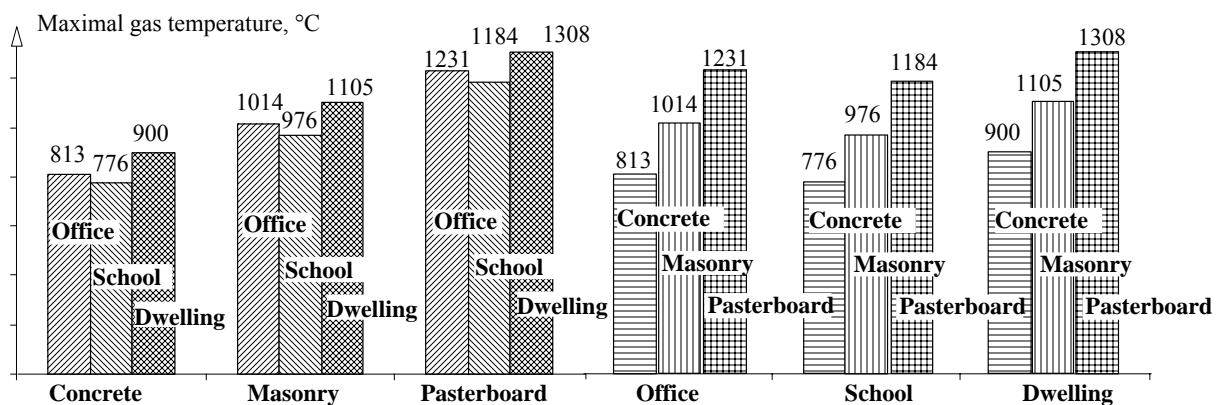


Fig. 7 – The calculated maximal gas temperatures for different materials of enclosure

The detailed influence of concrete thermal properties is expressed at Fig. 8 for light weight concrete as $c_1 = 840 \text{ J kg}^{-1} \text{ K}^{-1}$, $\rho_1 = 1600 \text{ kg m}^{-3}$, $\lambda_1 = 0,8 \text{ W m}^{-1} \text{ K}^{-1}$, middle weight concrete $c_2 = 1000 \text{ J kg}^{-1} \text{ K}^{-1}$, $\rho_2 = 1800 \text{ kg m}^{-3}$, $\lambda_2 = 1,15 \text{ W m}^{-1} \text{ K}^{-1}$ and normal weight concrete $c_3 = 1000 \text{ J kg}^{-1} \text{ K}^{-1}$, $\rho_3 = 2300 \text{ kg m}^{-3}$, $\lambda_3 = 1,6 \text{ W m}^{-1} \text{ K}^{-1}$ for the parametric fire model according to [5]. The results of calculation by zone model OZONE 2.2 [6] with the similar properties of enclosures, ventilation conditions and fire load are shown on Fig. 9.

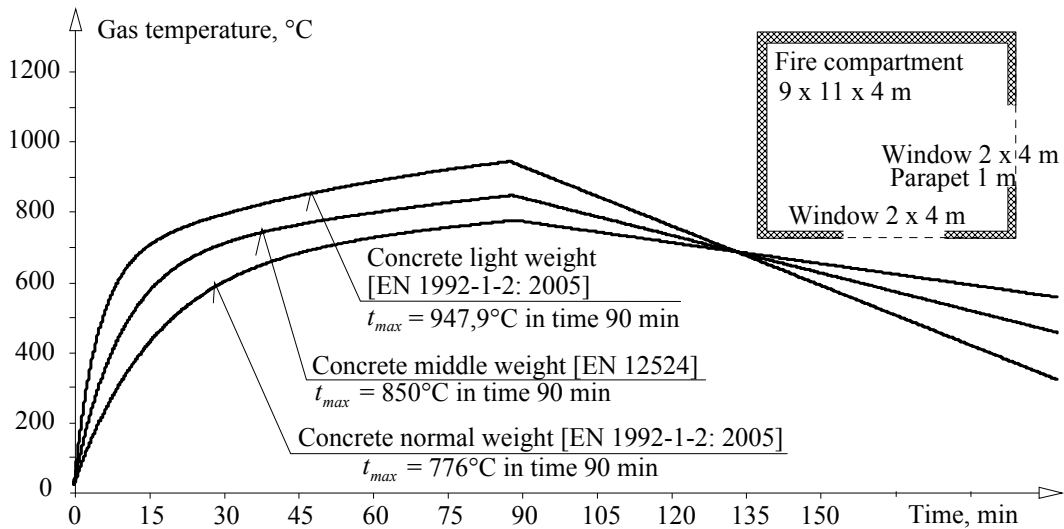


Fig. 8 – Time temperature diagram for concrete enclosures of different fire properties by parametric fire curve according to [5]

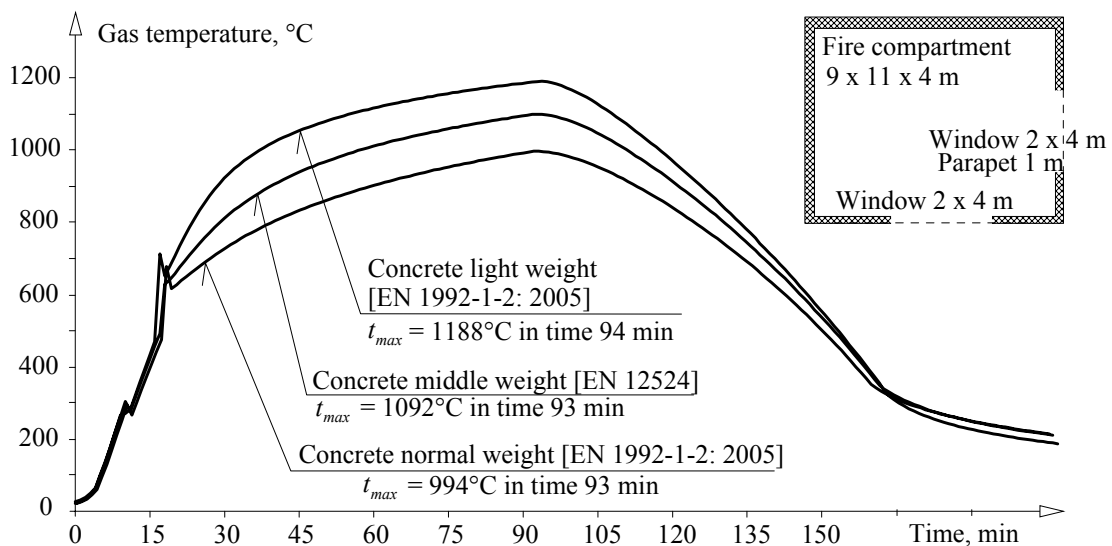


Fig. 9 – Time temperature diagram for concrete enclosures of different fire properties by zone fire model OZONE 2.2 [6]

The thermal properties of materials of enclosure may be described by the thermal permeability, capacity and emissivity of the surface. Fig. 10 shows the influence of the specific heat of enclosure to the shape of the parametric fire curve in case of $\rho = 2000 \text{ kg m}^{-3}$, $c = 920 \text{ J kg}^{-1} \text{ K}^{-1}$; the fire compartment $11,1 \times 9 \times 4 \text{ m}$ with $A_v = 16 \text{ m}^2$; $A_t = 360 \text{ m}^2$, $h_{eq} = 2,0 \text{ m}$; $O = 0,0627 \text{ m}^2$. Fig. 10 includes the resulting fire curves in previous case simulated by the zone model OZONE 2.2. The parametric fire cures shows more conservative results in the time to the maximal temperature and in the reached maximal temperatures. In described case varies the maximal predicted temperature by parametric curves from 844°C for to $\lambda = 1,6 \text{ W m}^{-1} \text{ K}^{-1}$ to 947°C for $\lambda = 0,8 \text{ W m}^{-1} \text{ K}^{-1}$ and from 817°C for to $\lambda = 1,6 \text{ W m}^{-1} \text{ K}^{-1}$ to 921°C for $\lambda = 0,8 \text{ W m}^{-1} \text{ K}^{-1}$.

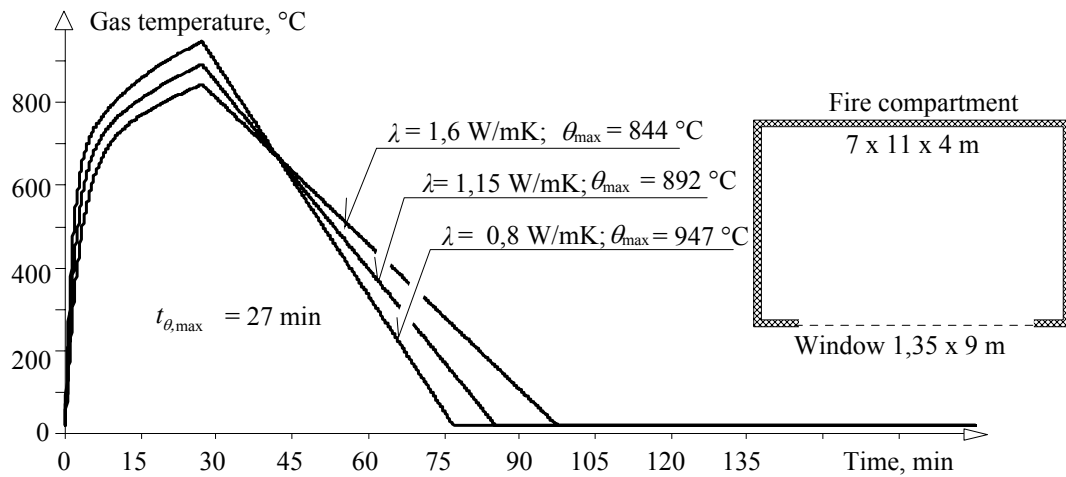


Fig. 10 – Influence of the specific heat of enclosure to the parametric fire curve

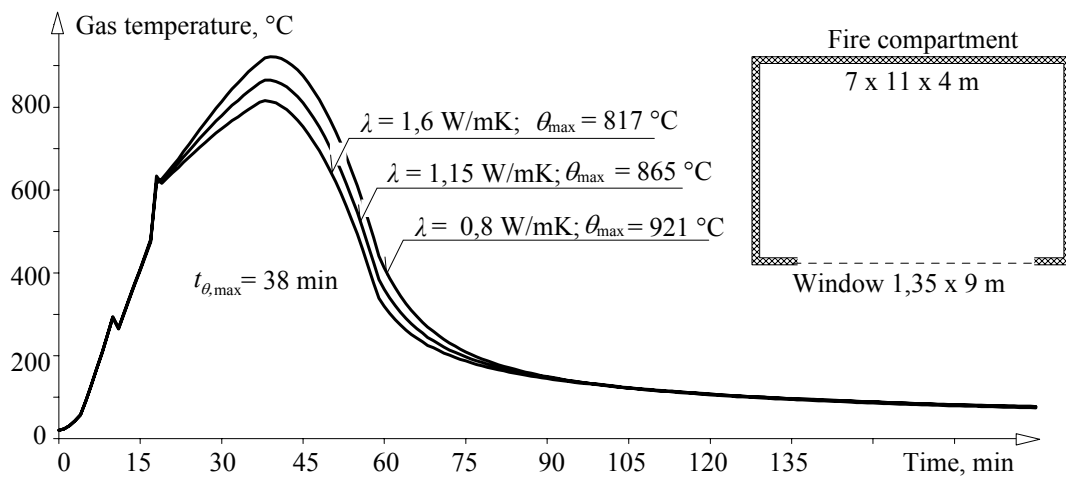


Fig. 11 – Influence of the specific heat of the enclosure to the fire curve by zone model

The error in estimation of the maximal temperature due to variation of the thermal properties of the fire compartment depends widely on the fire load, the ventilation conditions, and the rate of heat release. The error is studied in terms of inaccuracy of prediction of properties of walls in %, e.g. inaccuracy 25 % means 25 % difference in prediction of quality of walls, with ceiling and floor from the normal weight concrete. The sensitivity of the error in estimation of the maximal temperature to the fire load and heat release due to simplification of the prediction of the properties of enclosures is demonstrated on Fig. 12 in case of masonry enclosures. In the graph is shown on the horizontal axes the inaccuracy in estimation of the thermal property of the enclosure represented by $A_v = 8 \text{ m}^2$; $A_t = 360 \text{ m}^2$, $h_{eq} = 2,0 \text{ m}$; $O = 0,0314 \text{ m}^2$ and design fire load density related to the floor area $q_{f,d} = 347 \text{ MJ/m}^2$. The inaccuracy in estimation till 45 % is creating the error of prediction of temperature till 5 %.

Fig. 13 shows the error in estimation of maximal temperature due to inaccuracy of modelling of surfaces for three characteristic enclosures normal weight concrete ($b = 1698 \text{ J m}^{-2} \text{ s}^{-1/2} \text{ K}^{-1}$), plasterboard ($1254 \text{ J m}^{-2} \text{ s}^{-1/2} \text{ K}^{-1}$) and sandwich panes ($1093 \text{ J m}^{-2} \text{ s}^{-1/2} \text{ K}^{-1}$) in case of dwelling 100 m^2 , for details see [7]. In case of concrete the inaccuracy in estimation till 25 % creates the error of prediction of temperature till 5 %; for plasterboards and sandwiches inaccuracy 50 % till 3 %.

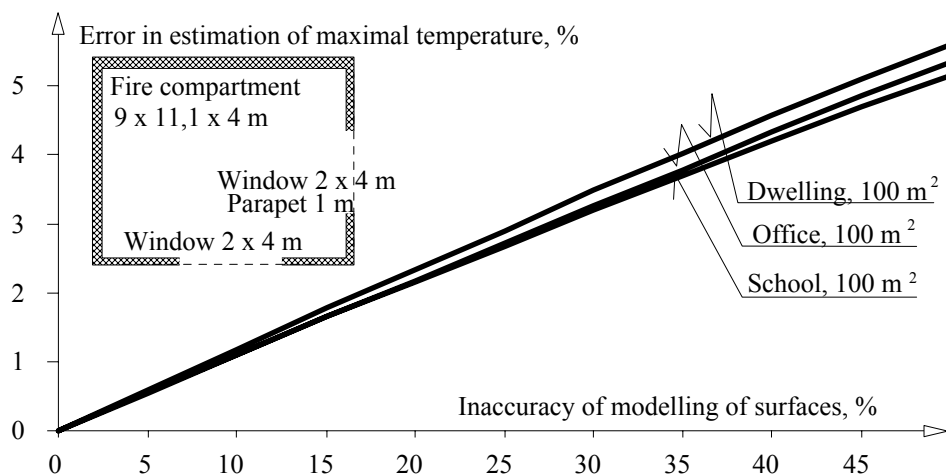


Fig. 12 – Error in estimation of maximal temperature due to inaccuracy of modelling of surfaces for three characteristic fires in case of masonry enclosures

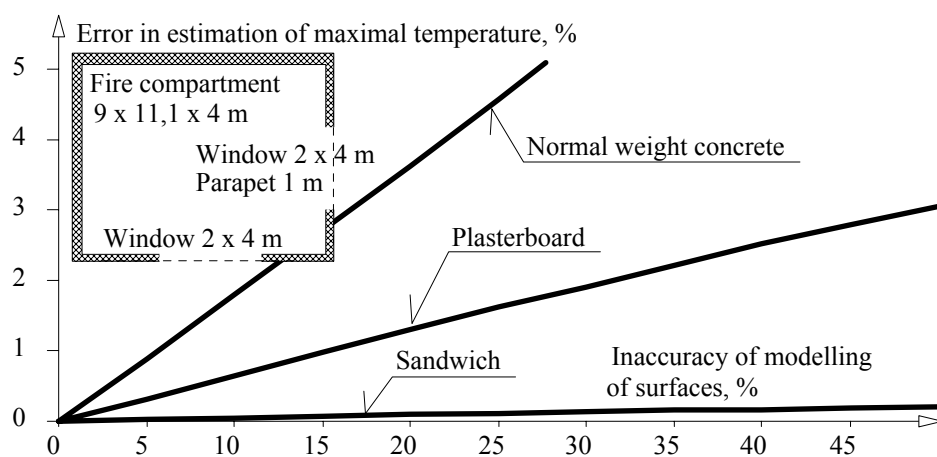


Fig. 13 – Error in estimation of maximal temperature due to inaccuracy of modelling of surfaces for three characteristic enclosures in case of dwelling 100 m²

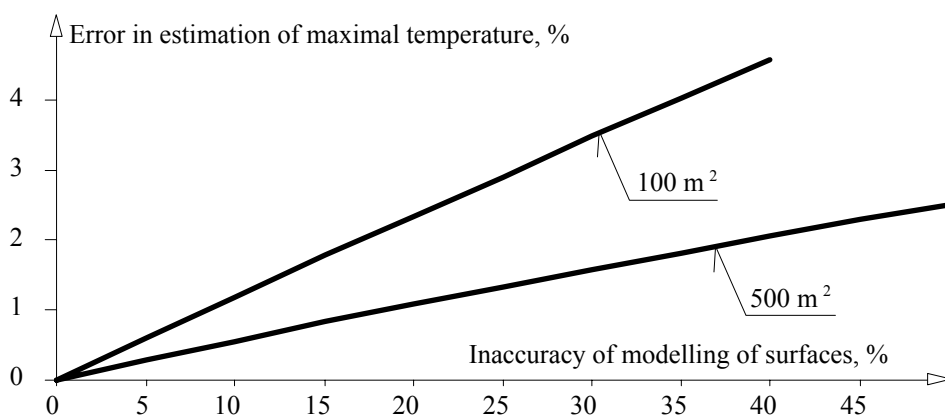


Fig. 14 – Error in estimation of maximal temperature due to inaccuracy of modelling of surfaces for medium and large fire compartment in case of dwelling

Error in estimation of maximal temperature due to inaccuracy of modelling of surfaces for medium and large fire compartment in case of dwelling demonstrates Fig. 14, for compartments 10 x 10 x 4 m with window 4 x 2 m and 20 x 25 x 4 m with three windows 4 x 3 m. The inaccuracy in estimation till 40 % creates the error of prediction of temperature till 5 %.

4. CONCLUSIONS

The test shows a good conservative prediction of the gas temperature during the compartment fire temperature by zone models as well as parametric fire curves.

Influence of the boundary enclosure to the prediction of the temperature in the fire compartment is not dominant. The difference in the prediction is most sensitive by the massive enclosure as concrete. By variation of the fire load is the difference in prediction of enclosures changing insignificantly. The presented study shows, that the estimation of the type of enclosure with difference of 25 % is ensuring the accuracy of prediction of the maximal temperature till 5 %.

5. ACKNOWLEDGEMENT

This outcome has been achieved with the financial support of the Czech Ministry of Education, Youth and Sports, project No. 1M680470001, within activities of the CIDEAS research centre.

6. REFERENCES

- [1] Buchanan A. H.: Structural design for fire safety, John Wiley & Sons, Chichester 2003, ISBN 0-471-89060-X.
- [2] Reichel V.: Design of fire safety of industrial buildings, in Czech, Navrhování požární bezpečnosti výrobních objektů, in Zabraňujeme škodám, Vol. 17, Česká pojišťovna, Praha 1987.
- [3] Wald F. at al.: Calculation of fire resistance of structures, in Czech, Czech technical University in Prague, Praha 2005, p. 336, ISBN 80-0103157-8.
- [4] Wald F., Silva S., Moore D.B, Lennon T., Chladná M., Santiago A., Beneš M.: Experimental behaviour of a steel structure under natural fire, The Structural Engineer, New Steel Construction, 3/2005, pp. 24-27, ISSN 0968-0098.
- [5] EN 1991-1-2:2003, Eurocode 1: Actions on structures, Part 1-2: General actions – Actions on structures exposed to fire, CEN, Brussels, 2003, p. 60.
- [6] Franssen J. M.: OZone V2, Université Liege, URL: www.ulg.ac.be/matstruc, Liege 2004.
- [7] Uhlíř A., Baierle T., Wald F.: Enclosure Structures and Fire Modelling, research report, CIDEAS, CTU Praha, 2005, p. 28.

Other Topics



AN EXPERIMENTAL INVESTIGATION OF GYPSUM BOARD PARTITION ASSEMBLY PERFORMANCE UNDER REAL FIRE EXPOSURES

Samuel L. MANZELLO¹ and Richard G. GANN²

ABSTRACT

The present paper compares the responses of wall-size partition assemblies, composed of either type X or type C gypsum wallboard panels over steel studs, when each were exposed to an intense room fire. The exposures lasted from the time of ignition to beyond flashover. Heat flux gauges provided time histories of the energy incident on the partitions, while thermocouples provided data on the propagation of heat through the partitions and on the progress toward perforation. Visual and infrared cameras were used to image partition behavior during the fire exposure. Contraction of the seams of the two types of assemblies occurred under similar thermal conditions on the unexposed surface. However, there were noticeable differences in cracking behavior. Reduced-scale experiments were performed in conjunction with the real-scale fire tests to provide insight into the contraction and cracking behavior of the different gypsum board types. Results obtained from these experiments are discussed.

1. INTRODUCTION

Traditional fire resistance testing in the United States has been based upon ASTM standard E119, “Standard Test Methods for Fire Tests of Building Construction and Materials”¹. The similar international standard is ISO 834². In these tests, building components are subjected to a constantly increasing furnace temperature intended to represent a standard fire. The components are then rated, with units of time, on their ability to withstand the exposure up to a criterion that is defined as a failure point. This criterion may be either based on the temperature rise of the unexposed face of the partition assembly or the efflux of hot gases or flames. Generally, the relative ratings of similar construction types are

¹ PhD, Mechanical Engineer, Building and Fire Research Laboratory, National Institute of Standards and Technology, Gaithersburg, MD 20899 USA, email: samuel.manzello@nist.gov

² PhD, Senior Research Scientist, Building and Fire Research Laboratory, National Institute of Standards and Technology, Gaithersburg, MD 20899 USA, email: richard.gann@nist.gov

Official contribution of the National Institute of Standards and Technology, not subject to copyright in the United States of America.

accurate, *i.e.*, if Construction A obtains a higher rating than Construct B in the test, then it is reasonable to expect that it will contain heat, flames, and smoke longer in an actual fire. Current model building codes in the United States of America prescribe specific ratings for construction assemblies.

There are limitations to this approach in providing a known degree of fire safety. The test is concluded when the first failure criterion is met. For wall, floor, and ceiling assemblies, this is almost always an excessive temperature on the unexposed face. The more serious fire hazard is the passage of smoke and flames through the partition, and the time to this failure is rarely measured. In addition, there is no method available to relate the response of the partition under this standard exposure to its response to a different (more realistic) design fire. Most realistic fires do not heat a partition uniformly. Real fires can recede, allowing the partition to cool while still in the presence of smoke and flames.

With these issues in mind, the model building codes in the United States of America (and formal building codes elsewhere) accept the use of performance-based design³⁻⁴, and the fire protection engineering profession is developing first-generation tools to support this practice⁵⁻⁶. Under this approach, the designs of construction assemblies are assessed on how they would be expected to perform during selected design fires, with their thermal and radiative exposures. However, it is not feasible, either practically or economically, to test in the full-scale all assemblies under a variety of fires, while making quantitative measurements of their responses. A more pragmatic approach would be the use of (perhaps semi-empirical) models capable of accurately predicting the response of construction assemblies to a wide range of fire conditions. These models would draw upon a small subset of full-scale and reduced-scale tests to yield the predicted response.

The present work develops needed physical understanding of the phenomena that govern the performance of a common wall assembly: a non-load-bearing wall of gypsum panels attached with screws to steel studs. To this end, real-scale compartment tests exposed two different types of gypsum wall board to real fire exposures. Reduced-scale experiments were performed in conjunction with the real-scale fire tests to provide insight into the contraction and cracking behavior of the different gypsum board types. For a performance-based design approach, it is important to know when wall assemblies collapse and when their effectiveness as a smoke and flame barrier is compromised due to gypsum board shrinkage and cracking. The results obtained from these experiments are being used to validate a complimentary modeling effort aimed at predicting the response of gypsum wall assemblies exposed to fires⁷.

2. EXPERIMENTAL DESCRIPTION

Two non-load bearing walls consisting of gypsum panels attached to steel studs were constructed for fire testing. Figures 1 and 2 display exposed face and unexposed face construction for Assembly One and Assembly Two, respectively. Each assembly consisted of two single (1.22 m by 2.44 m), gypsum panels vertically mounted on the interior side of the steel studs. The dimensions of each assembly were 2.44 m by 2.44 m. For Assembly One, steel studs (width: 92 mm, thickness: 20 gauge) were spaced at 609 mm, and type X gypsum panels (USG Fire Code Core³) with a thickness of 15.9 mm were attached vertically to the studs using type S drywall screws spaced at 305 mm. For Assembly Two, the stud and screw spacing were identical to Assembly One, but type C gypsum panels (USG Fire Code C Core), also with a thickness of 15.9 mm, were used. Joints were taped and spackled prior to fire initiation within the compartment. The partitions were constructed under ASTM guidelines for non-load bearing wall assemblies⁸⁻¹¹.

³ Certain commercial products are identified to adequately describe the experimental procedure. This in no way implies endorsement from NIST.

Assembly One and Assembly Two are not common constructions (due to the lack of gypsum panels attached on the unexposed side), but were built to visualize the front gypsum partition response to the fire load. To facilitate the explanation of partition behavior observed during the fire exposures, the space between the studs was designated as section 1 thru section 4 (See figure 2).

To model the unexposed surface temperatures accurately, one must account for the thermal resistance induced by the pads¹². Accordingly, temperatures were obtained using type K thermocouples (22 gauge) attached to both sides of the gypsum panels. Bare thermocouples were used on the exposed face. Thermocouples at the unexposed face were placed under insulating pads, as specified in ASTM E119¹, in order to compare these measurements to the failure modes of the standard. The locations of the thermocouples were identical for the two assemblies and are displayed in figure 2.

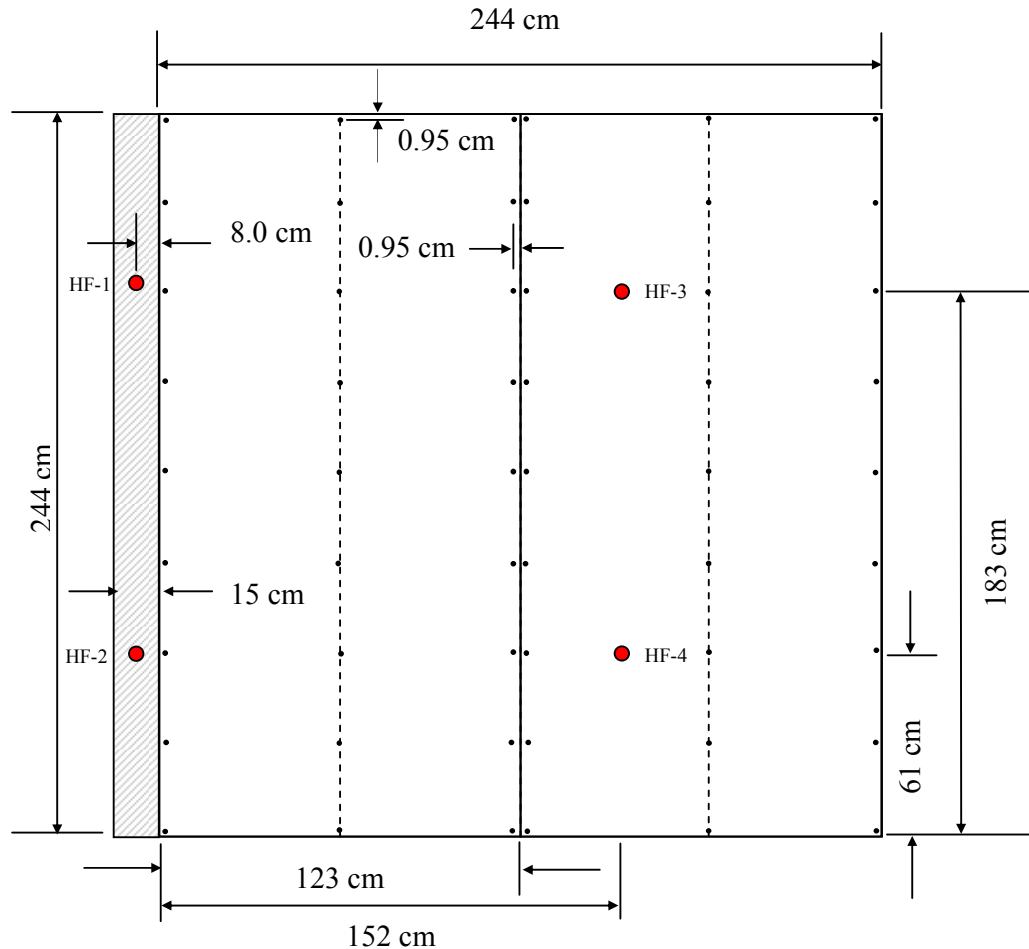


Fig. 1 Drawing of Assembly One and Assembly Two construction at the exposed face.

Four Schmidt-Boelter water-cooled total heat flux gauges were used to measure the heat flux incident on the partitions. The position of all four gauges (designated as HF1, HF2, HF3, and HF4) was the same for both partitions assemblies tested. (See figure 1). Two gauges were mounted flush to the exposed face of the gypsum panels, and two gauges were mounted flush to the column adjacent to the other vertically mounted gypsum panel. The gauges were mounted on the column in order to have one of the gypsum panels free from the

holes necessary for gauge mounting. For the gauges mounted on the gypsum panel, a custom bracket was constructed to support the weight of the gauges and water lines.

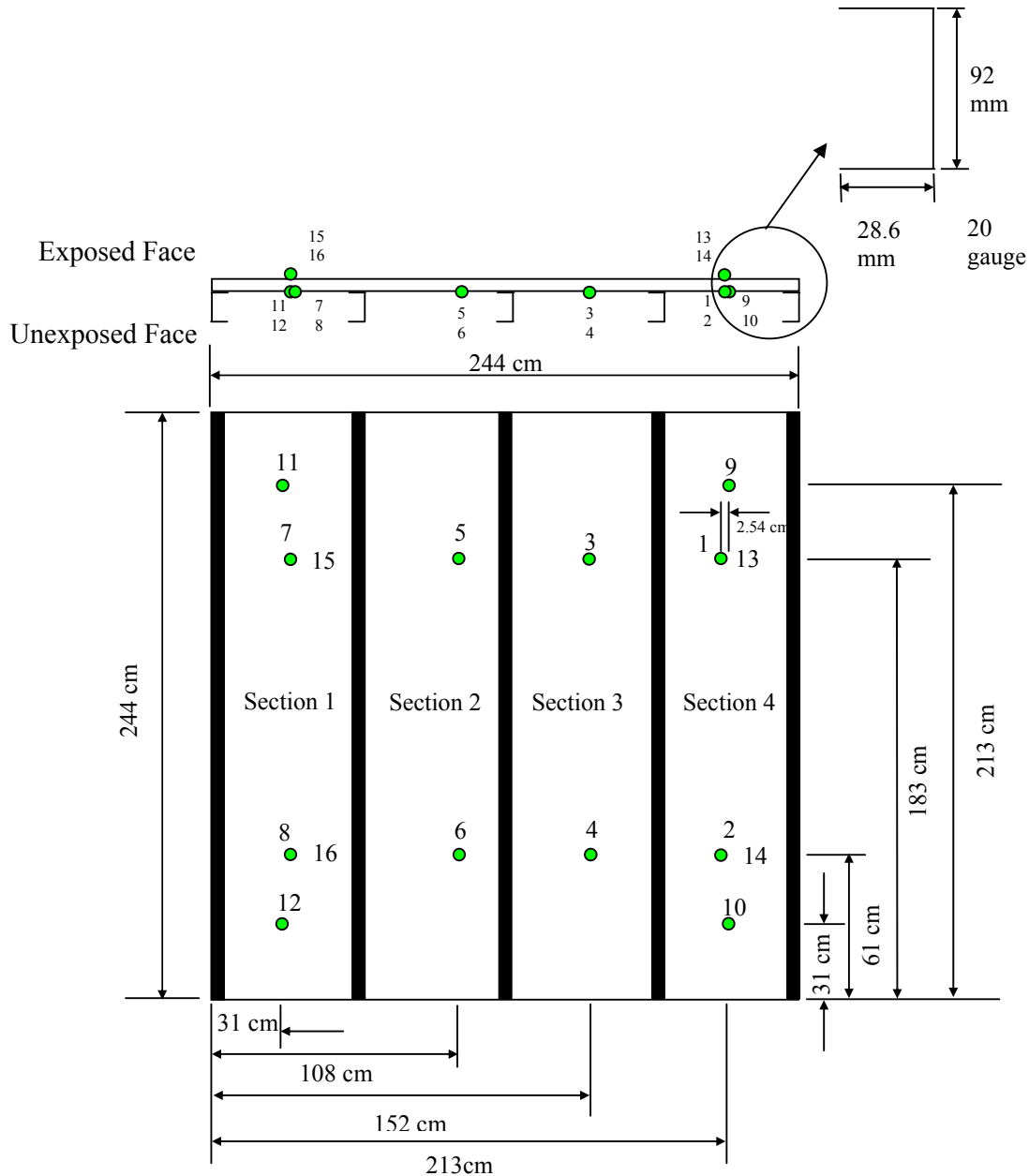


Fig.2 Drawing of Assembly One and Assembly Two, showing the location of the unexposed face temperature measurements.

To mitigate water condensation on the gauge surface, each gauge was water cooled to $75\text{ }^{\circ}\text{C} \pm 5\text{ }^{\circ}\text{C}$, which is well above the dew point. Since soot deposition on the gauge surface was not desired, each gauge was purged with nitrogen for 3 s, every 120 s, during the test. The purge signal was apparent in the flux data and was subsequently removed from the temporal heat flux trace. Although each gauge was provided with a calibration from the manufacturer, the gauges were re-calibrated at NIST at $75\text{ }^{\circ}\text{C}$, prior to the test series. The

response of the gauges was re-calibrated upon completion of the test series. The calibrations before and after the test series agreed to within the uncertainty of the calibration procedure.

The unexposed face of each partition assembly was imaged using a standard (visual) video camera with a framing rate of 30 frames/s. In addition, an infrared camera was used to image the unexposed face, also at 30frames/s. Prior to each test, photographs were taken at 2048 x 1024 pixel resolutions of both the exposed and unexposed faces using a digital camera fitted with a zoom lens. Another series of photographs were taken of both faces upon completion of each test.

The size of the compartment for the fire experiments was 10.7 m long by 7.0 m wide by 3.4 m high. A 2.44 m by 2.44 m opening was constructed on the lower 7.0 m side of the compartment so that each partition assembly could be switched out easily for each fire test. A photograph of the fire compartment is shown in figure 3.

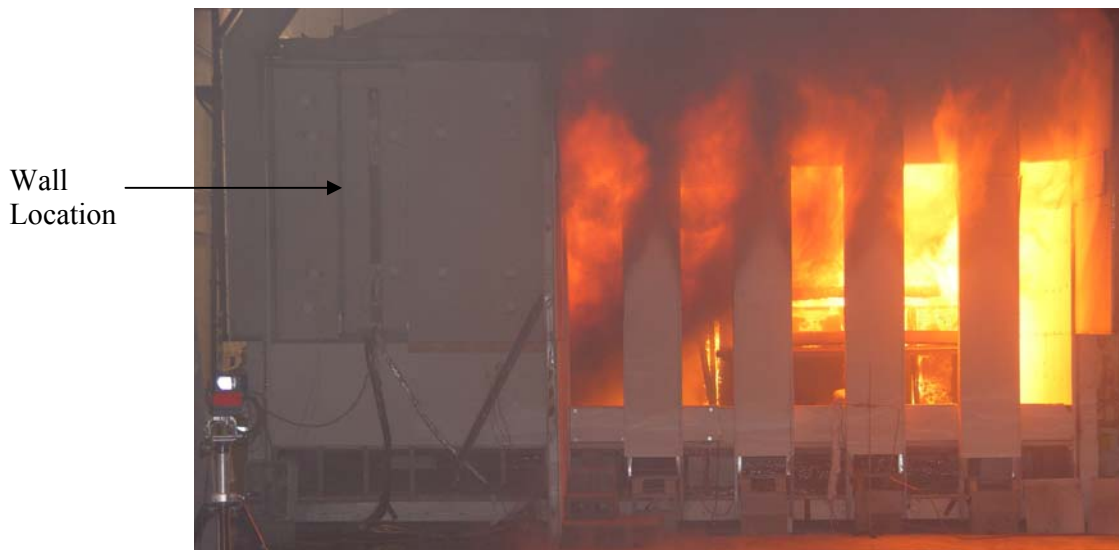


Fig. 3 Photograph of the compartment where Assembly One and Assembly Two were installed.

The compartment was constructed to simulate a common office space that would be found in a commercial building. Accordingly, the combustibles within the compartment consisted of three workstations for each of the fire exposures reported here. The fires were ignited using a spray burner. The fire exposures had peak heat release rates (HRR) of 12.0 MW at 825 s after ignition and 10.5 MW at 912 s after ignition for Assembly One and Assembly Two, respectively. The total burn time for each fire was approximately 45 minutes. Further details of the compartment and the combustibles within the compartment are available elsewhere¹³.

3. RESULTS AND DISCUSSION

Figure 4 (a) is a picture of Assembly One taken immediately after the fire test.. It is well known that, upon heating, gypsum panels contract due to dehydration¹². The opening along the seams of the two gypsum panels due to contraction is clearly visible. Cracks were observed to occur at the screw locations. The formation of cracks at the screw locations was expected since it is these locations that experience the greatest mechanical stress. In addition, a series of transverse cracks was observed to form in both gypsum panels. Both gypsum panels were intact upon completion of the fire test. Overnight, during the cooling process, the

gypsum board began to fall apart, resulting in the missing sections. (Entry was not permitted into the fire compartment until the next day due to safety concerns.)

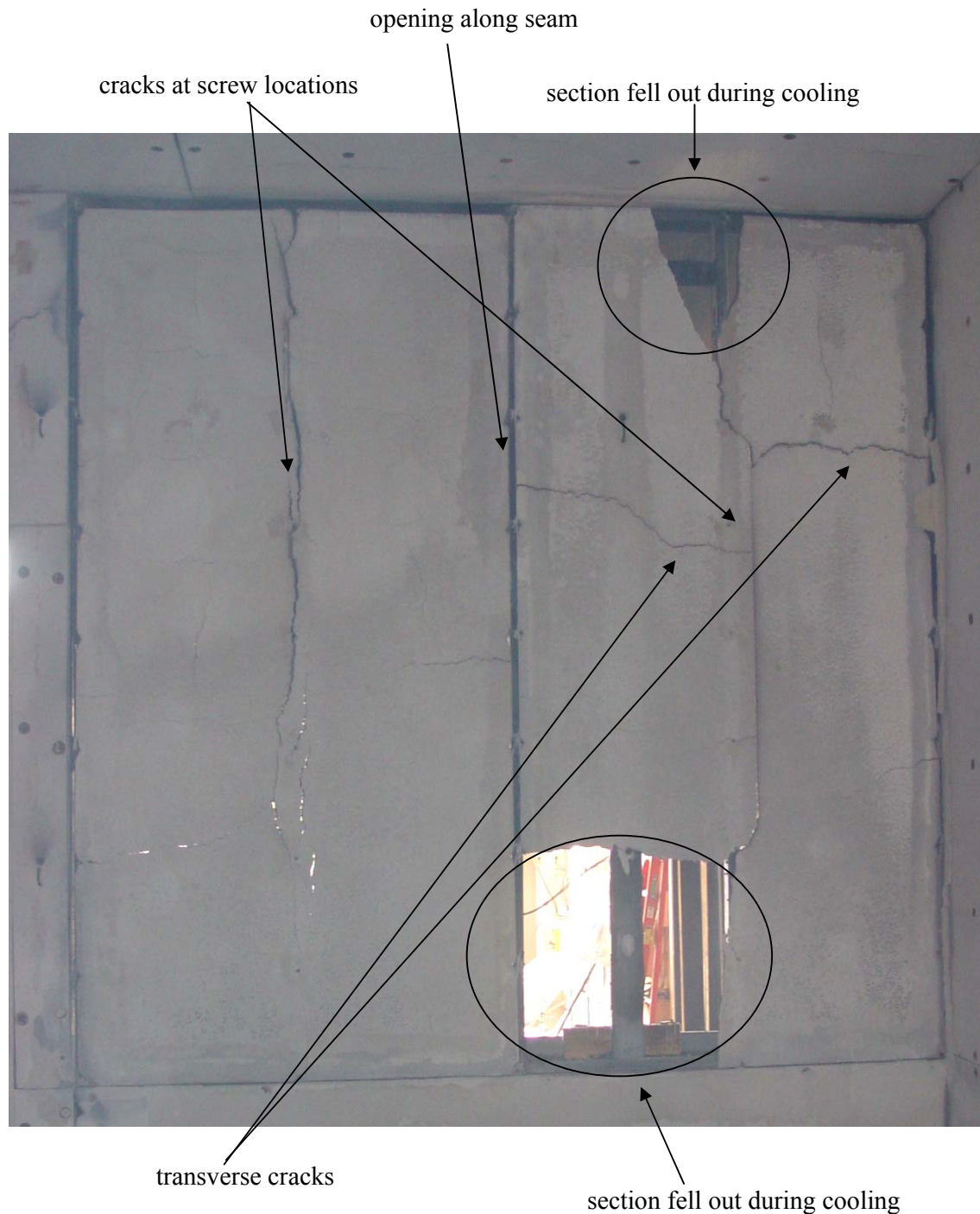


Fig. 4 (a) Digital pictures of the exposed face of Assembly One (post-fire).

The temporal evolution of openings and crack propagation was analyzed and was observed to occur in the following order: opening at the joint between the two vertically mounted gypsum panels (initiation at $t = 1243$ s), cracks at the screw locations along studs (initiation at $t = 1550$ s, first visible in the upper portion of section 3), transverse cracks

(initiation in section 2 at $t = 2200$ s). The transverse cracks that formed on the exposed face, corresponding to section 3 and section 4 on the unexposed face, were not visible on the unexposed face during the fire exposure.

There were distinct differences between the behaviors of the assemblies with the two types of gypsum board. An image of the exposed face of Assembly Two is displayed in figure 4 (b). The paper on the exposed face burned off, and the opening along the seams of the two gypsum panels due to contraction is clearly visible. No cracks were observed at the screw locations, nor were transverse cracks observed. The opening at the joint between the two vertically mounted gypsum panels was observed to occur at 1370 s after ignition. As was observed for Assembly One, both gypsum panels were intact upon completion of the fire test, *i.e.* the opening in the picture did not occur during the fire exposure, but during the overnight cool down process.

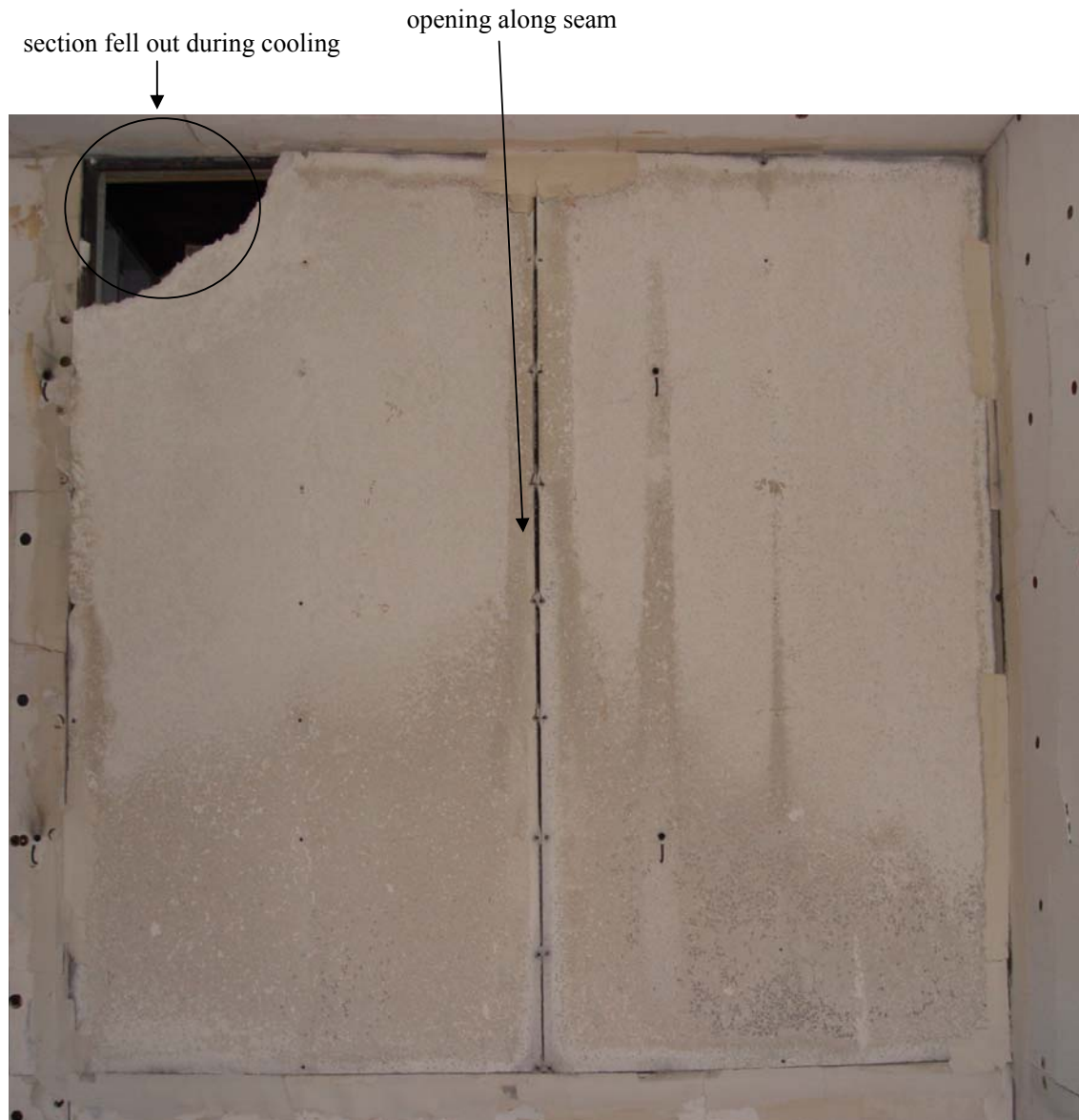


Fig. 4(b) Digital pictures of the exposed face of Assembly Two (post-fire).

Although many investigators have recognized the importance of modeling the response of both wood-framed and steel-framed partition assemblies to fire exposure^{12,14-19}, such models can generally only predict the behavior of the partition up to the point of insulation failure, as specified under ASTM E119 and ISO 834. The standard insulation criterion is itself of marginal value in assessing fire hazard. Auto-ignition of combustibles on the far side of the wall requires both much higher temperatures and good thermal contact between the wall and the combustibles. Information on the additional failure modes is needed for a model to estimate how long a partition can contain flames and smoke. The model of Takeda¹⁴ has begun to address some of this by incorporating the contraction of gypsum board on the exposed face at the seams in his model.

In order to compare the performance of the two types of assemblies, the total heat flux and gypsum board temperature profiles were analyzed at the time when the openings of the gypsum board at the seams were observed on the unexposed face (from camera IR view). The average total heat flux profiles were obtained by averaging the spatial resolved heat flux data as a function of time. Overall, the two profiles were similar, which demonstrates that the thermal load due to the fire exposure was similar.

For Assembly One, the average gypsum board temperature (average based on exposed and unexposed face temperature measurement) and the average total heat flux were 417 °C and 140 kW/m², respectively, when contraction of the gypsum board at the seams were observed on the unexposed face. For Assembly Two, the average gypsum board temperature (exposed and unexposed face) and the average total heat flux were 412 °C and 143 kW/m², respectively, when contraction of the gypsum board at the seams were observed on the unexposed face.

Since soot was not allowed to accumulate on the gauge surface due to the nitrogen purge system, the two main sources of uncertainty in total heat flux measurement were: (1) calibration uncertainty, (2) uncertainty associated with the voltage reading process. Uncertainty exists with the calibration itself and the fluctuation of the cooling water temperature during the test, since the calibration was based on a water temperature of 75 °C. Accordingly, the combined uncertainty in the total heat flux measurements was $\pm 10\%$. It is estimated that the combined uncertainty for the exposed face temperature measurements is $\pm 10\text{ °C}$ for temperatures lower than 200 °C and $\pm 30\text{ °C}$ for temperatures higher than 200 °C.

In the same series of experiments, Manzello *et al.*²⁰ exposed an assembly identical to Assembly One (designated Assembly One in that paper) to a different fire exposure. For that test, the average gypsum board temperatures (exposed and unexposed face) and exposed face total heat flux measured were 416 °C and 148 kW/m², when contraction of the gypsum board at the seams were observed on the unexposed face. Since these values are virtually the same as those observed for Assembly One, they suggest that the contraction leading to the seam opening is a relatively fast process and is less dependent on the earlier thermal history.

Additional measurements were performed under reduced-scale to provide further insights into gypsum board contraction. Triplicate samples of 15.9 mm thick Type X gypsum board (USG Fire Code Core) and Type C gypsum board (USG Fire Code C Core) were cut into 50 mm by 152 mm rectangles from single sheets of each type and inserted into an oven.

A series of scoping experiments was conducted in which samples were heated to a selected temperature and their mass measured as a function of time. Further weight loss was insignificant after about 3 h in the oven.

Fresh samples were then heated in 100 °C steps. At the end of each step (3 h), a sample was removed from the oven, its width was measured using high precision calipers (1/100 mm resolution), and the sample was returned to the oven within 30 s. The results of these measurements are displayed in Table 1. The combined uncertainty in these measurements is $\pm 10\%$.

The linear shrinkage of the gypsum board samples was clearly a function of temperature and gypsum board type. For temperatures below 400 °C, the degrees of shrinkage of the two types of gypsum board were not significantly different. At 500 °C, a minor dip was observed in the degree of shrinkage (as compared to measurements at 400 °C) for the two types of gypsum board. As the temperature was increased, the degree of shrinkage increased dramatically for the type X gypsum board with respect to the type C gypsum board. For example, at 600 °C, the degree of shrinkage of type X board was more than two times larger than type C board.

Takeda [14] has measured contraction of 50 mm by 200 mm by 12.7 mm thick samples of type X gypsum board as a function of temperature in an oven up to 700 °C. The shrinkage of the gypsum board increased, reaching 1.7 % at 700 °C. This is significantly lower than the value measured here and indicates a difference in the boards tested, an effect of the dimensions of the boards, or a difference in the heating protocol.

Heating T (°C)	% Shrinkage from the initial Sample Dimension			
	Type X Board		Type C Board	
	Heating only	Heating and Cooling to 120 °C	Heating only	Heating and Cooling to 120 °C
200	0.15	0.22	0.15	0.20
300	0.39	0.52	0.39	0.53
400	1.19	1.50	0.80	1.17
500	1.13	1.56	0.50	1.0
600	1.71	2.29	0.78	1.31
700	2.65	3.43	1.23	1.72
800	2.58	3.50	1.14	1.98
900	3.69	4.67	1.97	3.08

Table 1 Measured gypsum board contraction as a function of temperature for type X and type C gypsum board samples.

In addition to gypsum board contraction measurements, we measured the mass loss of 50 mm by 152 mm by 15.9 mm thick gypsum board samples of both types as a function of temperature. The mass loss of the gypsum board samples was obtained using a load cell (resolution of 5 mg – for reference the initial gypsum board samples had a mass of 80 g (type X) to 100 g (type C), and the results of these measurements are shown in figure 5. Three replicate experiments were performed at each temperature, with the error bars representing the standard deviation in the measurements at each temperature.

A significant amount of mass was lost for both gypsum board types for temperatures up to 400 °C. This was expected since the core of type X gypsum board is known to contain approximately 21 % by mass of chemically bound water. For type X gypsum board, the 21 % was reached at about this temperature, but there was further mass loss up to about 600 °C.

The type C gypsum board reached 21 % mass loss at about 400 °C, stabilized, and then lost additional mass up to 700 °C. At 700 °C, all six samples had lost about 23 % of their mass.

Understanding of this mass loss behavior and the difference between the two types of gypsum board lies in the details of the composition of the two materials. ASTM C1396/C1396M²¹ contains specifications for type X gypsum board. Type X gypsum board contains a fibrous glass mesh which is designed to hold the gypsum board in place after the dehydration reactions have occurred. There is no ASTM standard for type C gypsum board. As a result, type C gypsum board is generally manufacturer-specific. It is common practice to include other additives, in addition to a fibrous glass mesh, with vermiculite being commonly used. As the gypsum board is heated and the dehydration reactions occur, resulting in contraction of the gypsum, the vermiculite expands. The combination of the fibrous glass mesh and expanding vermiculite act to mitigate contraction and ultimately reduce cracking in the gypsum board. The present experiments, both real-scale and reduced-scale, confirm this behavior.

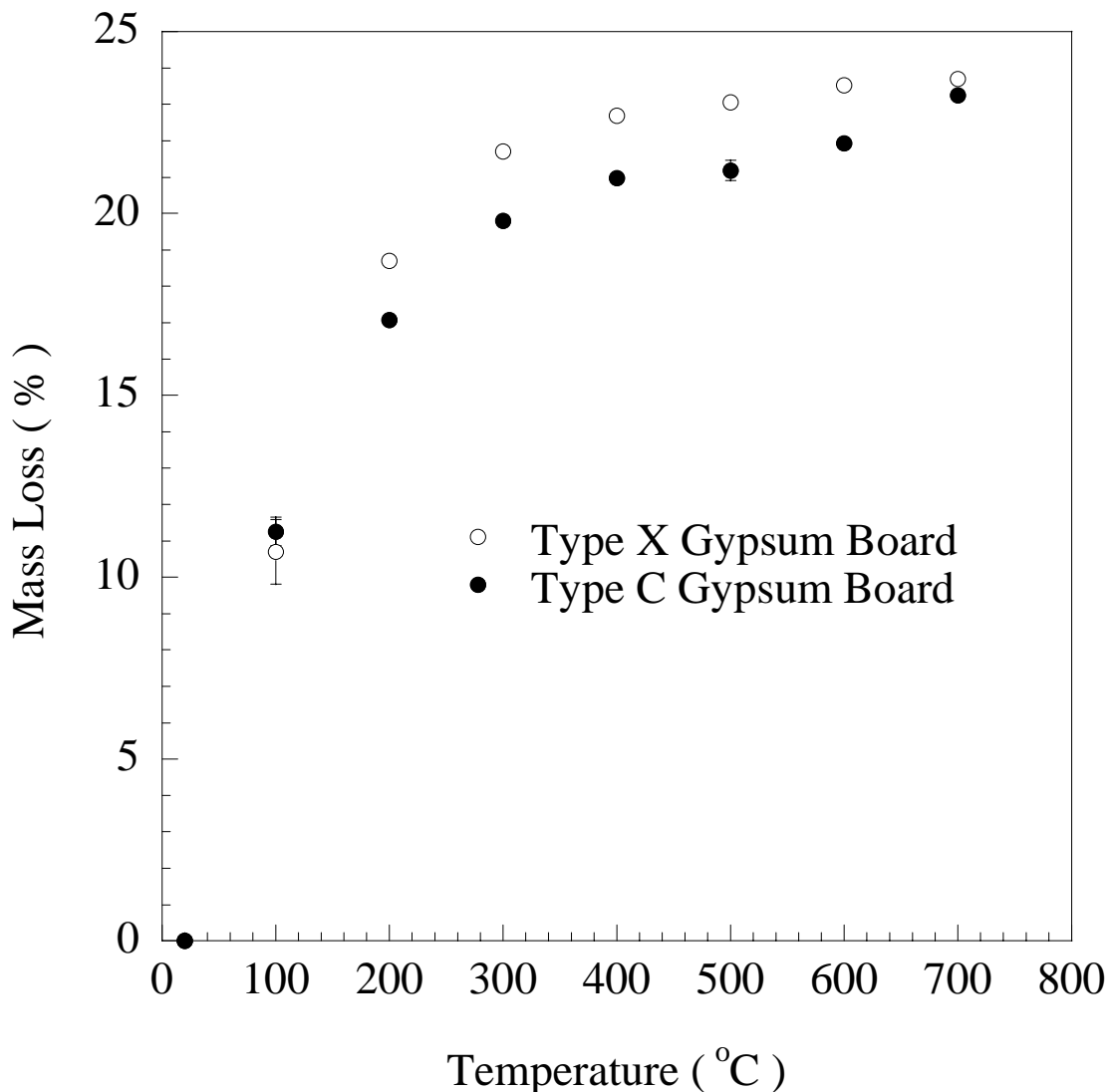


Fig. 5 Measured mass loss of type X and type C gypsum board samples as a function of temperature.

When cracks were observed at the screw locations for Assembly One, the average temperature of the gypsum board (exposed and unexposed face) was 600 °C and the average exposed face heat flux was 137 kW/m². For the identical assembly but different fire exposure²⁰ mentioned above, the average gypsum board temperatures (exposed and unexposed face) and exposed face total heat flux measured were similar: 589 °C and 115 kW/m², when cracks were observed at the screw locations.

It is known that the screw locations are the points where the greatest mechanical stress exists, due to screw penetration. The data from the real-scale experiments showed that as the average temperature of type X gypsum board approached 600 °C, significant cracking occurred. The type C gypsum board for Assembly Two also reached 600 °C, but cracks at the screw locations did not materialize throughout the test. It is suggested that these cracks formed because the type X gypsum board contracted to such a degree that the gypsum board pulled away from screws. The type C gypsum board contraction at 700 °C was equivalent to type X gypsum board contraction at only 400 °C. No cracks were observed for type X board at 400 °C. Thus, the lack of cracking at the screw locations in the type C board may be due to the lower degree of contraction at the screw locations.

The transverse cracks that were observed to form in Assembly One occurred after the fire reached its peak heat release rate and was in the decay phase. At this time, the gypsum board was cooling down as well. It was hypothesized that as the gypsum board cools, it may continue to contract. To test this supposition, gypsum board samples were heated to one of several prescribed temperatures for 3 h, then transferred to another oven at 120 °C, where it remained for another 3 h. The contraction of the sample from the initial dimension was then measured. Especially for temperatures at or above 400 °C, the contraction is considerably larger than the contraction measured when the gypsum board samples are at the elevated temperatures. This is further shown in table 1.

4. CONCLUSIONS

Both full-scale and reduced-scale experiments were performed to gain insight into the behavior of type X and type C gypsum board partitions, especially the cracking that could lead to wall perforation and the passage of smoke and flames into adjacent compartments. The opening of the seam between adjacent panel occurred at similar board temperatures and incident total heat fluxes on the exposed face. The type X panels showed cracking at the mounting screws and transverse cracking at longer times and higher temperatures; the type C panels did not. Reduced-scale experiments replicated the shrinkage, suggesting that such (less costly) measurements might be a predictor of crack formation at seams and mounting screws. The reduced shrinkage of type C board, relative to type X board, at higher temperatures is a plausible explanation for the non-formation of cracks in the real-scale test.

5. ACKNOWLEDGEMENTS

The authors are indebted to the staff of the Large Fire Laboratory (LFL) at NIST for assistance in the experiments. In particular, we are grateful to Mr. Alexander Maranghides (Facility Manager), Mr. Jay McElroy, Mr. Lauren DeLauter, Mr. Ed Hnetovsky, Mr. Gale Miller, and Mr. Marco Fernandez. Dr. S. Kukuck of the Army Research Laboratory is acknowledged for useful discussion. Mr. J. Shields and Dr. D. Lenhart of BFRL-NIST are acknowledged for performing some of the gypsum board contraction measurements.

6. REFERENCES

1. Test Method for Fire Resistance Tests of Building Construction and Materials, ASTM E119-00a, ASTM International, West Conshohocken, PA.

2. Fire Resistance Tests – Elements of Building Construction, ISO 834 Parts 1 through 9, International Organization for Standardization, Geneva Switzerland.
3. NFPA 5000, Building Construction and Safety Code, 2003 Edition, National Fire Protection Association, Quincy, MA.
4. International Building Code (IBC), 2003 Edition, International Code Council, Falls Church, VA.
5. R.W. Bukowski, Prediction of the Structural Fire Performance of Buildings, *8th Fire and Materials Conference*, San Francisco, CA (2003).
6. CIB-W14, Rational Fire Safety Engineering Approach to Fire Resistance of Buildings, Publication 269 (2001).
7. S.L. Manzello, R.G. Gann, S.R. Kukuck, K. Prasad, and W.W. Jones, Real Fire Performance of a Non-Load Bearing Steel Stud Gypsum Wall Assembly: Experiments and Modeling, *Fire and Materials*, in review (2006).
8. Standard Specification for Installation of Steel Framing Members to Receive Screw-Attached Gypsum Panel Products, ASTM C754-00, ASTM International, West Conshohocken, PA.
9. Standard Specification for Application of Finishing of Gypsum Board, ASTM C840-03, ASTM International, West Conshohocken, PA.
10. Standard Specification for Nonstructural Steel Framing Members, ASTM C645-00, ASTM International, West Conshohocken, PA.
11. Standard Specification for Steel-Piercing Tapping Screws for the Application of Gypsum Panel Products or Metal Plaster Bases to Wood or Steel Studs, ASTM C1002-01, ASTM International, West Conshohocken, PA.
12. M.A. Sultan, A Model for Predicting Heat Transfer Through Noninsulated Unloaded Steel-Stud Gypsum Board Wall Assemblies Exposed to Fire, *Fire Technology*, 32:239-259 (1996).
13. A. Hamins, A., Maranghides, K. McGrattan, T. Ohlemiller, and R. Anleitner, *Federal Building and Fire Safety Investigation of the World Trade Center Disaster: Experiments and Modeling of the Multiple Workstations Burning in a Compartment*. NIST NCSTAR 1-5E, National Institute of Standards and Technology, Gaithersburg, MD, (2005).
14. H. Takeda, A Model to Predict the Fire Resistance of Non-Load Bearing Wood-Stud Walls, *Fire and Materials*, 27:19-39 (2003).
15. H. Takeda, J.R. Mehaffey, Wall2D: A Model for Predicting Heat Transfer through Wood-Stud Walls Exposed to Fire, *Fire and Materials*, 22:133-140 (1998).
16. L.R. Richardson, M. Batista, Revisiting the Component Additive Method for Light-Frame Walls Protected by Gypsum Board, *Fire and Materials*, 21:107-114 (1997).
17. O. Axenenko, G. Thorpe, The modeling of dehydration and Stress Analysis of Gypsum Plasterboards Exposed To Fire, *Comp. Mat. Sci.* 6:281-294 (1996).
18. J.R. Mehaffey, P. Cuerrier, G. Carisse, A Model for Predicting Heat Transfer through Gypsum-Board/Wood-Stud Walls Exposed to Fire, *Fire and Materials*, 18: 297-305 (1994).
19. B. Fredlund, Modeling of Heat Transfer and Mass Transfer in Wood Structures During Fire, *Fire Safety Journal*, 20:39 (1993).
20. S.L. Manzello, R.G. Gann, S.R. Kukuck, K. Prasad, and W.W. Jones, Real Fire Performance of Partition Assemblies, *Fire and Materials*, 29:351-366 (2005).
21. Standard Specification for Gypsum Board, ASTM C1396/C1396M-01, ASTM International, West Conshohocken, PA.



EXPERIENCE WITH THERMO IMAGING CAMERAS ON FIRE TESTS

Jan PAŠEK¹, František WALD² and Antonín UHLÍŘ³

ABSTRACT

The paper is focussed to the experiences with measurements by the thermo imaging cameras during the fire test on the 4th floor of the testing steel-concrete structure in the Cardington BRE laboratory performed January 16, 2003. The work presents analyses of the development of the temperature in the connections and elements, readings of temperatures on the structure and observations of the buckling of the lower flange of primary beam. The prediction of the emissivity from the reported matrix is discussed.

1. INTRODUCTION

The instrumentation used in the seventh large test in BRE Cardington laboratory performed January 16, 2003 included thermocouples, strain gauges and displacement transducers, see [1]. A total of 133 thermocouples were used to monitor the temperature of the connections, the steel beams within the compartment, the temperature distribution through the slab and the atmosphere temperature within the compartment, see Fig. 1. An additional 14 thermocouples were used to measure the temperature of the fire protected columns. In the exposed and un-protected elements (fin plate and end plate – minor axis) nine high temperature strain gauges were used. In the protected columns and on the slab a total of 47 ambient strain gauges were installed. Twenty-five displacement transducers were attached along the 5th floor to measure the vertical deformation of the concrete slab. An additional 12 transducers were used to measure the horizontal movement of the columns and the slab.

Ten video cameras and two thermo-imaging cameras, FLIR 695 PM, recorded the fire and smoke development, the deformations and temperature distribution, see Fig. 1 [2]. The thermo-imaging cameras were focused primarily on the development of the temperature

¹ Lecturer, Czech Technical University in Prague, Dept. Building Structures, CZ166 29 Praha, Czech Republic
email: jan.pasek@fsv.cvut.cz

² Professor, Czech Technical University in Prague, Dept. Steel & Timber Struct., CZ166 29 Praha, Czech Rep.
email: wald@fsv.cvut.cz

³ Research assistant, Czech Technical University in Prague, Dept. Steel & Tim. S., CZ166 29 Praha, Czech Rep.
email: antonin.uhlir@fsv.cvut.cz

at the connections. The cameras were recording the matrix of the measured temperatures on the structure. The perpendicular projection dimension of the observed points (pixels) on the structure were due to resolution of the camera detector matrix 320 x 240 pixels, applied lens of 6° viewing field and the distance between cameras and the measured surfaces of 20 m about 5 mm. The temperatures scanned by the cameras were corrected by the temperatures measured by the thermocouples at the beam-to-beam and beam-to-column connections as well as the atmosphere temperature to precise the temperature on the connection surface.

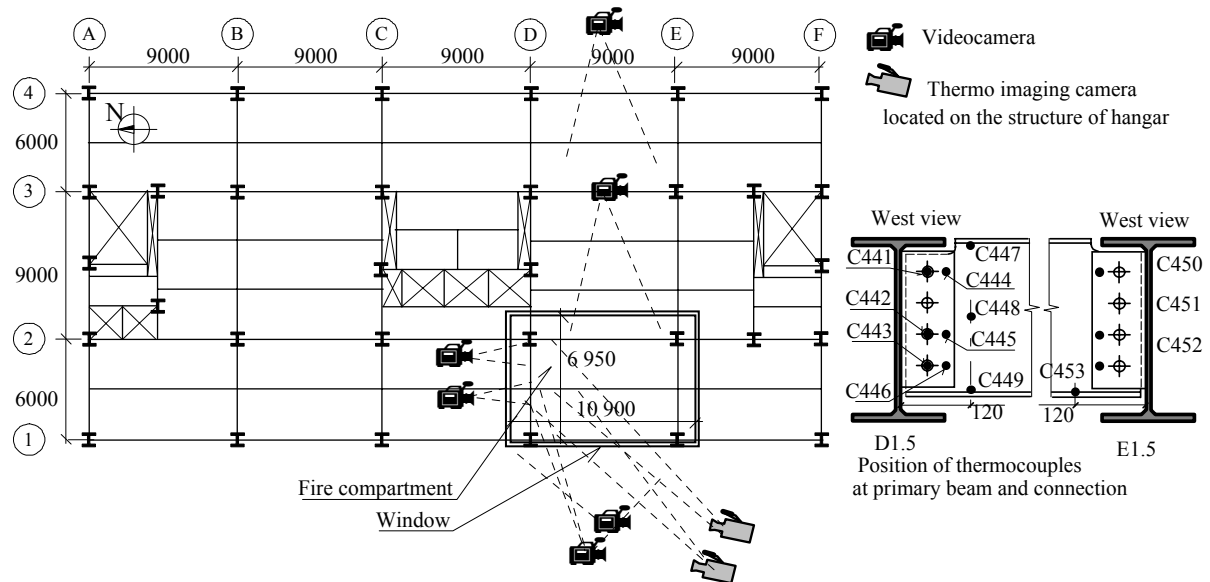
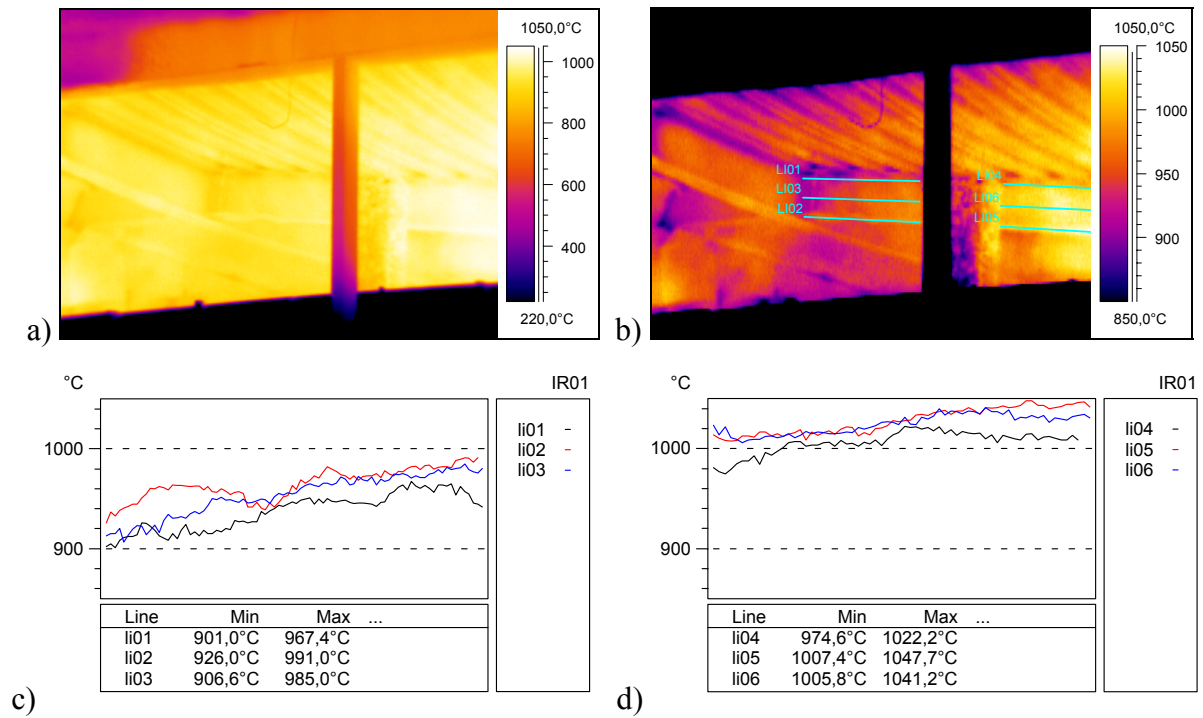


Fig. 1 – Positions of the thermo imaging cameras on the structure of hangar

2. TEMPERATURE

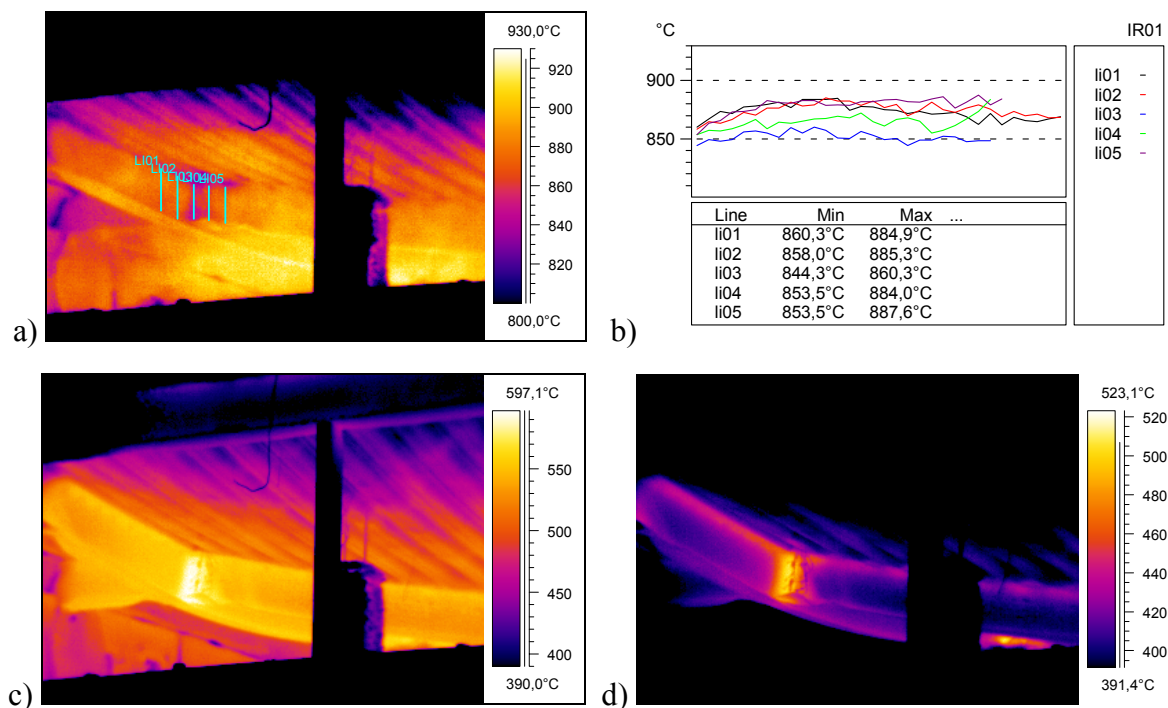
The thermo imaging cameras enable to visualise the development of the surface temperatures during the natural fire. The measured surface temperatures matrix 320 x 240 points obtained from camera was calibrated by temperature values of the visible thermocouples to increase the accuracy, which is limited due to changes of the temperature dependent emissivity, temperature changes of surrounding surfaces, reflected temperature development dependent on the radiation of surrounding surfaces and flames and their emissivity and last but not least chemical changes of gas (atmosphere) in the compartment resulting into the changes of emissivity and transparency of gas.

Fig. 2a illustrates the matrix of temperatures after 57 min of the experiment, corresponding to the maximum temperature measured by the thermocouple on the lower flange of the secondary beam, 1088 °C. The matrix is visualised by colours (or gray on black and white copy) in whole compartment temperature range from 220 °C to 1050 °C. Because of better readability, in Fig. 2b the range is shortened from 850 °C to 1050 °C. Detailed temperature readings along lines 01 to 06 (marked on Fig. 2b) are illustrated in Fig. 2c and 2d; continuance of the lines 01+04, 02+05 and 03+06 is discontinued by the tested specimen hung in the view field of the camera detector.



Note: Scale of greys on figures is different to visualise temperatures.

Fig. 2 – The visualisation of the beam maximal temperature, in 57 min of the experiment; a) thermogram with full matrix; b) the same record with limited temperature scale and marked measured lines; c) and d) the temperature profiles at the lines marked above



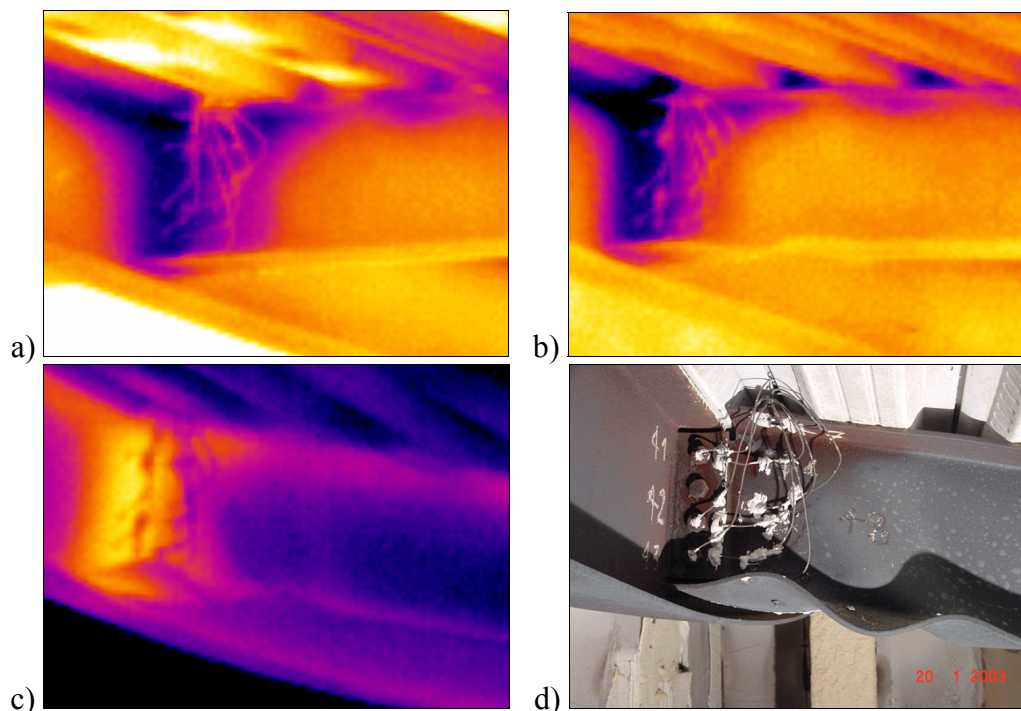
Note: Scale of greys on figures is different to visualise temperatures.

Fig. 3 – Imagine at a) maximal connection temperature in 63 min of experiment; b) the temperature profiles on lines in 63 min of experiment, where the fin plate reached 908,3 °C; and c) in 92 min of experiment by the highest temperature differences; d) continuing cooling of the structure surfaces

The maximum temperature on the fin plate connection was measured after 63 min of the experiment. Fig. 3a illustrates the observed vertical lines positions in the connection; the influence of the developed fire flames temperature on total surface temperature detected by camera is clear. Fig. 3b shows the adequate measured temperatures at marked lines. On cooling the joints are hotter than the surrounding structure surfaces. The highest difference between the temperatures of the connection and the beam was reported after 92 min, see Fig. 3c. The continuing cooling of the connection and whole structure surfaces is reported on Fig. 3d.

3. LOCAL BUCKLING

The experiment in BRE Cardington laboratory January 16, 2003 was oriented to the connections behaviour and their reliability. Two video cameras were placed behind the windows in the plasterboard walls. Both cameras failed due to burning of cables for lightning. The visibility in the wavelength radiation observed by the thermo imaging cameras allows reporting the mechanical behaviour during the test even in the phases with heavy smoke development. The used lens 6° view field and distance of cameras leads to visualized points of size about 5 x 5 mm, which enable to observe the behaviour of local flange. The development of the local buckling is shown in 25 min of fire at Figs 4a, in 35 min 4b and in 110 min 4c. The Fig. 4d shows the observed beam to beam fin plate connection after the experiment.



Note: Scale of greys on figures is different to visualise contours.

Fig. 4 – The observed connection with visible local buckling of the lower flange of the primary beam a) in 25 min of fire b) in 35 min; c) in 110 min; and d) after cooling of the structure

4. EMISSIVITY'S TEMPERATURE DEPENDANCY

The thermo cameras measurement enables to calculate the temperature of observed surface based on the non-contact scanned infrared radiation emitted by this surface. The accuracy of prediction depends on correct estimation of external factors affecting the calculation; see [3] and [4]. One of the major parameters is the emissivity of the scanned surface ε . The non-contact temperature measurement is often utilised vice versa to calculate the emissivity based among others on exact contact technique measured temperature in the points of interest and surrounding surfaces as well as on atmosphere temperature.

For the emissivity prediction the primary beam – secondary beam connection surface without corrosion after its scorch and the measured point identical with position of thermocouple were used. The point C442 was chosen inside the structure (in the corner of primary and secondary beam connection) where the impact of the thermal radiation emitted by the surrounding surfaces on the point of interest temperature was estimated from $2/3$ till $3/4$, see Tab. 1. The gas temperature was measured, see [1]. The temperature dependent emissivity of the gas was expected from 0,42 to 0,29 according to [5]. The contamination of the air by the products of combustion changes rapidly the transparency of air and its permeability for thermal radiation detected by thermocamera. These affects were eliminated so that the emissivity analysis was done on the thermograms created on the structure after combustion during cooling part of experiment.

Tab. 1 – Estimation of the emissivity of steel structure

Time, min	Steel temperature θ_a °C , Thermocouple C442	Gas temperature θ_g °C , Thermocouple C525	Emissivity ε for 66 % radiation of surrounding surfaces	Emissivity ε for 75 % radiation of surrounding surfaces	Estimated emissivity ε
66	880	899	0,65	0,56	0,59
76	800	749	0,63	0,54	0,58
92	700	550	0,61	0,50	0,57
106	600	386	0,60	0,48	0,56
116	500	215	0,58	0,47	0,55
128	400	197	0,57	0,46	0,54
148	300	146	0,56	0,45	0,53

5. CONCLUSIONS

The thermo imaging cameras helped to visualise the development of the temperatures during the natural fire experiment. With support of measurements by thermocouples located in the observed field of the camera the surface temperatures were predicted with good accuracy.

The non-contact measured matrix of temperatures showed the structural behaviour and its contours in cases where the visibility of the video cameras is limited. The calculation of the relative change of the position may enable to observe the deflections as well.

For known temperatures of the structure surfaces, surrounding structures and atmosphere the surface emissivity of the structure during the natural fire may be observed with limited accuracy due to the complexity of radiation.

The non-contact temperature measurements by thermo imaging camera brings a good experiences in development of fire safe connection of sandwich panels, see [6].

6. ACKNOWLEDGEMENT

This outcome has been achieved with the financial support of the Czech Ministry of Education, Youth and Sports, projects No. VZ MSM 6840770005 and MSM 6840770001.

7. REFERENCES

- [1] Wald F., Silva S., Moore D. B, Lennon T., Chladná M., Santiago A., Beneš M.: Experimental behaviour of a steel structure under natural fire, *The Structural Engineer, New Steel Construction*, 3/2005, pp. 24-27, ISSN 0968-0098.
- [2] Wald F., Chladná M., Moore D., Santiago A.: Temperature distribution in a full-scale steel framed building subject to a natural fire; *Steel and Composite Structures*, Vol. 6, No. 2 (2006), in printing.
- [3] Madding R. P.: Emissivity measurement and temperature correction accuracy consideration, *proc. Thermosence XXI*, Vol. 3700, SPIE, 1993, pp. 393-401.
- [4] Pašek J., Svoboda J.: Physical aspects of the application of non-contact thermography in the analysis of external skin of buildings, *Stavební obzor*, 3/2004, pp. 82-91.
- [5] Ghojel J. I.: A new approach to modeling heat transfer in compartment fires, *Fire safety journal* 31, 1998, pp. 227-237.
- [6] Uhlíř A., Wald F.: On development of fire safe connection of sandwich panels, internal report, Czech Technical University in Prague, 2005, p. 26.



THERMAL STRESSES IN GLAZING SYSTEMS IN BUILDINGS

Piotr TOFILO¹, Michael DELICHATSIOS², Ali NADJAI³ and Jean-Marc FRANSSEN⁴

ABSTRACT

A thorough examination has been performed for the first time of the thermal stresses on a window in an enclosure fire environment. Analytical and numerical methods established the importance of bridling (due to axial elongation) and flexing stresses (due to normal deformation). Previous studies omitted the importance of flexing stresses. Maximum stresses on the sides have been calculated for varying aspect ratios of a rectangular window and for varying ratios of shaded width to the window sides. For uniform width and uniform heating (represented by constant temperature in the heated region), the maximum stresses are bridling and equal to those of an infinite strip shaded on two sides when the shaded width is less than 40% of the side. For non-uniform shading (e.g. due to radiation blockage) or non-uniform heating, flexing stresses contribute to the total stress by an increase up to 50%. These new results have been applied in predicting the magnitude of stresses and the location of first crack in well-controlled experiments and measurements.

1. INTRODUCTION

Cracking and subsequent fall out of glazing can change dramatically the fire intensity in enclosure fires by generating, for example, an additional opening feeding fresh combustion air into the fire. Thermal expansion of the glazing caused by heat fluxes from the fire produces stresses of sufficient magnitude to initiate cracks in the glazing. The relation between the stresses and the temperature distribution on the glazing enables the prediction of times to first crack and subsequent cracks. Recent work¹⁻⁶ suggests that this relationship is simple:

$$\varepsilon_b = \sigma_b/E = \beta\Delta T_b \quad (1)$$

¹ Research assistant, University of Ulster, Fire Safety Engineering Research and Technology Centre (FireSERT), Jordanstown, Shore Road, BT37 0QG, Northern Ireland; email: p.tofilo@ulster.ac.uk

² Professor, University of Ulster, Fire Safety Engineering Research and Technology Centre (FireSERT), Jordanstown, Shore Road, BT37 0QG, Northern Ireland; email: m.delichatsios@ulster.ac.uk

³ Professor, University of Ulster, Fire Safety Engineering Research and Technology Centre (FireSERT), Jordanstown, Shore Road, BT37 0QG, Northern Ireland; email: a.nadjai@ulster.ac.uk

⁴ Ass. Professor, University of Liege, ; email: jm.franssen@ulg.ac.be

Each term in Eq. (1) is the thermally induced strain at the edge of the glass at the breaking point. The first equation is Hook's Law and the second is the definition of the thermal coefficient of linear expansion, $\beta = (dl / dT) / l$. Using typical values for the glass breaking stress⁵, $10 < \sigma_b < 50$ MPa, and Young's Modulus, $E \sim 72$ GPa, in Hook's Law gives small breaking strains, $1.5 \times 10^{-4} < \epsilon_b < 7 \times 10^{-4}$; i.e., 0.015% to 0.07% thermal expansion suffices to break the glass. The frame offers no restraint to the glass since the maximum thermal expansion, < 1 mm, is less than the normal gap of several mm between the frame and the pane^{3,4}. From Eq. (1), assuming $\beta \sim 9 \times 10^{-6} \text{ K}^{-1}$, the spatially averaged glass temperature rise at breaking is $20^\circ\text{C} < \Delta T_g < 80^\circ\text{C}$. The spatially averaged glass temperature is defined through Fig.1 taken from³. Consider the framed windowpane shown in Fig. 1. The coordinate origin is placed at the inner edge of the shaded region of width s ; z is into the glass with zero on the fire side and the glass thickness is L so that $0 \leq z \leq L$; y is toward the center of the pane and x is along the edge of the shaded region.

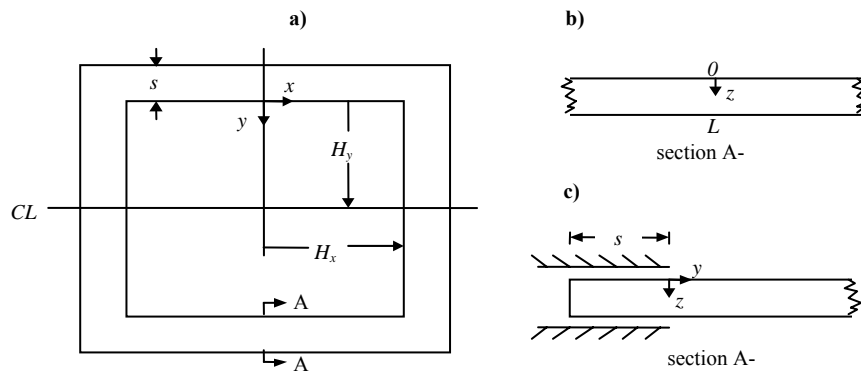


Fig. 1 – Window geometry: z is the depth, y is normal to the shaded region, x is along the shading, s is the width of the shading, H_y and H_x are the exposed pane half-lengths and L is the glass thickness.

It has been claimed^{3,4} that “the greatest simplification comes from recognizing that it is the difference between the integrated bulk temperature over the central pane and the coldest temperature on the pane edge which produces the strain that leads to cracking. As Keski-Rahkonen says: “maximum stresses are located at cold spots”^{1,2}. The point of crack origin will be the edge cold spot with the largest stress-concentrating defect. Then the ΔT_b in Eq.1 is:

$$\Delta T_b = \bar{T}_{\text{exposed}} - T_{\text{coldest}} \quad (2)$$

where

$$\bar{T}_{\text{exposed}} \equiv \int_0^L \int_0^{H_y} \int_0^{H_x} \frac{T(x, y, z, t_b)}{L H_y H_x} dx dy dz \quad (3)$$

with the upper right quadrant assumed to represent the whole pane.

The relation defined by Eqs.1,2,3 proposes that the thermal strain and stresses are independent of a) the detailed temperature distribution and b) the aspect ratio or shape of the window. Examination, however, of earlier work on thermal expansion of glazing in solar energy applications^{5,6,7} and theoretical analysis show that this conclusion and claim needs revisiting, which this paper presents. It is remarkable that the more recent fire related work¹⁻⁴ does not include references to those earlier papers related to solar radiation⁶⁻⁸.

2. THERMAL STRESS: ANALYTIC SOLUTIONS

Variations of stresses and temperature in depth can be neglected because the glazing thickness is much smaller than the other dimensions. Therefore, the development of stresses and the temperature distribution are two-dimensional so that the glazing behaves as a thin plate. This is the approximation all previous investigators have adopted¹⁻⁸. The analytic solutions of Keski-Rahkonen^{1,2} are examined in detail. These solutions were adopted by Pagni³⁻⁵ and represented by Eqs.1 and 2. Keski-Rahkonen^{1,2} examined two geometries, a long rectangular strip¹ and a circular glass plane having a radially symmetric temperature distribution². The solution for the circular glass plane can be found in standard books¹⁰ and shows that Eq.1 can indeed express the thermal stress where effective temperature rise is the average temperature of the circular pane of radius a :

$$\bar{T}_{\text{exposed}} = \frac{1}{\pi a^2} \int_0^a 2\pi T r dr \quad (4)$$

The solution for the long strip, however, being not accurate both in Ref¹ and in Ref³⁻⁵ is revised in the next section.

The Keski-Rahkonen¹ solution for a long strip of glazing

The investigation of thermal stresses starts with the examination of the solution of Keski-Rahkonen¹, also adopted by Pagni³. For quick reference, the complete stress equations for a rectangular thin plate and their boundary conditions are recast in Appendix A¹⁰. For common glazing applications, the edges, having space to expand, are traction free, which means that stresses normal to the edge are zero at each edge. A rectangular window ABCD of size $(2b \times 2c)$ is shown in Fig.2 having a x-y coordinate system with origin at the center of the window. For aspect ratios $b/c > 3$, numerical solutions^{7,12,13,14} show that the window behaves as an infinitely long strip.

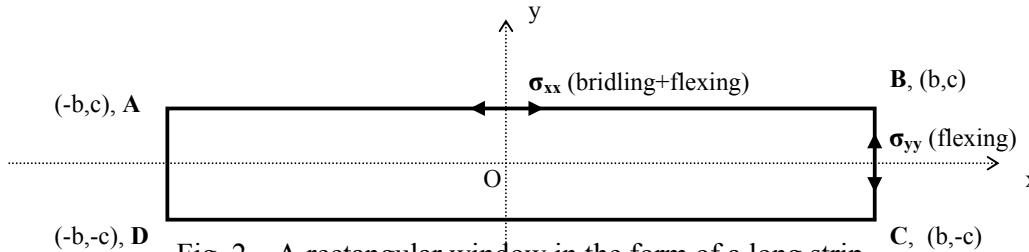


Fig. 2 – A rectangular window in the form of a long strip

The solution^{1,3} is derived for a temperature function of y only: $T = T(y)$. The traction free boundary conditions are (see Appendix A):

On sides AD and BC: normal and shear stresses are zero

$$\sigma_{xx} = \sigma_{yx} = 0 \quad (5a)$$

but the normal y -stress (flexing due to deformation) is not:

$$\sigma_{yy} \neq 0 \quad (5b)$$

On sides AB and DC: similarly, normal and shear stresses are zero

$$\sigma_{xy} = \sigma_{yy} = 0 \quad (5c)$$

but the normal x -stress (bridling due to axial tension) is not:

$$\sigma_{xx} \neq 0 \quad (5d)$$

A simplification of the stress relation near the center $x = 0$ of the strip is obtained by noting that the y stresses are zero $\sigma_{xy} = \sigma_{yy} = 0$ there and the remaining parameters are functions only of y near the center of the strip. But still the y normal stress is different from zero $\sigma_{yy} \neq 0$ on the sides AD and BC (specifically at their center) as it will be shown later when discussing the numerical solution in the next section. For the conditions near the y -axis, the compatibility relation in terms of the stresses (see Eq. A6) gives:

$$\frac{\partial^2 \varepsilon_{xx}}{\partial y^2} = 0 \quad (6a)$$

The x normal stress near the center axis Oy (Fig.2) is given by Eq.A5a,

$$\frac{1}{E} \sigma_{xx} = \varepsilon_{xx} - \beta T \quad (6b)$$

The solution of the system of Eqs.5 and 6 is simply:

$$\varepsilon_{xx} = Ay + B \quad (7a)$$

$$\frac{1}{E} \sigma_{xx} = Ay + B - \beta T \quad (7b)$$

where the constants A and B need two boundary conditions to be derived. These boundary conditions are related the boundary conditions for the normal x stress on sides AD and BC:

$$\int_{-c}^{+c} \sigma_{xx} dy = 0 \quad (8a)$$

$$\int_{-c}^{+c} y \sigma_{xx} dy = 0 \quad (8b)$$

The latter condition was not considered in references 1 and 3. It is essential when the temperature field is not symmetric in the y direction. The stress for any temperature distribution is given by:

$$A = \frac{3\beta}{2c^3} \int_{-c}^{+c} y T dy \quad (8c)$$

$$B = \beta \int_{-c}^{+c} \frac{T}{2c} dy \quad (8d)$$

$$\frac{1}{E} \sigma_{xx} = \frac{3\beta}{2c^3} y \int_{-c}^{+c} y T dy + \beta \int_{-c}^{+c} \frac{T}{2c} dy - \beta T = \beta (T_{av} - T) \quad (8e)$$

For a temperature variation symmetric in y , the coefficient $A=0$ and the coefficient B is equal to the average temperature of the strip $T_{av} = \beta \int_{-c}^{+c} \frac{T}{2c} dy$ and the x normal stress is:

$$\frac{1}{E} \sigma_{xx} = \beta \int_{-c}^{+c} \frac{T}{2c} dy - \beta T = \beta (T_{av} - T) \quad (9a)$$

The stress is tension at the edges and contraction near at the centre of the strip. The strain being independent of y in this case is equal to :

$$\varepsilon_{xx} = \beta T + \frac{1}{E} \sigma_{xx} = \beta T_{av} \quad (\text{independent of } y) \quad (9b)$$

The latter result means that there is no deformation of the long strip near its centre along the y -axis. The normal stresses caused by expansion but without deformation in the x direction are called bridling stresses. For an asymmetric distribution of temperature, the strain is a function of y and the strip sustains deformation so that even the stress σ_{xx} is the sum of a bridling and a flexing component.

Equation 9a is the same as the result given by Keski-Rahkonen¹, also adopted by Pagni³. However, there are some critical differences in the derivation and assumptions:

1. None of these derivations^{1,3} led to the general solution given by Eqs.7, 8a and 8b applicable for an arbitrary temperature distribution
2. Keski-Rahkonen's derivation¹ does not mention any boundary conditions whereas both Keski-Rahkonen¹ and Pagni³ assume a temperature profile even with y .
3. Both these derivations^{1,3} imply that the y normal stress is everywhere zero on the sides BC and AD, a result that is shown not to be correct by resorting to numerical solution in the next section. It is important to point out at this point that the y stresses caused on the sides BC and AD are due to their flexing and deformation by expansion. These stresses are called flexing stresses.

The previous derivations of stress relations in a rectangular strip^{1,3} have misled investigators to conclude that the simple Eq.1 gives the stress (where Eq.2 defines the temperature) regardless of the shaded area of the window, its aspect ratio or the temperature distribution. Moreover, the previous investigators did not consider the flexing stresses, which will be shown to have a significant contribution to the cracking of the glazing.

A complete numerical analysis is applied in the next section to determine the influence of the temperature distribution, aspect ratio and shaded area on the stresses. To focus the present investigation on the stresses in a fire environment, we bypass the discussion of the thermal field by considering the temperature to be constant in the exposed area and equal to zero in the shaded area. The shaded area is taken to have the same width all around the window (Fig.3a) or different widths in the vertical direction (Fig.3b). The chosen representation of the temperature field in Fig.3a is applicable for a window in the hot layer in an enclosure and for times prior to a temperature increase by diffusion at the outer cold edges of the plate. The situation of variable vertical shaded area in Fig.3b represents an anticipated and measured vertical variation of the heat fluxes from a fire in an enclosure when the window extends over the height of the enclosure from the hot to the cold layer.

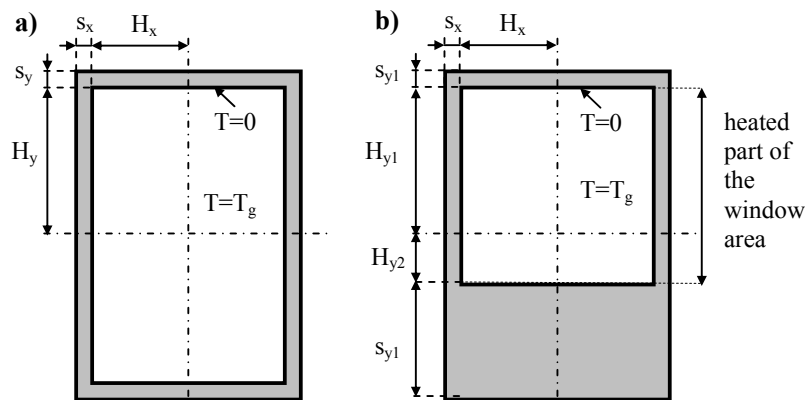


Fig.3 - A window heated with a shaded region of constant width representing a window located
a) totally in the hot layer b) partially in the hot and cold layers of an enclosure fire

3. NUMERICAL INVESTIGATION OF THERMAL STRESSES

The numerical investigation has been carried out using three different finite element codes computer codes^{12,13,14} for comparison and verification of the results. Moreover, an earlier numerical solution based on a collocation method⁷ was also consulted. The numerical results agreed with the exact solution for the infinite strip (e.g. Eqs 9a and 9b). Numerous calculations for the stresses were carried out to elucidate the physics¹⁵ but results are only discussed for the conditions of Figs.3a and 3b, which reproduce well more realistic distributions of temperatures near the shaded region¹⁵. These situations will be presented in a different paper.

From the linearity of the stress equation (see Appendix A) and computer calculations, we have found that all configurations in Figs.3a and 3b can be represented by multiple superposition of the solutions for a single strip shading (Fig.4a) and a corner shading (Fig.4b).

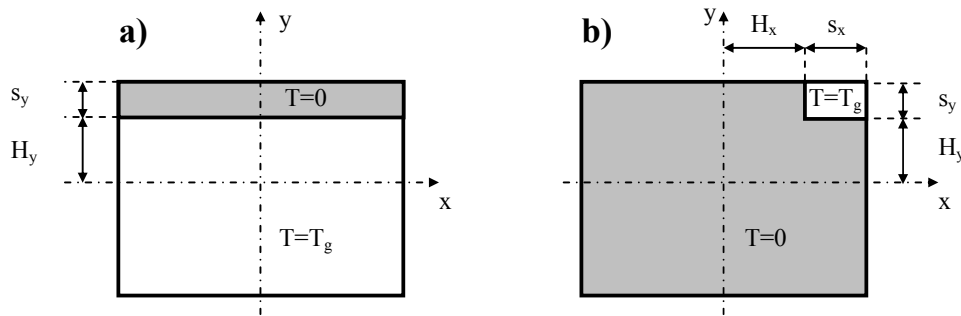


Fig. 4. Basic geometries for multiple superposition
a) single strip shaded b) everything but corner region shaded

For these two cases the stress tensor in any location can be expressed in terms of the following relations:

$$\frac{\sigma_{ij}(x,y)}{E\beta T_G} = \text{function} \left(\frac{s_y}{H_y}, \frac{H_x}{H_y} \right) \quad \text{for the single strip shading} \quad (10a)$$

$$\frac{\sigma_{ij}(x,y)}{E\beta T_G} = \text{function} \left(\frac{s_x}{H_x}, \frac{s_y}{H_y}, \frac{H_x}{H_y} \right) \quad \text{for the corner configuration} \quad (10b)$$

For calculating the breakage time, the maximum stresses (set equal to the yield stress) are needed at the edges; these stresses occur at the center of a side edge or at the edge junction of the large cold shaded area with the hot part of the window (Fig. 4b). The generalized functions in Eqs.10a and 10b have been obtained by using response surface functions derived from the numerical results. However, we present in this paper some representative cases for the configurations in Figs. 3a and 3b to effect modifications of Eqs.1 and 2 and provide simple useful results. The following results show the significance of the flexing stresses and demonstrate that stresses higher than the ones calculated from Eqs.1 and 2 could arise.

3.1 Stresses in a window with constant width of the shaded area (see Fig.3)

The stresses and temperature fields can be deduced from the superposition of the two strip configurations (horizontal and vertical), a corner configuration and a uniform temperature configuration (no stress) as shown in Fig.5a. All cases of aspect ratio and shaded width fraction (s_y / H_y) have been examined in Reference 15. We present here only the stresses for a square window (i.e. $H_x / H_y = 1$) utilizing the superposition shown in Fig.5a.

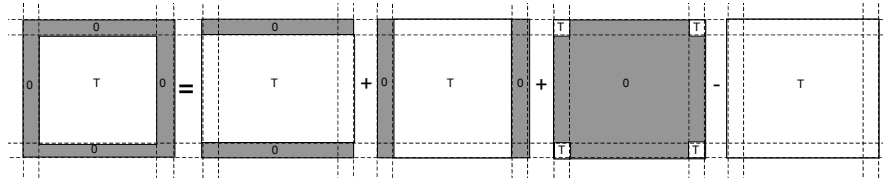
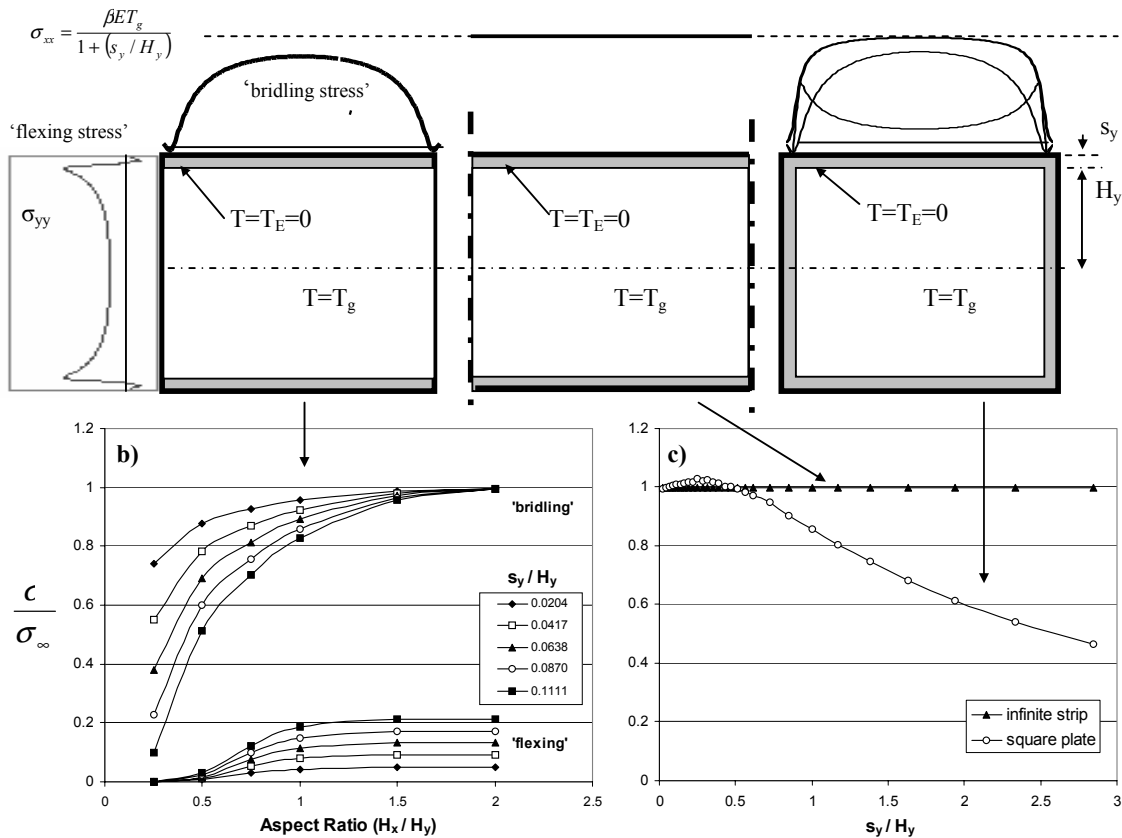


Fig. 5a – Superposition of simple configurations to represent a window with constant width of the shaded area

For shaded widths $s_y/H_y < 0.5$, the corner configuration does not contribute to the maximum stresses in the center of the edges as shown in Fig.5a and on top of Figs. 5b and 5c. The bridling and flexing stresses for the strip configuration of all aspect and width ratios are plotted in Fig.5b and the stresses for the square window are shown in Fig.5c. All stresses are normalized by the stress for an infinite strip at the center of the top edge:

$$c_{\infty} = \beta E T_g / (1 + s_y / H_y) \quad (\text{derived from Eq.9a}) \quad (11)$$



Figs. 5b, 5c – Stresses normalized by the bridling stress of an infinite strip
b) for a strip of variable aspect ratio c) for a square window and variable shaded width ratio

We make the following remarks regarding Figs 5b and 5c:

1. Both bridling and flexing stresses for the strip configuration (shaded on two opposite sides) are less than the maximum value for an infinite strip (see Fig.5b). Such an arrangement can be considered as a modification of current installation methods to reduce the maximum stresses and the propensity of window to break.
2. The stresses for the square window with constant shaded width are nearly equal to stresses for a infinite strip (see Fig.5c) for widths $s_y/H_y < 0.5$ (a slight insignificant increase can be observed for s_y/H_y around 0.25). These stresses are bridling stresses because the corner configuration in Fig.5a restricts the deformation of the edges. For larger widths $s_y/H_y > 0.5$ the stresses reduce and are proportional to the fraction of the area shaded¹⁵.

The stresses for a window of any aspect ratio with constant shaded width are given by the relation for the infinite strip as in Eq.11 if $s_y/H_y < 0.5$. The maximum stresses for both sides are the same and their magnitude depends on the maximum width ratio s_y/H_y or s_x/H_x to be used in Eq.11.

3.2 Stresses in a window with non-uniform heating or variable width of the shaded area in the vertical direction (see Fig.3b)

The stresses and temperature fields can be deduced from the superposition of simpler strip configurations as shown in Fig. 6a. We restrict the presentation here for a square window. Because the temperature field is asymmetric, flexing and bridling stresses are important for the vertical and horizontal sides both in the strip and the window configurations. The stresses are normalized by the maximum stress for an infinite two-sided strip having a shaded width equal to the smaller width in Fig.6a using Eq.11. The maximum stresses on the horizontal and vertical sides are plotted in Figs 6b and 6c against the fraction of the area heated as defined in Fig.6a.

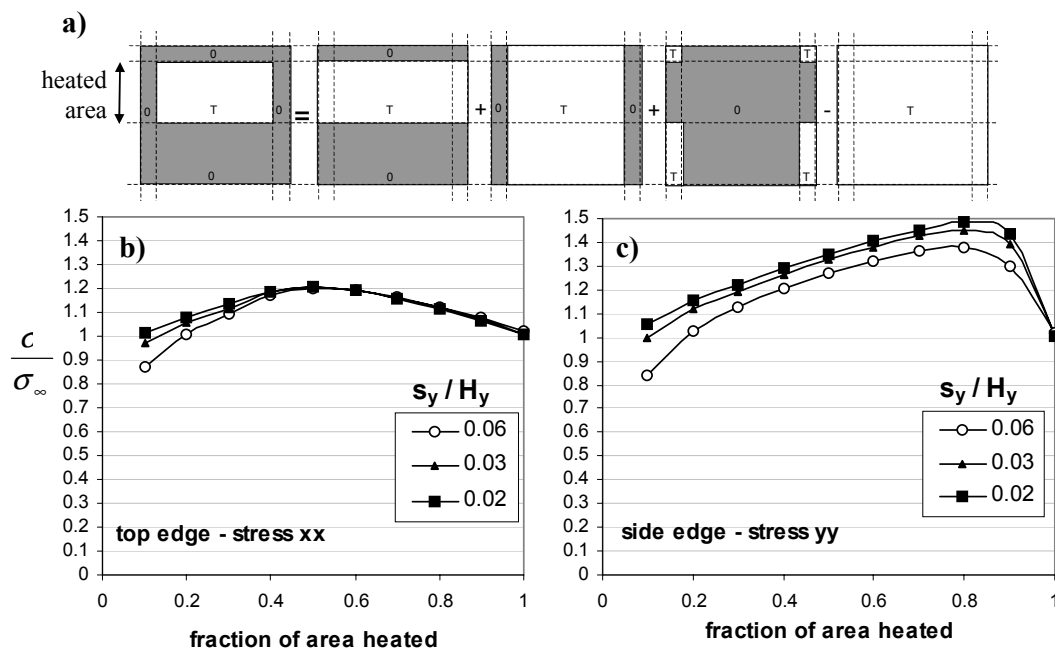


Fig. 6 – a) Superposition of simpler configurations to represent the temperature and stress in a window with non-uniform heating b,c) stresses normalized by the bridling stress in an infinite strip (Eq.11) for variable shaded width (s_y/H_y) and fraction of area heated

The results shown in Figs.6a, 6b and 6c are discussed for clarification:

1. The stresses are higher on the vertical side and about 50% more than the stress for uniform width and temperature. This applies to all aspect ratios¹⁵.
2. Both bridling and flexing stresses contribute to the total stress.

4. COMPARISONS WITH EXPERIMENTS

Experiments¹⁵ in enclosure fires have validated the previous analysis which also provided explanation why cracking occurs on the vertical side in these experiments (see Figs. 6a,6b,6c). Briefly, Fig. 7a and 7b outline the temperature profile on a window obtained by an infrared camera (darker areas denote lower temperatures) and Fig. 7c compares predicted with measured values of the strains. The first crack occurred on the vertical sides where the maximum stresses are expected (see Figs.6b and 6c), because significant shading (due to radiation blockage) was observed in the measurements of temperature distribution as shown in Fig. 7c.

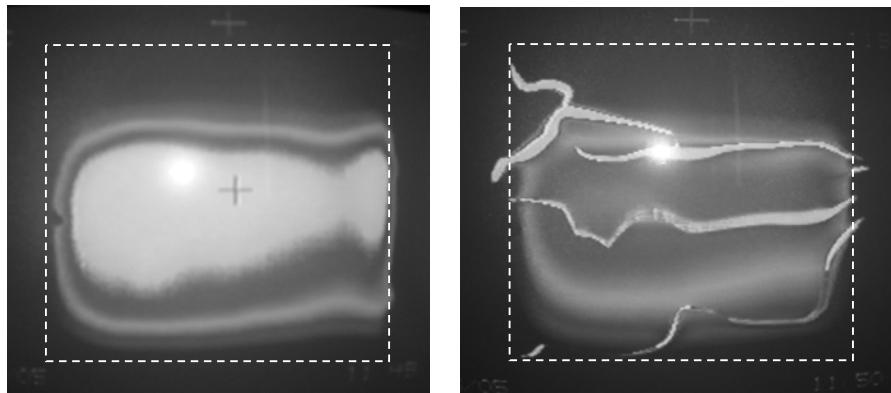


Fig. 7 – a,b) Temperature distribution and cracking patterns on glazing¹⁵

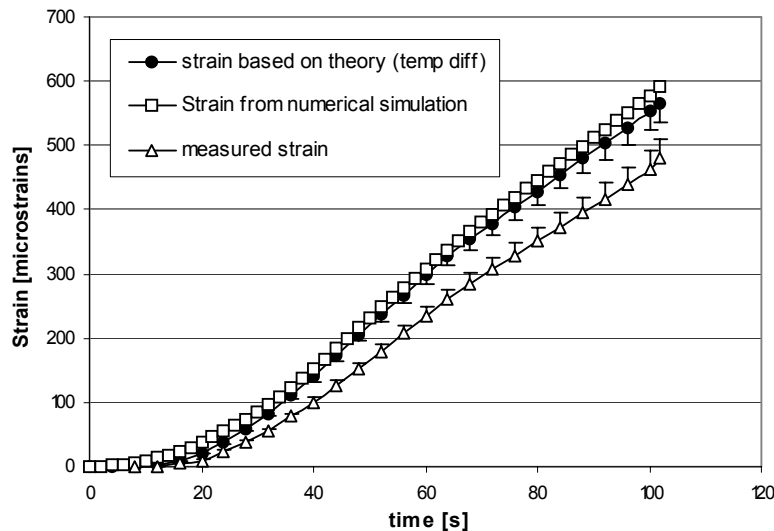


Fig. 7c – Comparison of measured and calculated strains in a glazing experiment¹⁵ (uniform heat flux was used over all the window area for simple calculation and numerical simulation)

5. CONCLUSIONS

Analytical equations developed in this work together with numerical simulations have been used to gain fundamental insight into the dominant mechanisms governing the experimental and measured stress magnitudes and the first crack locations.

The major conclusions of this work are:

1. Analytical and numerical solutions demonstrated the significance of the bridging and flexing stresses in calculating the maximum thermal stresses on a window in a enclosure fire environment.
2. For non-uniform heating or variable shaded width, the stresses increase by 50% owing to the contribution of flexing stresses added to the bridging stresses.
3. For uniform heating and equal shaded width of a rectangular window, the maximum stresses being bridging on both sides are the same and equal to those of an infinite strip corresponding to the long side.
4. These results were applied to predict the stresses, the breaking time and possible first crack location in well-controlled experiments and proper measurements.

Further research is needed to assess when the glazing will fall out after the first crack occurs.

6. REFERENCES

1. Keski-Rahkonen, O., "Breaking of Window Glass Close to Fire," *Fire and Materials*, **12**, 61-69, 1988.
2. Keski-Rahkonen, O., "Breaking of Window Glass Close to Fire, II: Circular Panes," *Fire and Materials*, **15**, 11-16, 1991.
3. Pagni, P., Thermal Glass Breakage, Howard W. Emmons Lecture, 7th International Symposium on Fire Safety Science, June 2002, Boston
Proceedings of the Seventh Symposium, ed. Evans, D., IAFSS, 2002, in press.
4. Joshi, A.A. and Pagni, P.J., "Fire-Induced Thermal Fields in Window Glass. I – Theory," *Fire Safety Journal*, **22**:1, 25-43, 1994.
5. Joshi, A.A. and Pagni, P.J., "Fire-Induced Thermal Fields in Window Glass. II – Experiments," *Fire Safety Journal*, **22**:1, 45-65, 1994.
6. Mai, Y.W., Jacob, L.J.S. "Thermal Fracture of Building Glass Subjected to Solar radiation" Volume 3, ICM 3, Cambridge, England, 1979.
7. Roberts, E. "Elastic Design Charts for Thin Plates with Spanwise and chordwise variations of Temperature" NASA, Technical Note, D-1182, 1962
8. Colvin, J.B. and Lightfoot, D.G. "Thermal Stress in non-rectangular Glazing" Pilkington, Technical Sales Laboratory, Report No 382, 1974.
9. Eckersley, D., "Calculation of Thermoelastic Stresses in Two Dimensions", Report PT/70/5, Pilkington, 1970
10. Landau, L.D, Lifshitz, E.M, "Theory of Elasticity", Pergamon Press, 2nd Ed., pp 22, 198
11. Harada, K., Enomoto, A., Ueda, K., and Wakamatsu, T., "Experimental Study on Glass Cracking and Fallout by Radiant Heat Exposure," *Fire Safety Science – Proceedings of the Sixth International Symposium*, ed. Curtat, M., IAFSS, 2000, pp. 1063-1074.
12. Ansys, Technical Documentation
13. SAFIR. A Thermal/Structural Program Modelling Structures under Fire, Franssen J.-M., Engineering Journal, A.I.S.C., Vol 42, No. 3 (2005), 143-158
14. FireCrack, Technical Documentation, University of Ulster
15. Tofilo, P., "Factors controlling the behaviour of glazing in enclosure fires", PhD thesis, University of Ulster, 2006

APPENDIX A**TWO –DIMENSIONAL FORMULATION OF STRESSES FOR THIN PLATES**¹⁰

The stress equations in orthogonal co-ordinates are:

$$\left(\frac{\partial^2}{\partial x^2} + \frac{\partial^2}{\partial y^2}\right)(\sigma_{xx} + \sigma_{yy}) + E\alpha\left(\frac{\partial^2}{\partial x^2} + \frac{\partial^2}{\partial y^2}\right)T(x, y) = 0 \quad (\text{compatibility equation}) \quad (\text{A1})$$

and

$$\frac{\partial \sigma_{xx}}{\partial x} + \frac{\partial \sigma_{xy}}{\partial y} = 0 \quad \text{and} \quad \frac{\partial \sigma_{yy}}{\partial y} + \frac{\partial \sigma_{yx}}{\partial x} = 0 \quad (\text{force equilibrium with no external forces}) \quad (\text{A2})$$

The boundary relations at the edges are for traction free conditions:

$$\sigma_{xx}n_x + \sigma_{xy}n_y = 0 \quad (\text{A3})$$

and

$$\sigma_{yx}n_x + \sigma_{yy}n_y = 0 \quad (\text{A4})$$

These relations mean that at the window side normal to x-axis $\sigma_{xx} = \sigma_{yx} = 0$ and at the window side normal to the y-axis $\sigma_{xy} = \sigma_{yy} = 0$. The plane strains are related to the stresses by the following equations:

$$\epsilon_{xx} = \frac{1}{E}(\sigma_{xx} - \nu\sigma_{yy}) + \beta T \quad (\text{A5a})$$

$$\epsilon_{yy} = \frac{1}{E}(\sigma_{yy} - \nu\sigma_{xx}) + \beta T$$

(A5b)

$$\epsilon_{xy} = 2\frac{E}{1+\nu}\sigma_{xy} \quad (\text{A5c})$$

Finally, there is strain in the direction z normal to the surface:

$$\epsilon_{zz} = -\frac{\nu}{E}(\sigma_{xx} + \sigma_{yy}) + \beta T$$

(A5d)

The compatibility Eq.A1 takes the following form in terms of the strains:

$$\frac{\partial^2 \epsilon_{yy}}{\partial x^2} + \frac{\partial^2 \epsilon_{xx}}{\partial y^2} = \frac{2\partial^2 \epsilon_{xy}}{\partial x \partial y} \quad (\text{A6})$$

Eq.A1 becomes formally simpler and Eq.A2 is not needed by introducing the Airy stress function $F(x, y)$ which is related to stresses by:

$$\sigma_{xx} = \frac{\partial^2 F}{\partial y^2}, \quad \sigma_{yy} = \frac{\partial^2 F}{\partial x^2}, \quad \sigma_{xy} = -\frac{\partial^2 F}{\partial x \partial y} \quad (\text{A6})$$

These equations have been solved numerically and simple solutions have been developed for example in Ref.⁷: “Elastic design charts for thin plates with span-wise and chord-wise variations in temperature”, NASA, Technical Note D-1182, 1962.



INVESTIGATION OF FIRE PERFORMANCE OF STRUCTURAL MEMBERS INCORPORATING FIBER REINFORCED PLASTIC COMPOSITES USED SCALED EXPERIMENTAL ENCLOSURE FIRES

Vahid MOTEVALLI¹ and Tahar EL-KORCHI²

ABSTRACT

Advances in fiber reinforced composite technology have resulted in the development of Fiber Reinforced Plastic (FRP) elements that exceed the tensile strength of steel at only fraction of the weight. The use of fiber reinforced plastics as structural components such as reinforcement rods in concrete, bridge grid segments and special building applications has become wide-spread. The motivation for use of FRP structural elements includes non-corrosive property as well as good weight to strength ratio and electrically non-conductive behavior. However, the use of FRP introduces new concerns about the fire resistance and endurance of such structural members. There are possible scenarios, which would justify such concerns. Several such situations are described herein to demonstrate the likelihood of bridges, parking garages and similar structures, when exposed to a fire, may result in the loss of structural integrity of FRP-reinforced structural members.

This paper discusses use of scale-fire models the fire performance of FRP structural members and concrete structural members reinforced with FRP. The issues are addressed in two parts: 1) Development of an experimental approach to for fire testing of reinforced concrete columns exposed to post-flashover enclosure fires, 2) A theoretical discussion of application of such methodology FRP structural members.

The results show that columns under compressive load and exposed to fires behave differently and the potential for exposure of FRP elements to temperatures above 100C is great.

¹ Associate Professor, , Ph.D., P.E., Civil and Environmental Engineering, 801 22nd St., NW, The George Washington University, Washington, DC 20052, e-mail: vahidm@gwu.edu

² Professor, Ph.D., P.E.Civil and Environmental Engineering, 100 Institute Rd, Worcester, MA 01609, e-mail: tek@wpi.edu

Use of scaled experimental simulation is an appropriate method to address evaluation of FRP reinforced structural members or their fire performance.

1. INTRODUCTION

Fiber Reinforced Plastic (FRP) composites, with different matrix material, in the form of bars, beams, grating, etc., and as a replacement for steel as reinforcement rods in concrete structural members has gained more acceptability in a variety of structural applications. Some applications of FRP include structural members on ships, oil platforms, and buildings such as hospitals and radar facilities.

Advances in fiber reinforced composite technology has resulted in the development of Fiber Reinforced Plastic (FRP) elements that exceed the tensile strength of steel at only one fourth of the weight. The use of FRP as primary or secondary structural members are being increasingly considered in three main areas; primary or secondary structural members, secondary reinforcement for retrofitting and rehabilitation, and as reinforcement (pre-stressing, post stressing and rebar tendons or rods) in concrete. The motivation for use of FRP structural elements has been strongly driven by their non-corrosive property. Aside from this property, FRP's light weight and electrically non-conductive behavior has made it a desirable structural material for many other applications such as; radar facilities, hospitals with X-ray and MRI (Magnetic Resonance Imaging) equipment and communication facilities. However, the use of FRP introduces new concerns about the fire resistance and endurance of such structural members. Several situations are described herein to demonstrate the likelihood of bridges, parking garages and similar structures exposed to fires, which may affect the structural integrity of members incorporating or made of FRP.

1. A fuel tanker accident on a bridge or under an overpass. In either of these cases, a large flame from the burning fuel could engulf portions of the bridge/overpass resulting in critical thermal stress conditions. Several such incidents have happened on major interstate highways, beltways, bridges and overpasses in the US (examples include, Washington, D.C., 1992 and , Philadelphia, 1995, I-95 Connecticut, 2004). In such scenarios, the excess heat may lead to a softening of the FRP, thus reducing the stiffness of FRP members used in girders and beams and possibly result in the collapse of highway structures (i.e. bridges or overpasses).
2. Car fire in a parking garage. Although many parking garages are protected with a sprinkler system and “fire proofing”, an automotive fire (particularly if accompanied with an explosion) could expose structural members incorporating FRP leading to significant weakening and possible failures.
3. Post-Flashover condition in a structurally critical area of a building. It is conceivable that facilities used by shipyards, navy and similar organizations as well as radar facilities, hospitals (Magnetic Resonance Imaging facilities) and telecommunication centers may use FRP which could be vulnerable to typical, compartment post-flashover fire scenarios leading to structural failures.

2. BACKGROUND

Description of FRP

The non-corrosive, light-weight, high strength FRP is a composite material made using impregnated high performance continuous or chopped fibers such as carbon, glass and aramid fibers with resin. The most commonly used fibers; glass, carbon and aramid fibers all have different characteristics and properties which in turn will affect the behavior of FRP composites depending on resin matrix, fiber type and volume loading. Tensile strength and durability properties of FRP are comparable and better than typical pre-stressed steel.

Matrix materials for FRP composites are commonly thermo-setting polyester, vinylester and epoxy resins. Although thermoplastic polymers may also becoming popular, polyester is more widely used especially for glass FRP. Polyester resins exhibit adequate resistance to water and aggressive chemicals, and environmental aging. Polyester resins are more economical than epoxy resins, which may have better performance. In addition, the thermo-setting FRP's are charring when exposed to fire, which is a critical factor in fire resistance considerations.

The two distinct advantages of the FRP when compared to steel are:

1. FRP do not rust and are immune to electrolytic corrosion and to a wide range of acids, salts and other chemicals that attack steel.
2. Fiber Reinforced Plastics are non-magnetic and electrically non-conducting.

Another advantage of FRP is its high strength-to-weight ratio compared to steel. FRP has twice the tensile strength of steel at one-fourth the weight. Although this property is less important for reinforcing concrete than for some other applications (e.g. fiberglass grating), FRP rebars are frequently used in architectural concrete casting because it is light and easy to handle and will not rust. The primary mechanical disadvantage of the FRP is its compressive strength compared to steel. Manufacturer reports that the high temperature becomes a factor if FRP is exposed to temperatures above 110°C (230°F) for extended periods.

2.1 Relevant Research on FRP Use in Structural Members

Since the introduction of FRP for use in structures, there have been two central issues in investigation of reinforced concrete structures; first is the performance evaluation of such structures under various loading conditions and mechanical behavior of FRP elements including bonding to concrete, second, is the thermal behavior and fire resistance and endurance of such members. In the second area, effect of temperature including thermal gradient effect has been studied which is described herein. However, only one research comes close to in-situ evaluation of structural member exposed to fire while under load and none discussed use of scaled experiment for this purpose.

Performance of steel reinforced concrete exposed to fires has been studied extensively (Fleischmann, 1989). These investigations have pointed out the need to increase concrete cover thickness or add fire proofing and insulation in order to increase their fire endurance. More importantly, several approaches have been developed to predict temperature distributions within concrete columns both analytically (Lie & Allen, 1972 and 1974) and numerically (Anderberg, 1990, Ng, et al., 1989 & 1990). These efforts have reached a certain level of success and have provided good predictions of the temperature time history inside a column. The degree of sophistication in these predictions may be demonstrated by examining Figure 1 (Ng, et al., 1989) which shows a temperature distribution in a concrete column exposed to fire. Most of the numerical predictions have been compared with test results generated from standard test method,

ASTM E119-05a (2005). Aside from the fact that this standard is criticized for not being the appropriate test for all types of structural members, it is also not clear if it provides the most severe or even a realistic test of fire endurance or resistance of a concrete structural member. For example, it may be a more severe condition for a column to be exposed to a fire on one side, or to a hot upper layer in a compartment. The higher severity of such test condition can be attributed to higher thermal gradients.

The mechanical performance of FRP reinforced concrete members (slabs, beams, etc.) has been studied in the past (for example Bank & Ozel, 1999; Benmokrane, et al., 1998; Abdelrahman & Rizkalla, 1997; Naaman and Park, 1999; Fukuyama, 1999, Brown & Bartholomew, 1990; Barbero, 1991a&b; Faza & GangaRao, 1991a-d; Goodspeed, 1991; Greene,

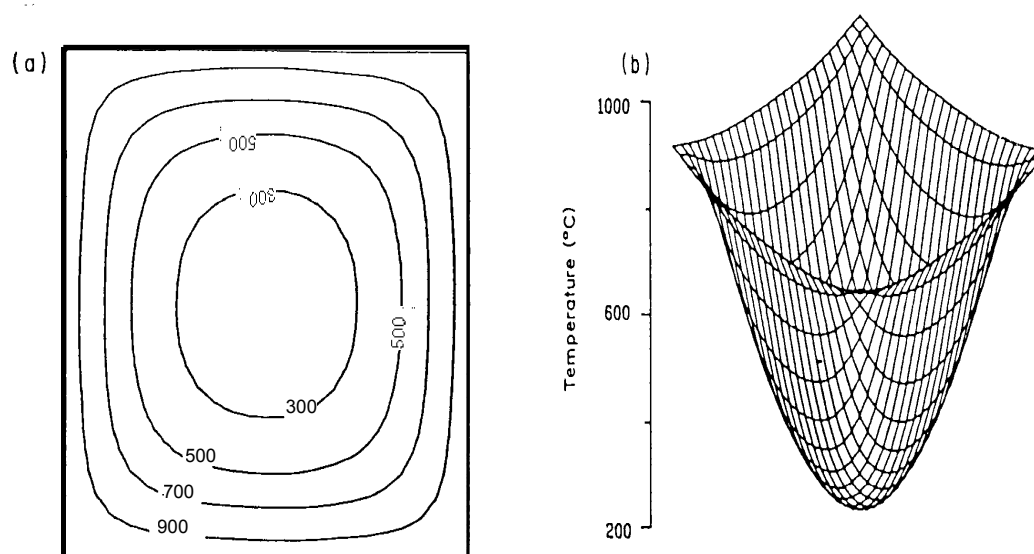


Figure 1 – Numerical prediction of temperature distribution in a column. a) Cross-sectional distribution, b) 3-D contours. (Ng, et al., 1989)

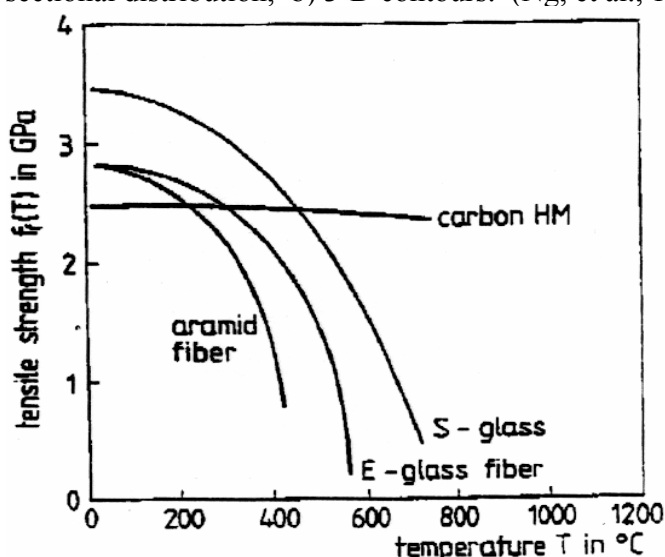


Figure 2 – Dependence of tensile strength of FRP elements on temperature rise (Katz, et al. 1999)

1987; Roll, 1991; Saadatmanesh & Ehsani, 1989). Studies of temperature dependence of FRP have taken place more recently. These studies typically include examination of performance evaluation of FRP member post exposure to thermal loading.

The temperature dependence on tensile strength for some fibers is shown in Figure 2 (Katz et al. (1999). It can be concluded that aramid and glass fibers will loose all strength at fire temperatures and carbon will incinerate at extremely high temperatures. The influence of elevated temperatures on matrix resins is more pronounced. Elevated temperatures decrease the modulus of elasticity,

strength and produce a time dependent strain. Temperature dependence on FRP elements is highly dependent on matrix type and volume. Katz et al. (1999) also evaluated the bond properties of (FRP) bars at temperatures ranging from (20°C) to high temperatures of up to 250°C. The bond properties in this temperature range were studied for a number of commercially produced rebars, where different bond "treatments" were applied to FRP rebars. Test results showed a reduction of between 80 and 90 percent in the bond strength as the temperature increased from 20 to 250°C. In comparison, ordinary deformed steel rebars showed a reduction of only 38 percent in the same temperature range. In addition, a reduction in the bond stiffness, which was determined from the slope of the ascending branch of the pullout load versus slip curve, was seen as the temperature increased. At elevated temperatures the post peak bond decrease was gradual as compared with the instantaneous drop at room temperature. Greater sensitivity to high temperatures was seen in FRP rebars, in which the bond relies mainly on the polymer treatment at the surface of the rod. Given that the post-flashover fire environment can expose structural members to temperatures as high as 1000°C the thermal effects can be extremely important. Furthermore, the dynamic thermal loading and the interaction between the fire gases and concrete are significant which are addressed in the discussion section. As part of a research project on "Fire resistance of concrete elements strengthened with externally bonded FRP reinforcement", Blontrock, et al. (1999) produced a synthesis report on the influence of elevated temperatures on the thermal and mechanical properties of FRP materials and resins. They also addressed the influence of elevated temperatures on the behavior of the interface between concrete and FRP. This work provides a good deal of background work for this research, but again does not address the particular fire environment.

There has been more recent research addressing the thermal behavior and thermal testing of FRP structures. Bausano, et al. (2003) show that fiber reinforced composite materials exposed to fire conditions exhibit reversible and irreversible loss in strength and stiffness due to the dependence of material properties on temperature and time. Wang, et al. (2005) conducted detailed experimental studies were conducted to determine the strength and stiffness properties of carbon fiber reinforced polyester and glass fiber reinforced polyester bars at elevated temperatures. Kodur et al. (2005) performed similar research for FRP reinforced concrete slabs. Abdolkarim and Paul (2005) proposed a model to predict the time to failure of FRP reinforced beams. A very relevant research performed by Elbadry and Elzaroug (2004) examined the effects of thermal incompatibility of carbon fiber reinforced polymers (CFRP) and concrete on the behavior of reinforced concrete members. Concrete beams reinforced with CFRP rebars were tested under the effects of temperature gradients while the rotations at the beam-ends are prevented.

The fire performance of FRP reinforced concrete is of even greater interest than in steel reinforced concrete structures due to the following concerns:

1. The FRP element could lose a significant portion of their load bearing capacity at slightly increased temperatures.
2. Due to differences in coefficients of thermal expansion and elastic moduli between fiber, resin matrix and concrete, a complex state of thermal stresses will develop and will require testing to verify analytical solutions. This condition may also result in debonding between the fiber and resin, especially at high temperatures.
3. It is a distinct possibility that a FRP element could be exposed to direct heat due to spalling (especially in high strength concrete) or cracking in the concrete. In such cases, while the steel reinforcements would not lose their structural integrity immediately, the FRP could potentially incinerate and result in catastrophic failure.

3. APPROACH

A scaled experiment was developed to demonstrate the potential for investigating a FRP reinforced high-strength column exposed directly to a flame or hot upper layer while under axial compression. The scaled model represents a room with a structural column in one of the corners. This is very similar to a corner office in a multi-story building with the load carrying column going through it. The scaled room accurately simulates flashover, thus creating a thermal step due to the upper layer. The fire next to the column exposes it to large vertical gradients.

4. THEORY

The work by Lie and co-workers in Canada (Lie, 1989, Ng, et al., 1989 & 1990), provides a good basis for development of scaled experiments to simulate fire testing of FRP reinforced structural members (beams, slabs, floor spans and other flexural members). They have identified the key scaling parameters for thermal modeling of structures using dimensional analysis. The variables include stress, σ , strain, ϵ , modulus of elasticity, E , Poisson's ratio, ν , coefficient of linear expansion, β , coefficient of thermal diffusivity, α , thermal conductivity, k , linear dimension, l , displacement, δ , temperature, θ , time, t , fire endurance, t_r , and loading force, F . Using force, length, time and temperature (F , l , t , θ , respectively) as the fundamental dimensions, nine dimensionless products can be derived using the Buckingham's Pi theorem. These non-dimensional products would represent stress, deformation or deflection, strain, Poisson's ratio, coefficient of linear expansion, time force, thermal conductivity and fire endurance. The scale factor for any physical quantity is defined as the ratio of its value for the prototype to its value for the model, e.g. the length scale factor, S_l , is defined as:

$$S_l = \frac{l_p}{l_m} \quad (1)$$

where the subscripts p and m refer to the prototype and the model, respectively.

The scaling consideration for simulating fire exposure intensity and true thermal modeling requires that a temperature scale factor of one be imposed, i.e.:

$$S_\theta = \frac{S_E S_l^2}{S_t S_k} = 1 \quad (2)$$

where S_E , S_t and S_k are the scale factors for the modulus of elasticity, time and thermal conductivity, respectively. By setting $S_\theta=1$, with appropriately scaled temperature-time characteristic, the model thermal stresses and strains will be identical to those in the prototype at the homologous points. Furthermore, the prototype response can be predicted from the model response using the similitude relations.

4.1 Scaling the Fire Exposure Intensity

The rate of fire exposure intensity for the model structure, which is a function of the variation of temperature of fire with time, is governed by the time-scale factor, $S_t = t_p/t_m = S_l^2/S_\alpha$, given by:

$$S_t = \frac{t_p}{t_m} = \frac{S_l^2}{S_\alpha} \quad \text{and} \quad t_m = \frac{S_\alpha}{S_l^2} t_p \quad (3)$$

where $S_\alpha = \alpha t/l^2$ is the Fourier's number for heat transfer which normally governs the time-scale in heat conduction and α is thermal diffusivity. Since the model time, t_m , is inversely proportional to the square of the length scale factor, S_l , it is possible to simulate long time thermal effects in a significantly reduced time. For example, using a 1/4 scale model the ASTM E119 test time can be reduced by a factor of 16, namely a 240 minutes long test can be reduced to only 15 minutes. Furthermore, Ng, et al., (1990) demonstrated the use of equivalent temperature-time history for a model which can be derived from the prototype temperature-time history. For example, if the model temperature is defined by the relation shown below:

$$\theta_m = c_1 + c_2 \left[1 - e^{c_3 \sqrt{t_m}} \right] + c_4 \sqrt{t_m} \quad (4)$$

Then, by substituting for t_m from above into eqn. (4), the temperature-time history for the prototype can be estimated according to eqn. (5):

$$\theta_p = c_1 + c_2 \left[1 - e^{c_3 \sqrt{\frac{S_\alpha}{S_l^2} t_p}} \right] + c_4 \sqrt{\frac{S_\alpha}{S_l^2} t_p} \quad (5)$$

Using this approach, Lie and co-workers (Ng, et al., 1990) have shown a good comparison between the internal temperature-time history of a prototype and 1/2.33 and 1/3.00 scale models.

The temperature of the steel reinforcement measured in that work also showed a very good comparison between the model and prototype. Similar close agreement has been demonstrated by these researchers for the simulation of axial deformation of the models and the prototype.

4.2 Fire Scaling Laws

Two set of scaling parameters are needed for the experimental simulations proposed here.

1. The scaling parameters described in the theory will be used to determine the load, geometry and characteristics of the structural members being tested.
2. Scaling laws for the simulation of the proper fire size representing an actual enclosure fire scenario will be used. These scaling parameters have been well established in fire research literature (Quintiere, 1989). The fire size in an enclosure may be scaled by:

$$\frac{\dot{Q}_p}{\dot{Q}_m} = \left(\frac{l_p}{l_m} \right)^{\frac{5}{2}} \quad (6)$$

where l is the appropriate length scale (normally the height of an enclosure).

5. DESCRIPTION OF THE EXPERIMENTS

The use of a small-scale experimental simulation of a fire scenario involving a steel reinforced concrete column was examined. Figure 3 shows the schematic of the scaled enclosure (0.6m cubic) which was made from gypsum board (15.875 mm thick). A premixed methane burner at the center of this enclosure provided a 15 kW fire source needed to produce flashover within the scaled enclosure. The heat release rate is arrived at by using well-known empirical relations. The upper layer temperature was monitored using a thermocouple. A concrete column (0.6 m high, 7.5 cm in diameter) reinforced with steel bars in this case was loaded to 80% of its design strength. The column was instrumented with thermocouples at 3 radial locations and at 4 different vertical stations. Strain gages

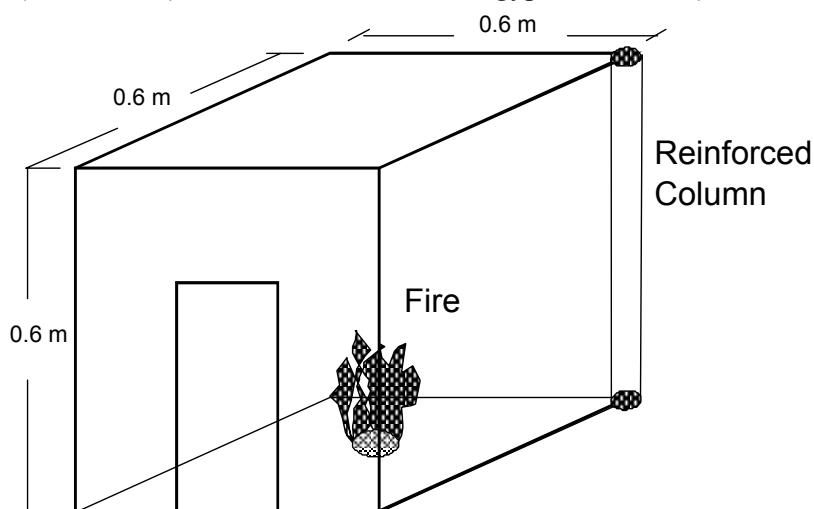


Figure 3 - Scaled enclosure used for fire simulation

were also used to monitor axial surface strain at 4 vertical locations (on the ambient side of the column). The experiment was also performed with fire source placed next to the column. These experiments show that a real enclosure fire scenario can be simulated and temperature distribution inside the column can be measured.

6. RESULTS AND DISCUSSION

The results presented here are limited to the experimental results of the scaled simulation of exposure of reinforced concrete columns to enclosure fire conditions. Test 1 refers to the fire being placed at the center of the enclosure, thus producing a hot upper layer which ultimately

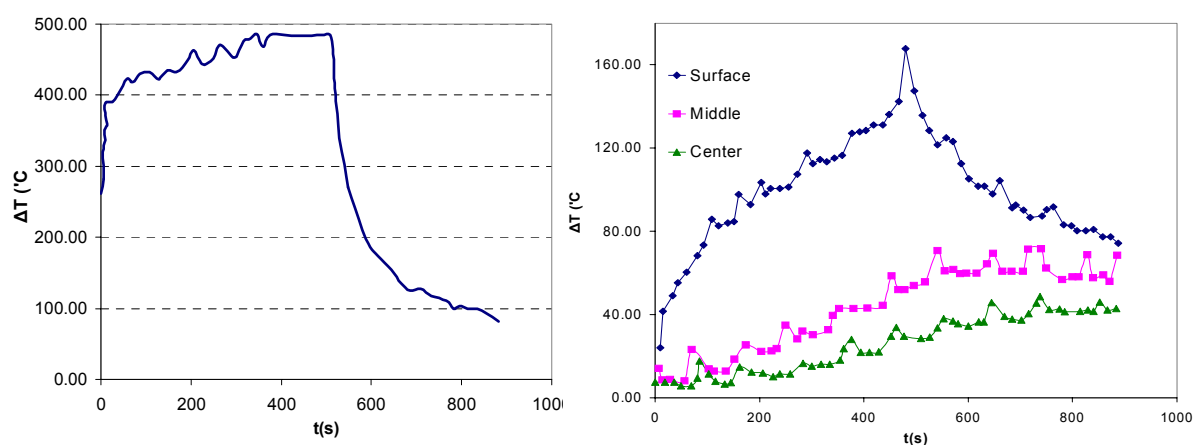


Figure 4 - Fire Test 1, Upper layer temperature measurement in the enclosure

results in a flashover conditions. Test 2 refers to the fire being placed next to the column with the flame extending to about half of the height of the column.

The results of the test 1 are shown in Figures 4-7. Figure 4 shows upper layer temperature change with time at the ceiling level of the enclosure. The temperature difference with the ambient (ΔT) reaches about 500°C and remains constant which is consistent with pre-flashover. The enclosure then transitioned to flashover and the burner was immediately turned off and temperature rapidly decays. The flashover was clearly observed. The flashover was achieved around 500 seconds which is consistent with the prediction of MQH model. The top of the column in this test experiences the highest temperatures and as expected, the thermocouple imbedded at the surface of the concrete column experiences the highest temperatures. Figure 5 shows the temperature rise at the three radial locations within the column. The temperature just below the surface rises rapidly and reaches a maximum temperature of 170 C corresponding to the time flashover was achieved. The temperature in the interior of the column rises more gradually due to lag in thermal propagation and levels off after the burner is turned off. Although the test is stopped at flashover, the time to flashover is only about 400 seconds (less than 7 minutes). Time to flashover is governed by a more complex relationship referred to as the MQH model. However, for the scaled model the flashover happens approximately 2/3 of the time of the large scale.

Figure 6 shows the strain measurements for fire test 1. The column in Test 1 is initially loaded to 5200 psi (35.86 MPa), which is approximately 80% of the column design strength. As the column temperature increases, additional stress increase due to thermal strain is recorded. Figure 7 shows the axial stress for both cases. The stress strain curves appear bimodal with a steeper slope up to the time flashover is achieved and then a smaller rate of increase thereafter. (The radial strains correlate well with the axial strain assuming poisson's ratio is less than 0.2). After 20 minutes the total stress in the column has reached 6900 psi (48 MPa). Since there is a large thermal gradient between the exterior and interior temperatures of the column a more complex stress profile exists and is beyond the scope of this study. The column for Test 2 is initially loaded to about 4000 psi (28 MPa). The stress remains steady and starts to increase substantially around 1800 seconds. A gradual stress increase was recorded until 2800 seconds where the stress reached 6800 psi (47 MPa).

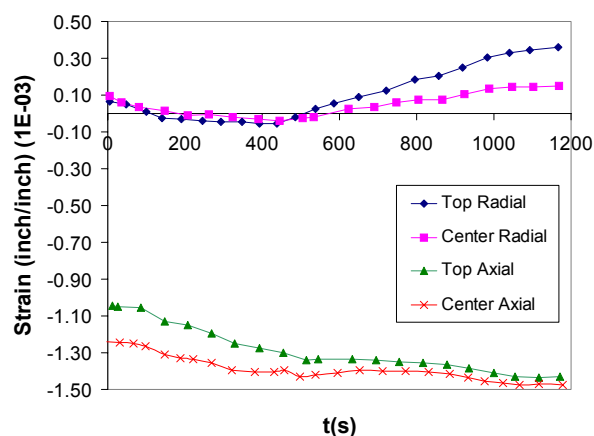


Figure 6- Fire Test 1 - Axial and Radial Strain

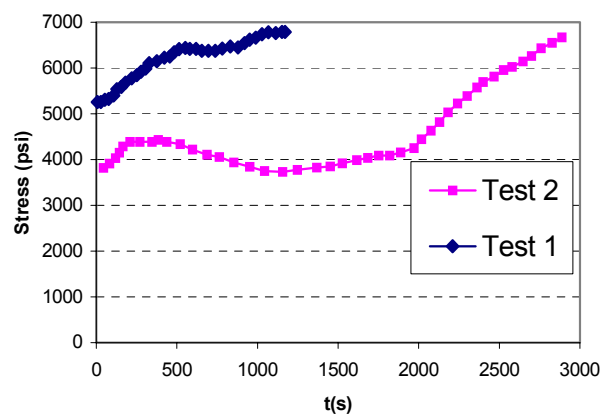


Figure 7 – Column Axial Stress, Fire Tests 1&2

Figure 8-11 show the results for the fire test 2 with the burner placed near the column. Figure 8 and 9 contain the temperature at the top and base of the column with thermocouples placed just below the surface of the column, at the center, and at half the radial depth. At the top of the column, it should be noted that the temperatures reach 100°C in the center and exceeded 450°C at the surface. At the bottom, the mid-way temperature has a slope the same as the surface and thus if the fire were continued, it could easily reach 100°C. In this test the temperature curves increase at a constant rate.

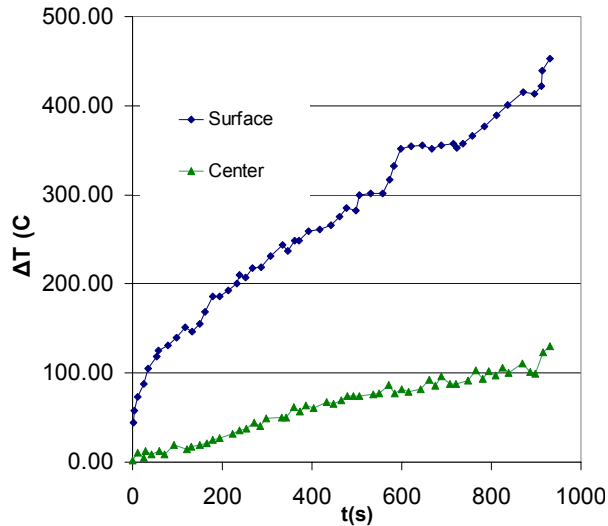


Figure 8 - Fire Test 2, Temperature measurements at top of the column

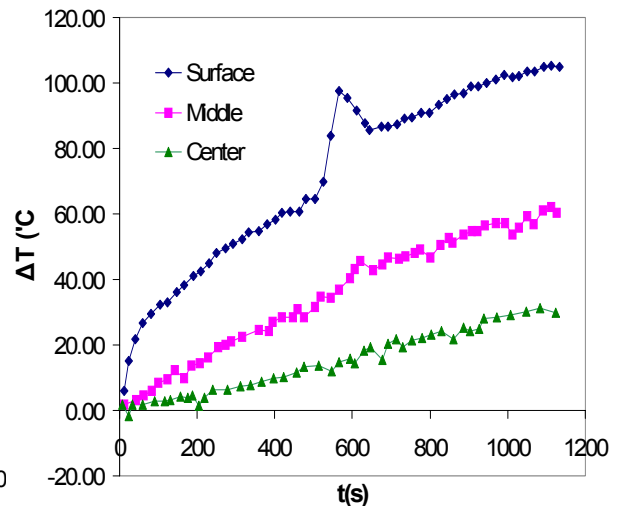


Figure 9 - Fire Test 2, Temperature measurements at bottom of the column

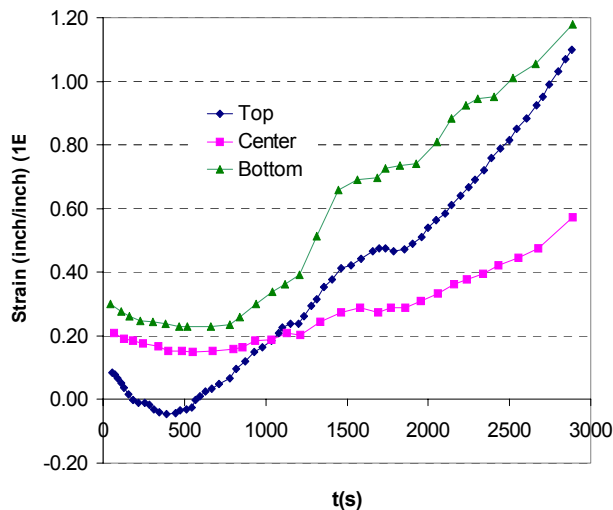


Figure 10 – Fire Test 2, Radial strain

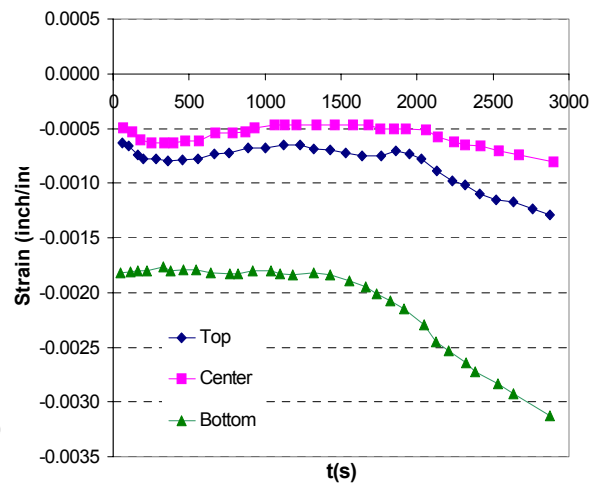


Figure 11 – Fire Test 2, Axial strain

In both cases, severe cracking at the top of the column due to the thermal stresses were observed. It is anticipated that such cracks formed in a FRP reinforced structural member may allow hot gases to reach the FRP rods reducing their performance significantly. The internal temperature distribution can be used to calculate the heat transfer within the column and to

estimate the temperature of the reinforcing elements. It is stipulated that the same enclosure can be used to test other compartment structural members such as load bearing walls; floor slabs, etc.

7. CONCLUSIONS

This research has demonstrated that enclosure fire scenarios involving structural members can be simulated using scaled experiments. The significant contribution of the work is that the reinforced structural columns being tested were under load thus creating realistic conditions for fire endurance. It is concluded that scaled experiments may be a more realistic option to test structural members under load and in a much less cost. Temperature distributions within concrete structural elements were measured and scaling factors can be used to predict temperatures in actual size structural elements reinforced with FRP. Measured stress-strain behavior during fire testing and column loading compares well with expected behavior even under complex thermal gradients within the concrete columns. The scaled experiment showed high potential of spalling of concrete and exposure of reinforcement bars. Furthermore, temperatures exceeding 100°C was reached easily within the column by the time of flashover indicating that for FRP reinforced structural members, concrete alone may not be adequate to insulate and protect against thermal degradation of FRP particularly for a 4 hour fire endurance requirement.

8. REFERENCES

- Abdelrahman, AA, Rizkalla, SH, "Serviceability Of Concrete Beams Prestressed By Carbon-Fiber-Reinforced-Plastic Bars", ACI Structural Journal, V 94 No. 4, 1997.
- Abdolkarim, A. and Paul J. H., "Prediction of the Failure Time of Glass Fiber Reinforced Plastic Reinforced Concrete Beams under Fire Conditions", Journals of Composites for Construction, Vol. 9, No. 5, October, 2005.
- Anderberg, Y., TCD 3.0 User's Manual, Fire Safety Design, Lund, Sweden, 1990.
- ASTM E119-05a, "Standard Test Methods for Fire Tests of Building Construction and Materials", American Society of Testing Material, West Conshohocken, Pennsylvania, 2005.
- Bank, LC, Ozel, M "Shear Failure Of Concrete Beams Reinforced With 3-D Fiber Reinforced Plastic Grids", Fourth International Symposium on Fiber Reinforced Polymer Reinforcement for Reinforced Concrete Structures, American Concrete Institute, 1999
- Barbero, E.J., Int. SAMPLE Symposium and Exhibition, 36: (1991a)
- Barbero, E.J., S-H. Fu, and I. Raftoyiannis, Jour. of Mat. in Civil Eng., (11), 1991b.
- Bausano, J.A., Case, S.W., Lesko, J.S: "Structural integrity of FRP composite structures during/following fire", Int. SAMPLE Symposium and Exhibition, Vol. 48 I, p. 908-921, 2003.
- Benmokrane, B, Masmoudi, R, Theriault, M "Flexural Behavior Of Concrete Beams Reinforced With Deformed Fiber Reinforced Plastic Reinforcing Rods", ACI Structural Journal V 95 No 6, 1998
- Blontrock, H. Matthys, S. Taerwe, L , "Properties Of Fiber Reinforced Plastics At Elevated Temperatures With Regard To Fire Resistance Of Reinforced Concrete Members", Fourth International Symposium on Fiber Reinforced Polymer Reinforcement for Reinforced Concrete Structures ,American Concrete Institute SP-188-5, 1999.
- Brown, V.L. and Bartholomew, C.L., "FRP Rebar in Reinforced Concrete Member", 8th ASCE Structures Congress, Baltimore, MD, April 1990.

- Elbadry, M., Elzaroug, O., "Control of cracking due to temperature in structural concrete reinforced with CFRP bars", *Composite Structures*, Vol. 64, No. 1, April, P.37-45, 2004.
- Faza, S. and GangaRao, H., "Behavior of Concrete Beams Post Tension with Fiber Reinforced Rods", 8th Annual Int'l Bridge Conf., Engineers' Society of Western Pennsylvania, June, 1991.
- Faza, S. and GangaRao, H., "Bending Response of Concrete Beams Reinforced with FRP Rebars for Varying Surface Conditions", *Trans. Res. Bd (TRB)*, Washington, DC, Jan., 1991.
- Faza, S. & GangaRao, H., "Bending Response of Beams Reinforced with FRP Rebars for Varying Concrete Strengths", *Adv. Comp. Mat. in Civil Eng. Str. ed. S. L. Hyer, Asce*, 1991.
- Faza, S. and GangaRao, H., "Bending and Bond Behavior of Concrete Beams Reinforced with Plastics Rebars", 3rd Bridge Conf., TRB, Denver, March 1991.
- "Fire Resistance of Concrete Slabs Reinforced by NEFMAC", Tech. Report. 3, NEFCOM Corp.
- Fleischmann, C., "Analytical Methods for Determining Fire Resistance of Concrete Members", *SFPE Handbook of Fire Protection Engineering*, Sec. 3, Ch. 7, p. 113-129, 1988.
- Fukuyama, H., "Frp Composites In Japan", *Concrete International*, V 21 No. 10 1999.
- Greene, A., "Glass Fiber Reinforced Composites in Building Construction", *Transportation Research Board (TRB) Record #1118*, Washington, DC, 1987.
- Goodspeed, C. et al., "Cyclical Testing of Concrete Beams Reinforced with Fiber Reinforced Plastic (FRP) Grids", *Adv. Comp. Mat. in CEng. Struct.*, ed. S.L. Hyer, ASCE, NY, 1991.
- Lie, T.T. and Allen, D.E., Tech. Paper No. 378, National Research Council of Canada, 1972.
- Lie, T.T. and Allen, D.E., Tech. Paper No. 416, National Research Council of Canada, 1974.
- Lie, T.T., "Fire Resistance of Concrete Columns: A Parametric Study", *J. of Fire Protection Engineering*, Vol. 1, No. 4, pp. 121-130, 1989.
- Katz N, Berman LC, Bank A, "Effect Of High Temperature On Bond Strength Of FRP Rebars", *Journal of Composites for Construction*, Vol. 3, No.2, ASCE, 1999.
- Kodur, V.K., Bisby, L.A., Foo, S.H., "Thermal behavior of fire-exposed concrete slabs reinforced with fiber-reinforced polymer bars", *ACI Structural Journal*, Vol. 102, No. 6, November/December, p. 799-807, 2005.
- McCaffrey, B.J., Quintiere, J.G. and Harkleroad, M.F., "Estimating Room Temperatures and the Likelihood of Flashover Using Fire Test Data Correlations", *F. Tech.*, 17, p. 98-119, 1981.
- Naaman, AE, Park, S "Shear Behavior Of Concrete Beams Prestressed With Frp Tendons", *PCI Journal*, Vol 44 No 1, 1999.
- Ng, A.B., Mirza, M.S. and Lie, T.T., "Fire Endurance Analysis of Reinforced Concrete Columns", *Can. J. Civ. Eng.* 16, p. 290-299, 1989.
- Ng, A.B., Mirza, M.S. and Lie, T.T., "Response of Direct Models of Reinforced Concrete Columns Subjected to Fire", *ACI Structural Journal*, May-June, 1990.
- Quintiere, J.G., "Scaling Applications in Fire Research", *Fire Safety J.*, Vol. 15, 1, 1989.
- Roll, R.D., Use of GFRP Rebar in concrete Structures", *Advanced Composite Materials in Civil Engineering Structures*, edited by S.L. Hyer, ASCE, NY, 1991.
- Saadatmanesh, H. and Ehsani, M., "Fiber Composite Bars for Reinforced Concrete Construction, Univ. of Arizona.
- Wang, Y.C., Kodur, V.S., "Variation of strength and stiffness of fiber reinforced polymer reinforcing bars with temperature", *Cement and Concrete Composites*, Vol. 27, No. 9-10, October/November, p. 864-874, 2005.

AUTHOR INDEX

ABU, Anthony K.	659
AIK KHOO, Heng	63
ALA-OUTINEN, Tiin	139
ALI, Faris	613, 813
ALLAM, Ahmed	813
ALONSO, C.	599
BADDERS, B. L.	931
BAHR, Oliver	837
BAIERLE, Tomáš	1035
BAILEY, Colin G	709
BAMONTE, Patrick	545
BATISTA, Eduardo de Miranda	427
BÉNICHOU, Noureddine	909
BENNETTS, Ian	161
BERGMEISTER, K.	983
BISBY, Luke A	791
BLAŽEVIČIUS, Žygimantas	63
BLOCK, Florian	345
BONG, Ming Wei	451
BORG, Audun	779
BOSTRÖM, Lars	757
BRADFORD, Mark A.	805
BRECCOLOTTI, Marco	587
BUCHANAN, Andrew H	451, 623,
BURGESS, Ian W	315, 345, 393, 561, 635, 659, 825
CAJOT, Louis-Guy	299
CAMERON, Neil	873
CANGIANO, Stefano	545
CARRÉ, H.	697
CEDERING, Magdalena	975
CHANG, Jeremy	623
CHANG, Peter C.	439
CHICA, Jose Antonio	213
CHOWDHURY, Ershad U.	791
COCCIA, Simona	767
COLOMBO, Matteo	721
COOKE, Gordon	101, 405
CRAFT, Steven	939
DAVISON, Buick	315, 345
DELICHATSIOS, Michael	1065
DESANGHERE, Sylvain	213
DHAKAL, Rajesh	451, 623
DHIERSAT, M.	683
DHIMA, Dhionis	405, 899, 1005
DOTREPPE, Jean-Claude	885
EL-DIB, Mohamed E.	13
ELGHAZOULI, A.Y.	379
EL-HUSSEINY, Ossama M.	13
EL-KORCHI, Tahar	1077
FAKURY, Ricardo Hallal	1023
FELICETTI, Roberto	721

FLETCHER, Ian	779
FLINT, Graeme	415, 527
FONTANA, Mario	113, 963
FORNATHER, J.	983
FOSTER, S. J.	635
FRANGI, Andrea	963
FRANSSEN, Jean-Marc	127, 151, 885, 1065
FROMY, Philippe	1005
FUJIMOTO, Kentaro	511
FUJITA, Masaru	511
GAMBAROVA, Pietro G	545
GANN, Richard G.	1047
GARDNER, Leroy	247
GARLOCK, Maria E.M.	175, 187
GAVILÁN, Ana Ramos	849
GILLIE, M.	861
GREEN, Mark F.	791
GRIJALVO, J.	1017
GUO, Shi Xiong	41
HADJISOPHOCLEOUS, George	63, 939
HAGER, I.	697
HALLER, Mike	299
HAMINS, Anthony	499
HASEMI, Yuji	225
HAWES, Mike	813
HEISE, Alexander	357, 487
HIRASHIMA, Takeo	511
HITCHEN, Neil	779
HUANG, Zhaohui	393, 561, 825
ISGOR, Burkan	939
IWANKIW, Nestor	993
IZZUDDIN, B.A.	379
JANSSON, Robert	747, 757
JOHNSTON, Louise	527
JOWSEY, Allan	259, 527
JOYEUX, Daniel	213
KAITILA, Olli	89, 139, 213
KÄLLSNER, Bo	951
KAMIKAWA, Daisuke	225
KANG, Yu	63
KAY, Alexandra	299
KETTNER, Florian	139
KNOBLOCH, Markus	113
KODUR, Venkatesh	573, 791, 837
KÖNIG, Jürgen	951, 983
KORHONEN, Timo	89
KORZEN, Manfred	273
KVEDARAS, Audronis Kazimieras	63
KWON, Kihyon	235
LA QUINTANA, J. de	1017
LABORDERIE, C.	697
LAMONT, Susan	259, 415, 487, 861
LANDESMANN, Alexandre	427
LANE, Barbara	259, 415, 487

LANGE, David	873
LAPLANCHE, Karine	899
LEE, Byoung-Jun	235
LI, Guo-Qiang	41, 327
LI, Yu Guang,	473, 511
LIANG, Hong,	287
LOPES, Nuno	127, 151, 463
LOU, Guo-Biao	327
MAHENDRAN, Mahen	29, 53
MALJAARS, Johan	75
MANZELLO, Samuel L.	1047
MATAR, Ehab B.	13
MATERAZZI, Annibale Luigi	587
MEDA, Alberto	647
MEHAFFEY, Jim	931, 939
MESQUITA, Luís	463, 849
MINDEGUIA, J.C.	683, 697
MIRAMBELL, Enrique	127
MOSS, Peter	451, 623
MOTEVALLI, Vahid	1077
NADJAI, Ali	613, 813, 1065
NAKAMURA, Masatoshi	225
NEVES, I. Cabrita	273
NIEDEREGGER, Philipp	113
OZAKI, Fuminobu	113
PANNONI, Fabio Domingos	1023
PAŠEK, Jan	1059
PERSSON, Bertil	735
PESSIKI, Stephen	235
PHAN, L.	573
PILOTO, Paulo	463, 849
PIMIENTA, P.	683, 697
PINTEA, Dan	885
PLANK, Roger	315, 345, 393, 561, 635, 671, 825
POZZI, Claudio	487
PRASAD, Kuldeep	499
PROE, David	161
QUIEL, Spencer E.	175, 187
QUINTIERE, James G.	439
RACHER, Patrick	899
RAFI, Muhammad Masood	613
RANAWAKA, Thanuja	29, 53
RENAUD, C.	199
RESZKA, Pedro	921
REY, F.	1017
RICHARDSON, L. R.	931
RINALDI, Zila	767
RINI, Darlene	259
RIVA, Paolo	647
ROBEN, Charlotte	527
RODRIGUES, Francisco Carlos	1023
RODRIGUES, João Paulo C.	273
SALEM, Osama F.	13
SARRAJ, M.	315

SCHAUMANN, Peter	139, 357, 837
SCHMIDT, J.	983
SEGAWA, Hirofumi	511
SILVA, Valdir Pignatta e	1023
SIMÕES DA SILVA, Luís	127, 151, 463
SIMON, A.	683
SOETENS, Frans	75
STREJČEK, Michal	371
SULONG, N.H. Ramli	379
TAILLEFER, Nicolas	1005
TALAMONA, Didier	613, 813
TAN, Kang-Hai	3
THOMAS, Ian	161
TICHÁ, Alena	371
TOFILO, Piotr	1065
TOH, Wee Siang,	709
TORERO, Jose	259, 415, 873, 921
TWILT, Leen	75
UESUGI, Hideki	473, 511
UHLÍŘ, Antonín	1035, 1059
UNANUA, J.	1017
USMANI, Asif	415 527, 861, 873
VALENTE, Joaquim C.	273
VASSART, Olivier	813
VENANZI, Ilaria	587
VILA REAL, Paulo	127, 151, 463
VIRDI, Kuldeep S.	101
WAKAMATSU, Takao	473
WALD, František	371, 1035, 1059
WANG, Ming	439
WANG, Zhi-Hua	3
WELCH, Stephen	287, 779
WINKLER, Wolfgang	873
YAMADA, Kaori	225
YU, Chaoming	393
YU, Ximmeng	825
ZEHFUSS, Jochen	519
ZHAO, B.	199